

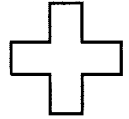
editors_
kurt aulenbacher
franco bradamante
andrea bressan
anna martin

20
04
spin 
16th international spin physics symposium

20
04
spin 
16th international spin physics symposium

This page intentionally left blank

spin²⁰¹⁶
16th international spin physics symposium



workshop on
polarized electron
sources and polarimeters

editors_

kurt aulenbacher

[mainz university]

franco bradamante

[trieste university and infn]

andrea bressan

[trieste university and infn]

anna martin

[trieste university and infn]

 World Scientific

NEW JERSEY • LONDON • SINGAPORE • BEIJING • SHANGHAI • HONG KONG • TAIPEI • CHENNAI

Published by

World Scientific Publishing Co. Pte. Ltd.

5 Toh Tuck Link, Singapore 596224

USA office: 27 Warren Street, Suite 401-402, Hackensack, NJ 07601

UK office: 57 Shelton Street, Covent Garden, London WC2H 9HE

Library of Congress Cataloging-in-Publication Data

SPIN 2004 (2004 : Trieste, Italy)

SPIN 2004 : proceedings of the 16th International Spin Physics Symposium and Workshop on Polarized Electron Sources and Polarimeters, Trieste, Italy, 10-16 October 2004 / editors, Franco Bradamante ... [et al.].

p. cm.

ISBN 981-256-315-6 (alk. paper)

1. Nuclear spin--Congresses. 2. Polarization (Nuclear physics)--Congresses. 3. Polarized beams (Nuclear physics)--Congresses. I. Bradamante, F. II. Workshop on Polarized Electron Sources and Polarimeters (2004 : Trieste, Italy). III. Title.

QC793.3.S6 S65 2004

539.7'25--dc22

2005047976

British Library Cataloguing-in-Publication Data

A catalogue record for this book is available from the British Library.

Copyright © 2005 by World Scientific Publishing Co. Pte. Ltd.

All rights reserved. This book, or parts thereof, may not be reproduced in any form or by any means, electronic or mechanical, including photocopying, recording or any information storage and retrieval system now known or to be invented, without written permission from the Publisher.

For photocopying of material in this volume, please pay a copying fee through the Copyright Clearance Center, Inc., 222 Rosewood Drive, Danvers, MA 01923, USA. In this case permission to photocopy is not required from the publisher.

Printed in Singapore by B & JO Enterprise

CONTENTS

SPIN2004	xix
Preface	xxv
Scientific Programme	xxxix

PLENARY TALKS

Present Understanding of the Nucleon Spin Structure	3
<i>A. Metz</i>	
Understanding Transversity: Present and Future	12
<i>V. Barone</i>	
Results and Future Prospects for Muon ($g - 2$)	22
<i>B. L. Roberts</i>	
The Jefferson Lab Contribution to the QCD Spin Structure of the Nucleon	30
<i>M. Garçon</i>	
Physics at HERMES	38
<i>D. Hasch</i>	
Physics Results from COMPASS	48
<i>A. Bressan</i>	
First Results from RHIC Spin Program and Future Prospects	58
<i>N. Saito</i>	
Soft Spin Physics at Jefferson Laboratory	70
<i>R. De Vita</i>	
Spin Physics in Nuclear Interactions	78
<i>K. Hatanaka</i>	
Spin Physics in NN Interactions at Intermediate Energies	86
<i>B. von Przewoski</i>	
Speculations in Hadron Spectroscopy	95
<i>J. M. Richard</i>	
V. W. Hughes: "To Learn Fundamental Things" 1921–2003	103
<i>G. Bunce</i>	

Searches for Permanent Electric Dipole Moments - Some Recent Developments <i>K. P. Jungmann</i>	108
Nucleon Form Factors <i>K. de Jager</i>	117
Low Energy Tests of the Standard Model <i>E. W. Hughes</i>	126
Memorial L.D. Soloviev <i>A. D. Krisch</i>	134
Experimental Status of the GDH Sum Rule <i>H. Arends</i>	136
Spin Physics at GSI <i>F. Rathmann</i>	145
Polarized Structure Functions with Neutrino Beams <i>S. Forte</i>	154
Status of Proton Polarization in RHIC and AGS <i>W. W. Mackay</i>	163
Summary of Parallel Sessions 1, Spin and Fundamental Symmetries, and 3, Spin Beyond Standard Model <i>O. V. Teryaev</i>	171
Summary of Parallel Session 2, The QCD Spin Structure of Nucleons <i>G. K. Mallot</i>	176
Summary of Parallel Session 8, Polarized Sources, Targets and Polarimetry <i>T. Wise</i>	184
Summary of Parallel Session 7, Acceleration, Storage, and Polarimetry of Polarized Protons <i>A. Lehrach</i>	186
Future Colliders <i>A. Deshpande</i>	192
Concluding Remarks <i>T. Roser</i>	201

WORKSHOP SUMMARIES

Summary of the X Workshop on High Energy Spin Physics (NATO ARW DUBNA-SPIN-03) <i>A. V. Efremov</i>	205
Summary of the 10 th Workshop on Polarized Sources and Targets (PST2003) <i>D. K. Toporkov</i>	209

Summary of the Advanced Studies Institute on Symmetries and Spin (Paha-Spin-2003 and Praha-Spin-2004)	210
<i>M. Finger</i>	
Summary of the Workshop on Spin Polarized Electron Sources and Polarimeters (PESP-2004)	215
<i>K. Aulenbacher</i>	
Summary of the 9 th International Workshop on Polarized Solid State Targets and Techniques	221
<i>H. Dutz</i>	
Pirelli International Award	227
<i>M. Armeni</i>	

SESSION 1

Spin and Fundamental Symmetries

Compton Polarizabilities of π -mesons in Relativistic Hamiltonian Dynamics	231
<i>V. V. Andreev</i>	
Vector and Axial-Vector Current Correlators within the Instanton Model of QCD Vacuum	235
<i>A. E. Dorokhov</i>	
The Polarization Effects in Neutrino-Lepton Processes in a Magnetic Field	239
<i>V. A. Huseynov</i>	
Correlated Quark Structure of the Proton and Spin Effects	243
<i>G. Musulmanbekov</i>	
Low-frequency Nuclear Spin Maser and Search for Atomic EDM of ^{129}Xe	247
<i>A. Yoshimi</i>	
Polarization Effects in the Reactions $p + {}^3\text{He} \rightarrow \pi^+ + {}^4\text{He}$, $\pi^+ + {}^4\text{He} \rightarrow p + {}^3\text{He}$ and Verification of the Consequences of Quantum-mechanical Coherence for the Correlation Tensor	251
<i>V. V. Lyuboshitz</i>	
Spinning Particle, Rotating Black Hole and Twistor-String	255
<i>A. Burinskii</i>	
Classical Elementary Spinning Particles, Zitterbewegung and Dipole Structure	259
<i>M. Rivas</i>	

SESSION 2

QCD Spin Structure of Nucleons

Measurement of the Gluon Polarization $\Delta G/G$ at COMPASS	265
<i>C. Schill</i>	

Transverse Spin at PHENIX and Future Plans <i>Y. Makdisi</i>	269
Calculations of Single-inclusive Cross Sections and Spin Asymmetries in pp Scattering <i>W. Vogelsang</i>	273
Transversity and Drell–Yan K -Factors <i>P. G. Ratcliffe</i>	278
Parton Intrinsic Motion: Unpolarized Cross Sections and the Sivers Effect in Inclusive Particle Production <i>F. Murgia</i>	282
Hermes Precision Results on g_1^p , g_1^d and g_1^n and the First Measurement of the Tensor Structure Function b_1^d <i>C. Riedl</i>	286
Generalization of the DGLAP for the Structure Function g_1 to the Region of Small x <i>B. I. Ermolaev</i>	290
Inclusive Spin-dependent Asymmetry A_1^d <i>D. Peshekhonov</i>	294
Spin Asymmetries for Events with High p_T Hadrons and an Evaluation of the Gluon Polarization from SMC Data <i>E. Rondio</i>	298
Flavour Decomposition of the Quark Helicity Distributions in the Nucleon from Semi-Inclusive Deep-Inelastic Scattering <i>J. G. Rubin</i>	302
The Role of Higher Twist in Determining Polarized Parton Densities from DIS Data <i>D. B. Stamenov</i>	306
The Gluon Spin Asymmetry as a Link to ΔG and Orbital Angular Momentum <i>G. P. Ramsey</i>	310
NLO QCD Procedure with Respect to First Moments of Polarized Quark Densities <i>O. Y. Shevchenko</i>	313
A Model-Independent Approach to Semi-Inclusive Deep Inelastic Scattering <i>E. Christova</i>	317
Spin Physics Progress with the STAR Detector at RHIC <i>J. Sowinski</i>	321
Probing Gluon Polarization with π^0 's in Longitudinally Polarized Proton Collisions at the RHIC-PHENIX Experiment <i>Y. Fukao</i>	325
Measurement of Prompt Photons in $\sqrt{s} = 200$ GeV pp Collisions <i>K. Okada</i>	329

Study of Gluon Polarization in the Proton with a Silicon Vertex Upgrade at RHIC/PHENIX <i>M. Togawa</i>	333
Spin Effects in Large Rapidity Neutral Pion Production at STAR <i>A. Ogawa</i>	337
Can the Collins Mechanism Explain the Large Transverse Single Spin Asymmetries Observed in $p^\uparrow p \rightarrow \pi X$? <i>U. D'Alesio</i>	341
The Gluon Sivers Distribution in D Production at RHIC <i>M. Boglione</i>	345
Double Transverse Spin Asymmetries at Next-to-leading Order in QCD <i>A. Mukherjee</i>	349
Spin Transfer to Λ_c^+ Hyperons in Polarized Proton Collisions at RHIC <i>V. L. Rykov</i>	353
Higher Twists Resummation in Inclusive and Semi-inclusive Spin-dependent DIS <i>O. V. Teryaev</i>	357
Spin Dependent Fragmentation Functions at BELLE <i>R. Seidl</i>	361
Azimuthal Single-Spin Asymmetries on a Transversely Polarized Hydrogen Target at HERMES <i>G. Schnell</i>	365
Measurements of Collins and Sivers Asymmetries at COMPASS <i>P. Pagano</i>	369
Transversity and Dihadron Fragmentation Functions <i>A. Bacchetta</i>	373
Two-hadron Single Target-spin Asymmetries: First Measurements by HERMES <i>P. B. van der Nat</i>	377
Transversity Signals in Two-hadron Correlation at COMPASS <i>R. Joosten</i>	381
Transversity of Quarks and Nucleons in SIDIS and Drell-Yan <i>L. P. Gamberg</i>	385
Comments on Cahn and Sivers Effects in SIDIS <i>A. Prokudin</i>	389
Longitudinal Polarization of Λ and $\bar{\Lambda}$ Hyperons in Deep-inelastic Scattering at COMPASS <i>V. Y. Alexakhin</i>	393
Measurement of Transverse Λ Polarisation at COMPASS <i>J. M. Friedrich</i>	396

Hyperon Production at HERMES <i>S. L. Belostotski</i>	400
LEPTO and Polarized SIDIS <i>A. Kotzinian</i>	404
Asymmetries in Semi-inclusive Deep Inelastic Scattering <i>E. Di Salvo</i>	409
Transversity in Drell-Yan Process of Polarized Protons and Antiprotons in PAX Experiment <i>A. V. Efremov</i>	413
Proton Transversity and Intrinsic Motion of the Quarks <i>P. Závada</i>	417
Spin Density Matrix Elements in Vector Meson Lepto-production <i>S. V. Goloskokov</i>	421
Results on Exclusive ρ^0 Production from COMPASS <i>D. Neyret</i>	425
Hard Exclusive Electroproduction of $\pi^+\pi^-$ Pairs at HERMES <i>R. Fabbri</i>	429
Exclusive Electroproduction of Pions and Vector Mesons at HERMES <i>A. Rostomyan</i>	434
A New Angular Momentum Sum Rule <i>E. Leader</i>	438
Factorization and Universality in Azimuthal Asymmetries <i>F. Pijlman</i>	442
A Planned Jefferson Lab Experiment on Spin-Flavour Decomposition <i>X. Jiang</i>	446
The Q^2 -dependence of the Generalised Gerasimov–Drell–Hearn Integral for the Deuteron, Proton and Neutron and Evidence for Quark-Hadron Duality in the Proton Spin Asymmetry A_1 <i>A. Nagaytsev</i>	450
Measurement of Deeply Virtual Compton Scattering at HERMES <i>H. Marukyan</i>	454
The HERMES Recoil Detector <i>J. Stewart</i>	458
Chiral-Odd Twist-3 Distribution Function $e(x)$ <i>M. Wakamatsu</i>	462
Pre-constraining Evolution of Parton Distributions in the Matrix Solution of DGLAP <i>M. Goshtasbpour</i>	466

SESSION 3

Spin Beyond the Standard Model

Identification of Graviton Exchange Effects at High Energy Colliders <i>A. A. Pankov</i>	473
Contact Interaction Searches at e^+e^- and e^-e^- Colliders: Role of Polarization <i>A. V. Tsytrinov</i>	477
Polarized Parton Distributions in the Approach of Complete Renormalization Group Improvement <i>A. Mirjalili</i>	481
Quark-gluon Helicity and Q^2 Dependence of Partonic Angular Momentum <i>A. N. Khorramian</i>	485
The Approach Unifying Spins and Charges and its Predictions <i>N. M. Borštnik</i>	489
New QCD Relations Between Magnetic Moments of Σ^0 and Λ Hyperons <i>V. S. Zamiralov</i>	493
Q_{weak} : A Precision Measurement of the Proton's Weak Charge <i>R. D. Carlini</i>	497
Four-spinon Contribution to the Dynamic Structure Factor in the Antiferromagnetic Heisenberg Model <i>B. Si Lakhali</i>	501

SESSION 4

Spin in Soft Hadronic Reactions

Measurement of the Analyzing Power in pp Elastic Scattering in the Peak CNI Region at RHIC <i>H. Okada</i>	507
Measurement of A_N in Elastic pp-scattering with Small Momentum Transfers at $\sqrt{s} = 200$ GeV at RHIC <i>I. G. Alekseev</i>	511
Measurement of the Analyzing Power of Proton-carbon Elastic Scattering in the CNI Region at RHIC <i>O. Jinnouchi</i>	515
Energy Dependence of pp and p-carbon CNI Analyzing Power <i>T. L. Trueman</i>	519
Energy Dependence of Helicity-Flip Amplitudes in the Small-Angle Elastic pp-Scattering <i>S. M. Troshin</i>	523

Large-distance Effects on Spin Observables at RHIC <i>O. V. Selyugin</i>	527
Spin Physics of NN Interactions at COSY <i>A. Kacharava</i>	531
Measurement of the Vector Analyzing Power in $pd \rightarrow (pp)n$ with Emission of a Fast Forward Diproton at ANKE/COSY <i>S. Yaschenko</i>	537
Results for the Asymmetry Measurement in Elastic Pion-Proton Scattering at 1.78 and 2.07 GeV/c <i>D. N. Svirida</i>	540
Lower Excitation Spectrum of the Nucleon and Δ in a Relativistic Chiral Quark Model with One-meson Exchange Forces <i>E. M. Tursunov</i>	544
Single Spin Asymmetry Measurements for π^0 Inclusive Productions in $p + p_{\uparrow} \rightarrow \pi^0 + X$ and $\pi^- + p_{\uparrow} \rightarrow \pi^0 + X$ Reactions at 70 and 40 GeV Respectively <i>S. B. Nurushev</i>	548
A_N at Small Negative Values of x_F in the Reaction $p + p_{\uparrow} \rightarrow \pi^0 + X$ at 70 GeV and Universal Threshold in Inclusive Pion Production <i>V. V. Mochalov</i>	551
Λ^0 Polarization in $pp \rightarrow p\Lambda^0 K^+(\pi^+\pi^-)^5$ at 27.5 GeV <i>J. Félix</i>	555
Spin Polarization of Hyperons in Hadron-Hadron Inclusive Collisions <i>K. Kubo</i>	558
Hyperon Polarization in Unpolarized hh/hA Collisions and Some Related Problems <i>Z. Liang</i>	562
Spin Effects at Fragmentation of GeV Polarized Deuterons into Pions with Large Transverse Momentum <i>L. Zolin</i>	565
Evidence of $S = +1$ Narrow Resonances in the System $K_s^0 p$ <i>P. Z. Aslanyan</i>	569
P-parity of the Pentaquark Θ^+ and Spin Observables in the Reaction $NN \rightarrow Y\Theta^+$ <i>Y. N. Uzikov</i>	572

SESSION 5

Soft Spin Physics with Photons and Leptons

Measurement of the Neutron Electric Form Factor at Low Momentum Transfer <i>V. Ziskin</i>	577
--	-----

A Precision Measurement of G_E^p/G_M^p at BLAST <i>C. B. Crawford</i>	581
Asymmetries Analysis from the Forward Angle Part of the G0 Experiment <i>J. Roche</i>	585
The Second Generation HAPPEX Experiments <i>D. Lhuillier</i>	589
Tensor Analyzing Power in Exclusive π^- -Meson Photoproduction on Deuteron <i>V. N. Stibunov</i>	593
Measurement of Tensor Analyzing Powers in Deuteron Photodisintegration <i>D. K. Toporkov</i>	597
Preliminary Results of ${}^2H(e, e'p)n$ in BLAST <i>A. Maschinot</i>	601
Λ Polarization in Exclusive Electro- and Photoproduction <i>M. D. Mestayer</i>	605
Spin Asymmetries A_{et} and A_t in Exclusive η Electroproduction from the Proton <i>P. E. Bosted</i>	609
Measurement of the Q^2 -evolution of the Bjorken Integral at Low Q^2 <i>A. Deur</i>	613

SESSION 6

Spin Physics in Nuclear Interactions

${}^4\text{He}(p, 2p)$ Reactions for Studying In-Medium NN Interactions <i>S. Asaji</i>	619
Spin Correlation Parameter C_{yy} of $p + {}^3\text{He}$ Elastic Backward Scattering at Intermediate Energy <i>Y. Shimizu</i>	623
Experimental Investigation of the Quasielastic Scattering of Polarised Protons on Nuclei at the JINR VB LHE Synchrophasotron <i>A. A. Yershov</i>	627
Measurements of $n + d$ Elastic Scattering at 250 MeV and the Three-nucleon Forces <i>Y. Maeda</i>	631
A Three-Body Effect in the Double Polarised ${}^3\text{He}(d, p){}^4\text{He}$ Reaction near Threshold <i>S. Oryu</i>	634
The Role of Spin Observables in Quasi-free η Meson Photoproduction from Nuclei <i>B. I. S. van der Ventel</i>	637

Unified Understanding of Spin Isospin Response Functions of Nuclei <i>M. Ichimura</i>	641
Isovector and Isoscalar Spin-Flip M1 Strengths in ^{11}B <i>T. Kawabata</i>	645
Tensor Analyzing Power of the $^{16}\text{O}(d, ^2\text{He})$ Reaction at 0 Degrees and Structure of the Spin-dipole Resonances <i>K. Suda</i>	649
Spin Effects and Neutrino Opacity to Cold Neutron Matter <i>G. I. Lykasov</i>	653
Asymmetry Measurement of Charged Hadron Production in $p\uparrow A$ Collisions at 40 GeV <i>V. Kryshkin</i>	657
Tensor Analyzing Power A_{yy} in Deuteron Inclusive Breakup at Large P_t and Spin Structure of the Deuteron at Short Internucleonic Distances <i>V. P. Ladygin</i>	661
Study of Corresponding Homologous States in ^{41}K and ^{42}Ca via (p, α) Reactions <i>P. Guazzoni</i>	665
High-accuracy Measurement of the Spin-dependent Neutron Scattering Length of the Deuteron <i>P. Hautle</i>	669

SESSION 7

Acceleration, Storage and Polarimetry of Polarized Beams

RHIC Polarized Proton New Working Point Commissioning <i>M. Bai</i>	675
Snake Resonance Observed in RHIC <i>V. Ptitsyn</i>	679
Acceleration of Polarized Protons in the AGS with a Helical Partial Snake <i>H. Huang</i>	683
Acceleration of Polarized Beams Using Multiple Strong Partial Siberian Snakes <i>T. Roser</i>	687
Spin Manipulating 2 GeV/c Polarized Protons and Deuterons Stored in COSY <i>A. D. Krisch</i>	691
Polarised Deuterons at the JINR Accelerator Nuclotron <i>Y. K. Pilipenko</i>	696
Spin Dependence in Elastic Scattering in the CNI Region <i>A. Bravar</i>	700

Deuteron Polarization Determination at High Energies <i>N. H. Buttimore</i>	706
Design and Test of a Prototype Cavity for a Stern-Gerlach Polarimeter <i>P. R. Cameron</i>	710
The MIT-Bates Compton Polarimeter for the South Hall Ring <i>W. A. Franklin</i>	714
Local Polarimetry for Proton Beams with the STAR Beam Beam Counters <i>J. Kiryluk</i>	718
<i>p</i> -Carbon CNI Polarimeters at BNL: The Fastest Physics Setup in the World <i>D. Svirida</i>	722
Spin Oscillations in Storage Rings <i>A. J. Silenko</i>	726
Suppression of Coherent Betatron Oscillations in the Muon (g-2) Experiment <i>Y. M. Shatunov</i>	730
The MIT-Bates South Hall Ring: A Unique Instrument for Studying Polarization <i>W. A. Franklin</i>	734
Polarisation in the eRHIC Electron (Positron) Ring <i>D. P. Barber</i>	738
Polarized Beams in the High-Energy Storage Ring of the Future GSI Project <i>A. Lehrach</i>	742
Polarized Proton Acceleration at the J-PARC Accelerator Complex <i>H. Sato</i>	746

SESSION 8

Polarized Sources, Targets and Polarimetry

Beam Induced Depolarization in the HERMES Transversely Polarized Hydrogen Target <i>D. Reggiani</i>	753
Polarized Hydrogen Jet Target for Measurement of RHIC Proton Beam Polarization <i>T. Wise</i>	757
Atomic Beam Studies in the RHIC H-JET Polarimeter <i>A. Zelenski</i>	761
Polarized Electron Photoinjector for Future Linear Colliders Using the Plane Wave Transformer (PWT) Design <i>D. Yu</i>	765
Polarization Measurements of the Polarized ^3He Target with Water and DPPH <i>W. Kim</i>	770

IUCF Polarized Ion Source CIPIOS for JINR Accelerator NUCLOTRON <i>V. V. Fimushkin</i>	774
Atomic Beam Polarization Measurement of the RHIC Polarized H-Jet Target <i>A. Nass</i>	776
Estimates of Intra-Beam Scattering in Atomic Beam Sources <i>M. Stancari</i>	779
Direct Measurement of Intra-Beam Scattering in Atomic Beam Sources <i>Z. Ye</i>	783
Polarized Electrons for Linear Colliders <i>J. E. Clendenin</i>	787
The COMPASS Polarized Target <i>F. Gautheron</i>	791
Polarization Build Up in COMPASS ⁶ LiD Target <i>J. Koivuniemi</i>	796
The Polarized Internal Gas Target of ANKE at COSY <i>K. Grigoriev</i>	800
Michigan Ultra-Cold Spin-Polarized Hydrogen Jet Target <i>R. S. Raymond</i>	804
Performance of the HERMES Polarized Hydrogen and Deuterium Gas Targets <i>P. Lenisa</i>	808
Frozen-spin Polarized HD Target for Spin Asymmetry Experiments <i>T. Kageya</i>	812
Features of Dynamic Nuclear Polarization in Irradiated LiD Target Material <i>Y. Kisselev</i>	816
Optical Spectrometer for Measuring the Ratio of Atomic Hydrogen and Molecular Hydrogen in an ABS <i>L. Barion</i>	820
Hydrogen/Deuterium Polarized Target at MIT-BATES <i>E. Tsentalovich</i>	824
Participants	829
Photos	849
Appendix A <i>Novosibirsk Deuteron Collaboration</i>	877

PESP2004

Preface	881
Scientific Programme	883
Workshop Agenda	887

The Status of Gallium Arsenide Photoemission Guns at Jefferson Lab <i>M. Poelker</i>	891
Operation of the MIT-Bates Polarized Source for a High Average Current Storage Ring <i>M. Farkhondeh</i>	897
Present Status of 200 keV Polarized Electron Gun at Nagoya University <i>M. Yamamoto</i>	902
Maximal Spin Orientation in Electron Photoemission from Strained Semiconductor Superlattices <i>L. G. Gerchikov</i>	908
High Performance Polarized Electron Photocathodes Based on InGaAlAs/AlGaAs Superlattices <i>Y. A. Mamaev</i>	913
Polarized Electron Emission from Strained GaAs/GaAsP Superlattice Photocathodes <i>T. Maruyama</i>	917
Time Resolved Depolarization Measurements on Superlattices with Strained Wells <i>K. Aulenbacher</i>	922
The Compton Backscattering Polarimeter of the A4 Experiment <i>Y. Imai</i>	926
Ferromagnetic Thin Layers for Spin Polarimetry <i>D. Lamine</i>	930
Highly-Polarized Electron Emission from Strain Compensated InAlGaAs-GaAsP Superlattices <i>L. G. Gerchikov</i>	935
Laser Development for Future Photocathode Research at SLAC <i>A. Brachmann</i>	939
Performance of the Cold Photocathode Gun at the Electron Target of the Heidelberg TSR <i>D. A. Orlov</i>	943
Lifetime Measurements Using the Jefferson Lab Load-Lock Electron Gun <i>J. Grames</i>	948
Recent PES Photocathode R&D at Nagoya University <i>M. Kuwahara</i>	953
Quality Characterization of NEA-photocathode for PES by Means of Photoemission from Defect States <i>A. A. Pakhnevich</i>	959
Properties of Field Emission Dark Current from Molybdenum and Titanium Electrodes <i>F. Furuta</i>	964

The Mainz A4 Parity Violation Experiment Single Spin Asymmetries in Elastic Scattering <i>F. E. Maas</i>	970
Photocathode Life Time Research at MAMI <i>K. Aulenbacher</i>	975
Cesium Adsorption on GaAs(001) Surface: Adsorbates Geometry and Sb Influence <i>S. E. Kulkova</i>	980
Atomic Hydrogen Cleaning of Polarized GaAs Photocathodes <i>T. Maruyama</i>	985
Polarized Electron Sources for Future Electron Ion Colliders <i>M. Farkhondeh</i>	990
Helical Undulator Based Production of Polarized Positrons and Status of the E166 Experiment <i>K. Laihem</i>	995
PESP2004 - Participants	1001
Author Index	1005



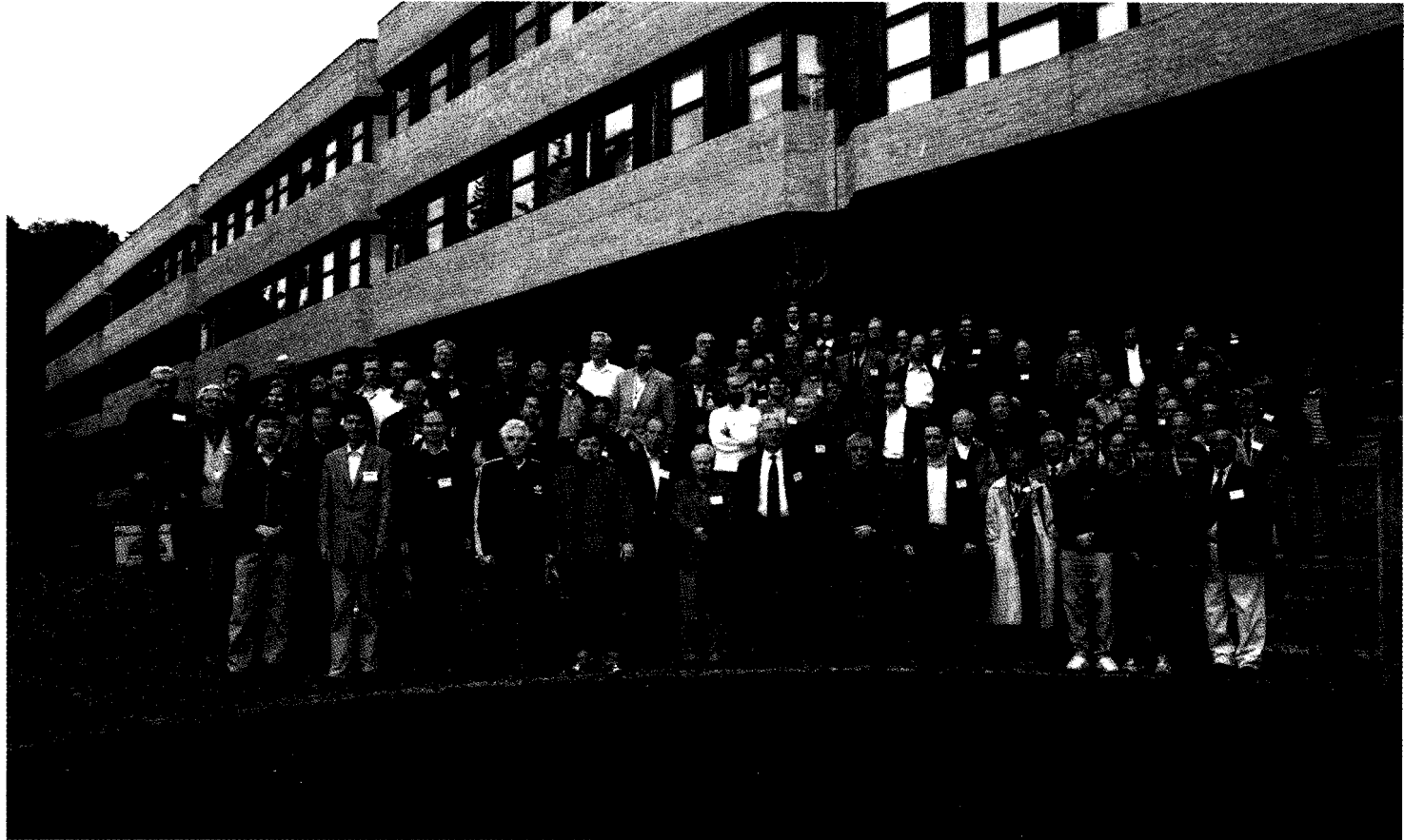
trieste, italy
october 10_16 2004

editors_

franco bradamante
[trieste university and infn]

andrea bressan
[trieste university and infn]

anna martin
[trieste university and infn]





This page intentionally left blank

organized by..



Istituto Nazionale di Fisica Nucleare

hosted at..



the Abdus Salam International Centre for Theoretical Physics

supported by..

International Spin Committee



International Union of Pure and Applied Physics



Central Europe Initiative



Physics Consortium – Trieste



Consorzio Sviluppo Internazionale Università di Trieste



Sissa – International School for Advanced Studies



Regione Friuli Venezia Giulia



Provincia di Trieste



Comune di Trieste

PREFACE

It has been a great pleasure and an honour to host the 16th International Spin Physics Symposium (SPIN2004) in Trieste, Italy, during October 10-16, 2004. The Symposium was organised by the Trieste Section of Istituto Nazionale di Fisica Nucleare (INFN), and was a hosted activity of the Abdus Salam International Centre for Theoretical Physics (ICTP) in Miramare, Trieste.

SPIN2004 is the third Symposium of a new series in which the International Conference on Polarization Phenomena in Nuclear Physics and the International Symposia on High Energy Spin physics joined together. Thus the scientific programme of this Symposium includes topics of relevance to spin physics in medium-low energy reactions and polarization phenomena in nuclear physics, as well as those relevant to high energy spin physics. The previous two editions of the new series of Symposia were held in Osaka, Japan (October 2000) and at BNL, USA (September 2002). As announced during the Symposium, the next one will be held in Kyoto, Japan.

Spin is a key element in the present and future development of particle and nuclear physics. Indeed spin has always played a paramount role in studies of fundamental symmetries, static particle properties, and the structure of fundamental interactions. On top of that, for 15 years Spin Physics has been enjoying a true "Renaissance", and many enthusiastic young people, both theoreticians and experimentalists, have been attracted by the new ideas and by the new experimental opportunities, and have entered the field. Over 300 spin physics enthusiasts showed up at the beautiful Miramare campus, and participation in SPIN2004 was highly diversified. Twenty-nine different countries were represented. The largest single community came from the USA, followed by those from Italy, Russian Federation, Germany, and Japan. A unique feature of this edition of the Symposium was the large participation from developing countries, which was possible thanks to support from the ICTP and to the very special rates the organisers could thus offer to these participants.

The Symposium was structured in plenary sessions in the mornings and in parallel sessions in the afternoons. The complete scientific programme is given at page xxxiii. As at SPIN2002, no poster session was set up: although a large number of contributions was expected an effort was made to accommodate all the talks in short communications in the parallel sessions, thus giving everybody an opportunity to stand up and present his or her work. The result was that the afternoon sessions were quite dense, never ending before 7 pm, particularly so for the session on "QCD Spin Structure of Nucleons", where 55 talks were given. On the other hand, the excellent plenary talks were almost one hour

long, covered all the topics of the Symposium, and were routinely followed by interesting discussions. Another important decision of the Local Organizing Committee was privilege for invited talks by young scientists. Also, in view of the variety of talks covered at the Symposium, rather than having a single “Concluding Remarks” talk, four rapporteurs were asked to report the highlights of the corresponding parallel sessions.

In the plenary sessions reports were also given on the specialized Workshops on Spin Physics, which took place over the past two years and were supported by the International Spin Committee: “X Workshop on High Energy Spin Physics (NATO ARW DUBNA-SPIN-03)” in Dubna, “10th Workshop on Polarized Sources and Targets” in Novosibirsk, “Advanced Studies Institute on Symmetries and Spin (Praha-Spin-2003 and Praha-Spin-Praha)” in Prague, “9th International Workshop on Polarized Solid State Targets and Techniques” in Bad Honnef, and “Workshop on Spin Polarized Electron Sources and Polarimeters (PESP-2004)” in Mainz. Following tradition, this last workshop took place the week before SPIN 2004, and the the PESP-2004 Proceedings can be found in the second part of this book.

During the Symposium tributes were paid to two distinguished members of the International Spin Committee who passed away since SPIN2002, V.W. Hughes and L.D. Soloviev. Both Myriam Hughes and Tatiana Solovieva attended the Symposium and could feel the friendship and the gratitude of many colleagues of Vernon and Lev.

These proceedings collect all 31 talks given in the plenary sessions, and 164 of the 173 talks in the parallel session. We are grateful to the authors for having submitted their written versions on time.

Here we would like to express our gratitude to the agencies and the institutions whose support has been essential for the success of the Symposium. In addition to the INFN and ICTP, we would like to thank the International School for Advanced Studies, the Consortium for the International Development of the University of Trieste, the Trieste Physics Consortium, the Central European Initiative, the Friuli-Venezia Giulia Region, the Province of Trieste, the City of Trieste, the International Union of Pure and Applied Physics, and the International Spin Physics Committee, for their support. We are indebted to the Director of the ICTP, Prof. K. Sreenivasan, for providing us the facilities and infrastructure, and to the ICTP support service staff for their invaluable work, and in particular to D. Giombi, F. Giorgi, L. Iannitti, E. Jost, A. Lusenti, D. Pothiou, R. Sain, D. Sauleek, T. Wardel, and M. Zorzin. We would also like to acknowledge here the great help we received from Prof. S. Fantoni, Director of SISSA, where at very short notice we could move the plenary sessions and some of the parallel sessions.

It would not have been possible to organise this Symposium without the full collaboration and support of the former and present Directors of the Trieste Section of INFN, Prof. N. Paver and Dr. A. Vacchi respectively, whom we would like to thank explicitly here. Our thanks also go to the administrative staff of the Trieste Section of INFN, A. Filippi, M. Giugovaz, R. Gomezel, R. Iacovelli, S. Rizzarelli, C. Sparagna, C. Strizzolo, T. Tenze, and A. Tirel, and particularly to A. Cappelletti and E. Novacco, who constituted the backbone of the whole enterprise. The fruitful collaboration of D. Pierluigi from LNF is here acknowl-

edged, as well as the help of L. De Marco, P. Fabbri, and C. Nuncibello from the Ferrara and Turin INFN Sections during the Symposium.

The design of the Symposium poster, the logo, and all the material which was distributed to the participants is the work of M. Cetin, M. Sterle, and M. Stulle (emme-emme).

Finally we would like to thank A. Mielech, P. Pagano and F. Sozzi for their valuable support during the sessions of the Symposium, V. Duic for his help on several practical aspects, and Dr. J.F. Crawford for his help in editing these Proceedings.

F. Bradamante
A. Bressan
A. Martin

Trieste, ITALY
28 February 2005

This page intentionally left blank

INTERNATIONAL SPIN PHYSICS COMMITTEE

T. Roser (Chair)	– Brookhaven USA
A.D. Krisch (Past-Chair)	– Michigan USA
F. Bradamante	– Trieste Italy
O. Chamberlain*	– Berkeley USA
D.G. Crabb	– Virginia USA
E.D. Courant*	– BNL USA
A.V. Efremov	– JINR Russia
G. Fidecaro*	– CERN Switzerland
W. Haeberli*	– Wisconsin USA
K. Hatanaka	– RCNP Japan
K. Imai	– Kyoto Japan
R.G. Milner	– MIT USA
Y. Mori	– KEK Japan
W.T.H. van Oers	– Manitoba Canada
C.Y. Prescott	– SLAC USA
F. Rathmann	– COSY Germany
Yu.M. Shatunov	– Novosibirsk Russia
V. Soergel	– Heidelberg Germany
E. Steffens	– Erlangen Germany
N.E. Tyurin	– IHEP Russia

* Honorary Members

LOCAL ORGANIZING COMMITTEE

G. Altarelli	– Geneva Switzerland
M. Anselmino	– Turin Italy
D. Barber	– Hamburg Germany
R. Bertini	– Turin Italy
F. Bradamante (Chair)	– Trieste Italy
S. Dalla Torre	– Trieste Italy
P. F. Dalpiaz	– Ferrara Italy
E. De Sanctis	– Frascati Italy
M. Finger	– Prague Czech Republic
T. Johansson	– Uppsala Sweden
E. Leader	– London England
D. Lhuillier	– Saclay France
A. Martin (vice-Chair)	– Trieste Italy
W. Meyer	– Bochum Germany
S. Nurushev	– Protvino Russia
N. Paver	– Trieste Italy
A. Penzo	– Trieste Italy
A. Sissakian	– Dubna Russia
J. Soffer	– Marseille France
G. van der Steenhoven	– Amsterdam Netherlands
T. Walcher	– Mainz Germany



SCIENTIFIC PROGRAMME

This page intentionally left blank

SPIN2004 SCIENTIFIC PROGRAMME

October 11, 2004

PLENARY SESSION

9:00 *Welcome Address:*

F. Bradamante	Local Organizing committee
G. Del Fabbro	Central European Initiative
U. Dosselli	INFN - Management Board
S. Fantoni	SISSA
G.C. Ghirardi	Physics Consortium Trieste
M.P. Pagnini	Comune di Trieste
D. Romeo	Trieste University
T. Roser	International Spin Physics Committee
C. Tuniz	ICTP
A. Vacchi	INFN - Trieste Section

chairperson A. Vacchi

9:40 A. Metz

Present understanding of the Nucleon Spin Structure

10:30 V. Barone

Understanding Transversity: present and future

11:20 *coffee break*

chairperson G. Fidecaro

11:40 M. Armeni

Pirelli International Award

11:50 B.L. Roberts

New results on g-2

12:40 A. Efremov

Summary of the X Workshop on High Energy Spin Physics
(NATO ARW DUBNA-SPIN-03)

13:00 *end of session*

PARALLEL SESSION 2: QCD Spin Structure of Nucleons (I)

chairperson Ch. Prescott

- 14:30 C. Schill Measurement of the gluon polarisation $\delta G/G$ at the COMPASS experiment
- 14:50 Y. Makdisi Current and future transverse spin physics with the PHENIX experiment at RHIC
- 15:10 W. Vogelsang Calculations of cross sections and spin asymmetries for single-inclusive reactions in pp scattering
- 15:30 P.G. Ratcliffe Transversity and Drell-Yan K -factors
- 15:50 F. Murgia Parton intrinsic motion: unpolarized cross sections, single spin asymmetries and the Sivers effects
- 16:10 C. Riedl Precision results on g_1 for proton, deuteron and neutron and first measurement of the tensor structure function b_1 of the deuteron
- 16:30 *coffee break*

PARALLEL SESSION 1: Spin and Fundamental Symmetries (I)

chairperson N. Paver

- 17:00 V.V. Andreev Compton polarizabilities of π -mesons in relativistic Hamiltonian dynamics
- 17:20 A.E. Dorokhov Vector and axial-vector current correlators within the instanton model of QCD vacuum
- 17:40 V.A. Huseynov The polarization effects in neutrino-lepton processes in a magnetic field
- 18:00 G. Musulmanbekov Spin structure of proton in dynamical model of correlated quarks
- 18:20 *end of session*

PARALLEL SESSION 2: QCD Spin Structure of Nucleons (II)*chairperson J. Nassalski*

- 17:00 B.I. Ermolaev Generalization of the DGLAP-evolution for the structure function g_1 to the small- x region
- 17:15 D. Peshekhonov Inclusive spin-dependent asymmetry $A_1^d(x, Q^2)$
- 17:30 E. Rondio Spin asymmetries for events with high p_T hadrons and an evaluation of the gluon polarization from SMC data
- 17:50 J.G. Rubin Flavor decomposition of the sea quark helicity distributions in the nucleon from semi-inclusive deep-inelastic scattering
- 18:10 D.B. Stamenov The role of higher twists in determining polarized parton densities from DIS data
- 18:25 G.P. Ramsey The gluon spin asymmetry as a link to the polarized gluon distribution and orbital angular momentum
- 18:40 O.J. Shevchenko NLO QCD procedure with respect to first moments of polarized quark densities
- 19:00 E. Christova A model independent approach to Semi-Inclusive Deep Inelastic Scattering
- 19:15 *end of session*

PARALLEL SESSION 6: Spin Physics in Nuclear Interactions (I)*chairperson K. Imai*

- 17:00 S. Asaji $^4\text{He}(p, 2p)$ reactions for studying in-medium NN interactions
- 17:20 Y. Shimizu Spin correlation parameter C_{yy} of proton- ^3He elastic backward scattering at intermediate energy
- 17:40 A.A. Yerшов Experimental investigation of the quasielastic scattering of polarized protons on nuclei at the JINR VBLHE synchrotron
- 18:00 Y. Maeda Measurements of the $n + d$ elastic scattering at 250 MeV and the three-nucleon forces
- 18:20 S. Oryu A three-body effect on the double polarized $^3\text{He}(d, p)^4\text{He}$ reaction near the threshold
- 18:40 *end of session*

PARALLEL SESSION 7: Acceleration, Storage, and Polarimetry of Polarized Beams (I)

chairperson A.U. Luccio

- | | | |
|-------|-----------------------|---|
| 17:00 | M. Bai | RHIC polarized proton new working point commissioning |
| 17:20 | V. Ptitsyn | Snake depolarizing resonance observed in RHIC |
| 17:40 | H. Huang | Acceleration of polarized protons in the AGS with a helical partial snake |
| 18:00 | T. Roser | Acceleration of polarized beams using multiple strong partial siberian snakes |
| 18:20 | A.D. Krisch | Spin manipulating 2 GeV/c polarized protons and deuterons stored in COSY |
| 18:55 | Yu.K. Pilipenko | Polarized Deuterons at the JINR Accelerator Nuclotron |
| 19:15 | <i>end of session</i> | |

October 12, 2004**PLENARY SESSION***chairperson D.G. Crabb*

- | | | |
|-------|------------------------------|--|
| 9:00 | M. Garçon | JLab contribution to the QCD spin structure of the nucleon |
| 9:50 | D. Hasch | Physics results from HERMES |
| 10:40 | <i>coffee break</i> | |
| | <i>chairperson R. Milner</i> | |
| 11:10 | A. Bressan | Physics results from COMPASS |
| 12:00 | N. Saito | Physics results from RHIC |
| 12:50 | D.K. Toporkov | Summary of the 10 th Workshop on Polarized Sources and Targets (PST2003) Workshop Summary |
| 13:00 | <i>end of session</i> | |

PARALLEL SESSION 2: QCD Spin Structure of Nucleons (III)*chairperson E.C. Aschenauer*

- | | | |
|-------|-----------------------|--|
| 14:30 | J. Sowinski | Spin Physics Progress with the STAR detector at RHIC |
| 14:50 | Y. Fukao | Probing gluon polarization with π^0 's in longitudinally polarized proton collisions at the RHIC-PHENIX experiment |
| 15:05 | K. Okada | Measurement of the direct photon cross section in proton-proton collisions at 200 GeV in RHIC-PHENIX |
| 15:20 | E. Kinney | Proposed upgrades of the PHENIX forward spectrometers for spin physics |
| 15:35 | M. Togawa | Study of the gluon polarization in the proton with a silicon vertex upgrade at RHIC/PHENIX |
| 15:50 | A. Ogawa | Spin effects in large rapidity neutral pion production at STAR |
| 16:05 | <i>end of session</i> | |

PARALLEL SESSION 4: Spin in Soft Hadronic Reactions (I)

chairperson L. Bland

- 14:30 H. Okada Measurement of the analyzing power in pp elastic scattering in the peak CNI region at RHIC
- 14:50 I.G. Alekseev Measurement of A_N in the elastic pp scattering with small momenta transferred at $\sqrt{s} = 200$ GeV at RHIC
- 15:10 O. Jinnouchi Measurement of the analyzing power of proton-carbon elastic scattering in the CNI region at RHIC
- 15:30 T.L. Trueman The energy dependence of proton-carbon analyzing power and the spin-dependent coupling of the Pomeron
- 15:50 S.M. Troshin Energy dependence of helicity-flip amplitudes in the small-angle elastic pp-scattering
- 16:10 O.V. Selyugin Large distance effects on spin observables at RHIC
- 16:30 *end of session*

PARALLEL SESSION 6: Spin Physics in Nuclear Interactions (II)

chairperson P. Haulte

- 14:30 B.I.S.
Van der Ventel Quasifree photoproduction of η mesons from nuclei in a relativistic approach
- 14:50 M. Ichimua Unified understanding of spin isospin response functions of nuclei
- 15:10 T. Kawabata Isovector and isoscalar spin-flip M1 strengths in ^{11}B
- 15:30 A. Prokofiev Study of inelastic αp - and dp -scattering in Roper resonance region
- 15:50 K. Suda Tensor analyzing power of the $^{16}\text{O}(d, ^2\text{He})$ reaction at 0° and structure of the spin-dipole resonances
- 16:10 G.I. Lykasov Spin effects and opacity of nuclear matter to neutrino
- 16:30 *coffee break*

PARALLEL SESSION 2: QCD Spin Structure of Nucleons (IV)*chairperson E. Christova*

- 16.50 U. D'Alesio Can the Collins mechanism explain the large transverse single spin asymmetries observed in $p^\uparrow p \rightarrow \pi X$?
- 17.10 M. Boglione Accessing Sivers gluon distribution via transverse spin asymmetries in D production processes at RICH
- 17.30 A. Mukherjee Double transverse spin asymmetries at next-to-leading order in QCD
- 17:50 V.L. Rykov Spin transfer studies in polarized proton collisions at RHIC
- 18:05 O.V. Teryaev Higher twists resummation in inclusive and semi-inclusive spin-dependent DIS
- 18.20 R. Seidl Status of spin dependent fragmentation analysis at Belle
- 18:40 *end of session*

PARALLEL SESSION 3: Spin Beyond the Standard Model (I)*chairperson A. Dorokhov*

- 17:00 A.A. Pankov Search for and identification of graviton exchange effects at high energy colliders
- 17:20 A.V. Tsytrynau Contact interaction searches at e^+e^- and e^-e^- linear colliders: role of polarization
- 17:40 A. Mirjalili Polarized parton distributions in the approach of complete renormalization group improvement
- 18:00 A. Khorrarnian Spin dependence of constituent quarks and structure function g_1
(A. Mirjalili)
- 18:20 *end of session*

PARALLEL SESSION 4: Spin in Soft Hadronic Reactions (II)

chairperson S. Troshin

- | | | |
|-------|-----------------------|---|
| 17:00 | A. Kacharava | Spin Physics of NN Interactions at COSY
(invited speaker) |
| 17:30 | S. Yashchenko | Measurement of the vector analyzing power in $pd \rightarrow (pp)n$ with emission of a fast forward diproton at ANKE/COSY |
| 17:45 | D.N. Svirida | Results for the asymmetry measurement in the elastic pion-proton scattering at 1.78 and 2.07 GeV/c |
| 18:00 | E.M. Tursunov | Lower excitation spectrum of the Nucleon and Δ in a relativistic chiral quark model |
| 18:20 | S.B. Nurushev | Single spin asymmetry measurements for π^0 inclusive productions in $pp^\uparrow \rightarrow \pi^0 X$ and $\pi p^\uparrow \rightarrow \pi^0 X$ interactions at 70 and 40 GeV/c respectively |
| 18:40 | V.V. Mochalov | A_N at small negative values of x_F in the reaction $pp^\uparrow \rightarrow \pi^0 X$ at 70 GeV and universal threshold in inclusive pion production |
| 19:00 | V.V. Sumachev | New experimental facets of the πN interaction investigations in the resonance region |
| 19:15 | <i>end of session</i> | |

PARALLEL SESSION 6: Spin Physics in Nuclear Interactions (III)

chairperson F. Hinterberger

- | | | |
|-------|----------------------------|---|
| 17:00 | V. Kryshkin | Asymmetry measurement of charged hadron production in $p^\uparrow A$ collisions at 40 GeV |
| 17:20 | V.P. Ladygin
(L. Zolin) | Tensor analyzing power A_{yy} in deuteron inclusive breakup at large P_t and spin structure of deuteron at short internucleonic distances |
| 17:40 | P. Guazzoni | Study of corresponding homologous states in ^{41}K and ^{42}Ca via (p, α) reactions |
| 18:00 | P. Hautle | High-accuracy measurement of the spin-dependent neutron scattering length of the deuteron |
| 18:20 | <i>end of session</i> | |

October 13, 2004**PLENARY SESSION***chairperson V. Soergel*

- | | | |
|-------|--------------------------------|--|
| 9:00 | R. De Vita | Soft spin physics at JLab |
| 9:50 | K. Hatanaka | Spin physics in nuclear interactions |
| 10:40 | <i>coffee break</i> | |
| | <i>chairperson A.D. Krisch</i> | |
| 11:10 | B. von Przewoski | Spin physics in NN interactions at intermediate energies |
| 12:00 | J.M. Richard | Status of hadron spectroscopy |
| 12:50 | G. Bunce | Memorial V. W. Hughes |
| 13:10 | <i>end of session</i> | |

October 14, 2004**PLENARY SESSION***chairperson W.T.H. van Oers*

- | | | |
|-------|--------------------------------|--|
| 9:00 | K.P. Jungmann | New EDM measurements |
| 9:55 | K. De Jager | The EM and weak nucleon form factors (and the strangeness content of the nucleon) |
| 10:50 | <i>coffee break</i> | |
| | <i>chairperson N.E. Tyurin</i> | |
| 11:15 | E.W. Hughes | Low energy tests of the Standard Model |
| 12:10 | M. Finger | Summary of the Advanced Studies Institute on Symmetries and Spin (Praha-Spin-2003 and Praha-Spin-2004) |
| 12:30 | K. Aulenbacher | Summary of the Workshop on Spin Polarized Electron Sources and Polarimeters (PESP-2004) |
| 12:50 | A.D. Krisch | Memorial L. D. Soloviev |
| 13:10 | <i>end of session</i> | |

PARALLEL SESSION 2: QCD Spin Structure of Nucleons (V)

chairperson M. Grosse Perdekamp

- 14:30 G. Schnell Measurement of transversity at HERMES
14:50 P. Pagano Measurements of Collins and Sivers asymmetries at COMPASS
15:10 E. Kinney Measurement of single-spin azimuthal asymmetries in semi-inclusive electroproduction of mesons
15:30 A. Bacchetta Transversity and 2-hadron fragmentation function
15:45 P.B. Van Der Nat First measurement of interference fragmentation function on longitudinally polarized deuteron target at HERMES
16:00 R. Joosten Transversity signals in two pion correlation at COMPASS
16:15 L.P. Gamberg Transversity of quarks and nucleons in SIDIS and Drell-Yan
16:35 *end of session*

PARALLEL SESSION 4: Spin in Soft Hadronic Reactions (III)

chairperson M. Sapozhnikov

- 14:30 S. Paul Transverse hyperon polarization revisited (invited speaker)
15:00 J. Felix Λ^0 polarization in $pp \rightarrow p\Lambda^0 K^+(\pi^+\pi^-)^5$ at 27.5 GeV
15:20 K. Kubo Spin polarization of hyperons in the hadron-hadron inclusive collisions - mechanisms and dynamics
15:40 Z. Liang Hyperon polarization in unpolarized h-h collisions and some related problems
16:00 *end of session*

PARALLEL SESSION 7: Acceleration, Storage, and Polarimetry of Polarized Beams (II)

chairperson D. Underwood

- 14:30 A. Bravar Spin dependence in elastic scattering in the CNI region (invited speaker)
- 15:00 N.H. Buttimore Deuteron polarization determination at high energies
- 15:20 P.R. Cameron Design and test of a prototype cavity for a Stern-Gerlach polarimeter
- 15:40 W.A. Franklin The MIT-Bates Compton polarimeter for the South Hall Ring
- 16:00 J. Kiryluk Local Polarimetry for proton beams with the STAR beam
- 16:20 *end of session*

PARALLEL SESSION 8: Polarized Sources, Targets, and Polarimetry (I)

chairperson W. Haeberli

- 14:30 D. Reggiani Beam induced depolarization in the HERMES transversely polarized Hydrogen target
- 14:50 T. Wise Polarized Hydrogen jet target for measurement of RHIC proton beam polarization
- 15:10 A. Zelenski Studies of atomic beam production in the polarized H-jet polarimeter for RHIC
- 15:30 W. Kim Polarization measurements of the polarized ^3He target with water and DPPH
- 15:50 D. Yu A Polarized Electron PWT photoinjector
- 16:10 N. Piskunov Results and future measurements of the analyzing powers for the proton-polyethelene scattering
- 16:30 *coffee break*

PARALLEL SESSION 2: QCD Spin Structure of Nucleons (VI)

chairperson U. D'Alesio

- 17:05 A. Prokudin The role of Cahn and Sivers effects in Deep Inelastic Scattering
- 17:25 V.Y. Alexakhin Longitudinal polarization of Λ and $\bar{\Lambda}$ hyperons in deep-inelastic scattering at COMPASS
- 17:40 J.M. Friedrich Transverse Λ polarisation at COMPASS
- 17:55 S. Belostotski (G. Schnell) An overview of the recent results on hyperon production at HERMES
- 18:10 A. Kotzinian LEPTO and polarized SIDIS
- 18:25 E. Di Salvo Asymmetries in Semi-Inclusive Deep Inelastic Scattering
- 18:40 *end of session*

PARALLEL SESSION 4: Spin in Soft Hadronic Reactions (IV)

chairperson V. Mochalov

- 16:45 L. Zolin Spin effects at fragmentation of GeV polarized deuterons into pions with large transverse momentum
- 17:00 P.Zh. Aslanyan Evidence of $S=+1$ narrow resonances in the system $K_s^0 p$
- 17:15 Yu.N. Uzikov P-parity of the pentaquark Θ^+ and spin observables in the reaction $NN \rightarrow Y\Theta^+$
- 17:30 *end of session*

PARALLEL SESSION 7: Acceleration, Storage, and Polarimetry of Polarized Beams (III)

chairperson M. Tannenbaum

- 16:50 D. Svirida p-Carbon CNI Polarimeters at BNL - the fastest physics setup in the world
- 17:10 A.J. Silenko Spin oscillations in storage rings
- 17:30 Yu.M. Shatunov Suppression of coherent betatron oscillations in muon (g-2) experiment
- 17:50 W. Franklin The Bates south hall ring: a unique instrument for studying polarization
- 18:10 D.P. Barber Polarisation in the eRHIC electron(positron) ring
- 18:30 A. Lehrach Polarized beams in the high-energy storage ring of the future GSI project
- 18:50 H. Sato Polarized proton acceleration at the J-PARC accelerator complex
- 19:10 *end of session*

PARALLEL SESSION 8 - Polarized Sources, Targets, and Polarimetry (II)

chairperson W. Haeberli

- 17:00 V.V. Fimushkin IUCF polarized ion source CIPIOS for JINR accelerator Nuclotron
- 17:20 A. Nass Atomic beam polarization measurement of the RHIC polarized H-jet target
- 17:40 M. Stancari Studies and planned measurements of beam formation and attenuation for future high intensity ABS design
- 18:00 Z. Ye Direct measurements of intra-beam scattering in atomic beam sources
- 18:20 *end of session*

October 15, 2004

PLENARY SESSION

chairperson S. Fantoni

9:10 H. Arends Experimental status of the GDH sum rule

10:00 F. Rathmann Spin physics at GSI

10:50 *coffee break*

chairperson Yu.M. Shatunov

11:20 S. Forte Spin physics at a neutrino factory

12:10 W.W. MacKay Status of proton polarization at RHIC and AGS

12:30 *end of session*

PARALLEL SESSION 1: Spin and Fundamental Symmetries (II)

chairperson R. Gasimova

14:30 A. Yoshimi Low-frequency nuclear spin maser and search for atomic EDM of ^{129}Xe

14:50 V.V. Lyuboshitz Polarization effects in the reaction $p + {}^3\text{He} \rightarrow \pi^+ + {}^4\text{He}$, $\pi^+ + {}^4\text{He} \rightarrow p + {}^3\text{He}$ and verification of the consequences of quantum-mechanical coherence for the correlation tensor

15:10 A. Burinskii Spinning particle and stingy system of the rotating black hole solution

15:30 M. Rivas Classical spinning elementary particles, Zitterbewegung and dipole structure

15:50 *end of session*

PARALLEL SESSION 2: QCD Spin Structure of Nucleons (VII)*chairperson P. Di Nezza*

- 14:30 A.V. Efremov Transversity distribution function in hard scattering of polarized protons and antiprotons in the PAX experiment
- 14:50 P. Zavada Proton transversity and intrinsic motion of quarks
- 15:05 S.V. Goloskokov Spin density matrix elements in vector meson leptonproduction
- 15:20 D. Neyret Results on exclusive ρ^0 production from COMPASS at CERN
- 15:40 R. Fabbri Hard exclusive electroproduction of $\pi^+\pi^-$ pairs
- 15:55 A. Rostomyan Exclusive electroproduction of pions and of vector mesons at HERMES
- 16:15 E. Leader A critique of the angular momentum sum rules and a new angular momentum sum rule
- 16:35 *end of session*

PARALLEL SESSION 5 - Soft Spin Physics with Photons and Leptons (I)*chairperson P. Bosted*

- 14:30 V. Ziskin Measurement of the neutron electric form factor at low momentum transfer
- 14:50 C.B. Crawford Measurement of G_E^p/G_M^p in the range $Q^2 = 0.1-0.9$ (GeV/c)² at BLAST
- 15:10 J. Roche Parity-violating asymmetries from the G0 experiment
- 15:30 D. Lhuillier The second generation HAPPEX experiments
- 15:50 V.N. Stibunov Tensor analyzing power in exclusive π^- -meson photoproduction on deuteron
- 16:10 D.K. Toporkov Measurement of tensor analyzing powers in deuteron photodisintegration
- 16:30 *end of session*

PARALLEL SESSION 8 - Polarized Sources, Targets, and Polarimetry (III)

chairperson Y. Kisselev

- 14:30 J.E. Clendenin Polarized electrons for linear colliders
14:50 F. Gautheron The COMPASS polarized target
15:10 J. Koivuniemi Polarization build up in the large COMPASS ${}^6\text{LiD}$ target
15:30 K. Grigoriev The polarized internal gas target of ANKE at COSY
15:50 R.S. Raymond Michigan ultra-cold spin-polarized Hydrogen jet target
16:10 P. Lenisa The HERMES polarized Hydrogen and Deuterium internal target

16:30 *coffee break*

PARALLEL SESSION 2 - QCD Spin Structure of Nucleons (VIII)

chairperson H. Fischer

- 17:05 F. Pijlman New observables from color gauge invariance
17:25 X. Jiang A proposed measurement of polarized sea flavor asymmetry at Jefferson Lab Hall C
17:45 A. Nagaytsev The Q^2 -dependence of the generalised GDH integral and evidence for quark-hadron duality in A_1^p
18:05 H. Marukyan Measurement of Deeply Virtual Compton Scattering at HERMES
18:20 J. Stewart The HERMES recoil detector
18:35 M. Wakamatsu Chiral-odd twist-3 distribution function $e(x)$
18:50 M. Goshtasbpour Pre-constraining evolution of parton distributions in the matrix solution of DGLAG
19:05 *end of session*

PARALLEL SESSION 3 - Spin Beyond the Standard Model (II)*chairperson A. Pankov*

- 16:40 N.S. Mankoc Borsnik The approach unifying spin and charges
- 17:00 V.S. Zamiralov New QCD relation between magnetic moments of Σ^0 and Λ hyperons
- 17:20 R.D. Carlini The JLab Qweak experiment
- 18:00 B. Si Lakhali Four-spinon contribution to the dynamic structure factor in antiferromagnetic Heisenberg model
- 18:20 *end of session*

PARALLEL SESSION 5: Soft Spin Physics with Photons and Leptons (II)*chairperson E. De Sanctis*

- 17:00 A. Maschinot Quasi-elastic ep scattering from vector/tensor polarised deuterium
- 17:20 M. Mestayer Polarization in exclusive electro- and photoproduction at CLAS
- 17:40 P.E. Bosted Spin asymmetries in exclusive electron scattering from polarized protons with CLAS
- 18:00 A. Deur Measurement of the Q^2 -dependence of the Bjorken integral in the resonance region
- 18:20 *end of session*

PARALLEL SESSION 8: Polarized Sources, Targets, and Polarimetry (IV)

chairperson P. Lenisa

- | | | |
|-------|------------------------------|---|
| 17:00 | T. Kageya | Status of frozen-spin polarized HD targets for spin asymmetry measurement experiments |
| 17:20 | Y. Kisselev | Features of Dynamic Nuclear Polarization in irradiated LiD target material |
| 17:40 | S. Atutov
(L. Barion) | Optical spectrometer for measuring the relative density of the atomic hydrogen and molecular hydrogen in the ABS source |
| 18:00 | E. Tsentalovich | Polarized Hydrogen/Deuterium internal gas target |
| 18:20 | A. Zelenski
(R.G. Milner) | A proposal of a polarized $^3\text{He}^{++}$ ion source with the EBIS ionizer for RHIC |
| 18:40 | <i>end of session</i> | |

October 16, 2004

PLENARY SESSION

chairperson E. Steffens

- | | | |
|-------|---------------------------------|---|
| 9:00 | O.V. Teryaev | Parallel Sessions 1 and 3 Summary |
| 9:30 | G.K. Mallot | Parallel Sessions 2 Summary |
| 10:00 | H. Dutz | Summary of the 9 th International Workshop on Polarized Solid State Targets and Techniques |
| 10:20 | T. Wise | Parallel Sessions 8 Summary |
| 10:40 | <i>coffee break</i> | |
| | <i>chairperson F Bradamante</i> | |
| 11:10 | A. Lehrach | Parallel Sessions 7 Summary |
| 11:40 | A. Desphande | Future facilities |
| 12:30 | T. Roser | Concluding Remarks |

End of the Symposium



PLENARY TALKS

This page intentionally left blank

PRESENT UNDERSTANDING OF THE NUCLEON SPIN STRUCTURE*

A. METZ

Institut für Theoretische Physik II, Ruhr-Universität Bochum, Bochum, Germany

The present understanding of the spin structure of the nucleon is briefly reviewed. The main focus is on parton helicity distributions, orbital angular momentum of partons as defined through generalized parton distributions, as well as single spin asymmetries and time-reversal odd correlation functions.

1. Introduction

The history of the non-trivial nucleon spin structure started as long ago as in 1933 with the discovery of the anomalous magnetic moment of the proton by Frisch and Stern [1]. This observation led to the important conclusion that the nucleon cannot be point-like.

In the meantime the field has grown tremendously. This short review concentrates on the QCD spin structure of the nucleon, which is usually quantified in terms of various parton distributions. In this context one is dealing with three kinds of parton distributions: (1) forward distributions (quark and gluon helicity distribution), (2) generalized parton distributions (GPDs) which contain information on the orbital angular momentum of partons, (3) transverse momentum dependent distributions (TMDs) which can lead to single spin asymmetries (SSAs). Related experiments are currently running at CERN, DESY, Jefferson Lab, and RHIC.

Many issues like the transversity distribution, parton distributions for $x \rightarrow 0, 1$, various sum rules, subleading twist etc. cannot be covered. For such topics the reader is referred to existing review articles (like, e.g., [2]– [5]) and refereces therein, as well as these proceedings.

*This work has been supported by the Sofia Kovalevskaya Programme of the Alexander von Humboldt Foundation and by the Deutsche Forschungsgemeinschaft.

2. Parton helicity distributions

2.1. Quark helicity distribution

Up to now our knowledge about the quark helicity distribution Δq has mostly come from inclusive lepton scattering off the nucleon. By measuring double spin asymmetries (polarized lepton beam and polarized target) one can extract the structure function $g_1(x, Q^2)$ which is given by

$$g_1^{p,n} = \frac{1}{9}\Delta\Sigma \pm \frac{1}{12}\Delta q_3 + \frac{1}{36}\Delta q_8, \quad (1)$$

with the flavour combinations

$$\begin{aligned} \Delta\Sigma &= (\Delta u + \Delta\bar{u}) + (\Delta d + \Delta\bar{d}) + (\Delta s + \Delta\bar{s}), \\ \Delta q_3 &= (\Delta u + \Delta\bar{u}) - (\Delta d + \Delta\bar{d}), \\ \Delta q_8 &= (\Delta u + \Delta\bar{u}) + (\Delta d + \Delta\bar{d}) - 2(\Delta s + \Delta\bar{s}). \end{aligned} \quad (2)$$

In the past many QCD analyses, using (slightly) different assumptions and different schemes, of polarised DIS data were performed. Information on the first moment of Δq_3 and Δq_8 from beta decay of the neutron and hyperons usually serves as an important independent constraint. The results of such QCD analyses can be summarized roughly as follows: while $\Delta\Sigma$ and Δq_3 are fairly well known, Δq_8 is not known with the same accuracy. In particular, this means that there still exists a considerable uncertainty about the distribution of strange quarks. Most importantly, however, inclusive DIS measurements do not permit the determination of Δq and $\Delta\bar{q}$ separately.

At this point additional information can be obtained from semi-inclusive DIS, where one extracts the double spin asymmetry

$$A^h \propto \frac{\sum_q e_q^2 \Delta q(x) D_q^h(z)}{\sum_q e_q^2 q(x) D_q^h(z)}. \quad (3)$$

Detecting one hadron h in the final state not only addresses the distribution of specific quark flavours (e.g., by looking at kaons one can learn something about the strange-quark distribution), but also makes it possible to separate the quark and antiquark distributions, since the fragmentation functions D_q^h , $D_{\bar{q}}^h$ put different weights on Δq and $\Delta\bar{q}$. The results for such an analysis from the HERMES Collaboration [6] are shown in Fig. 1, where, in particular, it turned out that the data are consistent with a vanishing sea quark distribution for all three flavours. It has been claimed, however, that the extraction method used in [6] has some model dependence [7]. Recently, there has been considerable activity aimed at an entirely model-independent analysis of semi-inclusive DIS data [8, 9].

Measuring a parity-violating SSA in $\bar{p}p \rightarrow W^\pm X$ can provide complementary information on the helicity distribution of the light flavours [10, 11], where for W^+ production one has

$$A_L^{W^+} = \frac{\Delta u(x_1)\bar{d}(x_2) - \Delta\bar{d}(x_1)u(x_2)}{u(x_1)\bar{d}(x_2) + \bar{d}(x_1)u(x_2)}. \quad (4)$$

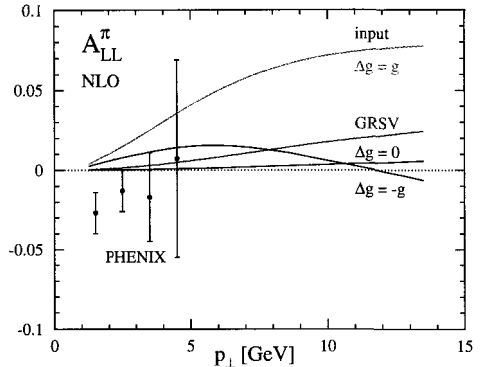
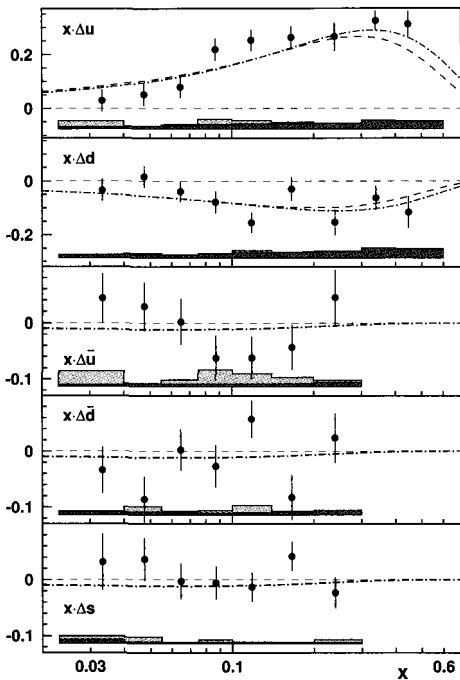


Fig. 1. Quark helicity distributions at $\langle Q^2 \rangle = 2.5 \text{ GeV}^2$ from HERMES [6] (left panel), and longitudinal double spin asymmetry for $\bar{p}\bar{p} \rightarrow \pi^0 X$ from PHENIX [18] (right panel).

Since x_1 and x_2 are fixed by external kinematics one can disentangle the contributions of the different flavours. If, e.g., x_1 is large, then both $\Delta \bar{d}$ and \bar{d} are small and one can extract the ratio $\Delta u/u$. On the other hand the ratio $\Delta \bar{d}/\bar{d}$ can be obtained if x_2 is large. Analogously, production of W^- allows one to measure $\Delta d/d$ and $\Delta \bar{u}/\bar{u}$. This method is rather clean and is planned to be exploited at RICH. Eventually, polarized neutrino DIS could be used to get additional information on Δs and $\Delta \bar{s}$.

2.2. Gluon helicity distribution

In order to get information on the gluon helicity distribution Δg of the nucleon, one studies lepton nucleon scattering as well as pp -collisions, where different final states are considered in both cases.

In the DIS measurements one tries to isolate the partonic subprocess of photon-gluon fusion (PGF), $\gamma g \rightarrow q\bar{q}$. From the experimental point of view, inclusive DIS represents the simplest reaction containing PGF. However, since it only enters through evolution, this process merely provides a rather indirect measurement of Δg . Because of the limited range in x and Q^2 , the currently available data put no strong constraint on Δg , even though a positive Δg is preferred in the analyses. This is in contrast to the situation of the unpolarized gluon distribution, where a lot of information is coming from unpolarized inclusive DIS which has been explored in a wide kinematical region.

A more direct measurement of the PGF process is possible by detecting high- p_T jets or hadron pairs in the final state (see, e.g., [2]–[5] and referenes therein). In this context

a special role is played by the production of a pair of charmed mesons created through $\gamma g \rightarrow c\bar{c}$, because background processes like the QCD-Compton reaction $\gamma q \rightarrow gq$ are automatically suppressed without making specific kinematical cuts. To measure Δg via charm production is a central aim of the COMPASS Collaboration [12].

The only published numbers for Δg from such reactions come from the production of high- p_T hadron pairs. The measurements of the HERMES [13] and SMC [14] Collaborations, performed at different average values of x , yielded

$$\Delta g/g|_{\langle x \rangle=0.17} = 0.41 \pm 0.18(\text{stat}) \pm 0.03(\text{syst}) \quad (\text{from [13]}), \quad (5)$$

$$\Delta g/g|_{\langle x \rangle=0.7} = -0.20 \pm 0.28(\text{stat}) \pm 0.10(\text{syst}) \quad (\text{from [14]}). \quad (6)$$

Unfortunately, these data still suffer from large statistical errors. While the SMC result was obtained in the DIS regime ($Q^2 > 1 \text{ GeV}^2$), HERMES used photoproduction, which led to speculations about background contributions from resolved photons.

The second class of processes providing information on Δg are longitudinal double spin asymmetries in proton-proton collisions. To be specific, the following reactions are considered: prompt photon production ($\vec{p}\vec{p} \rightarrow \gamma X$), production of heavy flavours ($\vec{p}\vec{p} \rightarrow c\bar{c}X, b\bar{b}X$), jet production ($\vec{p}\vec{p} \rightarrow \text{jet}X$), as well as inclusive production of hadrons ($\vec{p}\vec{p} \rightarrow hX$). The processes have already been computed up to NLO in QCD. A detailed discussion of the advantages and drawbacks of the different reactions can be found in [4, 11, 15–17] and references therein. At RICH there are extensive ongoing activities in order to study the various channels for different kinematics.

The first published data are from the PHENIX Collaboration for inclusive production of neutral pions [18]. The asymmetry is shown in Fig.1 as function of the transverse momentum of the pion, and compared to a NLO calculation [15]. Measuring A_{LL}^π with good statistics at higher values of p_\perp , where the sensitivity of the asymmetry to the gluon helicity is larger as compared to the low p_\perp region, can already provide an important constraint on Δg .

3. Generalized parton distributions and orbital angular momentum

Knowing the helicity distributions is not sufficient to understand how the spin of the nucleon is decomposed. One also needs information on the orbital angular momentum of the partons. In 1996 it was shown [19] that generalized parton distributions (see, e.g., [20, 21]) can provide the pertinent information. GPDs appear in the description of hard exclusive processes like deep-virtual Compton scattering off the nucleon and meson production, where in both cases data have already been published. Neglecting the scale dependence, GPDs are functions of three variables, x, ξ, t . While ξ and t , describing the longitudinal and total momentum transfer to the nucleon, are fixed by the external kinematics of an experiment, x is integrated over, which complicates the extraction of the x -dependence of GPDs.

GPDs contain a vast amount of physics, and show several interesting properties which put strong constraints on models. They are related to forward parton distributions and nucleon form factors, obey the so-called polynomiality condition [22], and satisfy positivity

bounds [23]. Moreover, they contain information on the shear forces experienced by partons in the nucleon [24]. In particular, they can provide a 3-dimensional picture of the nucleon [25].

Concerning the nucleon spin structure, it is important that the total angular momentum (for longitudinal polarization) of quarks is related to the GPDs according to [19]

$$J_q^z = \frac{1}{2} \int_{-1}^1 dx x \left[H_q(x, \xi, t=0) + E_q(x, \xi, t=0) \right], \quad (7)$$

where $H_q(x, 0, 0) = q(x)$, while the GPD E_q has no relation to a normal forward distribution. For J_g^z an analogous formula holds. Knowing both the total angular momentum and the helicity of partons allows one to address the orbital angular momentum by means of the decomposition

$$\frac{1}{2} = \sum_q J_q^z + J_g^z = \sum_q \left[\frac{1}{2} \int_0^1 dx \left(\Delta q(x) + \Delta \bar{q}(x) \right) + L_q^z \right] + \Delta g + L_g^z. \quad (8)$$

(Note that also for a transversely polarized nucleon a decomposition like in (8) has been proposed [26].) Recently, Lattice QCD as well as models and phenomenological parametrizations of GPDs were used to estimate the orbital angular momentum of the quarks. Lattice data, e.g., result in a small contribution to the angular momentum if one sums over the quarks, but the uncertainties of these calculations are still large.

4. Single spin asymmetries

Single spin asymmetries are currently under intense investigation from both the experimental and theoretical point of view. For the process $p^\uparrow p \rightarrow \pi X$, e.g., Fermi-Lab [27] observed large transverse SSAs (up to 40%) at the *cm*-energy $\sqrt{s} = 20 \text{ GeV}$, and recent results from the STAR Collaboration [28] have shown that the effect survives at $\sqrt{s} = 200 \text{ GeV}$ (see Fig.2). Also for pion production in semi-inclusive DIS, non-vanishing transverse SSAs have been observed [29] (see Fig.2).

In general, SSAs are generated by so-called time-reversal odd (T-odd) correlation functions (parton distributions and fragmentation functions). They vanish in leading twist collinear factorization. To get non-zero effects one has to resort to (collinear) twist-3 correlators [30] or to transverse momentum dependent functions [31]. There exist four T-odd leading twist TMD correlation functions, where the Sivers function f_{1T}^\perp [32], describing the azimuthal asymmetry of quarks in a transversely polarized target, is the most prominent T-odd parton distribution. In the case of fragmentation, the Collins function [33] (transition of a transversely polarized quark into an unpolarized hadron) has attracted a lot of interest, since in semi-inclusive DIS it gets coupled to the transversity distribution of the nucleon.

For A_N in pp -collisions both TMD twist-2 and collinear twist-3 correlators were used to describe the data as can be seen in Fig. 2. For the twist-2 analysis, very recently the invoked kinematics has been revisited carefully. As a result it turns out that the Collins mechanism actually cannot explain the data [34], while the Sivers mechanism could well do so [35]. In contrast to A_N , in semi-inclusive DIS at low transverse momentum of the detected hadron, one can unambiguously select the Sivers mechanism shown in Fig. 2.

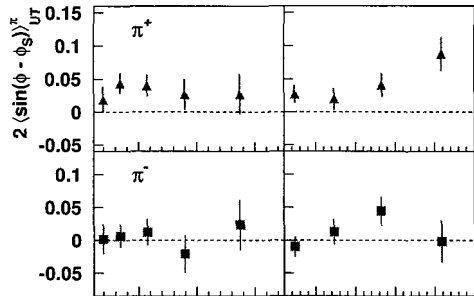
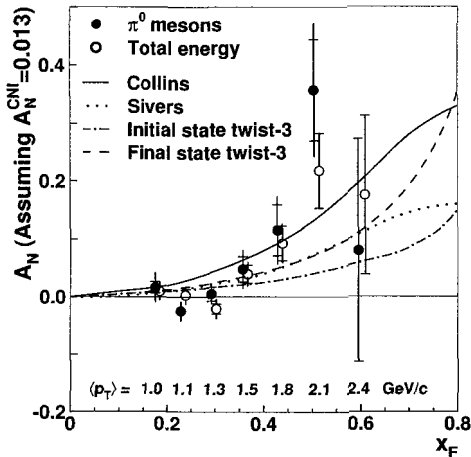


Fig. 2. Transverse single spin asymmetries: A_N in $p^\dagger p \rightarrow \pi^0 X$ from STAR [28] (left panel), and Siverson asymmetry in $ep^\dagger \rightarrow e\pi X$ as functions of x (*lhs*) and z (*rhs*) from HERMES [29](right panel).

For quite some time it was believed that T-odd TMD distributions like the Siverson function should vanish because of T-invariance of the strong interaction [33], whereas T-odd fragmentation functions may well exist because of final state interactions [33]. However, in 2002 a simple spectator model calculation provided a non-zero SSA in DIS [36]. A reanalysis then revealed that in fact the Siverson function can be non-zero, but only if the Wilson-line ensuring color gauge invariance is taken into account in the operator definition [37]. The presence of the Wilson line, which can be process-dependent, in turn endangers the universality of TMD correlation functions [37, 38]. This problem also affects the soft factor appearing in factorization formulae for transverse momentum dependent processes. The schematical structure of the factorization formula for semi-inclusive DIS is [39, 40]

$$\sigma_{DIS} \propto \text{pdf} \times \text{frag} \times \hat{\sigma}_{part} \times \text{soft}. \quad (9)$$

For unintegrated Drell-Yan and $e^+e^- \rightarrow h_1 h_2 X$, if the two hadrons are almost back-to-back one is dealing with corresponding formulae. While time-reversal can be used to relate parton distributions in DIS which contain future-pointing Wilson lines to distributions in Drell-Yan with past-pointing lines, this is not possible for fragmentation functions. Nevertheless, by considering the analytic properties of the fragmentation correlator, it can be shown that fragmentation functions are universal [40, 41]. This result, in particular, justifies the relation of the Collins function in e^+e^- -annihilation and semi-inclusive DIS. Also for the soft factor universality between the three mentioned processes can be established [40]. Only T-odd parton distributions are non-universal in the sense that they have a reversed sign in DIS as compared to Drell-Yan, i.e.,

$$f_{iT}^\perp \Big|_{DY} = -f_{iT}^\perp \Big|_{DIS}. \quad (10)$$

This relation should be checked experimentally.

There are many more interesting developments in the field of SSAs. For instance, a relation between the sign of the Siverson function and the anomalous magnetic moment of a given quark flavour was given [42]. Moreover, a sum rule relating the Siverson effect for quarks and

gluons was derived [43]. It was also proposed to measure the gluon Sivers function through jet correlations in $p^\uparrow p$ -collisions [44], and charm production ($p^\uparrow p \rightarrow DX$) [45].

5. Conclusions

We have briefly reviewed the status of the QCD spin structure of the nucleon. Currently, an enormous amount of activities is dealing with this vast and very interesting field.

Historically, the first subject which was studied intensely is the physics of parton helicity distributions, and today we already have a considerable knowledge about the quark helicity distribution. Uncertainties still exist in the strange quark sector and in the separation of valence and sea quark distributions, but many current activities are aimed at an improvement of this situation. In contrast to Δq , the gluon helicity distribution is still only weakly constrained. Nevertheless, a lot of new information, which is supposed to come in the near future from COMPASS and the various measurements at RHIC, will certainly increase our knowledge about Δg .

Also generalized parton distributions can provide important information in order to resolve the spin puzzle of the nucleon, because the orbital angular momentum of partons is related to these objects. Using Lattice QCD as well as phenomenological approaches, people have exploited this connection to determine the orbital angular momentum of quarks. At present, the situation is not yet conclusive, but should definitely improve in the future. In particular, many new preliminary data for hard exclusive reactions on the nucleon from COMPASS, HERMES, and Jefferson Lab exist. These data will also help to clarify the role played by orbital angular momentum in the spin sum rule of the nucleon.

The discovery that time-reversal odd parton distributions in general are non-zero gave a strong boost to the interesting subject of single spin asymmetries over the past three years. Since then a lot of progress has been made on both the theoretical but also the experimental side. In this context it has been a crucial discovery that the presence of the Wilson line in transverse momentum dependent correlation functions is mandatory. Because this field in some sense is still rather young, more fundamental results are to be expected. The large amount of already existing, preliminary, and forthcoming data from lepton-nucleon and proton-proton collisions will further improve our understanding of the origin of single spin asymmetries.

References

1. R. Frisch and O. Stern, *Z. Phys.* **85**, 4 (1933).
2. M. Anselmino, A. V. Efremov, and E. Leader, *Phys. Rep.* **261**, 1 (1995).
3. B. Lampe and E. Reya, *Phys. Rep.* **332**, 1 (2000).
4. B. W. Filippone and X. Ji, *Adv. Nucl. Phys.* **26**, 1 (2001).
5. S. D. Bass, hep-ph/0411005.
6. HERMES Collaboration (A. Airapetian *et al.*), *Phys. Rev. Lett.* **92**, 012005 (2003); hep-ex/0407032.
7. A. Kotzinian, hep-ph/0410093.
8. E. Christova and E. Leader, *Nucl. Phys.* **B 607**, 369 (2001).
9. A. N. Sissakian, O. Yu. Shevchenko, and O. N. Ivanov, hep-ph/04112243.

10. N. S. Craigie *et al.*, *Phys. Rep.* **99**, 69 (1983); and references therein.
11. G. Bunce *et al.*, *Ann. Rev. Nucl. Part. Sci.* **50**, 525 (2000).
12. COMPASS proposal, CERN/SPSLC 96-14, SPSLC/P297, (1996); F. Bradamante, hep-ex/0411076.
13. HERMES Collaboration (A. Airapetian *et al.*), *Phys. Rev. Lett* **84**, 2584 (2000).
14. SMC Collaboration (B. Adeva *et al.*), *Phys. Rev. D* **70**, 012002 (2004).
15. B. Jäger *et al.*, *Phys. Rev. D* **67**, 054005 (2003).
16. B. Jäger *et al.*, *Phys. Rev. Lett* **92**, 121803 (2004).
17. B. Jäger, M. Stratmann, and W. Vogelsang, *Phys. Rev. D* **70**, 034010 (2004).
18. PHENIX Collaboration (S. S. Adler *et al.*), *Phys. Rev. Lett* **93**, 202002 (2004).
19. X. Ji, *Phys. Rev. Lett.* **78**, 610 (1997).
20. D. Müller *et al.*, *Fortsch. Phys.* **42**, 101 (1994).
21. M. Diehl, *Phys. Rep.* **388**, 41 (2003).
22. X. Ji, *J. Phys.* **G 24**, 1181 (1998).
23. P. V. Pobylitsa, *Phys. Rev. D* **65**, 114015 (2002).
24. M. V. Polyakov, *Phys. Lett. B* **555**, 57 (2003).
25. M. Burkardt, *Int. J. Mod. Phys. A* **18**, 173 (2003).
26. B. L. G. Bakker, E. Leader, and T. L. Trueman, hep-ph/0406139.
27. E704 Collaboration, (D. L. Adams *et al.*), *Phys. Lett. B* **264**, 462 (1991).
28. STAR Collaboration, (J. Adams *et al.*), *Phys. Rev. Lett.* **92**, 171801 (2004).
29. HERMES Collaboration, (A. Airapetian *et al.*), hep-ex/0408013.
30. A. V. Efremov and O. V. Teryaev, *Phys. Lett. B* **150**, 383 (1985).
31. J. P. Ralston and D. E. Soper, *Nucl. Phys. B* **152**, 109 (1979).
32. D. W. Sivers, *Phys. Rev. D* **41**, 83 (1990); *Phys. Rev. D* **43**, 261 (1991).
33. J. C. Collins, *Nucl. Phys. B* **396**, 161 (1993).
34. M. Anselmino *et al.*, hep-ph/0408356.
35. U. D'Alesio and F. Murgia, *Phys. Rev. D* **70**, 074009 (2004).
36. S. J. Brodsky, D. S. Hwang, and I. Schmidt, *Phys. Lett. B* **530**, 99 (2002).
37. J. C. Collins, *Phys. Lett. B* **536**, 43 (2002).
38. D. Boer, P. J. Mulders, and F. Pijlman, *Nucl. Phys. B* **667**, 201 (2003).
39. J. C. Collins and D. E. Soper, *Nucl. Phys. B* **193**, 381 (1981).
40. J. C. Collins and A. Metz, hep-ph/0408249.
41. A. Metz, *Phys. Lett. B* **549**, 139 (2002).
42. M. Burkardt, *Phys. Rev. D* **66**, 114005 (2002).
43. M. Burkardt, *Phys. Rev. D* **69**, 091501 (2004).
44. D. Boer and W. Vogelsang, *Phys. Rev. D* **69**, 094025 (2004).
45. M. Anselmino *et al.*, *Phys. Rev. D* **70**, 074025 (2004).

DISCUSSION

E. Leader:

Question: You said that COMPASS will have an excellent determination of $\Delta G(x)$ by detecting pairs of D-mesons. I wish that were true! In reality statistics will limit them to detecting only one D, so the interpretation will be a little less unambiguous. But still it is an excellent way to try to study $\Delta G(x)$.

Answer: I agree!

N. Saito:

Comment 1: A_{LL} for hadron production is proportional to $\left[\frac{\Delta g}{g}(x)\right]^2$ when $g-g$ scattering dominates, but it is proportional to $\frac{\Delta g}{g}(x) \cdot A_1^p(x)$ in prompt γ production where gluon Compton process dominates.

Comment 2: PHENIX measurement of $A_{LL}(pp \rightarrow \pi^0 X)$ is not the only constraints from hadro-production. Fermilab E704 measured $A_{LL}(pp \rightarrow \pi^0 X)$, $A_{LL}(\bar{p}p \rightarrow \pi^0 X)$ and $A_{LL}(pp \rightarrow \text{multi-photon pair } X)$ to provide some constraints on $\frac{\Delta g}{g}(x)$.

Answer to the second comment: I agree.

S. B. Nurushev:

Question: There are two types of experiments for measuring ΔG : a) polarized lp scattering, and b) hh (pp or $\bar{p}p$) scattering. I thought that the second one is preferable and suitable for extracting ΔG . What do you personally think about this subject?

Answer: In my opinion it is not clear why pp -collisions should be better. Typically everything depends on the quality of the data, the chosen kinematics and in particular the observed final state.

A. Deshpande:

Comment 1: About S. B. Nurushev question "Is determination of ΔG better in pp or lp experiments?": one should not view this as one better of the other: they are independent measurements with identical fundamental underlying physics. They are complementary.

2. About A. Metz comment "No gluon (polarized) constraints have come from DIS": it is often mentioned that DIS cannot constraint ΔG . This is wrong! The best value of unpolarized gluon distribution does come from QCD evolution of S.F.s at NLO. The only reason that has not happened yet for polarized DIS is that there is no data in the wide x, Q^2 range for that method to be effective. Future may change this. It should not be ignored that PRD58, 112002, 112003 papers by SMC and SLAC E143 have addressed this issue rigorously.

Answer to the second comment: my statement about a badly constrained gluon-distribution from inclusive DIS through evolution is of course to be understood in view of the currently available data. I didn't want to say something beyond that.

UNDERSTANDING TRANSVERSITY: PRESENT AND FUTURE

V. BARONE

Università del Piemonte Orientale and INFN, Gruppo Collegato di Alessandria, Alessandria, Italy

I review the present state of knowledge concerning transversity distributions and related observables. In particular, I discuss the phenomenology of transverse asymmetries in ep^\dagger , pp^\dagger , $p^\dagger p^\dagger$ and $\bar{p}^\dagger p^\dagger$ scattering, and the perspectives for ongoing and future research.

1. General properties of transversity

The transverse polarization, or *transversity*, distribution of quarks $h_1(x)$ – also called $\Delta_T q(x)$ – has been the subject of intense theoretical work in the last decade (for reviews, see Refs. 1 and 2), and the corresponding observables are now actively being investigated in many experiments.

Let us start by recalling the partonic definition of $h_1(x)$. Given a transversely polarized hadron, if we denote by $q_\uparrow(q_\downarrow)$ the number density of quarks with polarization parallel (antiparallel) to that of the hadron, the transversity distribution is the difference $h_1(x) = q_\uparrow(x) - q_\downarrow(x)$. In field-theoretical terms, $h_1(x)$ is given by (P and S are the momentum and the spin of the hadron, respectively)

$$h_1(x) = \int \frac{d\xi^-}{4\pi} e^{ixP^+\xi^-} \langle P, S | \bar{\psi}(0) \gamma^+ \gamma_\perp \gamma_5 \psi(\xi) | P, S \rangle \Big|_{\xi^+ = \xi_\perp = 0}, \quad (1)$$

and is a *leading-twist* quantity, like the number density $f_1(x)$ (also called $q(x)$) and the helicity distribution $g_1(x)$ (more often, and less ambiguously called $\Delta q(x)$). A Wilson line $W(0, \xi)$ should be inserted between the quark fields in (1), in order to ensure gauge invariance. In the light-cone gauge, W reduces to unity and can be omitted (this is no more true for k_T -dependent distributions, see below). The tensor charge δq is defined by

$$\langle P, S | \bar{\psi}(0) i\sigma^{\mu\nu} \gamma_5 \psi(0) | P, S \rangle = 2 \delta q S^{[\mu} P^{\nu]}, \quad (2)$$

and corresponds to the first moment of $h_1 - \bar{h}_1$: $\delta q = \int dx (h_1^q - \bar{h}_1^q)$.

An important peculiarity of h_1 is that it has no gluonic counterpart (in spin-1/2 hadrons). Therefore, it does not mix with gluons, and behaves as a non-singlet distribution.

At low x , it turns out to rise slower than g_1 by QCD evolution [3]. An angular momentum sum rule for transversity,

$$\frac{1}{2} = \frac{1}{2} \sum_{a=q,\bar{q}} \int dx h_1^a(x) + \sum_{a=q,\bar{q},g} \langle L_T \rangle^a, \quad (3)$$

has been recently proved in the framework of the quark-parton model [4]. Since transversity decreases with increasing Q^2 , the orbital angular momentum $\langle L_T \rangle$ must increase (assuming an initial zero value). Of course, it would be very interesting to study this sum rule in perturbative QCD.

The transversity distributions have been computed in a variety of models (for a review, see Ref. 1). Generally, one finds $h_1 \approx g_1$ at the model scale, i.e. for $Q^2 \lesssim 0.5 \text{ GeV}^2$ (the difference between the two quantities comes from the lower components of the quark wavefunctions). Tensor charges have been also evaluated in lattice QCD and by QCD sum rules. A summary of all estimates is: $\delta u \sim 0.7 - 1.0$, $\delta d \sim -(0.1 - 0.4)$ at $Q^2 = 10 \text{ GeV}^2$.

Examining the operator structure in (1) one sees that $h_1(x)$ is *chirally-odd*. Now, fully inclusive DIS proceeds via the so-called handbag diagram, which cannot flip the chirality of quarks. Thus, transversity distributions are *not* observable in inclusive DIS. In order to measure h_1 , the chirality must be flipped twice, so one needs either two hadrons in the initial state (hadron-hadron collisions), or one hadron in the initial state and one - at least - in the final state (semi-inclusive deep inelastic scattering, SIDIS).

2. k_T -dependent distributions related to transversity

If we ignore (or integrate over) the transverse momenta of quarks, $f_1(x)$, $g_1(x)$ and $h_1(x)$ completely describe the internal dynamics of hadrons. Taking the transverse motion of quarks into account, the number of distribution functions increases. At leading twist there are eight k_T -dependent distributions [5, 6], three of which, upon integration over \mathbf{k}_T^2 , yield $f_1(x)$, $g_1(x)$ and $h_1(x)$. The remaining five distributions are new and disappear when the hadronic tensor is integrated over \mathbf{k}_T . They are related to various correlations between \mathbf{k}_T , \mathbf{S}_T and \mathbf{S}_{qT} (the quark spin). The spin asymmetry of transversely polarized quarks inside a transversely polarized proton is given by

$$\begin{aligned} \mathcal{P}_{q^\dagger/p^\dagger}(x, \mathbf{k}_T) - \mathcal{P}_{q^\dagger/p^\dagger}(x, \mathbf{k}_T) &= (\mathbf{S}_T \cdot \mathbf{S}_{qT}) h_1(x, \mathbf{k}_T^2) \\ &- \frac{1}{M^2} \left[(\mathbf{k}_T \cdot \mathbf{S}_{qT})(\mathbf{k}_T \cdot \mathbf{S}_T) + \frac{1}{2} \mathbf{k}_T^2 (\mathbf{S}_T \cdot \mathbf{S}_{qT}) \right] h_{1T}^\perp(x, \mathbf{k}_T^2), \end{aligned} \quad (4)$$

and contains not only the unintegrated transversity distribution $h_1(x, \mathbf{k}_T^2)$, but also another distribution function, called $h_{1T}^\perp(x, \mathbf{k}_T^2)$. Both h_1 and h_{1T}^\perp contribute to single-spin asymmetries in SIDIS (via Collins effect), but with different angular distributions, $\sin(\phi_h + \phi_S)$ and $\sin(3\phi_h - \phi_S)$ respectively (see below). Consider now unpolarized quarks inside a transversely polarized proton. They may have an azimuthal asymmetry of the form

$$\mathcal{P}_{q/p^\dagger}(x, \mathbf{k}_T) - \mathcal{P}_{q/p^\dagger}(x, -\mathbf{k}_T) = \frac{(\mathbf{k}_T \times \hat{\mathbf{P}}) \cdot \mathbf{S}_T}{M} f_{1T}^\perp(x, \mathbf{k}_T^2), \quad (5)$$

where f_{1T}^\perp is the *Sivers distribution function* [7]. Specularly, transversely polarized quarks inside an unpolarized proton admit a possible spin asymmetry of the form

$$\mathcal{P}_{q^\dagger/p}(x, \mathbf{k}_T) - \mathcal{P}_{q/p}(x, \mathbf{k}_T) = \frac{(\mathbf{k}_T \times \hat{\mathbf{P}}) \cdot \mathbf{S}_{qT}}{M} h_1^\perp(x, \mathbf{k}_T^2), \quad (6)$$

where h_1^\perp is the so-called *Boer–Mulders distribution function* [8]. The two distributions f_{1T}^\perp and h_1^\perp are associated with the *T-odd* correlations $(\hat{\mathbf{P}} \times \mathbf{k}_T) \cdot \mathbf{S}_T$ and $(\hat{\mathbf{P}} \times \mathbf{k}_T) \cdot \mathbf{S}_{qT}$. To see the implications of time-reversal invariance, let us write the operator definition of the Sivers function:

$$f_{1T}^\perp(x, \mathbf{k}_T^2) \sim \int d\xi^- \int d\xi_T e^{ixP^+ \xi^- - ik_T \cdot \xi_T} \times \langle P, S_T | \bar{\psi}(\xi) \gamma^+ W(0, \xi) \psi(0) | P, S_T \rangle \quad (7)$$

If we naïvely set the Wilson link W to $\mathbb{1}$, the matrix element in (7) changes sign under time reversal T ; hence the Sivers function must be zero [9]. On the other hand, a direct calculation [10] in a quark-spectator model shows that f_{1T}^\perp is non-vanishing: gluon exchange between the struck quark and the target remnant generates a non-zero Sivers asymmetry (the presence of a quark transverse momentum smaller than Q ensures that this asymmetry is proportional to M/k_T , rather than to M/Q , and therefore is a leading-twist observable). The puzzle is solved by carefully considering the Wilson line in (7) [11]. For the case at hand (SIDIS), $W(0, \xi)$ includes a link at ∞^- which does not reduce to $\mathbb{1}$ in the light-cone gauge [12]. Time reversal changes a future-pointing Wilson line into a past-pointing Wilson line, and therefore invariance under T , rather than constraining f_{1T}^\perp to zero, gives a relation between processes that probe Wilson lines pointing in opposite time directions. In particular, since in SIDIS the Sivers asymmetry arises from the interaction between the spectator and the outgoing quark, whereas in Drell-Yan processes it is due to the interaction between the spectator and an incoming quark, one gets $f_{1T}^\perp(x, \mathbf{k}_T^2)_{\text{SIDIS}} = -f_{1T}^\perp(x, \mathbf{k}_T^2)_{\text{DY}}$. This is an example of the “time-reversal modified universality” of distribution functions in SIDIS, Drell-Yan production and e^+e^- annihilation studied by Collins and Metz [13]. More complicated Wilson link structures in various hard processes have been investigated by Bomhof, Mulders and Pijlman [14]. The issue is not completely settled and more theoretical work seems to be needed in order to fully clarify the universality properties of k_T -dependent distributions. Finally, it is known [15] that at twist 3, effective *T-odd* distributions emerge from gluonic poles. The precise connection between k_T -dependent and twist-3 distributions is another problem that deserves further study.

3. Probing transversity

3.1. *Semi-inclusive deep inelastic scattering*

Let us start with the single-spin process $e p^\uparrow \rightarrow e' \pi X$, for which some data are already available. In order to have a non-vanishing asymmetry, one must consider the transverse motion of quarks. The non-collinear factorization theorem has been recently proven by Ji, Ma and Yuan [16] for $P_{hT} \ll Q$. A single-spin transverse asymmetry is due either to: *i*) a

spin asymmetry of transversely polarized quarks fragmenting into the unpolarized hadron, the so-called *Collins effect* involving

$$\mathcal{N}_{h/q\uparrow}(z, \mathbf{P}_{hT}) - \mathcal{N}_{h/q\downarrow}(z, \mathbf{P}_{hT}) = \frac{(\hat{\mathbf{k}}_T \times \mathbf{P}_{hT}) \cdot \mathbf{S}_{qT}}{z M_h} H_1^\perp(z, \mathbf{P}_{hT}^2), \quad (8)$$

a T -odd function not forbidden by time reversal invariance (due to final-state interactions); or to *ii*) an azimuthal asymmetry of unpolarized quarks inside the transversely polarized proton, the so-called *Sivers effect*, involving f_{1T}^\perp . The differential cross section for $e p^\uparrow \rightarrow e' \pi X$ is

$$\begin{aligned} d\sigma \sim A(y) \mathcal{J} \left[\frac{\boldsymbol{\kappa}_T \cdot \hat{\mathbf{P}}_{hT}}{M_h} h_1 H_1^\perp \right] \sin(\phi_h + \phi_S) \\ + B(y) \mathcal{J} \left[\frac{\mathbf{k}_T \cdot \hat{\mathbf{P}}_{hT}}{M_h} f_{1T}^\perp D_1 \right] \sin(\phi_h - \phi_S) \\ + C(y) \mathcal{J} \left[\lambda(\mathbf{k}_T, \boldsymbol{\kappa}_T, \hat{\mathbf{P}}_{hT}) h_{1T}^\perp H_1^\perp \right] \sin(3\phi_h - \phi_S), \end{aligned} \quad (9)$$

where $\mathcal{J}[\dots]$ is a convolution integral over \mathbf{k}_T and $\boldsymbol{\kappa}_T$. As one can see, there is a variety of angular distributions which combine in different ways the two physical angles ϕ_h and ϕ_S . In particular, the Collins effect is associated with $\sin(\phi_h + \phi_S)$, and also with $\sin(3\phi_h - \phi_S)$ if the transverse motion of quarks inside the target is not neglected, whereas the Sivers effect is associated with a $\sin(\phi_h - \phi_S)$ distribution. One can disentangle these angular distributions by taking the azimuthal moments of the asymmetries. For instance, the Collins moment is

$$\langle \sin(\phi_h + \phi_S) \rangle \equiv \frac{\int d\phi_h d\phi_S \sin(\phi_h + \phi_S) [d\sigma(\phi_h, \phi_S) - d\sigma(\phi_h, \phi_S + \pi)]}{\int d\phi_h d\phi_S [d\sigma(\phi_h, \phi_S) + d\sigma(\phi_h, \phi_S + \pi)]}. \quad (10)$$

Recently, the HERMES Collaboration [17] reported the first measurement of the Collins moment $\langle \sin(\phi_h + \phi_S) \rangle$ and of the Sivers moment $\langle \sin(\phi_h - \phi_S) \rangle$, in the region $0.02 < x < 0.4$, $0.2 < z < 0.7$, at $\langle Q^2 \rangle = 2.4 \text{ GeV}^2$. The Collins asymmetry $A_T^{\pi^+}$ is found to be positive, whereas $A_T^{\pi^-}$ is negative. This is consistent with the fact that $h_1^u > 0$ and $h_1^d < 0$. However, $A_T^{\pi^-}$ is negative and its absolute value $|A_T^{\pi^-}|$ is larger than $|A_T^{\pi^+}|$, whereas one expects from models $|h_1^d| \ll |h_1^u|$. Recalling that $A_T^{\pi^+}$ and $A_T^{\pi^-}$ involve the following combinations of distribution and fragmentation functions ('fav' = favoured, 'unf' = unfavoured)

$$A_T^{\pi^+} : 4h_1^u H_1^{\perp \text{fav}} + h_1^d H_1^{\perp \text{unf}}, \quad A_T^{\pi^-} : h_1^d H_1^{\perp \text{fav}} + 4h_1^u H_1^{\perp \text{unf}} \quad (11)$$

one sees that the π^- data seem to require large unfavoured Collins functions, with $H_1^{\perp \text{unf}} \approx -H_1^{\perp \text{fav}}$. It would be very useful to get some independent information on H_1^\perp from other processes: in this respect, the forthcoming extraction of H_1^\perp from e^+e^- annihilation data in the Belle experiment at KEK will be extremely important [18]. There are also preliminary HERMES results on the π^0 asymmetry, showing a largely negative $A_T^{\pi^0}$, similar to $A_T^{\pi^-}$. This is quite a controversial finding, as it conflicts with expectations based on isospin invariance. The Collins asymmetry has also been measured by the COMPASS Collaboration with a deuteron target [19]. In the $x \lesssim 0.1$ region, it is found to be compatible with zero for both π^+ and π^- , as expected quite generally at small x . Concerning Sivers asymmetries, HERMES

find $A_T^{\pi^+} > 0$: this is the first evidence of a non-vanishing Siverson function f_{1T}^\perp , although – due to the smallness of $A_T^{\pi^+}$ and the present uncertainties – more precise data are needed to draw a definite conclusion.

Another access to transversity in the context of SIDIS is offered by the double-spin process $e p^\uparrow \rightarrow e' \Lambda^\uparrow X$ (transversely polarized Λ production), which probes the fragmentation analog of h_1 , i.e. $H_1(z) = \mathcal{N}_{h^\uparrow/q^\uparrow}(z) - \mathcal{N}_{h^\uparrow/q^\downarrow}(z)$. Unfortunately, it is hard to predict the Λ polarization, because $H_{1\Lambda}$ is unknown (see, however, some attempts in Ref. 20). An analysis of data on transversely polarized Λ production is currently being performed by the COMPASS Collaboration [21].

A third promising process to detect transversity is two-pion production in $e p^\uparrow$ scattering. In this case, after integrating the cross sections over \mathbf{P}_{hT} , one finds that the single-spin asymmetry depends on an interference fragmentation function $I(z, M_h^2)$, arising from the interference between different partial waves of the two-pion system [22]. The extraction of this function is under way [23].

3.2. Pion hadroproduction

Collins and Siverson effects also manifest themselves in pion hadroproduction with a transversely polarized target. A non-vanishing asymmetry is generated either by quark transverse momenta or by higher-twist effects. The non-collinear factorization formula is, in this case, only conjectured. Assuming its validity, the Collins asymmetry reads

$$d\sigma^\uparrow - d\sigma^\downarrow \sim \sum_{abc} [h_1(x_a, \mathbf{k}_T^2) + (\mathbf{k}_T^2/M^2) h_{1T}^\perp(x_a, \mathbf{k}_T^2)] \otimes f_1(x_b, \mathbf{k}_T'^2) \\ \otimes \Delta_{TT} \hat{\sigma}(a^\uparrow b \rightarrow c^\uparrow d) \otimes H_1^\perp(z, \kappa_T^2),$$

whereas the Siverson asymmetry is

$$d\sigma^\uparrow - d\sigma^\downarrow \sim f_{1T}^\perp(x_a, \mathbf{k}_T^2) \otimes f_1(x_b, \mathbf{k}_T'^2) \otimes d\hat{\sigma}(ab \rightarrow cd) \otimes D_1(z, \kappa_T^2). \quad (12)$$

An extensive and detailed treatment of single-spin asymmetries in the framework of non-collinear factorization has been presented in Refs. 24 and 25. The main finding is that the Collins asymmetry alone is unable to reproduce the E704 [26] and STAR [27] data: the Collins effect turns out to be suppressed due to kinematic phases occurring in non-collinear partonic subprocesses (this does not imply anything about the magnitude of H_1^\perp). On the contrary, the Siverson mechanism is not affected by a similar suppression. A major shortcoming of pion hadroproduction is that it depends on one physical angle only, so that all asymmetry mechanisms are entangled. A possible way to avoid this problem is to study a less inclusive process, such as pion + jet production, as advocated by Teryaev (private communication).

In a recent paper, Bourrely and Soffer [28] argued that, since collinear pQCD correctly reproduces the large- \sqrt{s} STAR unpolarized cross sections but fails to describe the small- \sqrt{s} E704 data, the single-spin asymmetries measured by these two experiments are actually different phenomena, and in particular the E704 asymmetry “cannot be attributed to pQCD”. Two comments are in order: first of all, higher-twist effects might be important, since $\langle P_{hT} \rangle$

is not so large (typically, around 1-2 GeV). Second, as shown by D'Alesio and Murgia [25], quark transverse momenta considerably improve the agreement of the pQCD calculations with the small- \sqrt{s} unpolarized cross sections.

3.3. Drell-Yan processes

Drell-Yan production in $p^\uparrow p^\uparrow$ collisions is the cleanest process that probes transversity. The double-spin asymmetry A_{TT}^{DY} , in fact, contains only combinations of the transversity distributions. At leading order, for instance, one has

$$A_{TT}^{DY}(pp) \sim \frac{\sum_q e_q^2 h_1^q(x_1, M^2) \bar{h}_1^q(x_2, M^2) + [1 \leftrightarrow 2]}{\sum_q e_q^2 f_1^q(x_1, M^2) \bar{f}_1^q(x_2, M^2) + [1 \leftrightarrow 2]}. \quad (13)$$

It turns out, however, that at the energies of RHIC (where this process will be studied [29]) this asymmetry is rather small [30, 31] (about 1 – 2%; similar values are found for transverse double-spin asymmetries in prompt photon production [32]). The reason is twofold: 1) $A_{TT}^{DY}(pp)$ contains antiquark transversity distributions, which are small; 2) RHIC kinematics ($\sqrt{s} = 200$ GeV, $M < 10$ GeV, $x_1 x_2 = M^2/s \lesssim 3 \times 10^{-3}$) probes the low- x region, where h_1 rises slowly. The problem could be circumvented by considering $\bar{p}^\uparrow p^\uparrow$ scattering at more moderate energies. In this case a much larger asymmetry is expected [30, 33, 34], since $A_{TT}^{DY}(\bar{p}p)$ contains products of valence distributions at medium x . The PAX Collaboration has proposed to study $\bar{p}^\uparrow p^\uparrow$ -initiated Drell-Yan production at the High-Energy Storage Ring of GSI, in the kinematic region $30 \text{ GeV}^2 \lesssim s \lesssim 45 \text{ GeV}^2$, $M \gtrsim 2 \text{ GeV}$, $x_1 x_2 \gtrsim 0.1$ [35]. Leading-order predictions for the $\bar{p}p$ asymmetry in this regime are shown in Fig. 1 (left). $A_{TT}^{DY}(\bar{p}p)$ is as large as 0.3 at $M = 4$ GeV, but counting rates are small and this makes the measurement arduous. Things become easier if one looks at the J/ψ peak, where the production rate is larger by two orders of magnitude. Assuming the dominance of $q\bar{q}$ fusion (as suggested by a comparison of pp and $\bar{p}p$ cross sections at the CERN SPS), the J/ψ production double transverse asymmetry $A_{TT}^{J/\psi}(\bar{p}p)$ has the same structure as Eq. (13), with the electric charges replaced by the $q\bar{q} - J/\psi$ couplings. These cancel out in the ratio, and hence $A_{TT}^{J/\psi}(\bar{p}p)$, which is dominated by the u sector, becomes

$$A_{TT}^{J/\psi}(\bar{p}p) \sim \frac{h_1^u(x_1, M_{J/\psi}^2) h_1^u(x_2, M_{J/\psi}^2)}{f_1^u(x_1, M_{J/\psi}^2) f_1^u(x_2, M_{J/\psi}^2)}. \quad (14)$$

This asymmetry is also of the order of 0.3 (Fig. 1, right) and, by measuring it, one can directly extract the u transversity distribution.

4. Conclusions and perspectives

Transversity is currently a very hot topic in high-energy spin physics. From the theoretical point of view, a lot of work has been done and h_1 is by now rather well known. On the experimental side, the era of data has at last arrived: single-spin processes are under study and the first results are already a matter of phenomenological analysis. Double-spin processes

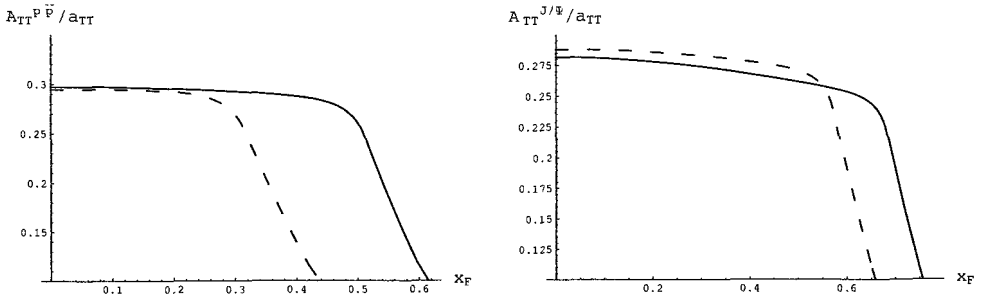


Fig. 1. Transverse double spin asymmetry in $\bar{p}^\uparrow p^\uparrow$ Drell-Yan production at $M = 4 \text{ GeV}$ (left) and for J/ψ production (right), as a function of $x_F = x_1 - x_2$. Solid (dashed) lines correspond to $s = 45$ (30) GeV^2 .

are experimentally more difficult but theoretically cleaner, and their investigation is certainly worth the effort. While we look forward to more - and more precise - data, the main goal of theory is to achieve a solid picture of single-spin transverse asymmetries (shedding further light on k_T and higher-twist effects), in view of future global studies of transversity measurements.

Acknowledgments

I am grateful to the organizers of SPIN04 for their invitation to this beautiful Symposium. I would also like to thank M. Anselmino, U. D'Alesio, A. Efremov, L. Gamberg, A. Kotzinian, A. Prokudin, P. Ratcliffe and O. Teryaev for useful discussions.

References

1. V. Barone, A. Drago and P.G. Ratcliffe, *Phys. Rep.* **359**, 1 (2002).
2. V. Barone and P.G. Ratcliffe, *Transverse Spin Physics*, World Scientific, Singapore, 2003.
3. V. Barone, *Phys. Lett.* **B409**, 499 (1997). V. Barone, T. Calarco and A. Drago, *Phys. Lett.* **B390**, 287 (1997).
4. B.L.G. Bakker, E. Leader and T.L. Trueman, hep-ph/0406139.
5. P.J. Mulders and R.D. Tangerman, *Nucl. Phys.* **B461**, 197 (1996).
6. A. Kotzinian, *Nucl. Phys.* **B441**, 234 (1995).
7. D. Sivers, *Phys. Rev.* **D41**, 83 (1990).
8. D. Boer and P.J. Mulders, *Phys. Rev.* **D57**, 5780 (1998).
9. J.C. Collins, *Nucl. Phys.* **B396**, 161 (1993).
10. S.J. Brodsky, D.S. Hwang and I. Schmidt, *Phys. Lett.* **B530**, 99 (2002).
11. J.C. Collins, *Phys. Lett.* **B536**, 43 (2002).
12. A.V. Belitsky, X. Ji and F. Yuan, *Nucl. Phys.* **B656**, 165 (2003).
13. J. C. Collins and A. Metz, hep-ph/0408249.
14. C. J. Bomhof, P. J. Mulders and F. Pijlman, *Phys. Lett.* **B596**, 277 (2004).
15. D. Boer, P.J. Mulders and O.V. Teryaev, *Phys. Rev.* **D57**, 3057 (1997).
16. X. Ji, J. P. Ma and F. Yuan, *Phys. Lett.* **B597**, 299 (2004).
17. A. Airapetian et al. (HERMES), hep-ex/0408013.
18. R. Seidl (Belle), contribution to these Proceedings.
19. P. Pagano (COMPASS), contribution to these Proceedings.
20. M. Anselmino, M. Boglione and F. Murgia, *Phys. Lett.* **B481**, 253 (2000).

21. A. Bressan (COMPASS), contribution to these Proceedings.
22. R.L. Jaffe, X.-M. Jin and J. Tang, *Phys. Rev. Lett.* **80**, 1166 (1998). M. Radici, R. Jakob and A. Bianconi, *Phys. Rev.* **D65**, 074031 (2002). A. Bacchetta and M. Radici, *Phys. Rev.* **D67**, 094002 (2003).
23. R. Joosten (COMPASS), contribution to these Proceedings.
24. M. Anselmino et al., hep-ph/0408356.
25. U. D'Alesio and F. Murgia, *Phys. Rev.* **D70**, 074009 (2004).
26. D.L. Adams et al. (E704), *Phys. Lett.* **B264**, 462 (1991). A. Bravar et al. (E704), *Phys. Rev. Lett.* **77**, 2626 (1996).
27. J. Adams et al. (STAR), *Phys. Rev. Lett.* **92**, 171801 (2004).
28. C. Bourrely and J. Soffer, *Eur. Phys. J.* **C36**, 371 (2004).
29. G. Bunce, N. Saito, J. Soffer and W. Vogelsang, *Ann. Rev. Nucl. Part. Sci.* **50**, 525 (2000). N. Saito, contribution to these Proceedings.
30. V. Barone, T. Calarco and A. Drago, *Phys. Rev.* **D56**, 527 (1997).
31. O. Martin, A. Schäfer, M. Stratmann and W. Vogelsang, *Phys. Rev.* **D57**, 3084 (1998).
32. A. Mukherjee, M. Stratmann and W. Vogelsang, *Phys. Rev.* **D67**, 114006 (2003).
33. M. Anselmino, V. Barone, A. Drago and N. N. Nikolaev, *Phys. Lett.* **B594**, 97 (2004).
34. A.V. Efremov, K. Goeke and P. Schweitzer, *Eur. Phys. J.* **C35**, 207 (2004).
35. F. Rathmann, contribution to these Proceedings.

DISCUSSION

R. Bertini:

Comment: you forgot to mention the ASSIA LoI at GSI, that looks for transversity.

Question: what can be said about the relationship between f_{1T}^\perp and h_1^\perp ?

Answer: The ASSIA proposal is about $\bar{p}p^\dagger$ scattering, whereas I focused on double-spin Drell-Yan processes. Concerning f_{1T}^\perp and h_1^\perp , they are independent functions. So, any relation between them that one may find in a model calculation depends on the assumptions of the model (see, e.g., L. Gamberg's talk).

S. B. Nurushev:

Question: I was surprised to hear about the polarized quark distribution inside an unpolarized proton. May be I missed some essential element in your explanation. No spin-orbit interaction (I assume external) can lead to polarized quarks. Please explain me this subject.

Answer: the distribution of transversely polarized quarks inside an unpolarized proton (the so-called Boer - Mulders function h_1^\perp) arises from a correlation between the quark transverse momentum \vec{k}_T and the quark transverse spin \vec{S}_{qT} .

O. Teryaev:

Comment: I would like to support the relevance of higher twists for the difference between E704 and RHIC pointed out by Bourrely and Soffer. Indeed for E704 larger partonic x are relevant, where higher twists are known to rise. They are related by positivity to particular QCD twist-3 mechanisms (gluonic pole), which are definitively important at E704 but may be rising too strongly for RHIC. Bourrely and Soffer conclusion may be therefore

rephrased as that unpolarized cross-section indicate the relevance of different QCD mechanisms at E704 and RHIC.

A. Efremov:

Comment: First, let me notice that the observed $A_T^{\pi^0} \approx A_T^{\pi^-}$ contradicts the x and z factorization, which gives

$$A_T^{\pi^0} = \frac{\sigma^{\pi^+}}{\sigma^{\pi^+} + \sigma^{\pi^-}} A_T^{\pi^+} + \frac{\sigma^{\pi^-}}{\sigma^{\pi^+} + \sigma^{\pi^-}} A_T^{\pi^-},$$

or

$$A_T^{\pi^0} - A_T^{\pi^-} = \frac{\sigma^{\pi^+}}{\sigma^{\pi^+} + \sigma^{\pi^-}} (A_T^{\pi^+} - A_T^{\pi^-}),$$

since the r.h.s. is definitely different from zero. So, the x and z factorization should be carefully checked. Second, I would like to draw the attention to the $\sin 2\phi_h$ asymmetry for longitudinal target polarization which is only due to Collins fragmentation function and transversity, and was experimentally measured by the CLAS Collaboration.

Answer: I agree with you that the preliminary data on the π^0 asymmetry raise some doubts, and that the assumption of x and z factorization should be checked. As for the $\sin 2\phi_h$ asymmetry, I did not mention it since it involves not h_1 (which was the subject of my talk) but another transverse polarization distribution called h_{1L}^\perp .

F. Rathmann:

Comment: The speaker mentioned that \bar{p} polarization in the HESR of GSI could reach 5%. The achievable polarization is strongly energy dependent and with a dedicated \bar{p} polarizer ring, polarizations of about 0.2 - 0.4 are reachable (see my talk at this Symposium).

Answer: I mentioned the \bar{p} polarization value of 5% used in the PAX Letter of Intent to estimate the expected uncertainties on double-spin asymmetries. Higher antiproton polarizations are obviously welcome.

E. Leader:

Comment: You have mentioned some problems or difficulties in some of the HERMES results, especially involving π^0 s. I just want to draw attention to a recent paper of Kotzinian which raises some doubts about the reliability of the method of analysis used by HERMES.

Answer: Yes, I did not have time to discuss all of the problems raised by the data.

A.D. Krisch:

Question: I am very pleased that you indicated that transversity is one of the hot topics in spin physics. When this Symposium series started in 1974, transversity was also a hot topic because all polarized beams and targets were transversely polarized. Moreover the 1978 double-spin experiments at the ZGS on high p_T elastic scattering found that the spin-parallel cross-section was four times larger than the spin-antiparallel cross-section. This completely disagreed with QCD as it existed at that time. Then in the 1980's similar elastic

single-spin experiments found large one-spin asymmetries which grew larger as p_T increased, again in total disagreement with the modified QCD which existed in 1985 and then 1990. Has any progress been made in understanding theoretically, these large, clear, and unexpected effects in the last three decades?

Answer: When we speak today about “transversity”, we refer to transverse polarization effects in hard processes, probing the perturbative dynamics of quarks and gluons. In this sense, “transversity” is a relatively new subject, developed in the 90’s. As you recalled, in the 70’s-80’s there were a wealth of transverse spin measurements in exclusive processes, such as elastic scattering. As far as I know, this phenomenology is not fully understood yet from a theoretical point of view (in particular, it is not clear to what extent one can apply perturbative QCD to exclusive reactions). I would like to add that some mechanisms proposed in the past to explain transverse spin phenomena in soft physics reappeared recently in the context of modern “transversity” [see, e.g., P. Cea, G. Nardulli and P. Chiappetta, *Phys. Lett.* **B209**, 333 (1988)].

RESULTS AND FUTURE PROSPECTS FOR MUON ($g - 2$) *

B. L. ROBERTS

Department of Physics, Boston University, Boston, USA

(on behalf of the Muon ($g - 2$) Collaboration.^{11,12,13})

Spin physics had its beginnings in the famous experiments of Stern and Gerlach, which eventually resulted in the postulation of spin by Goudsmit and Uhlenbeck. The Stern-Gerlach experiment told us that the g -value of the electron was 2, but we now know that because of radiative corrections, the g -value of the leptons is slightly greater than 2, the lowest-order contribution being α/π , where α is the fine-structure constant. Measurements of the magnetic dipole moments of the electron and muon have played a major role in our understanding of QED and of the standard model. In this talk I discuss the progress on measurements and theory of the magnetic dipole moment of the muon.

1. Theory of the Lepton Anomalies

Over the past 83 years, the study of dipole moments of elementary particles has provided a wealth of information on subatomic physics, and more recently has provided topics of interest to this conference. The pioneering work of Stern [1] led to the discovery of spin, and showed that $g_e \simeq 2$. This set the stage for the precision measurements by Foley and Kusch [4], which showed g was not exactly 2, but rather slightly larger, which was explained by Schwinger [5] and played an important role in the development of QED. Subsequently Stern [2] showed that $g_p \simeq 5.5$, and Alvarez and Bloch [3] found that the neutron had a magnetic moment, which eventually helped lead to the quark models of the baryons. In the 1980s, measuring hyperon magnetic moments to test quark models became an industry that was well covered in earlier installments of these spin conferences, and in which I had the pleasure of participating.

A charged particle with spin \vec{s} has a magnetic moment

$$\vec{\mu}_s = g_s \left(\frac{e}{2m} \right) \vec{s}; \quad a \equiv \frac{(g_s - 2)}{2}; \quad \mu = (1 + a) \frac{e\hbar}{2m}; \quad (1)$$

where g_s is the gyromagnetic ratio, a is the anomaly, and the latter expression is what one finds in the Particle Data Tables [6].

For point particles, the anomaly arises from radiative corrections. The QED contribution to a (or g) is an expansion in $\left(\frac{\alpha}{\pi}\right)$, $a = \sum_{n=1} C_n \left(\frac{\alpha}{\pi}\right)^n$, with one diagram for the

*This work is supported in part by the U.S. National Science Foundation and the U.S. Department of Energy.

Schwinger (second-order) contribution (where $C_1 = 0.5$), five for the fourth order, 40 for the sixth order, and 891 for the eighth order. The QED contributions to electron and muon ($g-2$) have now been calculated through eighth order, $(\alpha/\pi)^4$, and the tenth-order contribution has been estimated [7].

The electron anomaly is measured to a relative precision of about 4 parts in a billion (ppb) [8], which is better than the precision on the fine-structure constant α , and Kinoshita has used the measured electron anomaly to give the best determination of α [9]. The electron anomaly will be further improved over the next few years [10].

The muon anomaly has been measured to 0.5 parts per million (ppm) [11–13]. The relative contributions of heavier particles to a scales as $(m_e/m_\mu)^2$, so the muon has an increased sensitivity to higher mass scale radiative corrections of about 40,000 over the electron. At a precision of ~ 0.5 ppm, the muon anomaly is sensitive to ≥ 100 GeV scale physics.

The standard model value of a_μ has measurable contributions from three types of radiative processes: QED loops containing leptons (e, μ, τ) and photons; [7] hadronic loops containing hadrons in vacuum polarization loops; [14–18] and weak loops involving the W and Z weak gauge bosons (the standard model Higgs contribution is negligible) [14], $a_\mu(\text{SM}) = a_\mu(\text{QED}) + a_\mu(\text{Had}) + a_\mu(\text{Weak})$. A significant difference between the experimental value and the standard model prediction would signify the presence of new physics. A few examples of such potential contributions are lepton substructure, anomalous $W - \gamma$ couplings, and supersymmetry [14].

The CERN experiment [19] observed the contribution of hadronic vacuum polarization shown in Fig. 1(a) at the eight standard deviation level. Unfortunately, the hadronic contribution cannot be calculated directly from QCD, since the energy scale is very low ($m_\mu c^2$), although Blum [20] has performed a proof of principle calculation on the lattice. Fortunately dispersion theory gives a relationship between the vacuum polarization loop and the cross section for $e^+e^- \rightarrow \text{hadrons}$,

$$a_\mu(\text{Had}; 1) = \left(\frac{\alpha m_\mu}{3\pi}\right)^2 \int_{4m_\pi^2}^{\infty} \frac{ds}{s^2} K(s) R(s); \quad R \equiv \frac{\sigma_{\text{tot}}(e^+e^- \rightarrow \text{hadrons})}{\sigma_{\text{tot}}(e^+e^- \rightarrow \mu^+\mu^-)} \quad (2)$$

and experimental data are used as input. The factor s^{-2} in the dispersion relation means that values of $R(s)$ at low energies (the ρ resonance) dominate the determination of $a_\mu(\text{Had}; 1)$. In principle, this information could be obtained from hadronic τ^- decays such as $\tau^- \rightarrow \pi^- \pi^0 \nu_\tau$, which can be related to e^+e^- annihilation through the CVC hypothesis and isospin conservation [15]. However, inconsistencies between information obtained from e^+e^- annihilation and hadronic tau decays, plus an independent confirmation of the CMD2 high-precision e^+e^- cross-section measurements by the KLOE collaboration [21], have prompted Davier, Höcker, et al., to state that until these inconsistencies can be understood only the e^+e^- data should be used to determine $a_\mu(\text{Had}; 1)$ [17].

The hadronic light-by-light contribution (see Fig. 1(e)) has been the topic of much theoretical investigation [18]. Unlike the lowest-order contribution, it can only be calculated from a model, and this contribution is likely to provide the ultimate limit to the precision of the standard-model value of a_μ .

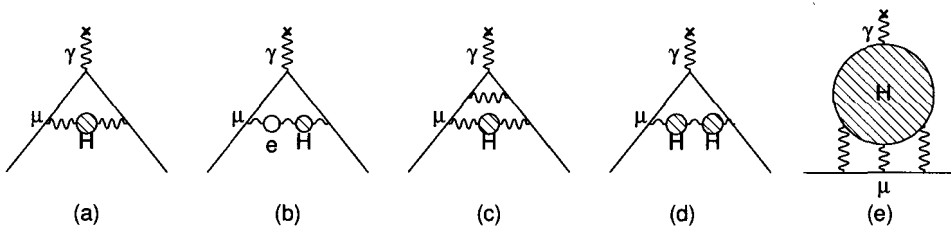


Fig. 1. The hadronic contribution to the muon anomaly, where the dominant contribution comes from (a). The hadronic light-by-light contribution is shown in (e).

One of the very useful roles the measurements of a_μ have played in the past is placing serious restrictions on physics beyond the standard model. With the development of supersymmetric theories as a favored scheme of physics beyond the standard model, interest in the experimental and theoretical value of a_μ has grown substantially. Contributions to a_μ from SUSY or other new dynamics at the several hundred GeV scale could be at a measurable level in a broad range of models. Furthermore, there is a complementarity between the SUSY contributions to the magnetic (MDM) and electric dipole (EDM) moments, and the transition moment for the lepton-flavor violating (LFV) process $\mu^- \rightarrow e^-$ in the field of a nucleus. The MDM and EDM are related to the real and imaginary parts of the diagonal element of the slepton mixing matrix, and the transition moment is related to the off-diagonal one. See Klaus Jungmann's talk from this conference for a discussion of electric dipole moments.

2. Measurement of the muon anomaly

The methods used in the third CERN experiment and the BNL experiment are very similar, save the use of direct muon injection [22] into the storage ring [23, 24], which was developed by the E821 collaboration. These experiments are based on the fact that for $a_\mu > 0$ the spin precesses faster than the momentum vector when a muon travels transversely to a magnetic field. The spin precession frequency ω_S consists of the Larmor and Thomas spin-precession terms. The spin frequency ω_S , and the momentum precession (cyclotron) frequency ω_C , are given by

$$\omega_S = \frac{geB}{2mc} + (1 - \gamma) \frac{eB}{\gamma mc}; \quad \omega_C = \frac{eB}{mc\gamma}; \quad \omega_a = \omega_S - \omega_C = \left(\frac{g-2}{2} \right) \frac{eB}{mc}. \quad (3)$$

The difference frequency ω_a is the frequency with which the spin precesses relative to the momentum, and is proportional to the anomaly, rather than to g . A precision measurement of a_μ requires precision measurements of the muon spin precession frequency ω_a , and the magnetic field, which is expressed as the free-proton precession frequency ω_p in the storage ring magnetic field.

The muon frequency can be measured as accurately as the counting statistics and detector apparatus permit. The design goal for the NMR magnetometer and calibration system

was a field accuracy of 0.1 ppm. The B which enters in Eq. 3 is the average field seen by the ensemble of muons in the storage ring. In E821 we reached a precision of 0.17 ppm in the magnetic field measurement.

An electric quadrupole field [25] is used for vertical focusing, taking advantage of the “magic” $\gamma = 29.3$ at which an electric field does not contribute to the spin motion relative to the momentum. With both an electric and a magnetic field, the spin difference frequency is given by

$$\vec{\omega}_a = -\frac{e}{mc} \left[a_\mu \vec{B} - \left(a_\mu - \frac{1}{\gamma^2 - 1} \right) \vec{\beta} \times \vec{E} \right], \quad (4)$$

which reduces to Eq. 3 in the absence of an electric field. For muons with $\gamma = 29.3$ in an electric field alone, the spin would follow the momentum vector.

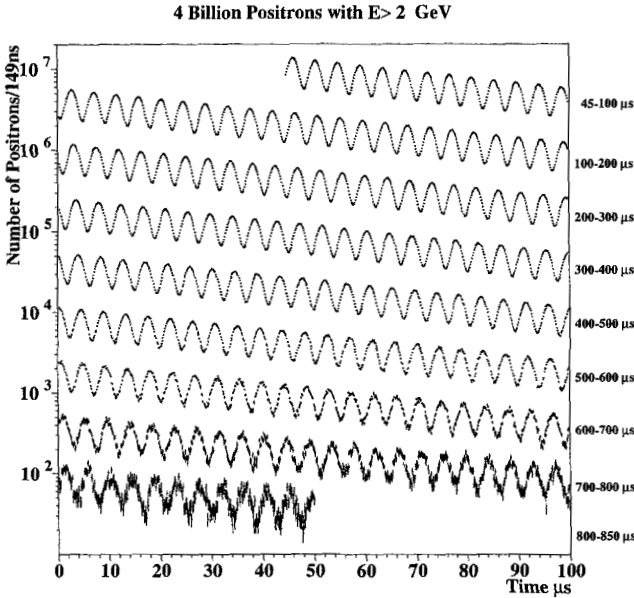


Fig. 2. The time spectrum of positrons with energy greater than 2.0 GeV from the year 2000 run. The endpoint energy is 3.1 GeV. The time interval for each of the diagonal “wiggles” is given on the right.

The experimental signal is the e^\pm from μ^\pm decay, which were detected by lead-scintillating fibre calorimeters [26]. The time and energy of each event were stored for analysis off-line. Muon decay is a three-body decay, so the 3.1 GeV muons produce a continuum of positrons (electrons) from the end-point energy down. Since the highest energy e^\pm are correlated with the muon spin, if one counts high-energy e^\pm as a function of time, one gets an exponential from muon decay modulated by the $(g-2)$ precession. The expected form for the positron time spectrum is $f(t) = N_0 e^{-\lambda t} [1 + A \cos(\omega_a t + \phi)]$; however in analyzing the data it is necessary to take a number of small effects into account in order

to obtain a satisfactory χ^2 for the fit [12, 13]. The data from our 2000 running period are shown in Fig. 2.

The experimental results from E821 are shown in Fig. 3, with the average

$$a_\mu(\text{E821}) = 11\,659\,208(6) \times 10^{-10} \quad (\pm 0.5 \text{ ppm}) \quad (5)$$

which determines the “world average”. The theory value [7, 14, 17] $a_\mu(\text{SM}) = 11\,659\,182.8(7.3) \times 10^{-10}$, (± 0.7 ppm) is determined using the strong interaction contribution from Höcker et al. [17], which updates their earlier analysis [15] with the KLOE data [21]. The value of Hagiwara et al. [16], gives an equivalent answer. The hadronic light-by-light contribution of $(12.0 \pm 3.5) \times 10^{-10}$ is taken from Davier and Marciario [14]. When the experimental value is compared to the standard model value using either of these two analyses [16, 17] for the lowest-order hadronic contribution, one finds $\Delta a_\mu(\text{E821} - \text{SM}) = (25.2 \text{ to } 26.0 \pm 9.4) \times 10^{-10}$, (2.7 standard deviations).

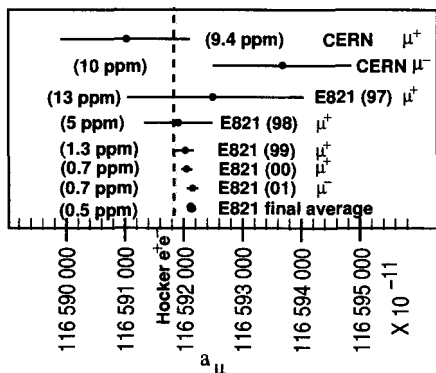


Fig. 3. Measurements of a_μ compared with the theory value described in the text.

To show the sensitivity of our measurement of a_μ to the presence of virtual electroweak gauge bosons, we subtract off the electroweak contribution of $15.4(0.1)(0.2) \times 10^{-10}$ from the standard model value, compare with experiment, and obtain $\Delta a_\mu = (40.6 \pm 9.4) \times 10^{-10}$, a 4.3 standard deviation discrepancy. This difference shows conclusively that E821 was sensitive to physics at the 100 GeV scale. At present, it is inconclusive whether we see evidence for contributions from physics beyond the standard-model gauge bosons.

With each data set, the systematic error was reduced, as can be seen from Table 1, and the experiment was statistics limited when running was ended. Given the tantalizing discrepancy between our result and the latest standard-model value, and the fact that the hadronic error could be reduced by about a factor of two over the next few years [14], we submitted a new proposal to Brookhaven to further improve the experimental measurement. The goal of this new experiment is ± 0.2 ppm total error, with the aim of controlling the total systematic errors on the magnetic field and on the muon frequency measurement to 0.1 ppm each.

Table 1. Systematic and statistical errors from the three major E821 data runs.

Data Run	ω_p (B -Field) Systematic Error (ppm)	ω_a Systematic Error (ppm)	Total Systematic Error (ppm)	Total Statistical Error (ppm)
1999	0.4	0.3	0.5	1.3
2000	0.24	0.31	0.39	0.62
2001	0.17	0.21	0.27	0.66
E969 Goal	0.1	0.1	0.14	0.14

Our proposal [27] was given enthusiastic scientific approval in September 2004 by the Laboratory, and has been given the new number E969. Negotiations are underway between the Laboratory and the funding agencies to secure funding.

The upgraded experiment will use a backwards muon beam to reduce background in the electron calorimeters. A new inflector magnet with open ends will be employed. The beamline improvements will increase the stored flux in the ring by ~ 5 , and the detectors, electronics and data acquisition system will be replaced with components which can handle the increased rates with reduced systematic errors.

In E821, the magnetic field was uniform to about one ppm, as can be seen from Figure 4. To improve our knowledge of the field from 0.17 ppm to 0.1 ppm, we will further shim the storage ring and improve on the calibration, monitoring and measurement of the magnetic field.

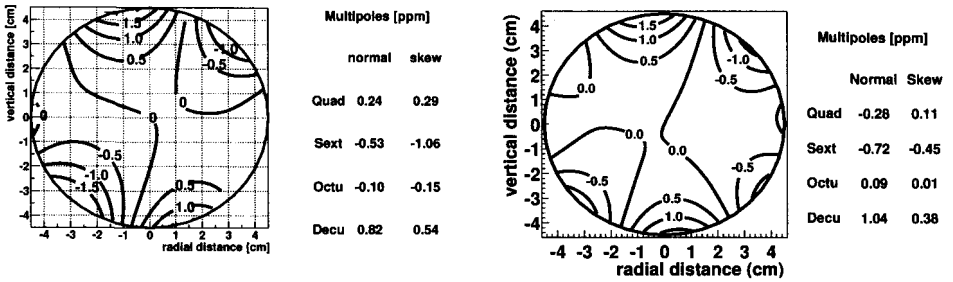


Fig. 4. The magnetic field averaged over azimuth in the storage ring for the 2000 (μ^+) (left figure) and 2001 (μ^-) (right figure) running periods. Contours represent 0.5 ppm changes. The multipole content is in ppm relative to the dipole field.

A letter of intent (LOI) for an even more precise ($g-2$) experiment was also submitted to J-PARC [28]. In that LOI we proposed to reach a precision below 0.1 ppm. Since it is not clear how well the hadronic contribution can be calculated, and whether the new Brookhaven experiment E969 will go ahead, we will evaluate whether to press forward with this experiment at a later time. Our LOI at J-PARC [28] was predicated on pushing as far as possible at Brookhaven before moving to Japan.

3. Summary and Conclusions

Muon ($g - 2$) has played an important role in constraining the standard model for many years. With the sub-ppm accuracy now available for the muon anomaly [11–13], there may be indications that new physics is beginning to appear in loop processes [29]. An enormous amount of work continues worldwide to improve on our knowledge of the hadronic contribution, and we can look forward to a factor of about two improvement over the next few years. We have proposed to improve on the precision of the measurement by a factor of two and a half. These two improvements will provide a much more sensitive confrontation with the standard model in the next few years.

Acknowledgments

I wish to thank my colleagues on the muon ($g - 2$) experiment, as well as M. Davier, J. Ellis, T. Kinoshita, E. de Rafael, W. Marciano and T. Teubner for helpful discussions. Special thanks to David Hertzog, Jim Miller and Yannis Semertzidis for helpful comments on this manuscript.

References

1. O. Stern, *Z. Phys.* **7**, 249 (1921), W. Gerlach and O. Stern, *Ann. Physik*, **74**, 1924.
2. R. Frisch and O. Stern, *Z. Phys.* **85**, 4 (1933).
3. Luis W. Alvarez and F. Bloch, *Phys. Rev.* **57**, 111 (1940).
4. H.M. Foley and P. Kusch, *Phys. Rev.* **73**, 4121 (1948).
5. J. Schwinger, *Phys. Rev.* **73**, 416L (1948).
6. Particle Data Group, *Phys. Lett.* **B 592**, Part 1 (2004).
7. T. Kinoshita and M. Nio, *Phys. Rev. Lett.* **90**, 021803-1, Toichiro Kinoshita and M. Nio, *Phys. Rev.* **D70**, 113001 (2004).
8. R.S. Van Dyck et al., *Phys. Rev. Lett.*, **59**, 26(1987) and in *Quantum Electrodynamics*, (Directions in High Energy Physics Vol. 7) T. Kinoshita ed., World Scientific, 1990, p.322.
9. T. Kinoshita, *Rep. Prog. Phys.* **59**, 1459 (1996) which is updated in Ref. [7].
10. G. Gabrielse and collaborators have constructed a new trap, and expect to improve on the electron anomaly by a factor of 10 to 100 over the measurements of Ref. 8.
11. H.N. Brown, et al., (Muon ($g - 2$) Collaboration), *Phys. Rev. Lett.* **86** (2001) 2227.
12. G.W. Bennett, et al., (Muon ($g - 2$) Collaboration), *Phys. Rev. Lett.* **89**, 101804 (2002)
13. G.W. Bennett, et al., (Muon ($g - 2$) Collaboration), *Phys. Rev. Lett.* **92**, 161802 (2004).
14. M. Davier and W. Marciano, *Ann. Rev. Nucl. Part. Sci.* **54**, 115 (2004). For a slightly more up-to-date and more inclusive review, see M. Passera, hep-ph/0411168, 2004 and *J. Phys.* **G** to be published.
15. M. Davier, S. Eidelman, A. Höcker, and Z. Zhang, *Eur. Phys. J. C* **31**, 503 (2003).
16. K. Hagiwara, A.D. Martin, Daisuke Nomura, and T. Teubner, *Phys. Lett.* **B557**, 69 (2003), and *Phys. Rev.* **D69** 093003 (2004).
17. A. Höcker, ICHEP04, hep-ph/0410081, 2004; also M. Davier 8th International Workshop on Tau-Lepton Physics, September 2004, <http://www.hepl.phys.nagoya-u.ac.jp/public/Tau04/>
18. J. Bijnens, E. Pallante and J. Prades, *Nucl. Phys.* **B474**, 379 (1996) and *Nucl. Phys.* **B626**, 410 (2002). M. Hayakawa and T. Kinoshita *Phys. Rev.* **D57**, 465(1998) and hep-ph/0112102 (2002). Marc Knecht, Andreas Nyffeler, *Phys. Rev.* **D65**, 073034 (2002), M. Knecht, A. Nyffeler, M.

- Perrottet, E. De Rafael, Phys. Rev. Lett. **88**, 071802 (2002). I. Blokland, A. Czarnecki and K. Melnikov Phys. Rev. Lett. **88**, 071803 (2002). K. Melnikov and A. Vainshtein, Phys. Rev. **D70**, 113006 (2004).
19. J. Bailey, et. al, Nucl. Phys. **B150**, 1 (1979).
 20. T. Blum, Phys. Rev. Lett. **91**, 052001-1 (2003).
 21. A. Aloisio, et al., (KLOE Collaboration) arXiv hep-ex/0407048, July 2004, and Phys. Lett. **B** in press.
 22. E. Efsthadiadis, et al., Nucl. Inst. and Meth. **A496**,8-25 (2002).
 23. G.T. Danby, et al., Nucl. Instr. and Methods, **A 457**, 151-174 (2001).
 24. A. Yamamoto, et al., Nucl. Inst. and Meth. **A496**,8-25 (2002).
 25. Y.K. Semertzidis, et al., Nucl. Inst. and Meth. **A503**, 458-484 (2003).
 26. S.A. Sedyk, et al., Nucl. Inst. and Meth., **A455** 346, (2000).
 27. A ($g - 2$) $_{\mu}$ *Experiment to ± 0.2 ppm Precision* R.M. Carey, A. Gafarov, I. Logashenko, K.R. Lynch, J.P. Miller, B.L. Roberts (co-spokesperson), G. Bunce, W. Meng, W.M. Morse (resident spokesperson), Y.K. Semertzidis, D. Grigoriev, B.I. Khazin, S.I. Redin, Yuri M. Shatunov, E. Solodov, Y. Orlov, P. Debevec, D.W. Hertzog (co-spokesperson), P. Kammel, R. McNabb, F. Mülhauser, K.L. Giovanetti, K.P. Jungmann, C.J.G. Onderwater, S. Dhamija, T.P. Gorringe, W. Korsch, F.E. Gray, B. Lauss, E.P. Sichtermann, P. Cushman, T. Qian, P. Shagin, S. Dhawan and F.J.M. Farley, which can be found at: <http://g2pc1.bu.edu/~roberts/>
 28. J-PARC Letter of Intent L17, *An Improved Muon ($g - 2$) Experiment at J-PARC*, B.L. Roberts contact person.
 29. W.J. Marciano, J. Phys. **G29**, 23 (2003), and J. Phys. **G29**, 225 (2003).

DISCUSSION

V. A. Huseynov:

Question: In your report you spoke about electro-weak corrections. In these corrections a muon neutrino appears. Does the anomalous magnetic moment (AMM) of a muon depend on the nature of the neutrino mass? Because, as you know, the Dirac neutrino has an AMM. The Majorana neutrino does not have an AMM.

Answer: These effects are much smaller than the experimental sensitivity.

S. B. Nurushhev:

Question: The discrepancy between the $g - 2$ experimental data and the theoretical calculations means that we go beyond the S.M.. Can you put from your data an upper limit on the muon neutrino mass?

Answer: Since the neutrino mass is so small the effects on the S.M. value are negligible.

O. Teryaev:

Question: What about scenario 3, if Higgs would not be found in LHC? And are there possibilities to substantially improve the accuracy, by one or two orders of magnitude?

Answer: This is an interesting suggestion. If no Higgs is found at LHC, then looking for effects of "virtual" new physics becomes even more important.

As far as $g - 2$ goes, we are thinking how to do an order of magnitude better, and there is a letter of intent to JPARC to do this.

THE JEFFERSON LAB CONTRIBUTION TO THE QCD SPIN STRUCTURE OF THE NUCLEON

M. GARÇON

DAPNIA/SPhN, CEA-Saclay, Gif-sur-Yvette, France

From inclusive to semi-inclusive and exclusive (polarized) deep inelastic scattering, the quark structure of the nucleon is being studied with increasingly precise experiments at Jefferson Lab. We will review here the ongoing programs to determine polarized parton distributions - helicity and transversity - as well as generalized parton distributions, addressing the question of intrinsic spin and orbital angular momentum of quarks in the nucleon.

1. A window into the deep inelastic regime

With electron beams in the 4-6 GeV energy range, the CEBAF accelerator gives the experimentalist the possibility to probe the nucleon structure in the deep inelastic scattering regime (DIS), here defined by the kinematical condition that the energy W of the $\gamma^* p$ system is above most nucleon resonances, typically 2 GeV, and the virtuality Q^2 of the exchanged photon larger than 1 GeV². Though the available range in W is rather modest compared to higher energy machines, it is an interesting finding, developed in this paper, that the (mostly valence) quark structure of the nucleon can be accessed in precise measurements of inclusive, semi-inclusive and exclusive electron scattering.

Figure 1 shows the typical kinematical coverage achieved with a 5.75 GeV beam and the CEBAF large acceptance spectrometer (CLAS). The higher boundary is due to the beam energy, and to a lesser extent to the electron scattering angle. For $W > 2$ GeV, a significant coverage of the valence quark region ($0.15 < x_B < 0.65$) can be obtained, albeit at moderate values of Q^2 . There is however accumulating evidence, from the evolution of parton distributions, from first results on exclusive virtual Compton scattering, and from the description of the $\gamma^* \gamma \pi^0$ form factor in $e^+ e^-$ collisions [1] with a handbag diagram similar to the one describing the $\gamma^* p \rightarrow \gamma^{(*)} p$ reaction, that this reaction can indeed be interpreted in terms of parton distributions at Q^2 as low as 1 or 2 GeV². It is certainly one of the goals of the experiments described here to put this on a firm footing.

The transition from the resonance region to the deep inelastic regime is also studied in great detail at JLab, addressing for example the question of higher twists and duality [2].

2. Experimental equipment

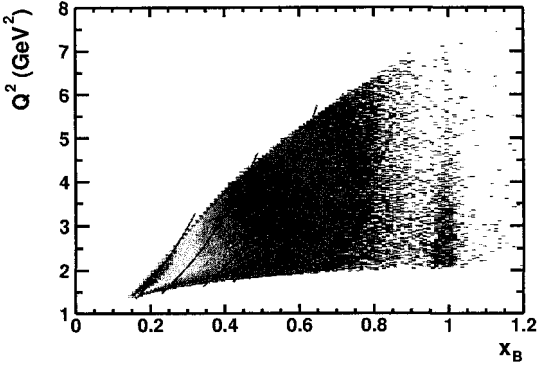


Fig. 1. Kinematical coverage for a typical CLAS experiment with a 5.75 GeV electron beam. The lines correspond to constant values of W (1.8, 2, 2.4 and 2.8 GeV from right to left).

with subsequent spin exchange between Rb and ^3He . In Halls B (CLAS) and C, solid longitudinally polarized NH_3 or ND_3 targets have been installed. Hall C has in addition the capability of target transverse polarization, and is planning to use LiD in coming experiments (deuterated lithium has a higher figure of merit than deuterated ammonium).

In addition to the standard magnetic spectrometers available in the three Halls, dedicated detectors are being used or developed for specific experiments described below.

3. Helicity dependent parton distributions

3.1. Inclusive scattering

Using a longitudinally polarized electron beam incident upon a longitudinally ($//$) or transversely (\perp) polarized target, double spin asymmetries are measured in inclusive $e'\vec{N} \rightarrow e'X$ scattering. The asymmetries $A_{//}$ and A_{\perp} with respect to the beam direction are translated into asymmetries A_1 and A_2 with respect to the virtual photon direction. These in turn, using the known unpolarized structure functions appearing in their denominators, determine the two polarized structure functions $g_1(x, Q^2)$ and $g_2(x, Q^2)$. In the quark parton model, g_1 has the well-known probability interpretation in the Bjorken regime ($Q^2 \rightarrow \infty$):

$$g_1(x) = \frac{1}{2} \sum_{q, \bar{q}} e_q^2 [q^\uparrow(x) - q^\downarrow(x)] = \frac{1}{2} \sum_{q, \bar{q}} e_q^2 \Delta q(x) \quad (1)$$

It measures the contribution of the quark intrinsic spin to the nucleon spin. g_2 represents interaction beyond the quark parton model, and as such is a good tool to study higher twist effects and is sensitive to quark-gluon correlations.

The behaviour of these asymmetries and polarized structure functions is hardly explored at high values of x . Yet it could lead to significant constraints on the valence quark distributions, whose x -dependence is often parameterized as $x \rightarrow 1$; it is useful to calculate (high) moments of these distributions for direct comparison with lattice QCD calculations;

One of the main specificities of JLab is the high luminosity, or product luminosity \times acceptance, which can be achieved using the highly polarized electron beam (about 80 % polarization).

Polarized targets are being used in all three experimental Halls. In Hall A, a high density polarized ^3He target has been developed, which gives an excellent opportunity to study polarized parton distributions in the neutron. This target is based on optical pumping of Rb atoms,

and it poses interesting theoretical problems since the QCD factorization and evolution may break down at the limit of very high x [3].

It is an experimental challenge to perform such measurements, since both the Mott cross section and the unpolarized quark distributions $q(x)$ decrease as x increases.

New results on the proton and deuteron asymmetries (A_{1p} and A_{1d}) from CLAS [4] were shown at this conference and will soon be available. The neutron asymmetry A_{1n} has recently been measured in Hall A [5]. Three precise data points at $0.32 < x < 0.6$ give the first clean signature of positive A_{1n} at high x . The trend deviates from PQCD predictions based on hadron helicity conservation, which states that a quark with $x \rightarrow 1$ has the same helicity as the nucleon. This finding points to the role of quark orbital angular momentum in the nucleon.

Using parametrizations of unpolarized structure functions F_1 , world data for g_1^p/F_1^p and neglecting strangeness at high x , the quantities $(\Delta u + \Delta \bar{u})/(u + \bar{u})$ and $(\Delta d + \Delta \bar{d})/(d + \bar{d})$ were extracted [5]. Since the difference $(\Delta q + \Delta \bar{q})/(q + \bar{q}) - \Delta q_v/q_v$, is smaller than experimental uncertainties, the polarized valence quark distributions Δq_v may be determined from these ratios (see Figure 2). This new measurement constrains especially Δd_v .

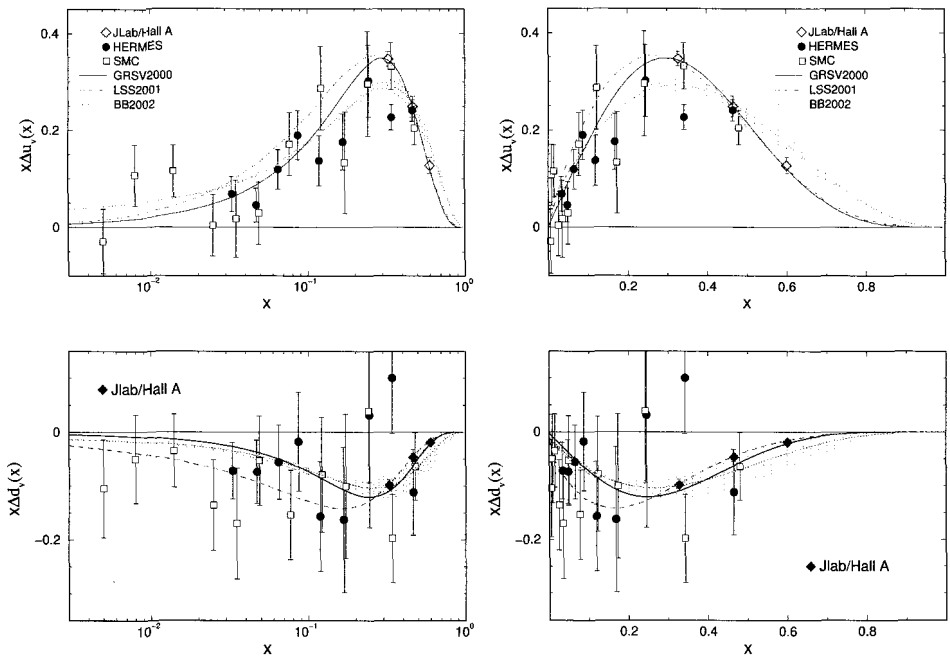


Fig. 2. Polarized valence quark distributions in the nucleon calculated using the JLab/Hall A results [5]. Adapted from Figure 16.5 of [6], which contains all references to previous experiments and parameterizations. x -scale is logarithmic on the left, linear on the right.

Even higher values of x will be accessible with the planned 12 GeV upgrade of the CEBAF accelerator [7] and/or from measurements in the resonance region provided quark-

hadron duality is established [2].

3.2. Semi-inclusive scattering (SIDIS) and flavour decomposition

Detecting the hadron from the current quark fragmentation in the semi-inclusive process $\vec{e}\vec{N} \rightarrow ehX$, a double spin asymmetry A_{11}^h can be measured, using longitudinally polarized beam and target. Assuming leading order $x-z$ factorization, one gets for each detected hadron species h an asymmetry

$$A_{1N}^h(x, Q^2, z) \equiv \frac{\Delta\sigma^h(x, Q^2, z)}{\sigma^h(x, Q^2, z)} = \frac{\sum_q e_q^2 \Delta q(x, Q^2) \cdot D_q^h(z, Q^2)}{\sum_q e_q^2 q(x, Q^2) \cdot D_q^h(z, Q^2)} \quad (2)$$

where D_q^h describes the fragmentation of the quark q in a hadron h of energy $z \times$ the virtual photon energy.

The so-called ‘‘Semi-SANE’’ program [8] is to measure eight such asymmetries, for $h = \pi^\pm$ and K^\pm , for both proton and deuteron (NH_3 and LiD polarized targets) in Hall C. Together with the two inclusive asymmetries A_{1N} , this will lead to the extraction of five polarized quark distributions Δu , $\Delta \bar{u}$, Δd , $\Delta \bar{d}$ and Δs . The originality of this experiment will be the use of a non-magnetic spectrometer in direct view of the target to detect the scattered electrons. The Big Electron Telescope Array (BETA), under construction, will consist of a 1744 blocks lead-glass calorimeter, a gas Cerenkov detector for pion rejection, and a lucite hodoscope array for tracking and redundant particle identification. It will cover a solid angle close to 200 msr. In conjunction with the standard Hall C HMS spectrometer, also equipped with gas Cerenkov and aerogel detectors for π/K identification, luminosities of the order of $10^{35} \text{ cm}^{-2}\text{s}^{-1}$ should be achieved. Anticipated results were discussed at this conference [8].

4. Tests of factorization in SIDIS

At the relatively low energies used at JLab for these experiments, one could question the validity of the (leading order) $x-z$ factorization, resulting in Eq. (2). There is increasing evidence that this factorization is not, or not much, violated at 6 GeV. For example, cross sections for the $H(e, e' \pi^-)X$ reaction measured in Hall C are in excellent agreement with Monte-Carlo work based on LO $x-z$ factorization [9]. Also semi-inclusive asymmetries $A_{1p}^{\pi^+}$ measured with CLAS agree with HERMES and SMC data, and fall on the same curve as the inclusive A_{1p} ; within experimental errors, no z dependence is observed [10].

5. Transversity

In SIDIS, at leading order, eight response functions characterize the distribution of cross section. Three contributions are associated with a transversely polarized target, two of which should be measurable. The transverse nucleon polarization

- affects the quark transverse momentum: this asymmetric k_\perp distribution, combined with the usual fragmentation function D , gives rise to the Sivers effect, characterized by a $\sin(\phi_h - \phi_S)$ dependence in the $\vec{N}(e, e'h)X$ cross section.

- induces quark transverse polarization: this may manifest itself through the Collins fragmentation function which describes the correlation of the outgoing hadron (transverse) momentum with the quark transverse polarization; this effect is characterized by a $\sin(\phi_h + \phi_S)$ dependence.

The ϕ angles refer here to the final hadron (h) and target spin (S) azimuthal angles with respect to the electron scattering plane. Both effects are the subject of intense studies. The Collins effect is of particular interest, since its measurement would lead to the determination of the transversity distribution [11]. Let us recall that the transversity and helicity distributions are identical in a non relativistic quark model picture of the nucleon, and that transversity does not mix with gluons in its evolution and is suppressed at low x with respect to $\Delta q(x)$. Finally, its first moment yields the nucleon “tensor charge” δq calculable in lattice QCD.

Using the polarized ^3He target and the newly installed Bigbite detector in Hall A, a dedicated high precision experiment [12] will disentangle these two effects, measure the transversity distribution in the neutron (sensitive to δd), and probe other k_{\perp} -dependent quark distribution functions. Such single spin asymmetries measurements using a transversely polarized ^3He target are complementary to HERMES and COMPASS transversity measurements, respectively on the proton and on the deuteron, and are performed at x values where transversity might be larger.

6. Other single spin asymmetries (SSA)

There is a rich phenomenology associated with various SSA linked to transverse momentum distributions of partons, and to orbital angular momentum. One example is the determination of the scalar distribution $e_q(x)$ [13]. On the experimental side, the consistency (through a model) between HERMES and CLAS results [10, 14] of A_{LU} and A_{UL} measurements (using either polarized beam or target) may be interpreted as a further indication of the applicability of factorization. Definitive conclusions on the measurability of several quark transverse momentum distributions require more data and higher accuracy, in order to disentangle various azimuthal dependences as well as to distinguish between twist-2 and twist-3 contributions. JLab is also pursuing this path.

7. Generalized parton distributions

Generalized Parton Distributions (GPDs) have emerged as an attractive, powerful and unifying concept for the nucleon structure [15]. Besides offering a link between “ordinary” parton distributions and elastic form factors, they contain the interferences, or coherences, between states of different parton longitudinal momentum fractions, and they include correlations between transverse position and longitudinal momentum. Last but not least, their determination could yield the total angular momentum (intrinsic spin + orbital angular momentum) carried by the quarks in the nucleon. Recent theoretical progress includes lattice QCD calculations of GPD moments [17], and refined phenomenological analyses of the link with form factors [18].

GPDs enter the leading order description of deeply exclusive leptonproduction of photons - DVCS - and of mesons (see e.g. [16]).

7.1. Deeply virtual Compton scattering (DVCS)

After the first observation of DVCS at H1 (in the gluon sector) and at CLAS and HERMES, preliminary CLAS results obtained at 4.8 and 5.75 GeV were shown in this talk. Increased statistics allow for a finer binning (in Q^2 , x and t), but the separation between $ep \rightarrow ep\gamma$ and $ep \rightarrow ep\pi^0$ reactions is increasingly difficult. Dedicated DVCS experiments at JLab will detect all three particles in the final state. Their primary objective is to establish on firm grounds the link between observables and GPDs. This goes through the study of characteristic scaling laws in observables. If scaling laws are manifest, or deviations thereof understood, then these measurements will put stringent constraints on GPD models or parameterizations.

The dedicated Hall A experiments on $\bar{e}p \rightarrow ep\gamma$ [19] and $\bar{e}n \rightarrow en\gamma$ [20] (quasi-free reaction on a deuterium target) were completed in the Fall 2004. The CLAS/DVCS experiment [21] will run in the Spring 2005. The observable being measured is the beam spin cross section difference, which originates from the interference between the DVCS (photon emission from the nucleon) and the Bethe-Heitler (photon emission from the incident or scattered electron) processes:

$$\Delta\sigma = \sigma^+ - \sigma^- = \Gamma \cdot (\mathcal{A} \sin\phi + \dots) \quad (3)$$

or the beam spin asymmetry $\Delta\sigma/(2\sigma)$, where Γ is a known factor and

$$\mathcal{A} = F_1(t) \cdot \mathcal{H} + \frac{x_B}{2 - x_B} [F_1(t) + F_2(t)] \cdot \tilde{\mathcal{H}} - \frac{t}{4M^2} F_2(t) \cdot \mathcal{E}. \quad (4)$$

Here F_1 and F_2 are the elastic nucleon form factors (originating from the Bethe-Heitler amplitude) while the GPDs H^q , \tilde{H}^q and E^q enter the imaginary part of the DVCS amplitude through $\mathcal{H} = \pi \sum_q e_q^2 [H^q(\xi, \xi, t) \pm H^q(-\xi, \xi, t)]$ and similar expression for $\tilde{\mathcal{H}}$ and \mathcal{E} . Note that the dominant term in Eq. (4) is the first one for DVCS on the proton, while the last term dominates in the case of the neutron. The neutron experiment has then the potential to access the less constrained GPD E and thus yield information on the quark orbital angular momentum. While the $\sin\phi$ dependance in Eq. (3) originates from the helicity conserving leading twist contributions, the additional terms will be determined as well, and provide a quantitative measure of higher-twist contributions.

For these experiments, new compact electromagnetic calorimeters were developed (PbF₂ in Hall A, equipped with fast digitizing electronics, PbWO₄ in CLAS, in conjunction with a background sweeping superconducting solenoid) for the detection of the photons originating from DVCS.

7.2. Hard exclusive meson electroproduction

Deeply virtual vector meson production is complementary to DVCS since it could give access to the flavour separated H and E GPDs. The contribution to observables from the

longitudinal photons must be isolated, and one must reach higher Q^2 since the additional gluon exchange necessary to produce the meson increases the higher-twist contributions.

Longitudinal cross sections have been extracted for ρ electroproduction at 4.2 GeV, and are in qualitative agreement with a model based on GPDs [22]. For the ω channel however, recent CLAS data at 5.75 GeV show that the handbag diagram does not dominate [23]. This is specific to the case of the ω , as the t -channel π^0 exchange was shown to dominate the cross section, even at relatively high Q^2 .

8. Conclusions

Inclusive and semi-inclusive deep inelastic scattering are being understood at moderate values of Q^2 , yielding information about the quark structure of the nucleon. Factorization is shown to work at lower energies than previously thought. Jefferson Lab, with the CEBAF beam energy nearing 6 GeV for the past two years, contributes and will contribute fully to the determination of polarized quark distributions (valence helicity distributions were presented, and transversity measurements are being prepared). In addition, a rich phenomenology in quark transverse momentum distributions is being explored experimentally through single spin asymmetries.

JLab, with its high luminosity and high resolution detectors, is especially well equipped for the measurement of deep exclusive reactions. Once proper scaling laws are verified for DVCS (and possibly for hard meson electroproduction), significant constraints on the generalized parton distributions will be set by new dedicated experiments. A complete mapping and measurement of GPDs will probably have to await the planned 12 GeV upgrade [7] of the CEBAF accelerator and of the Halls' detectors.

References

1. J. Gronberg *et al.* (CLEO collaboration), *Phys. Rev.* **D57**, 33 (1998).
2. R. De Vita, these proceedings.
3. X. Ji, Proc. of the HiX2004 Workshop on the Structure of the Nucleon at Large Bjorken x , Marseille (2004), to be published; W. Vogelsang, *ibidem*.
4. G. Dodge, S. Kuhn, M. Taiuti *et al.* (CLAS collaboration), private communication.
5. X. Zheng *et al.*, *Phys. Rev. Lett.* **92**, 012004 (2004); and *Phys. Rev.* **C70**, 065207 (2004).
6. Particle Data Group, *Phys. Lett.* **B592**, 1 (2004).
7. Preliminary Conceptual Design Report, http://www.jlab.org/div_dept/physics_division/GeV/index.html
8. X. Jiang, contribution to this conference.
9. R. Ent, private communication.
10. H. Avakian (CLAS collaboration), private communications.
11. V. Barone, these proceedings.
12. J.P. Chen, X. Jiang, J.C. Peng *et al.*, CEBAF experiment E03-004.
13. A.V. Efremov *et al.*, *Phys. Rev.* **D64**, 114014 (2003); M. Wakamatsu, contribution to this conference.
14. H. Avakian *et al.*, *Phys. Rev.* **D69**, 112004 (2004).
15. X. Ji, *Phys. Rev. Lett.* **78**, 610 (1997) and *Phys. Rev.* **D55**, 7114 (1997); A. Radyushkin, *At the Frontier of Particle Physics / Handbook of QCD*, M. Shifman ed., World Scientific, Singapore (2001) [hep-ph/0101225].

16. M. Garçon, *Eur. Phys. J. A* **18**, 389 (2003); and references therein.
 17. M. Gockeler *et al.* (QCDSF Collaboration), hep-lat/0410023.
 18. M. Diehl *et al.*, hep-ph/0408173; M. Guidal *et al.*, hep-ph/0410251.
 19. P. Bertin, C. Hyde-Wright, R. Ransome, F. Sabatié *et al.*, CEBAF experiment 00-110.
 20. P. Bertin, C. Hyde-Wright, F. Sabatié, E. Voutier *et al.*, CEBAF experiment 03-106.
 21. V. Burkert, L. Elouadrhiri, M. Garçon, S. Stepanyan *et al.*, CEBAF experiment 01-113.
 22. C. Hadjidakis *et al.* (CLAS collaboration), hep-ex/0408005.
 23. M. Garçon *et al.* 10th Int. Symp. on *Meson-Nucleon Physics and the Nucleon Structure*, Beijing (2004).
-

DISCUSSION

Teryaev:

Question: The possible violation of factorization due to fracture function should increase with decreasing Q^2z/x . Can you test it at smaller z ?

Answer: Measurements at small z are certainly possible. In CLAS data, events at $z < 0.5$ are present but are cut in the results which I presented.

E. Leader:

You mentioned using a Monte Carlo program to study $x - z$ factorization. Is this Monte Carlo different from those used by HERMES and COMPASS?

Answer (given after the session): Yes, it is a different Monte Carlo program, developed at JLab, with factorization built in.

PHYSICS AT HERMES

D. HASCH

I.N.F.N., Laboratori Nazionali di Frascati, Frascati, Italy

(for the HERMES Collaboration)

HERMES is a second generation experiment for the study of the spin structure of the nucleon by measuring not only inclusive but also semi-inclusive and exclusive processes in deep-inelastic lepton scattering. An overview is given of new and finalised results since the Spin2002 conference.

1. Introduction

In the last few decades, one particular issue which has received much attention is how to perform measurements that dissect the spin structure of the nucleon. The nucleon spin can be decomposed conceptually into the spin of its constituents according to

$$\langle s_z^N \rangle = \frac{1}{2} = \frac{1}{2} \Delta \Sigma + \Delta G + \Delta L_z, \quad (1)$$

where the three terms are the contributions from quark and gluon spins and the total orbital angular momenta of the quarks and gluons, respectively. From early measurements it was realised that simple leading order considerations without the inclusion of contributions from gluons were too naive. More recent next-to-leading order treatments provide a picture more consistent with our present understanding of QCD. The key to further progress is more specific probes of the individual contributions of Eq. (1) to the nucleon spin.

In the following section, after a brief description of the experiment, are presented the final results for the polarised structure function g_1 of the proton, the deuteron and the neutron, from measurements with longitudinally polarised beams and targets. By also observing a produced hadron it has been possible to extract the helicity distributions of individual quark flavours in the nucleon. The first experimental results from measurements of single-spin asymmetries for charged pions from deep-inelastic scattering off a transversely polarised target are discussed. Moreover, new results from hard exclusive electroproduction of π^+ and from deeply-virtual Compton scattering (DVCS) are presented and compared to Generalised Parton Distribution calculations. The results presented in this contribution are discussed in more detail elsewhere at this conference [1]. Further HERMES results have been discussed during this conference [2] too.

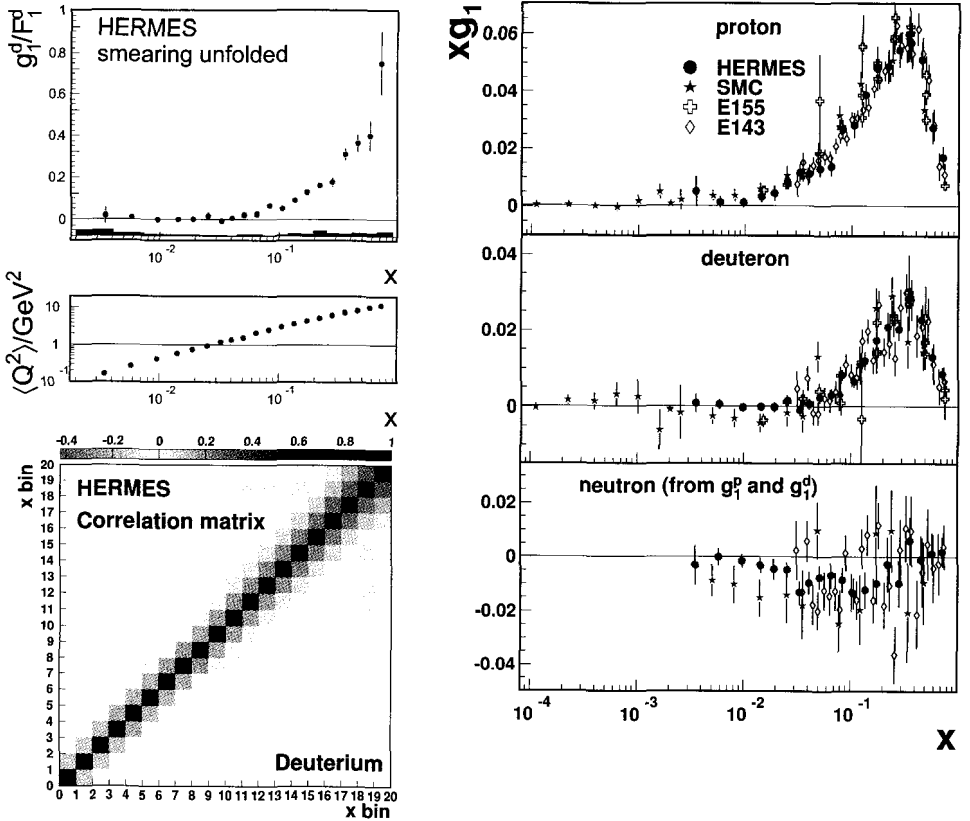


Fig. 1. Left: The smearing unfolded g_1/F_1 of the deuterium (top panel) and the correlation matrix between statistical errors (bottom panel). Error bars are statistical, displaying the diagonal elements of the correlation matrix only. Right: World data on the x -weighted spin SF g_1 for the proton (top panel), the deuteron (middle panel) and the neutron obtained from proton and deuteron data (bottom panel). Error bars show the quadratic sum of statistical and systematic uncertainties.

The HERMES experiment has been taking data at the HERA accelerator in Hamburg, Germany since 1995. HERMES scatters longitudinally polarised electron and positron beams of 27.5 GeV from longitudinally or transversely polarised targets internal to the beam pipe. Featuring polarised beams and targets, and an open-geometry spectrometer [3] with excellent particle identification, HERMES is well suited to study the spin-dependent inclusive and semi-inclusive DIS reactions. The PID capabilities of the experiment were significantly enhanced in 1998 when the threshold Cerenkov detector (used to identify pions above 4 GeV) was upgraded to a dual Ring Imaging system (RICH). This new detector provides full separation between charged pions, kaons and protons over essentially the entire momentum range of the experiment.

2. Inclusive spin asymmetries

Final results for the polarised structure function (SF) $g_1(x, Q^2)$ are obtained from a refined analysis of data taken with longitudinally polarised hydrogen and deuterium targets in the kinematic range $Q^2 > 0.1 \text{ GeV}^2$ and $W > 1.8 \text{ GeV}$. For both targets, g_1 is determined from the ratio g_1/F_1 , which is approximately equal to the virtual photon asymmetry A_1 measured via the longitudinal cross section asymmetry $A_{||}$. The neutron spin SF is calculated as a linear combination of g_1^p and g_1^d .

The measured asymmetries have been corrected for detector smearing and QED radiative effects in a rigorous model-independent unfolding procedure in which Monte Carlo is used to compute the migration of events between kinematic bins. As this method assumes no functional form for the underlying physics, there is an apparent inflation of error bars which reflects the uncertainty contributions from all possible kinematic correlations. When incorporated into models and world fits (i.e. when a functional form is assumed) and the correlation matrix is taken into account, the uncertainties become significantly smaller.

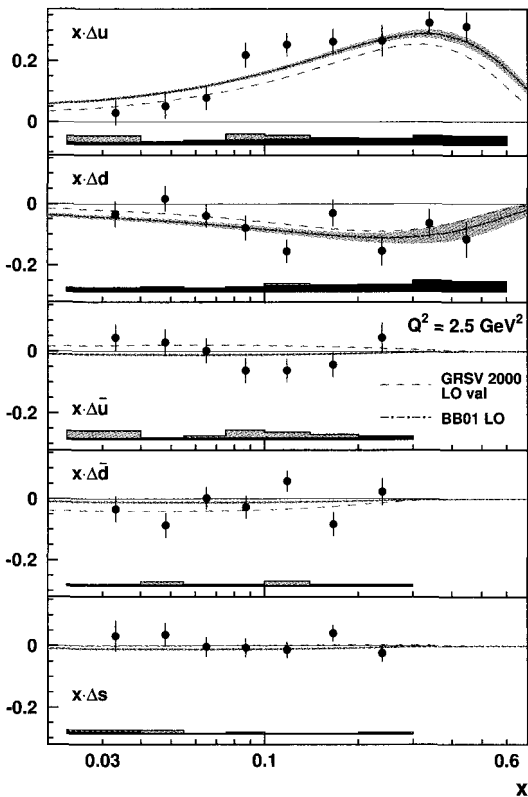


Fig. 2. The quark helicity distributions $x\Delta q(x, Q_0^2)$ evaluated at a common value of $Q_0^2 = 2.5 \text{ GeV}^2$ as a function of x . The curves show LO QCD analyses of polarised data (see text).

The smearing unfolded asymmetry g_1/F_1 of the deuterium is shown in the left hand side of Fig. 1 (top panel) together with the correlation matrix (bottom panel). A compilation of the world data on the x -weighted SF g_1 is presented in the right hand side of Fig. 1 at their measured Q^2 .

3. Flavour decomposition

Semi-inclusive deep-inelastic scattering is a powerful tool to determine the separate contributions $\Delta q_f(x)$ of the quarks and antiquarks of flavour f to the total spin of the nucleon. By means of the technique of flavour tagging, individual spin contributions can be determined directly from spin asymmetries of hadrons with the appropriate flavour content. The measured semi-inclusive photon-nucleon asymmetry, A_1^h , for the hadron of type h , is related to the quark and antiquark polarisations $\Delta q_f(x)$ through the so-called purity matrix P_f^h , representing

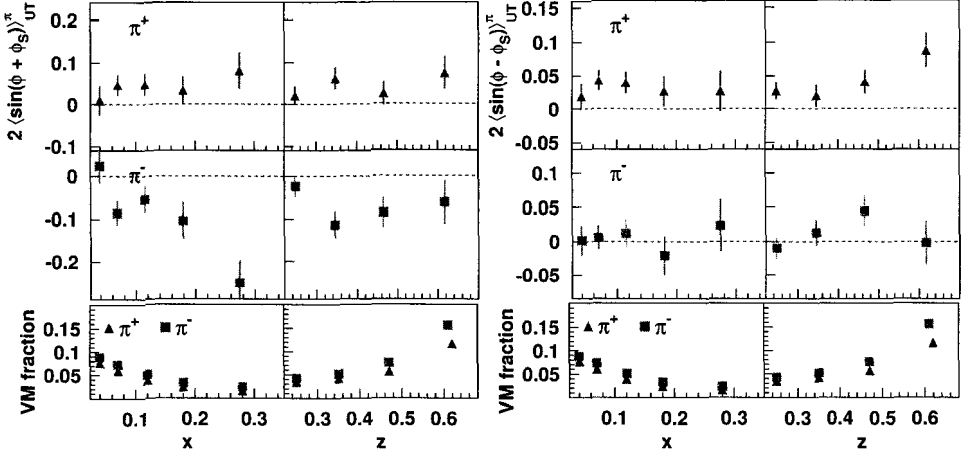


Fig. 3. Virtual-photon Collins (left) and Sivers (right) moments for charged pions as function of x and z . Error bars represent the statistical uncertainties. In addition, there is a common 8% scale uncertainty. The lower panels show the relative contributions to the data from simulated exclusive vector meson production.

the probability that the quark q_f was struck in the DIS event. The purities are obtained from Monte Carlo simulations based on the Lund string fragmentation model tuned to HERMES kinematics. The parameters of the fragmentation model were determined by fitting various measured hadron multiplicities. For the first time, a global analysis of the smearing unfolded inclusive spin asymmetries and semi-inclusive spin asymmetries for π^+ , π^- , K^+ , and K^- has been carried out for longitudinally polarised targets of hydrogen, and deuterium [4]. The results of the decomposition are presented in the left hand panel of Fig. 2 and compared to LO QCD analyses [5, 6]. In the analysis $\Delta\bar{s} = 0$ is assumed. As expected, the results show that $x\Delta u(x)$ is positive and $x\Delta d(x)$ is negative, and that both reach their maximum magnitude in the valence quark region. The polarised sea quark distributions are all consistent with zero, and show a hint for a small positive s -quark polarisation.

4. Transverse spin asymmetries

Apart from the structure functions $F_1(x)$ and $g_1(x)$, a third distribution function $h_1(x)$, known as the transversity distribution, is required to provide a complete description of the quark structure of the nucleon at leading order.

Due to its chiral-odd nature, transversity cannot be measured in inclusive DIS, but only in a process in which it is combined with another chiral-odd object. Using a transversely polarised nucleon target, the transversity enters the cross section combined with the chiral-odd fragmentation function (FF) known as Collins function [7].

Azimuthal spin asymmetries can also be generated by the T-odd Sivers distribution function $f_{1T}^\perp(x, k_T)$ [8] that appears in the cross section together with the unpolarised FF, D_q^h . The DF $f_{1T}^\perp(x, k_T)$ describes a correlation between the transverse polarisation of the target nucleon and the \vec{p}_T of the struck quark. The characteristic signature of the Collins (Sivers) effect is a $\sin(\phi + \phi_S)$ ($\sin(\phi - \phi_S)$) modulation of the cross section in the distri-

bution of the azimuthal angle ϕ of the pion around the virtual photon direction and relative to the lepton scattering plane, and ϕ_S , the angle between the scattering plane and the transverse spin component of the target nucleon.

The extracted Collins (left) and Sivers (right) moments for charged pions [9] are shown in Fig. 3. The bottom panels present simulations based on PYTHIA6, tuned for HERMES kinematics, of the fractions of the semi-inclusive pion yield from exclusive production of vector mesons, the asymmetries of which are poorly determined. The averaged Collins moment for π^+ is positive at $0.021 \pm 0.007(\text{stat})$, while it is negative at $-0.038 \pm 0.008(\text{stat})$ for π^- . To the extent that δu is positive and δd is negative the data is similar to model predictions. However, the magnitude of the negative π^- moment appears to be at least as large as that for π^+ . This trend becomes more pronounced as the magnitude of the transverse moments increase at large x where valence quark effects dominate, as they do in previously measured longitudinal spin asymmetries [10]. Unlike the case of π^+ where u-quark dominance is expected, large negative π^- moments are a surprise, because neither quark flavour dominates π^- production, and one expects $|\delta d| < |\delta u|$ in analogy with $|\Delta d| < |\Delta u|$. One explanation of the larger negative π^- azimuthal moments could be a substantial magnitude with opposite sign for the disfavoured Collins function.

The HERMES results for the Sivers moment is found to be non-zero at $0.017 \pm 0.004(\text{stat})$ for π^+ , providing an indication for non-zero orbital angular momenta of quarks in the nucleon. However, it may be due to a much larger apparent π^+ asymmetry in a small contamination from exclusive production of ρ^0 mesons.

The data displayed in Fig. 3 represent only one third of the total data set collected with a transversely polarised target up to August 2004.

5. Hard exclusive processes

An exciting new field is opened up with measurements of hard exclusive production of mesons and real photons (deeply virtual Compton scattering). The parton correlation functions (known as Generalised Parton Distributions, GPDs) accessible in these processes are related to the total angular quark momentum contribution in the nucleon [11]. Thus, with prior knowledge of $\Delta\Sigma$ (Eq. 1), the orbital angular momentum of the quarks L^q may become accessible. Such studies appear to mark a major advance in unravelling the spin structure of the nucleon.

Since in the present HERMES apparatus the recoiling target nucleon is not detected, the exclusivity of the processes was ensured by the missing mass or missing energy technique. The non-exclusive background has been subtracted.

5.1. Exclusive pion production

The factorisation theorem for hard exclusive production of mesons has been proved for longitudinal photons only. However, the transverse contribution to the cross section is predicted to be suppressed by a power of $1/Q^2$ with respect to the longitudinal one [12] which is expected to fall like $1/Q^6$.

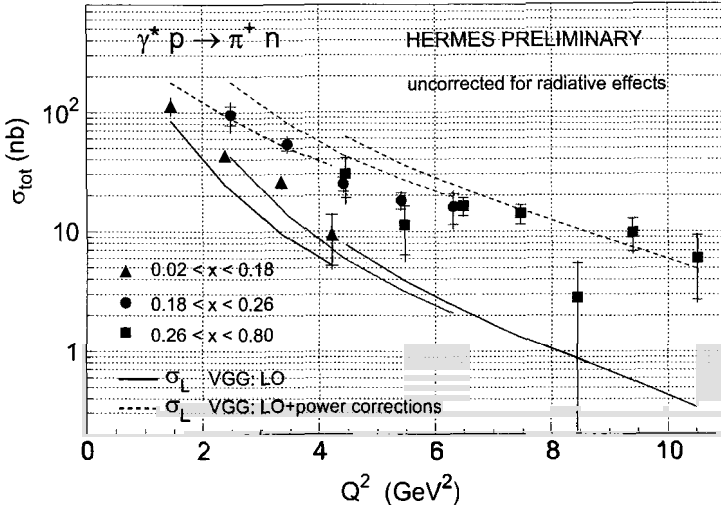


Fig. 4. Total cross section for exclusive π^+ production as function of Q^2 for three different x ranges, integrated over t . The curves represent calculations based on a GPD-model.

HERMES has measured the total cross section for exclusive π^+ production shown in figure 4 as a function of Q^2 for three different x -ranges. These preliminary data have not yet been corrected for radiative effects, which have been roughly estimated to be as large as 20% with little dependence on x or Q^2 . The data is compared to calculations for the longitudinal part of the cross section computed from a GPD-model [13]. At HERMES the separation of the transverse and longitudinal component of the cross section is not feasible. However, since the transverse contribution is predicted to be suppressed, and since the virtual photon polarisation parameter ε ranges from 0.8 to 0.95, the data at larger Q^2 are expected to be dominated by the longitudinal part. The full lines in Fig. 4 show the leading-order calculation computed for the mean x and Q^2 corresponding to the data and integrated over t . The dashed lines include power corrections due to intrinsic transverse momenta of the partons in the nucleon and due to soft overlap contributions. The Q^2 dependence is in general agreement with theoretical expectation. While the leading-order calculations underestimate the data, the evaluation of the power corrections appears too large. As the data contain some x dependence, a reduced cross section has been evaluated [14] in order to remove kinematic factors which depend strongly on x : $16\pi(1-x)/x^2 Q^4 \sqrt{1+4x^2M^2/Q^2} \sigma^{\gamma^* p \rightarrow n\pi^+}(x, Q^2)$ where M is the proton mass. The reduced cross section represents the squared amplitude of the process, averaged over initial and summed over final proton helicities. A fit to the reduced cross section of the form: $1/Q^p$ leads to $p = 1.9 \pm 0.5$, 1.7 ± 0.6 and 1.5 ± 1.0 respectively for the low, middle and high x -bin. Within the uncertainties, the Q^2 dependence of the reduced cross section is in good agreement with the $1/Q^2$ theoretical expectation.

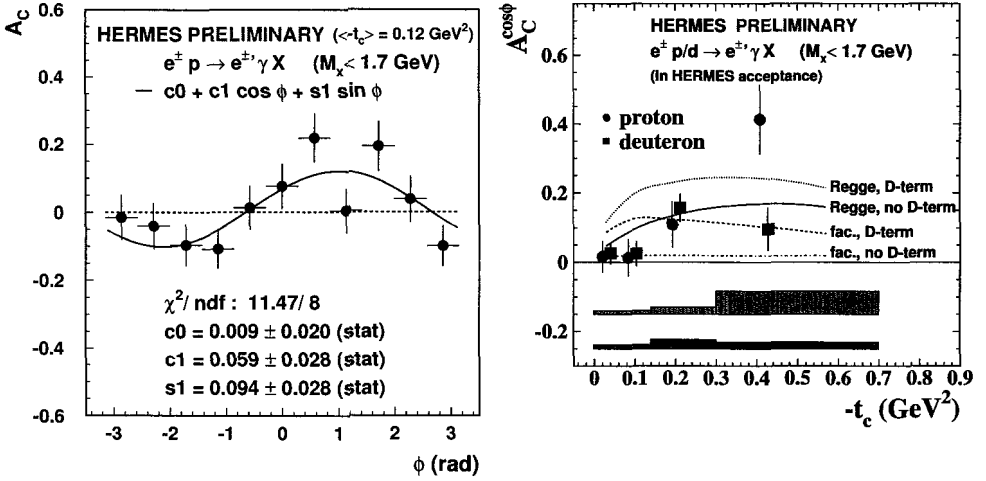


Fig. 5. Left: Beam-charge asymmetry (BCA) for hard electroproduction of photons on the proton as a function of the azimuthal angle ϕ . The solid curve shows the result of the indicated fit. Right: The $\cos \phi$ amplitude of the BCA for proton and deuteron as a function of $-t$. The curves represent model calculations based on different GPD parametrisations (see text).

5.2. Deeply-virtual Compton scattering (DVCS)

The hard exclusive electroproduction of a real photon appears to provide the theoretically cleanest access to GPDs. DVCS amplitudes can be determined through a measurement of the interference between the DVCS and Bethe-Heitler (BH) processes, in which the photon is radiated from a parton and from the lepton, respectively. Measuring the ϕ -dependence of a cross section asymmetry with respect to the charge (spin) of the lepton beam provides information about the real (imaginary) part of the DVCS amplitude. The real (imaginary) part of the DVCS amplitude manifests itself as a $\cos \phi$ ($\sin \phi$) modulation of the cross section asymmetry. HERMES has already measured azimuthal asymmetries with respect to the beam helicity [15]. Fig. 5 shows the first measurement of the beam-charge asymmetry A_C from hydrogen and deuterium targets. The left hand side presents A_C for the proton as a function of the azimuthal angle ϕ . As the two beams have different average polarisations, the $\sin \phi$ -dependent part of the interference term also contributes, and the asymmetry is fitted with the function $P_1 \cos \phi + P_2 \sin \phi$. The right hand side of Fig. 5 shows the $\cos \phi$ amplitudes derived from the two-parameter fits and corrected for background as a function of the four-momentum transfer to the target $-t$ for the proton and the deuteron. The data is compared to GPD-based model calculations [13], assuming a factorised or Regge-inspired t -dependence with and without the D-term contribution [16]. It is apparent that measurements of the beam-charge asymmetry have high sensitivity to different GPD parametrisations.

6. Prospects for HERMES spin physics

In spite of many years of experiments, a detailed decomposition of the spin of the nucleon remains elusive. HERMES will continue taking data with a transversely polarised target till mid 2005, and will significantly improve the statistical precision of the Collins and Sivers asymmetries. In 2005 a major upgrade of the spectrometer with a recoil detector is foreseen. HERMES will then emphasise measurements in the exciting new field of hard exclusive production of mesons and real photons with positron and electron beams.

References

1. H. Marukyan, C. Riedl, A. Rostomyan, J. Rubin, G. Schnell; these proceedings.
2. S. Belostoski, R. Fabbri, E. Kinney, A. Nagaitsev, P. van der Nat; these proceedings.
3. HERMES Collab., K. Ackerstaff *et al.*, *Nucl. Inst. Meth.* **A417**, 230 (1998).
4. HERMES Collab., A. Airapetian *et al.*, *Phys. Rev. Lett.* **92**, 012005 (2004); *Phys. Rev. D* (in press).
5. M. Glück, E. Reya, M. Stratmann, W. Vogelsang, *Phys. Rev.* **D63**, 094005 (2001).
6. J. Blümlein and H. Böttcher, *Nucl. Phys.* **B636**, 225 (2002).
7. J.C. Collins, *Nucl. Phys.* **b396**, 161 (1993).
8. D.W. Sivers, *Phys. Rev.* **D43**, 261 (1991). S.J. Brodsky, D.S. Hwang, I. Schmidt *Phys. Lett.* **B530**, 99 (2002).
9. HERMES Collab., A. Airapetian *et al.*, *Phys. Rev. Lett.* (in print).
10. HERMES Collab., A. Airapetian *et al.*, *Phys. Lett.* **B535**, 85 (2002).
11. X. Ji, *Phys. Rev. Lett.* **78**, 610 (1997); *Phys. Rev.* **D55**, 7114 (1997).
12. J.C. Collins, L. Frankfurt, M. Strikman, *Phys. Rev.* **D56**, 2982 (1997).
13. M. Vanderhaegen, P.A.M. Guichon, M. Guidal, *Phys. Rev.* **D60**, 094017 (1999).
14. M. Diehl, *private communication*.
15. HERMES Collab., A. Airapetian *et al.*, *Phys. Rev. Lett.* **87**, 182001 (2001).
16. M. Polyakov, C. Weiss *Phys. Rev.* **D60**, 114017 (1999).

DISCUSSION

M. Garçon:

Question: In the case of exclusive single and double pion production, I am concerned with the fact that the longitudinal part of the process is not isolated and still you compare the results to models valid for longitudinal photon only. More specifically:

- a good half of the $\pi^+\pi^-$ events are to be associated with transverse photons;
- the $1/Q^2$ theoretical corrections to $ep \rightarrow e\pi^+$ are large.

Why do you then assume that σ_T is negligible?

Answer: For exclusive meson production the transverse part of the cross-section is suppressed by $1/Q^2$ compared to the longitudinal part for which factorisation has been proven. Moreover, the ratio σ_L/σ_T is always larger than 0.8 in the presented measurements.

- In case of $\pi^+\pi^-$ production, the reasonable agreement of the leading twist predictions for the $m_{\pi\pi}$ -dependence of the $\langle P_1 \rangle$ data may tentatively be understood as arising from the cancellation of higher twist effects in this moment.

- The Q^2 dependence of the measured total cross-section of $ep \rightarrow e\pi^+$ is found to agree

with the $1/Q^6$ behaviour expected for the σ_L part. The $1/Q^2$ corrections (power corrections) are very sensitive to the choice of the pion form factor. Therefore the overestimation of the data when including power corrections may indicate that the chosen parametrisation of the pion form factor does not reproduce its behaviour at higher Q^2 values.

V. A. Huseinov:

Question: In your investigation you consider longitudinally polarized electron or positron beam. The anomalous magnetic moment of the charged lepton destroys the longitudinal polarization. Under the real conditions of modern storage rings it happens quite fast. How do you manage to keep the longitudinally polarized electron or positron beams stable?

Answer: In the HERA electron storage ring a transverse polarization is achieved and monitored. Just in front of the HERMES experiment the transverse spin orientation is rotated into a longitudinal one by means of spin rotators and rotated back into transverse direction after the experiment. This procedure was proven in the work of Barber et al. PLB 343(1995)436. However, the longitudinal polarization is measured continuously by a Compton-backscattering polarimeter and compared to the measurement of the transverse beam polarization. The two are found to agree within about 2%.

E. Leader:

Comment: I would just like to draw your attention to the fact that there is now an angular momentum sum rule for transversely polarized nucleons. What is interesting is that in this you must ADD the contributions of quarks and antiquarks in h_1 i.e. $h_1^q + h_1^{\bar{q}}$, whereas in the calculation of the tensor charge there occur $h_1^q - h_1^{\bar{q}}$.

Answer: I am aware of this sum rule and I hope that HERMES will contribute in measuring it with both, transversity measurements and exclusive reaction measurements.

O. J. Nassalski:

Your semi-inclusive analysis relies on the fragmentation functions from the Monte-Carlo; Question 1: what is the systematic error on your polarized quark distribution do to this; e.g. SMC modified MC fragmentation functions (E. Rondio talk) in order to describe the data? Question 2: are you planning to determine fragmentation functions?

Answer:

1. The fragmentation is modeled in the LUND string model implemented in JETSET and the string breaking parameters were found to fit the hadron multiplicities measured at HERMES. The uncertainty of the fragmentation model to the polarized quark distributions was estimated by comparing the purities obtained with the best tune of JETSET parameters to a set which was derived earlier from a reduced set of measured hadron multiplicities.

2. Certainly yes; we are going to derive the fragmentation functions at HERMES kinematics from our measured hadron multiplicities and to use them in an extraction of the quark polarizations.

S. B. Nurushev:

Question: You stated that in HERMES there are essential azimuthal asymmetries. This large negative asymmetry means that Collins effect leads to large negative spin asymmetry. In a recent theoretical paper (Anselmino, Leader et al.) the Collins effect does not lead to large asymmetry. What do you think?

answer: The measured large negative π^- Collins asymmetries imply that the unfavoured Collins fragmentation function is negative and large in size compared to the favoured one. Anselmino et al. demonstrated in their recent work that for the Collins effect in hadron hadron collisions the hard scattering part appears to be very small. Therefore Collins asymmetries in pp scattering are expected to be small even though the distribution and/or fragmentation functions may be large. The group is going to repeat their calculations also for the SIDIS case.

F. Pijlman:

Question: Did you try to extract the Sivers function from the A_{UL} asymmetry?

Answer: The A_{UL} asymmetry receives contributions from the Collins effect, the Sivers effect and from distribution and fragmentation functions which contain twist-3 dependent interaction parts. Experimentally, there is no way to distinguish the different contributions. On the other hand, using the recently measured A_{UT} asymmetry from HERMES, where Collins and Sivers effect are distinguished, one can subtract this contributions from the A_{UL} and can therefore obtain the twist-3 dependent part only. We will use the y -dependence of the A_{UL} to further try to distinguish the Collins and Sivers part in A_{UL} as they appear with different kinematic factors (mainly depending on y).

D. Stamenov:

Comment: The HERMES result on the first momentum of $\Delta s(x)$ leads to very strong breaking of the SU(3) symmetry (more than 35%) of the semi-leptonic hyperon β -decays. We don't see such a big violation of the SU(3) symmetry in these processes.

Answer: The expectation of a sizeable (about -12%) strange sea polarization originates from the violation of the Ellis-Jaffe sum rule. Even if in this context the HERMES result for $\Delta s = 0.028 \pm 0.034$ within the measured range $0.023 < x < 0.3$ is surprising one should take into account that:

- the measured strange density is in agreement with two parton helicity distributions derived from LO fits to inclusive data (GRVS 2001, and Blümlein and Böttcher, 2002);
- the extrapolation in kinematic regions where no data exist is highly model dependent (especially for $x \rightarrow 0$) for both, the quark polarizations and g_1 (in order to calculate the Ellis-Jaffe SR).

Therefore the statement of a 35% violation of SU(3) symmetry should be weakened.

PHYSICS RESULTS FROM COMPASS

A. BRESSAN

University of Trieste and INFN, Sezione di Trieste, Trieste, Italy

(on behalf of the COMPASS Collaboration)

The COMPASS Experiment at the CERN SPS has a broad physics program focused on the nucleon spin structure and on hadron spectroscopy, using muon and hadron beams. Main objectives for the spin program with the muon beam are the direct measurement of the gluon contribution to the spin of the nucleon, semi-inclusive measurements, and the measurement of the transverse spin distribution $\Delta_{Tq}(x)$. The COMPASS apparatus consists of a two-stage large acceptance spectrometer designed for high data rates and equipped with high-resolution tracking, particle identification and electromagnetic and hadronic calorimetry.

The data taking is ongoing since 2002 and till now was mainly devoted to the spin programme using a 160 GeV/c naturally polarized, μ^+ beam and a polarized ^6LiD target. First physics results from the 2002 and 2003 runs are presented.

1. Introduction

The COMPASS [1] experiment is focused on a deeper understanding on how the constituents contribute to the spin of the nucleon. The main goal is a direct measurement of the gluon polarization $\Delta G/G$, obtained by measuring the spin dependent asymmetry of open charm production in the photon-gluon process. The determination of the transversity distribution function $\Delta_{Tq}(x)$ and studies of transverse spin effects; accurate measurements of the flavour decomposition of the quark helicity distributions, vector meson exclusive production, and Λ physics are also important parts of the program. The hadron spectroscopy is dedicated to measurements of the mass and decay patterns of light hadronic systems and leptonic decays of charmed mesons, as well as π and K polarizabilities (Primakoff reactions), and extensive meson spectroscopy to investigate the presence of exotic states.

The experiment, performed by a collaboration of about 270 physicists from 27 institutes and 11 countries, was set up in 1998–2000 and a technical run took place in 2001. The runs from 2002 to 2004 were mainly devoted to the spin programme with a polarized muon beam and a polarized ^6LiD target. After the 2005 technical shut-down at CERN, COMPASS will run at the SPS at least until 2010.

The talk is focused on the results of the 2002 and 2003 runs, during which a total of 500 TB of data have been collected.

2. The COMPASS Apparatus

The COMPASS experiment has been set up in the CERN SPS M2 beam line. It combines high rate beams with a modern two stage magnetic spectrometer [2]. Both stages are equipped with hadronic calorimetry and muon identification by filtering through thick absorbers. In the first stage a RICH detector is also installed, allowing the identification of charged hadrons up to 40 GeV. Detectors, electronics and data acquisition system are able to handle beam rates up to 10^8 muons/s and about 5×10^7 hadrons/s with a maximal interaction rate of about 2×10^6 /s. The triggering system and the tracking system of COMPASS have been designed to stand the associated rate of secondaries, and to use state-of-the-art detectors. Also, fast front-end electronics, multi-buffering, and a large and fast event store, are essential.

The layout of the spectrometer for the 2004 running period is shown in Fig. 1. The

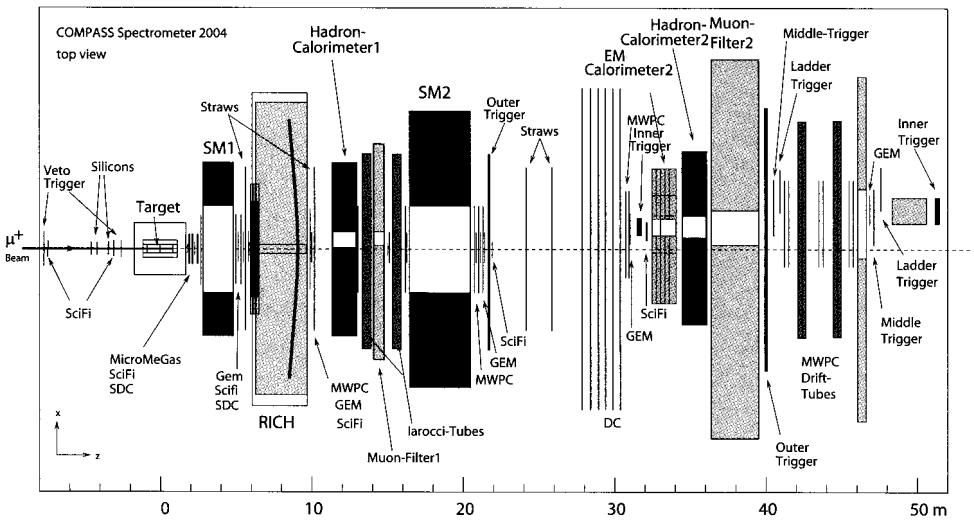


Fig. 1. Top view of the lay-out of the spectrometer for the COMPASS experiment in 2004. The labels and the arrows refer to the major components of the tracking, trigger, and PID systems.

experiment has been run at a muon energy of 160 GeV. The beam is naturally polarized by the π -decay mechanism, and the beam polarization is estimated to be 76%. The beam intensity is 2×10^8 muons per spill (4.5 s long).

We use the polarized target system of the SMC experiment [4], which allows for two oppositely polarized target cells, 60 cm long each. The PT magnet can provide both a solenoid field (2.5 T), to hold the longitudinal (with respect to the beam direction) polarization, and a dipole field (0.5 T), needed for adiabatic spin rotation and for holding the transverse polarization. The use of two different target materials, NH_3 as proton target and ${}^6\text{LiD}$ as deuteron target, is foreseen. Polarizations of 85% and 50% have been reached, respectively. In so far we have used ${}^6\text{LiD}$ because its favourable dilution factor [5] of >0.4 is

particularly important for the measurement of $\Delta G/G$. In 2006 the installation of a new PT magnet build by Oxford-Danfysik, with an increased inner bore radius matching the full acceptance of the spectrometer (± 180 mrad), is foreseen. As a result, an increased acceptance at large x_{Bj} and a better sensitivity to the charm channel will improve the figure of merit of the experiment.

Different tracking devices are used to cope with different fluxes and to fit the needed resolution. The small area trackers (SAS), sitting on or close to the beam line, consist of several stations of scintillating fibres, silicon detectors, micro-pattern gaseous detectors like Micromegas [6], and GEMs [7]. Large area tracking (LAS) devices are made from gaseous detectors (the Saclay Drift Chambers, Straw tubes [8], MWPCs, and the W4/5 Drift Chambers) placed around the two spectrometer magnets. Table 1 summarizes the spatial resolution and the timing properties of the tracking detectors, as derived from the 2002 data. Muons are efficiently identified by large detector planes placed before and after a 60 cm

Table 1. Trackers performances in the 2002 run.

Detector	coordinates	efficiency	resolution	timing
Scintillating fibres	21	94 %	130 μm	0.45 ns
Micromegas	12	95 - 98 %	65 μm	8 ns
GEM	40	95 - 98 %	50 μm	12 ns
SDC	24	94 - 97 %	170 μm	
Straw tubes	18	> 90 %	270 μm	
MWPC	32	97 - 99 %		
W4/5	8	> 80 %		

thick iron absorber. Aluminium Iarocci-type limited streamer and drift tubes planes are used in the LAS and the SAS respectively.

Hadron identification in the LAS is provided by RICH-1 [9], designed to separate π and K over the whole LAS angular acceptance at up to 60 GeV. RICH-1 consists of a 3 m long C_4F_{10} radiator at atmospheric pressure, a wall of spherical mirrors (3.3 focal length) covering an area of >20 m^2 , and two sets of far UV photon detectors placed above and below the acceptance region. The Cherenkov photons are detected by MWPCs equipped with CsI photo-cathodes [10], segmented into $83000 \times 8 \times 8$ mm^2 pads read-out by a system of front-end boards [11] with local intelligence.

The trigger is formed by two hadron calorimeters and several hodoscope systems. Coincidences 2 ns wide between more than 500 elements select the scattered muons in the kinematics region of interest, on the bases of target pointing and energy release. A hadron shower in the hadronic calorimeter provides more selective triggering. The overall typical trigger rate was 5 kHz with a dead time of about 7%. The acceptance in Q^2 goes from quasi-real photons $\sim 10^{-4}$ $(\text{GeV}/c)^2$ up to ~ 100 $(\text{GeV}/c)^2$, while x_{Bj} is from $10^{-4} < x_{Bj} < 0.7^a$.

The readout system [12] uses a modern concept, involving highly specialized integrated circuits. The readout chips are placed close to the detectors and the data are concentrated at a very early stage via high speed serial links. At the next level high bandwidth optical links

^afor $Q^2 > 1$ $(\text{GeV}/c)^2$ the lower limit for the range in x_{Bj} is $\simeq 4 \times 10^{-3}$.

transport the data to a system of readout buffers. The event building is based on PCs and Gigabit or Fast Ethernet switches, and is highly scalable. This high performance network is also used to transfer data, via optical link, to the Central Data Recording (CDR) in the computer center for database formatting, reconstruction, analysis and mass storage.

The computing power needed to process the huge amount of data (~ 300 TB/year) is about 100 kSI2k. The raw data processing is centrally performed at CERN, while the DST and mDST analysis, as well as the large Monte Carlo production, are done on satellite farms in the major home institutes. Event reconstruction is performed by a fully object oriented program, with a modular architecture, written in C++ (CORAL). C++ has also been used to write the analysis program PHAST, while the Monte Carlo program COMGEANT is based on GEANT3.

3. First Physics Results

Many physics channels are under investigation, and important flavours of the ongoing work were given in the parallel sessions:

- A_1^d , the virtual photon asymmetry in both inclusive and semi-inclusive DIS [13],
- $\Delta G/G$ from open charm and from production of pairs of high- p_T hadrons [14],
- transverse spin asymmetries [15, 16],
- exclusive vector meson production to test s-channel helicity conservation [17],
- spontaneous Λ polarizations [18, 19].

Due to limited space, in this contribution only some of the relevant results of first three items will be summarized.

3.1. Inclusive and Semi-Inclusive Asymmetries

The preliminary results from COMPASS, based on 2002-2003 data, are shown in figure 2, where results from previous measurements are also given [20–22]. The COMPASS data are in good agreement with the other data sets, and are compatible with zero in the low- x region. Moreover, the COMPASS data at low- x (fig. 2(b)) already have smaller statistical errors than SMC, thanks to higher luminosity and dilution factor, and will contribute to improving the precision on the spin dependent structure function $g_1^d(x)$ and its first moment Γ_1^d . Figures 2(c) and 2(d) show semi-inclusive asymmetries A_1^h for hadrons of positive charge (c) and negative charge (d), compared with existing data [23, 24]. In this case statistical errors at low- x are also smaller than previous measurements. Those hadron samples are dominated by pions ($\sim 80\%$), and at this stage of the analysis the RICH information is not yet used. Even using PID, a full flavour decomposition from the deuteron data alone is not possible, and there is a need to extend the measurement by also collecting data with a proton target; nevertheless one can extract $\Delta u + \Delta d$, $\Delta \bar{u} + \Delta \bar{d}$ and from kaon samples $\Delta s = \Delta \bar{s}$, i.e. the strange quark helicity distribution function. With the accumulated statistics from 2002 to 2004, COMPASS will extend by one order of magnitude, in the low- x region, the existing results [25] on $\Delta s(x)$, decreasing the uncertainties on the first moment.

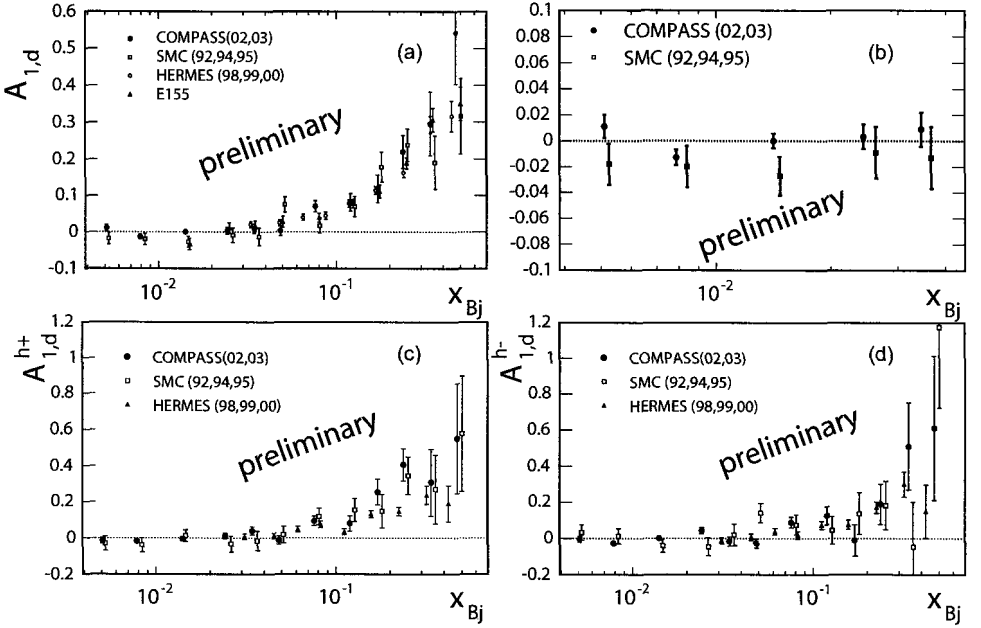


Fig. 2. (a) Measured asymmetry $A_{1,d}^d$ from COMPASS 2002-2003 runs compared with the existing data. (b) Same measurement for the low- x region compared with SMC data only. (c) Semi-inclusive spin asymmetry $A_{1,d}^{h+}$ as a function of x for positively charged hadrons. (d) Semi-inclusive spin asymmetry $A_{1,d}^{h-}$ as a function of x for negatively charged hadrons.

3.2. Gluon polarization $\Delta G/G$

In COMPASS the gluon polarization $\Delta G/G$ is accessed by identifying the photon-gluon fusion process, tagged either by open-charm production or by the production of pair of high- p_T hadrons.

Open-charm events are selected by reconstructing D^0 and D^* mesons from their decay products, i.e. $D^0 \rightarrow K\pi$ and $D^* \rightarrow D^0\pi^0 \rightarrow K\pi\pi^0$. In the first case, cuts on the K direction in the D^0 rest frame ($|\cos(\theta_K^*)| < 0.5$) and on the D^0 energy fraction ($z_D = E_D/E_{\gamma^*} > 0.25$) are needed to reduce the still dominant background. The second case is much cleaner given the unique kinematics. Figure 3(a) shows the D^0 peak reconstructed from the 2003 run, by selecting D^0 coming from D^* decays. The projected error from the open charm, including all the 2002–2004 data, is $\delta(\Delta G/G) = 0.24$.

$\Delta G/G$ from pairs of high- p_T hadrons has, compared to open charm, the advantage of better statistics, even if the extraction of the gluon polarization is more difficult due to the contribution of competitive processes to the asymmetry. Selecting events with $Q^2 > 1$ (GeV/c)² drastically cuts the contribution from resolved photons, at the price of a $\sim 1/10$ reduction of the data sample. Selecting events with high- p_T hadrons reduces the contribution from the leading order process $\gamma q \rightarrow q$ (LO), and increases the QCD-Compton process $\gamma q \rightarrow \gamma q(gq)$ and the photon-gluon fusion (PGF) creation of a light $q\bar{q}$ pair. An additional

selection $x_{Bj} < 0.05$ allows us to restrict the data to a region where $\Delta q/q$ is close to zero, and therefore the contribution to the asymmetry from background processes (LO and QCD-Compton) can be neglected. With this assumption we can relate the preliminary virtual

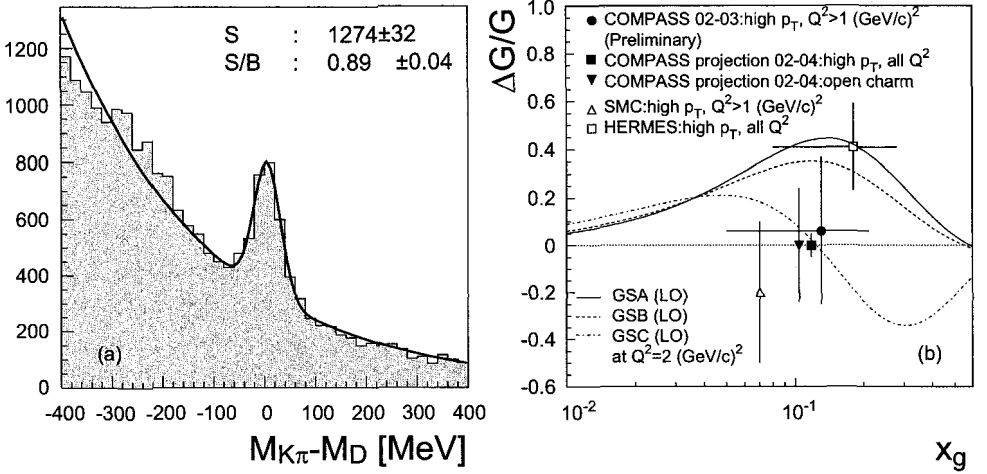


Fig. 3. (a) Reconstructed D^0 in the $K\pi$ invariant mass distribution tagged from the D^* decay. (b) Preliminary result for ΔG from COMPASS high- p_T production and $Q^2 > 1$ (GeV/c^2), together with the results from HERMES ($\langle Q^2 \rangle = 0.06$ (GeV/c^2) and SMC ($Q^2 > 1$ (GeV/c^2)). Also shown are the projected error bars for the open charm high- p_T (all Q^2) for the whole 2002–2004 data. The curves show the parametrization A–C of [31].

photon-deuteron asymmetry $A^{\gamma d}$ resulting from high- p_T pair production from the 2002–2003 data at $Q^2 > 1$ (GeV/c^2) ($A^{\gamma d} = -0.015 \pm 0.080$ (stat) ± 0.013 (syst.)) to $\Delta G/G$:

$$A^{\gamma d} = \frac{A_{LL}^{ud \rightarrow hhX}}{D} \approx \left\langle \frac{\hat{a}_{LL}^{PGF}}{D} \right\rangle \left\langle \frac{\Delta G}{G} \right\rangle \frac{\sigma^{PGF}}{\sigma^T}$$

where \hat{a}_{LL} is the analyzing power of the process at the partonic level, D is the depolarization factor, and σ^{PGF}/σ^T is the fraction of PGF processes in the selected sample. For COMPASS we have estimated, from Monte-Carlo using LEPTO [26], $\langle \hat{a}_{LL}/D \rangle = -0.74 \pm 0.05$ and $\sigma^{PGF}/\sigma^T = 0.34 \pm 0.07$, allowing the extraction of $\Delta G/G = 0.06 \pm 0.31$ (stat.) ± 0.06 (sys.) at a mean gluon momentum fraction $x_g = 0.13$.

For the whole period 2002–2004 one can determine $\Delta G/G$ with an accuracy $\simeq 0.17$ for events with $Q^2 > 1$ (GeV/c^2), while allowing for all Q^2 gives a statistical error of 0.05. The preliminary results from high- p_T are shown in figure 3(b), together with measurements from HERMES [27] and SMC [28].

3.3. Collins and Sivers Effects

The chirally-odd transversity distributions $\Delta_T q(x)$ can be accessed, as suggested by Collins [29], in semi-inclusive interactions of leptons with transversely polarized nucleons in combination with the chirally-odd fragmentation function $\Delta D_q^h(z, p_T)$. At first order

the measured azimuthal asymmetry A_{Col} can be written as:

$$A_{\text{Col}} = \frac{\sum_a e_a^2 \cdot \Delta_T q_a(x) \cdot \Delta D_a^h(z, p_T)}{\sum_a e_a^2 \cdot q_a(x) \cdot D_a^h(z)} = \frac{1}{\sin \Phi_C D_{NNf}} \cdot \frac{N^+ - N^-}{N^+ + N^-}$$

A different mechanism may also give rise to an asymmetry in the scattering of leptons off transversely polarized nucleons. Accounting for an intrinsic momentum k_T dependence of the quark distribution in the nucleon $\Delta_0^T q_a(x, k_T^2)$ may induce an azimuthal asymmetry (Sivers effect [30]) in:

$$A_{\text{Siv}} = \frac{\sum_a e_a^2 \cdot \Delta_0^T q_a(x, k_T^2) \cdot D_a^h(z)}{\sum_a e_a^2 \cdot q_a(x) \cdot D_a^h(z)} = \frac{1}{\sin \Phi_S D_{NNf}} \cdot \frac{N^+ - N^-}{N^+ + N^-}$$

To measure transverse asymmetries, COMPASS has taken SIDIS data with the ^6LiD polarized orthogonally to the incoming μ momentum for about 20% of the running time.

Figure 4 shows preliminary results [15] of the first ever measured single hadron Collins asymmetry on a deuteron target, separately for positive and negative hadrons produced in struck quark fragmentation, as a function of x_{Bj} , $z = E_h / (E_\mu - E_{\mu'})$ and the transverse momentum of the hadron p_T (first row). The Sivers asymmetry, also on a deuteron target, is shown in the second row. The small values of the Collins asymmetries at all x might

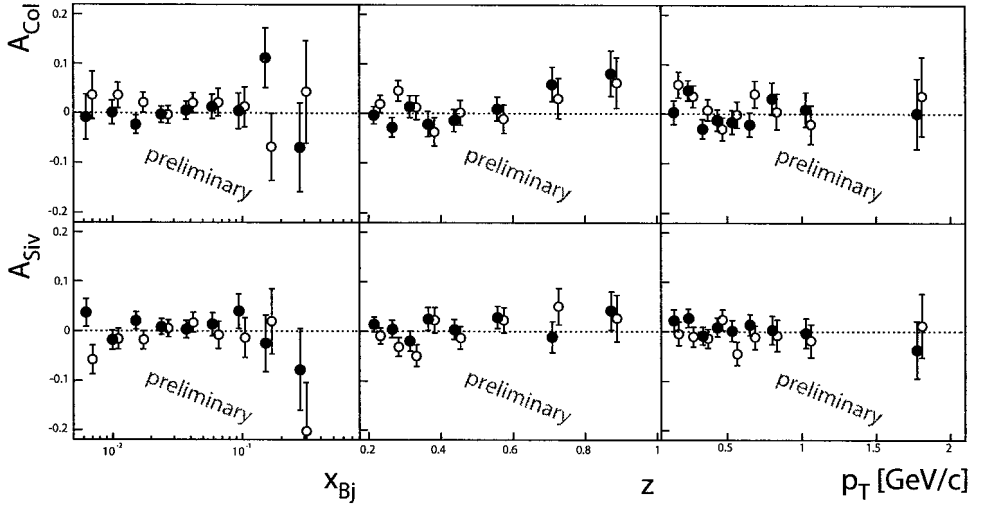


Fig. 4. Collins (top) and Sivers (bottom) asymmetries as a function of x_{Bj} , z and p_T for positively (open triangles) and negatively (closed squares) charged hadrons.

imply either a cancellation between the proton and the neutron asymmetries, or a small Collins effect in the fragmentation ΔD_q^h . Also the Sivers asymmetry is small and, with these statistical errors, compatible with zero, which may indicate a small value of $\Delta_0^T q$ in the x range covered. These results are based on the 2002 run only; the full analysis of the 2002-2004 data will allow us to reduce the statistical errors by a factor of two.

Other promising channels, such as the asymmetries in the two-hadron [16], inclusive vector mesons production, and Λ production are also under study, and will soon yield important new insights into nucleon spin structure.

4. Conclusion

The CERN COMPASS experiment has been on the floor taking data since 2002. Many novel detectors and LHC techniques were integrated into the experiment and are performing according to expectations. The new and modern analysis system has also required great efforts within the collaboration, but is now running in top gear and very interesting results are arriving.

First physics results have been produced and have been shown here and in parallel sessions of this conference, while many others will appear in the near future. The first three years of data taken had shown that COMPASS is fully able to perform complete its broad physics programme, allowing CERN to bring new pieces of information to the spin puzzle. After the accelerator technical shut-down in 2005, COMPASS will run till 2010.

References

1. G. Baum *et al.*, COMPASS proposal, CERN-SPSLC-96-14 (1996).
2. G.K. Mallot, *Nucl. Instr. Methods A* 518 (2004) 121.
3. D. Adams *et al.* [Spin Muon Collaboration], *Nucl. Instr. Methods A* 443 (2000) 1.
4. F. Gautheron *et al.*, "The COMPASS polarized target", these Proceedings.
5. N. W. Schellinghouth *et al.*, *Phys. Rev. C* 48 (1993) 2714.
6. Y. Giomataris *et al.*, *Nucl. Instr. Methods A* 376 (1996) 29; F. Kunne, *Nucl. Phys. A* 721 (2003) 1087.
7. F. Sauli *et al.*, *Nucl. Instr. Methods A* 386 (1997) 531; B. Ketzer *et al.*, *IEEE Trans.Nucl.Sci.* 49 (2002) 2403.
8. V.N. Bychkov *et al.*, *Particles and Nuclei Letters* 2 (2002) 111.
9. E. Albrecht *et al.*, *Nucl. Instr. Methods A* 504 (2003) 354.
10. F. Piuze, *Nucl. Instr. Methods A* 371 (1996) 96.
11. G. Baum *et al.*, *Nucl. Instr. Methods A* 502 (2003) 246.
12. L. Schmitt *et al.*, "The DAQ of the COMPASS experiment", 13th IEEE-NPSS Real Time Conference 2003, Montréal, Canada, May 18-23 2003.
13. D. Peshekhonov *et al.*, "Inclusive spin dependent asymmetry $A_1(x, Q^2)$ ", these Proceedings.
14. C. Schill *et al.*, "Measurement of gluon polarization $\Delta G/G$ at the COMPASS Experiment", these Proceedings.
15. P. Pagano *et al.*, "Measurement of Collins and Sivers asymmetries at COMPASS", these Proceedings.
16. R. Joosten *et al.*, "Transversity signals in two pion correlation at COMPASS", these Proceedings.
17. D. Neyret *et al.*, "Results on exclusive ρ^0 production from COMPASS at CERN", these Proceedings.
18. V. Yu. Alexakhin *et al.*, "Longitudinal polarization in Λ and $\bar{\Lambda}$ hyperions in Deep Inelastic Scattering at COMPASS", these Proceedings.
19. J. Fridrich *et al.*, "Transverse Λ polarization at COMPASS", these Proceedings.
20. B. Adeva *et al.*, *Phys. Rev. D* 58 (1998) 112001.

21. The SLAC E143 Collaboration, K. Abe *et al.*, *Phys. Rev. D* 58 (1998) 112003; The SLAC E155 Collaboration, P.L. Anthony *et al.*, *Phys. Lett. B* 463 (1999) 339 and *Phys. Lett. B* 493 (2000) 19.
22. A. Airapetian *et al.*, *Phys. Lett. B* 442 (1998) 442.
23. B. Adeva *et al.*, *Phys. Lett. B* 420 (1998) 180.
24. A. Airapetian *et al.*, *Phys. Lett. B* 562 (2003) 182.
25. A. Airapetian *et al.*, *Phys. Rev. Lett.* 92 (2004) 012005.
26. G. Ingelman, A. Edin and J. Rathsman, *Comp. Phys. Commun.* 101 108 (1997).
27. A. Airapetian *et al.*, *Phys. Rev. Lett.* 84 (2000) 2584.
28. B. Adeva *et al.* *Phys. Rev. D* 70 (2004) 012002.
29. J. Collins, *NPB* 369 (1993) 161.
30. D. Sivers, *PRD* 41 (1990) 83.
31. T. Gehrmann and W.J. Sterling, *Z. Phys. C* 65 (1994) 461.

DISCUSSION

D. Peshekhonov:

There is a correction for the statistics you have quoted for the inclusive analysis. We used not 22.5×10^6 events (which is the number for pure inclusive trigger), but 34.5×10^6 events.

Answer: Thank you for the clarification.

W. Volgestan:

You showed the nice results for dN/dP_T^2 for the hadron pairs. Has that been compared to a theory calculation?

Answer: The shape of dN/dP_T^2 has been compared with the Monte Carlo distribution based on a modified Lepto generator and the agreement is satisfactory. For what concerns the extraction of the differential cross-section from the data, I have to say that the measure is tuned on an asymmetry extraction and the determination of an absolute normalization is very difficult.

M. J. Tannenbaum:

Since you show the Collins and Sivers asymmetries both compatible with zero, how does that affect the explanation of the single spin asymmetry in pp collisions?

Answer: First of all, those are the first measurement of the Collins and Sivers asymmetries performed on deuteron, while the measurements reported by Hermes (ep) and STAR (pp) are “testing” the transverse distribution of the proton.

Event if statistically compatible with zero, the measured Collins asymmetry is also compatible with Efremov predictions (not shown in my presentation) which foresee a lower signal on deuteron as compared with the proton only. It is possible that a cancellation occurs between p and n in the case of the deuteron.

J. Sowinski:

How does the average x in the ΔG measurement change when the new large acceptance target magnet is installed?

Answer: For DIS and SIDIS measurements the larger acceptance results in an increased acceptance at large x .

Concerning the ΔG measurement and the average x_g , this doesn't change, while $\langle x_g \rangle$ is increased (decreased) by increasing (decreasing) the beam energy.

FIRST RESULTS FROM RHIC SPIN PROGRAM AND FUTURE PROSPECTS

N. SAITO

Physics Department, Kyoto University, Kyoto, Japan

Spin physics with hadrons has entered a new era with the completion of the first polarized proton collider, RHIC, at Brookhaven National Laboratory. The spin physics program at RHIC provides a unique opportunity to elucidate the spin structure of the nucleon and to investigate the symmetries embedded in nature. The first set of physics results from the program are described, along with near future prospects.

1. Introduction

Since the discovery of the spin anomaly in the proton by the EMC collaboration [1], there has been a series of dedicated efforts to elucidate the spin structure of the nucleon. The paper has received more than 1,200 citations to date, representing the impact of the discovery.

It is very difficult to design a complete experiment to elucidate the origin of proton spin, because any measurements are done in finite ranges of x and Q^2 , and also the type of the probe is limited. A major source of polarized structure information has been limited to polarized deep-inelastic scattering (DIS) experiments, which are done with polarized photons on a polarized nucleon target, while the unpolarized structure has been determined using additional data sets from Drell-Yan production of lepton pairs, charged current DIS, and jet/prompt photon productions. Therefore it is crucial to extend the data set to include hadron-hadron reactions as well as global QCD analysis of all available experimental data.

The current understanding of the spin structure of the proton can be seen in one of the global QCD analyses. Figure 1 shows the polarized parton distributions, $x\Delta u_v(x)$, $x\Delta d_v$, $x\Delta g$, and $x\Delta q_{sea}(x)$ at $Q^2 = 1.0 \text{ GeV}^2$, with the uncertainty band of 68% confidence level derived from the HESSIAN method [2].

From this analysis we conclude the following.

- Polarized valence quark distributions are determined to reasonable precision. Precision data from J-lab experiments with the “neutron” target (not included in the analyses so far) will further constrain Δd_v .
- The largest uncertainty resides in the polarized gluon density. $\Delta g(x)$ can be either positive or negative. This is still the biggest problem in the resolution of the proton spin crisis. Furthermore, separation of quark distributions (into flavour singlet and

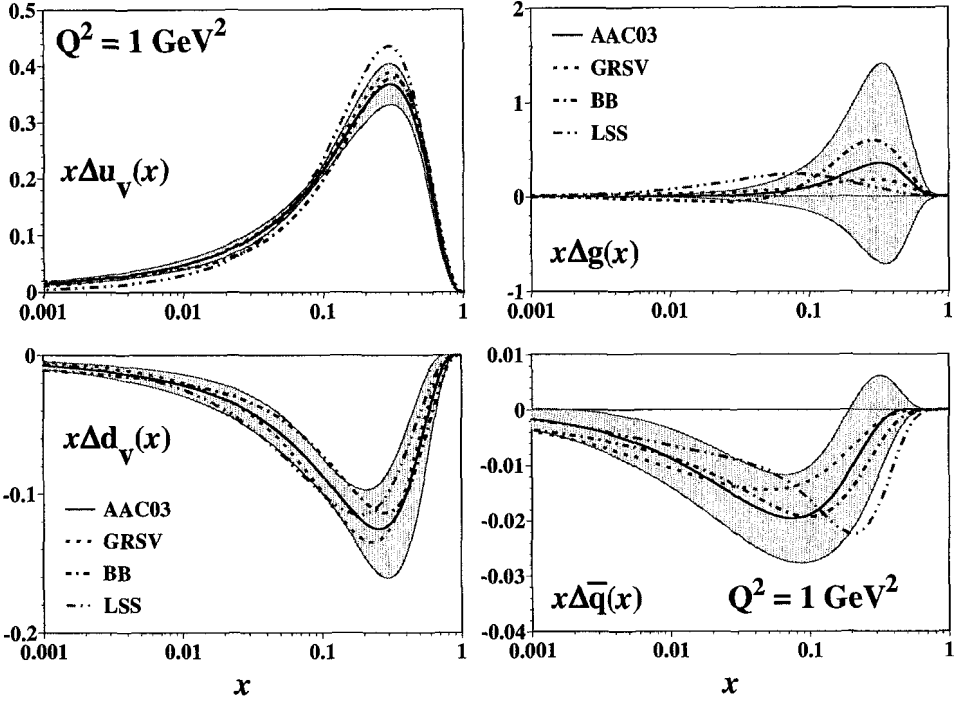


Fig. 1. Polarized parton distribution functions with “ 1σ ” uncertainties extracted from polarized DIS data (AAC03). The relevant first moments at $Q^2=1 \text{ GeV}^2$ are $\Delta\Sigma = 0.21 \pm 0.14$, $\Delta g = 0.50 \pm 1.27$, and $\Delta\bar{q} = -0.06 \pm 0.02$. Distributions are compared with other models (GRSV, BB, LSS).

non-singlet) relies on their coupling with gluon polarization in their Q^2 -evolution. Therefore new data sets to constrain $\Delta g(x)$ are essential not only for the spin sum rule, but also for a better understanding of polarized quark distributions. In addition, a possible axial-anomaly interpretation of the spin crisis has to be revisited, once $\Delta g(x)$ is measured to reasonable precision. In this sense, the impact of $\Delta g(x)$ determination is vast.

- Polarized sea-quark distributions are poorly constrained. This is understandable, since the photon does not distinguish between quark and anti-quark. In most of the global analyses, only the average of $\Delta u_{sea}(x)$, $\Delta d_{sea}(x)$, and $\Delta s(x)$ and their charge conjugations are determined.

In addition to these issues, there are significant uncertainties in the extrapolation of the measurements to $x \rightarrow 0$ and $x \rightarrow 1$. In fact, a significant fraction of the information on spin structure is obtained from the analysis of β -decay constants of octet baryons, where the first moments of polarized quark distributions are directly obtained. The uncertainties involved in the extrapolation will, however, be reduced by extending the measured x - and Q^2 -ranges by collider experiments e.g. RHIC and eRHIC (or ELIC) [6], as was done in the unpolarized case by TEVATRON and HERA. Furthermore, the role of lepton-nucleon elastic scattering has to be revisited, since it also provides the first moment directly [7].

2. RHIC Spin Program

The RHIC at Brookhaven National Laboratory was built originally for heavy ion physics, to search for the new state of matter, quark gluon plasma. We have extended the capability of the machine by adding spin control magnets (Siberian Snake and Spin Rotators) to accelerate and collide polarized proton beams at high luminosity and polarization [8]. The physics program is described in our review article [9].

Every year the spin program receives some fraction of beam time at RHIC for machine development and physics. Selected progress is summarized in Table 1.

Table 1. Selected progress of RHIC as a polarized collider.

Run (begin date)	progress
Run-1 (2000.9)	first injection and acceleration of polarized proton beam at RHIC
Run-2 (2001.12)	first collision of polarized proton beams at $\sqrt{s}=200$ GeV
Run-3 (2003.3)	first operation of spin rotators for PHENIX and STAR
Run-4 (2004.4)	new snake magnet in AGS; \bar{H} target ; new β -tron tune working-point for polarization and luminosity improvements
Run-5 (2005.3)	further polarization and luminosity improvements with super-conducting snake magnet in the AGS and NEG-coating in RHIC

There was a major breakthrough in the machine performance in the last run (Run-4) and we were unexpectedly able to accumulate a similar quality of data for A_{LL} in only four days compared to a dedicated four-week physics run in Run-3. In addition to physics results from the runs up to Run-3, results from the just-finished Run-4 will be discussed later, and also in contributions to these proceedings [10–12]. Details of the machine development are described in MacKay’s contribution [13].

3. First Results from RHIC Spin Program

As discussed in the introduction, one of the major missing pieces in the proton spin puzzle is the polarized gluon in the proton. The RHIC spin program will reveal it with the polarized quark and gluon itself as probes. Since whole idea of the measurements is to utilize perturbative QCD (pQCD) to elucidate the spin structure of the proton, pQCD is required to be reliable for the reactions of interest. In this sense, the precision test of pQCD should be one of the most important prerequisites for the extraction of any spin-structure information about the proton.

In this section, we will first see how pQCD will confront precision data from RHIC. Then spin asymmetry results will be described.

3.1. Precision test of perturbative QCD

As mentioned above, it is important to check how pQCD describes the reactions of interest before we use it to extract structure information. In the factorized picture of hadron reactions, a reaction is divided into three stages; 1) initial state hadrons “emit” partons 2) partons go through hard interactions 3) the final state partons fragment into hadrons. Therefore the cross section for a typical hadron reaction, $pp \rightarrow \pi X$ can be described at leading order as;

$$\begin{aligned}
 E \frac{d^3 \sigma}{dp^3} \sim & g(x_a) \otimes g(x_b) \otimes \frac{d\hat{\sigma}}{dt}(gg \rightarrow gg) \otimes D_{\pi/g}(z) \\
 & + g(x_a) \otimes q(x_b) \otimes \frac{d\hat{\sigma}}{dt}(gq \rightarrow gq) \otimes D_{\pi/(g \text{ or } q)}(z) \\
 & + q(x_a) \otimes q(x_b) \otimes \frac{d\hat{\sigma}}{dt}(qq \rightarrow qq) \otimes D_{\pi/q}(z) + \dots
 \end{aligned} \tag{1}$$

where $f(x_i)$ ($f = g$ or q), $d\hat{\sigma}/dt$, and $D_{\pi/f}(z)$ ($f = g$ or q) describes the probability for a gluon or quark to carry a momentum fraction between x_i and $x_i + dx_i$, the hard scattering cross section, and the fragmentation function to describe the probability for parton f to fragment into π with the energy fraction between z and $z + dz$, respectively. The symbol \otimes represents integration over the appropriate phase space.

The factorization theorem guarantees that the quark distributions and fragmentation functions appearing in the above expression are identical to the ones in DIS and $e^+e^- \rightarrow$ hadrons + X , respectively. Therefore it is possible to extract e.g. gluon distributions from hadron scattering data such as jet/prompt γ production, with only particle momenta in initial and final states. To perform this “trace back” reliably, we have to know how accurately the pQCD can describe the process.

Such a test was done for neutral pion production in PHENIX [14] and STAR [15] at $\sqrt{s} = 200$ GeV, the highest energy pp collisions. PHENIX measured π^0 production in the central rapidity ($|\eta| \leq 0.35$), while STAR measured in the forward rapidity region $\eta = 3.4 - 4.0$, in addition to the central rapidity covered by the newly installed EM calorimeter [16]. As shown in Figure 2, the data are described by the pQCD [17] over several orders of magnitude. This agreement justifies the use of this reaction to extract parton information in the proton. Furthermore, the cross section for $pp \rightarrow \gamma X$ newly obtained by PHENIX is reproduced by the pQCD calculation very well; see Figure 3. Details are discussed in Okada’s contribution to these proceedings [18].

3.2. Gluon polarization in the proton

Since the discovery by EMC of the proton spin crisis, there has been a number of attempts to constrain the gluon polarization in the proton. The E704 experiment at Fermilab has measured the double helicity asymmetries A_{LL} for π^0 production in pp and $\bar{p}p$ collisions [19], and for multi-photon pairs in pp collisions [20]. Measured asymmetries are compared with the model calculations with various

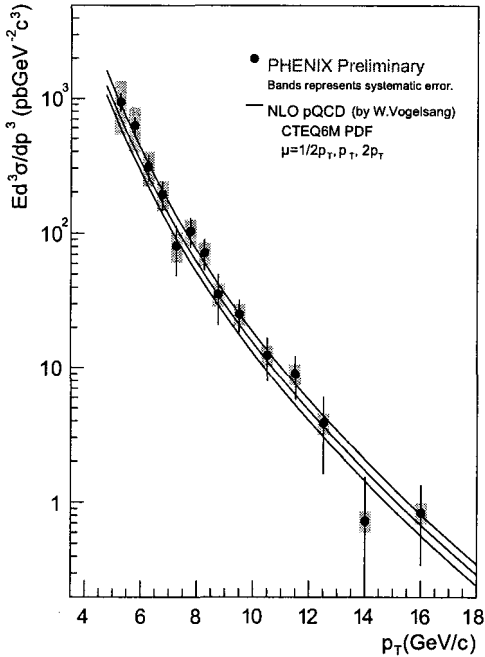
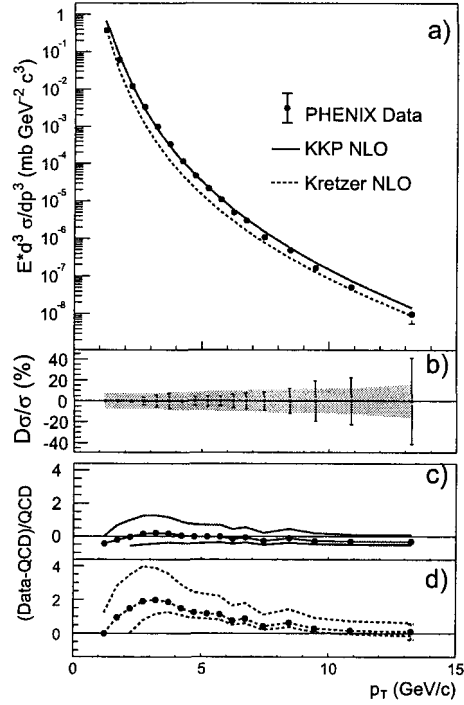


Fig. 3. Cross section for prompt photon production in pp collisions at $\sqrt{s} = 200$ GeV, measured by PHENIX experiment.

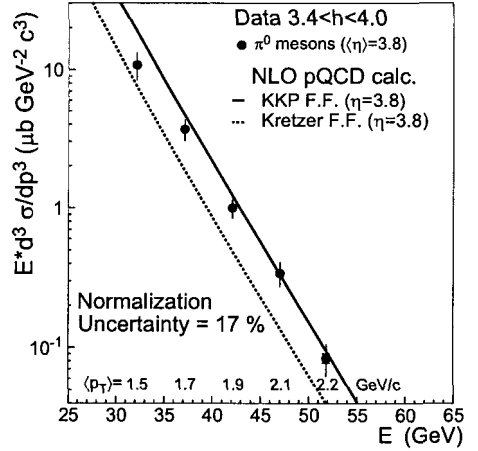


Fig. 2. Cross section for π^0 production in pp collisions at $\sqrt{s} = 200$ GeV, measured at central rapidity by PHENIX (*Left*) and at forward rapidity by STAR (*Right*) experiments.

gluon polarization, and the data seem to favour smaller gluon polarization in the proton.

The SMC experiment has extracted $\Delta g(x)$ from the next-to-leading order (NLO) QCD analysis [21]. Uncertainties in $\Delta g(x)$ span positive and negative regions, when we include the experimental and theoretical uncertainties.

The HERMES experiment has extracted $\Delta g(x)/g(x)$ at $x = 0.17$ utilizing hadron pair production at large transverse momentum [22]. There are still controversies about the extraction based on the LUND model [23] and concerns originating in its scale dependence; it provides a hint for a possible gluon polarization in the proton. The SMC experiment employed the same technique to extract $\Delta g/g(x)$ [24]. In addition, the COMPASS experiment has just released a new data point in this sympo-

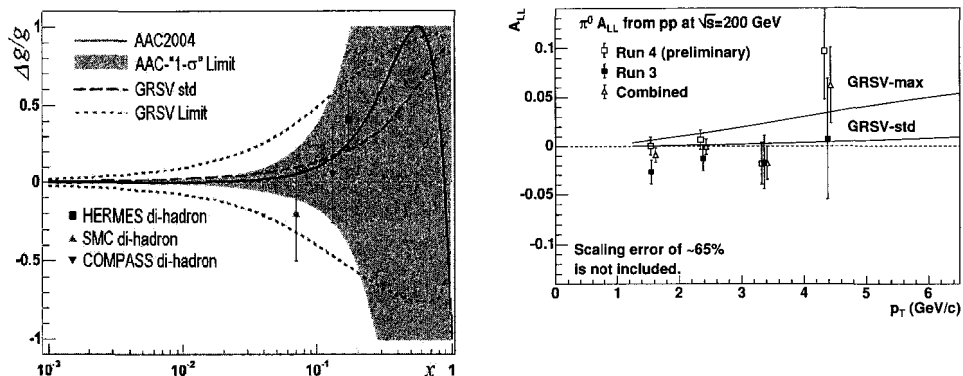


Fig. 4. *Left* Current phenomenological and experimental constraints on gluon polarization $\Delta g/g(x)$. *Right* Combined results on $A_{LL}(pp \rightarrow \pi^0 X)$ at $\sqrt{s} = 200$ GeV.

sium from the same technique [25]. These are summarized in Figure 4, together with phenomenological limits from pQCD analyses of inclusive DIS measurements. The GRSV limits originate in the saturated gluon polarization in the initial scale of the model ($Q^2=0.6$ GeV 2), namely $\Delta g(x) = \pm g(x)$. Due to the large difference between the polarized and unpolarized splitting functions, this reduces to smaller $|\Delta g/g(x)|$ when extrapolated to $Q^2 = 5.0$ GeV 2 , where pQCD can be reasonably applied. The AAC limits reflect the 68% confidence level of $x\Delta g(x)$ shown in Figure 1. Currently available data remain within phenomenological limits.

The PHENIX experiment has published the first measurement of A_{LL} for $pp \rightarrow \pi^0 X$ in the central rapidity region [26]. The data provided the first constraints on gluon polarization from the polarized hadron collider. During Run-4 more data were accumulated and the combined results have just been released at this symposium [10]. Their statistical significance is much better, thanks to the higher polarization during Run-4^a. The data seem to favour the GRSV-std theoretical model rather than the $\Delta g(x) = g(x)$ model, although more direct interpretation is underway.

As we discussed in the previous subsection, the process is described by pQCD very well. According to the pQCD picture, the process is a mixture of gg , qg and qq scattering. In the lower p_T region, the process is dominated by gg and gq scattering, and the A_{LL} becomes quadratic in $\Delta g(x)/g(x)$;

$$A_{LL} \sim \alpha \left[\frac{\Delta g(x)}{g(x)} \right]^2 + \beta \left[\frac{\Delta g(x)}{g(x)} \right] + \gamma, \quad (2)$$

where the coefficients α , β , and γ reflect the relative fraction of the gg , gq , and qq contributions, and the partonic asymmetries a_{LL} for these processes. Because of this quadratic

^aAverage polarization in Run-3 was 27% and it was 40% in Run-4. Since the figure of merit for double spin asymmetries such as A_{LL} and A_{TT} scales to the forth power of polarization, this polarization improvement had a significant impact on our data set.

nature, experimental results could provide two possible ranges of gluon polarization^b. However such ambiguity can be resolved when we combine with other processes to be measured at RHIC e.g. prompt photon production, $pp \rightarrow \gamma X$. The asymmetry A_{LL} for this process can be written at the leading order as

$$A_{LL} \sim \frac{\Delta g(x)}{g(x)} \otimes \frac{\Sigma_q e_q^2 \Delta q(x)}{\Sigma_q e_q^2 q(x)} \otimes a_{LL}(gq \rightarrow \gamma q), \quad (3)$$

with some corrections due to annihilation process, $q\bar{q} \rightarrow \gamma g$. We can extend the determination to the lower x region, by using asymmetric collisions of gg measured in heavy flavour production in the forward muon arms in PHENIX, or forward pion and/or prompt photon production in STAR. As described in these proceedings, the upgrade of the PHENIX experiment will also help [27] to extend the x region.

3.3. Single transverse-spin asymmetries

The single transverse-spin asymmetry, A_N has been measured for many years using a polarized beam and/or polarized target. The reactions under study are either inclusive particle production or elastic scattering. Such non-zero asymmetries arise only when the spin-flip scattering amplitude exists with a different phase from the non-spin flip amplitudes. This can be understood as follows: the initial state hadron is in the transverse spin state, either $|\uparrow\rangle = (|+\rangle + i|-\rangle)/\sqrt{2}$ or $|\downarrow\rangle = (|+\rangle - i|-\rangle)/\sqrt{2}$, where $|+\rangle$ and $|-\rangle$ denote the helicity states of the initial hadron.

$$A_N \sim |\langle X|T|\uparrow\rangle|^2 - |\langle X|T|\downarrow\rangle|^2 = 2 \text{Im} \{ \langle -|T^\dagger|X\rangle \langle X|T|+\rangle \}. \quad (4)$$

At RHIC we have measured non-zero A_N in three different levels of the strong interaction, as we will see in the following subsections.

3.3.1. Inclusive hadron production

There are a number of experimental results on the single transverse-spin asymmetries in inclusive pion productions [28]. One of the most frequently cited results is the E704 experiment, which shows surprisingly *symmetric* asymmetries, A_N for π^+ and π^- in a large- x_F region in $p^\uparrow p$ collisions at $\sqrt{s} = 19.4$ GeV [29]. The asymmetry for π^0 production was about a half of the π^+ asymmetry [30]. This experiment also measured asymmetries with a polarized \bar{p}^\uparrow beam, which again shows *symmetric* asymmetries for π^+ and π^- , in which the sign is flipped compared to $p^\uparrow p$ collisions, while the π^0 asymmetry stayed the same [30,31].

There have been many proposals to explain the origin of the asymmetries, but so far there is no conclusive explanation. Proposed origin(s) of the asymmetries are (i) imbalance in the intrinsic transverse momentum k_T in the initial state parton distributions (Sivers effect) [32], or (ii) spin dependent fragmentation function (Collins-Heppelman effect) [33], (iii) twist-3 effects [34,35], (iv) or a combination of these. In either case, spin flip is involved, either in initial or final states.

^bThis situation is unchanged for jet production, since it is also a mixture of gg , gq and qq scatterings.

Since these effects are based on the hard scattering picture, the asymmetry should persist at higher energies such as at RHIC, provided we stay in the appropriate kinematic region, e.g. similar x_F and p_T regions. Indeed sizable asymmetries were observed by the STAR experiment in π^0 production in the forward rapidity region [15]. The measurement was extended to more forward and also backward rapidities [36], as shown in Figure 5.

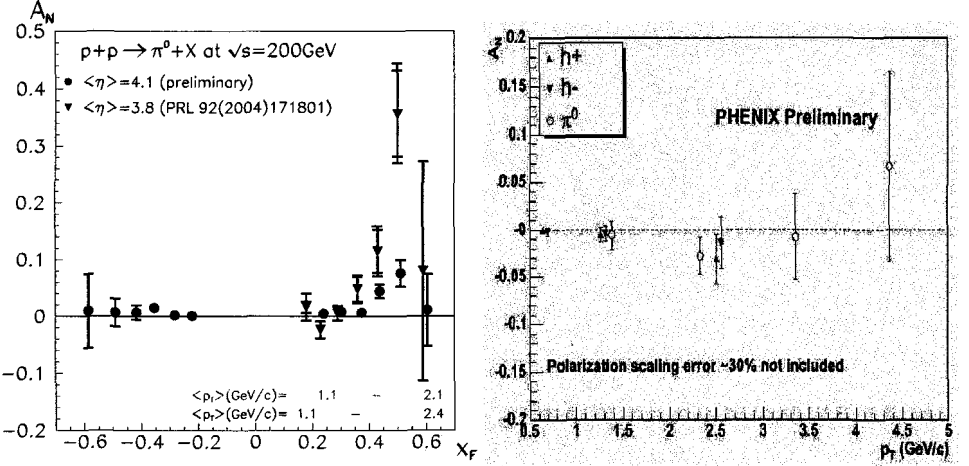


Fig. 5. Single transverse-spin asymmetry A_N in π^0 production in pp collisions at $\sqrt{s}=200$ GeV at forward rapidity measured by STAR (Left), and in π^0 and charged hadron production at central rapidity measured by PHENIX experiment (Right).

On the other hand, measurements in the central rapidity region ($x_F \sim 0$) by PHENIX show essentially zero asymmetries in π^0 , and charged hadron production [37]. These results can be compared with the E704 measurement of π^0 production at 90° in the centre-of-mass system, which also measured zero asymmetry [38].

In addition to efforts to extend the kinematical coverage planned by STAR and BRAHMS experiments, it seems important to separate initial state effects (such as the Sivers effect) from final state effects (such as the Collins effect). There are attempts to disentangle these effects in semi-inclusive production of charged hadrons in deep-inelastic scattering by HERMES [39] and COMPASS [40]. Their effects are extracted as distinctive Fourier components of azimuthal angles of target polarization, pion momentum, and lepton scattering plane. However, current data precision and possible vector meson contributions frustrate a definitive understanding of the origin of the transverse-spin asymmetries. More precise data and an analogous approach in pp collisions [16, 41] are desirable.

It would be useful to investigate a process which does not have a fragmentation contribution, such as Drell-Yan production of lepton pairs. If the asymmetry still survives in this process, the origin should reside in the initial states. This will become possible as the RHIC polarized collider reaches its full design performance within the next few years. Another important input can be expected from e^+e^- collisions, where an extraction of the square of the spin-dependent fragmentation functions is being explored [42].

3.3.2. pp and pC elastic scattering

Another interesting asymmetry awaiting further investigation is elastic scattering of hadrons. Significant asymmetry is predicted in the forward region, where Coulomb interaction and nuclear interaction interfere. In the case of pp elastic scattering, the Coulomb scattering includes a spin flip amplitude, and the interference with nuclear interaction, *which is often assumed to be spin non-flip*, can produce an asymmetry as large as 4-5% [43].

One question is the spin non-flip assumption about the nuclear part, which has never been explored. To further clarify the situation, it would be useful to list the most fundamental observables in pp scattering in terms of parity-conserving helicity amplitudes:

$$\phi_1 \equiv M_{++}^{++}, \phi_2 \equiv M_{++}^{--}, \phi_3 \equiv M_{+-}^{+-}, \phi_4 \equiv M_{+-}^{+-}, \phi_5 \equiv M_{+-}^{+-}. \quad (5)$$

Here $M_{\lambda_3\lambda_4}^{\lambda_1\lambda_2}$ denotes pp scattering amplitude with initial state helicities $(\lambda_1\lambda_2)$ to a final state with $(\lambda_3\lambda_4)$. The spin-flip amplitude in question is ϕ_5 . As can be seen in Table 2, which summarizes selected observables and their representations in the helicity amplitude formalism, A_N plays a crucial role in the determination of ϕ_5 .

We have taken data with a successfully operated polarized gas-jet target [44] and polarized proton beams of 24 GeV/c and 100 GeV/c. The PP2PP experiment also measured A_N with colliding beams at $\sqrt{s} = 200$ GeV [45].

In this symposium, we reported preliminary results for the small $-t$ region at 100 GeV/c [11, 12], as shown in *Left* panel in Figure 6. Our measurements revealed the detailed shape of the asymmetry around the peak region for the first time. The asymmetry is well described by theory in the $-t$ region. We already have a data set for the high $-t$ -region and we hope that we can constrain ϕ_5 significantly when the analysis is completed. Similar effects sur-

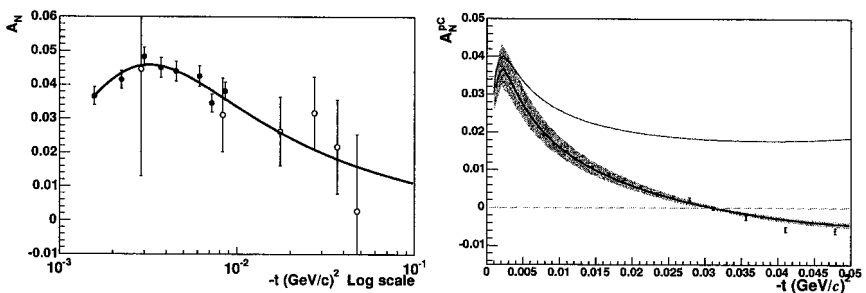


Fig. 6. Single transverse-spin asymmetry A_N in pp (*Left*) and pC (*Right*) elastic scattering. *Left* Our data are shown as closed circles, and previous measurements by E704 are shown as open circles; *Right* The upper curve is a theoretical prediction assuming spin non-flip.

vive in pC elastic scattering, even with “smearing” by nuclear effects. The asymmetry A_N has been measured at a beam momentum of 21.7 GeV/c at AGS (E950) [46]. The data is well described by the theoretical curve by Kopeliovich and Trueman [47]. Polarimetry at RHIC also makes use of this process, with its very large cross section, to measure polarization quickly. This helps machine studies substantially because it is sensitive to possible

polarization changes even over a short time scale [48].

We have released precision data on A_N from the RHIC polarimeter at this conference [49], as shown in *Right* panel in Figure 6. The data are consistent with E950, which revealed significantly non-zero ϕ_5 , while the beam momentum (100 GeV) is significantly higher than that of E950. This represents a significant contrast with the pp data, which is still consistent with $\phi_5 = 0$, although we need to wait for the high $-t$ results for a more conclusive picture. Motivation for more investigation is further strengthened by the newly released PP2PP data on $A_N(pp \rightarrow pp)$ at $\sqrt{s} = 200$ GeV, which again indicates significantly non-zero ϕ_5 in the higher $-t$ region [45]. Obviously only ϕ_5 in lower energy pp data does not show an apparent deviation from zero. It would be very useful to compare A_N in the same $-t$ region, which can be done when the higher $-t$ data analysis is completed.

Table 2. Selected observables in pp elastic scattering and their representation in the helicity amplitude formalism.

observable	helicity amplitudes
σ_{tot}	$\frac{4\pi}{s} \text{Im} \{ \phi_1 + \phi_3 \} _{t=0}$
$\frac{d\sigma}{dt}$	$\frac{2\pi}{s^2} \{ \phi_1 ^2 + \phi_2 ^2 + \phi_3 ^2 + \phi_4 ^2 + 4 \phi_5 ^2 \}$
$A_N \frac{d\sigma}{dt}$	$-\frac{4\pi}{s^2} \text{Im} \{ \phi_5^* (\phi_1 + \phi_2 + \phi_3 - \phi_4) \}$
$A_{NN} \frac{d\sigma}{dt}$	$\frac{4\pi}{s^2} \{ 2 \phi_5 ^2 + \text{Re}(\phi_1^* \phi_2 - \phi_3^* \phi_4) \}$

3.3.3. Particle production in the extremely forward region

Now we extend the discussion to diffractive process. We have already reported the significantly large asymmetry observed in the extremely forward production of neutrons (~ 3 mrad in the centre-of-mass system) in pp collisions at $\sqrt{s}=200$ GeV [50]. Its cross section was measured at ISR in the mid-70's at $\sqrt{s} = 30.6 - 62.7$ GeV [51], and the cross section was well described by one-pion exchange (OPE). Since OPE is a fully spin-flip process, one can expect non-zero A_N . Indeed a negative asymmetry as large as -10% in size was observed, as shown in Figure 7.

The process has been utilized for local polarimetry at the PHENIX collision point. In fact the polarimeter saved the entire program by finding a mis-cabling in the spin-rotator magnets [13]. In STAR, charged particle production measured by the beam-beam counter (BBC) is used for polarimetry, and works very well [52]. Since these are very forward phenomena, it is plausible that diffractive processes are playing an important role, and further investigation is planned by both experiments.

We have seen single transverse-spin asymmetries in very different reactions, elastic scattering, inclusive particle production, and presumably diffractive processes. While these reactions involve different levels of strong interaction, it is interesting that they can be understood in terms of a universal picture of interference of spin-flip and non-flip amplitudes.

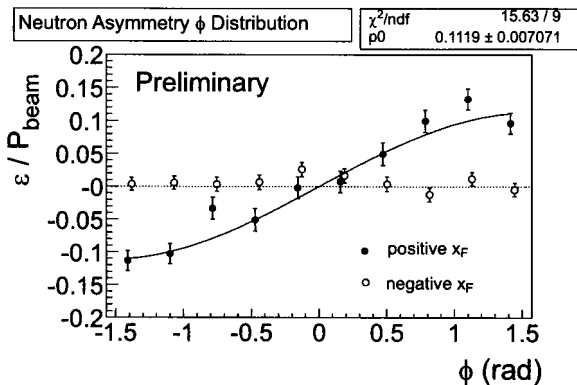


Fig. 7. Single transverse-spin asymmetry A_N for $pp \rightarrow nX$ in extremely forward rapidity at $\sqrt{s} = 200$ GeV.

4. Summary

The RHIC spin program has started to produce physics results in the area of precision tests of perturbative QCD, gluon polarization, and single-spin asymmetries. We have not described many other topics e.g. W -physics, transversity etc., which can be found in the review article [9]. Machine commissioning in the last run was very successful, and we expect more physics results from the next run, which is scheduled from March, 2005. The physics program will be further extended by the detector upgrades planned by both PHENIX and STAR experiments.

Acknowledgment

I would like to thank entire RHIC Spin Collaboration for the materials for the talk and for this manuscript. In preparation of the talk, discussions, plots, and calculations by Y. Fukao, M. Hirai, Y. Koike, M. Stratmann, and W. Vogelsang were very helpful. The RHIC spin program is supported by MEXT, RIKEN, KEK, DOE, and NSF. The work by the author is supported by the JSPS Grant-in-Aid for Scientific Research (No. 16340072).

References

1. J. Ashman *et al.*, *Phys. Lett.* **B206** 364 (1988).
2. M. Hirai, S. Kumano, and N. Saito, *Phys. Rev.* **D69** 054021 (2004).
3. M. Glück, E. Reya, M. Stratmann and W. Vogelsang, *Phys. Rev.* **D63** 094005 (2001).
4. J. Blümlein and H. Böttcher, *Nucl. Phys.* **B636** 225 (2002).
5. E. Leader, A.V. Sidorov, and D.B. Stamenov, *Eur. Phys. Jour.* **C23** 479 (2002) and references therein.
6. A. Deshpande, these proceedings.
7. G.T. Garvey, W.C. Louis, D.H. White, *Phys. Rev.* **C48** 761 (1993).
8. “*Design Manual: Polarized Proton Collider at RHIC*”,
<http://www.agrnhichome.bnl.gov/RHIC/Spin/design/contents.pdf>
9. G. Bunce, N. Saito, J. Soffer and W. Vogelsang, *Ann. Rev. Nucl. Part. Sci.* **50** 525 (2000).
10. Y. Fukao for the PHENIX Collaboration, these proceedings.

11. H. Okada *et al.*, these proceedings.
12. A. Bravar, these proceedings.
13. W. MacKay *et al.*, these proceedings.
14. PHENIX Collaboration (S.S. Adler *et al.*), *Phys. Rev. Lett.* **91** 241803 (2003).
15. STAR Collaboration (J. Adams *et al.*), *Phys. Rev. Lett.* **92** 171801 (2004).
16. J. Sowinski for the STAR Collaboration, these proceedings.
17. F. Aversa, P. Chiappetta, M. Greco, and J.P. Guillet, *Nucl. Phys.* **B327** 105 (1989), B. Jager, A. Schäfer, M. Stratmann, and W. Vogelsang, *Phys. Rev.* **D67** 054005 (2003), B.A. Kniehl, G. Kramer, B. Potter, *Nucl. Phys.* **B597** 337 (2001), S. Kretzer, *Phys. Rev.* **D62** 054001 (2000).
18. K. Okada for the PHENIX Collaboration, these proceedings.
19. E581/E704 Collaboration (D.L. Adams *et al.*), *Phys. Lett.* **B261** 197 (1991).
20. E581/704 Collaboration (D.L. Adams *et al.*), *Phys. Lett.* **B336** 269 (1994).
21. SMC (B. Adeva *et al.*), *Phys. Rev.* **D58** 112002 (1998).
22. HERMES Collaboration, *Phys. Rev. Lett.* **84** 2584 (2000).
23. T. Sjostrand, *Comput. Phys. Commun.* **82** 74 (1994).
24. SMC (B. Adeva *et al.*) *Phys. Rev.* **D70** 012002 (2004).
25. A. Bressan for the COMPASS collaboration, these proceedings.
26. PHENIX Collaboration (S.S. Adler *et al.*), *Phys. Rev. Lett.* **93** 202002 (2004).
27. M. Togawa for the PHENIX Collaboration, these proceedings and E. Kinney for the PHENIX Collaboration, *ibid.*
28. There are number of references which can be found in E925 Collaboration (C. E. Allgower *et al.*), *Phys. Rev.* **D65** 092008 (2002).
29. E704 Collaboration (D.L. Adams *et al.*), *Phys. Lett.* **B264** 462 (1991).
30. E581/E704 Collaboration (D.L. Adams *et al.*), *Phys. Lett.* **B261** 201 (1991).
31. E704 Collaboration (A. Bravar *et al.*), *Phys. Rev. Lett.* **77** 2626 (1996).
32. D.W. Sivers, *Phys. Rev.* **D41** 83 (1990).
33. J.C. Collins, *Nucl. Phys.* **B396** 161 (1993).
34. J. Qiu and G. Sterman, *Phys. Rev. Lett.* **67** 2264 (1991).
35. Y. Kanazawa, Y. Koike, *Phys. Lett.* **B478** 121 (2000).
36. A. Ogawa for the STAR Collaboration, these proceedings.
37. Y. Makdisi for the PHENIX Collaboration, these proceedings.
38. E704 Collaboration (D.L. Adams *et al.*), *Phys. Rev.* **D53** 4747 (1996).
39. HERMES Collaboration (A. Airapetian *et al.*) e-Print: hep-ex/0408013.
40. P. Pagano for the COMPASS Collaboration, these proceedings.
41. D. Boer and W. Vogelsang, *Phys. Rev.* **D69** 094025 (2004).
42. K. Hasuko *et al.*, *AIP Conf. Proc.* **698** 628 (2003).
43. N.H. Buttmore *et al.*, *Phys. Rev.* **D59** 114010 (1999).
44. Contributions of A. Nass, T. Wise, and A. Zelenski in these proceedings.
45. I. Alekseev *et al.*, these proceedings.
46. J. Tojo *et al.*, *Phys. Rev. Lett.* **89** 052302 (2002).
47. B.Z. Kopeliovich and T.L. Trueman, *Phys. Rev.* **D64** 034004 (2001).
48. D. Svirida *et al.*, these proceedings.
49. O. Jinnouchi *et al.*, these proceedings.
50. A. Bazilevsky *et al.*, *AIP Conf. Proc.* **675** 584 (2003).
51. W. Flauger and F. Monnig, *Nucl. Phys.* **B109** 347 (1976).
52. J. Koryluk for the STAR Collaboration, these proceedings.

SOFT SPIN PHYSICS AT JEFFERSON LABORATORY

R. De VITA

Istituto Nazionale di Fisica Nucleare, Sezione di Genova, Genova, Italy

An extensive experimental program to study spin physics at low and moderate four-momentum transfer, Q^2 , is in progress at Jefferson Lab. In this regime, soft processes such as resonance excitation and higher twist contribution play a dominant role, and the measurement of spin observables is a fundamental tool to understand such phenomena and identify the relevant degrees of freedom. In these proceedings I will describe the ongoing experimental program and discuss preliminary and final results.

1. Physics Motivation

In the last three decades extensive studies of the spin properties of the nucleon have been carried out at large momentum transfer Q^2 . Measurements of the spin-dependent structure functions g_1 and g_2 have been performed at several facilities such as SLAC, CERN, and DESY [1] in the DIS region, providing first information on the spin-dependent parton distribution functions.

As Q^2 decreases, non-perturbative effects such as resonance excitations start to play a dominant role, and the connection between the nucleon properties and its elementary constituents, i.e. quarks and gluons, becomes highly non-trivial. In particular at low Q^2 , a better description of the nucleon can be obtained in terms of hadronic degrees of freedom.

Understanding the transition region between hadronic and partonic degrees of freedom is a key issue in strong interaction physics, and spin observables are a fundamental tool to improve our knowledge of these phenomena.

A broad program to study the nucleon spin structure in the soft regime is in progress at Jefferson Lab, involving the three experimental Halls of the facility with the goal of mapping this kinematic region. This ongoing program includes measurements of the nucleon spin structure functions in the resonance region and of their integrals, measurements of nucleon spin polarizabilities at low Q^2 , test of duality of spin structure functions, study of higher twist contributions, and study of polarization observables in exclusive and semi-inclusive meson production. In the next sections I will describe the experimental setups used in such measurements, and I will then discuss a selection of the already available results focusing on the low Q^2 domain. Other information on the Jefferson Lab spin physics program and results can be found in [2–5].

2. Experimental Setup

The core of Jefferson Lab is the CEBAF accelerator (Continuous Electron Beam Accelerator Facility). This consists of two superconducting linacs connected by recirculation arcs. The superconducting cavities operate at a frequency of 1.497 GHz, resulting in a 2.0 ns duty cycle beam for the three experimental halls (Hall A, B, and C). The electron beam is produced by illuminating a strained GaAs cathode with a gain switched laser diode operating at 780 nm. The resulting electron polarization has typical values of 70-80%. The injected electrons can circulate up to five times, reaching a maximum energy of 5.75 GeV.

The three experimental halls are equipped with complementary instrumentation.

The Hall A spin physics experiments [6–11] have been performed using a polarized Helium-3 gas target as an effective polarized neutron target [12]. The ^3He nuclei are polarized through spin exchange with optically pumped Rubidium atoms, reaching typical polarization of 35%. The scattered electrons are detected by two identical high resolution spectrometers. The orientation of the spectrometers with respect to the electron beam line was varied to cover a wide range of Q^2 and invariant mass W .

Hall B is equipped with the CEBAF Large Acceptance Spectrometer (CLAS) [13]. Exploiting the large acceptance of the detector, inclusive, semi-inclusive, and exclusive measurements [14–17] were performed simultaneously using a solid state NH_3/ND_3 target, polarized longitudinally through Dynamic Nuclear Polarization [18].

Finally Hall C is instrumented with two spectrometers with different resolution and acceptance. Measurement of inclusive asymmetries and structure functions on proton and deuteron [19] were performed using a NH_3/ND_3 target [20]. The target polarization can be both parallel and perpendicular to the electron beam direction, allowing full separation of the nucleon structure functions g_1 and g_2 .

The complementarity of the experimental setups of the three Halls has allowed the completion of a broad and extensive physics program, and has allowed the performance of important checks of possible systematic effects in the extraction of the observables of interest.

3. Sum Rules and Integrals of Spin Structure Functions

One of the primary goals of the Jefferson Lab spin physics program is the measurement of the spin structure functions $g_1(x, Q^2)$ and $g_2(x, Q^2)$ of the proton and neutron, and the extraction of their integrals $\Gamma_1(Q^2) = \int g_1(x, Q^2) dx$ and $\Gamma_2(Q^2) = \int g_2(x, Q^2) dx$. These are connected to important sum rules such as the Bjorken sum rule, which relates the difference ($\Gamma_1^p - \Gamma_1^n$) to the axial form factor of the nucleon in the infinite Q^2 limit [21], and the Burkhardt-Cottingham sum rule which predicts $\Gamma_2(Q^2)$ to be zero [22].

The Γ_1^p and Γ_1^n integrals have been measured at large Q^2 at SLAC, CERN, and DESY, and have been found to be respectively positive and negative, consistent with what is expected from the Bjorken sum rule and pQCD calculations. On the other hand, both integrals are expected to be negative at very low Q^2 and to approach zero for $Q^2 \rightarrow 0$ with a negative slope, based on the relation between the Γ_1 integral and the Gerasimov-Drell-Hearn sum rule [23, 24]. This sum rule relates the difference of the helicity-dependent total photoab-

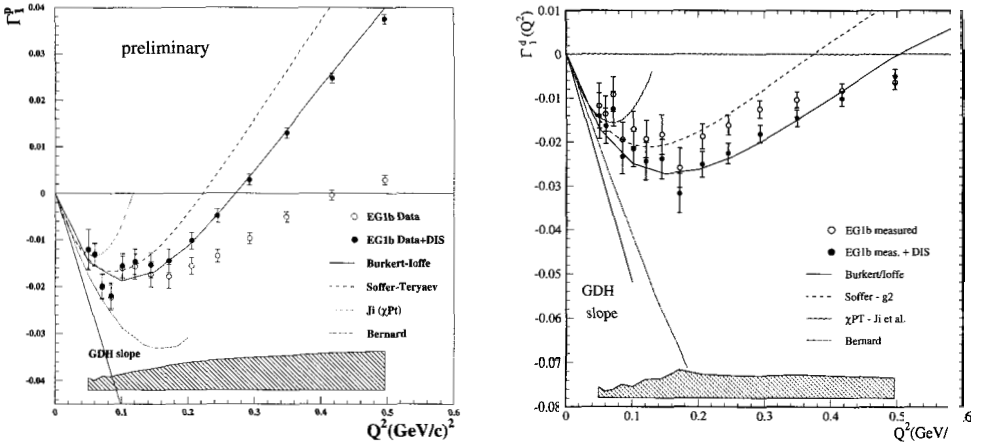


Fig. 1. Preliminary results on $\Gamma_1(Q^2)$ for the proton (left) and the deuteron (right), obtained by CLAS. The open circles are the CLAS data integrated over the measured region, while the full circles include the DIS contribution. The shaded band shows the systematic error associated with the measurement. At low Q^2 the slope given by the GDH sum rule and chiral perturbation theory calculations from [25] and [26] are indicated. The dashed and dotted lines are model predictions of [27] and [28].

sorption cross sections to the anomalous magnetic moment of the the nucleon, and is based on very general assumptions such as gauge invariance, causality, and analyticity. Because of this constraint, the Γ_1 integral in particular for the proton must undergo to a dramatic change as Q^2 varies from the photon point to the perturbative domain.

The proton and deuteron Γ_1 integrals have been measured in Hall B with CLAS, while Γ_1^n has been extracted from the ^3He measurement performed in Hall A. Figure 1 shows the CLAS measurements on protons and deuterons at up to $Q^2 = 0.5 \text{ GeV}^2$. The open circles show the integral of g_1 over the measured region, while the full circles include the extrapolation at small x evaluated using a parameterization of the world data. The error bars represent the statistical error while the shaded band shows the systematic uncertainty. At low Q^2 the slope given by the GDH sum rule is shown, as well as the chiral perturbation theory predictions of Bernard [25] and Ji [26]. The dashed and dotted line are model predictions of [27] and [28]. The measured integrals are consistent with the expected behavior both for the proton and deuteron, showing the change in slope for $Q^2 \sim 0.1 - 0.2 \text{ GeV}^2$. The comparison with χPT predictions shows good agreement only at lower Q^2 , while significant discrepancies are found at higher values.

Figure 2 shows the Γ_1 (left) and Γ_2 (right) integrals for the neutron, measured in Hall A [29]. The Γ_1 integral measured over the resonance region is shown by open circles, while the full circles include the extrapolation in the unmeasured region based on the parameterization by Bianchi and Thomas [31]. The size of the points represents the statistical error, while the shaded band shows the systematic uncertainty. Previous measurements from SLAC and HERMES, and different theoretical predictions from [25–28,32] are shown. The new Hall A data agree fairly well with the previous measurements with much improved accuracy, extending the coverage at very low Q^2 where χPT predictions are available. The

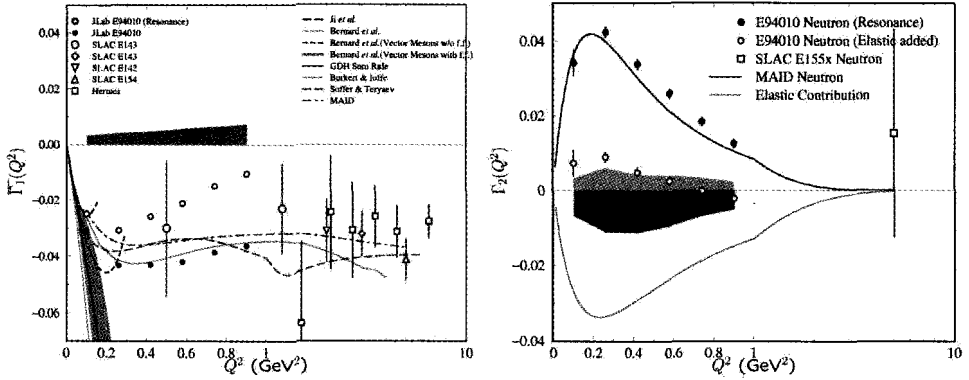


Fig. 2. Left: Γ_1 integral for the neutron. The open circles show the integral over the measured region while the full circles include the extrapolation to small x . The previous SLAC and Hermes measurements are shown for comparison. Right: Γ_2 integral for the neutron. The full circles show the measured integral while the open circle include the elastic contribution (lower curve). The positive shaded band shows the experimental uncertainties, while the negative band shows the effect of the extrapolation to small x .

Burkhardt Cottingham sum rule for the neutron has been tested integrating the structure function $g_2(x, Q^2)$. The results shown in the right panel of figure 2 seem to indicate that the sum rule is verified to within the experimental uncertainty.

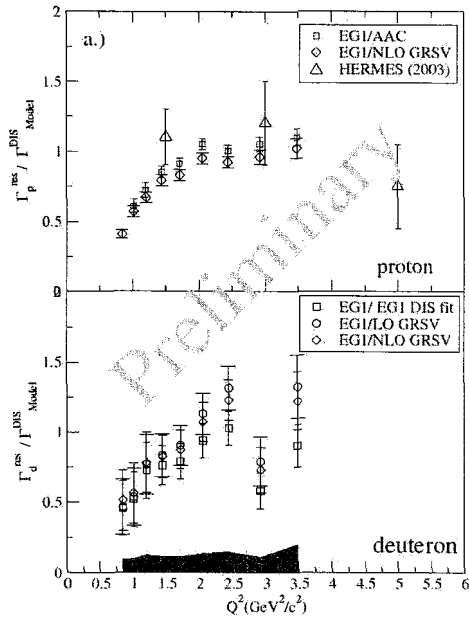


Fig. 4. $\Gamma^{RES}(Q^2)/\Gamma^{DIS}$ as a function of Q^2 measured by CLAS. The top plot shows the results for the proton while the bottom plot shows the results for the deuterium. The Hermes data are shown for comparison.

The Hall A and Hall B measurements of Γ_1 on proton, deuteron, and neutron have been combined to extract the Bjorken integral [30]. Details of this analysis and results can be found in [3].

4. Duality in Spin Structure Functions

The dual nature of the nucleon structure functions was first observed in the unpolarized sector by Boom and Gilman [33], who noticed that the nucleon structure function $\nu W(x, Q^2)$ measured in the resonance region at low Q^2 was equivalent to the structure function $F_2(x)$ measured in the DIS regime when averaged over the same range of the scaling variable $\xi = 2x/(1 + \sqrt{1 + 4M^2x^2/Q^2})$. Duality for unpolarized structure functions has been found to hold at the 10% level down to $Q^2 \sim 1 \text{ GeV}^2$.

In the polarized sector, the situation is

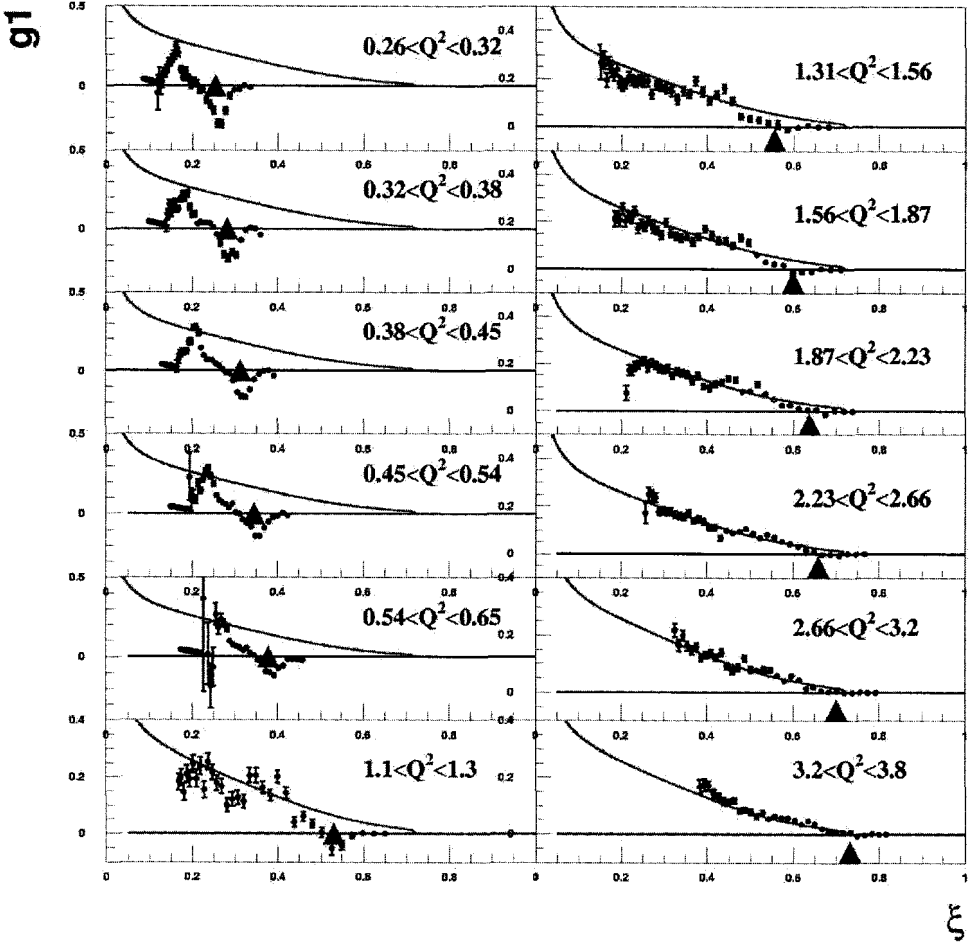


Fig. 3. g_1 structure function of the proton from CLAS. The line shows a parameterization of the world data evolved at $Q^2 = 10 \text{ GeV}^2$. The triangle indicates the position of the $\Delta(1232)$ resonance.

more complicated due to the resonance contribution, which can cause the structure functions to have negative values as shown in Figure 3.

A first test of duality of the proton structure function g_1 was performed by the HERMES Collaboration, who compared the integral of g_1 over a specific x range in the resonance region, $\Gamma_1^{RES}(Q^2) = \int_{x_1}^{x_2} g_1(x, Q^2) dx$, with that over an equivalent region of x in the DIS regime, $\Gamma_1^{DIS} = \int_{x_1}^{x_2} g_1(x) dx$. The HERMES Collaboration found $\Gamma_1^{RES}(Q^2)/\Gamma_1^{DIS}$ to be consistent with unity at the 20% level down to the minimum Q^2 of $\sim 1.5 \text{ GeV}^2$ [34]. A similar analysis has been performed using the CLAS data for the proton and deuteron structure functions. Figure 4 shows the $\Gamma_1^{RES}(Q^2)/\Gamma_1^{DIS}$ ratio for the proton (top) and deuteron (bottom) as a function of Q^2 . The CLAS preliminary results are in general agreement with the HERMES data, but provide a much more precise and detailed picture of the onset of

duality. The CLAS ratio test begins to fail at the two sigma level when Q^2 becomes less than 1 GeV^2 . The ratio is also consistent with unity at the 10% level for the proton, and the 30% level for the deuteron when Q^2 goes beyond 2 GeV^2 .

5. Higher Twist Contribution to Spin Structure Function

Understanding the origin and quantify higher twist contributions to the structure functions is one of the key issues in the phenomenology of nucleon structure in the soft regime. In the case of spin structure functions, an interesting feature of $g_2(x, Q^2)$ is that it contains twist-3 contributions at leading order. As a result, the integral $d_2 = \int x^2 (2g_1(x, Q^2) + 3g_2(x, Q^2)) dx$ gives a measure of the higher twist contribution to g_2 . Figure 5 shows the Hall A measurement of d_2 on the neutron for $Q^2 = 0.2 - 0.9 \text{ GeV}^2$. The data are in good agreement with the prediction of the MAID model [32], while χ PT calculations overestimate the integral even at the smaller Q^2 . At $Q^2 = 5 \text{ GeV}^2$ the SLAC data give a large and positive value for the integral, while lattice QCD calculations give a small and negative value, in better agreement with the trend of the present measurement.

6. Summary and Outlook

Extensive measurements of spin observables in the soft regime have been performed at Jefferson Lab involving the three experimental Halls. These measurements aim at understanding the transition region between hadronic and partonic degrees of freedom, investigating phenomena such as resonance excitation, duality in spin structure functions, and higher twist contribution. The high precision results obtained from such experiments provide stringent constraints for theories in a kinematic region that was not explored in detail in the past.

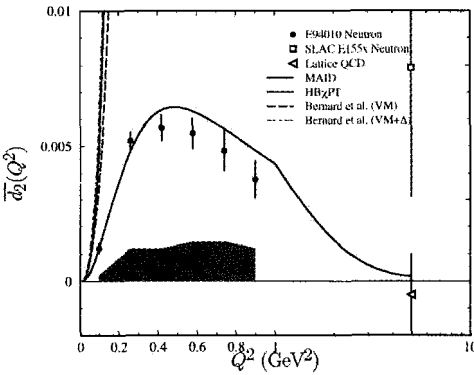


Fig. 5. $d_2(Q^2)$ integral for the neutron measured in Hall A. The smooth curve shows the prediction of the MAID model. At 5 GeV^2 the SLAC data give a positive value while lattice QCD calculations give a small and negative value.

In addition to the measurements already completed, new experiments are currently under analysis or planned for the near future.

These include an extension of the Hall A and Hall B measurement of spin structure functions at very low Q^2 [9, 35], with the goal of reaching a minimum Q^2 of 0.01 GeV^2 in the measurement of Γ_1 to study the behavior of the integral at very low Q^2 and to test chiral perturbation theory predictions. Furthermore, extensions of the duality studies on spin structure functions are planned in Hall A and C by means of experiment E01-012 [11]

which is presently under analysis, and experiment E03-106 [36] which will take data in the near future.

The already available data as well as the new data provided by the upcoming experiments, will provide high precision information on spin observables, and will hopefully allow us to reach a complete understanding of the nucleon spin structure in the soft regime.

Acknowledgments

I am grateful to the many members of the Hall A, CLAS, and Hall C Collaborations whose work I have reported here. The Southeastern Universities Research Association (SURA) operates the Thomas Jefferson National Accelerator Facility for the United States Department of Energy under contract DE-AC05-84ER40150.

References

1. For a recent review see: B. W. Filippone and X. D. Ji, hep-ph/0101224 (2001), and references therein.
2. M. Garcon, *these proceedings*.
3. A. Deur, *these proceedings*.
4. P. Bosted, *these proceedings*.
5. M. D. Mestayer, *these proceedings*.
6. S. Frullani, J. Kelly, and A. Sarty, Jefferson Lab Proposal E91-011, (1991).
7. G. Cates, J. P. Chen and Z. E. Meziani, Jefferson Lab Proposal E94-010, (1994).
8. T. Averett and W. Korsch, Jefferson Lab Proposal E97-103, (1997).
9. J. P. Chen, A. Deur and F. Garibaldi, Jefferson Lab Proposal E97-110, (1997).
10. J. P. Chen, Z. E. Meziani and P. Souder, E99-117, (1999).
11. J. P. Chen, S. Choi, and N. Liyanage, Jefferson Lab Proposal E01-012, (2001).
12. J. Alcorn *et al.*, Nucl. Instrum. and Meth. **A522**, 171 (2004).
13. B. Mecking *et al.* (CLAS Collaboration), Nucl. Instrum. and Meth. **A503** (2003) 513.
14. V. D. Burkert, D. G. Crabb and R. Minehart, Jefferson Lab Proposal E91-023, (1991).
15. S. E. Kuhn, G. E. Dodge and M. Taiuti, Jefferson Lab Proposal E93-009, (1993).
16. M. Anghinolfi, R. Minehart and H. Weller, Jefferson Lab Proposal E93-036, (1993).
17. P. Stoler, R. Minehart and M. Taiuti, Jefferson Lab Proposal E94-003, (1994).
18. C. D. Keith *et al.*: Nucl. Instrum. and Meth. **A501** (2003) 327.
19. JLab E01-006, Spokesperson O. Rondon-Aramayo.
20. D. G. Crabb *et al.*, Nucl. Instrum. and Meth. **A356**, 9 (1995); T. Averett *et al.*, Nucl. Instrum. Meth. **A427**, 440 (1999).
21. J. D. Bjorken, Phys. Rev. **148**, 1467 (1966).
22. H. Burkhardt and W. N. Cottingham, Annals of Physics **56**, 453 (1970).
23. S. B. Gerasimov, Sov. J. Nucl. Phys. **2**, 430 (1966).
24. S. D. Drell and A. C. Hearn, Phys. Rev. Lett. **16**, 908 (1966).
25. V. Bernard *et al.*, hep-ph/0203167 (2002).
26. X. D. Ji *et al.*, Phys. Lett. **B472**, 1 (2000).
27. V. D. Burkert and B. L. Ioffe, Phys. Lett. **B296**, 223 (1992); J. Exp. Theor. Phys. **78**, 619 (1994).
28. J. Soffer and O. V. Teryaev, Phys. Rev. Lett. **70**, 3372 (1993), Phys. Rev. **D51**, 25 (1995), Phys. Lett. **B 545**, 232 (2002).
29. M. Amarian *al.*, Phys. Rev. Lett. **92**, 022301 (2004).
30. A. Deur *et a.*, Phys. Rev. Lett. **93**, 212001 (2004).
31. E. Thomas and N. Bianchi, Nucl. Phys. **B82**, 256 (2000).

32. D. Drechsel *et al.*, Nucl. Phys **A645**, 145 (1999).
33. E. D. Bloom and F. J. Gilman, Phys. Rev. Lett. **25**, 1140 (1970).
34. A. Airapetian *et al.*(HERMES Collaboration), Phys. Rev. Lett.. **90**, 092002 (2003).
35. M. Battaglieri, A. Deur, R. De Vita, and M. Ripani, *The GDH Sum Rule with Nearly Real Photons and the g_1 Structure Function of the Proton at Very Low Q^2* , Jefferson Lab Proposal E03-006, (2003).
36. M. Jones *et. al*, Jefferson Lab Proposal E03-106, (2003).

DISCUSSION

O. Teryaev:

Comment 1: The QCD-based model by J. Soffer and myself contains the QCD radiative and power corrections as inputs. We did not not evaluate them 10 years ago, as we did not expect such a remarkable accuracy. Now this was done and reported by J. Soffer at the GDH Conference this summer, and also in my talk in a parallel session. The results are much closer to the data than the old curves shown in the plots.

Comment 2. There are QCD-based arguments which which I also presented in the parallel session, that duality should work better for the structure function $g_T = g_1 + g_2$ than for g_1 itself. It would be interesting to check this.

Answer: Comment 1: As you said in the last few year, Jefferson Lab has provided high precision data in the low Q^2 region. It is very important to see that these new results are stimulating new theoretical activity in this field. In the future we will surely compare the JLab results with the new theoretical predictions from Soffer and Teryaev.

Comment 2: The test of duality on g_T is a very interesting issue. This can be studied in Hall A and Hall C at Jefferson Lab where they have measurements both of g_1 and g_2 . I think this topic will be certainly considered in the near future.

SPIN PHYSICS IN NUCLEAR INTERACTIONS*

K. HATANAKA

Research Center for Nuclear Physics, Osaka University Ibaraki, Japan

There have been extensive studies to construct effective interactions, modified so as to account for the presence of the many body environment, which are used to investigate the properties of nuclear matter or nuclear reactions. High precision experimental data have become available and owing to the rapid development of computers, large scale calculations have become possible based on more fundamental theories. Three topics are discussed by comparing experimental data at intermediate energies with sophisticated calculations; (p,2p) reactions, spin isospin responses in nuclei, and few nucleon systems.

1. Introduction

One of the goals of nuclear physics is to understand the structure of nuclei and the dynamics of nuclear reactions in terms of the underlying interactions between nucleons. For the strong interaction, meson theory was proposed by Yukawa 70-years ago [1]. Since then, many models of nucleon-nucleon (NN) interactions were proposed to reproduce NN scatterings. Meson exchange interactions depend strongly on the spin, parity and isospin of the interacting NN system [2]. These characteristics of the NN interactions lead to rich nuclear structures and nuclear reaction dynamics. It is well known, free NN interactions are too attractive to describe properties of nuclei. There have been extensive studies to construct effective interactions, modified so as to account for the presence of the many body environment, which are used to investigate the properties of nuclear matter or nuclear reactions.

Over the past decades, high precision experimental data have become available and owing to the tremendous development of computers, large scale calculations have become possible based on more fundamental theories. In this talk, I will discuss medium effects on NN interactions by comparing recent high precision experimental data at intermediate energies with sophisticated and rigorous calculations on the following three topics:

- (1) The relativistic prescription of spin observables for exclusive proton knockout reactions
- (2) Spin isospin responses in nuclei studied by the Gamow-Teller quenching value Q and the longitudinal/transverse excitations by quasi elastic (p,n) scatterings

*This work is supported in part by the grant-in-aid for scientific research no. 14340074 of the ministry of education, culture, sport, science and technology of Japan

- (3) Three nucleon forces and relativistic effects explored through nucleon-deuteron scatterings.

2. Modification of NN Amplitude Studied by Exclusive Proton Knockout Reactions

The exclusive proton knockout (p,2p) reaction has advantages over the quasi elastic scattering by electrons. A simple reaction mechanism is expected for this reaction at intermediate energies. Same spectroscopic factors are obtained as (e,e'p) reactions and have much larger cross sections. It is well known that spin observables provide stringent tests of theoretical models. Among various models, the relativistic (Dirac)-Brueckner-Hartree-Fock (DBHF) approach provides a consistent description of such medium effects as the Pauli principle and density dependent NN amplitudes [3]. Simple relativistic models give an excellent description of spin observables for elastic and inelastic proton-nucleus scattering [4]. Only very sophisticated state-of-the-art non-relativistic models can describe elastic proton scattering with the same level of accuracy [5]. It is possible to incorporate spinor modification by the relativistic Love Franey model in a self-consistent way [6]. The scaling conjecture of the hadron masses and coupling constants is attributed to the partial restoration of the Chiral symmetry in the nuclear medium [7].

The (p,2p) reaction is considered to be nucleon-nucleon scattering in the nuclear field, and should be different from the scattering in a free space. If we can control the density of the medium where the scattering occurs, we can extract the density dependence of NN amplitudes. Thus, in the meson exchange model, we can specify the density dependence of the spinor modifications. At TRIUMF, distinct reductions of the analyzing power were found for the (p,2p) reaction leading to $1s_{1/2}$ -hole state on ^{16}O [8]. No calculation could reproduce the large reductions, even though the empirical density dependence was taken into account in the interaction. By selecting kinematical conditions in measurements, we knock out an $s_{1/2}$ nucleon at rest in the nucleus, and this process has several advantages:

- (1) Simple reaction mechanisms and nuclear structures are expected.
- (2) There is a large contribution from the nuclear interior.
- (3) The target nucleon is completely unpolarized.
- (4) Spin-dependent distortion is negligible.

In the exclusive measurement, we explained how to estimate the average density of the medium where the scattering occurs, and the experimental data showed a clear dependence on the estimated average density [9]. Non-relativistic calculations could not reproduce the experimental results even if we introduced density dependent interactions. By incorporating a relativistic Love Franey model and the Brown Rho scaling conjecture, PWIA gave a good description of the experimental data.

At higher energies we can cover a wider momentum transfer (q) region. This q dependence is expected to be able to distinguish the effects of meson-mass, nucleon-mass and coupling constant modifications [10]. Figure 1 shows our results at 1 GeV compared with theoretical predictions. This is the induced polarization for $1s_{1/2}$ proton knockout from ^{12}C ;

measurements [11] were performed at PNPI, Russia. Non-relativistic PWIA and DWBA calculations fail to describe the data, and non-relativistic distortion effects are negligible. On the other hand, a relativistic DWIA calculation gives much better descriptions. In the right panel of Fig. 1, the reduction of the polarization is well explained when the smaller scaling factor is applied for hadron masses and coupling constants [7]. It is interesting as well to see that relativistic distortion effects are very important at 1 GeV, and that density-dependent corrections to the NN interaction play a significant role. Recently, it has been reported the relativistic DWIA calculations describe the analyzing powers of the (p,2p) at 200 MeV quite well [14]. Figure 2 shows the results at 392 MeV. The distortion effects are smaller than at either 200 MeV or 1 GeV. The following points summarise this section:

- (1) Relativistic calculations reproduce the experimental data of (p,2p) reaction at intermediate energies very well
- (2) Spin observables of (p,2p) reactions are sensitive to relativistic optical potentials
- (3) Density-dependent corrections to the free NN interactions are required to describe the induced polarization for $1s_{1/2}$ knockout from ^{12}C at 1 GeV
- (4) More data on a complete set of spin observables are needed to establish the theory and to study medium modifications of NN interactions [15]. They can be measured at the RCNP, PNPI and iThemba Laboratories.

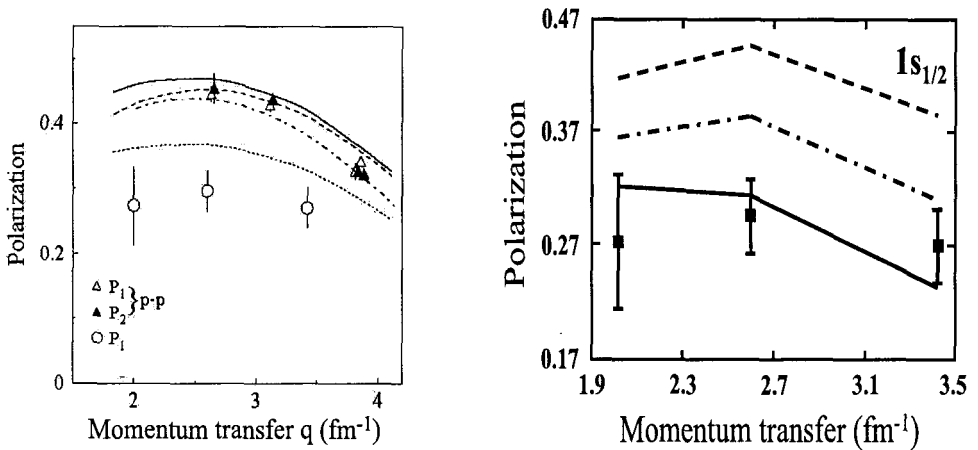


Fig. 1. Left panel: Momentum transfer dependence of the polarization for $p-p$ scattering and the $^{12}\text{C}(p,2p)$ reaction. P_1 and P_2 are the polarization of forward and backward outgoing protons, respectively. The dot-dashed curve represents the results of a phase-shift analysis for the $p-p$ scattering. The dashed and solid curves represent results of the PWIA and DWIA calculations with the NN interaction in free space, respectively. The dotted curve is the DWIA result, in which the relativistic effect is taken into account in a Schrödinger-equivalent form [12]. Right panel: The dashed line is the relativistic PWIA result. The dot-dashed line and solid lines represent the relativistic DWIA results with scaling factors of 1.0 and 0.55, respectively [13].

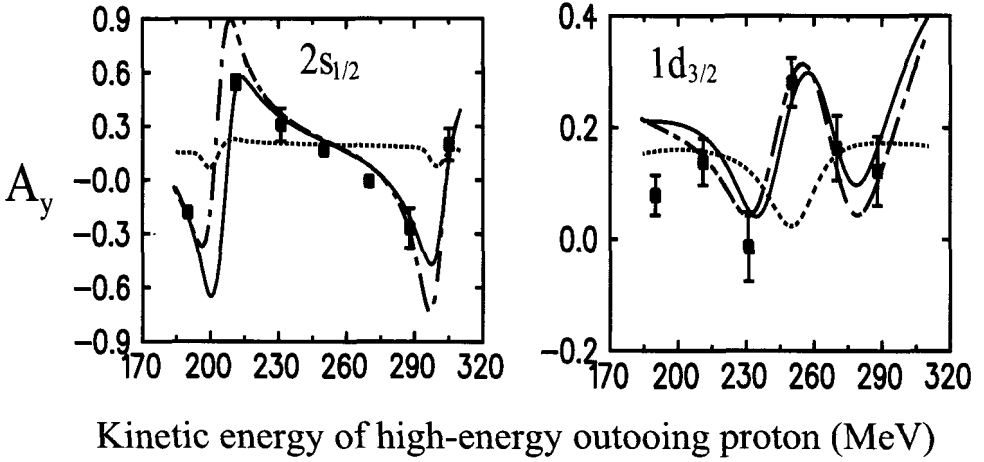


Fig. 2. Analyzing power of the $^{40}\text{Ca}(p,2p)^{39}\text{K}$ reaction at 392 MeV for the knockout of $2s_{1/2}$ (left) and $1d_{3/2}$ (right) protons, respectively. High- and low-energy protons were detected at 32.5 degrees and 50.0 degrees, respectively. The dotted curve, the dot-dashed curve and the solid curve represent results of the non-relativistic DWIA, the relativistic PWIA, and the relativistic DWIA by Hillhouse, respectively [13].

3. Pionic Correlation in Spin Isospin Excitations

Since Yukawa proposed the pion exchange mechanism as a dominant carrier of the nuclear force in 1935, pionic nuclear collectivity (enhancement) has been the heart of nuclear physics. The strong attraction produced by pions is expected to lead to various interesting phenomena such as pion condensation or its precursor phenomena, although they have hardly been observed [16, 17].

I discussed recent results on pionic correlation in spin isospin excitations by (p,n) and (n,p) reactions. However, since details are described in these Proceedings by M. Ichimura et al. [18], only the conclusions are summarized below:

- (1) From the energy and quenching factor of Gamow-Teller excitations in $^{90}\text{Zr}(p,n)/(n,p)$ reactions, the Landau-Migdal parameters were determined as $g'_{NN}=0.6$, $g'_{N\Delta}=0.28\pm 0.13$ with $g'_{\Delta\Delta}=0.5$ (assumed) [19]. Therefore, the universality ansatz does not hold.
- (2) The critical density of the pion condensation ρ_c is estimated to be about $2\rho_0$, and condensation is more likely on a neutron star [20].
- (3) The enhancement of the longitudinal response ID_q from the Random Phase Approximation (RPA)+ Δ is important [21]. The experimental data are well described with parameters $g'_{NN}=0.7\pm 0.1$, $g'_{N\Delta}=0.4\pm 0.12$, which are insensitive to the parameter $g'_{\Delta\Delta}$.
- (4) Two-step contributions are important in the transverse response ID_p , but they are insufficient to explain the underestimation of ID_p around the quasielastic peak [21]. Similar underestimation is observed for the transverse responses of (p,p') inelastic scatterings to unnatural parity states [22].

4. Few-Body System

Few-body system and three nucleon force (3NF) are one of recent hot topics in nuclear physics. Fujita and Miyazawa proposed a 3NF which takes account of a 2π -exchange between three nucleons with an intermediate Δ excitation [23]. Several present day 3NF are based on more fundamental theories, but they are also limited to 2π -exchange process [24]–[27]. The first evidence of the 'static' 3NF effects appeared to explain the binding energy of the ${}^3\text{H}$ nucleus. Calculations with only a two nucleon (2N) force are underbound by 0.5–1.0 MeV. 3NF fills this gap with a cut-off parameter Λ . The Hannover group could reproduce the ${}^3\text{H}$ binding energy with a coupled channel calculation taking account of Δ particles explicitly [28]. Recently, H. Witała proposed to study nucleon-deuteron (Nd) scatterings at intermediate energies to investigate 'dynamical' properties of 3NF, especially its dependence on the spin degrees of freedom [29]. Elastic Nd scattering is very attractive since it is simple and offers a rich set of spin observables.

A large amount of data has been accumulated for Nd elastic scattering at 70–400 MeV/u [30]. They include various kinds of spin observables; analyzing powers, polarization transfer coefficients and spin correlation parameters. By comparing experimental data with rigorous Faddeev calculations, the following conclusions have been drawn [30, 31]:

- (1) Discrepancies between data and calculations based on 2NF only are clearly seen in the cross section minimum region, and become larger as an energy increases.
- (2) 2π -exchange 3NFs improve the description of the differential cross section and some polarization observables, but are not always successful in explaining existing data.
- (3) 3NFs are clearly needed, but there are defects in spin dependent parts of 3NF.
- (4) Coupled channel calculations with Δ -degrees of freedom give comparable descriptions to 3NFs.
- (5) Discrepancies remain for the differential cross section and the proton analyzing power at 250 MeV.

Several possibilities have been proposed for better descriptions of data. New 3NFs may be introduced by taking account of ρ - ρ and ρ - π exchanges, or many Δ -contributions with π -rings. On the other hand, the baryon-baryon interaction has been proposed by the Kyoto-Niigata group based on the QCD-inspired spin-flavor SU6 model. The 2N interaction of the most recent model, fss2, is accurate enough to compare with the modern meson-exchange model [32]. These quark-model interactions are used for realistic calculations of few-baryon and few-cluster systems by the resonating-group method (RGM). Other 2N potentials based on Chiral Effective Field Theory (EFT) become available to analyze hadron systems at low energy [33], where perturbative expansion of QCD in powers of the coupling constant cannot be applied. In the chiral perturbation theory, one expands chiral πN Lagrangians in powers of the relevant momenta to masses (pion mass), relative to the QCD scale at $\Lambda_{\text{QCD}} \sim 1$ GeV. All pion-exchange diagrams are taken into account up through a given chiral order. It is shown that next-next-leading-order (NNLO) calculations give a comparable description of data to Faddeev calculations with 3NF [33, 34]. Recently, a relativistic Lippman-Schwinger equation has been solved by taking account of

the boosted potential arising from the Lorentz transformation of three nucleon system [35]. The boosted potential was approximated by expanding the general results in terms of the momenta of two nucleon subsystems [36]. In Fig. 3, relativistic calculations are compared with experimental data and non-relativistic calculations. Only small effects are observed with exception of backward angles for the cross section. The increase of the relativistic phase-space factor by about 17 % was predicted in the Nd total cross section [37], but it is found to be compensated by the transition matrix which describes the 'dynamical effects'. It seems that discrepancies between data and theories observed at higher energies originate totally from 3NFs, and short range contributions may be required to 3NFs.

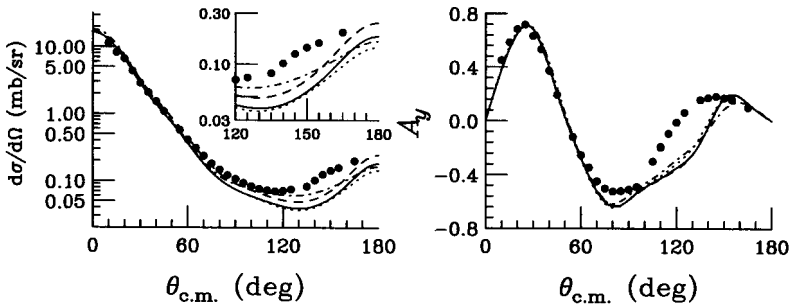


Fig. 3. The differential cross section (left) and proton analyzing power (right) of the elastic pd scattering at $E_p=250$ MeV. The dotted and dot-dashed curves are non-relativistic Faddeev results with CD-Bonn only and CD-Bonn+TM99, respectively. The solid and dashed curves represent the relativistic calculations with a boosted potential and no boost at all, respectively. Calculations were performed by H. Witała.

5. Summary

Over the past decade, high precision experimental data have become available at intermediate energies for various reactions and in a wide energy range. They include a rich set of spin observables: analyzing powers, polarization transfer coefficients, spin correlation parameters as well as cross sections. Owing to the rapid developments of computers, rigorous calculations become possible based on fundamental theoretical bases. Theories that explain experimental data deepen the understanding of the interactions and dynamics in the nuclear field. These are important ingredients to understand phenomena in such extreme conditions as astrophysics, unstable nuclei, high density nuclei and so on.

Acknowledgments

I am very much indebted to my many collaborators. In particular, T. Wakasa, K. Sekiguchi and Y. Shimizu helped me in preparing the figures which I presented. I would like to thank G.C. Hillhouse and H. Witała for helpful discussions and allowing me to use their calculations and results prior to the publication.

References

1. H. Yukawa, *Proc. Phys. Math. Soc. Japan* **17**, 48 (1935).
2. for example, T. Hamada and I.D. Johnston, *Nucl. Phys.* **34**, 382 (1962).
3. R. Brockmann and R. Machleidt, *Phys. Rev.* **C42**, 1965 (1990).
4. F. Sammarruca and E.J. Stephenson, *Phys. Rev.* **C64**, 034006 (2001) and references therein.
5. D.P. Murdock and C.J. Horowitz, *Phys. Rev.* **C35**, 1442 (1987).
6. C.J. Horowitz, *Phys. Rev.* **C31**, 1340 (1985).
7. G.E. Brown and Mannque Rho, *Phys. Rev. Lett.* **66**, 2720 (1991).
8. C.A. Miller *et al.*, *Phys. Rev.* **C57**, 1756 (1998).
9. K. Hatanaka *et al.*, *Phys. Rev. Lett.* **78**, 1014 (1997).
10. T. Noro, *Proc. 14th Int. Spin Physics Symposium, AIP Conf. Proc.* **570**, 228 (2001).
11. V.A. Andreev *et al.*, *Phys. Rev.* **C69**, 024604 (2004).
12. N.S. Chant and P.G. Roos, *Phys. Rev.* **C27**, 1060 (1983).
13. G.C. Hillhouse, private communication.
14. G.C. Hillhouse *et al.*, *Phys. Rev.* **C67**, 064604 (2003).
15. G.C. Hillhouse *et al.*, *Phys. Rev.* **C68**, 034608 (2003).
16. T.N. Taddeucci *et al.*, *Phys. Rev. Lett.* **73**, 3516 (1994).
17. H. Sakai, *Proc. 14th Int. Spin Physics Symposium, AIP Conf. Proc.* **570**, 218 (2001).
18. M. Ichimura *et al.*, in these Proceedings.
19. H. Sakai and K. Yako, *Nucl. Phys.* **A731**, 94 (2004).
20. S. Tsuruta *et al.*, *Astro. Phys. J.* **571**, L143 (2002).
21. T. Wakasa *et al.*, *Phys. Rev.* **C69**, 054609 (2004).
22. F. Sammarruca *et al.*, *Phys. Rev.* **C61**, 014309 (1999).
23. J. Fujita and H. Miyazawa, *Prog. Theor. Phys.* **17**, 360 (1957).
24. S.A. Coon *et al.*, *Nucl. Phys.* **A317**, 242 (1979)
25. J. Carlson *et al.*, *Nucl. Phys.* **A401**, 59 (1983)
26. H.T. Coelho *et al.*, *Phys. Rev.* **C28**, 1812 (1983)
27. U. van Kolck *et al.*, *Phys. Rev.* **C49**, 2932 (1994).
28. S. Nemoto *et al.*, *Phys. Rev.* **C58**, 2599 (1998).
29. H. Witała *et al.*, *Phys. Rev. Lett.* **81**, 1183 (1998).
30. K. Sekiguchi *et al.*, *Phys. Rev.* **C65**, 034003 (2002); *ibid.*, *Phys. Rev.* **C70**, 014001 (2004); H.O. Meyer *et al.*, *Phys. Rev. Lett.* **93**, 112502 (2004) and references therein.
31. K. Hatanaka *et al.*, *Phys. Rev.* **C66**, 044002 (2002).
32. Y. Fujiwara *et al.*, *Phys. Rev.* **C66**, 021001(R) (2002).
33. E. Epelbaum *et al.*, *Phys. Rev.* **C66**, 064001 (2002).
34. K. Sekiguchi, private communication.
35. H. Witała, private communication.
36. H. Kamada *et al.*, *Phys. Rev.* **C66**, 044010 (2002).
37. H. Witała *et al.*, *Phys. Rev.* **C59**, 3035 (1999).

DISCUSSION

E. Turnusov:

Question: When we calculate the energy of the ^3H and ^3He including 3N forces (TM, 3N potential,...), we do not have convergence. For instance we get for the binding energy of ^3H :

Answer: In the Faddeev calculations, we use expansions in the angular momentum. Convergence is well achieved.

25 channels	40 channels	60 channels
-8.30	-8.60	-8.40

N.S. Mankoč Borštnik:

Comment 1: More than 20 years ago the importance of taking into account the relativistic effects in scattering processes properly was strongly recognised. Bunny Clark even wrote a book on this topic.

Comment2: More than 20 years ago we studied the N-N potential as an effective potential between two clusters of quarks (Phys. Lett. 93B, 489 (1980), 99B, 486 (1981)). It became very clear to me that the definition of the N-N potential is not unique and that one must take into account strongly the momentum dependence of a force, for example. This is stressed in the paper J. Phys. G 7, 1385 (1981).

Question: Are you sure that the N-N potential you have used does take into account this effect properly? Higher body forces always appear when you cut the Hilbert space. But with them you can also connect the N-N force. It is, I would guess, very important to know for understanding physics behind the right reason for real agreement between experiments and the theoretical predictions.

Answer: Thank you for comments and a question. The importance of the relativistic effects had been recognised since long time ago. My point is that it recently became possible to calculate observables by taking account of the effects and to compare them with experimental results owing to developments of computers. There are several effective or realistic N-N potentials. Some are local and others non-local. In the calculations I showed, they use realistic potentials which reproduce existing N-N data quite well. I agree with you that effects of the truncation of the Hilbert space should be carefully examined.

SPIN PHYSICS IN NN INTERACTIONS AT INTERMEDIATE ENERGIES

B. von PRZEWOSKI

Indiana University Cyclotron Facility, Bloomington, USA

Nucleon-nucleon scattering experiments in hadron storage rings with a polarized beam and a polarized internal target are reviewed. The review also includes selected few nucleon experiments.

1. Polarized Beam and Target in a Ring

1.1. *Spin Dynamics*

A polarized beam from an ion source is injected into a storage ring. If the field integral around the ring is vertical, the spin closed orbit is vertical everywhere, but spin rotators (so-called snakes) can be used to produce non-vertical spin orientation. A longitudinal solenoid field is an example of a spin rotator.

Crossing a spin resonance at slow speed (adiabatic passage) causes the spin closed orbit to flip by 180° . It has been demonstrated [1–3] that the crossing of an induced resonance (by varying the RF frequency) flips the sign of the polarization (transverse as well as longitudinal) of protons with better than a few percent loss in polarization. This can be an important tool in eliminating systematic errors in polarization experiments.

1.2. *Polarized Internal Targets*

The attainable production rate by standard methods for atoms with nuclear polarization satisfies the requirements for an internal target. The atomic beam is either crossed with the beam in the ring or injected into a storage cell. The gas flow impedance of such a storage cell enhances the target thickness by several orders of magnitude. A guide field over the target region defines the spin alignment axis. Polarized internal targets are pure, not susceptible to radiation damage, and offer complete freedom in choosing the direction of the polarization, including rapid reversal of its sign. The ability to use such targets is perhaps the most important benefit of the storage ring environment for nuclear physics.

1.3. *Detector Considerations*

The ϕ dependences of spin observables are simple trigonometric functions. Each observable is associated with a known, characteristic ϕ dependence. This dependence is crucial

in distinguishing observables from each other when analyzing the data. For this reason, it helps to have a detector with full azimuthal coverage.

2. Proton-Proton Elastic Scattering at IUCF and COSY

A fair number of experiments with the Indiana Cooler were aimed at the analyzing power A_y and three of the four spin correlation coefficients, C_{xx} , C_{yy} , C_{xz} (in pp scattering, often called A_{xx} , A_{yy} , A_{xz} , or A_{SS} , A_{NN} , A_{SL}). Initial measurements near 200 MeV [4–7] were accompanied by the development of the new technology and novel analysis tools [8]. Finally, a general survey of these observables from 200 to 450 MeV [9], using up- and down-ramping to export the polarization calibration, resulted in an impressive body of data with statistical uncertainties of about 0.01 and an overall normalization error of 2.4%. A measurement of the fourth correlation coefficient C_{zz} at 200 MeV [10] made use of a solenoid snake to generate a beam with longitudinal polarization at the target.

The EDDA collaboration at COSY subsequently extended these measurements to higher energies, resulting in analyzing power and spin correlation coefficients between 450 MeV and 2.5 GeV [11].

The high precision of the data, and the fact that the clean definition of the scattering events made the small angles of the Coulomb-nuclear interference region accessible, made it possible to demonstrate, for the first time, a significant effect due to the interaction of the magnetic moments. However, a more important consequence of the Indiana data was that they required an update of the phenomenological description of NN scattering in terms of empirical phase shifts. This is even truer at GeV energies, where the new COSY data had a significant impact on the pp phase shift analysis in this energy range [12]. The NN phase shifts constitute the basis for numerous models in nuclear physics.

3. Meson Production in p+p Collisions

Compared to a two-particle final state, we need to specify a third momentum vector to describe the final-state kinematics. This brings the number of kinematic variables to five.

But this is not all. Since in a three-body final state, parity conservation no longer constrains any observables, we must now also consider the longitudinal analyzing powers A_{z0} and A_{0z} , and the correlation coefficient C_{xy} - C_{yx} . In addition, we must address the dependence on the energy-sharing parameter ε (for instance, by studying the dependence on ε of the unpolarized cross section and the spin-dependent total cross sections $\Delta\sigma_T$ and $\Delta\sigma_L$). The formal aspects of polarization observables in reactions with a three-particle final state are treated in detail in [13].

In meson production near threshold, relatively few partial waves contribute. For the reaction $pp \rightarrow pp\pi^0$, at up to about 400 MeV bombarding energy, the final-state angular momenta of the two nucleons (L_{NN}) and of the pion (l_π) are both either 0 or 1, and within the first 20 MeV above threshold just a single partial wave (${}^3P_0 \rightarrow {}^1S_0(l_\pi = 0)$) is important. Early pion-production experiments in this energy region yielded the first evidence for the importance of heavy meson exchange [14] and the associated enhancement of the axial

current in a nuclear system. But the theoretical situation is far from settled, since other contributions (such as off-shell pion rescattering) may also be relevant. A meaningful test of models, at this stage, needs more than just the strength of the $L_{NN}=l_{\pi}=0$ amplitude. Such information is provided by polarization observables.

3.1. Pion Production Experiments at the Indiana Cooler

The first pion production polarization experiments at the Cooler were measurements near threshold of cross section and analyzing power for the reactions $pp \rightarrow d\pi^+$ [15] and $pp \rightarrow pn\pi^+$ [16, 17]. After the polarized internal target became available, a program to study spin correlation in $pp \rightarrow pp\pi^0$ was initiated [18, 19], and it was demonstrated that model-independent information on the contribution of a single partial-wave amplitude can be deduced from the spin-dependent cross sections $\Delta\sigma_T$ and $\Delta\sigma_L$ alone [20]. This effort eventually led to a complete measurement of all observables of $pp \rightarrow pp\pi^0$ with polarization in the initial state, everywhere in the three-body phase space, up to 400 MeV [13]. This data set provides sufficient information to experimentally determine all 12 amplitudes for which L_{NN} and l_{π} are either 0 or 1. Perhaps the single most interesting result was the observation that the longitudinal analyzing power A_z (normally forbidden by parity conservation) can well be large in a reaction with a three-body final state [21]. Concurrently with the $pp \rightarrow pp\pi^0$ experiment, data on the spin correlation coefficients in $pp \rightarrow d\pi^+$ [22] and in $pp \rightarrow pn\pi^+$ [23, 24] were also obtained.

3.2. Meson Production at COSY

At COSY, the first polarization data in meson production begin to emerge: very recently the COSY-11 collaboration has reported a measurement of the analyzing power (with respect to the meson) of $pp \rightarrow pp\eta$, 40 MeV above threshold [25].

4. Adding a Third Nucleon: p+d Reactions below the Pion Threshold

4.1. Proton-Deuteron Elastic Scattering

When the spin-1 particles are vector-polarized, the situation is analogous to the spin-1/2 on spin-1/2 case: there are a total of seven observables, namely two analyzing powers and five vector spin correlation coefficients. For tensor-polarized spin-1 particles there is some added complexity. Good introductions to tensor observables, terminology and conventions are given, e.g., by Haeberli [26], and Darden [27]. The additional observables are the three tensor analyzing powers A_{xx} , A_{yy} and A_{xz} , and the seven tensor correlation coefficients $C_{xx,y}$, $C_{xy,x}$, $C_{xy,z}$, $C_{xz,y}$, $C_{xz,z}$, $C_{yy,y}$ and $C_{yz,x}$. Thus, apart from the unpolarized cross section, there are a total of 17 polarization observables that can be measured in p+d elastic scattering with polarized collision partners (for a formal discussion of spin correlation measurements, see Ohlsen [28]).

A number of measurements of the proton analyzing power, and the deuteron vector and tensor analyzing powers, exist at proton bombarding energies between 100 and 200

MeV (see references given in [29]). The first spin correlation measurement ($C_{y,y}$), together with the deuteron vector analyzing power, has been carried out at 200 MeV [30] at the Indiana Cooler, using a laser-driven polarized target. More recently, the PINTEX group has measured all but two of the 17 possible polarization observables [31]. This experiment has been carried out at two beam energies (135 and 200 MeV stored, polarized protons including longitudinal polarization) and an atomic-beam deuterium target with either pure vector or pure tensor polarization.

4.2. *Physics Interest: the Three-Nucleon Force*

It is believed that today's state-of-the-art Faddeev calculations, solving the three-nucleon problem with a phenomenological NN input, are telling us how nature would behave if there were only two-nucleon forces. They neglect the Coulomb force but there is evidence that this does not matter above 100 MeV and for $\Theta_{cms} \geq 30^\circ$. Comparing such calculations with a complete set of polarization data thus promises to reveal information about the three-nucleon force, in particular its spin dependence. The general features of the p+d elastic scattering results of ref. [31] are reproduced rather well by the most recent 2N Faddeev calculations [32]. The remaining discrepancies are most pronounced for center-of-mass angles greater than 70° and forward of 30° (the latter presumably because of Coulomb effects). The observables with the largest discrepancies are the tensor analyzing powers.

The differences between our measurements and the Faddeev calculation with the CD-Bonn potential are plotted in Figs. 1 and 2, i.e., the calculation is the zero line. The effect of including the old (TM) or the new (TM') Tucson-Melbourne 3NFs is shown by the solid and dashed lines respectively. A comparison of these curves with the data is justified if calculations with different NN potentials agree with each other. To illustrate this, the difference between calculations with the AV18 and the CDBonn potentials, both without a 3NF, is shown as a dotted line. This difference is indeed generally small, but there are many cases where the variation between the two potentials competes in size with the 3NF effects.

As can be seen from Figs. 1 and 2, the two 3NFs agree with each other for some observables and in some angular regions (e.g., in A_y^d), but in numerous cases the predictions with the TM and the TM' 3NF are quite different. Both sometimes improve the agreement with the data (e.g., in A_y^d), but equally often this is not the case. Thus, neither 3NF is a successful representation of the discrepancies between the p+d spin observables and Faddeev calculations without a 3NF.

Clearly, much more theoretical work is needed to quantitatively explain the disparity between experiment and 2NF calculations. It may also be worthwhile to search for a phenomenological three-nucleon potential that would explain the data, much along the lines of the phenomenological potentials that we employ to describe the NN interaction.

4.3. *Deuteron Break-up Reaction and Axial Observables*

When searching for 3NF effects, the break-up into three nucleons has an advantage since the kinematic freedom in the final-state offers the possibility to select configurations, which

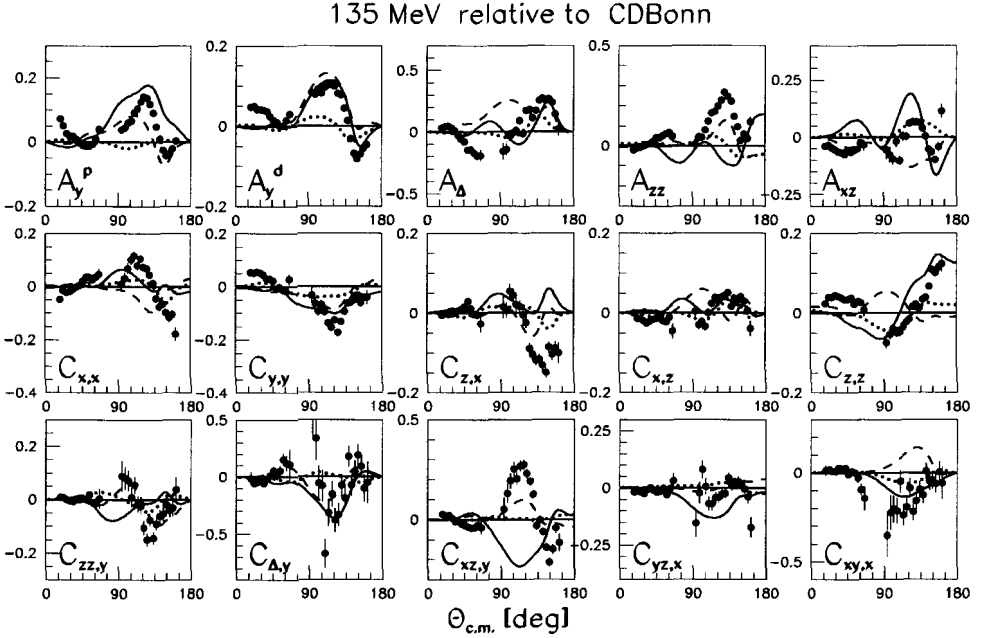


Fig. 1. Difference between the IUCF data at 135 MeV and the Faddeev calculation with the CDBonn potential. The effect of including the old or the new Tucson-Melbourne 3NFs is shown by the solid lines (TM) and the dashed lines (TM'). The dotted lines show the difference between calculations with the AV18 and the CDBonn potentials, both without a 3NF.

differ in their sensitivity to 3N forces. On the other hand the complexity of the spin-1/2 - spin-1 spin space combined with a three-body phase space is mind-boggling, and a measurement clearly needs some guidance. Such guidance is provided, for instance, by the following argument. It was pointed out by Knutson [33] that three-body potentials involve spin operators of a type that is not allowed for ordinary two-body interactions. These operators affect the so-called axial observables. An example of an axial observable is the longitudinal analyzing power A_z . In reactions with two outgoing particles this observable must vanish by parity conservation, but it is unconstrained when there are outgoing particles with lab momenta that are not co-planar. An attempt to observe a non-zero A_z in $pd \rightarrow ppn$ with a longitudinally polarized 9 MeV proton beam [34] failed (an upper limit of 0.003 was established, in agreement with Faddeev predictions). Somewhat surprisingly, the same calculations at 135 MeV predict a much larger value for A_z . This opens up the exciting possibility of an experiment that addresses the 3NF where the choice of the quantity to be measured is motivated by a theoretical argument.

4.4. Measurement of Axial Observables at 135 MeV

One of the last experiments with the Indiana Cooler was a measurement of three out of five possible axial observables, A_z , $C_{y,x} - C_{x,y}$ and $C_{zz,z}$, in $pd \rightarrow ppn$ at 135 MeV (proton energy) [35]. The experiment was carried out with a 270 MeV deuteron beam on a proton

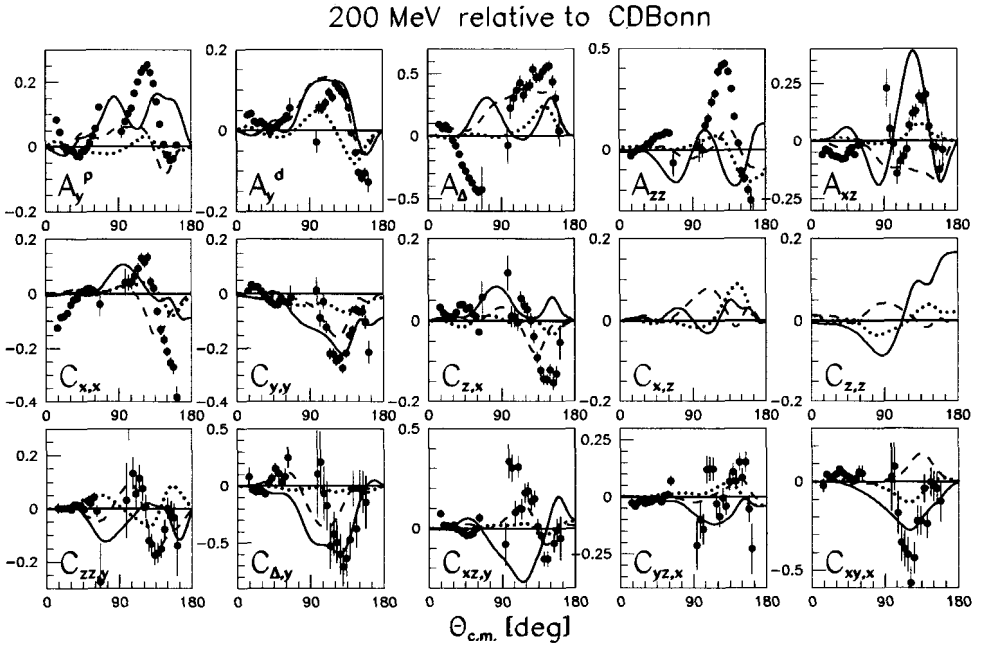


Fig. 2. Difference between the IUCF data at 200 MeV and the Faddeev calculation with the CDBonn potential. Otherwise, the caption of Fig. 1 applies

target. The other two axial observables would have required longitudinal beam polarization. As for pd elastic scattering it was found that none of the available 3NF potentials consistently improve the agreement between theory and data.

4.5. $p+d$ Reactions at GeV Energies

4.5.1. $p+d$ Break-up

As the bombarding energy increases beyond the pion threshold, Faddeev calculations can not yet be used to describe the three-nucleon continuum. On the other hand, one might hope that few-nucleon reactions get simpler as the energy is increased. However, this does not seem to be the case, given the very limited success of the impulse approximation to describe, e.g., $p+d$ break-up. We are thus relegated to models, evaluating contributions from various postulated reaction mechanisms. Selective tests of such models make use of a specific choice of the final-state kinematics, and of the observation of polarization observables. Recently, the ANKE experiment at COSY has measured the analyzing power of pd break-up with a proton pair with low relative energy (presumably in a 1S_0 state) in the final state [25]. Eventually, these experiments will also cover spin-correlation observables.

4.5.2. *p+d Total Cross Section: Time Reversal Invariance*

It is commonly thought that many of the systematic errors that make the classical tests for charge symmetry, parity violation and time reversal invariance hard, are easier to handle in a storage ring environment. Yet such experiments are slow in coming. One experiment that probably can only be done in a storage ring is described below.

One of the contributions to the spin-dependence of the total cross section of the $p+d$ reaction, the tensor correlation coefficient $C_{yz,x}C_{xz,y}$, can be shown to vanish under time reversal if one includes all exit channels (but only then) [36]. There exists a proposal to exploit this observable for a time reversal invariance test at COSY [37], using a vertically polarized proton beam and a tensor-polarized, internal deuteron target. A similar experiment at very high energy has also been discussed for RHIC.

5. Summary and Outlook

Nucleon-nucleon scattering experiments with storage rings have produced a wealth of data. The Indiana Cooler, where much of the new technology and novel analysis tools were developed, was shut down in 2002. Today, COSY builds on past experience and uses polarization as a tool to extend the knowledge of nucleon-nucleon scattering to higher energies.

Beyond experiments involving only two nucleons in the entrance channel, experimental programs that use a polarized deuteron beam and/or target have begun to emerge. The aim of two such experiments at the Indiana Cooler was to investigate the role of three-nucleon forces below the pion production threshold. The ANKE collaboration at COSY has embarked on an experimental program that will eventually lead to a measurement of spin correlation parameters in $p+d$ scattering at GeV energies. Stay tuned!

References

1. D.D. Caussyn et al., *Phys. Rev. Lett.* **73**, 2857 (1994)
2. B. v. Przewoski et al., *Rev. Sci. Instr.* **67**, 165 (1996)
3. B.B. Blinov et al., *Phys. Rev. Lett.* **88**, 014801-1 (2002)
4. W.K. Pitts et al., *Phys. Rev.* **C45**, R1 (1992)
5. W.K. Pitts, *Phys. Rev.* **C45**, 455 (1992)
6. W. Haeberli et al., *Phys. Rev.* **C55**, 597 (1997)
7. F. Rathmann et al., *Phys. Rev.* **C58**, 658 (1998)
8. H.O. Meyer, *Phys. Rev.* **C56**, 2074 (1997)
9. B. v. Przewoski et al., *Phys. Rev.* **C58**, 1897 (1998)
10. B. Lorentz et al., *Phys. Rev.* **C61**, 054002 (2000)
11. F. Bauer et al., *Phys. Rev. Lett.* **90**, 142301 (2003)
12. M. Altmeier et al., *Phys. Rev. Lett.* **85**, 1819 (2000)
13. H.O. Meyer, et al., *Phys. Rev.* **C63**, 064002 (2001)
14. T.S.H. Lee and D.O. Riska, *Phys. Rev. Lett.* **70**, 2237 (1993)
15. P. Heimberg et al., *Phys. Rev. Lett.* **77**, 1012 (1996)
16. W.W. Daehnick et al., *Phys. Lett.* **B423**, 213 (1998)
17. R.W. Flammang et al., *Phys. Rev.* **C58**, 916 (1998)
18. T. Rinckel et al., *Nucl. Instr. Meth.* **A439**, 117 (2000)
19. H.O. Meyer et al., *Phys. Rev. Lett.* **81**, 3096 (1998)

20. H.O. Meyer et al., *Phys. Rev. Lett.* **83**, 5439 (1999)
21. H.O. Meyer et al., *Phys. Lett.* **B480**, 7 (2000)
22. B. v. Przewoski et al., *Phys. Rev.* **C61**, 064604 (2000)
23. Swapan K. Saha et al., *Phys. Lett.* **B461**, 175 (1999)
24. W.W. Daehnick et al., *Phys. Rev.* **C65**, 024003 (2002)
25. COSY Annual Report 2001, Forschungszentrum Juelich, 2002
26. W. Haeberli, *Nucl. Spectroscopy and Reactions, Part A*, ed. Cerny, Academic press, NY 1974, p.151
27. S.E. Darden, in Proc. 3rd Int. Symp. On Polarization Phenomena in Nuclear Reactions, eds. H.H. Barschall and W. Haeberli, Univ. of Wisconsin Press, Madison, 1971, p.39.
28. G.G. Ohlsen, *Rep. Prog. Phys* **35**, 717 (1972)
29. H.O. Meyer, Proc. 8th Conf. On Mesons and Light Nuclei, Prague, Czech Republic, ed. J. Adam, P BydOvsk and J. Mare, AIP Conf. Proc. v.603, 2001, p. 113
30. R.V. Cadman et al., *Phys. Rev. Lett.* **86**, 967 (2001)
31. B. v. Przewoski et al., <http://lanl.arXiv.org/abs/nucl-ex/0411019>
32. H. Witala et al., *Phys. Rev.* **C63**, 024007 (2001)
33. L.D. Knutson, *Phys. Rev. Lett.* **23**, 3062 (1994)
34. E.A. George et al., *Phys. Rev.* **C54**, 1523 (1996)
35. H. O. Meyer et al. *Phys. Rev. Lett* **93**, 112502
36. H.E. Conzett, *Phys. Rev.* **C48**, 423 (1993)
37. P.D. Eversheim, Proc. 4th Int. Conf., Bloomington, IN, September 1999, eds. H.O. Meyer and P. Schwandt, API Conference Proceedings 512, Am. Inst. of Physics, New York, 2000.

DISCUSSION

N.S. Mankoč Borštnik:

Comment: Whenever one cuts the Hilbert space, the many body forces appear to mimic all that has been left out. Definition of the N-N force is a complicated many body problem and one must in addition carefully define the way of expansion of the N-N force (which must be momentum dependent, see ref. in my comment to Hatanaka talk) to see at which extend the 3N (and higher) are really responsible for non agreement between predictions and theory.

Answer: It is true that one has to be careful that the addition of 3N forces to a model does not simply absorb other deficiencies in the 2N calculation such as relativistic effects for example.

M. Garcon:

Comment 1: I want to mention the usefulness of the recent phase shift analysis in the 1 GeV range (with input from COSY and SATURNE data) in understanding e, e'p reaction at JLab (calculations of J.M. Laget). This is crucial before reaching conclusions on two-nucleon correlation in nuclei.

Comment 2: Since you mentioned SATURNE NN data only in connection with a weak evidence for dibaryons, I would like to remind the audience that there were also three precise experiments in elastic pp scattering that put stringent limits (at the level of a few %) to the elasticity of hypothetical dibaryions. As a side remark, to be fair towards other claims in

production experiments, NN elastic experiments can only set upper limits on elasticity, but not discard definitively dibaryons.

Answer: I agree that a precise knowledge on the NN phase shift or potentials is crucial for the theoretical interpretation of many experimental results. E. g. in order to draw any conclusions about 3N forces the NN interaction must first be well known.

SPECULATIONS IN HADRON SPECTROSCOPY

J. M. RICHARD

Laboratoire de Physique Subatomique et Cosmologie, Université Joseph Fourier, Grenoble, France

A selected survey is presented of recent progress in hadron spectroscopy. This includes spin-singlet charmonium states, excitations of charmonium and open-charm mesons, double-charm baryons, and pentaquark candidates. Models proposing exotic bound states or resonances are reviewed. The sector of exotic mesons with two heavy quarks appears particularly promising.

1. Introduction

A dramatic revival of hadron spectroscopy has been observed for several months. In high-energy experiments, a larger part of the analysis effort is devoted to the search for new hadrons. Theorists also rediscover how challenging are the issues raised by confinement in QCD.

Some problems have been here for years. Progress is sometimes slow but effective: for instance, the data accumulated by the annihilation experiments at LEAR shed valuable light on the sector of scalar mesons, where an excess of states is observed, as compared with counting based solely on orbital excitations of $(\bar{q}q)$ or $(\bar{s}s)$ configurations. Here q denotes any light quark u or d . Progress is more rapid for the singlet-states of charmonium, with the recent discovery of the long-awaited η'_c and h_c states. Another example, now on the theory side, deals with the Roper resonance in the spectrum of nucleon excitations. In conventional approaches, it comes too high, above the negative-parity excitations. Simple models with Goldstone-boson exchange, or more elaborate lattice simulations [1] with low value for the mass of the light quarks, clearly show that the level ordering is due to chiral dynamics.

Other problems were bothering only a group of pioneers, and have been unveiled by the recent experimental findings. Immediately comes to mind the existence of a low-lying pentaquark anti-decuplet, predicted by chiral-soliton models. Another issue deals with stable or narrow $D\bar{D}^*$ molecules. Also hot is the question of parity partners lying close above some ground-state configurations, and remarkably illustrated by the so-called $D_{s,J}$ resonances.

These sectors will now be discussed, and then I shall comment on the possibility of predicting stable, exotic multi-quark states from our present knowledge of quark dynamics. I apologise in advance for being unable, due to the lack of space, to cite all the relevant references to new results and new ideas which are proposed almost every day.

2. Charmonium

Thanks to an energetic coordination, the “Yellow Report” of the *Quarkonium Working Group* [2] is now finished, and provides a summary of experimental and theoretical aspects, with many references. For this spin conference, it seems appropriate to focus on the spin-dependent forces between quarks. The non-observation in e^+e^- of any 3D_1 of $(b\bar{b})$ confirms that if the ψ'' state of the charmonium family is seen formed in e^+e^- , this is due to its 3S_1 mixing induced by tensor forces, suppressed by $(m_c/m_b)^2$ for Upsilon, and to the particular coupling induced by the neighbouring $D\bar{D}$, a situation without analogue for the 2S level of $(b\bar{b})$. The $^3S_1 \leftrightarrow ^3D_1$ orbital mixing also influences the decay properties of ψ' and ψ'' states.

While radial (ψ' , ψ''' , ...) or orbital (χ_J , ψ'' , ...) excitations of the J/ψ were identified rather early in e^+e^- experiments, and confirmed in production and $\bar{p}p$ formation experiments, the spin-singlet partners have been more elusive. This was expected, but not at that level.

The $\eta_c(1S)$ was first found 300 MeV below the J/ψ , before a more reasonable hyperfine splitting of about 120 MeV was measured. Its radial excitation, η'_c , or $\eta_c(2S)$ was searched for in several experiments, including ψ' radiative decay, $\gamma\gamma$ fusion or $\bar{p}p$ formation. The embarrassing absence of a reliable η'_c is over now, with the observation by the Belle collaboration of η'_c in two different measurements [2]. The first is double-charm production in e^+e^- collisions, that is to say, $J/\psi + X$. The Zweig rule strongly suggests that $c\bar{c}$ recoils against $c\bar{c}$. There is, however, some debate on the cross-section for these double-charm events. The second Belle analysis deals with B decay. The final state $KKK\pi$ exhibits a peak in the $KK\pi$ mass spectrum. The η'_c has also been seen in other experiments [2]. The η'_c is closer to ψ' than expected in simple charmonium models. This is probably due to the coupling to the open-charm threshold [2]. The η'_c does not link to $D\bar{D}$, due to its pseudoscalar nature, but the ψ' does, and is pushed down.

The 1P_1 state of charmonium, h_c , was searched for actively. It was suspected in the R704 experiment at CERN ISR, and seen for a while in the Fermilab $\bar{p}p$ experiment, not confirmed in the first analysis of further runs, eventually seen by looking at another final state, and also detected at CLEO [2, 3]. The mass lies, as expected, at the centre of gravity of 3P_0 , 3P_1 and 3P_2 triplet states. This means that, in a perturbative analysis of spin forces within the potential models, there is no spin-spin interaction acting on the P-state multiplet. There are presumably several corrections to this simple analysis, which tend to cancel out on the whole. Higher-order QCD corrections give some corrections to the 1P_1 mass, and indeed the spin-spin potential obtained from lattice calculation is not strictly of zero range. However, if the spin-orbit and tensor forces are treated non perturbatively, the 1P_1 should not be compared to the naive centroid $(^3P_0 + 3^3P_1 + 5^3P_2)/9$, but to an improved average which is higher by a few MeV. The energy of triplet states is, indeed, not a linear, but a concave function of the coefficients of the spin-orbit and tensor components.

Higher states of charmonium might reveal new structures. The $\psi(4040)$ has an interesting history in this respect. It was found to have preferential decay into $D\bar{D}^*$ (an implicit $+c.c.$ is implied here and in similar circumstances). This suggested a molecular descrip-

tion of this state [4]. In fact, the groups at Orsay and Cornell understood that the unorthodox pattern of the branching ratios to $D\bar{D}$, $D\bar{D}^*$ and $D^*\bar{D}^*$ is due to the radial structure of $\psi(4040)$, as a mere $(c\bar{c})$ state [5]. The spatial wave function has nodes. In momentum space, there are also oscillations. Hence, if a decay calls for a momentum whose probability is low, it is suppressed.

A more recent state in the charmonium mass-range is the X(3872) [6], seen in several experiments, as a clear signal above the background, and hence considered as very safely established. The X(3872) is not seen in two-photon production at CLEO, thus constraining the possible quantum numbers. Though experts have learned to be careful from the lesson of the $\psi(4040)$, a molecular interpretation of this state is very tempting, as it lies almost exactly at the $D^0\bar{D}^{*0}$ threshold, and none of the charmonium assignment (D-state, radially excited P-state, etc.) survives scrutiny, although the production is rather reminiscent of the pattern observed for usual charmonium states. Such a molecule was predicted on the safe ground of the Yukawa interaction between two hadrons, and recently generalised to bound states of charmed baryons [7].

More recently, another state has been seen in this region, let us call it X(3941), decaying into $J/\psi + \omega$. As noted in the paper revealing its existence [8], it bears some properties of the charmonium hybrid, as predicted by Giles and Tye, Mandula and Horn, Hasenfratz et al., and many others [9]. Hybrid mesons have an explicit constituent gluon, and this allows for exotic quantum numbers that are not permitted for $(Q\bar{Q})$, and also leads to supernumerary states with ordinary quantum numbers. Though the first experimental candidates for hybrid mesons were proposed in the light sector, the heavy sector offers the advantage of a cleaner knowledge of ordinary $(Q\bar{Q})$, on top of which the unusual states are better singled out.

3. Open-charm mesons

States with $(c\bar{s})$ flavour content were found at the Babar experiment of SLAC, and confirmed at CLEO, Fermilab, etc. [10]. The masses, 2317 and 2458 MeV, can be compared with 1968 for the pseudoscalar and 2112 MeV for the vector ground state of $(c\bar{s})$. This is rather low for the lowest P-state, from our present understanding of spin-orbit forces. The small widths are also rather intriguing. Views about these states schematically fall into two categories:

- (1) These new states are understood as the chiral partners of the ground-state multiplet. Some authors insist that this is not an ad-hoc explanation just for these two states, but a recurrent phenomenon for light quarks surrounding a heavy core [11].
- (2) Barnes et al. [12] and several other authors proposed a four-quark interpretation, $(cq\bar{s}\bar{q})$, with, however, a possible breaking of isospin symmetry.

Further investigation is needed to decide whether the new $D_{s,J}$ states are just the usual excitations, shifted in mass and made narrower than expected, or supernumerary states.

This summer, a new state, $D_s(2632)$, was announced by the Selex collaboration, again rather narrow, and decaying more often into $D_s\eta$ than into DK [13]. It has not been con-

firmed [14]. Several interpretations have been proposed for the $D_s(2632)$, among them a four-quark structure ($cq\bar{s}\bar{q}$), somewhat reminiscent [15] of the baryonium states proposed in the late 70s.

4. Double-charm baryons

According to the results shown by Selex at the INPC conference, the lowest $\Xi_{cc}^+(ccd)$ state is now seen in two different weak-decay modes. Problems remain: Selex is the only experiment to have seen these baryons yet; the isospin splitting between this Ξ_{cc}^+ and the lowest Ξ_{cc}^{++} candidate is larger than expected; the puzzling excitations about 60 MeV above the ground state need confirmation with higher statistics.

Anyhow, the Selex results have stimulated further studies on hadrons with two heavy quarks. The (QQq) baryons are perhaps the most interesting of ordinary hadrons, as they combine in a single object two extreme regimes: the slow motion of two heavy quarks in an effective potential generated by light degrees of freedom, as in charmonium or Upsilon systems; the ultra-relativistic motion of a light quark around a heavy colour source, as in D and B mesons. The large Q/q mass ratio, which implies a hierarchy $r(QQ) \ll r(Qq)$ of mean radii, suggests valuable approximation schemes [2] such as a diquark–quark picture or a Born–Oppenheimer treatment of (QQq) .

As pointed out [11], one expects chiral partners of (QQq) baryons, similar to the chiral partners of $(Q\bar{q})$ mesons. However, a universal spacing of about 300 MeV is empirically observed between any hadron and its chiral partner. Hence the small spacing suggested by the Selex results is difficult to understand.

5. Pentaquarks

A baryon with charge $Q = +1$ and strangeness $S = +1$, i.e., minimal quark content ($\bar{s}uudd$) has been seen at the Spring8 facility in Japan, and in several other experiments. However, this state is not seen in a number of high-statistics experiments with a very good particle identification, and for some of them, with very good record in hadron spectroscopy. Hence, the status of the θ^+ is more than shaky [16].

The situation is even worse for the Ξ^{--} member of the putative anti-decuplet, since it has been claimed by only a fraction [17] of the NA49 collaboration, and not seen in any other analysis [18] looking for it. It has also been proposed that some baryon resonances with ordinary quantum numbers contain a large fraction of pentaquark configurations, to explain their intriguing properties. This concerns, e.g., the Roper resonances and the $\Lambda(1405)$.

On the theory side, the situation is also rather confusing, even for experts. The pioneers on chiral soliton dynamics, and in particular, the Skyrminion model, made the remarkable prediction [19] of an anti-decuplet ($\bar{10}$) of baryons on almost the same footing as the familiar octet (N, Λ, Σ, Ξ) and decuplet (Δ, \dots, Ω^-). The positive-parity assignment is crucial in this picture, and is confirmed in simpler constituent models [20] mimicking the chiral effects by spin–flavour terms.

Moreover, lattice QCD calculations and QCD sum rules have seen either negative parity, or positive parity, or both, or no state at all. Critical surveys [21] exist. As in ordinary few-body quantum mechanics, it is essential to demonstrate a clear separation between the continuum dissociation threshold and possible resonances on the top of this background.

Constituent models have been worked at very hard, perhaps too hard, to accommodate the announced pentaquark. In particular, astute diquark or even triquark clustering has been devised, that, once accepted, naturally leads to a pentaquark [22]. Note that early promoters of the diquark in soft physics do not fully endorse this use of the diquark [23].

In the past, diquarks were successfully advocated to explain why mesons and baryons exhibit the same Regge slope, but the $[qq] - q$ clustering of orbitally excited baryons was later demonstrated citeMartin:1985hw to occur in a large class of potential models. However, $[qq] - [\bar{q}\bar{q}]$ clustering was also postulated for four-quark states, leading to the prediction of many baryonium states, but these states were never confirmed, and, to my knowledge, no serious four-body calculation was ever attempted to support this type of clustering.

In most of the models explaining the light pentaquark with strangeness $S = +1$, a heavy ($\bar{Q}qqqq$) version, tentatively more stable against dissociation, exists. Heavy pentaquarks have already a long history. A first candidate was proposed in 1987 independently in a paper by the Grenoble group, where the word “pentaquark” was seemingly used for the first time, and another one by Lipkin [25]. It consists of ($\bar{Q}qqqq$), with the light–strange sector q^4 forming a flavour triplet of SU(3). The parity is negative in the original model, very much inspired by Jaffe’s H($uudds$), the binding being due to attractive coherences in the chromomagnetic interaction.

6. Stability of multiquark states

It is sometimes claimed, even in otherwise remarkable papers [26], that the potential models produce a large number of stable or metastable states, and hence, are ruled out by the scarce evidence for such states. However, the reverse is true: potential models, supplemented by the most current ansatz for the colour dependence of the interaction, predict that multiquarks do *not* bind below their dissociation threshold, except for the rare configurations where a special coherence benefits the collective quark system, and not its decay products. Stability of few-body systems should, indeed, be seen as a competition between a collective behaviour and preference for dissociation.

For a Hamiltonian with a pairwise potential $V \propto \sum \lambda_i^c \cdot \lambda_j^c v(r_{ij})$, with the usual (though questionable) colour dependence, it is found that baryons are heavier *per quark* than mesons [27], and further, for equal mass quarks, that $(qq\bar{q}\bar{q}) \geq 2(q\bar{q})$. Some effects, however, might tend to reverse this inequality, and its analogues such as $(qqqq\bar{q}) \geq (qqq) + (q\bar{q})$, $(q^6) \geq 2(q^3)$, etc. This includes, for instance, spin–colour forces, or spin–flavour forces.

Another, simpler, effect deals with mass differences. In a (flavour independent) confining potential, heavy quarks take better advantage of the binding, in exactly the same way as a particle in a harmonic well has its binding energy $\propto \mu^{-1/2}$ decrease when its mass μ increases. This makes ($QQ\bar{q}\bar{q}$) take advantage of the heavy–heavy interaction, that is absent

in the threshold made of two separate $(Q\bar{q})$ mesons.

There is also something special with light quarks that cannot be extrapolated from potential models tuned to heavy quarks. This goes beyond the necessary account for relativistic effect. The following exercise is instructive: take a simple linear potential λr , or an improved $\lambda r - a/r$; use relativistic kinematics, and tune the parameters (λ , a , quark masses), to reproduce the spin-average levels of charmonium and D meson. Then solve for (qqq) , (qqQ) , (qQQ) , $(QQ\bar{q}\bar{q})$, etc., so that the heavy–heavy effect is automatically taken into account. It is found that (ccq) comes out compatible with the Selex mass (if room is left for hyperfine effects), and that $(QQ\bar{q}\bar{q})$ becomes lower than $2(Q\bar{q})$ if quark-mass ratio M/m is large enough.

This model, however, will miss some of the light–light attraction, by overestimating (Qqq) by about 150 MeV, and (qqq) by 500 MeV. An additional dynamical ingredient, which breaks flavour independence, should be implemented. It is responsible for the nuclear forces among hadrons containing light quarks, and is approximately realised in empirical models with Yukawa-type scalar–isoscalar exchange between light quarks. Altogether, if one computes the $(cc\bar{q}\bar{q})$ mass with a model compatible with the $(c\bar{c})$ and $(c\bar{q})$ spectra, and adds about 100 to 150 MeV extra attraction for the light-quark pair, one finds a bound state that decays weakly.

In short, the $(cc\bar{q}\bar{q})$ configuration seems one of the most promising candidates for a stable multiquark state, since it benefits both from the heavy–heavy and light–light effects.

7. Conclusions

The last months have been very exciting for hadron spectroscopy. The $D_{s,J}$ resonances, the heavy baryons, the $X(3872)$, and the pentaquark candidates stimulated interesting studies on confinement dynamics.

The discovery of the η'_c shows that new means of investigation can solve the old problems, and it is hoped that the missing baryons and quarkonia will also be found with an appropriate production mechanisms.

For many years, hadrons with multiquark structure, or constituent glue, or revealing the power of chiral symmetry, have been searched for. Now, they are emerging perhaps too suddenly, and we would be rather embarrassed if all the recent candidates survive careful experimental scrutiny. We have to wait for the current next wave of experiments and analyses, especially concerning the controversial pentaquark.

Meanwhile, theorists should also refine and improve their tools. The history of poly-electrons is in this respect rather instructive. Around the year 1945, Wheeler proposed several new states, in particular the (e^+, e^+, e^-, e^-) , as being stable if internal annihilation is neglected. In 1946, Ore published an article where he concluded that stability is very unlikely, on the basis of a seemingly-solid variational calculation borrowed from a nuclear-physics picture of the α -particle as a four-nucleon system. Hylleraas, however, suspected that the trial wave function was not suited for long-range forces. Today, most of us, in similar circumstances, would rush to their computer and post a criticism on the web. These gentlemen, instead, combined their efforts, and in 1947, published a very elegant and rig-

orous proof of the stability [28].

Acknowledgments

I would like to thank Franco Bradamante and his colleagues for this beautiful conference. I benefitted from several discussions with Ica Stancu, useful remarks on the manuscript by Muhammad Asghar, and informative correspondence with Harry Lipkin and Stephan Paul.

References

1. S. J. Dong, T. Draper, I. Horvath, F. X. Lee, K. F. Liu, N. Mathur and J. B. Zhang, arXiv:hep-ph/0306199.
2. Quarkonium Working Group, *Heavy Quarkonium Physics*, arXiv:hep-ph/0412158, <http://www.qwg.to.infn.it/>.
3. A. Tomaradze, arXiv:hep-ex/0410090; C. Patrignani [FNAL-E835 Collaboration], arXiv:hep-ex/0410085.
4. M.B. Voloshin and L.B. Okun, JETP Lett. 23 (1976) 333; A. De Rujula, H. Georgi and S. L. Glashow, Phys. Rev. Lett. **38**, 317 (1977).
5. A. Le Yaouanc et al., Phys. Lett. B **72**, 57 (1977); E. Eichten et al., Phys. Rev. D **21**, 203 (1980).
6. B. Aubert *et al.* [BABAR Collaboration], arXiv:hep-ex/0406022.
7. N. A. Törnqvist, arXiv:hep-ph/0308277; T. E. O. Ericson and G. Karl, Phys. Lett. B **309**, 426 (1993); A. V. Manohar and M. B. Wise, Nucl. Phys. B **399**, 17 (1993); E. Braaten and M. Kusunoki, Phys. Rev. D **69**, 074005 (2004); B. Julia-Diaz and D. O. Riska, arXiv:nucl-th/0405061.
8. K. Abe *et al.* [Belle Collaboration], arXiv:hep-ex/0408126.
9. R. Giles and S. H. H. Tye, Phys. Rev. D **16** (1977) 1079; D. Horn and J. Mandula, Phys. Rev. D **17** (1978) 898; P. Hasenfratz, R. R. Horgan, J. Kuti and J. M. Richard, Phys. Lett. B **95** (1980) 299.
10. M. Bondioli [BABAR Collaboration], Nucl. Phys. Proc. Suppl. **133**, 158 (2004).
11. W. A. Bardeen, E. J. Eichten and C. T. Hill, Phys. Rev. D **68**, 054024 (2003); M. A. Nowak, arXiv:hep-ph/0407272.
12. T. Barnes, F. E. Close and H. J. Lipkin, Phys. Rev. D **68**, 054006 (2003).
13. A. V. Evdokimov *et al.* [SELEX Collaboration], arXiv:hep-ex/0406045.
14. B. Aubert *et al.* [BABAR Collaboration], arXiv:hep-ex/0408087.
15. B. Nicolescu and J. P. B. de Melo, arXiv:hep-ph/0407088; L. Maiani, F. Piccinini, A. D. Polosa and V. Riquer, Phys. Rev. D **70** (2004) 054009.
16. P. Rossi [CLAS Collaboration], arXiv:hep-ex/0409057.
17. C. Alt *et al.* [NA49 Collaboration], Phys. Rev. Lett. **92** (2004) 042003.
18. M. I. Adamovich *et al.*, Phys. Rev. C **70** (2004) 022201.
19. D. Diakonov, arXiv:hep-ph/0406043, and refs. therein.
20. F. Stancu and D. O. Riska, Phys. Lett. B **575** (2003) 242.
21. S. Sasaki, arXiv:hep-lat/0410016; R. D. Matheus and S. Narison, arXiv:hep-ph/0412063.
22. R. L. Jaffe, arXiv:hep-ph/0409065; M. Karliner and H. J. Lipkin, Phys. Lett. B **575** (2003) 249.
23. D. B. Lichtenberg, arXiv:hep-ph/0406198.
24. A. Martin, Z. Phys. C **32** (1986) 359.
25. C. Gignoux, B. Silvestre-Brac and J.-M. Richard, Phys. Lett. B **193** (1987) 323; H.J. Lipkin, Phys. Lett. B **195** (1987) 484.

26. J. Carlson and V. R. Pandharipande, Phys. Rev. D **43** (1991) 1652.
 27. S. Nussinov and M. A. Lampert, Phys. Rept. **362** (2002) 193.
 28. J.A. Wheeler, Ann. N.Y. Acad. Sci. **48** (1946) 219; A. Ore, Phys. Rev. **70** (1946) 90; E.A. Hylleraas and A. Ore, Phys. Rev. **71** (1947) 493; for a review, see, e.g., E.A.G. Armour, J.-M. Richard and K. Varga, arXiv:physics/0411204.

DISCUSSION

O. Teryaev:

In the QCD sum-rule approach of Ioffe and Oganesian, the small width of the θ^+ is explained by chiral invariance. If so, one may expect a large non-forward transversity distribution for the transition from nucleon to θ^+ , which may lead in turn to the electroproduction of θ^+ accompanied by transversely polarized K^* and longitudinally polarized ρ , in analogy to $\rho_L\rho_T$ production studied by Ivanov, Pire, Szymanowski and myself, which cannot be explained by the small width.

Answer: Yes, this is a very interesting remark by Ioffe and Oganesian, that certain transitions are suppressed by chiral symmetry considerations. Similar considerations have been proposed by Melikhov and Stech, and others^a. I also agree with your second point. More generally, spin observables are very useful to single out resonances whose signal is elusive in integrated cross sections.

K. Imai:

It is important to confirm θ^+ with high statistics and high precision. Experiments are being done at Spring8 and Jlab. The preliminary data from Spring8 have confirmed the previous result with higher statistics. We are now preparing an experiment to study θ^+ with a K^+ beam with 1 MeV resolution at KEK-PS. Since this is a spin symposium, I would like to comment that a measurement of polarization of the final proton, or an experiment with a polarized beam, is important for determining the spin and parity of θ^+ .

Answer: I agree with you both on the need for better statistics and the importance of spin observables for extracting the quantum numbers. When one reads the *Review of Particle Properties*, one is astonished to discover that for many hadrons, the quantum numbers are not determined by unambiguous measurements but simply deduced from the most plausible quark-model assignment. For the exotics whose structure is debated, the spin and parity have to be measured.

H. Sato:

Are there some interesting physics issues, in particular for hadronic interaction and hadron spectroscopy, accessible with a 50 GeV beam of polarized protons?

Answer: Yes, the potential of such machines is extremely rich, thanks in particular to the variety of secondary beams they can produce. In the particular sector of spectroscopy, these machines will however face competition from beauty factories.

^aSee, e.g., Matheus and Narison [21]

V. W. HUGHES: “TO LEARN FUNDAMENTAL THINGS” 1921-2003

G. BUNCE

RIKEN BNL Research Center, BNL, USA

A presentation in Vernon’s words, attempting to capture his sense of seriousness, humour, and justice.

The quotations used here are from the memoir written by Vernon Hughes, “Various Researches in Physics,” in the *Annual Review of Nuclear and Particle Science* 2000, 50:i-xxxvi (2000). This memoir was first presented to the 2003 Spin Conference in Dubna, Russia.

Vernon (I apologize for my informality, but I have a difficult time continually referring to “Professor Hughes” or whatever.) divided his life chronologically into several stages – the titles of the following sections are his.

1. “My Unprecocious Entry into Physics”

Vernon grew up in New York City, brought up by his mother, Jean Parr Hughes (his memoir is dedicated to her). He attended a small private school on the upper west side, the school having an “idealistic and humanistic orientation.”

Vernon first went to Columbia College in pre-law: “I planned a pre-law course of study with the intention of going to law school and then eventually doing good things for the world.” “A pre-law course entitled ‘Analysis of the Written Word’ was particularly stimulating and valuable with its emphasis on the exact meaning of the written word.” My realization from this emphasis is that every word that Vernon uses in his memoir (and in his publications) has been carefully chosen, for example in the quotations above and below.

Vernon took his first physics course in his sophomore year (2nd year). In his third year he majored in physics, and graduated, in 1941.

Vernon went to Caltech for graduate school. “President Robert Milikan gave a spirited but not humble course on modern physics.” Then, in December, Pearl Harbor was bombed. Vernon then went to work at the MIT Rad Lab – on radar, 1941–1945.

2. “World War II Years and Columbia Graduate School”

After the war ended, in 1946, Vernon went back to graduate school, but at Columbia. This was the period of QED, g-2 (electron), beta decay (Rabi, Lamb, Wu, ..). Vernon decided to work on nuclear electric quadrupole moments from the polarization of the nuclear core by an outer nucleon – his thesis used molecular beams, with Rabi as his advisor. “I was particularly interested at the time in building an apparatus by myself from scratch.” “I then worked out the theory for this two-photon transition for our case. At that time at Columbia theoretical course work was extensive and one was expected to handle the theory relevant to ones experiments.” “As a teacher, I found Rabi most inspiring, helpful, encouraging, and basically sane.”

Vernon laments missing doing hyperfine structure of hydrogen for his thesis (this led to the first observation of a discrepancy with QED, before the Lamb shift discovery). “My thesis was certainly satisfying and instructive. And it contributed a bit of new knowledge. This experience did instill in me the firm view that, to learn fundamental things, it is best to study a simple system where the theory should be adequate.”

Vernon received his Ph.D. in 1950: “Launched with a Ph.D. in 1950.”

3. “Atomic Physics Research”

Vernon joined Yale in 1954. He did helium research for 30 years, many ppm measurements: $\mu(^3He)/\mu(^1H) = 0.761\ 812\ 37\ (46)$ (0.6 ppm), to provide a test of modern QED theory of the two-electron system. He found good agreement at the ppm level.

($e^+ - e^-$): positronium was discovered in 1951 by Deutsch at MIT. Vernon measured the hyperfine interval with C.S. Wu to 3.6 ppm. Wu et al. then discovered parity violation in 1957. Vernon then did an experiment to measure the polarization of electrons from ^{60}Co decay. “Furthermore, believing that polarized electron sources would prove useful generally in atomic and high-energy physics, I began to study methods of producing a beam of polarized electrons with reasonable intensity.” This led to an electronically polarized K beam (via 6-pole magnets), with polarized electrons from photo-ionization. This new source, PEGGY, achieved $P=.8, 2 \times 10^8$ electrons in 1.5 μ sec pulse.

4. “Muonium”

($e^- - \mu^+$): Vernon’s search for muonium started within weeks of the parity violation discoveries (beta decay; π to μ to electron). Parity violation provided a tool to identify the muon spin state. Attempts from 1957-1960: a spin exchange between muonium and oxygen (an impurity in the argon gas in the apparatus) depolarized electrons and blocked discovery. Vernon and his group discovered muonium in 1960. “Muonium brought something new, interesting, and substantial into our world.”

Vernon developed plans for a meson factory at Yale using a linear accelerator that wasn’t built; but LAMPF was, following the Yale scheme (1972). Vernon then worked on developing the muon facility at LAMPF from the mid-1960s, leading to muonium experiments.

Gisbert zu Putnitz came to Yale, collaborating on muonium from 1967. "Gisbert and I, as well as our families, have been close friends for over 30 years. Our collaboration and friendship have been among the better experiences in my life."

5. "Polarized Leptons at High Energy"

The next chapter in Vernon's career led to the work that we are discussing at this meeting: polarized leptons at high energy. The Yale polarized source was brought to SLAC, leading to the development of a new field. "A second area in which our Yale group was able to bring something new, interesting, and important into the world was high energy polarized lepton-nucleon scattering." In 1968: the famous SLAC-MIT experiment with unpolarized $e + p$ discovered quarks. Vernon was initially interested in measuring the polarized proton structure function to provide the polarizability contribution to the hyperfine structure interval in hydrogen. This resulted in a plan to do a polarized electron-polarized proton scattering at SLAC. He used the Yale polarized electron source, and polarized target. This first measurement of $A_1(p)$ confirmed naive quark model expectations – the quarks carried much of the proton spin at large momentum fraction.

Also at this time Charles Prescott, with Vernon, did one of the most beautiful experiments: parity violation for polarized electron-unpolarized nucleon scattering, "which decisively established the validity of the unified electroweak theory."

Following the proton measurement of A_1 , a polarized electron-polarized neutron experiment was proposed and rejected by SLAC. Vernon attempted to develop interest in a polarized muon-polarized nucleon experiment at Fermilab with no success.

Vernon then joined the EMC experiment at CERN: polarized muon-polarized proton scattering, Gabathuler, Sloan, Hughes et al. The experiment uncovered the spin surprise/crisis/puzzle!

The SMC experiment was then proposed to focus on the polarized muon experiment. "Since NMC did not have anyone who had been active in the spin structure field (the British having left after EMC), it turned out that I became spokesman of SMC." The experiment obtained beautiful results – the Bjorken sum rule was confirmed to 10%. "The large amount of data on spin structure functions obtained by SMC and by SLAC confirmed but did not resolve the spin puzzle. Interest has focused on the polarized gluon contribution to nucleon spin."

Vernon's next step was to push to collide polarized electrons with polarized nucleons, at HERA. He advocated studies for polarized protons at HERA that were carried out; later, he supported studies for polarized electrons at RHIC. Vernon joined a collaboration for polarized proton beam polarimetry for RHIC and for a future polarized HERA.

RHIC Spin came in large part from the physics uncovered by Vernon on the spin structure of the proton. Vernon also played a direct role: he first suggested to Ernest Courant to study whether acceleration of polarized protons in a strong-focusing accelerator would be possible. He also supported the waveform digitizers from Yale (Satish Dhawan) that are a crucial part of proton polarimetry at RHIC. Vernon never joined polarized proton-polarized proton collision physics. I believe he thought protons too complicated as a probe.

6. “Muon g-2”

“The anomalous magnetic moment or g-value of the muon, like that of the electron, is a fundamental quantity of great interest.” By 1979 the third CERN muon g-2 experiment obtained a 7 ppm precision (syst. error 1 ppm). In 1978, R.W. Williams presented “Muon g-2 – the Last Word.” Vernon seemed to take this title as a challenge! In 1982, at the LAMPF II workshop, Vernon and others studied mounting a new g-2 experiment (the LAMPF II intensity was expected to be 100 x CERN). This work led to the formation of a new muon g-2 experiment at the AGS, when the AGS booster had been proposed, which would give a proton intensity for the AGS of about 30 x CERN.

“The value of the muon anomalous magnetic moment may be considered a sum rule of present physics. Any deviation of a_μ (experiment) from a_μ (theory) indicates physics beyond the standard model.” While writing the paper showing a 2.5 sigma deviation from theory (the 1999 BNL result), Vernon told me “we are very lucky.” However, while preparing a press release, Vernon was quoted that a deviation can come from 1) we are wrong, 2) the theory is wrong, and 3) new physics (this is paraphrased).

The last result from the present BNL experiment, announced in January, 2004, reached a precision of 0.5 ppm. Whether there is a significant difference from theory is uncertain at present, due to ongoing theoretical work. The present difference between theory and experiment is 2.7 standard deviations, using the standard e^+e^- data to obtain the hadronic contribution. The theory is closer to experiment when τ data are used, but there are now questions about the assumptions necessary to use the τ data.

7. “An Administrative Addendum”

Associated Universities Incorporated (AUI) established BNL in 1947, and Vernon was trustee from 1962. AUI was removed from managing BNL in 1998 by the U.S. Department of Energy, due to a furore over a High Flux Beam Reactor tritium leak. The leak amounted to about 1 exit sign worth of tritium (tritium is commonly used in exit signs for buildings). This was not fought legally by AUI. “I regret this lack of legal response because I believe that a vigorous AUI defense could have clarified many aspects of the situation and would have been a positive move toward strengthening a spirit of mutual respect and trust between federal agencies and the scientific community.”

Finally, from “A Festschrift in honor of Vernon W. Hughes” edited by M.E. Zeller, World Scientific 1991 (on the occasion of Vernons 70th birthday): “Being descended from Iowa stock, which included an evangelical Methodist minister, I should probably have some moral, wise thoughts to offer. However, I don’t have anything very original to say. Surely the important driving force for research is one’s own interest in the topic. One shouldn’t be too influenced by other people’s opinions, or by current fads or speculations. I have found, on several occasions, progress in research has been slowed at least partly due to the injection of criteria extraneous to the research itself, e.g. consideration of credit to individuals, a teaching objective or some political funding matter. Effective collaboration in small or large groups requires the closest possible communication among their members and maximum input from everyone. I have derived great satisfaction from the warm human

relationships with physicists with whom I have worked or shared common interests."

"I have felt for a long time, as I believe many of us do, that a particular importance of our profession is its international aspect. We have a rather unique opportunity, largely independent of politics, to communicate and work and to become friends with physicists from almost any country which has activity in our field. Our collaborations are not only a great professional and personal pleasure but also an important contribution to international understanding and peace."

SEARCHES FOR PERMANENT ELECTRIC DIPOLE MOMENTS - SOME RECENT DEVELOPMENTS*

K. P. JUNGMANN

Kernfysisch Versneller Instituut, Rijksuniversiteit Groningen, Groningen, The Netherlands

Searches for permanent electric dipole moments (EDMs) of fundamental particles provide an opportunity to discover New Physics beyond the present Standard Theory. New ideas for experiments have come up recently which may allow present limits to be lowered substantially, or even unambiguous effects to be found. Such effects are predicted by a variety of speculative models. The identification of potential sources for CP and T-violation will require the study of several systems, all of which have different sensitivities to possible mechanisms generating EDMs.

1. Introduction

The Standard Model (SM) provides a remarkable framework for describing observations in particle physics. Despite the success of the SM^a, a number of most intriguing questions remain in modern physics. Among those are the observation of exactly three generations of fundamental particles and the hierarchy of the fundamental fermion masses. In addition, the electro-weak SM has a rather large number of some 27 free parameters, all of which have to be extracted from experiment [1].

In modern physics - and in particular in the SM - symmetries play an important and central role. Whereas global symmetries relate to conservation laws, local symmetries yield forces [2]. It is rather unsatisfactory that within the SM the physical origin of the observed breaking of discrete symmetries in weak interactions, e.g. of parity (P), of time reversal (T) and of combined charge conjugation and parity (CP), remains unrevealed, although the experimental findings can be well described.

The speculative models beyond the present standard theory include some which involve Left-Right symmetry, fundamental fermion compositeness, new particles, leptoquarks, supersymmetry, supergravity and many more. Interesting candidates for an all-encompassing quantum field theory are string or membrane (M) theories which in their low energy limit may include supersymmetry. Without secure experimental evidence to be gained in future, all of these speculative theories will remain without status in physics, independent of their

*This work is supported by the Dutch Foundation for Fundamental Research (FOM)

^aWe do not consider the necessary modifications to the SM to accommodate recent observations in neutrino physics that strongly indicate the existence of neutrino oscillations.

mathematical elegance and partial appeal. Experimental searches for predicted unique features of those models - such as breaking of symmetries - are therefore essential to steer theory towards a better and deeper understanding of fundamental laws of nature. Such experiments can be carried out in a complementary manner at high energy accelerators and also at lower energies - typically in the regime of atomic physics - in high precision measurements, such as EDM searches.

2. Discrete Symmetries

In this article we are concerned with discrete symmetries. A permanent electric dipole moment (EDM) of any fundamental particle or quantum system violates both parity (P) and time reversal (T) symmetries [3].

The violation of P is well established in physics [4], and its accurate description has contributed significantly to the credibility of the SM. The observation of neutral currents, together with the observation of parity non-conservation in atoms, were important in verifying the validity the SM. The fact that physics over 10 orders in momentum transfer - from atoms to the highest energy scattering - yields the same electro-weak parameters may be viewed as one of the biggest successes in physics to date. However, at the level of highest precision electro-weak experiments questions arose, which ultimately may call for a refinement.

The predicted running of the weak mixing angle $\sin^2\Theta_W$ appears not to be in agreement with observations [5]. If the value of $\sin^2\Theta_W$ is fixed at the Z^0 -pole, deep inelastic electron scattering at several GeV appears to yield a considerably higher value. A reported disagreement from atomic parity violation in Cs has disappeared after a revision of atomic theory [6]. A new round of experiments is being started with the Q_{weak} experiment [7] at the Jefferson Laboratory in the USA. For atomic parity violation, in principle higher experimental accuracy will be possible from experiments using Fr isotopes [20, 21] or single Ba or Ra ions in radiofrequency traps [22]. Although the weak effects are larger in these systems due to their high power dependence on the nuclear charge, this can be exploited only after improved atomic wave function calculations become available, as the observation is always through an interference of weak with electromagnetic effects [23].

The violation of the combined charge conjugation (C) and parity (P) operations was first observed in the neutral Kaon decays, and can be described with a phase in the Cabbibo-Kobayashi-Maskawa formalism [24]. CP-Violation is particularly interesting because of its possible relation to the observed matter-antimatter asymmetry in the universe. A. Sakharov [25] has suggested that the observed dominance of matter could be explained via CP-violation in the early universe in a state of thermal non-equilibrium and with processes violating baryon number.^b CP violation as described in the SM is insufficient to satisfy the needs of this elegant model. This strongly motivates searches for yet unknown sources of CP-Violation.

^bWe note here that the existence of additional sources of CP-Violation is not a necessary condition to explain the matter-antimatter asymmetry. Other viable routes could lead through CPT violation and would not even need thermal non-equilibrium [26].

Table 1. Some actual limits on EDMs and the improvement factors necessary in experiments to reach SM predictions. It appears that for electrons, neutrons and muons the region where speculative models have predicted a finite value for an EDM can be reached with presently proposed experiments in the near future.

Particle	Limit/Measurement [e cm]	Method employed in latest experiment	Standard Model Limit [factor to go]	Possible New Physics [factor to go]
e	$< 1.6 \times 10^{-27}$	Thallium beam [8]	10^{11}	≤ 1
μ	$< 2.8 \times 10^{-19}$	Tilt of precession plane in anomalous magnetic moment experiment [9]	10^8	≤ 200
τ	$(-2.2 < d_\tau < 4.5) \times 10^{-17}$	electric form factor in $e^+e^- \rightarrow \tau\tau$ events [10]	10^7	≤ 1700
n	$< 6.3 \times 10^{-26}$	Ultra-cold neutrons [11]	10^4	≤ 60
p	$(-3.7 \pm 6.3) \times 10^{-23}$	120kHz thallium spin resonance [12]	10^7	$\leq 10^5$
Λ^0	$(-3.0 \pm 7.4) \times 10^{-17}$	Spin precession in motional electric field [13]	10^{11}	10^9
$\nu_{e,\mu}$	$< 2 \times 10^{-21}$	Inferred from magnetic moment limits [14]		
ν_τ	$< 5.2 \times 10^{-17}$	Z decay width [15]		
Hg-atom	$< 2.1 \times 10^{-28}$	mercury atom spin precession [16]	$\leq 10^5$	various

Note: Interesting systems such as deuterons and Ra atoms are not listed, because no experiments have been performed yet. However, higher sensitivity to non-SM EDMs has been predicted compared to neutrons (e.g. more than one order of magnitude for certain quark chromo EDMs [17]) and Hg atoms (e.g. more than three orders of magnitude for an electron EDM [18] and two orders for nuclear EDMs [19]).

3. Searches for Permanent Electric Dipole Moments

Excellent opportunities to find such new CP-Violation are provided through possible EDMs. With the assumption of CPT invariance, CP- and T-violation can be considered equivalent [3], and therefore an EDM also violates CP. For all particles, CP-Violation as it is known from the K and B mesons causes EDMs to appear through higher order loops [3]. These are at least 4 orders of magnitude below the present experimental limits (see Table 1). Several speculative models foresee EDMs which could be as large as the present experimental bounds just allow.^c

EDMs have been searched for in various systems with different sensitivities (Table 1). The spectrum of activities has been frequently reviewed in the recent past [3, 28–30]. A number of distinctively different precision experiments to search for an EDM in one or another system are under way, and several ideas for significant improvements have been made public. Still, the electron and the neutron get the largest attention from experimental groups. In composed systems such as molecules or atoms, fundamental particle dipole moments of constituents may be significantly enhanced [28]. For the electron significant enhancement factors are planned to be exploited, such as those associated with the large internal electric fields in polar molecules [31].

The physical systems investigated fall into five groups, i.e. (i) 'point' particles (e, μ , τ), (ii) nucleons (n, p), (iii) nuclei (^2H , ^{223}Fr , ...), (iv) atoms (Hg, Xe, Tl, Cs, Rn, Ra,...) and (v) molecules (TlF, YbF, PbO, ...), where each investigated object has its own particular advantages. Among the methods employed are (i) Classical approaches using optical spectroscopy of atoms and molecules in cells, as well as atomic and molecular beams or with contained cold neutrons, (ii) Modern atomic physics techniques such as traps, fountains and interference techniques; (iii) Innovative approaches involving radioactive species, storage rings, particles in condensed matter, 'masers', and more. It will remain to be seen, which of all these promising approaches will succeed in providing new limits or even find an EDM.^d

We must note that there is no preferred system for an EDM search. In fact, many systems need to be examined, because depending on the underlying processes different systems have in general quite different susceptibility to acquire an EDM through a particular mechanism (see Figure 1). An EDM may be found as an "intrinsic property" of an elementary particle as we know it, because the underlying mechanism is not accessible at present. However, it can also arise from CP-odd forces between the constituents under observation, e.g. between nucleons in nuclei or between nuclei and electrons. Such EDMs could be much higher [17] than those expected for elementary particles originating within the popular models, usually from New Physics.

^cHistorically the non-observation of any EDM has ruled out more speculative models than any other experimental approach in all of particle physics [27].

^dAn all-encompassing review of all the relevant aspects and giving justice to all the new ideas in this rapidly growing field can not even be attempted in this article.

4. Some New Developments in the Field of EDM Searches

This highly active field of research benefited recently from a plurality of novel ideas. These have led to new activities in systems not investigated so far. Among them are in particular radioactive atoms and charged particles.

4.1. Radioactive Systems

New facilities around the world make more short-lived radioactive isotopes available for experiments. Of particular interest is the Ra atom, which has rather close lying states of opposite parity. This accidental quasi-degeneracy of the $7s7p^3P_1$ and $7s6d^3D_2$ states has led to the prediction of a significant enhancement of an electron EDM [18] - much higher

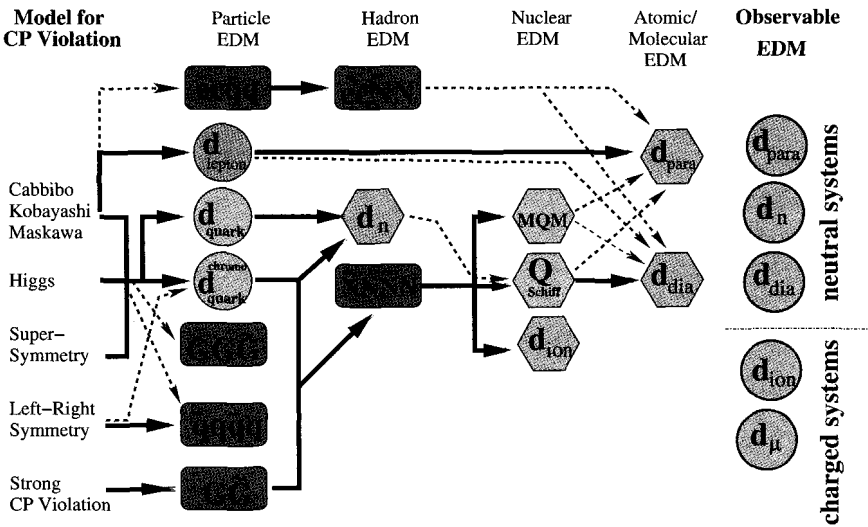


Fig. 1. A variety of theoretical speculative models exists in which an EDM could be induced through different mechanisms, or a combination of them, in fundamental particles and composed systems for which an EDM would be experimentally accessible. Up to now very sensitive experiments were carried out only with composed neutral systems. A novel technique may allow us to sensitively access EDMs also with charged fundamental particles and ions. (Figure adapted from C.P. Liu³³)

than for any other atomic system. Furthermore, the nuclei of many Ra isotopes are within a region where (dynamic) octupole deformation occurs, which also enhances the effect of a nucleon EDM substantially, i.e. by some two orders of magnitude [19]. From a technical point of view the Ra atomic levels of interest for an experiment are easily accessible spectroscopically, and the isotopes can be produced in sufficient quantities in nuclear reactions. The advantage of an accelerator-based Ra experiment is apparent, because nuclear EDMs are possible only in nuclei with spin, and all Ra isotopes with non-vanishing nuclear spin are relatively short-lived [32].

4.2. Searches for EDMs in charged Particles

A very novel idea was introduced recently for measuring an EDM of charged particles directly. For such experiments the high electric field is exploited, which charged particles experience at relativistic speeds in a magnetic storage ring. In such a setup the Schiff theorem, which had excluded charged particles from experiments due to the Lorentz force acceleration, can be circumvented because of the non-trivial geometry of the problem [28]. With an additional radial electric field in the storage region, the spin precession due to the magnetic moment anomaly can be compensated if the effective magnetic anomaly a_{eff} is small, i.e. if $a_{eff} \ll 1$ [34].

The method was first considered for muons. For longitudinally polarized muons injected into the ring, an EDM would express itself as a spin rotation out of the orbital plane. This can be observed as a time dependent (to first order linear in time) change of the above/below the plane of orbit counting rate ratio. For the possible muon beams at the future J-PARC facility in Japan a sensitivity of 10^{-24} e cm is expected [35, 36]. In such an experiment the possible muon flux is a major limitation. For models with nonlinear mass scaling of EDMs such an experiment would already be more sensitive to some certain new physics models than the present limit on the electron EDM [37]. For certain Left-Right symmetric models a value of d_μ up to 5×10^{-23} e cm would be possible. An experiment carried out at a more intense muon source could provide a significantly more sensitive probe of CP violation in the second generation of particles without strangeness.^e

The deuteron is the simplest known nucleus. Here an EDM could arise not only from a proton or a neutron EDM, but also from CP-odd nuclear forces [40]. It has been shown very recently [17] that the deuteron can in certain scenarios be significantly more sensitive than the neutron. In equation (1) this situation is evident for the case of quark chromo-EDMs:

$$\begin{aligned} d_{\mathcal{D}} &= -4.67 d_d^c + 5.22 d_u^c, \\ d_n &= -0.01 d_d^c + 0.49 d_u^c. \end{aligned} \quad (1)$$

It should be noted that because of its rather small magnetic anomaly the deuteron is a particularly interesting candidate for a ring EDM experiment, and a proposal with a sensitivity of 10^{-27} e cm exists [41]. In this case scattering off a target will be used to observe a spin precession. As possible sites of an experiment the Brookhaven National Laboratory (BNL), the Indiana University Cyclotron Facility (IUCF) and the Kernfysisch Versneller Instituut (KVI) are considered.

^eA New Physics (non-SM) contribution a_μ^{NP} to the muon magnetic anomaly and muon EDM d_μ are the real and imaginary parts of a single complex quantity related through $d_\mu = 3 \times 10^{-22} \times (a_\mu^{NP} / (3 \times 10^{-9})) \times \tan \Phi_{CP}$ e cm with a yet unknown CP violating phase Φ_{CP} . The problems around the SM model value for a_μ [38, 39], which cause difficulties for the interpretation of the recent muon g-2 experiment in terms of limits for or indications of New Physics, make a search for d_μ attractive as an important alternative, as the SM value is negligible for the foreseeable future.

5. T-violation Searches other than EDMs

Besides EDMs there exist more possibilities to find T-Violation. Among those certain correlation observables in β -decays offer excellent opportunities to find such new sources [30, 42, 43]. In β -neutrino correlations the 'D'-coefficient [42] (for spin polarized nuclei) offers great potential to observe new interactions in a region of possible New Physics which is less accessible to EDM searches. However, the 'R'-coefficient [42] (observation of β -particle polarization) would explore the same areas as present EDM searches or β -decay asymmetry measurements. Such experiments are under way at a number of laboratories worldwide [43].

6. Conclusions

There is a large field of searches for EDMs in a large number of systems. Novel ideas to use not yet studied systems have emerged recently, and newly suggested experimental approaches offer excellent opportunities to complement the more traditional experimental approaches on neutron-, atom- and electron-EDMs, which have yielded the best limits to date. Any successful search in the future will have to be complemented by experiments on other systems in order to pin down eventually the mechanisms leading to the observed EDMs.

7. Acknowledgments

The author is grateful to his colleagues C.P. Liu, C.J.G. Onderwater, R.G.E. Timmermans, L. Willmann, H. Wilschut, the members of the BNL based edm-collaboration and the KVI TRi μ P group for recent discussions around the exciting subject of EDM searches.

References

1. S. Eidelmann et al., Phys. Lett. **B 592**, 1 (2004)
2. T.D. Lee and C.N. Yang, Phys. Rev. **98**, 1501 (1955)
3. I.B. Khriplovich and S.K. Lamoreaux, "CP Violation Without Strangeness", Springer, Berlin (1997)
4. E. Hughes, this volume
5. A. Czarnecki and W. Marciano, Int.J.Mod.Phys. **A13**, 2235 (1998)
6. W.C. Haxton and C.E. Wieman, Ann.Rev.Nucl.Part.Sci. **21**, 261 (2001); see also: J. Sapirstein and K.T. Cheng, physics/0409147 (2004) and references therein.
7. D. Armstrong et al, proposal E02-020 to Jefferson Lab (2002)
8. B.C. Regan et. al., Phys. Rev. Lett., **88**, 071805(2002)
9. R. McNabb et al., hep-ex/0407008 (2004)
10. K. Inami et. al., Phys. Lett. B, **551**, 16 (2002)
11. P. G. Harris et. al., Phys. Rev. Lett, **82**, 904 (1999)
12. D. Cho et. al., Phys. Rev. Lett., **63**, 2559 (1989)
13. L. Pondrom et. al., Phys. Rev. D, **23**, 814 (1981)
14. F. del Aguila and M. Sher, Phys. Lett. B, **252**, 116 (1990)
15. R. Escribano and E. Masso, Phys. Lett. B, **395**, 369 (1997)
16. M. Romalis, W. Griffith and N. Fortson, Phys.Rev.Lett. **86**, 2505 (2001)

17. C.P Liu and R.G.E. Timmermans, Phys.Rev.C **70**, 055501(2004); see also: O. Lebedev et al., Phys. Rev. D **70**, 016003 (2004)
18. V. Dzuba et al., Phys. Rev. A **63**, 062101 (2001)
19. J. Engel, this volume; J. Engel et al., Phys. Rev. C **68**, 025501 2003
20. S.N. Atutov et al., Hyperfine Interactions **146-147**, 83 (2003)
21. E. Gomez et al., physics/0412073 (2004)
22. N. Fortson, in: "Parity Violation in Atoms and Polarized Electron Scattering", B. and M.Bouchiat (eds.), World Scientific, Singapore, p. 244 (1999)
23. J. Sapirstein and K.T. Cheng, physics/0409147 (2004)
24. J.W. Cronin, Rev.Mod.Phys. **53**, 373 (1981); M. Neubert, Int.J.Mod. Phys. **A11**, 4173 (1996); O. Long, hep-ex/0412047 (2004)
25. A. Sakharov, JETP **5**, 32 (1967); M. Trodden, Rev.Mod.Phys. **71**, 1463 (1999)
26. O. Bertolami et al., Phys.Lett. **B395** 178 (1996)
27. N. Ramsey, at "Breit Symposium", Yale (1999)
28. P.G.H. Sandars, Contemp. Phys. **42**, 97 (2001)
29. Y. Semertzidis, Proceedings SIGHAD03 Workshop, Pisa, Italy, hep-ex/0401016 (2004)
30. K. Jungmann et al., in: "NuPECC Long Range Plan 2004", M.N. Harakeh et al. (eds.), (2004)
31. M.G. Kozlov and D. DeMille, Phys.Rev.Lett. **89**, 133001 (2002); D. Kawall et al., Phys.Rev.Lett.**92**, 13307 (2004)
32. K. Jungmann, Acta Phys. Pol., **33** 2049 (2002)
33. C.P. Liu, Workshop on Fundamental Interactions, Trento, Italy (2004)
34. I.B. Khriplovich, Phys.Lett. **B444**, 98 (1998)
35. Y. Semertzidis et al., J-PARC Letter of Intent L22 (2003)
36. F.J.M. Farley et al., Phys. Rev. Lett. **93**, 052001 (2004)
37. K.S. Babu, B. Dutta and R. Mohapatra, Phys.Rev.Lett. **85** 5064 (2000); B. Dutta and R. Mohapatra, Phys. Rev. **D68** (2003) 113008
38. B.L. Roberts, this volume
39. G.W. Bennett et al., Phys. Rev. Lett.**92**, 168102 (2004) see also: Phys. Rev. Lett. **89**,101804 (2002) and H.N. Brown et al., Phys.Rev.Lett.**86**, 2227 (2001)
40. J. Hisano, hep-ph/0410038 (2004)
41. Y. Semertzidis et al., AIP Conf. Proc. **698**, 200 (2004)
42. P. Herczeg, Prog. Part. and Nucl. Phys. **46**, 413 (2001)
43. K. Jungmann, Proceedings INPC04, Goeteborg, Sweden (2005)

DISCUSSION

W.T.H. van Oers:

Question: You have stressed in your talk the importance of atomic and nuclear multiplication factors for the measurements of EDM's. But given a non-zero measurement how will it be possible to unravel the atomic and nuclear structure effects with some certainty?

Answer: You mention correctly the importance of atomic and molecular calculations. The case of atomic parity violation has demonstrated that for alkali systems calculations at the percent level are possible (as a historical note, in the parity case less than optimal care in doing and interpreting calculations has caused some excitement, unjustified by nature). At present, calculations relating to EDM enhancements are typically of order 25% accurate. That's by far sufficient to select the right systems for our research. Once there will be a signal, I am convinced that these calculations will improve. Along that way, the calcula-

tions in Ra and Ba, being performed right now on properties of these atoms, may serve as an indication of what is possible. For Ra we will depend on calculations to find some lines with laser spectroscopy.

M. Garcon:

Question: In various scenarii beyond the Standard Model, is there a flavour-dependence of the quark electric dipole moment? Could it be that the linear combination of the quark EDM involved in the neutron or deuteron EDM yield very small values?

Answer: The answer to this question of possible cancellations of quark EDM's depends on the New Physics Model one chooses. Some models have a large number of CP-violating phases which may allow a "conspirative" cancellation mechanism. In general, looking at different systems, e.g. neutron AND deuteron, allows to investigate different linear combinations of quark EDM's and therefore is expected to shine more light onto possible underlying mechanisms.

M. Giorgi:

Question: When you mentioned a "Lorentz violation" did you mean an explicit T violation?

Answer: The CPT violation research I was referring to is not particularly connected to T-violation. The point was that there are other ways to explain the matter-antimatter asymmetry but CP violation as suggested by Sacharov. One way would be the CPT (and Lorentz violation) as suggested by Kosteleckj et al., where explicit T violation or CP violation is not needed.

A. Burinskii:

Question: The word "point" in one of your transparencies is in quotes before the word "electron". Is it assumed that the electron is not a point-like particle?

Answer: The electron is point-like, as it is checked in the deep inelastic scattering processes. However, it has a virtual photon structure in the Compton region.

NUCLEON FORM FACTORS

K. de JAGER

Thomas Jefferson National Accelerator Facility, Newport News, U.S.A.

The experimental and theoretical status of elastic electron scattering from the nucleon is reviewed. As a consequence of new experimental facilities, data of unprecedented precision have recently become available for the electromagnetic and the strange form factors of the nucleon.

1. Introduction

Nucleon electro-magnetic form factors (EMFFs) are optimally studied through the exchange of a virtual photon, in elastic electron-nucleon scattering. More than 40 years ago Akhiezer *et al.* [1] (followed 20 years later by Arnold *et al.* [2]) showed that the accuracy of nucleon charge form-factor measurements could be increased significantly by scattering polarized electrons off a polarized target (or equivalently by measuring the polarization of the recoiling proton). However, it took several decades before technology had sufficiently advanced to make the first of such measurements feasible, and only in the past few years has a large number of new data with a significantly improved accuracy become available. For G_E^p measurements the highest figure of merit at Q^2 -values larger than a few GeV^2 is obtained with a focal plane polarimeter. For studies of G_E^n one needs to use a magnetic spectrometer to detect the scattered electron in order to clearly identify the reaction channel. As a consequence, the figure of merit of a polarized ^3He target is comparable to that of a neutron polarimeter. A more detailed overview of the subject is available in [3].

There are experimental indications that strange quarks can contribute to the nucleon mass (from pion-proton scattering results) and to its spin (from spin-dependent deep-inelastic scattering data). Parity-violating elastic electron-nucleon scattering can access the contribution of strange quarks to the charge and magnetization distributions of the nucleon. In order to study this, one needs to scatter longitudinally polarized electrons off unpolarized protons and measure the effect of changing the beam helicity. A rough estimate of that beam asymmetry yields:

$$A^{PV} \propto \frac{\sigma_R - \sigma_L}{\sigma_R + \sigma_L} \approx \frac{A_Z}{A_Y} \approx \frac{4\pi\alpha}{Q^2} \approx 10^{-4} Q^2, \quad (1)$$

where $\sigma_{L(R)}$ is the cross section for scattering of left(right)-handed electrons. A^{PV} is proportional to the interference between those processes in which a virtual photon, or a neutral

Z-boson, is exchanged. The equation implies that the effect to be measured is of the order of a few parts per million (ppm). In the past decade the helicity-correlated properties of electron beams have improved such that systematic errors of a few parts per billion are becoming achievable. Still, specially designed instrumentation is required to achieve a comparable statistical error.

2. Electromagnetic Form Factors

2.1. Experimental Results

In the past decade a series of double-polarization measurements of neutron knock-out from a polarized ^2H or ^3He target have provided accurate data on G_E^n . The ratio of the beam-target asymmetry with the target polarization perpendicular and parallel to the momentum transfer is directly proportional to the ratio of the electric and magnetic form factors. A similar result is obtained with an unpolarized deuteron target when one measures the polarization of the knocked-out neutron as a function of the angle over which the neutron spin is precessed with a dipole magnet. The latest data from Hall C at Jefferson Lab, using either a polarimeter [5] or a polarized target [6], extend up to $Q^2 \approx 1.5 \text{ GeV}^2$ with an overall accuracy of $\sim 10\%$, in mutual agreement.

A significant break-through for G_M^n was made by measuring the ratio of quasi-elastic neutron and proton knock-out from a deuterium target. A study for G_M^n at Q^2 -values up to 5 GeV^2 has recently been completed in Hall B at Jefferson Lab. [4]. Preliminary results indicate that G_M^n is within 10% of the dipole form factor G_D over the full Q^2 -range (0.5-4.8 GeV^2).

In elastic electron-proton scattering a longitudinally polarized electron will transfer its polarization to the recoil proton. In the one-photon exchange approximation, the ratio of the charge and magnetic form factors is directly proportional to the ratio of these polarization components. The greatest impact of the polarization-transfer technique was made by the two recent experiments [7, 8] in Hall A at Jefferson Lab, which measured the ratio G_E^p/G_M^p in a Q^2 -range from 0.5 to 5.6 GeV^2 . The most striking feature of the data is the sharp, practically linear, decline as Q^2 increases. Since it is known that G_M^p closely follows G_D , this implies that G_E^p falls more rapidly with Q^2 than G_D . This significant fall-off of the form-factor ratio is in clear disagreement with earlier results using the Rosenbluth extraction. Qattan *et al.* [9] performed a high-precision Rosenbluth extraction in Hall A at Jefferson Lab, designed specifically to significantly reduce the systematic errors compared to earlier Rosenbluth measurements. The results of this experiment, covering Q^2 -values from 2.6 to 4.1 GeV^2 , are in excellent agreement with previous Rosenbluth results. This basically rules out the possibility that the disagreement between Rosenbluth and polarization-transfer measurements of the ratio G_E^p/G_M^p is due to an underestimate of ϵ -dependent uncertainties in the Rosenbluth measurements.

2.2. Two-Photon Exchange

Blunden *et al.* [10] carried out the first modern calculation of the elastic contribution from two-(or more-)photon exchange (TPE) effects. However, the size of the correction only resolves about half of the discrepancy. A different approach was used by Chen *et al.* [11], who related the elastic electron-nucleon scattering to the scattering off a parton in a nucleon through generalized parton distributions. Their results for the TPE contribution practically reconcile the Rosenbluth and the polarization-transfer data.

Hence, it is becoming more and more likely that TPE processes have to be taken into account in the analysis of Rosenbluth data, and that they will affect polarization-transfer data only at the few percent level. Of course, further effort is needed to investigate the model-dependence of the TPE calculations. The most direct test would be a measurement [12] of the positron-proton and electron-proton scattering cross-section ratio at small ε -values.

3. Form-Factor Behaviour at Low and at High Q^2 -values

3.1. Experimental Review and Outlook

Table 1 lists the results for the charge and magnetization rms radii, related to the slope of the form factor at $Q^2=0$. For an accurate extraction of the radius Sick [13] has shown that it is necessary to take into account Coulomb distortion effects and higher moments of the radial distribution. Within error bars, the rms radii for the proton charge and magnetization distribution and for the neutron magnetization distribution are equal.

Table 1. Values for the nucleon charge and magnetization radii

Observable	value \pm error	Reference
$\langle (r_E^p)^2 \rangle^{1/2}$	0.895 ± 0.018 fm	[13]
$\langle (r_M^p)^2 \rangle^{1/2}$	0.855 ± 0.035 fm	[13]
$\langle (r_E^n)^2 \rangle$	-0.119 ± 0.003 fm ²	[14]
$\langle (r_M^n)^2 \rangle^{1/2}$	0.87 ± 0.01 fm	[15]

In the asymptotically free limit, QCD can be solved perturbatively, providing predictions for the EMFF behavior at large Q^2 -values. Recently, Brodsky *et al.* [16] and Belitsky *et al.* [17] have independently revisited the pQCD domain. Belitsky *et al.* derive the following large Q^2 -behavior:

$$\frac{F_2}{F_1} \propto \frac{\ln^2 Q^2 / \Lambda^2}{Q^2}, \quad (2)$$

where Λ is a soft scale related to the size of the nucleon. This behaviour (calculated for $\Lambda = 300$ MeV in Fig. 1) is in excellent agreement with the data for $Q^2 \geq 1$ GeV². It predicts that G_E^p/G_M^p will cross zero at $Q^2 \approx 8$ GeV² and that G_E^n drops off much more gradually than expected.

3.2. Model Calculations

The recent production of very accurate EMFF data, especially the surprising G_E^p data from polarization transfer, has prompted the theoretical community to intensify their investigation of nucleon structure. The first EMFF models were based on vector meson dominance (VMD). With this model Iachello *et al.* [18] predicted a linear drop of the proton form factor ratio, similar to that measured by polarization transfer, more than 20 years before the data became available. Bijker and Iachello [19] have extended the original calculations by including a meson-cloud contribution in F_2 . These new calculations are in good agreement with the proton form-factor data, but do rather poorly for the neutron (Fig. 1).

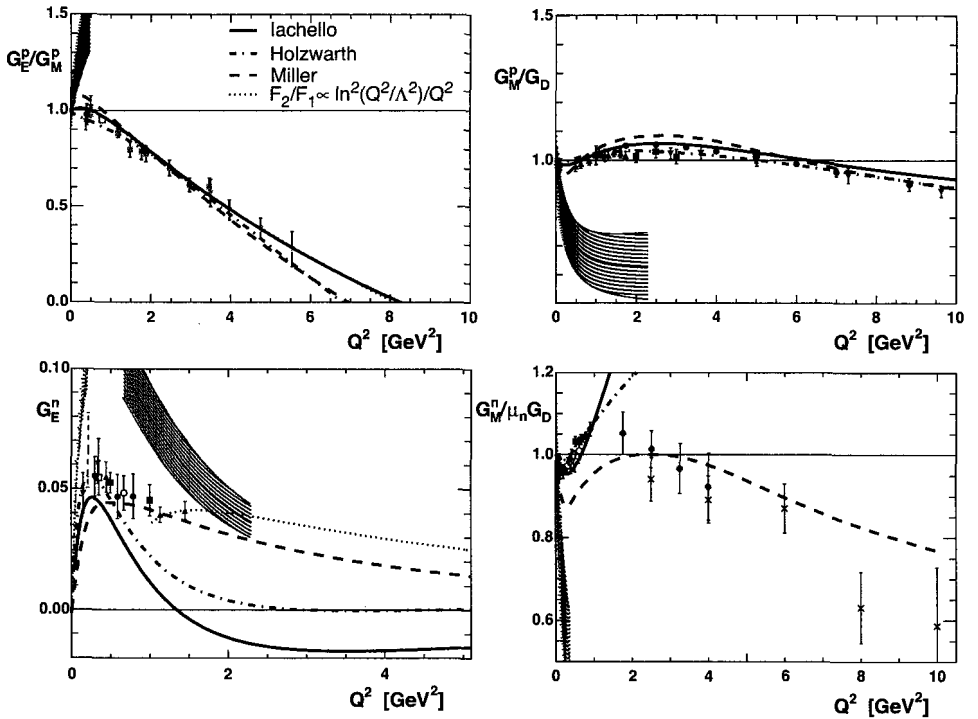


Fig. 1. Comparison of various calculations ([19–21]) with available EMFF data (see Hyde-Wright ([3]) for references). For G_E^p/G_M^p only polarization-transfer data are shown. The shaded band indicates the uncertainty in the extrapolation [23] of the Lattice QCD calculations [22]. Where applicable, the calculations have been normalized to the calculated values of $\mu_{p,n}$. Also shown is the Q^2 -behaviour [17] of G_E^p/G_M^p and G_E^n , normalized to the datum at the largest Q^2 -value.

Many recent theoretical studies of the EMFFs have applied various forms of a relativistic constituent quark model (RCQM). Because the momentum transfer can be several times the nucleon mass, the constituent quarks require a relativistic quantum mechanical treatment. Miller [20] uses an extension of the cloudy bag model, three relativistically moving (in light-front kinematics) constituent quarks, surrounded by a pion cloud. The calculations

of Miller do well for all EMFFs, except for G_M^n at low Q^2 -values.

Before the Jefferson Lab polarization transfer data on G_E^p/G_M^p became available, Holzwarth [21] predicted a linear drop in a chiral soliton model. In such a model the quarks are bound in a nucleon by their interaction with chiral fields. His later calculations provide excellent agreement for the proton data, but only a reasonable description of the neutron data.

Only lattice gauge theory can provide a truly ab initio calculation, but accurate lattice QCD results for the EMFFs are still several years away. One of the most advanced lattice calculations of EMFFs has been performed by the QCDSF collaboration [22]. The technical state of the art limits these calculations to the quenched approximation (in which sea-quark contributions are neglected), to a box size of 1.6 fm, and to a pion mass of 650 MeV. Ashley *et al.* [23] have extrapolated the results of these calculations to the chiral limit, using chiral coefficients appropriate to full QCD. The agreement with the data (Figure 1) is poorer than that of any of the other calculations, a clear indication of the technology developments required before lattice QCD calculations can provide a stringent test of EMFF data.

4. Strange Form Factors

The parity-violating asymmetry can be expressed explicitly in terms of the electromagnetic Sachs form factors $G_{E,M}^{p,n}$, the Weinberg angle θ_W , and the Fermi constant G_F :

$$A^{PV} = -\frac{G_F Q^2}{4\alpha\pi\sqrt{2}} \left[(1 - 4\sin^2\theta_W) - \frac{\varepsilon G_E^p (G_E^n + G_E^s)}{\varepsilon(G_E^p)^2 + \tau(G_M^p)^2} \right. \\ \left. + \frac{\tau G_M^p (G_M^n + G_M^s) - 2\varepsilon'(1 - 4\sin^2\theta_W) G_M^p G_A^{Zp}}{\varepsilon(G_E^p)^2 + \tau(G_M^p)^2} \right] \quad (3)$$

where τ , ε and ε' are kinematic factors. G_A^{Zp} contains two terms, the neutral-current axial form factor, and electro-weak radiative effects. The neutral current axial form factor is to first order given by the sum of the charged-current form factor and the first moment of the strange quark distribution. The radiative effects either have to be calculated or can be determined by a separate measurement from a deuterium target. In the past decade four separate efforts have been initiated to study the strange form factors G_E^s and G_M^s , the characteristics of which are listed in Table 2.

Table 2. Overview of parity-violating studies of strange form factors

Name	Facility	Technique	Q^2 -range [GeV ⁻²]	Kinematics	Target
SAMPLE	MIT-Bates	integrating	0.04-0.1	backward	H,D
HAPPEX-I	JLab Hall A	integrating	0.47	forward	H
A4	MAMI	counting	0.1- 0.3	for/backward	H,D
HAPPEX-II	JLab Hall A	integrating	0.1	forward	H, ⁴ He
G ^o	JLab Hall C	counting	0.2-0.8	for/backward	H,D

The first experiment to start running was SAMPLE at the MIT-Bates facility, which

used a 200 MeV polarized electron beam incident on a liquid hydrogen (and later deuterium) target. The Čerenkov light induced in air by electrons elastically scattered through an angle between 130° and 170° were detected in an array of ten large phototubes, covering an angular acceptance of 1.5 sr. At the beam energy of 200 MeV, electrons from inelastic events do not produce Čerenkov light in air. Initial results yielded a value for the electroweak radiative corrections (including anapole effects) in disagreement with a detailed calculation by Zhu *et al.* [24] In a recent reanalysis [25], corrections were applied for electromagnetic radiative effects, for the background due to threshold photo-pion production, and due to charged particles not blocked by the shutters in front of the phototubes. The final result overlaps the calculation of Zhu *et al.*, and results in a value for the strange magnetic form factor of $G_M^s(Q^2 = 0.1) = 0.37 \pm 0.20 \pm 0.26 \pm 0.07$, where the uncertainties are statistical, experimental systematic, and due to electroweak radiative corrections.

In the HAPPEX experiment the electrons scattered over an angle of 12.5° were detected in a pair of high-resolution magnetic spectrometers. The spectrometer optics cleanly separates elastic events from inelastic ones, while at such a forward angle even the limited acceptance (≈ 6 msr) of the spectrometers covers a significant fraction of the full azimuthal range. A CW beam of ≈ 3.3 GeV impinged on a 15 cm long LH2 target. The detector in the focal plane consisted of a lead-lucite sandwich viewed by a single phototube. The beam helicity was flipped with a frequency of 30 Hz and the detector signal was integrated over a 32 ms window. The experiment [26] yielded a linear combination of the strange electric and magnetic form factors $G_E^s + 0.392G_M^s(Q^2 = 0.48) = 0.014 \pm 0.020 \pm 0.010$, where the first error constitutes a quadratic sum of the experimental statistical and systematic errors, and the second arises from the EMFF data.

In the A4 experiment at the Mainz-MAMI facility, individual events are counted in an array of 1022 tapered PbF_2 crystals with an angular acceptance of 0.7 sr. Light from each 3×3 array of crystals is digitized and histogrammed with custom-built electronics. In this way all inelastic events are rejected. In the first stage of this experiment [27] the detector was centered at 35° , and data were taken at beam energies of 570 and 854 MeV. This has yielded combinations of the strange electric and magnetic form factors at two Q^2 -values: $G_E^s + 0.225G_M^s(Q^2 = 0.23) = 0.039 \pm 0.034$ and $G_E^s + 0.106G_M^s(Q^2 = 0.11) = 0.071 \pm 0.036$, where the error constitutes a quadratic sum of the experimental statistical and systematic errors. In the next phase the detector will be rotated to 145° , and data will be taken on hydrogen and deuterium at Q^2 -values of 0.23 and 0.47 GeV^2 .

The G^0 program [29] aims at a separation of G_E^s and G_M^s over a Q^2 -range from 0.2 to 0.8 GeV^2 . It uses a large superconducting toroidal magnet as a spectrometer, in which recoil protons from elastic scattering at forward angles are detected with plastic scintillators with an angular acceptance of 0.9 sr. The elastic protons are identified by time of flight. Backward-angle asymmetries will be measured by reversing the orientation of the spectrometer w.r.t. the beam direction. In that set-up, elastically scattered electrons will be detected at a scattering angle of $\approx 110^\circ$. Inelastic electrons will be discriminated against with additional scintillators. Additional runs from a deuterium target at the backward angle are scheduled to study electroweak radiative effects. The forward-angle run has been

completed in 2004 and the analysis of the data is in progress.

In the second phase of the HAPPEX experiments a pair of septum magnets allows the detection of electrons scattered over 6° in the magnetic spectrometers. In addition, various aspects of the instrumentation have been improved, among which a super-lattice GaAs photocathode (which provided a record 88% beam polarization), racetrack target cells with improved boiling characteristics, and radiation-hard Čerenkov detectors. In addition a set of luminosity monitors was installed for a quantitative study of the helicity-correlated beam properties and target boiling effects. In a preliminary run data were taken on both hydrogen and ^4He targets. Because the ^4He nucleus is isoscalar, the parity-violating asymmetry is sensitive only to the strange electric form factor. Although less than 10% of the final statistics was accumulated, the preliminary results shown in Fig. 2 already provides an accuracy comparable to the results from SAMPLE and A4:

$$G_E^s(Q^2 = 0.1) = -0.019 \pm 0.041 \pm 0.026 \quad \text{and} \quad (4)$$

$$G_E^s + 0.08 G_M^s(Q^2 = 0.1) = 0.034 \pm 0.028 \pm 0.010 \pm 0.09, \quad (5)$$

where the statistical and systematic errors are quoted separately. The final run, scheduled in 2005, will reduce the statistical errors by a factor of three.

All four experiments have measured [30] or have plans to measure the vector analyzing power in elastic electron-proton scattering. This observable is sensitive to the imaginary part of the TPE amplitude and can be accessed by measuring the azimuthal dependence of

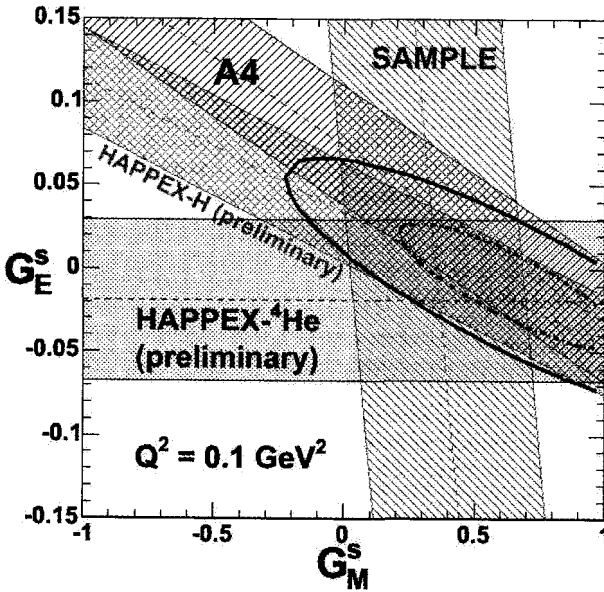


Fig. 2. The results at $Q^2 = 0.1 \text{ GeV}^2$ of the experiments described in the text.

the single-spin asymmetry for electrons polarized transverse to the scattering plane.

5. Summary

In recent years highly accurate data on the nucleon form factors have become available from various facilities around the world, made possible by the development of high luminosity and novel polarization techniques. These have established some general trends in the Q^2 -behavior of the four EMFFs. The two magnetic form factors G_M^p and G_M^n are close to identical, following G_D to within 10% at least up to 5 GeV², while G_E^p/G_M^p drops linearly with Q^2 . Once the upgrade to 12 GeV has been implemented at Jefferson Lab, it will be possible to extend the data set on G_E^p and G_M^n to 14 GeV² and on G_E^n to 8 GeV². Highly accurate measurements with the Rosenbluth technique have established that the discrepancy between results on G_E^p/G_M^p with the Rosenbluth techniques and with polarization transfer is not an instrumentation problem. Recent advances on two-photon exchange contributions make it highly likely that the application of TPE corrections will resolve that discrepancy. Similar advances have already yielded results of unprecedented precision for the strange nucleon form factors. As yet these have not provided quantitative evidence for the contribution of strange form factors, in agreement with recent Lattice QCD calculations [31, 32] which predict very small effects. However, the results of even more accurate measurements can be expected within a couple of years.

Acknowledgments

This work was supported by DOE contract DE-AC05-84ER40150 Modification No. M175, under which the Southeastern Universities Research Association (SURA) operates the Thomas Jefferson National Accelerator Facility.

References

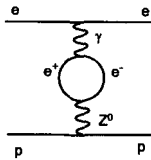
1. A.I. Akhiezer, L.N. Rozentsweig, and I.M. Shmushkevich, *Sov. Phys. JETP* **6**, 588 (1958).
2. R. Arnold, C. Carlson and F. Gross, *Phys. Rev. C* **23**, 363 (1981).
3. C.E. Hyde-Wright and K. de Jager, *Annu. Rev. Nucl. Part. Sci.* **54**, 217 (2004).
4. W. Brooks and M.F. Vineyard, spokespersons, Jefferson Lab experiment E94-017; private communication.
5. R. Madey *et al.*, *Phys. Rev. Lett.* **91**, 122002 (2003).
6. G. Warren *et al.*, *Phys. Rev. Lett.* **92**, 042301 (2004); H. Zhu *et al.* *Phys. Rev. Lett.* **87**, 081801 (2001).
7. V. Punjabi *et al.*, submitted to *Phys. Rev. C*; M.K. Jones *et al.*, *Phys. Rev. Lett.* **84**, 1398 (2000).
8. O. Gayou *et al.*, *Phys. Rev. Lett.* **88**, 092301 (2002).
9. I.A. Qattan *et al.*, nucl-ex/0410010.
10. P.G. Blunden *et al.*, *Phys. Rev. Lett.* **91**, 142304 (2003).
11. Y.C. Chen *et al.*, *Phys. Rev. Lett.* **93**, 122301 (2004).
12. W. Brooks *et al.*, spokespersons, Jefferson Lab experiment E04-116.
13. I. Sick, *Phys. Lett. B* **576**, 62 (2003); private communication (2004).
14. S. Kopecky *et al.*, *Phys. Rev. C* **56**, 2229 (1997).
15. G. Kubon *et al.*, *Phys. Lett. B* **524**, 26 (2002).

16. S.J. Brodsky *et al.*, *Phys. Rev. D* **69**, 076001 (2004).
17. A.V. Belitsky, X. Ji and F. Yuan, *Phys. Rev. Lett.* **91**, 092003 (2003).
18. F. Iachello, A. Jackson and A. Lande, *Phys. Lett. B* **43**, 191 (1973).
19. R. Bijker and F. Iachello, *Phys. Rev. C* **69**, 068201 (2004).
20. G.A. Miller, *Phys. Rev. C* **66**, 032001R (2002).
21. H. Holzwarth, *Z. Phys. A* **356**, 339 (1996); hep-ph/0201138.
22. M. Göckeler *et al.*, hep-lat/0303019.
23. J.D. Ashley *et al.*, *Eur. Phys. Jour. A* **19** (Suppl. 1), 9 (2004).
24. S.-L. Zhu *et al.*, *Phys. Rev. D* **62**, 033008 (2000).
25. D.T. Spayde *et al.*, *Phys. Lett. B* **583**, 79 (2004).
26. K.A. Aniol *et al.*, *Phys. Rev. C* **69**, 065501 (2004).
27. F.E. Maas *et al.*, *Phys. Rev. Lett.* **93**, 022002 (2004); nucl-ex/0412030.
28. D. Lhuillier, Contribution to these Proceedings.
29. J. Roche, Contribution to these Proceedings of.
30. S.P. Wells *et al.*, *Phys. Rev. C* **63**, 064001 (2001); F.E. Maas *et al.*, nucl-ex/0410013.
31. D. Leinweber *et al.*, hep-lat/0406002.
32. R. Lewis, W. Wilcox and R.M. Woloshyn, *Phys. Rev. D* **67**, 013003 (2003).

DISCUSSION

V. A. Huseynov:

Comment: you investigate ep scattering and you consider exchange via photon (γ) or neutral Z^0 boson. To increase the precision of the calculations or measurements it would be better to take into account quantum loops (radiative corrections) like photon + electron-positron loop + Z^0 boson etc. in the future investigations.



M. Mestayer:

Question: Is the Super-Rosanbluth data consistent with non-linear t -dependence expected from 2-photon exchange?

Answer: 2-photon exchange does not necessarily imply a non-linear t -dependence.

LOW ENERGY TESTS OF THE STANDARD MODEL

E. W. HUGHES

California Institute of Technology, Kellogg Radiation Laboratory, Pasadena, USA

Low-energy precision measurement of fundamental parameters in the electroweak theory provide information on new physics at high mass scales, beyond the reach of present-day colliders. Historically, low energy tests of the electroweak theory were critical in establishing the validity of the Standard Model; however, today the motivation for performing precision low-energy measurements is to search for beyond Standard Model physics. We review briefly the study of low energy measurements of the electroweak mixing angle, with a focus on a new measurement coming from the observation of a parity-violating asymmetry in the scattering of high energy polarized electrons by unpolarized electrons in a liquid hydrogen target. The experiment was performed at the Stanford Linear Accelerator Center. The present experiment is sensitive to new physics at the TeV energy scale. We also compare the results to other low-energy tests of the electroweak theory, and briefly discuss future planned low-energy measurements.

1. Introduction

Low energy measurements have played a pioneering role in establishing the Standard Model, and continue to be important in the search for new interactions beyond the Standard Model. Some of the important low energy tests require studying spin-dependent effects, such as measurements of parity violation. Therefore, this topic is relevant to the Spin Conference series. We have heard here already two plenary talks that fall under the category of "Low Energy Tests of the Standard Model", namely the $g-2$ experiment described by Lee Roberts [1] and the search for electric dipole moments described by Klaus Jungmann [2]. These are important efforts in the search for new interactions beyond the Standard Model, but did not play a large role in establishing the electroweak theory. For example, only recently has the precision of the $g-2$ measurements reached the level of requiring electroweak radiative correction diagrams. Also, up to now, no electric dipole moments have been observed in neutral atoms or molecules.

My talk will focus on the measurement of the electroweak mixing angle, including a brief review of the history of low energy measurements, followed by a description of today's results, whose goal is to search for physics beyond Standard Model. Three measurements of the electroweak mixing angle have continually played an important role in testing the Standard Model, one coming from the study of parity violation in electron scattering, one coming from atomic parity violation measurements, and one coming from the

measurement of the neutral current (NC) to charged current (CC) cross sections in neutrino scattering.

Finally, this talk will concentrate, in particular, on measurement of parity violation in electron scattering. This measurement is the only new result in the field since the last spin conference two years ago.

2. The Past

Parity violation measurements in electron scattering and in atoms played a large role in establishing the electroweak theory, and provided definitive proof that there is, indeed, a mixing between the Z-boson exchange and photon exchange. The most important experiment that firmly established parity violation was a polarized electron scattering experiment performed at SLAC called E122 [3, 4]. The experiment, led by Charles Prescott, involved deep inelastic scattering of a ~ 20 GeV polarized electron beam off a liquid deuterium target. The pioneering step in the measurement was the use of a new solid state source, made of GaAs, which enabled the production of a high current polarized beam. In fact, the average beam current of $10 \mu\text{A}$ represented a factor of 100 increase in current compared to previous attempts in SLAC Experiments E80 [5] and E95 [6]. The factor of 100 improvement in statistics translated into a factor of 10 increased sensitivity to the parity-violation effect, ultimately allowing for a 10% measurement of the parity violating asymmetry.

The philosophy and fundamental techniques used in the E122 experiment were reintroduced in today's experiment, especially with regard to beam control and beam systematics. In particular, the E122 experiment made use of a rapid reversal of the beam helicity by controlling the helicity of a source laser with a pockel cell. Two important systematic studies of false asymmetries were performed in the experiment. One used a prism to reverse the laser helicity independent of the pockel cell. A second test was performed by running the longitudinally polarized electron beam at different beam energies, which corresponded to an independent reversal, since the electron beam helicity undergoes a g-2 precession before it enters the experimental hall. Running the experiment at 19 and 22 GeV, for example, corresponded to a 180 degree reversal of the electron beam helicity, resulting in a sign reversal of the physics asymmetry.

These same reversals and checks for possible false asymmetries were performed in the SLAC E158 experiment discussed in the next section. The final result from the E122 experiment was the measurement of a parity-violating asymmetry 10 standard deviations away from zero, resulting in a measurement of the electroweak mixing parameter of $\sin^2 \theta_w = 0.224 \pm 0.020$, consistent within uncertainties with today's precision results from e^+e^- collider measurements, namely $\sin^2 \theta_w = 0.23126 \pm 0.00017$.

First parity-violating measurements from atomic experiments using bismuth atoms were also published the same year [3]. However, the history of these measurements was much rockier. A number of atomic physics groups found no parity violation, and the atomic physics theoretical uncertainties also changed dramatically with time. Surprisingly, about half the atomic experiments found no evidence for parity violation, whereas the other half found strong evidence for parity violation, many standard deviations away from zero. In

the midst of these discrepancies, SLAC Experiment E122 was critical for resolving these difficulties in favour of the Standard Model.

Ahead of the parity violation measurements was another extremely important test of the Standard Model coming from the measurement of the NC to CC cross section in neutrino scattering. However, even these measurements had a rough start. Figure 1a shows measurements of the NC/CC ratio for neutrino and anti-neutrino scattering from the first round of experiments, namely the Gargamelle experiment [7] at CERN and the HPWF experiment [8] at Fermilab. The situation as a test of the Standard Model was unclear in 1974, but got cleaned up by 1978 with further measurements coming from FERMILAB with the CCFR experiment [9], and CERN from the CDHS experiment [10], as shown in Figure 1b.

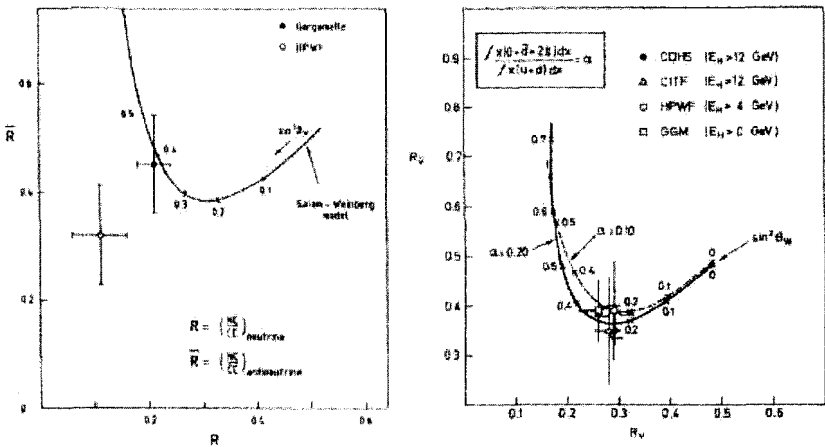


Fig. 1. Measurements of the NC/CC cross section in anti-neutrino versus neutrino scattering from CERN and FERMILAB. The left figure are results from 1974 and the right figure are results from 1978.

3. The Present

Jumping ahead twenty years, measurements from e^+e^- collider experiments from LEP at CERN and from SLD at SLAC have produced parity-violation asymmetry measurements that allow one to extract the electroweak mixing parameter $\sin^2 \theta_w$, to a precision on average of ± 0.0017 . The measurements are, in general, in excellent agreement with one another. However, all these measurements come at one energy point, namely that set by the mass of the Z^0 boson. One might ask how well these measurements have been performed at lower energy scales. Figure 2 presents the results as of 1997 on the measurement of $\sin^2 \theta_w$ coming from the collider experiments and from the best low energy measurements. All measurements with error bars too large to fit on the graph have been excluded. One sees only two remaining points, one coming from an unpublished paper from a FERMILAB

neutrino experiment called NuTeV, and the other coming from an atomic parity violation measurement in atomic cesium by the Weiman group at Boulder [11].

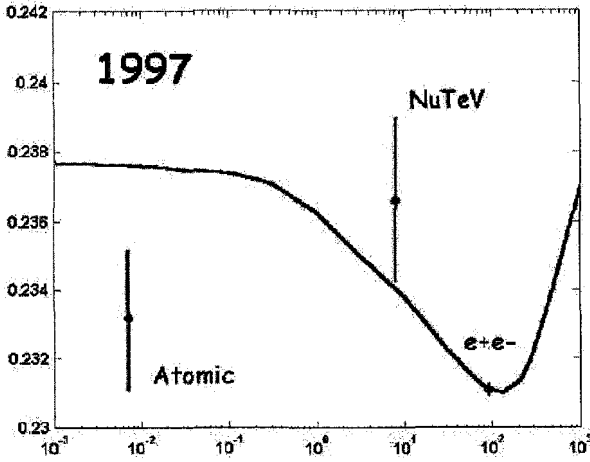


Fig. 2. Measurements of the electroweak mixing parameter, $\sin^2 \theta_w$, versus average four-momenta as of 1997.

The interest in making a precise low energy measurement of $\sin^2 \theta_w$ is both to test the prediction that $\sin^2 \theta_w$ changes with energy [12], and to test for new physics at higher energy scales that may appear as new radiative corrections. It was in this environment that SLAC Experiment E158 was approved to perform a 'precision' measurement of $\sin^2 \theta_w$ at low energy. At this point, we now focus on the measurement from SLAC Experiment E158.

SLAC Experiment E158 was an electron scattering experiment that involved elastic scattering of a high-energy high-current polarized electron beam by the unpolarized electrons in a liquid hydrogen target. A specially designed spectrometer selected electrons from specific scattering angles and energies that optimized the presence of those originating from Moller scattering. By detecting scattered electrons in an integrating calorimeter, a parity-violating asymmetry, A^{PV} is found, where $A^{PV} = \frac{\sigma_R - \sigma_L}{\sigma_R + \sigma_L}$ and σ_R and σ_L correspond to the scattering cross sections for left and right handed polarized electrons, respectively. At tree level, the relationship between A^{PV} and $\sin^2 \theta_w$ is given by

$$A^{PV} = \frac{mEG_F}{\sqrt{2}\pi} \cdot \frac{16\sin^2\theta}{3 + \cos^2\theta} \left[\frac{1}{4} - \sin^2 \theta_w \right],$$

where m is the electron mass, E is the beam energy, G_F is the Fermi coupling constant and θ is the scattering angle between the beam and target in the center of mass frame. There are some interesting features of this formula. First, the Fermi constant G_F is small, and this sets a scale for the measurement, namely that the asymmetry is extremely small. In fact, the expected electroweak prediction for the raw value of A^{PV} is $\sim 10^{-7}$ (100 ppb). Secondly, A^{PV} increases with beam energy. This implies that one needs a high-energy beam

(~ 50 GeV from SLAC) to have a sufficiently large asymmetry for the electron-electron scattering process. Finally, the asymmetry measurement provides a direct measurement of the difference between $\sin^2 \theta_w$ and 0.25. This detail is important, since $\sin^2 \theta_w$ turns out to be close to 0.25 ($\sin^2 \theta_w \sim 0.23$). Therefore, a 10% measurement of A^{PV} results in an uncertainty on $\sin^2 \theta_w$ of 0.002 from the tree level calculation. It turns out that another factor of two is gained coming from the electroweak radiative corrections. In the end, the SLAC E158 measurement of A^{PV} to a $\sim 10\%$ relative precision provides a result on $\sin^2 \theta_w$ with an uncertainty near ± 0.001 .

The E158 experiment was conditionally approved in the autumn of 1997 and collected data over three run periods in 2002 and 2003. Results from the first run period have been published [13], and preliminary results from the full data sample are presented at the end of this section. The measurement of such a small asymmetry, ~ 100 ppb, brought about numerous challenges. The primary challenges for the experiment can be categorized into four types: (1) statistics, (2) beam resolution effects originating from pulse-to-pulse fluctuations, (3) false asymmetries, and (4) backgrounds. Two of these challenges, statistics and false asymmetries, are discussed briefly here.

In order to make a 10% relative measurement on a 10^{-7} asymmetry, one needs enough events to measure A^{PV} to 10^{-8} . The primary means to maximize the statistics

for the experiment was to collect data with the maximum beam current that SLAC could deliver, build and operate an extremely long hydrogen target, and collect all Moller scattered electrons into a full acceptance azimuthally symmetric detector. The details work out as follows. With SLAC operating at $10 \mu\text{A}$ (same current as SLAC Experiment E122), using a 1.5 meter long liquid hydrogen target, the rate of Moller scattered electrons into our detector was on the order of 10^7 per pulse. The repetition rate of the accelerator was 120 Hz, resulting in 10^9 electrons scattered per second. There are 10^5 seconds in a day, giving 10^{14} scattered electrons per day. And the experiment collected data for a total of approximately 100 days. So approximately 10^{16} scattered electrons were recorded, which is the number needed for a 10^{-8} asymmetry measurement.

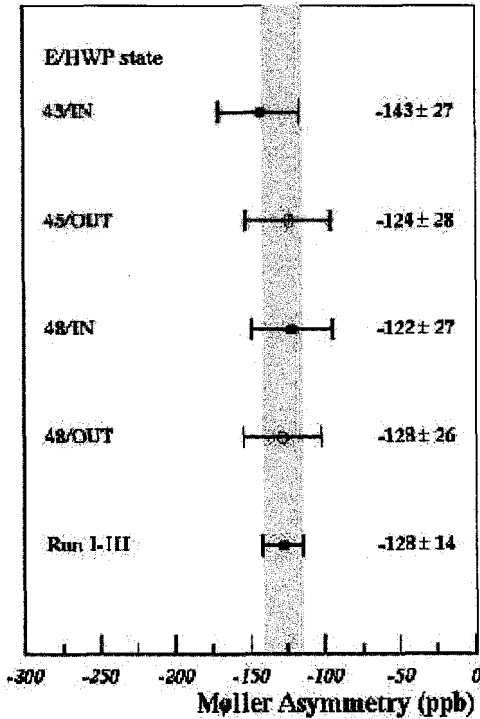


Fig. 3. Measurements of the parity violating asymmetry from SLAC Experiment E158, divided into different half-wave plate and beam energy states.

A second challenge for the measurement of such a tiny asymmetry was performing checks to assure that one has not

introduced a false non-physics asymmetry, due to some helicity dependence for some part of the experiment. A large effort was invested at the polarized source, where a complex optical feedback system was developed to zero out helicity-dependent systematics originating from the front end of the accelerator. Similar to SLAC Experiment E122, a reversal of the physics asymmetry was checked by frequently changing a half-wave plate installed at the source optics and by running the experiment at two different beam energies, namely 45 GeV and 48 GeV. Over this 3 GeV energy step, the electron spin undergoes a 180 degree rotation of its spin direction, thereby reversing its helicity. Figure 3 shows the asymmetry results coming from the E158 experiment for the four different conditions, of half-wave plate in or out, and two beam energies. One sees that the results are in excellent agreement with one another.

The final result for the experiment as shown in Figure 3 is $A^{PV} = -128 \pm 14$ (stat) ± 12 (syst) ppb. The asymmetry can be converted to a value of $\sin^2 \theta_w = 0.2330 \pm 0.0011$ (stat) ± 0.0010 (syst.). Probably the most significant implication of this result is that it puts reasonably stringent limits on the possible production of a new $SO(10) Z'$ (greater than 900 GeV at the 95% confidence level), and puts a limit of $\Lambda_{LL} \sim 10$ TeV at the 95% confidence level on a possible new four-fermion interaction.

Figure 4 presents the results from SLAC Experiment E158 compared to updated results from the cesium atomic parity violation experiment and the final published results from the NuTeV experiment [14]. Taken all together, the low energy measurements still fall significantly short of the precision coming from the collider experiments, but provide a reasonable consistency test of the Standard Model, though the NuTeV result for $\sin^2 \theta_w$ is somewhat high.

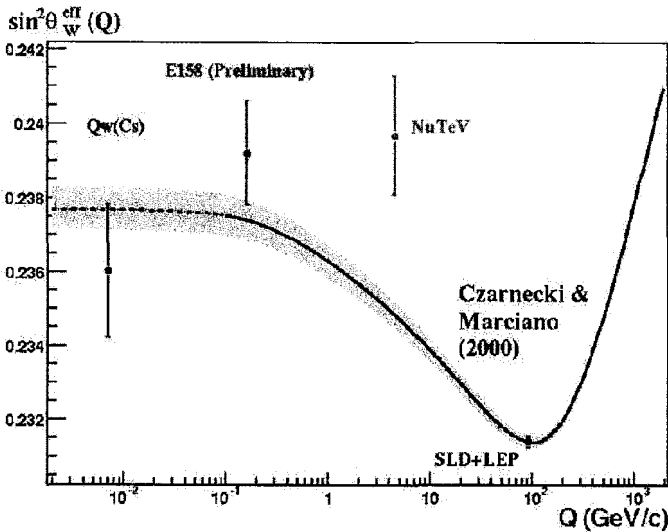


Fig. 4. Today's measurements of the electroweak mixing parameter, $\sin^2 \theta_w$, versus average four-momenta.

4. The Future

The future of the field of parity violation in electron scattering is bright, but will be focused at one location, Jefferson Laboratory in Virginia. Already, an experiment called Qweak [15], very similar in style to SLAC Experiment E158, has been approved to collect data to make a precision measurement of $\sin^2 \theta_w$ in the elastic scattering of polarized electrons by unpolarized protons. As proposed, Qweak will make a measurement of $\sin^2 \theta_w$ with an uncertainty three times smaller than that achieved in SLAC Experiment E158t. This would be a powerful measurement and would test for new physics at substantially higher energy scales.

In addition, as Jefferson Laboratory proceeds to build a 12 GeV high current polarized electron scattering fixed target program, it is likely and planned that proposals will come in to make a further parity violation measurement from deep inelastic scattering, similar to the original SLAC Experiment E122, but with a higher precision. A second attempt to measure $\sin^2 \theta_w$ from Moller scattering similar to SLAC Experiment E158 will likely be performed in this program. At 12 GeV the asymmetry to be measured will be smaller than SLAC's, where one had a 20 to 50 GeV polarized electron beam. But the high current coming from the CEBAF facility offers the opportunity to perform a much higher counting rate measurement.

The long tradition of studying parity violation to perform precision tests of the Standard Model continues. The challenge ahead for these technically demanding endeavours will be to compete with the potential direct production of new particles and new interactions coming out of the LHC program at CERN at the end of this decade.

5. Acknowledgements

I would like to thank the organizers of SPIN2004 for the invitation to give a review talk in beautiful Trieste. And, I would like to thank especially Alan Krisch, Gerry Bunce and Franco Bradamante for the session honouring the memory of my father, Vernon Hughes. This work was supported in part by the U.S. National Science Foundation Grant No. PHY-0244245.

References

1. B.L. Roberts, these proceedings.
2. K.P. Jungmann, these proceedings.
3. C.Y. Prescott, "Weak-Electromagnetic Interference in Polarized Electron-Deuteron Scattering", *Rise of the Standard Model: A History of Particle Physics from 1964 to 1979*, p. 459.
4. C.Y. Prescott, *Phys. Lett.* **77B**, 347 (1978).
5. M.J. Alguard *et al*, *Phys. Rev. Lett.* **37**, 1261 (1976).
6. W.B. Atwood *et al*, *Phys. Rev.* **D18**, 2223 (1978).
7. F.J. Hasert *et al*, *Nucl. Phys.* **B46**, 1 (1974).
8. A. Benvenuti *et al*, *Phys. Rev. Lett.* **32**, 800 (1974).
9. B.C. Barish *et al*, *Phys. Rev. Lett.* **34**, 538 (1975).
10. M. Holder *et al*, *Phys. Lett.* **B71**, 222 (1977).

11. C.S. Wood, S.C. Bennett, D. Cho, B.P. Masterson, J.L. Roberts, C.E. Tanner, C.E. Wieman, *Science* **275**, 1759 (1997).
 12. A. Czarnecki and W.J. Marciano, *Phys. Rev.* **D53**, 1066 (1996).
 13. P.L. Anthony *et al*, *Phys. Rev. Lett.* **92**, 181602-1 (2004).
 14. G.P. Zeller *et al*, *Phys. Rev. Lett.* **88**, 091802-1 (2002).
 15. D. Armstrong *et al*, "The Qweak Experiment: A Search for New Physics at the TeV Scale via a Measurement of the Proton's Weak Charge", Jefferson Laboratory Proposal E02-020, December 2001.
-

DISCUSSION

M.J.Tannenbaum:

Question: You showed beautiful measurements using parity violation to test the Standard Model, with excellent agreement. I remember that there was a spin related asymmetry of B meson production at SLD which disagreed with the Standard Model. Has that gone away?

Answer: The SLD b-quark asymmetry did, indeed, differ from the Standard Model prediction; however, this discrepancy disappeared with an increased data sample. On the other hand, the average LEP measurement of this quantity now differs from the Standard Model by about 3 standard deviations. My plot is a bit out of data, showing only a 2 standard deviation difference. Nevertheless, the main point of my plot was to show that overall the e^+e^- collider asymmetry measurements represent an enormously successful test of the Standard Model at high precision.

MEMORIAL L.D. SOLOVIEV

A. D. KRISCH

Spin Physics Center, University of Michigan, Ann Arbor, U.S.A.

The first part of this Memorial lecture was a detailed review of the Memorial article that was published in CERN Courier in October 2003; it is reprinted on the next page as Fig. 1. It was written by IHEP's founding director, A.A. Logunov, IHEP's present director, N.E. Tyurin, and me. Together, we could much better summarize Professor Soloviev's long and admirable career than I could alone.

Now I will end with a few personal thoughts. Professor Lev D. Soloviev was a friend and colleague that I admired greatly. He was trained as a theorist and a mathematician; moreover, he was a very practical man. For 19 years he was not only the director of the former Soviet Union's largest high-energy physics facility; he was also effectively the mayor of Protvino. He was a modest man, who did not seek personal publicity; he was also very responsible and kind. He once told me that one of his most difficult jobs was dealing with a large group of unhappy mothers, who wanted to discuss a problem with some kindergarten teacher in Protvino; he never told me how he solved that problem.

He was also very wise about international matters. You may recall that in the early 1980s, the relations between Russia and America were strained; in 1982 he and I exchanged letters, which neither of us wanted to write. After relations had improved in the late 1980s, during a pleasant dinner together in Protvino, Lev said:

“Sometime this might happen again; we might have to again do what we must do. But we should remember that we were friends and may be friends again after the difficult times pass.”

Unfortunately, unlike many theoretical predictions, Lev's prediction of new problems was experimentally confirmed: first in Washington in February 2002 and then at Moscow Airport in March-November 2002. Fortunately, Lev's wise advice was followed, and friendly discussions have continued with my many IHEP friends, including Nikolai Tyurin, who chaired this Memorial session. However, these discussions now mostly occur by telephone or e-mail or in neutral places such as ICTP Trieste. Let us all hope that: the problems will soon be history; the 50-year-long US/Russian Peaceful Use of Atomic Energy Agreement

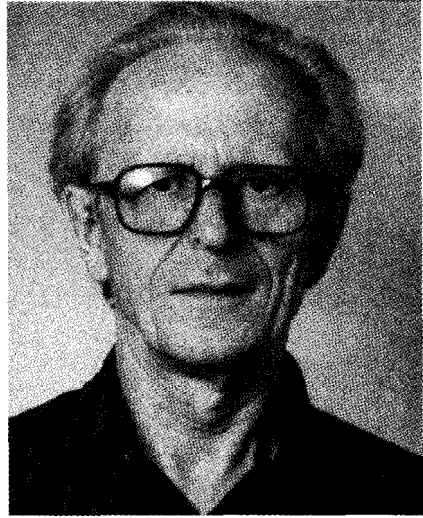
Lev D. Soloviev, an outstanding Russian theoretical physicist and director of the Institute for High Energy Physics (IHEP) in Protvino, Russia, from 1974 to 1993, passed away on 6 July 2003 after a long illness.

Soloviev's scientific career began in 1956 in the Steklov Institute in Moscow, Russia's famous centre of mathematics, after graduating with excellent results from Moscow State University and following a post-graduate course. When his scientific interests became focused on nuclear physics, he began to work at the Joint Institute for Nuclear Research (JINR) in Dubna.

Soloviev then moved to IHEP-Protvino soon after its creation in 1963 to construct the 70 GeV U-70 proton accelerator. This was the world's highest energy facility until CERN's Intersecting Storage Rings and Fermilab began operation in the early 1970s. At IHEP he continued his theoretical research, and his notable uses of modern mathematics in high-energy physics soon became recognized in the scientific world. These included the theory of low-energy photoproduction and electroproduction, the S-matrix theory of high-energy electromagnetic interactions, and relativistic string theory. Soloviev's name is also connected with the famous finite-energy sum rules, which served as a basis for the creation of the duality concept, and then superstring theory.

Soloviev was a scientist of rare ability. He combined distinguished scientific work with 19 years' service as director of the IHEP, Russia's largest high-energy physics institute. During those years, IHEP was developing both its experimental and accelerator capabilities. Soloviev constantly paid great attention to the further improvement of scientific personnel in what was then the USSR and is now Russia. There were many talented scientists among his students who gained fame both in Russia and abroad. One major factor in this success was the example he set of high scientific and personal standards. His many contributions to the development of science were highly valued by his home country.

After his term as director, Soloviev continued as IHEP's senior scientist. Despite his grave illness, he continued both his well-loved physics research and his teaching as chairman of the



Moscow Physical-Technical Institute's branch in Protvino, until almost the last day of his life.

Soloviev was also a leading figure in the international high-energy physics community. He was one of the first young Soviet physicists to make an extended stay at the Niels Bohr Institute in Copenhagen. From 1976 to 1982 he served as a member and then from 1982 to 1984 as chairman of the IUPAP's Commission on Particles and Fields. In 1977 he was a founding member of the International Committee for High Energy Spin Physics Symposia, and became its first Russian honorary member in 2002. Moreover, he chaired the first Russian Spin Physics Symposium, which was held at IHEP-Protvino in 1986. After a long period of strained East-West relations, this historic symposium served as a model for further scientific cooperation. When his directorship ended, Soloviev became a visiting professor at the University of Michigan, where he wrote some significant papers on theoretical spin physics.

The best memorial for Lev Soloviev will come from the similar work of all those who knew and respected him, and who will try to follow his example.

A.A. Logunov, N.E. Tyurin, IHEP, and A.D. Krisch, University of Michigan.

Fig. 1. Article from CERN Courier 43, No. 8, p. 41 (October 2003).
CERN Courier.

Reprinted with permission of

will soon be restarted; and our much-loved SPIN@U-70 experiment at IHEP-Protvino can restart. This would be a memorial that would please Lev Soloviev.

EXPERIMENTAL STATUS OF THE GDH SUM RULE

H. ARENDS

Institut für Kernphysik, Johannes Gutenberg-Universität Mainz, Mainz, Germany

An experimental program to investigate the Gerasimov-Drell-Hearn (GDH) sum rule on protons and neutrons has been carried out by the GDH collaboration at MAMI (Mainz) and ELSA (Bonn), using circularly polarized photons and the Bonn-Bochum longitudinally polarized frozen-spin target together with two different detector setups. For the proton, results in the photon energy range 200 - 2985 MeV are published. Preliminary data from JLab extend the energy range to 5.2 GeV. For $E_\gamma < 800$ MeV the helicity structure of partial reaction channels has been studied in detail at MAMI. Data from polarized deuterons have also been taken at photon energies 200 - 800 MeV (MAMI) and 815 - 1825 MeV (ELSA). Preliminary results and future perspectives are presented and discussed.

1. Introduction

The GDH sum rule relates the total absorption cross section of circularly polarized real photons on longitudinally polarized nucleons to the static properties of the nucleon [1]. The two relative spin configurations, parallel or antiparallel, determine the two absorption cross sections $\sigma_{3/2}$ and $\sigma_{1/2}$. The integral over the photon energy ν of the difference of these two cross sections, weighted by the inverse of ν , is related to the mass M and anomalous magnetic moment κ of the nucleon as follows:

$$\int_{\nu_0}^{\infty} (\sigma_{3/2} - \sigma_{1/2}) \frac{d\nu}{\nu} = \frac{2\pi^2\alpha}{M^2} \kappa^2 \quad (1)$$

where ν_0 is the pion photoproduction threshold and α the fine-structure constant. The GDH sum rule results from basic principles and a non-subtraction hypothesis which assumes that the integrand of the sum rule vanishes at high photon energy fast enough to assure convergence of the integral. A generalized GDH integral is defined for virtual photons, i.e. for Q^2 values different from zero. The physics and experimental status in the transition region is covered by several contributions to this conference, see [2].

2. Experimental Setups

Polarized electrons with typical degrees of polarization of 65 to 80% are available from sources using the photoeffect on strained GaAs crystals [3]. The electron polarization is monitored during the experiments by means of Møller polarimetry. Circularly polarized photons are produced by bremsstrahlung of longitudinally polarized electrons with an

energy-dependent degree of polarization according to [4]. The photon energy is determined by tagging spectrometers.

For the experiments at MAMI and ELSA, a frozen-spin target [5] has been developed, providing polarized protons or deuterons (using butanol, D-butanol or ^6LiD as target materials). The system consists of a horizontal dilution refrigerator and a superconducting magnet (≈ 2.5 T), used in the polarization phase, together with a microwave system for dynamic nuclear polarization. During the measurement, the polarization was maintained in the frozen-spin mode at a temperature of about 50 mK and a magnetic field of 0.4 T, supplied by a small superconducting holding coil inside the cryostat. Maximum polarization

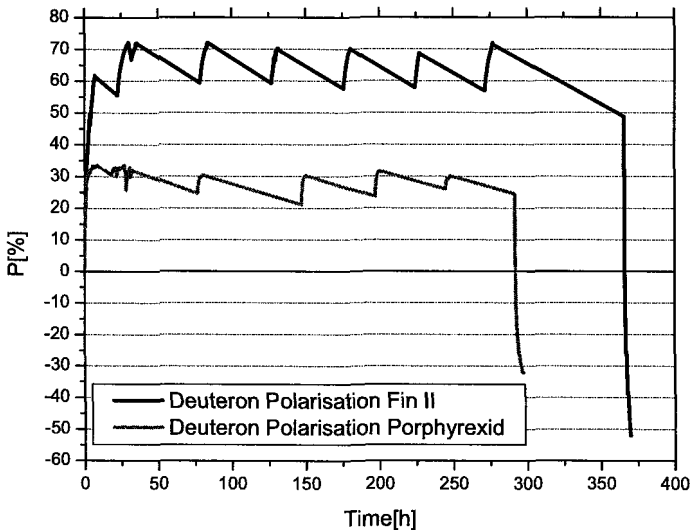


Fig. 1. Progression of the target polarization during the 2003 data taking period at MAMI with the standard and the new target material (labelled Fin II).

values close to 90% for protons and about 35% for deuterons with relaxation times in the frozen-spin mode of about 200 h have been regularly achieved. In the course of the 2003 data taking period at MAMI, the degree of deuteron polarization could be dramatically increased to more than 70% due to a new target material based on trityl-doped D-butanol, which has been developed by the Bochum group [6]. This development is a major step forward in polarized target technology. The progression of the target polarization measured during the experiment with the two target materials, using NMR techniques, is shown in Fig. 1.

Different detector concepts were used for the different energy ranges. The DAPHNE detector [8] at MAMI is well suited for charged particle detection and the identification of individual reaction channels. The GDH detector [9] at ELSA, consisting of lead-scintillator

sandwiches, detects at least one reaction product with a very high overall acceptance as a signature of a hadronic reaction.

In the GDH test measurement [12] carried out at JLab, a dynamically polarized NH₃ target was used with the CLAS detector.

3. GDH Sum Rule for the Proton

A summary of the present experimental results is shown in Fig. 2, where the helicity difference $\Delta\sigma = \sigma_{3/2} - \sigma_{1/2}$ for the total cross section on the proton [10, 11] is compared to the unpolarized cross section [15, 16]. The large “helicity-blind” background of non-resonant

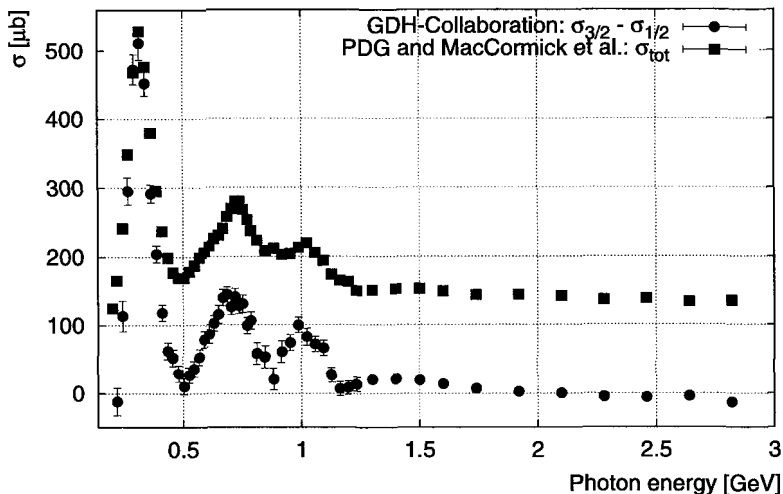


Fig. 2. Helicity difference $\Delta\sigma(\nu)$ in and above the resonance region [10, 11], compared to the unpolarized cross section of the proton [15, 16].

photoproduction has almost disappeared in $\Delta\sigma$. There is a change of sign in $\Delta\sigma$ at about 2.1 GeV. This behaviour is supported by the preliminary data [12] from JLab extending up to 5.2 GeV, see Fig. 3. Negative values are also expected from models based on a Regge fit to polarized deep inelastic scattering data [13, 14]. The running GDH integral is shown in Fig. 4. The offset of $-27.5 \mu\text{b}$ takes into account the contribution of the unmeasured low-energy part below 200 MeV, which is due to the E_{0+} multipole, as given by MAID [17]. The integral clearly exceeds the sum rule value at about 900 MeV. The change of sign in $\Delta\sigma$ leads to a turn-over. The Regge models predict a contribution of about $-14 \mu\text{b}$ for the high-energy part, which would make the experiment consistent with the GDH sum rule.

4. Partial Reaction Channels

In addition to checking the sum rule experimentally, there is a strong motivation to carefully measure the integrand and the helicity dependence of partial reaction channels such as

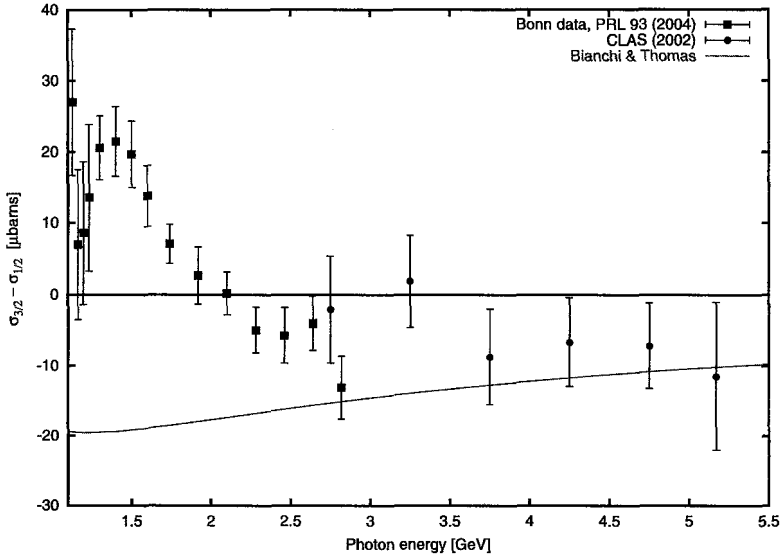


Fig. 3. Behaviour of $\Delta\sigma$ at higher energies. The data from ELSA [11] and JLab [12] are compared to Regge predictions [13].

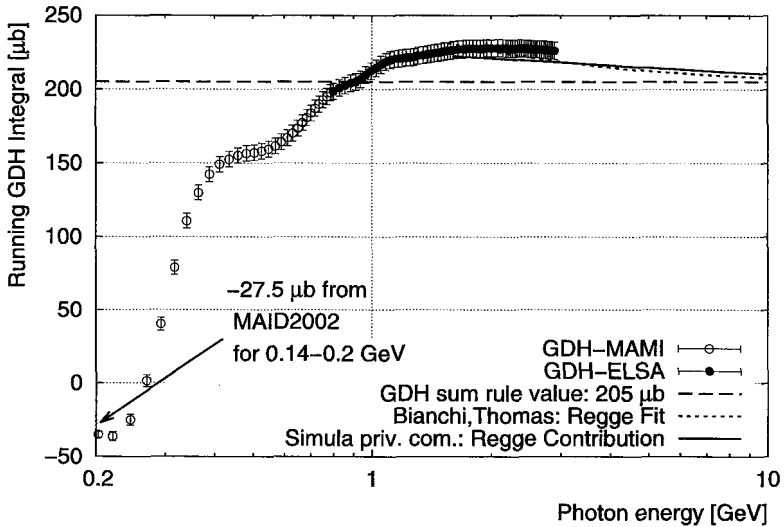


Fig. 4. Running GDH integral measured at MAMI [10] and ELSA [11] up to 2.9 GeV with Regge predictions [13, 14] for the high energy development.

single or double pion photoproduction [19], which provides completely new and up to now inaccessible information on partial wave amplitudes. Two examples in the region of the second resonances, where the resonance properties are not known very well, are given in the following. Here, the helicity difference reveals a high sensitivity to the $D_{13}(1520)$ -resonance. The multipoles E_{2-} and M_{2-} ($E1$ and $M2$ transitions, respectively) are related

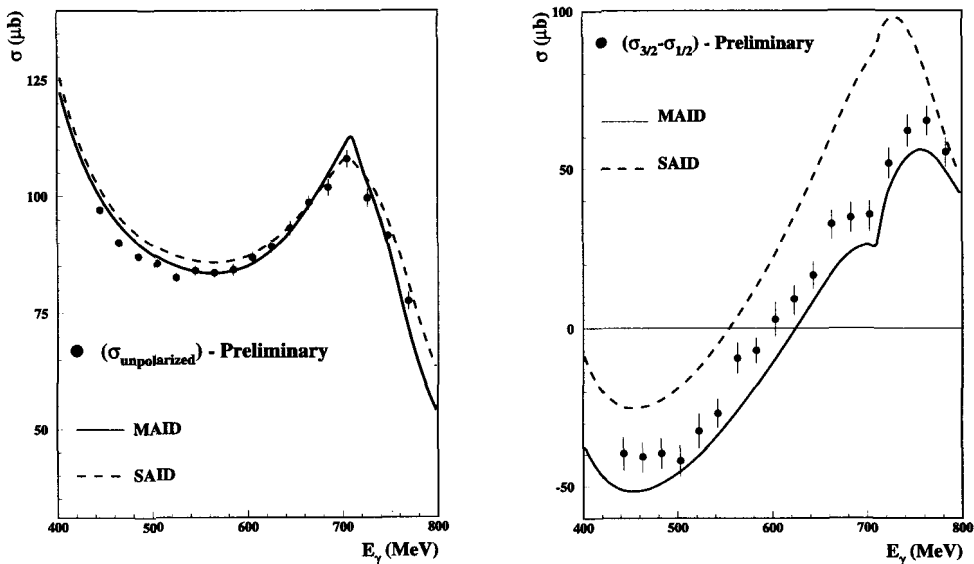


Fig. 5. The preliminary total cross section (left) and helicity difference $\Delta\sigma = \sigma_{3/2} - \sigma_{1/2}$ (right) for the reaction $\gamma p \rightarrow n\pi^+$ in comparison with results from MAID [17] and SAID [18].

to the helicity amplitudes in the following way:

$$A_{1/2}(D_{13}) \sim E_{2-} - 3M_{2-}, \quad A_{3/2}(D_{13}) \sim \sqrt{3}(E_{2-} + M_{2-}).$$

Our new results [20] on π^0 production are $A_{1/2} = -38 \pm 3$ (PDG [22]: -24 ± 9) and $A_{3/2} = 147 \pm 10$ (PDG [22]: 166 ± 5), all in units of $10^{-3} \text{ GeV}^{-1/2}$. Expressed in terms of the CGLN multipoles, the ratio M_{2-}/E_{2-} has increased from 0.45 (PDG values) to 0.56.

In a similar way the single- π^+ production was investigated in the second resonance region. Preliminary data [21] on the total unpolarized and polarized cross section are shown in Fig. 5, in comparison with the results of MAID [17] and SAID [18]. The differences of the two analyses are much more pronounced in the polarized case. This originates from significant differences in the balance of the E_{0+} and E_{2-} multipoles, which enter with opposite signs in $\Delta\sigma$.

From these examples it becomes obvious that these double-polarization experiments serve many more purposes than just measuring the GDH integral; in particular they provide a very sensitive tool to study resonance properties.

5. Deuteron Experiments

The situation is much less clear in the case of the neutron, for which the GDH sum rule predicts the value $I_n = 233.2 \mu\text{b}$. Since no free neutron target is available, experiments have to be done on deuteron or ^3He targets. The GDH sum rule for the deuteron is $I_d = 0.65 \mu\text{b}$, whereas the corresponding sum for proton and neutron is $438 \mu\text{b}$. This high nucleonic contribution therefore has to be almost completely compensated by nuclear effects, mainly

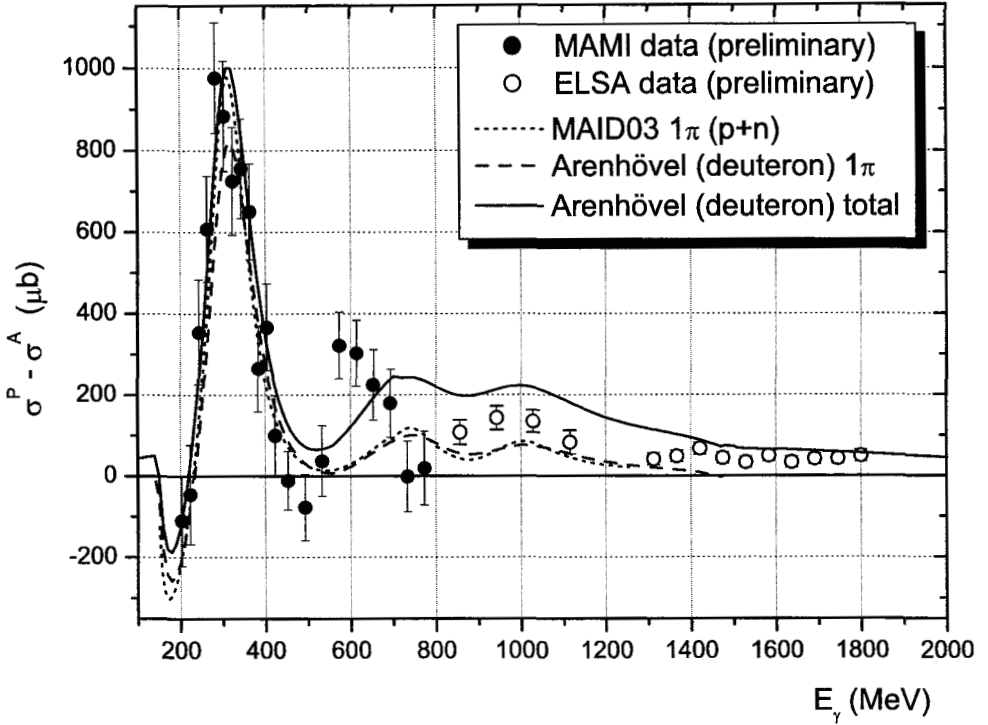


Fig. 6. Preliminary data for the deuteron from MAMI and ELSA compared to predictions from MAID [17] and Arenhövel et al. [23]. σ^P (σ^A) denotes the total cross section for parallel (antiparallel) spin configuration.

deuteron disintegration just above break-up threshold. Due to these nuclear effects, a direct extraction of the neutron spin asymmetries is not possible but requires detailed theoretical support.

First preliminary data on the deuteron above pion threshold measured by the GDH collaboration at MAMI [24] and ELSA [26] are shown in Fig. 6, in comparison with current theoretical calculations [23]. In the MAMI energy range partial reaction channels such as quasifree pion production or deuteron disintegration have also been analyzed [24]; a high-statistics run is under analysis.

At higher energies, where nuclear effects are expected to play a minor role, the difference between the deuteron and proton results can be taken as an estimate for the neutron spin asymmetries; see Fig. 7. Within the larger error bars the neutron data show a similar behaviour to the proton data [25, 26]. Whereas the one-pion contribution from [17] describes the proton data in the 3rd resonance region reasonably well, there is a significant discrepancy in the case of the neutron. This could indicate either an important contribution from multi-pion production, or a failure of MAID for the neutron. This open question remains to be solved by future experiments, e.g. with the Crystal Ball at MAMI-C [27], which will disentangle the partial reaction channels contributing in this energy region.

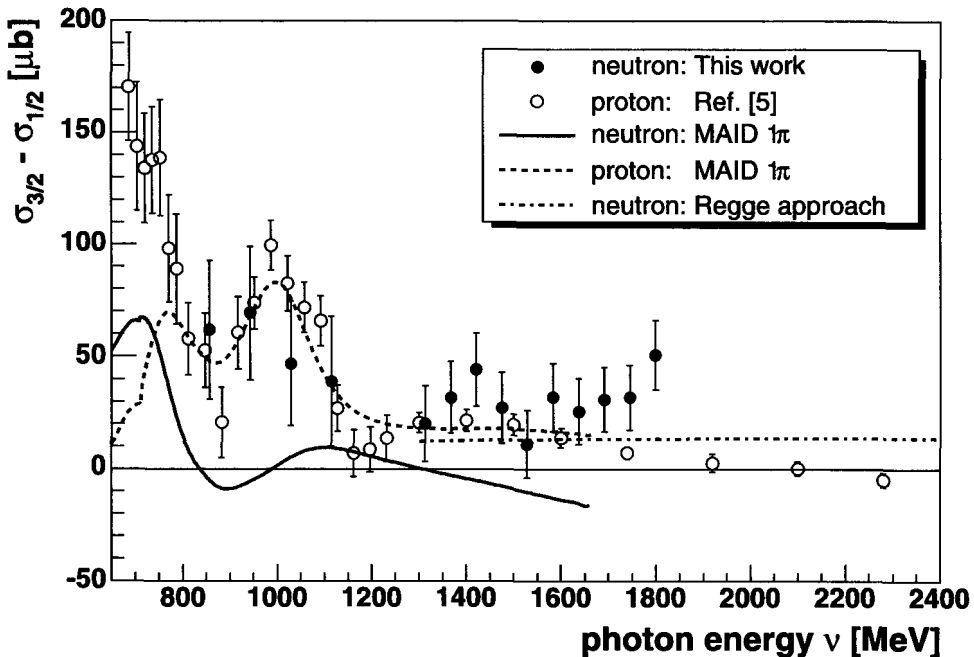


Fig. 7. Preliminary data for the neutron from ELSA [26] compared to predictions from MAID [17]

Table 1. GDH activities in progress or preparation.

<i>facility</i>	E_{γ}^{\max} [GeV]	<i>method</i>	<i>target</i>
HIγS	0.225	Compton backscattering (CB)	frozen-spin
LEGS	0.47	CB	HD
MAMI C	1.5	bremsstrahlung (BS)	frozen-spin
GRAAL	1.8	CB	HD
SPring-8	2.8	CB	frozen-spin
ELSA	3	BS	frozen-spin
JLab	6	BS	frozen-spin
SLAC	40	BS (not funded)	

6. Summary and Outlook

The GDH experiments carried out so far have verified the GDH sum rule at about the 10% level. First preliminary data on deuteron targets are available from MAMI and ELSA. The GDH sum rule for the neutron is a challenge and requires detailed theoretical support. Helicity observables for partial reaction channels carry valuable information on resonance properties. There is great activity in progress at several laboratories, see Table 1, in order to improve the data quality and energy range.

References

1. S.B. Gerasimov, *Sov. J. Nucl. Phys.* **2**, 430 (1966). S.D. Drell and A.C. Hearn, *Phys. Rev. Lett.* **16**, 908 (1966).
2. R. de Vita, contribution to this conference.
3. K. Aulenbacher, contribution to this conference.
4. H. Olsen and L.C. Maximon, *Phys. Rev.* **114**, 887 (1959).
5. C. Bradtke et al., *Nucl. Instr. Methods* **A436**, 430 (1999).
6. St. Goertz et al., Highest polarizations in deuterated compounds, to be published in *Nucl. Instr. Methods* **A**.
7. H. Dutz, report at this conference on the 9th International Workshop on Polarized Targets and Techniques, Bad Honnef (2003).
8. G. Audit et al., *Nucl. Instr. Methods* **A301**, 473 (1991).
9. K. Helbing et al., *Nucl. Instr. Methods* **A484**, 129 (2002).
10. J. Ahrens et al., *Phys. Rev. Lett.* **87**, 022003 (2001).
11. H. Dutz et al., *Phys. Rev. Lett.* **93**, 032003 (2004).
12. D. Sober et al., Proc. GDH2002, Genova, (World Scientific, Singapore, 2003).
13. N. Bianchi and E. Thomas, *Phys. Lett.* **B450**, 439 (1999).
14. S. Simula et al., *Phys. Rev.* **D65**, 034017 (2002).
15. Particle Data Group, D.E. Groom et al., *Eur. Phys. J. C* **15**, 1 (2000).
16. M. MacCormick et al., *Phys. Rev.* **C53**, 41 (1996).
17. D. Drechsel et al., *Nucl. Phys.* **A645**, 145 (1999), L. Tiator, Proceedings of GDH2002, Genova, (World Scientific, Singapore, 2003).
18. R.A. Arndt et al., *Phys. Rev.* **C66**, 055213, (2002).
19. P. Pedroni, Proceedings of GDH2004, Norfolk, VA. (2004).
20. J. Ahrens et al., *Phys. Rev. Lett.* **88**, 232002 (2002).
21. T. Rostymian, PhD thesis (Gent), in preparation.
22. K. Hagiwara et al., (Particle Data Group Collaboration), *Phys. Rev.* **D66**, 010001 (2002).
23. H. Arenhövel, A. Fix, and M. Schwamb, *Phys. Rev. Lett.* **93**, 202301 (2004).
24. O. Jahn, Proceedings of GDH2004, Norfolk, VA. (2004).
25. K. Helbing, Proceedings of GDH2004, Norfolk, VA. (2004).
26. H. Dutz et al., to be published, J. Krimmer, Ph.D. thesis, Tübingen, 2004.
27. R. Beck and A. Starostin, *Eur. Phys. J. A* **19**, 279 (2004).

DISCUSSION

O. Teryaev:

Comment: One may deduce a sort of “asymptotic theorem” valid in the limit of negligible AMM and binding energy of the deuteron. Photo-disintegration contribution exactly cancels the sum of free protons and neutron ones, and from the calculation you presented this seems to be not too far from reality.

Answer: Thank you for this comment.

F. Bradamante:

Question: For the 2003 run at MAMI you have mentioned the use of a new polarized deuteron target. How does the figure of merit of that new material compare with that of ^6LiD ? And what is its density?

Answer: This new target material developed by the Bochum group has slightly higher den-

sity, higher polarization but smaller dilution factor. In total this results in a comparable or even higher figure-of-merit compared to ${}^6\text{LiD}$.

W. Meyer:

Comment: This material will soon be tested at COMPASS.

K. Kurek:

Question: Is it possible to increase the number of photons in MAMI facility in the future?

Answer: In the experiments that I showed the photon flux was limited due to the detector, trigger, and data acquisition capabilities. We can produce tagged photon fluxes of about $10^8 \gamma/\text{s}$.

S. Fantoni:

Question: What do you think to be more needed from theorists: to look at the high energy tail of the GDH SR or to the neutron GDH SR?

Answer: Our lack of knowledge on the neutron is still large. So my preference would be on the neutron GDH SR.

M. Giorgi:

Question: With the finite energy sum rules of many years ago you could foresee the Regge behaviour of the high energy region knowing the resonances. What do you learn more with these sum rules?

Answer: We do not question the fundamental ingredients to the sum rule. The only questionable piece may be the no-subtraction hypothesis. The energy-dependence of the integrand carries much more detailed information.

SPIN PHYSICS AT GSI*

F. RATHMANN

Institut für Kernphysik, Jülich, Germany

Polarized antiprotons produced by spin filtering with an internal polarized gas target provide access to a wealth of single- and double-spin observables, thereby opening a window to physics uniquely accessible with the HESR at FAIR. This includes a first measurement of the transversity distribution of the valence quarks in the proton, a test of the predicted opposite sign of the Sivers-function, related to the quark distribution inside a transversely polarized nucleon, in Drell-Yan (DY) as compared to semi-inclusive DIS, and a first measurement of the moduli and the relative phase of the time-like electric and magnetic form factors G_{EM} of the proton. In polarized and unpolarized $p\bar{p}$ elastic scattering open questions like the contribution from the odd charge-symmetry Landshoff-mechanism at large $|t|$ and spin-effects in the extraction of the forward scattering amplitude at low $|t|$ can be addressed.

1. Physics Case

The polarized antiproton-proton interactions at the High Energy Storage Ring (HESR) at the future Facility for Antiproton and Ion Research (FAIR) will provide unique access to a number of new fundamental physics observables, which can be studied neither at other facilities nor at HESR without transverse polarization of protons and antiprotons.

1.1. *The transversity distribution*

is the last leading-twist missing piece of the QCD description of the partonic structure of the nucleon. It describes the quark transverse polarization inside a transversely polarized proton [2]. Unlike the more conventional unpolarized quark distribution $q(x, Q^2)$ and the helicity distribution $\Delta q(x, Q^2)$, the transversity $h_1^q(x, Q^2)$ can neither be accessed in inclusive deep-inelastic scattering of leptons off nucleons nor can it be reconstructed from the knowledge of $q(x, Q^2)$ and $\Delta q(x, Q^2)$. It may contribute to some single-spin observables, but always coupled to other unknown functions. The transversity distribution is directly accessible only via the **double transverse spin asymmetry** A_{TT} in the Drell-Yan production of lepton pairs. The theoretical expectations for A_{TT} in the Drell-Yan process with transversely polarized antiprotons interacting with a transversely polarized proton target at

*A short version of this report can be found in Ref. ¹.

HESR are in the 0.3–0.4 range [3, 4]; with the expected beam polarization achieved using a dedicated low–energy antiproton polarizer ring (AP) of $P \approx 0.3$ and the luminosity of HESR, the PAX experiment^a is uniquely suited for the definitive observation of $h_1^q(x, Q^2)$ of the proton for the valence quarks. The determination of $h_1^q(x, Q^2)$ will open new pathways to the QCD interpretation of single–spin asymmetry (SSA) measurements. In conjunction with the data on SSA from the HERMES collaboration [5], the PAX measurements of the SSA in Drell–Yan production on polarized protons can for the first time provide a test of the theoretical prediction [6] of the reversal of the sign of the Sivers function [7] from semi–inclusive DIS to Drell–Yan production.

1.2. *Magnetic and electric form factors*

The origin of the unexpected Q^2 –dependence of the ratio of the magnetic and electric form factors of the proton as observed at the Jefferson laboratory [8] can be clarified by a measurement of their relative phase in the time–like region, which discriminates strongly between the models for the form factor. This phase can be measured via SSA in the annihilation $\bar{p}p^\uparrow \rightarrow e^+e^-$ on a transversely polarized target [9, 10]. The first ever measurement of this phase at PAX will also contribute to the understanding of the onset of the pQCD asymptotics in the time–like region and will serve as a stringent test of dispersion theory approaches to the relationship between the space–like and time–like form factors [11–13]. The double–spin asymmetry will independently allow the $G_E - G_M$ separation and serve as a check of the Rosenbluth separation in the time–like region which has not been carried out so far.

1.3. *Hard scattering*

Arguably, in $p\bar{p}$ elastic scattering the hard scattering mechanism can be checked beyond $|t| = \frac{1}{2}(s - 4m_p^2)$ accessible in the t – u –symmetric pp scattering, because in the $p\bar{p}$ case the u –channel exchange contribution can originate only from the strongly suppressed exotic dibaryon exchange. Consequently, in the $p\bar{p}$ case the hard mechanisms [14–16] can be tested at t almost twice as large as in pp scattering. Even unpolarized large angle $p\bar{p}$ scattering data can shed light on the origin of the intriguing oscillations around the s^{-10} behaviour of the 90° scattering cross section in the pp channel, and put stringent constraints on the much disputed odd–charge conjugation Landshoff mechanism [17–20]. If the Landshoff mechanism is suppressed then the double transverse asymmetry in $p\bar{p}$ scattering is expected to be as large as the one observed in the pp case.

2. *Towards an asymmetric polarized antiproton–proton collider at FAIR*

The possibility to test the nucleon structure via double spin asymmetries in polarized proton–antiproton reactions at the HESR ring of FAIR at GSI was suggested in 2004 by

^aPAX collaboration (Polarized Antiproton EXperiments). For the web–site, see <http://www.fz-juelich.de/ikp/pax>.

the PAX collaboration [21]. Since then, there has been much progress, both in understanding the physics potential of such an experiment [3, 4, 22, 23] and in studying the feasibility of efficiently producing polarized antiprotons [24]. The physics program of such a facility would extend to a new domain the exceptionally fruitful studies of nucleon structure performed in unpolarized and polarized deep inelastic scattering (DIS), which have been at the center of high energy physics during the past four decades. As mentioned earlier, a direct measurement of the transversity distribution function $h_1^q(x, Q^2)$, one of the last missing fundamental pieces in the QCD description of the nucleon, is unique. In the available kinematic domain of the proposed experiment, which covers the valence region, the Drell–Yan double transverse spin asymmetry was recently predicted to be as large as 0.3 [3, 4]. Other novel tests of QCD at such a facility include the polarized elastic hard scattering of antiprotons on protons, and the measurement of the phases of the time-like form factors of the proton (see Ref. [21]). A viable practical scheme^b which allows us to reach a polarization of the stored antiprotons at HESR–FAIR of $\simeq 0.3$ has been worked out and published in Ref. [24].

The PAX Letter-of-Intent was submitted on January 15, 2004. The physics program of PAX has been positively reviewed by the QCD Program Advisory Committee (PAC) on May 14–16, 2004 [28]. The proposal by the ASSIA collaboration [29] to utilize a polarized solid target and bombard it with a 45 GeV unpolarized antiproton beam extracted from the synchrotron SIS100 has been rejected by the GSI management. Such measurements would not allow one to determine $h_1^q(x, Q^2)$, because in single spin measurements $h_1^q(x, Q^2)$ always appears coupled to another unknown fragmentation function. Following the QCD–PAC report and the recommendation of the Chairman of the committee on Scientific and Technological Issues (STI) [28] and the FAIR project coordinator, the PAX collaboration has optimized the technique to achieve a sizable antiproton polarization, and the proposal for experiments at GSI with polarized antiprotons [24]. From various working group meetings of the PAX collaboration, presented in part in 2004 at several workshops and conferences [28], we conclude:

- Polarization buildup in the HESR ring, operated at the lowest possible energy, as discussed in PAX LoI, does not allow one to achieve the optimum degree of polarization in the antiproton beam. The goal of achieving the highest possible polarization of antiprotons and optimization of the figure of merit dictates that one polarizes antiprotons in a dedicated low-energy ring. The transfer of polarized low-energy antiprotons into the HESR ring requires pre-acceleration to about 1.5 GeV/c in a dedicated booster ring. Simultaneously, the incorporation of this booster ring into the HESR complex opens up, quite naturally, the possibility of building an asymmetric antiproton–proton collider^c.

^bThe basic approach to polarizing and storing antiprotons at HESR–FAIR is based on solid QED calculations of the spin transfer from electrons to antiprotons [25], which is being routinely used at Jefferson Laboratory for electromagnetic form factor separation [26], and which has been tested and confirmed experimentally in the FILTEX experiment [27].

^cIt should be noted that within the PAX collaboration we realized the possibility of building an asymmetric collider

The PAX collaboration proposes an approach that is composed of two phases. During these the major milestones of the project can be tested and optimized before the final goal is approached: An asymmetric proton–antiproton collider, in which polarized protons with momenta of about 3.5 GeV/c collide with polarized antiprotons with momenta up to 15 GeV/c. These circulate in the HESR, which has already been approved and will serve the PANDA experiment. In the following, we will briefly describe the overall machine setup of the HESR complex, schematically depicted in Fig. 1.

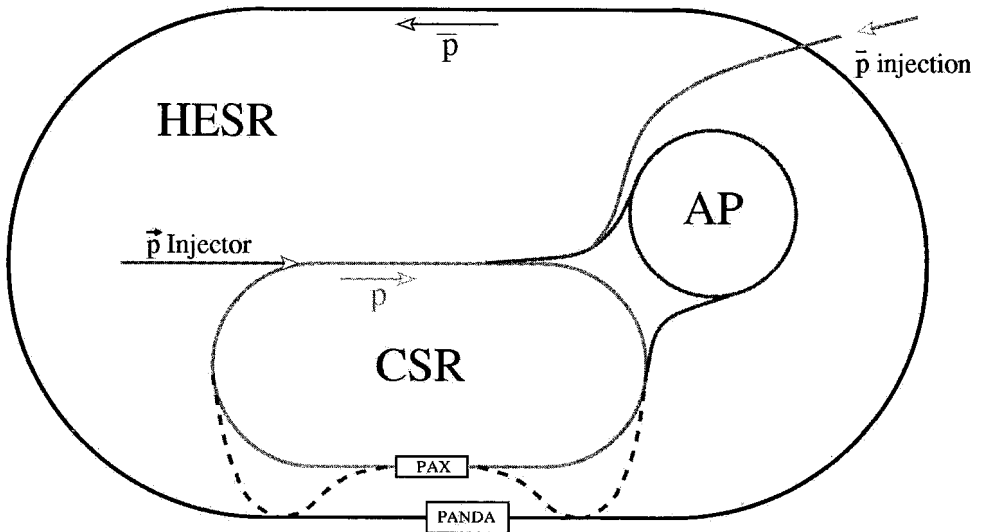


Fig. 1. The proposed accelerator set-up at the HESR (black), with the equipment used by the PAX collaboration in Phase I: CSR (light grey), AP, beam transfer lines and polarized proton injector (dark grey). In Phase II, by adding two transfer lines (dashed), an asymmetric collider is set up. It should be noted that, in this phase, fixed target operation at PAX is also possible.

Let us summarize the main features of the accelerator setup:

1. An Antiproton Polarizer (AP) built inside the HESR area with the crucial goal of polarizing antiprotons at kinetic energies around ≈ 50 MeV ($p \approx 300$ MeV/c), to be accelerated and injected into the other rings.
2. A second Cooler Synchrotron Ring (CSR, COSY-like) in which protons or antiprotons can be stored with a momentum up to 3.5 GeV/c. This ring shall have a straight section, where a PAX detector could be installed, running parallel to the experimental straight section of HESR.
3. By deflection of the HESR beam into the straight section of the CSR, both the collider or the fixed-target mode become feasible.

It is worthwhile to stress that, through the employment of the CSR, effectively a second interaction point is formed with minimum interference with PANDA. The proposed solution opens the opportunity to run two different experiments at the same time.

In the following sections, we discuss the physics program, which should be pursued in two different phases.

2.1. Phase I

A beam of unpolarized or polarized antiprotons with momentum up to 3.5 GeV/c in the CSR ring, colliding with a polarized hydrogen target in the PAX detector. This phase is independent of the HESR performance.

This first phase, at moderately high energy, will allow for the first time the measurement of the time-like proton form factors in single and double polarized $\bar{p}p$ interactions in a wide kinematical range, from close to threshold up to $Q^2 = 8.5 \text{ GeV}^2$. It would enable the determination of several double spin asymmetries in elastic $\bar{p}^\uparrow p^\uparrow$ scattering. By detecting back scattered antiprotons one can also explore hard scattering regions of large t : In proton–proton scattering the same region of t requires twice the energy. There are no competing facilities at which these topical issues can be addressed. For the theoretical background, see the PAX LoI [21] and the recent review paper [10].

2.2. Phase II

This phase will allow the first ever direct measurement of the quark transversity distribution h_1 , by measuring the double transverse spin asymmetry A_{TT} in Drell–Yan processes $p^\uparrow \bar{p}^\uparrow \rightarrow e^+ e^- X$ as a function of Bjorken x and Q^2 ($= M^2$)

$$A_{TT} \equiv \frac{d\sigma^{\uparrow\uparrow} - d\sigma^{\uparrow\downarrow}}{d\sigma^{\uparrow\uparrow} + d\sigma^{\uparrow\downarrow}} = \hat{a}_{TT} \frac{\sum_q e_q^2 h_1^q(x_1, M^2) h_1^{\bar{q}}(x_2, M^2)}{\sum_q e_q^2 q(x_1, M^2) \bar{q}(x_2, M^2)},$$

where $q = u, \bar{u}, d, \bar{d}, \dots$, M is the invariant mass of the lepton pair and \hat{a}_{TT} , of the order of one, is the calculable double–spin asymmetry of the QED elementary process $q\bar{q} \rightarrow e^+e^-$. Two possible scenarios might be foreseen to perform the measurement, which are discussed below.

2.2.1. Asymmetric collider

A beam of polarized antiprotons from 1.5 GeV/c up to 15 GeV/c circulating in the HESR, colliding with a beam of polarized protons with momenta up to 3.5 GeV/c circulating in the CSR. This scenario however requires to demonstrate that a suitable luminosity is reachable. Deflection of the HESR beam to the PAX detector in the CSR is necessary (see Fig. 1).

By proper variation of the energy of the two colliding beams, this setup would allow a measurement of the transversity distribution h_1 in the valence region of $x > 0.05$, with corresponding $Q^2 = 4 \dots 100 \text{ GeV}^2$ (see Fig. 2). A_{TT} is predicted to be larger than 0.3 over

the full kinematic range, up to the highest reachable center-of-mass energy of $\sqrt{s} \sim \sqrt{200}$. The cross section is large as well: with a luminosity of $5 \cdot 10^{30} \text{ cm}^{-2} \text{ s}^{-1}$ about 2000 events per day can be expected^d. For the transversity distribution h_1 , such an experiment can be considered as the analogue of polarized DIS for the determination of the helicity structure function g_1 , i.e. of the helicity distribution $\Delta q(x, Q^2)$; the kinematical coverage (x, Q^2) will be similar to that of the HERMES experiment.

2.2.2. High luminosity fixed target experiment

If the required luminosity in the collider mode is not achievable, a fixed target experiment can be conducted. A beam of 22 GeV/c (15 GeV/c) polarized antiprotons circulating in the HESR is used to collide with a polarized internal hydrogen target. Also this scenario requires the deflection of the HESR beam to the PAX detector in the CSR (see Fig. 1).

A theoretical discussion of the significance of the measurement of A_{TT} for a 22 GeV/c (15 GeV/c) beam impinging on a fixed target is given in Refs. [3, 4, 23] and the recent review paper [10]. The theoretical work on the K -factors for the transversity determination is in progress [30, 31]. This measurement will explore the valence region of $x > 0.2$, with corresponding $Q^2 = 4 \dots 16 \text{ GeV}^2$ (see Fig. 2). In this region A_{TT} is predicted to be large (of the order of 0.3, or more) and the expected number of events can be of the order of 2000 per day.

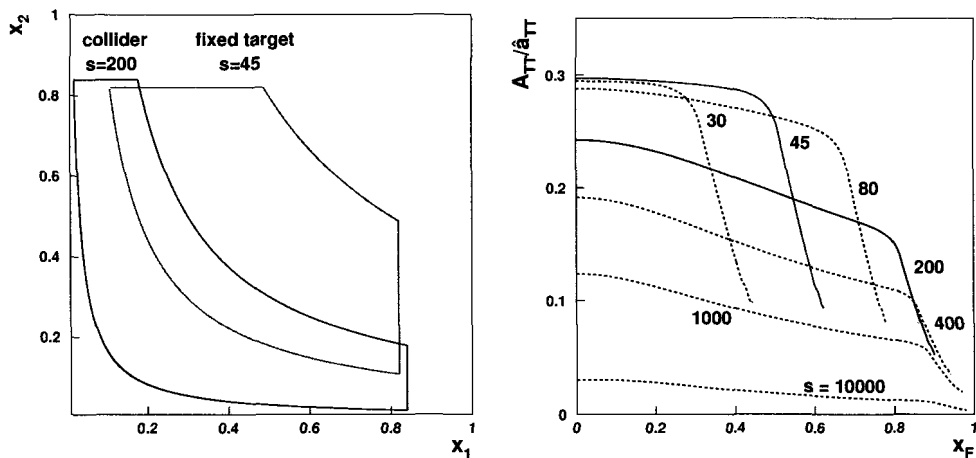


Fig. 2. Left: The kinematic region covered by the h_1 measurement at PAX in phase II. In the asymmetric collider scenario antiprotons of 15 GeV/c impinge on protons of 3.5 GeV/c at c.m. energies of $\sqrt{s} \sim \sqrt{200} \text{ GeV}$ and $Q^2 > 4 \text{ GeV}^2$. The fixed target case represents antiprotons of 22 GeV/c colliding with a fixed polarized target ($\sqrt{s} \sim \sqrt{45} \text{ GeV}$). Right: The expected asymmetry as a function of Feynman x_F for different values of s and $Q^2 = 16 \text{ GeV}^2$.

^dA first estimate indicates that in the collider mode luminosities in excess of $10^{30} \text{ cm}^{-2} \text{ s}^{-1}$ could be reached. We are currently evaluating the influence of intra-beam scattering, which seems to be one of the limiting factors.

We would like to mention that we are also investigating whether the PANDA detector, properly modified, is compatible with the transversity measurements in the collider mode, where an efficient identification of the Drell–Yan pairs is required. At the interaction point, the spins of the colliding protons and antiprotons should be vertical, with no significant component along the beam direction.

3. Conclusion

To summarize, we note that the storage of polarized antiprotons at HESR will open unique opportunities to test QCD in hitherto unexplored domains. This will provide another cornerstone for the antiproton program at FAIR.

Acknowledgments

The author would like to especially thank Paolo Lenisa for his contribution to the PAX project. In addition, the help of M. Anselmino, D. Chiladze, M. Contalbrigo, P.F. Dalpiaz, E. De Sanctis, A. Drago, A. Kacharava, A. Lehrach, B. Lorentz, G. Macharashvili, R. Maier, S. Martin, C. Montag, N.N. Nikolaev, E. Steffens, D. Prasuhn, H. Ströher, and S. Yaschenko is gratefully acknowledged.

References

1. P. Lenisa et al., “QCD physics with polarized antiprotons at GSI,” <http://lanl.arXiv.org/abs/hep-ex/0412063> (2004).
2. A comprehensive review paper on the transverse spin structure of the proton can be found in: V. Barone, A. Drago and P. Ratcliffe, *Phys. Rep.* **359**, 1 (2002).
3. M. Anselmino, V. Barone, A. Drago and N. Nikolaev, *Phys. Lett. B* **594**, 97 (2004).
4. A. Efremov, K. Goecke and P. Schweitzer, *Eur. Phys. J* **35**, 207 (2004).
5. HERMES Collaboration, A. Airapetian et al., *Phys. Rev. Lett.* **84**, 4047 (2000); *Phys. Rev. Lett.* **90**, 092002 (2003); *Phys. Rev. D* **64**, 097101 (2001); K. Rith, *Progress in Part. and Nucl. Phys.* **49**, 245 (2002) 245.
6. J.C. Collins, *Phys. Lett. B* **536**, 43 (2002).
7. D. Sivers, *Phys. Rev. D* **41**, 83 (1990); *Phys. Rev. D* **43**, 261 (1991).
8. M. K. Jones et al., [Jefferson Lab Hall A Collaboration], *Phys. Rev. Lett.* **84**, 1398 (2000). O. Gayou et al., [Jefferson Lab Hall A Collaboration], *Phys. Rev. Lett.* **88**, 092301 (2002).
9. A. Z. Dubnickova, S. Dubnicka, and M. P. Rekaló, *Nuovo Cimento* **109**, 241 (1966).
10. S.J. Brodsky et al., *Phys. Rev. D* **69**, 054022 (2004).
11. For a discussion on the validity of continuing space-like form factors to the time-like region, see, B. V. Geshkenbein, B. L. Ioffe, and M. A. Shifman, *Sov. J. Nucl. Phys.* **20**, 66 (1975) [*Yad. Fiz.* **20**, 128 (1974)].
12. H.–W. Hammer, U.–G. Meißner and D. Drechsel, *Phys. Lett. B* **385**, 343 (1996); H.–W. Hammer and U.–G. Meißner, *Eur. Phys. J. A* **20**, 469 (2004).
13. E. Tomasi–Gustafsson and M.P. Rekaló, *Phys. Lett. B* **504**, 291 (2001); *Nuovo Cimento* **109**, 241 (1996).
14. V. Matveev et al., *Lett. Nuovo Cimento* **7** (1972) 719.
15. S. Brodsky and G. Farrar, *Phys. Rev. Lett.* **31**, 1153 (1973) and *Phys. Rev. D* **11**, 1309 (1973).
16. M. Diehl, T. Feldmann, R. Jakob and P. Kroll, *Phys. Lett. B* **460**, 204 (1999).

17. P. Landshoff, *Phys. Rev. D* **10**, 1024 (1974); P. Landshoff and D. Pritchard, *Z. Phys.* **C6**, 69 (1980).
18. J.P. Ralston and B. Pire, *Phys. Rev. Lett.* **61**, 1823 (1988); *ibid.* **49**, 1605 (1982); *Phys. Lett. B* **117**, 233 (1982).
19. G. P. Ramsey and D. W. Sivers, *Phys. Rev. D* **52**, 116 (1995); *Phys. Rev. D* **47**, 93 (1993); *Phys. Rev. D* **45**, 79 (1992).
20. D. Dutta and H. Gao, “The Generalized Counting Rule and Oscillatory Scaling”
<http://lanl.arXiv.org/abs/hep-ph/0411267> (2004).
21. PAX Letter-of-Intent, spokespersons: P. Lenisa and F. Rathmann,
<http://www.fz-juelich.de/ikp/pax>
22. S. Brodsky, “Testing Quantum Chromo Dynamics with antiprotons”,
<http://lanl.arXiv.org/abs/hep-ph/0411046> (2004).
23. P. Zavada, “Proton transversity and intrinsic motion of the quarks,”
<http://lanl.arXiv.org/abs/hep-ph/0412206> (2004).
24. F. Rathmann et al., “A method to polarize stored antiprotons to a high degree”,
<http://lanl.arXiv.org/abs/physics/0410067>,
accepted for publication in *Phys. Rev. Lett.* (2004).
25. H.O. Meyer, *Phys. Rev. E* **50**, 1485 (1994); C.J. Horowitz and H.O. Meyer, *Phys. Rev. Lett.* **72**, 3981 (1994).
26. R. Madey et al., *Phys. Rev. Lett.* **91**, 122002 (2003); S. Strauch et al., *Phys. Rev. Lett.* **91**, 052301 (2003); O. Gayou et al., *Phys. Rev. Lett.* **88**, 092301 (2002).
27. F. Rathmann et al., *Phys. Rev. Lett.* **71**, 1379 (1993).
28. For a list of PAX collaboration meetings, conference presentations, QCD-PAC and STI reports, please visit the PAX web-site at <http://www.fz-juelich.de/ikp/pax>
29. ASSIA Letter-of-Intent, spokesperson: R. Bertini,
<http://www.gsi.de/documents/DOC-2004-Jan-152-1.ps>
30. P. G. Ratcliffe, “Transversity K Factors for Drell-Yan,”
<http://lanl.arXiv.org/abs/hep-ph/0412157> (2004).
31. V. Barone, C. Corianò and P. Ratcliffe, in preparation.

DISCUSSION

W. Meyer:

Question: What is the current of polarized antiprotons in the stored beam?

Answer: The beam current is calculated from the number of stored antiprotons $N_{\bar{p}}$ in HESR times the orbit frequency f_{HESR} . For HESR in equilibrium, the stored current at $T = 15$ GeV corresponds to $I_{\bar{p}} = N_{\bar{p}} \cdot f_{HESR} = 5.6 \cdot 10^{10} \cdot 6.8 \cdot 10^5 = 3.8 \cdot 10^{16} \bar{p}/s$.

M. Pusterla:

Question: Have you considered the possibility of separating the two spin states of the unpolarized antiprotons (after accumulation) via the Stern-Gerlach interaction?

Answer: Yes, we know about this possibility. However, to our knowledge, up to now, there is no experimental proof that spin-splitting actually works.

W. Volgelsang:

Comment: in the kinematic region you are considering, that is $\sqrt{s} \simeq 6$ or 7 GeV and Drell-

Yan masses of 2 or 3 GeV, higher order QCD corrections will be very large. K-factors could be 3 or 4, higher twist correction could be important as well.

M. Anselmino:

Answering to W. Volgelsang's comment about QCD corrections at small \sqrt{s} and Drell-Yan masses values, corrections will be evaluated. They are certainly significant for cross-sections, and are expected to cancel in A_{TT} . Measurements of cross-sections are also important.

POLARIZED STRUCTURE FUNCTIONS WITH NEUTRINO BEAMS

S. FORTE

Dipartimento di Fisica, Università di Milano and INFN, Sezione di Milano, Milano, Italy

We review the potential impact of neutrino data on the determination of the spin structure of the nucleon. We show that a flavour decomposition of the parton structure of the nucleon as required by present-day precision phenomenology could only be achieved at a neutrino factory. We discuss how neutrino scattering data would allow a full resolution of the nucleon spin problem.

1. Physics with neutrino beams

Physics with neutrino beams has played a crucial role in establishing the standard model and its structure, specifically in leading to the discovery of weak neutral currents and their properties [1]. Currently, while the physics *of* neutrinos gives us the first evidence of physics beyond the standard model [2], the use of neutrinos as probes appears to be the only way of accessing subtle details of the structure of the standard model, on the one hand, and of the nucleon, on the other. This is due to the obvious fact that weak currents, unlike the electromagnetic current, couple nontrivially to spin and flavour.

Current data offer tantalizing evidence of this situation: neutrino scattering data from the NuTeV collaboration [3] provide evidence for unexpected effects, either in the standard model, or in the structure of the nucleon [4]. However, existing beams are insufficient to exploit the potential of neutrino probes, because of low intensity and lack of control of the beam spectrum, due to the fact that neutrinos are obtained from the decay of secondary beams (pions). This has recently led to several proposals for facilities at which neutrinos would be produced as decay products of a primary beam: either muons (neutrino factories [5]) or radioactive nuclei (β -beams [6]). This would allow the production of $\sim 10^{20}$ neutrinos/year (neutrino factory) or $\sim 10^{18}$ neutrinos/year (β -beam) with full control of the energy spectrum, to be compared with $\sim 10^{16}$ neutrinos/year of present-day experiments. The prospects for the construction of such facilities, which are being studied in Europe, Japan and the U.S.A., have recently improved, in particular due to a renewed commitment of CERN to future neutrino facilities [7].

2. Deep-inelastic scattering with neutrino beams

2.1. Structure functions and parton distributions

Inclusive DIS is the standard way of accessing the parton content of hadrons. The use of neutrino beams allows one to study DIS mediated by the weak, rather than electromagnetic, interaction. The neutrino-nucleon deep-inelastic cross section for charged-current interactions, up to corrections suppressed by powers of m_p^2/Q^2 is given by

$$\frac{d^2\sigma^{\lambda_p\lambda_\ell}(x,y,Q^2)}{dx dy} = \frac{G_F^2}{2\pi(1+Q^2/m_W^2)^2} \frac{Q^2}{xy} \left\{ \left[-\lambda_\ell y \left(1 - \frac{y}{2}\right) x F_3(x, Q^2) \right. \right. \\ \left. \left. + (1-y) F_2(x, Q^2) + y^2 x F_1(x, Q^2) \right] - 2\lambda_p \left[-\lambda_\ell y (2-y) x g_1(x, Q^2) \right. \right. \\ \left. \left. - (1-y) g_4(x, Q^2) - y^2 x g_5(x, Q^2) \right] \right\}, \quad (1)$$

where λ are the lepton and proton helicities (assuming longitudinal proton polarization), and the kinematic variables are $y = \frac{p \cdot q}{p \cdot k}$ (lepton fractional energy loss), $x = \frac{Q^2}{2p \cdot q}$ (Bjorken x). The neutral-current cross-section is found from Eq. (1) by letting $m_W \rightarrow m_Z$ and multiplying by an overall factor $[\frac{1}{2}(g_V - \lambda_\ell g_A)]^2$.

The advantage of W and Z -mediated DIS over conventional γ^* DIS is clear from inspection of the parton content of the polarized and unpolarized structure functions F_i and g_i . Up to $O(\alpha_s)$ corrections, in terms of the unpolarized and polarized quark distribution for the i -th flavour $q_i \equiv q_i^{\uparrow\uparrow} + q_i^{\uparrow\downarrow}$ and $\Delta q_i \equiv q_i^{\uparrow\uparrow} - q_i^{\uparrow\downarrow}$

NC	$F_1^\gamma = \frac{1}{2} \sum_i e_i^2 (q_i + \bar{q}_i)$	$g_1^\gamma = \frac{1}{2} \sum_i e_i^2 (\Delta q_i + \Delta \bar{q}_i)$
NC	$F_1^Z = \frac{1}{2} \sum_i (g_V^2 + g_A^2)_i (q_i + \bar{q}_i)$	$g_1^Z = \frac{1}{2} \sum_i (g_V^2 + g_A^2)_i (\Delta q_i + \Delta \bar{q}_i)$
NC	$F_3^Z = 2 \sum_i (g_V g_A)_i (q_i + \bar{q}_i)$	$g_3^Z = - \sum_i (g_V g_A)_i (\Delta q_i + \Delta \bar{q}_i)$
CC	$F_1^{W^+} = \bar{u} + d + s + \bar{c}$	$g_1^{W^+} = \Delta \bar{u} + \Delta d + \Delta s + \Delta \bar{c}$
CC	$-F_3^{W^+} / 2 = \bar{u} - d - s + \bar{c}$	$g_3^{W^+} = \Delta \bar{u} - \Delta d - \Delta s + \Delta \bar{c}$
	$F_2 = 2x F_1$	$g_4 = 2x g_5$

Here e_i are the electric charges and $(g_V)_i, (g_A)_i$ are the weak charges of the i -th quark flavour. If $W^+ \rightarrow W^-$ (incoming $\bar{\nu}$ beam), then $u \leftrightarrow d, c \leftrightarrow s$. Of course, beyond leading order in the strong coupling each quark or antiquark flavour's contribution receives $O(\alpha_s)$ corrections proportional to itself and to all other quark, antiquark and gluon distributions. However, the gluon correction is flavour-blind, and thus decouples from the parity-violating structure functions F_3, g_4 and g_5 .

In neutral current DIS only the C-even combinations $q_i + \bar{q}_i$ and $\Delta q_i + \Delta \bar{q}_i$ are accessible. Furthermore, the structure functions F_3, g_4 and g_5 are parity-violating, and therefore not accessible in virtual photon scattering. In the presence of weak couplings, more independent linear combination of individual quark and antiquark distributions are accessible, thereby allowing one to disentangle individual flavours and antiflavours [8, 9].

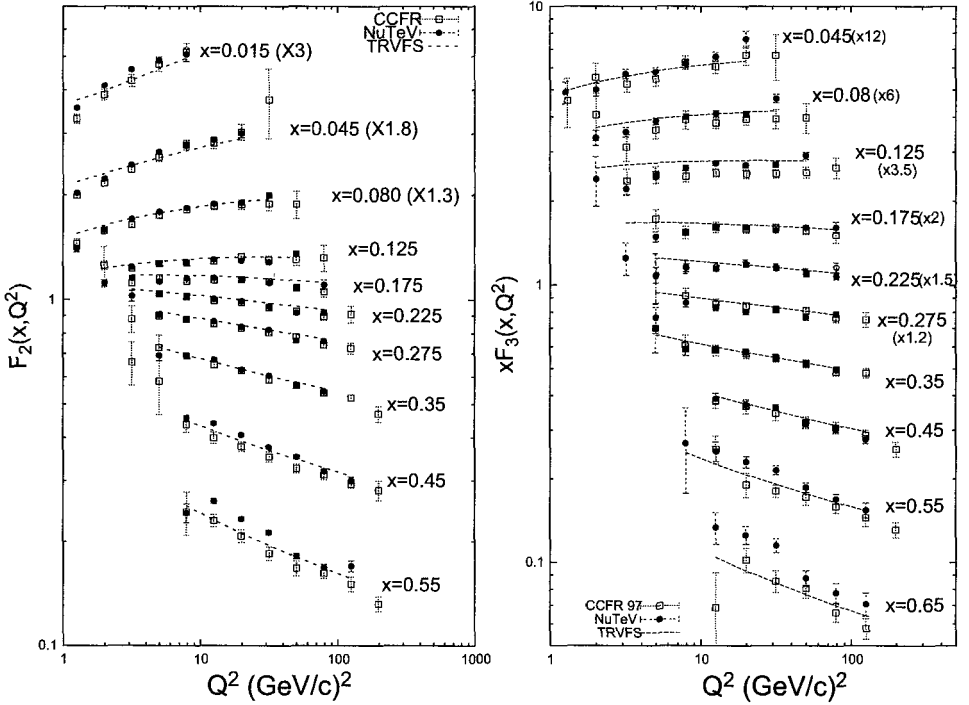


Fig. 1. Current unpolarized proton structure functions from μ scattering (from ref. [10]). The structure functions shown are $\nu + \bar{\nu}$ averages.

2.2. Current data and future prospects

Structure function measurements with neutrino beams have been performed recently by the CCFR/NuTeV collaboration [10], while DIS results have been announced, but not yet published, by the CHORUS [11] and NOMAD [12] collaborations. Older results, including historic bubble-chamber data, have been reanalyzed and collected in [13]. The recent NuTeV structure function data, based on a sample of 8.6×10^5 ν and 2.3×10^5 $\bar{\nu}$ DIS events, have led to reasonably precise determinations of the structure functions F_2 and F_3 (see fig.1). However, they still have rather lower accuracy than charged-lepton DIS data. Furthermore, only $\nu + \bar{\nu}$ structure function averages are determined: $F_3^{\nu} + F_3^{\bar{\nu}}$ (compare eq. (1)), from the difference $\sigma^{\nu} - \sigma^{\bar{\nu}}$, and $F_2^{\nu} + F_2^{\bar{\nu}}$ from the average $\sigma^{\nu} + \sigma^{\bar{\nu}}$ using a theoretical determination of F_3 . Hence, results are not free from theoretical assumptions, and only some linear combinations of parton distributions are accessible. Finally, present-day neutrino target-detectors are very large in order to ensure reasonable rates with available beams: e.g. the NuTeV target-calorimeter consists of 84 iron plates, 10 m \times 10 m \times 10 cm. Clearly, this could not be placed inside a polarizing magnet.

At a neutrino factory (in the CERN scenario [5, 14]) the neutrino beam originates from the decay of 10^{20} μ per year, stored in a 50 GeV ring. With a target effective density of 100 g/cm 2 , corresponding to, say, a 10 m long deuterium target [8] and a radius of 50 cm,

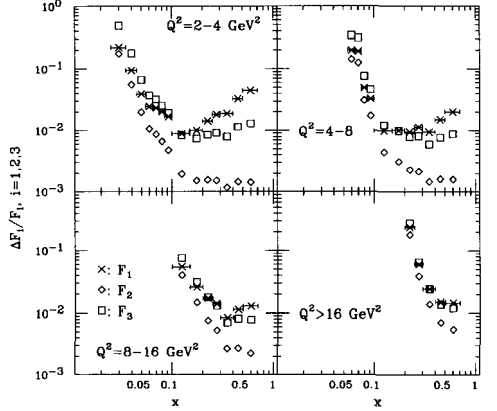
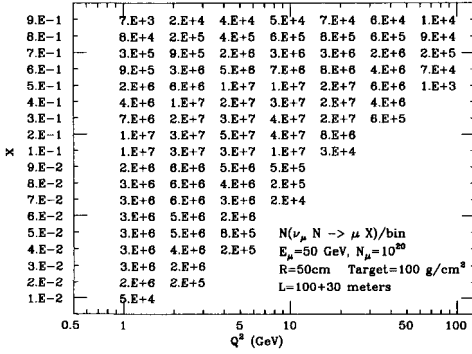


Fig. 2. Unpolarized DIS event rates (left) and errors on unpolarized parton distributions (right) for one year of running in the CERN neutrino factory scenario (from ref. [14]).

one could then count on 5×10^8 DIS events per year, with the rates in individual bins shown in fig.2. Furthermore, taking advantage of the fact that $y = Q^2 / (2xm_p E_\nu)$, at fixed x and Q^2 , y varies with the incoming ν energy. Because the beam at a neutrino factory is broad-band, if the kinematics of the DIS event can be fully reconstructed on an event-by-event basis, it is then possible to disentangle the contributions of the individual structure functions to the cross section Eq. (1) by fitting the y dependence of the data for fixed x and Q^2 . The errors on individual structure functions obtained through such a procedure are shown in fig.2, and are in fact rather smaller than those on current charged-lepton DIS structure functions.

Recent results of the NuTeV collaboration on the CC/NC total neutrino DIS cross sections highlight the potential and limitations of current neutrino data. The NuTeV data [3] allow a determination of the Paschos-Wolfenstein [15] ratio

$$\begin{aligned}
 R^- &= \frac{\sigma_{NC}(\nu) - \sigma_{NC}(\bar{\nu})}{\sigma_{CC}(\nu) - \sigma_{CC}(\bar{\nu})} \\
 &= \left(\frac{1}{2} - \sin^2 \theta_W \right) + 2 \left[\frac{(u - \bar{u}) - (d - \bar{d})}{u - \bar{u} + d - \bar{d}} - \frac{s - \bar{s}}{u - \bar{u} + d - \bar{d}} \right] \\
 &\quad \left[\left(\frac{1}{2} - \frac{7}{6} \sin^2 \theta_W \right) + \frac{4}{9} \frac{\alpha_s}{2\pi} \left(\frac{1}{2} - \sin^2 \theta_W \right) + O(\alpha_s^2) \right] + O(\delta(u-d)^2, \delta s^2)
 \end{aligned} \tag{2}$$

where u , d , s , etc. denote the second moments of the corresponding parton distributions. All dependence on parton distributions disappears assuming isospin for an isoscalar target, if one also assumes $s = \bar{s}$ (which is nontrivial for second moments).

Using these assumptions, NuTeV has arrived at a determination of $\sin^2 \theta_W$ which differs by about three sigma from the current standard best-fit. This indicates either physics beyond the standard model, or a nucleon structure which is subtler than expected [4]. Small violations of isospin are produced by QED corrections, and in fact phenomenological evidence supports an isospin violation which reduces the observed discrepancy by about one σ [16]. Also, a global fit to world data favours a strangeness asymmetry of the size and

magnitude required to remove the effect entirely [17]. However, in both cases the null assumption which leads to the discrepancy with the standard model cannot really be excluded within the required precision. Whereas less inclusive data, such as W production at hadron colliders, might give us some extra handle on the flavour decomposition of parton distributions [18], only a neutrino factory would allow a full determination of the flavour and antiflavour content of the nucleon [14], as required for this kind of precision physics.

3. Polarized physics with neutrino beams

3.1. Polarized DIS and the proton spin puzzle

The determination of the polarized structure of the nucleon has progressed considerably since the surprising discovery of the smallness of the nucleon’s singlet axial charge a_0 [20]. The focus of current phenomenological activity has shifted from inclusive deep-inelastic scattering to less inclusive data, largely driven by the desire to access quantities, such as transversity, which decouple from inclusive DIS. Whereas semi-inclusive data give us some hint of the flavour structure of the nucleon [21], experience in the unpolarized case [18] shows that they cannot compete in accuracy with DIS data, while hadron collider data play a complementary role.

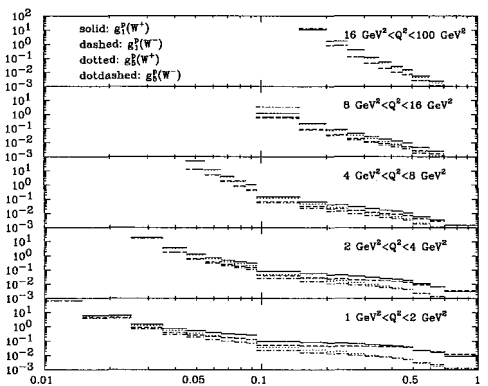
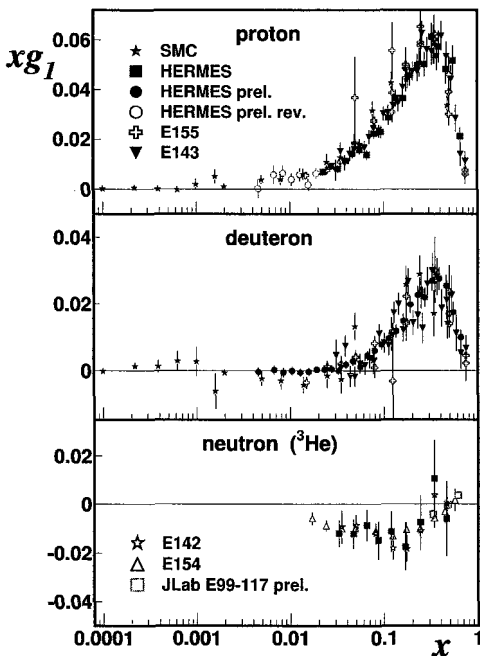


Fig. 3. Current polarized structure function data (left, from ref. [19]) and expected accuracies in the CERN neutrino factory scenario (right, from ref. [14]).

However, a detailed understanding of the flavour and antiflavour content of the nucleon is mandatory if one wishes to elucidate its spin structure [22]. Indeed, the reason why the smallness of the singlet axial charge a_0 is surprising is that it signals a departure from the

quark model, in which a_0 is the total quark spin fraction, and $a_0 \approx a_8$, the difference being due to the strange contribution, which is expected to be small from the Zweig rule. The octet axial charge a_8 cannot in practice be determined from neutral-current DIS data, hence it is currently determined using SU(3) from baryon β -decay constants: $a_8 = 0.6 \pm 30\%$, while $a_0 = 0.10^{+0.17}_{-0.11}$ (at $Q^2 = \infty$). Whereas a_8 does not depend on Q^2 , a_0 does: because of the axial anomaly, $\partial_\mu j_5^\mu \neq 0$. It turns out, however, that it is possible to choose a factorization scheme in such a way that the quark distribution is scale-independent. In such a case a_0 and the total quark spin fraction $\Delta\Sigma$ are no longer equal:

$$\begin{aligned}
 a_3 &= \Delta u + \Delta\bar{u} - (\Delta d + \Delta\bar{d}) \\
 a_8 &= \Delta u + \Delta\bar{u} + \Delta d + \Delta\bar{d} - 2(\Delta s + \Delta\bar{s}) \\
 \Delta\Sigma &= \Delta u + \Delta\bar{u} + \Delta d + \Delta\bar{d} + \Delta s + \Delta\bar{s} \\
 a_0 &= \Delta\Sigma - \frac{n_f \alpha_s}{2\pi} \Delta G
 \end{aligned} \tag{3}$$

where Δq_i and ΔG are respectively the quark and gluon spin fractions.

One can then envisage various scenarios for the nucleon spin content [9, 22]. A first possibility is that perhaps, even though a_0 is small, $\Delta\Sigma$ eq. (3) is large, because $\alpha\Delta g$ is large ('anomaly' scenario). If instead $\alpha\Delta g$ is small, there are two possibilities: either the determination of a_8 from octet decays using isospin is incorrect, the Zweig rule in actual fact holds, $a_0 \approx a_8$, and the strange spin fraction $\Delta s + \Delta\bar{s}$ is small; or $\Delta s + \Delta\bar{s}$ is large, i.e. comparable to $\Delta u + \Delta\bar{u}$ and $\Delta d + \Delta\bar{d}$. This is predicted, for instance, to happen in instanton models or in Skyrme models. These two cases, however, predict respectively that Δs and $\Delta\bar{s}$ are separately large ('instanton' scenario) or that $\Delta s \ll \Delta\bar{s}$ ('skymion' scenario). In short, different models of the nucleon spin structure lead to distinct predictions for its polarized content.

Table 1. Quark and gluon first moments. Both statistical and systematic errors are given for current values (from ref. [23]) statistical only for the neutrino factory scenarios (from ref. [9]).

	present	anomaly	instanton	skymion
Δg	$0.8 \pm 0.2 \pm 0.4$	0.86 ± 0.10	0.20 ± 0.06	0.24 ± 0.08
$\Delta\Sigma$	$0.38 \pm 0.03 \pm 0.04$	0.39 ± 0.01	0.321 ± 0.006	0.324 ± 0.008
a_3	$1.11 \pm 0.04 \pm 0.04$	1.097 ± 0.006	1.052 ± 0.013	1.066 ± 0.014
a_8	$0.6 \pm 0.2(?)$	0.557 ± 0.011	0.572 ± 0.013	0.580 ± 0.012
$\Delta s - \Delta\bar{s}$?	-0.075 ± 0.008	-0.007 ± 0.007	-0.106 ± 0.008

Current data provide a fairly accurate determination of $g_1^\gamma(x, Q^2)$ (Figure 3). From these only the C-even combination $\Delta q_i + \Delta\bar{q}_i$ can be determined, while Δg can be extracted from scaling violations, albeit with large errors [23]. A reasonably accurate determination of the isotriplet component is then possible, especially its first moment. However, the individual

valence flavours can be determined much less accurately, partly because of their admixture with the gluon eq. (3). In fact, only first moments can be determined with reasonable accuracy (Table 1), while the shape of individual parton distributions is known only rather poorly (Figure 4).

3.2. The spin of the nucleon at a neutrino factory

At a neutrino factory, significant rates could be achieved with small targets [8]: even with a rather conservative effective density of 10 g/cm^2 . With a detector radius of 50 cm, the structure functions g_1, g_5 could still be independently measured with an accuracy which is about one order of magnitude better than that with which g_1 is determined in present charged lepton DIS experiments (Figure 3). On the basis of such data, the flavour structure of the nucleon could be entirely disentangled [23]: in particular, the difference of any two flavour or antiflavour fractions could be determined, typically with uncertainties of the order of 1% (Table 1).

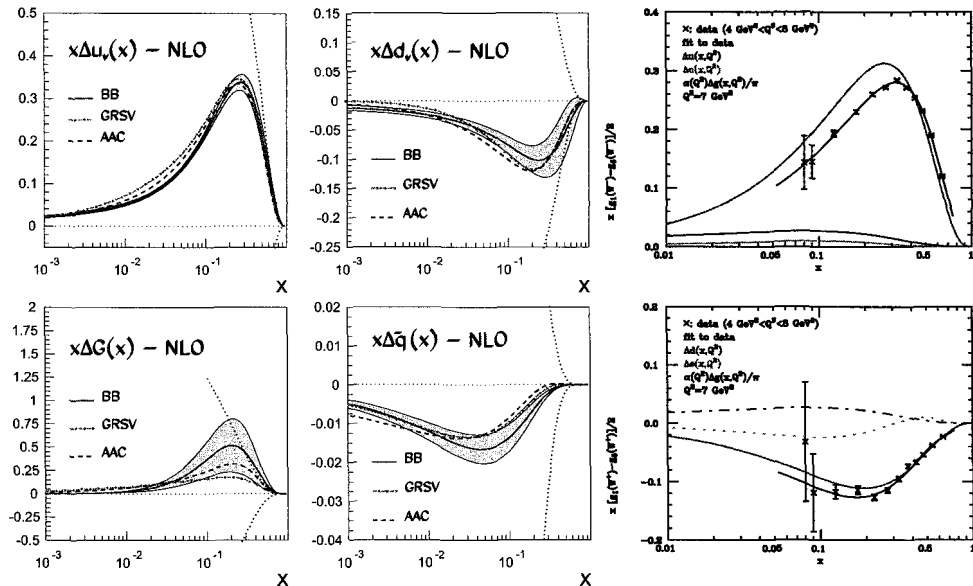


Fig. 4. Current errors on polarized parton distributions (left, from ref. [24]) and expected errors in the CERN neutrino factory scenario (right, from ref. [9]).

The absolute value of each quark distribution, however, is affected by the gluon admixture eq. (3). Therefore, the precision in the determination of a_0 is set by the accuracy in the knowledge of Δg . The determination of the latter at a neutrino factory would improve somewhat thanks to the accurate knowledge of scaling violations, but it would be very significantly hampered by the limited kinematic coverage, in Q^2 and especially at small x . On the other hand, by the time a neutrino factory comes into operation Δg is likely to

have been determined at collider experiments such as RHIC [20]. Hence, hadron colliders and the neutrino factory have complementary roles. The same applies to the determination of the shape of individual parton distributions (Figure 4). While structure functions would be measured very accurately, the dominant uncertainty of quark distributions would come from the polarized gluon.

Less inclusive measurements at a neutrino factory could provide a very clean handle on individual observables: for example, strangeness could be studied through charm production, just as in the unpolarized case. Thanks to high event rates, it would be possible to measure even elusive quantities such as those related to polarized fragmentation, or even generalized parton distributions [14].

4. Do we need a neutrino factory?

Alternative high-intensity neutrino sources, such as β beams, provide attractive opportunities for the study of neutrino oscillations. They share the same advantages as the neutrino factory, but with a somewhat lower flux and much lower energy: e.g. at a β beam one would expect $\sim 10^{18}$ β decays per year with an average ν energy ~ 200 MeV. With such a beam only elastic or quasi-elastic scattering on nucleons can be performed. However, effective field theory results [26] relate the matrix elements measured in low-energy scattering to polarized partonic observables: e.g. $\langle p | j_5^{\mu Z} | p \rangle = \Delta u - \Delta d - \Delta s = -\frac{1}{3}a_0 + a_3 + \frac{1}{3}a_8$, up to computable corrections related to higher-dimensional operators. This would allow e.g. a direct determination of a_8 and thus of the total polarized strangeness, if not the separation of Δs and $\Delta \bar{s}$. The full impact of such measurements on high-energy nucleon observables is currently under investigation [27].

In sum, a full determination of the polarized flavour structure of the nucleon will only be possible at a neutrino factory, with collider data providing complementary information on the polarized glue. Low-energy facilities such as β -beams would have a more limited though not negligible impact.

Acknowledgments

I thank F. Bradamante for inviting me at this stimulating meeting. This work was completed at KITP Santa Barbara, supported in part by the National Science Foundation under grant PHY99-0794.

References

1. See e.g. A. De Rujula, in "Fifty years of Yang-Mills theories" (G. 't Hooft, ed), World Scientific, Singapore 2004; hep-ph/0404215, and ref. therein.
2. See e.g. G. Altarelli, hep-ph/0410101 and ref. therein.
3. G. P. Zeller *et al.* [NuTeV Collaboration], Phys. Rev. Lett. **88** (2002) 091802 [Erratum-ibid. **90** (2003) 239902]
4. S. Davidson, S. Forte, P. Gambino, N. Rius and A. Strumia, JHEP **0202** (2002) 037
5. See A. Blondel *et al.*, CERN-2004-002; T. Adams *et al.*, hep-ph/0111030 and ref. therein.
6. P. Zucchelli, Phys. Lett. B **532** (2002) 166; see also M. Mezzetto, hep-ex/0410083 and ref. therein.

7. See J. Dainton,
http://hep.ph.liv.ac.uk/~jbd/CERN_seminar_Villars_released_public.ppt
8. R. D. Ball, D. A. Harris and K. S. McFarland, hep-ph/0009223.
9. S. Forte, M. L. Mangano and G. Ridolfi, Nucl. Phys. B **602** (2001) 585.
10. D. Naples *et al.* [NuTeV Collaboration], hep-ex/0307005.
11. R. G. C. Oldeman [CHORUS Collaboration], Nucl. Phys. Proc. Suppl. **79** (1999) 96;
12. R. Petti [NOMAD Collaboration], hep-ex/0411032.
13. V. Barone, C. Pascaud and F. Zomer, Eur. Phys. J. C **12** (2000) 243.
14. M. L. Mangano *et al.*, hep-ph/0105155.
15. E. A. Paschos and L. Wolfenstein, Phys. Rev. D **7** (1973) 91.
16. A. D. Martin, R. G. Roberts, W. J. Stirling and R. S. Thorne, hep-ph/0411040;
 Eur. Phys. J. C **35** (2004) 325.
17. F. Olness *et al.*, hep-ph/0312323.
18. See e.g. W. K. Tung, hep-ph/0409145 and ref. therein.
19. U. Stösslein, Acta Phys. Polon. B **33** (2002) 2813.
20. See W. Vogelsang, hep-ph/0405069;
 A. Metz, hep-ph/0412156, *these proceedings*, and ref. therein.
21. A. Airapetian *et al.* [HERMES Collaboration], hep-ex/0407032; D. Hasch, *these proceedings*;
 E. Christova and E. Leader, Nucl. Phys. B **607** (2001) 369; hep-ph/0412150, *these proceedings*.
22. S. Forte, hep-ph/9409416; hep-ph/9610238.
23. G. Altarelli, R. D. Ball, S. Forte and G. Ridolfi, Nucl. Phys. B **496** (1997) 337; Acta Phys. Polon. B **29** (1998) 1145;
 G. Ridolfi, eConf **C030614**, 019 (2003).
24. J. Blümlein and H. Böttcher, Nucl. Phys. B **636** (2002) 225.
25. Y. Goto *et al.* [Asymmetry Analysis Collaboration], Phys. Rev. D **62** (2000) 030417
26. D. B. Kaplan and A. Manohar, Nucl. Phys. B **310** (1988) 527.
27. P. Ferrario and S. Forte, *in preparation*.

DISCUSSION

N. Saito:

Question: The statistical accuracy mentioned for ν -factory seems to be very small, where the error involved in the extrapolation down to $x = 0$, and to $x = 1$ should be significant.

Answer: The error due to small- x extrapolation is very large (more than 50%) when determining the first moment of Δg , because the shape of $\Delta g(x)$ is poorly known. The neutrino factory cannot improve significantly this situation. However, the corresponding error on quark first moments is already moderate ($\sim 10 - 20\%$) and will be substantially improved by the neutrino factory, with reasonable assumptions on the small- x behaviour. However, an infinitely large contribution from the experimentally inaccessible $x \rightarrow 0$ region cannot be ruled out in principle.

STATUS OF PROTON POLARIZATION IN RHIC AND AGS*

W. W. MACKAY², M. BAI², H. HUANG², L. AHRENS², I. G. ALEKSEEV³, A. BRAVAR², K. BROWN²,
G. BUNCE^{2,6}, R. CALAGA², E. D. COURANT², A. DREES², W. FISCHER², C. GARDNER²,
J. W. GLENN², R. GUPTA², G. IGO⁹, U. IRISO², O. JINNOUCHI⁶, K. KURITA⁸, A. U. LUCCIO², Y. LUO²,
Y. MAKDISI², G. MARR², C. MONTAG², A. NASS², H. OKADA⁵, M. OKAMURA⁷, F. PILAT²,
V. PTITSYN², T. ROSER², N. SAITO⁵, T. SATOGATA², H. SPINKA¹, E. J. STEPHENSON⁴,
D. N. SVIRIDA³, J. TAKANO^{7,2}, S. TEPIKIAN², R. TOMAS², N. TSOUPAS², D. UNDERWOOD¹,
C. WHITTEN⁹, J. WOOD⁹, J. van ZELJTS^{2,11}, A. ZELENSKI², K. ZENO², S. Y. ZHANG²

1-ANL, Argonne, IL 60439 USA; 2-BNL, Upton, NY 11973 USA;

3-ITEP, Moscow 117259 Russia; 4-Indiana U., Bloomington, IN 47405, USA; 5-Kyoto Univ., Kyoto 606-8502
Japan; 6-RBRC, Upton, NY 11973 USA;

7-RIKEN, Wako, Saitama 351-0198 Japan;

8-Rikkyo Univ., Toshima-ku, Tokyo 171-8501, Japan;

9-UCLA, Los Angeles, CA 90095 USA;

11-present address Bear-Stearns & Co., 383 Madison Ave., New York, 10179 NY USA

The Relativistic Heavy Ion Collider (RHIC) has collided protons with both transverse and longitudinal polarization at a centre-of-mass energy of 200 GeV. Future running will extend this to 500 GeV. This paper describes the methods used to accelerate and manipulate polarized proton beams in RHIC and its injectors. Special techniques include the use of a partial Siberian snake and an AC dipole in the AGS. In RHIC we use superconducting helical Siberian snakes for acceleration, and eight superconducting helical rotators for independent control of polarization directions at two interaction regions. The present status and future plans for the polarized proton program will be reviewed.

1. Introduction

RHIC has been described in detail elsewhere [1], but it is worth noting (see Fig.1) the particular components used for spin control. First an H^- beam with polarized protons is produced by the optically pumped polarized ion source [2], and then accelerated in the RFQ and linac to a kinetic energy of 200 MeV ($\gamma = 1.21$). The beam is then stripped on injection into the Booster and accelerated to 2.46 GeV ($\gamma = 2.62$). Acceleration continues in the AGS up to 24.3 GeV ($\gamma = 25.94$), followed by transfer into either of the RHIC rings. There are several polarimeters to measure the polarization at various stages: one at the source, another at the end of the linac, three p+C CNI (Coulomb Nuclear Interference) polarimeters in the AGS and each RHIC ring, as well as local polarimeters at the STAR and PHENIX detectors. There is a partial Siberian snake in the AGS and a pair of full Siberian

*Work performed under the auspices of the U. S. DOE (Contract # DE-AC02-98CH10886) and RIKEN of Japan.

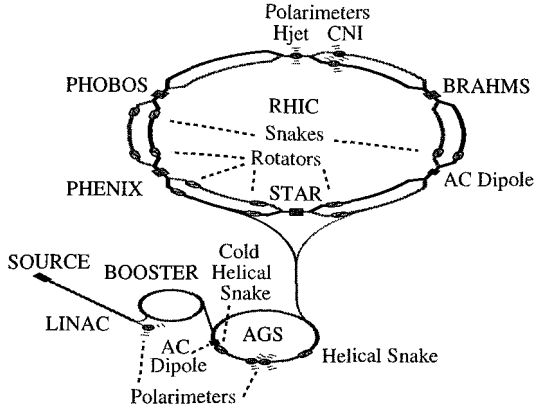


Fig. 1. The accelerator complex for polarized protons. The beam in the RHIC Blue (dark) ring goes clockwise and in the Yellow ring (light) counterclockwise.

snakes in each of the RHIC rings. Around each of the STAR and PHENIX detectors are four rotators to manipulate the polarization direction through the experiment. There is an AC dipole magnet in the AGS to aid in spin resonance crossing. RHIC has an additional AC dipole which will be used for spin flipping. A hydrogen jet polarimeter [12–15] was installed and commissioned during the latest run to provide an absolute calibration of the CNI polarimeters in RHIC.

2. Spin dynamics

In the local rest frame of the proton, the spin precession of the proton obeys the Thomas-Frenkel (BMT) equation [4]

$$\frac{dS}{dt} = \frac{g}{\gamma m} S \times \left[(1 + G\gamma) B_{\perp} + (1 + G) B_{\parallel} \right] \quad (1)$$

where the magnetic fields and time are expressed in the lab coordinates and electric fields have been ignored. Here $G = (g - 2)/2 = 1.792847$ for the proton. A comparison with the Lorentz force equation:

$$\frac{dp}{dt} = \frac{g}{\gamma m} S \times \left[\begin{array}{c} p \\ \end{array} \right] \quad (2)$$

shows that for a proton orbiting in planar ring with no vertical oscillations and a vertical bend field, the horizontal components of spin will precess a factor of $1 + G\gamma$ faster than the orbit in a fixed lab system. In the rotating coordinate system moving with the beam, any horizontal spin components will precess $\nu_s = G\gamma$ times in one turn. The number of precessions ν_s per turn, called the spin tune, is proportional to the energy of the proton.

A radial field component causing a vertical deflection of the particle by an angle ϕ will cause the spin to precess about the radial direction by an angle $(1 + G\gamma)\phi$. Since rotations about different axes do not commute, such vertical excursions can modify the amount of

precession and hence also the spin tune. In addition the local axes about which the spins precess may move away from the vertical.

Imperfection resonances, caused by misalignments of magnets, happen when $G\gamma$ is an integer and can be quite strong, producing flips of the polarization direction as the energy is ramped. For protons the energy separation of the imperfection resonances is 523 MeV.

The deflections of the vertical betatron oscillation also cause radial precessions which can build up when the spin tune matches the vertical betatron tune Q_v . This type of resonance is called an intrinsic resonance. For the most common resonances (intrinsic and imperfection) the resonance condition may be written as

$$\nu_s = N + N_v Q_v, \quad (3)$$

where N and N_v are integers. With horizontal-vertical coupling from rotated quadrupoles or solenoids, there may be an additional term $N_h Q_h$.

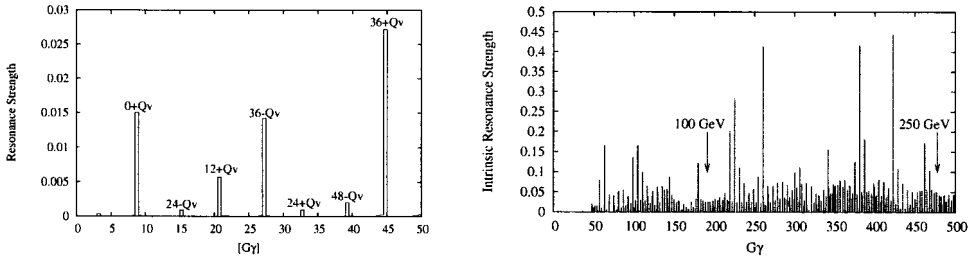


Fig. 2. a) Calculated relative strengths of intrinsic resonances in the AGS with no snake. It should be noted that there are 12 superperiods in the AGS, so the strongest intrinsic resonances occur when N is a multiple of 12 and $N_v = \pm 1$. b) Relative strengths of intrinsic resonances in RHIC with no snakes. These resonance spectra were calculated for protons on vertical emittance ellipses of $\pi\epsilon = 10\pi \mu\text{m}$, $Q_v = 8.7$ in the AGS and $Q_v = 29.219$ in RHIC. Note the different vertical scales in a and b.

As the energy increases the radial precessions are amplified, so that the resonance strengths increase with energy (see Fig. 2). The resonance strength ϵ is the angle of rotation away from the vertical divided by 2π that a proton right on resonance would experience in one turn. The Froissart-Stora formula [20] gives the ratio of final to initial polarization for an isolated resonance crossing:

$$\frac{P_f}{P_i} = 2 \exp\left(-\frac{\pi|\epsilon|^2}{2\alpha}\right) - 1, \quad (4)$$

where $\alpha = d(G\gamma)/d\theta$ is the ramp rate in units of $G\gamma$ per radian of bend around the ring. For a strong resonance, the spin can essentially completely flip over. Relative intrinsic resonance strengths for the AGS and RHIC are shown in Fig. 2.

3. The real machines

The linac provides a beam with about 80% polarization. In the Booster ($G\gamma$ from 2.18 to 4.5), we cross two imperfection resonances with harmonic orbit corrections to cancel any

depolarization at the integers 3 and 4. The beam gets extracted at $G\gamma = 4.5$ below the first intrinsic resonance ($\nu_s = Q_v = 4.9$).

In the AGS, with a more complicated resonance structure, the acceleration goes from $G\gamma = 4.5$ up to 46.5. Here we use a partial snake to cause a larger lattice disturbance with a rotation of the spin about the longitudinal axis and enhanced spin flipping at the imperfection resonances. A single partial snake in the ring will open up stop bands in the spin tune at the integer as shown in Fig. 3a. If $G\gamma$ is equal to an integer plus one half, then the stable spin direction is tilted away from the vertical by half of the snake-rotation angle; at integer values of $G\gamma$ the closed-orbit stable spin direction is in the horizontal plane.

An AC dipole can be made to vertically shake the beam near the betatron tune line, so that large amplitude oscillations will enhance the spin resonance, thus inducing more spin flip at the corresponding intrinsic resonance. We use the AC dipole to enhance spin flipping at four intrinsic resonances: $\nu_s = 0 + Q_v$, $12 + Q_v$, $36 - Q_v$, and $36 + Q_v$. Due to a lack of strength of the AC dipole we expect a loss of polarization at the $36 + Q_v$, with a decrease by a factor of about 0.85 at this resonance.

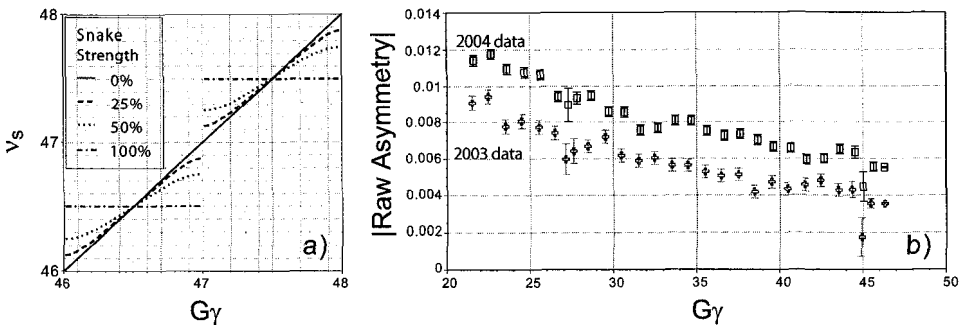


Fig. 3. a) A single partial snake in a ring opens up stop bands for the spin tune. The percentage refers to the amount of spin rotation from the snake: 100% corresponds to 180° of rotation. b) Absolute value of polarization asymmetry in AGS on ramp for runs in 2003 and 2004. At extraction ($G\gamma = 46.5$) the asymmetries corresponds to polarizations of 28% in 2003 and 42% in 2004.

In previous years the partial snake was a solenoid which introduced a large amount of horizontal-vertical coupling. For the latest run, we replaced the solenoid with a warm helically twisted dipole in order to reduce the contribution from coupling depolarizing resonances. Figure 3b shows the absolute value of the polarization asymmetry along the AGS ramp during the last two runs, in 2003 with the solenoidal snake and in 2004 with the helical snake [8]. Most of the increase was due to the new helical snake with smaller coupling; a few percent was due to improved performance of the polarized source.

With a single full snake in a ring the fractional part of ν_s will be an integer plus a half, and the intrinsic resonances go away, since we never operate with Q_v at an integer plus a half. With a single full snake, the stable spin direction is in the horizontal plane, which makes it difficult to match polarization from one ring to the next. There are however still some snake resonances [7, 20]. As we increase energy, more precessions happen in

the space between snake crossings, and the deleterious effects still build up, so that at RHIC energies up to 250 GeV ($G\gamma = 478$) a single snake would not be enough to maintain a reasonable amount of polarization. Higher energies require more snakes. In RHIC we inject and ramp with two full snakes on opposite sides of the rings (see Fig. 4).

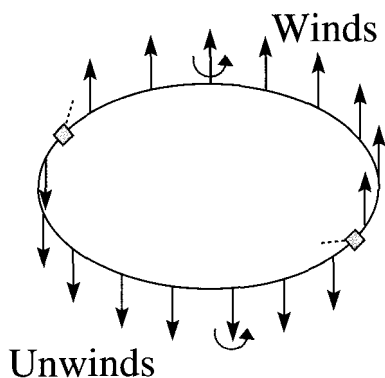


Fig. 4. With two full snakes on opposite sides of the ring that have rotation axes perpendicular to each other, the stable spin direction will be vertically up in one half of the ring and down in the other half, and the spin tune will be 0.5.

A snake is an insertion device which rotates the spin about an axis in the horizontal plane. The simplest type of snake is a solenoid which rotates the spin around the longitudinal axis. As can be seen from Eq. 1 the amount of rotation in a longitudinal field decreases with energy, so a solenoid becomes less effective for higher energy machines. Another drawback of solenoids is orbital coupling. In order to maintain a spin tune of 0.5 with two snakes on opposite sides of the ring, the rotation axes of the two snakes must be kept perpendicular. If the axes were parallel, the spin tune would be zero – a bad situation for maintaining polarization.

The RHIC snakes are constructed of four helical superconducting dipoles with right-handed pitch and fields. In contrast with the solenoidal snake, in a helical snake spin rotation is primarily due to the transverse fields so that the rotation is essentially independent of energy. Each snake is driven by two power supplies: The outer pair of helices are connected in series with opposite polarity to one supply, and the inner pair are likewise connected in series with opposite polarity to the second supply. This orientation of fields guarantees that the snake will act as an insertion device with minimal impact on the orbit outside the snake.

The spin rotators for longitudinal polarization are made of four helical superconducting dipoles. In this case we alternate the handedness of the pitch rather than polarity. Moving clockwise around both rings the pattern at each rotator is: right-left-right-left. For a rotator the field at the end of each helix is horizontal. Each pair (inner and outer) of helices within a rotator is again connected in series to a different power supply. The rotation axis of this kind of rotator lies in the plane perpendicular to the beam and not necessarily in the horizontal plane as in a snake. The rotators are laid out around one of the experiments as indicated in

Fig. 5

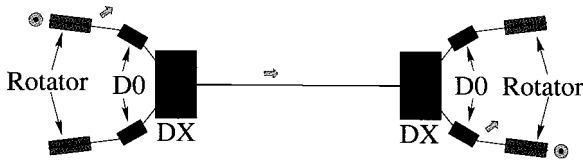


Fig. 5. There are two rotators in each ring on either side of both the STAR and PHENIX detectors. Between the rotators and experiment are four dipoles (D0 and DX) to steer the beams into head-on collisions. The final-focus triplets (not indicated) are located between the rotators and D0 magnets. For each ring the incoming rotator and outgoing rotator are parallel. There is a net bend angle of ± 3.675 mrad from the rotator to the collision point.

As with the snakes the amount of rotation is essentially independent of energy. However due to the net horizontal bend between the rotator and interaction region, there is an energy dependent precession which must be compensated to achieve a longitudinal polarization at the collision point. Figures 6a,b,c show transverse polarization asymmetries measured by

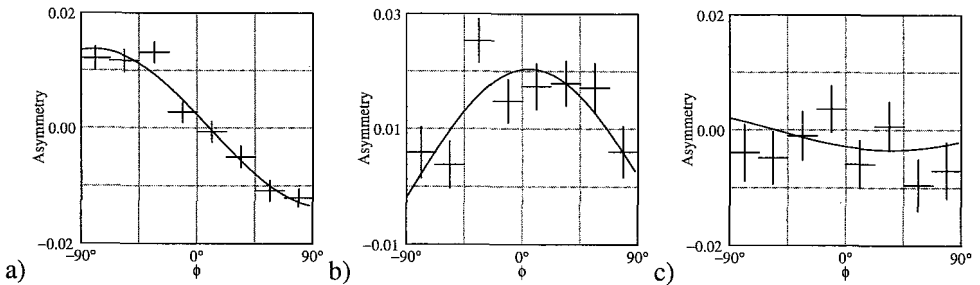


Fig. 6. Transverse polarization asymmetry at PHENIX with a) rotators off, b) rotators with wrong polarity, c) rotators with correct polarity.

the PHENIX experiment with three rotator settings [19]. The asymmetry is plotted as the “left-right” asymmetry relative to a transverse angle ϕ measured away from the vertical. In Fig. 6a we see a vertical polarization with the rotators turned off. With the currents accidentally reversed (Fig. 6b) the polarization was essentially radial, and with the correct polarity (Fig. 6c) the measured asymmetry was essentially zero with no appreciable loss of polarization measured by the CNI polarimeter outside the rotator region. Similar results confirmed longitudinal polarization by PHENIX in the Yellow ring and by STAR in both rings.

4. Status and future plans

To date we have achieved a polarization of 50% in the AGS at extraction with a bunch intensity of 1×10^{11} . We changed to a new betatron tune working point in RHIC to reduce beam loss from the beam-beam interaction and improve the luminosity – details are given

in [6]. At $\sqrt{s} = 200$ GeV in RHIC we have collided beams with an average luminosity of $4 \times 10^{30} \text{ cm}^{-2}\text{s}^{-1}$ and an average polarization of about $40 \pm 5\%$. Preliminary results [15] from the H-jet polarimeter give an A_N consistent with theory without hadron spin-flip as well as with the FNAL E704 experiment [16].

For the next run we will upgrade the solenoid for the OPPIS source, and expect to increase the polarization from the source from 80% to 85%. In the AGS we will also be adding a superconducting helical partial snake [9], which can reach 25% strength. We plan to commission this new snake during the next run in a mode which uses both the existing warm helical snake and the new superconducting snake. By placing the second snake one third of the way around the ring from the other, the snakes can be made to add in strength at spin tunes of multiples of three where the worst imperfection resonances lie, and subtract at spin tunes 1.5 units away where we inject ($G\gamma = 4.5$) and extract ($G\gamma = 46.5$). (See citeROSER.) The addition of this superconducting partial snake should allow us to extract 2×10^{11} protons per bunch with $> 70\%$ polarization from the AGS.

To date we have only accelerated polarized protons up to an energy of 100 GeV, although a top energy of 250 GeV is possible. Since the rate of spin precession about transverse fields is proportional to energy, we expect more stringent requirements on the orbit flatness as we increase the energy. In the next run we plan to spend a fraction of the time developing acceleration to higher energies in RHIC. This summer we realigned quadrupoles in the vicinity of the north interaction area (location of Hjet in Fig. 1). We are planning a complete realignment of the ring next summer. The electronics for our beam position monitors is being upgraded to have fewer radiation induced glitches, and we removed some mechanical microwave switches which caused serious drift problems in the reported beam positions. With the quadrupole realignments and more reliable position readback, we expect to achieve a much flatter orbit thus reducing the size of depolarizing resonances.

We are installing NEG-coated beam pipes in the warm sections of RHIC to increase vacuum pumping as well as reduce secondary emission of electrons; at present we are about half completed and will finish adding the NEG coated pipes during the next summer shutdown. This NEG-coated pipe should help minimize the vacuum problems which are limiting beam intensity and thus luminosity.

Over the next few years we are aiming to reach an enhanced luminosity of $1.5 \times 10^{32} \text{ cm}^{-2}\text{s}^{-1}$ with a polarization of at least 70% at 250 GeV ($\sqrt{s} = 500$ GeV).

Other development plans in RHIC include commissioning the AC dipole as a spin flipper and calibrating the snakes for the correct spin rotation. We plan to calibrate the beam energy by tilting the spin away from the vertical direction with one of the PHENIX rotators and measuring the oscillation of the radial component of spin at the CNI polarimeters as a function of energy.

In the long term, we are designing an electron ring (or possibly a linac) for collisions with heavy ions and polarized protons in at least one interaction area. For the ring design the electron beam will be polarized as discussed in [17]. An overview of the eRHIC plan was presented in the final plenary talk by Abhay Deshpande [18].

References

1. I. Alekseev *et al.*, NIM **A499**, 392 (2003). **C34**, 1729 (1980).
2. A. Zelenski *et al.*, SPIN2002, AIP Conf. Proc. 675, 881 (2003)
3. W. W. MacKay *et al.*, Proc. of the 2003 Part. Accel. Conf., 405 (2003).
4. L. H. Thomas, *Phil. Mag. S. 7*, **3**, 1 (1927); J. Frenkel, *Z. Physik.* **37**, 243 (1926); V. Bargmann *et al.*, *Phys. Rev. Lett.*, **2**, 435 (1959).
5. W. W. MacKay *et al.*, Proc. of the 2003 Part. Accel. Conf., 1697 (2003).
6. M. Bai *et al.*, these proceedings.
7. V. Ptitsyn *et al.*, these proceedings.
8. H. Huang *et al.*, these proceedings.
9. R. Gupta *et al.*, Proc. of the 2003 Part. Accel. Conf., 1936 (2003).
10. T. Roser *et al.*, these proceedings.
11. D. Svirida *et al.*, these proceedings.
12. T. Wise *et al.*, these proceedings.
13. A. Zelenski *et al.*, these proceedings.
14. A. Nass *et al.*, these proceedings.
15. H. Okada *et al.*, these proceedings.
16. D. L. Adams *et al.*, *Phys. Lett.*, **B264**, 462 (1991).
17. D. Barber, these proceedings.
18. A. Deshpande, these proceedings.
19. W. W. MacKay *et al.*, PAC03 Proceedings, 1697 (2003).
20. S. Y. Lee, *Spin Dynamics and Snakes in Synchrotrons*, World Scientific, Singapore (1997).

DISCUSSION

S. B. Nurushev:

Question 1: What is the polarization relaxation time during the 10 hour storage at RHIC?

Answer: With polarized protons the typical store length is only about 5 hours. In general we see no loss of polarization during the store; although on some occasions with nonoptimal conditions such as the vertical tune too close to a depolarizing resonance, we have seen a decrease.

Question 2: How large is the variation of the beam polarization from one bunch to another?

Answer: We fill the two rings with bunches having a different pattern of spins. In one ring we typically inject a spin pattern: up, down, up, down..., and in the other ring a pattern: up, up, down, down... This gives all four possible combinations for the collisions.

For most bunches the polarization magnitude appears to be the same; however there are a few special bunches such as one bunch which gets kicked periodically for tune measurements. This kicked bunch which usually has a lower intensity and fatter emittance has had a lower polarization on occasion.

SUMMARY OF PARALLEL SESSIONS 1, SPIN AND FUNDAMENTAL SYMMETRIES, AND 3, SPIN BEYOND STANDARD MODEL

O. V. TERYAEV

Joint Institute for Nuclear Research, Dubna, Russia

The main topics of 16 talks presented at these related sessions include spin-related signals of new physics and fundamental symmetries, alternative descriptions of spin, and manifestation of symmetries in dynamical calculations

1. Introduction

The two sections I am going to summarize are indeed closely related and their description in this common summary talk is therefore quite justified. The key common issue here is the close dependence of particle interactions on their spin, so that the underlying symmetries and indications of new physics directly influence the various spin effects.

The main topics may be described as:

- i) Spin-related tests of new physics.
- ii) Spin-related tests of fundamental symmetries
- iii) Alternative descriptions of spin.
- iv) Miscellaneous, which may be roughly characterized as manifestations of fundamental symmetries in spin-related dynamical calculations.

In total, taking into account all the cancellations, 16 talks were given, eight at each session. One should also mention here the three plenary talks [1–3]

In what follows I am going to review briefly the talks at parallel sessions and also to make a guess about the development of these important fields in the near future.

2. Spin-related tests of new physics

The talk of R. Carlini [4] was devoted to the field of low-energy [2] spin-exploring searches for new physics. This is complementary to the use of high-energy colliders to find its signatures. Although the new physics scale is typically assumed to be large, the size of the corresponding effects at low energy is suppressed. However, the use of high intensity beams and polarization may compensate for this. This is exactly what should happen in the QWEAK experiment, which is intended to measure the weak charge of the proton with 4% accuracy. This in turn will allow a check of $\sin \theta_W$ running due to Standard Model radiative

corrections at 10σ level of accuracy. The variation would be a signal of new physics. This study will be performed through the measurement of parity-violating asymmetry in the scattering of longitudinally polarized 1.2GeV electron beam on the LH_2 target. The very accurate (1.5%) measurement of beam polarization will be achieved by upgrading the existing Compton polarimeter and developing a new one.

Another concept, perhaps the most popular spin precession test for new physics, is provided by the muon $g - 2$ measurement extensively described in the plenary talk of L. Roberts [3]. This subject was addressed in the talk of Alexander Dorokhov [5], who studied the hadronic contribution to $g - 2$ in the framework of instanton-based model of QCD vacuum. He studied separately correlators of vector and axial current, achieving as a result a good description of ALEPH and OPAL data. The model hadronic contribution is in agreement with numbers extracted from e^+e^- annihilation and τ -decay data.

Two talks by A. Pankov [6] and A/ Tsitrinov [7] presented studies of new physics effects performed by scientists from Trieste and Gomel. The talk of A. Pankov was devoted to studies of (strong) graviton exchanges and lepton and hadron (LHC) high-energy colliders, making use of a new observable the author calls centre-edge asymmetry, which is proportional to the difference in differential cross-section within and without some arbitrary c.m. scattering angle. The author shows that this observable is quite sensitive to a graviton contribution, and claims that it can be measured accurately enough, if the acceptance effects are taken into account. The talk of A. Tsitrinov presents the studies of contact interactions in elastic processes at high-energy lepton collider, and shows, that beam polarization leads to a significant increase in the potential for discovery.

3. Spin-related tests of fundamental symmetries

A study of a spin-related T-invariance test and new physics search via electric dipole moment precession [1] was presented in a parallel session by A. Yoshimi [8]. This speaker described a new nuclear spin maser using polarized ^{129}Xe operating at much lower frequencies (34Hz) than usual, achieved by advanced optical feedback. However, as became clear during the interesting discussion after the talk, such a system requires special care in data handling and processing.

The theory of new spin-related tests of fundamental symmetries were discussed, strictly speaking, only in the talk of V. Lyuboshitz [9]. He considered spin correlations in the reaction $p + He^3 \rightarrow \pi^+ He^4$, whose advantage is the presence of two scalar particles in the final state, simplifying the structure of the correlation tensor. This reaction may be therefore considered as an analog of the famous Einstein-Podolsky-Rosen thought experiment, while the constraints derived by the authors are simplified analogs of the Bell inequalities. The emerging opportunities to test the basic principles of quantum mechanics in high energy experiments seem to be promising, and deserve further theoretical and, especially, experimental investigation.

4. Alternative description of spin

Alternative descriptions of the very concept of particle spin are explored in the talk of N. Mankoc-Borstnik [10], who suggested an alternative to the Standard Model based on the $SO(1, 13)$ group. In this approach only one (Weyl) fermion field in $d = (1 + 13)$ -dimensional space exists, while all the degrees of freedom of observable particles are related to their spin components. This model predicts the existence of new a quark flavour with mass $\sim 210\text{GeV}$, making it falsifiable in the near future.

There were some attempts at a semiclassical description of fermion spin, the first presented by Martin Rivas [11], in which a classical picture of a Dirac fermion as a sort of vortex was suggested. The crucial element of such a model is the separation of mass and charge, leading to a picture of particle scattering that was represented during the talk via computer simulations. However, an open problem remains the correspondence of this picture with the standard quantum description of scattering, as well as the interpretation of the electric dipole moment, which is zero when the particle is at rest but, as the author suggests, may be manifested at high energies.

The analogy between the Dirac fermion and a black hole was explored by A. Burinskii [12]. It is based on the remarkable property of a black hole that it has the Dirac value of magnetic moment, as discovered by B. Carter about 30 years ago. The current analysis includes interesting mathematical observations of peculiar stringy structures, but the analogy is still far from either theoretical completeness or phenomenological consequences.

The talk of G. Musulmanbekov [13] contained a discussion of the qualitative semiclassical explanation of single spin asymmetries as emerging due to collisions of quarks considered as vortices which may be distinguished as “left” and “right”. Quantitative results are to be investigated in the future.

5. Manifestation of symmetries in spin-related dynamical calculations

The exploration of symmetries in dynamical calculations was a subject of several rather diverse talks. V. Zamiralov [14] presented a study of $SU(3)$ symmetry manifestation in QCD sum rules calculations. He showed that the symmetry may be implemented at the level of quark current, resulting in exact relations for baryon magnetic moments.

The two talks presented by A. Mirjalili [15] were devoted to the description of the evolution of spin-dependent parton distributions in the framework of the valons model, a sort of dressed quark concept. While the former explored the so-called complete renormalization group improvement, the latter was aimed specifically at the evolution of parton angular momenta.

Another fundamental ingredient of hadronic structure, Compton polarizabilities of the pion, was discussed in the talk of V. Andreev [16]. The pion was considered as a relativistic bound state of quark and antiquark, and the values for electric (magnetic) polarizabilities obtained are $5.26(-2.03)10^{-4}Fm^3$.

Finally, the talk of B. Si Lakhali [17] was devoted to sum rules for the four-spinon dynamic structure factor of the Heisenberg spin chain, and therefore belonged to condensed matter physics. Still, an experimental test may be performed by the studies of spin effects

in neutron scattering, demonstrating the broad scope of particle spin physics.

6. Conclusions and outlook

The talks presented show that spin remains an essential tool to test fundamental symmetries and explore new physics beyond them. The new possibility emerging now is to use high accuracy experiments [4] at relatively low [2] energies. Possible indications of new physics are significantly lower than may be expected at high energy accelerators, but the high accuracy may compensate for this. Another new feature is the development of new methods and technologies [8] to make advances in the well-established method of spin precession.

There is still interest in an alternative description of spin degrees of freedom, which may result in a theoretical alternative to the Standard Model [10] which allows for an experimental check. On the other hand, new attempts to relate spin to classical notions and to gravity are continuing and may provide new theoretical insight.

Let me also suggest that the start of the LHC program might lead to a significant increase in the analysis of various aspects of spin effects [6, 7], including simulations and taking into account the detector acceptance. The mentioned sensitivity of spin effects to new physics makes their dedicated study at LHC an important and interesting problem. Unfortunately, LHC beams will not be polarized. However, there is an opportunity to study various spin correlations in the initial state, which are sensitive to details of fundamental interactions. The QCD background here is as important as in many studies of new physics (recall the hadronic contribution [5] to $g - 2$), and here the recent experience of studies of various QCD-induced spin effects [18, 19] may be very useful. One cannot exclude some manifestation of new physics at RHIC, especially when interference effects are considered, which are proportional to the amplitude of the new physics contribution, rather than to its square ^a.

Bearing such perspectives in mind, it seems important to bring together experts in spin physics and new physics, together with theorists and experimentalists, to have a broad exchange of ideas and to select the best spin-related signals at LHC and at other accelerators. For this purpose, round tables are planned at spin meetings in Prague [20] next July and in Dubna [21] next September, and I would like to use this opportunity to invite everybody interested to attend them. Hopefully, we will hear much more on the exciting subject of the fundamental aspects of spin physics at SPIN-2006.

Acknowledgements

I am most thankful to Organizers and, in particular, to Franco Bradamante, for warm hospitality in Trieste and financial support.

References

1. K. Jungmann, These Proceedings

^aOne may think, say, on the (strong) gravity-nuclear interference, similar to CNI

2. E. Hughes, These Proceedings
3. L. Roberts, These Proceedings
4. R. Carlini, These Proceedings
5. A. Dorokhov, These Proceedings
6. A. Pankov, These Proceedings
7. A. Tsitrinov, These Proceedings
8. A. Yoshimi, These Proceedings
9. V. Lyuboshitz, These Proceedings
10. N. Mankoc-Borstnik, These Proceedings
11. M. Rivas, These Proceedings
12. A. Burinskii, These Proceedings
13. G. Musulmanbekov, These Proceedings
14. V. Zamiralov, These Proceedings
15. A. Mirjalili, These Proceedings
16. V. andreev, These Proceedings
17. B. Si Lakhali, These Proceedings
18. A. Metz, These Proceedings
19. V. Barone, These Proceedings
20. M. Finger, These Proceedings
21. A. Efremov, These Proceedings

SUMMARY OF PARALLEL SESSION 2, THE QCD SPIN STRUCTURE OF NUCLEONS

G. K. MALLOT

CERN, Geneva, Switzerland

This paper attempts to summarise the highlights of the talks presented in Parallel Session II of the SPIN 2004 Symposium dedicated to the QCD spin structure of nucleons. Emphasis is put on new data and theoretical developments.

1. Introduction

The enormous interest in the spin structure of nucleons is reflected in the 55 accepted parallel talks in this session, comprising about equal numbers of theoretical and experimental presentations. About two-thirds of the experimental results came from lepton–nucleon scattering, while the rest were from pp interactions. A focus of the theory contributions was on transversity and single-spin asymmetries. This paper will not attempt to cover the excellent plenary talks on spin structure nor can it do justice to all the excellent talks in the parallel session.

2. Quark Helicity Distributions

The spin-dependent structure functions $g_1(x, Q^2)$ of the proton, the deuteron and the neutron are well known by now. However, the lack of data from colliders at small x and large Q^2 limits the information obtainable from an analysis of the Q^2 evolution. HERMES at DESY completed its programme with longitudinal polarisation and presented their quasi-final results [1] for g_1 of the proton, the deuteron and the neutron. COMPASS showed its first A_1 deuteron data [2] from the 2002 and 2003 runs. For $x < 0.03$ these are the most precise data yet (Fig. 1). The somewhat negative tendency of the SMC data in this region is not reproduced. During 2004 about the same amount of data was recorded and the larger- x region will additionally profit from an improved trigger set up.

In the valence-quark region $x > 0.2$, new highly precise data became available from Jefferson Lab. The ^3He neutron data [3] from E99-117 show for the first time a clearly positive asymmetry A_1^n for $x \simeq 0.6$. The deviation from pQCD predictions may hint at a possible effect due to quark orbital angular-momentum [3].

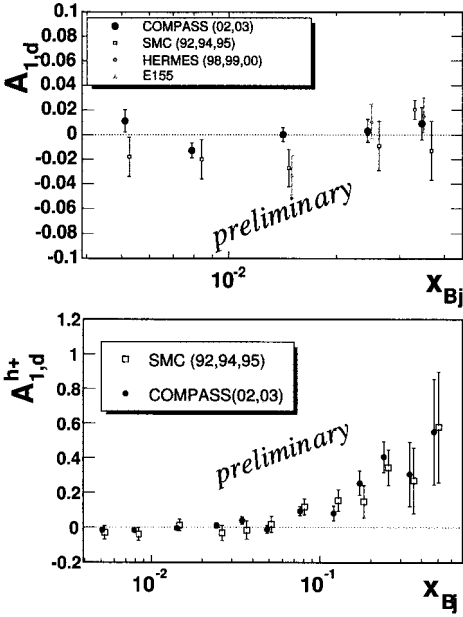


Fig. 1. Virtual photon asymmetry A_1^d for the deuteron from COMPASS 2002 and 2003 data [2]: inclusive asymmetry for $x < 0.04$ (top), asymmetry for positive hadrons (full x -range, bottom).

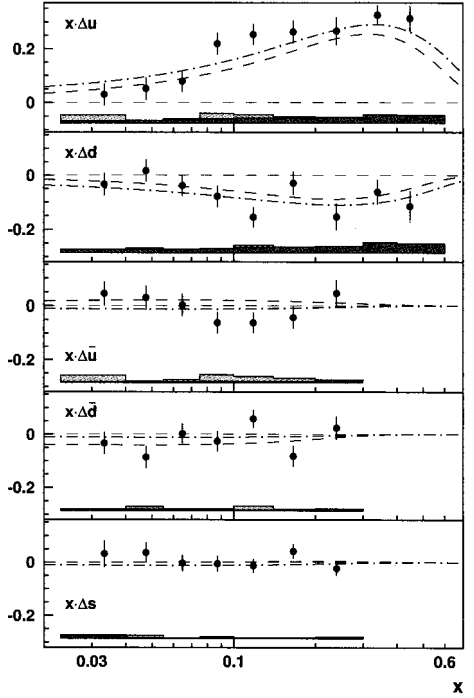


Fig. 2. The quark helicity distributions $x\Delta q(x)$ at fixed $Q^2 = 2.5 \text{ GeV}^2$ from HERMES [4]. The strange quark distribution $x\Delta s$ was determined assuming $x\Delta \bar{s} \equiv 0$.

To disentangle the contributions of the various quark flavours to g_1 requires semi-inclusive deep inelastic scattering, where the detected final-state hadron ‘remembers’ the flavour of the originally hit quark. In particular the interesting polarisation of the strange quarks cannot be determined by inclusive DIS off proton and neutron (deuteron) targets. New semi-inclusive asymmetries were presented by COMPASS [2]. In Figure 1 (bottom) the asymmetries for positive hadrons are shown extending down to $x \simeq 5 \cdot 10^{-3}$ for $Q^2 > 1 \text{ GeV}^2$. Similar results exist for negative hadrons, while the kaon asymmetries are still being analysed. HERMES analysed its data, including the asymmetries from identified kaons, in terms of the five quark distributions [4] : Δu , Δd , $\Delta \bar{u}$, $\Delta \bar{d}$ and Δs at fixed $Q^2 = 2.5 \text{ GeV}^2$ and assuming $\Delta \bar{s} \equiv 0$. The up and down quark data confirm, with higher precision, earlier results. The up and down antiquark distributions as well as that of the strange quarks are compatible with zero (Fig. 2).

It is well known that there is a strong isospin asymmetry [5] in the unpolarised quark distributions $\bar{u}(x) - \bar{d}(x) \neq 0$, first observed as a violation of the Gottfried sum rule. The models describing this asymmetry also predict an isospin asymmetry for $\Delta \bar{u}(x) - \Delta \bar{d}(x)$. The HERMES data [4] are shown in Fig. 3 with two model predictions [6]. The data rather favour a symmetric sea. High precision data for $\Delta \bar{u}(x) - \Delta \bar{d}(x)$ with $x > 0.1$ are expected

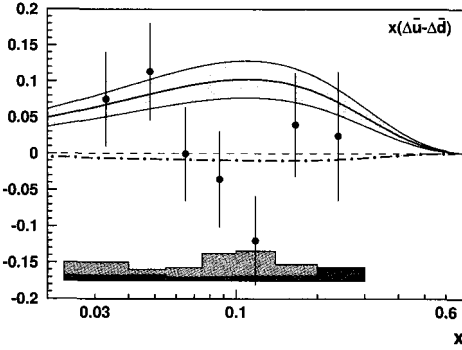


Fig. 3. The difference $x(\Delta\bar{u} - \Delta\bar{d})$ as a function of x from HERMES [4] at $Q^2 = 2.5 \text{ GeV}^2$.

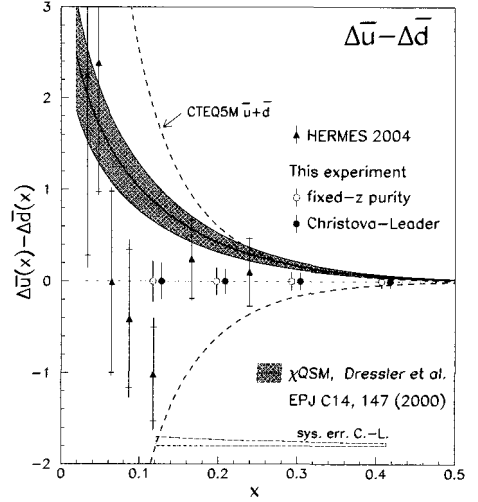


Fig. 4. Results for $\Delta\bar{u}(x) - \Delta\bar{d}(x)$ expected from Semi-SANE [7].

from a new JLAB experiment, semi-SANE (E04-113) [7]. In Figure 4 the projected results are shown. The scattered electron is detected in a calorimeter, while the final-state hadron is detected in a magnetic spectrometer. The inversion of the magnetic field yields the same acceptance for oppositely charged hadrons, while leaving the scattered-electron acceptance untouched. This opens the way to using a model-independent NLO method [8] involving positive and negative hadron data, in which the fragmentation functions cancel. A method using the first moments of the quark helicity distributions to determine $\Delta\bar{u}(x) - \Delta\bar{d}$ was also discussed [9].

Higher-twist effects, double logarithm resummation, and matrix solutions for PDFs were presented in separate contributions [10].

3. Gluon Polarisation

Still little is known about the gluon helicity distribution, ΔG , which can be determined in DIS either from the Q^2 evolution of the quark helicity distributions, or from processes involving photon-gluon fusion (PGF). The longitudinal double-spin asymmetry

$$A^{\ell N \rightarrow \ell' hhX} = \frac{\Delta G}{G} \langle \hat{a}_{LL} \rangle^{PGF} R^{PGF} + \frac{\Delta q}{q} \{ \langle \hat{a}_{LL} \rangle^{LP} R^{LP} + \langle \hat{a}_{LL} \rangle^{QCDC} R^{QCDC} \}$$

contains terms involving $\Delta G/G$ and those involving $\Delta q/q$. The latter is rather well known experimentally and the size of the relative contributions R must be estimated by Monte Carlo simulations. The partonic asymmetries $\langle \hat{a}_{LL} \rangle$ are known from theory. Determinations of $\Delta G/G$ from PGF using unidentified high- p_T hadron pairs and $Q^2 > 1 \text{ GeV}^2$ were reported by SMC [11] and by COMPASS [12] (2002–2003 data). The results are shown in

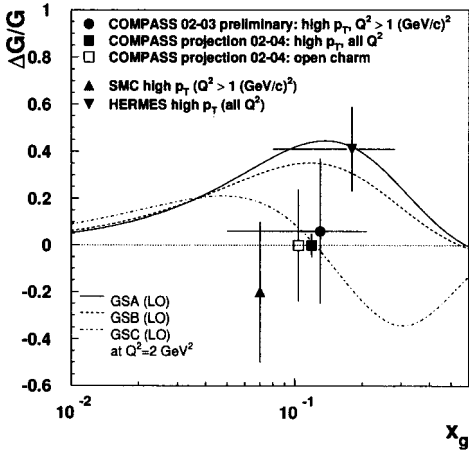


Fig. 5. Gluon polarisation $\Delta G/G$ as a function of x -gluon. The triangles and the circle correspond to data [11–13] while the squares indicate COMPASS projections [12].

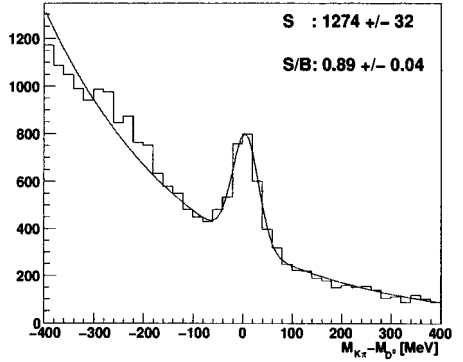


Fig. 6. COMPASS invariant mass peak $M_{K\pi} - m_{D^0}$ from the $D^0 \rightarrow \pi K$ decay [12].

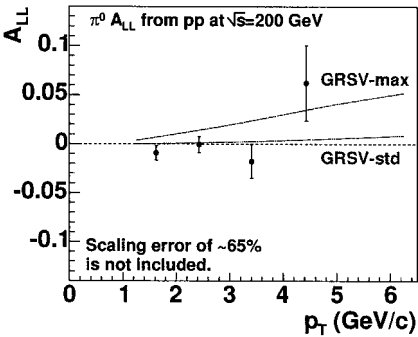


Fig. 7. Double-spin asymmetry A_{LL} for π^0 production as a function of p_T from PHENIX [14]. The curves correspond to the respective GRSV [18] input gluon-distributions.

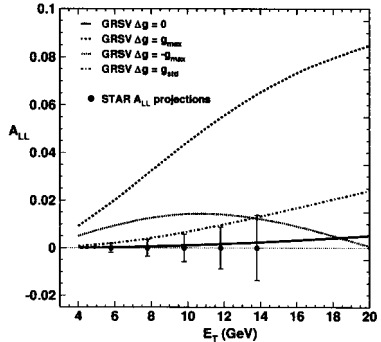


Fig. 8. Projected data for A_{LL} from $pp \rightarrow \text{jet} + X$ at STAR. The curves correspond to GRSV [18]: g_{max} , g_{std} , $g = 0$, $-g_{max}$ (top to bottom on right side).

Fig. 5 together with a previous result from HERMES [13] (all Q^2). Both new results are compatible with zero and smaller than the HERMES value. Hadron pairs at $Q^2 < 1$ GeV are 10 times more abundant at COMPASS, but their analysis is more model dependent and must take into account contributions from resolved photon processes. The cleanest signature for a PGF process is open-charm in the final state. COMPASS showed the first mass peak for D mesons (Fig. 6). The projected precision for $\Delta G/G$ from D^0 asymmetries and from all- Q^2 hadron pairs for their 2002–2004 data are also shown in Fig. 5.

The polarised proton–proton collisions at RHIC offer many channels to study the gluon polarisation. Given the limited beam polarisation (2003) and beam time (2004), the most promising channel is double spin asymmetry in π^0 production, $pp \rightarrow \pi^0 X$. The results [14]

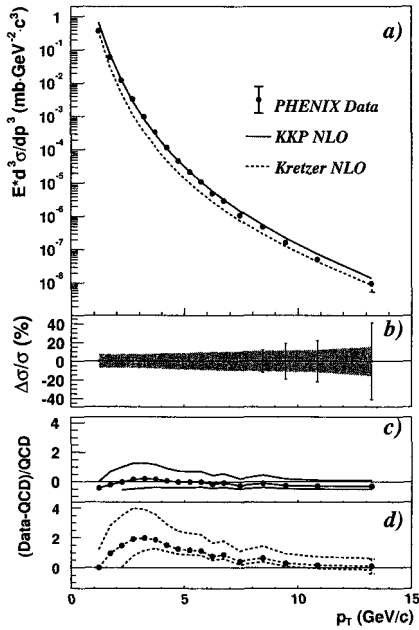


Fig. 9. The invariant differential cross-section for inclusive π^0 production from PHENIX as a function of p_T [19, 20]. For details see [20].

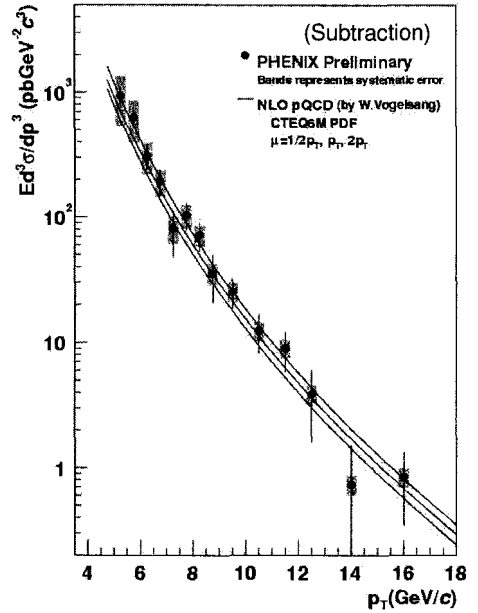


Fig. 10. The invariant differential cross-section for photon production from PHENIX as a function of p_T [21].

from PHENIX are shown in Fig. 7. The statistical significance is still very limited, but the big potential of this measurement becomes apparent taking into account the improvement in 2004 with respect to the 2003 data [15], which is largely due to the improved beam polarisation. The STAR experiment also expects significant data [16] for the gluon polarisation from the process $pp \rightarrow \text{jet} + X$ from the 2005 run (Fig. 8). In pp collisions gluon–gluon, gluon–quark and quark–quark partonic processes contribute, yielding terms proportional to $(\Delta G/G)^2$, $(\Delta G/G)(\Delta q/q)$ and $(\Delta q/q)^2$. As a consequence an ambiguity concerning the sign of ΔG arises. Because of the quadratic term in ΔG there is almost no opportunity to generate a negative asymmetry [17] as illustrated in Figs. 7 and 8.

Of central importance for the determination of $\Delta G/G$ from π^0 or prompt-photon production at RHIC is that the cross-section is well understood and reproduced by theory. Figures 9 and 10 demonstrate the good level of agreement for collider c.m.s. energies. Next-to-leading logarithm resummation and power corrections are an important element in the calculation [19, 22].

The determination of the first moment of ΔG requires an extension of the limited kinematic range in which the gluon momentum fraction x_g is accessible with the present RHIC detectors. A considerable upgrade programme [23] is proposed for PHENIX, which will extend the limits down to $x_g \simeq 0.001$ at $\sqrt{s} = 200$ GeV. Hyperon polarisation and new observables in pp collisions were also discussed [24].

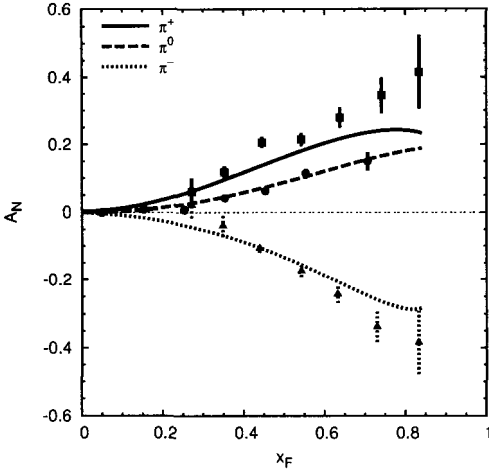


Fig. 11. E704 data [29] described by the Siverts effect in the k_T model [27, 28].

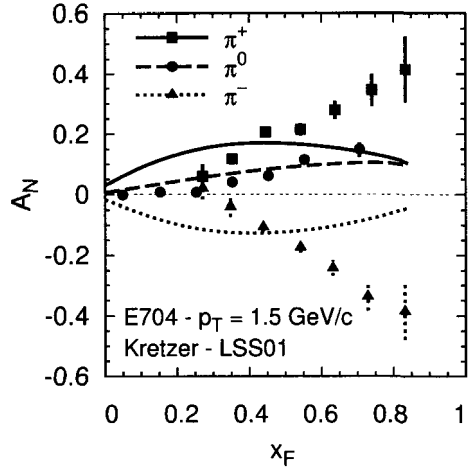


Fig. 12. Attempt to describe the E704 data [29] purely by the Collins effect [28, 30].

4. Transverse Spin

New measurements of the single-spin transverse asymmetry A_N for neutral pion production were reported by PHENIX [25] for $x_F = 0$ and by STAR [26] for $0.2 < |x_F| < 0.6$. The asymmetry is consistent with zero for $x_F < 0.4$ and positive for larger x_F . This behaviour is reproduced [27] by the Siverts effect in a generalised leading-order pQCD model [28] using k_T -dependent PDFs and fragmentation functions. The model also describes the FNAL-E704 pion data [29] by the Siverts effect (Fig. 11). On the other hand even a fully saturated Collins mechanism [30] cannot reproduce these data (Fig. 12). In the same model it was shown that D-meson production at RHIC in $p \uparrow p \rightarrow DX$ is an ideal place to study the gluon Siverts-distribution [31]. Also the Siverts asymmetries from HERMES [32] can be described in this model [33].

A full next-to-leading order calculation [34] is now available for prompt-photon production and other cross-sections in $p \uparrow p \uparrow$ collisions. The scale dependence is strongly reduced as compared with LO calculations.

Both COMPASS [35] and HERMES [32], presented first results on Collins and Siverts asymmetries (Figs. 13 and 14). For the deuteron, both the Collins and Siverts asymmetries are compatible with zero, while for the proton there is a hint of positive values for favoured and of negative values for unfavoured fragmentation. For both experiments more data are available and being analysed. New quark polarimeters may help to get a better handle on the transversity distributions. The experiments have already had a first look [36] at the proposed di-hadron fragmentation [37], which avoids a k_T convolution. Drell-Yan processes in polarised pp collisions and even $p\bar{p}$ collisions at the future PAX experiment are other channels to look for transversity [38].

New precise COMPASS data [39] on the spin transfer to lambdas and anti-lambdas and the spin density matrix in exclusive ρ production are in good agreement with previous data.

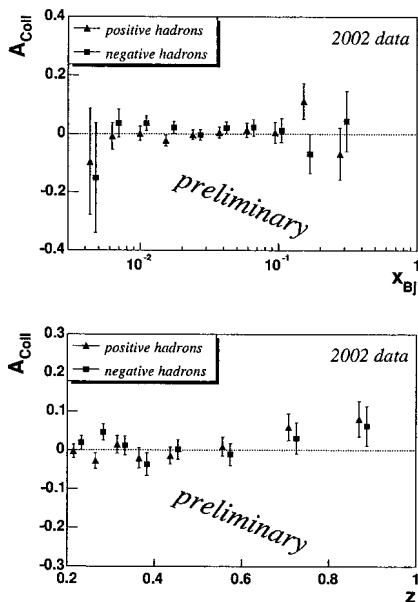


Fig. 13. COMPASS 2002 deuteron data [35]: Collins asymmetries as functions of x_{Bj} (top) and of z_h (bottom) for positive and negative hadrons.

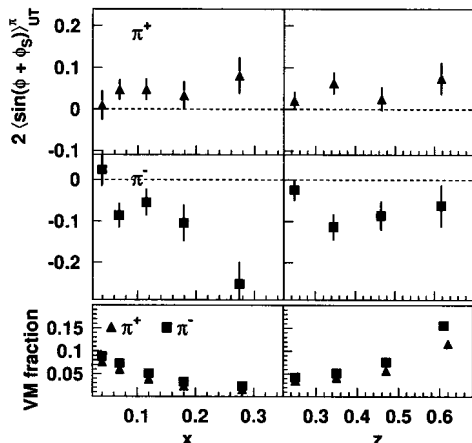


Fig. 14. HERMES 2002/3 proton data [32]: Collins asymmetries as functions of x_{Bj} (left) and of z_h (right) for positive (top) and negative (bottom) pions. The bottom panel shows the indicated contribution from exclusively produced vector mesons from PHYTHIA Monte Carlo.

New data were also presented on transverse lambda polarisation [40].

In the context of Generalised Parton Distributions, HERMES presented new results for the beam-charge asymmetry in deeply-virtual Compton-scattering off a deuteron target and for vector meson production [41].

5. Outlook

A wealth of new experimental results was presented at the Spin Symposium, including first data from COMPASS and RHIC. A precise measurement of the gluon polarisation in lepton–nucleon and in pp interactions is around the corner and first results were already presented. The second missing piece in our understanding of the nucleon’s spin structure is transversity, and here too we saw the first data from COMPASS and HERMES. The progress of the phenomenological models as well as in NLO QCD theory will allow us to take full advantage of the wealth of experimental results.

References

1. HERMES, C. Riedl, these proceedings.
2. COMPASS, D. Peshekhonov, these proceedings.
3. JLab Hall A Collaboration, X. Zeng *et al.*, *Phys. Rev. Lett.* **92**, 012004 (2004) and arXiv:nucl-ex/0405006; M. Garçon, these proceedings.
4. HERMES, J. Rubin, these proceedings; HERMES, A. Airapetian *et al.*, arXiv:hep-ex/0407032.

5. NMC, P. Amaudruz *et al.*, *Phys. Rev. Lett.* **66**, 2712 (1991); FNAL-E866, E. A. Hawker *et al.*, *Phys. Rev. Lett.* **80**, 3715 (1998).
6. B. Dressler *et al.*, *Eur. Phys. J. C* **14**, 147 (2000); F.-G. Cao and I.A. Signal, *Phys. Rev. D* **68**, 074002 (2003).
7. Jiang, these proceedings.
8. E. Christova and E. Leader, these proceedings, arXiv:hep-ph/0412150.
9. O.Y. Shevchenko, these proceedings; A.N. Sissakian, O.Y. Shevchenko and O.N. Ivanov, *Phys. Rev. D* **70** 074032 (2004).
10. Stamenov, these proceedings; Ermolaev *ibid.*, Goshtasbpour, *ibid.*
11. SMC, E. Rondio, these proceedings; SMC, B. Adeva *et al.*, *Phys. Rev. D* **70**, 012002 (2004).
12. COMPASS, C. Schill, these proceedings.
13. HERMES, A. Airapetian *et al.* *Phys. Rev. Lett.* **84**, 2584 (2000).
14. PHENIX, Y. Fukao these proceedings.
15. PHENIX, S.S. Adler *et al.*, *Phys. Rev. Lett.* **93**, 202002 (2004).
16. STAR, J. Sowardski, these proceedings, arXiv:hep-ex/0501001.
17. B. Jäger *et al.*, *Phys. Rev. Lett.* **92**, 121803 (2004).
18. M. Glück *et al.*, *Phys. Rev. D* **63**, 094005 (2001).
19. W. Vogelsang, these proceedings.
20. PHENIX, S.S. Adler *et al.* *Phys. Rev. Lett.* **91**, 241803 (2003).
21. PHENIX, K. Okada, these proceedings.
22. G. Sterman and W. Vogelsang, arXiv:hep-ph/0409234.
23. PHENIX, E. Kinney, these proceedings; M. Togawa, *ibid.*
24. Q. Xu, these proceedings; V.L. Rykov *ibid.*
25. PHENIX, Makdisi, these proceedings.
26. STAR, A. Ogawa, these proceedings; STAR, J. Adams *et al.* *Phys. Rev. Lett.* **92**, 171801 (2004).
27. F. Murgia, these proceedings.
28. U. D'Alesio and F. Murgia, *Phys. Rev. D* **70**, 074009 (2004).
29. E704, A. Bravar *et al.*, *Phys. Rev. Lett.* **77**, 2626 (1996).
30. U. D'Alesio, these proceedings; M. Anselmino *et al.*, arXiv:hep-ph/0412236.
31. M. Boglione, these proceedings; M. Anselmino *et al.*, arXiv:hep-ph/0412022.
32. HERMES, G. Schnell, these proceedings; HERMES, A. Airapetian *et al.*, arXiv:hep-ex/0408013.
33. A. Prokudin, these proceedings; M. Anselmino *et al.*, arXiv:hep-ph/0412316.
34. A. Mukherjee, these proceedings; A. Mukherjee, M. Stratmann and W. Vogelsang, *Phys. Rev. D* **67**, 114006 (2003).
35. COMPASS, P. Pagano, these proceedings.
36. COMPASS, R. Joosten, these proceedings; HERMES, P.B. van der Nat, *ibid.*
37. A. Bacchetta, these proceedings; A. Bacchetta and M. Radici, arXiv:hep-ph/0412141.
38. A. Efremov, these proceedings; P. Ratcliffe, *ibid.*
39. COMPASS, V. Alexakhin, these proceedings; D. Neyret *ibid.*
40. COMPASS, J. Friedrich, these proceedings; HERMES, S. Belostotski, *ibid.*
41. HERMES, H. Marukyan, these proceedings; HERMES, R. Fabbri *ibid.*;
HERMES, A. Rostomyan *ibid.*

SUMMARY OF PARALLEL SESSION 8, POLARIZED SOURCES, TARGETS AND POLARIMETRY

T. WISE

University of Wisconsin, Madison, USA

The presentations of parallel session eight are summarized.

1. Introduction

This diverse session consisted of two talks related to polarized electron sources, ten on various aspects of thermal velocity atomic H and D sources used as jets or to feed storage cells, two on proposed ion sources, one on a polarimeter for a ^3He gas target, and five describing solid targets.

2. Electron sources

Of the above categories, the development of pulsed polarized electron sources for linear colliders appears to be developing most rapidly. A well characterized commercially available gun was described. The performance includes 2 nC per bunch with 50 femto-second bunch lengths and operating vacuum of 10^{-10} . Polarizations exceeding 85% are now obtainable with MBE grown GaAs cathodes. Another talk concluded that the even more demanding needs of future colliders can be met.

3. Polarized thermal velocity H and D targets

This rather broad topic dominated the session. H or D gas targets are currently installed or are under construction at five facilities.

The Hermes group reported on their recent running experience with a transverse guide field and their successful efforts to avoid the very narrowly spaced resonances between hyperfine states 2-4. At Bates an atomic beam source and target has been installed inside the magnetic field of the BLAST spectrometer. Solutions to several unexpected problems related to the immersion of the entire source in the strong field of the BLAST spectrometer were described. The target is currently in use for data taking. At COSY a storage cell target system is nearing completion. Their atomic beam source is operational and tests of prototype storage cells are in progress. The ultra cold jet at Michigan is finally nearing

completion. The last major component, a large cold bore RF transition, is being designed and will be installed in the near future. At BNL a polarized H jet was installed in RHIC early in 2004, and during that run the performance of the jet exceeded expectations on two fronts. The beam intensity and therefore target thickness was higher than the predictions of modeling codes and exceeded previous records. Secondly, the RF transitions had efficiencies of 99.7% resulting in high and stable target polarization. The jet was successfully used to calibrate the polarization of the RHIC proton beam. At the same time the analyzing power A_n for the p-p elastic reaction at low momentum transfer was measured.

Several talks presented systematic studies of the processes used to produce polarized thermal velocity atomic beams. One study, in the very early stages, is attempting to develop a model of beam formation and scattering by tracking the collisions of individual atoms with their neighbours.

4. Proposed ion sources

The CIPIOS pulsed polarized H and D ion source previously used at IUCF will be upgraded for use at the new JINR superconducting NUCLOTRON accelerator. At RHIC there is a possibility to accelerate polarized $^3\text{He}^{++}$. To this end a feasibility study for production of polarized ^3He gas by metastability exchange, followed by transfer of the gas into the new EBIS pulsed ionizer was presented.

5. Solid targets

Presentations on solid targets included three talks on the COMPAS LiD target at CERN. The reported improvements were attributed to cryogenic upgrades which allow larger target volumes at colder temperatures, and to fine tuning of the buildup process. The buildup time to 40% deuteron polarization has been reduced to 48 hours and reaches a maximum of +57% or -52% in five days. One talk presented a possible explanation for the puzzling observation of unequal positive and negative saturation values.

SUMMARY OF PARALLEL SESSION 7, ACCELERATION, STORAGE, AND POLARIMETRY OF POLARIZED PROTONS

A. LEHRACH

Institut für Kernphysik, Jülich, Germany

In total 18 talks were presented in session seven, focusing on the acceleration, storage, spin flipping, and polarimetry of polarized beams at existing facilities, and discussing plans for polarized beams at future machines.

1. Introduction

Over the last decades many efforts have been made to accelerate polarized beams in the GeV energy range. This includes development of techniques to overcome depolarizing resonances, improvements of polarimetry as well as performing benchmarking experiments and applying new theoretical approaches to describe spin dynamics in circular machines. In session seven, recent developments and experiences at existing facilities, present status and new ideas of polarimetry, and future plans for polarized beams were presented. In the plenary talk of the session W.W. Mackay discussed the status of polarized protons in AGS and RHIC, emphasizing recent developments and future plans.

2. Acceleration, Storage, and Spin Flipping at Existing Facilities

In this part of the session the acceleration, storage, and spin flipping at different facilities like the Brookhaven Alternating Gradient Synchrotron AGS and Relativistic Heavy-Ion Collider RHIC, the Cooler-Synchrotron COSY at Jülich, the JINR Nuclotron at Dubna, and the Bates South Hall Ring at MIT-Bates were discussed.

Two talks were given on the status of the AGS polarized proton beam and measures to improve the polarization. H. Huang reported the progress of polarized proton acceleration. In 2004 a new warm helical snake was installed, replacing the old solenoidal snake. This snake was built in very short time by M. Okamura et al. from Riken (Japan). It provides an up to 8% partial snake in the energy range of the AGS with low transverse phase space coupling. The effect of horizontal parameters like beam emittance and betatron tune is now of less concern compared to the situation with the old solenoidal snake. By this means

together with the existing AC dipole and improvements to the polarized source, the polarization at AGS extraction could be improved significantly from roughly 40 to 50%. The AGS CNI polarimeter, which is able to measure polarization during acceleration, greatly supported this progress. T. Roser discussed orbit and optics matching needed for the ion optical integration of the new 30% super-conducting helical snake into the lattice. This new strong partial snake is planned to be installed in the AGS in 2005. Furthermore, spin tracking results were shown, confirming the feasibility of accelerating highly polarized beams in the AGS. It was also proposed to operate the two new helical snakes simultaneously. This is to some extent similar to the operation of two full snakes in RHIC. If the vertical tune and super-periodicity have common factors, as in the AGS, and a proper position of the two snakes in the ring is chosen, the strength of the two snakes adds during strong resonance crossing and almost cancels at injection and extraction, where the invariant spin axis should be almost vertical. Implementing this new scheme will further increase the performance of the AGS with respect to high polarization, opening the way to providing highly polarized beams for the RHIC Spin Physics Program.

Recent developments and future plans for polarized beam in RHIC were presented by M. Bai. During the run in 2004, different working points have been experimentally investigated to improve beam polarization and beam lifetime. The performance of polarized beam was further improved by scanning snake currents at injection. A new setup of the machine has been established, demonstrating better luminosity and polarization transmission efficiency. The observation of a $3/4$ snake resonance in RHIC was reported by V. Ptitsyn. The source for this type of spin resonance is orbit distortions due to relative quadrupole misalignments and snake field errors. Misalignment data are utilized to perform orbit correction with rms values down to less than 1 mm. The question was raised whether the ideal orbit is centered in the quadrupoles or in the beam position monitors. For the preparation of the next run with polarized beams in RHIC, improved orbit control, optimized snake setup, and proper choice of betatron tune, have highest priority.

Spin manipulation studies of vertical polarized protons, vector and tensor polarized deuterons, and the investigation of higher order resonances, were carried out by the international Spin@COSY collaboration, extending the unique spin experiments done at the IUCF cooler ring to higher energies at COSY. The experimental results were presented by A.D. Krisch, spokesperson of this collaboration. For these experiments very high beam polarization of above 80% for protons and up to 70% for deuterons was provided at about 2 GeV/c beam momenta in COSY. A remarkably high measured proton spin-flip efficiency of $99.92 \pm 0.04\%$ was achieved with a strong ferrite-core water-cooled RF dipole. With polarized deuterons, a very good spin-flip efficiency of $97 \pm 1\%$ was also measured, proving that spin-flip efficiency as well as resonance strength for vector and tensor polarization are in good agreement within the errors. The striking behavior of the spin-1 tensor polarization during spin-flips recently found at IUCF was confirmed. For higher order spin resonance studies, a well-elaborated procedure to move betatron tunes during the COSY cycle was applied. As expected, total spin-flip was observed at a very strong first-order intrinsic spin resonance. Third-order spin resonances were measured to be much stronger than second-

order spin resonances for the experimental conditions.

The 10 GeV Synchrotron at JINR Dubna, serving over 20 years for intense study of polarization phenomena in high-energy spin physics, was finally shut down in 2002. Yu.K. Pilipenko gave a historical overview of milestones for spin physics technology and reported on recent polarized deuteron beam acceleration at the new super-conducting JINR Nuclotron accelerator. Utilizing the present one-turn injection mode with a D^+ beam provided by the existing POLARIS source, an intensity of $1.3 \cdot 10^8$ polarized deuterons per pulse was realized with a high vector polarization of more than 60%. As simulations indicate, depolarizing resonances for deuterons are absent in the energy range of the Nuclotron, and vector polarization of deuterons could be preserved during acceleration. The required polarized beam intensity for the physics program of roughly 10^{10} deuterons per pulse is planned to be reached by multi-turn charge exchange injection of polarized D^- ions. The existing D^+ plasma charge exchange ionizer has therefore to be modified to a D^- ionizer.

In a talk by W. Franklin about the Bates South Hall Ring, opportunities for the study of polarization phenomena with polarized electrons were emphasized. Different devices, such as a Compton polarimeter for polarization monitoring, a full Siberian snake delivered by the Budker Institute at Novosibirsk to prepare longitudinal polarized beam at the target, and an RF dipole from Michigan to allow spin reversal of stored beams, are the ingredients for this ring to be a unique instrument for spin physics experiments. A way to calibrate the strength of the Siberian snake and to measure spin tunes was highlighted, utilizing the spin-flip device. Fill-by-fill polarization results were presented, showing high and reliable polarization with an average value of 66.2%, continuously monitored over many months.

3. Polarimetry

Several talks were given on polarimetry, discussing the performance of Compton and CNI polarimeters, presenting calculations for the determination of deuteron polarization at high energy, proposing a Stern-Gerlach polarimeter, and showing polarization measurements performed by Beam-Beam Counters at an experimental installation.

A second talk by W. Franklin dealt with the MIT-Bates Compton polarimeter. Compton polarimetry is well established at high energy. At lower energies the analyzing power drops dramatically to below 0.05. Nevertheless, Bates aims for precise polarization measurements on a fill-to-fill base. Typically between 4 and 5% precision has been reached. High and reliable polarization was monitored during a run period of ten months for the BLAST experiment.

Two talks were given on CNI polarimetry at AGS and RHIC. In his invited talk, A. Bravar discussed spin dependence in elastic pp and pC scattering in the CNI region. Different measurements for elastic pC and pp scattering up to 100 GeV at RHIC, and results from the pC polarimeter at AGS, were compared with theoretical predictions. Analyzing powers in the CNI region indicate that pp does not need a hadronic spin-flip term for its explanation, whereas pC data essentially require hadronic spin-flip. The status of the new polarized atomic beam target needed for absolute polarimetry at RHIC was presented;

this achieved remarkable performance in terms of target thickness and polarization. All CNI polarimeters in Brookhaven's AGS and RHIC operate reliably, and serve as precise diagnostics tools for polarized beam setup and monitoring. A. Svirida's talk was focused on the pC polarimeter in the AGS and RHIC, pointing out that these experimental setups reached outstanding performance, accumulating one million events per second thanks to deadtime free data acquisition with in-flight carbon event selection and powerful electronic module design. The AGS and RHIC polarization measurement history of the 2004 run was shown. CNI polarimetry was utilized to setup the accelerators for polarized beams. The pC polarimeters at AGS and RHIC meet all requirements, operate with excellent performance, allow spin dynamics studies, and in addition provide interesting spin physics which contributes to the understanding of the hadronic spin-flip contribution to elastic scattering in the CNI region.

In a theoretical study, N.H. Buttimore investigated the analyzing power for deuteron carbon scattering at high energy. Introducing a kinematically scaled ratio between helicity flip and non-flip, he calculated analyzing powers including electromagnetic and hadronic amplitudes of dC scattering. Depending on the ratio for the helicity flip, large analyzing powers above 1% are expected in the t range of about $0.05(\text{GeV}/c)^2$.

The design and test of a prototype cavity for a Stern-Gerlach polarimeter installed at the MIT-Bates accelerator complex was presented by P. Cameron. This concept could provide a cheap, fast, accurate, and non-destructive polarimeter. The cavity is operated in a TE011 mode and requires high precision alignment at a level of a few micro radian, sophisticated mode damping, and frequency tuning. Design work for dampers and tuners is under way. Requirements and restrictions for the operation of such a polarimeter at RHIC energies or even higher energies were discussed, and seemed ambitious.

Results for local polarimetry of proton beams with the STAR Beam-Beam Counters (BBC) were presented and discussed by J. Kiryluk. Procedures have been developed to provide a very fast, non-destructive local on-line polarimeter for both colliding beams at the STAR interaction point. Cross calibration with the RHIC polarimeter shows unexpected BBC analyzing power for single spin asymmetry, of unknown origin. Strong pseudorapidity dependence of analyzing power was observed. Furthermore, systematic studies were carried out for random spin fill patterns. A method to tune the spin rotators for longitudinal polarized beam at the STAR interaction region was also established. It allows the adjustment and monitoring of longitudinal polarization, with contributions from vertical and radial beam polarization components below the 5% level.

4. Spin Motion in Circular Machines

In two talks the influence of coherent betatron oscillations on spin dynamics in circular machines was discussed.

The effect of coherent betatron oscillations on spin motion was investigated by A. Silenko for the $g - 2$ and EDM experiment. The exact formula describing the dependence of the particle rotation frequency on the particle orbit perturbation was derived. Co-

herent betatron oscillations on the spin tune and vertical motion of spin give only small contributions, and corrections can be neglected.

A scheme to suppress coherent betatron oscillations due to injection mismatch of muons in the $g - 2$ experiment utilizing nonlinear fields was proposed by Yu.M. Shatunov. Simulation showed that coherent betatron oscillation can be damped within the first 30 turns after injection with moderate requirements for the damping device. A layout for an octupole magnet system was presented, which would meet the requirements in terms of field strength and time structure of the field. The next step is to simulate this effect with more realistic phase space distribution of the circulating muons.

5. Plans for Polarized Beams at Future Machines

Three talks were given on plans for polarized beams at future projects: the Electron-Ion Collider eRHIC at Brookhaven, the High-Energy Storage Ring HESR at the new Facility for Antiprotons and Ion Research (FAIR) at GSI in Darmstadt, and the Japan Proton Accelerator Research Project J-Parc currently being constructed by JAERI and KEK at the JAERI Tokai campus in Japan.

The project plan, polarization issues like self polarization, depolarization and spin matching for the eRHIC electron (positron) ring, were discussed by D.P. Barber. One of the main design criteria is the integration of this ring into the existing RHIC collider facility, especially with respect to the interaction region. A layout was presented which meets all requirements, including spin preparation for the interaction, and spin matching needed for polarization build up. Spin tracking simulations using the SLICK code were performed, including magnet misalignments to estimate the maximum equilibrium polarization, and polarization build up times. High degrees of polarization in acceptable buildup times are expected, taking first-order spin resonances into account. To simulate higher order spin resonance effects, Monte-Carlo spin diffusion simulations are being carried out, calibrated with the SLICK spin tracking code. In the next step, simulations with thick polarized beams including detector fields are to be performed.

A scheme to polarize antiprotons by a technique called spin-filtering in a dedicated antiproton-polarizer ring was presented in a plenary talk by F. Rathmann. A. Lehrach discussed how to accelerate this polarized antiproton beam in the HESR, which is proposed as a 15 GeV/ c antiproton storage ring. A synchrotron mode would have to be added, and additional devices included for measuring and preserving beam polarization. Two solutions were presented to preserve polarization during acceleration, a full Siberian snake combining helical and solenoidal magnetic fields, and a strong solenoidal snake including skew quadrupoles for phase space decoupling. A decision for one of the two solutions should be taken after intense particle and spin tracking studies, including higher order field errors and feasibility studies of the snake magnets.

The status of construction, the main parameters, and the option for polarized beams at the J-PARC accelerator complex, were presented by H. Sato. Calculation of resonance strength has been performed for the 3 GeV PS booster and the 50 GeV PS driver ring. Dif-

ferent schemes to preserve polarization during acceleration were discussed for these rings. Further investigations are being carried out by an international collaboration to strengthen the polarized proton program and provide a conceptual design for polarized beams at J-PARC.

6. Highlights and Outlook

Existing accelerator facilities show excellent performance with highly polarized beams and reliable beam operation. Experiments to study spin dynamics with and without Siberian snakes were performed at different facilities like the AGS/RHIC complex, MIT-Bates, COSY and the JINR Nuclotron accelerator complex. The observation of snake and higher order spin resonances, different ways to calibrate Siberian snakes and spin rotators, and investigation of spin-flip of polarized protons and deuterons, are all important activities with respect to existing and future machines for polarized beams and mandatory for successful polarized beam setup. The installation of new strong partial snakes in the AGS is an essential task towards 70% polarized beams for the RHIC Spin Physics Program. Applying two partial snakes in the AGS simultaneously can potentially further improve the performance of polarized beams in the RHIC collider complex. Different polarimeters and new ideas for future devices were presented. Existing polarimeters operate with high performance and greatly support the setup of polarized beams, as well as provide spin physics output. In particular, polarimetry in the CNI region looks very promising for new projects with polarized protons or deuterons, even at very high energy. The effect of coherent betatron oscillations on spin motion for the $g - 2$ and EDM experiments seems not to be of major concern from the theoretical point of view, and can be damped in the $g - 2$ experiment by applying non-linear fields. Proposals and conceptual designs for polarized beams in new projects like eRHIC, HESR and J-PARC were presented. Concepts and feasibility studies are carried out in international collaborations to ensure world-class solutions and performance for polarized beams. These new projects promise a bright future for spin physics experiments.

FUTURE COLLIDERS

A. DESHPANDE

Department of Physics & Astronomy, SUNY-Stony Brook, Stony Brook, U.S.A.
RIKEN-BNL Research Center, Brookhaven National Laboratory Upton, U.S.A.

I review initiatives for future lepton hadron colliders being pursued by the particle and nuclear physics communities in the US. The first one is the eRHIC at Brookhaven National Laboratory (BNL), which will require construction of a high intensity, polarized electron beam facility next to the Relativistic Heavy Ion Collider (RHIC) complex that is just becoming fully functional. It will also need modification of the hadron rings, but these changes will disrupt neither the heavy ion physics nor the RHIC spin program that has just started, both of which are expected to continue into early in the next decade. The second option recently being considered is the construction of a hadron ring next to the existing CEBAF electron beam facility at the Jefferson Laboratory. While severe physical and geographical constraints exist for this proposal, the use of futuristic technology in the project may allow polarized electron light ion collisions at unusually high luminosities. It is hoped that at least one of these proposals will eventually be built.

1. Electron Ion Collider & Fundamental Questions in QCD

By the end of this decade, the advance of current and planned research into the fundamental structure of matter will require a new facility, the Electron Ion Collider (EIC). The EIC will collide high-energy beams of polarized electrons with polarized protons and neutrons, and unpolarized beams of electrons with atomic nuclei with unprecedented intensity. Research at the EIC will lead to a detailed understanding of the structure of the proton, neutron, and heavy nuclei as described by Quantum Chromo-Dynamics (QCD), the accepted theory of the strong interaction. The EIC will establish quantitative answers to important questions by delivering dramatically increased precision over existing and planned experiments, and by providing completely new experimental capabilities. Indeed, the EIC will probe QCD in a manner not possible previously.

This paper summarises the scientific case, possible designs and operating scenarios of the EIC. While realization of the EIC requires a significant advance in the development of efficient means of producing powerful beams of energetic electrons, an important consideration for choosing the site of the EIC is the planned upgrade to the Relativistic Heavy Ion Collider (RHIC) at Brookhaven National Laboratory. The upgrade planned for RHIC will fully meet the requirements for the ion beam for the EIC, providing a distinct advantage in terms of cost, schedule and the final operation. This realization of the EIC will be called eRHIC in this paper.

Another idea being considered for EIC is a possible construction of a hadron beam facility at Jefferson Laboratory. This will augment the existing electron beam facility (CEBAF) and provide a high luminosity polarized collider, although according to present expectations, only a few low mass ion beams would be possible and the center of mass energy would be about half that of eRHIC. This version of the EIC will be called the Electron Light Ion Collider (ELIC) in this paper.

The EIC will probe in detail the framework of Quantum Chromo-Dynamics. QCD was developed in the 1970s, primarily from the experimental discovery at Stanford Linear Accelerator Center of hard electron scattering from point-like constituents in the proton. Since then, hard scattering experiments carried out at high-energy physics laboratories have provided information that determined, with good precision, the momentum distribution of the quarks in the nucleon, and have shown that the energy dependence of hard scattering is described well by QCD. An important discovery that helped establish QCD was the determination of the running of the strong coupling constant and the property of asymptotic freedom of the strong interaction. However, there are still many unanswered questions:

- How do we understand the momentum distribution and spin structure of the proton and neutron in terms of the fundamental quarks and gluons? Does the orbital angular momenta of partons play a significant role?
- In the hard scattering process, quarks or gluons are knocked out but only hadrons are seen in the final state. Can we understand this phenomenon of hadronization in terms of QCD?
- What is the role of quarks and gluons in understanding the microscopic structure of atomic nuclei, the basis of the physical world? In particular, what is the nature of short range internucleon forces?
- Can we observe new phenomena predicted by QCD, involving saturation of gluons at high energies, similar to the Bose-Einstein condensation in atomic nuclei at low temperatures?

2. Physics with an Electron Ion Collider

Most important results from fixed target DIS experiments performed so far have made inclusive measurements of structure functions, primarily because the hadronic final states in hard collisions in fixed target experiments are difficult to isolate and identify. The eRHIC at BNL will make these in the widest $x - Q^2$ range available so far [1]. The Collider geometry in general offers a unique capability for measuring “flavour tagged” structure functions by providing access to a wide range of final states arising from the virtual photon-parton hard scattering. The collider geometry makes measurement of semi-inclusive reactions very efficient, so that quark and gluon distributions in nucleons, nuclei, and possibly even mesons, can be mapped in a flavour-tagged mode. This will provide a decomposition of the parton densities, over a large kinematic range, into the contributions from different parton types: up, down and strange quarks as well as gluons. The ability to tag the hadronic final state will allow measurements of the nucleon structure function at large x , so that a reliable and

precise determination of the ratio of the quark distribution in neutrons and protons can be made in a regime where several competing theoretical predictions exist.

Fixed target polarized DIS experiments yielded the surprising information that the quark spins account for only 30% [2] of the total spin of the nucleon. Recent results [3], with large uncertainty, indicate that gluons may play a significant role in constituting the nucleon's spin. While experiments with polarized protons at the Relativistic Heavy Ion Collider (RHIC) [4] will provide significant information for unraveling the role of gluonic spin, energetic collisions using polarized electrons and protons will provide important complementary, and in some instances essential, new information using well established experimental methods and theoretical techniques currently used by the DIS community at HERA. The eRHIC, running at its highest energy, will provide crucial data at lower x than has been possible in any previous experiment. At small x it will provide separation between the polarization effects in the vacuum and nonvacuum channels. Determination of spin structure functions in this yet unmeasured low x region will bring a unique perspective to our understanding of pQCD. Direct measurement of the polarization of quarks in a broad range of x are needed to determine the polarization of quarks and antiquarks in the sea, currently a matter of controversy within sophisticated and successful models of the nucleon.

A complete characterization of the partonic substructure of the nucleon must go beyond a picture of collinear non-interacting partons. It must include a description of the correlations between the partons densities over impact parameters, and a comparison of the parton wave functions of different baryons. Progress in this direction can be realized by measuring hard exclusive processes where, in the final state, a photon, a meson or several mesons are produced along the virtual photon direction, and a baryon is produced in the nucleon fragmentation region. These processes are expressed, as a result of the new QCD factorization theorems, through a new class of parton distributions termed Generalized Parton Distributions (GPD). The collider kinematics are optimal for detecting these processes. The presence of polarization provides additional exciting opportunities, for example comparisons of the spin structure of hyperons and nucleons. If successful, such a program would greatly expand our knowledge about the role of non-perturbative QCD in hadronic structure.

Most hadronic matter exists in the form of nuclei. The ability of the EIC to collide electrons with light (heavy in case of eRHIC) nuclei opens horizons fundamental to nuclear physics. For example, the role of quarks and gluons in nuclei may be investigated by comparing the changes in parton distributions per nucleon as a function of the number of nucleons. Seminal DIS experiments off nuclei a) showed that the distribution of quarks is altered by the nuclear medium from that observed in nucleons, b) led to the discovery of the lack of enhancement of sea quarks in the nuclei that was expected based on models of the meson picture of nuclear forces, and c) provided tantalizing indications of significant modifications of the gluon distributions at moderate x . Studies of parton modifications at $x \approx 0.1$ will be most sensitive to the underlying quark-gluon structure of the internucleon interactions that are usually described within effective low energy mesonic theories. It is

particularly important to establish the quark distributions at small values of x where the presence of the other nucleons in the nucleus will alter (“shadow”) the partonic distributions. A nuclear enhancement of valence quarks, sea quarks, or gluons would indicate the relative importance of meson, quark, and gluon exchange at various distance scales.

How do the coloured quarks and gluons knocked out of nucleons in DIS evolve into the colourless hadrons that must eventually appear? This process is one of the clearest manifestations of confinement: the asymptotic physical states must be colour-neutral. Hadronization is a complex process that involves both the structure of hadronic matter and the long range non-perturbative dynamics of confinement. A fundamental question related to hadronization is how and to what extent the spin of the quark is transferred to its hadronic daughters. The ability to “tag flavour” and a facility that creates readily detectable jets are crucial for these experiments. The EIC makes it possible to strike quarks and observe the complete array of decay products from the nucleon or nucleus. The fact that nuclei also may be used is essential to this study. The ability to place varying amounts of nuclear matter in proximity to the system produced forward along the photon direction and the recoiling quark system, allows one to perturb in a controlled way the early stages of its space-time evolution, and to measure the energy imparted to the nuclear matter by the emerging parton. At eRHIC very high energy DIS on heavy nuclear targets with electromagnetic probes offers new opportunities for studying partonic matter under extreme conditions. Particularly intriguing is the regime of very low x ($x < 10^{-3}$) where gluons dominate. Measurements of the proton structure function showed that the gluon distribution grows rapidly at small x for Q^2 greater than a few GeV^2 . When the density of gluons becomes large, they may saturate and give rise to a new form of partonic matter: a colour glass condensate [5]. It is a coloured glass because the properties of the colour-saturated gluons are analogous to that of a spin glass system in condensed matter physics. It is a condensate because the gluons have a large occupation number and are peaked in momentum about a typical scale of the saturation momentum Q_s .

This state of strongly interacting matter would be universal in that it is insensitive to the hadronic matter in which it resides. The gluonic density/ cm^2 is enhanced in nuclei relative to that in individual nucleons by a factor $A^{1/3}$. Therefore, high parton density effects will appear at much lower energies in nuclei than in protons. The Electron Ion Collider at BNL, the eRHIC, with its heavy nuclear beams and e^- - A center-of-mass energies of at least 60 GeV, and ability to study inclusive and semi-inclusive observables, will probe this novel regime of Quantum Chromo Dynamics.

3. Realization of the EIC at BNL: eRHIC

The eRHIC Zeroth Design Report (ZDR) [6], is the first detailed document on the studies addressing how the accelerator and the interaction region of this collider might be constructed. The ZDR resulted of several month studies performed jointly by BNL and MIT-Bates, with close collaboration with scientists from BINP (Novosibirsk) and DESY (Hamburg). The goal of this study was to develop an initial design for the eRHIC to investigate accelerator physics issues most important for its design and to evaluate the luminosities

that could be achieved in such a collider if it were to be built in near future with minimal R&D. Other aims included identifying specific accelerator parameters, improvements to which would need varying levels of R&D but would lead to significantly higher luminosity. Finally, we were also charged with making a preliminary but realistic cost estimate for the new electron accelerator facility and the modifications of the RHIC rings to incorporate the interaction region. One of the working assumptions while developing this design was that the time scales for realizing this collider would be short enough, as such at least one or two experiments at RHIC would still be taking data with the upgraded RHICII collider and upgraded RHIC detectors. The eRHIC and those experiments would share one of the hadron beams in RHIC.

The physics program overview presented in the previous section demands nominally an e-p collision luminosity of $10^{33} \text{ cm}^{-2} \text{ sec}^{-1}$ and CM energies around 100 GeV to probe deep inside the nucleon. It also requires high beam polarization for proton beams at the high energy, and it was deemed important that a neutron rich nucleus such as $^3\text{He}^{++}$ or deuteron be storable. The RHIC proton and heavy ion beam can be stored at 250 GeV and 100 GeV per nucleon, respectively as per its design, but they can also be stored at lower energies. The proton beams in RHIC are polarized and can be manipulated either to collide longitudinally or transversely in experimental areas. The eRHIC will utilize this for collisions with variable center of mass energies and have the following additional abilities: It will allow longitudinal or/and transverse polarization in the interaction region (IR) for both the electron and the polarized hadron beams. It is expected that if a high enough intensity polarized source of He is prepared in the near future, RHIC will be able to accelerate He^{++} to its top energy without significant loss in polarization. The main design line for eRHIC presented in the ZDR is based on the construction of a 10 GeV electron/positron storage ring, adjacent to either 12 or 4 o'clock collision point of the RHIC, and will collide with one of the RHIC hadron beams. The electron beam energy will be variable down to 5 GeV with minimal loss in luminosity and in polarization for collisions. The electron beam injector system will have a re-circulating linac fed by a polarized electron source. With this design it was concluded that we can achieve of the order of $5 \times 10^{32} \text{ cm}^{-2} \text{ s}^{-1}$ luminosity for the high-energy mode ($10\text{GeV} \times 250\text{GeV}$) of e-p collisions, if the electron beam facility is designed using today's state-of-the-art but tested and reliable accelerator technology without an extensive R&D program. For the electron-gold ion collisions ($10\text{GeV} \times 100\text{GeV/u}$) this design, results in a luminosity of $5 \times 10^{30} \text{ cm}^{-2} \text{ s}^{-1}$. The potential to go to significantly higher luminosities by increasing the electron beam intensity is being considered now. A polarized positron beam of 10 GeV energy and high intensity will also be possible: starting with an unpolarized positron source, accelerating them to top energy in the linac, and then storing them in the ring at full energy results in self-polarization due to synchrotron radiation.

The eRHIC will require modifications of the RHIC hadron rings. Most important among them are a) the addition of electron cooling system, to achieve and maintain small beam emittance (this is also required for the RHICII upgrade plans), and b) the increase in the ion intensity by increasing the number of bunches in each ring. The ZDR assumes 360

bunches per ring will be possible, which is consistent with the capacity of the present RF system, although in RHIC design only 120 bunches are planned to be filled. The feasibility of such intensity increases requires studies on topics such as the effect of possible electron cloud formation associated with high bunch numbers. These will be pursued in the next few years.

A possible alternative design for eRHIC using an electron accelerator based on an energy recovery superconducting linac, instead of a storage ring, is also being studied and is presented in the ZDR as an appendix. Preliminary estimates show that this design option will produce higher luminosity, but would require more R&D for the polarized electron source and the energy recovery technology. Consequently this has a longer time horizon and at present has a larger uncertainty in the estimation of costs involved. It is expected that work on both options for eRHIC will continue in the foreseeable future until the final construction time demands freezing the design, and the technology.

A design for the interaction region for the eRHIC has been developed. It provides the necessary focusing at the collision point as well as fast, effective beam separation for the hadron and electron beams. The non-colliding RHIC ion beam avoids the IR region by excursion of its trajectory (at the outskirts of the detector volume). The IR design includes spin rotators in both electron and ion rings. Preliminary issues related to the integration of the detector into the IR design have also been considered, including the regions of intense synchrotron radiation by the bends in the electron beams. Acceptable solutions seem possible. The interaction region of the linac-ring design allows distinct advantages for the detector design, as it allows long ($\pm 5\text{m}$) element free spaces which would potentially inhibit the interesting acceptances for low Q^2 physics.

4. Realization of the EIC at Jlab: ELIC

While a detailed study of the realization of ELIC, the Electron Light Ion Collider, at Jlab has not taken place as yet, serious attempts to reach at least 10-50 times more luminosity compared to those deemed realistic at eRHIC are attempted. The design is based on a linac-ring collider concept. The idea is complementary to eRHIC: there exist a high intensity 5 GeV electron beam facility CEBAF at Jlab. The realization of ELIC would need construction of a high intensity hadron beam facility. CEBAF will be used for one pass acceleration of electrons. Energy Recovery (ER) is used for rf power saving and beam dump requirements. A Figure-8 storage ring for hadrons is planned, which should allow flexible spin manipulation of all ions of interests: protons, deuterons and helium. Unpolarized beams up to Calcium may be possible. A circulator ring for the electrons may be used in addition for high current polarized photo-injector requirements. Luminosities of the order of few times $10^{34} \text{ cm}^{-2} \text{ sec}^{-1}$ are aimed for in each interaction region. The Figure-8 design allows four interaction regions, a distinct advantage compared to the eRHIC design, which nominally allows one interaction region in its ring-ring design. The linac ring design of eRHIC would allow more IRs but at substantial extra cost. The physical size of the Jefferson laboratory site limits the maximum length of the hadron ring to about 1.2 km, which makes the highest reachable beam energies 100 GeV for protons, although recently possibilities

of 150 GeV proton beams have been discussed. The design luminosity calls for putting about 2000 bunches in the 1.2 km hadron ring. For comparison, at eRHIC there would be 360 bunches spread over 3.8 km, and with present understanding of the RHIC hadron ring that is considered a significant R&D project needing much attention and study over the next few years. It is in this type of machine parameter that the ELIC design presents itself as a truly futuristic machine requiring more R&D costs and time compared to eRHIC, and making the time horizon for its realization longer than that pursued for eRHIC.

While number of extremely challenging collider related issues remain to be resolved, aggressive R&D effort on the following items has already begun: a) Conceptual design of the circulator ring to reduce the high current photo injector and ER linac requirements that will eventually lead to a realistic luminosity limits, b) Simulations of electron cooling and achieving the required short bunches, beam-beam interactions, energy recovery linac physics, and c) experimental tests to address the ERL issues in large scale systems, as well as cooperative R&D efforts between Jlab, Cornell and BNL to address the high current ERL issues.

5. A e-A/p Detector in the Next Decade

The experience gained at HERA with H1 and ZEUS detectors provides significant guidance for the conceptual design of a detector that will measure a complete event (4π -coverage) produced in collisions of energetic electrons with protons and ions, at different beam energies and polarizations. The detector design directly impacts the interaction region design and hence the accelerator parameters for the two beam elements and the effective interaction luminosity. It is expected that the detector and IR design will proceed iteratively in the next few years as the consequence of each beam element on the detector acceptance and each detector element on the collider luminosity are accessed. The e-p and e-A collisions at EICs will produce very asymmetric event topologies, not unlike HERA events. These asymmetries are an advantage if exploited properly. They allow a precise measurement of energy and colour flow in collisions of large and small x partons. They also allow observation of interactions of electrons with photons that are coherently emitted by the relativistic heavy ions. The detector for EIC must detect the scattered electrons, the quark fragmentation products, and the centrally produced hadrons. In addition, it will be the first detector to measure the fragmentation region of the proton or nucleus, a domain not covered effectively at HERA. Further the detector design should pose no difficulties for important measurements such as precision beam polarizations (electron as well as hadron beam) and collision luminosity.

The EIC detector design will allow measurements of partons from hard processes in the region around 90 degrees to the beam pipes, hence called the central region. This region could have a jet tracker with an EM calorimeter backed by an instrumented iron yoke. Electrons from DIS are also emitted into this region and will utilize the tracking and the EM calorimetry. Electrons from photo-production and from DIS at intermediate and low momentum transfer will be detected by specialized backward detectors. With these guiding ideas, one could imagine that the EIC barrel might have a time projection chamber

(TPC) backed by EM Calorimeter inside a superconducting coil. One could use spaghetti calorimetry (SPACAL) for endcaps, and a gem type micro-vertex detector to complement the tracking capacity of the TPC. This type of central detector is fairly standard, and details of the design could be finalized in the next few years using the state of the art technology and experience from more recent detectors SLAC and in Japan.

Forward and backward regions (hadron and electron beam directions) in e-p collisions were instrumented at HERA up to a pseudo rapidity region of ≈ 3.5 . Specialized detectors added later extended this range with difficulty to ≈ 4.5 . One of the most surprising physics that was discovered at HERA concerned diffractive physics, and the final states from these events went to extreme forward and backward areas of $\eta > 3.5$. It is imperative that for the EIC detector this region is not a corner of the acceptance but one a principal focus of investigation. A recent detector design for eRHIC led by the experimental group at MPI, Munich accomplishes just this by allowing continuous access to physics up to an $\eta \approx 6$. The design principles and detector specifics of that detector will be central to the forward and backward detector design of the eRHIC. Additionally, far away from the EIC central detector and IR, there will be roman pots, high rigidity spectrometers including EM calorimetry, and forward electron taggers, all placed to improve the physics of low angle scattering at high energy.

6. Concluding Remarks & An Invitation

The idea of a polarized lepton hadron collider at high energy has now existed for at least 10 years. Various options in Europe have been tried unsuccessfully. Now the EIC designs considered in the US show unusual promise. It is hence time for the nuclear, high energy and hadron physics communities around the world, interested in exploring the most fundamental open questions of QCD, to come together and realize at least one of them. The EIC at BNL eRHIC has been studied in great detail for its feasibility and shows no show stoppers. It is a design that can be realized in good time for continuation of the field of nucleon spin. If pursued and supported aggressively, eRHIC could begin data taking in the first half of the next decade. A community that will carry out physics at this facility currently exists at RHIC, Jlab and at DESY. However, with the impending demise of HERA in the next two to three years, the DESY component, the experts in the field with the largest single block of experience in this type of physics, will have to make decisions regarding their future. If eRHIC is not on the time horizon by then, they may be lost for ever for other large experimental projects coming along in those time scales. It is hence imperative that the EIC community first comes behind the eRHIC project and gives its best to realize this collider. The physics is compelling, hence the case is easy to make. If this is not realized in the aggressive time scale promoted in this paper, other options such as ELIC at Jlab or the linac-ring option at RHIC will become technologically feasible towards the end of next decade.

Having argued that the future lepton hadron machine should be built early and with maximum flexibility, let us realize that no matter which machine and detector ideas become reality, an exciting physics program awaits us. Those of us who are already pursuing this

dream invite those not on board to join the effort. The work done so far is preliminary at best and it can absorb many new interesting, exciting physics ideas and goals as well as details of the detector design. Let me end this article with an invitation [9] to anyone, interested in experimentally exploring the deepest vistas of QCD in a manner unprecedented in its scope and sensitivity, to join this effort.

Acknowledgments

I would like to thank the organizers of this Symposium, in particular Professor F. Bradamante, for inviting me to give this talk. This trip was supported by the RIKEN-BNL Research Center.

References

1. eRHIC White Paper 2002, BNL-68933-02/07-REV
2. EMC, J. Ashman et al., Nucl. Phys. **B 328** 1 (1989)
3. SMC, B. Adeva et al., Phys. Rev. **D58**, 112002 (1998); E143, K. Abe et al. Phys. Rev. **D58**, 112003 (1998), G. Altarelli et al., Nucl. Phys. **B 534**, 277 (1998);
4. G. Bunce et al., Prospects of Spin Physics at RHIC, Ann. Rev. of Nucl. and Part. Science, bf 50 525-575 (2000)
5. L. McLerran, What is the Evidence for Color Glass Condensate? hep-ph/0402137; L. McLerran, The Color Glass Condensate and Small x Physics: 4 Lectures, Lect. Notes Phys. **583** (2002) 291-334
6. Zero-th Design Report for eRHIC, BNL C-A/AP/142, March 2004
7. L. Merminga, Proceedings of the CIPANP2003 Conference
8. I. Abt et al., A detector for forward physics at eRHIC: Feasibility Study, hep-ex/0407053
9. Register yourself for various email information servers for EIC Project related news: <http://www.bnl.gov/eic> or/and contact the author.

CONCLUDING REMARKS

T. ROSER

Brookhaven National Laboratory, Upton, U.S.A.

At the conclusion of the 16th International Spin Physics Symposium, that can be well summarized as “Exciting Spin Physics in a Beautiful Setting”, I would like to express many thanks and give a round of applause to the Symposium Chair Prof. Franco Bradamante and Vice-Chair Dr. Anna Martin for a very successful conference. I would also like to briefly report on the meeting of the International Spin Physics Committee held on Tuesday, October 12. Two new members have been added, Dr. G. Mallot from CERN and Dr. E. Stephenson from Indiana, and two new honorary members were elected, Prof. V. Soergel from Heidelberg and Prof. W.T.H. van Oers from Manitoba. The Committee also elected Prof. K. Imai as new Chair-Elect. Prof. Imai will take over as new Chair of the International Spin Physics Committee on January 1, 2007. Three workshops were approved for sponsorship during 2005: the Workshop on Polarized Sources and Targets (PST2005) held in Tokyo and chaired by Prof. H. Sakai from Tokyo University; the Workshop on High Energy Spin Physics (DUBNA SPIN-2005) chaired by Prof. A. Efremov; and the Advanced Study Institute (ASI) PRAGUE-2005 chaired by Prof. M. Finger. Finally the Committee selected the location of the 17th International Spin Physics Symposium. SPIN2006 will be hosted by Kyoto University in the beautiful city of Kyoto and chaired by Prof. Ken Imai. I hope to see you all again in two years in Kyoto.

This page intentionally left blank



WORKSHOP SUMMARIES

This page intentionally left blank

SUMMARY OF THE X WORKSHOP ON HIGH ENERGY SPIN PHYSICS (NATO ARW DUBNA-SPIN-03)*

A. V. EFREMOV, O. V. TERYAEV

Joint Institute for Nuclear Research, Dubna, Russia

A short description of the X Workshop on High Energy Spin Physics held in Dubna is given.

The X Workshop on High Energy Spin Physics held in Dubna, September 16–20, 2003 was devoted to the memory of Vernon Hughes and L.D. Soloviev. It continued a series of similar meetings, the first of which took place 23 years ago in 1981 under the initiative of the outstanding Russian theoretician Lev Lapidus. Since then, each odd year similar meetings have been carried out in Dubna or in Protvino between the biannual International Spin Symposia. Our meetings enable one to discuss the news accumulated during a year. Its other very important feature has always been an opportunity of participation for a large number of physicists from (former) USSR and East Europe, for which distant trips are complicated for financial (and earlier also by political and bureaucratic) reasons.

The present meeting as well as the previous ones was organized jointly with Poland by professors A.V.Efremov (Dubna) and J. Nassalski (Poland) as co-chairmen. The specific feature of the present meeting was a greater than usual number of participants from abroad (36 out of 96). This became possible not in the least instance owing to the support of JINR, the NATO Science Program, and the Russian Foundation for Basic Research.

The reason of the increased popularity of the ARW became, apparently, that this year has brought a lot of new experimental results, and even more are expected in the near future. First of all, it concerns the spin program of the accelerator RHIC (BNL, USA) to which a number of reports were devoted (I.Alekseev, G.Bunce, L.Bland, A.Bravar, A.Deshpande, S.B.Nurushev, A.Bazilevski, A.Taketani). Collisions of two polarized proton beams accelerated to the highest energies allow one to investigate the important elements of the spin structure of a nucleon, first of all the longitudinal spin contribution of gluons, and also various parton distribution functions and the correlations connected with the polarization.

*This work is partially supported by grants INTAS 00/587, RFBR 03-02-16816 and DFG-RFBR 03-02-04022.

Both the first experimental results and immediate prospects were discussed in the submitted reports.

Other experiments at high energy use the scattering of polarized leptons on polarized nucleons: HERMES at DESY (H.Marukyan -Erevan, A.Nagajtsev - Dubna), CLAS at the JLab (P.Bosted, H.Avakian - JLab), NOMAD (A.Chukanov - Dubna) and COMPASS at CERN (F.Bradamante - Trieste, J.Marroncle - Saclay, M.Sapozhnikov - Dubna).

Very interesting results from the WA99 collaboration on Λ polarization produced by a Σ^- beam were presented by Yu.Alexandrov (Moscow). They showed that the polarization had a maximum at $p_t \approx 1 \text{ GeV}/c$ and decreased at higher p_t . New results on A_N in $\pi^- p_{\uparrow} \rightarrow \pi^0 X$ and $pp_{\uparrow} \rightarrow \pi^0 X$ were presented by PROZA-M collaboration (V.Mochalov, Protvino).

The joint description of so different high-energy processes becomes possible through the application of the fundamental theory of strong interactions - Quantum Chromodynamics (QCD) - and to the remarkable factorization property that the only process-dependent contributions are weak, and therefore can be calculated within the framework of perturbation theory. At the same time, not allowed for such calculations (and demanding, therefore, attraction of model nonperturbative methods) parton distribution and fragmentation functions and parton correlations are universal and do not depend on the process. The theoretical description of the processes with spin participation are more complicated, as always, so the number of such functions increases and the picture connected to them loses the simplicity of the parton model with its probabilistic interpretation.

At present, quark spin distribution functions are the most extensively studied. Modern experimental data are precise enough to include in their QCD analysis not only the perturbative corrections, but also contributions of higher twists connected with transversal motion of quarks inside the nucleon, and transverse components of gluon fields (D.Stamenov - Sofia). Thus, one can exclude with high probability positive polarization of strange quarks. This coincides with the conclusions from the analysis of hyperon anomalous magnetic moments presented in the talk of S.B.Gerasimov (Dubna). The gluon polarization turns out to be large and positive, which supports an explanation of the so-called Spin Crisis due to the axial anomaly contribution. A more direct and accurate measurement of the gluon polarization is possible in semi-inclusive processes. In her talk K.Kowalik (Warsaw) presented this sort of analysis for earlier data from the SMC collaboration, important from a methodical point of view for the analysis of expected data of COMPASS collaboration. In particular, the role of gluons grows, thus demanding a special analysis in the small x region (B.Ermolaev - St. Petersburg) and in diffractive processes (N.Nikolaev - Julich and S.Goloskokov - Dubna).

Other important spin distribution functions are revealed in the scattering of transversely polarized particles. Especially interesting and complicated from the point of view of the theory (and relatively simple from the point of view of experiment) are the processes in which polarization of a single particle, initial or final, is measured. Such single spin asymmetries refer to T-odd effects, i.e. those that violate time reflection invariance. Here, however, we deal with an effective interaction, connected not with a true fundamental T-invariance breaking interaction (in our case, strong, described by QCD), but with subtle effects of fi-

nal state interactions simulating it. Such effects have been studied by theorists for 20 years but have received a new impact in recent years in connection with new experimental data. Though as a whole they are well described by existing theory (A.Efremov, Dubna), development continues. In particular, T-odd distribution functions arising here can lose key properties of universality (A.Metz - Bochum, O.Teryaev - Dubna) and relativistic invariance (P.Schlegel - Bochum).

One more new class is generalized parton distribution functions that appear in the analysis of exclusive hard processes with all final particle registration. There are therefore plenty of spin effects (D.Ivanov - Novosibirsk, M.Burkardt - New Mexico, L.Enkovsky - Kiev, L.Szymanowski and L.Mankiewicz - Warsaw).

An excellent review of density matrix formalism and positivity conditions for general multiple spin asymmetries was presented by X.Artru (Lion).

Research of tensor polarization of vector particles at high energies allows one to investigate mechanisms of lepton, hadron, and nuclear reactions (Z.-T.Liang - Shandong, S.Shimansky -Dubna, V.Saleev - Samara and B.Ioffe - Moscow) and reveal a graceful analogy to graviton formation, discussed also in connection with the possible existence of additional spatial dimensions (A.Pankov - Gomel). Some reports were devoted to tensor polarization of the deuteron, and spin dependence of nucleon-nucleon scattering at intermediate energies (D.Nikolenko - Novosibirsk, J.Uzikov, V.Ladygin, L.Strunov, L.Azhgirej, I.Sitnik and M.Janek - Dubna, V.Kanavetz, D.Novinski, V.Sumachev, D.Svirida - St.Petersburg)

The permanent subject of spin conferences is the so-called Gerasimov-Drell-Hearn Sum Rule proposed for the first time over 30 years ago in Dubna. The results and further prospects for its experimental testing (A.Thomas - Mainz), and the theoretical analysis of parity-violating contributions (K.Kurek - Warsaw) were discussed.

As always, physics and techniques of polarimetry (A.Bravar, O.Jinnouchi, A.Zelensky - Brookhaven, O.Selyugin - Dubna) and the polarized targets and beams (D. Reggiani - DESY, A.Silenko - Minsk and Yu.Pilipenko - Dubna) were discussed as well.

In conclusion, it would be desirable to dwell on the reports which can serve as the "first signs" of a new direction. One of the groups (Spring8) reported (Y. Ohashi - Japan) on the results on recently discovered exotic baryons with the obvious positive strangeness interpreted as a "pentaquark". For the present, polarizing effects for studying its properties are not used. However, since the spin asymmetries are rather sensitive to its (and similar baryons) quantum numbers, so far unknown, there is no doubt that reports on this subject will become usual at forthcoming spin conferences and meetings. This subject should also be added to the spin research program of Dubna's Nuclotron with the new polarized deuteron beam, submitted by Yu.Pilipenko (Dubna).

Another prospective subject that will certainly take on great significance at future spin meetings is the physics of neutrinos. The consideration of spin variables is necessary in studying nucleon-neutrino scattering (V.Ljubushkin - Dubna). It shows a very interesting connection between electroweak processes both at ultra-high and intermediate energies, and neutrino interactions with dense matter (G.Lykasov - Dubna).

All this, as well as the reports given at the final session about the electron beam as a

possible adjunct to the proton accelerator RHIC (project eRHIC, A.Deshpande - BNL) and the ARW Summary by F.Bradamante (Trieste) made an impression that new, interesting events in spin physics are pending.

The Proceedings of the ARW with talks and discussions are published by the JINR Publishing Department (E1,2-2004-80) and sent to all participants, members of the International Committee for Spin Physics Symposia, and to libraries of leading high energy research centres. The XI Workshop on High Energy Spin Physics is planned to be held in September 2005 in Dubna.

SUMMARY OF THE 10th WORKSHOP ON POLARIZED SOURCES AND TARGETS (PST2003)

D. K. TOPORKOV

Budker Institute of Nuclear Physics, Novosibirsk, Russia

The 10th International Workshop on Polarized Sources and Targets was held on September 22-26, 2003 in Akademgorodok, Novosibirsk, Russia. The Workshop was hosted by the Budker Institute of Nuclear Physics of the Siberian Branch of the Russian Academy of Sciences. Over forty physicists representing the major scientific centres from USA, Italy, Germany, The Netherlands, Switzerland, Russia, China and Japan participated in the Workshop. The Workshop is the most recent one of a series held at two-year intervals, the previous one being held in Nashville, Indiana, USA in 2001. The Workshop has covered a wide range of subjects concerned with polarized targets and sources for physics applications. About forty talks were given during the Workshop. The topics included polarized gas targets, polarized solid targets, polarized electron sources, polarized ion sources, photo cathodes, laser driven sources and targets, and polarimetry. An overview talk on each topic was given followed by contributed papers and discussions. The Workshop has shown a great progress made in these fields during the past two years.

The Proceedings of the Workshop will be published soon as a special issue of Nuclear Instruments and Methods in Physics Research, Section A.

The Workshop was supported by grants from the International Committee on High Energy Spin Physics, International Science and Technology Center (SWA 08-03) and Russian Foundation for Basic Research.

SUMMARY OF THE ADVANCED STUDIES INSTITUTE ON SYMMETRIES AND SPIN (PRAHA-SPIN-2003 AND PRAHA-SPIN-2004)

M. FINGER

Charles University, Faculty of Mathematics and Physics, Praha, Czech Republic

The topics, scope and scientific programme of the last two Advanced Studies Institutes (ASI) on Symmetries and Spin, SPIN–Praha–2003 and SPIN–Praha–2004 are summarized. The ASI were devoted to symmetry and polarization phenomena in various physics disciplines in general, and in particle and nuclear physics in particular. The theoretical and experimental aspects of large high-priority experiments in all leading world laboratories were presented and discussed.

1. Introduction

The Advanced Studies Institutes (ASI) on Symmetries and Spin, Praha–Spin–2003 and Praha–SPIN–2004 were the 19th and 20th in the series of international meetings, that began with the first meeting at the Joint Institute for Nuclear Research, (JINR, Dubna, Russia) in 1975, and continued after that from 1976 on a regular basis in the Czech Republic with the Faculty of Mathematics and Physics of the Charles University in Prague serving as host. The organization of the ASI in 2003 and 2004 was supported by International Committee for Spin Physics Symposia, JINR, Charles University and Czech Technical University in Prague, Technical University in Liberec, Institute of Scientific Instruments of Czech Academy of Sciences in Brno (Czech Republic), and University of Florida, Gainesville (USA).

2. ASI topics, scope and characteristic features

The Prague ASI meetings cover topics related to symmetry and polarization phenomena in particle and nuclear physics. Subjects which are covered usually include: (1) Symmetries and spin, (2) Super symmetry in particle and nuclear physics; (3) Spin physics and QCD; (4) Spin physics beyond standard model; (5) Spin physics in weak interactions in nuclei and atoms; (6) Spin structure of the nucleon; (7) Spin physics in hadronic and leptonic reactions, (8) Spin physics in nuclear interactions; (9) Spin physics with polarized photons; (10) Polarized beams and polarimeters; (11) Polarized ion sources and targets; (12) New projects and perspectives.

The aim of the ASI is: (1) to take the broadest possible view of the discipline by inviting distinguished speakers, both theoreticians and experimentalists, from different collaborations aiming at research on symmetry phenomena in various physics disciplines; (2) to promote contacts among researchers with different physics backgrounds, to review and discuss the status and perspectives of their research; (3) to help to form new collaborations; (4) to help young researchers and students to take an active part in the respective international research programmes.

Prague Advanced Studies Institutes combine: (1) advanced lectures programme of tutorial character, which span several days; (2) several advanced research workshops dedicated to selected topics, which are concentrated into 2–3 days each. The overview and dedicated talks are presented here; (3) seminars and/or students sessions, where young researchers and students can present their results; (4) poster sessions. The theoretical and experimental aspects of the large high-priority spin physics experiments, which are going on or are in preparation at existing accelerators at JINR, CERN, BNL, COSY, DESY, GANIL, GSI, JLAB (CEBAF), JYFL, RCNP, RIKEN etc. are presented and discussed.

The number of participants is limited to about 100. The Proceedings of the Prague ASI are published as special volumes of the Czechoslovak Journal of Physics. Proceedings published so far are Czech. J. Phys., volumes: 49/S2 (1999) – 54 (2004), 55 (2005) in preparation.

3. SPIN–Praha–2003, Prague, July 12–19, 2003

The Prague 2003 ASI meeting was dedicated to the memory of Vernon W. Hughes, the distinguished physicist whose contribution to our field of research was exceptional. There were 98 participants from 15 countries, CERN and JINR taking part in SPIN–Praha–2003. There were two obituary lectures, four series of lectures, two public lectures, 24 overview talks, 16 dedicated presentations, nine presentations on special neutrino and astrophysics session and four poster presentations included in the scientific programme:

3.1. *Obituary to Vernon W. Hughes*

G. zu Putlitz: *Muonium*. A. Desphande: *In quest of nucleon spin—Vernon W. Hughes, the last decade 1993–2003*.

3.2. *Lectures*

E. Predazzi: *General introduction on diffraction*. A. Belkov: *Experimental and theoretical status of CP violation in K- and B-meson decays*. E. Hughes: *Polarized Deep Inelastic Scattering*. T. Kajino: *QCD-driven cosmological nucleosynthesis and supernova nucleosynthesis*.

3.3. *Public lectures*

S. Kapitsa: *The statistical theory of global population growth*. G. Cates: *Medical imaging with laser polarized noble gases*.

3.4. Overview presentations related to the large spin physics experiments

COMPASS: M. Finger: *The COMPASS experiment.*

JLab: G. Cates: *Spin physics programme in JLab Hall A.* R. de Vita: *Spin physics programme in JLab Hall B.* O. A. Rondon: *Spin physics programme in JLab Hall C.*

HERMES: K. Rith: *Selected recent results from HERMES.* I.-M. Gregor: *Recent results from HERMES.*

RHIC: E. Predazzi: *Spin physics and diffraction at RHIC.* H. Spinka: *Polarimetry at RHIC and AGS.* K. Barish: *Spin physics with PHENIX at RHIC, first results and prospects.* M. Tokarev: *Hard probes and STAR spin program.* L. Nogach: *STAR forward pion detector—preliminary.* H. Spinka: *Some spin physics measurements with STAR.*

RNCP: K. Hatanaka: *Experimental studies on spin physics at RCNP.*

TRIUMF: D. W. Ramsay: *Parity violation experiments and the proton.*

JINR: P. Rukoyatkin: *An experimental estimation of momentum spread of a beam slowly extracted from the Nuclotron.* V. Sharov: *Measurements of energy behaviors of spin dependent np observables over a GeV region.* L. Strunov: *Measurement of neutron-proton spin observables using highest energy d,n probes.*

IHEP: L. Nogach: *Single-spin asymmetry in π^0 inclusive production measured at the Protvino 70 GeV accelerator.*

RIBF JINR: R. Oganessian: *Status of the Dubna RIBF.*

HRIBF Oak Ridge: D. Stracener: *Overview of Radioactive Ion Beam production at HRIBF.* R. Varner: *Recent experiments at HRIBF.*

RIBF RIKEN: A. Yoshimi: *Nuclear spin oscillator search for atomic EDM of ^{140}Xe .* J. Murata: *Fundamental beta decay experiments at RIKEN.*

GSI: G. Munzenberg: *Nuclear structure research at GSI and the new GSI projects.*

3.5. Dedicated presentations

Theory: A. Efremov: *Collins analyzing power and azimuthal asymmetries in SIDIS.* S. Goloskokov: *Spin effects in vector meson production.* M. Kolesár: *Some aspects of eta to two pion two γ -decay in chiral perturbation theory.* E. Kuraev: *Intercept of odderon and the one-spin correlations in proton-proton inelastic scattering.* H. Leeb: *The relevance of pseudospin symmetry in proton-neutron scattering.* V. Luboshitz: *Spin correlations in the decays of two unstable particles.* J. Manjavidze: *Bjorken sum rules in the frame of topological QCD.* P. Ratcliffe: *Hyperon β -decay and the CKM matrix.* O. Selyugin: *Hadron spin-flip amplitude in nucleon-nucleon and nucleon-nuclei reaction.* D. Stamenov: *The role of higher twists in determining polarized parton densities.* P. Starovoitov: *Angular distribution of heavy lepton pairs produced through photon-photon fusion at Large Hadron Collider.* M. Tokarev: *Z-scaling and anisotropy of energy momentum space in p-D Collisions.* P. Závada: *Proton spin structure and valence quarks.*

Experiment: J. Blaha: *Scintillating and light guide fibres in radiation fields.* Z. Dlouhý: *New insight to the structure of neutron-rich nuclei near the drip-line.* V. Novitski: *Methods of precise polarization attitude control for neutrons.*

3.6. Neutrino and astrophysics session

J. Vergados: *Review of theoretical aspects of dark-matter physics*. S. Petcov: *Neutrino masses and mixing and neutrino-less two-beta decay*. J. Suhonen: *Nuclear structure calculations for neutrino physics and dark matter physics*. T. Kajino: *Quest for the origin of dark matter, dark energy and dark radiation*. H. Ejiri: *Future experiments of two-beta decays*. Z. Sujkovski: *Neutrino-less two-beta decay—the key to contemporary neutrino physics*. C. Augier: *NEMO experiment, past, present and future*. J. Bonn: *Neutrino mass limits from tritium beta decay, present status and perspectives for KATRIN Project*. H. Ejiri: *The MOON Project*.

4. SPIN–Praha–2004, Prague, July 5–10, 2004

At the Prague 2004 ASI meeting there were 85 participants from nine countries, plus CERN and JINR, taking part. The scientific programme of the ASI included a series of lectures, 18 overview talks, 20 dedicated presentations, eight presentations on special pentaquark session, eight presentations on special students session and eight poster presentations:

4.1. Lectures

E.-M. Kabuss: *The spin structure of the nucleon*.

4.2. Overview presentations related to the large spin-physics experiments

COMPASS: F. Bradamante: *The COMPASS experiment at CERN*. E. Weise: *Spin Physics with COMPASS*. N. Doshita: *The COMPASS polarized target*. M. Colantoni: *Measurement of electric and magnetic polarizabilities with Primakoff reaction at COMPASS spectrometer*. A. Ferrero: *Status and perspectives of the COMPASS experiment at CERN*.

JLab: N. Liyanage: *The Hall A Spin Program at JLab*. R. Mineharp: *The Hall B Spin Program at JLab*. F. Wesselmann: *Spin Physics in Jefferson Lab's Hall C*.

HERMES: K. Rith: *Overview of recent HERMES results*.

RHIC: A. Bazilevski: *PHENIX Spin Program, recent results*. Yu. Panebratsev: *JINR LHE participation in the STAR experiment at RHIC*.

RNCP/Spring8: H. Ejiri: *Low energy neutrinos and GeV–MeV photons in astroparticle physics at RCNP/Spring-8*.

LEPS/Spring8: T. Hotta: *Recent results at LEPS/Spring-8*.

JINR: A. Malakhov: *Polarization investigations at the Nuclotron*. V. Sharov: *Measurements of energy behaviors of spin dependent neutron-proton observables over a GeV region*. A. Litvinenko: *The study of deuteron spin structure in experiments with hadronic probes*. B. Vasilishin: *Beam slow extraction from Nuclotron*. A. Isupov: *DAQ systems for the high energy and Nuclotron internal target polarimeters*.

GSI: C. Schwarz: *FAIR, the Facility for Antiprotons and Ion Research at GSI*. M.-P. Busa: *The PANDA experiment at FAIR*. M. Maggiora: *Spin physics with antiprotons*.

4.3. Dedicated presentations

Theory: I. Anikin: *Study of deep electroproduction of exotic hybrid mesons.* A. Burinski: *Spinning particle, strings and black holes.* A. Dorokhov: *Hadronic contribution to the muon anomalous magnetic moment $g-2$ in a nonlocal chiral quark model.* A. Efremov: *On single spin asymmetries in hard processes.* S. Gerasimov: *Quark-hadron duality sum rules for spin-dependent photon-nucleon and photon-photon resonance interactions.* N. Golovanova: *Including spin dependence in scattering amplitudes in mathematical eiconal methods.* R. Mir-Kasimov: *The Newton-Wigner localization concept and non-commutative space.* O. Selyugin: *Impact of saturation on spin effects in the proton-proton scattering.* A. Sidorov: *Higher twist contribution and QCD analysis of g_1 .* O. Teryaev: *k_T -dependent fragmentation and distribution functions and higher twists resummation.* E. Tomasi-Gustavsson: *Associative charm photoproduction.*

Experiment: R. Alarcon: *Spin-dependent electron scattering at intermediate energies.* A. Aldushenkov: *About an opportunity of research P,T -violating asymmetry in measurements of linear polarization of γ -quantum at decay of the aligned isomer states of nucleus.* A. Beda: *Aligned nuclear targets for investigation of time reversal invariance.* D. Kameda: *g -factor measurements for ^{30}Al and ^{32}Al .* F. Maas: *Parity violating scattering: An overview.* F. Maas: *The Mainz A4 parity violation experiment.* A. Prokofiev: *Study of α - p and d - p inelastic scattering in the Roper resonance region.* H.-W. Siebert: *A measurement of Λ and Ξ^- polarization in inclusive production by Σ^- of 340 GeV/c in Cu and C targets.*

4.4. Pentaquark session

M. Karliner: *Pentaquarks.* D. Barna: *Pentaquark baryons in the CERN NA49 experiment.* J. Cvach: *Evidence for a narrow exotic anti-charmed baryon state.* T. Hotta: *Pentaquark research at LEPS/SPring-8.* P. Rossi: *Pentaquark research at JLab.* H.-W. Siebert: *A search for the exotic Ξ^{--} (1860) in the hyperon beam experiment WA89.* M. Ostrick: *Pentaquarks, experimental overview.*

4.5. Students session

A. Král: *Online monitoring system for the COMPASS experiment.* M. Král: *Feasibility study of an experiment to measure the Magnetic Birefringence in Vacuum.* V. Kozhukalov: *Elastic hadron-deuteron scattering in the Bethe-Salpeter approach.* T. Liška: *The CDR subsystem of the COMPASS experiment.* A. Morozov: *Delta-Sigma experiment. Some preliminary physics results.* E. Rogochaya: *Deuteron electrodisintegration in the Bethe-Salpeter approximation.* R. Shindin: *Delta-Sigma experiment. Some preliminary physics results.* J. Valenta: *The RODs for ATLAS pixel detector.*

SUMMARY OF THE WORKSHOP ON SPIN POLARIZED ELECTRON SOURCES AND POLARIMETERS (PESP-2004)

K. AULENBACHER

Institut für Kernphysik der Universität Mainz, Mainz , Germany

This is a summary report concerning results reported within the contributions to the PESP-2004 workshop. Progress in cathode technology and basic understanding of photoemission processes was reviewed, together with performance improvements for operating sources at accelerators. Important subsystems such as polarimeters, laser sources and high voltage design were also presented, showing a variety of improvements and innovations.

1. Introduction

The PESP-2004 workshop took place at Mainz/Germany from 7 to 9 October 2004. We hosted 34 people from 20 institutions; 25 talks were presented in eight sessions. The following summary first deals with recent developments in photocathode research, to which nine talks were devoted. Seven talks dealt with the performance of existing source systems and exploration of their possible limitations, the subject of the second section. Another section, summarizing the contents of six talks, is on technological developments in the field of important subsystems like polarimeters, lasers, high voltage/high gradient design, etc. Another important part of the workshop (five talks and a round table discussion) was aimed at clarifying the need for future accelerator projects like TESLA. This summary is by no means complete. Only a limited selection of the multitude of interesting results can be mentioned here. Since the proceedings of PESP will be included in this volume, the interested reader will be able to find further reading by selecting the name of a speaker mentioned in this article from the author index.

The workshop was sponsored by the Deutsche Forschungsgemeinschaft (DFG), the Committee for Spin Physics Symposia, and by the Johannes-Gutenberg University in Mainz.

2. Photocathode research

The practical goal of research in this field is to produce photocathodes with higher values of quantum efficiency (QE) and polarization (P) than are available from strained layer cathodes. Such cathodes are widely used at present: high polarization of conduction band

electrons is achieved by the heavy hole/light hole (hh/lh-) splitting that is generated by reducing the symmetry of the semiconductor crystal by strain deformation. The size of this splitting is important, since too small a value will give rise to an admixture of the 'wrong' electron spin and hence a reduction of polarization. In addition, large splitting will allow operation with a larger energy difference compared to the photoabsorption edge. This leads to stronger photoabsorption and hence to larger quantum efficiency. Unfortunately, strain splitting and layer thickness (absorption) can be varied only within certain limits; the limiting factor is the instability of the crystal due to strain relaxation. After several years of improvement, the best compromise found for strained layers seems to be $P=80\%$ and $QE=0.4\%$ (corresponding to a Photosensitivity of $2.5 \mu A/mW$ at 800 nm).

Recent research and development has been focused on the more complicated superlattice (SL) structures. Typically they consist of a periodic repetition of thin semiconductor 'heterostructures'. These are made up of two semiconductors of different composition and consequently different band gap. The typical period of the superlattice is about 10 nm . The small longitudinal extension of the regions with different band gap causes quantum confinement effects. The different layers are called 'wells' and 'barriers'.

Due to the completely different lattice constant and potential in the directions perpendicular to the individual films, SL-cathodes show lh/hh-splitting even without using strained semiconductors. The application of strained films increases this natural splitting to the extent that it may exceed the achievable values for strained layer cathodes. The choice of the optimum composition of the two compounds was the task addressed in several talks during the workshop.

T. Maruyama (SLAC) presented results for the $\text{GaAs}/\text{GaAs}_{1-x}\text{P}_x$ System. The QE-spectra of these structures show features which can be attributed to the two dimensional density of states expected from the superlattice-symmetry (see Figure 1). A splitting of 89 meV was observed at SLAC for a phosphorus content of $x = .36$, resulting in polarizations of 86% at a QE of 1.2% . M. Kuwahara from Nagoya reported 92% at 0.5% quantum efficiency^a for a similar GaAsP/GaAs -SL-cathode. It was observed by a phenomenological approach that, besides the importance of the lh/hh-splitting, the details of the band structure must be considered. In addition it was observed that the strain relaxation was minimized. This reduces the anisotropy of absorption with respect to the direction of linearly polarized components of incident light. This in turn leads to a reduction of emission-current asymmetry, which is important for parity violation experiments.

Another strain optimized structure was presented by Y. Mamaev from SPTU (St. Petersburg). In this case $\text{In}_x\text{Al}_y\text{Ga}_{1-x-y}\text{As}/\text{GaAlAs}$, a 'strained well' superlattice, was investigated. This structure achieves high QEs ($> 1\%$) with polarizations in the 80% range. Time resolved polarization measurements at Mainz observed relatively slow extraction of the electrons from the SL, leading to depolarizations of $8-10\%$ in this structure. This suggests that polarizations in excess of 90% can be achieved if the transport is optimized. Indeed for an $\text{InAlGaAs}/\text{GaAs}$ structure, which should show optimized transport (minimized con-

^aIn comparing absolute polarizations, one must take into account the typical error bar of measurements with a Mott polarimeter, which is of the order of $3-6\%$.

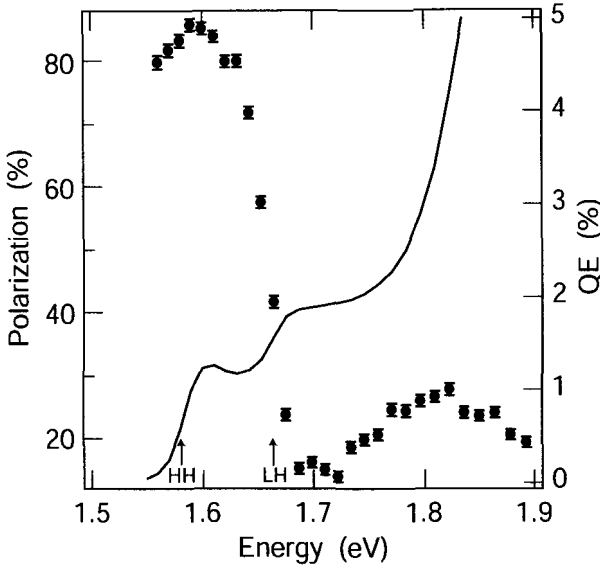


Fig. 1. QE and P-spectra for GaAsP/GaAs superlattice cathode.

duction band offset), a polarization in excess of 90% was reported. InGaAsAl/GaAlAs SL can be grown in standard MBE apparatus, and new growth technology allows for very low activation temperatures ($< 500\text{C}$) for the photocathode activations. This represents a considerable practical advantage by avoiding surface damage and diffusion of dopant from the highly doped surface layer. This unwanted phenomenon is frequently observed after heating to more elevated temperatures.

Two talks from SPTU given by L. Gerchikov addressed the interpretation of QE and P-spectra from the theoretical viewpoint. The main results were that a) in optimized SL-cathodes the losses in photoabsorption are $< 3\%$ (from theoretical investigations of an optimized SL-band structure), b) that highly doped GaAs capping layers (used for optimized QE) contribute to polarization losses, and that c) in the best photocathodes, depolarization processes during electron transport in the conduction band and during emission lead to a loss of $< 5\%$. The points b) and c) require experimental input for each type of photocathode, since the surface and transport effects involved here are not completely controllable. However it was shown that interpretation of QE and P-spectra is possible in a rather consistent way.

Since it is very desirable to keep the highly doped GaAs-surface layer, the application of strain-compensated SL-cathodes was suggested: in these structures the tensile strain of one layer is compensated by compressive strain in the other. This allows for higher thickness of the photoactive region, hence larger QE and a relatively reduced contribution from the less polarized electrons in the surface region.

Two talks addressed the problem of NEA-activation of the semiconductor activation layer, which consists of a Cs:O structure of still not completely understood structural pa-

rameters. S. Kulkova from Tomsk presented ab initio calculations for cesium deposition on GaAs (001). A. Terekhov from Novosibirsk presented experimental data for photoemission from surface states. Their conclusion is that for adequately activated structures, the contribution of surface states - which provide essentially unpolarized electrons - is negligible, but that surface contributions may reduce polarization for sub-optimal situations.

It is obvious that SL-cathodes have matured during the last few years. They offer several percent higher polarization together with a large enhancement of QE. Several accelerator centers (e.g. JLAB, SLAC, MAMI) have started operation with those structures or intend to do so in the near future.

3. Polarized source development and operation for experiments

Polarized source operation at existing machines is characterized at present by stable conditions. Parity experiments such as G0 and Happex at JLAB, Sample at MIT-Bates, or PVA4 at MAMI still require skilful beam adjustment and installation of several stabilisers, usually realized by feedback mechanisms (Talks by Farkondey(MIT-Bates), Poelker(JLAB), and Maas(MAMI)). All parity experiments mentioned have achieved sufficiently good beam parameters. A typical set of helicity correlated beam parameters, taken from the talk of M. Poelker, is presented in table 1

Table 1. Preliminary run-averaged helicity-correlated beam asymmetries for parity violation experiments recently conducted at CEBAF. Numbers may change slightly as data reduction continues. Error bars are forthcoming.

Experiment	Intensity	Position X	Position Y	Energy
G0 Forward Angle	0.14 ppm	3 +/- 4 nm	4 +/- 4 nm	10 ppb
HAPPEX-II He	0.4 ppm	3 nm	2 nm	2.6 ppb
HAPPEX-II H	0.2 ppm	2.2 nm	2.3 nm	2 ppb

Electron ion colliders which are currently in the design/planning stage require an increase over present-day polarized source intensities of (at least) one order of magnitude. Experiments at JLAB (J. Grames) and MAMI (R. Barday) have revealed the importance of reducing transmission losses, and optimum vacuum conditions. First experiments with DC currents in the milliampere region have started.

Very high current in combination with low emittance can be achieved only by using high source potentials together with high gradients. Besides the possibility of using an RF-source the investigation of extremely high DC-voltage operation is ongoing. A new 200 keV polarized electron source is now operating at Nagoya (talk by M. Yamamoto, see Figure 2).

The group at Heidelberg (talk by D. Orlov) has succeeded in producing ultra-cold (transverse energy of electron motion $< 1 meV$) and intense electron beams at DC currents of $200 \mu A$, from a GaAs cathode. Simultaneously they have demonstrated the possibility of sufficient cooling of the photocathode during operation, achieving a temperature increase of $< 20K/W$. Using this power with a modern SL-cathode would allow for highly polarized

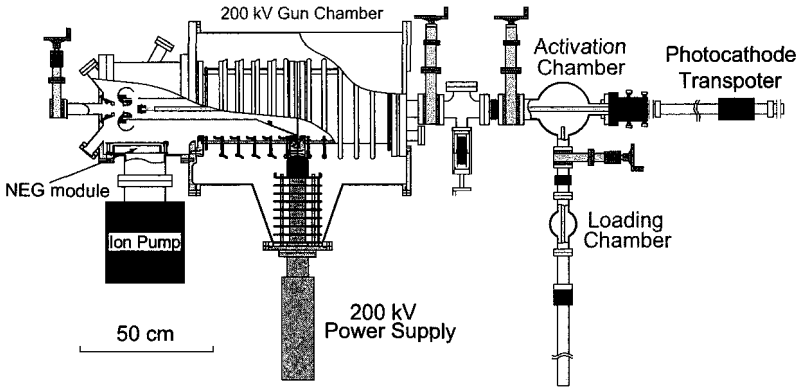


Fig. 2. QE and P-spectra for GaAsP/GaAs superlattice cathode.

beam production in the several mA region.

Omori (KEK) and Leihem (DESY/BNL) gave an overview of the status of polarized *positron* sources. The principle consists of generating polarized electron/positron bunches from circularly polarized *gamma*-radiation. Two approaches are being explored in order to generate sufficiently intense circularly polarized *gammas*: BNL uses electron bunches passing through a pulsed helical undulator, whereas KEK uses Compton backscattering of laser pulses off electron bunches. Both projects have reached important milestones in dedicated proof of principle experiments.

4. Tehnological development in polarized source subsystems

Only a few topics may be mentioned here:

Polarimeters: Y. Imai (MAMI/Mainz) reported on the Compton backscattering polarimeter at MAMI. The novel feature is the laser/electron beam overlap in the laser cavity itself. D. Lamine (Palaiseau) reviewed the spin filtering technique with magnetic thin films.

Field emission and HV By choosing titanium as a cathode and molybdenum as anode, an optimum static gradient of 120MV/m was achieved at a potential of 60kV at Nogaya (Yamamoto). They were able to disentangle primary and secondary field emission effects.

Surface activation Hydrogen cleaning has proved to be an efficient and rigorous cleaning method. Either plasma discharges (Maruyama, SLAC) or dissociators can be used (Orlov, Heidelberg)

5. Polarized sources for a future linear collider and for an electron/Ion collider

A lively discussion took place on source requirements for the next linear collider, in the light of the recent decision to favour the construction of a future collider using 'cold' (superconducting) RF-technology at 1.3 GHz. This choice has considerable impact on the required source parameters, since superconducting technology is characterized by somewhat relaxed beam emittance parameters, single bunch charge, and bunch spacing.

M. Farkondeh (MIT/Bates) reported on the planning status of electron/ion colliders (ERHIC/ELIC). To achieve very high luminosity, either a storage ring or a linac design with extremely high average current (and energy recovery) is needed. Storage ring options would require average currents of highly polarized electrons in the few milliampere region, generated by macropulses with high repetition rate and high peak current (several hundred milliampere). Such demands are about an order of magnitude higher than currently achieved; however in the light of present knowledge on limiting factors, they seem feasible. In any case considerable R&D work on the polarized source and its subsystems is required to provide a reliable source to meet these demands.

SUMMARY OF THE 9th INTERNATIONAL WORKSHOP ON POLARIZED SOLID STATE TARGETS AND TECHNIQUES*

H. DUTZ

Physikalisches Institut, Universität Bonn, Bonn, Germany

The workshop was held in Bad Honnef, Germany, from October the 27th to the 29th 2003. Remarkable progress has been made in the field of polarized solid targets since the preceding workshop in 1996. We now have a deeper understanding of the physics of dynamic nuclear polarization (DNP), resulting in new highly polarizable deuteron target materials doped using chemicals or radiation. Polarization measurements, usually done using nuclear magnetic resonance (NMR), can now be further improved to yield unprecedented levels of precision. Equally important advances have been achieved concerning other parts of the instrumentation of a polarized solid target, leading to target setups that are better matched to the requirements of present and future particle physics experiments.

1. Introduction

The 9th International Workshop on Polarized Targets and Techniques, organized by the Institut für Experimentalphysik der Ruhr-Universität Bochum and the Physikalisches Institut der Universität Bonn, was held at the Physikzentrum in Bad Honnef (Germany) on October 27–29, 2003.

The workshop was attended by 48 participants from 10 countries, who presented new developments and exciting results. The developments were concentrated on substantial polarization improvements in deuterated target materials, prepared for the dynamic nuclear polarization process by radiation or chemical doping methods, nuclear magnetic resonance techniques, and for the first time the application of polarized target substances for magnetic resonance imaging.

If one takes a look back over the series of Workshops, detailed improvements in target materials, cryogenics, magnets and NMR technology have led to major steps either in an upgraded luminosity L – defined as the product of the beam current I and the areal target thickness n_t – of the performed scattering experiments, or an enhancement of the 'figure of merit' (FOM) of the polarized target set-up. Both quantities characterize the quality of the combination of polarized target, particle beam, and detection system, for a given running time t and counting rate N or cross section σ of the scattering reaction of interest. The

*October 27-29, 2003 Bad Honnef, Germany

running time required to achieve a chosen accuracy ΔA in the measured polarization observable A in a scattering experiment is $t \approx 1/L\sigma f^2 P^2 (\Delta A)^2$, where f is the target material quality factor – in the literature often labeled as ‘dilution factor’ – defined as the ratio of the number of polarizable nucleons to the total number of nucleons in the target material, and P is the degree of polarization.

A ‘figure of merit’ FOM for the solid polarized targets used in particle physics experiments can be defined by $FOM = \sigma \cdot n_t \cdot P^2 \cdot f^2$. The optimization of the FOM especially of P and f is a multi-step procedure. Let us first focus on the nucleon polarization P ; this is a function of the external magnetic field B and the lattice temperature T of the material, and can be expressed as $P = (\mu B)/(2kT)$. P is thereby directly influenced by the instrumentation (cryogenics and magnet systems) of the target system. The product $n_t \cdot P^2 \cdot f^2$ depends on the specific properties of the target material used. To maximize it, one has to

- select a material with a high-quality factor f
- find for this material an appropriate radical doping method to make use of the DNP process to maximize P
- find an optimal radical concentration for a short polarization build-up time and long relaxation time for frozen spin target operation
- determine the resistance of the polarization to ionizing radiation (normally done during the particle physics experiment).

Following this scheme, this summary will focus on new developments in target instrumentation and, finally and more comprehensively, on improvements in target material research and results presented on the workshop.

2. Instrumentation

Within the last few years the cryogenic and magnetic equipment of the various polarized target facilities has not been changed in general. Following the requirements of the physics program, either high intensity (electron) beam scattering experiments measuring inclusive observables, or low intensity (e.g. real photon) beam with large angular acceptance detection systems observing exclusive reactions, use ^4He – evaporation or $^3\text{He}/^4\text{He}$ – dilution refrigerators and superconducting magnet systems.

2.1. Cryogenic and magnet systems

The high beam flux experiments are the domain of the ‘continuous mode’ polarized targets with a high field applied ($B_P \geq 5T$) to the target material cooled to 1K, and the permanent dynamic polarization of the nucleons during data taking. This type of target is operated by the polarized target group at the University of Virginia, which conducts experiments at both SLAC and JLab in which a high-intensity (up to 100 nA) electron beam is focused on a polarized target of ammonia and/or deuterated ammonia or lithium⁶.

At the COMPASS experiment at CERN a ‘continuous mode’ polarized target is used in combination with a large $^3\text{He}/^4\text{He}$ dilution refrigerator. The refrigerator is designed to cool 350g of target material for efficient DNP ($B_P = 2.5T$) down to around 300 mK with a

³He flow of 100 mmol/s. In order to keep the polarization in the frozen mode at 0.42 T, temperatures of about 65 mK are achievable^{138, 147}. In the case of reduced beam intensity scattering experiments, the measurement of polarization observables which are related to small cross sections require a large angular acceptance of the combined 'target-detection' system to keep a reasonable counting rate N and a large FOM . To open the geometry of the polarized target and to increase $\Delta\Omega$, the so-called 'frozen spin' technique is used by different groups at various places and accelerator facilities, such as Bochum, Bonn, Dubna¹⁵³, Mainz, PSI and TJNAF. The development of the internal holding coil technique, and the implementation into a horizontal dilution refrigerator, increases the geometric acceptance of the polarized target to almost 4π . This is the state of the art scheme for polarization experiments in large acceptance detection systems at ELSA/MAMI¹²⁶ and for future experiments at JLab, where a new frozen spin target is under construction for experiments in concert with the Hall-B CLAS detector¹³². For future large angular acceptance polarization experiments, a new concept has been presented by the Bonn polarized target group¹¹⁷. They propose to replace the internal holding coil by an internal polarizing magnet, providing a high and homogeneous enough field for continuous DNP in a large angular acceptance dilution refrigerator. This will be the next step in increasing the FOM of polarized solid state targets for scattering experiments in a 4π – detection system.

2.2. NMR – techniques

The continuous wave (CW) NMR-technique has been proved over years to be the standard high precision method for measuring the polarization of the nuclei in a dynamically polarized target⁶⁵. To get a quantitative estimate of the influence of various effects on the determination of the NMR-signal, a simulation of the Q-meter system has been performed⁷⁶. On this basis, one should be able to determine the deuteron polarization to a precision of 10^{-3} . The CW-NMR technique reaches its limits for small and wide signals. To improve the sensitivity for this case, a pulsed NMR-System has been discussed, and the first promising results have been presented by the Bochum Polarized Target group⁹⁶.

3. Target materials

The workshop was impressed by enormous efforts towards the theoretical understanding of polarization dynamics in various target substances²⁸. The systematic study of classic and new doping methods led to a substantial improvement of the maximum polarization in deuterated target materials.

3.1. Substances for DNP

The target materials used so far divided into two classes, one containing inorganic substances like ammonia (NH_3 , ND_3) or lithium deuteride (${}^6\text{LiD}$). They are highly polarizable and exhibit good radiation resistance together with a high quality (dilution) factor^{12,7}. The radiation resistance of the ammonia target materials has been extensively studied over the last 15 years by the Virginia Polarized Target Group. It is still the state of the art polarized

target material for high intensity (100nA) electron beam experiments⁶⁰. In particular ⁶LiD provides the highest available content of polarizable nucleons compared to all nucleons in the material. It was successfully used in the COMPASS-experiment at CERN, reaching deuteron polarization values up to 57% at a polarizing field of 2.5 T.

While for inclusive experiments at high energies, one may profit from the high dilution factor and in case of high intensities from the radiation hardness of the inorganic substances, for experiments at intermediate energies the problem arises, to what extent the experimental data are affected by background reaction on polarized nuclei of the materials. The second category of target materials are the organic substances such as alcohols or diols, traditionally doped with chemical radicals. Apart from the lower radiation hardness of these materials they suffer from another problem, namely limited deuteron polarization, which does not exceed 30-40%⁵³, compared to the 90% typically reached in protonated candidates under the same conditions¹. From this point of view, the development of deuterated organic target materials for maximum polarization as well as radiation hardness was a subject of research of the Bochum Polarized Target Group^{43,110}. They did systematic studies on the maximum polarization of deuterated organic substances as a function of the EPR-line width of various paramagnetic centres created chemically or by irradiation. In the search for radicals with a small EPR line width, any effect that tends to broaden the line has to be minimized. The anisotropic g-factor of the unpaired electron is a particular danger, because its influence on the line width increases with increasing magnetic field. Hyperfine interactions of the electron also cause broadening. Radiation doping of deuterated materials therefore appears useful because the resulting paramagnetic centres combine a small g-factor anisotropy with weak deuteron hyperfine splitting. In this way, irradiation doped deuterated materials show polarizations as high as 71% measured at 5 T in a dilution refrigerator by the Bochum Group⁴³, or of about 60% at 6.55 T and 1 K verified by the Virginia Group⁵⁶. A further substantial increase in deuteron polarization has been achieved in both D-butanol and D-propanediol, chemically doped with radicals of the trityl family (which were developed and delivered by Amersham Health, Malmö). Basically, the paramagnetic part of these molecules consists of a methyl-type radical with the three H-atoms replaced by larger but spinless complexes. They possess a very small EPR line width compared with those of the commonly used nitroxide radicals, porphyrexide and TEMPO²². Both D-butanol and D-propanediol doped with radicals of the trityl family could be polarized up to around 80 % in a magnetic field of 2.5 T. This material was recently successfully used for the measurement of the GDH-sum rule of the neutron at the Mainz microtron, MAMI. By doubling the average polarization of d-butanol, the measuring time required for a given statistical accuracy could be reduced by a factor of four!

An experimental approach to studying the nuclear polarization build-up around the paramagnetic centres during the DNP-process has been presented by the PSI-Target Group⁸¹. The simultaneous use of time-resolved polarized small-angle neutron scattering and nuclear magnetic resonance enables us to 'visualize' the nuclear polarization process, namely spin diffusion on a microscopic scale. This provides for the first time spatial information about the polarization evolution of protons close to a paramagnetic centre.

3.2. HD polarized target

An HD-target polarized by the DNP method is currently under development by the Bochum Group¹⁶⁸. The radiation doping is done so far by a radioactive source to create of the order of 10^{18} spins/cm³ paramagnetic centres. Up to now, no dynamic polarization could be achieved. The static or so-called 'brute-force' polarization scheme of HD samples is followed up by the Target Groups at BNL¹⁵⁷ and Orsay¹⁶³. For the first time a static polarized HD sample with a proton polarization of about 30% was provided by the BNL Target Group for a double polarization experiment at LEGS¹⁵⁷. Relaxation times of the order of 13 days have been achieved. To increase the in-beam proton and deuteron polarization of HD, several new improvements are being implemented. This includes a new in-beam cryostat to reach longer in-beam relaxation times with higher field and lower temperature, the construction of a new cold transfer cryostat to reduce polarization loss during target transfers, and the installation of a much improved NMR system to allow more precise measurement of the in-beam H- and D-polarization.

4. Conclusions

In this summary I have tried to at least mention the topics presented, and I apologize for not mentioning everyone by name. The Workshop was valuable in pulling together many issues. After more than 40 years the polarized solid state target is a very lively and innovative field of physics and is still the state of the art experimental tool for studying spin physics.

References

All citations given in the article refer to the page of a related article published in *Nucl. Instr. and Meth. A526* (2004), *Proceedings of the Ninth International Workshop on Polarized Solid Targets and Techniques*, Bad Honnef (Germany) 2003, Eds. St. Goertz, W. Meyer, G. Reicherz.

This page intentionally left blank



Pirelli INTERNETional Award

The world's first Internet multimedia award aimed at the diffusion of scientific and technological culture worldwide

This year the Pirelli INTERNETional Award launches a special award to mark the centenary of the publication of the Special Relativity Theory by Albert Einstein in 1905.



The award consists in a 25,000 Euro check (more than US \$ 30,000)

The submissions must be interactive multimedia presentations - in about five minutes - of Einstein' Special Relativity Theory. The work must be sent by FTP or by an e-mail attachment before March 31, 2005

Web Site: www.pirellaward.com/einstein.html

Contact Us: E-mail einstein@pirellaward.com

Telephone: +39-06-69517610

Fig. 1. Massimo Armeni presented the Pirelli International Award, for the centenary of the publication of the Special Relativity Theory

This page intentionally left blank



SESSION 1

Spin and Fundamental Symmetries

This page intentionally left blank

COMPTON POLARIZABILITIES OF π -MESONS IN RELATIVISTIC HAMILTONIAN DYNAMICS

V. V. ANDREEV*

Physics Department, Gomel State University, Gomel, Belarus

The electric and magnetic polarizabilities of the charged pion are studied in the framework of the Poincaré-covariant quark model. We consider the π^\pm -mesons as relativistic two-particle systems with a realistic potential describing the strong interactions between quarks. With the help of the dipole interaction term of bound quark systems in the one-photon exchange approximation, we find that static polarizabilities constitute only a minor fraction of the Compton polarizabilities.

1. Introduction

The electric and magnetic polarizabilities $\bar{\alpha}$ and $\bar{\beta}$ are important fundamental structure parameters. The experimental and theoretical investigation of the electromagnetic meson polarizabilities are therefore of great importance. The Compton electric polarizability $\bar{\alpha}$ of a spinless meson P can be represented as a sum [1]

$$\bar{\alpha} = \alpha_0 + \Delta\alpha = \frac{2}{3} \sum_{n \neq 0} \frac{|\langle n | \mathbf{D} | 0 \rangle|^2}{E_n - E_0} + \frac{e_P^2 \langle r_P^2 \rangle}{3M_P}. \quad (1)$$

Here α_0 is a static electric polarizability and $\Delta\alpha$ is a correction term. The operator \mathbf{D} is the internal electric dipole operator. The parameters e_P and M_P are the particle charge and mass, and r_P is the electric radius.

The expression for the magnetic polarizability has the form [1]

$$\bar{\beta} = \beta_0 + \Delta\beta = \frac{2}{3} \sum_{n \neq 0} \frac{|\langle n | \mathbf{M} | 0 \rangle|^2}{E_n - E_0} - \frac{e_q^2 \langle \psi | r_q^2 | \psi \rangle}{6m_q} - \frac{e_Q^2 \langle \psi | r_Q^2 | \psi \rangle}{6m_Q} - \frac{\langle \psi | \mathbf{D}^2 | \psi \rangle}{2M}, \quad (2)$$

where β_0 is the static magnetic polarizability. The operator \mathbf{M} is the internal dipole magnetic operator, and $r_{q,Q}$ are the corresponding internal radius vectors.

*Work partially supported by grant F003-112 of the Belarussian FFoundation Basic Researches.

There are many approaches to the description of hadron polarizabilities (more detailed reviews can be founded in [2, 3]). The aim of this work is to evaluate the Compton polarizabilities of π -mesons regarded as relativistic two-particle systems with a realistic potential describing the strong interactions between quarks.

2. The bound two-particle system in the RHD

In our approach the mesons are represented as bound states of relativistic point-like quarks q and antiquarks \bar{Q} , with masses m_q and m_Q , and electric charges e_q and e_Q . In this approach a meson with momentum \mathbf{P} , mass M_{meson} and spin J is described by the wave function $\Phi_{\mathbf{P};\lambda_1\lambda_2}^{J\mu}(\mathbf{k})$ of a quark-antiquark state, which satisfies the equation [4]

$$\begin{aligned} \sum_{\lambda_1, \lambda_2} \int < \mathbf{k}, \sigma_1, \sigma_2 \parallel V_{qQ} \parallel \mathbf{k}', \lambda_1, \lambda_2 > \Phi_{\mathbf{P};\lambda_1\lambda_2}^{J\mu}(\mathbf{k}') d\mathbf{k}' = \\ = (M_{meson} - \omega_{m_q}(\mathbf{k}) - \omega_{m_Q}(\mathbf{k})) \Phi_{\mathbf{P};\sigma_1\sigma_2}^{J\mu}(\mathbf{k}) \end{aligned} \tag{3}$$

with interquark potential V_{qQ} , relative momentum \mathbf{k} , and $\omega_{m_q}(\mathbf{k}) = \sqrt{\mathbf{k}^2 + m_q^2}$. For external electromagnetic fields (one-photon exchange approximation), Eq. (3) with $m_q = m_Q$ and $\mathbf{P} = \mathbf{0}$ is modified to

$$\begin{aligned} \sum_{\lambda_1, \lambda_2} \int < \mathbf{k}, \sigma_1, \sigma_2 \parallel \hat{V}_{qQ} \parallel \mathbf{k}', \lambda_1, \lambda_2 > \Psi_{\mathbf{P}=\mathbf{0};\lambda_1\lambda_2}^{J=0}(\mathbf{k}', \mathbf{E}(\mathbf{H})) d\mathbf{k}' = \\ = (M_{meson} + \Delta\varepsilon - 2 \omega_{m_q}(\mathbf{k}) - \Delta\hat{H}) \Psi_{\mathbf{P}=\mathbf{0};\sigma_1\sigma_2}^{J=0}(\mathbf{k}, \mathbf{E}(\mathbf{H})), \end{aligned} \tag{4}$$

where the operator $\Delta\hat{H}$ is determined by

$$\Delta\hat{H}_{\mathbf{E}} = -1/2(\mathbf{E}\mathbf{D}) \equiv -i/2(e_q - e_Q)(\mathbf{E}\nabla_{\mathbf{k}}) \text{ - electric field,} \tag{5}$$

$$\Delta\hat{H}_{\mathbf{H}} \equiv -1/2(\mathbf{M}\mathbf{H}) = \frac{i(e_q - e_Q)}{4 \omega_{m_q}(\mathbf{k})}(\mathbf{H}[\mathbf{k} \times \nabla_{\mathbf{k}}]) \text{ - magnetic field} \tag{6}$$

and $\Delta\varepsilon$ is the correction to the energy of the ground state.

The interquark potential in the coordinate representation is the sum of Coulomb-like, confining smeared potential and spin-spin interaction parts [5]

$$\hat{V}_{qQ}(r) = \hat{V}_{Coulomb}(r) + \hat{V}_{linear}(r) + \hat{V}_{SS}(r). \tag{7}$$

with $r = |\mathbf{r}|$. The Coulomb part of the interquark potential is determined by

$$\hat{V}_{Coulomb}(r) = -\frac{4}{3} \sum_{k=1}^3 \frac{\alpha_k}{r} \text{erf}(\tau_k r) \tag{8}$$

where $\text{erf}(x)$ is the error function. The parametrization of the coupling constant $\alpha_s(Q^2)$ has the convenient form

$$\alpha_s(Q^2) = \sum_{k=1}^3 \alpha_k \exp(-Q^2/4\gamma_k^2), \tag{9}$$

where $\alpha_1 = 0.43209$, $\alpha_2 = 0.13089$, $\alpha_3 = 0.11657$, $\gamma_1 = 0.65141$ GeV², $\gamma_2 = 187.13991$ GeV², $\gamma_3^2 = 5.45638$ GeV². The parameter τ_k is determined by $1/\tau_k^2 = 1/\gamma_k^2 + 1/\sigma^2$, and σ is the smearing parameter.

The confining part of the interaction has the form:

$$\hat{V}_{linear}(r) = b r \left[\frac{\exp(-\sigma^2 r^2)}{\sqrt{\pi} \sigma r} + \left(1 + \frac{1}{2\sigma^2 r^2} \right) \text{erf}(\sigma r) \right] + w_0. \quad (10)$$

The spin-spin part of the interaction is determined by

$$\hat{V}_{SS}(r) = -\frac{32\sigma^3}{9\sqrt{\pi}m_q m_Q} (\mathbf{S}_q \mathbf{S}_Q) \exp(-\sigma^2 r^2) \sum_k \alpha_k \text{erf}(\gamma_k r), \quad (11)$$

where $\mathbf{S}_q, \mathbf{S}_Q$ are quark spin operators.

3. Compton polarizabilities of π^\pm -mesons

With the help of variational methods and a harmonic oscillator wave function, we find a solution of the eigenvalue problem (3). Experimental π^\pm and ρ masses, and the π leptonic decay constant, lead to numerical values of the potential parameters:

$$\begin{aligned} \beta &= 0.4332 \text{ GeV}, \quad \sigma = 0.3518 \text{ GeV}, \\ w_0 &= -0.9391 \text{ GeV}, \quad m = m_u = 0.201 \text{ GeV} \end{aligned} \quad (12)$$

with the linear parameter (10) $b = 0.18$ GeV².

To evaluate the static electric polarizability we apply a procedure that includes the analytic calculation of contributions by means of perturbation theory and variational methods [6] (see, also [7]). The final result for the π^\pm -meson is

$$\alpha^0 = \frac{e^2 \sqrt{\pi} \exp(-V^2/2)}{48 m^2 \beta (V^2 K_0(V^2) - \beta^2 (V^2 - 1) K_1(V^2))}, \quad (13)$$

where $V = m/\beta$, $K_n(z)$ is the Bessel function of second kind, and $e^2 = 1/137.036$. The correction term can be represented by

$$\Delta\alpha = \frac{e^2 [\exp(V^2) (\sqrt{\pi} V (1 - \text{erf}(V)) + \int_{V^2}^{\infty} \exp(-t)/t dt)]}{8M_\pi \beta^2}. \quad (14)$$

Using Eq.(12) we obtain

$$\alpha_0^{\pi^\pm} = 0.14 * 10^{-4} \text{ Fm}^3, \quad \Delta\alpha^{\pi^\pm} = 5.26 * 10^{-4} \text{ Fm}^3. \quad (15)$$

For the magnetic polarizability we have

$$\begin{aligned} \beta_0 &= 0, \quad \Delta\beta = -\frac{(e_q^2 + e_Q^2)}{48V\beta^3} - \frac{3(e_q - e_Q)^2}{4M_\pi\beta^2} - \\ &-\frac{(e_q^2 + e_Q^2)}{12V\beta^3} (V^2 - \sqrt{\pi}V^3 \exp(V^2) (\text{erf}(V) - 1)) \end{aligned} \quad (16)$$

and

$$\bar{\beta} = -2.03 * 10^{-4} \text{ Fm}^3. \quad (17)$$

4. Summary and acknowledgments

We investigate the Compton polarizabilities of charged π^\pm within the framework of the relativistic quark model, based on a description of mesons as bound states of point-like quarks, with help of the instant form of relativistic Hamiltonian dynamics. From this investigation we conclude that the static polarizabilities constitute only a small fraction of the total polarizability of the π^\pm -meson in one-photon exchange approximation.

I would like to thank the organizers for warm and kind hospitality throughout the Conference. I thank the Central European Initiative(CEI) and the Abdus Salam ICTP for support.

References

1. V.A. Petrun'kin, *Sov.J. Part.Nucl.* **12**, 278 (1981).
2. A.I. L'vov, *Int. Journ. Mod. Phys.* **A8**, 5267 (1993).
3. J.Portoles, M.R. Pennington, arXiv: hep-ph/9407295.
4. B. D. Keister and W. N. Polyzou, *Adv. Nucl. Phys.* **20**, 225 (1991).
5. S. Godfrey and N. Isgur, *Phys. Rev.* **D 32**, 185 (1985).
6. V. V. Andreev and N. V. Maksimenko, *Proc. of Int. School-seminar "Actual problems of particle physics" Gomel, Belarus, 2001*, edited by the Ed. Board, **2** 128-139 (JINR, Dubna, 2002).
7. W. Lucha and F. F. Schöberl, *Phys. Lett.* **B544**, 380 (2002).

VECTOR AND AXIAL-VECTOR CURRENT CORRELATORS WITHIN THE INSTANTON MODEL OF QCD VACUUM

A. E. DOROKHOV

Bogoliubov Laboratory of Theoretical Physics, Joint Institute for Nuclear Research, Dubna, Russia

The pion electric polarizability, $\alpha_{\pi^\pm}^E$, the leading order hadronic contribution to the muon anomalous magnetic moment, $a_\mu^{\text{hvp}(1)}$, and the ratio of the $V - A$ and $V + A$ correlators are found within the instanton model of QCD vacuum. The results are compared with phenomenological estimates of these quantities from the ALEPH and OPAL data on vector and axial-vector spectral densities.

In the chiral limit, where the masses of u , d , s light quarks are set to zero, the vector (V) and axial-vector (A) current-current correlation functions in the momentum space (with $-q^2 \equiv Q^2 \geq 0$) are defined as

$$\begin{aligned} \Pi_{\mu\nu}^{J,ab}(q) &= i \int d^4x e^{iqx} \Pi_{\mu\nu}^{J,ab}(x) = (q_\mu q_\nu - g_{\mu\nu} q^2) \Pi_J(Q^2) \delta^{ab}, \\ \Pi_{\mu\nu}^{J,ab}(x) &= \langle 0 | T \{ J_\mu^a(x) J_\nu^b(0)^\dagger \} | 0 \rangle, \end{aligned} \quad (1)$$

where the QCD V and A currents are $J_\mu^a = \bar{q} \gamma_\mu \frac{\lambda^a}{\sqrt{2}} q$, $J_\mu^{5a} = \bar{q} \gamma_\mu \gamma_5 \frac{\lambda^a}{\sqrt{2}} q$, and λ^a are Gell-Mann matrices ($\text{tr} \lambda^a \lambda^b = 2 \delta^{ab}$) in flavour space. The momentum-space two-point correlation functions obey (suitably subtracted) dispersion relations,

$$\Pi_J(Q^2) = \int_0^\infty \frac{ds}{s + Q^2} \frac{1}{\pi} \text{Im} \Pi_J(s), \quad (2)$$

where the imaginary parts of the correlators determine the spectral functions $\rho_J(s) = 4\pi \text{Im} \Pi_J(s + i0)$ measured by ALEPH [1] and OPAL [2].

In the instanton liquid model (ILM) in the chiral limit the correlators have a transverse character [3]

$$\Pi_{\mu\nu}^J(Q^2) = \left(g_{\mu\nu} - \frac{q^\mu q^\nu}{q^2} \right) \Pi_J^{\text{ILM}}(Q^2), \quad (3)$$

and the dominant contribution to the correlators is given by the dynamical quark loop which was found in [3, 4], with the result for the vector current that

$$\begin{aligned} \Pi_V^{Q\text{Loop}}(Q^2) &= \frac{4N_c}{Q^2} \int \frac{d^4k}{(2\pi)^4} \frac{1}{D_+D_-} \left\{ M_+M_- + \left[k_+k_- - \frac{2}{3}k_\perp^2 \right]_{ren} \right. \\ &+ \frac{4}{3}k_\perp^2 \left[\left(M^{(1)}(k_+,k_-) \right)^2 (k_+k_- - M_+M_-) - \left(M^2(k_+,k_-) \right)^{(1)} \right] \left. \right\} \\ &+ \frac{8N_c}{Q^2} \int \frac{d^4k}{(2\pi)^4} \frac{M(k)}{D(k)} \left[M'(k) - \frac{4}{3}k_\perp^2 M^{(2)}(k, k+Q, k) \right], \end{aligned} \quad (4)$$

where the notations $k_\pm = k \pm Q/2, k_\perp^2 = k_+k_- - \frac{(k_+q)(k_-q)}{q^2}, D(k) = k^2 + M^2(k)$, and $M_\pm = M(k_\pm), D_\pm = D(k_\pm)$ are used. We also introduce the finite-difference derivatives defined for an arbitrary function $F(k)$ as

$$F^{(1)}(k, k') = \frac{F(k') - F(k)}{k'^2 - k^2}, \quad F^{(2)}(k, k', k'') = \frac{F^{(1)}(k, k'') - F^{(1)}(k, k')}{k''^2 - k'^2}. \quad (5)$$

The difference between the V and A correlators is free from any perturbative corrections for massless quarks and is very sensitive to the spontaneous breaking of chiral symmetry. The model calculations of the chirality flip $V - A$ combination provides

$$\begin{aligned} \Pi_{V-A}^{Q\text{Loop}}(Q^2) &= -\frac{4N_c}{Q^2} \int \frac{d^4k}{(2\pi)^4} \frac{1}{D_+D_-} \left\{ M_+M_- + \frac{4}{3}k_\perp^2 \cdot \right. \\ &\left. \left[-\sqrt{M_+M_-} M^{(1)}(k_+,k_-) + \left(\sqrt{M^{(1)}(k_+,k_-)} \right)^2 \left(\sqrt{M_+}k_+ + \sqrt{M_-}k_- \right)^2 \right] \right\}. \end{aligned} \quad (6)$$

The V and A correlators are separately dominated by perturbative massless quark loop diagrams in the high momentum region. In the model calculations this dominance is reproduced because in the chiral limit the dynamical quark mass generated in the instanton vacuum, $M(k)$, vanishes at large virtualities k^2 .

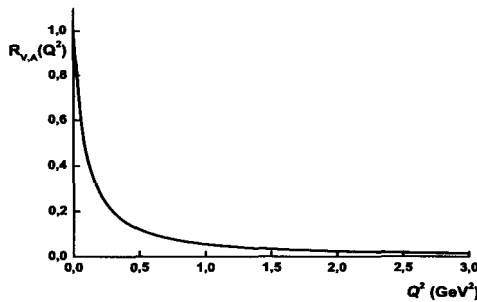


Fig. 1. Normalized $V - A$ correlation function Eq. (13) reconstructed from the ALEPH experimental spectral functions with next-to-leading accuracy in α_s .

With help of the Das-Mathur-Okubo (DMO) sum rule it is possible to estimate the electric polarizability of the charged pions by using the Gerasimov relation

$$\alpha_{\pi^\pm}^E = \frac{\alpha}{m_\pi} \left[\frac{\langle r_\pi^2 \rangle}{3} - \frac{I_{DMO}}{f_\pi^2} \right], \tag{7}$$

where I_{DMO} is the integral corresponding to the DMO sum rule

$$I_{DMO} = \frac{1}{4\pi^2} \int_0^\infty \frac{ds}{s} [\rho_V(s) - \rho_A(s)] = \frac{\partial}{\partial Q^2} [Q^2 \Pi_{V-A}(Q^2)] \Big|_{Q^2 \rightarrow 0}. \tag{8}$$

From (7), with values of charged pion radius and I_{DMO} obtained from the model (see for further details [4, 5]), one finds the result

$$[\alpha_{\pi^\pm}^E]_{\text{model}} = 2.9 \cdot 10^{-4} \text{fm}^3, \tag{9}$$

which is close to experimental data $[\alpha_{\pi^\pm}^E]_{\text{exp}}^{\text{OPAL}} = 2.71(88) \cdot 10^{-4} \text{fm}^3$ [2] and [6]

$$[\alpha_{\pi^\pm}^E]_{\text{exp}}^{\text{PIBETA}} = \begin{cases} 2.68(9) \cdot 10^{-4} \text{fm}^3 & \text{full data set,} \\ 2.90(9) \cdot 10^{-4} \text{fm}^3 & \text{kinematically restricted data set.} \end{cases} \tag{10}$$

New precise results on pion and kaon polarizabilities are expected from COMPASS [7].

The leading order hadronic vacuum contribution to the lepton anomalous magnetic moment is given by

$$a_\mu^{\text{hvp}(1)} = -\frac{2}{3} \alpha^2 \int_0^1 dx (1-x) \bar{\Pi}_V \left(\frac{x^2}{1-x} m_l^2 \right), \tag{10}$$

where $\bar{\Pi}_V(Q^2) = \Pi_V(Q^2) - \Pi_V(0)$, m_l is the lepton mass, and the charge factor 2/3 is taken into account. One gets the model estimate

$$[a_\mu^{\text{hvp}(1)}]_{\text{model}} = 6.2(0.4) \cdot 10^{-8} \tag{11}$$

which is in reasonable agreement with phenomenological results found from the precise determination of the low energy tail of the total $e^+e^- \rightarrow$ hadrons and τ lepton decay cross-sections [8]

$$[a_\mu^{\text{hvp}(1)}]_{\text{exp}} = \begin{cases} 6.934(88) \cdot 10^{-8}, & e^+e^-, \\ 7.018(90) \cdot 10^{-8}, & \tau. \end{cases} \tag{12}$$

As a by-product we estimate the anomalous magnetic moment of the τ lepton as [4] $[a_\tau^{\text{hvp}(1)}]_{\text{model}} = 3.1(0.2) \cdot 10^{-6}$.

The ratio of correlators

$$R_{V,A}(Q^2) = \frac{\bar{\Pi}_{V-A}(Q^2)}{\bar{\Pi}_{V-A}(Q^2) - 2\bar{\Pi}_V(Q^2)} \tag{13}$$

characterizes the dependence of the V,A asymmetry on momentum transfer squared. In (13) the axial-vector correlator is defined with the kinematical pole removed: $\bar{\Pi}_{V-A}(Q^2) = \Pi_{V-A}(Q^2) + f_\pi^2/Q^2$. This pole is not experimentally visible. On general grounds one expects that this ratio is unity at zero virtuality, and goes to zero at large virtualities where perturbative dynamics dominates. In Fig. 1 we present the ratio of correlators, $R_{V,A}$, reconstructed from ALEPH spectral data.

The region of intermediate momentum transfer provides a nontrivial transition between low energy dynamics described in terms of chiral symmetry structures, and high energy dynamics with relevant operator product expansion language. The problems of standard approaches are the rapid growth of independent operator structures with less sensitivity of their experimental determination when moving beyond the applicability region. Moreover, it is difficult to define an energy scale at which the standard expansions begin to work. These problems can be overcome with the aid of the instanton model of QCD vacuum. New data from ALEPH and OPAL on inclusive hadronic τ lepton decays are very helpful in the study of current correlators, one of the simplest objects, at intermediate momentum transfer.

Acknowledgments

The author thanks the Organizers of Spin 2004 for hospitality and financial support. The work is partially supported by RFBR (Grant nos. 04-02-16445, 03-02-17291, 02-02-16194).

References

1. R. Barate *et al.* [ALEPH Collaboration], *Eur. Phys. J.* **C4**, 409 (1998).
2. K. Ackerstaff *et al.* [OPAL Collaboration], *Eur. Phys. J.* **C 7** (1999) 571.
3. A. E. Dorokhov and W. Broniowski, *Eur. Phys. J.* **C32**, 79 (2003).
4. A. E. Dorokhov, *Phys. Rev.* **D70**, 094011 (2004); arXiv:hep-ph/0405153.
5. A. E. Dorokhov, A. E. Radzhabov and M. K. Volkov, *Eur. Phys. J.* **A 21** (2004) 155.
6. E. Frléz *et al.* [PIBETA Collaboration], arXiv:hep-ex/0312029; D. Počanić, private communication, (2004).
7. A. Bressan, *Physics Results from COMPASS*, talk at this conference.
8. B.L. Roberts, *New Results on Muon ($g-2$)*, talk at this conference.

THE POLARIZATION EFFECTS IN NEUTRINO-LEPTON PROCESSES IN A MAGNETIC FIELD

V. A. HUSEYNOV^{a,b}, R. E. GASIMOVA^a

^aDepartment of General and Theoretical Physics, Nakhchivan State University, Nakhchivan, Azerbaijan

^bLaboratory of Physical Research, Nakhchivan Division of Azerbaijan National Academy of Sciences, Nakhchivan, Azerbaijan

The cross sections of the neutrino-lepton processes $\nu_l e^- \rightarrow l^- \nu_e$, $\bar{\nu}_e e^- \rightarrow l^- \bar{\nu}_l$ and $\nu_l \bar{\nu}_e \rightarrow l^- e^+$ in a magnetic field are presented. The polarization effects in these processes and possible astrophysical applications are considered.

1. Introduction

Interest in neutrino (antineutrino)-electron scattering in a strong magnetic field is connected with its important role in astrophysics [1]. The strength of magnetic fields of neutron stars can be as large as $H \geq H_0 = m_e^2 c^3 / e \hbar = 4.41 \times 10^{13} G$ [2]. Fields of $H \sim 10^{15} - 10^{17} G^{\text{Ref.}}$ [3] are generated in supernova explosions. Therefore, for astrophysical applications, it is of great interest to take into account the effect of strong external magnetic field on neutrino (antineutrino)-lepton scattering.

We present the results of investigations on the processes $\nu_l e^- \rightarrow l^- \nu_e$, $\bar{\nu}_e e^- \rightarrow l^- \bar{\nu}_l$ and $\nu_l \bar{\nu}_e \rightarrow l^- e^+$ in a magnetic field. In this work we generalize the results obtained in [4, 5].

2. Inverse charged lepton decay $\nu_l e^- \rightarrow l^- \nu_e$ and the process $\bar{\nu}_e e^- \rightarrow l^- \bar{\nu}_l$

The gauge of the vector potential of the external field is $A^\mu = (0, 0, xH, 0)$. The quantum number $\zeta = +1(-1)$ specifies states with definite spin orientations. Let the initial neutrino travel along the magnetic field, i.e. $k^\mu = \omega(1, 0, 0, 1)$. Below, we restrict our analysis to the case in which the electron possesses a high transverse momentum $p_\perp = (2eHn)^{1/2} \gg m_l$ in the magnetic field of strength $H \ll H_l = m_l^2 / e$; in this case, the motion of the electron is semi-classical because $n \gg 1$. Performing a Lorentz boost along the z axis - this does not change the magnetic field \mathbf{H} - and employing the indicated kinematical condition, we go over to a reference frame where the longitudinal electron momentum is zero. We assume that the incident-neutrino energy ω lies in the range $eH/p_\perp \ll \omega \ll m_l$. Under the above conditions, the total probability of the process depends on only two invariant parameters

$\chi = (H/H_l)(p_{\perp}/m_l) = (e/m^3) [-(F_{\alpha\beta}p^\beta)^2]^{1/2}$ and $\kappa = 2\omega\varepsilon/m_l^2 = 2kp/m_l^2$ where $F_{\alpha\beta} = \partial_\alpha A_\beta - \partial_\beta A_\alpha$ is the tensor of the external field. We will use the invariant spectral variable u and the invariant angular variable τ

$$u = \frac{\chi}{\chi'} - 1 = \frac{p_{\perp}}{p'_{\perp}} - 1 \approx \frac{\omega'}{\varepsilon - \omega}, \quad \tau = \frac{e}{m_l^2} \cdot \frac{p^\alpha \tilde{F}_{\alpha\beta} k'^\beta}{\chi - \chi'} = \gamma \frac{k'_z}{\omega'} \approx \gamma\vartheta \quad (1)$$

where $\tilde{F}_{\alpha\beta} = (1/2)\varepsilon_{\alpha\beta\lambda\sigma}F^{\lambda\sigma}$, $\gamma^{-1} = m_l/\varepsilon$, $\vartheta = \pi/2 - \theta$ and θ is the angle between $\mathbf{k} \perp \mathbf{H}$ (in the region that is important for our analysis, we have $|\vartheta| \leq \gamma^{-1} \ll 1$). With allowance for particle polarizations, the cross sections are given by

$$\sigma_t(\zeta', \zeta) = \frac{G_F^2 m_l^2}{\pi^2} \int_{-\infty}^{+\infty} du \frac{u}{(1+u)^2} \int_{-\infty}^{+\infty} d\tau \left[(2\tilde{\chi})^{1/3} (1 + \tau^2 + \zeta'\tau)\Phi^2(y) + (2\tilde{\chi})^{1/3} \Phi'^2(y) + 2(\tau + \zeta')\Phi(y)\Phi'(y) \right] \quad (2)$$

$$\sigma_l(\zeta', \zeta) = 4 \frac{G_F^2 m_l^2}{\pi^2} \int_{-\infty}^{+\infty} du \frac{u}{(1+u)^2} \int_{-\infty}^{+\infty} d\tau \left[(2\tilde{\chi})^{1/3} \zeta_-(\zeta'_+ + \zeta'_-\tau^2)\Phi^2(y) + (2\tilde{\chi})^{1/3} \zeta_-\zeta'_-\Phi'^2(y) + 2\zeta_-\zeta'_-\tau\Phi(y)\Phi'(y) \right] \quad (3)$$

where $\tilde{\chi} = \chi/u$, $\zeta_{\pm} = (1 \pm \zeta)/2$, $\zeta'_{\pm} = (1 \pm \zeta')/2$, $\kappa_0 = 1 - (m_e/m_l)^2$, the argument of the Airy functions $\Phi(y)$ and $\Phi'(y) = d\Phi(y)/dy$ is $y = [u/2\tilde{\chi}]^{2/3} [1 + \tau^2 + (\kappa_0 - \kappa)/u]$ and the subscripts “ t ” and “ l ” label the cross sections referring to the cases of transverse and longitudinal polarizations, respectively. From 3, it follows that $\sigma_l \sim 1 - \zeta$ - that is, in the leading order in γ^{-1} , the process being considered is forbidden for electrons with right-hand circular polarization ($\zeta = 1$). That terms that are odd in the angular variable τ appear in the differential cross section $d^2\sigma_p/dud\tau$ ($p = t, l$ determined by the integrands in 2,3 is due to P non-conservation in weak interactions. This results in an asymmetry of final neutrino emission with respect to the xy plane chosen to be orthogonal to the magnetic field direction. The cross section of the process $\nu_l e^- \rightarrow l^- \nu_e$ is given by

$$\bar{\sigma}_t(\zeta', \zeta) = \frac{G_F^2 m_l^2}{\pi^2} \int_{-\infty}^{+\infty} du \frac{u}{(1+u)^4} \int_{-\infty}^{+\infty} d\tau \left[(2\tilde{\chi})^{-1/3} (\delta^2 + \tau^2 + 2\zeta\tau\delta)\Phi^2(y) + (2\tilde{\chi})^{1/3} \Phi'^2(y) - 2(\tau + \zeta\delta)\Phi(y)\Phi'(y) \right] \quad (4)$$

$$\bar{\sigma}_l(\zeta', \zeta) = 4 \frac{G_F^2 m_l^2}{\pi^2} \int_{-\infty}^{+\infty} du \frac{u}{(1+u)^4} \int_{-\infty}^{+\infty} d\tau \left[(2\tilde{\chi})^{-1/3} \zeta'_-(\zeta_+\delta^2 + \zeta_-\tau^2)\Phi^2(y) + (2\tilde{\chi})^{1/3} \zeta'_-\zeta_-\Phi'^2(y) - 2\zeta'_-\zeta_-\tau\Phi(y)\Phi'(y) \right] \quad (5)$$

where $\delta = m_e/m_l$. From 5 it follows that $\bar{\sigma}_l \sim 1 - \zeta'$; that is the process results in the production of only charged leptons having left-hand circular polarization. That the cross section σ and $\bar{\sigma}$ involve the variables ζ and ζ' in an asymmetric way is explained not only by P and C non-conservation in weak interactions but also by special kinematical features: left-handed electron neutrinos and right-handed charged lepton antineutrinos are emitted at small angles with respect to the ultrarelativistic-electron momentum.

3. Annihilation of a neutrino and an antineutrino into a charged lepton and a positron in a magnetic field

Here we consider the process $\nu_l + \bar{\nu}_e \rightarrow l_- + e^+$ in a constant magnetic field. Various processes induced by the inelastic scattering of ultrahigh-energy cosmic (anti) neutrinos on low-energy relic (anti) neutrinos in the Milky Way Galaxy are considered as possible sources of high-energy cosmic rays. The gauge of the 4-potential of the magnetic field is $A^\mu = (0, -yH/2, xH/2, 0)$. We restrict ourselves to the case where a neutrino and an antineutrino approach each other from opposite directions in the plane orthogonal to the field \mathbf{H} : $\kappa = \omega(1, 1, 0, 0)$, $\kappa' = \omega'(1, -1, 0, 0)$. Suppose that the energy of the neutrino and antineutrino, and the momentum transfer $q_\perp = |\omega - \omega'| \approx E \gg m_l$, are both much greater than m_l , and that the magnetic-field strength satisfies the condition $H \ll H_l = m_l^2/e$. We can introduce the field, the kinematical, and the mass parameters (κ , λ and δ , respectively)

$$\kappa = \frac{e}{m_l^3} \left[-(F_{\alpha\beta} q^\beta)^2 \right]^{1/2} = \frac{q_\perp H}{m_l H_l} \approx \frac{eHE}{m_l^3}, \quad \lambda = \frac{q^2}{m_l^2} = \frac{4\omega\omega'}{m_l^2}, \quad \delta = \frac{m_e}{m_l} \quad (6)$$

together with the spectral variable ν and the angular variable τ ,

$$\nu = \frac{\chi}{\chi + \chi'} \approx \frac{\varepsilon}{\varepsilon + \varepsilon'}, \quad \tau = \frac{e q^\alpha \tilde{F}_{\alpha\beta} p^\beta}{m_l^4 (\chi + \chi')} \approx \frac{p_z}{m_l} \quad (7)$$

where $\chi' = \chi(p \rightarrow p')$. The cross section for the production of transversely polarized leptons are given by

$$\begin{aligned} \sigma^{(+)}(\zeta', \zeta) &= \frac{G_F^2}{\pi^2} m_l^2 \int_0^1 d\nu \frac{\bar{\nu}}{\nu} \int_{-\infty}^{+\infty} d\tau \left[(2\bar{\kappa})^{-1/3} \tau^2 \Phi^2(y) + \right. \\ &\quad \left. + (2\bar{\kappa})^{1/3} \Phi'^2(y) - 2\tau\Phi(y)\Phi'(y) \right] \quad (\omega \gg \omega') \end{aligned} \quad (8)$$

$$\begin{aligned} \sigma^{(-)}(\zeta', \zeta) &= \frac{G_F^2}{\pi^2} m_l^2 \int_0^1 d\nu \frac{\bar{\nu}}{\nu} \int_{-\infty}^{+\infty} d\tau \left[(2\bar{\kappa})^{-1/3} (1 + \tau^2 + 2\zeta'\tau)\Phi^2(y) + \right. \\ &\quad \left. + (2\bar{\kappa})^{1/3} \Phi'^2(y) + 2(\zeta' + \tau)\Phi(y)\Phi'(y) \right] \quad (\omega \ll \omega') \end{aligned} \quad (9)$$

where $\bar{\kappa} = \kappa\nu\bar{\nu}$, the argument of the Airy function is determined at $\delta = 0$, and the upper and lower signs in the superscript refer to the cases of $q_x = \omega - \omega' > 0$ and $q_x = \omega - \omega' < 0$, respectively. The asymmetric dependence on the angular variable τ and the spin variables ζ and ζ' is due to P and C non-conservation in weak interactions and to the choice of kinematical conditions - an ultra-relativistic charged lepton and an ultra-relativistic positron are emitted at small angles with respect to the direction of the high-energy-(anti) neutrino momentum. The external-field effect on the process is described by the parameter $\eta = \kappa/(\lambda - 1)$. For $\eta \gg 1$ and $\kappa \gg 1$ (strong field), we obtain the asymptotic expression for the cross section

$$\sigma^{(-)}(\zeta', \zeta) = \frac{G_F^2}{4\pi^3} m_\mu^2 \left[c_2 (3\kappa)^{2/3} - c_1 (3\kappa)^{1/3} \zeta' \right], \quad \omega \ll \omega' \quad (10)$$

where $c_1 = (2/5)\Gamma^4(1/3)$, $c_2 = (15/14)\Gamma^4(2/3)$. Assuming that relic (anti)neutrinos are massless, we estimate their energy (that is the temperature of relic radiation) to be $\omega' \sim$

$2K \approx 1.7 \times 10^{-4}$ eV. Our results are valid in the region of cosmic-neutrino energies, $\omega \leq (m_l^2/\omega') \leq 10^{20}$ eV. For the field parameter, we have $\kappa < 10^{-7}(H/1G)$. For neutron stars $\kappa \leq 10^6$ and the cross section of the process in a magnetic field is much larger than the cross section for the free process owing to the factor $(3\kappa)^{2/3} \leq 10^4$. Thus, the process discussed can be a source of high-energy cosmic charged leptons.

Acknowledgements

We are very grateful to Franco Bradamante, Anna Martin and the organizing committee of SPIN 2004 Symposium for their invitation and warm hospitality. We very much appreciate valuable conversations with many participants of the symposium. We also would like to thank Isgender Jafarov, Vladimir Zhukovskii, Anatolii Borisov and Elchin Jafarov for many helpful discussions. This work was supported in part by Tempus Individual Mobility Grant under contract No IMG-AZB 2006-2004.

References

1. Bahcall J N 1989 Neutrino Astrophysics (Cambridge: Cambridge Univ. Press)
2. Lipunov V M 1987, Astrophysics of Neutron Stars (Moscow: Nauka)
3. Bysnovatyi-Kogan G S 1993 Astron. Astrophys. Trans. 3 287
4. Borisov A V, Guseinov V A and Pavlova O S 1998 Phys. At. Nuclei 61 94; 1998 Yad. Fiz. 61 103
5. Borisov A V, Guseinov V A and Zamorin N B 2000 Phys. At. Nuclei 63 1949; 2000 Yad. Fiz. 63 2041

CORRELATED QUARK STRUCTURE OF THE PROTON AND SPIN EFFECTS

G. MUSULMANBEKOV*

Joint Institute for Nuclear Research, Dubna,, Russia

It is shown that most observed polarization phenomena may be explained within the frame of the Strongly Correlated Quark Model proposed by author, where the proton spin emerges from the orbital momentum of the quark and gluon condensate circulating around valence quarks.

The aim of this paper is to propose one more possible explanation of SSA and AGS [1] data in the framework of the so-called Strongly Correlated Quark Model (SCQM), elaborated by the author [2]. The ingredients of the model are the following. A single quark of definite colour embedded in vacuum begins to polarize its surroundings, resulting in the formation of quark-gluon condensate. At the same time it experiences the pressure of the vacuum because of the zero-point radiation field or vacuum fluctuations, which act on the quark and tend to destroy the ordering of the condensate. Suppose that we place a corresponding antiquark in the vicinity of the first one. Owing to their opposite signs, their colour polarization fields interfere, cancelling each other in the region near the mid-point between the quarks. This effect reduces the condensate density in the region, and the overcompensation of the vacuum pressure acting on from further out on the quark-antiquark. As a result the attractive force between quark and antiquark emerges, and they start to move towards each other. The density of the remaining condensate around them is identified with the hadronic matter distribution. Maximum displacement of the $\bar{q}q$ - system corresponds to minimum overlap of the polarization fields, and the hadronic matter distributions have their maximum extent and size. The closer they are to each other, the larger is the destructive interference, the smaller are the hadronic matter distributions around quarks and the larger their kinetic energies. In this way the quark and antiquark start to oscillate around their mid-point. The generalization to three-quark system in baryons is performed according to $SU(3)_{colour}$ symmetry: in general, a pair of quarks has the coupled representation $3 \otimes 3 = 6 \oplus \bar{3}$, and for quarks within the same baryon only the $\bar{3}$ (antisymmetric) representation occurs. Hence, an antiquark can be replaced by two correspondingly coloured quarks to get a colour singlet

*Work partially supported by grants 04-07-90162, 04-02-27099 of the RFBR.

baryon, and destructive interference takes place between the colour fields of three valence quarks (VQs). Putting aside the mass and charge differences of valence quarks, we may say that inside a baryon three quarks oscillate along the bisectors of an equilateral triangle, turning synchronously from constituent quark states to current quark states and *vice versa*. Therefore, keeping in mind that the quark and antiquark in mesons and three quarks in baryons are strongly correlated, we can consider each of them separately as undergoing oscillatory motion for which the hamiltonian reads

$$H_{q(\bar{q})} = \left[\frac{m_{q(\bar{q})}}{(1 - \beta^2)^{1/2}} + U(x) \right], \quad (1)$$

where $U(x)$ is the potential energy of the quark or antiquark. The (anti)quark, along with the surrounding cloud (condensate) of sea quark-antiquark pairs and gluons (which is identified with the hadronic matter distribution), forms the constituent quark state, Q . It is natural to assume that the potential energy of the (anti)quark, $U(x)$, is equivalent to the mass, M_Q , of a constituent quark.

In our approach the spin of a hadron is composed, as in the naive quark model, of the spins of the VQs. The spin of a quark, in turn, is identified with the orbital momentum

$$\mathbf{s} = \mathbf{L} = \int_a^\infty \mathbf{r} \times (\mathbf{E}_{ch} \times \mathbf{B}_{ch}) d^3 \mathbf{r}. \quad (2)$$

The vector product inside the parentheses is the colour analogue of the Poynting vector which represents the circulating flow of energy created by the intersecting chromoelectric and chromomagnetic fields of the VQ. The condensate around the VQ carried along with this vector creates the hadronic current \mathbf{j} . Synchronous oscillations of quarks inside a hadron lead to periodic changes in values the of \mathbf{E}_{ch} and \mathbf{B}_{ch} . At maximum displacement of the quark from its origin of oscillation, \mathbf{E}_{ch} and \mathbf{B}_{ch} are maximally expanded around it (size of constituent quark) and so the circulating flow $\mathbf{S}_{ch} = \mathbf{E}_{ch} \times \mathbf{B}_{ch}$. At minimum displacement \mathbf{E}_{ch} and \mathbf{B}_{ch} , owing to the destructive interference described above, are confined to a small region around the quark, and the circulating flow of energy \mathbf{S}_{ch} and correspondingly the hadronic current, \mathbf{j} , are concentrated in a narrow shell. By analogy with hydrodynamics one can identify a single quark with the extended vortex, defined by a vorticity, ξ , and a velocity field \mathbf{v} :

$$\xi = \nabla \times \mathbf{v}. \quad (3)$$

If σ is the area (vortex size) covered by the velocity field of the vortex, then according to angular momentum conservation

$$\xi \cdot \sigma = \oint_\sigma \mathbf{v} \cdot d\mathbf{r} = const, \quad (4)$$

. This means that the larger the area of circulation the less the vorticity, and *vice versa*. In our case \mathbf{v} is the velocity of circulation, depending on the distance from the vortex center. Following these considerations we assume that the spin of quark is conserved during oscillation and

$$\mathbf{s} \propto \xi \cdot \sigma. \quad (5)$$

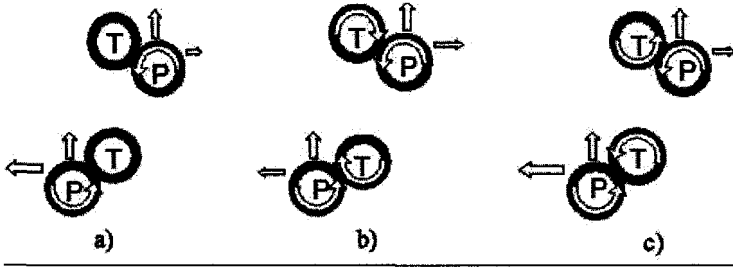


Fig. 1. Quark – quark (vortex – vortex) interactions in collisions of two protons: a) only the projectile proton is polarized; b) projectile and target protons are polarized antiparallel; c) projectile and target protons are polarized parallel. In the upper row the projectile quark (P) hits the target one (T) on the right side, and in the lower row on the left side. Up arrows point along the projectile beam; round arrows depict hadronic currents.

Rigorously, the case at hand is the conservation of individual quark spin because VQs inside hadronic systems can undergo spin-flip and what is conserved is the total angular momentum of the system. For consistency of the model we must demand that the spins of quarks are perpendicular to the plane of their oscillation. In [3] the model has been applied to estimate the spin content of the proton

In our approach mechanism of asymmetry is the same as proposed by Chou and Yang [4], with the difference that in their theory the hadronic current \mathbf{j} in a polarized proton is created by the orbital momentum of constituent quarks. In SCQM three VQs inside a proton look like three synchronously oscillating extended vortices (solitons) with varying sizes. According to (4) the tangential velocity \mathbf{v} is inversely proportional to distance from the center of the vortex. The smaller the vortex, the higher its tangential velocity. In SSA-experiments one of the colliding protons is polarized and the other unpolarized (Fig. 1a). Because of the higher relative velocity in the overlap region the transverse momentum is larger when the polarized quark hits the unpolarized one on the left, than on the right. The sizes of left and right arrows indicate the relative magnitudes of the transverse momenta. The smaller the quark vortex, the higher is the tangential velocity and the left-right asymmetry. Although quark polarization in our model follows the SU(6) wave function (in the proton $P_u = +2/3$ and $P_d = -1/3$), at small displacements the quark states with $P_u = +1$ and $P_d = -1$ dominate.

This mechanism also determines the behaviour of the analyzing power in elastic scattering of polarized protons at large transverse momenta. The larger the transverse momentum, the smaller is quark-vortex probed, and the larger the observed effect. Thus the increase in tangential velocity arising from a reduction in the size of a quark-vortex (large transversal momenta) results in a difference in the cross sections for elastic scattering of transversely polarized protons with parallel and antiparallel spins (Fig. 1b, 1c). Quantitative results will be published in a forthcoming paper.

References

1. P. R. Cameron *et al.*, *Phys. Rev. Rap. Comm.*, **D32**, 3070 (1985); D. G. Grabb *et al.*, *Phys. Rev. Lett.*, **65**, 3241 (1990).
2. G. Musulmanbekov *Frontiers of Fundamental Physics*, Kluwer Acad./Plenum Pub., New York, 2001, p. 109–120.
3. G. Musulmanbekov, *Proc. 15th Int. Symp. Spin Phys.*, 9 – 14 Sept. 2002, AIP Conf. Proc., **675**, New York 2003, p. 358 – 364.
4. T. T. Chou and C. N. Yang, *Nucl. Phys.*, **B107**, 1, (1976).

LOW-FREQUENCY NUCLEAR SPIN MASER AND SEARCH FOR ATOMIC EDM OF ^{129}Xe

A. YOSHIMI

RIKEN, Wako, Japan

K. ASAHI, S. EMORI, M. UCHIDA, S. OSHIMA

Department of physics, Tokyo Institute of Technology, Meguro, Japan

We have developed a nuclear spin maser in which highly polarized nuclei of the noble gas isotope ^{129}Xe oscillate at the low frequency of 34 Hz. The system is advantageous for detecting a small frequency shift of the nuclear spin precession. We are thus planning to apply this system to the search for an atomic electric dipole moment of ^{129}Xe . We here report the development of the system and its performance.

1. Introduction

Spin precession sometimes serves as an exclusive tool in fundamental physics studies. One of the most obvious examples would be found in the study of electric dipole moment (EDM) which, if non-vanishing, should constitute clear evidence for violation of time-reversal (T) and space inversion (P) invariance [1]. In the EDM search experiment, the small frequency shift of the spin precession due to the interaction between an applied electric field and the EDM must be detected. Therefore the precession frequency must be precisely measured. The frequency precision is ultimately governed by how long the precession is observed, but the observation time is usually limited by a finite transverse relaxation time T_2 for the spins. This limitation may be avoided by introducing a spin maser technique [2–4]. We have developed a nuclear spin maser using spin-polarized ^{129}Xe nuclei, which can operate at low frequency compared to the conventional spin maser, by incorporating an optical spin detection-feedback system. In such a system, the nuclear spin continuously precesses beyond the intrinsic T_2 , which is advantageous for EDM experiments.

2. Nuclear spin maser at low frequency

The nuclear spin maser, where the nuclear spins continuously precess without losing their transverse polarization, can oscillate when a transverse magnetic field, whose phase is

shifted by 90° to the transverse polarization component and whose amplitude is proportional to that of the transverse polarization, is applied to the precessing spin system [4, 5]. In order to produce the 'feedback' transverse field which rotates in synchronism with the nuclear spins, the instantaneous direction of the transverse spin polarization must be known. In the present system, we have adopted the optical spin detection system in order to obtain the instantaneous transverse polarization direction.

The experimental apparatus is shown in Fig. 1. A Xe gas (79% enriched ^{129}Xe) and Rb were confined in a spherical glass cell of 20mm diameter. The nuclear spin of ^{129}Xe

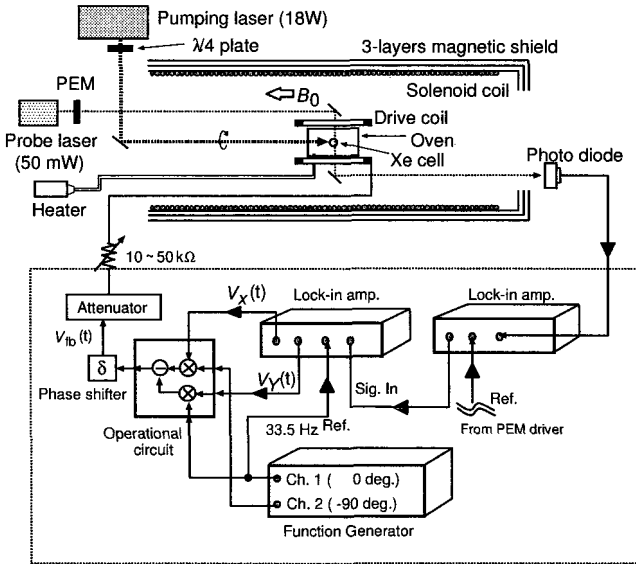


Fig. 1. Conceptual setup of a spin maser with the optical spin detection feedback.

is polarized by spin exchange with optically-pumped Rb atoms [6]. We typically obtained a polarization of $P_0 \approx 10\%$ at a ^{129}Xe density of 6×10^{18} atoms/cm³. A homogeneous static field $B_0 = 28.7$ mG applied to the Xe cell was produced by a solenoid coil installed inside a 3-layer magnetic shield. With the probe laser beam passing through the cell and a photoelastic modulator (PEM), the transverse Rb polarization is detected through circular dichroism. Since the transverse polarization of the ^{129}Xe nuclei induces a slight transverse polarization of Rb atomic spins (repolarization) through spin exchange, the ^{129}Xe precession signal appeared in the lock-in detection of the transmitted probe beam. In order to operate the nuclear spin maser, the optically detected precession signal is converted to the feedback signal with the lock-in amplifier and the operational circuit [4].

The typically measured oscillation signal is shown in Fig. 2. The precession signal appeared after the feedback system became active, and on a time scale of some thousand of seconds the signal approached the steady-state oscillation which eventually set in. The transient pattern of the maser amplitude toward the steady state oscillation was well reproduced

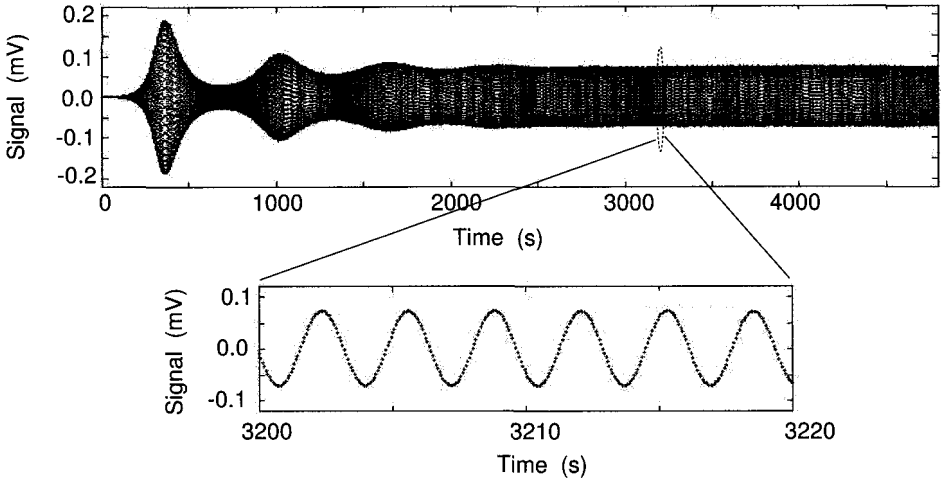


Fig. 2. The observed spin maser oscillation signal. (observed by lock-in detection with a reference frequency of 33.7 Hz)

by numerical simulations based on the modified Bloch equations.

The present nuclear spin maser is capable of operation at frequencies as low as $\nu = 34.0$ Hz. Such low-frequency operation provides a narrow absolute frequency width. The Fourier spectrum, obtained from one-hour continuous oscillation with the apparatus described above, and from the conventional spin maser setup with the spin-coil coupling operated earlier [5], are shown in Fig. 3 (a) and (b) respectively. The static fields in these

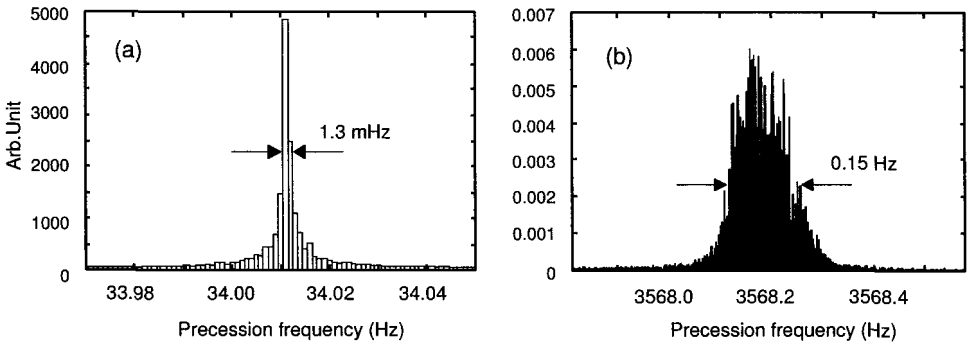


Fig. 3. Fourier spectrum of measured continuous oscillation. (a) The spectrum obtained from the operation of the optical spin detection-feedback spin maser described in the letter. (b) The spectrum obtained from the conventional spin maser.

experiments are respectively 28.7 mG and 3.01 G. The frequency width in the spin maser with the optical spin detection approaches 1.3 mHz, which is smaller by a factor of 100 than in a conventional spin maser. This is due to suppression of the static field fluctuations arising from current instability in the solenoid coil owing to the lower static field.

3. Summary and future

We have developed the nuclear spin maser with polarized ^{129}Xe nuclei by using optical detection of the instantaneous nuclear spin direction, leading to maser operation at the low frequency of 34 Hz. The frequency width of the spin maser became 2 orders narrower than the conventional spin maser. We are now planning to apply this system to search for an EDM in the ^{129}Xe atom. We have already constructed a 4-layer magnetic shield with a length of 1.60 m whose internal residual magnetic field is almost $50 \mu\text{G}$. In order to stabilize the B_0 field, a high-sensitivity magnetometer utilizing nonlinear magneto-optical rotation in Rb atoms [7] is under development. The static field is expected to be stabilized to a level of 10^{-13}G , which indicates that frequency fluctuations of ^{129}Xe precession can be reduced to below 0.1 nHz. Such a sensitive experiment will provide interesting information about the mechanism of CP-violation.

References

1. I.B. Kriplovich and S.K. Lamoreaux, *CP Violation Without Strangeness*, Springer-Verlag, Heidelberg, 1997.
2. M.G. Richards *et al.*, *J. Phys. B* **21**, 665 (1988).
3. T.E. Chupp *et al.*, *Phys. Rev. Lett.* **72**, 2363 (1994).
4. A. Yoshimi *et al.*, *Phys. Lett. A* **304**, 13 (2002).
5. K. Asahi *et al.*, *Czechoslovak J. Phys.* **50**, 179 (2000).
6. W. Happer *et al.*, *Phys. Rev. A* **29**, 3092 (1984).
7. D. Budker *et al.*, *Phys. Rev. A* **62**, 043403 (2000).

**POLARIZATION EFFECTS IN THE REACTIONS $p + {}^3\text{He} \rightarrow \pi^+ + {}^4\text{He}$,
 $\pi^+ + {}^4\text{He} \rightarrow p + {}^3\text{He}$ AND VERIFICATION OF THE CONSEQUENCES OF
 QUANTUM-MECHANICAL COHERENCE FOR THE CORRELATION TENSOR**

V. L. LYUBOSHITZ, V. V. LYUBOSHITZ

Joint Institute for Nuclear Research, Dubna, Russian Federation

Using the formalism of helicity amplitudes, polarization effects are studied in the reaction $p + {}^3\text{He} \rightarrow \pi^+ + {}^4\text{He}$ and in the inverse process $\pi^+ + {}^4\text{He} \rightarrow p + {}^3\text{He}$. It is shown that in the reaction $\pi^+ + {}^4\text{He} \rightarrow p + {}^3\text{He}$, the spins of the final proton and ${}^3\text{He}$ nucleus are strongly correlated. A structural expression through helicity amplitudes, corresponding to arbitrary emission angles, is obtained for the correlation tensor. It is established that in the reaction $\pi^+ + {}^4\text{He} \rightarrow p + {}^3\text{He}$ one of the “classical” incoherence inequalities of the Bell type for the sum of two diagonal components of the correlation tensor is necessarily violated.

1. Polarization effects in the reaction $p + {}^3\text{He} \rightarrow \pi^+ + {}^4\text{He}$

In the paper [1] the general consequences of T invariance for binary reactions $a + b \rightarrow c + d$, $c + d \rightarrow a + b$ with the spin-1/2 particles a and b were considered, and it was shown that due to T invariance, the dependence of the effective cross-section of the direct reaction $a + b \rightarrow c + d$ on the polarizations of initial particles *completely determines* the polarization vectors and spin correlations for the same particles a , b produced in the inverse reaction $c + d \rightarrow a + b$ with unpolarized primary particles^a.

Now let us consider, firstly, the direct reaction $p + {}^3\text{He} \rightarrow \pi^+ + {}^4\text{He}$. This reaction, of the type $1/2 + 1/2 \rightarrow 0 + 0$ (the proton and ${}^3\text{He}$ nucleus have spin 1/2, π^+ and ${}^4\text{He}$ have zero spin), can proceed *only from triplet* states of the system $(p, {}^3\text{He})^{\text{Ref.}}$ [3–5], as follows from parity and angular-momentum conservation, taking into account the negative internal parity of the π^+ -meson.

Let us choose the axis of the total-spin quantization z along the vector $\mathbf{l} = \mathbf{k}_p/k_p$, where \mathbf{k}_p is the proton momentum. There exist three possible triplet states of the $(p, {}^3\text{He})$ -system, characterized by the spin projections $+1$, -1 and 0 onto the axis z : 1) $|+1, \mathbf{l}\rangle = | + 1/2, \mathbf{l}\rangle^{(p)} \otimes | + 1/2, \mathbf{l}\rangle^{(He)}$; 2) $|-1, \mathbf{l}\rangle = | - 1/2, \mathbf{l}\rangle^{(p)} \otimes | - 1/2, \mathbf{l}\rangle^{(He)}$; and 3) $|0, \mathbf{l}\rangle = (1/\sqrt{2}) \left(| + 1/2, \mathbf{l}\rangle^{(p)} \otimes | - 1/2, \mathbf{l}\rangle^{(He)} + | - 1/2, \mathbf{l}\rangle^{(p)} \otimes | + 1/2, \mathbf{l}\rangle^{(He)} \right)$. Us-

^aPreviously a similar approach was used in [2] to study polarization effects in the scattering of spin-1/2 particles on an unpolarized target, basing on the T invariance of the differential cross-section of elastic scattering.

ing the technique of helicity amplitudes (the helicity amplitude $R_\lambda(E, \theta)$ is the amplitude of the reaction $p + {}^3\text{He} \rightarrow \pi^+ + {}^4\text{He}$ proceeding from the state $|\lambda, \mathbf{l}\rangle$; E is the total energy in the c.m. frame and θ is the emission angle), we may write for the cross-section $\sigma \equiv \sigma_{p+{}^3\text{He} \rightarrow \pi^+ + {}^4\text{He}}$ ^{Ref. [1]}:

$$\sigma(E, \theta) = \langle \psi | \hat{\rho}^{(p, He)} | \psi \rangle = \sum_{\lambda} \sum_{\lambda'} R_\lambda(E, \theta) \langle \lambda, \mathbf{l} | \hat{\rho}^{(p, He)} | \lambda', \mathbf{l} \rangle R_{\lambda'}^*(E, \theta); \quad (1)$$

here $|\psi\rangle = \sum_{\lambda=\pm 1, 0} R_\lambda^*(E, \theta) |\lambda, \mathbf{l}\rangle$ is the non-normalized initial two-particle spin state selected by the reaction (due to parity conservation, $R_{+1}(E, \theta) = -R_{-1}(E, \theta) \equiv R_1(E, \theta)$), and $\hat{\rho}^{(p, He)}$ is the two-particle spin density matrix for the $(p, {}^3\text{He})$ -system [1]. Finally, we find that the cross-section $\sigma_{p+{}^3\text{He} \rightarrow \pi^+ + {}^4\text{He}}$ (1) is described by the general structural formula for the cross-section $\sigma_{a+b \rightarrow c+d}$ (see [1]), where all the coefficients are bilinear combinations of the helicity amplitudes R_1, R_0 [1]; in particular, the cross-section for unpolarized primary particles is $\sigma_0 = (1/4)(|R_0(E, \theta)|^2 + 2|R_1(E, \theta)|^2)$.

For the cases $\theta = 0$ and $\theta = \pi$, when $R_1(E, \theta) = 0$ ^{Ref. [1]}, we obtain:

$$\sigma_{p+{}^3\text{He} \rightarrow \pi^+ + {}^4\text{He}} = \frac{1}{4} |R_0|^2 \left(1 + \mathbf{P}^{(p)} \mathbf{P}^{(He)} - 2(\mathbf{P}^{(p)} \mathbf{l})(\mathbf{P}^{(He)} \mathbf{l}) \right); \quad (2)$$

the coefficient at $|R_0|^2$ is the fraction of the state $|0, \mathbf{l}\rangle$ in the initial states.

2. Spin effects in the inverse reaction $\pi^+ + {}^4\text{He} \rightarrow p + {}^3\text{He}$

In the reaction $\pi^+ + {}^4\text{He} \rightarrow p + {}^3\text{He}$ the $(p, {}^3\text{He})$ -system is produced *in the triplet state only*. This state, being symmetric under the interchange of spin quantum numbers of the proton and ${}^3\text{He}$, is as follows (normalized to unity) [1]:

$$|\tilde{\psi}\rangle = \frac{1}{(|R_0(E, \theta)|^2 + 2|R_1(E, \theta)|^2)^{1/2}} \times [R_1(E, \theta) (|+1/2, \mathbf{l}\rangle^{(p)} \otimes |+1/2, \mathbf{l}\rangle^{(He)} - |-1/2, \mathbf{l}\rangle^{(p)} \otimes |-1/2, \mathbf{l}\rangle^{(He)}) + \frac{1}{\sqrt{2}} R_0(E, \theta) (|+1/2, \mathbf{l}\rangle^{(p)} \otimes |-1/2, \mathbf{l}\rangle^{(He)} + |-1/2, \mathbf{l}\rangle^{(p)} \otimes |+1/2, \mathbf{l}\rangle^{(He)})], \quad (3)$$

where $\mathbf{l} = \mathbf{k}_p/k_p$. The state $|\tilde{\psi}\rangle$ is similar in structure to the initial triplet state $|\psi\rangle$ selected by the direct reaction $p + {}^3\text{He} \rightarrow \pi^+ + {}^4\text{He}$, but differs by complex conjugation of *the same* helicity amplitudes.

Assuming the general consequences of T invariance, we obtain [1]:

1.) For the effective cross-section of the reaction $\pi^+ + {}^4\text{He} \rightarrow p + {}^3\text{He}$ in the c.m. frame, summed over the spin projections in the final state:

$$\tilde{\sigma}_0(E, \theta) = (k_p/k_\pi)^2 (|R_0(E, \theta)|^2 + 2|R_1(E, \theta)|^2); \quad (4)$$

2.) For the polarization vectors $\mathbf{P}^{(p)} = \langle \tilde{\psi} | \hat{\sigma}^{(p)} | \tilde{\psi} \rangle$ and $\mathbf{P}^{(He)} = \langle \tilde{\psi} | \hat{\sigma}^{(He)} | \tilde{\psi} \rangle$ of the proton and ${}^3\text{He}$ in the final system:

$$\mathbf{P}^{(p)}(E, \theta) = \mathbf{P}^{(He)}(E, \theta) = -A(E, \theta) \mathbf{n} = -2\sqrt{2} \frac{\text{Im}(R_1(E, \theta) R_0^*(E, \theta))}{|R_0(E, \theta)|^2 + 2|R_1(E, \theta)|^2} \mathbf{n}; \quad (5)$$

3.) For the correlation tensor of the $(p, {}^3\text{He})$ -system:

$$T_{ik}(E, \theta) = \langle \tilde{\psi} | \hat{\sigma}_i^{(p)} \hat{\sigma}_k^{(He)} | \tilde{\psi} \rangle = \delta_{ik} - \frac{2}{|R_0(E, \theta)|^2 + 2|R_1(E, \theta)|^2} \times \left[|R_0(E, \theta)|^2 l_i l_k + 2|R_1(E, \theta)|^2 m_i m_k - \sqrt{2} \text{Re}(R_1(E, \theta) R_0^*(E, \theta)) (l_i m_k + m_i l_k) \right]. \quad (6)$$

In the expressions (5,6) $\mathbf{l}, \mathbf{m}, \mathbf{n}$ are mutually perpendicular unit vectors. (The vector \mathbf{m} is directed in the reaction plane, the vector \mathbf{n} is directed along the normal to the reaction plane.)

In accordance with (5,6), the spins of the proton and the ${}^3\text{He}$ nucleus in the reaction $\pi^+ + {}^4\text{He} \rightarrow p + {}^3\text{He}$ must be *tightly correlated*, which in principle enables one to prepare a beam of ${}^3\text{He}$ nuclei with controllable polarization without acting directly on these nuclei (see [1] for more details).

3. Violation of the incoherence inequalities for the correlation tensor

As was established in the paper [6], in the case of incoherent mixtures of factorizable two-particle states of spin-1/2 fermions, the following inequalities for the sum of two diagonal components of the correlation tensor should be satisfied:

$$|T_{11} + T_{22}| \leq 1; \quad |T_{11} + T_{33}| \leq 1; \quad |T_{22} + T_{33}| \leq 1. \quad (7)$$

However, for *non-factorizable* quantum-mechanical superpositions these inequalities may be violated. The triplet state $|\tilde{\psi}\rangle$ (3) of the final system in the reaction $\pi^+ + {}^4\text{He} \rightarrow p + {}^3\text{He}$ represents a characteristic example of such non-factorizable spin states. (It is well seen that the state $|\tilde{\psi}\rangle$ cannot be reduced to the product of one-particle spin states.)

Calculating the components of the correlation tensor T_{ik} (6) for the system $(p, {}^3\text{He})$ in the coordinate frame used, with the axes $z \parallel \mathbf{l}$, $x \parallel \mathbf{m}$, $y \parallel \mathbf{n}$, we obtain the following expressions (indexes: $1 \rightarrow x$, $2 \rightarrow y$, $3 \rightarrow z$):

$$T_{11} = \frac{|R_0|^2 - 2|R_1|^2}{|R_0|^2 + 2|R_1|^2}; \quad T_{22} = 1; \quad T_{33} = \frac{2|R_1|^2 - |R_0|^2}{|R_0|^2 + 2|R_1|^2} = -T_{11}; \quad (8)$$

$$T_{13} = T_{31} = \frac{2\sqrt{2}}{|R_0|^2 + 2|R_1|^2} \text{Re}(R_1 R_0^*); \quad T_{12} = T_{21} = T_{23} = T_{32} = 0; \quad (9)$$

in doing so, $\text{tr}(T) = 1$. Thus, as follows from (8), in the reaction $\pi^+ + {}^4\text{He} \rightarrow p + {}^3\text{He}$ one of the incoherence inequalities (7) for the sum of two diagonal components of the correlation tensor is *necessarily* violated, irrespective of the specific mechanism of generation of the system $(p, {}^3\text{He})$. Indeed, if $|R_0|^2 > 2|R_1|^2$, we obtain $|T_{11} + T_{22}| > 1$; if, on the contrary, $|R_0|^2 < 2|R_1|^2$, then we have: $|T_{22} + T_{33}| > 1$. Meantime, in both cases the other two incoherence inequalities (7) are satisfied.

Acknowledgments

This work is supported by Russian Foundation for Basic Research (Grant No. 03-02-16210).

References

1. V.V. Lyuboshitz and V.L. Lyuboshitz, *Phys. At. Nucl.* **63**, 767 (2000).
2. V.V. Lyuboshitz and V.L. Lyuboshitz, *Phys. At. Nucl.* **62**, 1323 (1999).
3. S.M. Bilenky and R.M. Ryndin, *Phys. Lett.* **6**, 217 (1963).
4. V.L. Lyuboshitz, *Proceedings of the International Symposium Dubna-Deuteron-93*, JINR E2-94-95, Dubna, 1994, p.292.
5. V.L. Lyuboshitz, *Sov. J. Nucl. Phys.* **12**, 107 (1970).
6. R. Lednicky and V.L. Lyuboshitz, *Phys. Lett.* **B508**, 146 (2001).

SPINNING PARTICLE, ROTATING BLACK HOLE AND TWISTOR-STRING *

A. BURINSKII

NSI Russian Academy of Sciences, Moscow, RUSSIA

The structure of a spinning particle based on the rotating black hole solution is considered. It has gyromagnetic ratio $g = 2$ and nontrivial twistorial and stringy systems. The mass and spin appear from excitations of the Kerr circular string, while the Dirac equation describes excitations of an *axial* stringy system which is responsible for scattering. Complex Kerr geometry contains an open twistor-string, the target space of which is equivalent to Witten's 'diagonal' of the $\mathbf{CP}^3 \times \mathbf{CP}^{*3}$.

1. Rotating black hole as a spinning particle

In this paper we consider the model of a spinning particle [1] which is based on the Kerr rotating black hole solution and has rich spinor, twistor and stringy structures. Methods inspired by strings and twistors have led to great progress in computation of some scattering amplitudes [2]. In a recent paper [3] Witten suggested a 'twistor-string' which may be an element of the structure of fundamental particles. We show that a version of the 'twistor-string' is present in the Kerr spinning particle.

Twistors may be considered as lightlike world-lines [4]. The lightlike momentum p^μ may be represented in the spinor form $p^\mu = \bar{\psi}\sigma^\mu\psi$. A twistor is a generalization of the spinor which is necessary for the description of null world-lines carrying angular momentum $x^\mu(t) = x_0^\mu + p^\mu t$ with $x_0 \neq 0$. It contains two extra spinor components $\omega_{\dot{\alpha}} = \psi^\alpha x_0^\nu \sigma_{\nu\alpha\dot{\alpha}}$. The set $\{x^\mu, \psi^\alpha\}$, or the equivalent set $\{x^\mu, Y\}$, where $Y = \psi_2/\psi_1$ is a projective spinor, may also be considered as twistors.

A Black Hole which is neither 'Black' nor a 'Hole' - this joke by P. Townsend has a direct relation to the Kerr spinning particle. The ratio angular momentum/mass, $a = J/m$, for spinning particles is very high and the black-hole horizons disappear, revealing the naked singular ring which is the branch line of the Kerr space on the physical and 'mirror' sheets. The strings and twistors going through the Kerr ring pass into a 'mirror' world and appear semi-infinite. In [5] a model of spinning particle was suggested, where the quantum electromagnetic excitations of the Kerr ring generate the spin and mass.

*Work partially supported by grant 03-02-27190 of the RFBR

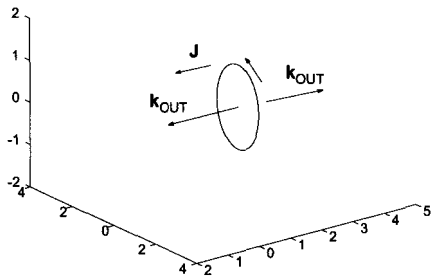


Fig. 1. Kerr’s singular ring and two semistrings (twistors) of opposite chiralities.

It was recognized that the Kerr ring is a closed string with traveling waves [6], and excitations of the Kerr ring lead to the appearance of the extra *axial* stringy system consisting of two semi-infinite singular strings of opposite chiralities [1] (Figure 1). These excitations generate the chiral traveling waves along the axial semistrings, and the Dirac spinor $\Psi = \begin{pmatrix} \phi_\alpha \\ \chi^{\dot{\alpha}} \end{pmatrix}$ describes in the Weyl basis an interplay of two axial traveling waves of opposite chiralities [1].

This axial stringy system plays important role in the formation of the third stringy structure, the *complex* twistor-string.

Basic properties of the Kerr spinning particle:

- The anomalous gyromagnetic ratio $g = 2$ is that of the Dirac electron,
- Twistorial and stringy structures,
- Mass and spin of the particle appear from electromagnetic excitations of the Kerr ring (traveling waves) - Wheeler’s ‘geon’,
- The Compton region is structured by the Kerr circular string.
- The Dirac equation describes traveling waves on two axial semistrings.

A few properties may also be related to the foundations of quantum theory:

- The wave function has a physical carrier - the axial stringy system.
- The axial string may control the motion of particle due to topological coupling to a circular string, reproducing the old de Broglie conjecture.
- The quantum property - absence of radiation by oscillations - is exhibited here at the classical level due to the twofolded nature of the Kerr space: the loss of energy on the ‘physical’ sheet of space is compensated by incoming radiation from the ‘mirror’ sheet.

Beyond that, there are connections to the Skirme and chiral bag models: the Kerr congruence is a twisting generalization of the ‘hedgehog’ Ansatz.

2. Complex Kerr geometry and twistor-string

In the **Kerr-Schild formalism** [7], the metric has the form $g_{\mu\nu} = \eta_{\mu\nu} + 2hk_\mu k_\nu$, where $\eta_{\mu\nu}$ is the metric of Minkowski space, $x^\mu = (t, x, y, z)$, and k_μ is a vortex of the null field which is tangent to the Kerr congruence of twistors $\{x^\mu, Y\}$ which is determined by the **Kerr theorem** [1, 4]. Congruence of twistors, a geodesic family of null rays, covers the Kerr space twice (see figures in [1, 6].) Two axial semistrings z^- and z^+ are created by two twistors corresponding to $Y = 0$ and $Y = \infty$.

The complex Kerr string appears naturally in the Newman-initiated *complex representation* of the Kerr geometry [8], which is generated by a complex world-line $X_0^\mu(\tau) \in \mathbf{CM}^4$. The complex time $\tau = t_0 + i\sigma$ forms a stringy world-sheet [9, 10]. The real fields on the real space-time x^μ are determined via a complex retarded-time construction, where the vectors

$K^\mu = x^\mu - X_0^\mu(\tau)$ have to satisfy the complex light-cone constraints $K_\mu K^\mu = 0$. This allows one to select two families of twistors: left (holomorphic) $\{X_0, Y\}$ and right (antiholomorphic) $\{\bar{X}_0, \bar{Y}\}$.

In the Kerr case $X_0^\mu(\tau) = (\tau, 0, 0, ia)$, and the complex retarded-time equation $t - \tau \equiv t - t_0 - i\sigma = \bar{r}$ (where $\bar{r} = r + ia \cos \theta$ is the Kerr complex radial distance and θ is an angular direction of twistor) shows that on the real space $\sigma = -a \cos \theta$. Therefore, the light-cone constraints select a strip on the τ plane, $\sigma \in [-a, +a]$, and the complex world-sheet acquires the boundary, forming an open string $X_0^\mu(t, \sigma)$.

This string is similar to the well known $N = 2$ string [9]. In \mathbf{CM}^4 it has only chiral left modes $X_0(\tau)$, while the complex conjugate string has only right ones, $\bar{X}_0(\bar{\tau})$. By imbedding this string into real space-time, the left and right structures are identified by orientifolding the world-sheet [10]. The resulting string describes a massive particle and has a broken $N=2$ supersymmetry. Its target space is equivalent to a 'diagonal' of $\mathbf{CP}^3 \times \mathbf{CP}^{*3}$.

The twistors, joined to the ends of the complex string $X_0^\nu(t \pm ia)$, have the directions $\theta = 0, \pi$ and are generators of the singular z^\pm semi-strings, so the complex string turns out to be a D -string which is stuck to two singular semistrings of opposite chiralities (Figure 2). These z^\pm singular semistrings may carry the Chan-Paton factors (currents) playing the role of quarks with respect to the complex string. The Kerr circular string is responsible for the

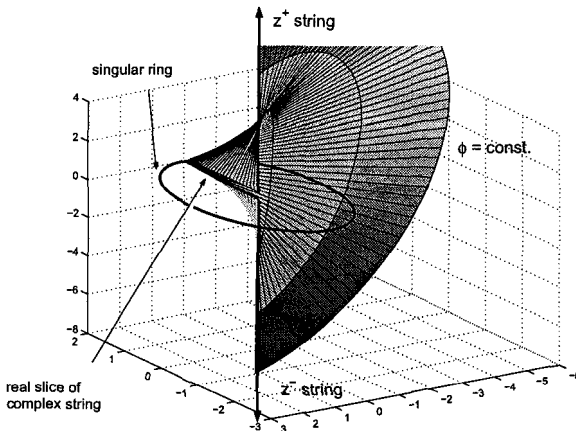


Fig. 2. The complex twistor-string is stuck to two semistrings by imbedding into the real Kerr geometry. The subset of semi-twistors at $\phi = \text{const.}$ is shown.

mass and spin of the particle, while the axial semistrings are responsible for the scattering processes.

Acknowledgments

The author thanks the ICTP and Organizers of the SPIN2004 Symposium for an invitation and financial support, and the RFBR for a travel grant.

References

1. A. Burinskii, *Phys. Rev. D***70** 086006 (2004), hep-th/0406063.
2. Z. Bern, L. Dixon and D. Kosower, *Ann. Rev. Nucl. Part. Sci.***46**, 109 (1996); V. P. Nair, *Phys. Lett.***B214**, 215 (1988).
3. E. Witten, hep-th/0312171.
4. R. Penrose, *J. Math. Phys.***8**, 345 (1967).
5. A. Burinskii, *Sov. Phys. JETP* **39** 193 (1974).
6. A. Burinskii, *Phys. Rev. D***68**, 105004 (2003).
7. G. C. Debney, R. P. Kerr, A. Schild, *J. Math. Phys.***10**, 1842 (1969).
8. E.T. Newman, *J. Math. Phys.* **15**, 44 (1974); *Phys. Rev. D***65**, 104005 (2002).
9. H. Ooguri, C. Vafa, *Nucl. Phys.***B361**, 469 (1991); **B367**, 83 (1991).
10. A. Ya. Burinskii, *Phys. Lett.***A185**, 441 (1994); gr-qc/9303003.

CLASSICAL ELEMENTARY SPINNING PARTICLES, ZITTERBEWEGUNG AND DIPOLE STRUCTURE*

M. RIVAS

Theoretical Physics Department, University of the Basque Country, Bilbao, Spain

The concept of elementary particle rests on the idea that it is a physical system with no excited states, so that all possible kinematical states of the particle are just kinematical modifications of any one of them. In this way describing the particle attributes amounts to describing the collection of consecutive inertial observers who describe the particle in the same kinematical state. The description of an elementary particle is thus related to the kinematical group of space-time transformations related to the relativity principle. The kinematical state space of an elementary particle is a homogeneous space of the kinematical group. We finally present the model of the electron predicted by this formalism.

1. What is an elementary particle?

To understand the spin structure of an elementary particle we have to understand first what is an elementary particle. The concept of an elementary particle rests on the idea that this ultimate indivisible object is such a simple mechanical system that it has no excited states. In a broad sense it is always in a single state which looks different for the different inertial observers, but the difference is only a matter of change of point of view and not a change of its intrinsic properties. It is only a kinematical change. All its possible states are just kinematical modifications of any one of them.

In the quantum case, once a single inertial observer O describes the state of the electron, the collection of the remaining states described by all other inertial observers completely generates the Hilbert space of all states. There is no other possible state of the electron which cannot be described by any one of the above states or any linear combination of them. The Hilbert space is the kinematical state space of an elementary particle.

This is Wigner's quantum definition of an elementary particle as a system whose Hilbert space of pure states is an invariant space under the group of space-time transformations. In group theoretical language, an elementary particle is thus a quantum system whose Hilbert space of states carries an irreducible representation of the kinematical group of space-time transformations [1].

*This work has been partially supported by the universidad del País Vasco/Euskal Herriko Unibertsitatea research grant 9/UPV00172.310-14456/2002.

It is clear that Wigner's irreducibility condition is a necessary condition for a quantum system to be considered as elementary. But, what is the classical equivalent requirement?

Let us assume that a particular inertial observer is describing the classical state of a particle by giving the values of the basic and essential variables which characterize its state. Now the particle, under some external influence, changes some of its variables and therefore it goes into a different state. Then, by assumption, if the particle is elementary it is always possible to select another inertial observer who describes the particle in the same state and with the same values of its variables as the previous observer. This is the idea about what an elementary particle should be from a theoretical viewpoint. Every change in the state of an elementary particle can always be compensated by choosing a new inertial reference frame.

If we call the kinematical variables of a system those variables which characterize the initial and final state of the system in a Lagrangian formalism, we conclude [2, 3] that the **kinematical space of a classical elementary particle must necessarily be a homogeneous space of the kinematical group**. This is the classical requirement, equivalent to the irreducibility condition of the quantum case, to define an elementary particle.

Although we have not made any assumption concerning the classical variables we need to describe an elementary particle, the above definition completely determines them. The classical variables which characterize the initial and final states of an elementary particle are t , r , v and α , interpreted respectively as the time, position of a point where the charge is located, velocity of the charge, and the orientation of the particle, which is expressed as a suitable parametrization of the rotation group. We see that these 10 variables are the variables we use to parametrize any element of the kinematical group, either the Galilei or Poincaré.

In particular, the point particle states are characterized by the variables t and r . It is an elementary particle according to this formalism, but it is spinless and it is not the most general elementary system we can describe. The additional variables v and α for the description of a general elementary particle, when compared with the point particle case, will give rise to the spin structure. Variables α mean that the particle changes its orientation in space and thus rotates, so that part of the spin will be related to its angular velocity of rotation. The analysis of the dependence of the velocity variables v will produce a general feature for spinning particles: the position of the charge and the center of mass of the particle will be different points. Only for spinless systems these two points are the same point. This separation contributes to the electric and magnetic dipole structure.

2. The classical description of the electron

The relativistic description of the electron leads to the dynamical equation of the free electron in the center of mass frame

$$r = \frac{1}{mc^2} S \times v,$$

where S is a constant spin vector in this frame. The solution is depicted in Figure 1.

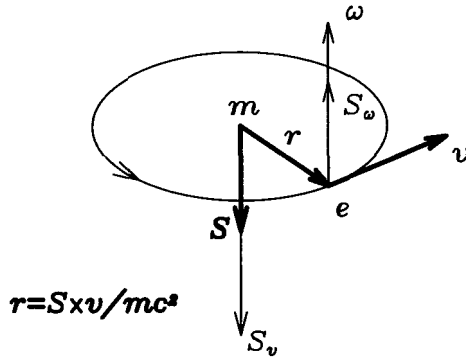


Fig. 1. The charge of the electron, located at point r , moves in circles at the speed of light in the center of mass frame. The body frame associated to this point, which rotates with angular velocity ω , is not depicted.

The structure of the spin is twofold $S = S_\omega + S_v$. One part S_ω is related to the rotation of the body frame and is directed along the angular velocity, and another S_v depends on the orbital motion of the charge of the electron, located at a single point r , around its center of mass, which is necessarily a different point for a spinning particle. This internal motion of the charge is at the speed of light, so that no inertial observer sees the charge of the electron at rest.

The magnetic moment of the electron is produced by this motion of the charge, and it is only related with the S_v part by the usual classical relation. The electron is just a current j^μ for every observer, the magnetic moment is a derived property, and this justifies that its interaction with an external electromagnetic field is given by the minimal coupling $j^\mu A_\mu$ without any further anomalous magnetic coupling.

The rotation part S_ω does not contribute to the magnetic moment. When we quantize the system, the total spin S is just half the orbital part S_v , so that when we express the magnetic moment in terms of the total spin we obtain that $g = 2$ by pure kinematical considerations [4].

The orbital motion of the charge around the center of mass is of radius $R = S/mc$ and angular frequency $\omega = mc^2/S$, and both S and m are unrestricted from the classical point of view. This motion is what Schrödinger called the *Zitterbewegung* of the electron. When we quantize the system the classical parameter $S = \hbar/2$. This classical model of an elementary particle describes a fermion when quantized.

We see that, in addition to the magnetic moment created by the motion of the charge, we also have with respect to the center of mass an electric dipole moment $d = er$. This oscillating electric dipole is of average value zero, and therefore when the electrons are far apart it produces no noticeable effect in low energy processes. But in high energy in-

teractions or in very close electron-electron interactions, it plays an important role. It has been recently shown that this separation between the center of mass and the charge position, which produces a nonvanishing electric moment, can justify the formation of bound electron pairs in a spin 1 state [5].

References

1. E.P. Wigner, *Ann. Math.* **40**, 149, (1939).
2. M. Rivas, *J. Phys. A*, 1971 (1985); *J. Math. Phys.* **30**, 318 (1989); *J. Math. Phys.* **35**, 3380 (1994).
3. M.Rivas, *Kinematical theory of spinning particles*, Kluwer, Dordrecht (2001).
4. M. Rivas, J.M. Aguirregabiria and A. Hernández, *Phys. Lett. A* **257**, 21 (1999).
5. M. Rivas, *J. Phys. A*, **36**, 4703, (2003); ArXiv:physics/0112005.

This set of states contains only kinematical modifications of any one of them.



SESSION 2

QCD Spin Structure of Nucleons

This page intentionally left blank

MEASUREMENT OF THE GLUON POLARIZATION $\Delta G/G$ AT COMPASS

C. SCHILL

Albert-Ludwigs-Universität Freiburg, Freiburg, Germany

(on behalf of the COMPASS Collaboration)

One of the key objectives of the COMPASS experiment at CERN is the determination of the gluon contribution to the nucleon spin. The gluon polarization is measured via photon-gluon fusion in deep-inelastic scattering of 160 GeV/c polarized muons on a polarized ${}^6\text{LiD}$ solid-state target. Photon-gluon fusion is tagged by the observation of charmed mesons or the production of hadron pairs with large transverse momenta p_t . The status of the analysis of the D^0 and D^{0*} events and of the high- p_t hadron pairs is shown. The gluon polarization $\Delta G/G$ has been determined from the asymmetry of high- p_t hadron pairs with $Q^2 > 1$ (GeV/c) 2 in an analysis of the 2002/03 data as $\Delta G/G = 0.06 \pm 0.31(\text{stat.}) \pm 0.06(\text{sys.})$.

1. Introduction

In an intuitive picture, the spin of the nucleon is carried by its valence quarks. However, deep inelastic scattering (DIS) experiments (EMC, SMC, SLAC, HERMES) have shown that only a small fraction of the nucleon spin is carried by quarks. Since then, one of the key questions in hadron physics has been how the total spin of the nucleon $\hbar/2$ is assembled. Candidates which may contribute, in addition to the quark spin $\Delta\Sigma$, are the helicity contribution of the gluon ΔG , together with the quark and gluon orbital angular momenta $L_{q,g}$:

$$\frac{1}{2} = \frac{1}{2}\Delta\Sigma + \Delta G + L_{q,g} \quad (1)$$

One of the main goals of the COMPASS experiment [1] is a measurement of the helicity contribution ΔG of the gluon to the nucleon spin, via the photon-gluon fusion process. Photon-gluon fusion is tagged by the production of charmed mesons D^0 and D^{0*} or of hadron pairs with large transverse momenta p_t . In addition to the gluon polarization, the COMPASS experiment investigates a broad physics program [2] in polarized semi-inclusive deep inelastic scattering and hadron spectroscopy.

2. The COMPASS experiment

The COMPASS experiment uses a 160 GeV/c polarized muon beam from the CERN SPS, scattering it off a polarized ${}^6\text{LiD}$ solid state target [3] at a high luminosity of about $4 \cdot$

$10^{32} \text{ cm}^{-2}\text{s}^{-1}$. From the counting rate difference in two oppositely polarized target cells, the photon-nucleon cross-section asymmetry A^{γ^*d} can be determined:

$$A^{\gamma^*d} = \frac{\Delta\sigma^{\gamma^*d}}{\sigma^{\gamma^*d}} = \frac{1}{P_b P_t f D} \cdot \frac{N_1^{\overline{\pi}} - N_2^{\overline{\pi}}}{N_1^{\overline{\pi}} + N_2^{\overline{\pi}}}, \quad (2)$$

where the muon beam polarization is $P_b \approx 0.76$, the target polarization $P_t \approx 0.5$, and the fraction of polarized material in the target $f \approx 0.4$. The depolarization factor $D(y)$ of the virtual photon γ^* can be calculated as a function of the fractional energy transfer y .

The particles produced in the interaction are detected in a two-stage forward spectrometer with high momentum resolution, high rate capability, and excellent particle identification using hadronic and electromagnetic calorimeters and a large ring-imaging Čerenkov detector, which is able to identify kaons and pions from the charmed meson decay. A special quasi-real photo-production trigger allows the detection of events with scattered muons down to $Q^2 = 10^{-4} (\text{GeV}/c)^2$. Data have so far been taken from 2002 until 2004.

3. Gluon polarization from open charm production

The ‘‘golden channel’’ for tagging photon-gluon fusion events is the production of a $c\bar{c}$ -quark pair, since the charm content of the nucleon is very small, and the hard scale is set by the charm mass for this channel. One of the charm quarks fragments into a D^0 or a D^{0*} meson, which is detected in our experiment. The D^0 and D^{0*} mesons are reconstructed from their invariant mass in the decays $D^0 \rightarrow K^- \pi^+$ and $D^{0*} \rightarrow D^0 + \pi$, and the charge-conjugated decays (Fig. 1). The gluon polarization $\Delta G/G$ can then be determined from the experimental asymmetry in open-charm production according to:

$$A^{\gamma^*d \rightarrow c\bar{c}} = \frac{\int d\hat{s} \Delta\sigma^{PGF}(\hat{s}) \Delta G(x_g, \hat{s})}{\int d\hat{s} \sigma^{PGF}(\hat{s}) G(x_g, \hat{s})} \approx \langle a_{LL} \rangle \frac{\Delta G}{G}, \quad (3)$$

where \hat{s} is the invariant mass $m_{c\bar{c}}^2$ of the charm quark pair. The polarized photon-gluon cross section $\Delta\sigma^{PGF}$ has been calculated in NLO by two groups [4, 5]. The analysis of the full 2002-2004 data set is in progress; the projected statistical error on $\Delta G/G$ is 0.24.

4. Gluon polarization from hadron pairs with large p_t

Another approach to tagging the photon-gluon fusion process is the detection of a hadron pair [6] with large transverse momenta p_t . The transverse momentum of each hadron relative to the virtual photon is required to be larger than $0.7 \text{ GeV}/c$, and $(p_{t1}^2 + p_{t2}^2) > 2.5 (\text{GeV}/c)^2$. To ensure that the hadrons originate from the current fragmentation region, cuts on $x_F > 0.1$ and $z > 0.1$ have been applied. Contributions from resonances are removed by a two-hadron invariant mass cut $m(h_1 h_2) > 1.5 \text{ GeV}/c^2$. Requiring $Q^2 > 1 (\text{GeV}/c)^2$ suppresses a possible contribution from resolved photon processes, where the hadronic structure of the photon is probed. Requiring $x_{Bj} < 0.05$ selects a kinematic region in which the asymmetry from leading order DIS and QCD-Compton scattering is small. From the selected high- p_t sample of events in the 2002/2003 data we have measured:

$$A_{LL}^{\gamma^*d \rightarrow hhX} = -0.015 \pm 0.080(\text{stat.}) \pm 0.013(\text{syst.}) \quad (4)$$

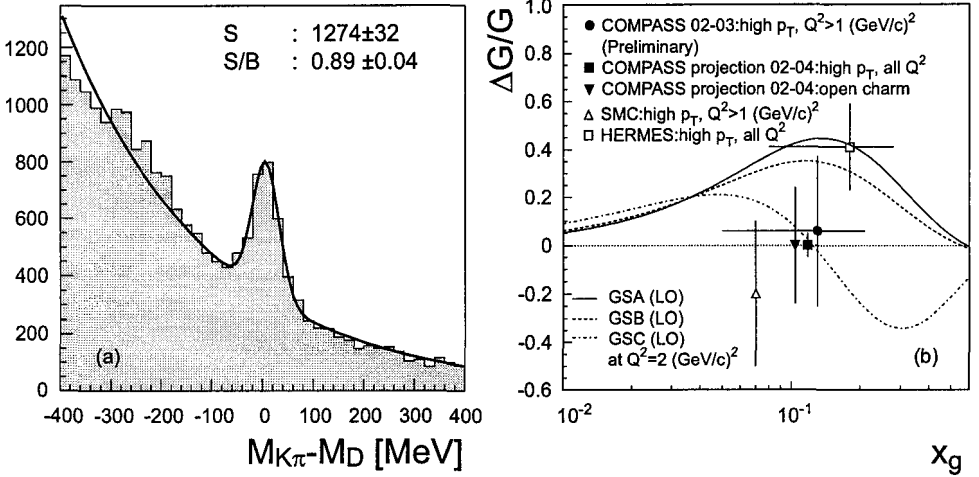


Fig. 1. Left: Reconstructed D^0 in the $K\pi$ invariant mass spectrum tagged by their decay from D^* (2003 data). Right: COMPASS result for $\Delta G/G$ from high- p_T hadron pairs with $Q^2 > 1$ (GeV/c) 2 from 2002/03 data compared to SMC [7] ($Q^2 > 1$ (GeV/c) 2) and HERMES [8] (all Q^2) measurements. In addition, projections for the statistical accuracy in $\Delta G/G$ from open charm production and high- p_T hadron pairs for all Q^2 are shown for the full 2002-04 dataset. The curves show the parameterizations A - C of [9].

The systematic uncertainty takes into account possible false asymmetries, the uncertainty in the measurement of the target and beam polarization, and the knowledge of the depolarization D and dilution factor f . The gluon polarization is calculated from the asymmetry $A_{LL}^{\gamma^* d \rightarrow hhX}$ as:

$$A_{LL}^{\gamma^* d \rightarrow hhX} = \left\langle \frac{\hat{a}_{LL}^{PGF}}{D} \right\rangle \frac{\sigma^{PGF}}{\sigma^{tot}} \frac{\Delta G}{G}, \quad (5)$$

where \hat{a}_{LL}^{PGF} is the analyzing power and $\sigma^{PGF}/\sigma^{tot}$ the fraction of photon-gluon fusion events. Background processes like QCD-Compton scattering and leading order DIS contribute only as a dilution of the measured signal: their asymmetry is proportional to $A_1^d(x)$, which is very small in the selected kinematic range $x_{Bj} < 0.05$. Their effect has been taken into account in the systematic uncertainty of the result. The analyzing power $\hat{a}_{LL}^{PGF} = -0.75 \pm 0.05(\text{syst.})$ and the fraction $\sigma^{PGF}/\sigma^{tot} = 0.34 \pm 0.07(\text{syst.})$ of photon-gluon fusion events were determined using a Monte-Carlo simulation (LEPTO) with a modified set of fragmentation parameters [7] and including radiative corrections (RADGEN). Our result for $\Delta G/G$ is (Fig. 1):

$$\Delta G/G = 0.06 \pm 0.31(\text{stat.}) \pm 0.06(\text{syst.}) \quad (6)$$

at a mean gluon momentum fraction $\langle x_g \rangle = 0.13 \pm 0.08(\text{RMS})$.

5. Outlook

The first COMPASS result on $\Delta G/G$ for high- p_T hadron pairs with $Q^2 > 1$ (GeV/c) 2 is shown in Fig.1, in comparison with other experiments [7,8]. Including the 2004 run will ap-

proximately double the data set. There are about 10 times more events at $Q^2 < 1$ (GeV/c)². However, at low Q^2 , a background of resolved photons enters as an additional theoretical uncertainty. The projected statistical accuracy on $\Delta G/G$ from open charm production and high- p_t hadron pairs for all Q^2 is shown in Fig.1. COMPASS will resume data taking in 2006 and will continue its physics program until at least 2010.

References

1. COMPASS collaboration, *CERN/SPSLC* 96-14 (1996).
2. A. Bressan, D. Peshekonov, R. Joosten, P. Pagano, D. Neyret, J. Friedrich, V. Alexakhin, *these proceedings*.
3. F. Gautheron, Y. Kisselev, J. Koivuniemi, *these proceedings*.
4. I. Bojak, and M. Stratmann, *Nucl. Phys.* **B 540**, 345 (1999).
5. Z. Merebashvili, A. P. Contogouris, and G. Grispos, *Phys. Rev.* **D 62**, 114509 (2000) and *Phys. Rev.* **D 69**, 019901(E) (2004).
6. A. Bravar *et al.*, *Phys. Lett.* **B 421**, 349 (1998).
7. E. Rondio, *these proceedings*; B. Adeva *et al.* (SMC), *Phys. Rev.* **D 70**, 012002 (2004).
8. A. Airapetian *et al.* (HERMES), *Phys. Rev. Lett.* **84**, 2584 (2000).
9. T. Gehrman, and W. J. Sterling, *Z. Phys.* **C 65**, 461 (1994).

TRANSVERSE SPIN AT PHENIX AND FUTURE PLANS

Y. MAKDISI

Brookhaven National Laboratory, Upton, USA

(for the PHENIX Collaboration)

The PHENIX experiment took data with transversely polarized proton beams in 2001-2002. It measured the transverse single-spin asymmetries in inclusive neutral pion and non-identified charge hadrons at midrapidity and $\sqrt{s}=200$ GeV. The data near $X_F \sim 0$ cover a transverse momentum range from 0.5 to 5.0 GeV/c. The observed asymmetries are consistent with zero with good statistical accuracy. This paper presents the current work in the light of earlier measurements at lower energies in this kinematic region, and future plans of the PHENIX detector.

1. Introduction

Large transverse single-spin asymmetries in $p\uparrow p$ collisions have been observed in a number of experiments at energies \sqrt{s} ranging from 5 to 10 GeV. Asymmetries approaching 30% were observed in inclusive pion production at large x_F [1, 2]. In the kinematic region at midrapidity at high x_T and p_T up to 2 GeV/c, large asymmetries were also observed in inclusive π^0 and π^+ production, but not in π^- production [3–5]. From the low energy data one could surmise that the asymmetries tend to grow and reach a maximum near the kinematic limits. At higher energies of 20 and 200 GeV, where pQCD is considered applicable, asymmetries at large x_F persisted [6, 7]. However the asymmetry in π^0 production at midrapidity was found to be zero up to a p_T of 4 GeV/c [8].

The data presented here were collected by the PHENIX detector in 2001-2002 with RHIC running with transversely polarized proton beams at $\sqrt{s}=200$ GeV. At these energies the measured unpolarized cross sections at midrapidity were found to agree well with the NLO pQCD calculations [13], providing confidence that perturbative calculations are applicable to the polarized data, Figure 1.

2. The experimental set up and data analysis

The RHIC beams had 56 bunches each, an average intensity of $5 \cdot 10^{10}$ per bunch, and bunch polarization $+ - + -$ and $+ + - -$ in each beam respectively. A total of 0.15 pb^{-1} was accumulated. The average beam polarization was 15% as measured by the p-Carbon CNI polarimeters, with an overall scale uncertainty of 35%, most of which is attributed to the

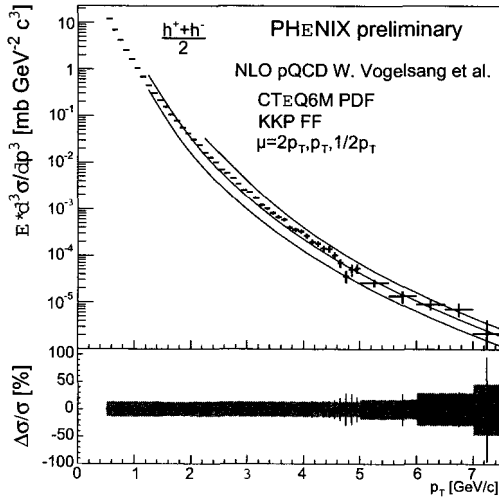


Fig. 1. Invariant cross section vs. p_T . The curves represent NLO pQCD calculations.

lack of analyzing power of the physics process [9]. The relative luminosity between bunch collisions was determined for each fill using two sets of 2π azimuthally symmetric Beam-Beam Counters (BBC) located ± 1.44 m from the interaction point. This was confirmed from a later run by a comparison with the Zero-Degree Calorimeters at ± 18 m that are sensitive to very forward neutrons. The accuracy was determined to about $2.5 \cdot 10^{-4}$.

The collision trigger utilized a coincidence between the BBCs, which accounts for approximately 50% of the proton-proton inelastic cross section at 200 GeV and provides minimal bias to vertical beam polarization. With a vertex position resolution of ≈ 2 cm the trigger accepted events within 75 cm. The analyzed sample had a vertex cut of ± 30 cm. In order to enhance the neutral pion sample, a photon energy threshold of 0.8 GeV was added in coincidence. Charge particle reconstruction was carried out using the drift and pad chambers, which cover $|\eta| < 0.35$ and $\Delta\phi = 90^\circ$. Conversion electrons were reduced to less than 1% by requiring no hits in the RICH counter with a pion threshold of 4.7 GeV/c. Decays from short-lived particles could not be removed but accounted for less than 5% at the highest momenta.

The two-photon effective mass was reconstructed using the EM-calorimeters, with trigger efficiencies ranging from 24% to 78%, and π^0 peak widths ranging from 13.2 to 10.6 MeV/c², as p_T ranged from low to high values. The yield was extracted at each transverse momentum within a mass cut of 0.12-0.16 GeV/c². The asymmetry in the background was calculated using 50 MeV/c² bins around the π^0 mass.

The asymmetries were calculated using the luminosity formula for each fill and then averaged over the whole run. With both beams polarized, single-spin analyses were carried out independently, using one polarized beam while averaging over the other. To assess the systematics, a bunch shuffling technique was also employed, in which the spin direction of each bunch was assigned randomly, assuring the same relative luminosities. The results

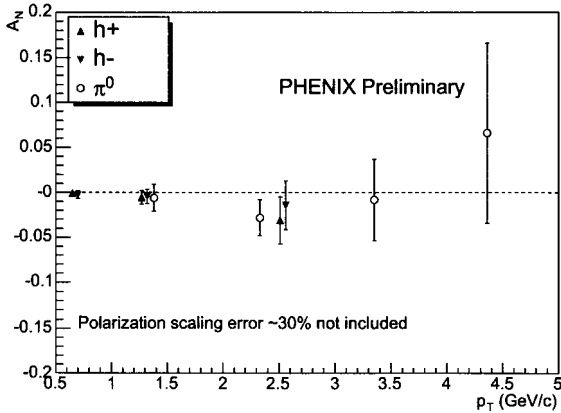


Fig. 2. Single-spin asymmetries in inclusive π^0 and unidentified hadron production.

indicate systematic uncertainties smaller than the statistical ones.

3. The results

The asymmetries in inclusive production at midrapidity and very low x_T in both neutral and unidentified charged hadrons are consistent with zero to within a few percent (figure 2). The data represent the first measurements at this energy and kinematic region. It is interesting to note that at transverse momenta below $p_T=3$ GeV/c, gluon-gluon partonic interactions dominate. These results could indicate a low gluon contribution to transverse asymmetries. The data are consistent with the results seen by E704 [8]. These should be contrasted with the large asymmetries observed at STAR [7] and more recently BRAHMS (unpublished) in inclusive pion production at forward x_F , where valence quark interactions are likely to dominate.

Recently several theoretical models [10–12] have been advanced to explain these asymmetries, including higher-twist contributions, modifications to the parton distribution functions (Sivers effect), and modifications to the fragmentation functions (Collins effect). These tend to explain the large x_F asymmetries, but they have yet to delve into the midrapidity domain.

4. Future plans

Since these data were taken, significant progress has been made in luminosity as well as polarization, so that it is reasonable to expect to accumulate more than 1 pb^{-1} per week of running at a polarization exceeding 40% (Run 5 in 2005). With 3 pb^{-1} PHENIX could extend the reach to $p_T \approx 10$ GeV/c with better than 5% statistical accuracy, well into the regime of gluon-quark interactions. The installation of an aerogel counter will extend the particle identification range from the current 3 GeV using the TOF to about 9 GeV. The charged hadron trigger at higher momenta can be augmented by the RICH.

In addition, PHENIX is planning to explore the Sivers effect using leading back-to-back hadrons. Further out, with the planned upgrade of a barrel Si vertex detector, back-to-back jets can be studied. In addition the Collins effect can be explored using $\pi\pi$ interference, which requires higher luminosities.

References

1. W.H. Dragoset et al., Phys. Rev. D18 (1978) 3939-3954.
2. C.E. Allgower et al., Phys.Rev.D65 (2002) 092008.
3. J. Antille et al., Phys.Lett.B94 (1980) 523.
4. S. Saroff et al. Phys. Rev. Lett. 64 (1990) 995.
5. V.D. Apokin et al., Phys. Lett. B243 (1990) 461-464.
6. D.L. Adams et al., Phys. Lett. B261 (1991) 201.
7. J. Adams et al., Phys. Rev. Lett. 92 (2004) 171801.
8. D.L. Adams et al., Phys. Lett. B264 (1991) 462.
9. O. Jinnouchi et al., 15th Int.Spin Phys.Symp.AIP Conf.Proc. 675 (2003) 817.
10. D.W. Sivers, Phys. Rev. D41 (1990) 83 and Phys. Rev. D43 (1991), 261.
11. J.C. Collins, Nucl. Phys. B396 (1933) 161.
12. J.W. Qui and G. Sterman, Phys. Rev. D59 (1999) 014004.
13. W. Vogelsang et al. Phys. Rev. D67 (2003) 054005.

CALCULATIONS OF SINGLE-INCLUSIVE CROSS SECTIONS AND SPIN ASYMMETRIES IN PP SCATTERING

W. VOGELSANG

Physics Department and RIKEN-BNL Research Center, Brookhaven National Laboratory, Upton, U.S.A.

We present calculations of cross sections and spin asymmetries in single-inclusive reactions in pp scattering. We discuss next-to-leading order predictions as well as all-order soft-gluon “threshold” resummations.

1. Introduction

Single-inclusive reactions in pp scattering, such as $pp \rightarrow \gamma X$, $pp \rightarrow \pi X$, $pp \rightarrow \text{jet} X$, play an important role in QCD. At sufficiently large produced transverse momentum p_T , QCD perturbation theory (pQCD) can be used to derive predictions for these reactions. Since high p_T implies large momentum transfer, the cross section may be factorized at leading power in p_T into convolutions of long-distance pieces representing the structure of the initial hadrons, and parts that are short-distance and describe the hard interactions of the partons. The long-distance contributions are universal, that is, they are the same in any inelastic reaction, whereas the short-distance pieces depend only large scales, and therefore can be evaluated using QCD perturbation theory. Because of this, single-inclusive cross sections offer unique possibilities to probe the structure of the initial hadrons in ways that are complementary to deeply-inelastic scattering. At the same time, they test the perturbative framework, for example the relevance of higher orders in the perturbative expansion, and of power-suppressed contributions to the cross section.

Of special interest is the case where the initial protons are polarized. At RHIC, one measures spin asymmetries for single-inclusive reactions, in order to investigate the spin structure of the nucleon [1]. A particular focus here is on the gluon polarization in the nucleon, $\Delta g \equiv g^\uparrow - g^\downarrow$.

In the following, we will present some theoretical predictions for cross sections and spin asymmetries for single-inclusive reactions. We will first discuss the double-longitudinal spin asymmetries A_{LL} for pion and jet production at RHIC and their sensitivities to Δg [2,3]. In the second part, we will give results for new calculations [4] of the unpolarized cross section for $pp \rightarrow \pi^0 X$ in the fixed-target regime, which show a greatly improved description of the available experimental data.

2. Spin asymmetries for $pp \rightarrow (\pi^0, \text{jet}) X$ at RHIC

We consider the double-spin asymmetry

$$A_{LL} \equiv \frac{\sigma^{++} - \sigma^{+-}}{\sigma^{++} + \sigma^{+-}} \equiv \frac{d\Delta\sigma}{d\sigma}, \quad (1)$$

where the superscripts denote the helicities of the initial protons. According to the factorization theorem, the spin-dependent cross section $\Delta\sigma$ can be written in terms of the spin-dependent parton distributions Δf as

$$\frac{d\Delta\sigma}{dp_T d\eta} = \sum_{a,b} \Delta f_a(x_a, \mu) \otimes \Delta f_b(x_b, \mu) \otimes \frac{d\Delta\hat{\sigma}_{ab}}{dp_T d\eta}(x_a, x_b, p_T, \eta, \mu), \quad (2)$$

where the symbols \otimes denote convolutions and where the sum is over all contributing partonic channels. We have written Eq. (2) for the case of jet production; for pion production there is an additional convolution with a pion fragmentation function. As mentioned above, the parton-level cross sections may be evaluated in QCD perturbation theory:

$$d\Delta\hat{\sigma}_{ab} = d\Delta\hat{\sigma}_{ab}^{(0)} + \frac{\alpha_s}{\pi} d\Delta\hat{\sigma}_{ab}^{(1)} + \dots, \quad (3)$$

corresponding to “leading order” (LO), “next-to-leading order” (NLO), and so forth. The NLO corrections for the spin-dependent cross sections for inclusive-hadron and jet production were published in [2, 5] and [3, 6], respectively. They are crucial for making reliable quantitative predictions and for analyzing the forthcoming RHIC data in terms of spin-dependent parton densities. The corrections can be sizable and they reduce the dependence on the factorization/renormalization scale μ in Eq. (2). In case of jet production, NLO corrections are also of particular importance since it is only at NLO that the QCD structure of the jet starts to play a role.

Figure 1 shows NLO predictions for the spin asymmetry A_{LL} for high- p_T pion production for collisions at $\sqrt{S} = 200$ GeV at RHIC. We have used various

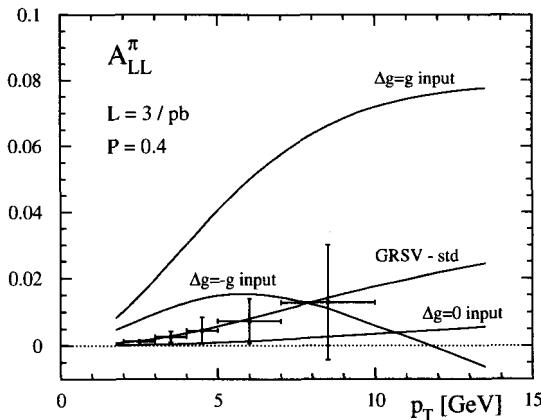


Fig. 1. NLO spin asymmetry² for π^0 production, using several GRSV polarized parton densities⁷ with different gluon polarizations.

sets of polarized parton densities of [7], which differ mainly in Δg . As one can see, the spin asymmetry strongly depends on Δg , so that measurements of A_{LL} at RHIC should give direct and clear information. The “error bars” in the figure are uncertainties expected for measurements with an integrated luminosity of 3/pb and beam polarization $P=0.4$. We note that PHENIX has already presented preliminary data [8] for A_{LL} . We also mention that the figure shows that at lower p_T the asymmetry is not sensitive to the *sign* of Δg . This is related to the dominance of the gg scattering

channel, which is approximately quadratic in Δg . In fact it can be shown that A_{LL} in leading-power QCD can hardly be negative at p_T of a few GeV [9]. One may obtain better sensitivity to the sign of Δg by expanding kinematics to the forward rapidity region.

Figure 2 shows predictions for the spin asymmetry A_{LL} for high- p_T jet production. The gross features are rather similar to the pion asymmetry, except that everything is shifted by roughly a factor two in p_T . This is due to the fact that a pion takes only a certain fraction of $\sim \mathcal{O}(50\%)$ of the outgoing parton's momentum, so that the hard scattering takes place at roughly twice the pion transverse momentum. A jet, however, will carry the full transverse momentum of a produced parton.

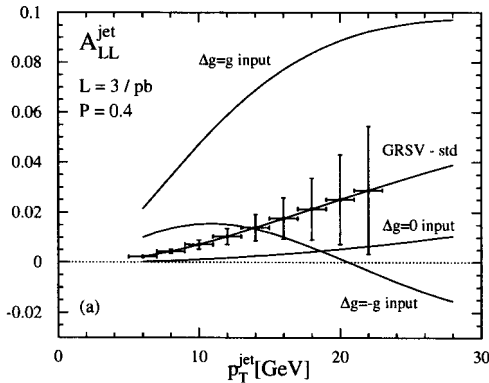


Fig. 2. Same as Fig. 1, but for inclusive jet production³ at RHIC.

We emphasize that PHENIX and STAR have presented measurements [10] of the unpolarized cross section for $pp \rightarrow \pi^0 X$. These are well described by the corresponding NLO QCD calculations [2, 5], providing confidence that the NLO pQCD hard-scattering framework is indeed adequate in the RHIC domain. This is in contrast to what was found in comparisons [11] between NLO theory and data for inclusive-hadron production taken in the fixed-target regime. We will turn to this issue next.

3. Threshold resummation for inclusive-hadron production

One may further improve the theoretical calculations by an all-order resummation of large logarithmic corrections to the partonic cross sections [4]. At partonic threshold, when the initial partons have just enough energy to produce a high-transverse momentum parton (which subsequently fragments into the observed pion) and a massless recoiling jet, the phase space available for gluon bremsstrahlung vanishes, resulting in large logarithmic corrections to the partonic cross section. For the rapidity-integrated cross section, partonic threshold is reached when $\hat{x}_T \equiv 2\hat{p}_T/\sqrt{\hat{s}} = 1$, where $\sqrt{\hat{s}}$ is the partonic center-of-mass (c.m.) energy, and \hat{p}_T is the transverse momentum of the produced parton fragmenting into the hadron. The leading large contributions near threshold arise as $\alpha_s^k \ln^{2k} (1 - \hat{x}_T^2)$ at the k th order in perturbation theory. Sufficiently close to threshold, the perturbative series will be only useful if such terms are taken into account to all orders in α_s , which is achieved by threshold resummation [12]. This resummation has been derived for a number of cases of interest, to next-to-leading logarithmic (NLL) order, in particular also for jet production [13] which proceeds through the same partonic channels as inclusive-hadron production.

The larger \hat{x}_T , the more dominant the threshold logarithms will be. Since $\hat{s} = x_a x_b S$, where $x_{a,b}$ are the partonic momentum fractions and \sqrt{S} is the hadronic c.m. energy, and since the parton distribution functions fall rapidly with increasing $x_{a,b}$, threshold effects

become more and more relevant as the hadronic scaling variable $x_T \equiv 2p_T/\sqrt{S}$ goes to one. This means that the fixed-target regime with $3 \text{ GeV} \lesssim p_T \lesssim 10 \text{ GeV}$ and \sqrt{S} of 20–30 GeV is the place where threshold resummations are expected to be particularly relevant and useful.

The resummation is performed in Mellin- N moment space, where the logarithms $\alpha_s^k \ln^{2k}(1 - \hat{x}_T^2)$ turn into $\alpha_s^k \ln^{2k}(N)$, which then exponentiate. For inclusive-hadron production, because of the color-structure of the underlying Born $2 \rightarrow 2$ QCD processes, one actually obtains a *sum* of exponentials in the resummed expression. Details may be found in [4]. Here, we give only a brief indication of the qualitative effects resulting from resummation. For a given partonic channel $ab \rightarrow cd$, the leading logarithms exponentiate in N space as

$$\hat{\sigma}_{ab \rightarrow cd}^{(res)}(N) \propto \exp \left[\frac{\alpha_s}{\pi} \left(C_a + C_b + C_c - \frac{1}{2} C_d \right) \ln^2(N) \right], \quad (4)$$

where

$$C_g = C_A = N_c = 3, \quad C_q = C_F = (N_c^2 - 1)/2N_c = 4/3. \quad (5)$$

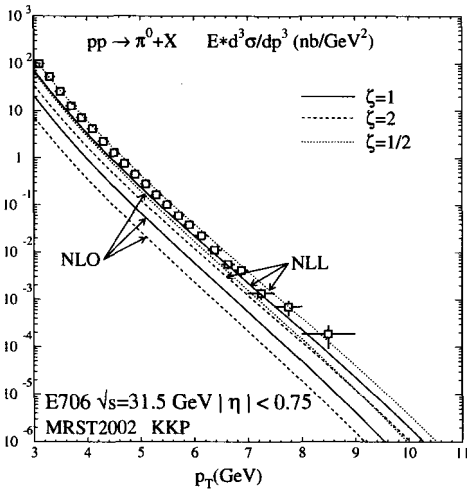


Fig. 3. NLO and NLL resummed⁴ results for the cross section for $pp \rightarrow \pi^0 X$ for E706 kinematics. Results are given for three different choices of scales, $\mu = \zeta p_T$, where $\zeta = 1/2, 1, 2$. Data are from¹⁴.

This exponent is clearly positive for each of the partonic channels, which means that the soft-gluon effects will lead to an enhancement of the cross section. Indeed, as may be seen from Fig. 3, resummation dramatically increases the cross section in the fixed-target regime. The example we give is a comparison of NLO and NLL resummed predictions at $\sqrt{S} = 31.5 \text{ GeV}$ with the data of E706 [14] at that energy. We have used the “KKP” set of pion fragmentation functions [15], and the parton distributions of [16].

Acknowledgments

I am grateful to D. de Florian, B. Jäger, S. Kretzer, A. Schäfer, and M. Stratmann for fruitful collaborations on the topics presented here.

I thank RIKEN, BNL and the U.S. DoE (contract number DE-AC02-98CH10886) for providing the facilities essential for the completion of his work.

References

1. G. Bunce, N. Saito, J. Soffer, and W. Vogelsang, *Annu. Rev. Nucl. Part. Sci.* **50**, 525 (2000).
2. B. Jäger, A. Schäfer, M. Stratmann, and W. Vogelsang, *Phys. Rev.* **D67**, 054005 (2003).
3. B. Jäger, M. Stratmann, and W. Vogelsang, *Phys. Rev.* **D70**, 034010 (2004).

4. D. de Florian and W. Vogelsang, in preparation.
5. D. de Florian, Phys. Rev. **D67**, 054004 (2003).
6. D. de Florian, S. Frixione, A. Signer, and W. Vogelsang, Nucl. Phys. **B539**, 455 (1999).
7. M. Glück, E. Reya, M. Stratmann, and W. Vogelsang, Phys. Rev. **D63**, 094005 (2001).
8. Y. Fukao, PHENIX Collab., these proceedings.
9. B. Jäger, S. Kretzer, M. Stratmann, and W. Vogelsang, Phys. Rev. Lett. **92**, 121803 (2004).
10. S.S. Adler *et al.*, PHENIX Collab., Phys. Rev. Lett. **91**, 241803 (2003);
J. Adams *et al.*, STAR Collab., Phys. Rev. Lett. **92**, 171801 (2004).
11. P. Aurenche, M. Fontannaz, J. P. Guillet, B. A. Kniehl, and M. Werlen, Eur. Phys. J. C **13**, 347 (2000); U. Baur *et al.*, arXiv:hep-ph/0005226; C. Bourrely and J. Soffer, Eur. Phys. J. C **36**, 371 (2004).
12. G. Sterman, Nucl. Phys. B **281**, 310 (1987); S. Catani and L. Trentadue, Nucl. Phys. B **327**, 323 (1989); Nucl. Phys. B **353**, 183 (1991).
13. N. Kidonakis and G. Sterman, Nucl. Phys. B **505**, 321 (1997); N. Kidonakis, G. Oderda, and G. Sterman, Nucl. Phys. B **525**, 299 (1998); *ibid.* B **531**, 365 (1998); N. Kidonakis and J. F. Owens, Phys. Rev. D **63**, 054019 (2001).
14. L. Apanasevich *et al.*, E706 Collab., Phys. Rev. D **68**, 052001 (2003).
15. B. A. Kniehl, G. Kramer, and B. Pötter, Nucl. Phys. B **582**, 514 (2000).
16. A. D. Martin, R. G. Roberts, W. J. Stirling, and R. S. Thorne, Eur. Phys. J. C **28**, 455 (2003).

TRANSVERSITY AND DRELL-YAN K -FACTORS

P. G. RATCLIFFE

Università degli Studi dell'Insubria and INFN - Sezione di Milano, Como, Italy

The Drell-Yan K -factors for transversely polarised hadrons are examined. Since transverse spin is peculiar in having no DIS reference point, the effects of higher-order corrections on DY asymmetries are examined via a DIS definition for transversity devised using a hypothetical scalar vertex. The results suggest that some care may be required when interpreting experimentally extracted partonic transversity, particularly when comparing with model calculations or predictions.*

1. Motivation

Transversity is the last, leading-twist piece in the partonic jig-saw puzzle that makes up the hadronic picture; the theoretical framework (*i.e.*, QCD evolution, partonic processes, radiative effects, *etc.*) is now rather solid [1, 2] while a number of experiments aimed at its measurement are on-line or under development: HERMES, COMPASS and the RHIC spin programme. Moreover, transverse-spin effects are notoriously surprising.

2. Transversity

2.1. Chirality and Hikasa's Theorem

QCD and electroweak vertices conserve quark chirality, so that transversity decouples from DIS (see Fig. 1a). Chirality flip is not a problem if the quarks connect to different hadrons, *e.g.*, as in Drell-Yan (DY) processes (see Fig 1b). A caveat to accessing transversity in DY is Hikasa's theorem [3]: chiral symmetry requires that the lepton-pair azimuthal angle remain unintegrated. No simple proof exists; it has to do with γ -matrix properties.

2.2. Higher-Order Corrections

Quark densities are usually defined in DIS, where the parton picture was first formulated and model calculations are performed. When translated to DY, large radiative K factors appear $\sim \mathcal{O}(\pi\alpha_s)$, enhancing the cross-section [4]. At RHIC energies the correction is roughly

*Following correction of an error in the code used for the numerical estimates, the results shown here are a little less dramatic than those actually presented at the symposium.

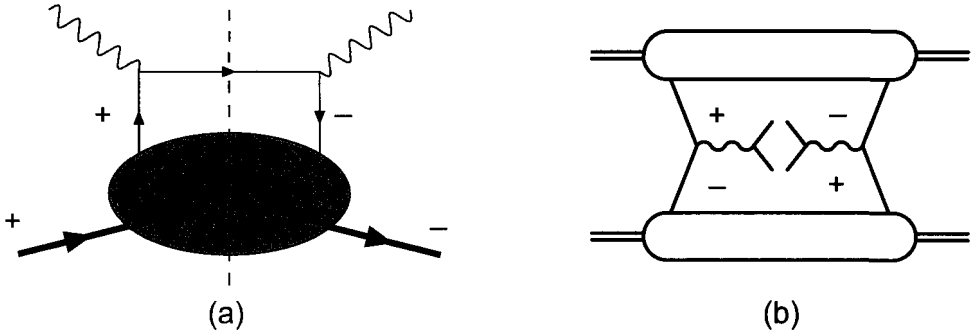


Fig. 1. (a) The forbidden chirality-flip DIS handbag diagram. (b) The Drell–Yan process for transversely polarised hadrons (\pm indicate quark chirality).

30%, while at EMC/SMC energies it becomes nearly 100%. Since spin asymmetries are ratios of differences and sums of cross-sections for different spin-alignment combinations, any strong polarisation dependence in the K factors could lead to dramatic variations in the asymmetries, with respect say to model predictions. For the $q\bar{q}$ annihilation contribution in the case of longitudinal polarised hadrons, this turns out *not* to be the case [5]. A partial explanation may be found in the helicity-conserving nature of vector interactions: only a single helicity combination contributes, to next-to-leading order (NLO).

However, the case of transversity is peculiar: as noted above, no DIS definition exists, nor is it obvious that quark helicity-conservation should still afford any protection. For pure DY, the NLO coefficient functions are known in various schemes [6, 7]; surprisingly, a new term $\propto \frac{z \ln^2 z}{1-z}$ appears, which is found neither for spin-averaged nor helicity-dependent DY.

Now, to study the K -factor problem, we need a DIS-like process to which transversity may contribute. We thus seek a DIS helicity-flip mechanism, which could be provided by either a quark mass (*i.e.*, in a propagator) or a scalar vertex (*e.g.*, a Higgs coupling). Although a quark mass does what is required, the contribution cancels via the equations of motion and gauge invariance (see, *e.g.*, [8]). However, a (single) Higgs-like vertex, replacing one of the photon vertices in Fig. 1a, allows a chiral-odd contribution to DIS ([9], from a suggestion by R.L. Jaffe). Indeed, such a *gedanken* process may be used to calculate the anomalous dimensions, but care is needed.

An attempt at calculating transversity anomalous dimensions γ via this method led to an apparent contradiction, which was corrected by [10]: the vector current J_V is conserved so $\gamma_V = 0$ but the scalar current J_S is not and $\gamma_S \neq 0$. The product of two currents may be expanded as

$$J_V(\xi) \cdot J_S(0) = \sum_n C(n; \xi) \mathcal{O}(n; 0), \tag{1}$$

where the RGE's for the Wilson coefficients $C(n; \xi)$ are

$$[\mathcal{D} + \gamma_V(g) + \gamma_S(g) - \gamma_{\mathcal{O}}(n; g)] C(n; \xi) = 0. \tag{2}$$

Thus, the ‘‘Compton’’ amplitude correction has coefficient

$$\gamma_C(n; g) = \gamma_{J_V}(g) + \gamma_{J_S}(g) - \gamma_\sigma(n; g) \tag{3}$$

and therefore $\gamma_\sigma \neq \gamma_C$!

Moreover, since the scalar current is not conserved, there is an extra UV contribution from the scalar vertex, which must be factorised into the Higgs coupling constant (or equivalently, the running quark mass). The results for the coefficient functions are (see [11])

$$C_{q,DY}^f - 2C_{q,DIS}^f = \frac{\alpha_s}{2\pi} C_F \left[\frac{3}{(1-z)_+} + 2(1+z^2) \left(\frac{\ln(1-z)}{1-z} \right)_+ - 6 - 4z + \left(\frac{4}{3}\pi^2 + 1 \right) \delta(1-z) \right], \tag{4a}$$

$$C_{q,DY}^g - 2C_{q,DIS}^g = C_{q,DY}^f - 2C_{q,DIS}^f + \frac{\alpha_s}{2\pi} C_F 2(1+z), \tag{4b}$$

$$C_{q,DY}^h - 2C_{q,DIS}^h = C_{q,DY}^f - 2C_{q,DIS}^f + \frac{\alpha_s}{2\pi} C_F \left[7 - \frac{6z \ln^2 z}{1-z} - 2(1-z) \ln(1-z) \right]. \tag{4c}$$

The origins of the larger differences in the last line may be traced to different phase-space restrictions in the transversity case. Fig. 2 shows a comparison of the Mellin moments of the above coefficients, and a simple purely valence estimate of the effects on a transverse asymmetry. The correction is rather more than twice that of the helicity case, reaching about 15%.

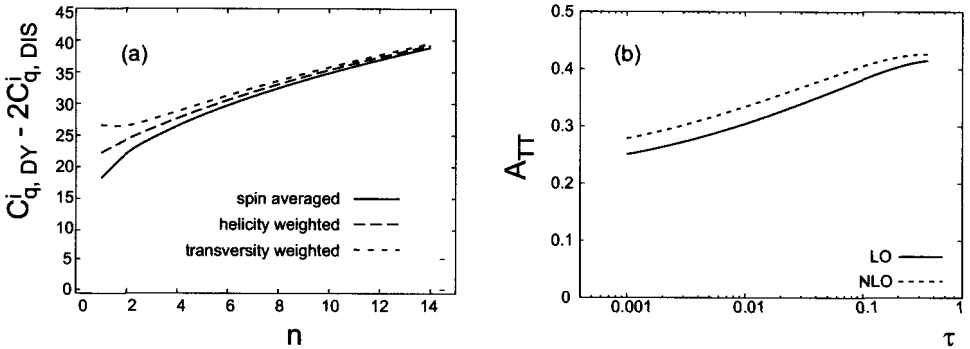


Fig. 2. (a) Spin-averaged, helicity- and transversity-weighted coefficient differences $C_{q,DY}^i - 2C_{q,DIS}^i$ (for $i = f, g, h$) in Mellin moment space. (b) LO and NLO transversity asymmetries (valence contributions only) for Drell-Yan ($\tau = Q^2/s, s = 1600 \text{ GeV}^2$).

It could be argued that it is the Higgs-like vertex that spoils the K -factor cancellation in the transversity case. However, DY processes can also be constructed in which an intermediate Higgs state produces the lepton pair. The presence of scalar (chirality-flip) vertices avoids Hikasa:1986qi’s theorem, and the final lepton-pair azimuth may be integrated out.

Likewise, a purely Higgs-exchange DIS process exists. In these cases the large K -factors are “well-behaved”. Thus, model calculations might not fare too well at first sight if not suitably corrected for the transition from DIS to DY.

3. Summary and Conclusions

A full description of the nucleon must include transversity. On the theory side, the standard QCD picture is complete to NLO, but only for DY or more exotic processes. We have no experimental data, though the future is promising. The phenomenology, while not dissimilar to the other leading-twist densities, has interesting peculiarities. Hikasa’s theorem forces us to keep the lepton-pair azimuth unintegrated in DY, leading to a new term in the NLO correction, which then affects the K -factor. Thus, comparison with model predictions and even the Soffer bound [12] could be misleading.

References

1. V. Barone, A. Drago and P.G. Ratcliffe, *Phys. Rep.* **359** (2002) 1.
2. V. Barone, these proceedings.
3. K.-I. Hikasa, *Phys. Rev.* **D33** (1986) 3203.
4. G. Altarelli, R.K. Ellis and G. Martinelli, *Nucl. Phys.* **B157** (1979) 461.
5. P.G. Ratcliffe, *Nucl. Phys.* **B223** (1983) 45.
6. W. Vogelsang and A. Weber, *Phys. Rev.* **D48** (1993) 2073.
7. A.P. Contogouris, B. Kamal and Z. Merebashvili, *Phys. Lett.* **B337** (1994) 169.
8. M. Anselmino, A. Efremov and E. Leader, *Phys. Rep.* **261** (1995) 1; *erratum, ibid.* 399.
9. B.L. Ioffe and A. Khodjamirian, *Phys. Rev.* **D51** (1995) 3373.
10. J. Blümlein, *Eur. Phys. J.* **C20** (2001) 683.
11. P.G. Ratcliffe, submitted to *Eur. Phys. J.*; hep-ph/0412157.
12. J. Soffer, *Phys. Rev. Lett.* **74** (1995) 1292.

PARTON INTRINSIC MOTION: UNPOLARIZED CROSS SECTIONS AND THE SIVERS EFFECT IN INCLUSIVE PARTICLE PRODUCTION

U. D'ALESIO, F. MURGIA

Università di Cagliari and INFN, Sezione di Cagliari, Cagliari, Italy

We present a detailed study, performed in the framework of LO perturbative QCD with the inclusion of spin and k_{\perp} effects, of unpolarized cross sections for the Drell-Yan process and for inclusive π and γ production in hadronic collisions, in different kinematical situations. We find satisfactory agreement between theoretical predictions and experimental data. This supports the study of spin effects and transverse single spin asymmetries (SSA) within the same scheme. We then present results for SSA, generated by the so-called Sivers effect, in inclusive pion production in proton-proton collisions.

It is known that collinear pQCD, even at NLO, often underestimates experimental results for inclusive pion and photon production in hadronic collisions in the central rapidity region and at moderately large p_T . It has also been shown that, in most cases, intrinsic parton momentum (k_{\perp}) effects reconcile theoretical calculations with experimental results. The role of k_{\perp} effects has been also studied in the context of *polarized* high-energy inclusive particle production at moderately large p_T , in particular at medium-large x_F . Two noticeable examples are the SSA observed in $p^{\uparrow}p \rightarrow \pi X$ processes, and the transverse Λ polarization measured in unpolarized hadronic collisions. It was originally suggested by Sivers [1] and Collins [2] that pQCD with proper inclusion of spin and k_{\perp} effects in parton distribution/fragmentation functions (PDF/FF) and in elementary dynamics could be able to explain experimental results on $A_N(\pi)$. This suggestion has been further extended in a number of subsequent papers [3]. Recently, however, Bourrely and Soffer [4] have claimed that most experimental data on SSA cannot be explained within pQCD, on the basis that collinear pQCD fails to reproduce the corresponding unpolarized cross sections by 1-2 orders of magnitude. As a matter of fact, in early pQCD-based approaches to SSA, careful analysis of unpolarized cross sections was not addressed. Therefore, it was timely to perform a detailed and comprehensive study of unpolarized cross sections and SSA within the same pQCD approach and at the same level of accuracy. In this contribution we summarize the main results of this program. A detailed presentation and a complete list of references can be found in [5].

In order to study the inclusive production of moderately large p_T particles in high-energy hadron collisions, the process $AB \rightarrow CX$, we generalize, by including spin and k_\perp effects, the well-known collinear pQCD factorized expression for the corresponding differential cross section:

$$\frac{E_C d\sigma^{AB \rightarrow CX}}{d^3 p_C} = \sum_{a,b,c,d} \int dx_a dx_b dz \prod_i d^2 k_{\perp i} \hat{f}_{a/A}(x_a, k_{\perp a}) \hat{f}_{b/B}(x_b, k_{\perp b}) \\ \times \frac{\hat{s}}{x_a x_b s} \frac{d\hat{\sigma}^{ab \rightarrow cd}}{d\hat{t}}(x_a, x_b, \hat{s}, \hat{t}, \hat{u}) \frac{\hat{s}}{\pi} \delta(\hat{s} + \hat{t} + \hat{u}) \frac{1}{z^2} J(z, |k_{\perp C}|) \hat{D}_{C/c}(z, k_{\perp C}).$$

The factors $\hat{s}/(x_a x_b s)$ and $J(z, |k_{\perp C}|)$ are due to k_\perp effects on the kinematics and become unity in collinear pQCD with massless partons. The rest of the notation should be obvious [5]. Additional contributions to the unpolarized cross section are in principle possible, but can be shown to be negligible [5, 6]. When considering SSA and Sivvers effects only, to get the numerator of the asymmetry (the denominator being twice the unpolarized cross section) one simply substitutes in this master formula the unpolarized PDF with the corresponding Sivvers function for the parton inside the initial polarized hadron. Notice that a formal proof of factorization with the inclusion of k_\perp effects is still lacking for $AB \rightarrow CX$ processes. Moreover, a complete formal definition of spin and k_\perp dependent PDF/FF, including their evolution and universality properties is also missing; we also lack a consistent higher-twist treatment including additional, unknown (higher-twist) PDF/FF and possible quark-gluon correlations. In fact, only ‘‘enhanced’’ higher-twist effects due to k_\perp ’s are included in our approach: i) the change of the $x_{a,b}$, z regions contributing mostly to the integrals in our master formula can have a substantial effect, particularly at large x/z values, where PDF/FF vary rapidly; ii) the partonic scattering angle in the AB c.m. frame might become much smaller than the hadronic production angle, thus enhancing the moderately large p_T production of particles.

Let us now summarize some basic details of numerical calculations: a) We use a factorized, Gaussian-like and flavour-independent behaviour for the k_\perp -dependent part of PDF/FF, e.g. $\hat{f}_{a/A}(x_a, k_{\perp a}) = f_{a/A}(x_a) (\beta^2/\pi) \exp[-\beta^2 k_{\perp a}^2]$ (where $1/\beta = \langle k_{\perp a}^2 \rangle^{1/2}$); b) We calculate partonic cross sections at LO in α_s , with k_\perp -modified partonic invariants \hat{s} , \hat{t} , \hat{u} , introducing a regulator mass, $\mu = 0.8$ GeV, so that $\hat{t} \rightarrow \hat{t} - \mu^2$, $\hat{u} \rightarrow \hat{u} - \mu^2$, $\hat{s} \rightarrow \hat{s} + 2\mu^2$; c) We use a unique scale for renormalization and factorization, $Q = \hat{p}_T^*/2$, \hat{p}_T^* being the transverse momentum of the fragmenting parton in the partonic c.m. frame; d) We properly take into account NLO corrections (K -factors); our LO numerical results are always rescaled in the plots by a K -factor, fixed (for a given curve), estimated by using the numerical code INCNLL [7]. e) We adopt MRST01 PDF, and Kretzer/KKP pion FF; f) No complete best-fit procedure has been attempted at this stage; therefore, in principle our results may be further improved.

The following processes and kinematical configurations have been considered: 1) $pp \rightarrow \mu^+ \mu^- X$, in the region $20 \leq \sqrt{s} \leq 60$ GeV, $5 \leq M \leq 10$ GeV, $q_T < 3$ GeV/c [used also to estimate $1/\beta = \langle k_{\perp a,b}^2 \rangle^{1/2} = 0.8$ GeV/c for PDF]; 2) $pp \rightarrow \gamma X$, $\bar{p}p \rightarrow \gamma X$, in the region $20 \leq \sqrt{s} \leq 60$ GeV, $1.5 \leq p_T \leq 10$ GeV/c, $|x_F| < 0.4$, and $\sqrt{s} \simeq 600$ GeV, $10 \leq p_T \leq 80$ GeV/c; 3) $pp \rightarrow \pi X$ in the region $20 \leq \sqrt{s} \leq 200$ GeV, $1.5 \leq p_T \leq 14$ GeV/c, $|x_F| < 0.8$

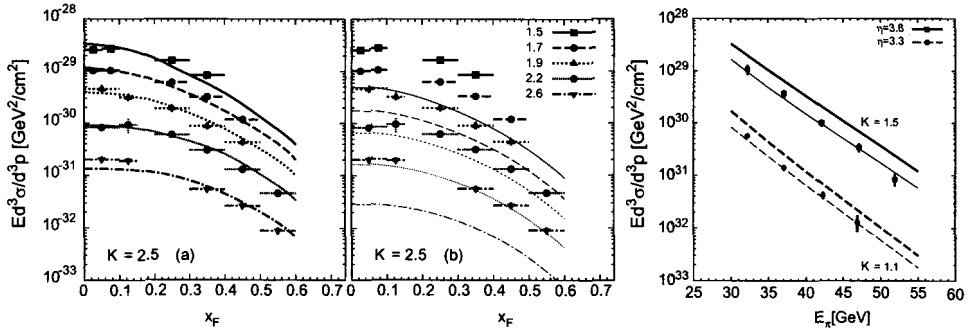


Fig. 1. Cross section for $pp \rightarrow \pi X$ process, with (thick lines) and without (thin lines) k_{\perp} effects, compared to FNAL [8] (left) and STAR [9] (right) data.

[used to estimate $1/\beta' = \langle k_{\perp}^2 \rangle^{1/2}$, see [5]]. We can present here only a few representative results: in Fig. 1 we show the differential unpolarized cross section for $pp \rightarrow \pi X$ in the kinematical configurations of [8] (left) and of the STAR experiment at RHIC (right); this gives a comparison between a calculation similar to that of [4] (thin lines) and our results including k_{\perp} effects (thick lines). In Fig. 2, we show $A_N(p^{\uparrow} p \rightarrow \pi X)$ in the kinematical configurations of the E704 experiment at FNAL (left) [used to fix the Sivvers function] and of the STAR experiment at BNL (right).

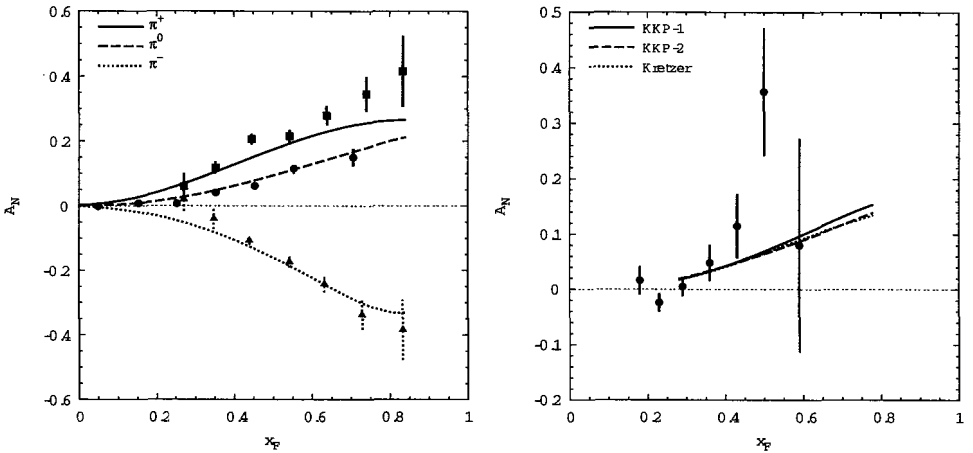


Fig. 2. $A_N(p^{\uparrow} p \rightarrow \pi X)$ compared to E704 [10] (left) and STAR [9] (right) data.

In conclusion, our LO approach (complemented with proper NLO K -factors) is in reasonable agreement with a large set of experimental data for unpolarized cross sections. This gives support to the validity of the same approach in the study of SSA. A detailed treatment of k_{\perp} effects confirms all main results and conclusions of our former studies on Sivvers effect performed keeping only leading contributions (in k_{\perp}) and using a simplified partonic

configuration (see the first of [3]). Let us finally notice that our approach is in principle able to reproduce most of the features of the experimental data available for $P_T^\Lambda(pp \rightarrow \Lambda^\uparrow X)$. A combined analysis of P_T^Λ and unpolarized cross sections, like that performed here for the Drell-Yan process and SSA in inclusive π and γ production, is under way.

References

1. D. Sivers, *Phys. Rev.* **D41**, 83 (1990); *Phys. Rev.* **D43**, 261 (1991)
2. J.C. Collins, *Nucl. Phys.* **B396**, 16 (1993)
3. See, e.g., M. Anselmino, F. Murgia, *Phys. Lett.* **B442**, 470 (1998); M. Anselmino, M. Boglione, F. Murgia, *Phys. Rev.* **D60**, 054027 (1999)
4. C. Bourrely, J. Soffer, *Eur. Phys. J.* **C36**, 371 (2004)
5. U. D'Alesio and F. Murgia, *Phys. Rev.* **D70** 074009 (2004)
6. M. Anselmino, M. Boglione, U. D'Alesio, E. Leader, F. Murgia, e-Print Archive: hep-ph/0408356 (*Phys. Rev. D*, in press)
7. P. Aurenche, *et al.*, *Nucl. Phys.* **B297**, 661 (1988)
8. G. Donaldson, *et al.*, *Phys. Lett.* **B73**, 375 (1978)
9. STAR Collaboration, J. Adams, *et al.*, *Phys. Rev. Lett.* **92**, 171801 (2004); S. Heppelmann, contribution to the Transversity Workshop, October 6-7, 2003, IASA, Athens, Greece
10. E704 Collaboration, D.L. Adams *et al.*, *Phys. Lett.* **B345**, 569 (1995); **261**, 201 (1991); **264**, 462 (1991)

HERMES PRECISION RESULTS ON g_1^p , g_1^d AND g_1^n AND THE FIRST MEASUREMENT OF THE TENSOR STRUCTURE FUNCTION b_1^d

C. RIEDL

Physikalisches Institut 2 der Universität Erlangen-Nürnberg,
Erlangen, Germany

(on behalf of the HERMES Collaboration)

Final HERMES results on the proton, deuteron and neutron structure function g_1 are presented in the kinematic range $0.0021 < x < 0.9$ and $0.1 < Q^2 < 20 \text{ GeV}^2$. These results are based on a refined analysis and are corrected for radiative and detector smearing effects using an unfolding algorithm. Furthermore, preliminary results on the first measurement of the tensor asymmetry A_{zz} and the tensor structure function b_1^d are presented.

Over the last 15 years, measurements of the polarized structure function g_1 by inclusive polarized deep-inelastic scattering (DIS) [1] have shed light on one basic ingredient of the spin puzzle: the quark contribution to the nucleon spin, $\Delta\Sigma$. For a spin-1 target, besides g_1 the quadrupole structure function b_1 is needed to parameterize the hadronic part of the interaction [2].

The final HERMES g_1 results presented here are based on a refined analysis of data taken with longitudinally polarized hydrogen [3] and deuterium [4] targets (4 resp. $11.5 \cdot 10^6$ DIS events), the b_1 results on a separate data set with a tensor-polarized deuterium target ($2.4 \cdot 10^6$ DIS events) [5]. The kinematic range covers $0.0021 < x < 0.9$ and $0.1 < Q^2 < 20 \text{ GeV}^2$.

In the fixed-target experiment HERMES, the 27.6 GeV lepton beam of the HERA storage ring is scattered off an internal pure-gas target. The lepton beam is transversely self-polarized, reaching an average polarization of 53% for the reported data; longitudinal beam polarization in the interaction region is obtained with pairs of spin rotators. The HERMES atomic gas target [6] consists of an Atomic Beam Source (ABS) to generate, and a Breit Rabi Polarimeter to measure, nuclear polarization; a tubular open-ended, cooled storage cell is mounted inside the beam pipe confining the gas fed from the ABS. The average vector polarization was 85%. Furthermore, the target design allowed for simultaneous setting of an average tensor polarization of -166% and a residual vector polarization of only $+1\%$, making it possible to decouple the b_1 and g_1 measurements.

The HERMES forward spectrometer [7] includes numerous tracking chambers in front and behind a 1.3 Tm magnetic field, and various detectors for particle identification. Electrons and hadrons are discriminated using a likelihood method based on the combination of four detectors [8]. The inclusive sample presented is contaminated with less than 1% hadrons.

The spin structure function $g_1(x, Q^2)$ for both the proton and the deuteron is determined from the ratio g_1/F_1 , which is approximately equal to the virtual photon asymmetry A_1 measured via the longitudinal cross section asymmetry $A_{||}$. For analysis details, see e.g. [3]. For the neutron, g_1^n is calculated as a linear combination of g_1^p and g_1^d .

The measured asymmetries have been corrected for detector smearing and QED radiative effects to obtain the Born asymmetries [8, 9]. These corrections have been applied using an unfolding algorithm that keeps track of the kinematic migration of events and does not require a fit to the data. The final Born asymmetries depend only on the measured data, on the detector model, on the known unpolarized cross sections, and on the model for background processes. Figure 1 shows the g_1/F_1 and xg_1 results with smearing unfolded, and

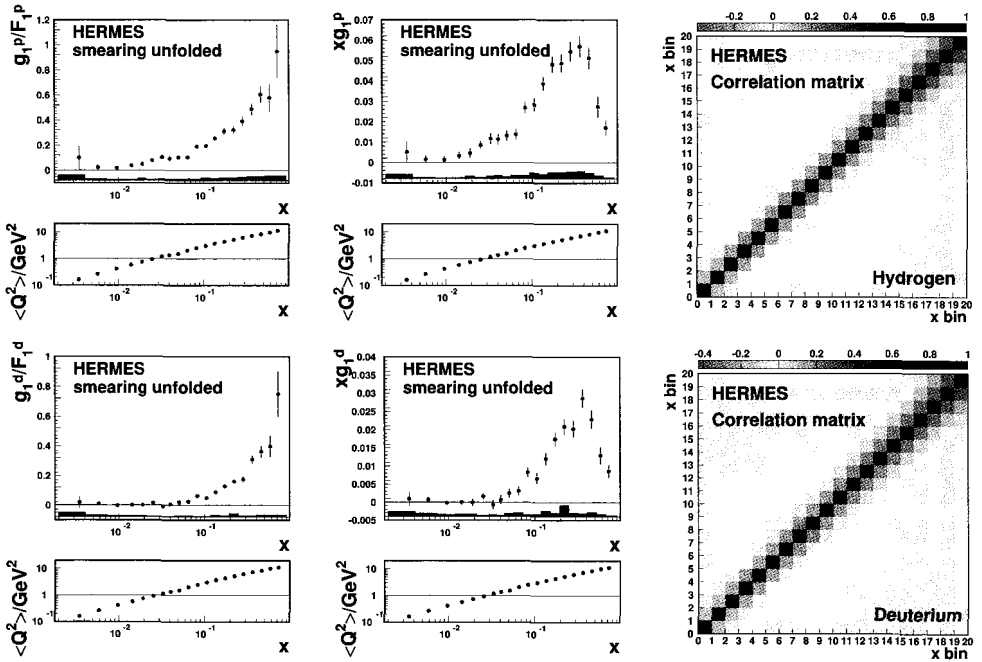


Fig. 1. Smearing-unfolded g_1/F_1 (left) and xg_1 (middle) as measured by HERMES, and the correlation matrix between statistical errors (right), for the proton (top row) and the deuteron (bottom row). Error bars are statistical, displaying only the diagonal element of the correlation matrix; shaded bands show the estimated systematic uncertainties

and, based on the simulated event migration, their statistical correlations which must be taken into account when e.g. calculating errors on moments or performing QCD fits to g_1 data [9]. The applied algorithm removes systematic correlations between data points. A

compilation of world data on g_1/F_1 and xg_1 is shown in Fig. 2 [10–12].

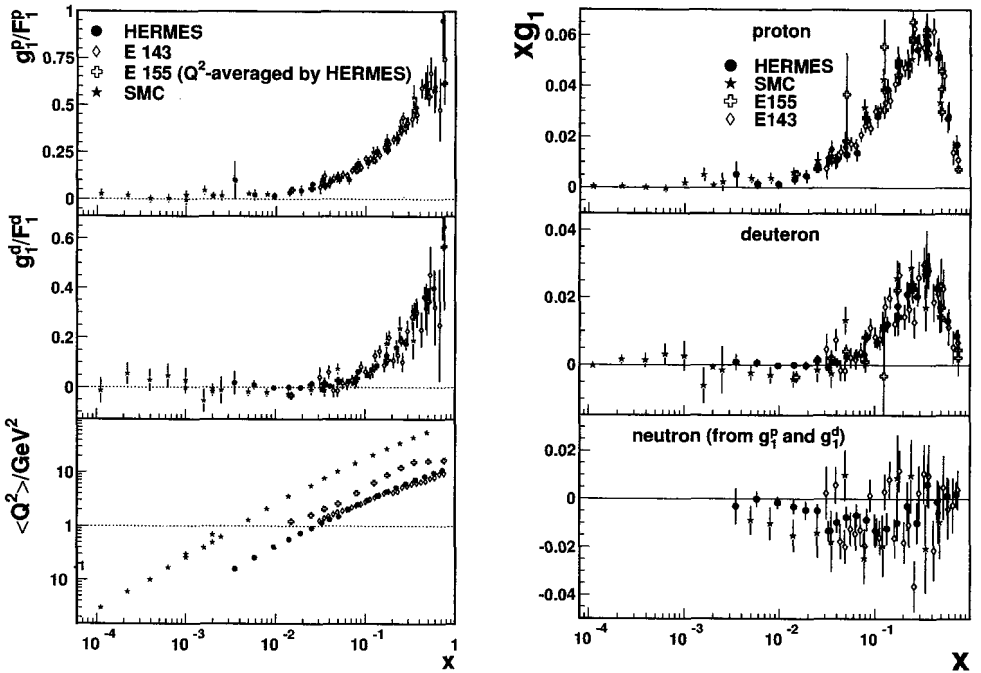


Fig. 2. HERMES g_1/F_1 (left) and xg_1 data (right) in comparison to SLAC and CERN data for the proton (top panels) and the deuteron (middle panels), and xg_1 for the neutron from p and d data (right bottom panel) at the measured Q^2 (left bottom). Error bars show the quadratic sum of statistical and systematic uncertainties.

The tensor structure function $b_1(x, Q^2)$ is obtained from the ratio b_1/F_1 , measured via A_{zz} which compares the helicity-0 state of the deuteron with its averaged non-zero states. In Fig. 3, A_{zz} and b_1 are displayed as measured for the first time by HERMES; A_{zz} is only of the order of 1%, implying the quadrupole contribution to the measurement of g_1 to be negligible. The steep rise of b_1 for small x suits the latest model calculations [5]. The unfolding algorithm discussed above will also be applied to these data [13].

Acknowledgments

I thank my HERMES colleagues, especially the inclusive group. Furthermore, I gratefully acknowledge the financial support by the German Bundesministerium für Bildung und Forschung (contract number 06 ER 125I).

References

1. For a compilation of polarized data see: <http://durpdg.dur.ac.uk/HEPDATA>
2. P. Hoodbhoy *et al.*, Nucl. Phys. B312 (1989) 571
3. HERMES Collaboration, A. Airapetian *et al.*, Phys. Lett. B442 (1998) 484

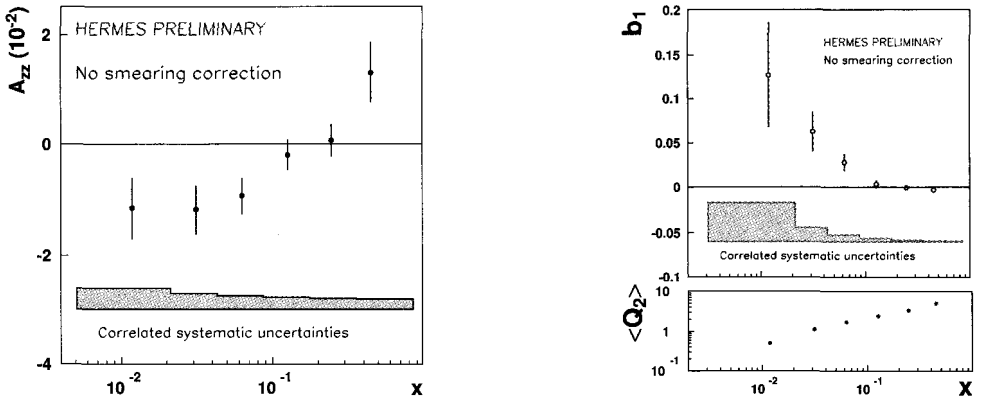


Fig. 3. The HERMES tensor asymmetry A_{zz} (left) and tensor structure function b_1^d (right; lower panel: average Q^2 for the measurements). The error bars are statistical only; shaded bands show the estimated systematic uncertainties.

4. L. De Nardo, for the HERMES Collaboration, *Proceedings from PRAHA-Spin-2001, Prague, Czech Republic, Jul 15 - 28, 2001*
5. M. Contalbrigo, for the HERMES Collaboration, *Proceedings from SPIN 2002, New York, USA, Sep 9 - 14, 2002*, hep-ex/0211014
6. HERMES Collaboration, A. Airapetian *et al.*, Nucl. Instr. and Meth. A (in press), hep-ex/0408013
7. HERMES Collaboration, K. Ackerstaff *et al.*, Nucl. Instr. **A417** (1998) 230
8. HERMES Collaboration, A. Airapetian *et al.*, Phys. Rev. D (in press), hep-ex/0407032
9. HERMES Collaboration, publication on g_1 in preparation
10. SMC Collaboration, B. Adeva *et al.*, Phys. Rev. **D60** (1999) 072004
11. E143 Collaboration, K. Abe *et al.*, Phys. Rev. **D58** (1998) 112003
12. E155 Collaboration, P.L. Anthony *et al.*, Phys. Lett. **B463** (1999) 339
13. HERMES Collaboration, publication on b_1 in preparation

GENERALIZATION OF THE DGLAP FOR THE STRUCTURE FUNCTION g_1 TO THE REGION OF SMALL x

B. I. ERMOLAEV

Ioffe Physico-Technical Institute, St.Petersburg, Russia

M. GRECO

Dept of Physics and INFN, University Rome III, Rome, Italy

S. I. TROYAN*

St.Petersburg Institute of Nuclear Physics, Gatchina, Russia

Explicit expressions for the non-singlet and singlet components of the DIS structure function g_1 , comprising DGLAP expressions for the coefficient functions and the anomalous dimensions, and accounting for the total resummation of the most singular contributions to them, are obtained.

1. Introduction

The standard theoretical instrument for studying the structure function g_1 is DGLAP. In this approach, $g_1(x, Q^2)$ can be represented as a convolution of the coefficient functions and the evolved quark distributions calculated with NLO approximation. Those results, having been completed with appropriate fits for the initial quark distributions, agree well with the available experimental data.

On the other hand, the DGLAP evolution was originally obtained for operating in the range of rather large x , where higher-loop contributions to the coefficient functions and the anomalous dimensions are small. It is clear that when x is decreasing, such corrections become more and more essential, and DGLAP should stop working well at some small value of x .

*Work partially supported by RSGSS-1124.2003.2 of the Russian State Grant for Scientific School.

In the present paper we use the results of our previous papers [2, 3] to demonstrate that the impact of the high-order corrections on the Q^2 and x -evolutions of the non-singlet structure functions is quite sizable for $x \leq 10^{-2}$.

2. Difference between DGLAP and our approach

The DGLAP expressions for the non-singlet structure functions are well-known. In order to make the all-order resummation of the double-logarithmic contributions to g_1 , in Ref. [1] an alternative approach was used, composing and solving the Infrared Evolution Equations. This approach was improved in Ref. [2], where the single-logarithmic contributions were accounted for and the QCD coupling was varied while in Ref. [1] it was considered as fixed. In contrast to the DGLAP parametrization $\alpha_s = \alpha_s(k_{\perp}^2)$, Ref. [2] used the other parametrization. The argument in favour of such a parametrization was given in Ref. [3]. In particular, it was shown there that this new parametrization coincides with the DGLAP parametrization when x is not far from 1, but these parameterizations differ a lot when $x \ll 1$. Ref. [2] suggests the following formula for the non-singlet component of g_1 ($\equiv g_1^{NS}$):

$$g_1^{NS}(x, Q^2) = (e_q^2/2) \int_{-\infty}^{\infty} \frac{d\omega}{2\pi i} (1/x)^\omega C_{NS}(\omega) \delta q(\omega) \exp(H_{NS}(\omega)y), \quad (1)$$

with $y = \ln(Q^2/\mu^2)$, so that μ^2 is the starting point of the Q^2 evolution. The new coefficient function C_{NS} is expressed in terms of new anomalous dimension H_{NS} :

$$C_{NS} = \omega / (\omega - H_{NS}(\omega)) \quad (2)$$

and the new anomalous dimension $H_{NS}(\omega)$, accounting for the total resummation of the double- and single-logarithmic contributions, is

$$H_{NS} = (1/2) \left[\omega - \sqrt{\omega^2 - B(\omega)} \right] \quad (3)$$

where B and related to it the Mellin transform of α_s , $A(\omega)$ are expressed in terms of $l = \ln(1/x)$, $b = (33 - 2n_f)/12\pi$ and the colour factors (see Ref. [2] for details).

3. Comparison of the x evolution for g_1^{NS} by DGLAP with the one by eq. (1)

Let us compare our results (1) with the expressions for g_1^{NS} obtained with the NLO DGLAP. In order to be independent of fits for δq , we use the bare quark input. In other words, we compare pure evolutions for the non-singlets. We compare them when x is changing while Q^2 is fixed. We define R_{NLO} as follows:

$$R_{NLO}(x) = g_1^{NS} / g_{1\ NLO}^{NS} \quad (4)$$

when Q^2 is fixed and the initial quark distribution corresponds to the bare quark. The results for $R_{NLO}(x)$ and are presented in Fig. 1. This shows that for $x \geq 0.05$ the NLO DGLAP evolution predicts higher values for the non-singlets than our evolution. However, for $x \leq 0.05$ the situation is the opposite. Therefore, we gather that $x \approx 0.05$ is the point where the impact of higher-loop contributions is sizable. However, it is known that DGLAP actually

works successfully at lower values of x . We have the following explanation for this fact: it is the impact of the fits used in DGLAP because they contain the singular terms when $x \rightarrow 0$ and therefore imitate the impact of the higher-loop contributions absent in DGLAP.

4. Combining DGLAP with our higher-loop contributions

Eq. (1) accounts for the total resummation double- and single-logarithmic contributions to the non-singlet anomalous dimension and the coefficient function. They are leading when x is small, but the method we have used does not account for the other contributions. One can neglect them when x is small but they become important when x is not far from 1. On the other hand, such contributions are accounted for in DGLAP where the non-singlet coefficient function C_{DGLAP} and anomalous dimension γ_{DGLAP} are known with two-loop accuracy:

$$C_{DGLAP} = 1 + \frac{\alpha_s(Q^2)}{2\pi} C^{(1)}, \quad \gamma_{DGLAP} = \frac{\alpha_s(Q^2)}{4\pi} \gamma^{(0)} + \left(\frac{\alpha_s(Q^2)}{4\pi} \right)^2 \gamma^{(1)} \quad (5)$$

We can therefore borrow from DGLAP formulae the contributions missing in Eq. (1) by adding C_{DGLAP} and γ_{DGLAP} to the coefficient functions and anomalous dimensions of Eq. (1). However, both C_{DGLAP} and γ_{DGLAP} also contain the terms already accounted for by Eqs. (1):

$$\tilde{C}_{NS} = 1 + B/(4\omega^2), \quad \tilde{H}_{NS} = B/(2\omega) + B^2/(16\omega^3). \quad (6)$$

Now let us make the new coefficient functions \hat{C}_{NS} and new anomalous dimensions \hat{H}_{NS} :

$$\begin{aligned} \hat{H}_{NS} &= [H_{NS} - \tilde{H}_{NS}] + \frac{A(\omega)}{16\pi^2 C_F} \gamma^{(0)} + \left(\frac{A(\omega)}{16\pi^2 C_F} \right)^2 \gamma^{(1)}, \\ \hat{C}_{NS} &= [C_{NS} - \tilde{C}_{NS}] + 1 + \frac{A(\omega)}{8\pi^2 C_F} C^{(1)}. \end{aligned} \quad (7)$$

The new coefficient function and anomalous dimension of Eq. (7) comprise the total resummation of the leading contributions from higher loops and the DGLAP expressions in which $\alpha_s(Q^2)$ is replaced by $A(\omega)$.

References

1. B.I. Ermolaev, S.I. Manaenkov and M.G. Ryskin. *Z.Phys.* **C69** 259 (1996); J. Bartels, B.I. Ermolaev and M.G. Ryskin. *Z.Phys.* **C70** 273 (1996); J. Bartels, B.I. Ermolaev and M.G. Ryskin. *Z.Phys.* **C72** 627 (1996).
2. B.I. Ermolaev, M. Greco and S.I. Troyan. *Nucl.Phys.* **B594** 71 (2001); *ibid* **B571** 137(2000); *Phys.Lett.* **B579** 321 (2004).
3. B.I. Ermolaev, M. Greco and S.I. Troyan. *Phys.Lett.* **B522** 57 (2001).

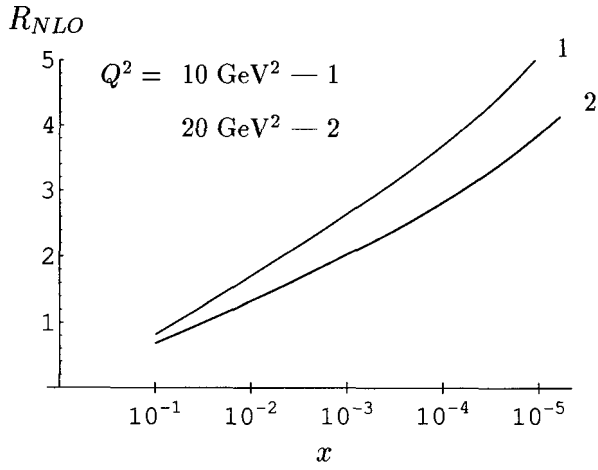


Fig. 1. Comparison of the x evolution of Eq. (1) for g_1^{NS} to that of NLO DGLAP.

INCLUSIVE SPIN-DEPENDENT ASYMMETRY A_1^d

D. PESHEKHONOV

Joint Institute of the Nuclear Research, Dubna, Russia

(on behalf of the COMPASS Collaboration)

First preliminary results from the COMPASS experiment on the inclusive asymmetry A_1 and on the semi-inclusive asymmetries A_1^{\pm} on deuterium obtained from 2002-2003 data are presented.

1. Introduction

COMPASS [1] is a fixed target experiment which has been taking data since 2002. Its is the measurement of polarized parton and gluon distributions in deep inelastic scattering (DIS) of longitudinally polarized muons on longitudinally polarized nucleons. One way to access the polarized quark distributions is the inclusive measurement of the photon-nucleon cross section asymmetry^a

$$A_1 = \frac{\sigma^{\uparrow\downarrow} - \sigma^{\uparrow\uparrow}}{\sigma^{\uparrow\downarrow} + \sigma^{\uparrow\uparrow}} = \frac{\sum_q e_q^2 (q^{\uparrow\downarrow} - q^{\uparrow\uparrow} + \bar{q}^{\uparrow\downarrow} - \bar{q}^{\uparrow\uparrow})}{\sum_q e_q^2 (q^{\uparrow\uparrow} + q^{\uparrow\downarrow} + \bar{q}^{\uparrow\uparrow} + \bar{q}^{\uparrow\downarrow})} = \frac{\sum_q e_q^2 (\Delta q + \Delta \bar{q})}{\sum_q e_q^2 (q + \bar{q})}$$

(exact formulas for deuterium are e.g. in [2]). The experimentally measurable quantity is the lepton-nucleon asymmetry A_{1N} , which is related to A_1 by:

$$A_{1N} \approx A_1 \cdot D = \frac{1}{P_l f P_b} \left(\frac{N_{\uparrow\downarrow} - N_{\uparrow\uparrow}}{N_{\uparrow\downarrow} + N_{\uparrow\uparrow}} \right).$$

Here P_b and P_l are the lepton and target polarization, f is the dilution factor, and $D \approx \frac{2y-y^2}{2-2y+y^2}$ is the kinematical variable known as the depolarization factor. $N_{\uparrow\downarrow}$ ($N_{\uparrow\uparrow}$) are the numbers of scattering events for antiparallel and parallel lepton and nucleon polarizations, respectively.

This study can be extended by measuring not only the lepton but also at least one hadron in the final state (so-called semi-inclusive DIS). Then the measured asymmetries depend on the fragmentation functions $D_{q(\bar{q})}^h$ - i.e. on the probabilities for the q or \bar{q} fragment to the

^a $\sigma^{\uparrow\uparrow(\uparrow\downarrow)}$ and $q(\bar{q})^{\uparrow\uparrow(\uparrow\downarrow)}$ denote γ -nucleon cross sections and quark(antiquark) distributions in the nucleon for parallel(antiparallel) virtual photon and nucleon(quark) spin orientations.

specified type of hadron:

$$A_1^h = \frac{1}{P_t f P_b D} \left(\frac{N_{\downarrow}^h - N_{\uparrow}^h}{N_{\downarrow}^h + N_{\uparrow}^h} \right) = \frac{\sum_q e_q^2 (\Delta q(x) \int D_q^h(z) dz + \Delta \bar{q}(x) \int D_{\bar{q}}^h(z) dz)}{\sum_q e_q^2 (q(x) \int D_q^h(z) dz + \bar{q}(x) \int D_{\bar{q}}^h(z) dz)}$$

Measuring different types of hadrons and using both proton and deuteron targets, full flavour separation of Δq can be done. In the following we present preliminary results on A_1 and A_1^h obtained from measurements on the deuterium target in 2002 and 2003.

2. The Apparatus

In 2002-2004 COMPASS [3] took data on the muon beam line of the CERN SPS with a μ^+ intensity of $2 \cdot 10^8$ per spill of 4.8 sec. The nominal beam momentum was 160 GeV on average, with a momentum spread of $\delta P/P$ of 0.05 and a mean polarization of 76%. The COMPASS target consists of two cylindrical cells, each 60 cm long and 3 cm in diameter, separated by 10 cm. They are filled with ${}^6\text{LiD}$, which is used as a deuteron target material, and are placed inside the solenoid to allow the material to be polarized by the dynamical nuclear polarization (DNP) technique [4]. The main advantage of the ${}^6\text{LiD}$ is its high dilution factor $f \approx 0.4$ which represents the fraction of scattering on the deuterons^b. The cells are longitudinally polarized in opposite directions. The typical polarization is above 50 %. In order to cancel out most of the systematic errors on the asymmetry measurements^c the polarization directions in target cells are reversed every 8 hours by rotating the magnetic field direction and, at least once per data-taking period, by changing the DNP microwave frequency. The measured asymmetry A_{exp} is then given by the average of the count rate asymmetries for the two different spin configurations $A_{exp} = \frac{1}{2} \left(\frac{N_u - N_d}{N_u + N_d} - \frac{N'_u - N'_d}{N'_u + N'_d} \right)$ where $N_{u(d)}$ and $N'_{u(d)}$ denote the number of scattering events observed in the upstream(downstream) target before and after polarization reversal.

3. The Inclusive Analysis

For the analysis we request that the primary vertex is inside one of the target cells, and that the incident muon has passed both target cells (to ensure the same muon flux for both cells). In addition, we apply the following kinematics cuts: $140 \text{ GeV} < E_\mu < 180 \text{ GeV}$, $Q^2 > 1 \text{ GeV}^2$ and $0.1 < y < 0.9$. The total statistics of DIS events after these cuts is 34.5 million events.

Our data span a range of Bjorken variable $0.004 < x < 0.7$. In Figure 1, our results are compared to previous experiments. Below $x < 0.04$, only data from SMC [5] exist so far. Our preliminary results have smaller statistical errors owing to the increase in luminosity by a factor 5 and higher f compared to the SMC experiment. This will help to better constrain the first moment of the spin dependent structure function g_1 , and thus $\Delta\Sigma$. Known sources of systematic errors are: $\sigma P_{target} = 5\%$, $\sigma P_{beam} = 3\%$, $\sigma f = 5\%$ and $\sigma D < 5\%$. Systematic

^b ${}^6\text{LiD} = \text{He} + \text{D}$

^ceffects of the beam flux, acceptance and time dependent changes in the spectrometer

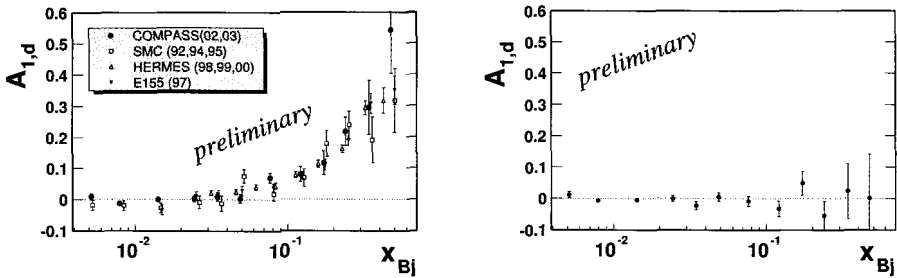


Fig. 1. Measured asymmetry A_1 compared with other published experimental results (left). Fake configuration asymmetry (right). Within the statistical accuracy, no asymmetry has been found.

errors from other sources can be estimated

- by combining data with the same spin configuration, such that the measured asymmetry (fake configuration asymmetry) should be zero^d. Our results obtained so far are compatible with zero within statistical error bars (see Figure 1);
- by using Monte Carlo simulation to study the effects of possible fluctuations in the detector efficiencies.

From the studies done so far, we estimate our systematic errors to be smaller than the statistical uncertainties.

4. Status of Semi-Inclusive Analysis

As described in the introduction, the measurement of the semi-inclusive asymmetries allows us to extract the contributions of the various quark flavours. At COMPASS we intend to measure six asymmetries ($A_1, A_1^{h^+}, A_1^{h^-}, A_1^{K^+}, A_1^{K^-}, A_1^{K_s^0}$). The upper index denotes which hadron type is detected in addition to the scattered muon. Figure 2 shows our preliminary result on the asymmetries $A_1^{h^\pm}$ obtained from our 2002-2003 data compared to the SMC result.

5. Conclusion

New preliminary results on both the inclusive, A_1 , and semi-inclusive, $A_1^{h^\pm}$, spin dependent asymmetries on deuterium in the kinematic range $Q^2 > 1 \text{ (GeV/c)}^2$ and $0.004 < x < 0.7$ have been obtained at COMPASS. Our results from 2002 and 2003 data are in good agreement with previous results from SMC, HERMES, SLAC experiments, and already show much improved statistical accuracy at low x compared to SMC, thanks to an increased beam flux and target dilution factor.

References

1. Proposal for COMPASS CERN/SPSLC 96-14, 1996.

^dtime dependent changes in the spectrometer

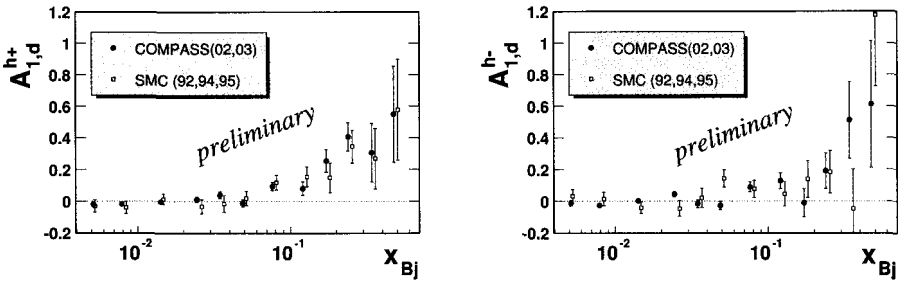


Fig. 2. Measured semi-inclusive asymmetries A_1^{h+} (left panel) and A_1^{h-} (right panel) compared with SMC published result.

2. B. Aveda et al., Phys.Rev. **D60** (1999) 072004.
3. G.K.Mallot, for the COMPASS collab., Nucl. Instr. Meth. A518 (2004) 121, A.Bressan et al., "Recent results from COMPASS", these proceedings.
4. J.Koivuniemi, talk on the 16th International Spin Physics Symposium, October 10-16 2004 Trieste, "Polarization build up in the large COMPASS 6LiD target".
5. B.Adeva et al., Phys.Rev. **D 58** (1998) 112001.

Spin asymmetries for events with high p_T hadrons and an evaluation of the gluon polarization from SMC data

E. RONDIO*

A. Soltan Institute for Nuclear Studies, Warsaw, Poland

representing Spin Muon Collaboration (SMC)

A measurement of the longitudinal spin cross section asymmetry for events with two high transverse momentum hadrons in DIS region performed by Spin Muon Collaboration is presented. From the asymmetries: $A_p^{\ell N \rightarrow \ell hhX} = 0.030 \pm 0.057 \pm 0.010$ and $A_d^{\ell N \rightarrow \ell hhX} = 0.070 \pm 0.076 \pm 0.010$ obtained in the DIS region, an averaged gluon polarization $\Delta G/G = -0.20 \pm 0.28 \pm 0.10$ is derived for an average fraction of nucleon momentum carried by gluons of $\langle \eta \rangle = 0.07$.

1. Introduction

A direct measurement of gluon polarization is possible via the Photon Gluon Fusion (PGF) process, which is illustrated in Fig.1, together with the two other lowest order diagrams: virtual photon absorption (leading process "LP"), and gluon radiation (QCD Compton scattering "QCDC"). Because the contribution of the PGF diagram to the deep inelastic scattering cross-section is small, it has to be increased by the event selection procedure, which should be very effective in selecting the PGF process. This is achieved by choosing events with hadrons of large transverse momenta (p_T) relative to the virtual photon direction [1, 2].

2. Formalism and applicability

Experimentally observed spin-dependent effects are small and have to be determined from the cross section asymmetry. The expression for the cross section asymmetry with production of at least two hadrons with large transverse momenta $A^{\ell N \rightarrow \ell hhX}$ at the parton level, consists of three terms corresponding to the processes shown in Fig. 1:

$$A^{\ell N \rightarrow \ell hhX} = \frac{\Delta q}{q} (\langle \hat{a}_{LL} \rangle^{LP} R_{LP} + \langle \hat{a}_{LL} \rangle^{QCDC} R_{QCDC}) + \frac{\Delta G}{G} \langle \hat{a}_{LL} \rangle^{PGF} R_{PGF}. \quad (1)$$

In this formula $\langle \hat{a}_{LL} \rangle$ is the average partonic asymmetry for a given process and R the ratio of its cross section to the total cross section for the selected sample of events. A

*Work partially supported by SPUB NO. 621/E-78/SPB/CERN/P-03/DWM 576

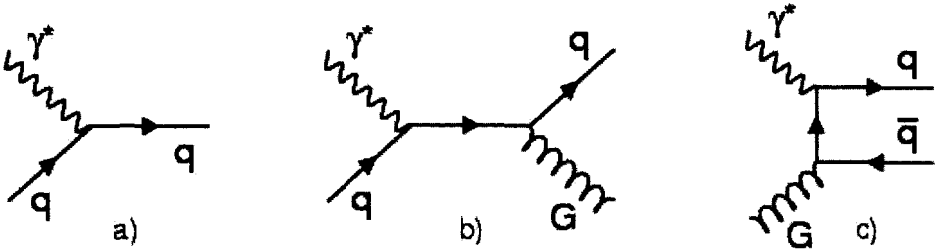


Fig. 1. Lowest order diagrams for DIS γ^* absorption: a) leading process (LP), b) gluon radiation (QCDC), c) photon-gluon fusion (PGF).

measurement of the asymmetry $A^{\ell N \rightarrow \ell h h X}$ thus permits an evaluation of the gluon polarization, $\Delta G/G$, if all other elements in Eq. (1) are known. The quark asymmetry $\Delta q/q$ can be approximated from the value of A_1 obtained in inclusive measurements. The partonic asymmetries \hat{a}_{LL} and ratios R are calculated for simulated events in the kinematic region covered by the data.

This method is restricted to the leading order QCD approach, when the three considered processes can be separated. The description of hadron production in DIS muon interaction in terms of the three processes of Fig. 1 with Monte Carlo event generator LEPTO has been successfully tested in EMC and E665 experiments. Other processes, such as those involving resolved photons, are expected to have small contributions for Q^2 above 1 GeV², and are not considered here.

3. Data selection

The analysis discussed here has been published [3]. An event sample for further studies was defined by requiring two hadrons with transverse momenta above 0.7 GeV and energy fraction above 0.1 (to reduce target fragmentation contribution). Events were also selected on kinematics, including $Q^2 \geq 1$ GeV², and on vertex position (for details see ref. [3]). After all selections, the total number of remaining events amounted to about 80k for the proton and 70k for the deuteron sample.

The data after selection were compared with the sample generated with LEPTO, taking into account experimental conditions. The detailed comparison can be found in Ref. [4]. In order to describe the data, it was found necessary to change the values of two parameters describing the quark fragmentation in JETSET [5].

The statistical precision of the gluon polarization determined from Eq. (1) depends on the precision of the measured asymmetry $A^{\ell N \rightarrow \ell h h X}$, and on the fraction of PGF events (R_{PGF}) in the final sample. The aim of the present analysis is therefore to select a large enough sample with a maximal contribution of PGF events.

Several additional selection methods were tried. The best results were obtained with the classification based on a neural network [6]. The procedure provides a single value, called "NN response", (range: 0-1) where high values correspond to events which are more likely to result from the PGF process. A comparison of selection efficiency and sample purity for

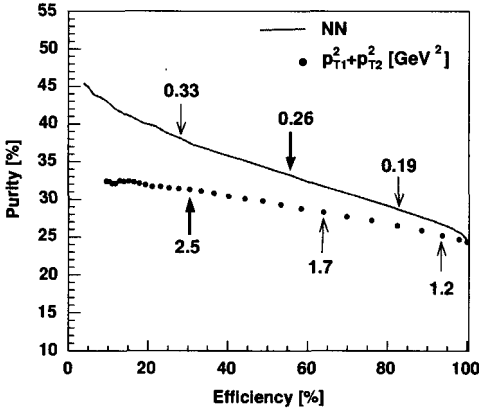


Fig. 2. Purity and efficiency obtained in the selection of the PGF process, with methods based on a cut on $\sum p_T^2$ and the NN response, applied to simulated events.

this method, and a cut on the sum $p_{T1}^2 + p_{T2}^2$, is shown in Fig.2. It is clear that a better statistical precision is obtained with the neural network method.

4. Spin asymmetries $A^{\ell N \rightarrow \ell hhX}$

The cross section asymmetry, $A^{\ell N \rightarrow \ell hhX}$, is related to the counting rate asymmetry A^{exp} by: $A^{exp} = P_B P_T f A^{\ell N \rightarrow \ell hhX}$, where f is the effective dilution factor, which takes into account the dilution of spin asymmetries by unpolarized nuclei in the target and by radiative effects on the nucleon; P_B and P_T are the beam and target polarizations.

The asymmetry calculations have been done for the entire sample with $p_{T1,2} \geq 0.7$ GeV and for the two selections enhancing R_{PGF} ($\sum p_T^2 > 2.5$ GeV² and NN response > 0.26). The results in Fig. 3 show that the asymmetries do not change significantly with the selection, and the asymmetries obtained for protons and deuterons are compatible within errors. The asymmetries obtained are compatible with zero.

5. Determination of the gluon polarization

The gluon polarization is evaluated from Eq. (1) using the measured $A^{\ell N \rightarrow \ell hhX}$ asymmetry, obtained for the samples with enhanced R_{PGF} by NN selection. The partonic asymmetries \hat{a}_{LL} of each sub-process are calculated for each Monte-Carlo event and averaged. The values of the ratios R provided by the simulation for the LP, QCDC and PGF processes are 0.38, 0.29 and 0.33 respectively. The contributions of different processes for the proton and deuteron samples differ by less than 0.02.

The gluon polarization is determined for the kinematic region covered by the selected sample and corresponds to a given fraction η of nucleon momentum carried by gluons. This quantity is known for simulated events but cannot be directly determined from the data. The averaged value for the selected PGF events $\eta = 0.07$ is used as the reference value for the result obtained on $\Delta G/G$.

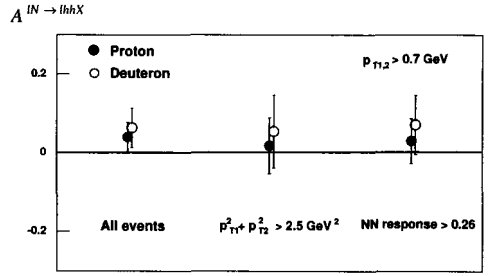


Fig. 3. Measured asymmetry $A^{\ell N \rightarrow \ell hhX}$, for proton and deuteron events with $p_{T1,2} > 0.7$ GeV cut (left) and after additional selection on $\sum p_T^2$ (center) or on the NN response (right).

Averaging the results for proton and deuteron obtained with the neural network classification, we obtain $\Delta G/G = -0.20 \pm 0.28 \pm 0.10$. This average gluon polarization obtained for the SMC data is close to zero with a large statistical error (~ 0.30). The accuracy is limited by the reduction to less than 1% of the DIS sample by the hadron selection requirements. The systematic errors contain dependence on the simulation parameters, scale dependence in the generation, and systematic uncertainty on the measured asymmetry. The dependence on Monte Carlo parameters is controllable and can be reduced for future high statistics measurements, which will allow even more precise comparison of the data with simulations.

References

1. R.D. Carlitz, J.C. Collins and A.H. Mueller, Phys. Lett. B **214**, 229 (1988).
2. A. Bravar, D. von Harrach and A. Kotzinian, Phys. Lett. B **421**, 349 (1998).
3. SMC Collaboration, B. Adeva *et al.*, Phys. Rev. D **70**, 012002 (2004).
4. K. Kowalik, Ph.D. Thesis, Institute for Nuclear Studies, Warsaw (2004).
5. T. Sjöstrand *et al.*, Comput. Phys. Commun. **135**, 238 (2001).
6. K. Kowalik *et al.*, Acta Physica Polonica B **32**, 2929 (2001).

FLAVOUR DECOMPOSITION OF THE QUARK HELICITY DISTRIBUTIONS IN THE NUCLEON FROM SEMI-INCLUSIVE DEEP-INELASTIC SCATTERING

J. G. RUBIN

University of Illinois Urbana-Champaign, Urbana, USA

(on behalf of the HERMES Collaboration)

Five-quark helicity distributions, including those for three sea quark flavours, were extracted from new SIDIS data on a deuterium target as well as previously published hydrogen target data. These distributions are consistent with zero for all three sea flavours. A recently predicted flavour asymmetry in the polarization of the light quark sea appears to be disfavoured by the data.

1. Introduction

Previous next-to-leading order extractions of the quark helicity distributions, made from inclusive deep inelastic scattering (DIS) measurements (SMC, E143, E155, HERMES), suffer from an inability to separate contributions of individual quark flavours without assuming SU(3) flavour symmetry and using data from hyperon β decay. An alternative leading order approach has been conducted at HERMES [1], [2]. By utilizing semi-inclusive DIS to measure A_1^h , where final state hadrons are measured in conjunction with the scattered lepton, the struck quark can be *flavour-tagged* and the individual quark contributions to A_1 can be unravelled.

2. Method

In leading order QCD, the longitudinal double-spin asymmetry can be written as follows:

$$A_1(x, Q^2) = \frac{\sum_q e_q^2 \Delta q(x, Q^2)}{\sum_q e_q^2 q(x, Q^2)}. \quad (1)$$

By measuring a hadron h in conjunction with the scattered lepton, one can rewrite the preceding formula,

$$A_1^h(x, Q^2, z) = \frac{\sum_q e_q^2 \Delta q(x, Q^2) D_q^h(z, Q^2)}{\sum_q e_q^2 q(x, Q^2) D_q^h(z, Q^2)} = \sum_q \mathcal{P}_q^h(x, Q^2, z) \frac{\Delta q(x, Q^2)}{q(x, Q^2)}, \quad (2)$$

where D_q^h are fragmentation functions, and $\mathcal{P}_q^h(x, Q^2, z)$ is the purity matrix which describes the likelihood that a hadron h is produced from a struck quark of flavour q . This

unpolarized purity matrix was generated through a LEPTO-based Monte Carlo simulation using CTEQ5L for unpolarized parton distribution functions and JETSET for fragmentation. The input parameters of the JETSET, Lund-string fragmentation model were tuned to unpolarized DIS data from HERMES. The systematic uncertainty contribution from the tune was estimated by computing a purity matrix at a tune that poorly describes the semi-inclusive yields observed at HERMES kinematics.

In terms of measured asymmetries and computed purities, one can express (2) as the matrix equation, $A_1(x) = \mathcal{N}(x)\mathcal{P}(x)Q(x)$, where the nuclear mixing matrix \mathcal{N} takes into account the probabilities of interacting with different nucleons in the deuteron. The vector $A(x)$ includes the inclusive and semi-inclusive asymmetries for each hadron species measured. The numbers of inclusive and semi-inclusive events included in this analysis are presented in Table 1. Finally, $Q(x) = \left(\frac{\Delta u}{u}(x), \frac{\Delta d}{d}(x), \frac{\Delta \bar{u}}{\bar{u}}(x), \frac{\Delta \bar{d}}{\bar{d}}(x), \frac{\Delta s}{s}(x) \right)$ is the vector of unknown quark helicity distributions. The expression, $\chi^2 = (A_1 - \mathcal{N}\mathcal{P}Q)^T v_A^{-1} (A_1 - \mathcal{N}\mathcal{P}Q)$, is numerically minimized to

Table 1. Total number of DIS events by target. Each column (both inclusive and semi-inclusive) reflects an asymmetry used in this analysis.

Target	DIS Events	π^+	π^+	K^+	K^-
H	1.7×10^6	117×10^3	82×10^3		
D	6.7×10^6	491×10^3	385×10^3	76×10^3	33×10^3

solve for $\Delta q(x)$. The matrix v_A is a statistical covariance matrix describing the correlations between bins. It is produced with a rigorous model-independent unfolding procedure in which Monte Carlo is used to compute the migration of events between kinematic bins resulting from acceptance and QED radiative smearing. Because this method assumes no functional form for the underlying physics, there is an apparent inflation of error bars which reflects the uncertainty contributions from all possible kinematic correlations. When incorporated into models and world fits (i.e. when a functional form is assumed) and the correlation matrix is taken into account, the uncertainties will become significantly smaller.

The configuration of the HERA beam and HERMES target was changed from year to year. Beam and target species and average polarizations are given in Table 2.

Table 2. Beam and target configuration by year.

Year	Beam and % Polarization	Target and % Polarization
1996	e^+ 52.8	H 78.8
1997	e^+ 53.1	H 85.0
1998	e^- 52.1	D 81.7
1999	e^+ 53.3	D 81.0
2000	e^+ 53.3	D 84.5

3. Results

The results of the five-flavour $\Delta q(x)$ extraction are presented in Fig. 1a. The sea quark distributions are all set to zero for $x > 0.3$, as they are poorly constrained by limited statistics in this range. $\Delta\bar{s}(x) \equiv 0$ for similar reasons. As expected, the results show that $\Delta u(x)$ is positive and $\Delta d(x)$ is negative, and that both reach their greatest magnitude in the valence quark range. The sea quark distributions are all consistent with zero. With respect to the zero polarization hypothesis, $\chi^2/NDF = 7.4/7$, $11.2/7$, and $4.3/7$ for the extracted $\bar{u}(x)$, $\bar{d}(x)$, and $s(x)$ respectively. The statistical precision is insufficient to distinguish the symmetric sea hypothesis from the GRSV 2000 LO or BB01 LO parameterizations. Unlike the

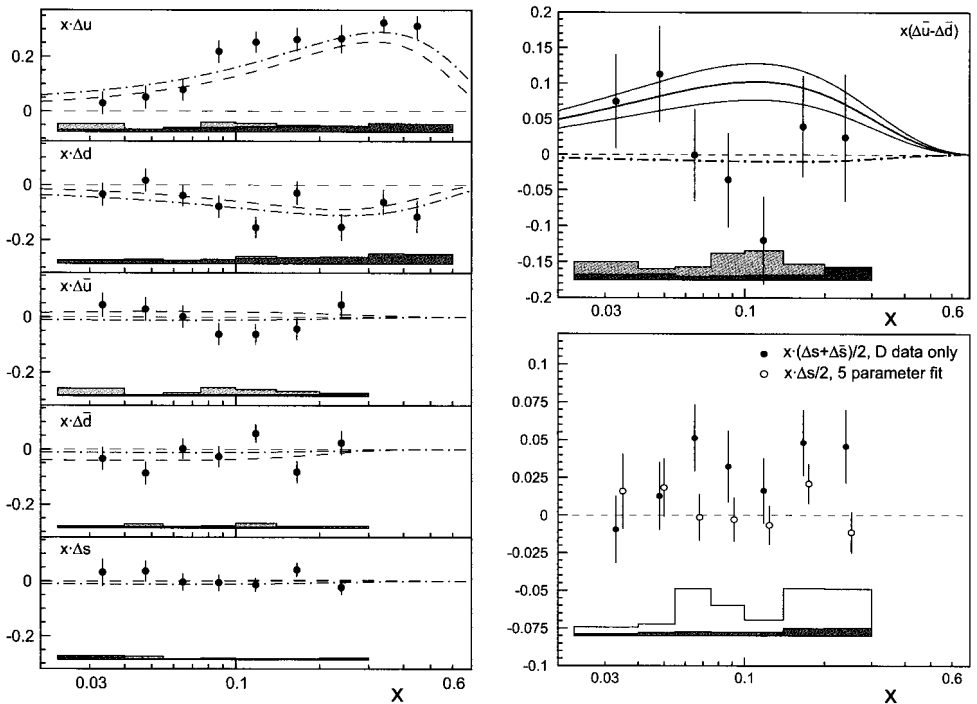


Fig. 1. a) Five-flavour $\Delta q(x)$ extraction. b) Extracted $x(\Delta\bar{u}(x) - \Delta\bar{d}(x))$ compared with Chiral Quark model (solid) and Meson Cloud model (dot-dashed) predictions. c) Comparison of five-flavour and isoscalar methods for strange sea extraction.

large asymmetry that has been observed for the unpolarized distributions $\bar{u}(x)$ and $\bar{d}(x)$, no evidence for a light sea polarization was found (Fig. 1b). Chiral quark soliton calculations predict a large positive $\Delta\bar{u}(x) - \Delta\bar{d}(x)$. Meson cloud models predict a small negative $\Delta\bar{u}(x) - \Delta\bar{d}(x)$. The symmetric sea hypothesis produced $\chi^2/NDF = 7.7/7$, the meson cloud model $\chi^2/NDF = 8.1/7$, and the Chiral Quark Soliton Model $\chi^2/NDF = 17.6/7$, when compared to the extracted distributions.

An alternative analysis was also performed to extract $\Delta s(x) + \Delta\bar{s}(x)$. Because the strange

quark helicity density $\Delta s(x) + \Delta \bar{s}(x)$ has no isospin, it can be extracted from the isoscalar deuteron alone. A simple purity matrix can be computed using kaon fragmentation functions from e^+e^- collider data describing specifically the likelihood of strange quark fragmentation into kaons. The result supports a symmetric strange sea polarization and is consistent with the five-flavour, Monte-Carlo based, extraction of $\Delta s(x)$ (Fig. 1c).

4. Conclusions

The HERMES collaboration has performed the first ever independent five-flavour $\Delta q(x)$ extraction. This semi-inclusive leading order approach takes advantage of the open geometry and excellent particle identification of HERMES to flavour-tag events and make possible such an extraction using a purity method. This measurement provides a first glimpse of antiquark polarization, which shows no evidence of the pronounced flavour asymmetry between \bar{u} and \bar{d} observed in the unpolarized sector.

References

1. A. Airapetian *et al.* (HERMES), Phys. Rev. Lett. **92**, (2004) 012005.
2. A. Airapetian *et al.* (HERMES), Phys. Rev. D (in press)

THE ROLE OF HIGHER TWIST IN DETERMINING POLARIZED PARTON DENSITIES FROM DIS DATA*

E. LEADER

Imperial College London, London, England

A. V. SIDOROV

Bogoliubov Theoretical Laboratory, Joint Institute for Nuclear Research, Dubna, Russia

D. B. STAMENOV

Institute for Nuclear Research and Nuclear Energy, Sofia, Bulgaria

Different methods to extract the polarized parton densities from the world polarized DIS data are considered. The higher twist corrections $h^N(x)/Q^2$ to the spin-dependent proton and neutron g_1 structure functions are found to be non-negligible and important in the QCD analysis of the present experimental data. Their role in determining the polarized parton densities in the framework of the different approaches is discussed.

One of the features of polarized DIS is that a lot of the present data are at low Q^2 ($Q^2 \sim 1 - 5 \text{ GeV}^2$). For this reason, to confront correctly the QCD predictions with experimental data and to determine the polarized parton densities, special attention should be paid to the non-perturbative higher-twist (powers in $1/Q^2$) corrections to the nucleon structure functions. The size of higher twist corrections (HT) to the spin structure function g_1 and their role in determining the polarized parton densities in the nucleon using different approaches of QCD fits to the data are discussed in this talk.

Up to now, two approaches have been mainly used to extract polarized parton densities (PPD) from world polarized DIS data. According to the first [1, 2] the leading twist

*This work is supported by the JINR-Bulgaria Collaborative Grant, by the RFBR (No 02-01-00601, 03-02-16816), INTAS 2000 (No 587) and by the Bulgarian National Science Foundation under Contract PH-1010.

LO/NLO QCD expressions for the structure functions g_1^N and F_1^N have been used to confront the data on spin asymmetry A_1 ($\approx g_1/F_1$) and g_1/F_1 . We have shown [3, 4] that in this case the “effective” HT corrections $h^{g_1/F_1}(x)$ to the ratio g_1/F_1

$$\frac{g_1(x, Q^2)}{F_1(x, Q^2)} = \frac{g_1(x, Q^2)_{LT}}{F_1(x, Q^2)_{LT}} + \frac{h^{g_1/F_1}(x)}{Q^2} \quad (1)$$

extracted from the world data, are negligible and consistent with zero within the errors, *i.e.* $h^{g_1/F_1}(x) \approx 0$. (Note that in QCD: $g_1 = (g_1)_{LT} + (g_1)_{HT}$; $F_1 = (F_1)_{LT} + (F_1)_{HT}$.) What follows from this result is that the higher twist corrections to g_1 and F_1 compensate each other in the ratio g_1/F_1 , and the PPD extracted this way are less sensitive to higher twist effects.

According to the second approach [6, 7], g_1/F_1 and A_1 data have been fitted using phenomenological parametrizations of the experimental data for the unpolarized structure function $F_2(x, Q^2)$, and the ratio $R(x, Q^2)$ of F_2 and F_1 (F_1 has been replaced by that usually extracted from unpolarized DIS experiments F_2 and R). Note that such a procedure is equivalent to a fit to $(g_1)_{exp}$, but it is more precise than the fit to the g_1 data themselves actually presented by the experimental groups because the g_1 data are extracted in the same way for all of the data sets.

If the second approach is applied to the data, the “effective higher twist” contribution $h^{g_1/F_1}(x)/Q^2$ to $A_1(g_1/F_1)$ is found [1] to be sizeable and important in the fit [the HT corrections to g_1 cannot be compensated because the HT corrections to F_1 (F_2 and R) are absorbed by the phenomenological parametrizations of the data on F_2 and R]. Therefore, to extract correctly the polarized parton densities from the g_1 data, the HT corrections to g_1 have to be taken into account. Note that a QCD fit to the data in this case, keeping in $g_1(x, Q^2)_{QCD}$ only the leading-twist expression (as it was done in [6, 7]), leads to some “effective” parton densities which themselves involve HT effects and are therefore not quite correct.

Keeping in mind the above discussion we have analyzed the world data on inclusive polarized DIS [5], taking into account the higher twist corrections to the nucleon structure function $g_1^N(x, Q^2)$. In our fit to the data we have used the following expressions for g_1/F_1 and A_1 :

$$\begin{aligned} \left[\frac{g_1^N(x, Q^2)}{F_1^N(x, Q^2)} \right]_{exp} &\Leftrightarrow \frac{g_1^N(x, Q^2)_{LT} + h^N(x)/Q^2}{F_2^N(x, Q^2)_{exp}} 2x \frac{[1 + R(x, Q^2)_{exp}]}{(1 + \gamma^2)}, \\ A_1^N(x, Q^2)_{exp} &\Leftrightarrow \frac{g_1^N(x, Q^2)_{LT} + h^N(x)/Q^2}{F_2^N(x, Q^2)_{exp}} 2x [1 + R(x, Q^2)_{exp}], \end{aligned} \quad (2)$$

where $g_1^N(x, Q^2)_{LT}$ is given by the leading twist QCD expression including the target mass corrections ($N=p, n, d$). The dynamical HT corrections $h^N(x)$ in (2) are included and extracted in a *model independent way*. In our analysis their Q^2 dependence is neglected. It is small and the accuracy of the present data does not allow us to determine it. The details of our analysis are given in [8]. Unlike [8], the polarized PD determined in this analysis are compatible with the positivity bounds imposed by the MRST’02 unpolarized PD instead

of the MRST'99 ones. The dependence of the polarized PD on the positivity constraints imposed will be discussed in detail in a forthcoming paper.

We have found that the fit to the data is significantly improved when the higher twist corrections to g_1 are included in the analysis, especially in the LO QCD case. The best LO and NLO($\overline{\text{MS}}$ scheme) fits correspond to $\chi_{\text{DF,LO}}^2 = 0.91$ and to $\chi_{\text{DF,NLO}}^2 = 0.89$, while in the case of LO and NLO($\overline{\text{MS}}$) fits, where HT effects are not included, $\chi_{\text{DF,LO}}^2 = 1.41$ and $\chi_{\text{DF,NLO}}^2 = 1.19$, respectively.

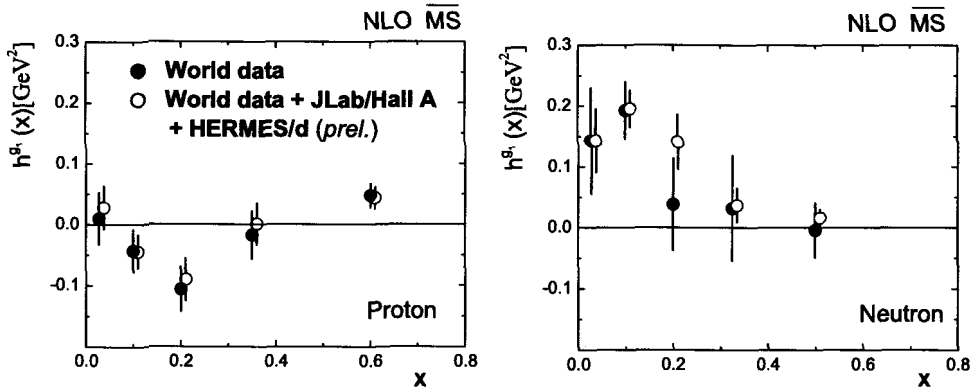


Fig. 1. Higher twist corrections to the proton and neutron g_1 structure functions extracted from the data on g_1 in the NLO QCD approximation for $g_1(x, Q^2)_{\text{LT}}$.

We have also found that the size of the HT corrections to g_1 is *not* negligible, and their shape depends on the target (see Fig. 1). In Fig. 1 shows our results on the HT corrections to g_1 (open circles), including in the world data set the recent JLab/Hall A [9] and preliminary HERMES [10] data. As seen from Fig. 1, the higher twist corrections to the neutron spin structure functions in the large x region are now much better determined. It was also shown that the NLO QCD polarized PD($g_1^{\text{LT}} + \text{HT}$) determined from the data on g_1 , including higher twist effects, are in good agreement with the polarized PD($g_1^{\text{NLO}}/F_1^{\text{NLO}}$) found from our analysis of the data on g_1/F_1 and A_1 , using for the structure functions g_1 and F_1 only their *leading* twist expressions in NLO QCD. This observation confirms once more that the higher twist corrections $h^{g_1/F_1}(x)$ to g_1/F_1 and A_1 are negligible, so that in the analysis of g_1/F_1 and A_1 data it is enough to account only for the leading twist of the structure functions g_1 and F_1 .

In conclusion, we have found that in order to confront the QCD predictions for the nucleon spin structure function g_1 to the present experimental data on g_1 and to extract correctly the polarized parton densities from these data, the higher twist corrections to g_1 have to be taken into account in the analysis. While, in the fit to g_1/F_1 and A_1 ($\approx g_1/F_1$) data it is enough to account only for the leading twist contributions to the structure functions g_1 and F_1 because the higher twist corrections to g_1 and F_1 compensate each other in the

ratio g_1/F_1 . Further investigations on the role of higher twist effects in semi-inclusive DIS processes would be important for the correct determination and flavor separation of the valence and light sea quark parton densities.

References

1. M. Glück, E. Reya, M. Stratmann and W. Vogelsang, *Phys. Rev.* **D63**, 094005 (2001).
2. E. Leader, A.V. Sidorov and D.B. Stamenov, *Eur. Phys. J.* **C23**, 479 (2002).
3. E. Leader, A.V. Sidorov and D.B. Stamenov, in *Particle Physics at the Start of the New Millennium*, edited by A.I. Studenikin, World Scientific, Singapore, May 2001, p. 76. (*Proceedings of the 9th Lomonosov Conference on Elementary Particle Physics, Moscow, Russia, 20-26 Sep 1999*).
4. E. Leader, A. V. Sidorov and D. B. Stamenov, in *Deep Inelastic Scattering DIS2003*, edited by V.Kim and L.Lipatov, PNPI RAS, 2003, pp. 790-794, e-Print Archive hep-ph/0309048.
5. EMC, J. Ashman et al., *Phys. Lett.* **B206**, 364 (1988); SLAC E142 Coll., P.L. Anthony et al., *Phys. Rev.* **D54**, 6620 (1996); SLAC/E154 Coll., K. Abe et al., *Phys. Rev. Lett.* **79**, 26 (1997); SMC, B. Adeva et al., *Phys. Rev.* **D58**, 112001 (1998); HERMES, K. Ackerstaff et al., *Phys. Lett.* **B404**, 383 (1997); *ibid* **B442**, 484 (1998); SLAC E143 Coll., K. Abe et al., *Phys. Rev.* **D58**, 112003 (1998); SLAC/E155 Coll., P.L. Anthony et al., *Phys. Lett.* **B463**, 339 (1999), *ibid* **B493**, 19 (2000).
6. SMC, B. Adeva et al., *Phys. Rev.* **D58**, 112002 (1998).
7. J. Blumlein and H. Bottcher, *Nucl. Phys.* **B636**, 225 (2002).
8. E. Leader, A.V. Sidorov and D.B. Stamenov, *Phys. Rev.* **D67**, 074017 (2003).
9. JLab/Hall A Coll., X. Zheng et al., *Phys. Rev. Lett.* **92**, 012004 (2004).
10. C. Weiskopf, DESY, Thesis 02-043, 2002.

THE GLUON SPIN ASYMMETRY AS A LINK TO ΔG AND ORBITAL ANGULAR MOMENTUM

G. P. RAMSEY

Physics Dept., Loyola University Chicago and
HEP Division, Argonne National Lab, IL, USA

The fundamental program in high energy spin physics focuses on the spin structure of the nucleon. The gluon and orbital angular momentum components of the nucleon spin are virtually unknown. The $J_z = \frac{1}{2}$ sum rule involves the integrated parton densities and can be used to extract information on the orbital angular momentum and its evolution. To avoid any bias on a model of ΔG , we assume that the gluon asymmetry $A = \Delta G/G$ can be used to extract ΔG over a reasonable kinematic region. Combining the results for ΔG with the evolution equations, we can determine a theoretical expression for the orbital angular momentum and its evolution.

1. Introduction

The $J_z = \frac{1}{2}$ sum rule involves the integrated densities.

$$J_z \equiv \frac{1}{2}\Delta\Sigma + \Delta G + (L_z)_q + (L_z)_G, \quad (1)$$

where $\Delta\Sigma$ is the total spin carried by all quarks, ΔG the spin carried by gluons, and $(L_z)_q$ and $(L_z)_G$ the orbital angular momenta of the quarks and gluons respectively. Recent DIS experiments have narrowed the quark spin contribution ($\Delta\Sigma$) to a reasonable degree. However, the gluon and orbital angular momentum components of the nucleon spin are virtually unknown. The purpose of this work is to estimate the gluon density through the use of the asymmetry $A = \Delta G/G$ and, with the evolution equations, determine a theoretical expression for the orbital angular momentum.

There are numerous models for the polarized quark distributions, most of which are in agreement with the polarized DIS data. We have chosen to use the model of Gordon, et. al. [1], which separates the valence and sea flavours and builds in an asymmetry of the quark and antiquark distributions. These polarized distributions depend upon the corresponding unpolarized distributions. To investigate the effects of a range of polarized PDFs, both CTEQ5 [2] and MRST2001 [3] unpolarized distributions are used. For the distributions considered, the x -dependence of the quark spin content is identical above $x=0.10$, but varies considerably for smaller x . Similarly, the different models for the unpolarized glue lead to a few percent differences in the gluon asymmetry and the x dependent values of L_z at small- x .

Our present knowledge of the polarized flavour distributions comes mostly from polarized deep-inelastic-scattering (PDIS). The up and down quark polarizations are fairly well established, but the strange and charm quark distributions are less known. Since these heavier quarks do not contribute more than a few percent to the proton spin, the overall quark spin $\Delta\Sigma$ is known to within a few percent. Most of the accepted values lie well within the range 0.20 – 0.35. The integrated polarized gluon distribution is virtually unknown, with estimates from almost zero to somewhat larger values around 2.0. This work consists of two parts. The first is to extract information about ΔG from the polarized gluon asymmetry $A = \Delta G/G$. This minimizes the bias of constructing an arbitrary model of ΔG . The assumptions of the asymmetry are based upon sound theoretical grounds and are directly verifiable by present experiments at DESY and RHIC at BNL. From the asymmetry and knowledge of the unpolarized gluon distributions (extracted from CTEQ and MRST to investigate the variation) we can extract the necessary information about ΔG . Coupled with the $J_z = \frac{1}{2}$ sum rule, we can then infer information about L_z and its evolution in Q^2 .

2. Asymmetry Model for ΔG and L_z

Experiments are underway and planned to measure both ΔG and the polarized gluon asymmetry $A = \Delta G/G$. To construct a theoretical model of the asymmetry, we assume that it has a scale independent part A_0 , plus a small piece that vanishes at some large scale so that ΔG can be written as $\Delta G = A_0 \cdot G + G_\epsilon$. The scale invariant A_0 is calculable and independent of theoretical models of ΔG . The second term is scale invariant and is interpreted as the difference between the measured polarized gluon distribution and that predicted by the calculated A_0 , combined with measurement of the unpolarized gluon density. Experimental results can be correlated by measuring the asymmetry A in a limited kinematic range of x for a fixed Q^2 (at HERMES and RHIC). The invariance of A_0 and G_ϵ can then be used to extract ΔG over an expanded kinematic region. Combining this with the extraction of ΔG in polarized pp collisions at RHIC can enhance the correlations of these experimental results. The model for A can thus be readily verified in separate sets of experiments.

We can write the asymmetry as

$$A(x, t) = A_0(x) + \epsilon(x, t) \equiv \Delta G/G \tag{2}$$

where $t \equiv \ln[(\alpha_s(Q_0^2))/(\alpha_s(Q^2))]$. Then ΔG can be written in terms of the calculated asymmetry $A_0(x)$ and a difference term. The calculable part can be found by taking the t -derivative of $A_0(x)$:

$$\frac{dA_0(x)}{dt} = \frac{\Delta G}{dt} - A_0 \cdot \frac{dG}{dt} = 0 \tag{3}$$

to a first approximation. Then $\frac{d\Delta G}{dt}$ and $\frac{dG}{dt}$ are calculated using the evolution equations. The result is a simple polynomial in x . Because the quantity $\epsilon(x, t) \cdot G(x, t)$ is scale-invariant at some large scale, $\frac{d\epsilon}{dt}$ is also calculable. From the counting rules, we bound $\epsilon(x, t)$ by $\epsilon(x, t) \leq c(t) \cdot x(1-x)$. We require $\epsilon(x, t)$ to be decreasing at some scale, since $\epsilon(x, t) \cdot G(x, t)$ is scale invariant. Then, the form for $\epsilon(x, t = 0) = x(1-x)^n$, where n is the power

of $(1-x)$ in $G(x)$ and we assume that $c(t) \equiv 1$. The calculation of L_z and its evolution involves using the $J_z = \frac{1}{2}$ sum rule and the DGLAP evolution equations.

$$L_z = \frac{1}{2} - \Delta\Sigma/2 - (A_0 + \epsilon) \cdot G. \quad (4)$$

From its derivative with respect to t and the evolution equations, the evolution of L_z is

$$\frac{dL_z}{dt} = -[\Delta P_{qq} \otimes \Delta q + \Delta P_{qG} \otimes (A_0 \cdot G)]/2 - A_0[P_{Gq} \otimes q + P_{GG} \otimes G]. \quad (5)$$

3. Results and Experimental Verification

A plot of the $L_z(x)$ is shown in figure 1. Differences in the MRS and CTEQ based distributions can be seen at small- x . The evolved L_z for the CTEQ based model is also shown in the figure as a dotted line. The evolution to 100 GeV^2 is not very significant at leading order.

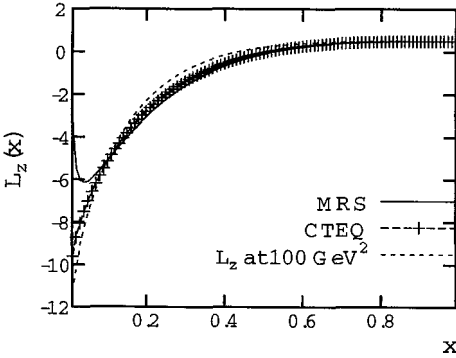


Fig. 1. Orbital angular momentum versus x generated by MRS (lines) and CTEQ (crosses) distributions and evolved to $Q^2 = 100 \text{ GeV}^2$ squared (dashes).

$A = \Delta G/G$. Experiments are outlined here to test the various assumptions and results obtained in this model.

Acknowledgments

This work is supported in part by the U.S. Department of Energy, Division of High Energy Physics, Contract W-31-109-ENG-38.

References

1. L. Gordon, M. Goshtasbpour and G. P. Ramsey, *Phys. Rev.* **D58**, 094017 (1998).
2. G. Pang and H. Zhao, *Phys. Rev.* **D65**, 014012 (2003)
3. A. D. Martin, *et. al.*, *Eur. Phys. J.* **C23**, 73 (2001).
4. L. Gordon and G. P. Ramsey, *Phys. Rev.* **D59**, 074018 (1999).
5. See papers by A. Metz, C. Schill, J. Sowinski and D. Hasch in this proceedings.

The model of the gluon asymmetry A can be tested by three separate experiments at DESY (HERA), BNL (RHIC) and CERN (COMPASS). First, ΔG can be measured via prompt photon production or jet production. These processes yield the largest asymmetries for the size of ΔG [4]. Also, measurement of $\Delta G/G$ in at least a small kinematic range of x and Q^2 will test this model [5]. The corresponding predictions for the orbital angular momentum L_z and its evolution can be measured via deeply-virtual Compton Scattering (DVCS) and vector-meson scattering.

We have proposed a way to calculate the orbital angular momentum and its evolution through use of the gluon asymmetry,

NLO QCD PROCEDURE WITH RESPECT TO FIRST MOMENTS OF POLARIZED QUARK DENSITIES

A. N. SISSAKIAN, O. Y. SHEVCHENKO, O. N. IVANOV

Joint Institute for Nuclear Research, Dubna, Russia

A procedure is proposed allowing the direct extraction of the first moments of the polarized quark distributions in the next to leading (NLO) QCD order from SIDIS data. The procedure is tested by appropriate simulations. It is shown that the extracted moments are in good agreement with the input parametrizations. The procedure is applied to recent HERMES data on pion asymmetries.

The main points of interests for the modern semi-inclusive deep inelastic scattering (SIDIS) experiments with longitudinally polarized beam and target are the strange quark, light sea quark and gluon contributions to the nucleon spin (see, for example [1] and references therein). Of special importance is also the still-open question of whether the polarized light sea quark is symmetric or not, i.e., if the quantity^a $\Delta_1\bar{u} - \Delta_1\bar{d}$ is equal to zero or not. At the same time it has been shown [2, 3] that to get reliable results on such tiny quantities as Δs and $\Delta_1\bar{u} - \Delta_1\bar{d}$ from the data obtained at the relatively small average Q^2 available to modern SIDIS experiments (such as HERMES and COMPASS), one should apply NLO QCD analysis. The appropriate procedure for Δ_1q extraction in NLO QCD have been proposed in [4]. In [4] it has been shown that the proposed procedure could be successfully applied to the *direct* extraction from the SIDIS data of the quantities Δ_1u_V , Δ_1d_V and, ultimately, of the quantity $\Delta_1\bar{u} - \Delta_1\bar{d}$. The equations for these quantities are

$$\Delta_1u_V = \frac{1}{5} \frac{A_p^{exp} + A_d^{exp}}{L_1 - L_2}; \quad \Delta_1d_V = \frac{1}{5} \frac{4A_d^{exp} - A_p^{exp}}{L_1 - L_2}, \quad (1)$$

for valence distributions and

$$\Delta_1\bar{u} - \Delta_1\bar{d} = \frac{1}{2} \left| \frac{g_A}{g_V} \right| - \frac{2A_p^{exp} - 3A_d^{exp}}{10(L_1 - L_2)} \quad (2)$$

for the $\Delta_1\bar{u} - \Delta_1\bar{d}$ respectively. All the quantities on the r.h.s. of these equations contain only already-measured unpolarized quark distributions and pion fragmentation functions

^aFrom now on the notation $\Delta_1q \equiv \int_0^1 dx \Delta q$ will be used to distinguish the local in Bjorken x polarized quark densities $\Delta q(x)$ and their first moments.

(favoured and unfavoured, entering the coefficients L_1 and L_2 , respectively), known NLO Wilson coefficients, and so-called “difference asymmetries” (see, for example, [1, 4, 5]) for pion production on proton and deuteron targets, $A_p^{\pi^+ - \pi^-}$ and $A_d^{\pi^+ - \pi^-}$, entering the quantities A_p^{exp} and A_d^{exp} . Thus, these difference asymmetries are the only unknown input which must be measured to find the quantities $\Delta_1 u_V$, $\Delta_1 d_V$ and $\Delta_1 \bar{u} - \Delta_1 \bar{d}$ using Eqs. (1) and (2).

The paper [4] reports a detailed analysis of the possibility of correctly extracting, in NLO QCD order, the quantities $\Delta_1 u_V$, $\Delta_1 d_V$ and $\Delta_1 \bar{u} - \Delta_1 \bar{d}$ in the real conditions of the HERMES and COMPASS experiments. Special attention was paid to such important questions as the statistical errors on the difference asymmetries^b and to the uncertainties caused by the low x_B regions inaccessible to HERMES and COMPASS. First of all, the analysis in [4] confirms that the proposed NLO QCD extraction procedure meets the main requirement: to reconstruct the quark moments in the accessible x_B region. On the other hand, it was shown that even with the rather overestimated low x_B uncertainties given in [4], one can conclude that the question whether $\Delta_1 \bar{u} - \Delta_1 \bar{d}$ is equal to zero or not could be answered even with the HERMES kinematics in the case of a strongly asymmetric polarized sea. In any case, the situation is much better in the x_B region accessible to COMPASS.

Let us now apply the proposed procedure to the real data^c from HERMES [6] on the asymmetries $A_{p,d}$, $A_{p,d}^{\pi^\pm}$. The proposed procedure in this case allows to obtain simple expressions for the NLO quantities $\Delta_1 u$, $\Delta_1 d$ and $\Delta_1 \bar{q} \equiv \Delta_1 \bar{u} = \Delta_1 \bar{d} = \Delta_1 s = \Delta_1 \bar{s}$ via the quantities $A_{(exp)p,d}$, $A_{(exp)p,d}^{\pi^\pm}$. The later, like the quantities A_p^{exp} , A_d^{exp} in the case of difference asymmetries [4], contain only already-measured unpolarized quark distributions, fragmentation functions^d, known NLO Wilson coefficients, and the measured asymmetries $A_{p,d}$, $A_{p,d}^{\pi^\pm}$. Certainly, one could choose only three equations (containing any three of six measured asymmetries) to obtain the minimal non-degenerate system which can be directly solved for NLO quantities $\Delta_1 u$, $\Delta_1 d$ and $\Delta_1 \bar{q}$. However, to increase the precision of extraction, we as usual use a fitting procedure which includes all six available quantities $A_{(exp)p,d}$, $A_{(exp)p,d}^{\pi^\pm}$ to calculate χ^2 .

First of all, we again perform the testing of our method using the GRSV2000(NLO) [8] parametrization as input. Comparing the upper and lower parts of Table 1, one can see that the results of the $\Delta_1 u$, $\Delta_1 d$ and $\Delta_1 \bar{q}$ reconstruction are in good agreement with the input parametrization. Thus, the testing performed shows that our procedure can be applied to $\Delta_1 u$, $\Delta_1 d$ and $\Delta_1 \bar{q}$ reconstruction.

^bAt first sight it could seem that the difference asymmetries suffer from the much larger errors in comparison with the usual asymmetries, because of the difference in π^+ and π^- counting rates in the denominator. Fortunately, however, for the proton and deuteron target this is not the case because on these targets (in contrast to the neutron target) π^+ production considerably exceeds π^- production. As a consequence, the statistical errors are quite acceptable [4].

^cSince the kaon fragmentation functions are still poorly known, at this point we would like to check the validity of the method itself (irrespective of this problem), considering the simplest case of pion production with the assumption $\Delta_1 \bar{u} = \Delta_1 \bar{d} = \Delta_1 s = \Delta_1 \bar{s} \equiv \Delta_1 \bar{q}$. The application of the method to the kaon asymmetries is now in preparation.

^dThe parametrization for the fragmentation functions from Ref. [7] is used for both testing with PEPSI [9] and reconstruction from the real HERMES data

Table 1. The upper part presents the results on $\Delta_1 u$, $\Delta_1 d$ and $\Delta_1 \bar{q}$ obtained from integration of the GRSV2000NLO parametrization (symmetric sea scenario). The lower part presents the results extracted from the simulated asymmetries applying the proposed NLO procedure with GRSV2000NLO parametrization entering the generator as an input.

x_B region	$\Delta_1 u$	$\Delta_1 d$	$\Delta_1 \bar{q}$
$0.023 < x_B < 0.6$	0.724	-0.302	-0.026
$0.023 < x_B < 0.6$	0.702 ± 0.020	-0.274 ± 0.025	-0.027 ± 0.013

Let us now perform NLO extraction of $\Delta_1 u$, $\Delta_1 d$ and $\Delta_1 \bar{q}$ from real HERMES data [6] on $A_{p,d}, A_{p,d}^{\pi^\pm}$. It is of importance that the unpolarized quark densities entering the quantities $A_{(exp)p,d}, A_{(exp),d}^{\pi^\pm}$ are obtained from the structure functions F_2 . Thus, when dealing with real data one should first express SIDIS structure function F_1^h (entering the quantities $A_{(exp)}$) via F_2^h : $F_1^h = 2xF_2^h(1 + R)$, and then use pQCD NLO expressions for F_2^h through the respective unpolarized quark densities and Wilson coefficients [10]. The respective results are presented in Table 2.

Table 2. The results on NLO extracted $\Delta_1 u$, $\Delta_1 d$ and $\Delta_1 \bar{q}$ from the HERMES data on asymmetries $A_{p,d}, A_{p,d}^{\pi^\pm}$.

$\Delta_1 u$	$\Delta_1 d$	$\Delta_1 \bar{q}$
0.624 ± 0.063	-0.355 ± 0.070	0.016 ± 0.038

It is instructive to compare the results of Table 2 with the appropriate integrals of the two latest NLO parametrizations [11]; see Table 3. It is seen that the results are in good agreement within the errors.

Table 3. The results on $\Delta_1 u$, $\Delta_1 d$ and $\Delta_1 \bar{q}$ obtained from the appropriate integrals of parametrizations AAC2003 and BB over the x_B region accessible to HERMES.

Parametrization	$\Delta_1 u$	$\Delta_1 d$	$\Delta_1 \bar{q}$
AAC2003	0.691	-0.293	-0.034
BB	0.667	-0.274	-0.024

Thus, the performed analysis suggests that the proposed procedure is acceptable for the extraction of $\Delta_1 q$ in the next-to-leading QCD order.

The authors are grateful to R. Bertini, M. P. Bussa, O. Denisov, O. Gorchakov, A. Efremov, N. Kochelev, A. Korzenev, A. Kotzinian, V. Krivokhizhin, E. Kuraev, A. Maggiora, A. Nagaytsev, A. Olshevsky, G. Piragino, G. Pontecorvo, J. Pretz, I. Savin and O. Teryaev, for fruitful discussions.

References

1. COMPASS collaboration (G. Baum et al.), “COMPASS: A proposal for a common muon and proton apparatus for structure and spectroscopy”, CERN-SPSLC-96-14 (1996).
2. E. Leader, D.B. Stamenov, *Phys. Rev.* **D67** (2003) 037503
3. A.N. Sissakian, O.Yu. Shevchenko and O.N. Ivanov, *Phys. Rev.* **D 68** (2003) 031502(R).
4. A.N. Sissakian, O.Yu. Shevchenko and O.N. Ivanov, *Phys. Rev.* **D 70** (2004) 074032.
5. E. Christova and E. Leader, *Nucl. Phys* **B 607** (2001) 369.
6. HERMES collaboration (A. Airapetian et al.), DESY-04-107, Jul 2004, hep-ex/0407032.
7. S. Kretzer, *Phys.Rev.* **D 62** (2000) 054001.
8. M. Gluck, E. Reya, M. Stratmann, W. Vogelsang, *Phys.Rev.* **D 63** (2001) 094005.
9. L. Mankiewicz, A. Schafer, M. Veltri, *Comput. Phys. Commun.* **71** (1992) 305-318.
10. D. de Florian and R. Sassot, *Phys. Rev.* **D 62** (2000) 094025.
11. Asymmetry Analysis Collaboration (M. Hirai et al), *Phys. Rev.* **D 69** (2004) 054021 (AAC2003); J. Blumlein, H. Bottcher *Nucl.Phys.* **B636** (2002) 225.

A MODEL-INDEPENDENT APPROACH TO SEMI-INCLUSIVE DEEP INELASTIC SCATTERING

E. CHRISTOVA*

Institute for Nuclear Research and Nuclear Energy, Sofia, Bulgaria

E. LEADER

Imperial College, London, England

We present a method for the extraction of detailed information on polarized quark densities from semi-inclusive deep inelastic scattering $l + N \rightarrow l + h + X$, in both LO and NLO QCD without any assumptions about fragmentation functions and polarized sea densities. The only symmetries utilised are charge conjugation and isotopic spin invariance of strong interactions.

1. At present the possibility of obtaining full information on the parton helicity densities in a polarized nucleon is related to semi-inclusive deep inelastic scattering (SIDIS) of polarized leptons on polarized nucleons:

$$\vec{\ell} + \vec{N} \rightarrow e + h + X, \quad h = \pi^\pm, K^\pm, \dots \quad (1)$$

The first polarized SIDIS measurements were done by the SMC [1] and HERMES [2] collaborations, where the asymmetry A_N^h was measured:

$$A_N^h = \frac{1 + (1 - y)^2}{2y(2 - y)} \frac{\Delta\sigma_N^h}{\sigma_N^h} = \frac{\sum e_q^2 (\Delta q D_q^h + \Delta \bar{q} D_{\bar{q}}^h)}{\sum e_q^2 (q D_q^h + \bar{q} D_{\bar{q}}^h)}, \quad (LO). \quad (2)$$

Here $\Delta\sigma_N^h$ (σ_N^h) is the measured polarized (unpolarized) cross section. Though this asymmetry allows, in principle, full extraction of the polarized parton densities, in practice it faces two major problems. Firstly, a good knowledge of the fragmentation functions (FFs) D_q^h is required. At present, these functions are rather poorly known, and a number of model-dependent assumptions are made. Secondly, it is not clear how to extend the ‘‘purity’’ method, used in the analysis in LO, to the case of NLO. As the completed and planned

*Work supported by grant Ph-1010 of the Bulgarian National Science Foundation.

measurements of polarized SIDIS are done at rather low Q^2 , NLO corrections have to be taken into account.

2. Here we show [3, 4] that a measurement of the difference asymmetries $A_N^{h^+-h^-}$ and ratios $R_N^{h^+-h^-}$:

$$A_N^{h^+-h^-} = \frac{1 + (1-y)^2}{2y(2-y)} \frac{\Delta\sigma_N^{h^+} - \Delta\sigma_N^{h^-}}{\sigma_N^{h^+} - \sigma_N^{h^-}}, \quad R_N^{h^+-h^-} = \frac{\sigma_N^{h^+} - \sigma_N^{h^-}}{\sigma_N^{DIS}}, \quad (3)$$

yields a lot of information on the polarized quark densities, in both LO and NLO, without any assumptions about the FFs. In general this can be traced as follows. C-invariance of strong interactions leads to $D_G^{h-\bar{h}} = 0$ and $D_q^{h-\bar{h}} = -D_{\bar{q}}^{h-\bar{h}}$, which immediately singles out in $A_N^{h^+-h^-}$ and $R_N^{h^+-h^-}$ quantities that are flavour non-singlets for both the parton densities and the FFs. This implies that: 1) the badly known gluons G , ΔG and $D_G^{h-\bar{h}}$ do not enter these asymmetries, 2) in its Q^2 -evolution $A_N^{h^+-h^-}$ and $R_N^{h^+-h^-}$ do not mix with other quantities, apart from those entering them and, 3) $A_N^{h^+-h^-}$ can give information only on non-singlet parton densities: Δu_V , Δd_V , $\Delta\bar{u} - \Delta\bar{d}$, $\Delta s - \Delta\bar{s}$, etc, but in a model-independent way. This holds in general and is true to any order in QCD. Depending on the SU(2) properties of the detected final hadron h , one obtains different pieces of information. This method for extracting the polarized quark densities will be used in the planned experiment E04-113, Semi-SANE, at Jefferson Lab. [5].

3. If $h = \pi^\pm$, SU(2) and C-invariance reduce the number of independent pion FFs: $D_u^{\pi^+-\pi^-} = -D_d^{\pi^+-\pi^-}$, $D_s^{\pi^+-\pi^-} = 0$. Then in LO we have:

$$A_p^{\pi^+-\pi^-} = \frac{4\Delta u_V - \Delta d_V}{4u_V - d_V}, \quad A_n^{\pi^+-\pi^-} = \frac{4\Delta d_V - \Delta u_V}{4d_V - u_V} \quad (4)$$

Thus the FFs completely cancel, and Δu_V and Δd_V are expressed algebraically solely in terms of measurable quantities and the known unpolarized u_V and d_V .

When going from LO to NLO, the principal differences are that the simple products are replaced by convolutions, and that gluons enter the cross sections. As explained above, in $A_N^{\pi^+-\pi^-}$ the gluon contributions always drop out and we obtain:

$$A_p^{\pi^+-\pi^-} = \frac{(4\Delta u_V - \Delta d_V)[1 + \otimes(\alpha_s/2\pi)\Delta C_{qq} \otimes] D_u^{\pi^+-\pi^-}}{(4u_V - d_V)[1 + \otimes(\alpha_s/2\pi)C_{qq} \otimes] D_u^{\pi^+-\pi^-}}$$

$$A_n^{\pi^+-\pi^-} = \frac{(4\Delta d_V - \Delta u_V)[1 + \otimes(\alpha_s/2\pi)\Delta C_{qq} \otimes] D_u^{\pi^+-\pi^-}}{(4d_V - u_V)[1 + \otimes(\alpha_s/2\pi)C_{qq} \otimes] D_u^{\pi^+-\pi^-}}. \quad (5)$$

The FF $D_u^{\pi^+-\pi^-}$, that enters (5), can be determined in unpolarized SIDIS:

$$R_p^{\pi^+-\pi^-} = \frac{(4u_V - d_V)[1 + \otimes(\alpha_s/2\pi)C_{qq} \otimes] D_u^{\pi^+-\pi^-}}{18F_1^p(1 + 2\gamma(y)R^p)}$$

$$R_n^{\pi^+-\pi^-} = \frac{(4d_V - u_V)[1 + \otimes(\alpha_s/2\pi)C_{qq} \otimes] D_u^{\pi^+-\pi^-}}{18F_1^n(1 + 2\gamma(y)R^n)}, \quad (6)$$

where $\gamma(y) = (1-y)/[1 + (1-y)^2]$.

Recently the HERMES collaboration published [6] very precise data for unpolarized SIDIS- π^\pm production, allowing the determination of $D_u^{\pi^+-\pi^-}$ directly. This was done in [7], combining the HERMES and the LEP e^+e^- inclusive data on π^\pm -production. For the first time the u -quark FFs of the pions were obtained by the EMC collaboration [8].

4. Having thus determined Δu_V and Δd_V , we can proceed to determine the SU(2) breaking of the polarized sea quarks. We have:

$$(\Delta\bar{u} - \Delta\bar{d}) = \frac{1}{6} [\Delta q_3 + \Delta d_V - \Delta u_V], \Delta q_3 = (\Delta u + \Delta\bar{u}) - (\Delta d - \Delta\bar{d}).$$

In LO the valence quarks are determined via (4), and Δq_3 is determined by $\Delta q_3 = g_1^p(x, Q^2) - g_1^n(x, Q^2)$. In NLO the valence quarks are determined via (5), and Δq_3 is obtained by the NLO expression:

$$g_1^p(x, Q^2) - g_1^n(x, Q^2) = \frac{1}{6} \Delta q_3 \otimes \left(1 + \frac{\alpha_s(Q^2)}{2\pi} \delta C_q \right). \quad (7)$$

Thus, $A_N^{\pi^+-\pi^-}$ and g_1^N determine Δu_V , Δd_V , and $\Delta\bar{u} - \Delta\bar{d}$, both in LO and NLO, without any assumptions. Note that, due to $D_s^{\pi^+-\pi^-} = 0$, even the commonly used assumptions $s = \bar{s}$ or $\Delta s = \Delta\bar{s}$ are not made.

5. If $h = K^\pm$ (and K^0) are not measured we cannot use isospin symmetry. However, if we make the natural assumption that unfavoured transitions for K^+ and K^- are equal (but not small): $D_d^{K^+-K^-} = 0$ we can use $A_N^{K^+-K^-}$ to determine $(\Delta s - \Delta\bar{s}) D_s^{K^+-K^-}$. As the strange quark is a valence quark for K^\pm , $D_s^{K^+-K^-}$ is not small, and $(\Delta s - \Delta\bar{s}) D_s^{K^+-K^-}$ would be nonzero only if $(\Delta s - \Delta\bar{s}) \neq 0$. In LO we have:

$$\begin{aligned} A_p^{K^+-K^-} &= \frac{4\Delta u_V D_u^{K^+-K^-} + (\Delta s - \Delta\bar{s}) D_s^{K^+-K^-}}{4u_V D_u^{K^+-K^-} + (s - \bar{s}) D_s^{K^+-K^-}} \\ A_n^{K^+-K^-} &= \frac{4\Delta d_V D_u^{K^+-K^-} + (\Delta s - \Delta\bar{s}) D_s^{K^+-K^-}}{4d_V D_u^{K^+-K^-} + (s - \bar{s}) D_s^{K^+-K^-}}. \end{aligned} \quad (8)$$

We determine $D_u^{K^+-K^-}$ and $(s - \bar{s}) D_s^{K^+-K^-}$ from unpolarized SIDIS:

$$\begin{aligned} R_p^{K^+-K^-} &= \left(4u_V D_u^{K^+-K^-} + (s - \bar{s}) D_s^{K^+-K^-} \right) / 18 F_1^p \\ R_n^{K^+-K^-} &= \left(4d_V D_u^{K^+-K^-} + (s - \bar{s}) D_s^{K^+-K^-} \right) / 18 F_1^n. \end{aligned} \quad (9)$$

Following the same argument as above, these ratios will shed light on the $(s - \bar{s})$ difference.

In NLO the same quantities enter, and the expressions are analogous to (8)-(9), where the simple products are replaced by convolutions [4].

6. If $h = \Lambda, \bar{\Lambda}$, then SU(2) invariance implies $D_u^{\Lambda-\bar{\Lambda}} = D_d^{\Lambda-\bar{\Lambda}}$ and no conditions on $D_s^{\Lambda-\bar{\Lambda}}$. Thus, $A_N^{\Lambda-\bar{\Lambda}}$ will give information on $(\Delta s - \Delta\bar{s})$ without any assumptions. The expressions can be found in [4].

References

1. B. Adeva *et al.*, (SMC) *Phys. Lett.* **B369**, 93 (1996); **B420**, 180 (1998)

2. K. Ackerstaff et al., (HERMES) *Phys. Lett.* **B464**, 123 (1999); hep-ex/0407032
3. E. Christova, E. Leader, *Phys. Lett.* **B468**, 299 (1999)
4. E. Christova, E. Leader, *Nucl. Phys.* **B607**, 369 (2001)
5. www.jLab.org/jiang/pac26/fact
6. A. Airepation et al., (HERMES) *Eur.Phys.J.* **C21**, 599 (2001)
7. S. Kretzer, E. Leader, E. Christova, *Eur.Phys.J.* **C22**, 269 (2001)
8. EMC: J.J. Aubert et al., *Phys.Lett* **B160** 417 (1985);
M. Arneodo et al., *Nucl. Phys.* **B321**, 541 (1989)

SPIN PHYSICS PROGRESS WITH THE STAR DETECTOR AT RHIC

J. SOWINSKI

Indiana University Cyclotron Facility, Bloomington, USA

(for the STAR Collaboration)

Progress in STAR over the last two years and projections for the coming two years are discussed. Important technical developments have been the completion of the barrel and endcap electromagnetic calorimeters. Measurement of inclusive jet and π_0 A_{LL} over the next two years are expected to show whether ΔG is a major contributor to the proton's spin. Transverse effects such as Collins and Sivers functions at mid-rapidity will also be investigated.

Since the first data from polarized proton collisions at RHIC were presented [1] at SPIN 2002, the STAR collaboration has continued to participate in the short data-acquisition periods provided as the beams were developed in 2003 and 2004. During these periods, characterized by increasing luminosity and beam polarization, STAR has been able to commission new detectors important to its spin program as well as take data that will help tune the detectors for the upcoming runs and provide "first looks" with limited statistics at spin observables needed to understand the spin structure of the nucleon. With luminosity and polarization continuing to improve [2], it is expected that extended running periods for polarized protons will be provided over the next few years, allowing significant constraints to be placed on ΔG , and investigations of transverse physics such as Sivers and Collins functions to be started. In the following I will review STAR's upgrades of the past few years, the measurements already made, and prospects for the next few years leading to SPIN 2006.

The STAR detector [3] is based on a large solenoidal magnet with much of its internal volume devoted to tracking charge particles with a time projection chamber (TPC) in a 5 kG magnetic field. A big effort has gone into providing electromagnetic calorimetry around the outer diameter of the TPC, the barrel electromagnetic calorimeter (BEMC) [4], and covering one poletip of the magnet, the endcap electromagnetic calorimeter (EEMC) [5]. Since 2002 subsets of these calorimeters have been installed and commissioned, with the installation of the final modules and electronics taking place in preparation for the 2005 run. This completes STAR's large solid angle capabilities allowing for the full reconstruction of jets (unique at RHIC), in addition to providing fast triggers, both essential to the spin program.

The two calorimeters are both lead/plastic-scintillator sampling calorimeters capable of measuring gamma rays from below 1 GeV to over 100 GeV in energy. The BEMC covers the range in pseudorapidity, $\eta = -\ln(\tan(\theta/2))$, of $-1 \leq \eta \leq 1$ ($\theta \geq 40^\circ$) with 4800 individually read out “tower” energy signals. The EEMC provides an additional 720 tower energy signals in a forward pseudorapidity range, $1.1 \leq \eta \leq 2$ ($37^\circ \geq \theta \geq 15^\circ$), important for reaching small x_{gluon} in partonic collisions. The first two active layers of each detector are read out twice, once as part of the tower sum, and independently as a pre-shower signal to help in π^0/γ and electron/hadron discrimination. The last layer of the EEMC is also read out twice, again in the tower sum and independently as a post-shower signal for e/h discrimination. Both detectors incorporate a finely segmented shower maximum detector (SMD) approximately 5 radiation lengths deep in the detector. The BEMC SMD is a gaseous proportional wire chamber, while the EEMC uses triangular scintillator strips laminated into two crossed planes. These SMDs are used to reconstruct the two showers from π^0 decay versus the single shower of direct photons. Although not complete over the full solid angle, the full functionality of these detector subsystems was used in the 2004 RHIC run. Currently algorithms such as those for finding π^0 s and jets are being fine tuned and physics analyses have begun.

It is well known that the spin of the quarks does not account for the spin of a proton [6]. Other contributions such as the spin of gluons (ΔG) or the orbital angular momentum are poorly constrained by existing data. Partonic scattering processes in $p-p$ scattering such as $q + g \rightarrow q + g$, $g + g \rightarrow g + g$ and $q + g \rightarrow q + \gamma$ detected as jets, and in the last case an isolated direct photon, have large spin sensitivities [6], opening a window to ΔG . The large solid angle of STAR is particularly well suited for detecting jets and direct-photon/jet coincidences over a range in pseudorapidity that helps cover a broad range in the partonic momentum fraction x .

A long-term goal for the STAR spin physics program is to measure $\Delta g(x)$, i.e. not just the integral ΔG over some region but the x dependence from $0.01 \leq x \leq 0.3$, using the $q + g \rightarrow q + \gamma$ (QCD Compton scattering) process. The coincident direct-photon and jet present a relatively clean experimental signal, the partonic sub-process dominates other partonic subprocesses generating the same signal, and two-body kinematics allows the reconstruction of the partons' x and scattering angle. However this is a rare process and will require over 100 pb^{-1} , so that the tens of pb^{-1} expected in the next two runs will serve primarily to tune the technique.

Although not as selective, A_{LL} measured with inclusive jets is sensitive [7] to ΔG as shown in Fig. 1, and jets are produced abundantly in the collisions at RHIC. The STAR detector has a large enough acceptance to reconstruct jets, and jet finding algorithms are being tuned on the 2004 data set. STAR triggers on jets either with a high tower trigger (largest tower above a threshold) or jet patch triggers (one of a predefined set of regions approximately 1×1 in $\eta \times \phi$ exceed a threshold). These triggers were tested and used during the 2004 run, and preliminary analyses indicate that approximately half of such triggers are found to contain jets with p_T over 5 GeV. It is expected that, when fully analyzed, the 2004 data will only be able to discriminate between the maximal ΔG and 0. The level of

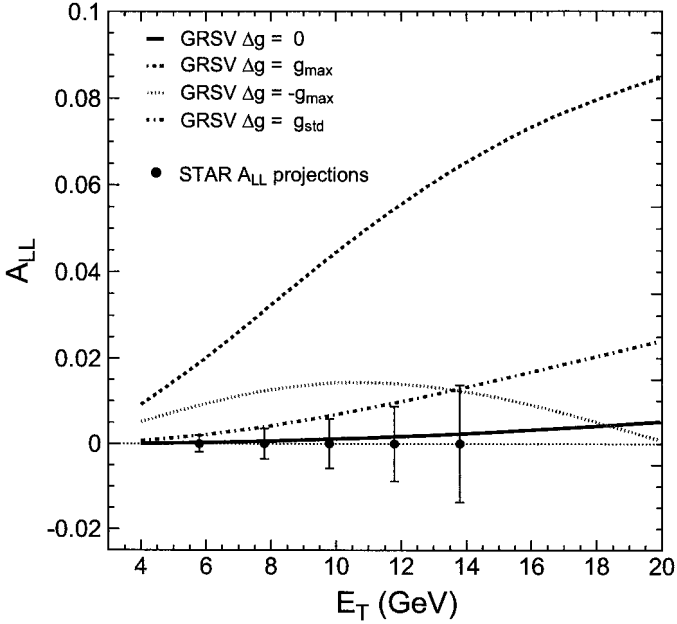


Fig. 1. Predictions of A_{LL} for inclusive jets [7] compared with the precision of measurements from data expected in the 2005 running period. An integrated luminosity of 7 pb^{-1} with a polarization of 0.4 as well as jet finding efficiencies from previous runs is assumed.

sensitivity expected with 2005 data is displayed in Fig. 1. The calorimeters in STAR are also capable of reconstructing π^0 s. Jäger et al. have shown [7] that jet sensitivity to ΔG is carried over to the inclusive π^0 A_{LL} . We expect that our inclusive π^0 results will have similar discriminating power to that of the jets, but with different sensitivities to trigger bias.

A number of mechanisms have been suggested for explaining the forward π^0 analyzing powers we have measured [1, 8]. STAR is also interested in pursuing effects arising from these at mid-rapidity. If the asymmetries in jet decays reflecting the showering quark's spin, as represented by Collins functions [9], turn out to be large enough, they can be used to gain access to transversity via spin transfer from the final to initial state quarks. Boer and Vogelsang have also recently pointed out possible effects at a measurable level resulting from gluonic Sivers functions in dijets [10]. The Sivers functions describe a correlation between the $k_T(x)$ of partons and the transverse spin of the proton. While these correlations integrate [11] to 0 over all partons and Bjorken x , they need not be zero for individual partons. STAR has already measured the unpolarized k_T distribution [12], which is of sufficient width that, with transverse data expected in the next few years, we should be able to observe signals of the predicted size [10].

Improving polarization and luminosity as well as significant running time for polarized protons at $\sqrt{s}=200$ GeV is expected over the next few years. In addition to continuing our studies of transverse physics, we hope that by spin 2006 we will be able to say whether

gluons are a major contributor to the proton's spin or not.

References

1. G. Rakness in *Spin 2002: 15th Int'l Spin Physics Symposium*, eds. Y.I. Makdisi, A.U. Luccio and W.W. McKay, (AIP, New York, 2003) p. 400; J. Adams *et al.*, Phys. Rev. Lett. **93** (2004) 012301.
2. W.W. MacKay, 'Status of Proton Polarization at RHIC and AGS', *these proceedings*.
3. K.H. Ackermann *et al.*, Nucl. Instrum. Meth. A **499**, 624 (2003).
4. M. Beddo *et al.*, Nucl. Instrum. Meth. A **499**, 725 (2003).
5. C.E. Allgower *et al.*, Nucl. Instrum. Meth. A **499**, 740 (2003).
6. G. Bunce *et al.*, Ann. Rev. Nucl. Part. Sci., **525** (2000).
7. B. Jager, M. Stratmann, W. Vogelsang, Phys.Rev. **D70**, 034010 (2004).
8. A. Ogawa, Spin Physics in Large Rapidity Neutral Pion Production at STAR, *these proceedings*.
9. J.C. Collins, S.F. Heppelmann, G.A. Ladinsky, Nucl. Phys. **B420**, 565 (1994).
10. D. Boer, W. Vogelsang, Phys.Rev. **D69**, 094025 (2004).
11. M. Burkardt, Phys.Rev. **D69**, 091501 (2004).
12. T. Henry, J.Phys. **G30** S1287 (2004).

PROBING GLUON POLARIZATION WITH π^0 'S IN LONGITUDINALLY POLARIZED PROTON COLLISIONS AT THE RHIC-PHENIX EXPERIMENT

Y. FUKAO

Kyoto University, Kyoto, Japan

(for the PHENIX Collaboration)

This report presents double-helicity asymmetry in inclusive π^0 production in polarized proton-proton collisions at a center-of-mass energy (\sqrt{s}) of 200 GeV. The data were collected with the PHENIX detector at the Relativistic Heavy Ion Collider (RHIC) during the 2004 run. The data are compared to a next-to-leading order perturbative quantum chromodynamic (NLO pQCD) calculation.

1. Introduction

Polarized lepton-nucleon deep inelastic scattering (DIS) experiments over the past 20 years have revealed that only $\sim 25\%$ of the proton spin is carried by the quark spin. Therefore the gluon spin and orbital angular momentum must contribute to the rest of the proton spin. In polarized proton-proton collisions one can explore the gluon polarization directly using the processes that gluons participate in. One of the promising probes is to measure the double longitudinal spin asymmetry (A_{LL}) in high p_T particle production.

The first measurement of A_{LL} in π^0 production at RHIC during the 2003 run (Run-3) has been published [1]. The present report shows the latest results of $\pi^0 A_{LL}$ for the range of 1–5 GeV/ c in transverse momenta (p_T) and from -0.35 to 0.35 in pseudorapidity (η) obtained during the 2004 run (Run-4).

A_{LL} is defined by the following formula.

$$A_{LL} = \frac{\sigma_{++} - \sigma_{+-}}{\sigma_{++} + \sigma_{+-}}, \quad (1)$$

where σ is the cross section of the process of interest, $++$ ($+-$) denotes that the variable is obtained in collisions with the same (opposite) helicity beams. Taking into account the beam polarizations and the luminosity variations between the two possible spin orientations, equation 1 becomes,

$$A_{LL} = \frac{1}{|P_{B_1}| |P_{B_2}|} \frac{N_{++} - RN_{+-}}{N_{++} + RN_{+-}}, \quad R = \frac{L_{++}}{L_{+-}}, \quad (2)$$

where P_{B_1} and P_{B_2} are the beam polarizations. N is the yield (of π^0 in this report), L is the integrated luminosity and R is what we call the relative luminosity. These $P_{B_1(B_2)}$, N , and R were measured in the experiment.

2. Experimental setup

RHIC was operated with both proton beams polarized longitudinally at $\sqrt{s}=200$ GeV. The machine performance in Run-4 is compared to Run-3 briefly in Table 1. For the double helicity asymmetry, the statistical figure of merit is expressed by $P_{B_1}^2 P_{B_2}^2 L$. Although Run-4 was short, the figure of merit is larger thanks to higher beam polarization. The beam po-

Table 1. PHENIX data summary in Run-3 and Run-4.

	run period	L (nb $^{-1}$)	$\langle P_B \rangle$ (%)	figure of merit (nb $^{-1}$)
Run-3	4 weeks	220	27	1.17
Run-4	4 days	75	40	1.92

larization was measured by the proton-Carbon CNI polarimeter [2] constructed near IP12, away from PHENIX, where the systematic error of the beam polarization was 32%. This affects the scaling error of the double helicity asymmetry by 65%.

Since the stable direction of the beam polarization is vertical in RHIC, we must rotate the beam polarization before and after the collision point to obtain longitudinal polarization. The PHENIX^a local polarimeter [1] confirmed that the direction of the proton spin in the PHENIX collision point was more than 99% longitudinal.

The relative luminosity, R , was evaluated using the beam-beam counter and the zero-degree calorimeter in PHENIX to be $\delta R = 5.8 \times 10^{-4}$, which corresponds to $\delta A_{LL} = 1.8 \times 10^{-3}$ for a beam polarization of 40%.

3. π^0 A_{LL} results

In the analysis, we did not subtract the background under the π^0 peak directly. Instead, we calculated A_{LL} in the two-photon invariant-mass range of ± 25 MeV around the π^0 peak (A_{LL}^{raw}), called the ‘‘signal’’ region, then corrected it by A_{LL} of the background (A_{LL}^{BG}) to extract A_{LL} of pure π^0 ($A_{LL}^{\pi^0}$) using

$$A_{LL}^{\pi^0} = \frac{A_{LL}^{raw} - rA_{LL}^{BG}}{1 - r}, \quad \Delta A_{LL}^{\pi^0} = \frac{\sqrt{(\Delta A_{LL}^{raw})^2 + r^2(\Delta A_{LL}^{BG})^2}}{1 - r}, \quad (3)$$

where r is the fraction of the background in the ‘‘signal’’ range and is obtained by fitting. A_{LL} of the background is evaluated using the mass range near the π^0 peak. Table 2 shows the statistics of π^0 's within the ‘‘signal’’ mass window and the fraction of BG under the π^0 peak. The systematic error of A_{LL} non-correlated between bunches or fills can be evaluated by

^aAn overview of PHENIX is found in [3].

Table 2. The statistics of π^0 s and the BG fraction.

p_T (GeV/c)	1-2	2-3	3-4	4-5
π^0 statistics ($\times 10^3$)	1151	510	91	17
BG fraction (%)	31	13	7	5

the ‘‘bunch shuffling’’ technique [1]. We found such systematics to be negligible compared to the statistical error. The systematic error correlated over all bunches or all fills comes mainly from the uncertainty on the beam polarization and the relative luminosity described above.

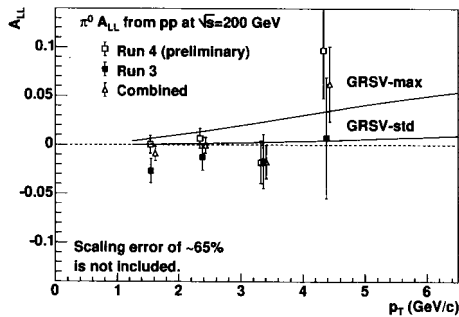
Figure 1 and Table 3 show Run-4 results for $\pi^0 A_{LL}$ as well as those from Run-3 [1], and their combination with the statistical errors. Two theoretical curves [4] are also drawn in the figure. The resulting confidence levels for our data from Run-3 and Run-4 combined was calculated to be 21-24% for the GRSV-standard model, 0.0-6% for the GRSV-maximum model, taking into account the polarization scale uncertainty. Our results favour the GRSV-standard model.

 Table 3. $\pi^0 A_{LL}$ in Run-4, Run-3 and their combination.

p_T (GeV/c)	1-2	2-3	3-4	4-5
Run 4 (%)	0.0 ± 0.9	0.7 ± 1.0	-1.8 ± 2.2	9.7 ± 4.9
Run 3 (%)	-2.7 ± 1.3	-1.3 ± 1.3	-1.7 ± 2.8	0.7 ± 6.2
Comb. (%)	-0.9 ± 0.7	0.0 ± 0.8	-1.8 ± 1.7	6.2 ± 3.8

4. Future plans

RHIC plans to operate with higher luminosity and polarization in the future. Figure 2 shows the expected $\pi^0 A_{LL}$ in proton Run-5, starting in February 2005, as well as in the next long pp run expected in 2006–7. The central values of those points follow the GRSV-standard. Three pQCD theory curves are also shown, calculated with $\Delta g = +g$ (same as GRSV-max in Fig.1), $\Delta g = -g$ and $\Delta g = 0$ at the input scale ($Q^2 = 0.4 \text{ GeV}^2$) [5]. We can further constrain Δg in Run-5.


 Fig. 1. $\pi^0 A_{LL}$ as a function of p_T .

However, A_{LL} for π^0 can be approximated by a quadratic function of $\Delta g/g$, and it is hard to determine the sign of Δg with only low p_T data due to the duality of the quadratic function. One solution of this problem is to measure $\pi^0 A_{LL}$ in the higher p_T region where the duality becomes less. (See Run-7 estimation in Fig.2.) The other way is to combine π^0 results with other channels, for example, A_{LL} of direct photons. This is a powerful probe and will be measured in future runs with higher statistics.

5. Summary

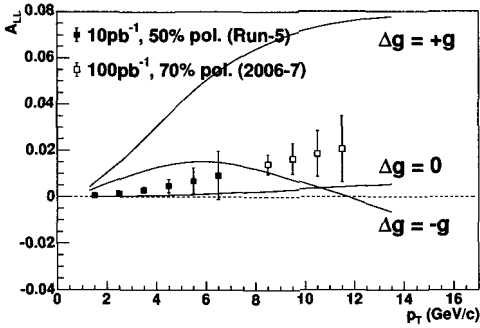


Fig. 2. $\pi^0 A_{LL}$ as a function of p_T .

We have reported the results of A_{LL} in π^0 production in polarized proton-proton collisions at $\sqrt{s} = 200$ GeV measured in 2004 with the PHENIX detector at RHIC. $\pi^0 A_{LL}$ was presented for 1–5 GeV/c in p_T and $|\eta| < 0.35$. The data was compared to NLO pQCD calculations and favours the GRSV-standard model on the gluon polarization. Expectations from future runs have also been discussed.

References

1. S. S. Adler *et al.*, *Phys.Rev.Lett.* **93**, 202002 (2004)
2. O. Jinnouchi *et al.*, RHIC/CAD Accelerator Physics Note 171 (2004)
3. K. Adcox *et al.*, *Nucl. Instrum. Meth.* **A499**, 469 (2003)
4. B. Jäger *et al.*, *Phys. Rev.* **D67**, 054005 (2003)
5. M. Glück *et al.*, *Phys. Rev.* **D63**, 094005 (2001)

MEASUREMENT OF PROMPT PHOTONS IN $\sqrt{s} = 200$ GeV pp COLLISIONS

K. OKADA

RIKEN-BNL Research Center, Brookhaven National Laboratory, Upton , USA

(for the PHENIX Collaboration)

This report presents the preliminary result for the prompt photon production cross section in proton-proton collisions in the mid-rapidity region using the PHENIX detector. The NLO pQCD calculation is in good agreement with the data. The measurement was made with and without an isolation cut. The isolation cut significantly improves the signal purity without reducing the signal yield. This is an important step for future spin asymmetry measurement.

1. Introduction

Prompt photon production in proton-proton collisions is a good probe of the parton structure in the proton. Its leading sub-process is gluon-quark Compton scattering. In polarized proton-proton collisions at RHIC, it is a good tool to access the spin structure function of the gluon in the proton. Two types of processes contribute to the prompt photon production cross section: the so-called 'direct' component, where the photon is emitted via point-like (direct) coupling to a quark, and the fragmentation component, in which the photon originates from the fragmentation of a final state parton. In the latter case, the photon is expected to be accompanied by hadronic activity. These processes are thought to be separated by applying an isolation cut on the photon. The cross section of the prompt photon at the mid-rapidity region in proton-proton collisions at $\sqrt{s} = 200$ GeV has been measured [1] using the PHENIX detector. In this paper, we report the measurement with increased statistics, and an isolation cut on photons is applied for the first time.

2. Experimental Setup

The analysis is based on the integrated luminosity of 266 nb^{-1} collected by the PHENIX detector [2] at the RHIC proton-proton run in May 2003. Photons are detected by electromagnetic calorimeters (EMCal) in the central arms, each of which has an azimuthal coverage of 90° and a pseudo-rapidity (η) coverage of ± 0.35 . In this paper, we report only on the measurement done with one arm. The EMCAL has such a very fine granularity ($10 \times 10 \text{ mrad}^2$) that we can efficiently identify background photons by reconstructing π^0 's. The energy scale and resolution were tuned by checking the π^0 mass peak position

and its width. In addition PHENIX has a tracking system in front of the EMCal which was useful to reject background clusters produced by charged hadrons. Data were collected with a minimum bias trigger provided by the beam-beam counters (BBC) placed in $3.0 < |\eta| < 3.9$ region and with an EMCal trigger. By requiring a high energy cluster with the EMCal trigger, event condensation by a factor of 120 was achieved. Fig. 1 shows that the trigger efficiency attains a plateau at 100% for single photons above $E \sim 3\text{GeV}$ for the active channels of EMCal.

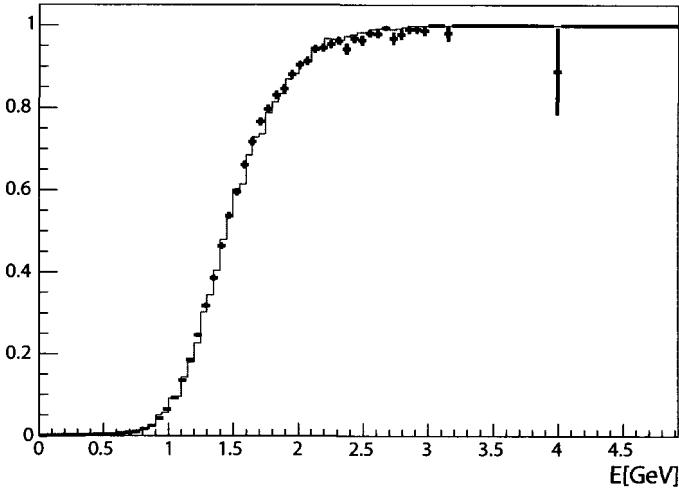


Fig. 1. Turn-on behaviour of the EMCal trigger. The line shows the expected behaviour.

3. Analysis Procedure

The prompt photon signal is obtained by subtracting known backgrounds from all EMCal clusters. The contribution from hadronic interactions is rejected by a photon shower shape cut and by requiring that no charged track is associated with the cluster. The dominant source of background is two-photon decays of π^0 's. This background is estimated by reconstructing π^0 's from two photons. A photon is rejected as a π^0 decay photon when the invariant mass of the photon and another photon in the same event is consistent with the mass of π^0 . Accidental coincidences are taken into account using the vicinity of the π^0 mass window. If only one of the two decay photons from a π^0 is detected, it mimics a prompt photon signal. This probability depends mainly on geometrical acceptance and kinematics of π^0 decays, which can be well reproduced by a Monte-Carlo simulation. Thanks to the highly segmented EMCal, two photon clusters from a π^0 are well separated in the p_T region of this measurement.

Besides the simple subtraction method, an isolation cut is applied to prompt photon candidates. This requires that the energy sum (E_{sum}) in an angular cone around a photon is

less than a certain fraction of the photon energy (Eq. 1).

$$E_{sum}(R < 0.5) < E_\gamma \times 0.1, R = \sqrt{\Delta\eta^2 + \Delta\phi^2} \quad (1)$$

The amount of photons from hadronic decays other than π^0 's is estimated based on the total amount of π^0 's.

In the subtraction method, of all photon clusters, 50% (20%) are tagged as photons from π^0 , and 85% (30%) are estimated as photons from all hadrons including missing π^0 's at $p_T = 5$ GeV/ c (16 GeV/ c). In the isolation method, ratios are improved to 25% (< 5%) and 65% (< 5%). The uncertainties of the energy scale, of the π^0 extraction, and of the hadron-to- π^0 production ratio are sources of systematic error.

After extracting the yield, correction factors such as acceptance, efficiency, luminosity, and BBC trigger bias are applied to calculate the cross section.

4. Results and Discussion

Fig. 2 (left) shows our measurement of the prompt photon cross section as a function of p_T . Bands correspond to systematic errors, which are listed in Table 1 for our lowest and highest p_T bins. Curves show a NLO pQCD calculation with three different scales [3]. The theory agrees well with our experimental measurement. In Fig. 2 (right), the two analysis methods are compared, and no significant reduction in the isolation method is observed. This suggests either (1) the 'direct' component is the dominant source of the prompt photon or (2) the reduction of the 'fragment' component by the isolation cut is small.

In summary, we have measured the cross section of prompt photons in proton-proton collisions at $\sqrt{s} = 200$ GeV. The NLO pQCD calculation agrees with the measurement very well. The isolation method significantly enhances the signal purity. These results are important for future spin asymmetry measurements of this channel.

Table 1. Systematic error table

	Subtraction		Isolation	
	Lowest 5 – 5.5 [GeV/ c]	Highest 15 – 17 [GeV/ c]	Lowest 5 – 5.5 [GeV/ c]	Highest 15 – 17 [GeV/ c]
π^0 photon estimation	30%	5	16	2
Non π^0 photon estimation	27	6	8	1
Photon acceptance and smearing	10	10	10	10
Photon conversion effect	1	1	1	1
Luminosity measurement	12	12	12	12
BBC trigger bias	3	3	3	3
Total	43%	18	24	16

References

1. S. S. Adler *et al.*: *Phys. Rev. D* (to be submitted)

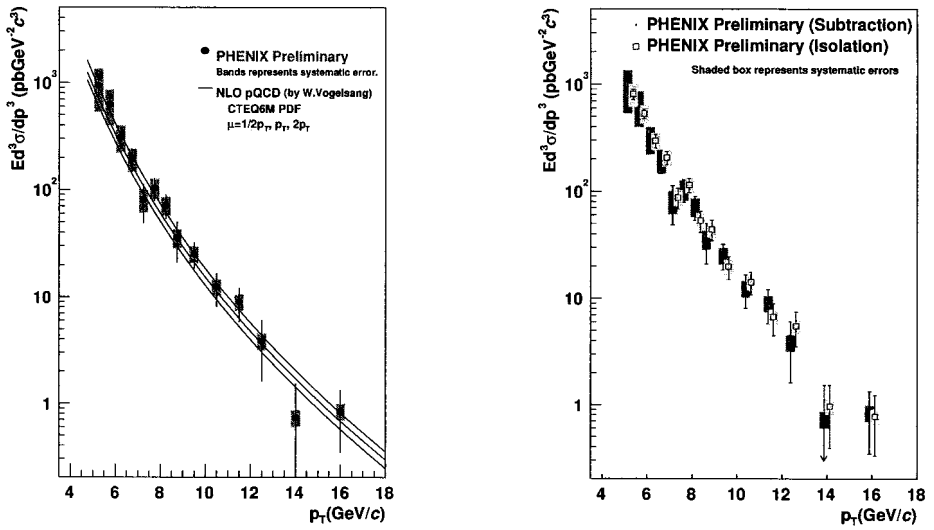


Fig. 2. [left] Result of the subtraction method with NLO pQCD calculation. [right] Comparison with the isolation method.

2. K. Adcox *et al.*: *Nucl. Inst. Meth.* **A499**, 469-602 (2003)
3. Private communication with Werner Vogelsang (RBRC)

STUDY OF GLUON POLARIZATION IN THE PROTON WITH A SILICON VERTEX UPGRADE AT RHIC/PHENIX

M. TOGAWA

Kyoto University, Kyoto, JAPAN &
Radiation Laboratory, RIKEN, Wako, JAPAN

(for the PHENIX Collaboration)

PHENIX has a well defined program for measuring the polarized gluon distribution in the nucleon. The measurements of gluon polarization *via* the direct-photon production and the heavy-flavour production can be significantly improved by the silicon vertex tracker upgrade. We have studied the possible improvements in gluon polarization measurements using Monte Carlo simulation. Results are shown and discussed.

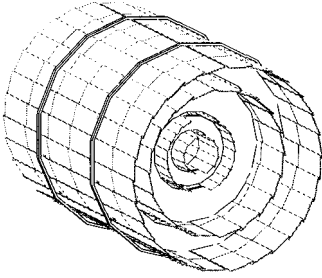
1. Introduction

One of the major goals of the PHENIX experiment at the Relativistic Heavy Ion Collider (RHIC) is a determination of gluon polarization in the proton [1]. The double longitudinal-spin asymmetry A_{LL} of π^0 production in longitudinally polarized p - p collisions at $\sqrt{s} = 200$ GeV has been measured [2]. In this process, the π^0 carries only a fraction of the momentum of the scattering quark or gluon. More direct information on the gluon polarization will be obtained by measuring A_{LL} in direct-photon and heavy-flavour production at $\sqrt{s} = 200$ GeV and 500 GeV. The sensitivity of the measurements will be improved by using a silicon vertex tracker (VTX), proposed as a PHENIX upgrade [3]. This consists of four layers of barrel detectors as shown in Fig.1, and covers 2π azimuthal angle and pseudo-rapidity $|\eta| < 1.2$. The inner two layers are silicon pixel detectors, while the outer two layers are silicon strip detectors [4]. In this paper, we discuss improvements to gluon polarization measurements, based on Monte Carlo simulations.

2. Direct-photon measurement

The direct-photon process is dominated by the gluon Compton process, whose contribution to the A_{LL} measurement is written as:

$$A_{LL}^{qg \rightarrow q\gamma}(p_T) \sim \frac{\Delta g(x_g)}{g(x_g)} \cdot A_1^p(x_q) \cdot \hat{a}_{LL}^{qg \rightarrow q\gamma} \quad (1)$$



Layer	Si	Radiation length	Radius (cm)
1	pixel	$\sim 1\%$	2.5
2	pixel	$\sim 1\%$	5.0
3	strip	$\sim 2\%$	10.0
4	strip	$\sim 2\%$	14.0

Pixel size ($50\mu\text{m} \times 425\mu\text{m}$)

Strip size ($80\mu\text{m} \times 3\text{cm}$)

Fig. 1. A view of Barrel part of VTX. Parameters are in the table.

where $A_1^P(x_q)$ shows the quark polarization measured by polarized-DIS experiments, and \hat{a}_{LL} is the calculable partonic level asymmetry of the gluon Compton process. x_g and x_q are momentum fractions of the gluon and quark, respectively. The gluon polarization, $\Delta g(x_g)/g(x_g)$, can be extracted with this formula.

Direct photons are detected by two Central Arms in the current PHENIX setup. A Central Arm is composed of a Electro-Magnetic Calorimeter (EMCal) system, a tracking system and the particle-ID detectors. It covers 90-degree azimuthal angle and $|\eta| < 0.35$. x_g and x_q are evaluated to be $\langle x_g \rangle = \langle x_q \rangle = 2 p_T / \sqrt{s}$ with photon's p_T as approximate average values.

With the VTX, we will also be able to identify *jets* by charged-particle tracking with expanded acceptance. The reconstruction resolution of the *jet*-axis is estimated to be 0.13 in RMS by PYTHIA simulation studies [5]. By detecting both the direct-photon and *jet* in one event, x_g and x_q can be evaluated under two assumptions: (a) p_T balance of the photon and *jet*, (b) x_g is smaller than x_q :

$$\begin{aligned}
 x_1 &= \frac{p_T}{\sqrt{s}} (e^{\eta_{jet}} + e^{\eta_\gamma}) & x_2 &= \frac{p_T}{\sqrt{s}} (e^{-\eta_{jet}} + e^{-\eta_\gamma}), \\
 x_g &= \min\{x_1, x_2\} & x_q &= \max\{x_1, x_2\}
 \end{aligned} \tag{2}$$

where η_{jet} and η_γ are the pseudo-rapidities of the *jet*-axis and direct-photon, respectively. Figure 2 shows a comparison of x_g from PYTHIA with the reconstructed x_g . A better correlation can be found in the right figure. Thus indicates that the determination of x_g improves with the VTX upgrade.

3. Single-electron measurement with a displaced vertex

In PHENIX, we measure *D*- and *B*-meson production *via* their decays to the single electron. Electrons are detected by the Central Arms, and well identified by ring-imaging Cherenkov detectors and EMCal [6].

Heavy-flavour production is dominated by the gluon fusion process. A_{LL} of the gluon fusion process is given by:

$$A_{LL}^{gg \rightarrow Q\bar{Q}} \sim \frac{\Delta g(x_1)}{g(x_1)} \cdot \frac{\Delta g(x_2)}{g(x_2)} \cdot \hat{a}_{LL}^{gg \rightarrow Q\bar{Q}} \tag{3}$$

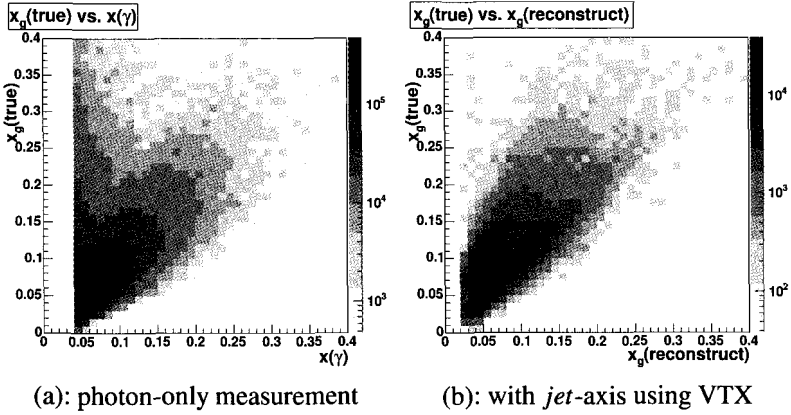


Fig. 2. Comparison of x_g from PYTHIA with reconstructed x_g . (a): x_g is calculated using the photon p_T (current setup). (b): x_g is calculated using equ.(2) with the VTX.

Since $\hat{a}_{LL}^{gg \rightarrow Q\bar{Q}}$ depends on the heavy-quark mass, $A_{LL}^{gg \rightarrow c\bar{c}}$ and $A_{LL}^{gg \rightarrow b\bar{b}}$ are different [7]. To extract the gluon polarization from the single-electron measurement, we need to distinguish these two cases.

Since D - and B -meson have long and different life times, they can be distinguished by measuring the Distance of Closest Approach (DCA) of the single electron track from the primary vertex. The VTX can determine the DCA with a vertex resolution of less than $50 \mu\text{m}$. We studied the ability of the VTX to distinguish single electrons from D -meson, B -meson and Dalitz decays by applying a DCA cut with PYTHIA, tuned to reproduce charm and beauty production at FNAL fixed-target experiments and the CDF [3]. The yield of electrons without and with the DCA cut, $N_e^{\text{no cut}}$ and N_e^{cut} respectively, can be written:

$$\begin{aligned} N_e^{\text{no cut}} &= N_e^{\text{Dalitz}} + N_e^D + N_e^B \\ N_e^{\text{cut}} &= R^{\text{Dalitz}} \cdot N_e^{\text{Dalitz}} + R^D \cdot N_e^D + R^B \cdot N_e^B \end{aligned} \quad (4)$$

R is the efficiency of each decay for the DCA cut, which can be estimated by Monte Carlo simulation including the life time.

4. Conclusion

The yield of electrons from the Dalitz decay (N_e^{Dalitz}) can be evaluated well from measured π^0 data, so that we can distinguish the yield of electrons from D -mesons (N_e^D) and that from B -mesons (N_e^B). Figure 3 shows the estimated errors in A_{LL} of single electrons from D - and B -meson decays, assuming a luminosity of $L = 320 \text{ pb}^{-1}$ and proton polarization of 70% at $\sqrt{s} = 200 \text{ GeV}$. We have studied the improvement of the gluon polarization measurement in the proton with the VTX upgrade at PHENIX. The determination of x_g in direct-photon production will be improved by measuring the jet -axis with the VTX. In heavy-flavour production, single electrons from D - and B -meson decays will be distinguished by measuring the DCA with precise determination of their track and the primary vertex of the collision.

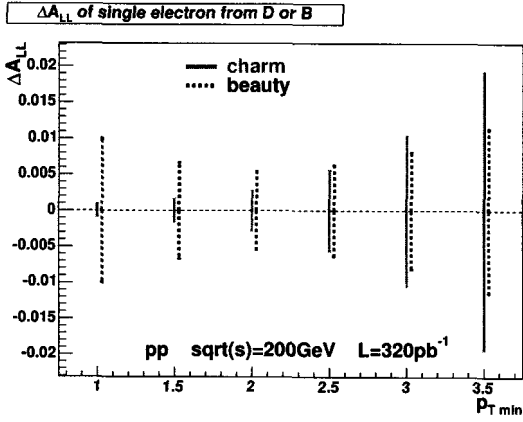


Fig. 3. The A_{LL} errors of electrons from charm and beauty. Each point shows the A_{LL} error of the p_T region above $p_{T \min}$.

The VTX will be installed in summer of 2007, and will be operated in the 2007-2008 RUN.

References

1. G. Bunce et al., *Ann. Rev. Nucl. Part. Sci.* **50**, 525(2000).
2. S. Adler et al. *Phys. Rev. Lett.* **93**, 202002,(2004).
3. Y. Akiba et al. *AIP Conf. Proc.* **698**, 785-788,(2004).
4. Z. Li et al. *Nucl. Instrum. Meth.* **A518**, 300-304,(2004).
5. T. Sjostrand, *Comput. Phys. Commun.* **135**, 238 (2001).
6. K. Adcox et al. *Phys. Rev. Lett.* **88**, 192303,(2002).
7. M. Karliner and R. Robinett, *Phys. Lett.* **B324**, 209-216,(1994).

SPIN EFFECTS IN LARGE RAPIDITY NEUTRAL PION PRODUCTION AT STAR

A. OGAWA

Brookhaven National Laboratory, Upton, USA

(for the STAR Collaboration)

First measurements of large Feynman x (x_F) neutral pion production in polarized proton collisions at $\sqrt{s} = 200$ GeV were reported previously. Cross section measurements at $\langle \eta \rangle = 3.3$ and 3.8 and analyzing power (A_N) measurements at $\langle \eta \rangle = 3.8$ were completed for $0.3 < x_F < 0.6$. The cross section was found to be consistent with next-to-leading order perturbative QCD calculations. In that framework, the dominant subprocess is partonic collisions of valence quarks on low Bjorken- x gluons. The A_N was found to be large, positive, increasing with x_F , and consistent with phenomenological calculations based on the Collins effect, the Sivers effect, and initial- and final-state higher twist contributions. Subsequent data have been acquired with transverse polarized proton collisions at RHIC at $\sqrt{s} = 200$ GeV. The status of the analysis and preliminary results will be presented.

In the perturbative QCD picture, high x_F hadron production in hadron-hadron collisions probes asymmetric partonic collisions. It is dominated by the collisions of a large- x quark on a low- x gluon. Since the longitudinal polarization of large- x quark is known to be large from polarized DIS experiments, this is an interesting place to study spin effects in the nucleon. It is also an ideal probe for low- x gluons because quarks directly couple with gluons.

An important question to address is whether fixed-order pQCD is appropriate to describe forward particle production in p+p collisions at $\sqrt{s}=200$ GeV. For $\sqrt{s} \leq 62$ GeV, next-to-leading order pQCD severely under-predicts measured π^0 cross sections [1]. At $\sqrt{s}=200$ GeV and larger collision energies, there is quantitative agreement between NLO pQCD calculations and measured cross sections at mid-rapidity [2]. This agreement has been found to extend to π^0 production at $\langle \eta \rangle = 3.8$ and 3.3 [3, 4].

Further tests of the underlying dynamics responsible for forward particle production can be obtained from the study of particle correlations. In particular, strong azimuthal correlations of hadron pairs are expected when particle production arises from $2 \rightarrow 2$ parton scattering. The azimuthal correlations of hadron pairs separated by large $\Delta\eta$ were reported [5], and found to be consistent with PYTHIA predictions [6].

In polarized proton-proton collisions, the transverse single spin asymmetry (A_N) for the $p_\uparrow + p \rightarrow \pi^0 + X$ reaction has been measured [3, 7] at $\sqrt{s} = 20$ and 200 GeV and found to be large. Semi-inclusive deep-inelastic lepton scattering experiments [8, 9] have reported measurements of transverse single-spin asymmetries which are significantly different from zero.

In perturbative QCD at leading twist with collinear factorization, A_N has to be zero. If one takes a step beyond this simple scheme and allows partons to have transverse momentum (k_T), there are three terms which can contribute to the asymmetry. The first is the Sivers effect [10], which is an initial state correlation between parton k_T and the transverse spin of the nucleon. The second is transverse polarization of the quark, or transversity, and the Collins effect [11] in the fragmentation process. The third involves a correlation between k_T and quark spin within the unpolarized nucleon, which is believed to be very small [12]. Calculations of twist-3 contributions [13, 14] also have three terms similar to the models with transverse momentum. While all these mechanisms can contribute at the same time, a recent study [15] shows that the Collins effect is suppressed due to cancellations in quantum phases.

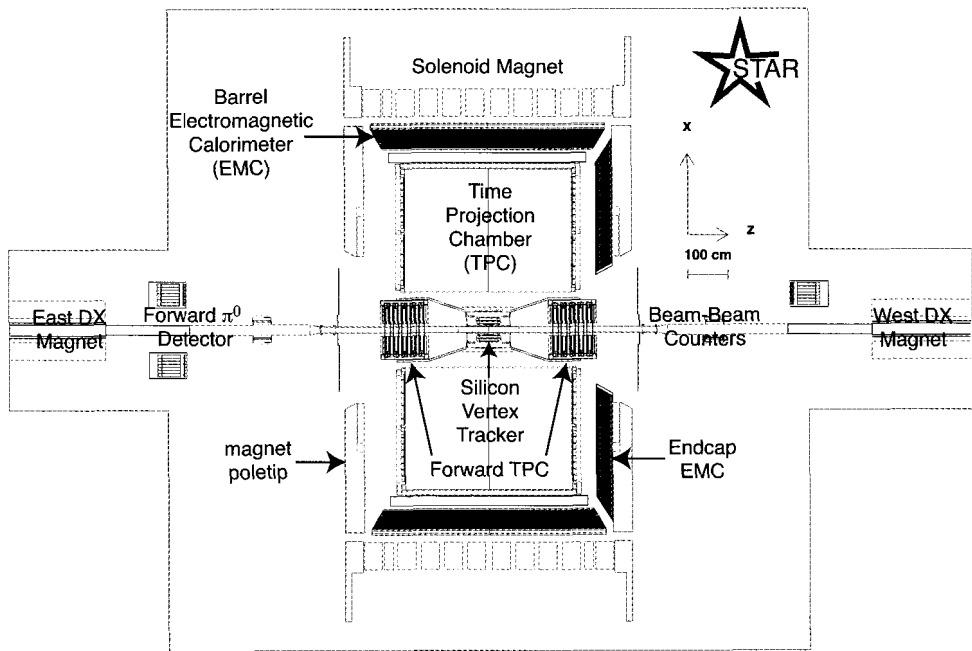


Fig. 1. Top view of the STAR detector.

The Solenoid Tracker at RHIC (STAR) is a multi-purpose detector at Brookhaven National Laboratory. One of its principal components is a time projection chamber (TPC and Forward-TPC) embedded in a 0.5 T solenoidal magnetic field used for tracking charged particles at $|\eta| < 1.2$ and $2.8 < |\eta| < 3.8$. To extend the rapidity coverage, a forward π^0

detector (FPD) was installed at STAR, as shown in Fig.1. The FPD is a 7×7 array of $3.8 \text{ cm} \times 3.8 \text{ cm} \times 45 \text{ cm}$ Pb-glass cells with individual photomultiplier tubes. For the 2003 RHIC run, both beam left and right detectors on the east side were installed, and a beam left detector was installed on the west side. The FPD provides triggering and reconstruction of neutral pions produced with $3.3 < \eta < 4.2$.

The energy calibration of the FPD is done using reconstructed π^0 mesons. The reconstruction method was extensively studied using GEANT Monte-Carlo simulations [16]. The absolute energy scale is known to better than 2%, and the reconstruction efficiency is found to be determined mostly by geometry. Photon conversion events, primarily in the beam pipe and producing hits in both the Forward-TPC and the FPD, were used to determine the position of the FPD.

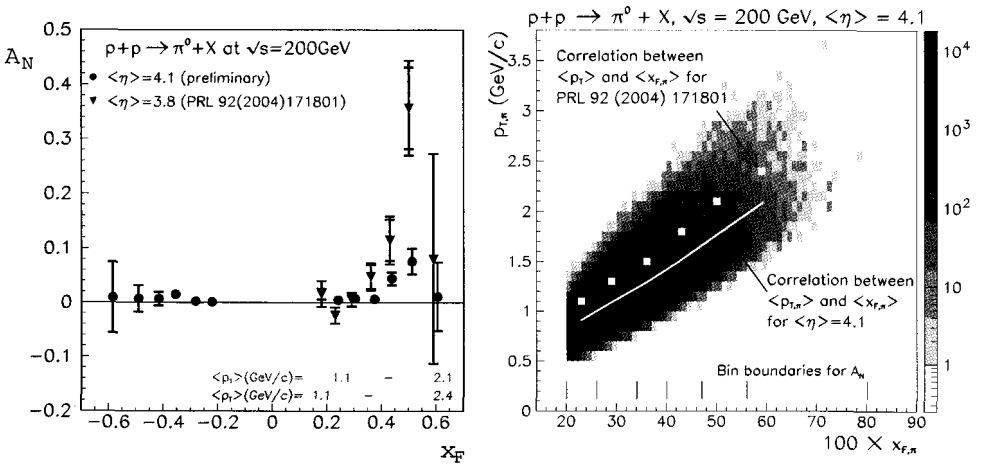


Fig. 2. Left: Preliminary results on analyzing power of $p + p \rightarrow \pi^0 + X$ as function of x_F at $\langle \eta \rangle = 4.1$ (circle), compared to published results at $\langle \eta \rangle = 3.8$ (triangle). Right: x_F and p_T range of the data. The line shows the correlation between $\langle x_F \rangle$ and $\langle p_T \rangle$ for $\langle \eta \rangle = 4.1$. The square dots shows the $\langle x_F \rangle$ and $\langle p_T \rangle$ for $\langle \eta \rangle = 3.8$.

In the 2003 RHIC run, $p+p$ collisions were studied at $\sqrt{s} = 200 \text{ GeV}$ with average polarization $\sim 25\%$ and integrated luminosity $\sim 0.5/pb$. The polarization was measured by the pC CNI polarimeter [18]. For the east side, the cross ratio method is used to obtain A_N . For the west side, the A_N is obtained from spin dependent yields normalized by the Beam-Beam Counter [17]. These two measurements are found to be consistent, and are combined. Positive (negative) x_F is defined when the π^0 is observed with the same (opposite) longitudinal momentum as the polarized beam. Positive A_N is defined as more π^0 going left of the upward polarized beam for both positive and negative x_F .

The preliminary results are shown in Fig.2. The A_N for positive x_F at $\langle \eta \rangle = 4.1$ is found to be significantly non-zero and positive, confirming earlier measurements. The first measurement of A_N at negative x_F has been done, and found to be consistent with zero. The negative x_F results may set an upper limit on the gluon Sivers function [15], which is

currently unknown.

Future studies using the STAR FPD will include measurements of the p_T dependence of A_N at fixed x_F di-hadron correlations, to distinguish the Collins effect from the Sivers effect and A_{LL} , which is sensitive to gluon polarization at low- x .

References

1. C. Bourrely and J. Soffer, Eur. Phys. J. **C36** 371-374 (2004).
2. S. S. Adler *et al.*, Phys. Rev. Lett. **91**, 241803 (2003).
3. STAR Collaboration, Phys. Rev. Lett. **92** (2004) 171801.
4. L.C. Bland, **hep-ex/0403012**.
5. A. Ogawa, **nucl-ex/0408004**.
6. T. Sjöstrand, Comp. Phys. Commun. **82**, 74 (1994).
7. A. Bravar *et al.*, Phys. Rev. Lett. **77** 2626 (1996) ; D. L. Adams *et al.*, Phys. Rev. **D53** 4747 (1996)
8. A. Airapetian *et al.*, Phys. Rev. Lett. **84**, 4047 (2000); Phys. Lett. B **535**, 85 (2002); **562**, 182 (2003).
9. A. Bravar *et al.*, Nucl. Phys. Proc. Suppl. **79**, 520 (1999).
10. D. W. Sivers, Phys. Rev. **D41** 83 (1990)
11. J. C. Collins, S. F. Heppelmann, G. A. Ladinsky, Nucl. Phys. **B396** 161 (1993);
12. D. Boer, AIP Conf. Proc. **675** 479-483 (2003).
13. J. Qiu and G. Sterman, Phys. Rev. D59, 014004 (1998).
14. Y. Koike, AIP Conf. Proc. **675**, 449 (2003).
15. M. Anselmino *et al.* **hep-ph/0408356**; U. D'Alesio, Proceedings of Spin2004
16. GEANT 3.21, CERN program library.
17. J. Koryluk, AIP Conf. Proc. **675**, 424 (2003).
18. O. Jinnouchi *et al.*, AIP Conf. Proc. **675**, 817 (2003).

CAN THE COLLINS MECHANISM EXPLAIN THE LARGE TRANSVERSE SINGLE SPIN ASYMMETRIES OBSERVED IN $p^\uparrow p \rightarrow \pi X$?

M. ANSELMINO¹, M. BOGLIONE¹, U. D'ALESIO², E. LEADER³, F. MURGIA²

¹Università di Torino and INFN, Sezione di Torino, Torino, Italy

²Università di Cagliari and INFN, Sezione di Cagliari, Cagliari, Italy

³Imperial College, London, England

We present a calculation of inclusive polarised and unpolarised cross sections within pQCD and the factorisation scheme, taking into account the parton intrinsic motion, k_\perp , in distribution and fragmentation functions, as well as in the elementary dynamics. We show, in contradiction with earlier claims, that the Collins mechanism is suppressed and unable to explain the large asymmetries found in $p^\uparrow p \rightarrow \pi X$ at moderate to large Feynman x_F . The Sivers effect is not suppressed.

In the standard perturbative QCD approach to inclusive particle production at high energies, intrinsic transverse motions are integrated out. Nevertheless, we know how they can help in describing experimental data for inclusive particle production in hadronic processes at moderately large p_T [1], otherwise heavily underestimated.

When we consider polarized cross sections, k_\perp could become essential: certain spin and k -dependent effects, generated by soft mechanisms, can be used to understand the large transverse single spin asymmetries (SSA) found in many reactions like $p^\uparrow p \rightarrow \pi X$.

For polarised processes, $(A, S_A) + (B, S_B) \rightarrow C + X$, by introducing in the factorisation scheme, in addition to the distribution functions, the helicity density matrices which describe the parton spin states, we have

$$d\sigma^{(A,S_A)+(B,S_B)\rightarrow C+X} = \sum_{a,b,c,d,\{\lambda\}} \rho_{\lambda_a,\lambda'_a}^{a/A,S_A} \hat{f}_{a/A,S_A}(x_a, k_{\perp a}) \quad (1)$$

$$\otimes \rho_{\lambda_b,\lambda'_b}^{b/B,S_B} \hat{f}_{b/B,S_B}(x_b, k_{\perp b}) \otimes \hat{M}_{\lambda_c,\lambda_d;\lambda_a,\lambda_b} \hat{M}_{\lambda'_c,\lambda'_d;\lambda'_a,\lambda'_b}^* \otimes \hat{D}_{\lambda_c,\lambda'_c}^{\lambda_C,\lambda'_C}(z, k_{\perp C}),$$

where $\{\lambda\}$ is a shorthand for all helicity indices involved. In Eq. (1), the $\hat{M}_{\lambda_c,\lambda_d;\lambda_a,\lambda_b}$'s are the helicity amplitudes for the hard process $ab \rightarrow cd$ and $\hat{D}_{\lambda_c,\lambda'_c}^{\lambda_C,\lambda'_C}(z, k_{\perp C})$ is the product of *fragmentation amplitudes* for the $c \rightarrow C + X$ process. The helicity density matrix, $\rho_{\lambda_a,\lambda'_a}^{a/A,S_A}$,

of parton a inside hadron A with polarisation S_A , is identically equal to

$$\begin{aligned} \rho_{\lambda_a, \lambda'_a}^{a/A, S_A} \hat{f}_{a/A, S_A}(x_a, k_{\perp a}) &= \sum_{\lambda_A, \lambda'_A} \rho_{\lambda_A, \lambda'_A}^{A, S_A} \int_{X_A, \lambda_{X_A}} \mathcal{F}_{\lambda_a, \lambda_{X_A}; \lambda_A} \mathcal{F}_{\lambda'_a, \lambda_{X_A}; \lambda'_A}^* \\ &= \sum_{\lambda_A, \lambda'_A} \rho_{\lambda_A, \lambda'_A}^{A, S_A} \hat{F}_{\lambda_A, \lambda'_A}^{a, \lambda_a, \lambda'_a}, \end{aligned} \quad (2)$$

where $\int_{X_A, \lambda_{X_A}}$ stands for a spin sum and phase space integration over all undetected remnants of hadron A , considered as a system X_A and the \mathcal{F} 's are the *helicity distribution amplitudes* for the $A \rightarrow a + X$ process.

By using Eq. (2), Eq. (1) becomes

$$\begin{aligned} d\sigma^{(A, S_A) + (B, S_B) \rightarrow C + X} &= \sum_{a, b, c, d, \{\lambda\}} \rho_{\lambda_A, \lambda'_A}^{A, S_A} \hat{F}_{\lambda_A, \lambda'_A}^{\lambda_a, \lambda'_a} \otimes \rho_{\lambda_B, \lambda'_B}^{B, S_B} \hat{F}_{\lambda_B, \lambda'_B}^{\lambda_b, \lambda'_b} \\ &\otimes \hat{M}_{\lambda_c, \lambda_d; \lambda_a, \lambda_b} \hat{M}_{\lambda'_c, \lambda'_d; \lambda'_a, \lambda'_b}^* \otimes \hat{D}_{\lambda_c, \lambda'_c}^{\lambda_c, \lambda'_c} \equiv \sum_{a, b, c, d} \int d[PS] \Sigma(S_A, S_B). \end{aligned} \quad (3)$$

Eq. (3) contains all possible combinations of different distribution and fragmentation amplitudes, with definite partonic interpretations.

Let us now study the processes $A^\uparrow(A^\downarrow)B \rightarrow \pi X$ in the AB center of mass frame, with the polarised beam moving along the positive Z -axis and the pion produced in the XZ plane. The $\uparrow(\downarrow)$ is the $+Y(-Y)$ direction. We focus only on the contribution of the Collins mechanism [3], that is the azimuthal dependence of the number of pions created in the fragmentation of a transversely polarised quark.

The helicity amplitudes \hat{M} in Eq. (3), defined in the hadronic c.m. frame, can be related to those given in the canonical partonic c.m. frame, \hat{M}^0 , with Z in the direction of the colliding partons and the XZ plane as the scattering plane. By performing a sequence of boost and rotations we get

$$\begin{aligned} \hat{M}_{\lambda_c, \lambda_d; \lambda_a, \lambda_b} &= \hat{M}_{\lambda_c, \lambda_d; \lambda_a, \lambda_b}^0 \\ &\times e^{-i(\lambda_a \xi_a + \lambda_b \xi_b - \lambda_c \xi_c - \lambda_d \xi_d)} e^{-i[(\lambda_a - \lambda_b) \tilde{\xi}_a - (\lambda_c - \lambda_d) \tilde{\xi}_c]} e^{i(\lambda_a - \lambda_b) \phi_c''}, \end{aligned} \quad (4)$$

where $\xi_i, \tilde{\xi}_i$ ($i = a, b, c, d$) and ϕ_c'' depend on parton momenta [2].

On summing over $\{\lambda\}$ [Eq. (3)], we obtain for the Collins contribution to the numerator of SSA ($qb \rightarrow qb, b = q, \bar{q}, g$):

$$\begin{aligned} [\Sigma(\uparrow, 0) - \Sigma(\downarrow, 0)] &= \left\{ F_{+-}^{+ -}(x_a, k_{\perp a}) \cos[\phi_a + \phi_c'' - \xi_a - \tilde{\xi}_a + \xi_c + \tilde{\xi}_c + \phi_\pi^H] \right. \\ &\quad \left. - F_{-+}^{+ -}(x_a, k_{\perp a}) \cos[\phi_a - \phi_c'' + \xi_a + \tilde{\xi}_a - \xi_c - \tilde{\xi}_c - \phi_\pi^H] \right\} \\ &\quad \times \hat{f}_{b/B}(x_b, k_{\perp b}) \hat{M}_{+, +; +, +}^0 \hat{M}_{-, +; -, +}^0 [-2iD_{+-}^\pi(z, k_{\perp \pi})] \end{aligned} \quad (5)$$

where $\pm = \pm 1/2$ (quarks), ± 1 (gluons), and ϕ_π^H is the azimuthal angle of the pion momentum in the fragmenting quark helicity frame. In the notations of [4] (details will be given

in [5], see also [6]), we have

$$F_{+-}^{+-}(x, k_{\perp}) = h_1(x, k_{\perp}) = h_{1T}(x, k_{\perp}) + \frac{k_{\perp}^2}{2M_p^2} h_{1T}^{\perp}(x, k_{\perp}) \quad (6)$$

$$F_{-+}^{+-}(x, k_{\perp}) = \frac{k_{\perp}^2}{2M_p^2} h_{1T}^{\perp}(x, k_{\perp}) \quad (7)$$

$$-2iD_{+-}^{\pi}(z, k_{\perp}) = \Delta^N D_{\pi/q^{\dagger}}(z, k_{\perp}) = \frac{2k_{\perp}}{zM_{\pi}} H_1^{\perp q}(z, k_{\perp}), \quad (8)$$

where M_p and M_{π} are respectively the proton and pion masses.

In all previous studies the large SSA found in the E704 experiment [7] was explained by either the Siverts [8] or the Collins mechanisms [9]. However, only a simplified kinematics was adopted. We now believe that the phases involved, when the kinematics is treated carefully, are crucial, and lead to a large suppression of the asymmetry due to the Collins mechanism. Almost no suppression of A_N from the Siverts mechanism is found [1].

In order to demonstrate the extent of the suppression, we choose for the unmeasured soft functions in Eq. (5) their known upper bounds [10], and adjust their signs so that the contributions from the valence flavours (up and down) reinforce each other. The results are presented in Fig. 1, which shows $(A_N)_{\max}^{\text{Collins}}$ as a function of x_F , at $p_T = 1.5 \text{ GeV}/c$ and $\sqrt{s} \simeq 19.4 \text{ GeV}$ together with the E704 data [7]. The only difference between the plots is given by different choices of the polarised distribution functions and/or the unpolarised fragmentation functions. In the upper-right plot the curves for charged pions obtained by setting all phases in Eq. (5) to zero are also given (thin lines). We can therefore conclude that the Collins mechanism alone, even maximising all its effects, cannot explain the observed SSA values.

An equally important consequence of keeping proper phases emerges in the calculation of SSA at $x_F < 0$: even maximising all contributions (Siverts mechanism too) one gets much smaller (a few %) A_N values [5].

Once more, the importance and subtleties of spin effects come out; phases, properly considered, often play crucial and unexpected roles.

References

1. U. D'Alesio and F. Murgia, *Phys. Rev.* **D70** (2004) 074009
2. M. Anselmino, M. Boglione, U. D'Alesio, E. Leader and F. Murgia e-Print Archive: hep-ph/0408356 (*Phys. Rev. D*, in press)
3. J.C. Collins, *Nucl. Phys.* **B396** (1993) 161
4. P.J. Mulders and R.D. Tangerman, *Nucl. Phys.* **B461** (1996) 197
5. M. Anselmino, M. Boglione, U. D'Alesio, E. Leader, S. Melis and F. Murgia, in preparation
6. A. Bacchetta, U. D'Alesio, M. Diehl, C. Andy Miller, e-Print Archive: hep-ph/0410050 (*Phys. Rev. D*, in press)
7. D.L. Adams *et al.*, *Phys. Lett.* **B264** (1991) 462; **B261** (1991) 201
8. M. Anselmino, M. Boglione and F. Murgia, *Phys. Lett.* **B362** (1995) 164; M. Anselmino and F. Murgia, *Phys. Lett.* **B442** (1998) 470

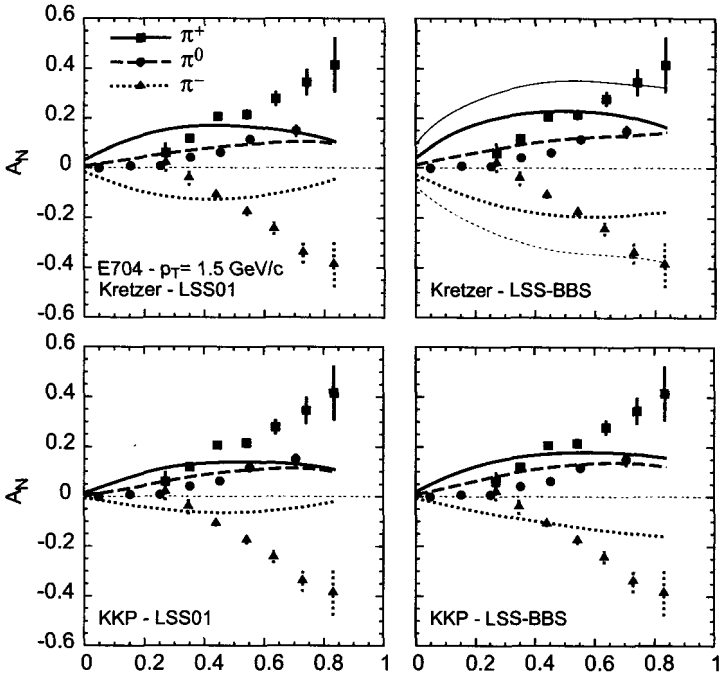


Fig. 1. Maximised values of A_N vs. x_F , as given by the Collins mechanism alone. Data are from [7]. See text for further details.

9. M. Anselmino, M. Boglione and F. Murgia, *Phys. Rev.* **D60** (1999) 054027
10. A. Bacchetta, M. Boglione, A. Henneman and P.J. Mulders, *Phys. Rev. Lett.* **85** (2000) 712

THE GLUON SIVERS DISTRIBUTION IN D PRODUCTION AT RHIC

M. ANSELMINO, M. BOGLIONE

Università di Torino and INFN, Sezione di Torino, Torino, Italy

E. LEADER

Imperial College, London, England

U. D'ALESIO, F. MURZIA

Università di Cagliari and INFN, Sezione di Cagliari, Cagliari, Italy

The single transverse spin asymmetry in D meson production at RHIC can provide a clean measure of the gluon Sivers distribution function. At intermediate rapidity, D production is largely dominated by the elementary $gg \rightarrow c\bar{c}$ channel, where there cannot be any transverse spin transfer. Therefore, any transverse single spin asymmetry observed for D 's produced in $p^\uparrow p$ interactions can only originate from the Sivers effect in the gluon distribution functions. A sizeable transverse single spin asymmetry measured by PHENIX or STAR experiments would then give direct information on the size of the gluon Sivers distribution function.

Parton distribution and fragmentation functions are phenomenological quantities which have to be obtained from experimental observation and cannot be theoretically predicted. When parton intrinsic transverse momenta are taken into account, a large number of pdf's and ff's arise: the main difficulties in gathering experimental information on these spin- and k_\perp - dependent functions is that most often more of them contribute to the same physical observable, making it extremely hard to estimate each one separately. The Sivers function $\Delta^N f(x, k_\perp)$ [1], which describes the probability density of finding unpolarized partons inside a transversely polarized proton, is one of these functions. It plays a crucial role since it can explain single spin asymmetries in terms of parton dynamics [2].

We suggest here an experiment to be conducted at RHIC which can isolate the gluon Sivers effect, making it possible to acquire direct independent information on the gluon

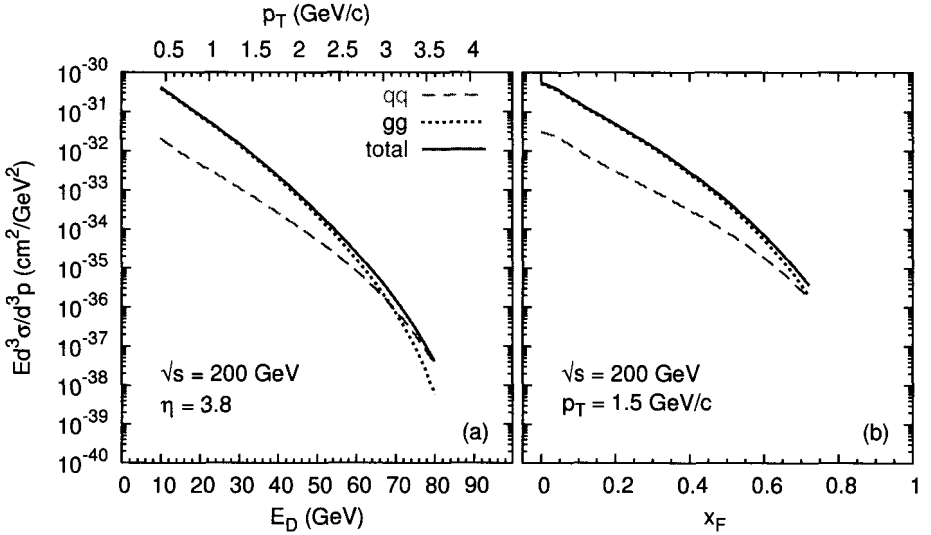


Fig. 1. The unpolarized cross section for the process $pp \rightarrow DX$ at $\sqrt{s} = 200$ GeV, as a function of E_D and p_T at fixed pseudo-rapidity $\eta = 3.8$ (a), and as a function of x_F at fixed transverse momentum $p_T = 1.5$ GeV/c (b).

Sivers distribution function $\Delta^N f_{g/p^\uparrow}(x, k_\perp)$. A full description can be found in a detailed, recently published paper [3].

Let us consider the single spin asymmetry $A_N = (d\sigma^\uparrow - d\sigma^\downarrow)/(d\sigma^\uparrow + d\sigma^\downarrow)$ for $p^\uparrow p \rightarrow DX$ processes at RHIC energy, $\sqrt{s} = 200$ GeV. These D mesons originate from c or \bar{c} quarks, which at LO can be created either via a $q\bar{q}$ annihilation, $q\bar{q} \rightarrow c\bar{c}$, or via a gluon fusion process, $gg \rightarrow c\bar{c}$. The elementary cross section for the fusion process is much larger than the $q\bar{q} \rightarrow c\bar{c}$ cross section. Therefore, the gluon fusion dominates the whole $p^\uparrow p \rightarrow DX$ process, up to $x_F \simeq 0.6$. In Fig. 1(a) we show the unpolarized cross section for the process $pp \rightarrow DX$ at $\sqrt{s} = 200$ GeV as a function of both the heavy meson energy E_D and its transverse momentum p_T , at fixed pseudo-rapidity $\eta = 3.8$. In Fig. 1(b) the same total cross section is presented as a function of x_F at fixed $p_T = 1.5$ GeV/c. The dashed and dotted lines correspond to the $q\bar{q} \rightarrow c\bar{c}$ and $gg \rightarrow c\bar{c}$ contributions respectively. These plots clearly show the striking dominance of the $gg \rightarrow c\bar{c}$ channel over most of the E_D and x_F ranges covered by RHIC kinematics.

As the gluons cannot carry any transverse spin, the elementary process $gg \rightarrow c\bar{c}$ results in unpolarized final quarks. In the $q\bar{q} \rightarrow c\bar{c}$ process, one of the initial partons can be polarized; however, at lowest order there is no single spin transfer in this s -channel interaction, so that the final c and \bar{c} are again not polarized. Consequently, the charmed quarks fragmenting into the observed D mesons cannot be polarized, and there cannot be any Collins fragmentation effect.

Therefore, transverse single spin asymmetries in $p^\uparrow p \rightarrow DX$ can be generated only by the Sivers mechanism, namely a spin- k_\perp asymmetry in the distribution of the unpolarized quarks and gluons inside the polarized proton, coupled to the unpolarized interaction process $q\bar{q} \rightarrow c\bar{c}$ and dominantly $gg \rightarrow c\bar{c}$, and the unpolarized fragmentation function of either the c or the \bar{c} quark into the final observed D meson. Detailed formulae for the A_N generated

by the Sivers effect can be found in a recent paper by U. D'Alesio and F. Murgia [4].

The Sivers distribution functions [1] for quarks and gluons are defined by

$$\Delta^N f_{a/p^\dagger}(x_a, k_{\perp a}) = \hat{f}_{a/p^\dagger}(x_a, k_{\perp a}) - \hat{f}_{a/p^\dagger}(x_a, -k_{\perp a}), \quad (1)$$

where a can either be a light quark or a gluon.

Here, we consider intrinsic transverse motions in the distributions of initial light quarks, in the elementary process and in the heavy quark fragmentation function, *i.e.* we consider a fully non-planar configuration for the partonic scattering. This has two main consequences: on one hand, taking into account three intrinsic transverse momenta makes the kinematics highly non-trivial; on the other hand it generates a large number of contributions, other than the Sivers effect, which originate from all possible combinations of k_{\perp} dependent distribution and fragmentation functions, each weighted by a phase factor. This is a crucial topic, extensively discussed by U. D'Alesio in these proceedings and in a paper dedicated to the suppression of Collins and other effects in proton-proton scattering [5]. We have explicitly verified that all contributions to the $p^\dagger p \rightarrow DX$ single spin asymmetry from k_{\perp} dependent pdf's and ff's, aside from those of the Sivers functions, are multiplied by phase factors which make the integrals over the transverse momenta either negligibly small or identically zero.

In the previous literature, analyses of single spin asymmetry data were performed under the assumption $\Delta^N f_{g/p^\dagger} = 0$. RHIC data on A_N in $p^\dagger p \rightarrow DX$ will enable us to test the validity of this assumption. In fact, as the $gg \rightarrow c\bar{c}$ elementary scattering largely dominates the process up to $x_F \simeq 0.6$ (see Fig. 1), any sizeable single spin asymmetry measured in $p^\dagger p \rightarrow DX$ at moderate x_F 's would be the direct consequence of a non-zero contribution of $\Delta^N f_{g/p^\dagger}$.

Since we have no information about the gluon Sivers function, we consider two opposite extreme scenarios: the first being the case in which the gluon Sivers function is set to zero, $\Delta^N f_{g/p^\dagger}(x_a, k_{\perp a}) = 0$, and the quark Sivers function $\Delta^N f_{q/p^\dagger}(x_a, k_{\perp a})$ is taken to be at its maximum allowed value at any x_a ; the second given by the opposite situation, where $\Delta^N f_{q/p^\dagger} = 0$ and $\Delta^N f_{g/p^\dagger}$ is maximized in x_a .

Fig. 2 shows our estimates for the maximum value of the single spin asymmetry in $p^\dagger p \rightarrow DX$. The dashed line shows $|A_N|$ when the quark Sivers function is set to its maximum, *i.e.* $\Delta^N f_{q/p^\dagger}(x) = 2f_{q/p}(x)$, while setting the gluon Sivers function to zero. Clearly, the quark contribution to A_N is very small over most of the kinematic region, in both cases (a) and (b). The dotted line corresponds to the SSA one finds in the opposite situation, when $\Delta^N f_{g/p^\dagger}(x) = 2f_{g/p}(x)$ and $\Delta^N f_{q/p^\dagger} = 0$: here the asymmetry presents a sizeable maximum in the central E_D and positive x_F energy region. This particular shape is given by the azimuthal dependence of the numerator of A_N [3].

By looking at Fig. 2 it is natural to conclude that any sizeable single transverse spin asymmetry measured by STAR or PHENIX experiments at RHIC in the region $E_D \leq 60$ GeV or $-0.2 \leq x_F \leq 0.6$, would give direct information on the size and importance of the gluon Sivers function.

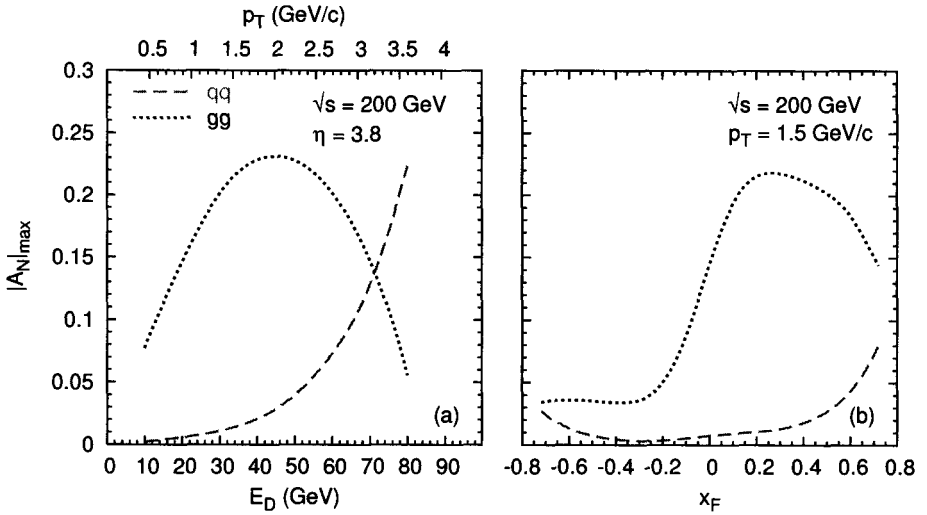


Fig. 2. Maximized values of $|A_N|$ for the process $p^\uparrow p \rightarrow DX$ as a function of E_D and p_T at fixed pseudo-rapidity (a), and as a function of x_F at fixed transverse momentum (b). The dashed line corresponds to a maximized quark Sivers function (with the gluon Sivers function set to zero), while the dotted line corresponds to a maximized gluon Sivers function (with the quark Sivers function set to zero).

References

1. D. Sivers, *Phys. Rev.* **D41**, 83 (1990); **D43**, 261 (1991).
2. M. Anselmino, M. Boggione and F. Murgia, *Phys. Lett.* **B362**, 164 (1995).
3. M. Anselmino, M. Boggione, U. D'Alesio, E. Leader, F. Murgia, *Phys. Rev.* **D70**, 074025 (2004).
4. U. D'Alesio and F. Murgia, *Phys. Rev.* **D70**, 074009 (2004).
5. M. Anselmino, M. Boggione, U. D'Alesio, E. Leader, F. Murgia, hep-ph/0408356.

DOUBLE TRANSVERSE SPIN ASYMMETRIES AT NEXT-TO-LEADING ORDER IN QCD

A. MUKHERJEE

Lorentz Institute, University of Leiden, Leiden, The Netherlands

M. STRATMANN

Institute für Theoretische Physik, Universität Regensburg, Regensburg, Germany

W. VOGELSANG

(1) Physics Department, Brookhaven National Laboratory, Upton, USA

(2) RIKEN-BNL Research Center, Brookhaven National Laboratory, Upton, USA

We present a technique to calculate the cross sections and spin asymmetries for transversely polarized pp collisions at NLO in QCD, and report on the use of this technique for the processes $p^\uparrow p^\uparrow \rightarrow \gamma X$, $p^\uparrow p^\uparrow \rightarrow \pi X$ and $p^\uparrow p^\uparrow \rightarrow l^+ l^- X$.

1. Introduction

Combined experimental and theoretical efforts in the past few years have led to an improved understanding of the unpolarized parton distributions $f(x, Q^2)$ and the helicity distributions $\Delta f(x, Q^2)$ of the nucleon. It is known that the complete understanding of the partonic structure of a spin $\frac{1}{2}$ object like a nucleon is given in terms of $f(x, Q^2)$, $\Delta f(x, Q^2)$, and by the transversity distributions $\delta f(x, Q^2)$, which give the number densities of partons having the same polarization as the nucleon, when the nucleon is transversely polarized, minus the number with opposite polarization. $\delta f(x, Q^2)$ remain the quantities about which we have the least knowledge and are at present the focus of much experimental activity.

Transversity will be probed in the double transverse spin asymmetries in transversely polarized pp collisions at the BNL Relativistic Heavy Ion Collider (RHIC). The potential of RHIC in accessing transversity through double transverse spin asymmetries A_{TT} in the Drell-Yan process was estimated in [1]. Other relevant processes include high p_T prompt

photon and jet production [2]. Apart from DY, the other calculations were done at leading order (LO). It is known that the next-to-leading order (NLO) QCD calculations are necessary in order to make a firm theoretical prediction.

2. Projection Technique

Apart from the motivations given above, interesting new technical questions arise beyond LO in the calculations of cross sections involving transverse polarization. Unlike the longitudinally polarized case, where the spin vectors are aligned with the momentum, the transverse spin vectors specify extra spatial directions, and as a result the cross section has non-trivial dependence on the azimuthal angle of the observed particle. For A_{TT} this dependence is always of the form [3]

$$\frac{d^3\delta\sigma}{dp_T d\eta d\Phi} \equiv \cos(2\Phi) \left\langle \frac{d^2\delta\sigma}{dp_T d\eta} \right\rangle, \quad (1)$$

for a parity conserving theory with vector coupling. Here the z axis is defined by the direction of the initial partons in their center-of-mass frame, and the spin vectors are taken to point in the $\pm x$ direction. Therefore the integration over the azimuthal angle is not appropriate. This makes it difficult to use here the standard techniques developed for NLO calculations of unpolarized and longitudinally polarized processes, because these techniques usually rely on the integration over the full azimuthal phase space and also on particular reference frames which are related in a complicated way to the center-of mass frame of the initial protons. In [4] a new general technique was introduced which facilitates NLO calculations with transverse polarizations by conveniently projecting on the azimuthal dependence of the cross section in a covariant way. The projector

$$F(p, s_a, s_b) = \frac{s}{\pi t u} \left[2(p \cdot s_a)(p \cdot s_b) + \frac{t u}{s} (s_a \cdot s_b) \right], \quad (2)$$

reduces to $\frac{\cos 2\phi}{\pi}$ in the center-of-mass frame of the initial protons. Here p is the momentum of the observed particle in the final state. The cross section is multiplied by the projector and integrated over the full azimuthal phase space. Integrations of the terms involving the product of the transverse spin vectors s_a, s_b with the momenta can be performed using a tensor decomposition. After this step, there are no scalar products involving s_i left in the matrix element. For the integration over the phase space, one can now use standard techniques from the unpolarized and longitudinally polarized cases. This method is particularly convenient at NLO, where one uses dimensional regularization and the phase space integrations are performed in n dimensions.

3. Applications

As an example, we discuss the use of this technique for high p_T prompt photon production. The LO process is $q\bar{q} \rightarrow \gamma g$. We multiply $\delta|M|^2$ by the projector $F(p, s_a, s_b)$ and integrate over the full $\Delta\phi$ in a covariant way. At NLO, two subprocesses contribute: $qq \rightarrow \gamma X$, where $X = qq$; and $q\bar{q} \rightarrow \gamma X$, where $X = q\bar{q} + gg + q'\bar{q}'$. For $2 \rightarrow 3$ processes, one integrates over

the phase spaces of the unobserved particles, after multiplying by the projector and eliminating the scalar products with the spin vectors using tensor decomposition. Owing to the presence of the ultraviolet, infrared and collinear singularities, one has to introduce a regulator. We choose dimensional regularization. UV poles in the virtual diagrams are removed by renormalization of the strong coupling constant. Infrared singularities cancel between the real emission and virtual diagrams. After this, only collinear singularities remain, which result from collinear splitting of an initial-state parton into a pair of partons. These correspond to long-distance contribution to the partonic cross section. From the factorization theorem, it follows that such contributions need to be factored into the parton distributions. We have imposed an isolation cut [5] to remove the background contribution. All final-state collinear singularities then cancel. The isolation constraint was imposed analytically by assuming a narrow isolation cone.

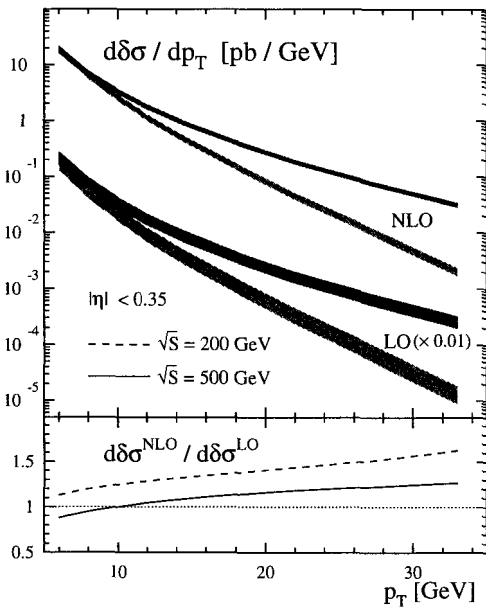


Fig. 1. Predictions for the transversely polarized prompt photon production cross sections at LO and NLO, for $\sqrt{s} = 200$ and 500 GeV. The LO results have been scaled by a factor of 0.01 . The shaded bands represent the theoretical uncertainty if $\mu_F (= \mu_R)$ is varied in the range $p_T/2 \leq \mu_F \leq 2p_T$. The lower panel shows the ratios of the NLO and LO results for both c.m.s. energies.

are $qq \rightarrow qX, q\bar{q} \rightarrow qX, q\bar{q} \rightarrow q'X, q\bar{q} \rightarrow gX$. At NLO there are $O(\alpha_s)$ corrections to the above processes and the additional channel $qq \rightarrow gX$. We have used the projection technique to calculate the cross section at NLO and the numerical results are in progress.

For our numerical predictions, we model the transversity distribution by saturating Soffer's inequality [6] at some low input scale $\mu_0 \approx 0.6$ GeV, and for higher scales $\delta f(x, \mu)$ are obtained by solving the QCD evolution equations. Figure 1 shows the results for the prompt photon production in transversely polarized pp collisions.

Our numerics apply to the PHENIX detector at RHIC. The lower part of the figure displays the 'K-factor', $K = \frac{d\delta\sigma^{\text{NLO}}}{d\delta\sigma^{\text{LO}}}$. The scale dependence becomes much weaker at NLO. The corresponding asymmetries are given in [4].

For the Drell-Yan lepton pair production in transversely polarized pp collisions the LO subprocess is $q\bar{q} \rightarrow l^+l^-$. The real emission $2 \rightarrow 3$ subprocess is $q\bar{q} \rightarrow l^+l^-g$. We multiply the squared matrix element by the projector and integrate over the phase space. We obtain the known result for the DY coefficient function in the $\overline{\text{MS}}$ scheme at NLO [4].

For inclusive pion production in transversely polarized process the LO channels

Acknowledgments

AM thanks the organizers of the 16 th International Spin Physics Symposium for a wonderful conference and hospitality and FOM for support. WV is grateful to RIKEN, Brookhaven National Laboratory and the U.S. Department of Energy (contract number DE-AC02-98CH10886) for providing the facilities essential for the completion of his work.

References

1. O. Martin, A. Schäfer, M. Stratmann, and W. Vogelsang, *Phys. Rev.* **D57**, 3090 (1998); **D60**, 117502 (1999).
2. J. Soffer, M. Stratmann, and W. Vogelsang, *Phys. Rev.* **D65**, 114024 (2002).
3. J.P. Ralston and D.E. Soper, *Nucl. Phys.* **B152**, 109 (1979).
4. A. Mukherjee, M. Stratmann, W. Vogelsang, *Phys. Rev.* **D 67**, 054005 (2003).
5. S. Frixione, *Phys. Lett.* **B429**, 369 (1998).
6. J. Soffer, *Phys. Rev. Lett.* **74**, 1292 (1995);
D. Sivers, *Phys. Rev.* **D51**, 4880 (1995).

SPIN TRANSFER TO Λ_c^+ HYPERONS IN POLARIZED PROTON COLLISIONS AT RHIC

V. L. RYKOV, K. SUDOH

RIKEN, Wako, Japan

The analysis [1] of helicity transfer to Λ_c^+ in polarized proton collisions is extended to the proton helicity correlations with the Λ_c^+ transverse polarization in the production plane (parameter D_{LS}). The available spin transfer observables for collisions of *two* longitudinally polarized protons are evaluated. It is shown that, in the central region at Λ_c^+ transverse momenta of a few GeV/c, D_{LS} parameters are of about the same size as the helicity-to-helicity correlations. The methodical issue of using spin transfers for cross-checks of systematic errors in cross-section A_{LL} measurements at polarized proton colliders is also briefly discussed.

1. Introduction

Spin transfers to inclusive strange and charmed hyperons in polarized proton collisions have been recently proposed [1, 2] as a probe for the polarized gluon distribution $\Delta G/G$ of the proton. Compared to the cross-section asymmetry usually considered for this purpose $A_{LL} = \frac{\sigma^{++} - \sigma^{+-}}{\sigma^{++} + \sigma^{+-}}$, where σ^{++} and σ^{+-} are the cross sections for same and opposite helicities of colliding protons, spin transfers are linear with $\Delta G/G$ while $A_{LL} \propto (\Delta G/G)^2$. This means that spin transfers might become more sensitive probes for polarized gluon distribution if $\Delta G/G$ appeared to be small. The other difference is that, unlike A_{LL} , spin transfer measurements generally do not require monitoring the relative luminosity of collisions with different polarizations of initial protons. Such monitoring is not a simple task at a proton collider with longitudinally polarized beams, and is always considered as a potential source of systematic errors. In general, measuring a number of sensitive characteristics rather than one, and comparing them to the predictions of theoretical models could serve as a good consistency check of the models' assumptions.

In the paper [1], measurements of the helicity-to-helicity transfer parameter D_{LL} in gluon fusion dominant Λ_c^+ production at RHIC with polarized protons have been proposed and studied^a. In this report, we extend this analysis to the proton helicity correlations with the Λ_c^+ transverse polarization in the production plane (parameter D_{LS})^b. Due to the large

^aThe notation A_{LL} has been used for D_{LL} in [1].

^b L and S axes here correspond to Z and X in the notation of the book [3].

c -quark mass, D_{LS} is also expected to be non-zero at Λ_c^+ transverse momenta (P_T) of a few GeV/c. Moreover, for each spin transfer LL and LS , we evaluated two more observables: $D_{L\Pi}^{++}$ and $D_{L\Pi}^{+-}$, $\Pi = L, S$, which will be measured at RHIC in collisions of *two* polarized protons of the same and opposite helicities:

$$D_{L\Pi}^{++} = \frac{\sigma_{L\Pi}^{+++} - \sigma_{L\Pi}^{++-} - \sigma_{L\Pi}^{--++} + \sigma_{L\Pi}^{--+-}}{\sigma_{L\Pi}^{+++} + \sigma_{L\Pi}^{++-} + \sigma_{L\Pi}^{--++} + \sigma_{L\Pi}^{--+-}},$$

$$D_{L\Pi}^{+-} = \frac{\sigma_{L\Pi}^{+-+} - \sigma_{L\Pi}^{+--} - \sigma_{L\Pi}^{-++} + \sigma_{L\Pi}^{-+-}}{\sigma_{L\Pi}^{+-+} + \sigma_{L\Pi}^{+--} + \sigma_{L\Pi}^{-++} + \sigma_{L\Pi}^{-+-}}, \quad \Pi = L, S \quad (1)$$

In Eqs. (1), σ_{LS}^{--++} , for example, is for the production cross-section of Λ_c^+ with the polarization “+1” along the S -axis in the collisions of two proton beams, both of *negative* helicity equal to “-1”.

Parameters $D_{L\Pi}$ for collisions of polarized and unpolarized protons are weighted with A_{LL} averages of $D_{L\Pi}^{++}$ and $D_{L\Pi}^{+-}$:

$$D_{L\Pi} = \frac{1}{2} [D_{L\Pi}^{++} (1 + A_{LL}) + D_{L\Pi}^{+-} (1 - A_{LL})] \quad (2)$$

In turn, if all three D 's for the same final spin component are measured, then A_{LL} can be derived, using Eq. (2). As mentioned above, A_{LL} determined in this way would potentially be free from systematics due to monitoring the relative luminosity with different beam polarizations. With this approach, the statistical error $\delta A_{LL} \approx \frac{2\sqrt{6}}{\alpha P |D_{L\Pi}| \sqrt{N}}$, where α is the hyperon decay asymmetry parameters, P is the beam polarization, and N is the combined statistics in the three measurements. This error would usually be noticeably larger than that of “direct” A_{LL} measurements. However, if systematic rather than statistical effects are an issue, then using spin transfers in high event rate processes, along with Eq. (2), could be an option.

2. Numerical results and discussion

The leading order calculations for pseudo-rapidity dependences of six spin transfer parameters, averaged over P_T interval from 2 to 5 GeV/c, are shown in Fig. 1. These results have been obtained under the same assumptions as in the analyses [1]. Only the dominant partonic sub-process of gluon fusion, $gg \rightarrow c\bar{c}$, was taken into account. The same spin dependent fragmentation function $\Delta\mathcal{D}(z) = \mathcal{C}(z) \cdot \mathcal{D}(z)$ was used for both the longitudinal and transverse spin transfers from c -quark to Λ_c^+ , where $\mathcal{D}(z)$ is the “unpolarized” quark fragmentation function. For the $\mathcal{C}(z)$, two options are compared: $\mathcal{C}(z) = 1$ and $\mathcal{C}(z) = z$. The statistical errors shown are for the integrated luminosity of 320 pb⁻¹ and beam polarization of 70%, assuming that the decay chain $\Lambda_c^+ \rightarrow \Lambda^0 \pi^+ \rightarrow p \pi^- \pi^+$ is to be used for measuring the Λ_c^+ polarization, with a detection efficiency of $\sim 10\%$.

In the central region of $|\eta| < 1$, D_{LL} 's and D_{LS} 's are all about ~ 5 –15%. As η increases, all D_{LL} 's increase to ~ 20 –30% at $\eta \sim 2$ for the AAC parameterization [4], while D_{LS}^{+-} stays almost flat. The achievable statistical errors of about 1% are small enough to clearly separate predictions for the models shown even in the central rapidity region. Since only

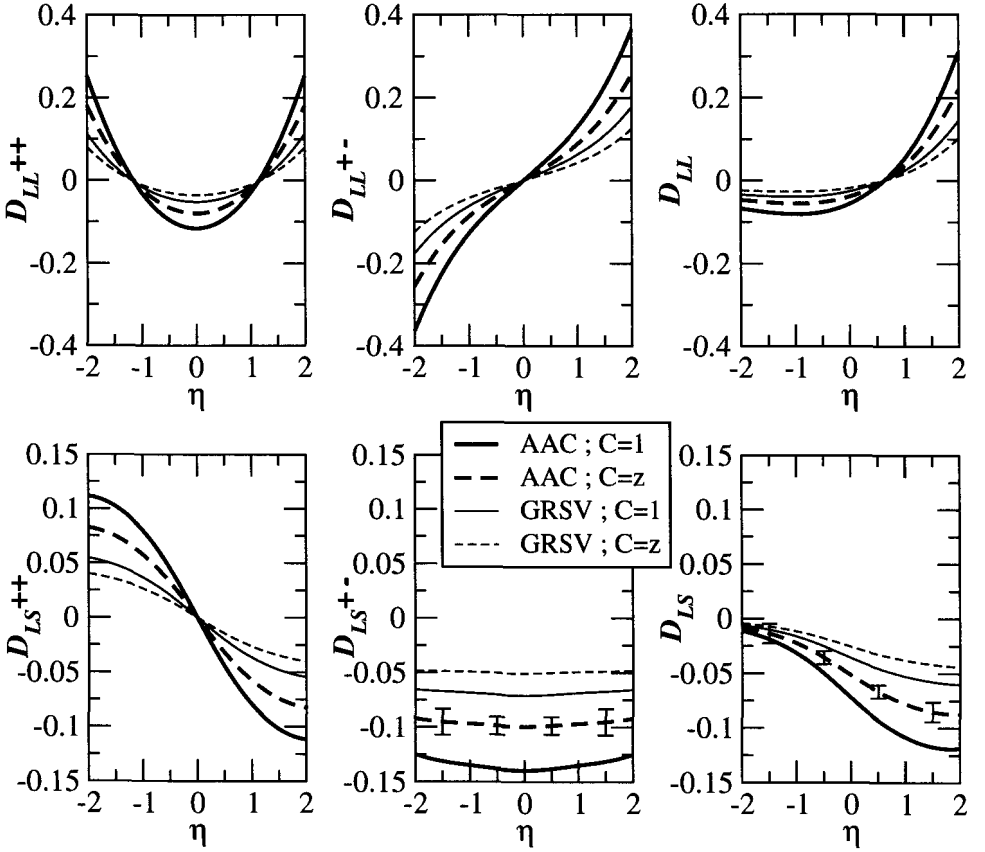


Fig. 1. η -dependences of spin transfer parameters for inclusive Λ_c^+ production in polarized proton collisions at $\sqrt{s}=200$ GeV. The leading order predictions for AAC [4] and GRSV [5] polarized gluon distributions are compared. Each error bar is for the integrated statistics within a pseudo-rapidity interval of $\Delta\eta = 1$. See text for other details.

half the total luminosity will be utilized for measuring $D_{L\Pi}^{++}$, and the other half will go to the measurements of $D_{L\Pi}^{+-}$, the statistical errors for these parameters would be larger than for $D_{L\Pi}$ by a factor of $\sqrt{2}$. However, it is worth underlining that $D_{LL}^{++} \approx 2D_{LL}$ and $D_{LS}^{+-} \approx 2D_{LS}$ for η in the vicinity of zero. These relations follow from Eq. (2) with $|A_{LL}| \ll 1$, taking into account the “forward–backward” symmetry of the initial system of two colliding protons. As a result, in the central region, the statistical significance of measurements with two polarized beams would be higher compared to the case of only one beam being polarized.

3. Summary

It is shown that both components, D_{LL} and D_{LS} , of the proton helicity transfer to the polarization of inclusive Λ_c^+ hyperons are expected to be equally sensitive to $\Delta G/G$. In the central region, the expected effects at $\sim 5\text{--}15\%$ are well above the statistical errors achievable at RHIC, which are also small enough to distinguish the AAC [4] and GRSV [5] parameter-

izations for $\Delta G/G$. The really large spin transfers at the level of up to 20–30% are expected at $\eta \sim 2$ and beyond, which might be accessible at STAR [6], but would definitely be so with the recently proposed new RHIC-II detector [7].

Acknowledgments

It is our pleasure to thank H. En'yo, N. Saito and K. Yazaki for the useful discussions.

References

1. K. Ohkuma, K. Sudoh, T. Mori, *Phys. Lett.* **B491**, 117 (2001); K. Ohkuma, T. Mori, *hep-ph/0306285*.
2. Xu Qing-hua, Liang Zuo-tang, *Phys. Rev.* **D70**, 034015 (2004).
3. E. Leader, "Spin in Particle Physics", Cambridge University Press, 2001.
4. Y. Goto et al., *Phys. Rev.* **D62**, 034017 (2000).
5. M. Glück et al., *Phys. Rev.* **D63**, 094005 (2001).
6. K. H. Ackermann et al., *Nucl. Instrum. Meth.* **A499** 624 (2003).
7. P. Steinberg et al., "Expression of Interest for a Comprehensive New Detector at RHIC II", Presentation to the BNL PAC, BNL, September 8, 2004 (available at http://www.bnl.gov/HENP/docs/pac0904/bellwied_eoi.r1.pdf, unpublished).

HIGHER TWISTS RESUMMATION IN INCLUSIVE AND SEMI-INCLUSIVE SPIN-DEPENDENT DIS *

O. V. TERYAEV

Joint Institute for Nuclear Research, Dubna, Russia

The situations when all higher twists are potentially important include DIS in the resonance region and/or at low Q^2 as well as SIDIS at low k_T . The status of Bloom-Gilman duality in QCD is discussed and its validity for the structure function g_T is deduced. The special role of this function is also manifested in the analysis of GGDH sum rules. The analogs of TMD distribution and fragmentation functions in SIDIS in coordinate space are suggested and their similarity to non-local quark condensates is stressed.

1. Introduction

While the leading spin structures of the nucleon in hard processes are described in terms of two twist-2 parton distribution functions, helicity $g_1^a(x)$, and transversity $h_1^a(x)$, the contributions of the various higher twist (HT) distributions are very important when the transition region (with the typical scales of order of 1 GeV) is considered. Moreover, there are situations when an infinite set of higher twists is required to reproduce even the qualitative features of the result.

2. Bloom-Gilman duality: for which structure function is it better?

The first such example is represented by the resonance region, where the Bloom-Gilman (BG) duality requires an account [1] of why the large x -enhanced HT terms behave like $(M^2/(1-x)Q^2)^n \approx (M^2/s)^n$. The quantitative analysis of these terms may be performed by exploring the technique of Borel sum rules (SR), which is very popular when vacuum power corrections are considered [2], but to my knowledge, have never been applied to studies of BG duality. As soon as only these enhanced power corrections are considered, the Borel SR in the variable s is especially convenient. This results from the Borel transform of the dispersion relation in s . Assuming the ansatz for spectral density

$$\rho(s) = \theta(s - s_0)\rho^{pert}(s) + \theta(s_0 - s)\rho^{Res}(s), \quad (1)$$

*This work is partially supported by grants INTAS 00/587 and RFBR 03-02-16816.

where s_0 is the duality interval, and setting the Borel parameter to infinity, which leads to the disappearance of the power corrections, one gets

$$\int_{s_{min}}^{s_0} (\rho^{pert}(s) - \rho^{Res}(s)) = 0, \quad (2)$$

which is just BG duality. Note that the calculation of s_0 from QCD, which is the real problem of QCD SR, would require an explicit account of HT terms. However, even before fulfilling this ambitious program, useful results may be attained. Thus, one should expect BG duality to be valid for those structures which make a non-zero contribution at the Born level. It is also well-known that it is the spin-dependent structure $g_T = g_1 + g_2$, rather than g_1 or g_2 , which appears at the Born level. It is therefore the most natural candidate for BG duality. This suggestion is actually supported by the data, as it is known that BG duality for g_1 structure function is violated by the contribution of the $\Delta(1232)$ resonance [3]. At the same time, its dominant magnetic transition form factor contributes only to g_T [5]. This observation was made in the analysis of Generalized GDH (GGDH) SR, which is our next subject.

3. GGDH SR: role of g_T

The GGDH SR also represents the situation in which all the higher twist contributions are important. While at large Q^2 the form factor

$$I_1(Q^2) = \frac{2M^2}{Q^2} \Gamma_1(Q^2) \equiv \frac{2M^2}{Q^2} \int_0^1 g_1(x, Q^2) dx \quad (3)$$

behaves like $1/Q^2$, for lower Q^2 higher powers of $1/Q^2$ are manifested. At the same time, their infinite sum is required to get the GDH value at $Q^2 = 0$ (provided the elastic contribution is subtracted): $I_1(0) = -\mu_A^2/4$. As the large Q^2 value for the proton is positive, the corresponding I_1 must represent a dramatic structure. It has been suggested [6] that it emerges from the elastic contribution to a similar form factor I_2 , related to g_2 by in a way analogous to (3). This elastic contribution is in fact controlled by the Burkhardt-Cottingham sum rule, which was recently checked experimentally at low Q^2 [4]. At the same time, the similar form factor I_T was assumed to be smooth, which is natural from the point of view of QCD SR. Indeed, its real photon limit $I_T(0) = -\mu_A/4$ is linear in μ_A , and one may expect to get the corresponding low energy theorem from the Ward identities, analogously to, say, the low energy theorem for the pion form factor (see [5, 6] and Ref. therein). The model for I_T was first chosen [6] in a simplistic way neglecting all the possible corrections, and this allowed the prediction of the low crossing point for I_1 . At the same time, the current high accuracy of JLAB data requires the radiative and power corrections to be taken into account [7]. This leads to the following behaviour (Fig. 1a).

Implementing the smooth model [8] for I_T^{p-n} , which is also a linear function of μ_A^p , one easily gets a similar expression [7] for the neutron (Fig. 1b). The results are in good agreement with the recent JLAB data and the results of the resonance approach of Burkert and Ioffe [9]. The latter agreement may be the another manifestation of the fact that g_T is a good candidate for BG duality.

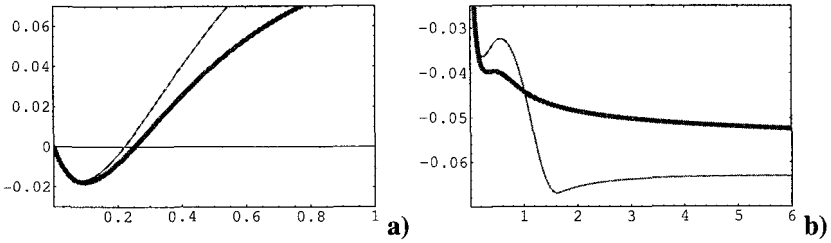


Fig. 1. a) The proton Γ_1 as a function of Q^2 . b) The neutron Γ_1 as a function of Q^2 . Solid lines correspond to perturbative and power corrections being included.

4. SIDIS: TMD functions and non-local condensates

In SIDIS the higher twist mass parameter contributions may be compensated by various kinematical variables, and terms $(M/p_T)^n$ are of most importance. It is these terms which are taken into account by the transverse momentum dependent (TMD) distribution and fragmentation functions. As these terms are not small at $M \sim p_T$, one is often speaking about leading twist effects. However, the analysis in the coordinate space [10] shows rather that one is dealing with the infinite sum of higher twists, exactly similar to the one appearing in the case of non-local quark condensates. The difference with TMD functions is mainly the following: for non-local condensates one is dealing with the vacuum matrix elements, but for TMD functions with the hadron ones. Let us say that the coordinate analog of the Collins fragmentation function is twist-3 and corresponds to the weighted k_T moment of the latter. In the coordinate space this consideration provides factorization proof for the (weighted) p_T -averaged cross-sections, analogous to the one deduced for the Drell-Yan process by Efremov and Radyushkin. Moreover, this provides a framework for regular calculations of NLO corrections, which should be very interesting. Let us say that the NLO correction for the Collins asymmetry should produce a Sivers-type asymmetry, independent of the lepton plane. This is the analog of the NLO effect in double transverse asymmetry in the Drell-Yan process, where one may easily see (although, up to my knowledge, this is absent in the vast literature [11] on the subject) the appearance of the infrared-finite term which is non-zero after integration over the produced dilepton angles (that is, the virtual photon tensor polarization), violating the so-called Hikasa theorem [12].

5. Conclusions

Since the theory of non-perturbative QCD is far from being complete, the problem of higher twist resummation is to large extent the problem of the choice of appropriate *ansatz*. It happens that the guidelines from QCD SR methods appear to be rather convenient when spin-dependent DIS or SIDIS is considered. Namely, the Borel sum rules provide the complementary description of BG duality and select the structure function g_T as a natural object of its application. This function also appears to be the useful object for study of GGDH SR, which is also supported by other reasoning from QCD SR. Passing to SIDIS case, the TMD function may be analyzed in coordinate space, where the analogs are quite similar to non-

local vacuum condensates. In such an approach the appearance of the resummed infinite set of higher twists, rather than leading twist, is clearly manifested.

References

1. A. De Rujula, H. Georgi and H. D. Politzer, *Phys. Rev. D* **15**, 2495 (1977).
2. M. A. Shifman, A. I. Vainshtein and V. I. Zakharov, *Nucl. Phys. B* **147**, 385 (1979).
3. S. Simula et al., *Phys. Rev.* **D65**, 034017 (2002).
4. R. de Vita, *These Proceedings*.
5. J. Soffer and O. Teryaev, *Phys. Rev.* **D51**, 25 (1995).
6. J. Soffer and O. Teryaev, *Phys. Rev. Lett.* **70**, 3373 (1993).
7. J. Soffer and O. Teryaev, arXiv:hep-ph/0410228, to appear in *Phys. Rev. D*.
8. J. Soffer and O. Teryaev, *Phys. Lett.* **B545**, 323 (2002).
9. A. Deur, *These Proceedings*.
10. O. V. Teryaev, arXiv:hep-ph/0310069, *Proceedings of DIS-03*, p.827; *Proceedings of SPIN-03*, p. 200.
11. W. Vogelsang and A. Weber, transversely polarized protons," *Phys. Rev. D* **48** (1993) 2073.
A. P. Contogouris, B. Kamal and Z. Merebashvili, *Corrections To Lepton Pair Production Hadrons*," *Phys. Lett. B* **337** (1994) 169. PHLTA,B337,169;
12. P. Ratcliffe, *These Proceedings*

SPIN DEPENDENT FRAGMENTATION FUNCTIONS AT BELLE

D. GABBERT, M. GROSSE-PERDEKAMP, R. SEIDL

University of Illinois at Urbana-Champaign, Urbana, USA

A. OGAWA

RIKEN Brookhaven Research Center, Upton, USA

K. HASUKO

RIKEN, Wako, Japan

The measurement of the so far unknown chiral-odd quark transverse spin distribution in either semi-inclusive DIS(SIDIS) or inclusive measurements in pp collisions at RHIC has an additional chiral-odd fragmentation function appearing in the cross section. This chiral-odd fragmentation functions (FF) can for example be the so-called Collins FF or the Interference FF. HERMES has given a first hint that these FFs are nonzero, however in order to measure transversity one needs these FFs to be precisely known. At the BELLE e^+e^- collider at the KEK-B factory a data set of about $30fb^{-1}$ can be used to obtain these functions.

1. Introduction

At leading twist three-quark distribution functions (DF) in the nucleon exist; the well known unpolarized quark DF, the somewhat known quark helicity DF, and the so far unknown transversity DF. The latter cannot be measured in inclusive DIS due to its chiral-odd nature, since all possible interactions are chiral-even for nearly massless quarks. Therefore one needs an additional chiral-odd function in the cross section to access transversity. This can either be achieved by an anti-quark transversity DF in double transversely polarized Drell-Yan processes, or one can have a chiral-odd fragmentation function in SIDIS or hadroproduction. The BELLE experiment at the asymmetric e^+e^- collider KEK-B at Tsukuba, Japan, is mainly dedicated to the study of CP violation in B meson decays. Its center of mass energy is tuned to the $\Upsilon(4S)$ resonance at $\sqrt{s} = 10.58 GeV$, whereas background studies are performed off-resonance at $10.52 GeV$. These off-resonance events are studied in order to measure spin-dependent and precise spin-independent fragmentation

functions. At present an integrated luminosity of about $30fb^{-1}$ has been accumulated in the off-resonance data sample. The aerogel Čerenkov counter (ACC), time-of-flight (TOF) detector, and the central drift chamber (CDC) allow good particle identification, which is crucial for these measurements. By requiring the tracks to originate in the primary vertex, applying the silicon vertex detector (SVD), one is able to reduce the background of pions created from heavy quark production.

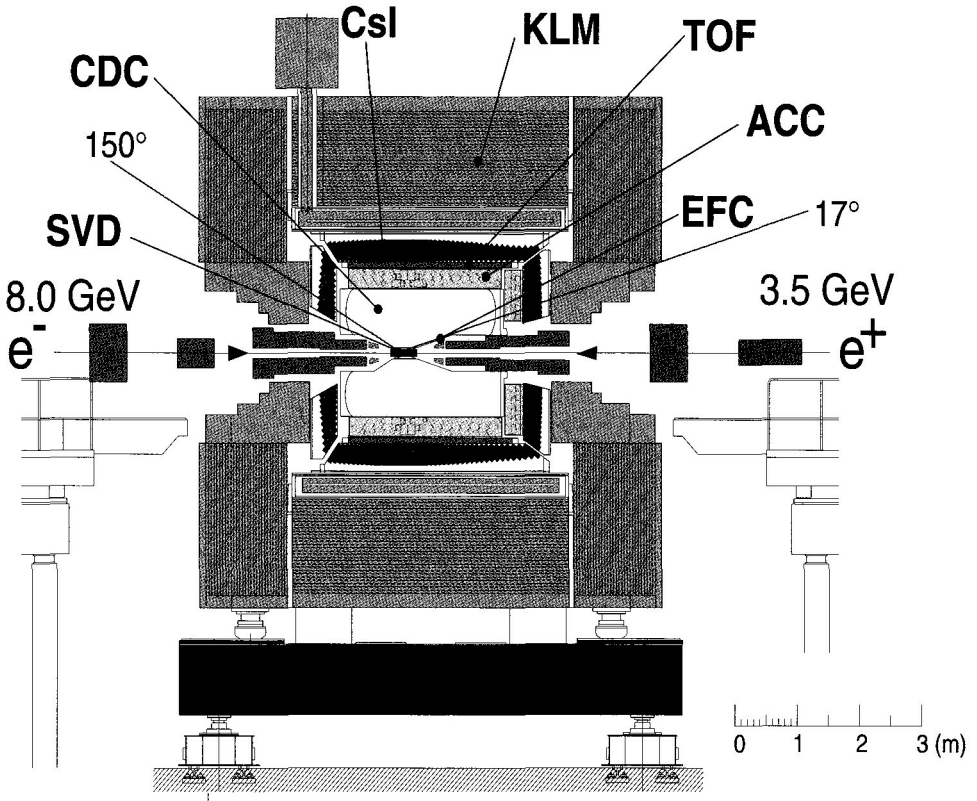


Fig. 1. A schematic side view of the BELLE detector.

To reduce the number of hard gluonic events, a cut on the kinematic variable thrust enhances the typical two-jet topology, and one can reconstruct the originally produced quark momenta quite well. To ensure that the pions did not originate in the decay of a vector meson and might be mistakenly put in the wrong hemisphere, a lower cut on the fractional energy of 0.2 is performed.

2. Collins FF

The most prominent member of these chiral-odd FFs is the Collins function [1] $H_1^\perp(z)$ which measures the difference between producing a pion to the left of the plane defined by the transversely polarized quark and its momentum, and producing a pion moving to the right. In $e^+e^- \rightarrow q\bar{q}$ one measures the azimuthal distribution of two pions in opposite hemispheres, as depicted in Fig. 2a. Following reference [2], one either computes the azimuthal angles of each pion relative to the thrust axis, which results in a $\cos(\phi_1 + \phi_2)$ modulation, or one calculates the azimuthal angle relative to the axis defined by the 2nd pion, which results in a $\cos(2\phi_0)$ modulation. While the first method directly accesses the Collins functions, the second also contains a convolution integral of the Collins FF over all involved transverse momenta. Due to holes in the acceptance near the beam pipe, the

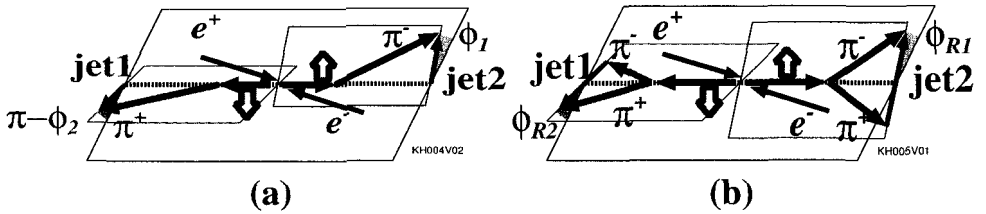


Fig. 2. Description of the azimuthal angles in the Collins and the interference fragmentation analysis.

corresponding raw asymmetries contain a large moment which can be reduced by fiducial and acceptance cuts concentrating only on pions detected in the central part of the detector. Additionally these moments are well described in MC such that one can cancel them out by dividing the azimuthal distributions of the data by their MC distributions. The second largest source of background asymmetries is of physical origin, as the emission of not too hard gluons can also produce $\cos(2\phi_0)$ and $\cos(\phi_1 + \phi_2)$ asymmetries. This contribution is calculable in pQCD, and is expected to be proportional to the unpolarized fragmentation functions $D_1(z)$ and $D_1(\bar{z})$, the strong coupling α_S , and the transverse momentum Q_T . These gluonic contributions will be independent of the pion charges, since they are proportional to the unpolarized fragmentation functions. Consequently, taking the ratio of the normalized distributions for unlike-sign over like-sign pairs, the gluonic distributions drop out in leading order:

$$R := \frac{N(\phi) |_{unlikesign}}{N(\phi) |_{likesign}} \approx 1 + r(y) \left(F \left(\frac{H_1^{\perp, fav}}{D_1^{fav}}, \frac{H_1^{\perp, disfav}}{D_1^{disfav}} \right) + \mathcal{O}(Q_T, \alpha_S)^2 \right) \cos(2\phi_0) \quad , \quad (1)$$

where $r(y)$ contains the ratio of the y -dependent prefactors, and favoured and disfavoured FF describe the fragmentation of a light quark into a pion of the same or opposite charge. y is defined as $y \stackrel{cms}{=} (1 + \cos \theta)/2$, where θ is the angle between the colliding leptons and

the produced hadron. Additionally one can check if these gluonic contributions are well described by the MC, and if so just use the data-to-MC ratios mentioned previously.

3. Interference FF

A second FF proposed in reference [3] does not rely on intrinsic transverse momentum, and is accessed by the interference of two pions or kaons in the vicinity of the ρ or Φ meson invariant mass. Here one measures the azimuthal distribution of the plane defined by the pions relative to the thrust axis in each hemisphere [4], as illustrated in Fig. 2b. The corresponding $\cos(\phi_{R1} + \phi_{R2})$ distribution still depends on the fractional energies z_1 and z_2 of the pion pairs and on their invariant mass. The invariant mass distribution of the asymmetry can either have a sign change at the ρ mass according to a pion phase shift analysis [3], or it could be flat as preferred by model calculations [5]. The BELLE measurements will be able to distinguish between these predictions, and a parameterization of the FF interference is possible.

References

1. J. C. Collins: Nucl. Phys **B396**(1993):161.
2. D. Boer, R. Jakob, P. J. Mulders: Phys. Let. **B 424**(1998):143
3. R. L. Jaffe, X. m. Jin and J. a. Tang: Phys. Rev. **D57**(1998):5920
4. X. Artru, J. Collins: Z. Phys. **C69**(1996):1166
5. M. Radici, R. Jakob, and A. Bianconi: Phys. Rev. **D65**(2002):074031.

AZIMUTHAL SINGLE-SPIN ASYMMETRIES ON A TRANSVERSELY POLARIZED HYDROGEN TARGET AT HERMES

G. SCHNELL*

Department of Physics, Tokyo Institute of Technology, Tokyo, Japan

(on behalf of the HERMES Collaboration)

Azimuthal Single-Spin Asymmetries for semi-inclusive electro-production of charged pions in deep-inelastic scattering of positrons off transversely polarized protons are presented. Different combinations of the azimuthal angles of the hadron momentum and the proton spin direction around the virtual photon direction allow separation of the so-called Collins and Sivers asymmetries.

1. Introduction

Single-spin asymmetries (SSA) in the azimuthal distribution of lepto-produced hadrons around the virtual photon direction are a valuable tool for exploring transverse spin and momentum degrees of freedom in the nucleon structure. Such SSA's in semi-inclusive deep-inelastic scattering (DIS) have already been observed with unpolarized beams and longitudinally polarized nucleons [1]. Recently [2], the HERMES experiment at DESY also measured SSA's on a transversely polarized target. While the interpretation of the data from longitudinally polarized targets is hampered by the fact that the various contributions can not be disentangled, a transversely polarized target allows simultaneous measurements of Collins and Sivers asymmetries. The Collins asymmetry involves transversity distribution [3] h_1 – the last leading-twist forward quark distribution to be measured. It describes the imbalance in the number of quarks with their spin (anti)aligned with the spin of a transversely polarized nucleon. It can not be measured in inclusive processes because of its chiral-odd character. However, it can appear in semi-inclusive DIS, e.g. in conjunction with the Collins fragmentation function [4] H_1^\perp – also chiral-odd and odd under naive^a time reversal (T-odd) – resulting in a sinusoidal distribution of produced hadrons around the virtual photon direction. The Sivers asymmetry, on the other hand, involves a naive T-odd distribution function. The Sivers function [5] f_{1T}^\perp was believed to vanish because of this property, but in the recent work initiated by [6] it was realized that final-state interactions

*This work is partially supported by Japan Society for the Promotion of Science

^aNaive time reversal is time reversal without interchange of initial and final states.

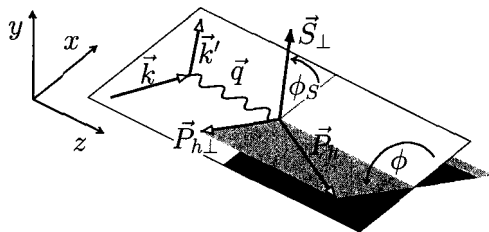


Fig. 1. The definitions of the azimuthal angles.

via soft gluons offer a mechanism to create the necessary interference of amplitudes for its naive T-odd nature. An interesting property of the Siverson function is its link to orbital angular momentum L_z – the Siverson function vanishes for zero L_z . It thus has the potential to lead to one way of measuring L_z .

2. Azimuthal Single Spin Asymmetries

Both the Siverson and the Collins functions belong to the group of unintegrated distribution (DF) and fragmentation functions (FF). They explicitly depend on intrinsic parton transverse momenta and do not survive integration over the latter. Hence a measurement needs to be sensitive to transverse momenta. One possibility is to study the azimuthal distribution of hadrons around the virtual photon direction. In the case of a transversely polarized target this distribution depends on two azimuthal angles ϕ and ϕ_S , as seen in Fig. 1.

The luminosity-normalized count-rate asymmetries between opposite target spin states (\uparrow, \downarrow) can be written as the sum of two sine functions [7]:

$$\frac{1}{S_{\perp}} \frac{N^{\uparrow}(\phi, \phi_S) - N^{\downarrow}(\phi, \phi_S)}{N^{\uparrow}(\phi, \phi_S) + N^{\downarrow}(\phi, \phi_S)} = \frac{B(\langle y \rangle)}{A(\langle x \rangle, \langle y \rangle)} A_{UT}^{\sin(\phi + \phi_S)} \sin(\phi + \phi_S) + A_{UT}^{\sin(\phi - \phi_S)} \sin(\phi - \phi_S). \tag{1}$$

Here S_T is the transverse polarization of the target, the subscript UT denotes unpolarized beam and transverse target polarization, x (Bjorken scaling variable) and y (fractional energy of the virtual photon) are the usual DIS Lorentz invariants, and $B(\langle y \rangle) \equiv (1 - y)$, $A(\langle x \rangle, \langle y \rangle) \equiv \frac{y^2}{2} + (1 - y)(1 + R(x, y))/(1 + \gamma(x, y)^2)$. The amplitudes of each sine term are proportional in leading order to a convolution integral over transverse momenta of both a DF and a FF:

$$A_{UT}^{\sin(\phi + \phi_S)} \propto \sum_q e_q^2 \mathcal{F} \left[\frac{k_T \cdot \hat{P}_{h\perp}}{M_h} h_1^q(x, p_T^2) H_1^{\perp, q}(z, z^2 k_T^2) \right] \tag{2}$$

$$A_{UT}^{\sin(\phi - \phi_S)} \propto - \sum_q e_q^2 \mathcal{F} \left[\frac{p_T \cdot \hat{P}_{h\perp}}{M} f_{1T}^{\perp, q}(x, p_T^2) D_1^q(z, z^2 k_T^2) \right], \tag{3}$$

where p_T (k_T) are the intrinsic quark transverse momenta, $\hat{P}_{h\perp}$ is the unit vector in the hadron's transverse momentum direction, and z is the fractional energy of the hadron. These

virtual-photon asymmetries were extracted by performing a two-dimensional fit of Eq. (1) in order to minimize uncertainties from systematic correlations.

3. Results

The measured asymmetries for the charged π mesons are plotted in Fig. 2 as functions of x and z . The Collins moments^b $\langle \sin(\phi + \phi_S) \rangle$ are positive for π^+ and negative for π^- . This is not unexpected as the two valence quark flavours of the proton are predicted to have transversity distributions of opposite sign, and they contribute to π^+/π^- production with different strength. The large moments for the π^- are somewhat unexpected however, but could be explained by a large disfavoured Collins FF (e.g. the fragmentation of up quarks into π^- mesons), which is also opposite in sign compared to the favoured one.

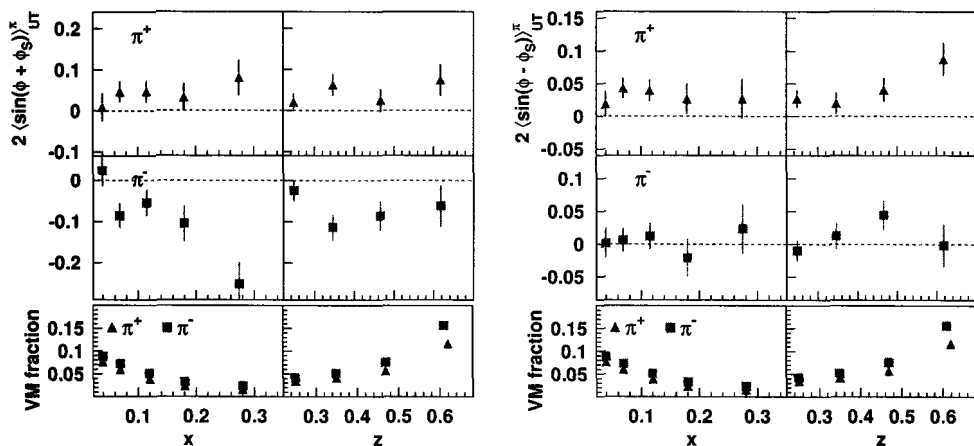


Fig. 2. Virtual-photon Collins (left) and Siverts (right) moments for charged π mesons as labelled in the upper panel, as functions of x and z . Error bars are statistical uncertainties only. There is a common 8% scale uncertainty dominated by the uncertainty in the target polarization value. The lower panel shows the relative contributions to the π sample from the decay of exclusive vector mesons (VM) evaluated using a PYTHIA-based Monte Carlo simulation.

The Siverts moments are positive for π^+ and consistent with zero for π^- . This agrees with e.g. the prediction in [9], and is the first direct sign of a T-odd DF in DIS. This observation is, however, weakened by the fact that a fraction of the observed π mesons comes from the decay of exclusively produced vector mesons, mainly ρ^0 mesons. These can not be reconstructed due to the limited detector acceptance, and could carry a large asymmetry not related to the Siverts function.

^bFollowing the Trento Conventions [8] azimuthal moments are denoted by either $A_{UT}^{\sin(\phi + \phi_S)}$ or $\langle \sin(\phi \pm \phi_S) \rangle \equiv \frac{1}{2} A_{UT}^{\sin(\phi \pm \phi_S)}$.

4. Outlook

These data are only a first glimpse on the total data set which HERMES will take with a transversely polarized target. The complete set will allow not only a more precise measurement of the presented moments, but also the extraction of the DF's and FF's involved. Furthermore, a measurement of the ρ^0 asymmetry will shed light on the question whether the measured Sivers moments are indeed a first observation of a T-odd DF in DIS, or whether they are entirely due to exclusive VM production.

References

1. A. Airapetian *et al.*, *Phys. Rev. Lett.* **84**, 4047 (2000).
A. Airapetian *et al.*, *Phys. Rev.* **D64**, 097101 (2001).
A. Airapetian *et al.*, *Phys. Lett.* **B562**, 182 (2003).
2. A. Airapetian *et al.*, *Phys. Rev. Lett.* (in press), arXiv:hep-ex/0408013.
3. J. P. Ralston and D. E. Soper, *Nucl. Phys.* **B152**, 109 (1979).
4. J. Collins, *Nucl. Phys.* **B396**, 161 (1993).
5. D. W. Sivers, *Phys. Rev.* **D41**, 83 (1990).
6. S. J. Brodsky, D. S. Hwang and I. Schmidt, *Phys. Lett.* **B530**, 99 (2002).
7. P. J. Mulders, R. D. Tangerman, *Nucl. Phys.* **B461**, 197 (1996).
D. Boer, P. J. Mulders, *Phys. Rev.* **D57**, 5780 (1998).
8. A. Bacchetta, U. D'Alesio, M. Diehl and C. A. Miller, arXiv:hep-ph/0410050.
9. M. Burkardt, *Nucl. Phys.* **A735**, 185 (2004).

MEASUREMENTS OF COLLINS AND SIVERS ASYMMETRIES AT COMPASS

P. PAGANO

Sezione INFN di Trieste, Trieste, Italy

(on behalf of the COMPASS Collaboration)

COMPASS is a fixed target experiment currently running at CERN. In 2002, 2003, and 2004 the experiment used a 160 GeV polarized muon beam coming from SPS and scattering on a ${}^6\text{LiD}$ target. The nucleons in the target can be polarized either longitudinally or transversely with respect to the muon beam, and 20% of the running time has been devoted to transverse polarization. From the transverse polarization data collected in 2002, which correspond to a total integrated luminosity of about 200 pb^{-1} , the Collins and the Sivers asymmetries have been determined separately, and the preliminary results are presented here.

1. The theoretical framework

The cross-section for polarized deep inelastic scattering [1] of leptons on spin 1/2 hadrons can be expressed, at the leading twist, as a function of three independent quark distribution functions: $q(x)$, $\Delta q(x)$ and $\Delta_T q(x)$. The latter is chiral-odd and can be measured in combination with a chiral-odd fragmentation function, the Collins function $\Delta D_a^h(z, p_T^h)$, via azimuthal single spin asymmetries [2] (SSA) in the hadronic end-product (semi-inclusive measurement). A similar effect can arise from a possible quark k_T structure of a transversely polarized nucleon (the Sivers function, $\Delta_0^T q$), which also causes an azimuthal asymmetry in the produced hadrons. Leptonproduction on transversely polarized nucleons is a favourable setting to disentangle the Collins and Sivers effects since they show a dependence on linearly independent kinematic variables.

According to Collins, the fragmentation function of a quark of flavour a in a hadron h can be written as [3]:

$$D_a^h(z, \mathbf{p}_T^h) = D_a^h(z, p_T^h) + \Delta D_a^h(z, p_T^h) \cdot \sin\Phi_C$$

where \mathbf{p}_T^h is the final hadron transverse momentum with respect to the quark direction – i.e. the virtual photon direction – and $z = E_h/(E_l - E_{l'})$ is the fraction of available energy carried by the hadron (E_h is the hadron energy, E_l is the incoming lepton energy and $E_{l'}$ is the scattered lepton energy). The angle appearing in the fragmentation function, known as “Collins angle” and denoted by Φ_C , is conveniently defined in the system where the z-axis is the virtual photon direction and the x-z plane is the muon scattering plane. In this frame

$\Phi_C = \Phi_h - \Phi'_s$, where Φ_h is the hadron azimuthal angle, and Φ'_s is the azimuthal angle of the transverse spin of the struck quark. Since $\Phi'_s = \pi - \Phi_s$, with Φ_s the azimuthal angle of the transverse spin of the initial quark (nucleon), the relation $\Phi_C = \Phi_h + \Phi_s - \pi$ is also valid. The fragmentation function $\Delta D_a^h(z, p_T^h)$ couples to the transverse spin distribution function $\Delta_T q(x)$, and gives rise to SSA (denoted as A_{Coll}) depending on the kinematic variables x , z and p_T^h .

Following the Sivers hypothesis, the difference in the probability of finding an unpolarised quark of transverse momenta \mathbf{k}_T and $-\mathbf{k}_T$ inside a polarised nucleon can be written as [6]:

$$P_{q/p^\uparrow}(x, \mathbf{k}_T) - P_{q/p^\uparrow}(x, -\mathbf{k}_T) = \sin \Phi_S \Delta_0^T q(x, k_T^2)$$

where $\Phi_S = \Phi_k - \Phi_s$ is the azimuthal angle of the quark with respect to the nucleon transverse spin orientation. It has been recently demonstrated by theoretical arguments [7, 8], that SSA (denoted as A_{Siv}) coming from the coupling of the Sivers function with the unpolarised fragmentation function $D_a^h(z, p_T^h)$ can be observed at the leading twist from polarised Semi-Inclusive DIS.

2. The COMPASS 2002 run for transversity

The COMPASS [3, 4] experiment makes use of a high energy, intense, polarised muon beam naturally polarised by the π^- decay mechanism. It uses the polarised target system of the SMC experiment, which consists of two ${}^6\text{LiD}$ cells, each 60 cm long, located along the beam one after the other in two separate RF cavities. Data are taken therefore on the two oppositely polarised target cells simultaneously.

Here we discuss the analysis of the data collected in 2002 with target polarisation oriented transversely to the beam direction. This sample (about 200 pb^{-1} in integrated luminosity) consists of two periods, each 5 days long, with two opposite settings of the target spin orientation. Events were selected in which a primary vertex (with identified beam and scattered muon) was found in one of the two target cells with a least one outgoing hadron. A clean separation of muon and hadron samples was achieved by cuts on the amount of material traversed in the spectrometer. In addition, the kinematic cuts $Q^2 > 1(\text{GeV}/c)^2$, $W > 5 \text{ GeV}/c^2$ and $0.1 < y < 0.9$ were applied to the data to ensure a deep-inelastic sample above the region of the nuclear resonances and within the COMPASS trigger acceptance. The upper bound on y also serves to keep radiative corrections small. SSA have been looked for in the leading hadron in the event, and in all hadrons. The leading hadron was determined as the most energetic non-muonic particle of the primary vertex having $z > 0.25$ and a transverse momentum $p_T^h > 0.1 \text{ GeV}/c$. When all the hadrons coming from the primary vertex were considered, the z cut was lowered to 0.20. The final data sample had an average values for $x = 0.034$, $y = 0.33$ and $Q^2 = 2.7 (\text{GeV}/c)^2$. The average value for z and p_T^h are 0.44 and $0.51 \text{ GeV}/c$ for the leading hadron analysis, 0.38 and $0.48 \text{ GeV}/c$ in the other case. In transverse polarisation, one can write the number of events as follows:

$$N(\Phi_{C/S}) = \alpha(\Phi_{C/S}) \cdot N_0 (1 + \epsilon_{C/S} \sin \Phi_{C/S}),$$

where ε is the amplitude of the experimental asymmetry and α is a function containing the apparatus acceptance. The former amplitude can be expressed as a function of the Collins and Sivers asymmetries through the expressions:

$$\varepsilon_C = A_{Coll} \cdot P_T \cdot f \cdot D_{NN} \qquad \varepsilon_S = A_{Siv} \cdot P_T \cdot f,$$

where P_T ($\simeq 0.45$) is the polarisation of the target, D_{NN} is the spin transfer coefficient, and f ($\simeq 0.40$) is the target dilution factor. To eliminate systematic effects due to acceptance, in each period the asymmetry ε_C (ε_S) is fitted separately for the two target cells from the event flux with the two target orientations using the expression:

$$\varepsilon_{C/S} \sin \Phi_{C/S} = \frac{N_h^\uparrow(\Phi_{C/S}) - R \cdot N_h^\downarrow(\Phi_{C/S} + \pi)}{N_h^\uparrow(\Phi_{C/S}) + R \cdot N_h^\downarrow(\Phi_{C/S} + \pi)}$$

where $R = N_{h,tot}^\uparrow / N_{h,tot}^\downarrow$ is the ratio of the total number of events in the two target polarisation orientations. The results of the asymmetries plotted against the kinematic variables x , z and p_T^h are shown in Fig. 1 for positive (full points) and negative (open points) hadrons, for the leading hadron only (top plot), and for all hadrons (bottom plot).

These are the first measurements of transverse spin effects on a deuteron target: within the statistical accuracy of the data, both the Collins and Sivers asymmetries turned out to be small and compatible with zero, with a marginal indication of a Collins effect at large z for both positive and negative charges.

References

1. V. Barone, A. Drago and P. G. Ratcliffe, Phys. Rept. **359** (2002) 1.
2. J. C. Collins, Nucl. Phys. B **396** (1993) 161.
3. G. Baum *et al.* [COMPASS Collaboration], CERN-SPSLC-96-14.
4. A. Bressan *et al.*, "Recent results from COMPASS", these proceedings.
5. D. W. Sivers, Phys. Rev. D **41** (1990) 83.
6. M. Anselmino, V. Barone, A. Drago, F. Murgia [arXiv:hep-ph/0209073].
7. S.J. Brodsky, D.S. Hwang, I. Schmidt, Phys. Lett. B **530** (2002) 99.
8. J. C. Collins, Phys. Lett. B **536** (2002) 43.

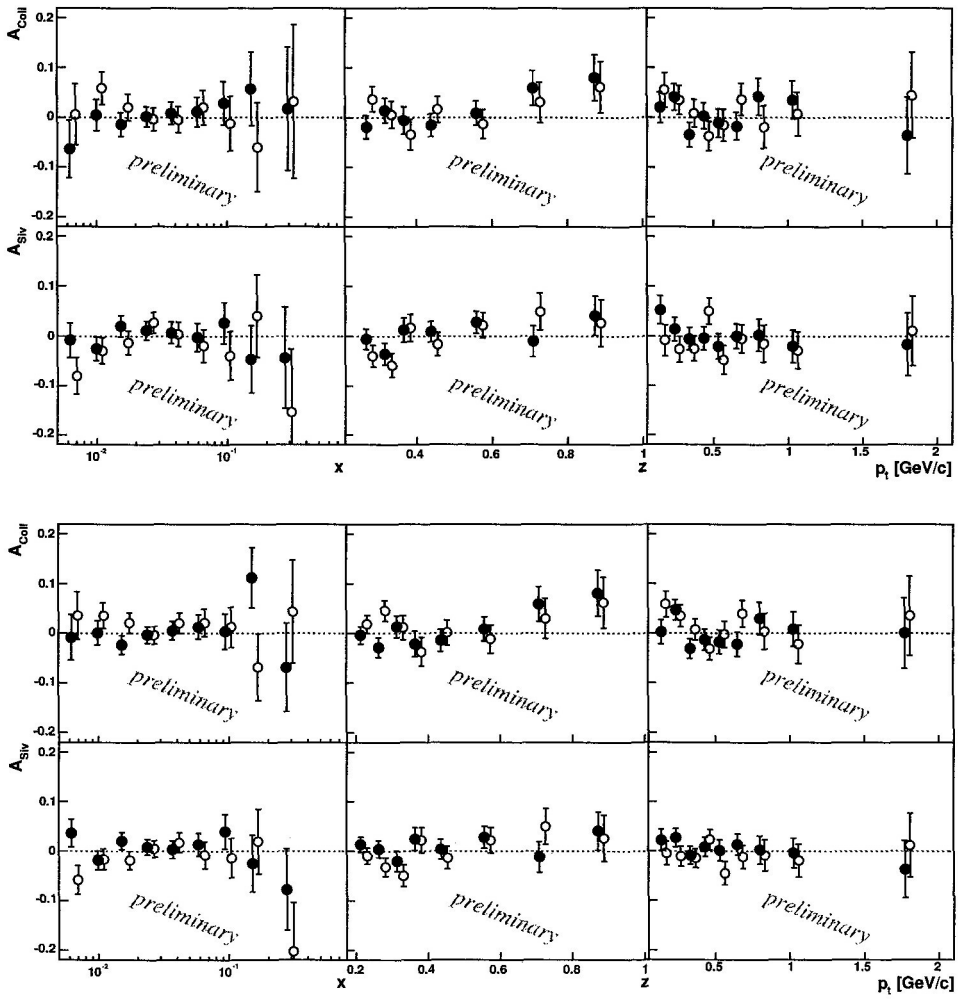


Fig. 1. Collins and Sivers asymmetry for positive (full points) and negative (open points) hadrons as a function of x , z and p_T^h . Leading hadrons analysis on top canvas, all hadrons on bottom canvas.

TRANSVERSITY AND DIHADRON FRAGMENTATION FUNCTIONS*

A. BACCHETTA

Institut für Theoretische Physik, Universität Regensburg, Regensburg, Germany

M. RADICI

Università di Pavia, and Istituto Nazionale di Fisica Nucleare, Sezione di Pavia, Pavia, Italy

The observation of the quark transversity distribution requires another soft object sensitive to the quark's transverse spin. Dihadron fragmentation functions represent a convenient tool to analyze partonic spin, which can influence the angular distribution of the two hadrons. In particular, the so-called interference fragmentation functions can be used to probe transversity both in semi-inclusive deep inelastic scattering as well as proton-proton collisions. We discuss two single-spin asymmetries sensitive to transversity in these two processes, at leading twist and leading order in α_S .

Transversity has received a lot of attention during this conference. Its measurement is on the agenda of several experimental collaborations. However, it is still not clear what will turn out to be the best way to access it. Different options will be explored in the next few years: polarized Drell-Yan, polarized Λ production, azimuthal asymmetries in pion production and, finally, azimuthal asymmetries in two-pion production.^a Each one of these processes has some advantages and drawbacks, making it necessary to explore all of them at the same time. Here, we focus on azimuthal asymmetries in two-hadron production.

First of all we consider lepton production of two hadrons in the current fragmentation region, i.e. the process $lp \rightarrow l'(h_1 h_2)X$. The outgoing hadrons have momenta P_1 and P_2 , masses M_1 and M_2 , and invariant mass M_h (which must be much smaller than the virtuality of the photon, Q). We introduce the vectors $P_h = P_1 + P_2$ and $R = (P_1 - P_2)/2$, i.e. the total and relative momenta of the pair, respectively. The angle θ is the angle between the direction of P_1 in the pair's center of mass and the direction of P_h in the lab frame [2]. We

*Work partially supported by the Alexander von Humboldt Foundation.

^aAt the moment, data are available only for azimuthal asymmetries in pion production [1].

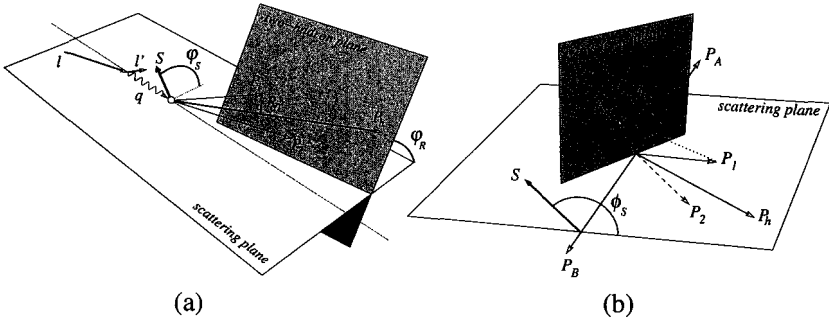


Fig. 1. Angles involved in the measurement of the transverse single-spin asymmetry in (a) deep-inelastic production of two hadrons in the current region, (b) proton-proton collisions into two hadrons belonging to the same jet.

also introduce the invariant

$$|\mathbf{R}| = \frac{1}{2} \sqrt{M_h^2 - 2(M_1^2 + M_2^2) + (M_1^2 - M_2^2)^2 / M_h^2}. \quad (1)$$

Cross-sections are assumed to be differential in dM_h^2 , $d\varphi_R$, dz , dx , dy , $d\varphi_S$, where z , x , y are the usual scaling variables employed in semi-inclusive DIS, the azimuthal angles are defined so that (see Fig. 1a)^b

$$\cos \varphi_S = \frac{(\hat{\mathbf{q}} \times \mathbf{l}) \cdot (\hat{\mathbf{q}} \times \mathbf{S})}{|\hat{\mathbf{q}} \times \mathbf{l}| |\hat{\mathbf{q}} \times \mathbf{S}|}, \quad \sin \varphi_S = \frac{(\mathbf{l} \times \mathbf{S}) \cdot \hat{\mathbf{q}}}{|\hat{\mathbf{q}} \times \mathbf{l}| |\hat{\mathbf{q}} \times \mathbf{S}|}, \quad (2)$$

$$\cos \varphi_R = \frac{(\hat{\mathbf{q}} \times \mathbf{l}) \cdot (\hat{\mathbf{q}} \times \mathbf{R}_T)}{|\hat{\mathbf{q}} \times \mathbf{l}| |\hat{\mathbf{q}} \times \mathbf{R}_T|}, \quad \sin \varphi_R = \frac{(\mathbf{l} \times \mathbf{R}_T) \cdot \hat{\mathbf{q}}}{|\hat{\mathbf{q}} \times \mathbf{l}| |\hat{\mathbf{q}} \times \mathbf{R}_T|}, \quad (3)$$

where $\hat{\mathbf{q}} = \mathbf{q}/|\mathbf{q}|$ and \mathbf{R}_T is the component of \mathbf{R} perpendicular to P_h .

The best observable to be measured in an attempt to extract transversity with dihadron fragmentation functions is probably the transverse spin asymmetry [4]

$$A_{UT}(x, M_h^2, \varphi_R, \varphi_S) = \frac{\int dz dy d^6\sigma_{UT}}{\int dz dy d^6\sigma_{UU}}, \quad (4)$$

where the unpolarized cross sections and the transversely polarized cross section (difference) read *up to leading twist only*^c

$$d^6\sigma_{UU} = \sum_a \frac{\alpha^2 e_a^2}{\pi Q^2 y} (1 - y + y^2/2) f_1^a(x) D_{1,oo}^a(z, M_h^2), \quad (5)$$

$$d^6\sigma_{UT} = - \sum_a \frac{\alpha^2 e_a^2}{4Q^2 y} \frac{|\mathbf{R}|}{M_h} |\mathbf{S}_\perp| (1 - y) \sin(\varphi_R + \varphi_S) h_1^a(x) H_{1,ot}^{Sa}(z, M_h^2). \quad (6)$$

Here, we assume that an integral over θ has been carried out. In the unpolarized case, the function $D_{1,oo}$ represents the sum of all resonances and backgrounds contributing to the

^bThe definition of the angles is consistent with the so-called Trento conventions [3].

^cFor subleading-twist corrections, see Refs. [5, 6]. NLO α_s corrections have not been studied yet.

two-pion spectrum, plus possible interference between pion pairs belonging to the same partial waves. The function $H_{1,ot}^{\leftarrow}$ in the transversely polarized case represent interference between s and p waves. It should be therefore sizeable only at values of the invariant mass where both waves contribute (e.g. in the neighbourhood of the ρ resonance), although the precise invariant-mass profile of this fragmentation function is at the moment unknown [7]. If information about the distribution over θ is retained, transversity could also be coupled to a pure p -wave fragmentation function, whose invariant-mass profile can be expected to follow a Breit-Wigner distribution peaked at the ρ resonance. Measurements of this kind of asymmetries are already in progress at HERMES and COMPASS [8].

Next we consider the production of two hadrons in the same jet in proton-proton collisions, i.e. the process $p_A p_B \rightarrow (h_1 h_2) X$. The two protons have momenta P_A and P_B . We assume that only proton B is polarized and has spin S . The transverse momentum of the hadron pair has to be large compared to all hadron masses, and to the invariant mass of the pair. We use the same variables introduced before to describe the hadron pair. Cross-sections are assumed to be differential in $d\eta$, $d|\mathbf{P}_{h\perp}|$, $d\cos\theta$, dM_h^2 , $d\phi_R$, $d\phi_S$, where η and $\mathbf{P}_{h\perp}$ are the pseudo-rapidity (defined with respect to P_A) and the transverse momentum of the hadron pair (i.e. of the sum of the outgoing hadron's momenta), and the azimuthal angles, shown in Fig. 1b, are defined as follows:

$$\cos\phi_S = \frac{(\hat{\mathbf{P}}_B \times \mathbf{P}_h)}{|\hat{\mathbf{P}}_B \times \mathbf{P}_h|} \cdot \frac{(\hat{\mathbf{P}}_B \times \mathbf{S})}{|\hat{\mathbf{P}}_B \times \mathbf{S}|}, \quad \sin\phi_S = \frac{(\mathbf{P}_h \times \mathbf{S}) \cdot \hat{\mathbf{P}}_B}{|\hat{\mathbf{P}}_B \times \mathbf{P}_h| |\hat{\mathbf{P}}_B \times \mathbf{S}|}, \quad (7)$$

$$\cos\phi_R = \frac{(\hat{\mathbf{P}}_h \times \mathbf{P}_A)}{|\hat{\mathbf{P}}_h \times \mathbf{P}_A|} \cdot \frac{(\hat{\mathbf{P}}_h \times \mathbf{R})}{|\hat{\mathbf{P}}_h \times \mathbf{R}|}, \quad \sin\phi_R = \frac{(\mathbf{P}_A \times \mathbf{R}) \cdot \hat{\mathbf{P}}_h}{|\hat{\mathbf{P}}_h \times \mathbf{P}_A| |\hat{\mathbf{P}}_h \times \mathbf{R}|}, \quad (8)$$

where $\hat{\mathbf{P}} = \mathbf{P}/|\mathbf{P}|$. The asymmetry to be measured is [9]

$$A_N(\eta, |\mathbf{P}_{h\perp}|, M_h^2, \phi_R, \phi_S) = \frac{d^5\sigma_{UT}}{d^5\sigma_{UU}}, \quad (9)$$

with

$$d^5\sigma_{UU} = 2|\mathbf{P}_{h\perp}| \sum_{a,b,c,d} \int \frac{dx_a dx_b}{4\pi^2 \bar{z}_c} f_1^a(x_a) f_1^b(x_b) \frac{d\hat{\sigma}_{ab \rightarrow cd}}{d\hat{t}} D_{1,oo}^c(\bar{z}_c, M_h^2), \quad (10)$$

$$d^5\sigma_{UT} = 2|\mathbf{P}_{h\perp}| \sum_{a,b,c,d} \frac{|\mathbf{R}|}{M_h} |\mathbf{S}_T| \sin(\phi_S - \phi_R) \quad (11)$$

$$\times \int \frac{dx_a dx_b}{16\pi \bar{z}_c} f_1^a(x_a) h_1^b(x_b) \frac{d\Delta\hat{\sigma}_{ab \rightarrow c \uparrow d}}{d\hat{t}} H_{1,ot}^{\leftarrow c}(\bar{z}_c, M_h^2),$$

$$\bar{z}_c = \frac{|\mathbf{P}_{h\perp}|}{\sqrt{s}} \frac{x_a e^{-\eta} + x_b e^{\eta}}{x_a x_b} \quad (12)$$

and $d\hat{\sigma}_{ab \rightarrow cd}$ denote the well-known unpolarized partonic cross sections, while $\Delta\hat{\sigma}_{ab \rightarrow c \uparrow d}$ denote the cross sections (differences) with transversely polarized partons b and c , to be found in [9]. This kind of asymmetry could be measured at RHIC.

Dihadron fragmentation functions could also be measured in e^+e^- annihilation, for instance at BELLE [10] and BABAR, and thus allow the extraction of transversity from the above-mentioned asymmetries.

Acknowledgments

The work of A. B. and his participation to the conference has been supported by the Alexander von Humboldt Foundation.

References

1. A. Airapetian *et al.* [HERMES Collaboration], arXiv:hep-ex/0408013; G. Schnell, these proceedings.
2. A. Bacchetta and M. Radici, Phys. Rev. D **67** (2003) 094002
3. A. Bacchetta, U. D'Alesio, M. Diehl and C. A. Miller, arXiv:hep-ph/0410050.
4. M. Radici, R. Jakob and A. Bianconi, Phys. Rev. D **65** (2002) 074031
5. A. Bacchetta and M. Radici, Phys. Rev. D **69** (2004) 074026
6. A. Bacchetta and M. Radici, proceedings of DIS 2004, arXiv:hep-ph/0407345.
7. R. L. Jaffe, X. Jin and J. Tang, Phys. Rev. Lett. **80** (1998) 1166
8. P. van der Nat, these proceedings; R. Joosten, these proceedings.
9. A. Bacchetta and M. Radici, Phys. Rev. D **70** (2004) 094032
10. R. Seidl, these proceedings.

TWO-HADRON SINGLE TARGET-SPIN ASYMMETRIES: FIRST MEASUREMENTS BY HERMES

P. B. van der NAT, K. GRIFFIOEN

Nationaal Instituut voor Kernfysica en Hoge-Energiefysica (NIKHEF), Amsterdam, The Netherlands

(on behalf of the HERMES Collaboration)

Single target-spin asymmetries in semi-inclusive two-pion production have been measured for the first time by the HERMES experiment, using a longitudinally polarized deuterium target. These asymmetries relate to the unknown transversity distribution function $h_1(x)$ through, also unknown, interference fragmentation functions. The results presented are compared with a model of the dependence of one of these interference fragmentation functions on the invariant mass of the pion pair.

1. Introduction

Of the three leading-twist quark distributions, the quark number density, the quark helicity, and the quark transversity distribution, only the last is so far unmeasured. The main reason for this is its chiral-odd nature, which requires a second chiral-odd object to couple to the transversity distribution in order to make it accessible to measurements. One candidate for such a chiral-odd fragmentation function is the so-called Collins fragmentation function appearing in pion lepton production. This has been studied by the HERMES experiment using a longitudinally polarized target [1], and recently using a transversely polarized target [2].

Another way of accessing transversity is offered by interference fragmentation functions, which appear in single target-spin asymmetries in two-pion semi-inclusive deep-inelastic scattering (DIS). One of the advantages of this method is that the azimuthal moment of the asymmetry is directly proportional to products of distribution and fragmentation functions, whereas in the case of one-hadron semi-inclusive DIS, these products are convoluted with the transverse momentum of the detected hadron. Although the interference fragmentation functions themselves are as yet unknown, they can be cleanly measured in e^+e^- experiments, such as Belle [3] and Babar.

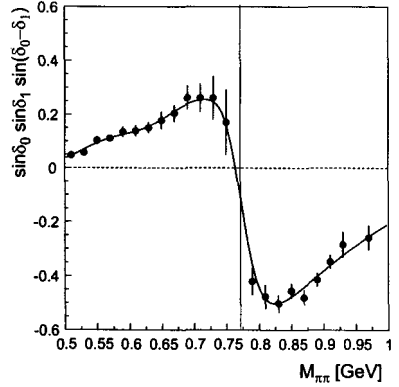
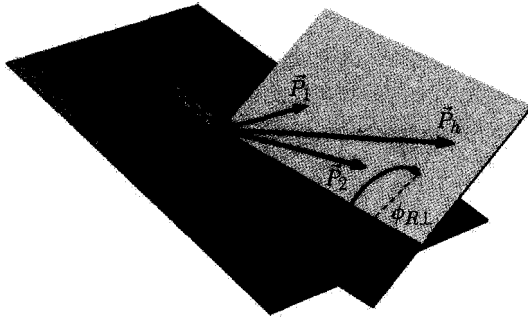


Fig. 1. Left: kinematic planes, where $\phi_{R\perp}$ is the angle between the plane spanned by the incident (k) and scattered leptons (k'), and the plane spanned by the two detected pions (P_1 and P_2 , with $P_h \equiv P_1 + P_2$). Right: the factor $\sin \delta_0 \sin \delta_1 \sin(\delta_0 - \delta_1)$, where the s- and p-wave phase shifts (δ_0 and δ_1) were obtained from pion-nucleon scattering experiments [8]. This factor shows the invariant mass-dependent part of $H_1^{\leftarrow,sp}$, as predicted by Jaffe *et al.* [5].

2. Single Spin Asymmetry

The transversity distribution can be accessed experimentally by measuring the single target-spin asymmetry, defined as:

$$A_{UL}(\phi_{R\perp}) = \frac{1}{|P_L|} \frac{N^{\rightarrow}(\phi_{R\perp})/N_d^{\rightarrow} - N^{\leftarrow}(\phi_{R\perp})/N_d^{\leftarrow}}{N^{\rightarrow}(\phi_{R\perp})/N_d^{\rightarrow} + N^{\leftarrow}(\phi_{R\perp})/N_d^{\leftarrow}} = \frac{\sigma_{UL}}{\sigma_{UU}}, \tag{1}$$

where N^{\rightarrow} (N^{\leftarrow}) is the number of $\pi^+\pi^-$ pairs detected with target spin anti-parallel (parallel) to the direction of the beam momentum. These numbers are normalized to the corresponding number of DIS events, N_d^{\rightarrow} and N_d^{\leftarrow} , respectively, and the entire ratio is divided by P_L , the longitudinal target polarization. The asymmetry is evaluated as a function of the azimuthal angle $\phi_{R\perp}$, which is shown in Fig. 1. In the last term, σ_{UL} and σ_{UU} are the polarized and unpolarized cross sections, respectively. According to Bacchetta *et al.* [6], σ_{UL} can be written at sub-leading twist as^a:

$$\sigma_{UL} \sim \sum_q e_q^2 \sin \phi_{R\perp} \sin \theta [K_1 |S_{||}| h_L - K_2 |S_{\perp}| h_1] (H_1^{\leftarrow,sp} + H_1^{\leftarrow,pp} \cos \theta), \tag{2}$$

where K_1 and K_2 are kinematic factors^b and θ is the angle between the direction of emission of the pion pair in its center-of-mass frame and P_h in the hadronic frame (see Fig. 1). Eq. 2 introduces the two-hadron interference fragmentation functions $H_1^{\leftarrow,sp}$ and $H_1^{\leftarrow,pp}$. They describe the interference between different production channels of the pion pair: $H_1^{\leftarrow,sp}$ relates to the interference between s- and p-wave states, and $H_1^{\leftarrow,pp}$ to the interference between two p-wave states. Both functions can be used *separately* to extract information on

^aEq. 2 was derived using the Wandzura-Wilczek approximation and is valid at low invariant mass $M_{\pi\pi}$ of the pion pair

^bSee the article by Bacchetta *et al.* [6] for the full expression.

the transversity distribution $h_1(x)$. In the present analysis the $\sin \phi_{R\perp}$ -moment of the asymmetry, $A_{UL}^{\sin \phi_{R\perp}}$ has been studied, which is sensitive only to $H_1^{\langle,SP}$, because in evaluating $A_{UL}^{\sin \phi_{R\perp}}$ the integral is taken over the polar angle θ .

A prediction has been given by Jaffe *et al.* [5] for the invariant-mass behavior of $H_1^{\langle,SP}$ in terms of s- and p-wave phase shifts. Fig. 1 shows that according to this model the asymmetry would change sign approximately at the ρ^0 mass. Note, however, that this model does not predict the size or sign of the asymmetry.

Two distribution functions appear in Eq. 2: the transversity distribution h_1 and the sub-leading-twist function h_L , which is related to h_1 through a Wandzura-Wilzcek relation. The contribution of these functions is proportional to the target polarization components transverse (S_{\perp}) and parallel (S_{\parallel}) to the virtual photon direction, respectively. In the data presented here the value of S_{\perp} increases from 3% of S_{\parallel} at low x to 9% at high x . For the present analysis, data were taken during the period 1998-2000 with a longitudinally polarized deuterium (gas) target. The average target polarization was 0.84 ± 0.04 .

3. Results

In Fig. 2 the $\sin \phi_{R\perp}$ -moment^c $A_{UL}^{\sin \phi_{R\perp}}$ is plotted versus the invariant mass of the pion pair^d $M_{\pi\pi}$ in panels of increasing x ($= Q^2/(2Mv)$) and z ($z \equiv E_{\pi\pi}/v$). The size of the asymmetries is on the order of a few percent. For all panels the asymmetries are not inconsistent with zero given the size of the statistical errors. No significant x - or z -dependence is observed. The shape of the asymmetries versus the invariant mass has been compared with the model prediction shown in Fig. 1. This was done by fitting the following function to the data:

$$f(M_{\pi\pi}) = c_1 \mathcal{P}(M_{\pi\pi}) + c_2 \quad (3)$$

where $\mathcal{P}(M_{\pi\pi})$ contains the invariant-mass dependence from the model prediction and c_1 and c_2 are free parameters of the fit. The resulting curves are included in Fig. 2. These curves show that in all panels, the results are consistent with the model. In the mid- x and low- z region the data hint at a sign change of the asymmetry at the ρ^0 mass.

Starting in 2002, HERMES has been taking data with a transversely polarized hydrogen target, with an average polarization of 0.78 ± 0.04 , which can result in much larger asymmetries. Data-taking will continue until the summer of 2005. The analysis of these data is ongoing and first results are expected in the near future.

References

1. A. Airapetian *et al.* (HERMES), *Phys. Lett. B* **562**, 182 (2003).
2. A. Airapetian *et al.* (HERMES), *Phys. Rev. Lett.* (in press), hep-ex/0408013.

^cUsing the definition of $\phi_{R\perp}$ shown in Fig. 1, $A_{UL}^{\sin \phi_{R\perp}}$ will differ by a sign, compared with the situation where the azimuthal angle is defined according to the Trento conventions [4].

^dFor these preliminary results, all hadron types were analyzed assuming they were pions. The corresponding uncertainty is not included in the quoted systematic error.

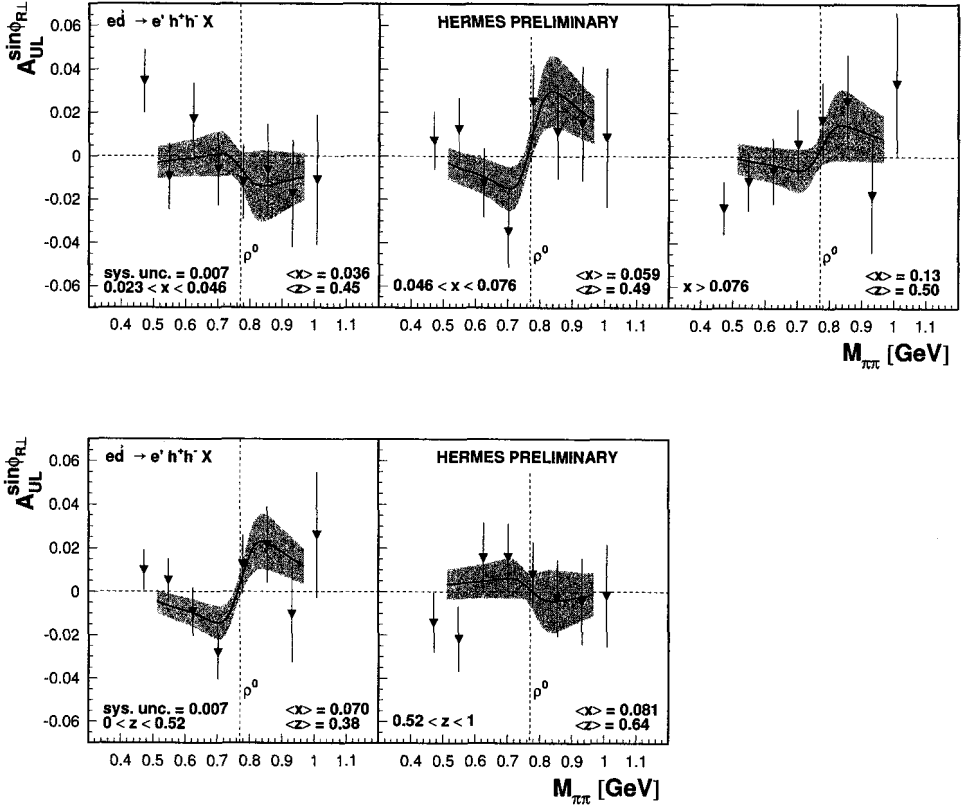


Fig. 2. The asymmetry-moment $A_{UL}^{\sin\phi_{RL}}$ as a function of the invariant mass $M_{\pi\pi}$ for different x -bins (top) and z -bins (bottom).

3. R. Seidl (Belle) these proceedings.
4. A. Bacchetta *et al.*, hep-ph/0410050 (2004)
5. R.L. Jaffe, X. Jin, and J. Tang. *Phys. Rev. Lett.* **80**, 1166 (1998).
6. A. Bacchetta and M. Radici, *Proceedings of DIS'2004* (2004), hep-ph/0407345.
7. A. Bacchetta and M. Radici, *Phys. Rev. D* **67**, 094002 (2003), hep-ph/0407345.
8. P. Estabrooks and A. Martin, *Nucl. Phys.* **B79**, 301 (1974).

TRANSVERSITY SIGNALS IN TWO-HADRON CORRELATION AT COMPASS

R. JOOSTEN

Helmholtz Institut für Strahlen- und Kernphysik, Bonn, Germany

(on behalf of the COMPASS Collaboration)

Measurement of two-hadron production, introducing the chiral odd interference fragmentation function H_1^{\perp} , is considered a new probe of the transverse spin distribution $\Delta_T q(x)$. COMPASS is a fixed target experiment on the SPS M2 beamline at CERN. Its target can be polarised both longitudinally and transversally with respect to the polarised 160 GeV/c μ^+ beam. In 2002, 2003, and 2004, 20% of the beam-time was spent in the transverse configuration on a ^6LiD target, allowing the measurement of transversity effects. First results of the analysis of two-hadron production will be reported.

1. Theoretical background

The cross-section for deep inelastic scattering on spin 1/2 hadrons can be parametrised, in leading order, in terms of three quark distribution functions: the helicity averaged distribution $q(x)$, the longitudinal helicity distribution $\Delta q(x)$, and the transverse spin distribution $\Delta_T q(x)$. This last distribution function, referred to as transversity, is chiral-odd and can be measured only in combination with another chiral-odd function. So far, attempts have been made to measure $\Delta_T q(x)$ in combination with the Collins fragmentation-function $\Delta D_a^h(z, p_T^h)$, requiring the partial detection of the hadronic products (semi-inclusive measurement) [1]. Another suggested and very promising probe is the measurement of two-hadron production, introducing the chiral-odd interference fragmentation function $H_1^{\perp}(z, M_h^2)$. The properties of interference fragmentation functions are described in [2–6].

At leading twist, the fragmentation function of a quark q into a pair h of hadrons h_1 and h_2 can be written as:

$$D_q^h(z, M_h^2) + H_1^{\perp}(z, M_h^2) \sin(\varphi_{RS}) \quad (1)$$

with $\varphi_{RS} = \varphi_R - \varphi_S = \varphi_R + \varphi_S - \pi$, where φ_S is the azimuthal angle of the struck quark, φ_S is the azimuthal angle of the initial quark spin, φ_R the angle of the hadron plane in the lepton scattering plane, and $\varphi_S = \pi - \varphi_S$. $z = z_1 + z_2 = (E(h_1) + E(h_2))/(E_l - E_{l'})$, E_l being the incoming and $E_{l'}$ the scattered lepton energy, is the fraction of the transferred energy carried by the two hadrons, and M_h^2 is their invariant mass squared. The angles are defined according to [7] (see Fig. 1), which follows the so-called *Trento conventions*.

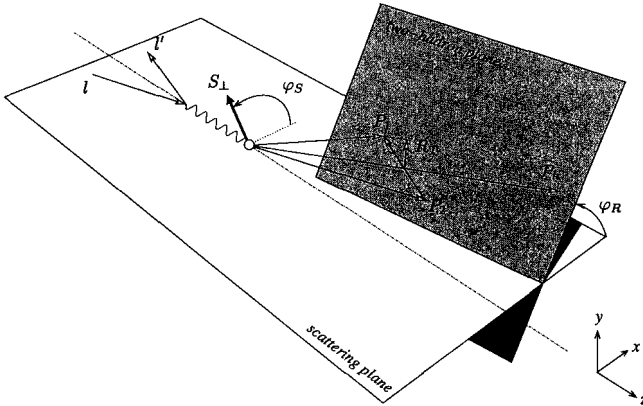


Fig. 1. Description of the angles involved in the measurement of single spin asymmetries in deep-inelastic production of two hadrons [7].

Therefore, an asymmetry is expected in the azimuthal angle of the hadron plane which depends on φ_{RS} . This asymmetry, which gives information on the transversity distribution, has not so far been measured on a transversely polarised target. A strong dependence of the fragmentation function $H_1^{\zeta}(z, M_h^2)$ on the invariant mass of the two-hadron system has even been predicted in the region of the ρ -mass [4], due to an interference term in two-pion production.

The measured raw asymmetry $A_{UT}^{\sin\varphi_{RS}}$ is connected to the physically relevant asymmetry $A_{\varphi_{RS}}$ by

$$\frac{A_{UT}^{\sin\varphi_{RS}}}{D_{NN}fP} = A_{\varphi_{RS}} = \frac{\sum_i e_i \Delta_T q_i(x) H_1^{\zeta h}(z, M_h^2)}{\sum_i e_i q_i(x) D_i^h(z, M_h^2)} \quad (2)$$

where f (≈ 0.4) is the dilution factor, P (≈ 0.45) the target polarisation, and $D_{NN} = (1 - y)/(1 - y + y^2/2)$ the depolarisation factor. Here, $y = (E_l - E_l')/E_l$ is the fraction of the incoming lepton energy transferred to the hadronic system.

2. Results from the COMPASS 2002 transversity run

The COMPASS experiment [8, 9] uses the high intensity 160 GeV secondary μ^+ -beam from π -decay in the CERN SPS M2 beamline. This beam is naturally longitudinally polarised with a polarisation of $\approx 76\%$.

The polarised target consists of two subsequent target cells filled with ${}^6\text{LiD}$, each 60 cm long, which can be individually polarised using separate RF-cavities. This allows data to be taken simultaneously on two target cells of opposite polarisation. The target can be polarised longitudinally or transversely with respect to the beam axis.

The data discussed here was taken in 2002 with a transversely polarised target. The sample consists of two data taking periods of approximately five days, where each period was split into two sub-periods with opposite spin orientation in the individual target cells.

The event selection is analogous to the analysis of the Collins and Sivers asymmetries [1]. The primary vertex, with identified incoming and scattered muon, is required to be in either of the two target cells. At least two hadrons are required to originate from the same vertex. The separation of muons and hadrons is primarily done by cutting on the amount of material traversed in the spectrometer. Moreover, the kinematic cuts $Q^2 > 1 (\text{GeV}/c)^2$, $W > 5 \text{GeV}/c^2$ and $0.1 < y < 0.9$ were applied to ensure a deep-inelastic scattering sample above nuclear resonances and within the COMPASS trigger acceptance. The final data sample had $x = 0.034$, $y = 0.33$, and $Q^2 = 2.7 (\text{GeV}/c)^2$ on average. The mean hadron multiplicity of the events selected by these kinematic cuts is 1.9 hadrons/event. As a first step, we selected the leading and next to leading hadron for further analysis. Here, the leading hadron is determined as the most energetic non-muonic charged particle of the primary vertex having $z > 0.25$. For the next to leading hadron, the second most energetic non-muonic charged particle from the primary vertex, no z cut is applied.

From the data, for each target cell and polarisation, the property

$$N(\varphi_{RS}) = N_0 \cdot (1 + A_{UT}^{\sin\varphi_{RS}} \cdot \sin\varphi_{RS}) \cdot F_{acc}(\varphi_{RS}) \quad (3)$$

can be derived, where $F_{acc}(\varphi_{RS})$ is the (unknown) angle dependant acceptance function of the detector. However, by comparing the sub-periods with opposite target spin, this acceptance function cancels, resulting in

$$A_{UT}^{\sin\varphi_{RS}} \cdot \sin\varphi_{RS} = \frac{N^\uparrow(\varphi_{RS}) - RN^\downarrow(\varphi_{RS})}{N^\uparrow(\varphi_{RS}) + RN^\downarrow(\varphi_{RS})} \quad (4)$$

where $R = N_{tot}^\uparrow/N_{tot}^\downarrow$ is the ratio of the events with opposite target polarisation. This procedure is repeated for both target cells and both periods. Finally, the weighted mean of the results is calculated.

The present status of the analysis does not yet allow results on the asymmetries to be stated. However, based on the first analysis and statistics, an error estimate for the 2002 data can be given. Fig. 2 shows the expected errors $\Delta A_{\varphi_{RS}} = \Delta A_{UT}^{\sin\varphi_{RS}} / D_{NN} fP$ vs. the invariant mass M_h of the hadron pair.

References

1. P. Pagano (COMPASS), these proceedings.
2. J.R. Collins, S.F. Heppelmann and G.A. Ladinsky, *Nucl. Phys.* **B420**, 565 (1994).
3. X. Artru and J. C. Collins, *Z. Phys.* **C69**, 277 (1996).
4. R. L. Jaffe, X. Jin and J. Tang, *Phys. Rev. Lett.* **80**, 1166 (1998).
5. A. Bianconi, S. Boffi, R. Jakob and M. Radici, *Phys. Rev.* **D62**, 034008 (2000).
6. A. Bacchetta and M. Radici, *Phys. Rev.* **D69**, 074026 (2004).
7. A. Bacchetta and M. Radici, Proceeding of DIS 2004, hep-ph/0407345 (2004).
8. G. Baum *et al.* [COMPASS Collaboration], CERN-SPSLC-96-14.
9. A. Bressan, "Recent results from COMPASS", these proceedings.

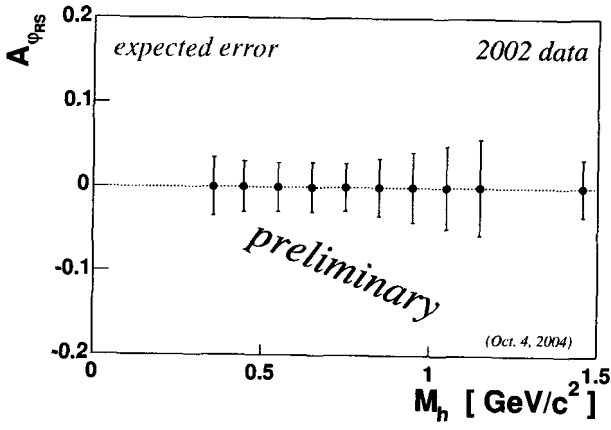


Fig. 2. Estimated error of the asymmetries $A_{\varphi_{RS}}$ for the 2002 data vs. invariant mass of the hadron pair. A binning of $100 MeV$ has been chosen except for the last point which covers the range from $1.2 GeV$ to $2.0 GeV$

TRANSVERSITY OF QUARKS AND NUCLEONS IN SIDIS AND DRELL-YAN

L. P. GAMBERG

Physics Department, Penn State-Berks, Reading, USA

G. R. GOLDSTEIN

Department of Physics and Astronomy, Tufts University Medford, Medford, USA

We consider the leading and sub-leading twist T -odd and -even contributions to the $\cos 2\phi$ azimuthal asymmetry in unpolarized dilepton production in Drell-Yan Scattering and semi-inclusive deep inelastic scattering of pions.

One of the persistent challenges confronting the QCD parton model is the explanation of the significant azimuthal and single spin asymmetries that emerge in inclusive and semi-inclusive processes [1–6]. Going beyond the collinear approximation in PQCD, recent progress has been achieved in characterizing these asymmetries in terms of absorptive scattering [7–9]. Such asymmetries involve time-reversal-odd (T -odd) transverse momentum dependent (TMD) distribution and fragmentation functions [10, 11]. They are indicative of correlations between transverse momentum of quarks and or hadrons, and the transverse spin of the reacting particles [12]. In SIDIS for unpolarized target, $s_T \cdot (p \times k_\perp)$ depicts a correlation of transverse quark polarization with the proton’s momentum and the intrinsic quark momentum in an unpolarized nucleon, while $s_T \cdot (p \times P_{h\perp})$, corresponds to that of a fragmenting quark’s polarization with quark and transverse pion momentum $P_{h\perp}$. These correlations enter the *unpolarized* cross-section convoluted with h_1^\perp [13] and the Collins fragmentation function H_1^\perp [11]. This $\cos 2\phi$ asymmetry is not suppressed by $1/Q$, where Q represents the hard QCD scale. Model estimates of absorptive scattering have led to colour gauge invariant [8, 14, 15] definitions of unsubtracted [16, 17] transverse momentum dependent distribution and fragmentation functions. h_1^\perp is projected from the correlation function for TMD distribution functions $\Phi(k, P)$, $\frac{1}{2} \int dk^- \text{Tr}(\sigma^{+\alpha} \gamma_5 \Phi(k, P)) = \dots \frac{\epsilon_{+ - \perp}^{\alpha} k_{\perp}^{\perp}}{M} h_1^\perp(x, k_\perp) \dots$. Similarly, the Collins function $H_1^\perp(z, p_\perp)$ is projected from the fragmentation matrix $\Delta(p, P_h)$. Using a parton model within the quark diquark spectator framework to model the quark-hadron interactions [9, 18]

$$h_1^\perp(x, k_\perp) = \frac{\mathcal{N}(m + xM)(1-x)e^{-2b(k_\perp^2 - \Lambda(0))}}{\Lambda(k_\perp^2)k_\perp^2} \left[\Gamma(0, 2b\Lambda(0)) - \Gamma(0, 2b\Lambda(k_\perp^2)) \right],$$

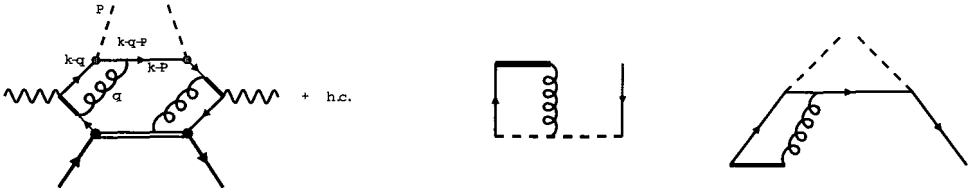


Fig. 1. Feynman diagram representing initial and final state interactions giving rise to T -odd contribution to quark distribution and fragmentation functions.

and the gauge link contribution to the Collins function are given by [19]

$$H_1^\perp(z, k_\perp) = \frac{\mathcal{N}' M_h \mu}{\Lambda(k_\perp^2) k_\perp^2} \frac{(1-z)e^{-2c(k_\perp^2 - \Lambda(0))}}{4z^3} \left[\Gamma(0, 2c\Lambda(0)) - \Gamma(0, 2c\Lambda(k_\perp^2)) \right].$$

Their contribution to the double T -odd azimuthal $\cos 2\phi$ asymmetry, in terms of initial and final (ISI/FSI) state interactions of active or “struck” and fragmenting quark [18, 19], are depicted in Fig. 1. Also, it was recognized by Boer [20] that the $\cos 2\phi$ azimuthal asymmetry in dilepton production in Drell-Yan scattering has a T -odd contribution at leading twist [21]. The latter process is interesting in the light of proposed experiments at Darmstadt GSI [22], where an anti-proton beam is ideal for studying transversity property of quarks due to the dominance of valence quark effects [23]. We explore the role that T -odd distribution and fragmentation functions play in unpolarized azimuthal asymmetries in SIDIS [18, 19, 23].

The angular asymmetries that arise in *unpolarized* Drell-Yan scattering [24] ($\bar{p} + p \rightarrow \mu^- \mu^+ + X$) and SIDIS [25] ($e + p \rightarrow e' hX$) are derived from the differential cross section expressions:

$$\frac{1}{\sigma} \frac{d\sigma}{d\Omega} = \frac{3}{4\pi} \frac{1}{\lambda + 3} \left(1 + \lambda \cos^2 \theta + \mu \sin^2 \theta \cos \phi + \frac{\nu}{2} \sin^2 \theta \cos 2\phi \right),$$

$$\frac{d\sigma}{dx dy dz dP_{h\perp}^2 d\phi_h} = A + B + C \cos \phi + D \cos 2\phi. \tag{1}$$

In the Drell-Yan process the angles refer to the lepton pair orientation in their rest frame relative to the boost direction and the initial hadron’s plane [24]. λ, μ, ν depend on s, x, m_μ^2, q_T . In SIDIS, the azimuthal angle refers to the relative angle between the hadron production plane and the lepton scattering plane. $A, B, C,$ and D are functions of $x, y, z, Q^2, |P_{h\perp}|$. ν is given by [20]

$$\nu_2 = \frac{\sum_a e_a^2 \mathcal{F} \left[(2\hat{h} \cdot k_\perp \cdot \hat{h} \cdot p_\perp - p_\perp \cdot k_\perp) h_1^\perp(x, k_\perp) \bar{h}_1^\perp(\bar{x}, p_\perp) / (M_1 M_2) \right]}{\sum_a e_a^2 \mathcal{F} \left[f_1(x, k_\perp) \bar{f}_1(\bar{x}, p_\perp) \right]}$$

where \mathcal{F} is the convolution integral. Collins and Soper [24] pointed out, well before h_1^\perp was identified, that there is a higher twist T -even contribution to the $\cos 2\phi$ asymmetry

$$\nu_4 = \frac{\frac{1}{Q^2} \sum_a e_a^2 \mathcal{F} \left[2(\hat{h} \cdot (k_\perp - p_\perp))^2 - (k_\perp - p_\perp)^2 f_1(x, k_\perp) \bar{f}_1(\bar{x}, p_\perp) \right]}{\sum_a e_a^2 \mathcal{F} \left[f_1(x, k_\perp) \bar{f}_1(\bar{x}, p_\perp) \right]}$$

This is not small at centre of mass energies of 50 GeV². We estimate the leading twist

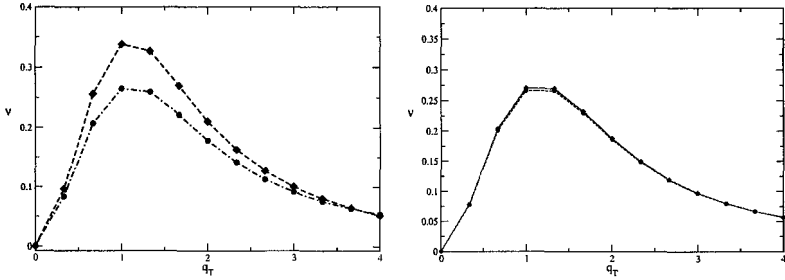


Fig. 2. v plotted as a function of q_T for $s = 50 \text{ GeV}^2$ and x in the range $0.2 - 1.0$, and q ranging from $2.5 - 5.0 \text{ GeV}$: Right panel: $s = 500 \text{ GeV}^2$ and q from $4.0 - 8.6 \text{ GeV}$.

2 and twist 4 contributions [23]. In Fig. 2, at a centre of mass energy of $s = 50 \text{ GeV}^2$, the T -odd portion contributes about 28% with an additional 10% from the sub-leading T -even piece. The distinction between the leading order T -odd and sub-leading order T -even contributions diminishes at a centre of mass energy of $s = 500 \text{ GeV}^2$. In Fig. 3, v is plotted versus x at $s = 50 \text{ GeV}^2$, where q_T ranges from 2 to 4 GeV. Again, the higher twist contribution is significant. In SIDIS a leading effect enters the $\cos 2\phi$ asymmetry with

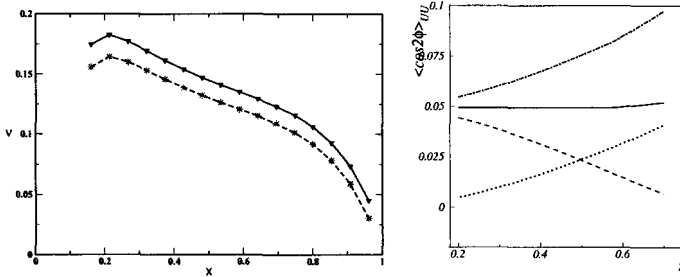


Fig. 3. Left panel: v plotted as a function of x for $s = 50 \text{ GeV}^2$ q_T ranging from 2 to 4 GeV. Right panel: The z -dependence of the $\cos 2\phi$ asymmetry at HERMES kinematics.

h_1^\perp convoluted with the Collins function, H_1^\perp [11]. The $\langle \cos 2\phi \rangle$ from ordinary sub-leading T -even and leading T -odd (up to a sign) contributions to order $1/Q^2$ is given by

$$\langle \cos 2\phi \rangle_{UU} = \frac{2 \frac{\langle k_\perp^2 \rangle}{Q^2} (1-y) f_1(x) D_1(z) \pm 8(1-y) h_1^{\perp(1)}(x) H_1^{\perp(1)}(z)}{\left[1 + (1-y)^2 + 2 \frac{\langle k_\perp^2 \rangle}{Q^2} (1-y) \right] f_1(x) D_1(z)}. \quad (2)$$

The z -dependence of this asymmetry at HERMES kinematics [6] is shown in the right panel of Fig. 3. The full and dotted curves correspond to the T -even and T -odd terms in the asymmetry, respectively. The dot-dashed and dashed curves are the sum and the difference of those terms. One can see that the double T -odd asymmetry behaves like z^2 , while the T -even asymmetry is flat over the whole range of z . Thus, aside from the competing T -even effect, the experimental observation of a strong z -dependence would indicate the presence

of T -odd structures in *unpolarized* SIDIS, implying that novel transversity properties of the nucleon can be accessed without invoking target polarization.

We conclude that T -odd correlations of intrinsic transverse quark momentum and transverse spin of reacting particles are intimately connected with studies of the $\cos 2\phi$ azimuthal asymmetries in Drell-Yan and SIDIS.

Work done in collaboration with G. R. Goldstein and K. A. Oganessyan. Acknowledgments to F. Pijlman, A. Metz and R. Seidl for useful discussions and the organizers of *SPIN04*.

References

1. K. Heller *et al.*, Phys. Rev. Lett. **41**, 607 (1978); Phys. Rev. Lett. **51**, 2025 (1983).
2. E615 Collaboration: J. S. Conway *et al.*, Phys. Rev. D **39**, 92 (1989).
3. E704 Collaboration: D. L. Adams *et al.*, Phys. Lett. B **261**, 210 (1991).
4. ZEUS Collaboration: J. Breitweg *et al.*, Phys. Lett. B **481**, 199 (2000).
5. STAR Collaboration: J. Adams *et al.* Phys. Rev. Lett. **92**, 171801, (2004).
6. A. Airapetian *et al.*, Phys. Rev. Lett. **84**, 4047 (2000); arXiv: hep-ex/0408013.
7. S. J. Brodsky, D. S. Hwang, and I. Schmidt, Phys. Lett. B **530**, 99 (2002).
8. X. Ji and F. Yuan, Phys. Lett. B **543**, 66 (2002).
9. G. R. Goldstein and L. P. Gamberg, arXiv:hep-ph/0209085, Proceedings ICHEP 2002.
10. D. Sivers, Phys. Rev. D **41**, 83 (1990).
11. J.C. Collins, Nucl. Phys. B **396**, 161 (1993).
12. M. Anselmino, M. Boglione and F. Murgia, Phys. Lett. B **362**, 164 (1995).
13. D. Boer and P. J. Mulders, Phys. Rev. D **57**, 5780 (1998).
14. J. C. Collins, Phys. Lett. B **536**, 43 (2002).
15. Daniel Boer, P.J. Mulders, F. Pijlman, Nucl.Phys. **B667**, 201 (2003).
16. J. C. Collins, Acta Phys. Polon. B **34**, 3103 (2003).
17. X. Ji, J. Ma, and F. Yuan; arXiv: hep-ph/0404183.
18. L. P. Gamberg, G. R. Goldstein and K.A. Oganessyan, Phys. Rev. D **67**, 071504 (2003).
19. L. P. Gamberg, G. R. Goldstein and K.A. Oganessyan, Phys. Rev. D **68**, 051501 (2003).
20. D. Boer, Phys. Rev. D **60**, 014012 (1999).
21. D. Boer, S. J. Brodsky, and D. S. Hwang, Phys. Rev D **67**, 054003 (2003).
22. *PAX* Letter of Intent, Jan. 15, 2003, Jülich; *ASSIA* Letter of Intent, Jan. 24, 2004.
23. L. P. Gamberg, G. R. Goldstein, and K. A. Oganessyan, arXiv:hep-ph/0411220.
24. J. Collins and D. E. Soper, Phys. Rev. D **16**, 2219 (1977).
25. R.N. Cahn, Phys. Lett. B **78**, 269 (1978); Phys. Rev. D **40**, 3107 (1989).

COMMENTS ON CAHN AND SIVERS EFFECTS IN SIDIS

M. ANSELMINO¹, M. BOGLIONE¹, U. D'ALESIO², A. KOTZINIAN³, F. MURGIA², A. PROKUDIN¹

¹Università di Torino and INFN, Sezione di Torino, Torino, Italy

²Università di Cagliari and INFN, Sezione di Cagliari, Cagliari, Italy

³Università di Torino and INFN, Sezione di Torino, Torino, Italy

The role of intrinsic k_{\perp} in semi-inclusive Deep Inelastic Scattering (SIDIS) processes ($\ell p \rightarrow \ell h X$) is studied within QCD parton model at leading order. The resulting picture is applied to the description of the weighted single spin asymmetry $A_{UL}^{\sin\phi_h}$ measured by HERMES. It is shown that these data could be described by the Siverts mechanism alone. However, the extracted Siverts functions fail to describe the HERMES data on $A_{UT}^{\sin(\phi_h - \phi_S)}$.

The role of intrinsic k_{\perp} is important in unpolarized SIDIS processes [1], and becomes crucial for the explanation of many single spin effects recently observed and still under active investigation in several ongoing experiments; spin and k_{\perp} dependences can couple in parton distributions and fragmentations, giving rise to unexpected effects in polarization observables. One such example is the azimuthal asymmetry observed in the scattering of unpolarized leptons off polarized protons [2, 3] and deuterons [4].

A recent analysis of SSA in $p^{\uparrow} p \rightarrow \pi X$ processes, with a separate study of the Siverts and Collins contributions, has been performed in [5] and [6] respectively, with the conclusion that the Siverts [7] mechanism alone can explain the data [8], while the Collins [9] mechanism is strongly suppressed.

We consider here the role of parton intrinsic motion in SIDIS processes within the QCD parton model at leading order. The average values of k_{\perp} for quarks inside protons, and p_{\perp} for final hadrons inside the fragmenting quark jet, are fixed by comparison with data [10] on the dependence of the unpolarized cross section on the azimuthal angle between the leptonic and hadronic planes, and on P_T . Such values are then used to compute the SSA for $\ell p^{\uparrow} \rightarrow \ell h X$ processes. We concentrate on the Siverts mechanism [7].

Within the factorization scheme, assuming an independent fragmentation process, the SIDIS cross section for the production of a hadron h in the current fragmentation region

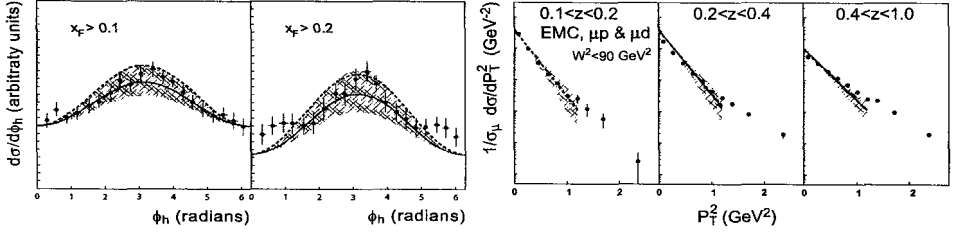


Fig. 1. Fits to the $\cos \phi_h$ dependence of the cross section and to $d\sigma/dP_T^2$.

with the inclusion of all intrinsic motions can be written as [11]

$$\frac{d^5 \sigma^{\ell p \rightarrow \ell h X}}{dx_B dQ^2 dz_h d^2 P_T} = \sum_q e_q^2 \int d^2 k_\perp f_q(x, k_\perp) \frac{2\pi\alpha^2}{x_B^2 s^2} \frac{\hat{s}^2 + \hat{u}^2}{Q^4} \times D_q^h(z, p_\perp) \frac{z}{z_h} \frac{x_B}{x} \left(1 + \frac{x_B^2 k_\perp^2}{x^2 Q^2}\right)^{-1}. \quad (1)$$

It is instructive, and often quite accurate, to consider the above equation in the much simpler limit in which only terms of $O(k_\perp/Q)$ are retained. In such a case $x \simeq x_B$, $z \simeq z_h$ and $p_\perp \simeq P_T - z_h k_\perp$. In what follows we assume, both for the parton densities and the fragmentation functions, a factorized Gaussian k_\perp and p_\perp dependence.

In this way the $d^2 k_\perp$ integration in Eq. (1) can be performed analytically, with the result, valid up to $O(k_\perp/Q)$:

$$\frac{d^5 \sigma^{\ell p \rightarrow \ell h X}}{dx_B dQ^2 dz_h d^2 P_T} \simeq \sum_q \frac{2\pi\alpha^2 e_q^2}{Q^4} f_q(x_B) D_q^h(z_h) \left[(1 + (1-y)^2) - 4 \frac{(2-y)\sqrt{1-y}\langle k_\perp^2 \rangle z_h P_T}{\langle P_T^2 \rangle Q} \cos \phi_h \right] \frac{1}{\pi \langle P_T^2 \rangle} e^{-P_T^2 / \langle P_T^2 \rangle}, \quad (2)$$

where $\langle P_T^2 \rangle = \langle p_\perp^2 \rangle + z_h^2 \langle k_\perp^2 \rangle$. The term proportional to $\cos \phi_h$ describes the Cahn effect [1].

By fitting the data [10] on unpolarized SIDIS we obtain the following values of the parameters: $\langle k_\perp^2 \rangle = 0.25 \text{ (GeV/c)}^2$, $\langle p_\perp^2 \rangle = 0.20 \text{ (GeV/c)}^2$. The results of the fits are shown in Fig. 1.

The unpolarized quark (and gluon) distributions inside a transversely polarized proton can be written as:

$$f_{q/p^\uparrow}(x, k_\perp) = f_{q/p}(x, k_\perp) + \frac{1}{2} \Delta^N f_{q/p^\uparrow}(x, k_\perp) S_T \cdot (\hat{P} \times \hat{k}_\perp), \quad (3)$$

where P and S_T are respectively the proton momentum and the transverse polarization vector, and k_\perp is the parton transverse momentum; transverse refers to the proton direction.

Eq. (3) leads to non-vanishing SSA, which can be calculated by substituting $f_{q/p}$ by f_{q/p^\uparrow} in Eq. (1). We parameterize, for each light quark flavour $q = u, d$, the Siverson function in the following factorized form: $\Delta^N f_{q/p^\uparrow}(x, k_\perp) = 2N_q(x) h(k_\perp) f_{q/p}(x, k_\perp)$, where $N_q(x) =$

$$N_q x^{a_q} (1-x)^{b_q} \frac{(a_q + b_q)^{(a_q + b_q)}}{a_q^{a_q} b_q^{b_q}}, \quad h(k_\perp) = \frac{2k_\perp M}{k_\perp^2 + M^2}, \quad \text{with } M^2 = \langle k_\perp^2 \rangle = 0.25 \text{ (GeV/c)}^2.$$

Our fit to the HERMES $A_{UL}^{\sin\phi_h}$ data [2] results in the following best values for the free parameters: $N_u = -1.0$, $N_d = 1.0$, $a_u = 0.1$, $a_d = 0.1$, $b_u = 0.3$, $b_d = 0.3$. The result of the fit is presented in the upper part of Fig. 2.

Having fixed all the parameters we can check the consistency of the model by computing $A_{UL}^{\sin\phi_h}$ for kaon and pion production on a deuteron target [4]; our results are given in the lower part of Fig. 2, showing very good agreement with data.

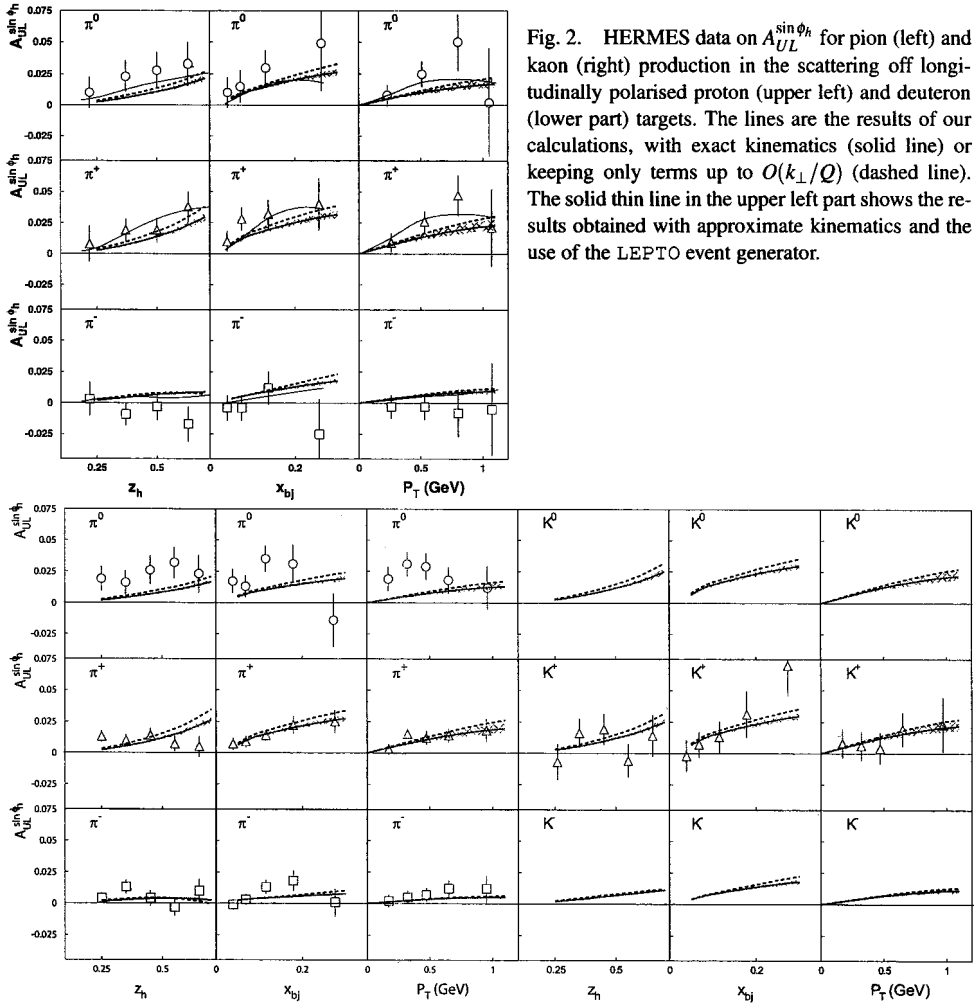


Fig. 2. HERMES data on $A_{UL}^{\sin\phi_h}$ for pion (left) and kaon (right) production in the scattering off longitudinally polarised proton (upper left) and deuteron (lower part) targets. The lines are the results of our calculations, with exact kinematics (solid line) or keeping only terms up to $O(k_{\perp}/Q)$ (dashed line). The solid thin line in the upper left part shows the results obtained with approximate kinematics and the use of the LEPTO event generator.

Looking only at the set of proton HERMES data [2] on $A_{UL}^{\sin\phi_h}$, one could conclude that the Sivers mechanism alone can explain such data and that the resulting model works well also for a deuteron target. However, one should not forget that the weighted SSA $A_{UL}^{\sin\phi_h}$ can also originate from the Collins mechanism and higher-twist contributions.

More recently, HERMES data on $A_{UT}^{\sin(\phi_h - \phi_s)}$ have become available [3]. Such data sin-

gle out the contribution of the Siverson mechanism alone. Therefore, we have computed $A_{UT}^{\sin(\phi_h - \phi_S)}$ with the Siverson functions extracted from $A_{UL}^{\sin\phi_h}$, under the assumption that only the Siverson mechanism is responsible for $A_{UL}^{\sin\phi_h}$. Our results for $A_{UT}^{\sin(\phi_h - \phi_S)}$ turn out to be much too large, and with opposite sign, when compared with HERMES data. This definitely shows that the observed $A_{UL}^{\sin\phi_h}$ must be dominated by contributions from higher-twist and/or Collins effects.

A direct extraction of the Siverson functions should be (and has been) performed [11] by first fitting the data on $A_{UT}^{\sin(\phi_h - \phi_S)}$. One can then check that, in such a case, the contribution of the extracted Siverson functions to $A_{UL}^{\sin\phi_h}$ is negligible [11].

References

1. R.N. Cahn, *Phys. Lett.* **B78** 269 (1978), *Phys. Rev.* **D40** 3107 (1989)
2. A. Airapetian *et al.*, HERMES Coll., *Phys. Rev. Lett.* **84** 4047 (2000); *Phys. Rev.* **D64** 097101 (2001)
3. A. Airapetian *et al.*, HERMES Coll., e-Print Archive: hep-ex/0408013
4. A. Airapetian *et al.*: HERMES Coll., *Phys. Lett.* **B562** 182 (2003)
5. U. D'Alesio and F. Murgia, *Phys. Rev.* **D70** 074009 (2004)
6. M. Anselmino, M. Boglione, U. D'Alesio, E. Leader and F. Murgia, e-Print Archive: hep-ph/0408356, (*Phys. Rev. D* in press)
7. D. Siverson, *Phys. Rev.* **D41** 83 (1990) ; **D43** 261 (1991)
8. D.L. Adams *et al.*, *Phys. Lett.* **B264** 462 (1991) ; A. Bravar *et al.*, *Phys. Rev. Lett.* **77** 2626 (1996)
9. J.C. Collins, *Nucl. Phys.* **B396** 161 (1993)
10. J.J. Aubert *et al.*: EMC Coll., *Phys. Lett.* **B130** 118 (1983); M. Arneodo *et al.*: EMC Coll., *Z. Phys.* **C34** 277 (1987); Fermilab E665 Coll., M.R. Adams *et al.*, *Phys. Rev.* **D48** 5057 (1993)
11. M. Anselmino, M. Boglione, U. D'Alesio, A. Kotzinian, F. Murgia, A. Prokudin, in preparation.

LONGITUDINAL POLARIZATION OF Λ AND $\bar{\Lambda}$ HYPERONS IN DEEP-INELASTIC SCATTERING AT COMPASS

V. Y. ALEXAKHIN

Joint Institute for Nuclear Research, Dubna, Russia

(on behalf of the COMPASS Collaboration)

The study of longitudinal polarization of Λ ($\bar{\Lambda}$) hyperons in deep-inelastic scattering is important because it can provide information on the fundamental properties of the nucleon, such as polarization of the strange quarks in the nucleon, and can determine the mechanism of spin transfer from a polarized quark to a polarized baryon. The production of Λ and $\bar{\Lambda}$ by polarized μ^+ s of 160 GeV/c on a polarized ${}^6\text{LiD}$ target has been studied using the COMPASS spectrometer. An important feature of the COMPASS experimental data sample is a large number of $\bar{\Lambda}$ hyperons, which is comparable with the number of Λ s. Preliminary results on the longitudinal polarization of Λ and $\bar{\Lambda}$ hyperons produced in the deep-inelastic scattering will be presented for the 2002 data set.

Measurements of Λ polarization in the target fragmentation region provide important information on the fundamental properties of the nucleon, such as the role of the $\bar{s}s$ pairs in the proton wave function [1]. The polarized nucleon intrinsic strangeness model [2, 3] predicts negative longitudinal polarization of Λ hyperons produced in target fragmentation region. The measurement of the Λ polarization in the current fragmentation region allows the investigation of another phenomenon, namely spin transfer from polarized quark to a polarized baryon. Recent theoretical models of Λ polarization in DIS can be found in [4]–[8]. Another interesting topic is the study of possible quark-antiquark asymmetries, in the quark to Λ fragmentation functions and/or in the quark and antiquark distributions of the target nucleon. Model calculations [8] show that spin transfer to Λ and $\bar{\Lambda}$ should be the same if standard quark distributions $s(x) = \bar{s}(x)$ are used. However there are difficulties in the interpretation of the results due to large contribution from the diquark fragmentation [3], and the significant fraction of Λ hyperons produced via decays of heavier hyperons.

The experimental situation for Λ and $\bar{\Lambda}$ production in DIS is summarized in Table 1. One can see that in the target fragmentation region the Λ polarization is negative; the spin transfer for current fragmentation region seems to be small.

COMPASS has studied Λ and $\bar{\Lambda}$ production by polarized muons of 160 GeV/c on a polarized ${}^6\text{LiD}$ target. The COMPASS spectrometer was constructed in the framework of

Table 1. Summary of experimental measurements of Λ hyperon polarization in DIS. The sign of polarization is given with respect to the virtual photon momentum.

Reaction Exp.	$\langle E_b \rangle$ (GeV)	x_F	N_Λ	P_Λ	$N_{\bar{\Lambda}}$	$P_{\bar{\Lambda}}$
$\bar{\nu}_\mu N_e$	40	$x_F < 0$	403	-0.63 ± 0.13		
WA59 [12]		$x_F > 0$	66	-0.11 ± 0.45		
μN	470	$0 < x_F < 0.3$	750	0.42 ± 0.17	650	-0.09 ± 0.20
E665 [13]		$x_F > 0.3$		0.09 ± 0.19		-0.31 ± 0.22
$\nu_\mu N$	43.8	$x_F < 0$	5608	-0.21 ± 0.04	248	0.23 ± 0.20
NOMAD [14]		$x_F > 0$	2479	-0.09 ± 0.06	401	-0.23 ± 0.15
eN	27.5	$x_F > 0$	16900	$\frac{P_\Lambda}{P_{BD}} =$	2500	
HERMES [15]				0.06 ± 0.09		

CERN experiment NA58 [9]. The total amount of collected data during the run in 2002 is about 260 TB, with a typical event size of 35 kB. This analysis uses all 2002 data obtained with the target longitudinally polarized. The data presented here are averaged over target polarization.

The selection criteria of Λ , $\bar{\Lambda}$ and K_s^0 (V^0) are the following. The primary vertex should be inside target cells, whereas the decay vertex of V^0 must be outside the target. The angle between the V^0 momentum and the vector between primary and V^0 vertices should be $\theta_{col} < 0.01$ rad. A cut on the transverse momentum of the decay products with respect to the direction of V^0 particle $p_t > 23$ MeV/c was applied to reject e^+e^- pairs from γ conversion. The standard DIS cuts $Q^2 > 1$ (GeV/c)² and $0.2 < y < 0.8$ have been used. After background subtraction, the experimental sample contains about 8000 Λ and 5000 $\bar{\Lambda}$. COMPASS is able to access mostly current fragmentation region with $\langle x_F \rangle = 0.2$, $\langle y \rangle = 0.45$, $\langle x_{Bj} \rangle = 0.02$ and $\langle Q^2 \rangle = 2.62$ (GeV/c)². The mean Λ momentum is 12 GeV/c, while the mean decay pion momentum is 2 GeV/c. Λ ($\bar{\Lambda}$) hyperon polarization can be measured via the asymmetry in the angular distribution of decay particles in $\Lambda \rightarrow p\pi^-$ ($\bar{\Lambda} \rightarrow \bar{p}\pi^+$) decays. We define the X-axis to be along the direction of the virtual photon in the V^0 rest frame. The angular distribution in the Λ ($\bar{\Lambda}$) rest frame is

$$\frac{dN}{d\cos\theta_X} = \frac{N_{tot}}{2}(1 + \alpha P \cos\theta_X) \quad (1)$$

where N_{tot} is the total number of events, $\alpha = +(-)0.642 \pm 0.013$ is Λ ($\bar{\Lambda}$) decay parameter, P is the projection of the polarization vector on the corresponding axis, and θ_X is the angle between the direction of the decay particle (proton for Λ , antiproton for $\bar{\Lambda}$) and X-axis. The acceptance correction was determined using unpolarized Monte Carlo simulation. The DIS events are produced by LEPTO 6.5.1 generator [10] and the apparatus is described by a full GEANT 3.21 [11] model.

The analysis was performed by slicing each angular distribution into ten bins and fitting the invariant mass distribution of the V^0 peak to obtain the number of events in the bin. Corrected angular distributions were fitted using equation (1).

The results for longitudinal polarization are $P_{K_s^0} = 0.007 \pm 0.017(stat.)$, $P_\Lambda = 0.03 \pm 0.04(stat.) \pm 0.04(syst.)$ and $P_{\bar{\Lambda}} = -0.11 \pm 0.06(stat.) \pm 0.05(syst.)$. All results were averaged over accessible kinematical region.

The spin transfer variable from beam to Λ was calculated as $S = \frac{P_\Lambda}{P_{BD}}$, where P_B is the

beam polarization and $D = (1 - (1 - y)^2) / (1 + (1 - y)^2)$ is the virtual photon depolarization factor. Spin transfer for world and COMPASS data are presented in Fig. 1 (Λ hyperons) and Fig. 2 (for $\bar{\Lambda}$ hyperons). Only points with $x_F > 0$ are shown. One can see that there is reasonable agreement between COMPASS and world data. There is an indication that spin transfer to $\bar{\Lambda}$ is non-zero and might be different from the Λ one.

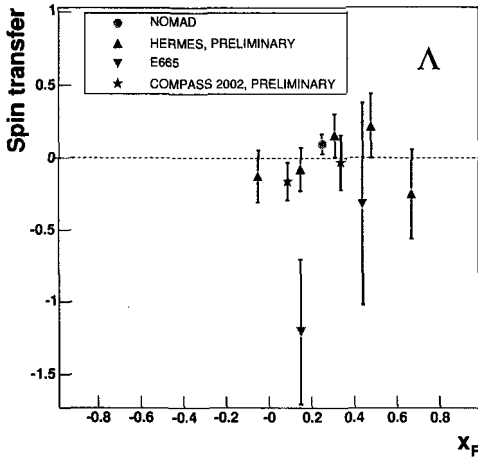


Fig. 1. Spin transfer for Λ hyperons.

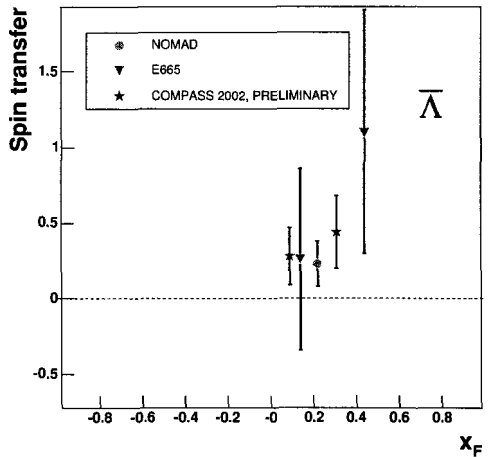


Fig. 2. Spin transfer for $\bar{\Lambda}$ hyperons.

The COMPASS 2002 data show good potential for Λ and $\bar{\Lambda}$ hyperon polarization measurement. Data samples collected in 2003 and 2004 will significantly increase the statistics.

References

1. J. Ellis et al, Phys.Lett., **B353** (1995) 319; Nucl.Phys., **A673** (2000) 256
2. J. Ellis, D. Kharzeev, A.M. Kotzinian, Z.Physik **C69** (1996) 467
3. J. Ellis, A.M. Kotzinian and D.V. Naumov, Eur. Phys. J., **C25** (2002) 603
4. M. Burkardt and R. L. Jaffe, Phys. Rev. Lett. **70** (1993) 2537
5. M. Anselmino, M. Boglione, U. D'Alesio, E. Leader and F. Murgia, Phys. Lett. B **509** (2001) 246,
6. A. M. Kotzinian, A. Bravar and D. von Harrach, Eur. Phys. J. **C2** (1998) 329,
7. C. Boros and L. Zuo-Tang, Phys. Rev. **D57** (1998) 4491.
8. B. Q. Ma, I. Schmidt, J. Soffer and J. J. Yang, Phys. Lett. **B488** (2000) 254
9. A. Bressan, contribution to these proceedings.
10. G. Ingelman, A. Edin and J. Rathsman Comp. Phys. Comm. **101** (1997) 108
11. GEANT, CERN Program Library Long Writeup W5013
12. Willocq S. et al. [WA59 Collaboration], Z.Phys. **C53**, (1992) 207
13. M. R. Adams et al. [E665 Collaboration], Eur. Phys. J. **C17** (2000) 263
14. P. Astier et al., [NOMAD Collaboration], Nucl. Phys. **B588** (2000) 3;
P. Astier et al. [NOMAD Collaboration], Nucl. Phys. **B605** (2001) 3
15. A. Airapetian et al. [HERMES Collaboration], Phys. Rev. **B64** (2001) 112005 S. Belostotski, talk at this conference.

MEASUREMENT OF TRANSVERSE Λ POLARISATION AT COMPASS*

J. M. FRIEDRICH

Physik Department, Technische Universität München, München, Germany

(on behalf of the COMPASS Collaboration)

Preliminary data on spontaneous transverse Lambda polarisation obtained at COMPASS are presented. While Λ polarisation transverse to the production plane is a well-established experimental fact in hadronic high-energy collisions, the underlying polarisation mechanism is not yet settled. COMPASS extends this field to high-energy photo production. We have extracted the polarisation at different values of the Feynman variable x_F and transverse momentum p_T . A bias-cancelling method has been used to reduce systematic effects.

1. Introduction

The polarisation of Λ particles from various high-energy processes is of interest in many respects. With polarised target or projectile, the respective spin dependent polarisation transfer can be understood in terms of polarised distribution and fragmentation functions [1], in the longitudinal as well as the transverse case. However, it has been known for a long time that polarisation of Λ is also observed in the collision of unpolarised particles, first in hadronic reactions at Fermilab [2]. This polarisation in proton-nucleus scattering is transverse to the production plane, and is found to be negative, as it almost always is for other hyperons, and linearly increasing with the transverse momentum of the Λ up to values of about 20%. The effects can at least be qualitatively understood in the phenomenological model of DeGrand and Miettinen [3], where the polarisation is explained semi-classically as a spin precession effect of the accelerated or decelerated strange quark.

COMPASS offers is able to study all aspects of Λ polarisation in detail, using muon and hadron beams on polarised and unpolarised targets. The analysis presented here considers the case of spontaneous transverse polarisation of Λ particles from a collision of a quasi-real photon with a nucleon. The coordinate system used is depicted in Fig. 1.

*This work is supported by BMBF and Maier-Leibnitz-Labor of LMU and TU Munich

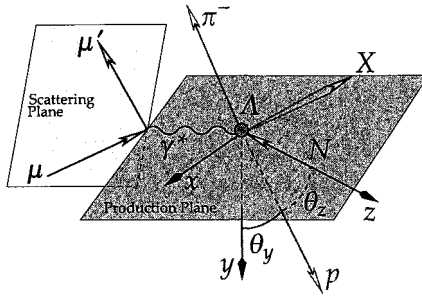


Fig. 1. Coordinates in the rest system of the produced Λ . The z axis is chosen along the Λ momentum in the laboratory frame, antiparallel to the target nucleon momentum in the Λ rest system. The y axis is normal to the production plane $y = \gamma \times z$, and $x = y \times z$

2. Measurement at COMPASS

COMPASS is a fixed target experiment at the CERN Super Proton Synchrotron, and accumulated data in 2002, 2003 and 2004. The analysis described in the following has been performed on the data taken in 2002, where a muon beam of 160 GeV/c momentum hit a solid-state ${}^6\text{LiD}$ target, which was polarised about 20% of the beam time transversely to, and 80% longitudinally with, the beam direction. Only data with longitudinally polarized target are considered in this analysis.

The tracks of the outgoing particles are measured in the spectrometer [4] with two stages for low and high momenta, respectively, each equipped with a combination of tracking detectors and calorimetry. Muons are identified using iron and concrete filters, especially in front of the trigger scintillator system.

The events are required to have a primary interaction with a fully reconstructed beam particle and scattered muon inside the polarised target volume. All vertices with two outgoing particles, not identified as muons of opposite charge, are investigated with the positive track assumed to be a p (π^+) and the negative to be a π^- (\bar{p}), to obtain the mass of the Λ ($\bar{\Lambda}$).

In order to suppress background from converted photons, small longitudinal decay angles are cut at $-0.7 < \cos \theta_z < 0.8$.

The Λ reveals its polarisation in the angular asymmetry of the weak decay $\Lambda \rightarrow p\pi^-$, with analysing power $\alpha = 62.4\%$. In order to reduce systematic effects, the complete sample is divided into two subsamples U and D , with the Λ momentum pointing up or down in the laboratory frame. Due to the parity flip when mirroring processes in the up and down halves of the spectrometer, the acceptances for the subsamples $U_+ = U(+\cos \theta_y)$ and $D_- = D(-\cos \theta_y)$ are related. It follows that in the definition

$$R = \frac{\sqrt{U_+ D_+} - \sqrt{U_- D_-}}{\sqrt{U_+ D_+} + \sqrt{U_- D_-}} = \alpha P_y \cos \theta_y, \quad (1)$$

acceptance effects (such as the cut in θ_z) cancel, and P_y can be directly extracted by fitting the distribution of R defined in Eq. 1.

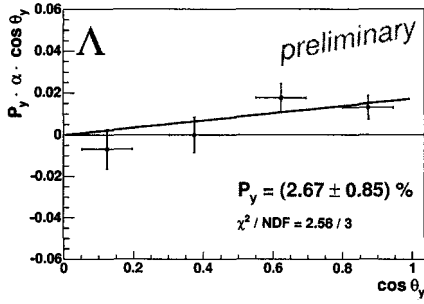


Fig. 2. The experimental data, presented in the form of Eq. 1

The distribution for Λ , including the fit result, is shown in Fig. 2, and the complete list of extracted polarisations for all examined particles is given in Fig. 3.

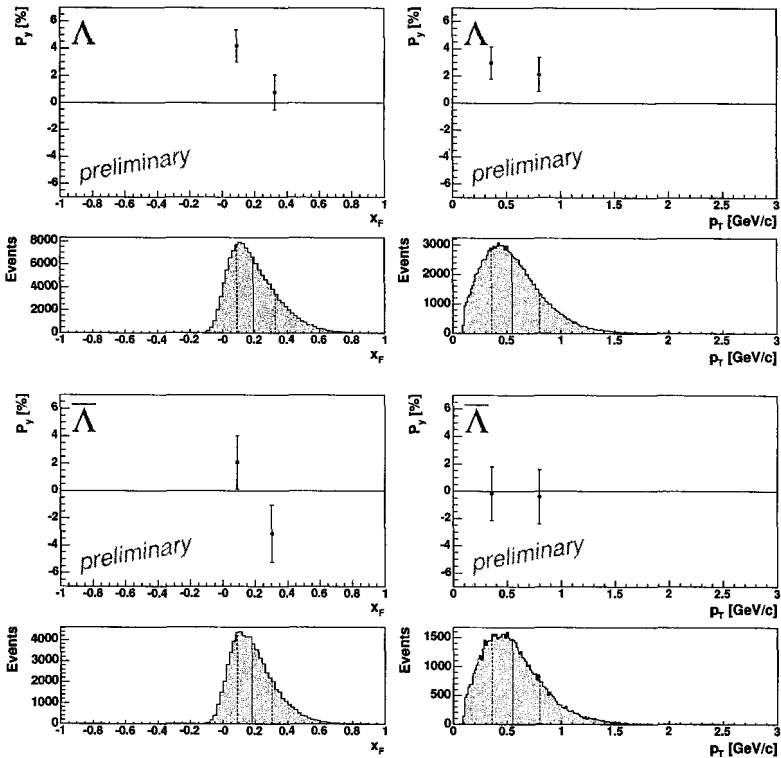


Fig. 3. Transverse Λ (upper plots) and $\bar{\Lambda}$ (lower plots) polarisation dependent on kinematical variables x_F (left) and p_T (right). The respective distributions of these variables are also shown.

3. Discussion

The spontaneous transverse polarisation of Λ produced in the collision of quasi-real photons on nucleons is found to be on average $+2.67 \pm 0.85\%$ in the kinematical range examined, while the polarisation of $\bar{\Lambda}$ is consistent with zero. The cross check on kaons yielded the expected unpolarised result.

The transverse Λ polarisation is positive, which may be understood in the semi-classical model of DeGrand and Miettinen [3] via the deceleration of a leading strange quark stemming from the hadronic $s\bar{s}$ component of the photon. The polarisation effect shows some increase towards smaller x_F , while no significant dependence on p_T is found. A significant increase in the number of reconstructed hyperons in the 2003 and 2004 data will allow more quantitative conclusions to be drawn.

References

1. M. Anselmino, Talk at Future Physics at COMPASS workshop, CERN Sept. 2002, hep-ph/0302008, and references herein
2. J. Lach, FERMILAB-Conf-92/378, and references herein
3. T.A. DeGrand, H.I. Miettinen, Phys. Rev. D24 (1981) 2419
4. G.K. Mallot f. the COMPASS collaboration, Nucl. Instr. Meth. A518(2004)121

HYPERON PRODUCTION AT HERMES

S. L. BELOSTOTSKI

Petersburg Nuclear Physics Institute, Gatchina, St Petersburg

(for the HERMES Collaboration)

A brief overview of hyperon production at HERMES is presented. The data were accumulated by the HERMES spectrometer using the 27.5 GeV longitudinally polarized HERA positron beam and the unpolarized (polarized) internal gas target. Semi-inclusive reactions with polarized Λ^0 hyperon in the final state have been studied. At the average fractional Λ energy $\langle z \rangle = 0.45$, the longitudinal spin transfer coefficient to the Λ^0 hyperon is found to be $0.04 \pm 0.08(stat) \pm 0.03(syst)$. The HERMES experiment has measured the transverse polarization of the Λ and $\bar{\Lambda}$ hyperons produced inclusively in quasi-real photon-nucleon interaction. Inclusively produced Σ^0 , Σ^{*+} , Σ^{*-} , and Ξ^- hyperons and their antiparticles have also been detected by the HERMES spectrometer.

1. Introduction. Λ hyperon spin structure

It is well-known that the spin structure of the proton and other baryons is non-trivial. In this respect the Λ^0 hyperon is of particular interest, as it is the lightest strange baryon of the SU(3)-flavour symmetry spin- $\frac{1}{2}$ octet. Using SU(3)-flavour symmetry formalism in conjunction with the experimental results on proton spin flavour decomposition [1], one obtains for the first moments of the spin-dependent quark distributions in the Λ^0 hyperon: $\Delta u^\Lambda + \Delta \bar{u}^\Lambda = \Delta d^\Lambda + \Delta \bar{d}^\Lambda = -0.07 \pm 0.06$ and $\Delta s^\Lambda + \Delta \bar{s}^\Lambda = 0.49 \pm 0.07$. According to this estimate, the u and d quarks in the Λ^0 hyperon carry a weak but non-zero net polarization opposite to the Λ^0 spin, whereas the Λ^0 spin direction is mostly defined by the s quark spin state.

One experimental possibility to probe hyperon spin structure is to measure spin transfer coefficients from a polarized quark to the (Λ^0) hyperon produced in the process of fragmentation. Longitudinal spin transfer was first studied by LEP experiments at an energy corresponding to the Z^0 pole [2, 3]. The OPAL and ALEPH (LEP) data show a significant polarization transfer from the $s(\bar{s})$ quark to the $\Lambda(\bar{\Lambda})$, thus confirming that Δs^Λ contribution dominates Λ spin.

In contrast to the LEP experiments, production of Λ^0 hyperons in the deep inelastic lepton scattering originated predominately from the u and d quarks in the proton [4, 5].

The HERMES spectrometer [9] has made a preliminary measurement of the longitudinal spin transfer to the Λ^0 using the 27.5 GeV polarized positron beam of the HERA

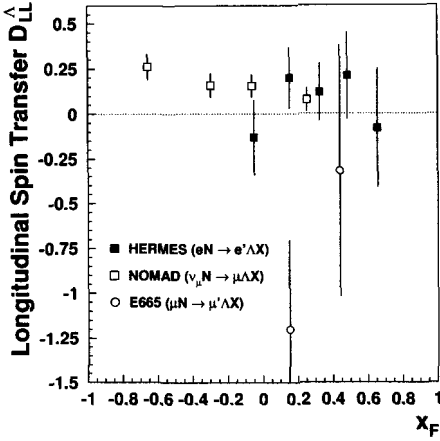


Fig. 1. Compilation of data on longitudinal spin transfer to the Λ^0 in lepton deep inelastic scattering.

In the Quark-Parton Model (QPM), spin-transfer integrated over x (the Bjorken variable) in the current-fragmentation region is expressed as follows [7, 8]:

$$D_{LL'}^{\Lambda}(z, Q^2) = \sum_q \omega_q^{\Lambda}(z, Q^2) D_{LL',q}^{\Lambda}(z, Q^2), \quad (1)$$

where the purity ω_q^{Λ} is the net probability that a Λ^0 was produced from a struck quark of flavour q , and $z = E_{\Lambda}/\nu$ is the fraction of the energy transfer $\nu = E - E'$ from the beam which is carried by the Λ^0 .

The ‘‘partial’’ spin transfer from a quark of flavour q to a Λ^0 hyperon $D_{LL',q}^{\Lambda}$ is defined by the process of fragmentation and cannot be evaluated at present from first principles. On the other hand, it is closely related to the spin structure of the produced Λ hyperon: $D_{LL',q}^{\Lambda} \simeq \frac{\Delta q^{\Lambda}}{q^{\Lambda}}$. The HERMES $D_{LL'}^{\Lambda}$ data plotted versus the Feynman- x variable x_F , together with NOMAD [4] and E665 [5] results, are shown in Fig.1. The average over the HERMES data set longitudinal spin transfer is found to be $D_{LL'}^{\Lambda} = 0.04 \pm 0.08(stat) \pm 0.03(syst)$ at the average $\langle z \rangle = 0.45$.

3. Transverse Λ^0 and $\bar{\Lambda}^0$ polarization

The HERMES experiment has measured the transverse polarization of Λ and $\bar{\Lambda}$ hyperons produced inclusively in quasi-real photon-nucleon interactions at a positron beam energy of 27.6 GeV. Since the scattered positron is not detected, the only possible direction of the measured polarization is along the normal to the Λ ($\bar{\Lambda}$) production plane. Dependences of measured polarizations on transverse Λ ($\bar{\Lambda}$) momentum p_T are shown in Fig.2. The data analysis is not yet finalized, and the presented results are very preliminary. A substantial

collider and the unpolarized gas target. This result [6] was based on very limited statistics.

In this talk the longitudinal spin transfer data with much better statistics ($\simeq 7000\Lambda^0$ events with $Q^2 > 0.8 \text{ GeV}^2$), allowing binning in z and x_f variables, are presented. Besides, we report here very briefly on transverse polarization of Λ^0 hyperons produced in photoproduction regime ($Q^2 \approx 0$), and on the detection of hyperons heavier than Λ^0 .

2. Longitudinal spin transfer to the Λ^0

In deep inelastic lepton scattering from an unpolarized target, the struck quark will acquire a polarization $P_q = P_b D_y$, where P_b is the beam polarization, and D_y describes the ‘‘depolarization’’ of the virtual photon. The polarization of the Λ^0 hyperon is then given by $P_{\Lambda} = P_b D(y) D_{LL'}^{\Lambda}$, where $D_{LL'}^{\Lambda}$ is the spin transfer coefficient.

part of the Λ^0 and $\bar{\Lambda}^0$ hyperons detected by HERMES originates from the decay of Σ^0 , $\Sigma(1385)$, Ξ , and their antiparticles. Measurement of the hyperon yields and hyperon polarization is of importance for Monte Carlo analysis of Λ^0 and $\bar{\Lambda}^0$ polarizations. Typical invariant mass spectra obtained at HERMES by detection of a Λ^0 ($\bar{\Lambda}^0$) in coincidence with a pion are shown in Fig.3. The Ξ and $\Sigma(1385)$ hyperons decaying to $\Lambda\pi$ are clearly identified in these spectra.

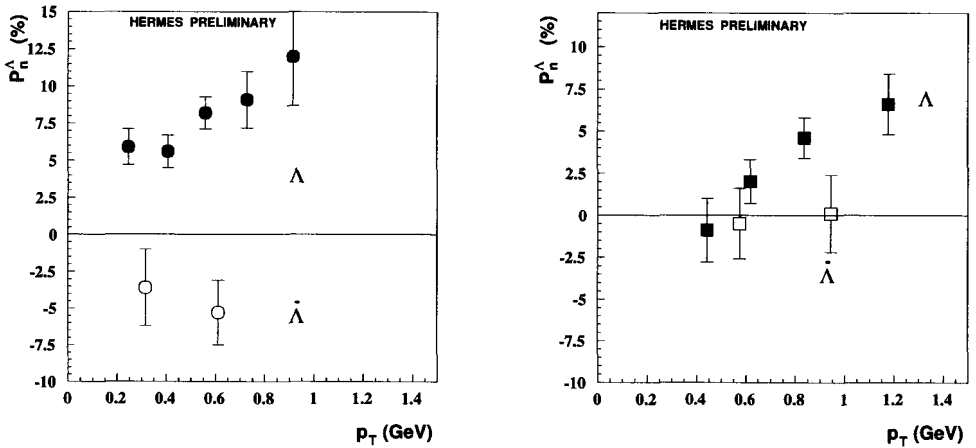


Fig. 2. Dependence of P_n on transverse Λ and $\bar{\Lambda}$ momentum for low longitudinal momenta $p_z/p_{beam} < 0.25$ (left panel) and for high longitudinal momenta $p_z/p_{beam} > 0.25$ (right panel).

4. Outlook

A substantial increase of the hyperon rate is expected after the Recoil Detector (RD) is installed this year. The RD, together with LW [10] (forward silicon detector), will provide practically full coverage for detection of the hyperons emitted from the target at large angles (compared to the standard HERMES acceptance), and increase considerably the hyperon detection efficiency, particularly in the target fragmentation region.

References

1. HERMES Collab., A. Airapetian *et al.*, *Phys. Rev. Lett.* **92**, 012005 (2004).
2. OPAL Collab., K. Ackerstaff *et al.*, *Eur. Phys. J. C.* **2**,49 (1998).
3. ALEPH Collab., D. Buskulic *et al.*, *Phys. Rev. Lett.* **374**, 319 (1996).
4. NOMAD Collab., P. Astier *et al.*, *Nucl. Phys.B* **588**,3 (2000).
5. E665 Collab., M.R. Adams *et al.*, *Eur. Phys. J. C.* **17**,263 (2000).
6. HERMES Collab., A. Airapetian *et al.*, *Phys.Rev.D* **64**, 112005 (2001).
7. R.L. Jaffe, *Phys.Rev.D* **54**, 6581 (1996).
8. P.J. Mulders and R.D. Tangerman, *Nucl. Phys.B* **461**,197 (1996).
9. HERMES Collab., K. Ackerstaff *et al.*, *NIM A* **417**, 230 (1998).
10. J.J.M.Steiger *et al.*, *NIM A* **453**, 98 (2000).

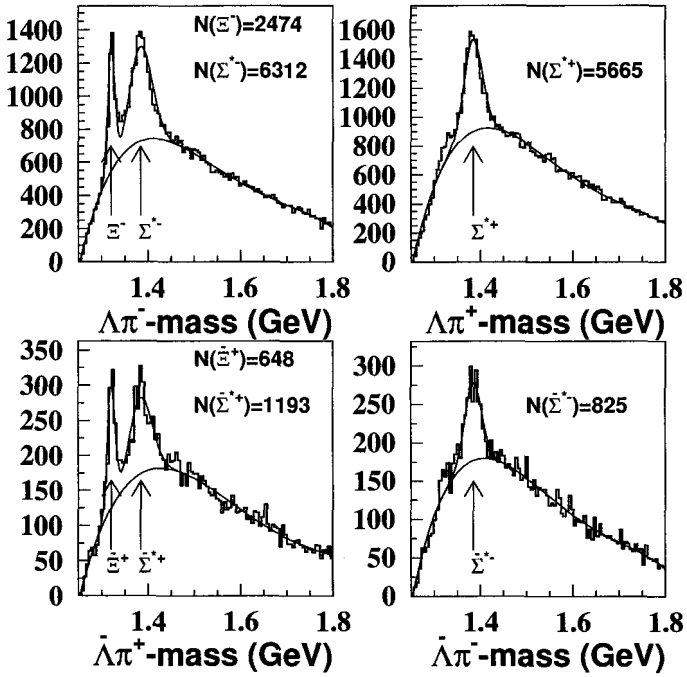


Fig. 3. Invariant mass distributions for the Ξ and $\Sigma(1385)$ hyperons detected by the HERMES spectrometer.

LEPTO AND POLARIZED SIDIS

A. KOTZINIAN

Università and INFN di Torino, Torino, Italy
Yerevan Physics Institute and JINR, Dubna, Russian Federation

A new formalism for *polarized* SIDIS is presented. It is shown that the purity method used by the HERMES collaboration cannot be considered a precise tool for the extraction of polarized quark distributions from measured SIDIS asymmetries.

Recently, the important issue of the extraction of polarized quark distributions was again addressed by the HERMES collaboration [1]. They have used the LO analysis of semi-inclusive deep inelastic scattering (SIDIS) based on the so-called purity method.

The virtual photon asymmetry for hadron h production can be written in the form

$$A_1^h(x, z, Q^2) = \sum_q \mathcal{P}_q^h(x, z, Q^2) \frac{\Delta q(x, Q^2)}{q(x, Q^2)}, \quad (1)$$

where the quark polarizations, $\Delta q/q$, are factored out and the *purities*,

$$\mathcal{P}_q^h(x, z, Q^2) = \frac{e_q^2 q(x, Q^2) D_q^h(z, Q^2)}{\sum_{q'} e_{q'}^2 q'(x, Q^2) D_{q'}^h(z, Q^2)}. \quad (2)$$

are calculated using the Monte Carlo unpolarized event generator LEPTO.

The main assumption of this method is that the hadronization mechanism in LEPTO is the same as in the naïve picture of SIDIS in which all hadrons in the current fragmentation region with $z > 0.2$ are produced in independent quark fragmentation. The quark-fragmentation functions depend by definition on the hadron type, quark flavour, and fraction z of the quark energy carried by the hadron (there is also a weak dependence on Q^2 due to perturbative QCD effects), and *are independent* of **a**) the Bjorken variable x , and **b**) the target type. Before using the LEPTO event generator to calculate purities, one has first to check if the conditions **a**) and **b**) are satisfied.

To this end, samples of SIDIS events were generated for HERMES experimental conditions using the settings of LEPTO as in [1].

In Fig. 1 the quark “fragmentation functions” to π^+ are presented. The available range of the Bjorken variable, x , was divided into two equally populated intervals: **1**) ($x < 0.074$)

and **2**) ($x > 0.074$). As one can see from the left panel of Fig. 1, the extracted “quark fragmentation functions” happen to be strongly dependent on the Bjorken x variable. Note that this cannot be attributed to the (weak) Q^2 -dependence of fragmentation functions. To demonstrate this, the LO Kretzer fragmentation functions, which includes the QCD evolution, are also presented in the same figure for mean values of Q^2 corresponding to Bjorken variable intervals **1**) ($Q^2 = 1.5(\text{GeV}/c)^2$) and **2**) ($Q^2 = 3.4(\text{GeV}/c)^2$).

In the right panel we see a dependence on the target type, which contradicts property **b**) of the fragmentation functions.

Such behavior of “fragmentation functions” extracted from the generated samples is also observed for the production of other types of light meson such as π^- , K^+ , K^- etc.

Now consider the string configuration in the simplest case where the valence u -quark is removed by hard scattering by a proton. The target remnant is then a scalar, $(ud)_0$, or vector, $(ud)_1$, diquark with probabilities $w_0 = 0.75$ and $w_1 = 1 - w_0 = 0.25$. In Fig. 2 the “fragmentation functions” are presented for the cases in which the generation has been done with the target remnant diquark chosen to be a 100% scalar ($w_0 = 1$) or a vector ($w_0 = 0$). We see a dependence on the target remnant spin state at the 5–10% level.

Let us turn to *polarized* SIDIS and again consider the simplest case, where a valence u -quark with positive (u^+) or negative (u^-) helicity is removed from a proton with positive helicity, p^+ . We get the following string configurations with corresponding probabilities, w ,

$$p^+ \ominus u^+ \Rightarrow \begin{cases} \{(ud)_{0,0} \cdots u^+\}, & w = 0.9, \\ \{(ud)_{1,0} \cdots u^+\}, & w = 0.1, \end{cases} \quad (3)$$

$$p^- \ominus u^+ \Rightarrow \{(ud)_{1,-1} \cdots u^+\}, \quad w = 1.0, \quad (4)$$

where $\{(q_1 q_2)_{i,k} \cdots q^+\}$ denotes the string formed by the struck quark q^+ and the diquark $(q_1 q_2)_{i,j}$.

The relations (3-4) demonstrate that the string configuration indeed depends not only on the struck quark type, but also on the target type and polarization. As a consequence, in polarized SIDIS the dependence on the target and struck quark polarizations appears.

The general expression for SIDIS cross section for arbitrary polarized beam (λ_l) and target (λ_N) becomes (for more details see [2])

$$\begin{aligned} \sigma_{N\lambda_l\lambda_N}^h &\propto [1 + (1-y)^2] \sum_q e_q^2 \{qH_{q/N}^h + \Delta q\Delta H_{q/N}^h\} + \\ &\lambda_l\lambda_N [1 - (1-y)^2] \sum_q e_q^2 \{\Delta qH_{q/N}^h + q\Delta H_{q/N}^h\}. \end{aligned} \quad (5)$$

The hadronization functions are defined as

$$\begin{aligned} H_{q/N}^h &= H_{q/N^{++}}^h + H_{q/N^{+-}}^h, \\ \Delta H_{q/N}^h &= H_{q/N^{++}}^h - H_{q/N^{+-}}^h, \end{aligned} \quad (6)$$

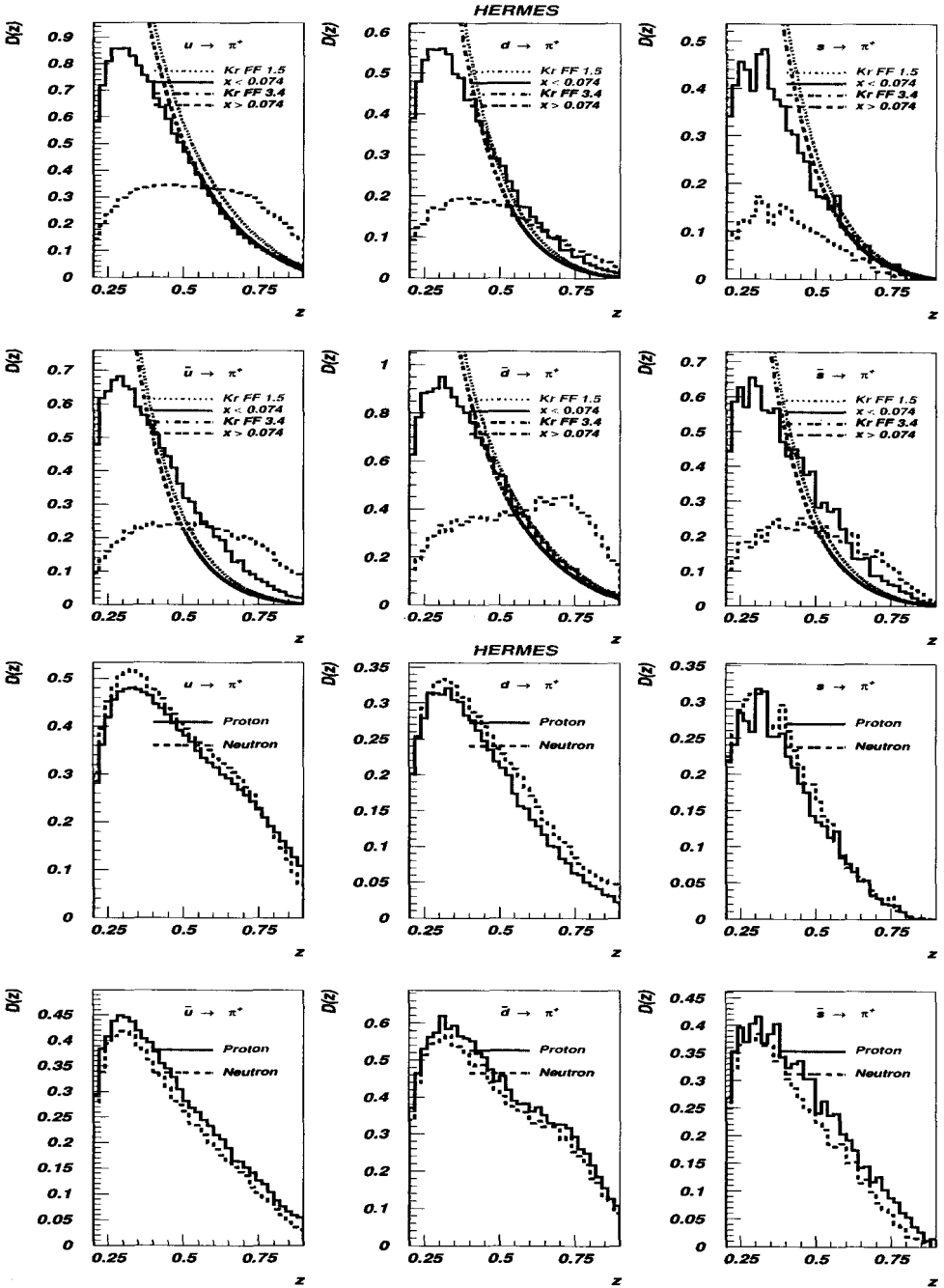


Fig. 1.

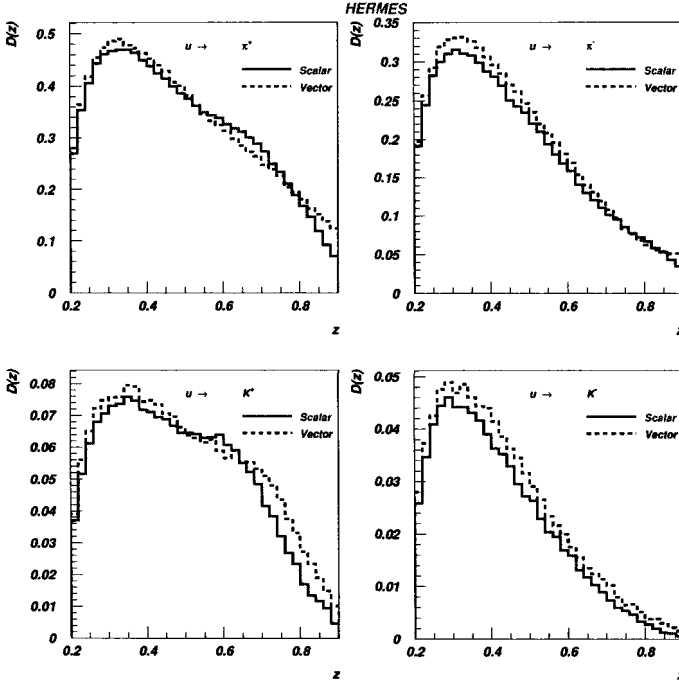


Fig. 2.

where $H_{q/N}^h$ stands for the case in which the quark with helicity λ_q is removed from the target nucleon with helicity λ_N .

The standard expression for the SIDIS description in the current fragmentation region is obtained if one assumes that

$$H_{q/N}^h(x, z, Q^2) \rightarrow D_q^h(z, Q^2) \quad (7)$$

and

$$\Delta H_{q/N}^h(x, z, Q^2) \rightarrow 0. \quad (8)$$

As we have demonstrated, relation (7) is not correct for the HERMES experimental conditions. On the other hand we have seen that hadronization in this model depends on the target remnant spin quantum numbers. In the case of polarized SIDIS the relative probabilities of different target remnant states depend on the target and struck quark polarizations; see Eqs. (3-4). There is then no reason to believe that relation (8) will hold for the polarized SIDIS at moderate energies. Thus, a *new non-perturbative input – the polarized hadronization functions*, $\Delta H_{q/N}^h(x, z, Q^2)$, are needed. In this case Eq. (1) is not exact, and

must be replaced by

$$A_1^h(x, z, Q^2) = \frac{\sum_q e_q^2 q(x, Q^2) H_{q/N}^h(x, z, Q^2) \left[\frac{\Delta q(x, Q^2)}{q(x, Q^2)} + \frac{\Delta H_{q/N}^h(x, z, Q^2)}{H_{q/N}^h(x, z, Q^2)} \right]}{\sum_q e_q^2 q(x, Q^2) H_{q/N}^h(x, z, Q^2) \left[1 + \frac{\Delta q(x, Q^2) \Delta H_{q/N}^h(x, z, Q^2)}{q(x, Q^2) H_{q/N}^h(x, z, Q^2)} \right]}, \quad (9)$$

with extra contributions in the numerator and denominator as compared to Eq. (1). Note that even if one can neglect the influence of this extra contribution in the denominator, the contribution to the numerator can be important for sea quarks.

One can check that the dependences on the Bjorken variable, the target type, and the target remnant spin state of the “quark fragmentation functions” extracted from generated samples for higher (COMPASS) energies, are less pronounced.

In conclusion, the purity method cannot be considered a precise tool for the extraction of polarized quark distributions from measured SIDIS asymmetries at moderate energies. More studies concerning the accuracy of the quark helicity distribution extraction are needed.

References

1. A. Airapetian *et al.*, [HERMES Collaboration], arXiv:hep-ex/0407032.
2. A. Kotzinian, arXiv:hep-ex/0410093.

ASYMMETRIES IN SEMI-INCLUSIVE DEEP INELASTIC SCATTERING

E. Di SALVO

Università di Genova, Genova, Italy

I briefly review the moments method for extracting azimuthal asymmetries from semi-inclusive deep inelastic scattering data. Further I suggest the exploitation of symmetry properties in data analysis, and I show applications of two recent theoretical results.

1. Introduction

The asymmetries in semi-inclusive deep inelastic scattering (SIDIS) can be disentangled by means of either the moments method [1], or best fits [2,3]. In any case the determinations of such asymmetries are affected by systematic errors. These can be reduced by various tricks, among which those based on symmetry considerations are especially intriguing. The main aim of my talk is to review the moments method, with particular reference to symmetry properties of the SIDIS differential cross section. Moreover I show applications of two new theoretical results.

The talk is organized as follows. First of all, I illustrate the formula for the polarized SIDIS cross section, and in particular the QCD leading order contributions. Secondly, I explain the moments method and deduce some useful symmetry properties of the cross section. Thirdly, I propose some applications of two recent theoretical results. Lastly, I give a short summary of the main results.

2. SIDIS Cross Section

I consider the SIDIS reaction $\ell p \rightarrow \ell' \pi X$, with a longitudinally polarized (charged) lepton and a transversely polarized proton, at not too high Q^2 , so that the weak neutral current can be neglected in comparison with the electromagnetic one. As usual [1, 4], I define the kinematic variables in the Breit frame, taking the z -axis along the direction of the virtual photon exchanged between the lepton and the nucleon. Among such variables, especially important are the difference angles

$$\phi = \varphi_\pi - \varphi_l, \quad \phi_S = \varphi_S - \varphi_l, \quad (1)$$

where φ_l , φ_π and φ_S denote the azimuthal angles of the lepton momentum, the pion momentum, and the nucleon polarization vector, respectively. The SIDIS differential cross section is denoted by $d\sigma/d\Gamma$, where $d\Gamma = d\Omega_\ell dx d^2q_\perp dz$ is the phase space element, the solid angle Ω_ℓ determines the direction of the final lepton, x is the longitudinal fractional momentum of the active quark, and \mathbf{q}_\perp and z are respectively the transverse momentum and the longitudinal fractional momentum of the final pion. According to the spin of the lepton and of the nucleon, one has four polarization combinations and, correspondingly, four different polarized cross sections, *i. e.*,

$$\left(\frac{d\sigma}{d\Gamma}\right)_{\rightarrow\uparrow}, \quad \left(\frac{d\sigma}{d\Gamma}\right)_{\rightarrow\downarrow}, \quad \left(\frac{d\sigma}{d\Gamma}\right)_{\leftarrow\uparrow}, \quad \left(\frac{d\sigma}{d\Gamma}\right)_{\leftarrow\downarrow}, \quad (2)$$

the arrows denoting respectively the longitudinal lepton polarization and the transverse nucleon polarization. In turn, each polarized cross section consists of four terms. For instance, one has

$$\left(\frac{d\sigma}{d\Gamma}\right)_{\rightarrow\uparrow} = \left(\frac{d\sigma}{d\Gamma}\right)_{UU} + \left(\frac{d\sigma}{d\Gamma}\right)_{UT} + \left(\frac{d\sigma}{d\Gamma}\right)_{LU} + \left(\frac{d\sigma}{d\Gamma}\right)_{LT}, \quad (3)$$

where U , L and T indicate the ‘‘unpolarized’’ (lepton or nucleon), ‘‘longitudinally polarized’’ (lepton) and ‘‘transversely polarized’’ (nucleon), respectively.

3. Leading Order Results

QCD predicts that, at leading order, and taking into account the intrinsic transverse momentum of the quarks inside the nucleon, each term on the r.h.s. of Eq. (3) results in a sum over different Fourier components [4] with respect to the angles (1); *e. g.*,

$$\begin{aligned} \left(\frac{d\sigma}{d\Gamma}\right)_{UT} &= B_{COL} \sin(\phi + \phi_S) + B_{SIV} \sin(\phi - \phi_S) \\ &+ B_\perp \sin(3\phi - \phi_S) + B_\parallel \sin 2\phi \cos \phi_S + O(g/Q), \end{aligned} \quad (4)$$

$$\left(\frac{d\sigma}{d\Gamma}\right)_{LT} = C_\parallel \cos \phi_S + C_\perp \sin(\phi - \phi_S) + O(g/Q). \quad (5)$$

Here g is the strong coupling constant and $Q = \sqrt{Q^2}$. Moreover the coefficients B and C of the Fourier components consist of convolutive products of distribution functions times fragmentation functions. In the notation of ref. 4, one has, *e. g.*,

$$B_{COL} \propto \frac{|\mathbf{q}_\perp|}{\mu_\pi} h_{1T} \otimes H_1^\perp \otimes w_{Col}, \quad B_{SIV} \propto \frac{|\mathbf{q}_\perp|}{\mu_N} f_1^\perp \otimes D \otimes w_{Siv}, \quad (6)$$

$$C_\perp \propto \frac{|\mathbf{q}_\perp|}{\mu_N} g_{1T} \otimes D \otimes w_{C_\perp}. \quad (7)$$

Here the μ s are energy scales - to be discussed below - and the w s are weight functions [4].

4. The Moments Method

Each term in the sum (4) or (5) corresponds to a given asymmetry: for instance, the first and the second term of Eq. (4) are known respectively as the Collins and the Sivers asymmetry. Moreover the Fourier components are all independent of one another [4]. Therefore, in order to disentangle an asymmetry, one can employ the moments method [5], consisting of weighting the cross section with an appropriate function, which includes the corresponding Fourier component. The resulting weighted asymmetry consists of a product of an ordinary distribution times an ordinary fragmentation function. As an example, one has [4]

$$\int d\mathbf{q}_\perp^2 d\phi d\phi_S W_{COL} \left(\frac{d\sigma}{d\Gamma} \right)_{\rightarrow\uparrow} \propto \frac{m_P}{\mu_\pi} h_1(x) H_1^{\perp(1)}(z). \tag{8}$$

Here h_1 is the transversity function, $H_1^{\perp(1)}$ the Collins fragmentation function, $W_{COL} = |\mathbf{q}_\perp| / (zm_\pi) \sin(\phi + \phi_S)$ is the weight function for the Collins asymmetry, and m_P and m_π are the proton and the pion masses. In principle, the leading order asymmetries could be extracted from any polarized cross section (2). However, in practice, imperfections of the experimental setup may produce fictitious asymmetries. These can be reduced - and simultaneously statistics can be improved - by weighting single terms on the r.h.s. of Eq. (3), resulting in combinations of the polarized cross sections (2). However, some experiments - *e.g.* COMPASS [1] - do not provide all such cross sections. I therefore suggest the exploitation of symmetry properties. In particular, parity and rotational invariance imply

$$\left(\frac{d\sigma}{d\Gamma} \right)_{\leftarrow\downarrow}(\phi, \phi_S) = \left(\frac{d\sigma}{d\Gamma} \right)_{\rightarrow\uparrow}(-\phi, \pi - \phi_S), \tag{9}$$

allowing the determination of the various terms on the r.h.s. of Eq. (3) with, *e.g.*, only one lepton polarization available [1].

5. Applications of Two Theoretical Results

A) I have shown [6–8] that the two energy scales μ_N and μ_π are equal to $Q/2$, contrary to the assumption of other authors [4], who have put them equal to hadron masses. The leading order asymmetries included in the SIDIS cross sections [4] - among them those described by Eqs. (4) and (5) - are then predicted to decrease with Q^2 , in contrast to previous treatments [4]. This prediction has been compared successfully with the Drell-Yan unpolarized azimuthal asymmetry [7].

B) The Politzer theorem on the equations of motion, when applied to QCD, implies [8, 9] that $g_{1T} = h_{1T}(1 - \varepsilon)$, where g_{1T} is the helicity density of a quark in a transversely polarized nucleon, h_{1T} the transverse momentum transversity, and ε a well-known function such that $|\varepsilon| \ll 1$. This relation, together with Eqs. (5) and (7), suggests an alternative method for determining transversity, through double-spin asymmetry [8, 9].

6. Summary

In singling out leading order asymmetries in SIDIS, space symmetries can be exploited in order to improve statistics and to make up for unavailable polarization combinations.

Moreover, the determination of these asymmetries allows the verification of predictions about their Q^2 dependence. Lastly, the double-spin asymmetry may be used for extracting transversity.

References

1. A. Martin, COMPASS coll., *Workshop on Hadron Structure and Spectroscopy*, Paris, March 1-5, 2004.
2. K. Rith, HERMES coll., *Workshop on Hadron Structure and Spectroscopy*, Paris, March 1-5, 2004.
3. J.C. Peng, *HiX2004 Workshop*, Marseille, July 26-28, 2004.
4. D. Boer, R. Jakob and P.J. Mulders, *Nucl. Phys.* **B564**, 471 (2000).
5. A.M. Kotzinian and P.J. Mulders, *Phys. Lett.* **B406**, 373 (1997).
6. E. Di Salvo, *AIP Conf. Proc.* **675**, 494 (2003);
7. E. Di Salvo, hep-ph/0407208.
8. E. Di Salvo, hep-ph/0408146.
9. E. Di Salvo, *Int. J. Mod. Phys.* **A18** 5277 (2003)

TRANSVERSITY IN DRELL-YAN PROCESS OF POLARIZED PROTONS AND ANTIPROTONS IN PAX EXPERIMENT*

A. V. EFREMOV^a, K. GOEKE^b, P. SCHWEITZER^b

^aJoint Institute for Nuclear Research, Dubna, Russia

^bInstitut für Theoretische Physik II, Ruhr-Universität Bochum, Bochum, Germany

Estimates are given for the double-spin asymmetry in lepton-pair production from collisions of transversely polarized protons and antiprotons for the kinematics of the recently proposed PAX experiment at GSI, on the basis of predictions for the transversity distribution from the chiral quark soliton model.

1. Introduction

The leading structures of the nucleon in deeply inelastic scattering processes are described in terms of three twist-2 parton distribution functions (PDF) – the unpolarized $f_1^a(x)$, helicity $g_1^a(x)$, and transversity $h_1^a(x)$. Owing to its chirally odd nature, $h_1^a(x)$ cannot be measured in DIS experiments. Transversity was originally introduced in the description of the Drell-Yan process of transversely polarized protons [1]. Alternative processes have also been discussed, e.g. the Collins effect in semi-inclusive deeply inelastic scattering experiments at HERMES, CLAS and COMPASS could be (partly) understood in terms of transversity [2]. However, in all these processes $h_1^a(x)$ enters in connection with some badly known [3] Collins fragmentation function. Moreover these processes involve the introduction of transverse parton momenta, and for none of them could a strict factorization theorem be formulated so far. Hence the Drell-Yan process still remains the theoretically cleanest and safest way to access $h_1^a(x)$.

The first attempt to study $h_1^a(x)$ by means of the Drell-Yan process is planned at RHIC. Dedicated estimates, however, indicate that at RHIC, access to $h_1^a(x)$ by means of the Drell-Yan process is very difficult. The main reason is that the observable double-spin asymmetry A_{TT} is proportional to the product of transversity quark and antiquark PDFs. The latter are small, although large enough to saturate the Soffer upper limit.

This problem can be circumvented by using an antiproton beam. Then A_{TT} is proportional to the product of transversity quark PDF from the proton and transversity antiquark PDF from the antiproton (which are equal due to charge conjugation). Thus in this case one

*This work is partially supported by grants INTAS 00/587, RFBR 03-02-16816 and DFG-RFBR 03-02-04022 and by Verbundforschung of BMBF.

can expect sizeable counting rates. The challenge of how to polarize an antiproton beam has recently been suggested in the PAX experiment at GSI [4]. The technically realizable polarization of the antiproton beam of more than (5 – 10)% [5] and the large counting rates make the program rather promising.

In the talk I briefly describe our quantitative estimates for the Drell-Yan double-spin asymmetry A_{TT} in the kinematics of the PAX experiment at LO QCD. (For more details and references see [6].) We will also estimate the recently suggested analogous double-spin asymmetry in J/Ψ production [7]. For the transversity distribution we shall use predictions from the chiral quark soliton model [8]. This model was derived from the instanton model of the QCD vacuum [9], and describes numerous nucleonic properties without adjustable parameters to (10 – 30)% accuracy. The field theoretic nature of the model allows the consistent computation of quark and antiquark PDFs, which agree with parameterizations [10] to the same accuracy. This gives us a certain confidence that the model describes $h_1^q(x)$ with a similar accuracy.

2. Lepton pair production in $p \uparrow \bar{p} \downarrow$

The process $p\bar{p} \rightarrow \mu^+ \mu^- X$ can be characterized by the invariants: Mandelstam $s = (p_1 + p_2)^2$, dilepton invariant mass $Q^2 = (k_1 + k_2)^2$, where $p_{1/2}$ and $k_{1/2}$ are the momenta of respectively the incoming proton-antiproton pair and the outgoing lepton pair, and the rapidity $y = \frac{1}{2} \ln \frac{p_1(k_1 + k_2)}{p_2(k_1 + k_2)}$. The double-spin asymmetry in Drell-Yan process is given by

$$\frac{N^{\uparrow\uparrow} - N^{\uparrow\downarrow}}{N^{\uparrow\uparrow} + N^{\uparrow\downarrow}} = D_P \frac{\sin^2 \theta}{1 + \cos^2 \theta} \cos 2\phi A_{TT}(y, Q^2), \quad (1)$$

where θ is the emission angle of one lepton in the dilepton rest frame, and ϕ its azimuth angle around the collision axis counted from the polarization plane of the hadron whose spin is not flipped in Eq. (1). The factor D_P takes into account polarization effects. At LO QCD A_{TT} is given by

$$A_{TT}(y, Q^2) = \frac{\sum_a e_a^2 h_1^a(x_1, Q^2) h_1^a(x_2, Q^2)}{\sum_b e_b^2 f_1^b(x_1, Q^2) f_1^b(x_2, Q^2)}, \quad (2)$$

where the parton momenta $x_{1/2}$ in Eq. (2) are $x_{1/2} = \sqrt{\frac{Q^2}{s}} e^{\pm y}$. In Eq. (2) use has been made of charge conjugation invariance.

In the PAX experiment an antiproton beam with energy in the range (15 – 25) GeV could be available, yielding $s = (30 – 50) \text{ GeV}^2$ for a fixed proton target. The region $1.5 \text{ GeV} < Q < 3 \text{ GeV}$, i.e. below the J/Ψ threshold but well above $\Phi(1020)$ -decays (and with sufficiently large Q^2) would allow the exploration of the region $x > 0.2$. However, in principle one can also address the resonance region itself, and benefit from large counting rates [7] since the unknown $q\bar{q}J/\Psi$ and $J/\Psi\mu^+\mu^-$ -couplings cancel in the ratio in Eq. (1), as argued in [7]. Keeping this in mind we present below estimates for $s = 45 \text{ GeV}^2$, and $Q^2 = 5 \text{ GeV}^2, 9 \text{ GeV}^2$ and 16 GeV^2 .

3. Double-spin asymmetry A_{TT} at PAX

The estimate for the double-spin asymmetry A_{TT} as defined in Eq. (2) for the PAX kinematics on the basis of the ingredients discussed above is shown in Fig. 1a. The exploitable rapidity range shrinks with increasing dilepton mass Q^2 . Since $s = x_1 x_2 Q^2$, for $s = 45 \text{ GeV}^2$ and $Q^2 = 5 \text{ GeV}^2$ (16 GeV^2) one probes parton momenta $x > 0.3$ ($x > 0.5$). The asymmetry A_{TT} grows with increasing Q^2 where larger parton momenta x are involved, since $h_1^a(x)$ is larger than $f_1^a(x)$ in the large x -region. The advantage of using antiprotons is evident from

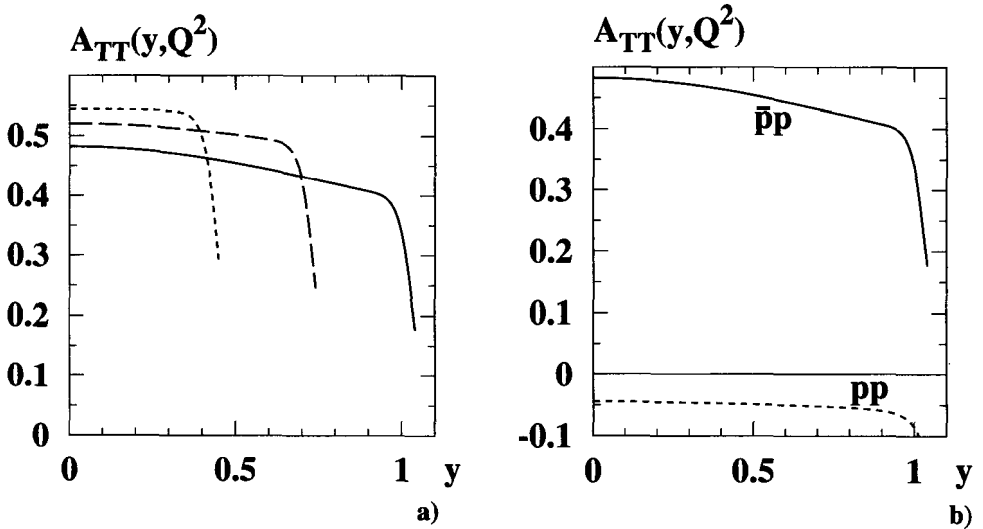


Fig. 1. a) The asymmetry $A_{TT}(y, M^2)$, cf. Eq. (2), as a function of the rapidity y for $Q^2 = 5 \text{ GeV}^2$ (solid) and 9 GeV^2 (dashed) and 16 GeV^2 (dotted line) for $s = 45 \text{ GeV}^2$. b) Comparison of $A_{TT}(y, M^2)$ from proton-antiproton (solid) and proton-proton (dotted line) collisions at PAX for $Q^2 = 5 \text{ GeV}^2$ and $s = 45 \text{ GeV}^2$.

Fig. 1b. The corresponding asymmetry from proton-proton collisions is an order of magnitude smaller (this observation holds also in the kinematics of RHIC [8]). At first glance this advantage seems to be compensated by the polarization factor in Eq. (1). For the antiproton beam polarization of $(5 - 10)\%$ and the proton target polarization of 90% , i.e. at PAX, $D_p \approx 0.05$. However, thanks to the use of antiprotons the counting rates are more sizeable. A precise measurement of A_{TT} in the region $Q > 4 \text{ GeV}$ is very difficult. However, in the dilepton mass region below the J/Ψ threshold [4] and in the resonance region [7], A_{TT} could be measured with sufficient accuracy in the PAX experiment.

A precise measurement would allow us to discriminate between different models for $h_1^a(x)$. Thus on the basis of the popular guess, motivated by the non-relativistic quark model, that $h_1^a(x) \approx g_1^a(x)$ (at some unspecified low scale), one would expect [7] an A_{TT} of about 30% , in contrast with the chiral quark soliton model estimate of about 50% .

At next-to-leading order in QCD one can expect corrections to this result which would reduce the asymmetry [11]. Similarly, large asymmetries can be also expected in the recently suggested process of lepton pair production *via* J/Ψ production [7].

References

1. J. P. Ralston and D. E. Soper, Nucl. Phys. B **152** (1979) 109.
R. L. Jaffe and X. D. Ji, Nucl. Phys. B **375** (1992) 527.
J. L. Cortes, B. Pire and J. P. Ralston, Z. Phys. C **55** (1992) 409.
2. A. V. Efremov, K. Goeke and P. Schweitzer, Phys. Lett. B **522** (2001) 37, B **544** (2002) 389E and B **568** (2003) 63; Eur. Phys. J. C **24** (2002) 407 and C **32** (2004) 337;
P. Schweitzer and A. Bacchetta, Nucl. Phys. A **732** (2004) 106.
3. A. V. Efremov, O. G. Smirnova and L. G. Tkatchev, Nucl. Phys. (Proc. Suppl.) **74** (1999) 49 and **79** (1999) 554 [hep-ph/9812522].
4. PAX Collaboration, "Antiproton-Proton Scattering Experiments with Polarization", Letter of Intent (Darmstadt, 2004), available at <http://www.fz-juelich.de/ikp/pax>.
5. F. Rathmann *et al.*, to appear in Phys. Rev. Lett. [arXiv:physics/0410067].
6. A. V. Efremov, K. Goeke and P. Schweitzer, Eur. Phys. J. C **35** (2004) 207 [arXiv:hep-ph/0403124].
7. M. Anselmino, V. Barone, A. Drago and N. N. Nikolaev, Phys. Lett. B **594** (2004) 97 [arXiv:hep-ph/0403114].
8. P. Schweitzer, D. Urbano, M. V. Polyakov, C. Weiss, P. V. Pobylitsa and K. Goeke, Phys. Rev. D **64** (2001) 034013; [arXiv:hep-ph/0101300].
9. For reviews see: D. I. Diakonov, Prog. Part. Nucl. Phys. **51** (2003) 173.
10. M. Glück, E. Reya and A. Vogt, Z. Phys. C **67** (1995) 433; Eur. Phys. J. C **5** (1998) 461. Phys. Rev. D **63** (2001) 094005.
11. W. Vogelsang and A. Weber, Phys. Rev. D **48** (1993) 2073.
A. P. Contogouris, B. Kamal and Z. Merebashvili, Phys. Lett. B **337** (1994) 169.

PROTON TRANSVERSITY AND INTRINSIC MOTION OF THE QUARKS

P. ZÁVADA

Institute of Physics, Academy of Sciences of the Czech Republic, Prague, Czech Republic

The spin structure of the system of quasi-free fermions having total angular momentum $J = 1/2$ is studied in a consistently covariant approach. Within this model the relations between the spin functions are obtained. Their particular cases are the sum rules Wanzura - Wilczek, Efremov - Leader - Teryaev, Burkhardt - Cottingham, and also the expression for the Wanzura - Wilczek twist 2 term g_2^{WW} . With the use of the proton valence quark distributions as an input, the corresponding spin functions including transversity are obtained.

1. Model

In this talk some results following from the covariant quark-parton model (QPM) will be briefly discussed, details of the model can be found in our recent papers [1–3]. In this version of QPM, valence quarks are considered as quasi-free fermions on the mass shell. Momenta distributions describing the quark intrinsic motion have spherical symmetry corresponding to the constraint $J = 1/2$, which represents the total angular momentum - generally consisting of spin and orbital parts. I shall mention the following items:

1. What sum rules follow from this approach for the spin structure functions?
2. How can the structure functions g_1, g_2 and transversity δq be obtained from the valence quark distributions u_V and d_V - if the $SU(6)$ symmetry is assumed?
3. Calculation of the transversity distribution.

The model is based on the set of distribution functions $G_{k,\lambda}(\frac{pP}{M})$, which measure the probability of finding a quark in the state:

$$u(p, \lambda \mathbf{n}) = \frac{1}{\sqrt{N}} \left(\begin{array}{c} \phi_{\lambda \mathbf{n}} \\ \frac{\mathbf{p}\sigma}{p_0+m} \phi_{\lambda \mathbf{n}} \end{array} \right); \quad \frac{1}{2} \mathbf{n}\sigma \phi_{\lambda \mathbf{n}} = \lambda \phi_{\lambda \mathbf{n}}, \quad \lambda = \pm \frac{1}{2},$$

where \mathbf{n} coincides with the direction of the proton polarization \mathbf{J} . Correspondingly, m and p are the quark mass and momentum; similarly M and P for the proton. With the use of these distribution functions one can define the function H , which in the target rest frame reads:

$$H(p_0) = \sum_{k=1}^3 e_k^2 \Delta G_k(p_0); \quad \Delta G_k(p_0) = G_{k,+1/2}(p_0) - G_{k,-1/2}(p_0), \quad (1)$$

In a previous study it was shown [1] how the spin structure functions can be obtained from the generic function H . If one assume $Q^2 \gg 4M^2x^2$, then:

$$g_1(x) = \frac{1}{2} \int H(p_0) \left(m + p_1 + \frac{p_1^2}{p_0 + m} \right) \delta \left(\frac{p_0 + p_1}{M} - x \right) \frac{d^3 p}{p_0}; \quad x = \frac{Q^2}{2Mv},$$

$$g_2(x) = -\frac{1}{2} \int H(p_0) \left(p_1 + \frac{p_1^2 - p_T^2/2}{p_0 + m} \right) \delta \left(\frac{p_0 + p_1}{M} - x \right) \frac{d^3 p}{p_0}.$$

Let me remark that the procedure for obtaining the functions g_1, g_2 from the distribution H is rather complex; nevertheless the task is well-defined and unambiguous. For the transversity, the corresponding expression reads

$$\delta q(x) = \varkappa \int H(p_0) \left(Mx - \frac{p_T^2/2}{p_0 + m} \right) \delta \left(\frac{p_0 + p_1}{M} - x \right) \frac{d^3 p}{p_0},$$

where the factor \varkappa depends on the approach taken in the calculation [3].

2. Sum rules

One can observe that the above functions have the same general form

$$\int H(p_0) f(p_0, p_1, p_T) \delta \left(\frac{p_0 + p_1}{M} - x \right) d^3 p \quad (2)$$

and differ only in the kinematic term f . This integral, due to spherical symmetry and the presence of the δ -function term, can be expressed as a combination of the momenta:

$$V_n(x) = \int H(p_0) \left(\frac{p_0}{M} \right)^n \delta \left(\frac{p_0 + p_1}{M} - x \right) d^3 p. \quad (3)$$

One can prove [2], that these functions satisfy

$$\frac{V_j'(x)}{V_k'(x)} = \left(\frac{x}{2} + \frac{x_0^2}{2x} \right)^{j-k}; \quad x_0 = \frac{m}{M}.$$

This relation then integral relations to be obtained between different functions having form (3) or (2). In particular for $g_1(x)$ and $g_2(x)$ one gets for $m \rightarrow 0$:

$$g_2(x) = -g_1(x) + \int_x^1 \frac{g_1(y)}{y} dy,$$

$$g_1(x) = -g_2(x) - \frac{1}{x} \int_x^1 g_2(y) dy.$$

Another rule, obtained in this approach, reads:

$$\int_0^1 x^\alpha \left[\frac{\alpha}{\alpha+1} g_1(x) + g_2(x) \right] dx = 0,$$

which is valid for any α , for which the integral exists. For $\alpha = 2, 4, 6, \dots$ the relation corresponds to the Wanzura - Wilczek sum rules [4]. Other special cases correspond to the

Burkhardt - Cottingham [5] ($\alpha = 0$) and the Efremov - Leader - Teryaev [6] (ELT, $\alpha = 1$) sum rules. For the transversity one gets

$$\delta q(x) = 2\kappa \left(g_1(x) + \int_x^1 \frac{g_1(y)}{y} dy \right).$$

3. Valence quarks

Now I shall apply the suggested approach to the description of the real proton. For simplicity I assume:

1) Spin contribution from the sea of quark-antiquark pairs and gluons can be neglected, so that the proton spin is generated only by the valence quarks. The negligible contribution from the quark sea was recently reported in [7].

2) In accordance with the non-relativistic $SU(6)$ approach, the spin contribution of individual valence terms is given by the fractions:

$$s_u = 4/3, \quad s_d = -1/3.$$

If the symbols h_u and h_d denote momenta distributions of the valence quarks in the proton rest frame, which are normalized as

$$\frac{1}{2} \int h_u(p_0) d^3 p = \int h_d(p_0) d^3 p = 1,$$

then the generic distribution (1) reads

$$H(p_0) = \sum e_j^2 \Delta h_j(p_0) = \left(\frac{2}{3}\right)^2 \frac{2}{3} h_u(p_0) - \left(\frac{1}{3}\right)^2 \frac{1}{3} h_d(p_0). \quad (4)$$

In the paper [11], using a similar approach, I also studied the unpolarized structure functions. The structure function F_2 can be expressed as

$$F_2(x) = x^2 \int G(p_0) \frac{M}{p_0} \delta \left(\frac{p_0 + p_1}{M} - x \right) d^3 p; \quad G(p_0) = \sum_q e_q^2 h_q(p_0).$$

On the other hand, for proton valence quarks one can write

$$F_2(x) = \frac{4}{9} x u_V(x) + \frac{1}{9} x d_V(x).$$

The combination of the last two relations gives:

$$q_V(x) = x \int h_q(p_0) \frac{M}{p_0} \delta \left(\frac{p_0 + p_1}{M} - x \right) d^3 p; \quad q = u, d.$$

Since this is again an integral having the structure (2), one can apply the technique of integral transforms and (instead of relations between $g_1, g_2, \delta q$) obtain the relations between $g_j^q, \delta q$ and q_V . For $m \rightarrow 0$ these relations read:

$$g_1^q(x) = \frac{\cos \eta_q}{2} \left(q_V(x) - 2x^2 \int_x^1 \frac{q_V(y)}{y^3} dy \right),$$

$$g_2^q(x) = \frac{\cos \eta_q}{2} \left(-q_V(x) + 3x^2 \int_x^1 \frac{q_V(y)}{y^3} dy \right),$$

$$\delta q(x) = \kappa \cos \eta_q \left(q_V(x) - x^2 \int_x^1 \frac{q_V(y)}{y^3} dy \right),$$

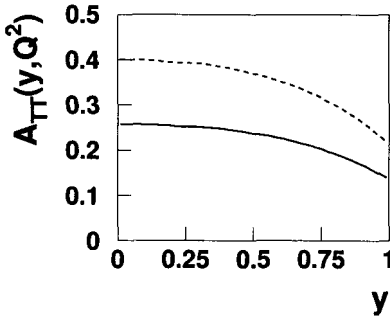


Fig. 1. Double spin asymmetry at $Q^2 = 4\text{GeV}/c$ calculated using two transversity approaches: Interference effects are attributed to quark level only (*solid line*). Interference effects at parton-hadron transition stage are included in addition (*dashed line*); this curve represents an upper bound only.

where $\cos \eta_q$ is corresponding $SU(6)$ factor. Now, taking quark charges and the $SU(6)$ factors as in Eq. (4), one can directly calculate g_1, g_2 and δq using only the input on the valence quark distributions $q_V = u_V, d_V$. More detailed discussion of the results obtained is in our cited papers. Here I mention our (A.Efremov, O.Teryaev and P.Zavada) quite recent result on double spin asymmetry $A_{TT}(y, Q^2)$, which is shown in Fig. 1. The calculation is done in accordance with the recent study [8, 9], but with the use of quark transversities obtained in the presented approach, which gives a slightly lower estimate of A_{TT} . It is expected that this function could be accessible in the PAX experiment [10], which will measure spin asymmetry of the lepton pairs produced in collisions of transversely polarized protons and antiprotons.

References

1. P. Závada, Phys. Rev. D **65**, 054040 (2002).
2. P. Závada, Phys. Rev. D **67**, 014019 (2003).
3. A.V. Efremov, O.V. Teryaev and P. Závada, Phys. Rev. D **70**, 054018 (2004).
4. S. Wanzura and W. Wilczek, Phys. Lett. B **72**, 195 (1977).
5. H. Burkhardt, W.N. Cottingham, Ann. Phys. **56**, 453 (1970).
6. A.V. Efremov, O.V. Teryaev, E. Leader, Phys. Rev. D **55**, 4307 (1997).
7. A. Airapetian et al., Phys. Rev. Lett. **92**, 012005 (2004).
8. A.V. Efremov, K. Goetze, P. Schweitzer, Eur. Phys. J. C **35**, 207 (2004).
9. M. Anselmino, V. Barone, A. Drago and N.N. Nikolaev, Phys. Lett. B **594**, 97 (2004).
10. PAX Collaboration, Antiproton-Proton Scattering Experiments with Polarization, Letter of Intent (Darmstadt, 2004), available at <http://www.fz-juelich.de/ikp/pax>.
11. P. Závada, Phys. Rev. D **55**, 4290 (1997).

SPIN DENSITY MATRIX ELEMENTS IN VECTOR MESON LEPTO-PRODUCTION *

S. V. GOLOSKOKOV

BLTP, Joint Institute for Nuclear Research, Dubna, Russia

P. KROLL

Fachbereich Physik, Universität Wuppertal, Wuppertal, Germany

An analysis of vector meson lepto-production at small Bjorken- x and large photon virtuality is reported, in an approach based on generalised parton distributions (GPDs). The approach leads to results for cross sections and spin density matrix elements for ρ and ϕ lepto-production in fair agreement with experiment.

Vector meson lepto-production at small Bjorken- x and large photon virtuality Q^2 factorises [1] into a hard partonic subprocess, vector meson lepto-production off gluons, and GPDs describing the collinear emission and reabsorption of gluons from the proton. The process of interest is dominated by transitions from longitudinally polarised photons to longitudinally polarised vector mesons, $\gamma_L^* \rightarrow V_L$, other transitions being suppressed by inverse powers of Q^2 . For experimentally accessible values of Q^2 , however, the $L \rightarrow L$ transition amplitude, calculated to leading-twist accuracy, leads to a cross section that exceeds experiment, typically by an order of magnitude [2]. Moreover, for Q^2 of the order of 10 GeV^2 , other transitions can not be ignored, as revealed by data on spin density matrix elements. A calculation of the transition amplitudes involving transversely polarised photons and/or vector mesons (T) in collinear factorisation is problematic since infrared singularities occur, indicating a break-down of factorisation [3].

We report here on work in progress in which the GPD approach is modified by employing the modified perturbative approach [4] in the calculation of the hard subprocess: the transverse degrees of freedom of the quarks building up the vector meson are retained, and

*This work is supported in part by the Russian Foundation for Basic Research, Grant 03-02-16816 and by the Heisenberg-Landau program

Sudakov suppressions are taken into account. This method provides a regularisation scheme for the infrared singularities mentioned above. In passing we note that our approach bears a resemblance to models proposed in [5] where, up to occasional corrections, the GPDs are replaced by the usual gluon distributions.

The gluon contribution to the lepto-production amplitude, calculated at the momentum transfer $t \simeq t_{\min} \simeq 0$ for a proton with positive helicity, reads

$$M_{\mu',\mu+} = \frac{e}{2} C_V \int_0^1 \frac{d\bar{x}}{(\bar{x} + \xi)(\bar{x} - \xi + i\epsilon)} \times \left[A_{\mu',\mu+}^V + A_{\mu',\mu-}^V \right] H^g(\bar{x}, \xi, t \simeq 0), \tag{1}$$

where μ (μ') denotes the helicity of the photon (meson). Proton helicity flip and contributions from the GPD \tilde{H}^q , which is much smaller than the GPD H^g at small \bar{x} , are neglected in (1). \bar{x} is the average momentum fraction of the gluons, and the skewness ξ is related to Bjorken- x by $\xi \simeq x_{Bj}/2$. The flavour factors are $C_p = 1/\sqrt{2}$ and $C_\phi = -1/3$.

The hard scattering amplitudes for the various helicity configurations are (the signs now label gluon helicities)

$$A_{\mu',\mu+}^V = \frac{2\pi\alpha_s(\mu_R)}{N_c} \int_0^1 d\tau \int \frac{dk_\perp^2}{16\pi^2} \Psi_V(\tau, k_\perp^2) K_{\mu'\mu}(\tau, \bar{x}, \xi, k_\perp^2, Q^2). \tag{2}$$

The hard scattering kernels K are calculated from the relevant Feynman graphs at $t \simeq 0$ (see for instance [6]), where only factors of $\sqrt{-t}$ required by angular momentum conservation are kept. The amplitude (2) is Fourier transformed to the impact parameter space, where the variable \mathbf{b} is canonically conjugated to \mathbf{k}_\perp . Multiplication with the b -space version of the Sudakov factor [4] completes the specification of the sub-process amplitude.

In the calculation of the sub-process, a spin wave function for the vector meson is used, which takes into account the quark transverse momentum, \mathbf{k}_\perp , linearly, and hence one unit of orbital angular momentum in a covariant manner [7]. For the momentum-space meson wave-function Ψ_V a simple Gaussian form is adopted [8]

$$\Psi_V(\mathbf{k}_\perp, \tau) = 8\pi^2 \sqrt{2N_c} f_V a_V^2 \exp \left[-a_V^2 \frac{\mathbf{k}_\perp^2}{\tau\bar{\tau}} \right], \tag{3}$$

where τ is the fraction of the meson momentum carried by the quark ($\bar{\tau} = 1 - \tau$). In the numerical evaluation of meson lepto-production the following values for the decay constants and the transverse size parameters are used: $f_\rho = 0.216$ GeV, $f_\phi = 0.237$ GeV, $a_\rho = 0.52$ GeV⁻¹ and $a_\phi = 0.45$ GeV⁻¹.

The GPD is modelled from a double distribution [9] for which the following ansatz is exploited:

$$f^g(\beta, \alpha, t \simeq 0) \sim \frac{[(1 - |\beta|)^2 - \alpha^2]^n}{(1 - |\beta|)^{2n+1}} g(\beta). \tag{4}$$

An appropriate integral over f^g leads to the GPD [9]. For the gluon distribution $g(\beta)$ we take the CTEQ5M parameterization [10]. The cases $n = 1$ and 2 lead to nearly the same results.

We have evaluated the amplitudes for $L \rightarrow L$, $T \rightarrow L$ and $T \rightarrow T$ transitions at small t , and neglected the $L \rightarrow T$ and $T \rightarrow -T$ ones since they are strongly suppressed in our approach. The three amplitudes are multiplied by exponentials $\exp[-B|t|/2]$ in order to make contact with experiment (or to extrapolate to $t = 0$). The integrated cross sections for $\gamma^* p \rightarrow V p$ are shown in Fig. 1. Good agreement with experiment is observed for ρ and ϕ mesons.

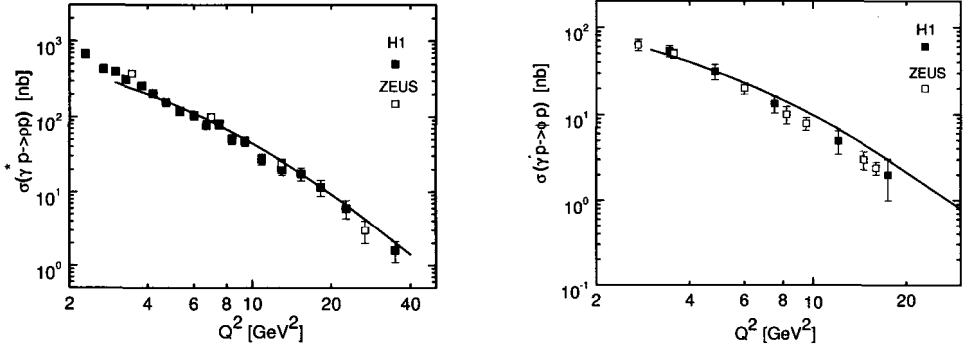


Fig. 1. The integrated cross section for $\gamma^* p \rightarrow \rho p$ (left) and $\gamma^* p \rightarrow \phi p$ (right) at $W \simeq 75$ GeV. Data taken from [11] (filled squares) and [12] (open squares). The solid lines represent our results.

In Fig. 2 two examples of predictions of spin density matrix elements are shown. Our results reproduce quite well the Q^2 dependence of the spin density matrix obtained at HERA experiments [11, 13].

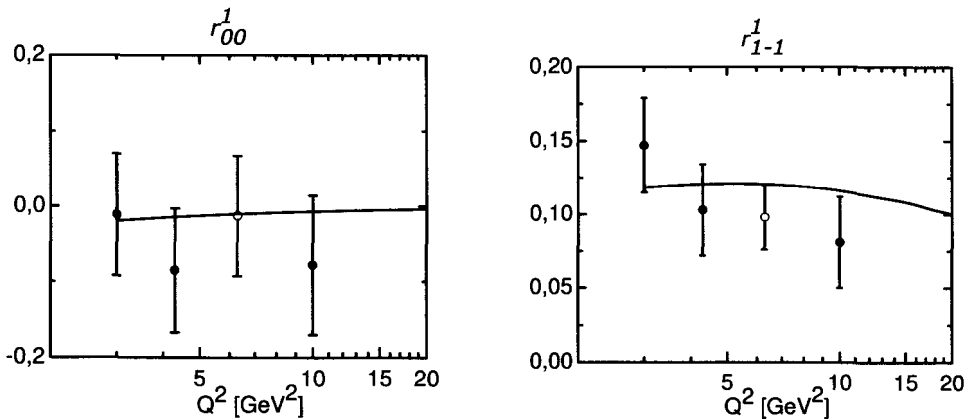


Fig. 2. Sample spin density matrix elements of electroproduced ρ at $W = 75$ GeV and $\langle -t \rangle = 0.15$ GeV². Data from [11] (filled circles) and [13] (open circles), are compared to our results (solid lines).

In summary, the GPD approach combined with the modified perturbative approach applied to the partonic subprocess allows for a calculation of various cross section and spin

density matrix elements at large Q^2 and small Bjorken- x . Fair agreement between theory and experiment for light vector meson lepto-production is found. It is important to extend our results to lower energies but larger Bjorken- x . This is the HERMES and COMPASS region where the quark GPDs have to be taken into account. Preliminary data for the spin density matrix elements have been presented by COMPASS at this conference [14].

References

1. X. Ji, *Phys. Rev.* **D55**, 7114 (1997); A.V. Radyushkin, *Phys. Lett.* **B380**, 417 (1996); J.C. Collins *et al.*, *Phys. Rev.* **D56**, 2982 (1997).
2. L. Mankiewicz, G. Piller and T. Weigl, *Eur. Phys. J.* **C5**, 119 (1998).
3. L. Mankiewicz and G. Piller, *Phys. Rev.* **D61**, 074013 (2000); I.V. Anikin and O.V. Teryaev, *Phys. Lett.* **B554**, 51 (2003).
4. J. Botts and G. Sterman, *Nucl. Phys.* **B325**, 62 (1989).
5. A.D. Martin, M.G. Ryskyn and T. Teubner, *Phys. Rev.* **D60**, 014022 (2000); L. Frankfurt, W. Koepf and M. Strikman, *Phys. Rev.* **D54**, 3194 (1996); D. Y. Ivanov and R. Kirschner, *Phys. Rev.* **D58**, 114026 (1998).
6. H. W. Huang and P. Kroll, *Eur. Phys. J.* **C17**, 423 (2000).
7. J. Bolz, J.G. Körner and P. Kroll, *Z. Phys.* **A350**, 145 (1994).
8. R. Jakob and P. Kroll, *Phys. Lett.* **B315**, 463 (1993); Erratum-ibid. **B319**, 545 (1993).
9. I. V. Musatov and A. V. Radyushkin, *Phys. Rev.* **D61**, 074027 (2000)
10. J. Pumplin, D. R. Stump, J. Huston, H. L. Lai, P. Nadolsky and W. K. Tung, *JHEP* **0207**, 012 (2002).
11. C. Adloff *et al.* [H1 Collaboration], *Eur. Phys. J.* **C13**, 371 (2000).
12. J. Breitweg *et al.* [ZEUS Collaboration], *Eur. Phys. J.* **C6** 603, (1999).
13. J. Breitweg *et al.* [ZEUS Collaborations], *Eur. Phys. J.* **C12**, 393 (2000).
14. D. Neyret, "Results on exclusive ρ^0 production from COMPASS at CERN", these proceedings.

RESULTS ON EXCLUSIVE ρ^0 PRODUCTION FROM COMPASS

D. NEYRET

DAPNIA/SPhN, CEA Saclay, Gif sur Yvette, France

(on behalf of the COMPASS Collaboration)

A study of the ρ_0 spin density matrices $r_{\lambda\lambda'}^\alpha$, using exclusive incoherent ρ^0 production events, was performed by the COMPASS collaboration. An overview of this analysis is presented, and preliminary results from the 2002 data are shown. These results are compatible with the previous experiments but with a better statistical accuracy and cover a larger range in Q^2 . The ratio R of the longitudinal to transverse virtual photon polarization cross sections for the studied process is deduced from r_{00}^{04} . The non-zero value of r_{1-1}^{04} indicates a weak violation of the s-channel helicity conservation.

1. Introduction

A study of the exclusive incoherent vector-meson production events is done by the COMPASS collaboration. The goal of such an analysis is to measure the elements of the ρ^0 spin density matrices $r_{\lambda\lambda'}^\alpha$, in order to test the s-channel helicity conservation (SCHC), to measure the ratio of the longitudinal to transverse virtual photon polarization cross sections for the studied process, and to get access to the longitudinal cross section related to Generalized Parton Distributions at high Q^2 .

2. Formalism of the exclusive ρ^0 production

We study ρ^0 exclusive production with $\mu + N \rightarrow \mu' + N' + \rho^0$, where the ρ^0 decays to $\pi^+\pi^-$. The cross section is proportional to the product of both leptonic and hadronic tensors $L_{\mu\nu}T^{\mu\nu}$. One defines a photon density matrix $\rho(\gamma)$ [1] proportional to the leptonic tensor, and from $\rho(\gamma)$ and the hadronic tensor, a ρ^0 density matrix $\rho(V)_{\lambda\lambda'} = 1/2T\rho(\gamma)T^+$ is expressed on the basis of ρ^0 helicity. The photon density matrix can be decomposed over nine independent virtual photon polarization states α : $\alpha = 0$ corresponds to the unpolarized transverse photons, 1 and 2 to the two linear polarizations, 3 to the circular photons, 4 to the longitudinally polarized photons, and 5 to 8 are the interference terms between transverse and longitudinal amplitudes. One defines the ρ^α matrices as the contribution to the ρ^0 density matrix $\rho(V)$ for these nine states. These matrices provide information on the spin characteristics of the hadronic tensor T. In particular, one could test the s-channel

helicity conservation hypothesis (SCHC), which means that the helicity of the virtual photon is entirely transferred to the outgoing vector meson. Assuming SCHC, it is possible to determine the value of the ratio $R = \sigma_L/\sigma_R$ of the longitudinal and transverse cross section.

3. ρ^0 production studies at COMPASS

The ρ^α matrices can all be extracted from the angular distributions of the ρ^0 production events $W(\cos\theta, \phi, \Phi)$ [1], where the three independent angles are: Φ between the leptonic scattering and ρ^0 production planes; ϕ between the ρ^0 production and $\rho^0 \rightarrow \pi^+\pi^-$ decay planes; and θ the polar angle between the ρ^0 momentum direction and the produced π^+ momentum in the vector-meson rest frame. The ρ^0 and ρ^4 matrices can be distinguished by a Rosenbluth method using two beam energies to separate the contribution of longitudinally and transversely polarized virtual photons. This is not yet done at COMPASS. One then measures $r_{\lambda\lambda'}^{04}$, which is proportional to a linear combination of ρ^0 and ρ^4 . We also define for homogeneity $r_{\lambda\lambda'}^\alpha$ proportional to the ρ^α matrices. For these preliminary results we do not use the full $W(\cos\theta, \phi, \Phi)$ distribution; the analysis is limited to the one-dimensional distributions $W(\cos\theta)$, $W(\phi)$ and $W(\psi)$, where $\psi = \phi - \Phi$. From these a few of the r^α matrix elements can be determined:

$$W(\cos\theta) = \frac{3}{4}((1 - r_{00}^{04}) + (3r_{00}^{04} - 1)\cos^2\theta) \quad W(\psi) = \frac{1}{2\pi}(1 - 2\epsilon r_{1-1}^1 \cos 2\psi) \quad (1)$$

$$W(\phi) = \frac{1}{2\pi}(1 - 2r_{1-1}^{04} \cos 2\phi + P_\mu \sqrt{1 - \epsilon^2} \text{Im} m r_{1-1}^3 \sin 2\phi) \quad (2)$$

In the above expression SCHC was used to obtain $W(\psi)$. The r_{00}^{04} matrix element allows the determination of the value of the ratio $R = \sigma_L/\sigma_T$, if SCHC is assumed. In parallel, SCHC can be tested from the values of r_{1-1}^{04} and the $\text{Im} m r_{1-1}^3$ matrix elements, which should be zero if it is valid.

4. Selection of the exclusive ρ^0 events

The COMPASS experiment studies the interaction of a beam of 160 GeV polarized muons (76% polarization) on a ${}^6\text{LiD}$ target. The detector is composed of two high resolution spectrometers; a more precise description can be found in [2]. Different criteria are applied to select exclusive ρ^0 production events. Topological selections will require an initial and scattered μ and two remaining tracks for the charged pions; the slow recoil target particles are not detected. Several cuts are applied to hadron tracks: a cut on the invariant mass of the two pions ($0.5 < m_{\pi\pi} < 1$ GeV) identifies the ρ^0 ; the exclusivity of the interaction is ensured by cuts on missing energy and transverse momentum ($-2.5 < E_{\text{missing}} < 2.5$ GeV, $p_t^2 < 0.5$ GeV 2), and coherent interactions on nuclei are rejected by $p_t^2 > 0.15$ GeV 2 . Kinematics regions where the systematics effects are too large are rejected ($E_{\mu'} > 20$ GeV, $Q^2 > 0.01$ GeV 2 , $\nu > 30$ GeV).

5. Correction for experimental effects

The event generator used in the Monte-Carlo used for this analysis is based on DIPSI [3], which is dedicated to exclusive vector-meson production. For this analysis, it has been

tuned to reproduce data from NMC [5] and E665 [6] experiments. Monte-Carlo events have been used to correct data for acceptance, efficiency and smearing effects. Correction functions have been determined using the numbers of generated and reconstructed events in each kinematical bin. These functions have been found to be approximately uniform as functions of the angles. Different Q^2 distributions of the generated events have been tested, but the differences obtained on the correction functions are less than 2%, well below the statistical errors of the Monte-Carlo.

6. Results

Matrix elements are extracted from the one-dimensional angular distributions of the COMPASS 2002 data in five bins in Q^2 from 0.01 up to 10 GeV^2 . The average value of W , after all the selection applied to the data, is around 10.4 GeV . Figure 1 shows the matrix element r_{00}^{04} determined from the $\cos\theta$ distribution as a function of Q^2 . It is compared to the published data of H1 [7], ZEUS [4] and E665 [6] experiments. Only statistical errors are shown. COMPASS data are in a good agreement with previous experiments, except for ZEUS, but with a much smaller statistical errors. COMPASS also covers a larger range at low Q^2 up to $2.5 \times 10^{-2} \text{ GeV}^2$. Using the measurement of r_{00}^{04} one can determine the value of the ratio $R = \sigma_L/\sigma_T$, if the SCHC hypothesis holds. Figure 2 shows the measurements of

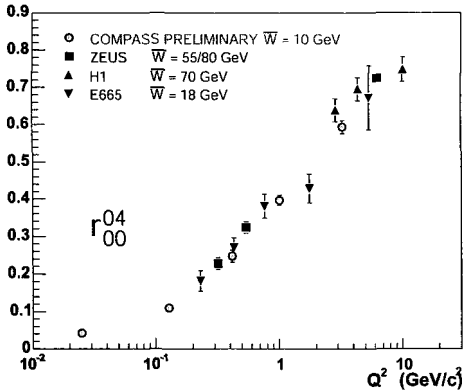


Fig. 1. Measured r_{00}^{04} (see text)

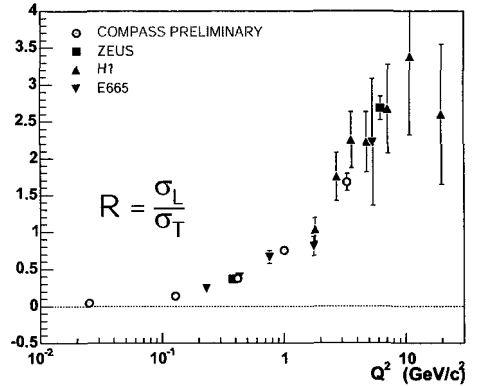


Fig. 2. Ratio of $R = \sigma_L/\sigma_T$ extracted from r_{00}^{04}

the ratio R , which are in agreement with other experiments. One can remark that at low Q^2 the production by transverse photons dominates, but becomes smaller than the longitudinal photons contribution at high Q^2 . From the ψ distribution one could extract the r_{1-1}^1 matrix element, assuming the validity of SCHC. This is shown in figure 3 and compared to other experiments, with the same conclusions as for r_{00}^{04} . The r_{1-1}^0 and $\text{Im} m r_{1-1}^3$ matrix elements are determined from the ϕ distribution. They are shown in figure 4 and compared with the previous experiments. $\text{Im} m r_{1-1}^3$ is not available from the HERA experiments, as its measurement requires a polarized lepton beam. One can note that if $\text{Im} m r_{1-1}^3$ is consistent with

0, but this is not the case for r_{1-1}^{04} . The measured values of the later one indicate a small contribution of amplitudes with helicity flip, which implies a mild violation of SCHC.

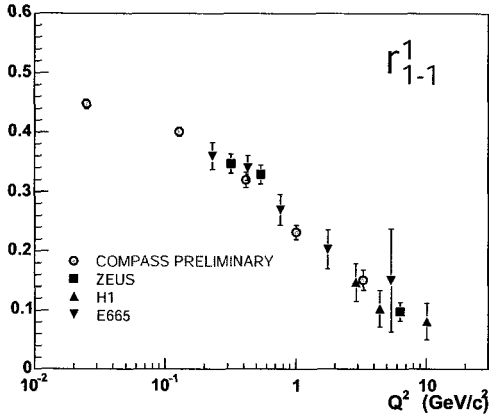


Fig. 3. Measured r_{1-1}^1 (see text)

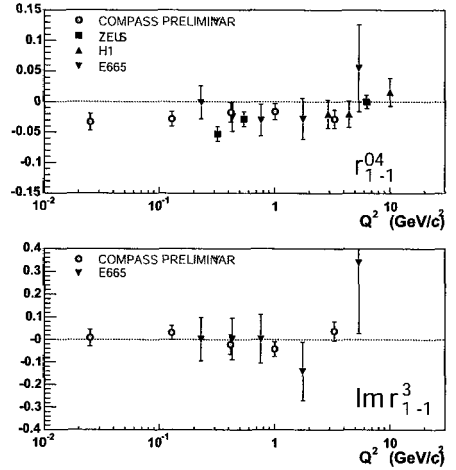


Fig. 4. Measured r_{1-1}^{04} and $\text{Im} r_{1-1}^3$ (see text)

7. Conclusion

A first determination of several ρ^α density matrix elements from the COMPASS 2002 data has been performed, leading to a measurement of r_{00}^{04} , r_{1-1}^1 , r_{1-1}^{04} , $\text{Im} r_{1-1}^3$ and R . These measurements have been done at an average value of W of 10.4 GeV and in a large Q^2 range between 0.01 and 10 GeV². These results are in good agreement with the previous experiments ZEUS, H1 and E665, with a better statistical accuracy and a larger Q^2 range. The data confirm an increase of R with Q^2 , and indicate a weak violation of SCHC. This analysis will be continued with more statistics using the 2003 and 2004 data, which will allow us to extend the high Q^2 range up to 25 GeV². Also the three-dimensional angular distribution $W(\cos \theta, \phi, \Phi)$ will be used to extract all the $r_{\lambda\lambda'}^\alpha$, spin density matrices.

References

1. K. Schilling and G. Wolf, Nucl. Phys. B61 (1973) 381
2. G.K. Mallot for the COMPASS Collaboration, Nucl. Instr. Meth. A518 (2004) 121
3. M. Arneodo, L. Lamberti, M.G. Ryskin, DIPSI: a Monte-Carlo generator for elastic vector-meson production in charged lepton-proton scattering., Comput. Phys. Commun. 100 (1997) 195, hep-ph/9610286
4. ZEUS Collab., J. Breitweg et al., Eur. Phys. J. C 13 (2000) 393
5. NMC Collab., M. Arneodo et al., Nucl. Phys. B 429 (1994) 503
6. E665 Collab., M.R. Adams et al., Z Phys. C 74 (1997) 237
7. H1 Collab., C. Adloff et al., Eur. Phys. J. C 13 (2000) 371, and H1 Collab., C. Adloff et al., Phys. Lett. B 539 (2002) 25

HARD EXCLUSIVE ELECTROPRODUCTION OF $\pi^+\pi^-$ PAIRS AT HERMES

R. FABBRI

NIKHEF, Amsterdam, The Netherlands

(on behalf of the HERMES Collaboration)

Hard exclusive electroproduction of $\pi^+\pi^-$ pairs on hydrogen and deuterium targets has been studied by the HERMES experiment at DESY. Legendre moments $\langle P_1 \rangle$ and $\langle P_3 \rangle$ of the angular distributions of π^+ mesons in the center-of-mass frame of the pair have been measured for the first time. Their dependence on the $\pi^+\pi^-$ invariant mass can be understood as being due to the interference between relative P -wave (isovector) and S, D -wave (isoscalar) states of the two pions. The increase in magnitude of $\langle P_1 \rangle$ as Bjorken x increases is interpreted in the framework of Generalized Parton Distributions as an enhancement of flavour non-singlet $q\bar{q}$ exchange for larger values of x , which leads to a sizable admixture of isoscalar and isovector pion pairs. In addition, the interference between P -wave and D -wave states separately for transverse and longitudinal pion pairs has been studied. The data indicate that in the $f_2(1270)$ region at $\langle Q^2 \rangle = 3 \text{ GeV}^2$, higher-twist effects can be as large as the leading-twist longitudinal component.

1. Introduction

This analysis reports the first experimental data for hard exclusive $\pi^+\pi^-$ pair production [1, 2]

$$e^+p \rightarrow e^+p \pi^+\pi^- \text{ and } e^+d \rightarrow e^+d \pi^+\pi^- . \quad (1)$$

Recent theoretical studies [3–5] have shown that the analyzed exclusive process can be described in the framework of Generalized Parton Distributions (GPDs) [6–8]. The diagrams relevant for this reaction at leading twist are shown in Fig. 1. The pion pairs may be produced through two-gluon (Fig. 1a) or quark-antiquark ($q\bar{q}$) exchange (Fig. 1b,c,d) with the target. In the range of the considered $\pi^+\pi^-$ invariant mass ($m_{\pi\pi}$), both resonant and non-resonant contributions are present. For the purpose of studying the interference between $\pi^+\pi^-$ production in P -wave ($I = 1$) and S, D -wave states ($I = 0$), the Legendre moments $\langle P_1(\cos\theta) \rangle$ and $\langle P_3(\cos\theta) \rangle$ are particularly useful because they are sensitive only to such interference. The Legendre moment of order n is given by

$$\langle P_n(\cos\theta) \rangle^{\pi^+\pi^-} = \frac{\int_{-1}^1 d\cos\theta P_n(\cos\theta) \frac{d\sigma^{\pi^+\pi^-}}{d\cos\theta}}{\int_{-1}^1 d\cos\theta \frac{d\sigma^{\pi^+\pi^-}}{d\cos\theta}} , \quad (2)$$

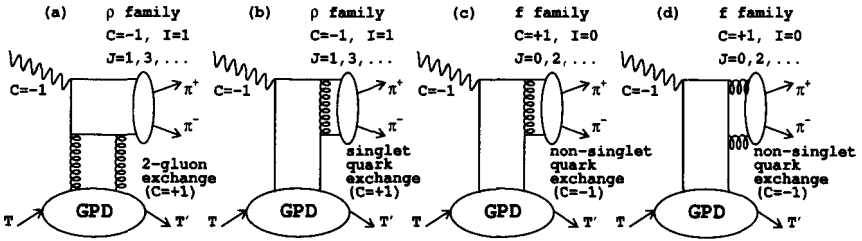


Fig. 1. Leading twist diagrams for the hard exclusive reaction $e^+T \rightarrow e^+T \pi^+\pi^-$. Gluon exchange (a) gives rise to pions in the isovector state only, while the quark exchange mechanism (b,c,d) gives rise to pions in both isoscalar and isovector states.

where θ is the polar angle of the π^+ meson with respect to the direction of the momentum of the $\pi^+\pi^-$ pair in the center-of-momentum frame of the virtual photon and target nucleon. In particular, $\langle P_1 \rangle$ is sensitive to P -wave interference with S and D -waves, whereas $\langle P_3 \rangle$ is sensitive only to P -wave interference with a D -wave.

In order to study the contribution of the $f_2(1270)$ resonance to the Legendre moments in more detail, the $m_{\pi\pi}$ -dependence of the purely longitudinal combination $\langle P_1 + \frac{7}{3} \cdot P_3 \rangle$, and of the combination $\langle P_1 - \frac{14}{9} \cdot P_3 \rangle$, which is believed to be dominated by the higher-twist transverse contribution to the excitation of the f_2 resonance [9], have been also measured in the f_2 domain.

2. Results

The exclusive data have been accumulated with the HERMES spectrometer [10], where the 27.6 GeV positron beam was scattered off hydrogen and deuterium targets, separately. Details of the analysis can be found in Ref. [1].

The $m_{\pi\pi}$ -dependence of $\langle P_1 \rangle$ and $\langle P_3 \rangle$ for exclusive $\pi^+\pi^-$ production on hydrogen and deuterium is presented in Fig. 2.

The moment $\langle P_1 \rangle$ shows a clear dependence on $m_{\pi\pi}$. At $m_{\pi\pi} < 0.6$ GeV this non-zero moment is interpreted as originating from the interference between the lower tail of the ρ^0 and the non-resonant $\pi^+\pi^-$ S -wave production. This interference is present over the entire invariant mass region considered. At $m_{\pi\pi} > 1.0$ GeV, additionally, an interference between the upper tail of the ρ^0 meson and the f -type mesons arises and is superimposed. In particular, the possible change of sign of the asymmetry at $m_{\pi\pi} \approx 1.3$ GeV may be understood as being caused by the interference of the broad ρ^0 tail and the $f_2(1270)$ resonance.

The Legendre moment $\langle P_3 \rangle$ is sensitive only to the interference of P -wave and D -wave states in $\pi^+\pi^-$ production. Consistent with the expectation that no resonance decay into $\pi^+\pi^-$ pairs in D -wave states occurs for $m_{\pi\pi} \leq 1$ GeV, no interference is observed in this invariant mass region. The $\langle P_3 \rangle$ moment for deuterium changes sign in the $f_2(1270)$ meson region, reflecting the interference of the P -wave and D -wave resonant $\pi^+\pi^-$ channels. On the other hand, no such signature is evident in the hydrogen data.

In Fig. 2 the $m_{\pi\pi}$ -dependence of $\langle P_1 \rangle$ for hydrogen is compared with theoretical calcu-

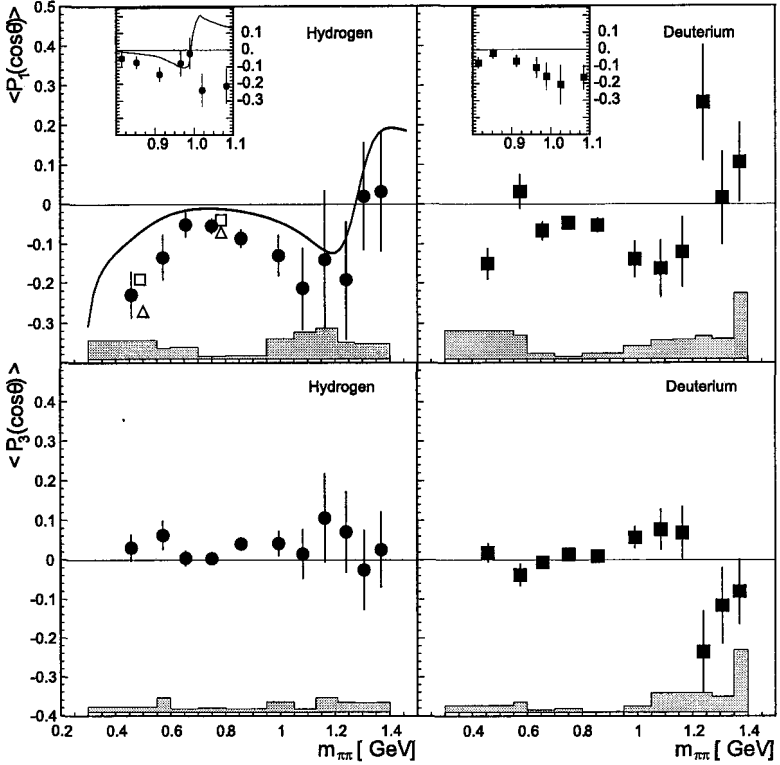


Fig. 2. The $m_{\pi\pi}$ -dependence of the Legendre moments $\langle P_1 \rangle$ (upper panels) and $\langle P_3 \rangle$ (lower panels) for hydrogen (left panels) and deuterium (right panels), for $x > 0.1$. The region $0.8 < m_{\pi\pi} < 1.1$ GeV is presented with finer bins to better investigate possible contributions from the narrow $f_0(980)$ resonance, as shown in the insert. In the upper panels, leading twist predictions for the hydrogen target including the two-gluon exchange mechanism contribution, LSPG [5, 11] (solid curve) at $x = 0.16$ are shown. A calculation without the gluon exchange contribution is shown for limited $m_{\pi\pi}$ values, LPPSG [4] (open squares at $x = 0.1$, open triangles at $x = 0.2$). In these calculations, the contribution from f_0 meson decay was not considered. Instead, the inset panel for the hydrogen target shows the prediction from [12], which includes the f_0 meson contribution. All experimental data have $\langle x \rangle = 0.16$, $\langle Q^2 \rangle = 3.2$ (3.3) GeV^2 , and $\langle -t \rangle = 0.43$ (0.29) GeV^2 for hydrogen (deuterium). The systematic uncertainty is represented by the error band.

lations based on the GPD framework [4, 5, 11]. A possible contribution from the f_0 meson was not considered in the calculations. To date, the f_0 contribution is taken into account only by Ref. [12]. The comparison with those predictions for $\langle P_1 \rangle$ on hydrogen is shown in the panel insert of Fig. 2.

The $m_{\pi\pi}$ -dependence of the purely longitudinal moments combination $\langle P_1 + \frac{7}{3} \cdot P_3 \rangle$ is presented in Fig. 3, upper panels, for both hydrogen and deuterium. For comparison, this figure also shows (bottom panels) the combination $\langle P_1 - \frac{14}{9} \cdot P_3 \rangle$, which is believed to be dominated by the higher-twist transverse contribution to the excitation of the f_2 resonance. The comparison between these two distributions suggests that the higher-twist transverse contribution to Legendre moments in the $f_2(1270)$ region is possibly as large as the longitudinal leading-twist production. The x -dependence of $\langle P_1 \rangle$ is shown in Fig. 4 for both targets

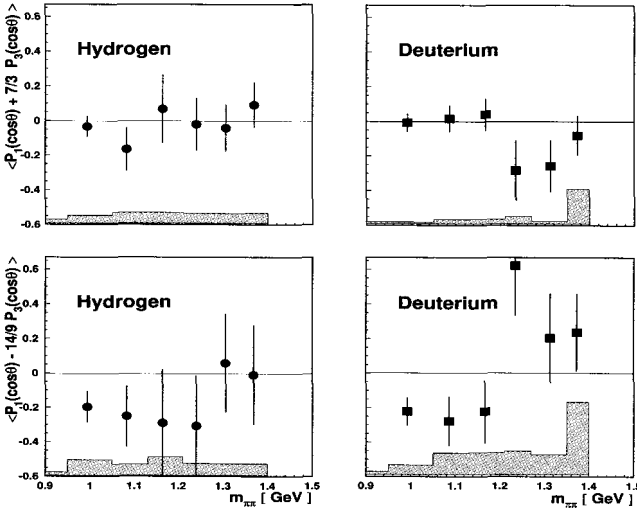


Fig. 3. The $m_{\pi\pi}$ -dependence of $\langle P_1 + 7/3 \cdot P_3 \rangle$ (upper panels) and $\langle P_1 - 14/9 \cdot P_3 \rangle$ (lower panels) for hydrogen (left panels) and deuterium (right panels). The data have $\langle x \rangle = 0.16$, $\langle Q^2 \rangle = 3.2$ (3.3) GeV^2 , and $\langle -t \rangle = 0.43$ (0.29) GeV^2 for for hydrogen (deuterium). The systematic uncertainty is represented by the error band.

in two regions of $m_{\pi\pi}$: $0.30 < m_{\pi\pi} < 0.60$ GeV and $0.60 < m_{\pi\pi} < 0.95$ GeV. The size of the $\langle P_1 \rangle$ increases with x , in agreement with theoretical expectations according to which at increasing x the $\pi^+\pi^-$ production becomes increasingly dominated by $q\bar{q}$ exchange, leading to a sizable admixture of isoscalar and isovector pion pairs. As explained above, this leads to an enhancement of the interference term.

3. Conclusions

The Legendre moments $\langle P_1(\cos\theta) \rangle$ and $\langle P_3(\cos\theta) \rangle$ for exclusive electroproduction of $\pi^+\pi^-$ pairs have been measured for the first time for hydrogen and deuterium targets. The data show signatures of the interference between the dominant isospin state $I = 1$ (P -wave) and $I = 0$ (S, D -wave) of these pion pairs. The interference of the ρ^0 amplitude with the non-resonant S -wave and resonant D -wave states appears to be larger than the interference with the resonant f_0 meson S -wave.

In the f_2 region, the combinations $\langle P_1 + 7/3 \cdot P_3 \rangle$ and $\langle P_1 - 14/9 \cdot P_3 \rangle$ are sensitive to the longitudinal and the transverse states of a D -wave $\pi^+\pi^-$ pair, respectively. Comparison of these combinations suggests that, at $\langle Q^2 \rangle = 3$ GeV^2 , the higher-twist transverse contribution to the Legendre moments in the f_2 domain can be as large as the leading-twist longitudinal contribution.

These results provide further constraints to models of the Generalized Parton Distributions.

References

1. A. Airapetian et al., (HERMES Collaboration), Phys. Lett. B **599** (2004), 212.
2. R. Fabbri, PhD Thesis, University of Ferrara 2003, HERMES-03-036.
3. J. C. Collins, L. Frankfurt and M. Strikman, Phys. Rev. D **56**, (1997) 2982.
4. B. Lehmann-Dronke et al., Phys. Lett. B **475**, (2000) 147.

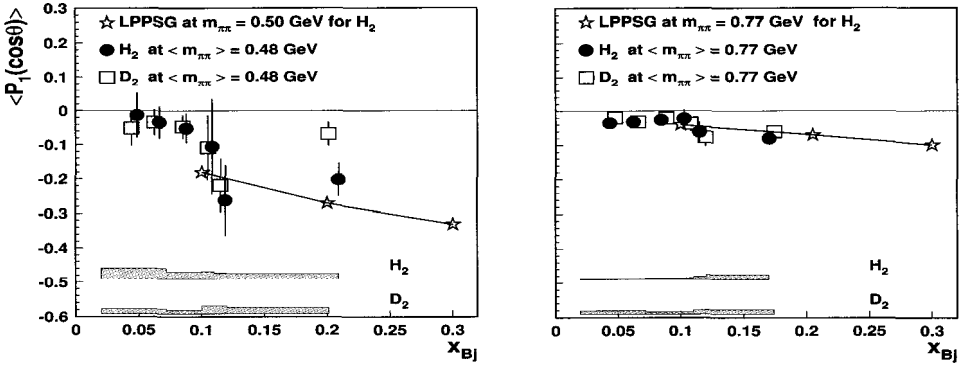


Fig. 4.

The x -dependence of the Legendre moments $\langle P_1 \rangle$ for both targets separately, in the regions $0.30 < m_{\pi\pi} < 0.60$ GeV (left panel) and $0.60 < m_{\pi\pi} < 0.95$ GeV (right panel).

The systematic uncertainty is given by the error band. Theoretical predictions (stars) from LPPSG [4] for hydrogen, which neglect two-gluon exchange mechanism, are compared with the data.

5. B. Lehmann-Dronke et al., Phys. Rev. D **63**, (2001) 114001.
6. D. Müller et al., Fortsch. Phys. **42** (1994) 101.
7. A. V. Radyushkin, Phys. Rev. D **56** (1997) 5524.
8. X. Ji, J. Phys. G **24** (1998) 1181.
9. M. Diehl, Phys. Rept. **388** (2003) 41.
10. K. Ackerstaff et al., (HERMES Collaboration), N.I.M. A **417**, 230 (1998).
11. B. Lehmann-Dronke, Private Communication.
12. Ph. Haegler et al., Phys. Lett.B **535** (2002), 117.

EXCLUSIVE ELECTROPRODUCTION OF PIONS AND VECTOR MESONS AT HERMES

A. ROSTOMYAN

HERMES/DESY, Hamburg, Germany

(on behalf of HERMES Collaboration)

Hard exclusive meson production in deep inelastic lepton scattering provides access to the unknown Generalized Parton Distributions (GPDs) in the nucleon. GPDs parameterize the nucleon structure and provide a unified description of exclusive/inclusive reactions. This paper reports on the measurement of hard exclusive π^+ and light vector meson production on an internal hydrogen gas target at HERMES using the 27.6 GeV HERA positron beam. First preliminary results for the total exclusive π^+ production cross section are presented and compared with GPD calculations. Spin density matrix elements have been determined for exclusive ρ^0 and ϕ productions, and the longitudinal component of the total cross section has also been compared to GPD calculations.

1. Introduction

Interest in hard exclusive electroproduction of mesons has grown since the QCD factorization theorem was proved for longitudinal polarized photons [1]. In that scheme, the target nucleon structure is parameterized by four Generalized Parton Distributions (GPDs). The quantum numbers of the produced meson select different GPDs. While exclusive vector mesons production is sensitive only to unpolarized GPDs (H and E), pseudoscalar meson production selects the polarized GPDs (\tilde{H} and \tilde{E}).

The data was collected using an internal hydrogen gas target in the 27.6 GeV HERA positron storage ring at DESY. The scattered positron and the produced mesons were detected by the HERMES spectrometer [2], which features excellent particle identification. The recoiling nucleon was not detected, and the exclusive process was identified via the missing mass or missing energy of the reaction.

2. π^+ production

The kinematic cuts applied on the scattered positron were: $Q^2 > 1 \text{ GeV}^2$, $0.02 < x < 0.8$ and $W > 2 \text{ GeV}$. The exclusive production of pions is selected by requiring the missing mass M_x of $ep \rightarrow e\pi^+X$ reaction to correspond to the nucleon mass. Due to limited experimental resolution, the exclusive channel cannot be separated from neighbouring non-exclusive

channels. As exclusive π^- production on a hydrogen target with a nucleon in the final state is forbidden, the non-exclusive π^+ background was estimated from the normalized number of π^- satisfying the same cuts as the π^+ ^{Ref.} [3]. The difference between the π^+ and π^- missing mass distributions shows a clear peak centred at the nucleon mass.

The photoproduction cross section for each x and Q^2 bin can be extracted as:

$$\sigma^{\gamma^* p \rightarrow \pi^+ n}(x, Q^2) = \frac{N_{\pi}^{excl}}{L \Delta x \Delta Q^2 \Gamma(\langle x \rangle, \langle Q^2 \rangle) \kappa(x, Q^2)} \quad (1)$$

where N_{π}^{excl} is the number of background corrected π^+ , L is the integrated luminosity, Γ is the virtual photon flux factor, Δ is related to the size of the x, Q^2 bins, and κ is the probability of detecting an exclusive π^+ in HERMES. A Monte Carlo based on GPD parameterization [4] was used to determine the detection probability. It varies between 0.02 and 0.25 according to the Q^2, x bins, with a relative systematic error evaluated to be smaller than 15%.

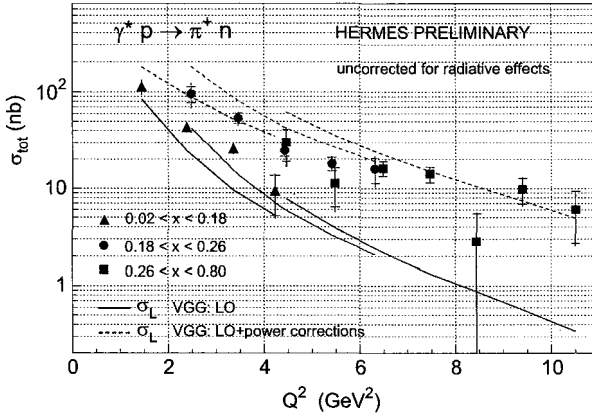


Fig. 1. The total cross section for exclusive π^+ production as a function of Q^2 for three different x ranges and integrated over t . The curves represent calculations based on a GPD-model [4].

The Q^2 dependence of the total cross section for three different x bins was obtained in Figure 1^{Ref.} [5]. These preliminary data have not been corrected yet for radiative effects, roughly estimated to be about 20% and showing no dependence on x or Q^2 . The total cross section σ_{tot} is the sum of the longitudinal (L) and transverse (T) parts, $\sigma_{tot} = \sigma_T + \epsilon \sigma_L$, where ϵ is the virtual photon polarization factor. Only the longitudinal part can be compared to GPDs. At HERMES, the separation of the transverse and longitudinal components is not feasible. However, since the transverse contribution is expected to be suppressed by $1/Q^2$ with respect to the longitudinal one, and ϵ ranges from 0.8 to 0.95, at large Q^2 the longitudinal part is expected to dominate. Calculations for HERMES kinematics based on Regge theory also predict the transverse part to be at least four times less than the longitudinal part. The solid lines show the leading-order calculation for the mean x and Q^2 corresponding to the data and integrated over t . The dashed lines include power correc-

tions. While the leading order calculations underestimate the data, the evaluation of power corrections appears to be too large. In general the Q^2 dependence is in agreement with the theoretical expectations.

3. Vector meson production

The vector mesons (VM) are identified through the following decay channels: $\rho^0 \rightarrow \pi^+\pi^-$ and $\phi \rightarrow K^+K^-$. For both samples, clear peaks have been observed in the invariant mass distributions in the expected regions. The exclusive events are concentrated in the low missing energy region ($\Delta E = M_x^2 - M_p^2/2M_p < 0.4$). The background contamination to the exclusive sample estimated by LEPTO Monte Carlo is about 10%.

In contrast to π^+ , the measured total VM production cross section can be splitted into longitudinal and transverse components assuming s-Channel Helicity Conservation. σ_L is related to the total VM production cross section $\sigma^{\gamma^* p \rightarrow \rho^0 p}$ via the ratio $R = \sigma_L/\sigma_T$

$$\sigma_L = \frac{R}{1 + \epsilon R} \sigma^{\gamma^* p \rightarrow \rho^0 p} \quad (2)$$

R is derived from the matrix element r_{00}^{04} extracted from the decay angle distribution of VM. The HERMES results for R for both ρ^0 and ϕ mesons are in good agreement with the world data [6]. The measurements of σ_L are compared to the results of E665 experiment and to the model calculation given by VGG [4, 7] (Figures 2, 3). The solid lines represent the results of these calculations. The dashed curves represent the quark exchange and the dotted lines the two-gluon exchange contribution. For ρ^0 mesons the quark exchange contribution dominates in the full range of the HERMES measurement. For ϕ mesons, only two-gluon exchange plays a role.

4. Prospects for exclusive meson production

Large target spin asymmetries (TSA) have been predicted for the exclusive production of mesons from a transversely polarized target [8]. They give access to linear combinations of GPDs \tilde{H} and \tilde{E} for π^+ and E and H for ρ^0 . In the case of ρ^0 the contribution of the GPD E dominates. It is related to the total angular momentum J of the quarks. Hence the TSA opens the perspective to extract J^u and J^d for the u and d quarks, respectively.

Since 2002, data has been collected with a transversely polarized hydrogen gas target. This running period, which will continue till summer 2005, will allow the measurement of TSA for π^+ and ρ^0 .

References

1. J.C.Collins, L.Frankfurt, M.Strikman, *Phys.Rev.* **D56**, 2982 (1997).
2. K.Ackerstaff et al.(HERMES), *Nucl.Instr.Meth.* **A417** 230 (1998)
3. A.Airapetian et al.(HERMES), *Phys.Lett.* **B535** 85 (2002)
4. M.Vanderhaegen, P.A.M Guichon, M.Guidal, *Phys.Rev* **D60** 094017 (1999)
5. C.Hadjidakis et al.(HERMES), hep-ex/0405078
6. A. Airapetian et al, *Eur. Phys. Jour.* **C 17** 389 (2000)

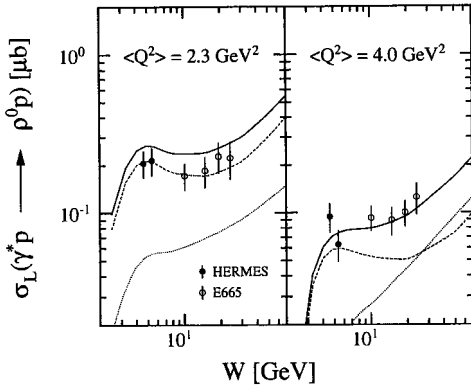


Fig. 2. The longitudinal component of the cross section for exclusive ρ^0 production.

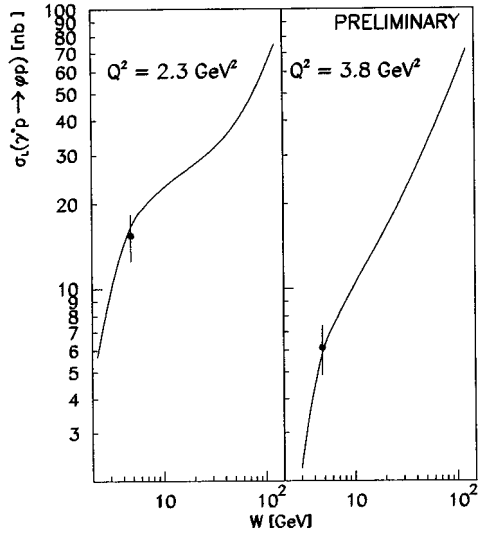


Fig. 3. The longitudinal component of the cross section for exclusive ϕ production.

7. M.Vanderhaegen, P.A.M Guichon, M.Guidal, *Phys.Rev.Lett* **80** 5064 (1998)
8. K.Goeke,M.V.Polyakov,M.Vanderhaegen, *Prog.Part.Nucl.Phys***47** 401 (2001)

A NEW ANGULAR MOMENTUM SUM RULE

B. L. BAKKER

Vrije Universiteit, Amsterdam, The Netherland

E. LEADER

Imperial College, London, United Kingdom

T. L. TRUEMAN

Brookhaven National Laboratory, Upton, USA

Sum rules, relating the total angular momentum of a nucleon to the spin and orbital angular momentum carried by its constituents, are interesting and important in understanding the internal structure of the nucleon. In a much cited paper, Jaffe and Manohar stressed the subtleties involved in deriving general angular momentum sum rules. As they point out, too naive an approach leads immediately to highly ambiguous divergent integrals, and a careful limiting procedure has to be introduced in order to obtain physically meaningful results. In this it is essential to work with non-diagonal matrix elements $\langle p', \sigma | \mathbf{J} | p, \sigma \rangle$, and this can have some unexpected consequences. Jaffe and Manohar comment that to justify rigorously the steps in such a procedure requires the use of normalizable wave packets, though they do *not* do this explicitly in their paper. *We show that the results in the literature are incorrect.* Surprisingly it turns out that the results are very sensitive to the type of relativistic spin state used to describe the motion of the particle *i.e.* whether a standard canonical (*i.e.* boost, as in *e.g.* Bjorken-Drell) state or a helicity state is utilized. We present results for the matrix elements of the angular momentum operators, valid in an arbitrary Lorentz frame, both for helicity states and canonical states. We present a new sum rule for transversely polarized nucleons.

1. The Origin of the Problem

In the standard approach one relates the matrix elements of the angular momentum operators to those of the energy-momentum tensor $T^{\mu\nu}(x)$, which is conserved. Typically one deals with expressions like

$$M^{\mu\nu\lambda}(x) \equiv x^\nu T^{\mu\lambda}(x) - x^\lambda T^{\mu\nu}(x) \quad (1)$$

The angular momentum operators are space integrals of the spatial components of these, so we would like to know the structure of the forward matrix elements

$$\mathcal{M}^{0ij}(p, s) \equiv \langle p, s | \int d^3x M^{0ij}(x, 0) | p, s \rangle. \tag{2}$$

We have:

$$\begin{aligned} \mathcal{M}^{0ij}(p, s) &= \int d^3x \langle p, s | x^i T^{0j}(x) - x^j T^{0i}(x) | p, s \rangle \\ &= \int d^3x x^i \langle p, s | e^{iP \cdot x} T^{0j}(0) e^{-iP \cdot x} | p, s \rangle - (i \leftrightarrow j) \\ &= \int d^3x x^i \langle p, s | T^{0j} | p, s \rangle - (i \leftrightarrow j). \end{aligned} \tag{3}$$

The integral in Eq. (3) is *totally ambiguous*, being either infinite or, by symmetry, zero. The essential problem is to obtain a sensible physical expression, in terms of p and s , for the above matrix element. The fundamental idea is to work with a *non-forward* matrix element, and then to try to approach the forward limit. This is similar to what is usually done when dealing with non-normalizable plane wave states, and it requires the use of wave packets for a rigorous justification.

2. The Source of Errors in the Literature

The spin state of the nucleon is labelled by the momentum and the *covariant* spin vector \mathcal{S} , and in these treatments [1,2] the most crucial error is the mishandling of the matrix elements of a covariant tensor operator. If $T^{\mu\lambda}$ transforms as a second-rank tensor its *non-forward* matrix elements do *not* transform covariantly [3]. The covariance is spoilt, for canonical spin states by the Wigner rotation, and for helicity states by the analogous Wick helicity rotation [4]. Only by first factoring out the wave-functions (in our case Dirac spinors) i.e. by writing

$$\langle p', \mathcal{S}' | T^{\mu\lambda} | p, \mathcal{S} \rangle = \bar{u}(p', \mathcal{S}') \mathcal{T}^{\mu\nu}(p', p) u(p, \mathcal{S}). \tag{4}$$

does the function, $\mathcal{T}^{\mu\nu}(p', p)$, transform covariantly.

3. Comparison of Our Results with those in the Literature

We have used three different approaches: a relativistic Dirac particle wave-packet, a field theoretic wave packet and a totally independent method based on the rotational properties of states. All give the same result [5]. The nicely covariant looking, but alas wrong, form of the expectation value of the angular momentum operators given by Jaffe-Manohar is:

$$\langle p, \mathcal{S} | \int d^3x M^{0ij}(x) | p, \mathcal{S} \rangle_{JM} = \left[2p^0 \epsilon^{j\beta\sigma} - p^i \epsilon^{0j\beta\sigma} + p^j \epsilon^{0i\beta\sigma} \right] \frac{p_\beta \mathcal{S}_\sigma}{4M p_0} \tag{5}$$

In terms of \mathbf{p} and \mathbf{s} this leads to

$$\langle J_i \rangle_{JM} = \frac{1}{4M p_0} \left\{ (3p_0^2 - M^2) s_i - \frac{3p_0 + M}{p_0 + M} (\mathbf{p} \cdot \mathbf{s}) p_i \right\} \tag{6}$$

for standard (e.g. Bjorken-Drell) canonical spin states, to be compared with our result

$$\langle J_i \rangle = \frac{1}{2} s_i \quad (7)$$

(In the above we have left out terms involving the derivative of a delta-function, which vanish for a symmetrical wave-packet). In general these are different. However, if $s = \hat{p}$ the J-M value agrees with Eq.(7), while if $s \perp \hat{p}$ they are not the same. Because our result Eq. (7) does not look manifestly covariant, we have shown in detail that it does in fact respect Lorentz invariance.

4. Sum Rules

Sum rules, relating the total angular momentum of a nucleon to the spin and orbital angular momentum carried by its constituents, are important in understanding the internal structure of the nucleon. In order to deal with the massless gluons we need the analogue of Eq. (7) for helicity states for which we find a surprisingly different result:

$$\langle p', \lambda' | J_i | p, \lambda \rangle = (2\pi)^3 2p_0 [\lambda \eta_i(p) \delta_{\lambda \lambda'}] \quad (8)$$

where

$$\eta_x = \cos(\phi) \tan(\theta/2), \quad \eta_y = \sin(\phi) \tan(\theta/2), \quad \eta_z = 1. \quad (9)$$

and (θ, ϕ) are the polar angles of p . The agreement between our results and those of J-M for canonical spin states when $s = \hat{p}$ is consistent with the intuitive sum rule

$$\frac{1}{2} = \frac{1}{2} \Delta \Sigma + \Delta G + \langle L^q \rangle + \langle L^G \rangle \quad (10)$$

In the case that $s \perp \hat{p}$ we find a new sum rule. For a proton with transverse spin vector s_T we find

$$\frac{1}{2} = \frac{1}{2} \sum_{q, \bar{q}} \int dx \Delta_T q^a(x) + \sum_{q, \bar{q}, G} \langle L_{s_T} \rangle^a \quad (11)$$

where L_{s_T} is the component of L along s_T . The structure functions $\Delta_T q^a(x) \equiv h_1^q(x)$ are known as the quark transversity or transverse spin distributions in the nucleon. Note that no such parton model sum rule is possible with the J-M formula because, as $p \rightarrow \infty$, Eq. (6) for $i = x, y$ diverges. The result Eq. (11) has a very intuitive appearance, similar to Eq. (10). Note that the RHS of Eq. (11) is different from the expression for the *tensor charge*, which involves the difference of the contributions of quarks and antiquarks. In Eq. (11) they are added. The structure functions $\Delta_T q^a(x) \equiv h_1^q(x)$ can be measured in doubly polarized Drell-Yan reactions, and also from the transverse single-spin asymmetry in semi-inclusive hadronic interactions.

5. Summary

1) The standard derivation of the tensorial structure of the expectation value of the angular momentum J , for a relativistic spin- s particle, in which the matrix elements of the angular

momentum operators are related to the matrix elements of the energy-momentum tensor, is rendered difficult by the singular nature of the operators involved. We have shown that the results in the literature are incorrect.

2) We have shown that, surprisingly, the results for helicity states are very different from those for standard canonical spin states.

3) Using a Fock-space picture of the proton, we have used our results to obtain a new sum rule for a transversely polarized nucleon, which involves the transverse spin or transversity distribution $\Delta_T q(x) \equiv h_1(x)$, and which is similar in form to the classic longitudinal spin sum rule.

References

1. R. L. Jaffe and A. Manohar, *Nucl. Phys.* **B 337**, 509 (1990)
2. G. M. Shore and B. E. White, *Nucl. Phys.* **B 581**, 409 (2000)
3. H. P. Stapp, *Phys. Rev.* **125**, 2139 (1962)
4. E. Leader, *Spin in Particle Physics*, Cambridge University Press (2001)
5. B.L.G.Bakker, E.Leader and T.L.Trueman, arXiv:hep-ph/0406139 v2 (2004)

FACTORIZATION AND UNIVERSALITY IN AZIMUTHAL ASYMMETRIES

F. PIJLMAN

Department of Physics, Vrije Universiteit Amsterdam, Amsterdam, The Netherlands

The theoretical status of transverse momentum dependent factorization in semi-inclusive DIS and Drell-Yan is not clear, in contrast to claims in the literature in which gauge links only at one loop were considered explicitly. Recently obtained results beyond this order question the validity of these claims and will be briefly discussed. Possible input from experiments to solve these matters will be outlined.

1. The present theoretical status

Single spin asymmetries (SSA's) are full of surprises and give rise to questions about factorization. In a factorized description of SSA's one needs a special class, called T-odd, of *transverse momentum dependent* distribution functions, or fragmentation functions. Three separate mechanisms were suggested to generate T-odd functions. The first [1] consists of non-zero gluon fields at infinity and was unified [2] with the second mechanism which is based on fully connected gauge links [3]. The non-trivial paths of these links connect the two quark fields in the distribution of fragmentation functions and could lead to SSA's. The third mechanism, appearing only for fragmentation functions, comes from final state interactions [4].

In a factorized description the gauge links have particular implications: T-odd distribution functions in semi-inclusive DIS (SIDIS) enter with a different sign in Drell-Yan (DY) [5]; T-odd distribution functions involve the gluon field in the nucleon [2]; gauge links violate naive Lorentz-invariance relations [6]; links can give rise to new functions [7]; and links might imply non-universal fragmentation functions [2]. This raises the question of whether a factorized description is allowed for transverse momentum dependent observables.

Several articles deal with factorization in SIDIS and DY. Recently a spin dependent factorization theorem for SIDIS and DY was claimed where the all-order argument is based on generalized Ward identities [8]. Subsequently, part of the relevant all-order calculations were presented [9], and possible problems on factorization in DY were pointed out [10]. Later, it was suggested that the fragmentation functions and soft factor in the factorization theorem should contain different gauge links, and the authors [11] claimed universality of

distribution, fragmentation functions and soft factors in SIDIS, e^+e^- annihilation and DY. The proof of universal fragmentation functions was formalized at one loop, but again the all-order arguments are based on Ward identities, and an explicit proof was not given.

Despite the claims of factorization and the significant progress made in the previous references, the present situation is not clear. However, factorization remains essential for comparing experimental results and relating them to theoretical predictions. In the next section gauge link derivations [9] and their consequences for factorization [10] will be briefly presented. As will be shown, Ward identities should be applied carefully. The last section will discuss how experiments and theory could contribute to solve these matters.

2. Gauge links and factorization

Gauge links for hard scattering diagrams can be derived by coupling on-shell longitudinally polarized gluons to the diagrams. The delicate use of Ward identities in these calculations is illustrated by the following QED example. When considering S-matrix elements, the sum of coupling a photon with $\varepsilon = p_1$ (and momentum $p_1 \sim n_+$) to all possible places in the tree-level amplitude $\gamma^*(q - p_1) + e(k) \rightarrow e(p)$ vanishes, giving the relation

$$\begin{array}{c} e(k) \longrightarrow e(p) \\ \left\{ \begin{array}{c} \text{---} \\ \text{---} \\ \text{---} \end{array} \right\} \begin{array}{c} p_1^\alpha \\ p_1^\alpha \\ p_1^\alpha \end{array} \\ \gamma^*(q - p_1) \end{array} = - \begin{array}{c} e(k) \longrightarrow e(p) \\ \left\{ \begin{array}{c} \text{---} \\ \text{---} \\ \text{---} \end{array} \right\} \begin{array}{c} p_1^\alpha \\ p_1^\alpha \\ p_1^\alpha \end{array} \\ \gamma^*(q - p_1) \end{array} . \quad (1)$$

However, in link derivations where the photon polarization is the momentum *direction*, the sum does not vanish. In fact, it equals a gluonic pole matrix element [2, 9] which could produce a SSA by itself

$$\begin{array}{c} e(k) \longrightarrow e(p) \\ \left\{ \begin{array}{c} \text{---} \\ \text{---} \\ \text{---} \end{array} \right\} \begin{array}{c} \text{dir}(p_1)^\alpha \\ \text{dir}(p_1)^\alpha \\ \text{dir}(p_1)^\alpha \end{array} \\ \gamma^*(q - p_1) \end{array} + \begin{array}{c} e(k) \longrightarrow e(p) \\ \left\{ \begin{array}{c} \text{---} \\ \text{---} \\ \text{---} \end{array} \right\} \begin{array}{c} \text{dir}(p_1)^\alpha \\ \text{dir}(p_1)^\alpha \\ \text{dir}(p_1)^\alpha \end{array} \\ \gamma^*(q - p_1) \end{array} = \begin{array}{c} e(k) \longrightarrow e(p) \\ \left\{ \begin{array}{c} \text{---} \\ \text{---} \\ \text{---} \end{array} \right\} \begin{array}{c} \text{dir}(p_1)^\alpha \\ \text{dir}(p_1)^\alpha \\ \text{dir}(p_1)^\alpha \end{array} \\ \gamma^*(q - p_1) \end{array} \left(\frac{1}{p_1^+ + i\epsilon} + \frac{1}{p_1^+ - i\epsilon} \right). \quad (2)$$

Since similar effects also appear in QCD we refrained from using identities like Eq.(1). Summing over the gluons explicitly the link is straightforwardly derived to all orders in the coupling, and allows for easy consistency checks by others (are the first orders of the link correct and is the quark-quark correlator gauge invariant?). Some obtained results [2, 9, 10] are given in Fig. 1.

Gauge links form an essential ingredient in considerations of factorization. In factorization one typically tries to absorb gluon radiation with small transverse momentum in a soft blob, hoping that the constructed soft blobs are in some sense universal. From Fig.1C it becomes clear that the behaviour of gauge links when gluons are radiated depends on the process. Although still calculable, the radiated gluon in DY in Fig.1C2 needs to be absorbed when constructing the upper blob, but since the gluon affects the gauge link of the lower blob, it will be difficult - if not impossible - to factorize such diagrams [10]. This result appears beyond the explicitly considered one-loop calculations of the references discussed earlier. Similar effects appear in other hadron-hadron scattering processes and in fragmentation functions in SIDIS. They do not appear in distribution functions in lepton or photon-hadron scattering, nor in fragmentation functions in e^+e^- annihilation.

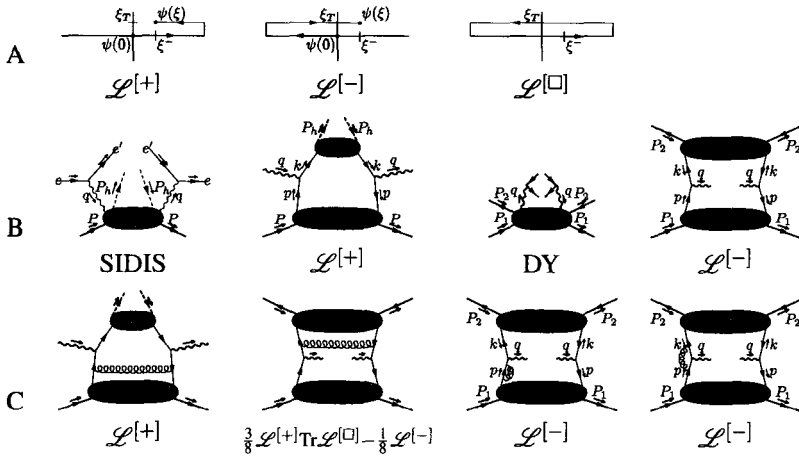


Fig. 1. The gauge links presented here are obtained as follows: (1) start with a certain hard scattering diagram with correlators containing no links, (2) sum over all diagrams of longitudinally polarized gluons connecting a considered soft blob and the hard diagram in the eikonal approximation. Gluons coupling directly to the quark of the considered correlator are already present in the soft blob definition, (3) the sum results in a link in the considered soft blob multiplied by the *same* hard scattering diagram.

A: various gauge links. B: tree-level SIDIS and DY, cross-sections and leading contributions in parton model with gauge links for Φ . C: corrections to SIDIS and DY with gauge links for lower blobs; the coupling of the longitudinally polarized gluons to the explicitly drawn gluon *has to be included* to obtain a proper gauge link; the gauge links for the virtual corrections have only been verified to the first non-trivial order.

3. Experimental and theoretical input

We would like to stress that in those processes where one is not sensitive to the transverse momenta of the quarks, one is dealing with transverse momentum integrated distribution and fragmentation functions. The links connect the two quark fields by a straight line and are process independent. Therefore, integrated SIDIS and DY have no problems regarding their link structures. As such, transversity can be best accessed via integrated DY, A polarization in SIDIS, or two hadron fragmentation in SIDIS [12].

To understand transverse momentum dependent factorization and universality we need experimental and theoretical input. A comparison of a T-odd distribution function, such as the Sivers function, in SIDIS and DY can have the following outcomes: (1) they only differ by a sign and the processes apparently factorize and links have predicting power, (2) they are both zero (for some unknown symmetry), a factorization theorem for DY probably exists, and the Lorentz invariance relations might hold, (3) they are totally different and factorization, as we understand it now, is violated.

It has been advocated [11, 13] that fragmentation functions are independent of the link direction. Although the supporting model [13] ignores non-perturbative quarks in the nucleon with $p^2 > m^2$ which could be sensitive to the link direction, the scenario remains possible. If fragmentation shows up to be link independent, then factorization in SIDIS is probably feasible. More complete models or experimental evidence (compare z dependences of $D_1(z, P_h^{\perp 2})$ or $H_1^{\perp(1)}(z)$ of SIDIS with e^+e^-) would contribute a lot.

This work, done in collaboration with C. Bomhof and P. Mulders, was presented at a nicely organized conference SPIN 2004 in Trieste. D. Boer, L. Gamberg, P. Hägler and A.

Metz are acknowledged for useful discussions.

References

1. A.V. Efremov and O.V. Teryaev, *Phys. Lett.* **B150**, 383 (1985),
J. Qiu and G. Sterman, *Phys. Rev. Lett.* **67**, 2264 (1991).
2. D. Boer, P.J. Mulders and F. Pijlman, *Nucl. Phys.* **B667**, 201 (2003).
3. A.V. Belitsky, X. Ji and F. Yuan, *Nucl. Phys.* **B656**, 165 (2003).
4. J.C. Collins, *Nucl. Phys.* **B396**, 161 (1993).
5. J.C. Collins, *Phys. Lett.* **B536**, 43 (2002).
6. K. Goeke, A. Metz, P. Pobylitsa, M. Polyakov, *Phys. Lett.* **B567**, 27 (2003).
7. A. Bacchetta, P.J. Mulders and F. Pijlman, *Phys. Lett.* **B595**, 309 (2004).
8. X. Ji, J. Ma and F. Yuan, hep-ph/0404183, *Phys. Lett.* **B597**, 299 (2004).
9. C.J. Bomhof, P.J. Mulders and F. Pijlman, *Phys. Lett.* **B596**, 277 (2004).
10. F. Pijlman, hep-ph/0409332.
11. J.C. Collins and A. Metz, hep-ph/0408249.
12. A. Bacchetta and M. Radici, *Phys. Rev.* **D69**, 074026 (2004)
13. A. Metz, *Phys. Lett.* **B549**, 139 (2002).

A PLANNED JEFFERSON LAB EXPERIMENT ON SPIN-FLAVOUR DECOMPOSITION

X. JIANG

Rutgers University, Piscataway, New Jersey, USA

P. BOSTED, M. JONES

Thomas Jefferson National Accelerator Facility, Newport News, USA

D. DAY

University of Virginia, Charlottesville, Virginia, USA.

Experiment E04-113 at Jefferson Lab Hall C plans to measure the beam-target double-spin asymmetries in semi-inclusive deep-inelastic $p(e, e'h)X$ and $d(e, e'h)X$ reactions ($h = \pi^+, \pi^-, K^+$ or K^-) with a 6 GeV polarised electron beam and longitudinally polarised NH_3 and LiD targets. The high statistics data will allow a spin-flavour decomposition in the region of $x = 0.12 \sim 0.41$ at $Q^2 = 1.21 \sim 3.14$ GeV^2 . In particular, leading order and next-to-leading order spin-flavour decomposition of Δu_v , Δd_v and $\Delta \bar{u} - \Delta \bar{d}$ will be extracted based on the measurement of the combined asymmetries $A_{1N}^{\pi^+ - \pi^-}$. The possible flavour asymmetry of the polarised sea will be addressed in this experiment.

1. Introduction

Remarkable progress in the knowledge of the polarised quark distributions $\Delta q_f(x)$ has been made in the last decade through inclusive deep-inelastic lepton scattering (DIS). However, the information available from inclusive DIS process has inherent limitations. As the cross sections are sensitive only to e_q^2 , an inclusive DIS experiment probes quarks and anti-quarks on an equal footing, and therefore is not sensitive to symmetry breaking in the sea sector. The sensitivity to each individual quark flavour can be realized in semi-inclusive deep inelastic scattering (SIDIS) in which one of the leading hadrons is also detected. Recently, the HERMES collaboration published the results of a leading order spin-flavour decomposition from polarised proton and deuteron data, and for the first time extracted the \bar{u} , \bar{d} and $s = \bar{s}$ sea quark polarisation [1].

The validity of the HERMES method of spin-flavour decomposition relies explicitly on several non-trivial assumptions. First, the leading-order “naive x - z factorization” was assumed, and the next-to-leading order terms were neglected. This implies that the cross sections factorize into the x -dependent quark distributions and the z -dependent fragmentation functions:

$$\sigma^h(x, z) = \sum_i e_f^2 q_f(x) \cdot D_{q_f}^h(z), \quad \Delta\sigma^h(x, z) = \sum_i e_f^2 \Delta q_f(x) \cdot D_{q_f}^h(z). \quad (1)$$

Furthermore, it was assumed that the quark fragmentation process and the experimental phase spaces were well-understood, so that a LUND model based Monte Carlo simulation program can reliably reproduce the “purity matrices” which account for the probability correlations between the detected hadrons and the struck quarks [1].

It was pointed out by Christova and Leader [2] that if the combined asymmetries $A_{1N}^{\pi^+-\pi^-}$ are measured, quark polarisation Δu_v , Δd_v and $\Delta\bar{u} - \Delta\bar{d}$ can be extracted at leading order without the complication of fragmentation functions. Even at next-to-leading order, information on the valence quark polarisations is well preserved in the combined asymmetries $A_{1N}^{\pi^+-\pi^-}$.

2. The Christova-Leader method at LO and NLO

At the leading order, under isospin symmetry and charge conjugation, the fragmentation functions cancel exactly in the combined asymmetry $A_{1N}^{\pi^+-\pi^-}$, the s -quark does not contribute, and we have [2] :

$$\begin{aligned} A_{1p}^{\pi^+-\pi^-} &= \frac{\Delta\sigma_p^{\pi^+} - \Delta\sigma_p^{\pi^-}}{\sigma_p^{\pi^+} - \sigma_p^{\pi^-}} = \frac{4\Delta u_v - \Delta d_v}{4u_v - d_v}, \\ A_{1d}^{\pi^+-\pi^-} &= \frac{\Delta\sigma_d^{\pi^+} - \Delta\sigma_d^{\pi^-}}{\sigma_d^{\pi^+} - \sigma_d^{\pi^-}} = \frac{\Delta u_v + \Delta d_v}{u_v + d_v}. \end{aligned} \quad (2)$$

Therefore, measurements of $A_{1N}^{\pi^+-\pi^-}$ on the proton and the deuteron can determine Δu_v and Δd_v . On the other hand, the existing inclusive DIS data already constrain another non-singlet quantity:

$$g_1^p(x, Q^2) - g_1^n(x, Q^2) = \frac{1}{6} [(\Delta u + \Delta\bar{u}) - (\Delta d + \Delta\bar{d})] |_{LO}. \quad (3)$$

The polarised sea asymmetry can be extracted at leading order following:

$$(\Delta\bar{u} - \Delta\bar{d})|_{LO} = 3(g_1^p - g_1^n)|_{LO} - \frac{1}{2}(\Delta u_v - \Delta d_v)|_{LO}. \quad (4)$$

At the next-to-leading order, x and z are mixed through double convolutions, and instead of Eq. 1, we have:

$$\begin{aligned} \sigma^h(x, z) &= \sum_f e_f^2 q_f \left[1 + \otimes \frac{\alpha_s}{2\pi} C_{qq} \otimes \right] D_{q_f}^h \\ &+ \left(\sum_f e_f^2 q_f \right) \otimes \frac{\alpha_s}{2\pi} C_{qg} \otimes D_G^h + G \otimes \frac{\alpha_s}{2\pi} C_{gq} \otimes \left(\sum_f e_f^2 D_{q_f}^h \right) \end{aligned} \quad (5)$$

and similarly for $\Delta\sigma^h$, where C_s are well-known Wilson coefficients. The convolution terms become much simpler [2] in quantities relate to $\sigma^{\pi^+} - \sigma^{\pi^-}$, since the gq and qg terms in Eq. 5 are identical for π^+ and π^- :

$$\begin{aligned} A_{1p}^{\pi^+-\pi^-} &= \frac{(4\Delta u_v - \Delta d_v)[1 + \otimes(\alpha_s/2\pi)\Delta C_{qq} \otimes](D^+ - D^-)}{(4u_v - d_v)[1 + \otimes(\alpha_s/2\pi)C_{qq} \otimes](D^+ - D^-)}, \\ A_{1d}^{\pi^+-\pi^-} &= \frac{(\Delta u_v + \Delta d_v)[1 + \otimes(\alpha_s/2\pi)\Delta C_{qq} \otimes](D^+ - D^-)}{(u_v + d_v)[1 + \otimes(\alpha_s/2\pi)C_{qq} \otimes](D^+ - D^-)}. \end{aligned} \quad (6)$$

in which Δu_v and Δd_v evolve as non-singlets and do not mix with gluon and sea distributions. Once we extract Δu_v and Δd_v at next-to-leading order from Eq. 6, $\Delta\bar{u} - \Delta\bar{d}$ can be determined to next-to-leading order using the well-known NLO form of Eq. 3.

3. The Jefferson Lab experiment E04-113

Experiment E04-113 at Jefferson Lab Hall C [3] is specifically designed to have well controlled phase space and hadron detection efficiencies such that the combined asymmetries $A_{1N}^{\pi^{\pm}\pi^{\mp}}$, in addition to the individual asymmetries A_{1N}^h ($h = \pi^+, \pi^-, K^+, K^-$), can be determined with high precision. The existing HMS spectrometer will be used as the hadron detector at 10.8° and a central momentum of 2.71 GeV/c, corresponding to $\langle z \rangle \approx 0.5$ to favour current fragmentation. For the electron detector, a combination of a large calorimeter array and a gas Cherenkov will be used. The experiment will cover $0.12 < x < 0.41$ with $1.21 < Q^2 < 3.14$ (GeV/c)² and $2.31 < W < 3.09$ GeV.

In addition to the Christova-Leader method, the ‘‘fixed- z purity’’ method of spin-flavour decomposition will be applied to provide a consistency check. At the well-defined z -value of this experiment, the ‘‘purity matrices’’ can be directly calculated, based on unpolarised PDFs and the ratio of fragmentation functions, rather than from a Monte Carlo simulation which involves a fragmentation model. The expected statistical accuracies and the estimated systematic uncertainties are shown in Fig.1.

4. Conclusions

Experiment E04-113 at Jefferson Lab plans to extract quark polarisations based on the measurement of the combined asymmetries $A_{1N}^{\pi^+-\pi^-}$. The much improved statistics over the HERMES data will present us with the first opportunity to probe the possible flavour asymmetry of the light sea quark polarisation.

We thank Drs. E. Christova, E. Leader, G.A. Navarro, R. Sassot, D. de Florian, A. Afanasev, W. Melnitchouk for many discussions. This work is supported in part by the US Department of Energy and the US National Science Foundation.

References

1. The HERMES collaboration, *Phys. Rev. Lett.* **92**, 012005 (2004).
2. E. Christova and E. Leader, *Nucl. Phys. B* **607**, 369 (2001).
3. Jefferson Lab experiment proposal E04-113, P. Bosted, D. Day, X. Jiang and M. Jones co-spokespersons (2004).

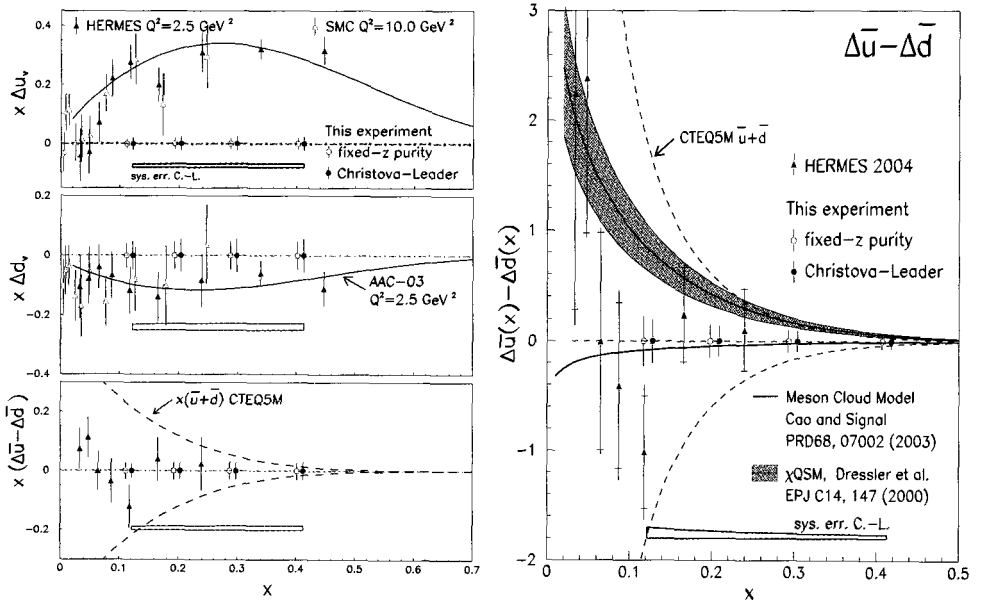


Fig. 1. The expected statistical accuracies of experiment E04-113 for two independent methods of flavour decomposition (Christova-Leader and “fixed-z purity”) are compared with the HERMES data [1] and the SMC data [4]. The open boxes represent the systematic uncertainties of the Christova-Leader method.

4. The Spin Muon Collaboration, *Phys. Lett. B* **420**, 180 (1998).

THE Q^2 -DEPENDENCE OF THE GENERALISED GERASIMOV–DRELL–HEARN INTEGRAL FOR THE DEUTERON, PROTON AND NEUTRON AND EVIDENCE FOR QUARK-HADRON DUALITY IN THE PROTON SPIN ASYMMETRY A_1

A. NAGAYTSEV

Joint Institute for Nuclear Research, Dubna, Russia

1. The Q^2 -dependence of the Generalised GDH Integrals

The Gerasimov–Drell–Hearn (GDH) [1] sum rule connects an energy–weighted integral of the difference of the helicity–dependent real–photon absorption cross sections with the anomalous contribution to the magnetic moment κ of the nucleon:

$$\int_{\nu_0}^{\infty} [\sigma_{\frac{1}{2}}(\nu) - \sigma_{\frac{3}{2}}(\nu)] \frac{d\nu}{\nu} = -\frac{2\pi^2\alpha}{M^2} \kappa^2, \quad (1)$$

where $\sigma_{\frac{1}{2}(\frac{3}{2})}$ is the photoabsorption cross section for total helicity of the photon-nucleon system equal to $\frac{1}{2}$ ($\frac{3}{2}$). The generalisation of the GDH integral to non-zero Q^2 allows us to connect the static ground state properties of the nucleon with its helicity structure as measured in inelastic scattering in the resonance and deep inelastic (DIS) regions [2, 3]:

$$\begin{aligned} I_{GDH}(Q^2) &= \int_{\nu_0}^{\infty} [\sigma_{\uparrow\downarrow}(\nu, Q^2) - \sigma_{\downarrow\uparrow}(\nu, Q^2)] \frac{d\nu}{\nu} \\ &= \frac{8\pi^2\alpha}{M} \int_0^{x_0} \frac{g_1(x, Q^2) - \gamma^2 g_2(x, Q^2)}{K} \frac{dx}{x}, \end{aligned} \quad (2)$$

where g_1 and g_2 are the polarised structure functions of the nucleon and K is the virtual-photon flux factor. The superscript $\uparrow\uparrow$ ($\uparrow\downarrow$) refers to the orientation of the target spin parallel (anti-parallel) to the electron beam polarisation. In the leading-twist approximation Eq.2 can be given as $I_{GDH}(Q^2) = \frac{16\pi^2\alpha}{Q^2} \Gamma_1$, where first moment of the the spin structure function g_1 , $\Gamma_1 = \int_0^1 g_1(x) dx$, is predicted by pQCD to have a logarithmic Q^2 evolution at large Q^2 . The HERMES polarised data taken with hydrogen and deuterium targets in 1997-2000 were used to extract the Q^2 dependence of the generalized GDH Integrals for the proton, deuteron and neutron. The full range in W^2 was separated into the resonance region ($1.0 < W^2 < 4.2$ GeV²) and the DIS region ($4.2 < W^2 < 45.0$ GeV²). The Bianchi-Thomas parameterization

was used for the unmeasured contribution at high energy [4]. The generalised GDH integral Eq.2 can be re-written in terms of the longitudinal virtual-photon asymmetry A_1 and the unpolarised structure function F_1 :

$$I_{GDH}(Q^2) = \frac{8\pi^2\alpha}{M} \int_0^{x_0} \frac{A_1(x, Q^2)F_1(x, Q^2)}{K} \frac{dx}{x}, \quad (3)$$

where K is the virtual-photon flux factor chosen in the Gilman convention [5]: $K = v\sqrt{1 + \gamma^2}$. The GDH integral for the neutron [6] was calculated from the deuteron I_{GDH}^d and the proton I_{GDH}^p reanalysed following the procedure detailed in [7]:

$$I_{GDH}^n = \frac{I_{GDH}^d}{1 - 1.5\omega_d} - I_{GDH}^p. \quad (4)$$

Here ω_d is the probability of the deuteron to be in a D-state.

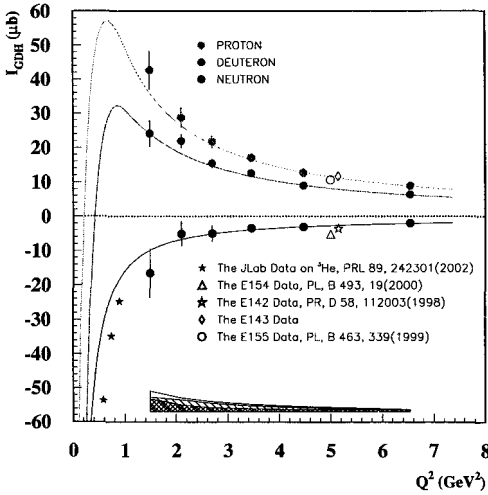


Fig. 1. The Q^2 dependence of the generalised GDH integrals. The curves shown are the predictions for the various targets according to the Soffer-Teryaev model.

Figure 1 shows the resulting Q^2 dependence of the full generalised GDH integrals [8]. The curves are Soffer-Teryaev model predictions [9] based on Q^2 evolution of g_1 and g_2 . The Q^2 -behaviour of I_{GDH} for proton and neutron can be also studied by dividing the GDH integral by the factor $16\pi^2\alpha/Q^2$, to get the Q^2 dependence expected from leading twist, as shown in Figure 2 (left panel). The data obtained for the proton and neutron over a large range in Q^2 and W^2 offer a unique possibility to evaluate the proton-neutron difference of the generalised GDH integrals. This difference is shown in Fig.2 (right panel). The data fall off as $1/Q^2$, indicating that leading twist dominates. It is found that $I_{GDH}^p - I_{GDH}^n = 14.3 \pm 0.9 \pm 1.3 \mu b$ at $Q^2 = 5 GeV^2$. This result is in agreement with

an experimental determination of the Bjorken sum rule by E143 [10], E155 [11], and is also in agreement with the Bjorken sum rule prediction of 0.182 ± 0.005 corresponding to $I_{GDH}^p - I_{GDH}^n = 16.33 \pm 0.45 \mu b$.

2. The Evidence for Quark-Hadron Duality in the Proton Spin Asymmetry A_1

The structure and the interaction of hadrons is generally described by two different but complementary approaches: the quark-gluon context at high energy, and the meson and baryon description at low energy. For some cases, the description in terms of quark-gluon degrees of freedom can be successfully extended at typically lower hadronic scales. This phenomena is called quark-hadron duality and it was introduced by Bloom and Gilman [12]. For the unpolarized structure functions, the duality was observed a long time ago, but

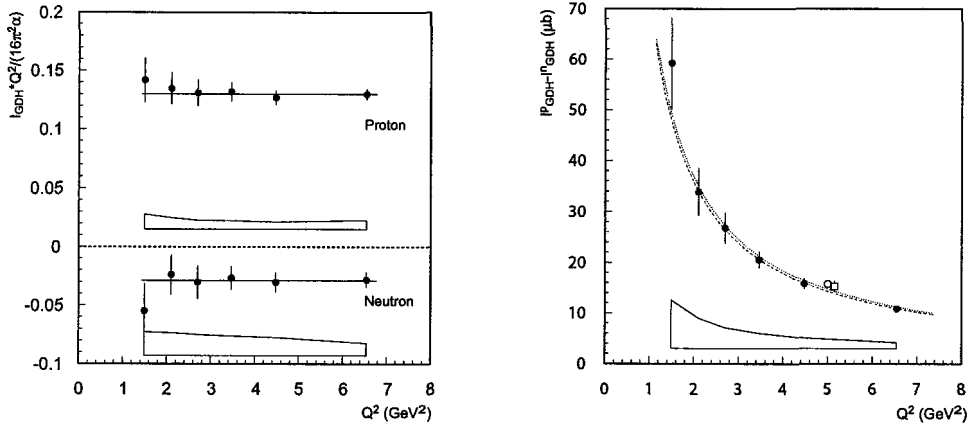


Fig. 2. Left Panel: The Q^2 dependence of the generalised GDH integrals for the proton (filled circles) and neutron (open circles) after the leading twist. Right Panel: The Q^2 dependence of the generalised GDH integral for the proton-neutron difference. The dotted curve represents the prediction from Soffer-Teryaev model. The dashed curve represents a $1/Q^2$ fit to the data. The open symbols represent the measurements of the Bjorken sum rule from E143 (square) and E155 (circle).

only recently for the polarized ones. Fig 1(left panel) shows the HERMES measurement A_1^{res} [13] in the nucleon resonance region, compared with A_1^{DIS} measured in the DIS at higher Q^2 and W^2 [10], [14], [15]. The curve is a Q^2 -independent fit to world DIS data [16] at $x > 0.3$, which fulfills the long standing SU(6)-breaking prediction of 1 at $x = 1$ [17]. The average ratio of the measured A_1^{res} to the DIS fit is $1.15 \pm 0.16 \pm 0.18$. This suggests that the description of the spin asymmetry in terms of quark degrees of freedom is also valid in the nucleon resonance region for the Q^2 range explored by the present experiment. The verification of the quark-hadron duality can be obtained by comparing the integrals of the polarised structure function g_1 in the resonance and DIS region in the same x interval. The integrals $\Gamma_1 = \int_{x_{min}}^{x_{max}} g_1(x) dx$ have been evaluated separately for the resonance and DIS domains [18]. The ratio $R = \Gamma_1^{RES} / \Gamma_1^{DIS}$ for three Q^2 values is shown in Fig. 1 (right). Also shown is the ratio R evaluated from the SLAC data, which shows a violation of duality at lower Q^2 .

In summary the generalised GDH integrals for the proton, deuteron and neutron are measured for the first time in both the resonance and DIS regions for the Q^2 range from 1.2 to 12.0 GeV². Above $Q^2=3$ GeV² the DIS contributions to the generalised GDH Integrals are dominant for all targets. Data show no indication for large non-leading twist effects. The data on generalized GDH proton-neutron difference yields good agreement with Bjorken sum rule prediction. The duality in polarized DIS was measured for the first time by HERMES. The spin asymmetry A_1 in resonance region is in agreement with DIS data at higher W^2 , Q^2 and same x . The duality ratio $R = \Gamma_1^{RES} / \Gamma_1^{DIS}$ is independent of Q^2 in measured range.

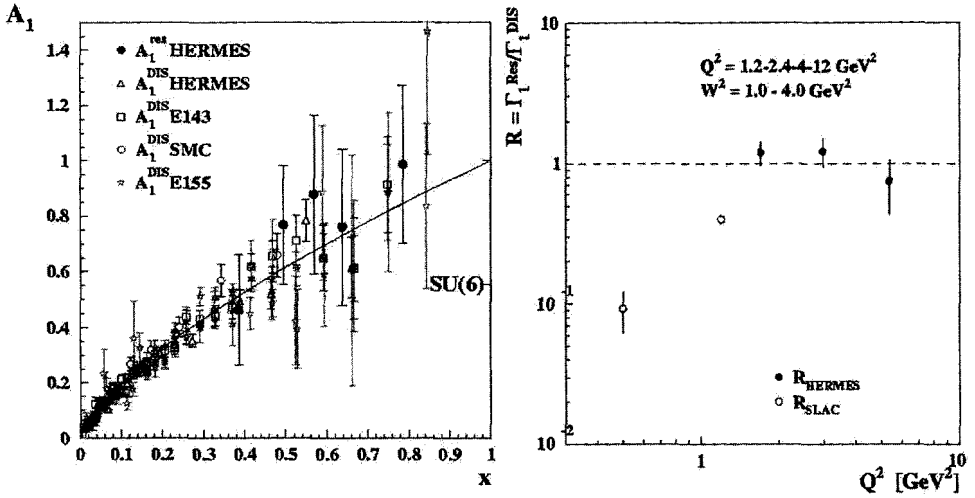


Fig. 3. Left Panel: Spin asymmetry A_1 as a function of x . The curve represents a fit to DIS data at large x . Right Panel: Ratio between Γ_1 in the resonance region and in DIS region as a function of Q^2 . The data from E143 are also shown.

References

1. S.B. Gerasimov, *Sov. J. Nucl. Phys.* **2**, (1966) 430;
S.D. Drell and A.C. Hearn, *Phys. Rev. Lett.* **16**, (1966) 908.
2. R. Pantförder, *PhD Thesis*, Universität Bonn (1998), BONN-IR-98-06, hep-ph/9805434 and reference therein.
3. D. Drechsel, S.S. Kamalov and L. Tiator, *Phys. Rev. D* **63** (2001), 114010.
4. N. Bianchi and E. Thomas, *Phys. Lett. B* **450**, (1999) 439.
5. F.J. Gilman, *Phys. Rev.* **167**, (1968) 1365.
6. C. Ciofi degli Atti et al., *Phys. Lett. B* **376**, (1996) 309.
7. HERMES Collaboration, A. Airapetian et al., *Phys. Lett. B* **494**, (2000) 1.
8. HERMES Collaboration, A. Airapetian et al., *EPJ C* **26**, (2003) 527.
9. J. Soffer and O.V. Teryaev, *Phys. Rev. D* **51**, (1995) 25;
J. Soffer and O.V. Teryaev, *Phys. Rev. Lett.* **70**, (1993) 3373.
10. E143 Collaboration, K. Abe et al., *Phys. Rev. D* **58** (1998) 112003.
11. E155 Collaboration, P. L. Anthony et al., *Phys. Lett. B* **493**, (2000) 19;
E155 Collaboration, P. L. Anthony et al., *Phys. Lett. B* **463**, (1999) 339.
12. E.D. Bloom and F.J. Gilman, *Phys. Rev. Lett.* **25**, 1140 (1970);
E.D. Bloom and F.J. Gilman, *Phys. Rev. D* **4**, 290 (1971);
13. HERMES Collaboration, A. Airapetian et al., *Phys. Rev. Lett.* **90**, (2003) 092002
14. HERMES Collaboration, A. Airapetian et al., *Phys. Lett. B* **442**, 484 (1998).
15. SMC Coll., B. Adeva et al., *Phys. Rev. D* **58**, 112001 (1998).
16. A.P. Nagaitsev et al., *JINR Rapid Commun.* N3(71), 1995, 59
17. F. Close, *Phys. Lett. B* **43**, (1973) 422
18. N. Bianchi, A. Fantoni and S. Liuti, *Phys. Rev. D* **69**, (2004) 014505

MEASUREMENT OF DEEPLY VIRTUAL COMPTON SCATTERING AT HERMES

H. MARUKYAN

Yerevan Physics Institute, Yerevan, Armenia

(on behalf of the HERMES Collaboration)

We report our latest observations of azimuthal asymmetries in deeply virtual Compton scattering with respect to the spin and the charge of the incoming lepton beam. The data have been accumulated by the HERMES experiment at DESY, scattering the HERA 27.6 GeV electron(positron) beam off hydrogen, deuterium, neon and krypton gas targets. Beam-spin asymmetries have been measured for all targets; results on beam-charge asymmetries are presented for the proton and the deuteron.

1. Introduction

Recent interest in hard exclusive processes has resulted from the theoretical description of these processes in terms of the Generalized Parton Distribution (GPD) formalism [1, 2]. This formalism offers a much more complete description of nucleon structure. It incorporates the well-known nucleon form factors determined from elastic scattering, as well as parton momentum distributions (PDFs) determined from measurements of inclusive and semi-inclusive deeply inelastic lepton-nucleon scattering (DIS). Interest in the GPD framework has also been motivated by the fact that the unknown total angular momentum components of the quarks and gluons are encoded in the GPDs [3].

One of the theoretically cleanest channels with which to probe GPDs is Deeply-Virtual Compton Scattering (DVCS), in which a highly virtual photon is absorbed on a parton within the target, producing a single real photon in the final state along with the intact recoiling nucleon (nucleus).

2. DVCS measurement at HERMES

Measurement of the DVCS process is intrinsically mixed with that of the Bethe-Heitler (BH) process, in which a real photon is radiated by the lepton rather than the quark. The cross section for the leptonproduction of real photons is therefore proportional to the square of the sum of the amplitudes:

$$d\sigma \propto |\tau_{BH}|^2 + |\tau_{DVCS}|^2 + \tau_{BH}^* \tau_{DVCS} + \tau_{DVCS}^* \tau_{BH}. \quad (1)$$

At HERMES kinematics the BH process dominates over DVCS in the cross section. However, the DVCS amplitude can be studied via the interference term by measuring various cross section asymmetries and their dependences on the azimuthal angle ϕ , defined as the angle between the lepton scattering plane and the photon production plane. The interference term $\tau_{BH}^* \tau_{DVCS} + \tau_{DVCS}^* \tau_{BH}$ (I) can be written as a series of Fourier moments in ϕ [4]

$$I \propto \pm \left(c_0^I + \sum_{n=1}^3 c_n^I \cos(n\phi) + \sum_{n=1}^3 s_n^I \sin(n\phi) \right) \quad (2)$$

where the $+(-)$ sign stands for the electron(positron) beam, and c_0^I , c_n^I and s_n^I are given by a linear combination of the Compton form factors (CFFs), which in general depend on beam helicity and target polarization. The CFFs can be expressed as convolutions of coefficient functions with the GPDs.

The squared DVCS and BH amplitudes are independent of the sign of the beam charge. Therefore the measurement of a cross section asymmetry with respect to the beam charge can be used to determine the real part of the interference term, while the imaginary part can be studied using longitudinally polarized lepton beam scattered off an unpolarized target.

In order to extract these asymmetries from the data, events were selected if they contained one photon and one scattered lepton track. Photons were identified by the energy deposition in the calorimeter and pre-shower counter in the absence of a track. The following requirements were imposed on the lepton kinematics: $Q^2 > 1 \text{ GeV}^2$; $W > 3 \text{ GeV}$. The opening angle $\Theta_{\gamma^* \gamma}$ between the virtual and real photon was limited to a range of 5 to 45 mrad.

Since the recoiling nucleon (or nucleus) was not detected, the exclusive DVCS events were selected by imposing an additional constraint on the missing mass M_x . The exclusive region was defined as $-1.5 < M_x < 1.7 \text{ GeV}$ (negative M_x values are obtained as a consequence of the finite energy resolution of the spectrometer).

3. Azimuthal asymmetries from HERMES

Azimuthal asymmetries with respect to the beam spin have been reported on hydrogen [5,6] as well as on deuteron and neon [7].

The azimuthal dependence of the beam-charge asymmetry A_C is extracted as

$$A_C(\phi) = \frac{N^+(\phi) - N^-(\phi)}{N^+(\phi) + N^-(\phi)} \quad (3)$$

where $N^+(\phi)$ and $N^-(\phi)$ represent the luminosity normalized yields of events in each ϕ bin for positron and electron beam, respectively. The ϕ dependences of the beam-charge asymmetry for the hydrogen and deuterium targets are shown in Figure 1, together with the results of fits to the data.

For the proton results, only data from unpolarized targets were used, while the deuteron results were obtained using both unpolarized and spin-averaged polarized target data. One

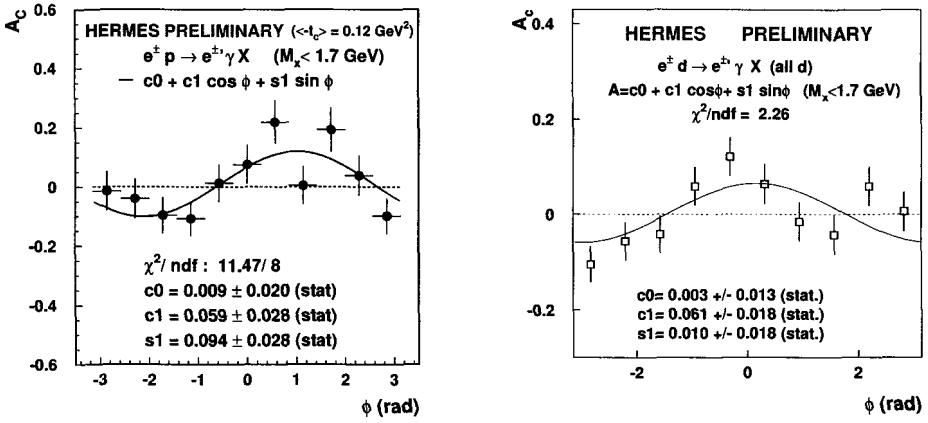


Fig. 1. Beam-charge azimuthal asymmetry A_C for the hard exclusive electroproduction of photons from hydrogen (left panel) and deuterium (right panel) targets.

can see the expected $\cos\phi$ behaviour for both targets, approximately with the same amplitudes, due to the fact that incoherent process on the nucleons in deuteron dominates over the coherent and resonance processes.

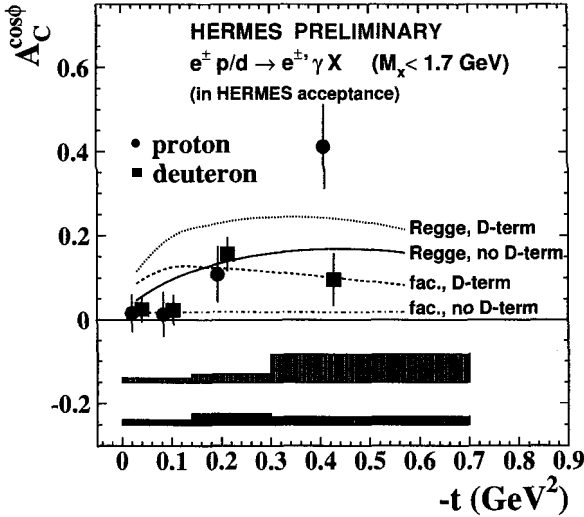


Fig. 2. The $\cos\phi$ amplitude of the beam-charge asymmetry on hydrogen and deuterium as a function of $-t$. The curves correspond to the GPD model calculations based on a factorized or Regge-inspired t -dependence with or without a D-term contribution.

Figure 2 shows the $\cos\phi$ amplitudes on deuterium and hydrogen derived from the fits in four bins in $-t$ (the square of the four-momentum transfer to the target). For both targets,

the amplitudes become sizable only at higher values of $-t$. The effects from the coherent scattering on the deuteron could be expected in the first $-t$ bin, but are not apparent. The difference in asymmetries at large $-t$ values can be explained by the contribution from incoherent scattering on the neutron inside the deuteron.

The theoretical calculations shown in Fig. 2 are based on a GPD model developed in Refs. [8, 9] carried out with two choices for the t -dependence of the GPDs: the simplest ansatz, where the t -dependence is factored from the t -independent part, or the Regge-motivated ansatz, with or without the so-called D-term. The data appear to favor the model with the non-factorized t -dependence but are not precise enough to test the D-term.

Acknowledgments

I wish to thank the organizers of SPIN2004 for their financial support.

References

1. F.M. Dittes et al., *Phys. Lett.* **B209**, 325 (1988).
2. D. Müller et al., *Fortsch. Phys.* **42**, 101 (1994).
3. X. Ji, *Phys. Rev. Lett.* **78**, 610 (1997).
4. A. V. Belitsky, D. Müller and A. Kirchner, *Nucl. Phys.* **B269**, 323 (2002).
5. HERMES coll., A. Airapetian et al., *Phys. Rev. Lett.* **87**, 182001 (2001).
6. CLAS coll., S. Stepanyan et al., *Phys. Rev. Lett.* **87**, 182002 (2001).
7. F. Ellinghaus, R. Shanidze and J. Volmer (for the HERMES Coll.), hep-ex/0212019.
8. M. Vanderhaeghen, P.A.M. Guichon and M. Guidal, *Phys. Rev.* **D60**, 094017 (1999).
9. K. Goeke, M.V. Polyakov and M. Vanderhaeghen, *Prog. Part. Nucl. Phys.* **47**, 401 (2001).

THE HERMES RECOIL DETECTOR

J. STEWART

DESY, Zeuthen, Germany

(for the HERMES Collaboration)

The HERMES collaboration at HERA is constructing a new detector system to greatly expand the experiment's tracking and identification capability for particles scattered at large angles. The detector is specifically designed to detect the recoil protons from exclusive processes and reject background from competing channels. The recoil detector system consists of a double layer silicon microstrip detector used as a ΔE -E telescope, a scintillating fibre tracker based magnetic spectrometer, and a three layer tungsten scintillator sampling calorimeter. The construction of the individual detector components is now finished and test beam studies are underway. Final assembly of the detector will be completed in Winter 2004/2005 and the detector will be installed in the HERMES experiment in Summer 2005.

1. Introduction

Recent exclusive electroproduction measurements, especially of Deeply Virtual Compton Scattering (DVCS) by HERMES [1] and other experiments, and the interpretation of this data in terms of Generalized Parton Distributions (GPDs) have produced enormous theoretical interest. A major improvement in the quality of the existing data requires both a large increase in statistics and improved suppression of unwanted background. The HERMES DVCS measurements use the polarized HERA lepton beam ($e^{+/-}$) with an unpolarized target. In case of running exclusively with the unpolarized target (density is 10 to 200 times the polarized target density) an integrated luminosity of 1 fb^{-1} is possible in one year. After the end of the transversely polarized target run in Summer 2005, HERMES is planning a two year high luminosity unpolarized run with roughly equal positron and electron statistics. A major upgrade to the spectrometer in the forward region for this running period has been constructed and is being tested.

2. Recoil Detector Description

The recoil detector is designed to precisely measure the momentum of the recoil protons from DVCS and extend the HERMES tracking capabilities to 90 degrees in the lab frame. The recoil protons from DVCS for the HERMES kinematics have a momentum of $0.05 < p < 1.4 \text{ GeV}/c$ and are scattered at angles between 0.1 and 1.35 rad. Design studies showed that to cover the whole momentum range a combined detector system was required.

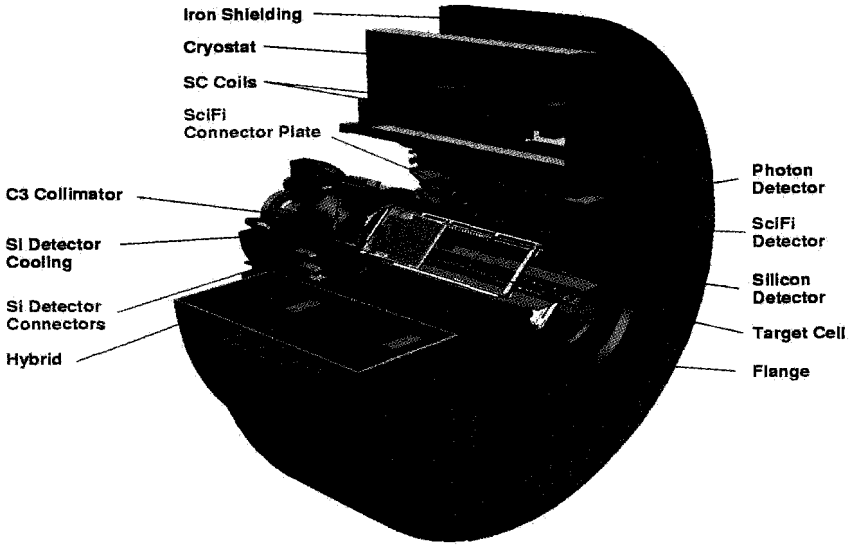


Fig. 1. 3D model of the new HERMES recoil detector system. The major components are a 1 T superconducting solenoidal magnet, a three layer tungsten-scintillator sampling calorimeter (photon detector), two cylindrical scintillating fibre trackers, and a two layer silicon strip detector package inside the HERA vacuum.

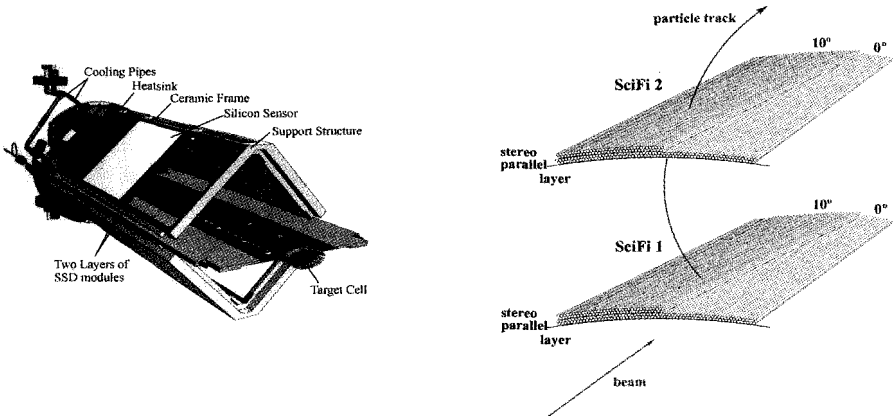


Fig. 2. Detailed view of the HERMES target cell and the surrounding silicon detector (left panel), and the conceptual design of the scintillating fibre tracker (right panel).

The 3-D model of the recoil detector is shown in Figure 1. The detector consists of a silicon microstrip detector for measurement of low momentum protons, a scintillating fibre tracker based magnetic spectrometer for higher momentum protons and detection of minimum ionizing particles, and a tungsten scintillator sampling calorimeter to detect photons from π^0 decay and to assist in particle identification. The innermost layer of the recoil detector is shown in the left panel of Figure 2. The HERMES target cell has been redesigned for ex-

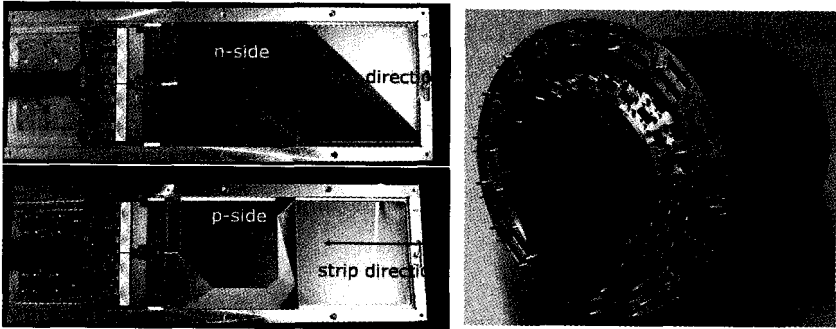


Fig. 3. Pictures of both sides of one of the silicon detector modules (left) and the finished scintillating fibre tracker (right).

clusive unpolarized running, and the cell walls reduced to $50\mu\text{m}$ to minimize the energy loss of the slow protons. As the low energy protons would be stopped in the wall of any vacuum chamber, a two layer silicon microstrip detector has been built which can be operated inside the HERA vacuum [2]. The silicon detector consists of eight detector modules mounted around the target cell, forming a two layer thick square tube. Each silicon module consists of two $99 \times 99 \text{ mm}^2$ $300 \mu\text{m}$ thick double sided silicon microstrip sensors. The readout strips have a pitch of $758 \mu\text{m}$ and are laid out in an X-Y orientation on the two sides so that both spatial coordinates are measured for each sensor. The length of the target cell was adjusted so that two sensors placed along the beamline cover $0.4 < \theta < 1.35 \text{ rad}$. In the low momentum range ($100\text{--}500 \text{ MeV}/c$), the energy loss in matter is roughly proportional to $1/\beta^2$. By measuring the energy loss in the two silicon layers the momentum of the proton can be reconstructed. The slow protons can deposit energies of up to 6 MeV in the detector, requiring a dynamic range of 70 for the readout electronics. A HELIX 3.0 based readout has been constructed whereby each strip is connected to two HELIX input channels via a capacitive charge sharing network fulfilling these requirements.

Above $300 \text{ MeV}/c$ the protons have sufficient momentum to pass through the silicon detector and the 1.2 mm thick wall of the aluminum vacuum chamber. These particles are detected in a scintillating fibre tracker (SciFi) shown schematically in Figure 2. Two cylindrical coaxial SciFi detectors (SciFi1 and SciFi2) with diameters 220 mm and 370 mm are used for tracking, with additional information from the silicon detector. The particle momentum is computed from the radius of curvature in the 1 T solenoidal magnetic field. Each of the SciFi cylinders consists of four layers of 1 mm Kuraray SCSF-78 scintillating fibres. The first two fibre layers are parallel to the beam, and the second two are constructed at a 10° stereo angle so that each SciFi detector yields a space point. The scintillating fibres are connected via 3.5 m long Kuraray light guides to Hamamatsu H-7548 64 channel PMTs. The PMTs are then interfaced to a preprocessing front-end readout system including GAS-SIPLEX chips. In addition, the Dynode 12 signal from the PMT is used to provide timing information for bunch selection. The completed detector components are shown in Figure 3. The space-point efficiency of the final silicon and SciFi detector modules for minimum ionizing particles was measured to be 98% in test beam. The response of the detector com-

ponents to low energy protons was measured at GSI (300 to 900 MeV/c) and for the silicon detector additionally at a 3.5 to 10 MeV tandem accelerator in Erlangen.

HERMES Monte Carlo simulations of the final detector show that below 250 MeV/c, where the protons stop in the second silicon detector, the momentum resolution $\Delta p/p$ is 3%. The resolution slowly decreases to 12% at the maximum DVCS proton momentum. The t -resolution $\Delta t/t$, which is especially important for GPD studies, is improved by an order of magnitude. The Monte Carlo studies indicate that the background from associated DVCS and other channels will be reduced to less than 1 percent.

References

1. HERMES Collaboration, A. Airapetian et al., Phys. Rev. Lett. **87** (2001) 182001. F. Ellinghaus (for the HERMES Collaboration), Nucl. Phys. **A711** (2002) 171.
2. M. Reinecke et al., IEEE Trans. Nucl. Sci., vol 51, pp.1111-1116, June 2004.

CHIRAL-ODD TWIST-3 DISTRIBUTION FUNCTION $E(x)$

M. WAKAMATSU, Y. OHNISHI

Department of Physics, Osaka University, Toyonaka, Japan

We clarify the non-perturbative origin of the δ -function singularity at $x = 0$ in the chiral-odd twist-3 distribution function $e(x)$ of the nucleon. We also compare a theoretical prediction for $e(x)$ based on the chiral quark soliton model with the empirical information extracted from the CLAS semi-inclusive DIS measurement.

1. Introduction

The subject of my talk here is the spin-independent chiral-odd twist-3 distribution function $e(x)$ of the nucleon. Why is it interesting? Firstly, its first moment is proportional to the famous πN sigma term. Secondly, within the framework of perturbative QCD, it was pointed out by Burkardt and Koike that this distribution function is likely to have a delta-function type singularity at $x = 0$ [1]. Unfortunately, the physical origin of this singularity was not fully clarified within the perturbative analysis.

The purpose of my present talk is two-fold. First, I want to show that the physical origin of this peculiar singularity is inseparably connected with the *non-trivial vacuum structure of QCD*. Secondly, I will show some theoretical predictions for this interesting quantity based on the Chiral Quark Soliton Model (CQSM), which can, for example, be compared with the recent CLAS measurement of semi-inclusive DIS scatterings [2].

2. Origin of delta-function singularity in $e(x)$

We start with the general definition of $e(x)$ given as

$$e(x) = M_N \int_{-\infty}^{\infty} \frac{dz^0}{2\pi} e^{-ixM_N z^0} E(z^0), \quad (1)$$

with

$$E(z^0) = \langle N | \bar{\psi}(-\frac{z}{2}) \psi(\frac{z}{2}) | N \rangle |_{z_3 = -z_0, z_{\perp} = 0}. \quad (2)$$

Here, the quantity $E(z_0)$ as a function of z_0 measures the light-cone quark-quark correlation of scalar type in the nucleon. The existence of a delta-function singularity in $e(x)$ indicates

that, when z_0 becomes large, $E(z_0)$ does not damp and approaches a certain constant such that

$$E(z^0) = E^{reg}(z_0) + \text{constant}, \quad (3)$$

with $E^{reg}(z^0) \rightarrow 0$ as $z^0 \rightarrow \infty$. In fact, within the framework of the CQSM, we have analytically confirmed this behavior [3]. As proved there, the existence of this infinite-range correlation is inseparably connected with the non-trivial vacuum structure of QCD, or more concretely, the appearance of non-vanishing quark condensate.

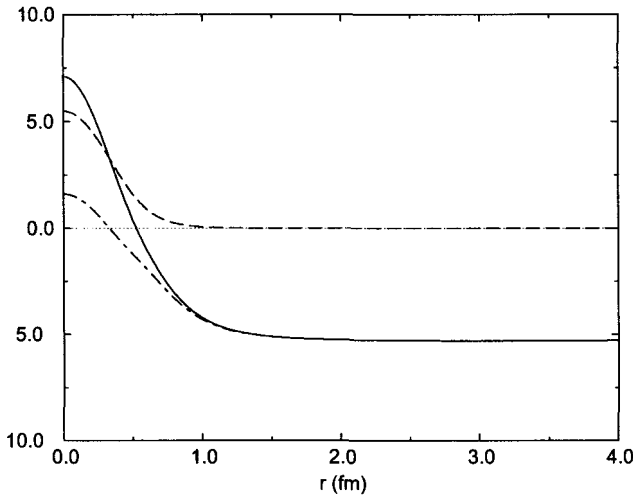


Fig. 1. The scalar quark density predicted by the CQSM.

A natural question is “Why does the vacuum property come into a localized hadron observable?”. This is due to the extraordinary nature of the scalar quark density inside the nucleon, as illustrated in Fig.1. (This is the prediction of the CQSM.) The long-dashed curve represents the contribution of three valence quarks in the hedgehog mean field, while the dash-dotted curve stands for the contribution of deformed Dirac-sea quarks. One sees clearly that, as the distance from the nucleon center becomes large, the valence quark contribution damps rapidly, while the Dirac-sea contribution does not damp, but approaches some *negative constant*, which is nothing but the *vacuum quark condensate*. The existence of an unending stretch of the region with non-zero scalar quark density is inseparably connected with the peculiar behavior of $E(z^0)$ as given by (3).

3. Numerical study of $e(x)$ in CQSM

Now we turn to the numerical study of $e(x)$ within the CQSM. In this theory, the isoscalar and isovector combinations of $e(x)$ have very different N_c dependences. The former is an order N_c quantity, while the latter a subleading quantity in N_c . We need very sophisticated

numerical methods to handle the isoscalar distribution function $e^{(T=0)}(x)$, which contains a delta-function type singularity. The details can be found in [4]. After all, we find that the total $e^{(T=0)}(x)$ is given as a sum of the two terms, i.e. the valence quark contribution, which has a peak around $x = 1/3$, and the Dirac-sea contribution

$$e^{(T=0)}(x) = e_{valence}^{(T=0)}(x) + e_{sea}^{(T=0)}(x). \quad (4)$$

The latter is further decomposed into two terms :

$$e_{sea}^{(T=0)}(x) = e_{sing}^{(T=0)}(x) + e_{regl}^{(T=0)}(x). \quad (5)$$

Here, the first is a singular term proportional to a delta function,

$$e_{sing}^{(T=0)}(x) = C \delta(x), \quad C \simeq 9.9, \quad (6)$$

while the second is a regular term, the magnitude of which turns out to be relatively small.

Particularly interesting here is the first moment sum rule for the isoscalar $e(x)$, which gives the nucleon scalar charge $\bar{\sigma}$, i.e. $\int_{-1}^1 e^{(T=0)}(x) dx = \bar{\sigma}$. Numerically, we find that

$$\bar{\sigma} = \bar{\sigma}_{valence} + \bar{\sigma}_{sea}^{regl} + \bar{\sigma}_{sea}^{sing} \simeq 1.7 + 0.18 + 9.92 \simeq 11.8, \quad (7)$$

which means that the singular term supplies the dominant contribution to this sum rule. With the standard values of the current quark mass $m_q \simeq (4 \sim 7) \text{ MeV}$, this nucleon scalar charge gives a fairly large πN sigma term

$$\Sigma_{\pi N} \equiv m_q \bar{\sigma} \simeq (47 \sim 83) \text{ MeV}, \quad (8)$$

which favors the recent analyses of low-energy πN scattering amplitudes [5].

For the isovector part of $e(x)$, we just comment that no singularity at $x = 0$ is observed. This is reasonable since there is no isovector quark condensate in the QCD vacuum. Combining the isoscalar and isovector distributions, we can predict any of the u, d, \bar{u}, \bar{d} distributions. Fig.2 shows the comparison of the predicted flavor combination $e^u(x) + (1/4)e^{\bar{d}}(x)$ with the empirical information extracted from the CLAS data by Efremov et al. under the assumption of Collins mechanism dominance [6]. One sees that the agreement between the theory and experiment is encouraging, although it would be premature to extract, from this crude comparison only, any definitive conclusion on the possible violation of the pion-nucleon sigma term sum rule due to the existence of the delta-function singularity at $x = 0$.

4. Summary and conclusion

Summarizing my talk, I have shown that the delta-function singularity in the chiral-odd twist-3 distribution $e(x)$ is a manifestation of the non-trivial vacuum structure of QCD in a hadron observable. Experimentally, the existence of this singularity will be observed as a violation of πN sigma-term sum rule of isoscalar $e(x)$. To confirm this interesting possibility, we certainly need more precise experimental information for $e(x)$ especially in the smaller x region.

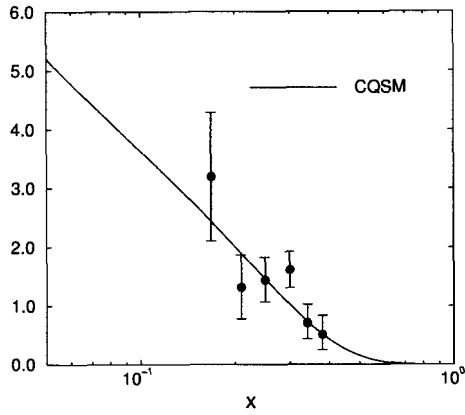


Fig. 2. Comparison with a parameterization of the CLAS data.

References

1. M. Burkardt and Y. Koike, *Nucl. Phys.* **B632**, 311 (2002).
2. CLAS Collaboration, H. Avakian et al., *hep-ex/0301005*.
3. M. Wakamatsu and Y. Ohnishi, *Phys. Rev.* **D67**, 114011 (2003).
4. Y. Ohnishi and M. Wakamatsu, *Phys. Rev.* **D69**, 114002 (2004).
5. M. M. Pavan et al., *PiN Newsletter* **16**, 110 (2002).
6. A. V. Efremov, K. Goeke, and P. Schweitzer, *Nucl. Phys.* **A711**, 84 (2002).

PRE-CONSTRAINING EVOLUTION OF PARTON DISTRIBUTIONS IN THE MATRIX SOLUTION OF DGLAP

M. GOSHTASBPOUR, F. QASSEMI

Department of Physics, Shahid Beheshti University, Tehran, Iran

In spite of the potential advantages of the 'matrix solution' to DGLAP, an instability in the set of linear decomposition equations obtained from it, when decomposing the structure function data, hinders its application. Here, we pre-constrain the solutions of the decomposition equations, based on the principle of positivity of the parton distributions and well-known facts such as the increasing nature of gluons with decreasing values of Bjorken x . Thus, reasonable solutions for evolved parton distributions may be extracted within this framework.

1. Introduction

There are potential advantages to the 'matrix solution' [1] of DGLAP evolution equations: e.g. it does not use any parametric fit to data and parton distributions as the existing solutions. However, there is an instability when decomposing the structure function data (e.g. F_1 or g_1) into parton distributions which hinders its application. These issues were discussed in the previous Symposium, Spin2002 [2]. Here, we propose a method of pre-conditioning or pre-constraining for the solutions of decomposition equations, by physical requirements (positivity, etc.), to control the instability.

2. Constraints

Using $F_1^{p,d}$ data [3] (except for the largest x , i.e. $x = .714$), parton distributions are extracted at the same x and Q^2 of the experiment, via a combination of the workings of DGLAP and constrained decomposition equations. With only positivity constraints on our parton distributions, the instability is removed; however, there remains a problem of the form or shape of the distributions, a slight kink in the gluon distribution $g(x)$.

Following the achievement of stability, we expect the shape problem to be generally correctable with additional constraints. Indeed, only constraining $g(x)$ to increase as x decreases seems to work well here, Figure 1.

If such a simple constraint had not responded so well, we could have made it stronger and eventually could have involved other parton distributions besides gluons. However, fortunately, it is the nature of the equations, rather than the constraining power of more

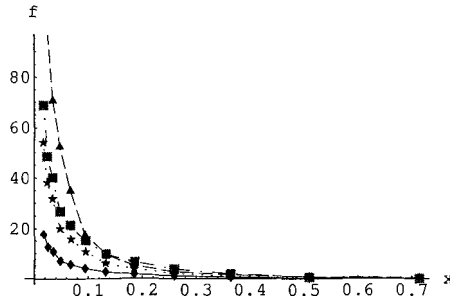


Fig. 1. Data points F_1^P (diamond) and the extracted parton distributions, octet q_8 (star), singlet q_0 (square) and gluons g (triangle), all points at x and Q^2 of the experiment. Constraints of positivity of parton distributions as well as increasing $g(x)$ with decreasing x are imposed.

strict constraints, that helps. We reach acceptable shapes for the parton distributions with relatively simple constraints.

3. Comparison with GRV

Our parton distributions obtained from decomposition and evolution of central values (no error bars) of $F_1^{P,d}$ data points are plotted in the first three graphs of Figure 2 in comparison with GRV's [4], using the same constraints as in Figure 1. The relative closeness of our parton distributions and GRV is a measure of the success of the present "pre-constraining" method to control the instability of the decomposition equations.

4. Implementation of the constraints

We introduced a parameter in each of the two evolved F_1^P at each x , within the decomposition equations [2]. We thought of implementing the constraints in two ways. In the first, we tried to determine the parameters by satisfying the constraints via conditional minimization of the distance of the parameterized F_1^P from the corresponding actual data point. However, there are some problems with jumps and discontinuities that make programming for dependable numerical solutions a bit hard.

In the second method, we tried to solve the inequalities of the constraints for the two parameters and then, within the range of the solutions, via a suitable function, we moved continuously towards those values of the parameters which give distributions with the desired scale. In other words, the correctly shaped distributions were scaled to the correct height by the use of two other continuous parameters, A and B , whose final values pick two points out of the two intervals in which our two evolved F_1^P lie.

In this process, we chose evolved the F_1^P themselves as parameters determined within two intervals via the constraint inequalities, together with DGLAP and decomposition equations. Then we chose the correct scale (height) of our distributions via A and B . The scales were set by GRV (which is going to be replaced by two data points F_1^P at each x corresponding to two higher Q^2 , in forthcoming data analysis).

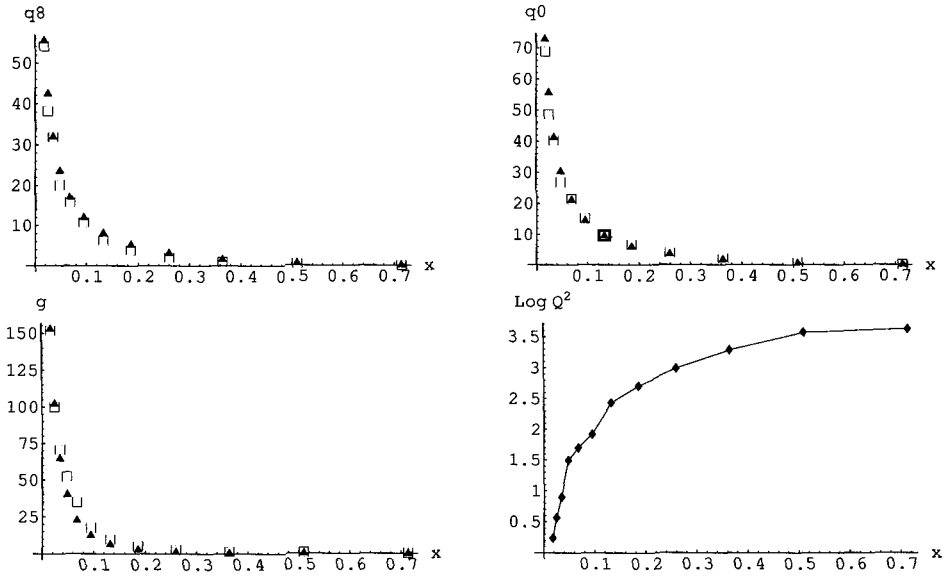


Fig. 2. Our parton distributions (triangles) obtained from $F_1^{P,d}$ data in comparison with GRV's (open squares), at the experimental values of x and Q^2 . Q^2 value at each x is indicated in the last graph.

In particular, the function $1/x^A$ was added to the lower limit of the first evolved F_1^P , and $1/x^B$ was used to select the point within the closed interval solution of the second evolved F_1^P , in the three decomposition equations [2]. Continuous change of A and B could guide the continuous motion to the desired scale. The choice of $A = 1.93$ and $B = .4$ is shown in Figure 2. A change in A selectively affects the scaling of $g(x)$, and a change in B selectively affects $q_8(x)$. The particular functional form with respect to x was chosen, among a set of possible functions, to have the desired increasing behavior with decreasing x .

4.1. Propagation of errors

We did simulations to get a first estimate of how the errors propagate. As a beginning, the experimental errors of F_1^P were multiplied by a large factor n . Then, the maximum deviation of the output parton distributions of a large number of runs m were taken as their error. Here, random numbers within the enlarged error interval were taken as input for F_1^P , instead of the central values of the data points. Figure 3 indicates some results with $n = 6, m = 100$, providing a first idea about propagation of errors. In the forthcoming publication, more comprehensive error analysis will be provided.

Acknowledgement

This research is based on the M.S. thesis of A. Shafi'i [2].

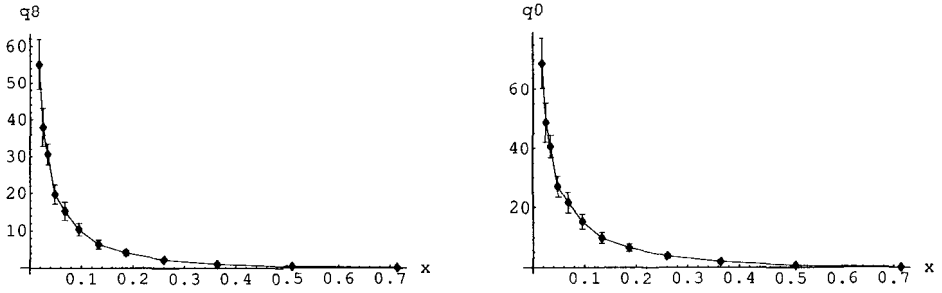


Fig. 3. Error bars of our some parton distributions generated via simulation.

References

1. P. G. Ratcliffe, *Phys. Rev.* **D63**, 116004 (2001).
2. M. Goshtasbpour and A. Shafi'i, 15th International Spin Physics Symposium, *AIP Conference Proceedings* **675**, 299 (2002).
3. Arneodo et al., *Nucl. Phys.* **B483**, 3 (1997).
4. M. Glück, E. Reya and A. Vogt, *Z. Phys.* **C67**, (1995).

This page intentionally left blank



SESSION 3

Spin Beyond the Standard Model

This page intentionally left blank

IDENTIFICATION OF GRAVITON EXCHANGE EFFECTS AT HIGH ENERGY COLLIDERS

A. A. PANKOV*

The Pavel Sukhoi Technical University of Gomel, Gomel, Belarus

We study the appropriate observables to uniquely identify the effects of graviton exchange within the Arkani-Hamed–Dimopoulos–Dvali (ADD) scenario from a large set of models beyond the Standard Model (SM) in fermion pair production processes at a linear e^+e^- collider (LC) and LHC.

New physics (NP) beyond the SM may manifest itself at future colliders either directly, as in the case of new particle production, or indirectly through deviations of observables from the SM predictions. There are numerous different NP scenarios that predict new particle exchanges which are described by contact interactions (CI) much below direct production thresholds. A partial list includes a Z' , leptoquarks, R -parity violating sneutrinos ($\tilde{\nu}$), bileptons, graviton Kaluza-Klein (KK) towers, gauge boson KK towers, etc. If contact interaction effects are experimentally observed one, must develop a technique which will divide the full set of all possible models into distinct sub-classes. In this note we propose a technique based on the center-edge asymmetries. This method provides an opportunity to uniquely identify graviton/spin-2 exchange envisaged by models of gravity in more than three spatial dimensions from other NP scenarios at LC and LHC [1]. One specific model involving extra dimensions will be considered, namely the ADD [2] scenario.

Let us consider the differential cross section for the process

$$e^+ + e^- \rightarrow f + \bar{f} \quad (1)$$

in the SM assuming $m_f = 0$ and $f \neq e$ for simplicity. The differential cross section can be written as

$$\frac{d\sigma^{\text{SM}}}{dz} = \frac{3}{8}\sigma^{\text{SM}}(1+z^2) + \sigma_{\text{FB}}^{\text{SM}}z, \quad (2)$$

where σ and σ_{FB} denote the total and forward-backward cross sections, respectively. They depend upon the electroweak quantum numbers of the fermion, f , as well as the center

*Work partially supported by the Abdus Salam International Centre for Theoretical Physics (Trieste, Italy).

of mass energy of the collision, \sqrt{s} . This structure is particularly interesting in that it is equally valid for a wide variety of NP models parameterized in form of the CI.

We define the center-edge (even) asymmetry A_{CE} as:

$$A_{CE} = \frac{\sigma_{CE}}{\sigma}, \tag{3}$$

where σ_{CE} is the difference between the ‘‘central’’ and ‘‘edge’’ parts of the cross section, with $0 < z^* < 1$:

$$\sigma_{CE}(z^*) = \left[\int_{-z^*}^{z^*} - \left(\int_{-1}^{-z^*} + \int_{z^*}^1 \right) \right] \frac{d\sigma}{dz} dz. \tag{4}$$

Clearly, from the definition (4), z -odd terms in the differential cross section cannot contribute to A_{CE} . Using Eq. (2), one immediately obtains in the SM, $A_{CE}^{SM}(z^*) = 0.5 z^* (z^{*2} + 3) - 1$.

If four-fermion CI are present in addition to the SM ones, the z -dependence of the resulting differential cross section has exactly the same structure as that of Eq. (2), up to superscript replacement $SM \rightarrow CI$. Consequently, the deviation of A_{CE}^{CI} from the SM prediction:

$$\Delta A_{CE}^{CI} = A_{CE}^{CI} - A_{CE}^{SM} = 0, \tag{5}$$

for any value of z^* . Correspondingly, such interactions are ‘‘filtered out’’ by the observable (3), in the sense that they produce *no* deviation from the SM.

We also define the center-edge-forward-backward asymmetry as follows:

$$A_{CE,FB} = \frac{\sigma_{CE,FB}}{\sigma}, \tag{6}$$

where, with $0 < z^* < 1$:

$$\sigma_{CE,FB} = \left[\left(\int_0^{z^*} - \int_{-z^*}^0 \right) - \left(\int_{z^*}^1 - \int_{-1}^{-z^*} \right) \right] \frac{d\sigma}{dz} dz \equiv (\sigma_{C,FB} - \sigma_{E,FB}). \tag{7}$$

In the SM, using Eq. (2) one immediately derives

$$A_{CE,FB}^{SM}(z^*) = A_{FB}^{SM}(2z^{*2} - 1). \tag{8}$$

In the case of the ‘‘conventional’’ current-current CI we have:

$$A_{CE,FB}^{CI}(z^*) = A_{FB}^{CI}(2z^{*2} - 1). \tag{9}$$

Furthermore, Eqs. (8) and (9) show that $A_{CE,FB}^{SM} = A_{CE,FB}^{CI} = 0$ at

$$z^* \equiv z_{CI}^* = 1/\sqrt{2} \approx 0.707, \tag{10}$$

corresponding to $\theta = 45^\circ$. The deviation of $A_{CE,FB}^{CI}$ from the SM prediction is given by:

$$\Delta A_{CE,FB}^{CI}(z^*) = A_{CE,FB}^{CI} - A_{CE,FB}^{SM} = \Delta A_{FB}^{CI} (2z^{*2} - 1). \tag{11}$$

Correspondingly, such interactions are also ‘‘filtered out’’ by $A_{CE,FB}$, when measured at $z^* = z_{CI}^*$. One can conclude that non-vanishing $A_{CE,FB} \neq 0$ at z_{CI}^* unambiguously signals the presence of NP *different* from CI.

Spin-2 KK graviton exchange provides a characteristic z -dependent contribution to the differential cross section [3] parameterized by a single variable, $\eta_G = \lambda/M_H^4$, where M_H is a cut-off on the summation over the KK spectrum expected of the order of TeV, and $\lambda = \pm 1$. The effective cross section is linear in η_G for the interference term, and quadratic in η_G for the pure graviton exchange term. In our numerical analysis we consider a LC with $\sqrt{s} = 0.5$ TeV and 1 TeV and time-integrated luminosity \mathcal{L}_{int} ranging from 50 up to 1000 fb^{-1} , and electron and positron beams with longitudinal polarization P_1 and P_2 , respectively. We assume $\Delta\mathcal{L}_{\text{int}}/\mathcal{L}_{\text{int}} = \Delta P_1/P_1 = \Delta P_2/P_2 = 0.5\%$, and $|P_1| = 80\%$ and $|P_2| = 60\%$ for electron and positron beams, respectively. In all cases a small angle cut of 10° around the beam pipe has been employed. Summing over μ, τ, c, b final states and combining A_{CE} and $A_{\text{CE,FB}}$ at $z^* = z_{\text{CI}}^*$ in the conventional χ^2 analysis, we obtain a 95% C.L. *identification reach* on the mass scale M_H as a function of luminosity shown in Fig. 1.

It should be interesting to make a comparison of the *identification reach* derived at the LC with the results on M_H potentially obtainable from the study of the inclusive di-lepton production process

$$p + p \rightarrow l^+ l^- + X \quad (12)$$

using A_{CE} at the proton-proton collider LHC [1]. This comparison is performed in Fig. 1 for the LHC with $\mathcal{L}_{\text{int}} = 100 \text{ fb}^{-1}$ and 300 fb^{-1} . This figure shows that the LC(0.5 TeV) will not improve the reach on M_H obtained at the LHC, whereas the LC(1 TeV) definitely provides the better limits for any value of the luminosity.

References

1. For details of the analysis and original references, see P. Osland, A. A. Pankov and N. Paver, *Phys. Rev.* **D68**, 015007 (2003); E.W. Dvergsnes, P. Osland, A. A. Pankov and N. Paver, *Phys. Rev.* **D69**, 115001 (2004).
2. N. Arkani-Hamed, S. Dimopoulos and G. R. Dvali, *Phys. Lett.* **B429**, 263 (1998).
3. J. L. Hewett, *Phys. Rev. Lett.* **82**, 4765 (1999).

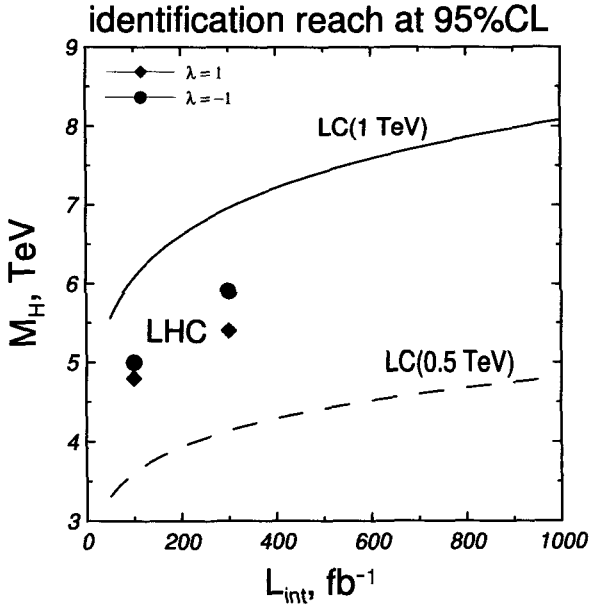


Fig. 1. 95% C.L. identification reach on the mass scale M_H vs. integrated luminosity obtained from the combined analysis of two polarized asymmetries, A_{CE} and $A_{\text{CE,FB}}$, for the process $e^+e^- \rightarrow f\bar{f}$, with f summed over μ, τ, b, c , at $z^* = z_{\text{C1}}^*$ and at the c.m. energy of 0.5 TeV and 1 TeV, and both beams polarized with $|P_1| = 0.8$ and $|P_2| = 0.6$. The reach on M_H from the dilepton production process at LHC is also shown for $\lambda = \pm 1$.

CONTACT INTERACTION SEARCHES AT e^+e^- AND e^-e^- COLLIDERS: ROLE OF POLARIZATION

A. V. TSYTRINOV, A. A. PANKOV

The Pavel Sukhoi Technical University of Gomel, Gomel, Belarus

We explore the potential of e^+e^- Linear Collider (LC), operating in the e^+e^- and e^-e^- modes, to study four-fermion contact interactions in muon pair production, Bhabha scattering and Møller scattering. We stress the role played by the initial state polarization in increasing the reach of this machine in the discovery of new phenomena. Discovery limits are discussed in a model-independent way.

A very general framework in which to search for the effect of new physics is the four-fermion contact interaction. In this framework the Standard Model (SM) Lagrangian for $e^+e^- \rightarrow \bar{f}f$ is extended by a term describing a new effective contact interaction (CI) with an unknown coupling constant g_{eff}^2 and an energy scale Λ . For the Bhabha scattering process

$$e^+ + e^- \rightarrow e^+ + e^-, \quad (1)$$

as well as for Møller scattering

$$e^- + e^- \rightarrow e^- + e^-, \quad (2)$$

we consider the flavor-diagonal, helicity-conserving $eeff$ contact-interaction effective Lagrangian [1]:

$$\mathcal{L}_{\text{CI}} = \frac{1}{1 + \delta_{ef}} \sum_{i,j} g_{\text{eff}}^2 \varepsilon_{ij} (\bar{e}_i \gamma_\mu e_i) (\bar{f}_j \gamma^\mu f_j). \quad (3)$$

In Eq. (3): $i, j = \text{L, R}$ denote left- or right-handed fermion helicities, $\delta_{ef} = 1$ for processes (1) and (2), and, if we assume lepton universality, the same Lagrangian, with $\delta_{ef} = 0$, is relevant to the annihilation process

$$e^+ + e^- \rightarrow \mu^+ + \mu^-. \quad (4)$$

The CI coupling constants in Eq. (3) are parameterized in terms of corresponding mass scales as $\varepsilon_{ij} = \eta_{ij}/\Lambda_{ij}^2$, and, according to the previous remarks concerning compositeness, one assumes $g_{\text{eff}}^2 = 4\pi$. Also, by convention, one takes $|\eta_{ij}| = 1$ or $\eta_{ij} = 0$, leaving the energy scales Λ_{ij} as free, *a priori* independent, parameters.

For the Bhabha process (1), Eq. (3) envisages the existence of three independent CI models, each one contributing to individual helicity amplitudes or combinations of them, with *a priori* free, and nonvanishing, coefficients (basically, ϵ_{LL} , ϵ_{RR} and $\epsilon_{LR} = \epsilon_{RL}$ combined with the \pm signs). The same is true for the Møller process (2). For $e^+e^- \rightarrow \mu^+\mu^-$ there are four independent CI couplings. Correspondingly, in principle, a model-independent analysis of the data should account for the situation where the full Eq. (3) is included in the expression for the cross section. Potentially, in this case, the different CI couplings may interfere and such interference could substantially weaken the bounds. To this end, in the case of the processes (1), (2) and (4) at the Linear Collider (LC) considered here, a possibility is offered by *initial beam polarization* to disentangle the constraints on the corresponding CI constants [2]. In this note, we wish to present a model-independent analysis of the CI based on the differential distributions of the final leptons. We stress the role played by the initial state polarization in increasing the reach of the LC in the discovery of the CI effects.

If electron and positron beams are polarized, with corresponding longitudinal polarization P^- and P^+ , the polarization of each beam can be changed on a pulse-by-pulse basis. This would allow the separate measurement of the polarized cross sections for each of the four polarization configurations $(P^-, P^+) = (P_1, P_2)$, $(-P_1, -P_2)$, $(P_1, -P_2)$ and $(-P_1, P_2)$, with $P_{1,2} > 0$. We take $P_1 = 0.8$ and $P_2 = 0.6$ for the LC, and impose a cut $|\cos \theta| < 0.9$ in the forward and backward directions. We divide this range into nine equal-size bins of width $\Delta z = 0.2$ ($z \equiv \cos \theta$). We also take the experimental efficiency for detecting the final e^+e^- pair to be $\epsilon = 0.9$. As for the systematic uncertainty, we take $\delta \mathcal{L}_{\text{int}}/\mathcal{L}_{\text{int}} = 0.5\%$, $\delta \epsilon/\epsilon = 0.5\%$, and, for the electron and positron polarizations, $\delta P_1/P_1 = \delta P_2/P_2 = 0.5\%$. The reach of the CI couplings, and the corresponding constraints on their allowed values if no effect is observed, can be estimated by a method based on the covariance matrix [3, 4] adapted for this kind of analysis. In this approach, model-independent allowed domains in the four-dimensional CI parameter space, to 95% confidence level, are obtained from the error contours determined by a quadratic form in ϵ_{ij} . For example, in case of three independent CI parameters, it can be written as:

$$(\epsilon_{LL} \ \epsilon_{LR} \ \epsilon_{RR}) W^{-1} \begin{pmatrix} \epsilon_{LL} \\ \epsilon_{LR} \\ \epsilon_{RR} \end{pmatrix} = w^2, \quad (5)$$

where W^{-1} is the inverse covariance matrix, and $w^2 = 7.82$ and 9.49 for processes (1), (2) and (4), respectively. The quadratic form (5) defines a three-dimensional ellipsoid in the $(\epsilon_{LL}, \epsilon_{LR}, \epsilon_{RR})$ parameter space. The matrix W has the property that the square roots of the individual diagonal matrix elements, $\sqrt{W_{ii}}$, determine the projection of the ellipsoid onto the corresponding i -parameter axis in the three-dimensional space, and has the meaning of the bound at 95% C.L. on that parameter regardless of the values assumed for the others. These model-independent limits are listed in Table 1.

All the numerical results exhibited in Table 1 can be represented graphically. As an example, in Figure 1 we show the planar ellipses that are obtained from Bhabha scattering by projecting onto the three planes $(\epsilon_{LL}, \epsilon_{LR})$, $(\epsilon_{LL}, \epsilon_{RR})$, $(\epsilon_{RR}, \epsilon_{LR})$ the 95% C.L. allowed

three-dimensional ellipsoid resulting from Eq. (5).

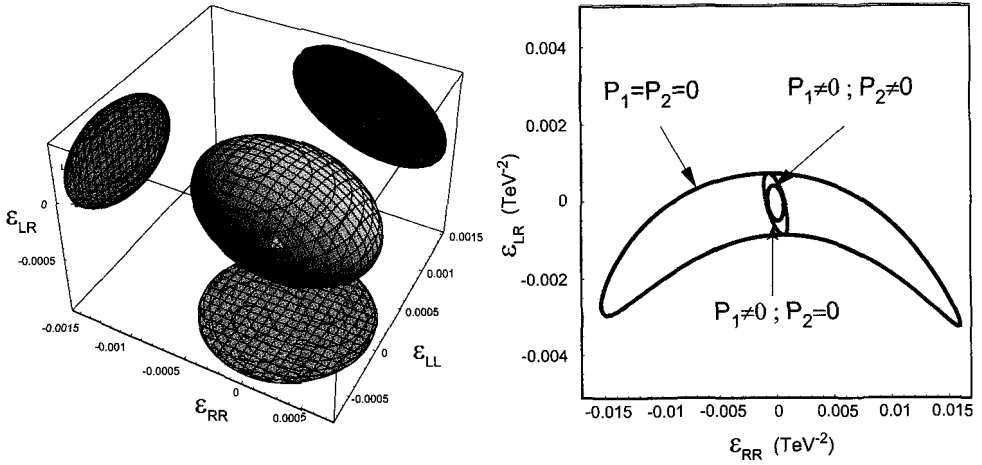


Fig. 1. Left panel: 95% C.L. allowed three-dimensional ellipsoid for Bhabha scattering at 500 GeV center of mass energy, $\mathcal{L}_{\text{int}} = 50 \text{ fb}^{-1}$ and $|P_e| = 0.8$ and $|P_{\bar{e}}| = 0.6$. Right panel: Two-dimensional projection of the 95% C.L. allowed region for unpolarized beams ($P_1 = P_2 = 0$), polarized only electrons ($P_1 \neq 0, P_2 = 0$) and with both beams polarized ($P_1 \neq 0, P_2 \neq 0$).

Figure 1 (right panel) shows the role of initial beam polarizations to increase the sensitivity of observables to CI parameters. Electron polarization is obviously essential, and the results in Table 1 show that the increase in sensitivity of the parameters Λ_{ij} , due to the availability of positron polarization, is appreciable.

Acknowledgments

This research has been supported by the Abdus Salam International Centre for Theoretical Physics (Trieste, Italy).

References

1. E. Eichten, K. Lane and M. E. Peskin, *Phys. Rev. Lett.* **50**, 811 (1983).
2. A. A. Pankov, N. Paver, *Eur. Phys. J.* **C29**, 313 (2003).
3. F. Cuypers, P. Gambino, *Phys. Lett.* **B388**, 211 (1996).
4. A. A. Babich, P. Osland, A. A. Pankov and N. Paver, *Phys. Lett.* **B518**, 128 (2001).

Table 1. Model-independent bounds on Λ_{ij} at 95% C.L. obtained from the processes $e^+e^- \rightarrow \mu^+\mu^-$, $e^+e^- \rightarrow e^+e^-$ and $e^-e^- \rightarrow e^-e^-$ at $E_{c.m.} = 0.5$ TeV, $\mathcal{L}_{int} = 50\text{fb}^{-1}$ and 500fb^{-1} , $|P_e| = 0.8$ and $|P_{\bar{e}}| = 0.0; 0.6$.

process	\mathcal{L}_{int} fb^{-1}	Λ_{LL} TeV	Λ_{RR} TeV	Λ_{LR} TeV	Λ_{RL} TeV
$\mu^+\mu^-$	50	31.5;32.9	31.1;32.6	29.1;29.7	29.5;29.9
	500	52.3;55.4	53.3;55.3	49.9;51.4	50.6;51.8
e^+e^-	50	31.4;37.7	30.8;37.4	36.0;47.1	36.0;47.1
	500	44.3;54.6	43.5;54.3	57.7;75.9	57.7;75.9
e^-e^-	50	44.8;46.6	45.3;47.9	13.0;29.6	13.0;29.6
	500	44.9;58.1	45.3;59.9	13.0;35.8	13.0;35.8

POLARIZED PARTON DISTRIBUTIONS IN THE APPROACH OF COMPLETE RENORMALIZATION GROUP IMPROVEMENT

A. MIRJALILI

Physics Department, Yazd University, Yazd, Iran &
Institute for Studies in Theoretical Physics and Mathematics, Tehran, Iran

S. A. TEHRANI

Physics Department, Persian Gulf University, Boushehr, Iran &
Institute for Studies in Theoretical Physics and Mathematics, Tehran, Iran

A. N. KHORRAMIAN

Physics Department, Semnan University, Semnan, Iran &
Institute for Studies in Theoretical Physics and Mathematics, Tehran, Iran

We use the valon model in the polarized case to obtain the parton distribution functions (PDFs). Valon is defined by the valence quark and associated sea quarks plus gluons in the dressing processes of QCD. The approach of complete renormalization group improvement is introduced. We employ this approach to obtain the polarized parton distribution functions which are based on using the phenomenological valon model. We compared singlet and non-singlet moments and also the obtained PDFs in our new approach and the conventional perturbative QCD approach. There is good agreement between the results of these two approaches.

1. Introduction

The idea of the valon model [1] is extended to the polarized case to describe the spin dependence of hadron structure function. The polarized valon distribution is derived from the unpolarized valon distribution [2]. After calculating polarized valon distributions and all parton distributions in a valon, the polarized parton density in a proton is calculable.

The idea of a complete RG-improvement approach is introduced, whereby QCD perturbative series can be reconstructed in a new form. In this approach, the perturbation series separates into infinite subsets of terms which when summed are renormalization

scheme (RS)-Invariant. Crucially, all ultraviolet logarithms involving the dimensional parameter Q on which the observable depends, are resummed, thereby building the correct Q -dependence [3].

The singlet and non-singlet moments of polarized valons are obtained, and the results in the conventional perturbative QCD approach and the CORGI approach are compared. To obtain the moments of PDFs in the proton, we need the convolution of two moments: the moment of partons in valon and the moment of valons in the proton. By employing the inverse Mellin technique, the PDFs in the proton can be obtained. The resulting PDFs are compared in a conventional QCD perturbative approach and in the CORGI approach.

2. Constituent quark model

2.1. Unpolarized case

The valon model describes the hadron structure relevant to multi-particles production. The valon is defined to be a dressed valence quark in QCD with a cloud of gluons and sea quarks which can be resolved by high Q^2 probes. At sufficiently low value of Q^2 the internal structure of a valon cannot be resolved, and hence it behaves as a valence quark. In the valon model we assume that a proton consists of three valons (UUD) that separately contain the three valence quarks [1] (uud). This picture suggests that the structure function of a hadron involves a convolution of two distributions: I) valon distributions in proton, II) quark distributions in a valon.

2.2. Polarized case

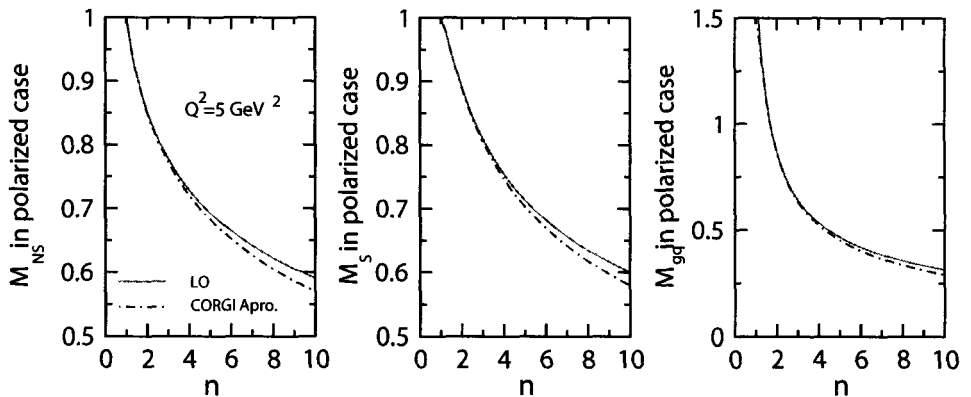


Fig. 1. Comparison of singlet, non-singlet and Gluonic moments in a conventional perturbative QCD approach (solid line) and in the CORGI approach (dashed-dotted line).

Unpolarized and polarized quark distributions are defined respectively as

$$q(x) = q^\uparrow(x) + q^\downarrow(x), \tag{1}$$

$$\delta q(x) = q^\uparrow(x) - q^\downarrow(x). \quad (2)$$

To determine the polarized parton distribution functions (PPDF's), the main step is to relate the polarized input densities to the unpolarized ones [4] using some intuitive theoretical argument as the guideline. We employ the general ansatz for the polarized parton distributions of [4], and introduce the following equations to relate the polarized and unpolarized valon distributions

$$\delta G_{j/p}(y) = \delta W_j(y) \times G_{j/p}(y), \quad (3)$$

where j refers to U and D type valons. The functions $\delta W_j(y)$ play an essential role in constructing the polarized valon distributions, $\delta G_{j/p}(y)$ from unpolarized ones. Using polarized valon distributions, the moments of polarized valon distributions, $\Delta M_{U/p}(n)$ and $\Delta M_{D/p}(n)$, can be easily calculated. The moments of polarized parton distributions in the proton, for instance Δu_v , can be written as follows

$$\Delta u_v(n, Q^2) = 2\Delta M^{NS}(n, Q^2) \times \Delta M_{U/p}(n). \quad (4)$$

Since ΔM^{NS} and ΔM^S depend on the evaluation parameter [2] defined by

$$L(Q^2) \equiv \frac{\alpha_s(Q^2)}{\alpha_s(Q_0^2)}, \quad (5)$$

it is possible to do our calculation in the CORGI approach and in LO approximation [3], where coupling constant α_s can be written in closed form in terms of the Lambert W -function [5], defined implicitly by $W(z) \exp(W(z)) = z$,

$$\alpha_s = -\frac{1}{c[1+W(z(Q))]}, \quad (6)$$

where

$$z(Q) \equiv -\frac{1}{e} \left(\frac{Q}{\Lambda_R} \right)^{-b/c}. \quad (7)$$

In Fig.1 we plotted singlet and non-singlet moments and compared the results in conventional QCD calculation and in the CORGI approach. There is a good agreement between these two results. In Fig.2 we plotted the results for polarized parton distributions in these two different approaches, where we used the convolution of moments as in Eq.(4) and employed inverse Mellin technique to get PPDFs. The results are again in good agreement with each other. Since in the CORGI approach each term indicates a resummation over infinite terms of specified order, we expect to get better consistency between theoretical results for structure function and available experimental data in this new approach.

References

1. R. C. Hwa and C. B. Yang, Phys. Rev. C **66** (2002)
2. Ali N.Khorramian, Abolfazl Mirjalili and S.atashbar Tehrani, *JHEP***10**, 062 (2004).
3. C.J.Maxwell and A.Mirjalili, *Nucl. Phys.* **B 577**, 209 (2000).
4. M. Glück, E. Reya, M. Stratmann and W. Vogelsang, Phys. Rev. D**63**,094005 (2001) ; M. Glück, E. Reya and W. Vogelsang, Phys. Lett. **B359** 201 (1995) .

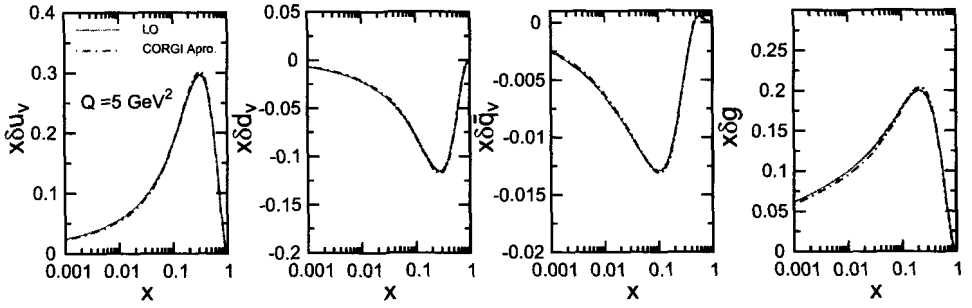


Fig. 2. Comparison of polarized valence u and d quark distributions and polarized gluon distribution in conventional perturbative QCD approach (solid line) and in CORGI approach (dashed-dotted line).

5. B. Magradze, hep-ph/9808247 and hep-ph/9911456; Einan Gardi, Georges Grunberg and Marek Karliner, JHEP **07** 007 (1998).

QUARK-GLUON HELICITY AND Q^2 DEPENDENCE OF PARTONIC ANGULAR MOMENTUM

A. N. KHORRAMIAN

Physics Department, Semnan University, Semnan, Iran &
Institute for Studies in Theoretical Physics and Mathematics, Tehran, Iran

A. MIRJALILI

Physics Department, Yazd University, Yazd, Iran &
Institute for Studies in Theoretical Physics and Mathematics, Tehran, Iran

S. A. TEHRANI

Physics Department, Persian Gulf University, Boushehr, Iran &
Institute for Studies in Theoretical Physics and Mathematics, Tehran, Iran

We use the improved valon model to obtain the spin dependence of parton distribution and proton structure. We compare our results for δu_v and δd_v with recent experimental data. We also calculate the Q^2 dependence of orbital angular momentum in valon model framework.

1. Introduction

Polarized deep inelastic scattering (DIS) is a powerful tool for the investigation of the nucleon spin structure. Measurements by the European Muon Collaboration (EMC) first indicated that only a small fraction of the nucleon spin is due to the spin of the quarks [1]. One of the hot problems in nucleon structure is the origin of the nucleon spin. In particular, it still remains a mystery how spin is shared among valence quarks, sea quarks, gluons and orbital momentum of nucleon constituents. Experimentally these question can not be answered by inclusive observables only.

The nucleon spin can be decomposed conceptually into the angular momentum contributions of its constituents according to the equation

$$\langle s_z^N \rangle = \frac{1}{2} = \frac{1}{2} \Delta \Sigma + \Delta g + L_z \quad (1)$$

where the three terms give the contributions to the nucleon spin from the quark, the gluon, and the quark-gluon orbital angular momentum, respectively. Early calculations based on relativistic quark models [2, 3] suggested $\Delta\Sigma \approx 2/3$, while more precise experiments on DIS at CERN, performed by the European Muon Collaboration (EMC) [1, 4], led to the conclusion that $\Delta\Sigma \approx 0.1 - 0.2$. We also had some experimental data from the HERMES group for $\delta q/q$ and $x\delta q$ the in range $0.033 \leq x \leq 0.447$ [5].

2. Polarized Parton Distributions (PPDs)

We have calculated polarized valon distributions (PVD's) by using an improved valon model in Next-to-Leading approximation [6]. The Non-singlet PVD's for U and D valons are:

$$\delta G_U = 0.278 y^{-0.395} (1-y)^{2.919} (1 - 0.155y^{0.5} + 10.654y), \tag{2}$$

$$\delta G_D = -0.177 y^{-0.536} (1-y)^{2.926} (1 - 0.841y^{0.5} + 9.620y). \tag{3}$$

For Singlet case, we have

$$\begin{aligned} \delta G_\Sigma = & (-0.002y^{-0.5} - 3.11 + 15.81y^{0.5} - 21.15y \\ & + 10.5y^{1.5} - 0.916y^2) \times (2\delta G_U + \delta G_D). \end{aligned} \tag{4}$$

According to the improved valon model, the polarized parton distribution is related to the polarized valon distribution. On the other hand, the polarized parton distribution of a hadron is obtained by convoluting two distributions: the polarized valon distributions in the proton, and the polarized parton distributions for each valon:

$$\delta q_{i/p}(x, Q^2) = \sum_j \int_x^1 \delta q_{i/j}\left(\frac{x}{y}, Q^2\right) \delta G_{j/p}(y) \frac{dy}{y}, \tag{5}$$

where the summation is over the three valons. Here $\delta G_{j/p}(y)$ indicates the probability for the ν -valon to have a momentum fraction y in the proton where $\delta q_{i/p}(x, Q^2)$ and $\delta q_{i/j}\left(\frac{x}{y}, Q^2\right)$ are respectively the polarized i -parton distribution in the proton and j -valon. Similarly for the unpolarized case, the polarized quark distribution can be related to a polarized valon distribution [7]. Using polarized sea quark distribution and having polarized valence quark distribution, we can obtain the contributions of $\delta q(x, Q^2) = \delta q_v(x, Q^2) + \delta \bar{q}(x, Q^2)$. In Fig.(1), we present the u and d quark helicity distributions $x\delta u(x, Q^2)$ and $x\delta d(x, Q^2)$ in $Q^2 = 2.5\text{GeV}^2$ as a function of x .

3. The Q^2 Dependence of L_z

The spin contribution of the valons to the proton can be analyzed through the valon model. The contribution of various polarized partons in a valon are calculable, and by computing their first moment, the spin of the proton can be computed. According to Eq.(1), the spin of the proton can be expressed in terms of the first moment of the total quark and gluon helicity distributions and their orbital angular momentum. To study the Q^2 dependence of the total orbital angular momentum of the quarks and gluons, e. g. L_z , the results of PPD's

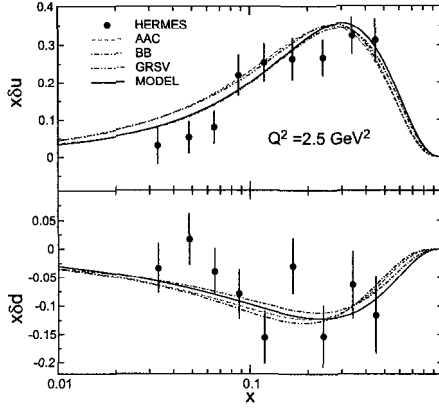


Fig. 1. The u and d quark helicity distributions, $x\delta u(x, Q^2)$ and $x\delta d(x, Q^2)$, evaluated at a common value of $Q^2 = 2.5 \text{ GeV}^2$ as a function of x . The dashed line is the AAC model (ISET=3)⁸, the dash-dotted line is the BB model (ISET=3)⁹, the dash-dot-dotted line is the GRSV model (ISET=1)¹⁰ and the solid line is our model.

in improved valon model in NLO approximation [6] can be employed. Using Eq.(5) the contributions of $\delta\Sigma(x, Q^2)$ and $\delta g(x, Q^2)$ in the proton can be calculated. Now we are in position to obtain their first moments as below

$$\Delta\Sigma^j = \int_0^1 \delta\Sigma^j(x, Q^2) dx, \quad \Delta g^j = \int_0^1 \delta g^j(x, Q^2) dx. \quad (6)$$

The resulting total quark and gluon helicity for a j -valon is $\frac{1}{2}\Delta\Sigma^j + \Delta g^j$. Since each proton involves 2 U -valons and one D -valon, the total quark and gluon helicity for the proton is

$$\frac{1}{2}\Delta\Sigma^p + \Delta g^p = 2\left(\frac{1}{2}\Delta\Sigma^U + \Delta g^U\right) + \frac{1}{2}\Delta\Sigma^D + \Delta g^D. \quad (7)$$

With the assumption that the polarized U and D valons have spins of $+\frac{1}{2}$ and $-\frac{1}{2}$ respectively, the determination of orbital angular momentum for each valon and finally for the proton, at different values of Q^2 , ($1 \leq Q^2(\text{GeV}^2) \leq 1000$), can be obtained from Eq.(1). As a result of our calculation, the Q^2 dependence of L_z can be given by $L_z(Q^2) = -5.10 + 4.96(Q^2)^{-0.04}$. In Fig.(2) we plot L_z as a function of Q^2 .

References

1. Ashman, J., et al., *Phys. Lett.* **B206**, 364 (1988).
2. R. L. Jaffe and A. Manohar, *Nucl. Phys.* **B 337**, 509 (1990).
3. K. Suzuki and W. Weise, *Nucl. Phys.* **A 634**, 141 (1998).
4. Ashman, J., et al., *Nucl. Phys.* **B328**, 1 (1989).
5. A. Airapetian, et al., hep-ex/0407032.
6. Ali N. Khorramian, A. Mirjalili, S. Atashbar Tehrani, *JHEP***10**, 062 (2004).
7. R. C. Hwa and C. B. Yang, *Phys. Rev. C* **66** (2002) 025204.

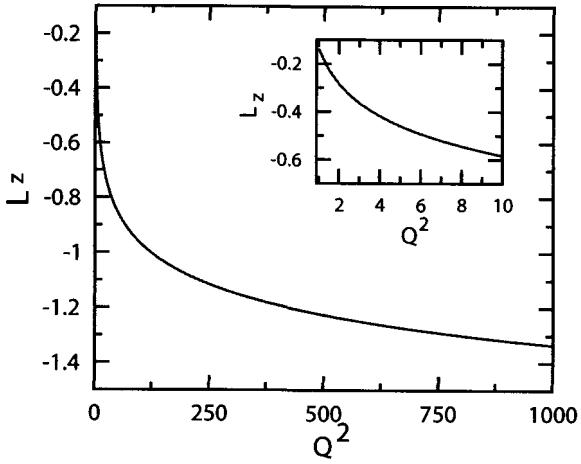


Fig. 2. The Q^2 dependence of L_z in NLO approximation.

8. Y. Goto and et al., Phys. Rev. D **62** (2000) 34017.
9. J. Blümlein, H. Böttcher, Nucl. Phys. B **636**(2002) 225.
10. M. Glück, E. Reya, M. Stratmann and W. Vogelsang, Phys. Rev. D **63**(2001) 094005.

THE APPROACH UNIFYING SPINS AND CHARGES AND ITS PREDICTIONS

A. B. BRAČIČ¹, N. M. BORŠTNIK²

¹ Educational Faculty, University of Ljubljana, Ljubljana, Slovenia

² Department of Physics, University of Ljubljana, Ljubljana, Slovenia

Ten years ago one of us (NMB) proposed an approach - a kind of the Kaluza-Klein-like theory - which unifies all the internal degrees of freedom of fermions and bosons - that is the spin and all the charges [1] within the group $SO(1, 13)$. Accordingly, there is only one fermion (one left-handed Weyl multiplet of the group $SO(1, 13)$) - with only one internal degree of freedom: the spin in the $d(= 1+13)$ -dimensional space. There is also only one gauge field: gravity. In this talk we briefly present the advances of the approach and its success in answering (some) of the open questions, which the standard electroweak model leaves open. We also present some of the (very preliminary) predictions of the approach: four generations of quarks and leptons, the mass of the fourth u- quark, and the mixing matrix for four generations of quarks. We comment on a possible way of breaking the group $SO(1, 13)$ leading to spins, charges and flavours of leptons and quarks and anti leptons and anti quarks.

1. Introduction

There is (almost) no experimental data yet which would not be in agreement with the standard electroweak model (we assume the non-zero neutrino masses to be a part of the model). But the standard electroweak model has more than 20 parameters and assumptions, the origin of which is not at all understood. There are also no theoretical approaches yet which could explain all these assumptions and parameters. We expect a lot from experiments on new extremely sophisticated and expensive accelerators and spectrometers, but measurements will first of all corroborate or not predictions for several events calculated with models and theories.

The great advantage of our approach, unifying spins and charges [1], is that it proposes possible answers to the open questions of the standard electroweak model. It turns out that *a (only one) left handed $SO(1, 13)$ Weyl spinor multiplet includes*, if the representation is interpreted in terms of the subgroups $SO(1, 3)$, $SU(2)$, $SU(3)$ and the sum of the two $U(1)$'s, *the spinors and the "anti spinors" of the standard model*. That is the left handed $SU(2)$ doublets and the right handed $SU(2)$ singlets, of the $SU(3)$ charged quarks and the $SU(3)$ chargeless leptons, while the "anti spinors" are oppositely charged and have opposite handedness. Right handed neutrinos and left handed antineutrinos - both weak and chargeless - are also included. We have succeeded in showing with one example that, when starting with a spinor of only one handedness, spinor representations of subgroups,

although they always contain representations of both handedness - with respect to each of the subgroups - can still have massless solutions, which chirally couple to the corresponding gauge field. Namely, the gauge Kaluza-Klein charges, which couple massless spinors to the corresponding gauge fields, are in this case proportional to the handedness [2].

In this talk we demonstrate, presenting the action, that the approach offers a possible explanation for families of spinors and their masses, since a part of the gravitational gauge fields originating in higher than four dimensions appears as terms which, together with the corresponding spinor operators, simulate the Yukawa couplings.

2. Lagrange function of the approach

Referring to earlier work [1] we write the action for a Weyl (massless) spinor and the gauge field in $d(= 1 + 13)$ - dimensional space as follows:

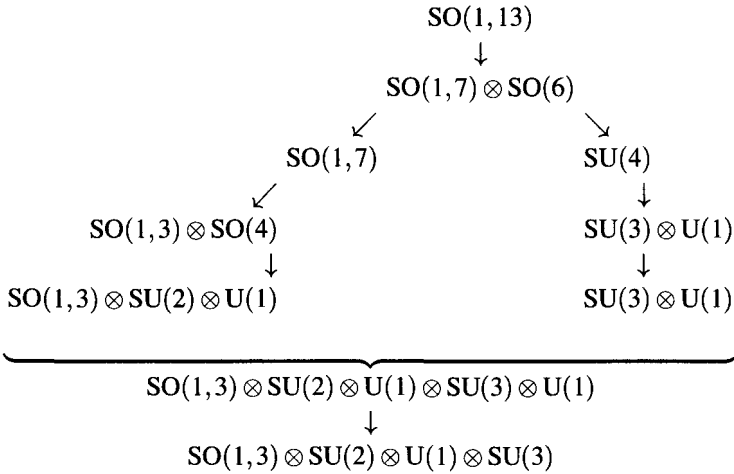
$$\begin{aligned}
 S &= \int d^d x E \mathcal{L} + \int d^d x ER, \text{ with} \\
 \mathcal{L} &= \bar{\Psi} \gamma^a p_{0a} \Psi = \bar{\Psi} \gamma^a f_a^\alpha p_{0\alpha} \text{ and } R = f^\alpha_{[a} f^{\beta}_{b]} (\omega^{ab}{}_{\alpha\beta} + \omega^a{}_{c\alpha} \omega^{cb}{}_{\beta}), \\
 p_{0\alpha} &= p_\alpha - \frac{1}{2} S^{ab} \omega_{ab\alpha} - \frac{1}{2} \tilde{S}^{ab} \tilde{\omega}_{ab\alpha}.
 \end{aligned} \tag{1}$$

Here f_a^α are vielbeins, while $\omega_{ab\alpha}$ and $\tilde{\omega}_{ab\alpha}$ are spin connections, the gauge fields of S^{ab} and \tilde{S}^{ab} , respectively. We point out that there are two kinds of the Clifford algebra objects [1]. (Besides the usual γ^a operators, there are also the operators $\tilde{\gamma}^a$, the first connected with left multiplication, the second with right multiplication. The two types of Clifford algebra objects anticommute ($\{\gamma^a, \tilde{\gamma}^b\}_+ = 0$), while the two corresponding types of generators of the Lorentz transformations commute ($\{S^{ab}, \tilde{S}^{cd}\}_- = 0$.)

To see that one Weyl spinor in $d = (1 + 13)$, with the spin as the only internal degree of freedom, (might) manifest itself in four-dimensional space as the ordinary ($SO(1,3)$) spinor with all the known charges of one family of the standard model, the reader must look at the ref. [1]. The gravitational field presented with spin connections and vielbeins (might) accordingly in four dimensions manifest as all the known gauge fields as well as the Yukawa couplings, if the symmetry breaking occurs in an appropriate way. When rewriting the spinor part of the Lagrangean of Eq.(1) as [1] $\mathcal{L} = \bar{\Psi} \gamma^a (p_\alpha - \sum_{A,i} g^A \tau^{Ai} A_\alpha^i) \Psi + i \Psi^+ S^{0h} S^{kk'} f_h^\sigma \omega_{kk'\sigma} \Psi + i \Psi^+ S^{0h} \tilde{S}^{kk'} f_h^\sigma \tilde{\omega}_{kk'\sigma} \Psi$, with Ψ , which is (for low energy solution) assumed not to depend on coordinates x^σ , $\sigma = \{5, 6, \dots, 14\}$, the second and the third term look like a mass term, since $f_h^\sigma \omega_{kk'\sigma}$ and $f_h^\sigma \tilde{\omega}_{kk'\sigma}$ behaves in $d(= 1 + 3)$ - dimensional part of space like a scalar field, while the operator S^{0h} , $h = 7, 8$, for example, transforms a right handed weak chargeless spinor into a left handed weak charged spinor, without changing the spin in $d = 1 + 3$ (just what the Yukawa couplings with the Higgs doublet included do in the standard model formulation. The reader should note that no Higgs weak charge doublet is needed here, as S^{0h} , $h = 7, 8$ does its job.)

3. Symmetry breaking from $SO(1, 13)$ to "physical" space

There are several ways of breaking the group $SO(1, 13)$. The approach unifying spins and charges suggests the following one



This symmetry breaking leads to the scheme of running coupling constants [1], without including additional degrees of freedom [3], as if it were a supersymmetry.

4. Predictions for masses and mixing matrices for four generations of fermions

The approach suggests four generations of quarks and leptons, and (approximate) symmetries, which lead, for example, to the (preliminary) mixing matrix for families of quarks [4] (the prediction is in boldface, while the rest represents the experimental data)

$$\begin{pmatrix}
 0.9730 - 0.9746 & 0.2174 - 0.2241 & 0.0030 - 0.0044 & \mathbf{0.039 - 0.044} \\
 0.213 - 0.226 & 0.968 - 0.975 & 0.039 - 0.044 & \mathbf{0.0030 - 0.0044} \\
 0 - 0.08 & 0 - 0.11 & \mathbf{0.900 - 0.935} & \mathbf{0.350 - 0.434} \\
 \mathbf{0.039 - 0.044} & \mathbf{0.0030 - 0.0044} & \mathbf{0.350 - 0.434} & \mathbf{0.900 - 0.935}
 \end{pmatrix}$$

while we find (preliminarily) for the mass of the fourth u quark the value $m_{u_4} = (210.5 \pm 11.5) GeV$.

5. Conclusions

In this talk we have briefly presented an approach which unifies spins and charges to only spins in $d = 1 + 13$ -dimensional space. The approach is very promising from the point of view that it offers answers to the open questions of the standard electroweak model. Only(!) one left handed Weyl multiplet of the group $SO(1, 13)$ contains, if represented so as to demonstrate the $SU(3), SU(2)$ and $U(1)$ substructure, *the spinors - the quarks and the leptons - and the "anti spinors" - the anti quarks and the anti leptons - of the standard electroweak and colour model*. The approach explains why the weak charge breaks parity while the colour charge does not, offers a non-standard way of breaking the group

$SO(1, 13)$ leading to the known spins, charges and flavours of leptons and quarks and anti leptons and anti quarks, and suggests that the spin connections and vielbeins appear not only as gauge fields connected with charges, but also as Yukawa couplings, determining accordingly masses of families. We predict the appearance of a fourth family, and present a (very preliminary) mixing matrix for the four generations of quarks as well as the mass of the fourth u quark.

References

1. A. Borštnik, N. S. Mankoč Borštnik and N. S. Mankoč Borštnik and H. Bech Nielsen, hep-ph/0401043, hep-ph/0401055, and other references, presented in this proceedings.
2. N. S. Mankoč Borštnik, H. Bech Nielsen, sent to Phys. Lett..
3. N. S. Mankoč Borštnik, H. Bech Nielsen, hep-ph/0401043, hep-ph/0401055.
4. M. Breskvar, J. Mravlje, N.S. Mankoč Borštnik, the paper in preparation.

NEW QCD RELATIONS BETWEEN MAGNETIC MOMENTS OF Σ^0 AND Λ HYPERONS

A. ÖZPINECI

ICTP, Trieste, Italy*

V. S. ZAMIRALOV, S. B. YAKOVLEV

D.V. Skobel'syn Institute of Nuclear Physics, Moscow State University, Moscow, Russia

It is shown that starting from the QCD Borel sum rule for μ_{Σ^0} and applying to it the transformations ($u \leftrightarrow s$) and ($d \leftrightarrow s$) it is straightforward to obtain the corresponding sum rule for the μ_{Λ} as well as the sum rule for $\mu_{\Lambda\Sigma^0}$

We propose here relations which connect QCD sum rules for μ_{Σ^0} with μ_{Λ} and *vice versa*, as well as formulae relating sum rules for μ_{Λ} or μ_{Σ^0} with the corresponding sum rule for $\mu_{\Lambda\Sigma^0}$. Their origin lies in relations between isotopic, U - and V -spin quantities.

The starting point is the two-point Green's function for hyperons Σ^0 and Λ of the baryon octet [1]:

$$\Pi^{\Sigma^0, \Lambda} = i \int d^4x e^{ipx} \langle 0 | T \{ \eta^{\Sigma^0, \Lambda}(x), \bar{\eta}^{\Sigma^0, \Lambda}(0) \} | 0 \rangle, \quad (1)$$

where the isovector and isoscalar field operators could be chosen as in [2]

$$\begin{aligned} \eta^{\Sigma^0} &= \frac{1}{2} \epsilon_{abc} [u^{aT} C s^b \gamma_5 d^c - d^{aT} C s^b \gamma_5 u^c - u^{aT} C \gamma_5 s^b d^c + d^{aT} C \gamma_5 s^b u^c], \\ \eta^{\Lambda} &= \frac{1}{2\sqrt{3}} \epsilon_{abc} [-2(u^{aT} C d^b) \gamma_5 s^c + (u^{aT} C s^b) \gamma_5 d^c + (d^{aT} C s^b) \gamma_5 u^c + \\ &\quad 2(u^{aT} C \gamma_5 d^b) s^c - (u^{aT} C \gamma_5 s^b) d^c - (d^{aT} C \gamma_5 s^b) u^c], \end{aligned} \quad (2)$$

where a, b, c are the colour indices, u, d, s are quark wave functions, and C is the charge conjugation matrix.

*presently at INFN, Sezione di Bari, Bari, Italy)

We show now that one can operate with the Σ hyperon and obtain results for the Λ hyperon. The reasoning would also be valid for charm and beauty Σ -like and Λ -like baryons.

In order to arrive at the desired relations we should write not only the isospin quantities of Eq.(2) but also the U -spin and V -spin ones. Let us introduce the U -vector and scalar field operators just by formally changing ($d \leftrightarrow s$) in Eq.(2) and similarly the V -vector and scalar ones changing ($u \leftrightarrow s$). Field operators of Eq.(2) can be related to these ones through

$$\begin{aligned} -2\tilde{\eta}^{\Lambda(d\leftrightarrow s)} &= \sqrt{3}\eta^{\Sigma^0} + \eta^{\Lambda}, & 2\tilde{\eta}^{\Sigma^0(d\leftrightarrow s)} &= \eta^{\Sigma^0} - \sqrt{3}\eta^{\Lambda}, \\ 2\tilde{\eta}^{\Lambda(u\leftrightarrow s)} &= \sqrt{3}\eta^{\Sigma^0} - \eta^{\Lambda}, & 2\tilde{\eta}^{\Sigma^0(u\leftrightarrow s)} &= \eta^{\Sigma^0} + \sqrt{3}\eta^{\Lambda}. \end{aligned} \tag{3}$$

Upon using Eqs.(2-3), the two-point functions of Eq.(1) for hyperons Σ^0 and Λ of the baryon octet can be related as

$$2 \cdot [\tilde{\Pi}^{\Sigma^0(d\leftrightarrow s)} + \tilde{\Pi}^{\Sigma^0(u\leftrightarrow s)}] - \Pi^{\Sigma^0} = 3\Pi^{\Lambda}, \tag{4}$$

$$2 \cdot [\tilde{\Pi}^{\Lambda(d\leftrightarrow s)} + \tilde{\Pi}^{\Lambda(u\leftrightarrow s)}] - \Pi^{\Lambda} = 3\Pi^{\Sigma^0}. \tag{5}$$

Moreover one can obtain the QCD Borel sum rule for the $\Sigma^0 - \Lambda$ transition magnetic moment using the relations

$$[\tilde{\Pi}^{\Sigma^0(u\leftrightarrow s)} - \tilde{\Pi}^{\Sigma^0(d\leftrightarrow s)}] = -[\tilde{\Pi}^{\Lambda(u\leftrightarrow s)} - \tilde{\Pi}^{\Lambda(d\leftrightarrow s)}] = \sqrt{3}\Pi^{\Lambda\Sigma^0}, \tag{6}$$

We have proved successfully the validity of these relations in the framework of light-cone QCD sum rules elaborated by one of us with coauthors [2].

But in order to demonstrate clearly how it works we preferred not to use these LC QCD sum rules, although they satisfy perfectly the relations (4-6), but instead to repeat calculations of the QCD Borel sum rules for magnetic moments of some known work (we have chosen [3]) conserving however non-degenerated quantities for u and d quarks. Our aim was to obtain QCD sum rules for μ_{Λ} and $\mu_{\Sigma^0\Lambda}$ using our relations for μ_{Σ^0} and to compare the results to some known works (we have chosen [4, 5]).

We construct a sum rule for μ_{Σ^0} along the lines of [3]

$$\begin{aligned} 2SR(\mu_{\Sigma^0}) &= \frac{M^6}{4L^{4/9}} 2(e_u + e_d) - \frac{L^{4/9}}{18M^2} a_u a_d 2(e_u + e_d + 3e_s) + \\ &\frac{M^2 b}{24L^{4/9}} [(2e_u + 2e_d + e_s) - \frac{1}{3} \cdot Ln \cdot (e_u + e_d + 2e_s) - \frac{4}{3} (Ln + 1 - \frac{M^2}{2\Lambda^2}) \times \\ &(e_u + e_d)] - \frac{1}{3L^{4/27}} [(M^2 - \frac{m_{(d)0}^2}{8L^{4/9}}) e_u (\chi_u a_u) a_d + (M^2 - \frac{m_{(u)0}^2}{8L^{4/9}}) e_d (\chi_d a_d) a_u] \\ &+ \frac{L^{4/9}}{18} [e_u (2\kappa_u - \xi_u) + e_d (2\kappa_d - \xi_d)] a_u a_d - \frac{M^2}{8L^{4/9}} 4[2(e_u a_u + e_d a_d) m_s \\ &- (e_u a_d + e_d a_u) m_s + 2e_s (m_u + m_d) a_s + 2(e_u a_u m_d + e_d a_d m_u) - \\ &(e_u m_d + e_d m_u) a_s] + \frac{M^2}{2L^{4/9}} 2 \cdot Ln \cdot (e_u m_u + e_d m_d) a_s \end{aligned} \tag{7}$$

$$\begin{aligned}
 & -\frac{M^4}{4L^{28/27}} [2(e_u a_u \chi_u m_d e_d a_d \chi_d m_u) - 2(e_u a_u \chi_u m_u + e_d a_d \chi_d m_d)] \\
 & + \frac{M^2}{6} [(2\kappa_u - \xi_u) - 3 \cdot \kappa_u \cdot Ln] e_u a_u m_d + \frac{M^2}{6} [(2\kappa_d - \xi_d)] - \\
 & \quad 3\kappa_d \cdot Ln] e_d a_d m_u = 2\beta_{\Sigma^0}^2 (\mu_{\Sigma^0} + AM^2) e^{-M_{\Sigma^0}^2/M^2}
 \end{aligned}$$

All quantities are defined in [1, 3], and $Ln = (\ln(M^2/\Lambda^2) - 1 - \gamma_{EM})$. Using the corollary of Eq.(4)

$$2 \cdot SR(\mu_{\Sigma_{sd}^0}) + 2 \cdot SR(\mu_{\Sigma_{su}^0}) - SR(\mu_{\Sigma^0}) = 3 \cdot SR(\mu_{\Lambda})$$

we arrive at the QCD Borel sum rule for μ_{Λ} [7] (here $m_{u,d} = 0$)

$$\begin{aligned}
 SR(\mu_{\Lambda}) &= \frac{M^6}{12L^{4/9}} (e_u + e_d + 4e_s) + \frac{M^2 b}{144L^{4/9}} (4e_u + 4e_d + 7e_s) \\
 & - \frac{L^{4/9}}{108M^2} [2(7e_u + 7e_d + e_s) + 8f(2e_u + 2e_d + e_s)] a^2 - \\
 & \frac{M^2 b}{192L^{4/9}} [Ln] (5e_u + 5e_d + 2e_s) - \frac{M^2 b}{108L^{4/9}} [Ln + 1 - \frac{M^2}{2\Lambda^2}] (e_u + e_d + 4e_s) \\
 & + [\frac{-\chi a^2}{18L^{4/27}} (M^2 - \frac{m_{(s)0}^2}{8L^{4/9}}) + \frac{L^{4/9}}{108} (2\kappa - \xi) a^2] [(e_u + e_d)(1 + 2f) + 4e_s \phi] \\
 & - \frac{15M^2}{36L^{4/9}} m_s (e_u + e_d) a + \frac{2m_s a e_s M^2}{3L^{4/9}} [Ln] \\
 & - \frac{M^2}{6L^{28/27}} (e_u + e_d - 2e_s \phi) m_s a \chi + (e_u + e_d) \frac{M^2}{18} [(2\kappa - \xi)] M^2 - \\
 & \quad 3\kappa \cdot Ln] a m_s = \beta_{\Lambda}^2 \mu_{\Lambda} e^{-M_{\Lambda}^2/M^2} (1 + A_{\Lambda} M^2)
 \end{aligned}$$

in agreement with [4] but with a factor 15/36 instead of 19/36 in the 7th term. This seems to be due to some diagram we have probably missed. The difference between the auxiliary sum rules for Σ_{sd}^0 and Σ_{su}^0 yields the sum rule for μ_{Σ^0} [7] :

$$\begin{aligned}
 (e_u - e_d) & [\frac{M^6}{4L^{4/9}} + \frac{L^{4/9}}{9M^2} a_s a + \frac{M^2 b}{24L^{4/9}} - \frac{M^2 b}{144L^{4/9}} [5 \cdot Ln + 4 - \frac{2M^2}{\Lambda^2}] \\
 & + [\frac{-\chi}{6L^{4/27}} (M^2 - \frac{m_{(s)0}^2}{8L^{4/9}}) + \frac{L^{4/9}}{36} (2\kappa - \xi)] a a_s + \frac{M^2}{L^{4/9}} (\frac{1^*}{4} - \frac{M^2}{4L^{16/27}} \chi) m_s a \\
 & + \frac{M^2}{18} [(2\kappa - \xi) - 3\kappa \cdot Ln] m_s a] = \beta_{\Sigma} \beta_{\Lambda} \sqrt{3} \mu_{\Sigma^0 \Lambda} e^{-\bar{m}^2/M^2} (1 + A_{\Sigma^0 \Lambda} M^2) \tag{8}
 \end{aligned}$$

in agreement with [5] but with a factor 1/4 instead of 1/3 in the term with * .

We have shown explicitly with the example of QDC Borel sum rules that starting from the sum rule for the μ_{Σ^0} , it is straightforward to obtain the corresponding sum rule for the μ_{Λ} , as well as the sum rule for $\mu_{\Sigma^0\Lambda}$. (The only divergence with [4] and [5] is discussed in the text.) We have also proved that starting from the QCD sum rule for μ_{Λ} with Eq.(5) we return to the initial sum rule for the magnetic moment of Σ^0 .

We have proved that Eqs.(4,5) are valid for the QCD Light-Cone sum rules [2].

The results will be published elsewhere. A similar result has earlier been proved for the QCD mass sum rules for Σ^0 and Λ [8], where the agreement with the sum rules of [6] has been found to be perfect.

The proposed relations Eqs.(4-6) can be used not only to obtain properties of the Λ -like baryons from those of Σ -like ones *et vice versa*, but also for mutual checks of many-term relations for the Σ -like and Λ -like baryons.

We thank T.Aliev, F.Hussain, B.L.Ioffe, G.Thompson for fruitful discussions. One of us (V.Z.) is grateful to Prof.S.Randjbar-Daemi for the hospitality extended to him at HE section of ICTP (Trieste, Italy). The financial support of the ICTP is gratefully acknowledged.

References

1. V.M.Belyaev, B.L.Ioffe, *JETP* **56**, 493 (1982); B.L.Ioffe, Smilga, *Nucl. Phys.* **B232**, 109 (1984); I. I. Balitsky and A. V. Yung, *Phys. Lett.* **B129**, 328 (1983).
2. T.M.Aliev, A.Özpineci, M.Savci, *Phys. Rev.* **D62**, 053012 (2000); *Nucl. Phys.* **A678**, 443 (2000).
3. Ch.B.Chiu, J.Pasupathy, S.L.Wilson, *Phys. Rev.* **D33**, 1961 (1986).
4. Ch.B.Chiu, S.L.Wilson, J.Pasupathy, J.P.Singh, *Phys. Rev.* **D36**, 1553 (1987); *ibid.* 1442.
5. Shi-lin Zhu, W-Y.P.Hwang and Ze-sen Yang, *Phys. Rev.* **D57**, 1527 (1998).
6. W-Y.P.Hwang and K.-C.Yang, *Phys. Rev.* **D49**, 460 (1994).
7. A.Özpineci, S.B.Yakovlev, V.S.Zamiralov, *hep-ph/0311271* (to be published in *Phys. Atom. Nucl.*).
8. A.Özpineci, S.B.Yakovlev, V.S.Zamiralov, *hep-ph/0310345* (to be published in *Messenger of the Moscow University*).

Q_{WEAK} : A PRECISION MEASUREMENT OF THE PROTON'S WEAK CHARGE*

R. D. CARLINI

Jefferson Laboratory, Newport News, USA

(for the Qweak Collaboration)

The Q_{weak} experiment at Jefferson Lab will measure the parity-violating asymmetry in e-p elastic scattering at low Q^2 using a polarized electron beam and a LH₂ target. The experiment will provide the first measurement of the weak charge of the proton to an accuracy of 4%. Q_w^p is related to the weak mixing angle, and thus provides the means for a precision test of the SM. Since the value of $\sin^2 \theta_w$ is approximately 1/4, the weak charge of the proton $Q_w^p = 1 - 4 \sin^2 \theta_w$ is suppressed in the SM, making it sensitive to the value of the mixing angle and to possible new physics. At the kinematics selected the systematic uncertainties from hadronic processes are strongly suppressed.

1. Scientific Motivation

We describe an experiment to make the first measurement of the weak charge of the proton, which is a well defined observable with a definite prediction in the Standard Model (SM). To lowest order, the weak charge can be expressed as $Q_w^p = 1 - 4 \sin^2 \theta_w$, where $\sin^2 \theta_w \approx 0.23$ is the weak mixing angle. The goal of the Q_{weak} experiment [1] is a 4% measurement of Q_w^p (combined statistical and systematic errors), which corresponds to a 0.3% measurement of $\sin^2 \theta_w$. A measurement of this precision is possible because the hadronic corrections are small at low Q^2 and measured by numerous experiments aimed at electromagnetic and weak hadronic form factors. The SM makes a prediction for Q_{weak} based on the running [2,3] of $\sin^2 \theta_w$ from the Z^0 pole. As shown in Fig. 1 the weak mixing angle is predicted to change (in the $\overline{\text{MS}}$ renormalization scheme) by $\sim 3\%$ from the energy scale of the Z pole (where a decade of measurements has been made at colliders like SLAC and CERN [4]) to the low energy scale of Q_{weak} . The proposed measurement will make a $\sim 10\sigma$ verification of this effect. A significant deviation from the SM prediction would imply new physics. Agreement with the SM would help constrain classes of extensions. If new physics is uncovered at the LHC, such as the Z' , then precision experiments undertaken at low Q^2 can aid in the determination of the charges, coupling constants, etc.

*This work is supported by DOE, NSF and NSERC.

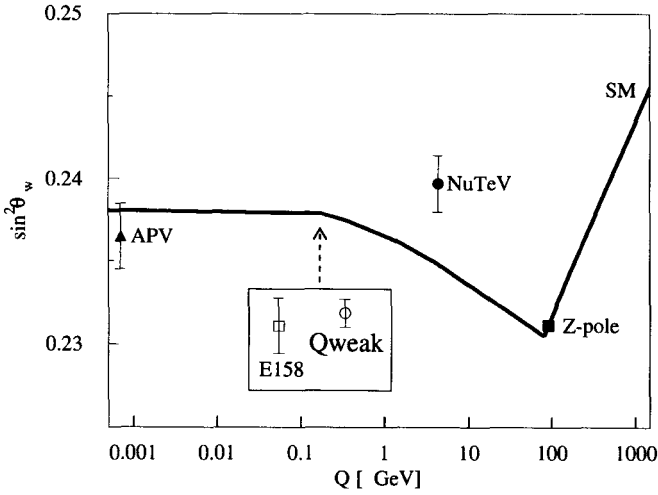


Fig. 1. Running of the weak mixing angle [2] in the SM, calculated in the \overline{MS} scheme. Shown are results from atomic parity violation [6–8], NuTeV [9], and the Z pole [4]. The error shown for the E158 [10] experiment is that anticipated for their final result.

The asymmetry between cross-sections for + and - helicity electrons in polarized elastic e–p scattering violates parity, and arises from the interference of electromagnetic and weak amplitudes (photon and Z boson exchange). At low energy scales, the asymmetry is a measure of Q_w^p , which is the strength of the weak vector coupling of the Z boson to the proton. In the limit of small scattering angle and small momentum transfer ($Q^2 \rightarrow 0$), the asymmetry is given by [5]:

$$\frac{\sigma_+ - \sigma_-}{\sigma_+ + \sigma_-} = \left[\frac{-G_F}{4\pi\alpha\sqrt{2}} \right] [Q^2 Q_w^p + Q^4 B(Q^2)] \tag{1}$$

$$\approx -0.3 \text{ ppm at } Q^2 = 0.03 \text{ GeV}^2$$

where $B(Q^2)$ is a contribution from electromagnetic and weak form factors. It is sensitive to $G_{E,M}^Y$ and $G_{E,M}^Z$, the target of many recent and ongoing experiments at Jefferson Lab, Bates, and MAMI. As equation 1 makes clear, the B term is suppressed as Q^2 goes to zero by an extra factor of Q^2 relative to Q_{weak} . On the other hand, the experimental asymmetry grows with Q^2 . At Jefferson Lab a Q^2 of ~ 0.03 has been chosen as the best compromise between these two competing considerations. The expected measured asymmetry of -0.29 ppm consists of three main terms. The largest is the term sought in this experiment, namely A_{qw} equal to -0.19 ppm. The second term (-0.09 ppm) arises from the hadronic form factors discussed above. It will be constrained by the measurements provided by HAPPEX, PVA4, and G0. The third term (axial) is only about 3% of the expected asymmetry. It contains G_A^E , and includes electroweak radiative corrections. It will be constrained by the SAMPLE and G0 experiments. When added in quadrature, the uncertainty from these terms contributes about 2% to the expected error on Q_{weak} .

2. Experimental Technique

A sketch of the Q_{weak} experiment is shown in Fig. 2. The experiment consists of scattering a longitudinally polarized 1.2 GeV electron beam by a 35 cm LH₂ target. Elastically scattered electrons at $8^\circ \pm 2^\circ$ are selected by a collimation system, and then focused by a large toroidal resistive magnet onto eight radiation hard synthetic quartz Čerenkov detectors. The expected event rate for scattered electrons is ~ 6 GHz. Therefore the experiment will use current mode detection and low noise electronics.

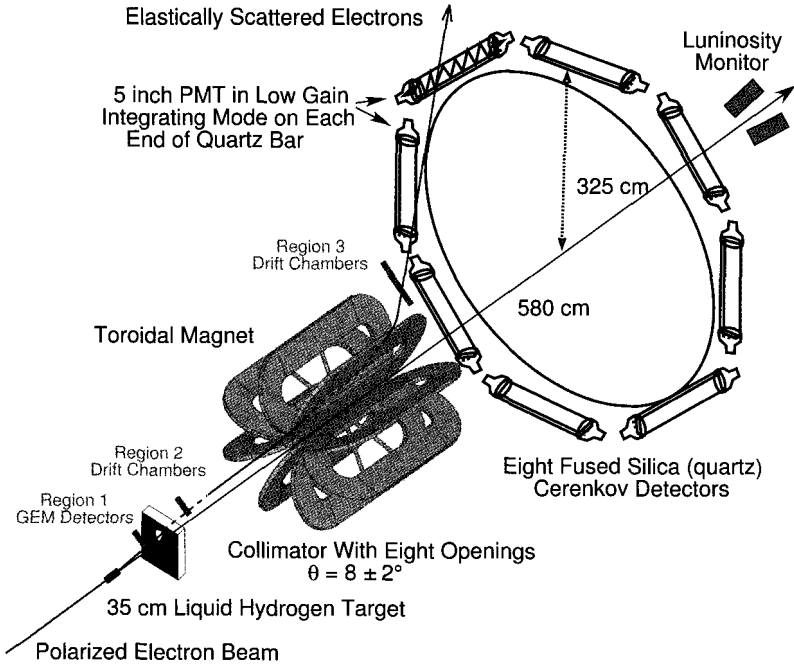


Fig. 2. Conceptual design for the Q_{weak} experimental setup at Jefferson Lab.

At a beam current of $180\mu\text{A}$, the LH₂ target will require 2.5kW of cooling power. An ancillary tracking system will be used, with the beam current reduced by four orders of magnitude, allowing individual events to be observed. This will enable a precise determination of the average Q^2 . Precision beam polarimetry is required in order to have a polarization contribution to the systematic error of less than 1.5%. To achieve this, efforts are underway to increase the operating current of the existing Møller polarimeter. In addition, a Compton polarimeter is being developed which should provide a continuous measurement of the beam polarization.

References

1. Q_{weak} Collaboration: Carlini, R. *et al.*, Jefferson Lab Proposal E-02-020. Proposal and collaboration list available at <http://www.jlab.org/qweak/>.

2. Erler, J., Kurylov, A., and Ramsey-Musolf, M.J., *Phys. Rev.* **D68**, (2003) 016006.
3. Kurylov, A., Ramsey-Musolf, M.J., and Su, S., hep-ph/0303026, to appear in *Phys. Rev. D*.
4. Particle Data Group: Hagiwara, K. *et al.*, *Phys. Rev.* **D66**, (2002) 010001.
In particular, the section *Electroweak Model and Constraints on New Physics*.
5. Musolf, M.J. *et al.*, *Phys. Rep.* **239**, (1994) 1.
6. Edwards, N.H. *et al.*, *Phys. Rev. Lett.* **74**, (1995) 2654.
7. Vetter, P.A. *et al.*, *Phys. Rev. Lett.* **74**, (1995) 2658.
8. Wood, C.S. *et al.*, *Science* **275**, (1997) 1759.
9. NuTeV Collaboration: Zeller, G.P. *et al.*, *Phys. Rev. Lett.* **88**, (2002) 091802.
10. Anthony, P.L., *et al.*, *Phys. Rev. Lett.* **92**, 181602 (2004) 181602.

FOUR-SPINON CONTRIBUTION TO THE DYNAMIC STRUCTURE FACTOR IN THE ANTIFERROMAGNETIC HEISENBERG MODEL

B. Si LAKHAL

Physics Department, Faculty of Science, University Saad Dahlab of Blida, Blida, Algeria

A. ABADA

Physics Department, Faculty of Science, United Arab Emirates University, Al Ain, United Arab Emirates

Sum rules are calculated for the exact four-spinon dynamic structure function (DSF) S_4 in the antiferromagnetic spin $1/2$ Heisenberg quantum spin chain. These sum rules are known to be exactly satisfied by the total DSF S . The sum rules for the two-spinon DSF S_2 have been evaluated in the literature and found to account for about 70%. The sum rules we consider are: the total integrated intensity, the first frequency moment, and the nearest-neighbour correlation function. The sum rules involve multiple integrals which are handled by Monte Carlo methods.

1. Exact Two-spinon DSF

The two-spinon contribution is given by [1]:

$$S_2(\omega, k - \pi) = \frac{\exp[-I(\rho)]}{\sqrt{\omega_{2u}^2 - \omega^2}} \Theta(\omega - \omega_{2l}) \Theta(\omega_{2u} - \omega), \quad (1)$$

where Θ is the Heaviside step function and the function $I(\rho)$ is given by:

$$I(\rho) = \int_{-\infty}^{+\infty} \frac{dt}{t} \frac{\cosh(2t) \cos(4\rho t)}{\sinh(2t) \cosh(t)} e^t. \quad (2)$$

In (1), $\omega_{2u(l)}$ are the upper and lower bounds of the two-spinon excitation energies. They read:

$$\omega_{2u} = 2\pi \sin(k/2); \quad \omega_{2l} = \pi |\sin k|. \quad (3)$$

The quantity $\rho \equiv \rho_1 - \rho_2$ is related to ω and k by the relation:

$$\cosh(\pi\rho) = \sqrt{\frac{\omega_{2u}^2 - \omega_{2l}^2}{\omega^2 - \omega_{2l}^2}}, \quad (4)$$

a relation obtained using the expressions of the spinon energy e_i and momentum p_i in terms of the spectral parameter ρ_i :

$$e(\rho_i) = \frac{\pi}{\cosh(2\pi\rho_i)} = -\pi \sin p_i; \quad \cot(p_i) = \sinh(2\pi\rho_i); \quad -\pi \leq p_i \leq 0; \quad i = 1, 2, \quad (5)$$

and the energy-momentum conservation laws:

$$\omega = e_1 + e_2; \quad k = -p_1 - p_2. \quad (6)$$

2. Exact Four-spinon DSF

The exact expression of the four-spinon DSF is more involved. It reads [2]:

$$S_4(\omega, k - \pi) = C_4 \int_{-\pi}^0 dp_3 \int_{-\pi}^0 dp_4 F(\rho_1, \rho_2, \rho_3, \rho_4). \quad (7)$$

The notation is as follows. C_4 is a numerical constant equal to [3]:

$$C_4 = \frac{1}{3 \times 2^{21} \times \pi^{14} \times \left| \Gamma\left(\frac{1}{4}\right) \right|^8 \times \left| A_-\left(\frac{i\pi}{2}\right) \right|^8}, \quad (8)$$

an expression in which Γ is Euler's gamma function and:

$$A_-(z) = \exp\left(-\int_0^\infty dt \frac{\sinh^2 t (1 - \frac{z}{i\pi}) \exp t}{t \sinh(2t) \cosh t}\right). \quad (9)$$

The integrand F in (7) is expressed by the relation:

$$F(\rho_1, \rho_2, \rho_3, \rho_4) = \sum_{(p_1, p_2)} \frac{\exp\left[-\sum_{1 \leq i \leq j \leq 4} I(\rho_{ij})\right] \sum_{l=1}^4 |g_l(\rho_1, \rho_2, \rho_3, \rho_4)|^2}{\sqrt{W_u^2 - W^2}}. \quad (10)$$

The different quantities involved in this expression are defined as follows:

$$W = \omega + \pi(\sin p_3 + \sin p_4); \quad W_u = 2\pi \left| \sin\left(\frac{K}{2}\right) \right|; \quad K = k + p_3 + p_4; \quad (11)$$

$$\cot p_j = \sinh(2\pi\rho_j), \quad -\pi \leq p_j \leq 0; \quad \rho_{ij} = \rho_i - \rho_j;$$

$$g_l = (-)^{l+1} (2\pi)^4 \sum_{j=1}^4 \cosh(2\pi\rho_j) \times \sum_{m=\Theta(j-l)}^4 \frac{\prod_{i \neq l} (m - \frac{1}{2} \Theta(l-i) + i\rho_{ji})}{\prod_{i \neq j} \pi^{-1} \sinh(\pi\rho_{ji})} \prod_{i=1}^4 \frac{\Gamma(m - \frac{1}{2} + i\rho_{ji})}{\Gamma(m + 1 + i\rho_{ji})}. \quad (12)$$

In relation (10), the sum is over the two pairs (p_1, p_2) and (p_2, p_1) solutions of the energy-momentum conservation laws:

$$W = -\pi(\sin p_1 + \sin p_2); \quad K = -p_1 - p_2. \quad (13)$$

They read:

$$(p_1, p_2) = \left(-\frac{K}{2} + \arccos\left(\frac{W}{2\pi \sin(K/2)}\right), -\frac{K}{2} - \arccos\left(\frac{W}{2\pi \sin(K/2)}\right) \right). \quad (14)$$

Note that (14) is allowed as long as $W_l \leq W \leq W_u$ where W_u is given in (11) and $W_l = \pi|\sin K|$. The behaviour of S_4 as a function of ω and k has been studied in [4]

3. Sum Rules

Sum rules are exact relations satisfied by the total S and some of its integrals [5]. We determine in the sequel three of these sum rules for S_2 and S_4 , using Monte Carlo integration methods. Note that in the following tables, σ_4 and χ^2 are respectively the standard deviation and the χ^2 -factor in the runs regarding S_4 .

3.1. First Frequency Moment

This is defined by:

$$K(k) \equiv \frac{1}{2\pi} \int_0^\infty d\omega \omega S(\omega, k) = \frac{8}{3} \left(\ln 2 - \frac{1}{4} \right) \sin^2\left(\frac{k}{2}\right). \quad (15)$$

We obtain the following results.

Table 1. First frequency moment for S_2 and S_4 .

k	$K_2(k)$ (10^{-2})	$K_4(k)$ (10^{-4})	σ_4 (10^{-5})	σ_4/K_4	χ^2	$K(k)$ (10^{-2})	K_2/K	K_4/K
0.1	0.2053042	0.80744	0.6305	7.8%	1.196	0.2951853	69.5%	2.7%
0.2	0.813574	3.08253	2.1058	6.8%	1.549	1.177792	69.1%	2.6%
0.3	1.799619	5.42950	2.8636	5.3%	0.208	2.639001	68.2%	2.1%
0.4	3.294491	12.70855	8.8941	7.0%	0.524	4.664213	70.6%	2.7%

3.2. Total Integrated Intensity

This is given by the following relation, which is followed by the corresponding results:

$$I = \frac{1}{\pi} \int_0^\pi dk I(k) = \frac{1}{2\pi^2} \int_0^\pi dk \int_0^\infty d\omega S(\omega, k) = \frac{1}{4}, \quad (16)$$

Table 2. The total integrated intensity for S_2 and S_4 .

I_2	I_4	σ_4	σ_4/I_4	χ^2	I	I_2/I	I_4/I
0.1845412	0.00629916	0.0004973	7.9%	0.430	0.25	73.8%	2.5%

3.3. Nearest-neighbour Correlation Function

This is defined by the following relations:

$$\langle \sigma_n^z \sigma_{n+1}^z \rangle \equiv \frac{1}{\pi} \int_0^\pi dk \exp^{-ik} I(k) = \frac{1}{2\pi^2} \int_0^\pi dk \exp^{-ik} \int_0^\infty d\omega S(\omega, k) = \frac{E_G}{3} \quad (17)$$

E_G is the ground-state energy per site given by $E_G = -(\ln 2 - 1/4)$. We have:

Table 3. Nearest-neighbour correlation for S_2 and S_4 .

$\langle \sigma_n^z \sigma_{n+1}^z \rangle_2$	$\langle \sigma_n^z \sigma_{n+1}^z \rangle_4$	σ_4	$\frac{\sigma_4}{ O_4 }$	χ^2	$\langle \sigma_n^z \sigma_{n+1}^z \rangle$	$\frac{O_2}{O}$	$\frac{O_4}{O}$
-0.105594	-0.0035309	0.000421	11.9%	0.580	-0.1477157	71.5%	2.4%

4. Conclusion

In this work, we have calculated three sum rules for the exact four-spinon dynamic structure factor S_4 in the Heisenberg antiferromagnetic quantum spin chain using Monte carlo methods. We notice that the contribution of S_4 to the total S is about 2.5%. It seems therefore that the contributions from the remaining $S_{n>4}$ are not negligible. The statistics of the Monte Carlo runs are in general satisfactory.

Acknowledgments

This work was done within the framework of the Associateship Scheme of the Abdus Salam International Centre for Theoretical Physics, Trieste, Italy.

References

1. A.H. Bougourzi, M. Couture and M. Kacir, Phys. Rev. **B54** (1996) 12669.
2. A. Abada, A.H. Bougourzi and B. Si Lakhali. Nucl. Phys. **B497** [FS] (1997) 733.
3. A.H. Bougourzi, Mod. Phys. Lett **B10** (1996) 1237.
4. B. Si Lakhali and A. Abada, J. Phys. A: Math. Gen. **37** (2004) 497.
5. P.C. Hohenberg and W.F. Brinkman, Phys. Rev. **B10** (1974) 128.



SESSION 4

Spin in Soft Hadronic Reactions

This page intentionally left blank

MEASUREMENT OF THE ANALYZING POWER IN PP ELASTIC SCATTERING IN THE PEAK CNI REGION AT RHIC

H. OKADA¹, I. G. ALEKSEEV², A. BRAVAR³, G. BUNCE^{3,4}, S. DHAWAN⁵, R. GILL³, W. HAEBERLI⁶, O. JINNOUCHI⁴, A. KHODINOV⁷, A. KPONOU³, Y. MAKDISI³, W. MENG³, A. NASS³, N. SAITO^{1,9}, H. SPINKA¹⁰, E. J. STEPHENSON¹¹, D. N. SVIRIDA², T. WISE⁶, A. ZELENSKI³

¹Kyoto University ²ITEP ³BNL ⁴RIKEN BNL Research Center ⁵Yale University ⁶University of Wisconsin-Madison ⁷Stony Brook University ⁸RIKEN ⁹ANL ¹⁰Indiana University

The analyzing power A_N for pp elastic scattering is expected to reach a peak value of 0.045 in the Coulomb Nuclear Interference (CNI) region at a momentum transfer $-t$ of 0.003 (GeV/c)². During the 2004 RHIC Run, we completed a measurement of A_N in the CNI region by detecting the recoil protons from pp elastic scattering, using a polarized atomic hydrogen gas jet target and the 100 GeV RHIC proton beam. We report the first measurements of the A_N absolute value and shape in the $-t$ range from 0.0015 to 0.010 (GeV/c)² with a precision better than 0.005 for each A_N data point. The recoil protons were detected with two arrays of Si detectors. The absolute target polarization as monitored by a Breit-Rabi polarimeter was stable at 0.924 ± 0.018 . This result allows us to further investigate the spin dependence of elastic pp scattering in the very low $-t$ region.

The elastic scattering of nucleons has been studied for a long time as the most fundamental reaction from which to extract information on the elementary building blocks of matter, nucleons. Regarding the initial and final states in the elastic scattering of protons, there are three types of processes ; no spin reversal, single spin reversal and double spin reversal. These processes can be described by the use of five independent helicity amplitudes which have hadronic and electromagnetic parts. The electromagnetic part of the helicity amplitudes is well understood from QED. On the other hand, the hadronic part is being studied [1]. The analyzing power (A_N) depends mainly on the single spin reversal process. At very small momentum transfer $-t = 0.001$ to 0.02 (GeV/c)², two helicity amplitudes (hadronic and electro magnetic) become similar in size and interfere with each other. We call this phenomenon Coulomb Nuclear Interference (CNI). The values of A_N is expected to reach a peak of 0.045 at $-t \sim 0.003$ (GeV/c)². The shape of A_N is related to the hadronic amplitude of the single spin reversal process. Experimental knowledge is needed to constrain theory. The only A_N data available in the CNI region is from E704 at Fermilab [2] with limited accuracy. Last spring (the 2004 RHIC run), we carried out a measurement of A_N in the peak CNI region using a polarized atomic hydrogen gas jet target.

Since the CNI process is ideal for use as a polarimeter for a high energy proton beam [3] and for the determination of the RHIC beam polarization, we have installed the RHIC Absolute Polarimeter [4]. This polarimeter consists of the silicon spectrometer and the polarized atomic hydrogen-jet target, which includes a Breit-Rabi polarimeter to obtain the precise absolute target polarization [5]. By knowing the absolute polarization of the target (P_{target}), we measured the absolute A_N from the scattering asymmetry with respect to the target spin sign (ϵ_{target}), that is, $A_N = \epsilon_{target}/P_{target}$. Since we are using the elastic scattering process with proton beam and target, we also obtain the absolute beam polarization from the scattering asymmetry with respect to the beam and A_N . Figure 1 sketches the setup. We detect the recoil particles by using three left-right pairs of silicon strip detectors. The strips run vertically with respect to the beam direction. The read out pitch is about 4 mm, and each channel outputs energy (T_R) and time of flight (tof). The readout channel number gives us the angle (θ_R) information as shown in Fig. 2.

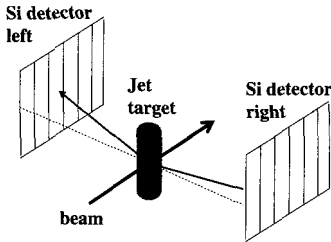


Fig. 1. Setup

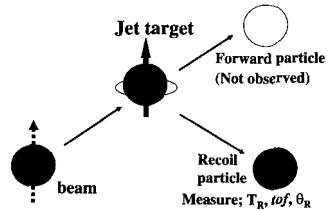


Fig. 2. Elastic scattering process

To get A_N , we measure the left-right asymmetry of the elastic event yield with respect to the target spin sign, then divide it by target polarization. The key points of this experiment are high target polarization and the ability to select the elastic events. The target polarization was quite high, accurate ($P_{target} = 0.924 \pm 0.018$) and stable [5]. We confirmed that both the recoil particle mass and the forward-scattered particle mass (missing mass) were consistent with that of the proton using the following two correlations. T_R and tof confirm the recoil particle is a proton (Fig. 3). T_R and channel number ($\propto \theta_R$) confirm the forward scattered particle is a proton (Fig. 4). We have focused on the smaller T_R region (< 5 MeV) which corresponds to $-t$ region of $0.0015 \sim 0.01 (\text{GeV}/c)^2$.

Figure 5 shows our result (closed circles) and E704 data (open circles). The errors are statistical only. We estimate the systematic error in A_N to be 0.0015, which is dominated by possible contributions of background (beam gas interaction etc.). The fraction of background is less than 5%.

We have measured A_N in the peak CNI region from 0.0015 to 0.010 $(\text{GeV}/c)^2$ in $-t$, and observed the peak shape of A_N for the first time.

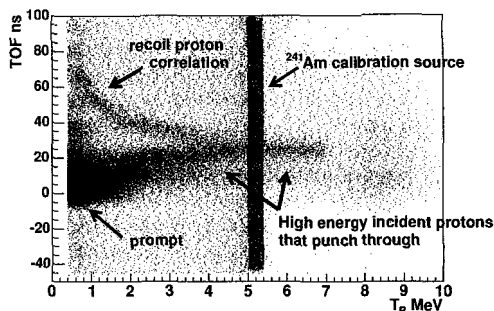


Fig. 3. The correlation of T_R and tof of one detector. This confirms the recoil particle is a proton.

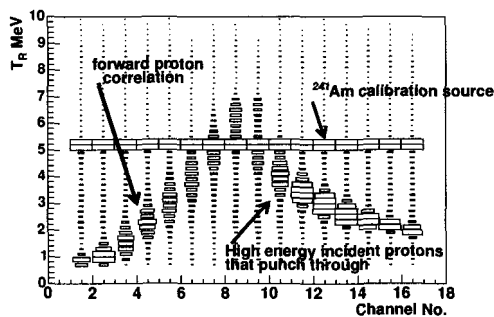


Fig. 4. The correlation of T_R and channel number ($\propto \theta_R$) of one detector. Each detector has 16 channels. This confirms the forward scattered particle is a proton (less than 5 MeV). Because the higher energy protons punched through the silicon detector, the measured T_R decreases beyond channel number 9.

The authors would like to thank the BNL Instrumental Division for their work on the silicon detectors and electronics. The work is performed under the auspices of U.S. DOE contract Nos. DE-AC02-98CH10886 and W-31-109-ENG-38, DOE grant No. DE-FG02-88ER40438, NSF grant PHY-0100348, and with support from RIKEN, Japan.

References

1. T.L. Trueman, these proceedings (2004).
2. N. Akchurin *et al.*, Phys. Rev. D **48**, 3026 (1993).
3. O. Jinnouchi *et al.*, these proceedings (2004) and AIP Conf. Proc. **675** (2003) 817.
4. A. Bravar *et al.*, these proceedings (2004) and AIP Conf. Proc. **675** (2003) 830.
5. A. Zelenski, T. Wise and A. Nass *et al.*, these proceedings (2004).

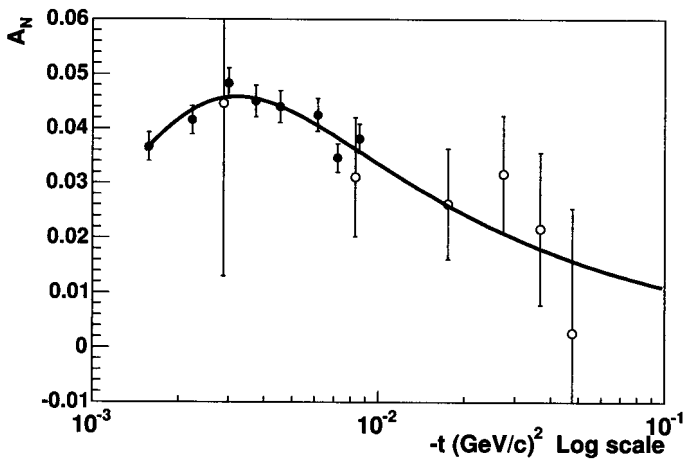


Fig. 5. A_N data for pp elastic scattering as a function of $-t$. The closed eight circles are the result; the open circles are from E704 [2]. The errors shown are statistical only. The solid line is a no hadronic spin flip calculation. $\chi^2/\text{d.o.f.} = 6/8$, which includes statistical and systematic errors.

MEASUREMENT OF A_N IN ELASTIC pp -SCATTERING WITH SMALL MOMENTUM TRANSFERS AT $\sqrt{s} = 200$ GeV AT RHIC

I. G. ALEKSEEV

Institute for Theoretical and Experimental Physics, Moscow, Russia

(for the pp2pp Collaboration)

The single spin analyzing power A_N has been measured at $\sqrt{s} = 100$ GeV using polarized protons at RHIC in the four momentum transfer range $-t = [0.01, 0.03]$ (GeV/c)². The scattered protons, having small scattering angles, travel inside the beam pipe following the accelerator lattice, and their trajectories are measured using silicon strip detectors placed in Roman Pots.

Although elastic scattering has been measured in $p\bar{p}$ collisions up to $\sqrt{s} = 1.8$ TeV, the highest energy pp data reach only 63 GeV. The pp2pp experiment [2] is designed to measure polarized pp elastic scattering at RHIC, which has been designed to provide proton beams with polarizations of 70% and luminosities up to 2×10^{32} cm⁻²sec⁻¹. The main goal of the experiment is to study the spin dependence of elastic scattering in the four-momentum transfer range $4 \times 10^{-4} \leq |t| \leq 1.3$ (GeV/c)² and $50 \leq \sqrt{s} \leq 500$ GeV. Our first results on the slope parameter measurement obtained in our first run can be found in Ref. [3].

By measuring the elastic scattering of polarized protons in the nonperturbative regime of QCD at RHIC, one has a unique opportunity to probe the spin structure of the nucleon interaction and of the exchanged mediators of the force, the Pomeron and its odd C-parity partner, the Odderon. The pp2pp experiment, part of the RHIC spin program, studies the physics of elastic scattering. It addresses the main unsolved problems in particle physics: long range QCD and confinement.

In RHIC the two protons collide at the interaction point (IP), and since the scattering angles are small, scattered protons stay within the beam pipe of the accelerator. They follow trajectories determined by the accelerator magnets until they reach the detectors, which measure the coordinates in the plane perpendicular to the beam axis. The coordinates are related by the beam transport equations to the coordinates and corresponding angles at the IP.

The layout of the experiment is shown in Fig. 1. The identification of elastic events

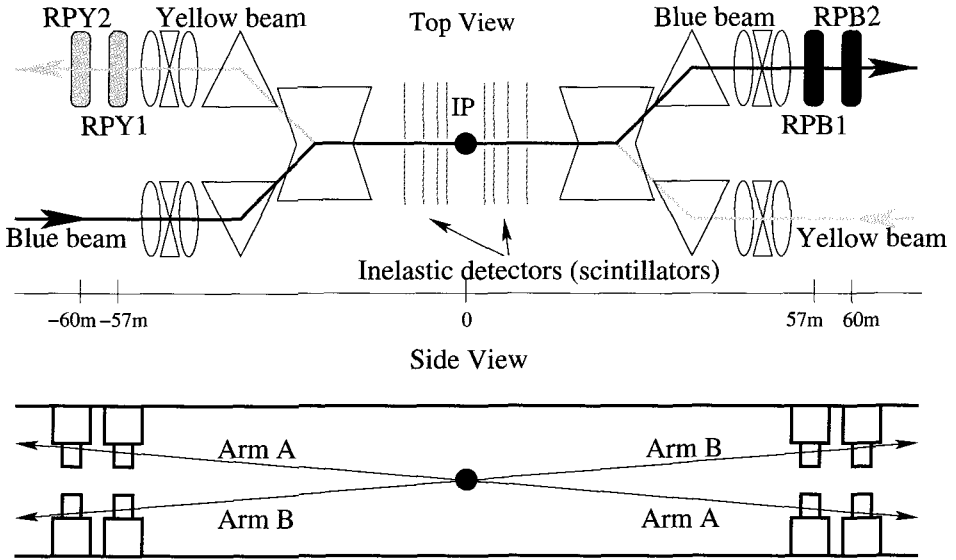


Fig. 1. Layout of the pp2pp experiment. Scattering is detected in either one of two arms: Arm A is formed from the upper half of RPY(1,2) and the lower half of RPB(1,2). Conversely, Arm B is formed from the lower half of RPY(1,2) and the upper half of RPB(1,2).

is based on the collinearity criterion; hence it requires the simultaneous detection of the scattered protons in the pair of Roman Pot (RP) detectors [4], RPY(1,2) and RPB(1,2), on either side of the IP. The RP's are insertion devices allowing four silicon strip detectors (SSD) to be positioned just above and below the beam orbits. Excellent performance of SSD was observed — we had only six dead strips among 14112 in the active area of the detectors [5, 6].

In this article we would like to present results of a 12 hour run in May 2003. The RHIC orbit betatron function at our IP was $\beta^* = 10$ m. A total number of $6.7 \cdot 10^6$ triggers were collected.

Only inner Roman Pots were used for elastic event reconstruction. Outer pots were used to get better knowledge of transport matrix parameters. Identification of elastic events is based on collinearity, which implies that the two coordinates obtained from the silicon detectors on either side of IP are correlated, i.e. the sum of coordinates measured by detectors on both sides is constant. An example of this correlation for the x plane is shown in Fig. 2-left. The widths of the distributions are determined by the beam emittance of about 15 mm-mrad and by an uncertainty of about 60 cm in the vertex position along the beam axis. $2.3 \cdot 10^6$ elastic events were selected for further processing.

The azimuthal angle dependence of the cross-section for elastic collisions of the vertically polarized protons is given by the equation:

$$2\pi \frac{d^2\sigma}{dt d\phi} = \frac{d\sigma}{dt} \cdot (1 + (P_B + P_Y)A_N \cos \phi + P_B P_Y (A_{NN} \cos^2 \phi + A_{SS} \sin^2 \phi)), \quad (1)$$

where P_B and P_Y are beam polarizations and ϕ is the azimuthal angle. Then square root

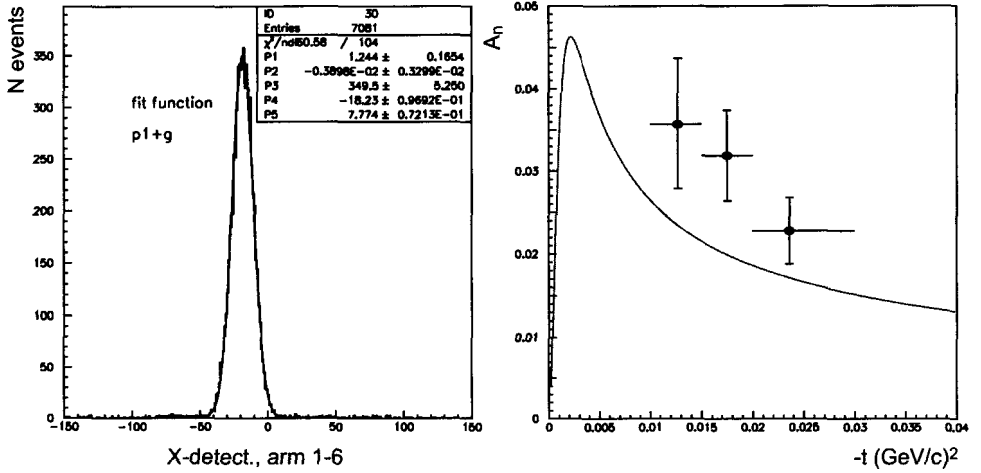


Fig. 2. (left) Elastic correlation in x -plane. (right) Single spin analyzing power in the elastic proton-proton scattering at $\sqrt{s} = 200$ GeV. Only statistical errors are shown (vertical). Horizontal error bars show the $-t$ -range. Solid curve corresponds to theoretical calculations without hadronic spin flip⁷.

formula for the single spin raw asymmetry can be written as:

$$\begin{aligned} \varepsilon(\phi) &= \frac{(P_B + P_Y) \cos \phi A_N}{1 + P_B P_Y (A_{NN} \cos^2 \phi + A_{SS} \sin^2 \phi)} \\ &= \frac{\sqrt{N^{++}(\phi) N^{--}(\pi - \phi)} - \sqrt{N^{--}(\phi) N^{++}(\pi - \phi)}}{\sqrt{N^{++}(\phi) N^{--}(\pi - \phi)} + \sqrt{N^{--}(\phi) N^{++}(\pi - \phi)}}, \end{aligned} \quad (2)$$

where $N^{ij}(\phi)$ are the numbers of elastic events for the corresponding beam bunch polarization pattern. As the term $P_B P_Y (A_{NN} \cos^2 \phi + A_{SS} \sin^2 \phi)$ is small compared with one, it can be neglected. A cosine fit to the raw asymmetry $\varepsilon(\phi)$ was used to calculate values of A_N . The results are presented in Fig. 2-right. A careful evaluation of possible sources of systematic errors was done. We found that the result on A_N depends only weakly on the variation of elastic events selection criteria and on the uncertainties in the transport matrix. The main contribution to the systematic error comes from statistical and systematic errors in the beam polarization which, given preliminary results from absolute beam polarization measurement with a polarized hydrogen gas jet [8–10], we estimate to be about 15% (relative).

Unlike proton-proton scattering at $\sqrt{s} = 14$ GeV, where experimental data [8, 10] are consistent with theoretical calculations without hadronic spin flip, and proton-carbon scattering at $P_{beam} = 22$ GeV/c, where experimental data [11] are below theoretical calculations without hadronic spin flip, the single spin analyzing power found in this experiment is larger than theoretical calculations without hadronic spin flip. This interesting situation requires theoretical understanding and inspires us to continue the measurements.

The research reported here has been performed in part under the US DOE contract DE-AC02-98CH10886, and was supported by the US National Science Foundation and the Polish Academy of Sciences. The authors are grateful for the help of N. Akchurin, D. Al-

burger, P. Draper, Y. Onel, A. Penzo, and P. Schiavon at an early stage of the experimental design and the support of the BNL Physics Department, Instrumentation Division, and C-A Department at the RHIC-AGS facility.

References

1. S. Bültmann, I. H. Chiang, R. E. Chrien, A. Drees, R. L. Gill, W. Guryan, J. Landgraf, T.A. Ljubičić, D. Lynn, C. Pearson, P. Pile, A. Rusek, M. Sakitt, S. Tepikian, K. Yip (*BNL, Upton, NY, USA*); J. Chwastowski, B. Pawlik (*INP, Cracow, Poland*); M. Haguenaer (*Ecole Polytechnique, Palaiseau, France*); A. A. Bogdanov, S. B. Nurushev, M. F. Runzo, M. N. Strikhanov (*MEPhi, Moscow, Russia*); I. G. Alekseev, V. P. Kanavets, L. I. Koroleva, B. V. Morozov, D. N. Svirida (*ITEP, Moscow, Russia*); A. Khodinov, M. Rijssenbeek, L. Whitehead (*Stony Brook University, NY, USA*); K. De, J. Li, N. Öztürk (*University of Texas at Arlington, TX, USA*); A. Sandacz (*INS, Warsaw, Poland*).
2. V. Kanavets, *Czech. J. Phys. Suppl. B*, **53**, B123 (2003)
3. S.L. Bültmann *et al.*, *Phys. Lett.* **B579**, 245 (2003); arXiv:nucl-ex/0305012
4. R. Battiston *et al.*, *Nucl. Instr. Meth.* **A238**, 35 (1985)
5. S.L. Bültmann *et al.*, Experiment pp2pp at RHIC, Proceedings of X Workshop on High Energy Spin Physics, p. 227, Dubna 2004.
6. S.L. Bültmann *et al.*, *Nucl. Instr. Meth.* **A535**, 415 (2004)
7. N.H. Buttimore *et al.*, *Phys. Rev.* **D59**, 114010 (1999)
8. A. Bravar *et al.*, Spin Dependence in the Elastic Scattering in the CNI Region, these proceedings.
9. O. Jinnouchi *et al.*, Measurement of the analyzing power of proton-carbon elastic scattering in the CNI region at RHIC, these proceedings.
10. H. Okada *et al.*, Measurement of the analyzing power in pp elastic scattering in the peak CNI region at RHIC, these proceedings.
11. J. Tojo *et al.*, *Phys. Rev. Lett.* **89**, 052302 (2002)

MEASUREMENT OF THE ANALYZING POWER OF PROTON-CARBON ELASTIC SCATTERING IN THE CNI REGION AT RHIC

O. JINNOUCHI¹, I. G. ALEKSEEV², A. BRAVAR³, G. BUNCE^{3,1}, S. DHAWAN⁴, H. HUANG³, G. IGO⁵, V. P. KANAVETS², K. KURITA^{6,1}, H. OKADA⁷, N. SAITO^{7,8,1}, H. SPINKA⁹, D. N. SVIRIDA², J. WOOD⁵

(1) RIKEN BNL Research Center, Upton, USA

(2) ITEP, Moscow, Russia

(3) Brookhaven National Laboratory, Upton, USA

(4) Yale University, New Haven, USA

(5) UCLA, Los Angeles, USA

(6) Rikkyo University, Tokyo, Japan

(7) Kyoto University, Kyoto, Japan

(8) RIKEN, Wako, Japan

(9) Argonne National Laboratory, Argonne, USA

The single transverse spin asymmetry, A_N , of the p-carbon elastic scattering process in the Coulomb Nuclear Interference (CNI) region was measured using an ultra thin carbon target and polarized proton beam in the Relativistic Heavy Ion Collider (RHIC) at Brookhaven National Laboratory (BNL). In 2004, data were collected to calibrate the p-carbon process at two RHIC energies (24 GeV, 100 GeV). A_N was obtained as a function of momentum transfer $-t$. The results were fitted with theoretical models which allow us to assess the contribution from a hadronic spin flip amplitude.

The elastic scattering of polarized protons off nuclei at RHIC energies (24 – 250 GeV) provides information on a spin dependent hadronic spin-flip amplitude. In the Coulomb-Nuclear Interference (CNI) region, i.e. $0.005 < -t < 0.05$ (GeV/c)² where $t = (p_{out} - p_{in})^2 \approx -2M_C T_{kin} < 0$, the single transverse spin asymmetry, A_N , of p-carbon elastic scattering is used to measure the beam polarization in RHIC. The data also provide physics information on the spin dependent hadronic contribution to the transverse asymmetry. For very small angle scattering, the elastic process dominates, and experimentally the elastic events are cleanly identified by measuring the recoil carbons for polar angles near 90° in the laboratory frame. In the CNI region, the electromagnetic and hadronic helicity amplitudes are comparable in size. A non-zero A_N arises mainly from the interference between the coulomb spin-flip amplitude (which generates the anomalous magnetic moment of the proton) and the hadronic non spin-flip amplitude. This interference term, called 'pure CNI' is precisely determined from QED calculations. However, a contribution to A_N can also come from the other interference term from the hadronic spin flip amplitude (coupling with

the coulomb non spin-flip amplitude), which can be described by Regge pole exchange phenomenology [1]. Since this hadronic term is in the non-perturbative QCD region, experimental data is indispensable.

Following the analogy to the helicity amplitude formalism of proton-proton elastic scattering, the pC process can be described by two amplitudes, spin non-flip $F_{+0}(s,t)$, and spin flip $F_{-0}(s,t)$. The spin flip amplitude parameter $r_5^{pC}(t)$ is defined as $r_5^{pC}(t) = mF_{-0}^h/(\sqrt{-t} \text{Im}F_{+0}^h)$, where m is the proton mass, and $F_{\pm 0}^h$ is the hadronic element of the helicity amplitudes. This may be connected to a t independent parameter r_5 for pp [7]. The AGS experiment E950 [2] has provided the only measurement of $A_N^{pC}(t)$, at 21.7 GeV/c. The r_5 result from E950 was $\text{Re } r_5 = 0.088 \pm 0.058 / \text{Im } r_5 = -0.161 \pm 0.226$ with a strong anti-correlation between real and imaginary parts.

For the current experiment, the polarized proton beam passes through an ultra-thin carbon ribbon target ($3.5\text{-}\mu\text{g}/\text{cm}^2$ thick [3]), and carbon recoils from CNI scattering are observed in six silicon strip detectors placed at 90° to the beam direction, 15 cm away from the target. Each detector has $10 \times 24\text{mm}^2$ active area divided into 12 strips, each directed parallel to the beam line. The six detectors are mounted inside the vacuum chamber with readout preamplifier boards directly attached to feed-through connectors on the detector ports. Data acquisition is based on waveform digitizer modules (WFD) [6]. The system reads out the data without deadtime to accommodate very high event rates. The waveforms from the strips are digitized, and energy (E) and time of flight (TOF) w.r.t. the RHIC RF clock are determined by on-board FPGA. Typically 2×10^7 samples of carbon events are stored in memory on board and are read out after the measurement.

Slow particles inside our kinematical acceptance follow the non-relativistic kinematics, i.e. $TOF = \sqrt{\frac{M_C L^2}{2}} \frac{1}{\sqrt{E}}$, which is slightly deformed by an energy loss correction in the inactive silicon surface. The size of the deformation is used to estimate the thickness of the inactive layer [4]. It is estimated to be $57 \pm 12 \mu\text{g}/\text{cm}^2$. The invariant mass of the recoil particle is reconstructed with the time and energy information. A three standard deviation cut around the carbon peak is applied for the carbon identification. The cut clearly separates the carbon events ($11.17 \text{ GeV}/c^2$) from α background ($3.7 \text{ GeV}/c^2$).

A raw asymmetry is calculated for carbon counts in left and right detectors using a geometric mean method, which takes advantage of the alternating spin patterns in RHIC [8]. Since each silicon strip can serve as an individual device measuring the asymmetry, the systematic uncertainty of the measurements is estimated from the size of fluctuation among the strips. Figure 1 shows the up-down asymmetry for the i -th ($i = 1 \cdots 72$) strip ($\equiv (N_i^u - R \cdot N_i^d)/(N_i^d + R \cdot N_i^u)$ where R is the luminosity ratio of up/down spin bunches). By allowing a phase shift to the $\sin \phi$ fit (two parameters: amplitude, phase), the χ^2/ndf is reduced to 70/68, whereas it is 104/69 for the one parameter fit. This χ^2/ndf value indicates there is a negligible systematic error in the measurement, and a spin tilt ($4 \sim 5$ degrees) from vertical.

A_N^{pC} is obtained by dividing the raw asymmetry of pC events by the beam polarization measured by the polarized hydrogen gas jet target [5]. Figure 2 shows $A_N^{pC}(t)$ at 100 GeV, where $P_{beam} = 0.386 \pm 0.033$ [5]. The thin line through the data points is from a fit allow-

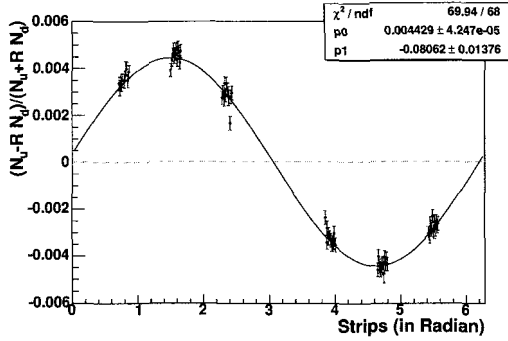


Fig. 1. Strip by strip asymmetry measurements. The raw up-down asymmetries are plotted as a function of strip location in radians. The curve is the best fit to the sine function allowing phase shift, i.e. $f(\phi) = P_0 \sin(\phi + P_1)$

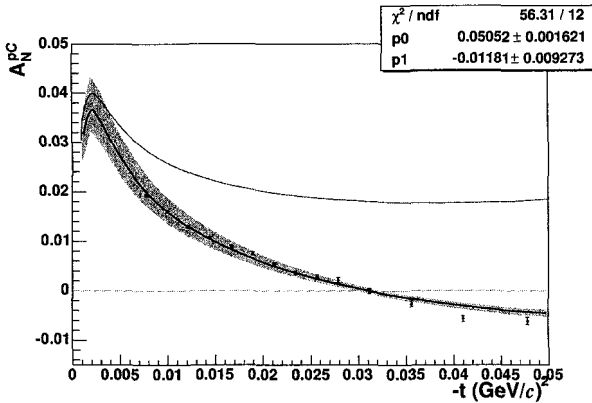


Fig. 2. Measured $A_N(t)$ at 100 GeV. The calibration is carried out with the polarization measured by the jet. The result is significantly different from the no-hadronic spin flip calculation (top curve). The shaded band represents the systematic uncertainty of the measurement

ing hadronic spin flip [1]. The error bars on the data points are statistical only. The size of systematic errors is shown by the shaded band. They are due to (i) the $-t$ ambiguity from the uncertainty in the inactive surface layer of the silicon, (ii) the error of the beam polarization measured with the jet. The r_5 value from the best fit results is $\text{Re } r_5 = 0.051 \pm 0.002$ and $\text{Im } r_5 = -0.012 \pm 0.009$. The uncertainty is mainly due to the two systematic error sources described above. The $1-\sigma$ error contour has a very strong anti-correlation between the real and imaginary part of r_5 , from $(\text{Re } r_5, \text{Im } r_5) = (0.070, -0.16)$ to $(0.035, 0.110)$. For 24 GeV, even though the absolute scale of $A_N(t)$ is not available yet from the hydrogen jet measurement, the shape is obtained and compared with 100 GeV for the range $0.008 < -t < 0.028$ $(\text{GeV}/c)^2$. The slope of $A_N^{PC}(t)$ at 100 GeV is significantly steeper than at 24 GeV.

Acknowledgments

We are grateful to W. Lozowski in Indiana University, Z. Li and S. Rescia in BNL for their hardware supports to this experiment. The authors thank the jet target collaboration for providing the absolute beam polarization value. This work is supported by the U.S. Department of Energy and by RIKEN Laboratory, Japan.

References

1. T.L. Trueman, *hep-ph/0305085* (2003).
2. J. Tojo et al. *Phys. Rev. Lett.* **89**, 052302 (2002).
3. W.R. Lozowski and J.D. Hudson, *NIM in Physics Research* **A334**, 173 (1993).
4. O. Jinnouchi et al. *RHIC/CAD Accelerator Physics Note 171* (2004).
5. A. Bravar et al. these proceedings (2004).; The talks on the jet, T. Wise et al., A. Nass et al., A. Zelenski et al., these proceedings (2004).
6. D.N. Svirida et al. detail description is found in these proceedings (2004).
7. B.Z. Kopeliovich and T.L. Trueman, *Phys. Rev.* **D64**, 034004 (2001).
8. G.G. Ohlsen and P.W. Keaton, *NIM in Physics Research* **109**, 41 (1973).

ENERGY DEPENDENCE OF pp AND p -CARBON CNI ANALYZING POWER*

T. L. TRUEMAN

Physics Department, Brookhaven National Laboratory, Upton, USA

The method described in my RHIC Spin Note (hep-ph/305085) is applied to recently reported data from RHIC experiments in order to obtain values for the spin-flip Regge couplings. The data comes from 100 GeV/c proton elastic scattering on both a carbon target and on the recently commissioned polarized hydrogen gas jet target. These couplings are used to predict the analyzing power for proton-carbon scattering at the top RHIC fixed target energy of 250 GeV/c and for pp scattering at RHIC collider energy.

1. Background

The Coulomb-nuclear interference induced asymmetry in proton elastic scattering has been seen to be a very sensitive and practical polarimeter for high energy proton beams [1, 2]. The main uncertainty in calculating this analyzing power is the unknown hadronic-spin flip amplitude, which we characterize by the quantity τ , the ratio of the single-flip to the non-flip proton scattering amplitude. τ cannot be calculated with the requisite precision and so it is necessary to calibrate the polarimeter. For a carbon target this is possible at AGS energy, about 24 GeV/c, where other means of determining the beam polarization are available, but it is not possible at higher energy. The goal of my RHIC Note [3] is to calculate the analyzing power at higher RHIC energy when the polarization is known at only the injection energy. This work relies heavily on earlier work [4] which shows, among other things, that it is quite reasonable to assume that τ for pC is equal to the $I = 0$ part of τ for pp , and that its variation with t over the CNI region can be neglected.

Its variation with s needs to be determined. (We will often use the beam momentum p and the proton-proton c.m. energy squared $s = 2m^2 + 2m\sqrt{p^2 + m^2}$ interchangeably.) To address this, I have taken a simple model that has been successfully used for unpolarized scattering over a wide energy range, namely the Regge pole model. For this work we chose the simple Regge pole model whose parameters are determined by [5]: three poles are found to contribute significantly: the pomeron; a $C = -1$ Regge pole, mainly the ω ; and a $C = +1$ Regge pole, mainly the f . We extend the model to polarized pC scattering by

*This work is authored under contract number DE-AC02-98CH10886 with the U.S. Department of Energy.

neglecting the small $I = 1$ contributions to the pp unpolarized scattering data used in the fit, and we introduce the spin-dependence through three real parameters τ_p, τ_f and τ_ω , that give the ratio of the spin-flip to non-flip Regge couplings for the pomeron, the f and the ω . They do not depend on the momentum of the beam. Until recently the only determination of the pC analyzing power at high energy with a beam of known polarization was E950 at the AGS with beam momentum of 21.7 GeV/c. $\tau(21.7)$ determined by this experiment is found to be non-zero and to have a significant imaginary part. The real and imaginary parts of $\tau(21.7)$ can be used with our model to determine two relations between the three real Regge spin-flip couplings in our model. With one more relation, the model would be completely determined.

A good measurement of the shape of the curve at a different energy with a polarized beam of unknown polarization can provide such a measurement because the shape of A_N , defined by,

$$S(s) = \frac{Im(\tau(s))}{\kappa/2 - Re(\tau(s))} \quad (1)$$

can be determined independently of P . We fit

$$\frac{A_N(s,t,\tau(s))}{A_N(s,t,0)} = \frac{2}{\kappa} \{ \kappa/2 - Re(\tau(s)) + f(s,t)Im(\tau(s)) \} \quad (2)$$

where $A_N(s,t,0)$ is the "pure" CNI" analyzing power in the absence of any hadronic spin flip, $\kappa = 1.79$, and $f(s,t)$ is a function that can be calculated using Glauber techniques without any spin-dependent information [4]. This is all valid for terms linear in $\tau(p)$. At the Spin2002, preliminary values for A_N at 100 GeV/c were reported [6], and in [3] we used them to determine $S(100 \text{ GeV/c})$. This gives us a third relation among the Regge couplings, and so we can calculate the analyzing power at 100 GeV/c without measuring the polarization at that energy. The prediction is $\tau(100) = -0.130 - 0.053i$ with an error of about ± 0.22 on the real part but only ± 0.012 on the imaginary part.

2. New pC results

At this meeting new results with much smaller errors and known beam polarization (as measured by the gas jet) at 100 GeV were reported [1]. By fitting this data one finds $\tau(100) = -0.017 - 0.049i$, within errors of the above prediction. The analyzing power is predicted by this model to be uniformly about 10% above the data (Note that for the data used, only statistical errors are now available. Systematic errors will be available soon.)

Since the errors on the new data are much smaller, let us turn the process around, and use the τ -value determined by the new 100 GeV/c data and just the shape from E950. This leads to a determination of the Regge couplings with much smaller errors than before [3]. See Fig. 1.

These can be used to predict the pC analyzing power at 250 GeV/c shown in Fig. 2. The thickness of the curve represents the statistical errors of this determination.

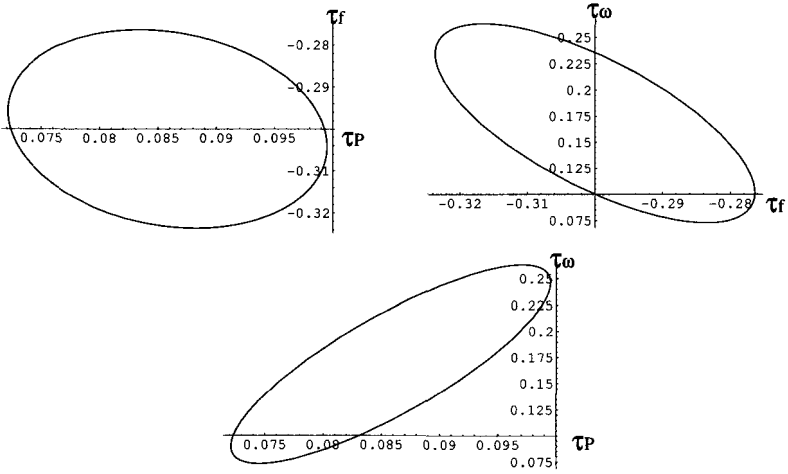


Fig. 1. 1-sigma error ellipses for the three Regge spin-flip couplings

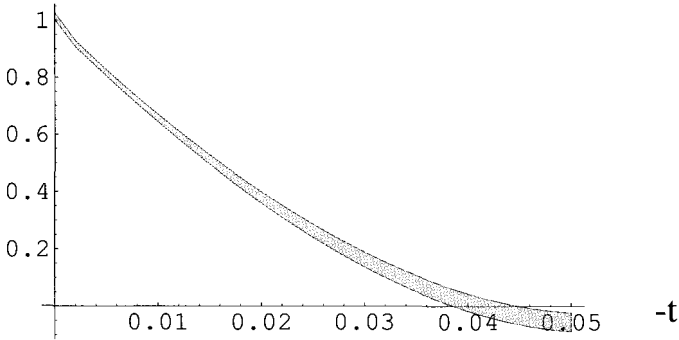


Fig. 2. Predicted $A_N(s, t, \tau(s))/A_N(s, t, 0)$ at 250 GeV/c

3. pp CNI

In order to extend the model and make predictions for high energy pp scattering asymmetries, we need information about the $l = 1$ Regge poles. The pomeron coupling is the same as already determined. We need in addition the ρ and the a_2 . If we assume that they are, respectively, degenerate with the ω and f , the pairs will enter the fit as only two Regge poles, one with $C = -1$ and one with $C = +1$. We are now blessed with the p -jet data at 100 GeV/c, and so have $A_N(100)$ [2]. So the real and imaginary parts of the corresponding spin-flip factor can be used to determine the two new constants, τ_- and τ_+ , and the model is completely determined. The values for the coupling are

$$\tau_p = 0.09 \qquad \tau_+ = -0.32 \qquad \tau_- = 1.06$$

We see from this that the a_2 coupling is rather small but the ρ coupling is enormous. This was to be expected [7].

These couplings can be used to predict the analyzing power in colliding beams of protons at high energy, such as in the recent $pp2pp$ experiment at RHIC. The prediction is $\tau(s = 200^2) = 0.08 - 0.007i$; the significant non-zero part has an error of about 2% due to the error in the pomeron coupling. The preliminary data reported to this conference [8] lies significantly above this prediction; this discrepancy will have to be addressed.

References

1. O. Jinnouchi, these proceedings.
2. H. Okada, these proceedings.
3. T. L. Trueman, hep-ph/305085.
4. B. Z. Kopeliovich and T. L. Trueman, Phys. Rev. **D64**:034004 (2001)
5. J. R. Cudell et al, Phys. Rev. **D61**:034019 (2000)
6. K. Kurita, for RHIC Spin Collaboration, Spin2002, Upton, NY, p.812.
7. E. L. Berger et al, Phys. Rev. **D17**, 2971 (1977)
8. I. Alexeev, these proceedings.

ENERGY DEPENDENCE OF HELICITY-FLIP AMPLITUDES IN THE SMALL-ANGLE ELASTIC pp -SCATTERING

S. M. TROSHIN, N. E. TYURIN

Institute for High Energy Physics, Protvino, Russia

We discuss the role of the double helicity-flip amplitudes and derive new unitary bounds for these amplitudes in elastic pp -scattering at small values of t . We show that the usual assumption on the smallness of such amplitudes can be justified only in the region of small t values which is shrinking with energy.

Discussion of the role and magnitude of helicity-flip amplitudes in small-angle elastic scattering has a long history and is an important issue in the studies of the spin properties of diffraction. Recently an interest in accounting for the contributions of helicity-flip amplitudes has become associated with CNI polarimetry related problems [1] as well. Not only non-flip and single helicity-flip amplitudes can give contributions and affect the estimates and bounds of the analyzing power A_N . Double helicity-flip amplitudes can also contribute to A_N , and their behaviour at high energies is also important for the spin correlation parameters and total cross-section differences in experiments with two polarized beams available at RHIC nowadays.

The double helicity-flip amplitudes are usually neglected since they are supposed to be small over the whole region of momentum transfer. But this assumption is based merely on the technical simplification of the problem, and is not valid at large momentum transfers in elastic pp -scattering, where double-flip amplitudes can play an important role and fill up multiple-dip structure in differential cross-section providing, correct description of the experimental data [2]. It is natural then to assess the role of double helicity-flip amplitudes at small and moderate values of t also.

The method we use is based on the unitarity equation for helicity amplitudes of elastic pp -scattering, i.e. we adhere to a rational form of unitarization which corresponds to an approximate wave function which changes both the phase and amplitude of the wave in potential scattering. For the helicity amplitudes of pp -scattering (i.e. for two-fermion

scattering), the corresponding solution of the unitarity equations

$$F_{\lambda_3, \lambda_4, \lambda_1, \lambda_2}(\mathbf{p}, \mathbf{q}) = U_{\lambda_3, \lambda_4, \lambda_1, \lambda_2}(\mathbf{p}, \mathbf{q}) + i \frac{\pi}{8} \sum_{\lambda', \lambda''} \int d\Omega_{\mathbf{k}} U_{\lambda_3, \lambda_4, \lambda', \lambda''}(\mathbf{p}, \mathbf{k}) F_{\lambda', \lambda'', \lambda_1, \lambda_2}(\mathbf{k}, \mathbf{q}), \tag{1}$$

in the impact parameter representation can be found explicitly in the following form:

$$\begin{aligned} f_1 &= \frac{(u_1 + u_1^2 - u_2^2)(1 + u_3 + u_4) - 2(1 + 2u_1 - 2u_2)u_5^2}{(1 + u_1 - u_2)[(1 + u_1 + u_2)(1 + u_3 + u_4) - 4u_5^2]}, \\ f_2 &= \frac{u_2(1 + u_3 + u_4) - 2u_5^2}{(1 + u_1 - u_2)[(1 + u_1 + u_2)(1 + u_3 + u_4) - 4u_5^2]}, \\ f_3 &= \frac{(u_3 + u_3^2 - u_4^2)(1 + u_1 + u_2) - 2(1 + 2u_3 - 2u_4)u_5^2}{(1 + u_3 - u_4)[(1 + u_1 + u_2)(1 + u_3 + u_4) - 4u_5^2]}, \\ f_4 &= \frac{u_4(1 + u_1 + u_2) - 2u_5^2}{(1 + u_3 - u_4)[(1 + u_1 + u_2)(1 + u_3 + u_4) - 4u_5^2]}, \\ f_5 &= \frac{u_5}{(1 + u_1 + u_2)(1 + u_3 + u_4) - 4u_5^2}, \end{aligned} \tag{2}$$

where for simplicity we have omitted the arguments of the functions $f_i(s, b)$ and $u_i(s, b)$. Unitarity requires that $\text{Re}u_{1,3}(s, b) \geq 0$, but the absolute values of the functions $u_i(s, b)$ should not be limited by unity. For the functions $u_{2,4}(s, b)$ we adhere to a simple general form (using arguments based on the analytical properties in the complex t -plane [4]):

$$u_2 \sim u_4 \sim s^\Delta e^{-\mu b}. \tag{3}$$

To get an upper bound for the amplitudes $F_{2,4}(s, t)$ we consider the case where $u_{2,4}(s, b)$ dominate. Then we have for the amplitudes $F_{2,4}(s, t)$ the following representations

$$F_2(s, t) = \frac{is}{\pi^2} \int_0^\infty b db \frac{u_2(s, b)}{1 - u_2^2(s, b)} J_0(b\sqrt{-t}) \tag{4}$$

and

$$F_4(s, t) = \frac{is}{\pi^2} \int_0^\infty b db \frac{u_4(s, b)}{1 - u_4^2(s, b)} J_2(b\sqrt{-t}) \tag{5}$$

Using for $u_{2,4}(s, b)$ the functional dependence in the form of Eq. (3), it can be shown that the amplitude $F_2(s, t = 0)$ cannot rise faster than $s \ln s$ at $s \rightarrow \infty$, and the function

$$\hat{F}_4(s, t = 0) \equiv \left[\frac{m^2}{-t} F_4(s, t) \right]_{t=0}$$

cannot rise faster than $s \ln^3 s$ at $s \rightarrow \infty$.

Thus, we can state that the explicit account of unitarity in the form of U - matrix approach leads to the following upper bound for the cross-section difference:

$$\Delta\sigma_T \leq c \ln s,$$

where

$$\Delta\sigma_T \equiv \sigma_{tot}(\uparrow\downarrow) - \sigma_{tot}(\uparrow\uparrow) \sim -\frac{1}{s}\text{Im}F_2(s, t=0).$$

It should be noted that the asymptotic behaviour of the amplitudes F_1 and F_3 are determined by the functions u_2 and u_4 , respectively, in the situation when these functions dominate; the Froissart–Martin asymptotical bound for these amplitudes remains under these circumstances, i.e. they are limited by $cs\ln^2 s$ at $t=0$.

Another related important consequence is the conclusion that one can neglect helicity-flip amplitudes F_2 , F_4 and F_5 in calculations of differential cross-section

$$\frac{d\sigma}{dt} = \frac{2\pi^5}{s^2} (|F_1(s, t)|^2 + |F_2(s, t)|^2 + |F_3(s, t)|^2 + |F_4(s, t)|^2 + 4|F_5(s, t)|^2)$$

and double helicity-flip amplitudes F_2 and F_4 in the calculation of analyzing power A_N

$$A_N(s, t) \frac{d\sigma}{dt} = \frac{2\pi^5}{s^2} \text{Im}[(F_1(s, t) + F_2(s, t) + F_3(s, t) - F_4(s, t))^* F_5(s, t)]$$

in the region of small values of t in the high energy limit. This conclusion is based on the above bounds for the helicity amplitudes and their small t dependence due to angular momentum conservation, i.e. at $-t \rightarrow 0$: $F_i \sim \text{const}$, ($i = 1, 2, 3$), $F_5 \sim \sqrt{-t}$ and $F_4 \sim -t$. However, the helicity-non-flip amplitudes ceases to dominate at fixed values of momentum transfers, where e.g. the amplitude F_4 can become a dominant one, since its growth with energy is limited by the function $s\ln^3 s$, while other helicity amplitudes cannot increase faster than $s\ln^2 s$.

One should recall that unitarity for the helicity amplitudes leads to a peripheral dependence of the amplitudes $f_i(s, b)$ ($i = 2, 4, 5$) on the impact parameter b at high energy, i.e.

$$|f_i(s, b=0)| \rightarrow 0$$

at $s \rightarrow \infty$. This is a consequence of the explicit unitarity representation for the helicity amplitudes through the U -matrix, and it is this which allows one to get better bounds for the helicity-flip amplitudes.

Thus, we have shown here and in [3], that the following asymptotic results should be valid:

- the ratio $r_5(s, 0) \equiv 2\hat{F}_5(s, 0)/[F_1(s, 0) + F_3(s, 0)]$ cannot increase with energy,
- the amplitude $F_2(s, t=0)$ cannot increase faster than $s\ln s$,
- the function $\hat{F}_4(s, t=0)$ should not rise faster than $s\ln^3 s$ at high energies.

Nowadays the RHIC spin program includes experiments with two polarized proton beams at the highest available energies, and the above bounds could be useful and provide grounds for the estimations of the spin observables in the forward region in these experiments. The above bounds provide a justification of the smallness of the double helicity-flip amplitudes in the low- t region, but at the same time they imply the importance of the double helicity-flip amplitudes at moderate values of momentum transfer. This result is in accordance with

an early analysis of experimental data performed in [2]. It is also evident that the momentum transfer region where helicity–flip amplitudes can be neglected is shrinking with energy, e.g. for the amplitude F_4 this shrinkage is proportional to $1/\ln s$. The magnitude of the helicity amplitude F_2 at $t = 0$ can be measured directly at RHIC through measurements of $\Delta\sigma_T$ [1], and it is definitely relevant to the study of the spin properties of diffraction. The experimental data for $\Delta\sigma_T(s)$ could also be a useful source of information on the low- x behaviour of the spin structure function $h_1(x)$.

Acknowledgments

We are grateful to the Local Organizing Committee of SPIN2004 for the warm hospitality in Trieste during the Symposium and one of us (S.T.) would also like to express his gratitude to the Local Organizing Committee for the financial support.

References

1. A. Bravar, invited talk at SPIN2004; these Proceedings.
2. V. F. Edneral, S. M. Troshin and N. E. Tyurin, *JETP Lett.* **30**, 330 (1979).
3. S. M. Troshin and N.E. Tyurin, *Phys. Lett.* **B459**, 641 (1999).
4. S. M. Troshin and N.E. Tyurin, *Phys. Lett.* **B580**, 54 (2004).

LARGE-DISTANCE EFFECTS ON SPIN OBSERVABLES AT RHIC

O. V. SELYUGIN^{1,2}, J. CUDELL¹, E. PREDAZZI³

¹Inst. de Physique, Univ. de Liège, Liège, Belgium

²BLTPb, JINR, Dubna, Russia.

³Dip. di Fisica Teorica - Univ. di Torino and Sezione INFN di Torino, Italy.

The impact of large-distance contributions on the behaviour of the slopes of the spin-non-flip and of the spin-flip amplitudes is analysed. It is shown that the long tail of the hadron potential in impact parameter space leads to a larger value of the slope for the spin-flip amplitude (without the kinematic factor $\sqrt{|t|}$) than for the spin-non-flip amplitude. This effect is taken into account in the calculation of the analysing power in proton-nucleus reactions at high energies.

The recent data from RHIC and HERA indicate that, even at high energy, the hadronic amplitude has a significant spin-flip contribution, \mathcal{A}_{sf}^h , which remains proportional to the spin-non-flip part, \mathcal{A}_{nf}^h , as energy is increased. Theoretically, when large-distance contributions are considered, one can obtain a more complicated spin structure for the pomeron coupling. The dependence of the hadron spin-flip amplitude on the momentum transfer at small angles is tightly connected with the basic structure of hadrons at large distances. We show that the slope of the “reduced” hadron spin-flip amplitude, (*i.e.* the hadron spin-flip amplitude without the kinematic factor $\sqrt{|t|}$), can be larger than the slope of the hadron spin-non-flip amplitude, as was observed long ago [1, 2]. This large slope has a small effect on the differential hadron cross section and on the real part of hadron non-flip amplitude [3].

The helicity amplitudes can be written

$$\Phi_i(s, t) = \phi_i^h(s, t) + \phi_i^{em}(t) \exp[i\alpha_{em}\varphi_{cn}(s, t)], \quad i = 1, \dots, 5$$

where $\phi_i^h(s, t)$ comes purely from strong interactions, $\phi_i^{em}(t)$ from electromagnetic interactions, ($\alpha_{em} = 1/137$ is the electromagnetic constant), and $\varphi_{cn}(s, t)$ is the electromagnetic-hadron interference phase factor. The “reduced” spin-flip amplitudes are defined as $\tilde{\mathcal{A}}_{sf}^h(s, t) = \phi_5^h(s, t)/(s\sqrt{|t|})$ and $\tilde{\mathcal{A}}_{sf}^c(s, t) = \phi_5^{em}(s, t)/(s\sqrt{|t|})$. As usual, we define the slope B of the scattering amplitudes as the derivative of the logarithm of the amplitudes with respect to t .

The contribution of large distances was studied in [4,5]. We present here the results of a numerical calculation of the relative contributions of small and large distances. We calculate the scattering amplitude in the Born approximation for form factors exponential or Gaussian in impact parameter space, as a function of the upper limit b of the corresponding integral

$$\phi_1^h(t) \sim \int_0^b \rho \, d\rho \, J_0(\rho\Delta) f_n, \quad \phi_5^h(t)/q \sim \int_0^b \rho^2 \, d\rho \, J_1(\rho\Delta) f_n. \quad (1)$$

with $f_n = \exp[-(\rho/5)^n]$, and $n = 1, 2$. We then calculate the ratio of the slopes of these two amplitudes $R_{BB} = B^{sf}/B^{nf}$ as a function of b for these two values of n . The result is shown in Fig.1. We

see that at small b the value of R_{BB} is practically the same in both cases. However, at large distances, the behaviour of R_{BB} depends on the form factor: in the Gaussian case, R_{BB} reaches its asymptotic value ($= 1$) quickly, but in the exponential case, it reaches its limit $R_{BB} = 1.7$ only at large distances. These calculations confirm our analytical analysis of the asymptotic behaviour of these integrals at large distances.

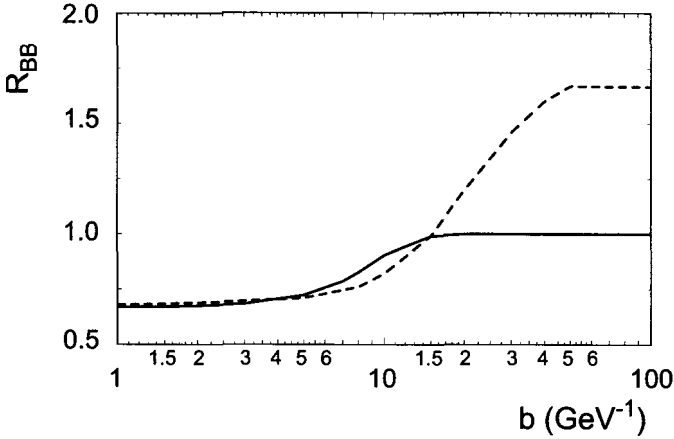


Fig. 1. The ratio R_{BB} of the effective slopes for $n = 1$ (dashed line) and $n = 2$ (solid line) versus the upper bound b of the integrals.

We can now use these results in the description of the analysing power at small momentum transfer, for which there are very few high-energy data. We take the hadron spin-non-flip amplitude in a simple exponential form, normalised to the total cross section [7], and with a size and energy dependence of the slope proportional to their values from pp -scattering [6].

We assume that the slope slowly rises with $\ln s$ in a way similar to the pp case, and normalise it so that the spin-non-flip amplitude has a slope of 62 GeV^{-2} at $p_L = 600 \text{ GeV}/c$ and $|t| = 0.02 \text{ GeV}^2$. We parametrise the spin-flip part of $p^{12}C$ scattering as

$$\mathcal{A}_{sf}^h(s, t) = (k_2 + i k_1) \frac{\sqrt{|t|} \sigma_{tot}^{pA}(s)}{4\pi} \exp\left(\frac{B^-}{2} t\right) \tag{2}$$

According to the above analysis, we investigate two extreme cases for the slope of the spin-flip amplitude: I - the spin-flip and the spin-non-flip amplitude have the same slope $B^- = B^+$; II - $B^- = 2B^+$. From the full scattering amplitude, the analysing power is given by

$$A_N \frac{d\sigma}{dt} = -4\pi [Im(\mathcal{A}_{nf})Re(\mathcal{A}_{sf}) - Re(\mathcal{A}_{nf})Im(\mathcal{A}_{sf})], \tag{3}$$

each term having electromagnetic and hadronic contributions.

In Fig. 2, we show A_N calculated for the two possible slopes of the hadron spin-flip amplitude (cases I and II). We see that in both cases we obtain a small energy dependence. In case I, when $B^- = B^+$, A_N decreases less with $|t|$ immediately after the maximum. But at large $|t| \geq 0.01 \text{ GeV}^2$ the behaviour of A_N is very different: we can obtain a zero for A_N at $|t| \approx 0.02 \text{ GeV}^2$, after which A_N becomes negative and grows in magnitude. In case II, when $B^- = 2B^+$, A_N approaches zero, may become slightly negative and then grows positive again.

When we come to super-high energies, there may be some additional effects connected with the saturation of the unitarity bound for some values of the impact parameter. This can lead to different

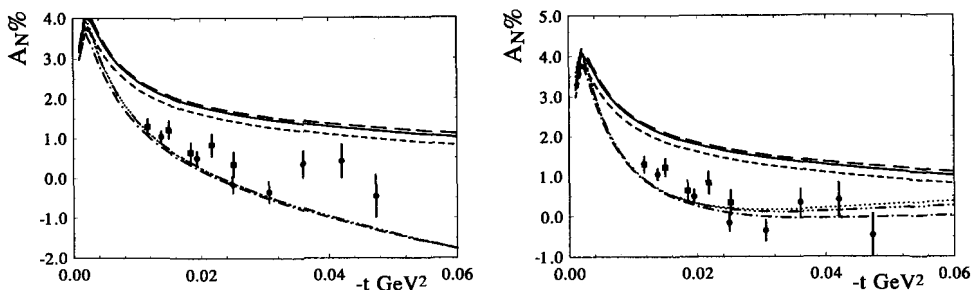


Fig. 2. Left: A_N with hadron-spin-flip amplitude in case I ($B^- = B^+$) for $p_L = 24, 100, 250$ GeV/c. (dash-dot, dashed-dots and dots correspondingly). Right: same as left, but in case II ($B^- = 2B^+$)

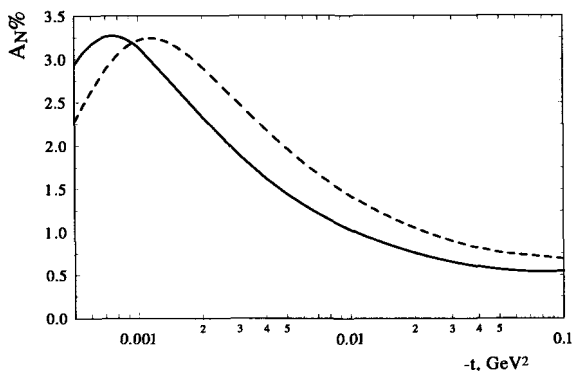


Fig. 3. A_N for pp -scattering (without hadron-spin flip amplitude) at $\sqrt{s} = 14$ TeV (hard and dashed lines - with and without saturation)

values for the analysing power. We calculate such effects in the framework of a model with two simple poles, the second one corresponding to contribution of the hard pomeron. Fig. 4 shows that the effect of the saturation moves the maximum of A_N to smaller values of t . Note that if we observe A_N only in a region of t after the maximum, it will seem smaller, and we may wrongly conclude that such an effect comes from the hadron spin-flip amplitude. This situation can also occur in pA -scattering at lower energies.

In conclusion, accurate measurements of the analysing power in the Coulomb-hadron interference region will reveal the structure of the hadron spin-flip amplitude. This in turn will give us further information about the behaviour of the hadron interaction potential at large distances. A definite example of the interplay between long and short distances can be found in the peripheral dynamic model [8, 9], which takes into account the contribution of the hadron interaction at large distances, and in which the calculated hadron spin-flip amplitude leads to a difference in the slopes of the “reduced” spin-flip and spin-non-flip amplitudes at small momentum transfer.

References

1. E. Predazzi, G. Soliani, *Nuovo Cim. A* **2**, 427 (1967); K. Hinotani, H.A. Neal, E. Predazzi and G. Walters, *Nuovo Cim. A* **52**, 363 (1979).
2. M. Sawamoto, S. Wakaizumi, *Progr. of Theor. Physics*, **62**, 1293 (1979).
3. O.V. Selyugin, *Mod. Phys. Lett. A* **9**, 1207 (1994).

4. E. Predazzi and O. Selyugin, *Eur. Phys. J. A* **13**, 471 (2002).
5. J.-R. Cudell, E. Predazzi and O. Selyugin, *Eur. Phys. J. A* **21**, 479 (2004).
6. U. Dersch et al., [SELEX Collaboration], *Nucl. Phys. B* **579**, 277 (2000), [arXiv:hep-ex/9910052].
7. J. R. Cudell et al., *Phys. Rev. D* **65**, 074024 (2002), [arXiv:hep-ph/0107219].
8. S. V. Goloskokov, S. P. Kuleshov and O. V. Selyugin, *Z. Phys. C* **50**, 455 (1991).
9. N. Akchurin, S. V. Goloskokov, O. V. Selyugin, *Int. J. of Mod. Phys., A* **14**, 253 (1999).

SPIN PHYSICS OF NN INTERACTIONS AT COSY *

A. KACHARAVA

Physikalisches Institut II, Universität Erlangen-Nürnberg, Erlangen, Germany

(on behalf of the ANKE Collaboration[†])

A survey is made of the current and future experimental programme on polarised nucleon-nucleon interactions at the COSY machine, with special emphasis on the recent results from the ANKE facility.

1. Introduction

The nucleon–nucleon (NN) interaction is fundamental to our understanding of nuclear physics. Elastic scattering data are an important ingredient in calculations of inelastic processes, nucleon–nucleus and heavy–ion reactions.

Below the pion production threshold, elastic scattering is well described by a number of models [1], both phenomenological and meson exchange, and also effective field theory. An unambiguous phase–shift analysis (PSA) has been achieved up to about 800 MeV. However, with increasing energy the number of partial waves grows, but the quality and density of the experimental database diminishes and above 1 GeV serious discrepancies between different PSAs exist [2, 3]. New, precise data, especially in observables not yet measured, are needed. Storage rings, such as COSY–Jülich, allow one to perform high statistics experiments with pure polarised targets and beams. COSY can contribute to the polarised np database by measuring breakup reactions of deuterium targets or deuteron beams.

2. Selected results from COSY

COSY is a COoler SYnchrotron and storage ring [4], providing high precision unpolarised and polarised beams of protons and deuterons with momenta in the range 0.3–3.7 GeV/c to a variety of experiments.

2.1. *PP experiments with EDDA*

The internal EDDA detector, consisting of two cylindrical hodoscope layers with a large solid angle, provides a high precision measurement of excitation functions of differential cross section, analysing power and spin–correlation parameters of elastic pp scattering during acceleration [5].

Measurements of spin–correlation parameters have been pioneered by the PINTEX group at energies between 200 and 450 MeV [6]. The EDDA Collaboration has similarly made a first measurement

*This work is supported by the COSY–FFE program of FZJ.

[†]See <http://www.fz-juelich.de/ikp/anke/>

of the spin–correlation parameters A_{NN} , A_{SS} and A_{SL} at 2.11 GeV [5]. The new data on A_{NN} are in good agreement with previous measurements and recent PSA solutions. However, for most of the angular range, A_{SS} , which was not present in the earlier database, disagrees with both PSA predictions [2, 3]. A_{SS} depends on the interference between double- and non-spin-flip amplitudes, and thus probes aspects of the spin–spin and spin–tensor parts of the NN interaction.

2.2. The NN programme at ANKE

ANKE, a magnetic spectrometer at an internal target position [7], consists of three dipole magnets. Detector systems for positively and negatively charged ejectiles are placed at the side, as well as in the forward and backward directions. A combination of scintillation and Čerenkov counters, together with wire chambers, is used for charged particle identification.

We have started a programme of single and double–polarisation np measurements [8], which should include:

(i) Studies of the small momentum transfer charge–exchange in the dp reaction with the forward emission of two protons. The first stage with an unpolarised target will be carried out early in 2005, with the aim of determining the magnitudes of the three np charge–exchange spin–flip amplitudes out to $\theta_{cm} \approx 15^\circ$, a region over which the one–pion–exchange amplitude varies significantly. To determine the relative phases of these amplitudes will entail measurements of spin–correlation parameters, requiring thus the polarised target [9]. It is important to stress that np data are almost non–existent above the Los Alamos energy of 800 MeV.

(ii) The deuteron beam only allows the investigation of np charge–exchange up to the maximum COSY energy of $\frac{1}{2}T_d \approx 1.1$ GeV. This can be extended to 3 GeV with a polarised proton beam incident on a polarised deuterium target and detecting two slow protons in an array of solid state spectator telescopes [10]. The interaction vertex is then very well located within the long target, making it unnecessary to measure the fast neutron in ANKE.

(iii) Simultaneously with the charge–exchange investigation we would measure a fast proton in ANKE in coincidence with one slow (spectator) proton in the telescope array. This would allow measurements of the elastic $pn \rightarrow pn$ polarisation observables for $\theta_{cm} < 30^\circ$. As a by–product we will also obtain data on inclusive pion production in polarised proton–neutron collisions, $pn \rightarrow \pi X$.

(iv) We have already investigated the high–momentum–transfer deuteron charge–exchange breakup reaction, $pd \rightarrow (pp)n$, with an unpolarised beam and target [11], as well as the proton analysing power at $T_p = 500$ and 800 MeV [12]. This will be complemented by the measurement of the deuteron tensor analysing power and the transverse pd spin–correlation parameter.

(v) The acceptance of ANKE for the production of a heavy meson X in proton–proton collisions *via* the missing mass is very good. We envisage studying double–polarisation observables in $pp \rightarrow ppX$ [13]. Of particular interest would be a comparison of the spin correlations in $pp \rightarrow pp\omega/\phi$ to check the OZI rule in well–defined spin states. With the spectator counters and a deuterium target, the $pn \rightarrow dX$ channels will also be accessed.

(vi) The reaction $pp \rightarrow pp\pi^0$, away from threshold but in the region of small pp excitation energies, is a good test-bed for pion–nucleon physics to parallel that of $pp \rightarrow d\pi^+$. The unpolarised reaction can be well identified in ANKE at small production angles [11], and this will be extended to spin observables. With a polarised deuterium target it will also be possible to extract the third independent isospin combination, *viz.* $pn \rightarrow pp\pi^-$.

2.3. Charge–exchange deuteron break–up at ANKE

Using the polarised deuteron Charge–Exchange (CE) break–up reaction $p(d, 2p)n$, where the final protons are in the 1S_0 state, we can access the spin–dependent amplitudes of the elementary np elastic scattering [14]. We are now exploring this process with a polarised deuteron beam and unpolarised

target. For collinear kinematics we can directly reconstruct the two spin amplitudes by measuring the cross section and T_{20} analysing power.

The first test measurement was carried out at ANKE using a polarised deuteron beam at $p_d = 2400$ MeV/c ($T_d = 1170$ MeV). Figure 1 shows the ANKE experimental acceptance for singly charged particles for different reactions as functions of the laboratory production angle and magnetic rigidity, together with loci for the kinematics of different allowed reactions. The $dp \rightarrow dp$ reaction has a significant acceptance for $4^\circ < \theta_{\text{lab}}^d < 10^\circ$. The observables A_y , A_{yy} and A_{xx} of this reaction were studied at Argonne [15] and SATURNE [16] for $T_d = 1198$ MeV.

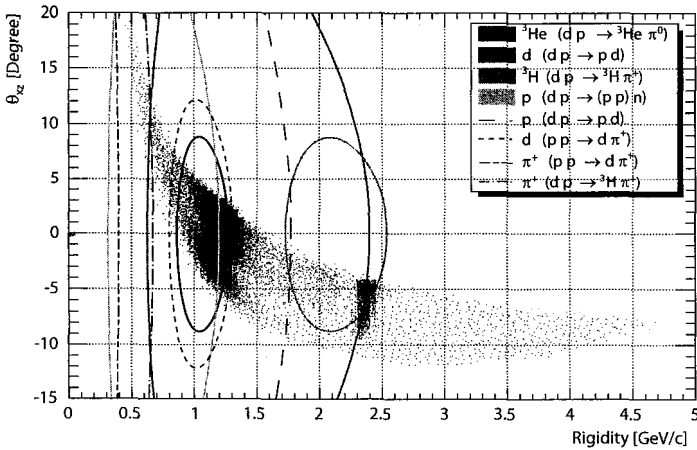


Fig. 1. ANKE experimental acceptance for different reactions in dp collisions at $T_d = 1170$ MeV.

The elastic peak region in the momentum spectrum of the single track events (left panel of Fig. 2) was fitted by the sum of Gaussian and linear functions, and events selected within 3σ of the mean. An example of such a fit is shown the right panel.

The $dp \rightarrow {}^3\text{He}\pi^0$ reaction can be studied using just the ${}^3\text{He}$ information. The high momentum branch of ${}^3\text{He}$ particles was isolated well in off-line analysis, applying two-dimensional cuts in ΔE versus momentum and Δt versus momentum for individual layers of the forward hodoscope.

The quasi-free $np \rightarrow d\pi^0$ can be clearly identified in ANKE by detecting two final charged particles in the $dp \rightarrow p_{sp}d\pi^0$ reaction, where p_{sp} is a spectator proton which has essentially half the beam momentum. The differential cross section should be half of that for $pp \rightarrow d\pi^+$, whereas all the analysing powers should be equal.

Using $dp \rightarrow dp$, $dp \rightarrow (2p)n$, $np \rightarrow d\pi^0$, and $dp \rightarrow {}^3\text{He}\pi^0$ reactions, which all have large and well determined analysing powers, simultaneous calibration of the vector and tensor components of the polarised deuteron beam at COSY becomes possible for the first time. The results are summarized in Table I [17].

The average of the two ANKE measurements is $\alpha_z^{\text{ANKE}} = 0.72 \pm 0.02$, which is completely compatible with EDDA. However, our mean tensor parameter, $\alpha_{zz}^{\text{ANKE}} = 0.52 \pm 0.03$, is about two standard deviations lower than EDDA. One possible source of this discrepancy is the difference of 30 MeV between the energy of our $dp \rightarrow dp$ measurement and that of Argonne [15] and Saturne [16], but other systematic effects have still to be investigated.

The $(d, 2p)$ charge-exchange process was identified from the missing-mass with respect to the proton pairs and time difference information. The spectra for all spin modes reveal a well defined

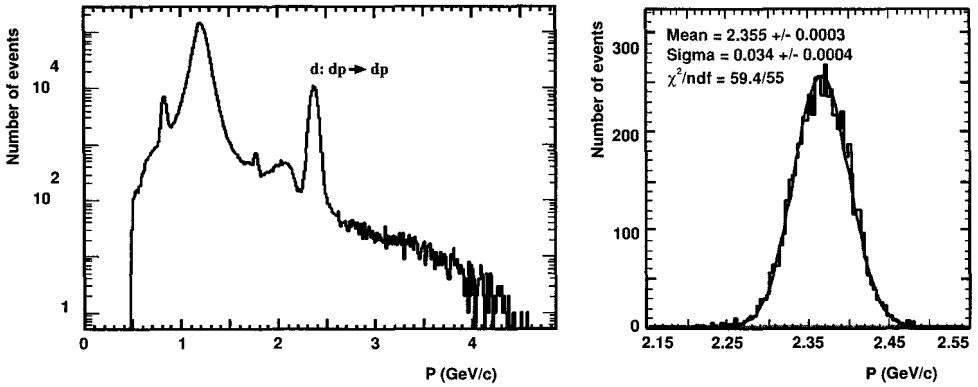


Fig. 2. Left: Single-track momentum spectrum for the dp data at 2.40 GeV/c. Right: Fit result of the elastic peak region with the sum of a Gaussian and linear function.

Table 1.

Reaction	Facility	α_{\pm}	$\alpha_{\pm\pm}$
$dp \rightarrow dp$	EDDA	0.74 ± 0.01	0.59 ± 0.02
$dp \rightarrow dp$	ANKE	0.73 ± 0.02	0.49 ± 0.02
$np \rightarrow d\pi^0$	ANKE	0.70 ± 0.03	—
$dp \rightarrow {}^3\text{He}\pi^0$	ANKE	—	0.58 ± 0.05
$dp \rightarrow (pp)n$	ANKE	—	0.48 ± 0.05

neutron peak with a mean value of $M_X = 940.4 \pm 0.2 \text{ MeV}/c^2$. The background was less than 2% and stable, so that the charge-exchange process could be reliably identified.

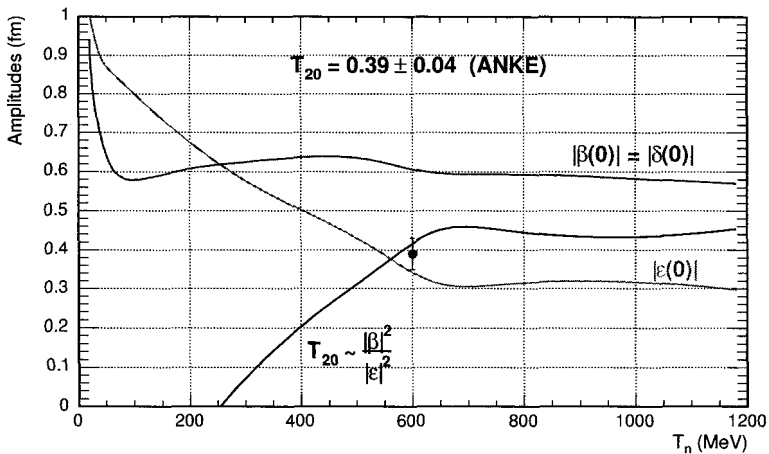


Fig. 3. Predictions for the moduli of the two independent $np \rightarrow pn$ scattering amplitudes at $t = 0$, taken from the SAID database [18], along with the associated prediction of T_{20} for $dp \rightarrow (pp)_{1S_0}n$ in the impulse approximation. The latter is compared to our preliminary value of $T_{20} = 0.39 \pm 0.04$ at $\frac{1}{2}T_d = 600 \text{ MeV}$.

Figure 3 shows predictions for the values of the moduli of the two forward spin-flip amplitudes, as functions of energy [18]. In the impulse approximation the forward differential cross section is proportional to $2|\beta(0)|^2 + |\varepsilon(0)|^2$ times form factors [14]. In the region $E_{pp} \leq 2$ MeV, the final pp system is essentially pure S -wave, and acceptance corrections largely cancel out for the analysing powers. Thus, in the forward direction,

$$T_{20} = \sqrt{2} \left(\frac{|\beta(0)|^2 - |\varepsilon(0)|^2}{2|\beta(0)|^2 + |\varepsilon(0)|^2} \right),$$

so that the ratio of the two forward spin-dependent $np \rightarrow pn$ amplitudes can already be deduced from our preliminary results.

The energy dependence of the predicted T_{20} using the SAID input is also shown in Fig. 3, along with our value of $T_{20} = 0.39 \pm 0.04$. Alternatively, using this value, we obtain $|\beta(0)|/|\varepsilon(0)| = 1.86 \pm 0.15$, to be compared to the SAID 1.79 ± 0.27 . Thus our statistical error is already superior.

2.4. Study of pd dynamics at ANKE

ANKE is well suited to study deuteron break-up reactions at GeV energies, in kinematics similar to backward elastic scattering $pd \rightarrow dp$. This provides a new tool to investigate pd dynamics at high-momentum transfer to gain more insight into systems composed of more than two nucleons. A measurement of the analysing power A_y for $pd \rightarrow (pp)n$ was carried out by detecting a fast forward proton pair of small excitation energy $E_{pp} \leq 3$ MeV. While at $T_p = 0.8$ GeV the measured analysing power A_y is small, it reaches almost unity at $T_p = 0.5$ GeV for neutrons emitted at $\Theta_{c.m.} = 166^\circ$ [12].

2.5. Meson production at COSY-11

The COSY-11 experimental facility [19], using a hydrogen cluster target in front of one of the regular COSY dipole magnets, acts like a magnetic spectrometer. Measurements of η meson production with a polarised proton beam, $pp \rightarrow pp\eta$, have been performed at three different excess energies, $Q=10, 37$ and 40 MeV and the dependence of A_y on the η meson production angle was studied [20]. The currently available cross section data near the threshold energy can be largely understood in terms of S and P waves, but any non-vanishing A_y must involve at least P waves. The current data are not yet sufficiently accurate to make a definitive statement as to the size of their contribution. Calculations for A_y show different results depending on the underlying assumption within the one meson exchange model [21, 22]. The data seem to favour the dominance of vector exchange. A model-independent extraction of the relevant amplitudes might be provided by the spin correlation parameters C_{ii} .

2.6. Hyperon-nucleon interaction

The TOF experiments [23] use an external large acceptance time-of-flight spectrometer. One of the main topics of the TOF experimental programme is associated strangeness production. The energy dependence of the Λ/Σ^0 production cross section ratio in pp interactions has been measured at TOF and COSY-11 [24]. The ratio shows a strong decrease from a threshold value of over 20 in the excess energy range from 10 to 20 MeV, and then gradually approaches the high energy limit of ≈ 2.5 .

Data with polarisation will be helpful to disentangle the contributing exchange mesons. In the reaction $NN \rightarrow NYK^+$, $Y = \Lambda(\Sigma)$, the final baryons are not identical. Therefore, even for pp induced reactions at threshold, two amplitudes are present (triplet \rightarrow singlet and triplet). At COSY it is possible to measure $d\sigma/d\Omega$, A_y , C_{NN} and D_{NN} for $pp \rightarrow p\Lambda K^+$ near threshold. Such data will provide us with unique information on the spin dependence of the S -wave hyperon-nucleon (YN) interaction in the final state. Moreover, polarisation observables can give an experimental signature of their parity when producing heavier hyperons, through the measurements of the sign of the spin correlation coefficient, or the polarisation transfer coefficient from initial proton to produced hyperon [25].

3. New equipment

3.1. Polarised internal target for ANKE

In order to perform double-polarised experiments at ANKE, the Polarised Internal Target (PIT) and spectator detector system [10] are required. The PIT, with its three main components of Atomic Beam Source, Lamb Shift Polarimeter, and storage-cell should be implemented at the ANKE platform and commissioning started in late 2005 [9].

3.2. Polarised target for TOF

The TOF collaboration published evidence for the Θ^+ pentaquark [26] and they are now taking more data. As a next step [25], they aim to measure its parity using the frozen spin target from the SPS185/3 LEAR experiment. Tests of the complete system are scheduled for autumn 2005.

References

1. R. Machleidt and I. Slaus, *J. Phys.* **G27**, R69 (2001), and references therein.
2. R. Arndt et al., *Phys. Rev.* **C62**, 34005 (2000).
3. J. Bystricky et al., *Eur. Phys. J.* **C4**, 607 (1998).
4. R. Maier, *Nucl. Instrum. Methods* **A390**, 1 (1997).
5. F. Bauer et al., *Phys. Rev. Lett.* **90**, 142301 (2003).
6. B. Lorentz et al., *Phys. Rev.* **C61**, 054002 (2000), and references [1–3] therein.
7. S. Barsov et al., *Nucl. Instrum. Methods* **A462**, 364 (2001).
8. A. Kacharava et al., www.fz-juelich.de/ikp/anke; March (2003).
9. K. Grigoriev, contribution to these proceedings.
10. I. Lehmann et al., *Nucl. Instrum. Methods* **A530**, 275 (2004).
11. V. Komarov et al., *Phys. Lett.* **B553**, 179 (2003).
12. S. Yaschenko et al., *arXiv:nucl-ex/0407018*, (2004), and contr. to these proc.
13. C. Hanhart, *J. Phys. Rep.* **397**, 155 (2004).
14. D.V. Bugg and C. Wilkin, *Nucl. Phys.* **A467**, 575 (1987).
15. M. Haji-Said et al., *Phys. Rev.* **C36**, 2010 (1987).
16. J. Arvieux et al., *Nucl. Instrum. Methods* **A273**, 48 (1988).
17. D. Chiladze et al., www.fz-juelich.de/ikp/anke, August (2004)
18. SAID database, <http://gwdac.phys.gwu.edu/analysis/>
19. S. Brauksiepe, *Nucl. Instrum. Methods* **A376**, 397 (1996).
20. P. Winter et al., *Phys. Lett.* **B544**, 251 (2002).
21. G. Fäldt and C. Wilkin, *Physica Scripta* **64**, 427 (2001).
22. K. Nakayama et al., *Phys. Rev.* **C65**, 045210 (2002).
23. K. Kilian, *Nucl. Phys.* **A629**, 303 (1998).
24. P. Kowina et al., *arXiv:nucl-ex/0402008*, (2004).
25. C. Hanhart et al., *Phys. Lett.* **B590**, 39 (2004).
26. TOF collaboration, *Phys. Lett.* **B595**, 127 (2004).

**MEASUREMENT OF THE VECTOR ANALYZING POWER
IN $pd \rightarrow (pp)n$ WITH EMISSION OF A FAST
FORWARD DIPROTON AT ANKE/COSY**

S. YASCHENKO^{1,2}, S. DYMOV², A. KACHARAVA^{1,3}, V. KOMAROV², G. MACHARASHVILI^{2,3},
F. RATHMANN⁴, S. BARSOV⁵, R. GEBEL⁴, M. HARTMANN⁴, A. KHOUKAZ⁶, P. KULESSA^{4,7},
A. KULIKOV², V. KURBATOV², N. LANG⁶, I. LEHMANN⁴, B. LORENTZ⁴, T. MERSMANN⁶,
S. MERZLIAKOV², S. MIKIRTYTCHIANTS⁵, A. MUSSGILLER⁴, M. NIORADZE³, H. OHM⁴,
D. PRASUHN⁴, R. SCHLEICHERT⁴, H. SEYFARTH⁴, H. J. STEIN⁴, H. STRÖHER⁴, Y. UZIKOV^{2,8},
B. ZALIKHANOV², N. ZHURAVLEV²

¹Physikalisches Institut II, Universität Erlangen-Nürnberg, Erlangen, Germany,

²Joint Institute for Nuclear Research, Dubna, Russia,

³High Energy Physics Institute, Tbilisi State University, Tbilisi, Georgia,

⁴Institut für Kernphysik, Forschungszentrum Jülich, Jülich, Germany,

⁵Petersburg Nuclear Physics Institute, Gatchina, Russia,

⁶Institut für Kernphysik, Universität Münster, Münster, Germany,

⁷Henryk Niewodniczanski Institute of Nuclear Physics, Cracow, Poland,

⁸Kazakh National University, Almaty, Kazakhstan

A measurement of the vector analyzing power A_y of the $pd \rightarrow (pp) + n$ reaction was carried out at the ANKE spectrometer at COSY at beam energies of 0.5 and 0.8 GeV by detection of a fast forward proton pair of small excitation energy $E_{pp} < 3$ MeV. While at $T_p = 0.8$ GeV the measured analyzing power A_y vanishes, it reaches almost unity at $T_p = 0.5$ GeV for neutrons emitted at $\theta_n^{c.m.} = 167^\circ$. The results are compared with a model taking into account one-nucleon exchange, single scattering, and $\Delta(1232)$ excitation in the intermediate state. The model describes fairly well the unpolarized cross section obtained earlier and the analyzing power at 0.8 GeV, but it fails to reproduce A_y at 0.5 GeV.

The structure of the lightest nuclei at short distances ($r_{NN} < 0.5$ fm) or high relative momenta ($q > 1/r_{NN} \sim 0.4$ GeV/c), and the closely related short-range part of nucleon-nucleon (NN) interaction, constitute fundamental problems in nuclear physics. Experimental investigations employ processes where the momentum transfer to the nucleus is large ($Q \sim 1$ GeV/c). The existing data on elastic electromagnetic deuteron form factors for $Q < 1$ GeV/c are in agreement with NN models based on the exchange of mesons [1, 2]. The situation above $Q \sim 1$ GeV/c becomes much less clear due to increasing contributions from meson-exchange currents in ed interactions and theoretical uncertainties in their treatment. Moreover, meson-exchange models have difficulty in explaining photo-disintegration data ($\gamma d \rightarrow np$) for energies $E_\gamma > 1$ GeV. Independent information about the short-range structure of nuclei can be obtained from hadronic interactions at large q . Recently, the unpolarized cross section of the $pd \rightarrow (pp)n$ reaction was measured at proton beam energies $T_p = 0.6$ to 1.9 GeV at kinematics similar to backward pd elastic scattering [3], with formation of a fast dipro-

ton in a 1S_0 state at low excitation energy ($E_{pp} < 3$ MeV). In $pd \rightarrow (pp)n$, the diproton provides two new features which are absent for isosinglet nucleon pairs. *i*) The contribution from three-body forces, related to two isovector meson exchanges, in particular the excitation of Δ and N^* resonances in the intermediate state, is suppressed by the isospin factor of 3 in the amplitude of this process [4]. *ii*) The S -wave dominates in the internal state of the diproton at $E_{pp} < 3$ MeV. Due to the repulsive NN core, the 1S_0 diproton wave function $\psi_{pp}(q)$ has a node at relative pp momenta $q \approx 0.4$ GeV/c [5], leading to a distinct energy dependence of various polarization observables [6] that helps to identify the dominant reaction mechanisms. The recent analysis [7] of the $pd \rightarrow (pp)_{^1S_0}n$ cross section, based on a model for the $pd \rightarrow dp$ process [8], includes the one-nucleon exchange (ONE), single scattering (SS), and double pN scattering with excitation of a $\Delta(1232)$ isobar. This analysis accounts for initial and final state interactions and employs modern NN potentials, based on the exchange of mesons, e.g. CD-Bonn [9]. Reasonable agreement with our recent data [3] is achieved. In contrast, the widely used NN potentials like the Paris [10] and especially the Reid Soft Core (RSC) potential [11] lead to strong disagreement with the data. These potentials apparently overestimate the high-momentum components of the NN wave function $\psi_{NN}(q)$.

New information about this reaction can be obtained from measurements of polarization observables. Here we report the first measurement [12] of the vector analyzing power A_y at $T_p = 0.5$ and 0.8 GeV of the reaction $p + d \rightarrow (pp)_{^1S_0} + n$, where $(pp)_{^1S_0}$ denotes a fast proton pair emitted in the forward direction with small excitation energy $E_{pp} < 3$ MeV. The two beam energies were chosen because of the difference in the reaction mechanisms predicted by the model [7].

The experiment was performed at the ANKE spectrometer [13] at the internal beam of COSY-Jülich [14] with about $3 \cdot 10^9$ vertically polarized stored protons. The deuterium cluster-jet [15] produced a target density of about $2 \cdot 10^{14}$ atoms/cm² with a target length along the beam of 12 mm and a width of 4.9 mm.

The beam polarization at $T_p = 0.8$ GeV was determined from precise pd -elastic analyzing power data [16]. Since there are no data available at 0.5 GeV, we resorted to the polarization export technique [17] to obtain a calibrated polarization for 0.5 GeV. This was achieved by setting up a cycle with a flat top at energy $T_p = 0.8$ GeV (I), followed by deceleration to a flat top at 0.5 GeV (II), and subsequent re-acceleration to a flat top at 0.8 GeV (III). Avoiding depolarization during crossing of the resonances, the measured beam polarizations $P_I = 0.564 \pm 0.003^{\text{stat.}} \pm 0.004^{\text{sys.}}$ and $P_{III} = 0.568 \pm 0.004^{\text{stat.}} \pm 0.005^{\text{sys.}}$ agree within errors. The weighted average of P_I and P_{III} was taken to be the beam polarization during flat top II and used to determine the angular distribution of the previously unknown analyzing power of pd elastic scattering at 0.5 GeV.

Protons from the breakup reaction with $E_{pp} < 3$ MeV are detected from $\theta_{\text{lab}} = 0^\circ$ to 6.5° at both energies; the polar angles of the proton pairs range from $\theta_{pp}^{c.m.} = 0^\circ$ to 14° . The uncertainty in E_{pp} ranges from 0.2 MeV at $E_{pp} = 0.3$ MeV to 0.3 MeV at $E_{pp} = 3$ MeV. The events of the deuteron breakup can be unambiguously identified via missing mass [3]. At both energies and for both orientations of the beam polarization, the missing mass peak is observed at the neutron mass with the (rms) peak widths of 16 MeV/c² ($T_p = 0.5$ GeV) and 20 MeV/c² ($T_p = 0.8$ GeV).

The obtained values of A_y in $pd \rightarrow (pp)n$ at 0.5 and 0.8 GeV are shown in Fig. 1 as a function of $\theta_n^{c.m.}$. The measured A_y is almost zero at 0.8 GeV, in agreement with the predictions of the ONE+SS+ Δ model. At this energy, the calculated A_y is almost insensitive to the spin structure of the Δ -mechanism, which completely dominates the process and produces alone a near zero value of A_y . A peculiarity of the data at 0.5 GeV is the rapid increase of A_y up to a value of 0.8 in a small angular interval from 180° to 167° . (In contrast, in the same angular interval the analyzing power of $pd \rightarrow dp$ scattering at comparable energies, 0.425, 0.68, 0.8 and 1.053 GeV, never exceeds 0.12.) The increase of A_y with decreasing energy from 0.8 to 0.5 GeV is expected from the ONE+SS+ Δ model; however the magnitude is grossly underestimated. Different NN -interaction potentials (RSC, Paris) do not improve the description. The inadequacy of the model to describe A_y at 0.5 GeV may be related to the spin structure of the Δ -mechanism, given here by the Born term of the $\pi + \rho$ meson exchange in

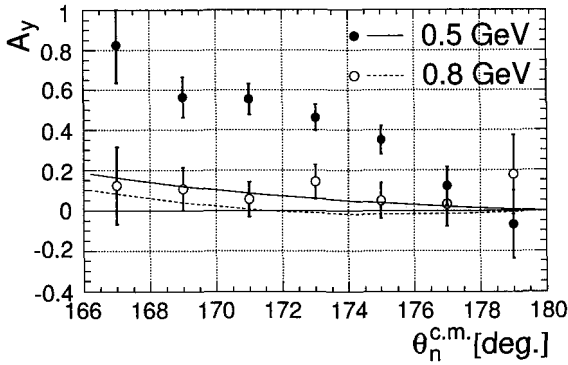


Fig. 1. Vector analyzing power A_y as a function of the neutron polar angle $\theta_n^{c.m.}$ for $T_p = 0.5$ (●) and 0.8 GeV (○). The lines show predictions for A_y at 0.5 GeV (solid) and 0.8 GeV (dashed) from the ONE + SS + Δ model, with the CD-Bonn potential. The figure is from Ref. [12].

the $NN \rightarrow \Delta N$ transition [7, 8]. Further insight into the short-range structure of the deuteron can be achieved from a measurement of the tensor analyzing power T_{20} in $pd \rightarrow (pp)_{1S_0}n$, in preparation at ANKE, for which the theoretical predictions are more robust than for A_y .

This work was supported by the BMBF (06 ER126), a BMBF grant to JINR, the BMBF/WTZ grants (Rus-667-97, Rus 00/211, Rus 01/691, Kaz 99/001, and Kaz 02/001) and the Heisenberg-Landau program.

References

1. M. Garçon and J.W. Van Orden, *Adv. Nucl. Phys.* **26**, 293 (2001).
2. R. Gilman and F. Gross, *J. Phys.* **G28**, R37 (2002).
3. V. Komarov *et al.*, *Phys. Lett.* **B553**, 179 (2003).
4. Yu.N. Uzikov, *JETP Lett.* **75**, 5 (2002).
5. O. Imambekov, Yu.N. Uzikov, *Sov. J. Nucl. Phys.* **47**, 862 (1990).
6. Yu.N. Uzikov *J. Phys.* **G28**, B13 (2002).
7. J. Haidenbauer and Yu.N. Uzikov, *Phys. Lett.* **B562**, 227 (2003).
8. L.A. Kondratyuk *et al.*, *Phys. Lett.* **B100**, 448 (1981).
9. R. Machleidt, *Phys. Rev.* **C63**, 024001 (2001).
10. M. Lacombe *et al.*, *Phys. Lett.* **B101**, 139 (1981).
11. J.R.V. Reid, *Ann. Phys. (N.Y.)* **50**, 411 (1968).
12. S. Yaschenko *et al.*, arXiv:nucl-ex/0407018.
13. S. Barsov *et al.*, *Nucl. Instrum. Methods* **A462**, 364 (2001).
14. R. Maier, *Nucl. Instrum. Methods* **A390**, 1 (1997).
15. A. Khoukaz *et al.*, *Eur. Phys. J.* **D5**, 275 (1999).
16. F. Irom *et al.*, *Phys. Rev.* **C28**, 2380 (1983).
17. R.E. Pollock *et al.*, *Phys. Rev.* **E55**, 7606 (1997).

**RESULTS FOR THE ASYMMETRY MEASUREMENT
IN ELASTIC PION-PROTON SCATTERING
AT 1.78 AND 2.07 GeV/c***

I. G. ALEKSEEV, P. E. BUDKOVSKY, V. P. KANAVETS, L. I. KOROLEVA, B. V. MOROZOV,
V. M. NESTEROV, V. V. RYLTSOV, A. D. SULIMOV, D. N. SVIRIDA, V. V. ZHURKIN

Institute for Theoretical and Experimental Physics, Moscow, Russia

Y. A. BELOGLAZOV, E. A. FILIMONOV, A. I. KOVALEV, S. P. KRUGLOV, D. V. NOVINSKY,
V. A. SHCHEDROV, V. V. SUMACHEV, V. Y. TRAUTMAN

Petersburg Nuclear Physics Institute, Gatchina, Russia

N. A. BAZHANOV, E. I. BUNYATOVA

Joint Institute for Nuclear Research, Dubna, Russia

New experimental results from the ITEP-PNPI collaboration are presented on the asymmetry in backward elastic scattering of negative pions on polarized protons in the resonance region. The data were obtained in the angular region ($150^\circ - 170^\circ$) c.m. at initial momenta 1.78 and 2.07 GeV/c. The results are compared to the predictions of partial wave analyses. The measurement was done at the ITEP accelerator.

1. Introduction

We present new experimental data on the asymmetry in backward $\pi^- p$ elastic scattering at 1.78 and 2.07 GeV/c. This experiment is the latest in a series of polarization parameter measurements by the ITEP-PNPI collaboration in the last decade. The momentum range (0.8-2.1) GeV/c available for our beam-line contains nearly 65 % of the known non-strange light quark resonances. There are three clusters of resonances in this region corresponding to the peaks in the total crosssection. The main goal of our experiment is to obtain the necessary information for the *unambiguous reconstruction* of the pion-proton elastic scattering amplitude by partial-wave analyses (PWA).

The physics interest in light baryon spectroscopy is enhanced by the fact that several observations do not fit the constituent quark model well. Example are: resonance clusters with masses 1.7

*This work was partially supported by the Russian Fund for Basic Research grant 02-02-16121 and Russian State Scientific Program "Fundamental Nuclear Physics".

and $1.9\text{ GeV}/c^2$, parity doublets, negative parity resonances in the peak at $\sqrt{s} = 1.9\text{ GeV}$, "missing resonances" near $\sqrt{s} = 2\text{ GeV}$.

The status of modern experimental light baryon spectroscopy is far from satisfactory. Resonances in the current issue of PDG are based mainly on two PWAs: CMB80 [1] and KH80 [2], both performed more than two decades ago. However more recent analyses by the VPI/GWU group [3] did not reveal 4 of 13 resonances in 1.7 and $1.9\text{ GeV}/c^2$ clusters. On the other hand, the new data by ITEP-PNPI collaboration on normal polarization [4] and spin rotation parameters [5] in backward $\pi^\pm p$ scattering did not confirm the CMB80 and KH80 predictions.

2. Experiment

The main elements of the experimental setup are [6]: a transversely polarized proton target inside a super-conducting solenoid, several sets of wire chambers for tracking the incident and scattered particles, and a TOF system for identifying beam particles. Additional chambers were used for the momentum analysis of the scattered pions.

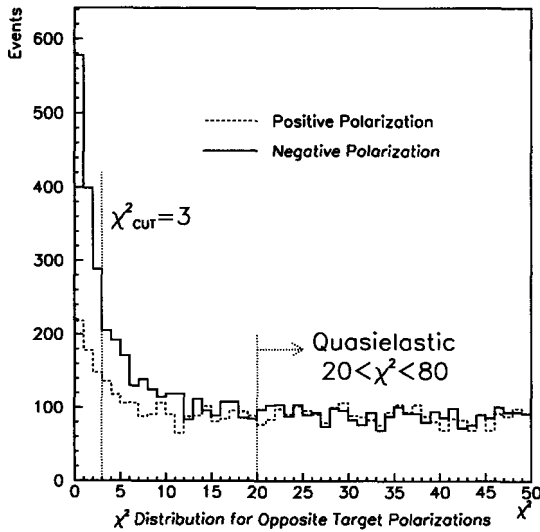


Fig. 1. χ^2 distributions for positive and negative target polarization.

The main difficulty of the measurements is the small elastic scattering cross-section in the explored domain. This leads to considerable background which has to be carefully subtracted. Elastic event selection was based on the joint χ^2 co-planarity and kinematic correlation criterion:

$$\chi^2 = \left(\frac{\Delta\varphi}{\sigma_\varphi} \right)^2 + \left(\frac{\Delta\theta}{\sigma_\theta} \right)^2,$$

where $\Delta\varphi$, $\Delta\theta$ are the deviations from the elastic kinematics, σ_φ and σ_θ the corresponding distribution widths. Typical χ^2 distributions for the positive and negative target polarization are shown in fig. 1. Minimal statistic errors are obtained at the optimal cut $\chi^2_{CUT} = 3$. Additional background suppression (factor 2 in S/B ratio) was achieved by pion momentum analysis. The background subtraction was done by linear extrapolation of the quasi-elastic part of the χ^2 distribution ($20 < \chi^2 < 80$)

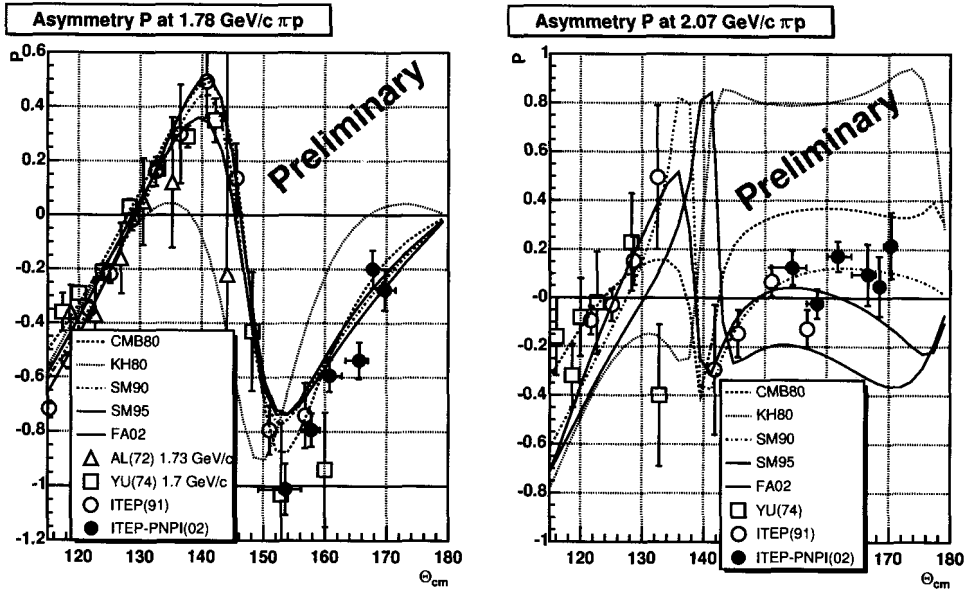


Fig. 2. Results on asymmetry in $\pi^- p$ elastic scattering at 1.78 and 2.07 GeV/c.

under the elastic peak. For the normalization of the counts with negative and positive target polarization two methods were used: one based on χ^2 distribution quasi-elastic wings, the other taking advantage of the beam particle counts. The results of both are well concordant.

3. Results and Conclusions

The results of the asymmetry measurements at 1.78 GeV/c are shown in fig. 2a. They agree with the CMB80 and FA02 (latest VPI/GWU) analyses and deviate significantly from the KH80 prediction. The data at 2.07 GeV/c (fig. 2b) manifest good agreement with the old analysis SM90 by the VPI group, reveal significant deviations from CMB80 and FA02 analyses, and definitely contradict KH80 predictions. The new data is well consistent with our previous experiment [4] in the angular interval where they overlap.

More general conclusions can be drawn from the discussion of the whole set of the latest experimental data on spin rotation parameters and asymmetry by ITEP-PNPI. It is clear that both old analyses (CMB80 and KH80) do not reconstruct properly the backward scattering amplitude. So one should be careful in comparing the theory with the present day spectrum and parameters of the light quark baryon resonances, because it is based mainly on these two old analyses. However one should mention the significant progress of the energy dependent partial wave analysis (DPWA) by the VPI/GWU group. Several versions of this DPWA, consistent with each other in their main features, are now at our disposal. Yet new data on spin rotation parameters and precise data on asymmetry are desirable to resolve the remaining PWA uncertainties. The development of a new energy independent partial wave analysis (IPWA) or the resurrection of the KH80 analysis [7] would be specially important for the modern experimental picture of the light quark baryon resonances.

Acknowledgments

We owe our heartiest gratitude to Professor G. Höhler for very interesting and fruitful discussion on the subject. We are grateful to the ITEP accelerator team for providing us with excellent beam conditions and to the ITEP cryogenic department for the supply of liquid helium and nitrogen.

References

1. R. E. Cutcosky, *Phys. Rev.* **D20**, 2839 (1979).
2. G. Höhler, *Handbook of Pion-Nucleon Scattering, Physics Data 12-1*, (Fachinformationzentrum, Karlsruhe, 1979).
3. R. A. Arndt et al., *Phys. Rev.* **C52**, 2120 (1995).
4. I. G. Alekseev et al., *Nucl. Phys.* **B348**, 257 (1991).
5. I. G. Alekseev et al., *Phys. Lett.* **B351**, 585 (1995);
I. G. Alekseev et al., *Phys. Lett.* **B485**, 32 (2000);
I. G. Alekseev et al., *Eur. Phys. J.* **A12**, 117 (2001).
6. Yu. A. Beloglazov et al., *Instr. and Exp. Tech.* **47**, 744 (2004)
7. P. Pirola, E. Pietarinen and M. E. Sainio, *πN -newsletter* **16**, 121 (2002).

LOWER EXCITATION SPECTRUM OF THE NUCLEON AND Δ IN A RELATIVISTIC CHIRAL QUARK MODEL WITH ONE-MESON EXCHANGE FORCES *

E. M. TURSUNOV

Institute of Nuclear Physics, Ulugbek, Tashkent, Uzbekistan

The lower excitation spectrum of the nucleon and Δ is calculated in a relativistic chiral quark model. It is shown that the relativistic structure of the one-meson exchange yields a splitting between negative parity $N^*(1/2^-)$ and $N^*(3/2^-)$ states, and also between $\Delta^*(3/2^-)$ and $\Delta^*(1/2^-)$ states

1. Introduction

The aim of the present work is to develop a relativistic chiral quark model based on a field-theoretical description of the interquark interaction for excited nucleon and Δ spectroscopy. The model was firstly suggested in [1] and used for the calculations of the nucleon ground state properties in [2, 3]. In these approaches baryons are considered as bound states of valence quarks surrounded by a cloud of Goldstone bosons (π -, K -, η - mesons) as required by the chiral symmetry.

The relativistic quark model is based on an effective chiral Lagrangian describing quarks as relativistic fermions moving in a confining static potential. The potential is described by a Lorentz scalar and the time component of a vector potential, where the latter term is responsible for short-range fluctuations of the gluon field configurations [4]. The model potential defines unperturbed wave functions of the quarks, which are subsequently used in the calculations of baryon properties. Interaction of quarks with Goldstone bosons is introduced on the basis of the nonlinear σ -model [5]. All calculations are performed at one loop or at order of accuracy $o(1/f_\pi^2, m)$. Due to negligible contribution of the K - and η - meson loop diagrams to the nucleon and Δ sectors in the model, we restrict ourselves to the π - meson loop diagrams.

2. Model

The effective Lagrangian of our model $\mathcal{L}(x)$ contains the quark core, the quark-pion interaction part, and the kinetic part of the pion field:

$$\begin{aligned} \mathcal{L}(x) = & \bar{\psi}(x)[i \not{\partial} - S(r) - \gamma^0 V(r)]\psi(x) \\ & - 1/f_\pi \bar{\psi}[S(r)i\gamma^5 \tau^i \phi_i]\psi + \frac{1}{2}(\partial_\mu \phi_i)^2 - \frac{1}{2}m_\pi^2 \Phi_i^2. \end{aligned} \quad (1)$$

*This work is supported in part by the DAAD research fellowship (Germany) and by the Belgian-state Federal Services for Scientific, Technical and Cultural Affairs (SSTC).

Here, $\psi(x)$ and $\phi_i, i = 1, 2, 3$ are the quark and pion field operators, respectively. The matrices $\tau^i (i = 1, 2, 3)$ are the isospin matrices. The pion decay constant is $f_\pi = 93$ MeV. The scalar part of the static confinement potential is $S(r) = cr + m$, where c and m are constants. The constant part of the scalar potential can be interpreted as the current quark mass term. At short distances, transverse fluctuations of the string are dominating [4], and they are given by a Coulomb type vector potential as $V(r) = -\alpha/r$, where α is approximated by a constant. The quark field operators are expanded over the basis of positive and negative energy eigenstates of the Dirac equation, with the corresponding scalar plus vector potentials

$$\psi(x) = \sum_{\alpha} u_{\alpha}(x)b_{\alpha} + \sum_{\beta} v_{\beta}(x)d_{\beta}^{\dagger}. \tag{2}$$

The expansion coefficients b_{α} and d_{β}^{\dagger} are operators which annihilate a quark and create an antiquark in the orbits α and β , respectively. The free pion field operator is expanded over plane-wave solutions.

Using the effective Lagrangian we calculate the lowest excitation spectrum of the nucleon and Δ . We resort to three approximate methods, which correct for the center of mass motion: the $R = 0$ [6], $P = 0$ [7] and LHO [8] methods. The second order perturbative corrections to the energy spectrum of the $SU(2)$ baryons due to pions ($\Delta E^{(\pi)}$) are calculated on the basis of the Gell-Mann and Low theorem.

3. Numerical results

In order to account for the finite size effect of the pion we introduce a one-pion vertex regularization function in momentum space, parametrized in the dipole form as $F_{\pi}(p^2) = \frac{\Lambda_q^2 - m^2}{\Lambda_q^2 + p^2}$. According to [4] we use the value $\alpha = 0.26 \approx \pi/12$. We choose two sets of parameters: model A and model B. The parameters of the confining potential (c and m) are fitted to reproduce the correct axial charge of the proton, which remains unaltered by the inclusion of the effects of the pion cloud, the empirical value of the pion-nucleon coupling constant $G_{\pi NN}^2/4\pi \approx 14$, and a normal value for the quark core RMS radius 0.5 – 0.6 fm of the proton. In the case of model A, a reasonable value (1280-1320 MeV) for the mass of the Δ is obtained. However, for the nucleon ground state the estimation is still large. In the second and fourth columns of Table 6 the quark core results are given without center of mass corrections. We note a good agreement of the theoretical value for the splitting of the first radial excitation of the nucleon, the Roper resonance $N^*(1440)(1/2^+)$. We also note that the splitting between Δ states is well reproduced.

Acknowledgments. The author thanks the Institut für Theoretische Physik, Universität Tübingen, the PNTPM group of ULB, Brussels, and the Abdus Salam International Center for Theoretical Physics for kind hospitality. He also deeply thanks Prof A. Faessler, Dr. Th. Gutsche and Prof D. Baye for valuable advice and discussion, and Prof. F.Stancu and Dr. A. Rakhimov for useful discussions.

References

1. E. Oset, R. Tegen, and W. Weise; Nucl. Phys. A **426**, 456 (1984)
2. T. Gutsche, Ph. D. Thesis, Florida State University, 1987 (unpublished).
3. T. Gutsche and D. Robson, Phys. Lett. **B229**, 333 (1989)
4. M. Lüscher, Nucl. Phys. **B180**, 317 (1981).
5. M. Gell-Mann and M. Levy, Nuovo Cim. **16** (1960) 1729
6. D.H.Lu, A.W.Thomas and A.G.Williams, Phys.Rev.C57(1998), 2628
7. R.Tegen, R.Brockmann and W.Weise, Z.Phys. A307(1982)339
8. L.Wilets, "Non-Topological Solitons (World Scientific, Singapoure, 1989

- 9. K. Hagiwara et al. (Particle Data Group), Phys.Rev. **D66**, 010001(2002)
- 10. R.A. Arndt, W.J. Briscoe, I.I. Strakovsky, R.L. Workman and M.M. Pavan Phys. Rev. **C69**, 035213(2004)

Table 1. Parameter sets for the models A and B and corresponding single quark energies in MeV

Model	c	m	Λ_π	α	$E(1S)$	$E(2S)$	$E(1P_{3/2})$	$E(1P_{1/2})$
	Gev ²	Gev	Gev		MeV	MeV	MeV	MeV
A	0.16	0.06	1.0	0.26	571.7	986.7	822.8	860.7
B	0.20	0.07	1.2	0.26	641.4	1105.71	922.0	964.4

Table 2. Quark core contributions to the static properties of the proton

Model	g_A	μ_p	RMS radius	$G_{\pi NN}^2/(4\pi)$
		N.M.	fm	
A	1.31	1.261	0.568	13.919
B	1.312	1.126	0.508	13.984

Table 3. Second order perturbative corrections due to one-pion self energy diagrams for the energy shift of the single valence quarks in MeV

Model	1S	2S	$1P_{3/2}$	$1P_{1/2}$
A	126.5	350	262	248
B	193	540	400	380

Table 4. Second order perturbative corrections due to one-pion exchange diagrams for the mass spectrum of lowest N and Δ states in MeV for the Model A

(J,T)	$(\frac{1}{2}, \frac{1}{2})$	$(\frac{3}{2}, \frac{1}{2})$	$(\frac{5}{2}, \frac{1}{2})$	$(\frac{1}{2}, \frac{3}{2})$	$(\frac{3}{2}, \frac{3}{2})$	$(\frac{5}{2}, \frac{3}{2})$
$(1S)^3$	-179.5					-35.9
$(1S)^2 2S$	-120.35					-24
$(1S)^2 1P_{1/2}$	3.7	-69.1		-23.8	-17.4	
$(1S)^2 1P_{3/2}$	-132.8	-150	10.8	-7.5	-17.6	-34.5

Table 5. The mass value of the g.s. nucleon in MeV with and without center of mass (CM) correction

Model		No CM	R=0 [6]	P=0 [7]	LHO [8]
A	E_Q	1715	940	985	966
	$E_Q + \Delta E$	1915	1140	1185	1166
B	E_Q	1924	1057	1110	1088
	$E_Q + \Delta E$	2225	1358	1411	1389

Table 6. Energy splitting values between lowest N and Δ states in MeV

	A, E_Q	A, ΔE	B, E_Q	B, ΔE	exp. [9]	exp. [10]
$N(939)(1/2^+) - \Delta(1232)(3/2^+)$	0	144	0	223	293	293
$N(939)(1/2^+) - N(1440)(1/2^+)$	415	284	464	439	$490 \div 530$	528 ± 4.5
$N(1440)(1/2^+) - N(1535)(1/2^-)$	-164	-101	-184	-161	$50 \div 125$	78 ± 6.5
$N(1520)(3/2^-) - N(1535)(1/2^-)$	0	17	0	26	$0 \div 30$	30.4 ± 3
$\Delta(1232)(3/2^+) - \Delta(1600)(3/2^+)$	415	237	464	366	$320 \div 470$	
$\Delta(1232)(3/2^+) - \Delta(1620)(1/2^-)$	251	166	280	250	$380 \div 445$	381 ± 2
$\Delta(1620)(1/2^-) - \Delta(1700)(3/2^-)$	0	-10	0	-15	$(-5) \div 185$	74 ± 3.5

SINGLE SPIN ASYMMETRY MEASUREMENTS FOR π^0 INCLUSIVE PRODUCTIONS IN $p + p \uparrow \rightarrow \pi^0 + X$ AND $\pi^- + p \uparrow \rightarrow \pi^0 + X$ REACTIONS AT 70 AND 40 GeV RESPECTIVELY*

A. M. DAVIDENKO, A. A. DEREVSCHIKOV, V. N. GRISHIN, V. Y. KHODYREV, Y. A. MATULENKO,
Y. M. MELNICK, A. P. MESCHANIN, V. V. MOCHALOV, L. V. NOGACH, S. B. NURUSHEV,
P. A. SEMENOV, A. F. PRUDKOGLYAD, K. E. SHESTERMANOV, L. F. SOLOVIEV, A. N. VASILIEV,
A. E. YAKUTIN

Institute for High Energy Physics, Protvino, Russia

N. S. BORISOV, V. N. MATAFONOV, A. B. NEGANOV, Y. A. PLIS, Y. A. USOV, A. N. FEDOROV

Joint Institute for Nuclear Physics, Dubna, Russia

A. A. LUKHANIN

Kharkov Physical Technical Institute, Kharkov, Ukraine

M. G. RYSKIN

Petersburg Nuclear Physics Institute, St. Petersburg, Russia

Inclusive π^0 asymmetries were measured in reactions $p + p \uparrow \rightarrow \pi^0 + X$ and $\pi^- + p \uparrow \rightarrow \pi^0 + X$ at 70 and 40 GeV/c respectively. The measurements were made in the central region (for the first reaction), and asymmetry is compatible with zero in the entire measured p_T region. For the second reaction the asymmetry is zero for small x_F ($-0.4 < x_F < -0.1$, $0.5 < p_T(\text{GeV}/c) < 1.5$) and increases with growth of $|x_F|$. Averaged over the interval $-0.8 < x_F < -0.4$, $1 < p_T(\text{GeV}/c) < 2$ the asymmetry was $-(13.8 \pm 3.8)\%$.

Two experiments were performed at the U70 GeV accelerator of IHEP with the aim of measuring single spin asymmetry (SSA) in inclusive π^0 productions. In one case we studied the reaction $pp \uparrow \rightarrow \pi^0 X$ at 70 GeV/c. Interest in such a study was stimulated by two experimental data relevant to above

*This work is supported by Russian Foundation for Basic Research, grant 03-02-16919.

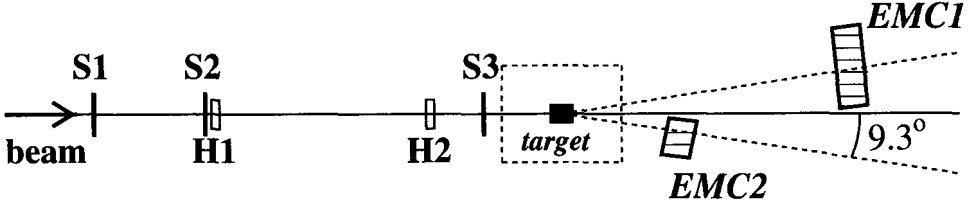


Fig. 1. Experimental Set-up PROZA-M; S1-S3 – Scintillation counters, H1-H2 – two-coordinate hodoscopes, EMC – electromagnetic calorimeter, *target* - polarized target.

reaction, namely, [1] at 24 GeV/c and [2] at 200 GeV/c. The proton beam of 70 GeV/c momentum was extracted from U70 by the thin Si crystal bent under 80 mrad [3].

The beam parameters measured by counters S1-S3 and hodoscopes H1,H2 (see Fig.1) were: intensity $\approx 1 \cdot 10^6$ p/cycle, $\sigma(x) = 4$ mm, $\sigma(x') = 2$ mrad, $\sigma(y) = 3$ mm, $\sigma(y') = 1$ mrad. The frozen spin polarized target (PT) was made of propandiole, had a length of 200 mm and a diameter of 20 mm. The average polarization was $\approx 80\%$.

Two electromagnetic calorimeters EMC1 (480 lead glass counters (LGC)) and EMC2 (144 LGC) were used. They were positioned at a π^0 emission angle of 90° in c.m.s. at 6.9 m and 2.8 m from the PT respectively. Both calorimeters were composed from the same lead glass cell of size $3.8 \times 3.8 \times 45$ cm^3 . The calorimeters were calibrated with an electron beam of 26.6 GeV. The energy resolution achieved was $\frac{\sigma(E)}{E} \approx 2.5\%$. The rate of data taking for pp-interactions was such that during 10 days running $2 \cdot 10^7$ events were accumulated, while for $\pi^- p$ it was around 300 events per cycle and 10^8 events were accumulated for 30 days.

The final results on the analyzing power for the reaction $p + p_\uparrow \rightarrow \pi^0 + X$ at 70 GeV are presented in Fig.2a (open squares). It is evident that the SSA is compatible with zero. The study of the reaction $\pi^- + p_\uparrow \rightarrow \pi^0 + X$ is similar to the previous one. The beam parameters were: intensity $1 \cdot 10^6$ p/cycle, momentum 40 GeV/c, the round beam size of 3.5 mm. In this case we use only one EMC with 720 LGC of the same type as before. The calorimeter was positioned at A distance of 2.3 m from the PT and the angle was varied. More details of the second experiment may be found in paper [4]. The results are presented in the Fig.2b (open square). If we average SSA over the interval $-0.8 < x_F < -0.4$ we get $A_N(\pi^0) = -(13.8 \pm 3.8)\%$, that is an essential spin effect. But for the interval $-0.4 < x_F < -0.1$ $A_N(\pi^0) \approx 0$.

A general overview of the theoretical interpretations of our data at 40 and 70 GeV/c leads to the following understandings. Most of the theoretical models based on pQCD are not applicable to our energy and transverse momentum ranges. There are several phenomenological models (orbiting quarks, Siverson and Collins mechanisms, high twist effects, etc.) explaining some but not all aspects of the data. In this situation we applied the model proposed recently in paper [5] to the present data. The slope parameter needed in this model for the calculation was taken either from our experimental data or from the published data [6]. The SSA results for the reaction $p + p_\uparrow \rightarrow \pi^0 + X$ at 70 GeV/c in CR [7] are presented in Fig.2a. The sign of the SSA as well as of x_F are changed in order to compare them with the E704 data presented in the same Figure. The dotted line is a prediction of the CMSM for 70 GeV/c, and the solid line is for the E704 data (see details in [5]). There is fair consistency between the experimental data and the model prediction.

New data on $\pi^- p_\uparrow \rightarrow \pi^0 X$ at 40 GeV/c are presented in Fig.2b (open squares). Since in this case x_F and x_T are comparable in magnitude, $A_N(in\%)$ is plotted versus x_R ($x_R = \sqrt{x_F^2 + x_T^2}$) using the following formula

$$A_N(\pi^0) = 11.7 \frac{x_R^{1.5}}{[x_R^{0.5} + 0.64 \cdot (1 - x_R)^{4.5}]}. \quad (1)$$

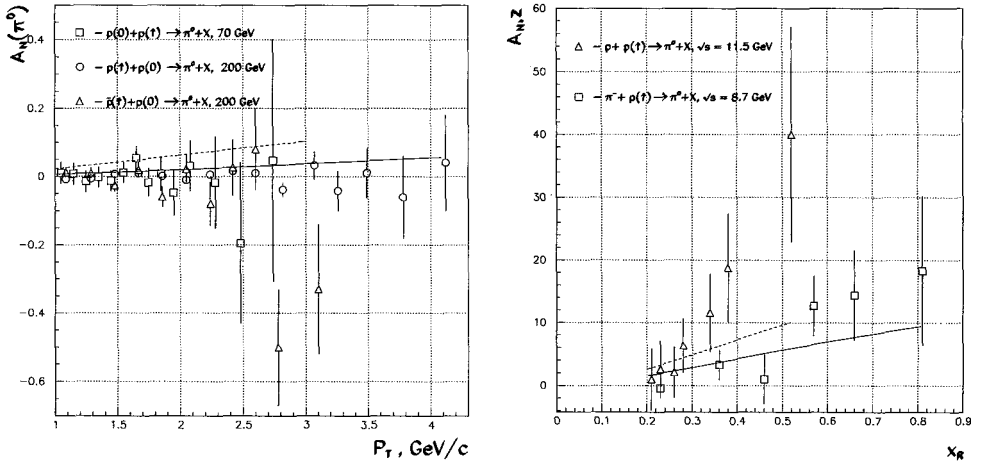


Fig. 2. SSA vs p_T for reaction $p + p_{\uparrow} \rightarrow \pi^0 + X$ (left) and SSA vs x_F for the reaction $\pi^- + p_{\uparrow} \rightarrow \pi^0 + X$ (right). Lines are the model prediction (see text)

As seen from Fig.2b (solid line) there is a fairly good description of our data. In the same Fig.2b the SSA data for reaction $pp_{\uparrow} \rightarrow \pi^0 X$ at 70 GeV/c are presented. A detailed discussion was given by Dr. Mochalov in this session [8]. The CMSM predicts the same formula as above but with parameter 20.0 replacing 11.7. In this case the model prediction (the dashed line) does not contradict the experimental data in the frame of the given error bars.

Summary

The experimental studies of the analyzing powers of reactions $p + p_{\uparrow} \rightarrow \pi^0 + X$ at 70 GeV and $\pi^- + p_{\uparrow} \rightarrow \pi^0 + X$ at 40 GeV allow us to draw the following conclusions. For the first time the single spin asymmetry was measured in the polarized target fragmentation region for reaction $\pi^- + p_{\uparrow} \rightarrow \pi^0 + X$ at 40 GeV/c. For the kinematical domain $-0.8 < x_F < -0.4$, $1 < p_T(\text{GeV}/c) < 2$, $A_N = -(13.8 \pm 3.8)\%$, while in the region $-0.4 < x_F < -0.1$, $0.5 < p_T(\text{GeV}/c) < 1.5$ the asymmetry is compatible with zero. The asymmetry measured in the CR is zero for region $1 < p_T(\text{GeV}/c) < 3$ for the reaction $p + p_{\uparrow} \rightarrow \pi^0 + X$ at 70 GeV/c. The results are consistent with E704 data at 200 GeV/c.

References

1. J. Antille *et al.* *Phys. Rev. Lett.* **B94**, 523 (1980).
2. D.L. Adams *et al.* *Phys. Rev.* **D53**, 4747 (1996).
3. A.A. Asseev *et al.* *Nucl. Instr. Meth.* **A330** (1993) 39.
4. A.N. Vasiliev *et al.* *Phys. of Atom. Nucl.* **67**, No 8, 1495 (2004); *Yad. Fizika* **67**, No 8, 1520 (2004); Prepr. IHEP 2003-21.
5. S.B. Nurushev and M.G. Ryskin, Preprint IHEP 2004-16, Protvino, 2004, Russia; hep-ph/0405041.
6. G. Donaldson *et al.* *Phys. Rev. Lett.* **36**, 1110 (1976).
7. A.N. Vasiliev *et al.* *Phys. of Atom. Nucl.* **67**, No 8, 1487 (2004), *Yad. Fizika* **67**, No 8, 1512 (2004); Prepr. IHEP 2003-22.
8. V.V. Mochalov talk, this conference.

**A_N AT SMALL NEGATIVE VALUES OF x_F IN THE REACTION
 $p + p_{\uparrow} \rightarrow \pi^0 + X$ AT 70 GeV AND UNIVERSAL THRESHOLD IN INCLUSIVE
PION PRODUCTION***

A. M. DAVIDENKO, A. A. DEREVSCHIKOV, V. N. GRISHIN, V. Y. KHODYREV, Y. A. MATULENKO,
Y. M. MELNICK, A. P. MESCHANIN, V. V. MOCHALOV, L. V. NOGACH, S. B. NURUSHEV,
P. A. SEMENOV, A. F. PRUDKOGLYAD, K. E. SHESTERMANOV, L. F. SOLOVIEV, A. N. VASILIEV,
A. E. YAKUTIN

Institute for High Energy Physics, Protvino, Russia

N. S. BORISOV, A. N. FEDOROV, V. N. MATAFONOV[†], A. B. NEGANOV, Y. A. PLIS, Y. A. USOV

JINR, Dubna, Russia

A. A. LUKHANIN

KhPTI, Kharkov, Ukraine

This paper continues the series of Single Spin Asymmetry (SSA) π^0 inclusive measurements carried out at the Protvino 70 GeV accelerator. The asymmetry in the polarized target fragmentation region grows in absolute value with decreasing x_F , and becomes $(-16 \pm 5)\%$ at $-0.4 < x_F < -0.25$. The result of the current experiment is in agreement with the universal threshold in pion asymmetries.

The experiment was carried out at the PROZA-M experimental set-up [1] at the U-70 Protvino accelerator at 1996. In previous measurements performed in Protvino [2]–[5] we observed significant asymmetries in the reaction $\pi^- + p_{\uparrow} \rightarrow \pi^0 + X$ at the central and the polarized target fragmentation regions, whereas the asymmetry in the reaction $p + p_{\uparrow} \rightarrow \pi^0 + X$ in the central region was compatible with zero. The present paper is devoted to SSA measurement at small negative values of x_F in the reaction $p + p_{\uparrow} \rightarrow \pi^0 + X$.

A 70 GeV proton beam extracted from the U-70 main ring with the use of a bent crystal had an intensity in the range $(3-6) \cdot 10^7$ protons/10 second cycle. The frozen polarized target ($C_3H_8O_2$) with a dilution factor $D \approx 10$ operated with 80% average polarization (see Fig. 1). γ -quanta were detected

*This work is supported by Russian Foundation for Basic Research, grant 03-02-16919.

[†]Deceased

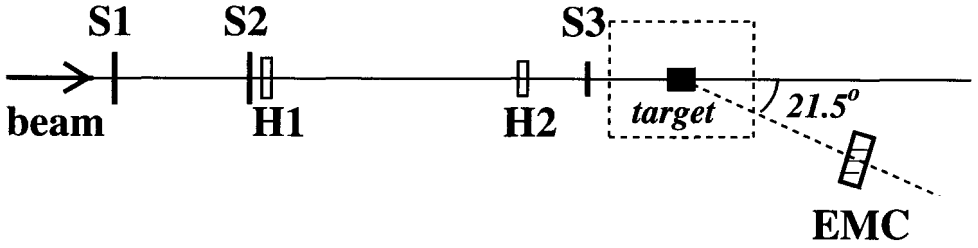


Fig. 1. Experimental set-up PROZA-M; S1-S3 – scintillation counters, H1-H2 – two-coordinate hodoscopes, EMC – electromagnetic calorimeter, *target* - polarized target.

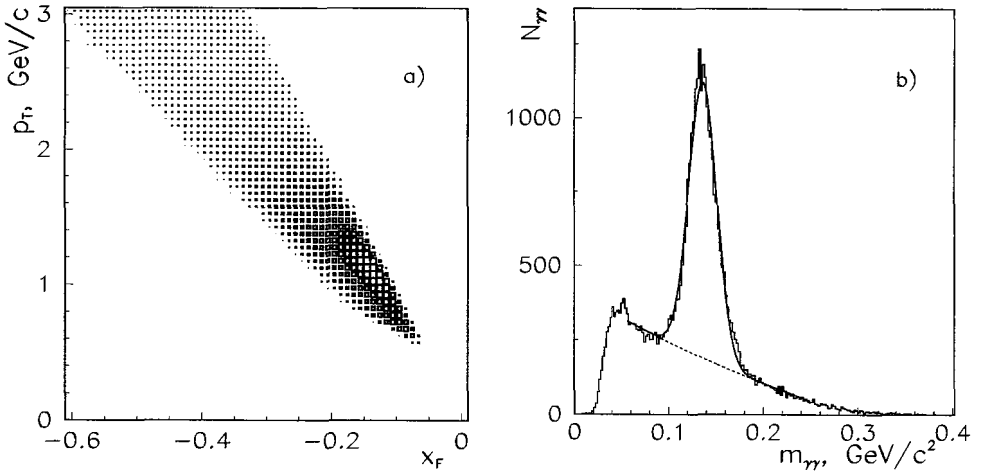


Fig. 2. Two-dimensional distribution versus p_T and x_F (a) and two-gamma mass spectrum (b)

by an electromagnetic calorimeter (144 lead glass counters) placed 2.8 m downstream target at 21.5° to the beam direction. Three scintillation counters S1-S3 and two hodoscopes H1-H2 were used for beam particle detection and the zero level trigger. The first level trigger provided event selection with more than 1 GeV energy deposited in the calorimeter.

The asymmetry was calculated as:

$$A_N = \frac{D(x_F, p_T)}{P_{target}} \cdot A_N^{raw}(x_F, p_T) = \frac{D(x_F, p_T)}{P_{target}} \cdot \frac{n_\uparrow(x_F, p_T) - n_\downarrow(x_F, p_T)}{n_\uparrow(x_F, p_T) + n_\downarrow(x_F, p_T)} \quad (1)$$

where P_{target} is the average target polarization, and D is the target dilution factor. Since the azimuthal angle was close to 180° , we neglected the SSA dependence on $\cos \phi$.

Measurements were performed at narrow solid angles (see Fig.2); the π^0 -mass width was in the range 11-17 MeV/c^2 for different kinematic regions.

The false asymmetry was compatible with zero (Fig. 3). The asymmetry was also close to zero at small absolute values of x_F and grew in magnitude as $|x_F|$ increased. The combined result $(-16 \pm 5)\%$ is in agreement with other experiments in the polarized particle fragmentation region: $A_N = (12.4 \pm 1.4)\%$ at E704 (FNAL) [6], $(14 \pm 4)\%$ at STAR (BNL) [7] in the reaction $p_\uparrow + p \rightarrow \pi^0 + X$ and $(13.8 \pm 3.8)\%$ in the reaction $\pi^- + p_\uparrow \rightarrow \pi^0 + X$ at PROZA-M (Protvino) [3].

The result is in good agreement with the observation of the universal threshold E_0^{cms} in SSA if the particle is formed from a valence quark, the polarization of which follows the nucleon polarization [8]. The summary of the universal threshold search for non-zero results is presented in Table 1. All the data were fitted by the function:

$$A_N = \begin{cases} 0 & , \text{if } E < E_0 \\ k \cdot (E - E_0) & , \text{if } E \geq E_0 \end{cases} \quad (2)$$

The value of E_0^{cms} equals (1.5 ± 0.2) GeV for the current experiment.

We are planning to carry out a new experiment to improve the accuracy and to measure the asymmetry at different angles. A detector with 720 cells will be placed at 30° to cover the $-0.8 < x_F < -0.25$ region.

Table 1. The search for the universal threshold in the centre of mass frame for different experiments

Reaction	Energy	E_0^{cms} , GeV	χ^2/N	$k \cdot (E_{max}^{cms} - E_0^{cms})$, %
$p_\uparrow + p \rightarrow \pi^+ + X$	13.3	1.26 ± 0.1	0.9	52 ± 6
$p_\uparrow + p \rightarrow \pi^+ + X$	18.5	1.46 ± 0.15	0.85	63 ± 16
$p_\uparrow + p \rightarrow \pi^+ + X$	21.92	1.57 ± 0.1	0.9	68 ± 6
$p_\uparrow + p \rightarrow \pi^+ + X$	40	1.64 ± 0.15		
$p_\uparrow + p \rightarrow \pi^+ + X$	200	1.68 ± 0.25	1.1	52 ± 5
$\pi^- + p_\uparrow \rightarrow \pi^0 + X$	40	1.67 ± 0.15	1.5	107 ± 26
$\pi^- + p_\uparrow \rightarrow \pi^0 + X$	40	1.76 ± 0.2	0.7	36 ± 14
$p + p_\uparrow \rightarrow \pi^0 + X$	24	1.7 ± 0.15	0.6	334 ± 165
$p + p_\uparrow \rightarrow \pi^0 + X$	70	1.5 ± 0.2	0.15	50 ± 15
$p_\uparrow + p \rightarrow \pi^0 + X$	200	2.1 ± 0.3	0.5	26 ± 5
$\bar{p}_\uparrow + p \rightarrow \pi^0 + X$	200	0.9 ± 0.6	0.5	13 ± 4
$p_\uparrow + p \rightarrow \pi^- + X$	21.92	1.95 ± 0.1	0.5	-87 ± 11
$p_\uparrow + p \rightarrow \pi^- + X$	200	2.9 ± 0.2	< 0.1	-51 ± 6
$\bar{p}_\uparrow + p \rightarrow \pi^+ + X$	200	3.1 ± 0.5	< 0.1	-59 ± 16
$\bar{p}_\uparrow + p \rightarrow \pi^- + X$	200	1.0 ± 2.2	0.1	25 ± 15

Conclusion

- SSA in the reaction $p + p \rightarrow \pi^0 + X$ was measured at 70 GeV in the kinematic region $-0.4 < x_F < -0.1$ and $0.9 < p_T < 2.5$ GeV/c.
- The asymmetry is zero at $-0.2 < x_F < -0.1$ and $0.5 < p_T < 1.5$ GeV/c, and $A_N = (-16 \pm 5)\%$ at $-0.4 < x_F < -0.25$ and $1.3 < p_T < 3.0$ GeV/c.
- The asymmetry starts to grow at $E_0^{cms} = (1.5 \pm 0.2)$ GeV in agreement with the universal threshold. This behaviour can be explained by the constituent quark model [9].

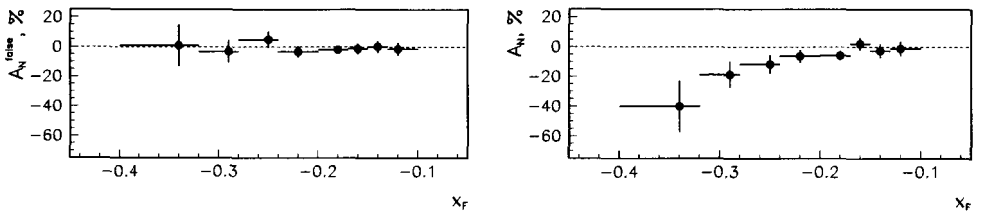


Fig. 3. False (left) and real (right) π^0 asymmetries

— New measurements will be carried out in the next two years of the $p + p_{\uparrow} \rightarrow \pi^0 + X$ reaction at the target fragmentation region.

References

1. V.D. Apokin *et al.* *Instrum. Exp. Tech.* **41**, 464 (1998).
2. V.D. Apokin *et al.* *Phys. Lett.* **B243**, 461 (1990).
3. A.N. Vasiliev *et al.* *Phys. of Atom. Nucl.* **67**, No 8, 1495 (2004); *Yad. Fizika* **67**, No 8, 1520 (2004); Prepr. IHEP 2003-21.
4. A.N. Vasiliev *et al.* *Phys. of Atom. Nucl.* **67**, No 8, 1487 (2004), *Yad. Fizika* **67**, No 8, 1512 (2004); Prepr. IHEP 2003-22.
5. S.B. Nurushev talk, this conference.
6. D.L. Adams *et al.* *Z.Phys.* **C56**, 181 (1992).
7. L.C. Bland *AIP Conf.Proc.* **675**, 98 (2003); e-Print Archive: hep-ex/0212013.
8. V. Mochalov and A. Vasiliev *Phys. of Atom. Nucl.* **67**, No 12, 2169 (2004); e-Print Archive: hep-ex/0312007.
9. V. Mochalov, S. Troshin and A. Vasiliev *Phys. Rev.* **D69**, 077503 (2004); e-Print Archive: hep-ph/0310224.

In this reaction Λ^0 is produced polarized, and this polarization is a function of x_F , P_T , and $M_{\Lambda^0 K^+}$.

This sample consists of fully reconstructed pp events at 27.5 GeV. All final-state particles are measured and identified. Two previous measurements have been published [5] of Λ^0 polarization from

$$pp \rightarrow p\Lambda^0 K^+ \pi^+ \pi^- \pi^+ \pi^- \pi^+ \pi^- \quad (2)$$

$$pp \rightarrow p\Lambda^0 K^+ (\pi^+ \pi^-)^N; N = 1, 2, 3, 4. \quad (3)$$

at 27.5 GeV, together with one measurement [2] of

$$pp \rightarrow p\Lambda^0 K^+. \quad (4)$$

at 800 GeV.

2. The BNL 766 Experiment and Λ^0 Data

The data for this study were recorded at the Alternating Gradient Synchrotron (AGS) at Brookhaven National Laboratories in experiment E766, described in detail elsewhere [6]. For this study, 1973 Λ^0 's satisfied the selection criteria reported elsewhere [6].

3. Λ^0 Polarization and Results

This study of Λ^0 polarization explores the dependence of the polarization on the kinematic variables P_T , x_F and $M_{\Lambda^0 K^+}$ in the final states represented by Eq. (1). The way these variables are defined and the way Λ^0 polarization is measured are explained elsewhere [5].

Λ^0 polarization has the same positive sign in both hemispheres $x_F > 0$ and $x_F < 0$, in contrast to Λ^0 polarization from the reactions of Eq. (2), which has opposite signs, negative in the $x_F > 0$ hemisphere and positive in the $x_F < 0$ one [2].

To improve the statistical power of the polarization measurements, Λ^0 polarizations from both hemispheres are summed directly. The results are shown in Figure 1, as a function of $M_{\Lambda^0 K^+}$. This Λ^0 polarization behaviour has been observed previously in other reactions [2]. A Monte Carlo analysis was used to study possible systematic effects, caused by finite acceptance and finite resolution, that might bias the Λ^0 polarization measurements. The Monte Carlo sample is generated with unpolarized Λ^0 's using a model for reactions (1) that faithfully reproduces all kinematic distributions. This sample of events is subjected to the same analysis programs and cuts used for the data. The measured polarization for this Monte Carlo sample, which is generated with zero polarization, is found to be consistent with zero as a function of x_F , P_T , and $M_{\Lambda^0 K^+}$.

In a second analysis that makes a direct comparison with data, Monte Carlo events are weighted by $(1 + \alpha \not{p} \cos \theta)$ with \not{p} measured, for each bin of $M_{\Lambda^0 K^+}$. The Λ^0 polarization in the Monte Carlo is in good agreement with the data, all the χ^2/dof between data and Monte Carlo distributions being close to 1. The $\cos \theta$ distributions are not quite linear, due to detector acceptance, and these acceptance induced variations in $\cos \theta$ are reproduced by the Monte Carlo.

Λ^0 polarization in reactions (1) depends on x_F , P_T , $M_{\Lambda^0 K^+}$; this polarization is similar to that determined in $pp \rightarrow p\Lambda^0 K^+$ at 800 GeV [2]. Therefore, provide that there is energy enough in the reaction to create Λ^0 , its polarization is independent of the beam energy.

References

1. K. Heller *et al*, Phys. Lett. **B68**, 480(1977). G. Bunce *et al*, Phys. Lett. **B86**, 386(1979).
2. T. Henkes *et al*, Phys. Lett. **B283**, 155(1992). J. Félix *et al*, Phys. Rev. Lett. **88**, 061801-4(2002).

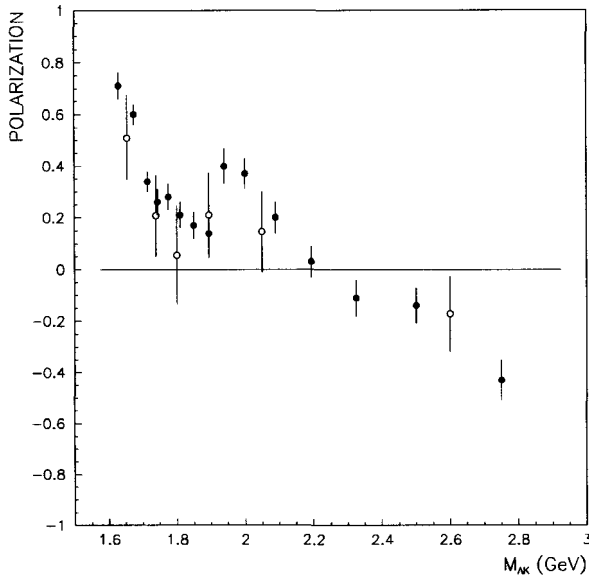


Fig. 1. Λ^0 Polarization as a function of the $M_{\Lambda^0 K^+}$ invariant mass. Open circles, this experiment; filled ones, Reference 2 (J. Félix *et al.*).

3. J. Duryea *et al.*, Phys. Rev. Lett. 67, 1193(1991). R. Rameika *et al.*, Phys. Rev. **D33**, 3172(1986). C. Wilkinson *et al.*, Phys. Rev. Lett. 58, 855(1987). B. Lundberg *et al.*, Phys. Rev. **D40**, 39(1989). F. Lomanno *et al.*, Phys. Rev. Lett. 43, 1905(1979). S. Erhan *et al.*, Phys. Lett. **B82**, 301(1979). F. Abe *et al.*, Phys. Rev. Lett. 50, 1102(1983). K. Raychaudhuri *et al.*, Phys. Lett. **B90**, 319(1980). K. Heller *et al.*, Phys. Rev. Lett. 41, 607(1978). F. Abe *et al.*, J. of the Phys. S. of Japan. 52, 4107(1983). P. Aahlin *et al.*, Lettere al Nuovo Cimento 21, 236(1978). A. M. Smith *et al.*, Phys. Lett. **B185**, 209(1987). V. Blobel *et al.*, Nuclear Physics **B122**, 429(1977).
4. T. A. DeGrand *et al.*, Phys. Rev. **D24**, 2419(1981). B. Andersson *et al.*, Phys. Lett. **B85**, 417(1979). J. Szweid *et al.*, Phys. Lett. **B105**, 403(1981). K. J. M. Moriarty *et al.*, Lett. Nuovo Cimento 17, 366(1976). S. M. Troshin and N. E. Tyurin, Sov. J. Nucl. Phys. 38, 4(1983). J. Soffer and N.E. Törnqvist, Phys. Rev. Lett. 68, 907(1992). Y. Hama and T. Kodama, Phys. Rev. **D48**, 3116(1993). R. Barni *et al.*, Phys. Lett. **B296**, 251(1992). W. G. D. Dharmaratna and G. R. Goldstein, Phys. Rev. **D53**, 1073(1996). W. G. D. Dharmaratna and G. R. Goldstein, Phys. Rev. **D41**, 1731(1990). S. M. Troshin and N. E. Tyurin, Phys. Rev. **D55**, 1265(1997). L. Zuo-Tang and C. Boros, Phys. Rev. Lett. 79, 3608(1997).
5. J. Félix *et al.*, Phys. Rev. Lett. 76, 22(1996). J. Félix, Ph.D. thesis, Universidad de Guanajuato, México, 1(1994). J. Félix *et al.*, Phys. Rev. Lett. 82, 5213(1999).
6. J. Uribe *et al.*, Phys. Rev. D49, 4373(1994). E. P. Hartouni *et al.*, Nucl. Inst. Meth. A317, 161(1992). E. P. Hartouni *et al.*, Phys. Rev. Lett. 72, 1322(1994). E. E. Gottschalk *et al.*, Phys. Rev. D53, 4756(1996). D. C. Christian *et al.*, Nucl. Instr. and Meth. A345, 62(1994). B. C. Knapp and W. Sippach, IEEE Trans. on Nucl. Sci. NS 27, 578(1980). E. P. Hartouni *et al.*, IEEE Trans. on Nucl. Sci. NS 36, 1480(1989). B. C. Knapp, Nucl. Instrum. Methods **A289**, 561(1980).

SPIN POLARIZATION OF HYPERONS IN HADRON-HADRON INCLUSIVE COLLISIONS

K. KUBO

School of Science, Tokyo Metropolitan University, Hachioji, Japan

K. SUZUKI

Division of Liberal Arts, Numazu College of Technology, Numazu, Japan

We discuss the interplay of the scalar and vector diquarks which determine the characteristics of the spin polarization as functions of p_T and x_F in a wide kinematical range. We demonstrate a significant effect of quark masses on the pair-creation probabilities from vacuum in $pp \rightarrow \Sigma^- X$ and $\gamma p \rightarrow \Lambda X$ collisions, and also a remarkable correction induced by the diquark form factor in $\Sigma^- p \rightarrow \Lambda X$ collision.

1. Introduction; the global model

High energy hadron-hadron collisions produce various hyperons, in which large spin polarizations perpendicular to a production plane are observed at high Feynman- x (x_F) and low transverse momentum p_T . For these collisions, we have proposed a global model on the basis of quark rearrangements concept [1]. In order to produce a final state hyperon at high x_F , we consider possible rearrangement processes allowed by $SU(6)$ symmetry, where valence quarks (diquarks) from the projectile combine with sea quarks created from the vacuum. Evaluation of rearrangement amplitudes in terms of relativistic quarks and diquarks with the confinement force in fact provides the spin asymmetry. We assume that the polarization is principally brought about by the rearrangement mechanism, while all other processes, such as standard fragmentation, which usually comes from showers of partons rather than from the valence quark of the projectile and is thus negligible at high x_F , are spin-independent. If this concept would work for the various hadron productions, we could consistently apply it to evaluations of the spin observables by any projectile collisions.

We have applied the model to the existing data and obtained a general success for the spin observables induced by the strong [1, 2], electromagnetic [3–5] and weak [4, 5] interactions, and also for the several so-called puzzling cases [6]. In this presentation, and from our recent work, we are concerned about two indications: the quark mass mechanisms (QMM); and the form factor dynamics (FFD) for the polarizations in $pp \rightarrow \Sigma^- X$, $\gamma p \rightarrow \Lambda X$ and $\Sigma^- p \rightarrow \Lambda X$ collisions.

2. The quark mass mechanisms

· The spin polarization of $pp \rightarrow \Sigma^- X$ at 400 GeV/c

Our global model calculation is compared to the Σ^- production data in Fig. 1; it predicts a large neg-

ative polarization, contrary to the positive values observed. In this process, a d -valence quark from the projectile p combines with scalar $(ds)^0$ or vector $(ds)^1$ diquarks created from the vacuum. The discrepancy arises from too much enhancement of the vector diquark contribution. To resolve the problem, we shall take into account the mass dependence of probabilities of creating sea diquarks. Within our framework, sea quarks are assumed to be produced non-perturbatively by string breaking in the hadronization process. In previous work [1, 3], we took the same production rate for the creation of all kinds of quarks. However, it has been suggested that probabilities of the pair-creation certainly depend on their masses [7]. Indeed, a simple calculation yields a rate of the pair-creation as, $C_{QMM}^i = \exp[-\pi(m_i^2 + k_T^2)/\kappa]$, where m , k_T , κ are the constituent mass of quark(s) i , the transverse momentum, and the string tension 1 GeV/fm, respectively. For the diquark creation we note that the diquark mass depends on its internal spin state, and the scalar diquark mass m_S is less than the vector one m_V . This is due to a property of the interaction acting between the two quarks: attractive for $S = 0$, while repulsive for $S = 1$. With $m_S = 0.8\text{GeV}$ and $m_V = 1\text{GeV}$, the spin polarization in our model [1] is then corrected to the form

$$P(x_F, p_T) = \frac{R_S \langle C_{QMM}^S \sigma_{dep}^S \rangle + R_V \langle C_{QMM}^V \sigma_{dep}^V \rangle}{\langle C_{QMM}^S \sigma_{ind}^S \rangle + \langle C_{QMM}^V \sigma_{ind}^V \rangle} \quad (1)$$

The correction is expected to reduce the vector diquark contribution dramatically, and in fact we have found a significant improvement in the calculation, as we can see in Fig.1.

·The spin polarization of $\gamma p \rightarrow \Lambda X$ at $v = 16\text{GeV}$

Further application of QMM has been made for the spin polarization of $\gamma p \rightarrow \Lambda X$ extracted from HERMES data. In this case, u, d, s quarks from γ contribute to the Λ production through the rearrangements $u + (ds)^{0,1}$, $d + (us)^{0,1}$, and $s + (ud)^0$. Our original model predicts the dashed curve in Fig.2, which is too big and negative, in contrast to the positive observation. When we include QMM we get the solid curve, which now reproduces well the observation with $m_{ud}^S = 0.6\text{GeV}$ and $m_{us}^V = m_{us}^S = 1\text{GeV}$.

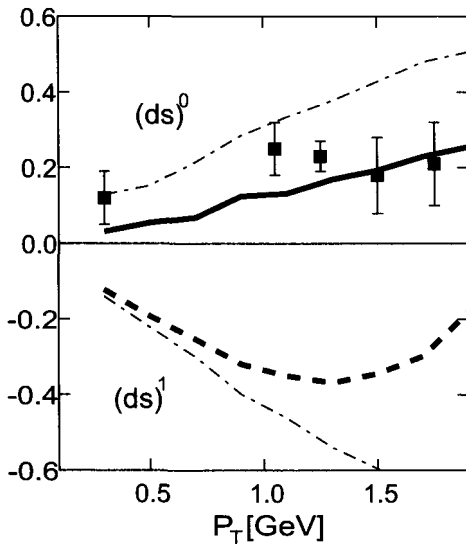


Fig. 1. Polarization of $pp \rightarrow \Sigma^- X$. The dashed and solid curves show the results without and with QMM.

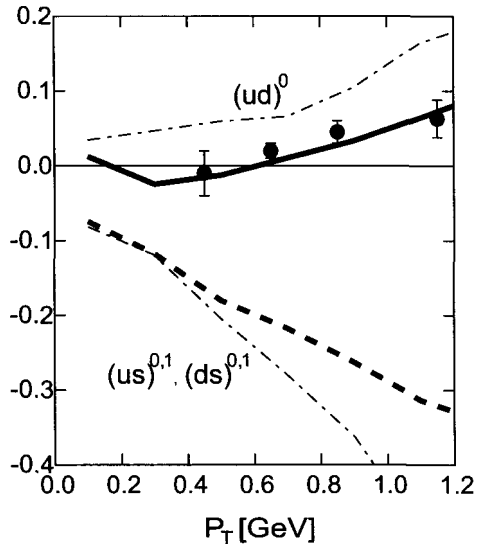


Fig. 2. Polarization of $\gamma p \rightarrow \Lambda X$. Notations are the same as those of Fig.1.

3. The form factor dynamics: $\Sigma^- p \rightarrow \Lambda X$ at 340 GeV/c

The polarization of $\Sigma^- p \rightarrow \Lambda X$ in a wide kinematical range has been fully observed. The most notable point in the observation is the change of sign of its p_T distribution around $x_F = 0.4$, the shape of which may not be reproduced by any theoretical calculation using the existing models. Our straight-forward calculation with the rearrangements $(ds)^0 + u$ and $(ds)^1 + u$ predicts only a monotonically increasing result in Fig.3a due to the dominance of the positive $(ds)^1$ contribution.

We now consider the property of the diquark wave functions in configuration space, which should be different between the scalar $(ds)^0$ and vector $(ds)^1$ diquarks due to the attractive or repulsive nature of the colour magnetic force. This interaction may induce a difference of sizes of diquarks, r_S and r_V , and indeed such a difference is observed within the rigorous three-body calculation of baryon structure [8].

To take it into account, it may be reasonable to introduce a form factor for the quark-diquark interaction vertex. We take a form $C_{FFD}^{S,V} = \exp(-r_{S,V}^2 p_T^2)$ to be multiplied by each cross section, similarly to eq. (1) with $r_S = 0.5\text{fm}$ and $r_V = 0.7\text{fm}$. We can see in Fig.3b that the FFD correction reduces the monotonic increase of the vector component previously seen. Therefore the new calculation with FFD provides a remarkable change and improves the calculation.

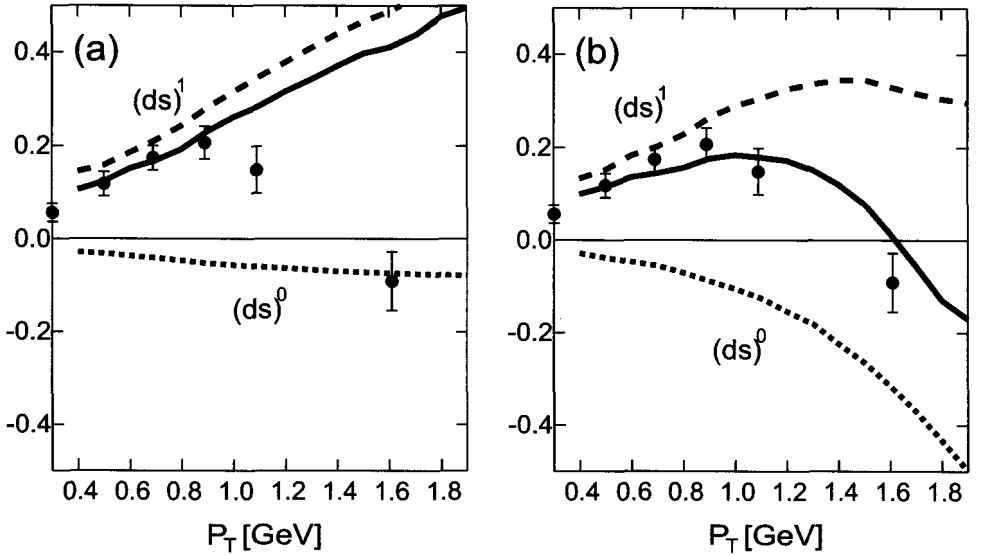


Fig. 3. Polarization of $\Sigma^- p \rightarrow \Lambda X$ without FFD (left) with FFD (right).

4. Conclusion

We discussed inclusive hyperon production and spin polarizations. We concentrated on the interplay of the scalar and vector diquarks. It has been found that in general the vector component shows too much predominance. Then we considered the quark mass mechanisms, which provide a significant improvement in the calculations by reflecting difference in masses of diquarks created from the vacuum. Form factor dynamics due to the diquark internal structure has been also found to provide a remarkable change in the calculation.

References

1. Y. Yamamoto, K.-I. Kubo and H. Toki, *Prog. Theor. Phys.* **98** (1997) 95.
2. K. Suzuki et al., *Mod. Phys. Lett.* **A14** (1999) 1403.
3. K. Suzuki, N. Nakajima, H. Toki and K.-I. Kubo, proceedings of the 14th Intern. Spin Phys. Symp. (Osaka 2000), *AIP Proc.* **570** (2001) 499.
4. K.-I. Kubo, K. Suzuki and N. Nakajima, *Proc. Symm. and Spin (Praha 2001)*, *Czech. J. Phys.* **52** (2002) C91.
5. K.-I. Kubo and K. Suzuki, proceedings of the 10th Intern. Conf. Nucl. Reaction Mechanisms (Varenna 2003), (2003) 559.
6. K.-I. Kubo, Y. Yamamoto and H. Toki, *Prog. Theor. Phys.* **101** (1999) 615.
7. See e. g., *The Lund Model*, Bo Andersson (Cambridge Univ. Press, 1998).
8. E. Hiyama et al., *Prog. Theor. Phys.* **112** (2004) 99.

HYPERON POLARIZATION IN UNPOLARIZED hh/hA COLLISIONS AND SOME RELATED PROBLEMS

Z. LIANG

Department of physics, Shandong University, Shandong, China

We proposed a picture that relates the transverse hyperon polarization observed in unpolarized hh/hA collisions to the left-right asymmetries observed in singly polarized hh collisions. We present the different ingredients of the picture and some of the main results, and discuss dedicated tests of them.

1. Introduction

There are two types of striking spin effect in inclusive production processes in high energy hh/hA collisions [1]: hyperon polarization (P_H) in unpolarized collisions, and left-right asymmetry (A_N) in singly polarized reactions. In both cases, we consider $AB \rightarrow hX$ and express the cross-section as, $d\sigma = d\sigma_0(1 + \alpha s \cdot n)$, where n is the normal to the production plane. For unpolarized reactions, s is taken as the spin of the produced $h = H$, while for the case of transversely polarized A (or B), $s = s_A$. P_H and A_N are respectively defined as the ratio of the difference of the cross sections for $n||s$ and $n||-s$ to the sum of them in the corresponding case. The definitions are quite similar. The experimental data also show the same features: both A_N and P_H are significant for large x_F and moderate p_T ; both of them depend on the flavour of the produced hadron; and both of them depend on the flavour of the incident hadron.

Inspired by these similarities, we proposed an approach [2, 3] to understand the origin(s) of P_H by relating it to A_N . We pointed out that these two striking spin phenomena should be closely related to each other and have the same origin(s). In the following, I will present the major ingredients of the proposed picture, the main results, and dedicated tests.

2. The picture and results

The physical picture proposed can be summarized as follows [2, 3]:

(i) Hadrons in the beam fragmentation region of $P + T$ collision are products of the following direct-fusion processes: (a) $q_v^P + \bar{q}_s^T \rightarrow M$, (b) $q_v^P + (q_s q_s)^T \rightarrow B$, and (c) $(q_v q_v)^P + q_s^T \rightarrow B$. Here, the superscript denotes projectile or target; the subscript denotes valence or sea.

(ii) In direct-fusion process (a) and (b), there exists a spin-correction so that the cross-section is of the form $\sigma = \sigma_0(1 + 2Cs_{q_v} \cdot n)$.

(iii) SU(6) wave-function is used to connect the polarizations of the quark and the produced hadron that contains the quark.

(iv) Since P has three valence quarks, direct fusion (c) is accompanied by (a), and the associatively produced M and B move in opposite directions.

(v) Spins of q_s and \bar{q}_s in the associated direct-fusion processes (a) $q_v^P + \bar{q}_s^T \rightarrow M$, and (c) $(q_v q_v)^P + q_s^T \rightarrow B$ are anti-aligned.

Point (i) is independent of the spin properties and has been tested in unpolarized reactions. In fact it was inspired by the data analysis of Qch and recombination models by Das and Hwa in the 1970s. The number density of hadrons produced in direct fusion is calculated from the quark distributions. E.g, for $q_v^P + \bar{q}_s^T \rightarrow M$, we have, $D(x_F, M|s) = \kappa_M q_v^P(x^P) \bar{q}_s^T(x^T)$, where $x^P \approx x_F$ and $x^T \approx m_M^2/(sx_F)$, following from energy-momentum conservation in the direct fusion process, s is the total c.m. energy squared; and κ_M is a constant. The model has also experienced a number of other tests that have been summarized in [4].

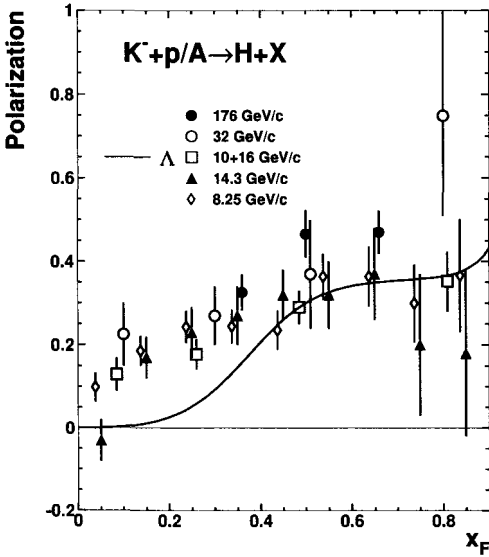


Fig. 1. P_Λ in $K^- + p \rightarrow \Lambda + X$ as a function of x_F . The figure is taken from [3].

tested.

Based on this picture, we can calculate P_H in hh/hA -collisions. We have applied the picture to pp , πp , $K^- p$ and $\Sigma^- p$ collisions since there are data for these reactions. We obtained the results for the polarization Λ , Σ^+ , Σ^- , Ξ^0 and Ξ^- in these collisions [2,3]. The qualitative features of the results are all in agreement with the available data [1].

As an example, we show P_Λ for $K^- + p \rightarrow \Lambda X$ in Fig.1. See [2, 3] for more.

3. Further tests

Encouraged by the success of the picture, we make further studies of different points mentioned in last section, in particular points (iii) and (v). Since we do not know how to derive them from QCD, we choose to apply them to some particularly chosen processes in order to make dedicated tests by experiments. Here I give a few examples.

First we found that Λ polarization in $pp \rightarrow p\Lambda K^+$ is ideal to test (v) [6]. This is because $pp \rightarrow p\Lambda K^+$ is the simplest channel for $pp \rightarrow \Lambda X$. Here, we definitely have Λ from $u_v d_v + s_s \rightarrow \Lambda$ and it is definitely associated with $u_v + \bar{s}_s \rightarrow K^+$. If (v) is true, $|P_\Lambda|$ in this channel should take the maximum among the different channels for $pp \rightarrow \Lambda X$, which is $P_\Lambda = -C = -0.6$. This result is in good agreement with the data [7] -0.62 ± 0.04 .

Another excellent place [8] that can give a good test of (v) is hyperon polarization in $e^- N \rightarrow e^- H K$. Here, the polarization of the quark which combines with a \bar{s} to form the K meson can be

Point (ii) is the starting point of the picture. It can be taken as derived from data on A_N . As we can see, if we apply it to $q_v(\uparrow) + \bar{q}_s \rightarrow M$, we find that M has an left-right asymmetry $A_N^D = C$. If we apply it to $q_v + q_s q_s \rightarrow B$ at a given n , we obtain a $P_{q_v} = C$ along n . By fitting the A_N data, we obtained [4] $C = 0.6$. In this way, we obtain the results for A_N in different reactions. We see in particular that the energy dependence of A_N comes merely from that of x^T as a result of energy-momentum conservation. It is interesting to see that the energy dependence obtained this way also agrees well with the data. (See [5]).

Point (iv) can be taken as a result of transverse momentum compensation among the valence quarks. It has a direct consequence that A_N for $p(\uparrow) + p \rightarrow \Lambda + X$ should be large and negative at large x_F . This is consistent with the E704 data [1]. (See [4]).

Point (v) is necessary to explain the large and negative Λ polarization in pp at large x_F based on (i) through (iv). It needs to be further

calculated in the deeply inelastic region. If (v) is true, we will obtain the polarization of the s quark that combines with the remaining di-quark of the incoming nucleon to form H . Together with the situation of the polarization of the diquark, we can calculate the polarization of H . Such calculations have been carried out. The results are given in [11]. Recently, the CLAS collaboration at CEBAF has measured the Λ polarization in this process [10]. The qualitative results are in agreement with our calculations.

Point (iii) is usually referred to as “spin transfer in fragmentation process”. This can be studied separately in reactions where quark fragmentation can be clearly separated and the quark polarization can be calculated. We found that Λ polarization in $e^+e^- \rightarrow Z^0 \rightarrow \Lambda X$ can give a good test of this point [12]. Experimental results have been obtained at LEP [11]. Calculations using different models have also been carried out. Unfortunately the data can not make a decisive judgement which model is most suitable. Although it seems that SU(6) picture results are favoured, other results are not excluded. We therefore made systematic calculations for other processes, such as polarized lepton-nucleon scattering in deeply inelastic region and $pp \rightarrow HX$ at very high p_T [13]. The results obtained can be used for further tests of (iii).

4. Summary

In summary, we proposed a picture that relates the transverse hyperon polarization observed in unpolarized hh/hA collisions to the left-right asymmetries observed in singly polarized hh collisions. The picture is composed of five different points. These points are based on different empirical facts and can be further tested by future experiments.

The author acknowledges the support of the Wong Kwan-cheng Education Foundation and the National Science Foundation of China (NSFC).

References

1. For a review of data, see e.g., A. Bravar, in Proc. of the 13th Inter. Sympo. on High Energy Spin Phys., Protvino, Russia, 1998, edited by N.E. Tyurin *et al.* (World Scientific, 1999), p. 167.
2. Z. Liang and C. Boros, Phys. Rev. Lett. **79**, 3608 (1997);
3. H. Dong and Z. Liang, Phys. Rev. D **70**, 014019 (2004).
4. Z. Liang, and C. Boros, Inter. J. Mod. Phys. **15**, 927 (2000).
5. H. Dong, F. Li, and Z. Liang, Phys. Rev. D **69**, 017501 (2004).
6. Z. Liang, and C. Boros, Phys. Rev. D **61**, 117503 (2000).
7. R608 Collaboration, T. Henkes, Phys. Lett. B **283**, 155 (1992).
8. Mac Mestayer, private communication (2000).
9. Z. Liang and Q. Xu, Phys. Rev. D **65**, 113012 (2002).
10. CLAS Collab., D.S. Carman *et al.*, Phys. Rev. Lett. **90**, 131804 (2003).
11. ALEPH Collab., D. Buskulic *et al.*, Phys. Lett. B **374**, 319 (1996); OPAL Collab., K. Ackerstaff *et al.*, Eur. Phys. J. C **2**, 49 (1998).
12. C. Boros and Z. Liang, Phys. Rev. D **57**, 4491 (1998).
13. C. Liu, and Z. Liang, Phys. Rev. D **62**, 094001 (2000); C. Liu, Q. Xu and Z. Liang, *ibid.* **64**, 073004 (2001); Q. Xu, C. Liu, and Z. Liang, *ibid.* **65**, 114008 (2002).

SPIN EFFECTS AT FRAGMENTATION OF GeV POLARIZED DEUTERONS INTO PIONS WITH LARGE TRANSVERSE MOMENTUM

L. ZOLIN, S. AFANASIEV, L. AZHGIREY, A. ISUPOV, A. KHRENOV, V. LADYGIN, A. LITVINENKO,
V. PERESEDOV, Y. PILIPENKO, V. ZHMYROV

Joint Institute for Nuclear Research, Dubna, Russia

I. DAITO, N. DOUSHITA, S. FUKUI, N. HORIKAWA, K. KONDO

Nagoya University, Nagoya, Japan

T. IWATA

Depat. of Physics, Faculty of Science, Yamagata University, Yamagata, Japan

V. PENEV

INPHE, Sofia, Bulgaria

The extracted polarized deuteron beam at the Dubna 10 GeV accelerator was used to study A_{yy} and A_y analyzing powers in the reaction $dA \rightarrow \pi(\theta)X$. Measurements at emission angles $\theta = 0, 135,$ and 180 mrad performed with 5 and 9 GeV/c deuterons showed a strong energy dependence of A_{yy} , and its linear rise at pion transverse momentum P_t from 0.4 to 0.8 GeV/c. The strong spin effects in this P_t -interval determined by D -state in the deuteron can be interpreted as evidence for correlation of meson-exchange (quark-exchange) currents in short range NN-interactions with orbital momentum of a strongly correlated NN-pair (6q-configuration).

The study of deuteron structure at small inter-nucleonic distances with both electromagnetic and hadron probes in the GeV energy region is continued. Several GeV polarized deuteron beams available in the 90s in Saclay and Dubna enabled us to examine predictions based on IA-calculations made with the use of realistic NN-potentials for spin observables in $A(d, p)X$, $H(d, p)d$ reactions at internal momentum up to $k=1$ GeV/c [1]. Measurements of tensor analyzing power T_{20} and polarization

transfer k_o^a showed considerable deviations from IA-predictions at $k > 0.25$ GeC/c ^b. In particular, no oscillating behaviour of T_{20} due to u - and w -component interference (Fig.1) was detected. A number of different models involving different mechanisms influencing the behaviour of the observables (FSI-interactions, $\Delta\Delta$ -, NN^* -, N^*N^* - components in DWF, P -wave admixture and so on) were proposed to explain this phenomenon. However, those ignoring quark-exchange mechanisms cannot give any satisfactory explanation of T_{20} or k_o behaviour in the whole k -region examined. This confirms that to study the spin structure of a strongly correlated NN-pair, non-nucleon degrees of freedom should be taken into account, including boson-exchange currents.

Hopefully, studying reactions $d \rightarrow \pi$ can reveal some new information on the contribution of meson components at small $r_{NN} (< 0.7 fm)$. At high enough transfer momentum the breakup process can be analyzed at the parton level as 6q-system fragmentation. The fact that pions bring spin information about parton PFF and PDF functions in the nucleon was demonstrated by large single spin asymmetries (SSA) in reactions $p(\bar{p})A \rightarrow \pi X$ within the beam fragmentation region at $P_t > 0.5$ GeV/c and $x_F > 0.5$ [2]. Thus, one could imagine remarkable spin effects in $d \rightarrow \pi$ at high P_t , x_F if similar mechanisms dominate in 3q- and 6q-system fragmentation.

Pions produced off a strong correlated NN-pair can be selected kinematically if the pions are observable with momentum well over the kinematical limit for free NN collisions, which is the cumulative regime [3]. The spectra of cumulative pions have a universal slope on the scale of the cumulative variable x_c^c . A detailed study of the $A(d,\pi)X$ reaction was performed at the Dubna 10 GeV accelerator, starting with a test of classical "direct" production mechanism (DPM) based on Fermi motion: $NN \rightarrow NN\pi$. The predicted behaviour of $T_{20}(k)$ at $\theta_\pi=0$ based on the DPM approach is shown at Fig.1. The DPM-hypothesis was not supported by the experiment as a working one [4]. This proved once again that an approach based on considerations of multi-quark configurations in nuclei [5] seems to be better grounded.

The experimental study of tensor and vector analyzing powers in the reactions $d + A \rightarrow \pi^\pm(\theta_\pi) + X$ was carried out with a focusing spectrometer [4] at P_d 5 and 9 GeV/c. The measurements with H-, Be-, and C-targets confirmed a weak A-dependence of observables in the beam fragmentation region. Three θ_π s were used: 0, 135, and 180 mrad. The summary data of tensor analyzing power vs x_c are shown in Fig.2. An analyzing power A_{yy} presentation in Cartesian form was used to compare data at different θ_s ($A_{yy} = -\frac{T_{20}}{\sqrt{2}}$ at $\theta=0$). A_{yy} was defined by measurements of pion yields at different tensor polarizations (p_{zz}) of the deuteron beam $\sigma(\theta) = \sigma_o(\theta)[1 + \frac{3}{2}p_{zz}A_y(\theta) + \frac{1}{2}p_{zz}A_{yy}(\theta)]$. An independent measurement of vector analyzing power A_y was carried out with a vector polarized deuteron beam at $P_d=9$ GeV/c (Fig.3). Comparing data for different P_d , θ_π , and q_π , one can come to the following conclusions.

The energy dependence of A_{yy} is very significant within the 5 to 9 GeV/c range: $A_{yy}(\pi^+)$ changes its sign at $P_d=5$ GeV/c within the emission angle from 0 to 180 mrad saving a weak x_c -dependence; at 9 GeV/c A_{yy} has negative sign and similar x_c -dependence for both π^\pm , demonstrating a steep rise with increasing θ_π at $x_c > 1$. This difference is related to the threshold behaviour of A_{yy} on the P_t -scale (Fig.4): an approximately linear increase of A_{yy} starts from $P_t \simeq 0.4$ GeV/c, as in the case of BNL-FNAL data for $p(\bar{p}) \rightarrow \pi$ [2]. One can conclude that the inner spin structure of both 3q- and 6q-systems begins to reveal itself when the parton mechanism starts working. According to the

^a T_{20} and k_o are related to S- and D-wave contributions in deuteron wave function (DWF) according to $T_{20} = -\frac{w^2 - \sqrt{2}uw}{u^2 + w^2}$, $k_o = \frac{u^2 - w^2 - uw/\sqrt{2}}{u^2 + w^2}$.

^b k stands for an internal momentum defined in light cone dynamics.

^c x_c is defined by 4-momentum conservation in the $ab \rightarrow hcX$ reaction: $x_c P_a + P_b = P_h + P_X$; x_c is quantitatively equal to the minimum beam fragmenting mass in M_N units to produce h if $P_{a,b}$ is the 4-momentum per nucleon. x_c rises to 1 for $NN \rightarrow \pi X$ and to 2 for $dp \rightarrow \pi X$. x_c from 1 to 2 corresponds to the cumulative region. At $E_d \gg M_N$ the scaling variable x_c is nearly the Feynman variable x_F ($\frac{x_c}{x_F} - 1 < 0.1$ at $E_d=9$ GeV) closely displaying a part of the momentum per nucleon of the fragmenting system carried out by the pion.

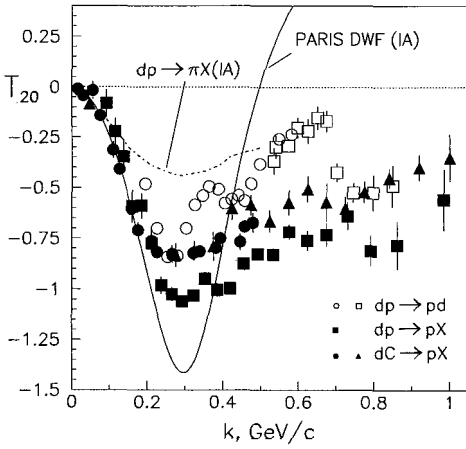


Fig. 1. Data for reactions induced by tensor polarized deuterons in the GeV region: breakup on H - and C -targets and dp backward elastic scattering. The dash-dotted line shows the IA prediction for $dp \rightarrow \pi X$.

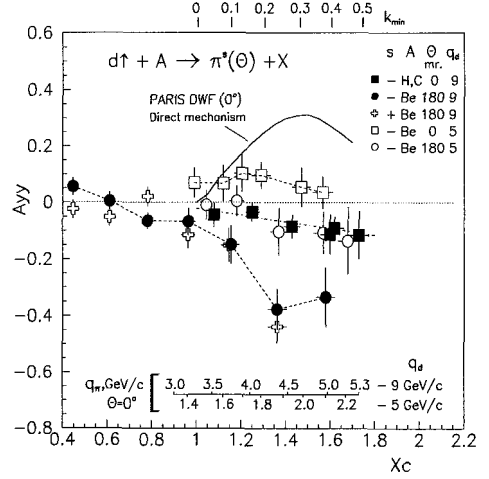


Fig. 2. A_{yy} vs x_c at fragmentation of 5 and 9 GeV tensor polarized deuterons. For $\theta=0^\circ$ are drawn the scales of pion momentum q_π and of minimum internal momenta k_{min} defined within the framework of DPM.

MQF-model [5] a cumulative hadron is produced at a soft hadronization of the spectator quark, which brings a high momentum as a result of momentum randomization in $6q$. In this case, the negative sign of A_{yy} indicates that the preferable direction of randomization is along the deuteron spin axis. The

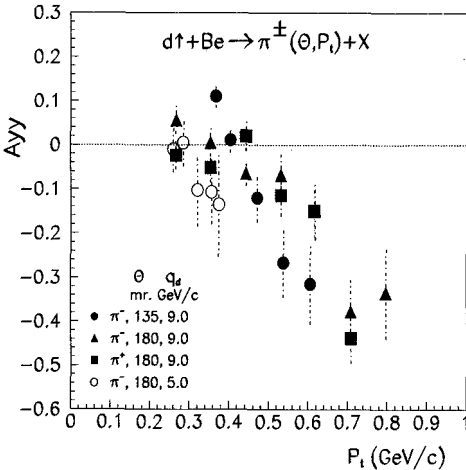


Fig. 3. Tensor analyzing power A_{yy} vs pion transverse momentum P_t .

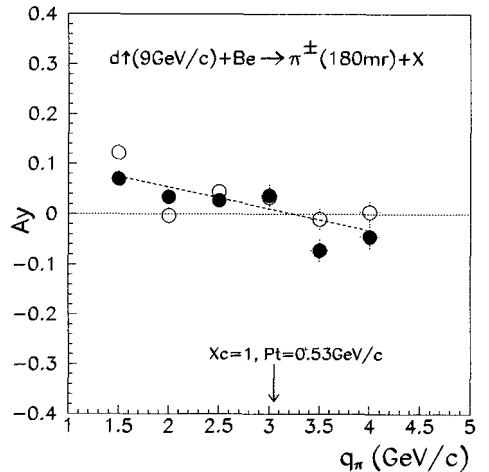


Fig. 4. Vector analyzing power A_y vs pion momentum q_π .

vector analyzing power A_y in $d \rightarrow \pi$ is small and has the same sign for π^\pm due to the quark content of the pn -system ($I=0$). A_y tends to rise with the negative sign at $x_c > 1$; it has to be checked in further

measurements at P_t from 0.7 to 0.9 GeV/c. Measurements within the same P_t -range are to be made to clarify the upper limit of the $A_{yy}(P_t)$ linear rise. To extract more information about the contribution of strangeness in the spin of a strong correlated NN-pair, a study of the reaction $d \rightarrow K^\pm$ in the cumulative regime is being considered. This can be done when the design parameters ($E_d = 12$ GeV, $I_d > 10^{10}$ d/spill) of the superconducting accelerator Nuclotron are reached.

References

1. V. Punjabi et al., Phys. Rev. **C39**, 608 (1989); T. Aono et al., Phys. Rev. Lett. **74**, 4997 (1995); V. Punjabi et al., Phys. Lett. **B350**, 178 (1995); L.S. Azhgirey et al., Phys. Lett. **B387**, 37 (1996) and Phys. Lett. **B391**, 22 (1997).
2. S.B.Nurushev, Intern. jour. of Modern Physics a, Vol. 12, No. 20 (1997) 3433.
3. A.M.Baldin, Nucl. Phys. **A 434** (1985) 695c.
4. A. Afanasiev et al., Phys. Lett. **B445**, 14 (1998).
5. V.V.Burov et al., Particles and Nuclei, **23** (1992) 721-766.

EVIDENCE OF $S = +1$ NARROW RESONANCES IN THE SYSTEM $K_S^0 p$

P. Z. ASLANYAN^{1,2}, V. N. EMELYANENKO¹, G. G. RIKHKVITZKAYA^{1*}

(1) Joint Institute for Nuclear Research, Dubna, Russia

(2) Yerevan State University, Yerevan, Armenia

Experimental data from the 2m propane bubble chamber have been analyzed to search for an exotic baryon state, the Θ^+ -baryon, in the pK_S^0 decay mode for the reaction $p+C_3H_8$ at 10 GeV/c. The pK_S^0 invariant mass spectrum shows resonant structures with $M_{K_S^0 p} = 1540 \pm 8, 1613 \pm 10, 1821 \pm 11$ MeV/c² and $\Gamma_{K_S^0 p} = 9.2 \pm 1.8, 16.1 \pm 4.1, 28.0 \pm 9.4$ MeV/c². The statistical significance of these peaks has been estimated as 5.5, 4.8 and 5.0 s.d., respectively. There are also small peaks in mass regions of 1487(3.0 s.d.), 1690(3.6 s.d.) and 1980(3.0 s.d.) MeV/c².

1. Introduction

Recent experimental efforts have been strongly motivated by Diakonov, Petrov and Polyakov [1] who studied antidecuplet baryons by using the chiral soliton (Skyrme) models. The lightest member of the pentaquark antidecuplet, the $\Theta^+(1530)$ -baryon, is predicted in [1]. Jaffe and Wilczek have suggested an underlying quark model structure of this state [2], which has also been predicted by others [3]– [6]. Experimental evidence for $\Theta^+(1530)$ -baryon with positive strangeness has recently come from several experimental groups (LEPS, DIANA-ITEP, CLAS, SAPHIR, HERMES, SVD-2 experiment, IHEP, Dubna-PBC, Dubna-HBC).

2. Experiment

The bubble chamber is the most suitable instrument for this purpose [7]– [10]. Experimental information from more than 700000 stereo photographs is used to select events with V^0 strange particles [10]. The effective mass distributions of 8657 Λ events 4122 K_S^0 events are consistent with their PDG values.

2.1. pK_S^0 -spectrum of identified protons with momentum $0.35 \leq P \leq 0.9$ GeV/c

The pK_S^0 effective mass distribution for 2300 combinations is shown in Fig. 1a. The solid curve is the sum of the background and four Breit-Wigner resonance curves.

The total experimental background has been obtained by two methods. In the first, the experimental effective mass distribution was approximated by a polynomial function after cutting out the resonance ranges. This distribution was fitted by an eighth-order polynomial. The second method,

*Work partially supported by grant 04-02-27111 from the Russian Foundation For Basic Research.

using the angle between K_s^0 and p for experimental events, is described in [11]. The two resulting distributions had the same coefficients and order of the polynomials.

The background for $\overline{K^0}p$ combinations has been estimated with the FRITIOF model to be no more than 10% (Fig. 1a).

2.2. pK_s^0 -spectrum of positively charged tracks with momentum $0.9 \leq P \leq 1.7$ GeV/c

The pK_s^0 invariant mass spectrum shows resonant structures with $M = 1515$ (5.3 s.d.) and 1690 MeV/c² (3.8 s.d.) in Fig. 1b. The backgrounds for $K_s^0\pi^+$ and $K_s^0K^+$ combinations are 46.6% and 4.4%, respectively. These peaks may come from the resonances $\Lambda(1520)$ and $\Lambda(1690)$ in reactions $p + C_3H_8 \rightarrow \pi^+ \overline{K^0} n X$, in cases in which the neutron was identified and the π^+ missed.

2.3. pK_s^0 -spectrum with momentum $P \geq 1.7$ GeV/c

The pK_s^0 invariant mass distribution with momentum $P \geq 1.7$ GeV/c is shown in Fig. 1c. The background analysis done by both methods has shown that these distributions had the same polynomial order and coefficients. The $K_s^0\pi^+$ and $K_s^0K^+$ backgrounds are 20% and 5%, respectively. The $\overline{K^0}p$ contribution is estimated with the FRITIOF model to be 8%.

The total pK_s^0 invariant mass distribution for identified protons and positively charged tracks $p_p \geq 1.7$ GeV/c is shown in Fig. 1d. The solid curve is the sum of the background and four Breit-Wigner resonance curves.

3. Conclusion

Examination of effective $K_s^0 p$ mass spectra in collisions of 10.0 GeV/c protons with C_3H_8 nuclei has resulted in the discovery of the peaks presented below (Table 1). Table 1 shows the effective resonance masses and widths (Γ), which are based on the data shown in Fig. 1a. The statistical significance in Table 1 is based on the data shown in Fig. 1d. There are small enhancements in mass regions at 1487, 1690 and 1980 MeV/c², the excess above background being 3.0, 3.6 and 3.0 S.D., respectively. The primary total cross section for $\Theta^+(1540)$ production in $p + C_3H_8$ -interactions is estimated to be $\approx 90\mu\text{b}$.

Table 1. Examination of effective $K_s^0 p$ mass spectra has resulted in the discovery of the peaks presented below.

Resonance system	M MeV/c ²	Γ_e MeV/c ² Experiment	Γ MeV/c ²	The statistical significance N_{sd}
$K_s^0 p$	1540±8	18.2±2.1	9.2±1.8	5.5±0.5
$K_s^0 p$	1613±10	23.6±6.0	16.1±4.1	4.8±0.5
$K_s^0 p$	1821±11	35.9±12.0	28.0±9.4	5.0±0.6

References

1. D. Diakonov, V. Petrov, and M. Polyakov, Z. Phys. A 359 , 305, 1997.
2. R.L. Jaffe, SLAC-PUB-1774 Talk presented at th Topical Conf. on Baryon Resonances, Oxford, Eng., Jul 5-9, 1976; arXiv:hep-ph/0307341, 2003.
3. M. Karliner and H.J. Lipkin, Phys. Lett. B, 575 , 249, 2003.
4. J. Ellis, M. Karliner, M. Praszalowich, hep-ph/0401127, 2004.

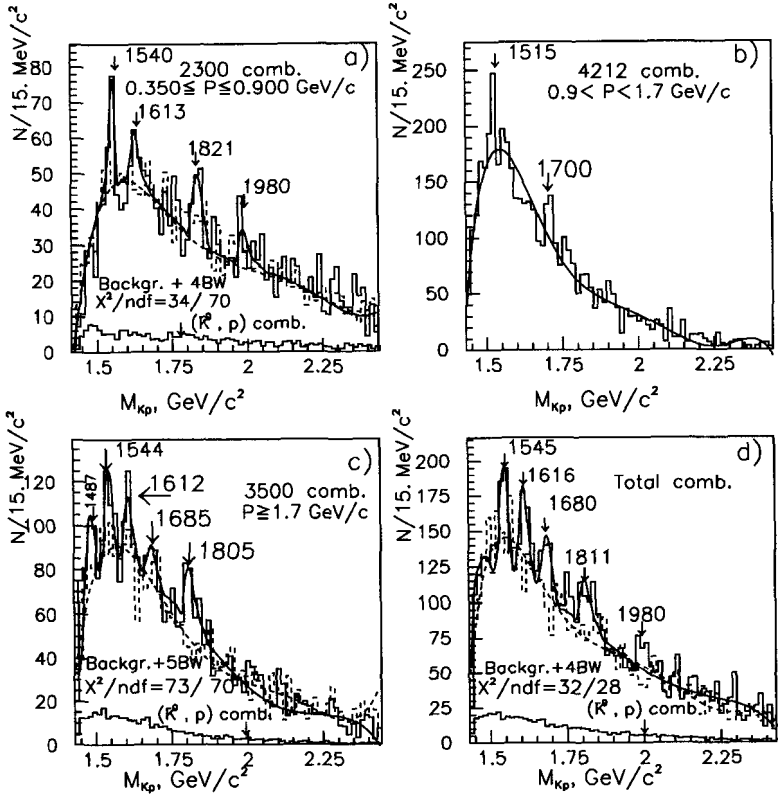


Fig. 1. The (pK_s^0) invariant mass spectra in the reaction $p+C_3H_8 \rightarrow (pK_s^0) + X$ with different track momentum P : a) $0.350 \leq P \leq 0.900 \text{ GeV}/c$ for identified protons; b) $0.9 \leq P \leq 1.7 \text{ GeV}/c$ for positively charged tracks; c) $p > 1.7 \text{ GeV}/c$ for positively charged tracks; d) $0.350 \leq P \leq 0.9 \text{ GeV}/c$ and $P > 1.7 \text{ GeV}/c$. The solid curve is the sum of the experimental background (by the first method) and Breit-Wigner resonance curves. The dashed histogram is the experimental background[11] taken in the form of by the polynomial(the dashed curve). The below histogram shows the simulated background for the spectrum of $K^0 p$ combinations.

5. D. Akers, arXiv.org:hep-ph/0310031, 2004.
6. A.A.Arhipov, arXiv:hep-ph/0403284, 2004.
7. DIANA Coll., V. Barmin et al., arXiv:hep-ex/0304040; Phys. At. Nucl., 66 , 1715-1718, 2003;
8. A.A.Kuznetsov, R.Togoo et al., Proc. of the Mangolian Academy of Sciences,v.170, N4,p.3,2003.
9. P.Z.Aslyan et al., hep-ex/0403044, 2004. P.Z.Aslyan et al., JINR Communications, E1-2004-137,2004.
10. Yu.A.Troyan et al.,JINR, D1-2004-39, Dubna, 2004;arXiv:hep-ex/0404003(2004).
11. V.L.Lyuboshits at al., JINR Rapid Comm., N6(74),p209, 1995.

P-PARITY OF THE PENTAQUARK Θ^+ AND SPIN OBSERVABLES IN THE REACTION $NN \rightarrow Y\Theta^+$ *

Y. N. UZIKOV

Joint Institute for Nuclear Research, Dubna, Russian Federation

H. SEYFARTH

Institut für Kernphysik, Forschungszentrum Jülich, Jülich, Germany

Double and triple spin correlations in the reaction $NN \rightarrow Y\Theta$ are analyzed at the threshold in a model independent way for an arbitrary spin of the Θ^+ . Measurement of some of these observables allows us to determine the P-parity of the Θ^+ unambiguously.

1. Introduction

Experimental determination of the quantum numbers (spin, parity, isospin) of the exotic baryon Θ^+ (1540), strongly indicated by recent experiments, will be essential to establish its underlying dynamics. According to a general theorem [1], in order to determine the parity of one particle in a binary reaction $1 + 2 \rightarrow 3 + 4$, one has to know at least the polarizations of two fermions participating in this reaction. Model independent methods for determination of the P-parity of the Θ^+ in pp-collision were suggested in [2, 3]. These methods are based on such general properties of the reaction amplitude as angular momentum and P-parity conservation, and on the generalized Pauli principle for nucleons. Assuming the spin of the Θ^+ , j_Θ , to be $\frac{1}{2}$, it was shown in [3] that the sign of the spin-spin correlation parameter $C_{y,y}$ unambiguously determines the P-parity of the Θ^+ in the reaction $pp \rightarrow \Sigma^+\Theta^+$. Another definite correlation between $C_{y,y}$ and π_Θ holds for the $pn \rightarrow \Lambda^0\Theta^+$ reaction [4, 5] if the isospin of the Θ^+ is zero. Furthermore, measurements of the spin-transfer coefficients $K_y^\lambda = K_x^\lambda$ or K_z^λ in these reactions also allow us to determine the P-parity unambiguously [4, 5]. Obviously, a double-spin measurement near threshold is an experimental challenge. In this connection, one should note that measurements of the polarization transfer from the initial nucleon to the hyperon in the reaction $NN \rightarrow Y\Theta^+$ can be performed by single spin experiments with only polarized beam or target, since the polarization of the hyperon can be measured via its weak decay.

Many quark models predict $j_\Theta = \frac{1}{2}$ for the spin of the Θ^+ . However, higher spin values $j_\Theta > \frac{1}{2}$ are also possible [6, 7]. It was noted in [8, 9], that a very narrow width of the Θ^+ can be explained if its spin-parity is $j_\Theta^\pi = \frac{3}{2}^-$. A generalization of the approach [2, 3] to arbitrary spin of the Θ^+ is therefore an important task. This problem was discussed in [10] and independently in [11].

*This work is supported by the grants of BMBF/WTZ KAZ 02/01, RFFI 04-02-27118-z.

2. The method

Let us denote the orbital momentum, spin, isospin and total angular momentum of the initial NN system in the reaction $NN \rightarrow Y\Theta^+$ as L, S, T and J , respectively. We assume that at threshold the s-wave dominates in the final state.

In this case there is only one spin-singlet amplitude ($S = 0$), whereas the number of independent spin-triplet ($S = 1$) amplitudes a_j^S is two for $j_\Theta = \frac{1}{2}$ and three for $j_\Theta \geq \frac{3}{2}$. The relation between the quantum numbers of the initial NN system and P-parity of the Θ^+ , π_Θ , is determined by P-parity conservation and the generalized Pauli principle as $(-1)^S = \pi_\Theta(-1)^{T+1}$. Therefore, in order to determine the P-parity of the Θ at a given isospin T , it is sufficient to determine the spin of the NN-system in the initial state of this reaction at threshold.

As was shown in [4], the spin-spin correlation parameters for the spin-triplet state can be written as

$$C_{x,x} = C_{y,y} = \frac{\sum_J |\sqrt{J} a_J^{J-1} - \sqrt{J+1} a_J^{J+1}|^2}{\sum_{JL} (2J+1) |a_J^L|^2}, \quad \text{if } S = 1, \quad (1)$$

$$C_{z,z} = 1 - 2C_{y,y}. \quad (2)$$

As seen from Eq. (1), the parameters $C_{x,x}, C_{y,y}$ are non-negative. On the contrary, for the spin-singlet state the correlation parameters are negative and maximal in absolute value: $C_{x,x} = C_{y,y} = C_{z,z} = -1$. These results do not depend on the spin of the pentaquark Θ^+ (and hyperon Y). This independence is relevant, because the spin of the Θ^+ is not yet known. The sign of $C_{y,y}$, measured near threshold, therefore determines the P-parity π_Θ^+ unambiguously.

2.1. Spin-tensor correlation in the final state induced by polarized beam

The spin-transfer coefficient for induced tensor polarization in the reaction $N + N \rightarrow Y + \Theta^+$ is defined as

$$K_{NM}^{J_Y M_Y, J_\Theta M_\Theta} = \frac{Sp \{ T_{J_Y M_Y}(Y) T_{J_\Theta M_\Theta}(\Theta) F T_{J_N M_N}(N) F^+ \}}{Sp F F^+}, \quad (3)$$

where F is the transition operator, $T_{J_i M_i}(i)$ is the tensor operator of rank J_i with magnetic quantum number M_i for the i -th particle. For the polarized nucleon and hyperon Y ($J_N = J_Y = 1$) and unpolarized Θ^+ ($J_\Theta = M_\Theta = 0$), Eq. (3) determines the spin transfer coefficient K_i^j (where $i, j = x, y, z$), considered in detail in [4, 5, 10, 11]. For unpolarized initial nucleons and the final hyperon ($J_y = M_y = 0$), Eq. (3) gives the tensor polarization of the Θ^+ , t_{J_Θ, M_Θ} .

If the spin of the Θ^+ is higher than $\frac{1}{2}$, then there are additional possibilities to determine the P-parity, because for an even rank J and $M = 0$ the tensor polarization t_{J0} of the resonance can be measured by angular distribution in the strong decay $\Theta^+ \rightarrow N + K$ [12]. We can show [13] that for even rank J the coefficients $K_{1y}^{1y, J0}$ and $K_{1z}^{1z, J0}$ are zero for the spin singlet, and non-zero for the spin-triplet states [13]. The same is true for the K_y^y coefficient. Therefore, for a given isospin and P-parity of the Θ^+ , the coefficient $K_{1y}^{1y, J0}$ is non-zero only for one isospin channel of the reaction $NN \rightarrow Y\Theta^+$, and equals zero for another one. This statement is valid for any spin of the Θ^+ . Thus, a measurement of both coefficients $K_{1y}^{1y, J0}$ and K_y^y in the reactions $pp \rightarrow \Sigma^+ \Theta^+$ and $pn \rightarrow \Lambda \Theta^+$ serves as a strong test for the P-parity determination. Simultaneously, it allows us to determine the isospin of the Θ^+ [10].

The spin-transfer coefficient $\bar{K}_{x,z}^y$, defined similarly to Eq. (3), is also non-zero only for the spin-triplet initial state, and can be measured in the reaction $NN \rightarrow Y\Theta^+$. This coefficient can therefore be used for P-parity determination in addition to a measurement of $C_{y,y}$.

2.2. Energy dependence near the threshold

Our analysis is restricted to the threshold region under the assumption that an s-wave dominates in the final state. This assumption is expected to be a reasonable approximation up to few MeV excess energy [2]. For high momentum transfer in the near-threshold regime, the final partial wave with orbital momentum l contributes to the reaction amplitude as $\sim (p'/Q)^l$, where p' is the final c.m.s. momentum and Q denotes an intrinsic scale of the process that is determined by the transferred momentum. Therefore the contribution of the higher partial waves ($l \neq 0$) is suppressed at the threshold ($p' < Q$) as compared to $l = 0$. An additional suppression of the $l \neq 0$ states can be provided by the centrifugal barrier, if the final state short-range interaction between the Θ^+ and hyperon Y is strong enough.

As was shown in [14], the spin-singlet and spin triplet unpolarized cross sections near the threshold have different dependencies on the excess energy W . So, if the transition to the final s -wave is forbidden for a spin \bar{S} (1 or 0) at threshold, then (due to the contribution

of the p-wave above the threshold) the cross section, corresponding to the initial NN spin state $|\bar{S}\bar{M}\rangle$, behaves as $^{2\bar{S}+1}\sigma_{\bar{M}}/p' \sim W$. On the other hand, for the other spin S only even partial waves l contribute to the final state. Therefore, near threshold $^{2S+1}\sigma_M/p'$ is approximately independent of W . Since the unpolarized cross section σ_0 can be separated into singlet and triplet parts by measurement of the spin correlation parameters $C_{i,i}$, ($i = x, y, z$), the energy dependence of $\sigma_0 C_{j,j}$ allows us to determine the P-parity (at $W < 50$ MeV) [14]. Similar arguments are valid for the W -dependence of the product of the spin-transfer coefficients given by Eq. (3) and the unpolarized cross section.

In conclusion, the developed formalism is general and can be applied for P-parity determination of other narrow resonances with arbitrary spins.

References

1. P.L. Csonka, M.J. Moravcsik, M.D. Scadron, *Phys. Lett.* **15**, 353 (1965).
2. A. Thomas, K. Hicks, A. Hosaka, *Prog. Theor. Phys.* **111**, 291 (2004).
3. Ch. Hanhart et al., *Phys. Lett.* **B 590**, 39 (2004).
4. Yu.N. Uzikov, hep-ph/0401150;
5. M. Rekaló and E. Tomasi-Gustafsson, *Phys.Lett.* **B 591**, 225 (2004).
6. T. Nishikawa et al., hep-ph/0411224.
7. S. Takeuchi and K. Shimizu, hep-ph/0410286.
8. R.L. Jaffe and A. Jain, hep-ph/0408046.
9. A. Hosaka, M. Oka, T. Shinozaki, hep-ph/0409102.
10. Yu.N. Uzikov, hep-ph/0402216; *Phys.Lett.* **B 595**, 277 (2004).
11. M. Rekaló and E. Tomasi-Gustafsson, hep-ph/0402227.
12. S.M. Berman and M. Jacob, *Phys. Rev.* **139**, B1023 (1965).
13. Yu.N. Uzikov, nucl-th/0411113.
14. Ch. Hanhart et al., hep-ph/0407107; hep-ph/0410293.



SESSION 5

Soft Spin Physics with Photons and Leptons

This page intentionally left blank

MEASUREMENT OF THE NEUTRON ELECTRIC FORM FACTOR AT LOW MOMENTUM TRANSFER

R. ALARCON, E. GEIS, M. KOHL, R. MILNER, V. ZISKIN

Massachusetts Institute of Technology, Cambridge, USA

(for the BLAST Collaboration)

Measurement of the neutron's electric form factor, G_E^n , by means of quasi-elastic electron scattering from polarized deuterium with polarized beam and target, ${}^2H(e, e'n)p$, is in progress in the South Hall Ring of the MIT-Bates Linear Accelerator Center using the Bates Large Acceptance Spectrometer Toroid (BLAST). The spin-perpendicular vector-polarized beam-target asymmetry, A_{ed}^V provides the ratio, G_E^n/G_M^n , over a range of momentum transfer Q^2 between 0.12 and 0.80 (GeV/c)². Preliminary results are presented.

1. Introduction

Measurements of nucleon form factors, such as the electric form factor of the neutron, are important for the understanding of the structure of baryons in the non-perturbative QCD regime. Until recently a purely phenomenological parametrization by Galster [1] has served as the best description of G_E^n data. Lately, calculations of G_E^n based on effective field theories of QCD have become available. The neutron's electric form factor provides a sensitive test of many of these models. Thus, precision G_E^n data at low momentum transfer is essential to constrain theoretical calculations of nucleon structure.

At the same time, precise knowledge of the neutron's electric form factor is important for an interpretation of the results from parity-violating scattering experiments designed to probe the strangeness content of the nucleon. Recent parity-violation experiments [2] have indicated that the uncertainty of the elastic form factors of the nucleons, G_E^n in particular, is one of the largest contributions to the systematic error. A special interest of the parity-violating experiments is in the region of extremely low Q^2 . This work should be of great value for such low momentum transfer experiments.

2. Measurement of G_E^n using the ${}^2H(e, e'n)p$ reaction

Since there are no free neutron targets, the form factors of the neutron are measured using nuclear targets where corrections due to the nucleon-nucleon interactions are small and well understood. Typically these targets are 2H and 3He , with a neutron detected in the

final state. At low momentum transfer, 2H is a substantially better approximation to a free neutron target than 3He . In unpolarized quasi-elastic scattering, however, the fact that G_E^n is order of magnitude smaller than G_M^n greatly limits the precision with which the G_E^n/G_M^n ratio can be measured. A new generation of polarization experiments makes use of scattering of longitudinally polarized electrons either from a vector polarized target or involve the polarimetry of the recoil neutron.

The differential cross section, $S(h, P_z, P_{zz})$, for beam-target polarized scattering can be written in terms of polarization observables as [3]

$$S(h, P_z, P_{zz}) = S(0, 0, 0) \left\{ 1 + \sqrt{\frac{3}{2}} P_z A_d^V + \sqrt{\frac{1}{2}} P_{zz} A_d^T + h \left(A_e + \sqrt{\frac{3}{2}} P_z A_{ed}^V + \sqrt{\frac{1}{2}} P_{zz} A_{ed}^T \right) \right\}, \quad (1)$$

where P_z, P_{zz} and h are the vector and tensor polarizations of the target, and the polarization of the beam, respectively. When the momentum transfer vector is perpendicular to the target polarization vector (spin-perpendicular kinematics), the beam-target vector asymmetry, $A_{ed}^V(\frac{\pi}{2}, 0)$ is given in Plane Wave Born Approximation (PWBA) by

$$A_{ed}^V(\frac{\pi}{2}, 0) = -\sqrt{\frac{3}{2}} h P_z \frac{2\sqrt{2}\tau\rho'_{LT} G_E^n G_M^n}{\rho_L (G_E^n)^2 + 2\tau\rho_T (G_M^n)^2}, \quad (2)$$

where ρ_L, ρ_T and ρ'_{LT} are kinematic factors and $\tau = \frac{Q^2}{4M^2}$.

3. The BLAST experiment

This measurement is performed at the South Hall Ring complex of the Bates Linear Accelerator Center using an internal target and the BLAST detector. The detector consists of eight magnetic coils producing a toroidal field, with two sectors symmetrically equipped with wire drift chambers, Cerenkov counters and thin time-of-flight plastic scintillators. The neutron detection capabilities (thick arrays of plastic scintillators) were enhanced in the right sector, where the momentum transfer vector is perpendicular to the direction of the target polarization. A combination of the drift chambers and time-of-flight scintillators provides a charged particle veto with an efficiency of $\sim 99.9\%$.

Polarized deuterium atoms are injected into the target by an atomic beam source (ABS), which randomly switches between three polarization states [4], $P_z = \pm 1$ and $P_{zz} = -2$. This allows us to measure all polarization observables in Eq. (1) simultaneously.

4. Preliminary results

The BLAST data cover a large momentum transfer range^a, $0.12 < Q^2 < 0.8$ (GeV/c)². At this time about 60% of the data taken in 2004 have been analyzed, corresponding to a collected charge of 250 kC in three spin states. The average stored beam current has been 100 mA. With a target gas thickness of 6×10^{13} atoms/cm², a luminosity of 4×10^{31} cm⁻²s⁻¹ has

^aIn this work only data up to $Q^2 = 0.35$ (GeV/c)² have been analyzed

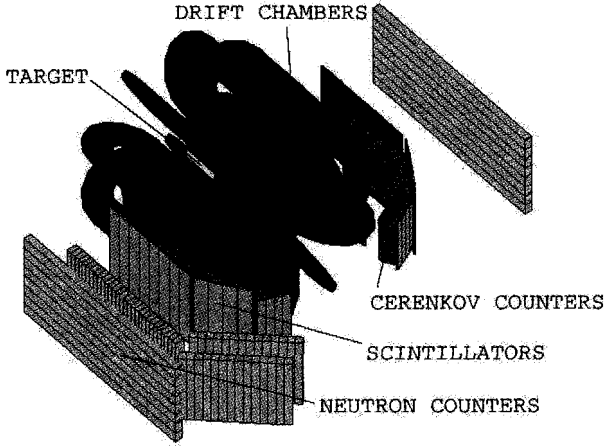


Fig. 1. Schematic of the BLAST detector. In the middle are the storage cell and the eight magnetic field coils. In the order away from the target are the wire drift chambers, Cerenkov counters, time-of-flight scintillators and neutron detectors.

been achieved. The vector polarization of deuterium atoms was $P_z \approx 72\%$ and remained stable over the course of the experiment.

The spin-perpendicular asymmetry $A_{ed}^V(\frac{\pi}{2}, 0)$ is compared to the BLASTMC Monte-Carlo simulations based on calculations by H. Arenhövel [3] and a GEANT model of the full BLAST detector. The radiative corrections are not yet performed.

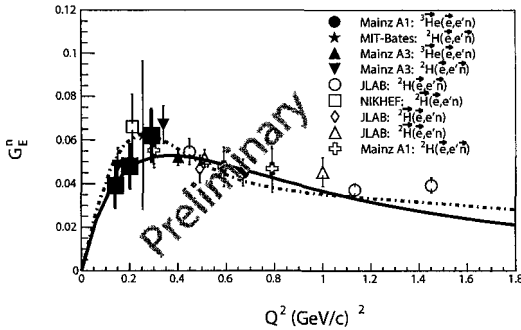


Fig. 2. Preliminary G_E^n data (large squares) from the BLAST experiment with the world's polarization data⁵⁻¹⁶. The solid line is the Galster parametrization, and the dot-dashed curve is a parametrization by Friedrich and Walcher [17] inspired by a non-relativistic constituent quark model.

Figure 2 shows in black squares three preliminary data points for G_E^n with purely statistical errors. Systematic errors are not finalized yet, but are expected to be small.

References

1. S. Galster et al. *Nucl. Phys.* **B32**, 221 (1971)
2. F. E. Maas et al. *Phys. Rev. Lett.* **93**, 022002 (2004)
3. H. Arenhövel et al., *Phys. Rev.* **C46**, 455 (1992)
4. E. Tsentalovich et al., *Spin2004 Conference Proceedings*, World Scientific (2004)
5. R. Madey et al., *Phys. Rev. Lett.* **91**, 122002 (2003)
6. J. Becker et al., *Eur. Phys. J.* **A6**, 329 (1999)
7. J. Golak et al., *Phys. Rev.* **C63**, 034006 (2001)
8. D. Rohe et al., *Phys. Rev. Lett.* **21**, 4257 (1999)
9. J. Bermuth et al., *Phys. Lett.* **B564**, 199 (2003)
10. I. Passchier et al., *Phys. Rev. Lett.* **82**, 4988 (1999)
11. H. Zhu et al., *Phys. Rev. Lett.* **87**, 081801 (2001)
12. T. Eden et al., *Phys. Rev.* **C4**, 1749 (1994)
13. M. Ostrick et al., *Phys. Rev. Lett.* **83**, 276 (1999)
14. C. Herberg et al., *Eur. Phys. J.* **A5**, 131 (1999)
15. G. Warren et al., *Phys. Rev. Lett.* **92**, 042301 (2004)
16. D. I. Glazier et al., *nucl-ex/0410026* (2004)
17. J. Friedrich and T. Walcher, *Eur. Phys. J.* **A17**, 607 (2003)

A PRECISION MEASUREMENT OF G_E^p/G_M^p AT BLAST

C. B. CRAWFORD

Massachusetts Institute of Technology, Cambridge, USA

(for the BLAST Collaboration)

We are undertaking a measurement of G_E^p/G_M^p at $Q^2 = 0.1\text{--}0.9(\text{GeV}/c)^2$ in the South Hall Ring of the MIT-Bates Linear Accelerator Facility. This experiment uses a polarized electron beam, a pure hydrogen internal polarized target, and the symmetric Bates Large Acceptance Spectrometer Toroid (BLAST) detector. By measuring the spin-dependent elastic $H(e, e'p)$ asymmetry in both sectors simultaneously, we can extract the form factor ratio independently of beam and target polarization. This is the first experiment to measure G_E^p/G_M^p using a polarized target, which is complementary to recoil polarimetry experiments. Preliminary results are presented.

1. Introduction

The electromagnetic form factors of the nucleon, G_E and G_M , are fundamental descriptions of its charge and magnetic distributions. The measurement of these quantities is an important test of various Vector Meson Dominance (VMD) and Constituent Quark (CQM) models as well as Lattice QCD calculations [1] of the nucleon form factors. The nucleon form factors have been measured during the last half century using L-T separations from unpolarized elastic electron-proton differential cross sections. Recent advances with polarized beams, targets and polarimetry have brought forth a new generation of precision measurements of G_E^p/G_M^p . Such experiments benefit from interference terms between G_E and G_M in the polarized response functions. Recent polarization transfer measurements of G_E^p/G_M^p at Jefferson Lab [2, 3] deviated significantly from the previous L-T separations at $Q^2 > 1(\text{GeV}/c)^2$, which has prompted new investigations to reconcile these two methods.

We are performing an experiment at MIT-Bates to measure G_E^p/G_M^p at $Q^2 = 0.1\text{--}0.9(\text{GeV}/c)^2$. This region, which overlaps the lowest Jefferson Lab Q^2 point, is sensitive to the structure of the meson cloud of the nucleon. This experiment exploits unique features of the Atomic Beam Source (ABS) target in an electron storage ring and the BLAST spectrometer to reduce systematic errors.

2. Formalism

The experimental double-spin asymmetry for elastic $H(e, e'p)$ scattering is the product of the beam and target polarizations, P_b and P_t , and the ratio of the polarized over the

unpolarized hydrogen elastic cross section [4]:

$$A_{exp} = P_b P_t \frac{z^* G_M^{p2} + x^* G_E^p G_M^p}{\tau G_M^{p2} + \varepsilon G_E^{p2}}, \quad (1)$$

where $\tau = Q^2/4M^2$, $\varepsilon = 1/(1 + 2(1 + \tau) \tan^2(\theta_e/2))$ is the longitudinal polarization of the virtual photon, and θ_e is the electron scattering angle. The terms including the kinematic factors z^* and x^* are proportional to the longitudinal and transverse components of the proton polarization with respect to the momentum transfer, q .

By simultaneously measuring the asymmetry for two different spin orientations at fixed Q^2 , one can form a super-ratio R_A of the asymmetries in which the beam and target polarizations and the unpolarized cross section all cancel. Given a symmetric detector, both asymmetries can be measured at the same time by orienting the target spin at the angle $\beta = 45^\circ$ to the left of the beam, so the asymmetry A_L (A_R) for electrons scattering to the left (right) is predominantly transverse (longitudinal). Then the form factor ratio $R = G_E^p/G_M^p$ can be extracted by inverting

$$R_A = \frac{A_L}{A_R} = \frac{z_L^* + x_L^* R}{z_R^* + x_R^* R}. \quad (2)$$

3. Experimental Setup

This experiment is being performed in the South Hall Ring [5] in the MIT-Bates Linear Accelerator Center, which can store a polarized electron beam ($P_b = 0.65 \pm 0.03$) of up to 250 mA at an energy of 850 MeV. A Siberian snake preserves the polarization, which is continuously monitored by a Compton polarimeter [6].

The internal target [7], consisting of an Atomic Beam Source (ABS) and a cryogenic storage cell, is embedded in the BLAST spectrometer. The ABS produces a highly polarized isotopically pure atomic beam, which is injected into a 15 mm diameter by 60 cm long T-shaped open-ended storage cell. The ABS is operated in single state mode in order to avoid depolarization due to hyperfine interactions. The ABS switches between states every five minutes, while the ring is filled with alternating polarizations every half hour.

The relatively low luminosity ($\mathcal{L} = 1.6 \times 10^{31} \text{ cm}^2 \text{ s}^{-1}$) of the internal gas target is compensated for by the large acceptance spectrometer. The detector package is built around eight copper coils which provide the 0.4 T BLAST toroidal magnetic field. Two of the sectors are instrumented with three drift chambers each for momentum, angular, and positional resolution, scintillators for triggering and time-of-flight, and Čerenkov detectors for pion rejection. Additional scintillators at backward angles beyond the drift chambers extend the acceptance to $Q^2 = 0.85 \text{ (GeV/c)}^2$.

4. Preliminary Results

The first production run in December 2003 accumulated 3.4 pb^{-1} of integrated luminosity with the target polarization $P_t = 0.48 \pm 0.04$ and the BLAST field reversed to extend to lower Q^2 . The second run in April 2004 accumulated 9.6 pb^{-1} with $P_t = 0.42 \pm 0.04$ and the

nominal BLAST field. We project another 67 pb^{-1} will be accumulated in the third run to be complete in December 2004, with target polarization improved to $P_t \sim 0.75$.

The elastic events are selected based on cuts from the reconstructed kinematic variables, including coplanarity and timing cuts from the scintillators. The timing cuts alone produce a clean elastic dataset with less than 1% background contamination in all Q^2 bins.

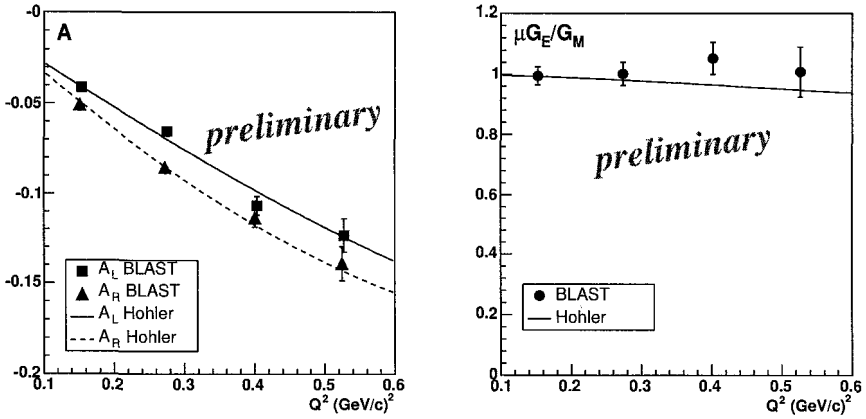


Fig. 1. Left: the $H(e, e'p)$ asymmetry in the left and right sectors of BLAST, compared to the asymmetry from the Höhler [8] parametrization of G_E^p and G_M^p . Right: preliminary results of $\mu G_E^p/G_M^p$ from the partial dataset also compared to Höhler.

Since the product of beam and target polarizations $P = P_b P_t$ is independent of Q^2 , the form factor ratio $R_i = G_E^p(Q_i^2)/G_M^p(Q_i^2)$ can be extracted by fitting the asymmetries to $A_{ij} = P(z_{ij}^* + x_{ij}^* R_i)/(\tau_i + \varepsilon_i R_i^2)$, where the Q^2 bin is labeled by i and the left/right sector by j . This method gives reduced statistical errors compared to the pure super-ratio method, which is equivalent to solving for both P_i and R_i independently in each Q^2 bin.

There are two important systematic errors which are currently being addressed. The first is in the uncertainty of z^* and x^* , which depend on $\theta^* = \beta - \theta_q$. The target spin angle β can be measured from tensor polarized $D(e, e'p)$ elastic scattering in BLAST, and the momentum transfer angle θ_q is overdetermined in elastic kinematics from both the momentum and scattering angle of the electron and proton. The second main contribution comes from the two detectors not being exactly symmetric, and we must account for the difference in Q^2 between the left and right sectors. The experimental asymmetry can be formed in four different ways from our experiment by reversing both the beam helicity and the target polarization directions in order to minimize the experimental false asymmetry.

Preliminary results are shown in Fig. 1 with statistical errors only. These results do not include the December 2004 run, in which we project to increase our effective statistics by a factor of 16.2. We have also taken 76 pb^{-1} of elastic $D(e, e'p)$ data of target vector polarization $P_z \sim 0.72$ with BLAST, which may be used to extract G_E^p/G_M^p for the deuteron.

Acknowledgments

This work is supported in part by the U.S. Department of Energy under contract number DE-FC02-94ER40818 and DE-FG02-03ER41231.

References

1. H. Gao, *Int. J. Mod. Phys. E* **12**, 1 (2003).
2. M. K. Jones *et al.*, *Phys. Rev. Lett.* **84**, 1398 (2000).
3. O. Gayou *et al.*, *Phys. Rev. Lett.* **88**, 092301 (2002).
4. T. W. Donnelly and A. S. Raskin, *Ann. Phys.* **169**, 247 (1986).
5. W. Franklin, in these proceedings.
6. W. Franklin, in these proceedings.
7. E. Tsentalovich, in these proceedings.
8. G. Höhler *et al.*, *Nucl. Phys.* **B114**, 505 (1976).

ASYMMETRIES ANALYSIS FROM THE FORWARD ANGLE PART OF THE G0 EXPERIMENT

J. ROCHE

Jefferson Lab, Newport-News, USA

(for the G0 Collaboration)

The G0 project is a parity violation experiment using elastic electron scattering. It is dedicated to the measurement of the contribution of strange quarks to the charge and magnetization distributions in the nucleon. After introducing the physics case this paper describes the analysis progress of the first part of the experiment.

1. Proton strange quark form factors measured by G0

Parity violation in elastic electron scattering arises through the interference of Z^0 and γ exchange. If one supposes the neutron and proton electromagnetic form factors to be known, the relative asymmetry [1], [2] of the cross-sections for the two helicity states of the beam (R or L), can be expressed as:

$$A = \frac{\sigma^R - \sigma^L}{\sigma^R + \sigma^L} = \eta + \xi G_E^s + \chi G_M^s + \phi G_A^e \quad (1)$$

where ξ , χ and ϕ are kinematic factors, G_E^s , G_M^s are the strange quark proton form factors, and G_A^e is the axial form-factor of the nucleon. η is a known asymmetry which, for G0, ranges between -1 and -35×10^{-6} . The G0 program [3] will completely separate G_E^s , G_M^s and G_A^e without any experimental assumptions. Asymmetries are measured with a hydrogen target at forward (7°) electron angle and hydrogen and deuterium targets at backward (110°) electron angles. Moreover, the evolution of those observables at momentum transfers below $Q^2 = 1$ (GeV/c)² will be measured. Figure 1 shows the expected total errors of the G0 measurements for G_E^s and G_M^s compared to other experimental data already available or planned. The projected errors presented here include the statistical ($\frac{\Delta A}{A} = 5\%$) and systematic errors. Also, in the backward angle configuration, the inelastic asymmetries will be measured simultaneously to the elastic ones measuring the parity violation effect in the N to Δ transition [7].

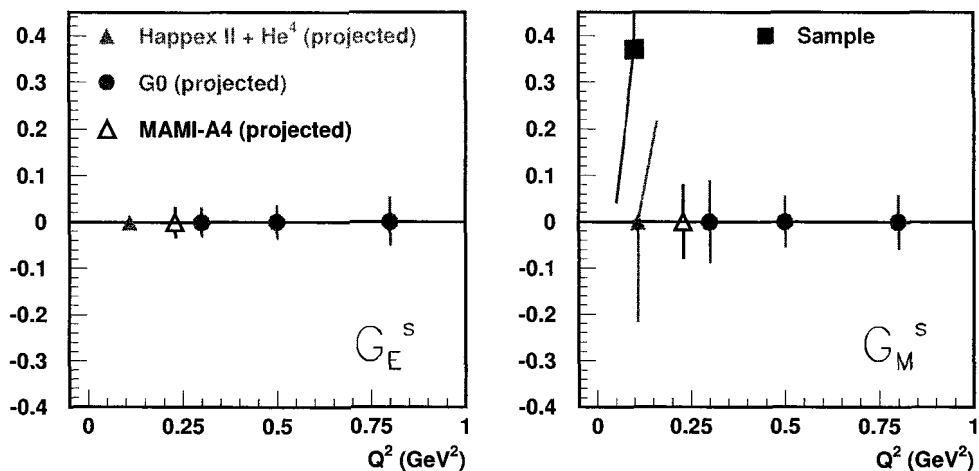


Fig. 1. Expected G0 results (full circles) as a function of Q^2 compared with world data (JLab-HAPPEX [4] generation two, MAMI-A4 [5] and BATES-SAMPLE [6]). Expected results on G_A^e can be found in reference [3].

2. The forward angle G0 data taking

The first part of the G0 program (forward angle) was carried out during the winter of 2004 in Hall C/JLab. It used a dedicated apparatus [3] of large solid angle (0.7 sr), operating at large luminosity ($2 \times 10^{38} \text{ cm}^{-2} \text{ s}^{-1}$) and able to handle large counting rates (2 MHz per detector). An azimuthally symmetric magnet bent the elastic recoil protons toward a specific focal plane detector (FPD) accordingly to the Q^2 of the reaction. In this configuration, the Q^2 range of G0 ranges from 0.1 to 1.0 (GeV/c)² and is measured in 16 FPDs.

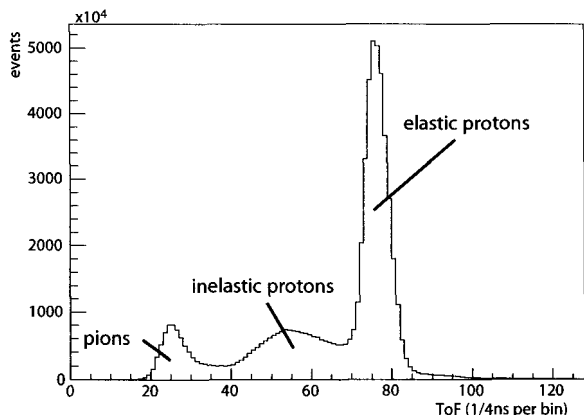


Fig. 2. Typical ToF spectra measurement of the G0 experiment

The measured signals are histograms of the Time of Flight (ToF) of the particles from the target to the detectors, which provide particle identification for the elastically scattered protons. In order to measure the ToF, the beam was pulsed at 31 MHz, although usually the beam delivered at JLab operates at 499 MHz. Figure 2 show the signal registered for each FPD and for each beam helicity window (R or L).

The statistical goal of the experiment was achieved, and most subsystems of the apparatus worked at or above their design goals. Especially, delivering beam with this time structure at 40 μA and tight helicity-correlated constraints required extensive development work on the part of the JLab accelerator group.

3. Data analysis of the forward angle data

The analysis of the forward angle data is currently underway. The data reduction from measured ToF and beam characteristics (charge, positions, angles and energy) is complete. Thanks to the active feedback systems, the helicity-correlated beam properties delivered during the run were such that the false asymmetries arising from them are estimated to be of the order of 0.01 ppm^a. The largest systematic error associated with the beam helicity properties arose from a leakage of the beam produced by the Hall A and B lasers^b. Only a thousandth of the beam current measured in Hall C was produced by the leaking lasers, but this beam component had a large charge asymmetry (~ 350 ppm) and a different time structure from the main G0 beam. It could not be measured by the beam current monitors. Dedicated measurements allowed us to quantitatively relate the charge asymmetry of the leakage current to the asymmetries measured by the FPDs in a range where no events produced by the main G0 beam are detected. For those measurements, the three lasers (A, B and C) were successively turned off. The correction to the asymmetry is of the order of 0.4 ppm, known with a precision of 0.1 ppm. This correction will dominate the systematic errors at small Q^2 . The current focus of the analysis is the extraction of the elastic asymmetry (A) from the measured one as background processes have their own asymmetries:

$$A_{measured} = f_{el}A + f_{bg}A_{bg} \quad (2)$$

where f_{el} (f_{bg}) is the fraction of events which are purely elastic (background) out of all events. Within a cut of 4 ns width centered around the elastic peak, the values of f_{bg} vary between 8 and 18% (depending on the FPD) coming roughly half from the entrance and exit windows and half from the hydrogen itself. This background measured on either side of the elastic peak (see figure 2) has a significant asymmetry. For low and medium Q^2 the background asymmetry varies slowly across the elastic peak, while for the larger Q^2 it shows a large variation across the peak. In this later case, the correction is likely to dominate the systematic error on the final elastic asymmetry. Figure 3 shows the preliminary results for the first 12 FPDs (low Q^2) including preliminary background corrections. These results are blinded by an overall multiplicative factor and should not be interpreted as anything other than an indication of the overall quality of the data and the present status of the analysis.

4. Summary

The forward part of the G0 program was completed in May 2004. The analysis of the data is underway. The turnaround and upgrade of the apparatus in preparation for the backward angle part has begun. The forward and backward measurements will provide a full separation of the electric and magnetic strange form-factors of the proton for a Q^2 ranging from 0.3 to 0.8 (GeV/c)².

^a 1 ppm= one Part Per Million = 10^{-6}

^b At JLab, three experimental halls A, B and C receive beam simultaneously.

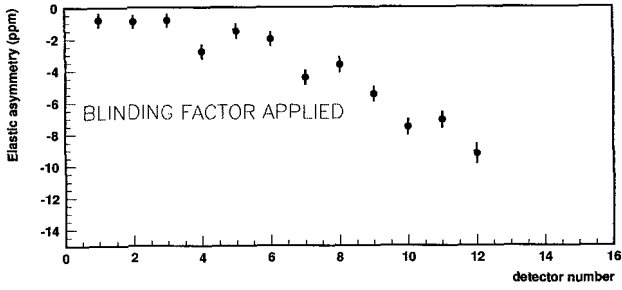


Fig. 3. Preliminary G0 forward angle data. The data are blinded by an overall multiplicative factor comprised between 0.75 and 1.25. The error bars are statistical only.

References

1. D.H. Beck and R.D. McKeown, *Ann. Rev. Nucl.* **51** (2001), 189.
2. K. de Jager, these proceedings.
3. JLab proposal E00-006 and E01-116, D.H. Beck spokesperson, <http://www.npl.uiuc.edu/exp/G0/g0Main.html>
4. D. Lhuillier, these proceedings.
5. F. Maas *et al.*, *Phys. Rev. Lett.* **93**, 022002 (2004).
6. T. Ito *et al.*, *Phys. Rev. Lett.* **92**, 102003 (2004).
7. JLab proposal E01-115, S.P. Wells and N. Simicevic spokespersons.

THE SECOND GENERATION HAPPEX EXPERIMENTS

D. LHUILLIER

CEA Saclay, DAPNIA/SPhN, Gif-sur-Yvette, France

(for the Hall A Collaboration)

The HAPPEX-II and HAPPEX-He experiments measure the parity violating asymmetry (A^{PV}) in polarized electron scattering from ^1H and ^4He respectively. At forward angles, A^{PV} is sensitive to a linear combination of the electric and magnetic strange form factors, and data from two different targets allow the separation of these two contributions. The experiments run in hall A at Thomas Jefferson National Accelerator Facility. We present the experimental setup of these new generation experiments and the analysis status of the summer 2004 run.

1. Introduction

The HAPPEX experiments measure the parity violating asymmetry (A^{PV}) in elastic scattering of polarized electrons from hadronic targets, giving access to the contribution of the strange quarks to the vector matrix element of the nucleon [1]. This contribution comes only from the $s\bar{s}$ fluctuations of the quark sea, and is parametrized by $G_{E(M)}^s$, the electric (magnetic) strange form factors. A clean measurement of these observables provides new insight into the role of the fundamental degrees of freedom of QCD and their dynamics in the non-perturbative structure of the nucleon.

2. Experimental Strategy

At tree level the parity violating asymmetry from protons is given by [4]

$$A^{PV} = -\frac{G_F|Q|^2}{4\pi\alpha\sqrt{2}} \times \left[(1 - 4\sin^2\theta_W) - \frac{\varepsilon G_E^{\gamma p}(G_E^{\gamma n} + G_E^s) + \tau G_M^{\gamma p}(G_M^{\gamma n} + G_M^s) - (1 - 4\sin^2\theta_W)\varepsilon' G_M^{\gamma p} G_A^e}{\varepsilon(G_E^{\gamma p})^2 + \tau(G_M^{\gamma p})^2} \right] \quad (1)$$

where $G_{E(M)}^{\gamma p(n)}$ are the electric (magnetic) Sachs form factors for the proton (neutron) and G_A^e is the axial form factor seen in PV electron scattering, all functions of the square of the momentum transfer Q^2 . τ , ε and ε' are kinematic factors which suppress the axial contribution for the forward scattering angles we are considering here.

The first HAPPEX experiment ran in 1998-99 and measured the following combination at $Q^2 = 0.5$ (GeV/c)²: $G_E^s + 0.392G_M^s = 0.014 \pm 0.020 \pm 0.010$, where the first error is experimental and the second is due to uncertainties in the electromagnetic form factors [2]. Beyond a strange contribution compatible with zero, this result has demonstrated the high

Table 1. Expected asymmetries and errors for H and 4He targets. When not specified all asymmetries are ppm units.

	A^{PV}	δA_{stat}	δA_{syst}	Sensitivity
H	-1.60	0.08 (5%)	0.04 (2.5%)	$\delta(G_E^s + 0.08G_M^s) = 0.010$
4He	+7.8	0.18 (2.2%)	0.18 (2.2%)	$\delta G_E^s = 0.015$

“parity quality” of the CEBAF beam and has motivated second generation experiments to answer the questions raised: the strange form factors may be small at this Q^2 , or there may be an accidental cancellation. Our strategy is thus to perform a measurement at a smaller Q^2 of 0.1 (GeV/c)², and separate the electric and magnetic form factors by using proton and 4He targets. Because it is an isoscalar nucleus, the scattering on 4He is sensitive only to the electric strange form factor:

$$A^{PV} = \frac{G_F |Q|^2}{4\pi\alpha\sqrt{2}} \left(4\sin^2\theta_W + \frac{2G_E^s}{G_E^{YP} + G_E^{YM}} \right) \quad (2)$$

With a 3 GeV beam and a mean scattering angle $\theta = 6^\circ$, the final expected asymmetries and sensitivities to the strange form factors are listed in table 1. Control of the systematic error at the 40 ppb level for hydrogen, as well as control of the normalization at the 2% level for helium, are the challenges being taken up by these measurements.

3. Instrumentation

In order to meet the required control and understanding of our systematics at a more precise level than in the past, a number of upgrades of the apparatus has been implemented including: various improvements at the polarized source; better polarimetry; new target cells; new septum magnets; new radiation hard Čerenkov detectors; new luminosity monitors; new profile scanners and an improved data acquisition system (Fig.1).

The false asymmetries induced by the beam parameters are first minimized by a careful setup of polarization and transport system of the laser beam at the polarized source. The beam current asymmetry is then further reduced by a feedback loop connecting the beam current readout in hall A and the laser intensity modulation at the source. The position fluctuations at the target depend strongly on the beam optics and are more difficult to control via a feedback loop. Besides the careful setup at the source, the HAPPEX experiments thus rely on the “damping” of the position differences inherent in the acceleration of the electron beam as well as on the control of the beam optics near the target. To correct the small remaining effects, the detector sensitivities to all beam parameters are monitored by the usual regression and dithering techniques [3]. Thanks to the hard work by the source

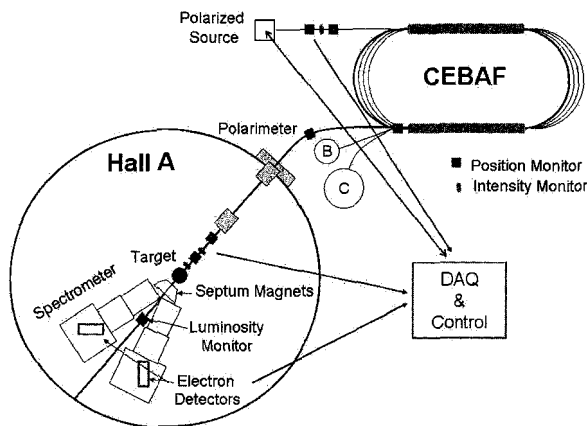


Fig. 1. Overview of HAPPEX experiment.

and accelerator groups in collaboration with HAPPEX personnel, the associated systematic error is kept small with respect to the statistical error.

The new “racetrack” design of the target cell features fluid flow transverse to the beam direction to reduce the target density fluctuations. These fluctuations are monitored by the new luminosity monitors mounted on the downstream beam line at very small scattering angles. The data show that they can be kept negligible with respect to the statistical width at high current provided that the beam is swept across a large enough surface (5x5 mm). In production mode the elastic rate is too high (up to 65 MHz) to get information on individual events. The signal is simply integrated by the HAPPEX detectors and the background rejection relies on the high resolution of the hall A spectrometers. Dedicated runs using the standard Hall A drift chamber package at low beam intensity allow an accurate study of the remaining background as well as the determination of the mean Q^2 intercepted by the detectors.

In order to achieve an accurate normalization of the helium asymmetry (table 1) the beam polarization is monitored by a Compton polarimeter. The use of a “super lattice” crystal at the source for part of the run has provided a record 88% polarization for the first time at JLab.

4. Extraction of strange form factors

Thanks to the various improvements described in Sec. 3 the corrections of the experimental asymmetries and the associated systematic errors are kept small. From the preliminary analysis of the summer 2004 data we have $A_{exp}^{PV}(^4He) = +7.40 \pm 0.89_{(stat)} \pm 0.57_{(syst)}$ and $A_{exp}^{PV}(H) = -1.10 \pm 0.27_{(stat)} \pm 0.10_{(syst)}$ at $Q^2 = 0.1$ (GeV/c)², from which we can extract:

$$G_E^S = -0.019 \pm 0.041_{(stat)} \pm 0.026_{(syst)} \quad (3)$$

$$G_E^S + 0.08G_M^S = 0.034 \pm 0.028_{(stat)} \pm 0.010_{(syst)} \pm 0.009_{(FF)}$$

where the last error is due mainly to the uncertainty on G_E^n . The helium measurement provides the first constraint on G_E^s . When combining Eqs.3 with the results of SAMPLE at MIT-Bates [5] and PVA4 at Mainz [6] for the same Q^2 , the trend of a potentially non-zero and positive magnetic strange form factor is confirmed, with a global one sigma contour of $G_M^s = +0.626 \pm 0.410$. In 2005 a second HAPPEX run will reduce the errors on $A_{exp}^{PV}(^4He)$ and $A_{exp}^{PV}(H)$ by factors three and two respectively. This high precision will either settle the existence of non-zero strange form factors at $Q^2 = 0.1$ (GeV/c)², or will constrain their contribution to the nucleon structure to a negligible level.

References

1. K.C. De Jager, "The Electromagnetic and Weak Nucleon Form Factors", *this conference* (2004).
2. K. Aniol *et al.*, *Phys. Rev. Lett.* **82**, 1096 (1999); K. Aniol *et al.*, *Phys. Lett.* **B509**, 211 (2001).
3. K. Aniol *et al.*, *Phys. Rev.* **C69**, 065501 (2004).
4. M.J. Ramsey-Musolf, *et al.*, *Phys. Rept.* **239**, 1-178 (1994)
5. D. Spayde, *et al.*, *Phys. Lett.* **B583**, 79-86 (2004) and references therein.
6. F.E. Maas, *et al.*, *Eur. Phys. J.* **A17**, 339 (2003).

TENSOR ANALYZING POWER IN EXCLUSIVE π^- -MESON PHOTOPRODUCTION ON DEUTERON*

V. N. STIBUNOV

Nuclear Physics Institute at Tomsk Polytechnic University, Tomsk, Russia

(for the Novosibirsk Deuteron Collaboration)

A new more precise measurement of the tensor target asymmetry for the exclusive π^- meson photoproduction on a deuteron for the high values of proton momenta is described. This measurement has been performed at the 2 GeV Novosibirsk VEPP-3 electron storage ring using the internal cell target method. Preliminary experimental results and the theoretical calculation are presented.

1. Introduction

The study of the exclusive π -meson photoproduction on tensor polarized deuterons is performed in the kinematic region at large polar angles of the outgoing protons, and of proton momenta above 250 MeV/c. This kinematic range is of interest because there is an opportunity to obtain new information on the dynamics of the NN -interaction at short distances. Our first measurement of the tensor analyzing power for this reaction [1] has low statistical accuracy. In order to obtain a reasonable statistical accuracy in the new experiment, both the cooling storage cell target and the novel high-intensity cryogenic atomic beam source (CABS) have been used, and the VEPP-3 electron beam optics has been modified [2].

2. Experimental Setup

This experiment has been performed on the internal tensor polarized deuterium target of the VEPP-3 electron storage ring simultaneously with measurement of the tensor analyzing power components in elastic ed -scattering [3]. The novel CABS fed the storage cell with the tensor polarized deuteron. The flux of polarized deuterium atoms reaching the storage cell is found to be $8.2 \times 10^{16} \text{ at/s}$. The CABS delivered two polarized states of the beam, one with $P_{zz}^+ = 1$ and the other with $P_{zz}^- = -2$. The vector polarization for both states is zero. The tensor polarization of the beam is monitored by the Breit-Rabi polarimeter and found to be more 98%.

*This work was supported in part by Ministry Education grant E02-3.3-216 and Russian Foundation for Basic Research grant 01-02-16929.

The storage cell fabricated from 30 μm thick aluminum foil had an elliptic cross section 13×24 mm and length 400 mm. In order to increase the target density the cell is cooled by liquid nitrogen. The inner surface of the cell is coated with drifilm to inhibit atom depolarization. The target thickness viewed by the detection system is found to be $8 \times 10^{13} \text{at}/\text{cm}^2$. Inside the storage cell the degree of the polarization of atoms becomes smaller, because there are depolarization effects. In order to determine the effective tensor polarization of the target, the low-Q polarimeter (LQP) is used. LQP is based on the measurement of the target asymmetry in elastic ed -scattering at momentum transfers around $Q^2 \approx 3 \text{fm}^{-2}$. At such Q^2 the theoretical predictions of the target asymmetry are reliable, and also an absolute measurement of the T_{20} component of tensor analyzing power had been performed in the past. The average degree of target polarization during the experiment is found to be $P_{zz}^+ = 0.397 \pm 0.013[\text{stat.}] \pm 0.018[\text{syst.}]$. The target polarization axis is fixed by a magnetic holding field H (with angles $\theta_H \approx 120^\circ$ and $\phi_H \approx 0^\circ$). The tensor polarization of the target was flipped every 30 s, between P_{zz}^+ and P_{zz}^- . The detector (Fig. 1) is composed

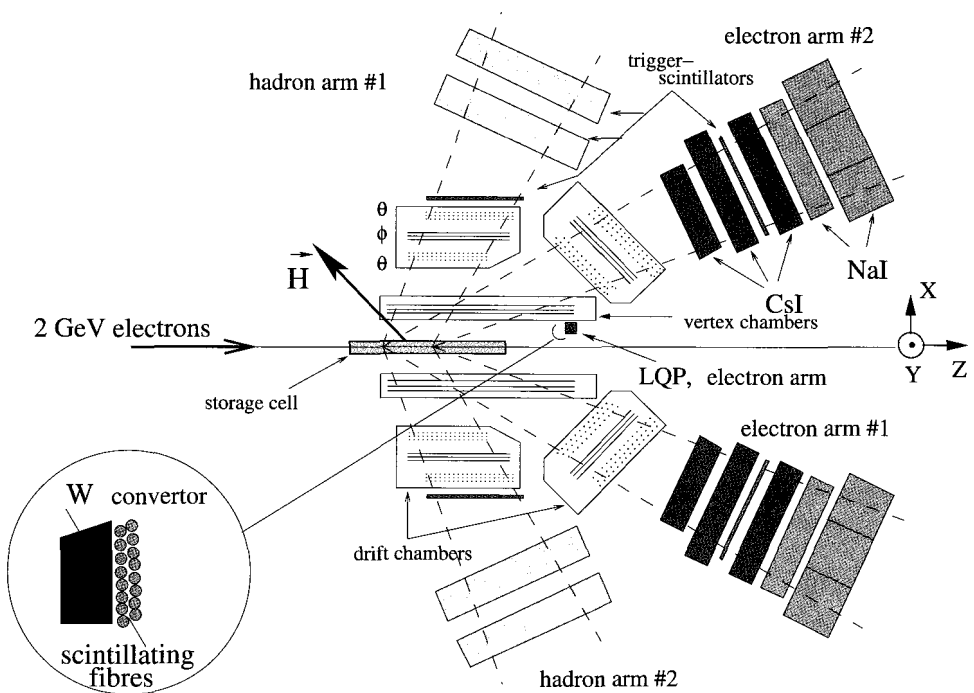


Fig. 1. Schematic overview of the detection system package. Side view.

of two nearly identical systems [3]. Each consisted of an electron arm and a hadron arm. Two hadron hodoscopes are used to detect two protons in coincidence. Around the storage cell and in front of the detector arms, drift chambers are positioned to register the particle tracks. Each hadron hodoscope included three plastic scintillator counters with total thicknesses 27 cm. For determination of the proton energy and particle identification, the energy

loss in two layers is required and the proton has to be stopped in the hodoscope. Therefore the proton detection energy ranges from 55 to 210 MeV. The angular acceptances of each hadron arm are $\theta_{1,2} = 55^\circ - 88^\circ$ and $\Delta\phi_{1,2} = 60^\circ$.

3. Results and Discussion

Specially developed analysis software is used for off-line data analysis. The calculations of the particle tracks, event vertexes, hodoscope responses, physics variables, and the selection of the events are performed by this software. The tensor target asymmetry is defined as:

$$A^t = \sqrt{2} \frac{(N^+ - N^-)}{(N^- P_{zz}^+ - N^+ P_{zz}^-)}, \quad (1)$$

where N^+ (N^-) are the normalized number of events measured from the positive (negative) polarized target. The T_{21} component of the tensor analyzing power is defined as:

$$T_{21} = \frac{k_\varphi}{2d_{21}} \left(A^t_{\varphi_s=0} - A^t_{\varphi_s=\pi} \right), \quad (2)$$

where $k_\varphi = 1.047$ is the azimuthal acceptance corrections, $d_{21} = \sqrt{3/8} \sin 2\theta_H = -0.53$, and φ_s is the azimuthal angle of the slow proton.

The measured data are compared with the theoretical calculation. The polarization observables of the reaction are calculated on the base of a diagram approach. In this model we take into account the contributions to the amplitude that come from diagrams corresponding to the spectator model, πN - and NN - rescattering [4]. The deuteron wave functions for both Bonn and Paris NN -potentials are used in the investigation.

In order to compare the theoretical predictions for the polarization observables with the experimental results, a Monte Carlo (MC) code was developed that performs the proper averaging of the theoretical calculation. This MC code generated exclusive π^- -meson photoproduction events on polarized deuterons, randomly over phase space. For each of these generated events the cross section and the polarization observables T_{20} , T_{21} , T_{22} and A^t are derived from the theoretical calculations.

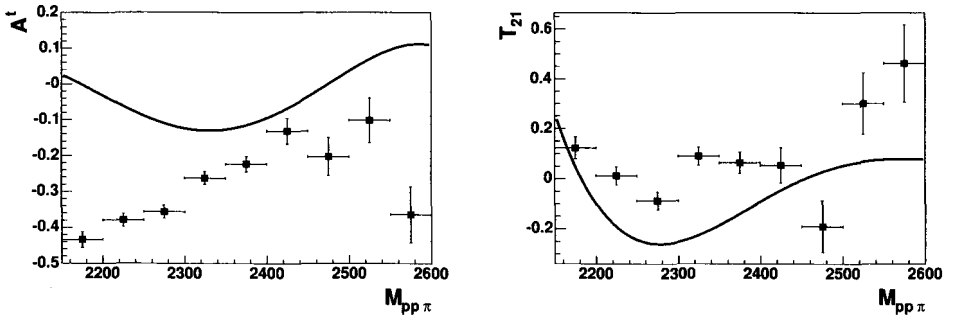


Fig. 2.

The experimental tensor target asymmetry and T_{21} -component of the tensor analyzing power as a functions of the $pp\pi$ - invariant mass are shown in Fig. 2. The theoretical predictions are shown by continuous curves. From this figure it can be seen that the theoretical prediction for the tensor target asymmetry disagrees with the experimental results.

References

1. A.Yu. Loginov et al. *JETF Letters*, **v.67**,N 10, 770 (1998).
2. M.V. Dyug et al. *Nucl. Instr. and Meth.*, **A495**, 8 (2002).
3. D.M. Nikolenko et al., *Phys. Rev. Lett.*, **90**, 072501 (2003).
4. A.Yu. Loginov et al., *Physics of Atomic Nuclei*, **63**, 391 (2000).

MEASUREMENT OF TENSOR ANALYZING POWERS IN DEUTERON PHOTODISINTEGRATION

D. K. TOPORKOV

BINP, 630090 Novosibirsk, Russia

(for the Novosibirsk Deuteron Collaboration)

Using a unique opportunity to operate the tensor-polarized deuterium gas target internal to an electron storage ring, we continue the study of tensor asymmetries in electromagnetic processes on the deuteron. Here we report on an experiment on photodisintegration of tensor polarized deuteron recently completed at the 2-GeV electron storage ring VEPP-3, Novosibirsk. The measurements were performed in the photon energy range 40 – 500 MeV and covered proton emission angles 20° – 40° and 80° – 100°. Preliminary results and comparison to existing theoretical predictions are presented.

1. Introduction

Deuteron two-body photodisintegration has been a subject of extensive experimental and theoretical studies for a long time. However data on tensor polarization observables are still very limited. There are data from only two experiments prior to the present one, both performed at BINP, Novosibirsk, at the electron storage rings VEPP-2 [1] and VEPP-3 [2]. Here we report on a new measurement of tensor analyzing powers of deuteron photodisintegration, recently completed at VEPP-3.

A general expression for the cross-section of two-body photodisintegration of the tensor-polarized deuteron can be written as follows:

$$\frac{d\sigma}{d\Omega} = \frac{d\sigma_0}{d\Omega} \left\{ 1 + 1/\sqrt{2} \cdot P_{zz} [(3 \cos^2 \theta^* - 1)/2 \cdot T_{20} + \sqrt{3/8} \cdot \sin 2\theta^* \cos \phi^* \cdot T_{21} \sqrt{3/8} \cdot \sin^2 \theta^* \cos 2\phi^* \cdot T_{22}] \right\},$$

where σ_0 – cross section for unpolarized deuteron, P_{zz} – degree of tensor polarization; the angles θ^* and ϕ^* define the orientation of the polarization axis relative to the photon momentum and the scattering plane. Tensor analyzing powers T_{20} , T_{21} , T_{22} are functions of photon energy and CM proton emission angle. The immediate observable is a target asymmetry, defined as $A^t = \sqrt{2} \frac{(N^+ - N^-)}{(N^- P_{zz}^+ - N^+ P_{zz}^-)}$, where N^+ and N^- are event counts for target polarization P_{zz}^+ and P_{zz}^- respectively. N^+ and N^- are normalized to the electron beam charge.

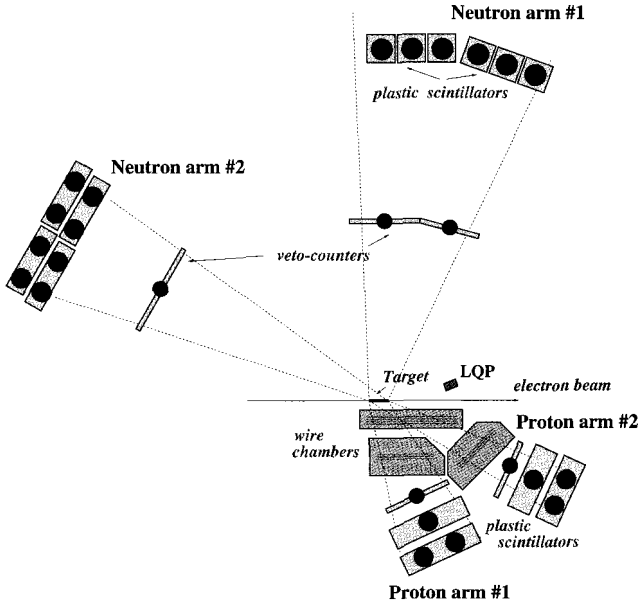


Fig. 1. The layout of the detector system, side view.

To separate the three analyzing powers one should do the measurements for three settings of polarization axis. We measured A_0^T , A_1^T and A_2^T for $\theta_0^* = 0^\circ$, $\theta_1^* \approx 55^\circ$ and $\theta_2^* \approx 125^\circ$ respectively, keeping $\phi^* \approx 0^\circ$. Then $T_{20} \sim A_0^T$, $T_{21} \sim (A_1^T + A_2^T)$ and $T_{22} \sim (A_1^T - A_2^T)$.

2. Tensor polarized deuterium target

The key improvement of the new experiment over our previous one [2] is the introduction of the new Cryogenic Atomic Beam Source [3] providing a record flux of polarized deuterium atoms $8.2 \times 10^{16} \text{ at/s}$, and a storage cell, cooled by liquid nitrogen. This resulted in an effective target thickness of 6.5×10^{13} , gaining two orders of magnitude over the target used in [2]. The average degree of tensor polarization was found to be $P_{zz} = 0.378 \pm 0.022$. It was obtained by a “low-Q” polarimeter, which measured an asymmetry in elastic ed – scattering, similar to what we did earlier [4].

3. Experimental set up

The particle detector consisted of two pairs of arms each detecting a proton and neutron in coincidence, see Fig 1. The proton arm includes wire chambers for tracking and three layers of scintillator plastics. The neutron arm is based on plastic scintillator bars placed at the largest available distance from the target (2.7 – 3 m) to provide the best energy (by TOF method) and angular resolution. Such a detector allowed us in a single run to collect data in a wide range of photon energy and emission angle: $E_\gamma \sim 40 - 500 \text{ MeV}$, $\theta_p^{cm} \sim 20^\circ - 40^\circ$ and $80^\circ - 100^\circ$.

4. Preliminary results

The preliminary results of data analysis are shown in Figs. 2 – 4. The data were divided into several bins of E_γ and θ_p^{cm} , and we present the histograms either for a selected E_γ -bin over θ_p^{cm} , or for a selected θ_p^{cm} -bin over E_γ . Only statistical errors are shown.

One can see that the new data are in good agreement with the earlier measurement (where the acceptances of the two experiments overlap). On the other hand one can see a substantial discrepancy between the experiment and theoretical predictions at E_γ above ~ 100 MeV, especially for T_{22} at large θ_p^{cm} and for T_{20} at small θ_p^{cm} . The origin of this discrepancy is not yet understood.

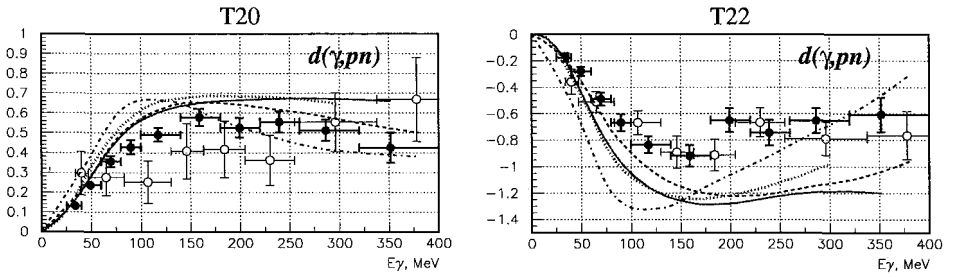


Fig. 2. Preliminary results for T20 and T22 plotted as functions of photon energy for $\theta_p^{cm} = 83^\circ - 93^\circ$. A fraction of new data (solid circles) that covered about the same E_γ - θ_p^{cm} acceptance as in the earlier experiment [2] (open circles) is shown.

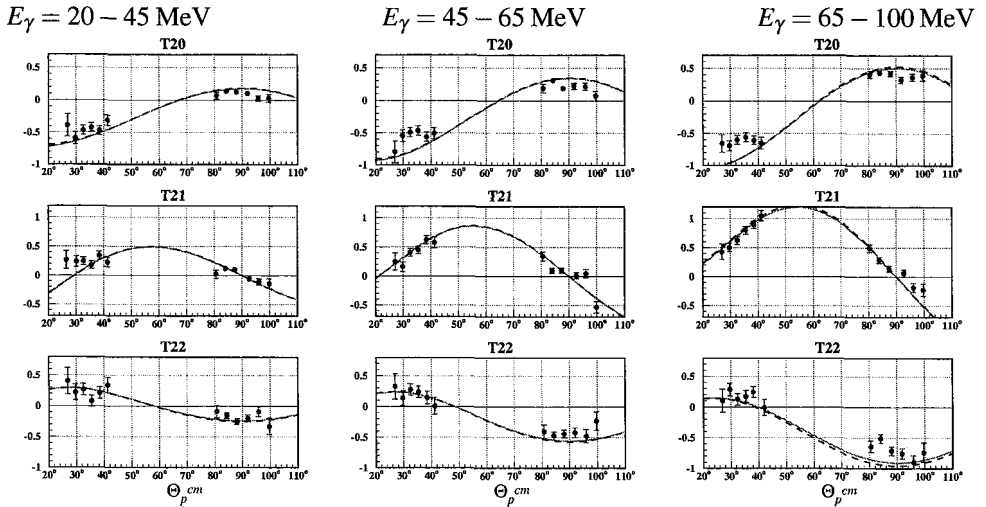


Fig. 3. Preliminary results for $E_\gamma = 25 - 150$ MeV. Theoretical curves are from Ref. [5] (solid line) and from Ref. [6] (dashed line).

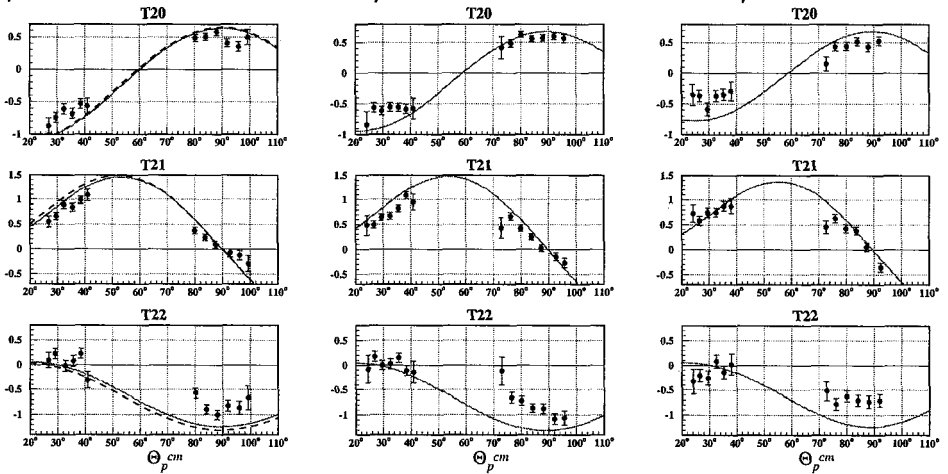
$E_\gamma = 100 - 150$ MeV $E_\gamma = 150 - 250$ MeV $E_\gamma = 250 - 400$ MeV

Fig. 4. Preliminary results for $E_\gamma = 150 - 400$ MeV. Notations as in Fig. 3.

This work was supported in part by Russian Foundation for Basic Research, grants 01-02-17276 and 01-02-16929.

References

1. M.V. Mostovoy *et al.*, Phys. Lett. **B189**, 181 (1987).
2. S.I. Mishnev *et al.*, Phys. Lett. **B302**, 23 (1993).
3. M.V. Dyug *et al.*, Nucl. Instrum. Methods **A495**, 8 (2002).
4. D.M. Nikolenko *et al.*, Phys. Rev. Lett. **90**, 072501 (2003).
5. K.-M. Schmitt and H. Arenhövel, Few Body Systems **7**, 95 (1989).
6. M.I. Levchuk, Few Body Systems **19**, 77 (1995).

PRELIMINARY RESULTS OF ${}^2\text{H}(e, e'p)n$ IN BLAST

A. MASCHINOT

Massachusetts Institute of Technology, Cambridge

(for the BLAST Collaboration)

Due to its simple composition, the deuteron has long been recognized as important in understanding the structure of the inter-nucleon potential. With this goal, a comprehensive study of low- Q^2 spin-dependent electron scattering from deuterium is currently underway using the polarized electron beam provided by the MIT-Bates linear accelerator. Using the BLAST (Bates Large Acceptance Spectrometer Toroid) detector together with an internal vector/tensor polarized deuterium target, a comprehensive spin-dependent analysis of proton scattering is being performed. Due to the detector's large acceptance and symmetric design, simultaneous determination of the deuteron's parallel and perpendicular asymmetries is possible over a Q^2 range between 0.1 and 0.5 GeV^2 . Preliminary asymmetry results are presented here along with a comparison with theory.

1. Introduction

The deuteron, being the only bound two-nucleon system and thus the simplest one in which the nuclear force is manifest, is a natural starting point for an investigation of the nuclear electromagnetic current. Additionally, due to the lack of free neutron targets, deuterium has often been used as a good approximation to a free neutron target, thus enabling the extraction of neutron-related physics measurables, such as G_E^n [1, 2]. However, in order to model deuterium as a free neutron target, one must be able to account for effects due to the neutron being bound within the deuterium nucleus. Accounting for such effects requires an accurate knowledge of the deuteron spin structure as well as the inter-nucleon potential along with reaction mechanisms, such as meson-exchange currents (MEC), isobar configurations (IC), and relativistic corrections (RC). For these reasons, comprehensive measurements of deuteron observables are essential.

Measurements of spin-dependent deuteron observables have the potential to enhance our understanding of nucleon and nuclear structure by providing access to small but dynamically-interesting amplitudes which otherwise disappear or get washed out in spin-independent processes [3]. In particular, coincidence ${}^2\text{H}(e, e'p)n$ reactions promise to advance our understanding of the inter-nucleon interaction.

The cross section for exclusive deuteron electrodisintegration can be written as fol-

lows [4]:

$$S(h, P_z, P_{zz}) = S(0, 0, 0) \left\{ 1 + \sqrt{\frac{3}{2}} P_z A_d^V + \sqrt{\frac{1}{2}} P_{zz} A_d^T + h \left(A_e + \sqrt{\frac{3}{2}} P_z A_{ed}^V + \sqrt{\frac{1}{2}} P_{zz} A_{ed}^T \right) \right\} \quad (1)$$

where h is the electron beam polarization, and P_z and P_{zz} are the respective deuterium target vector and tensor polarizations. The $A_{(d,e,ed)}^{(V,T)}$ terms are the various beam/target asymmetries, and $S(0, 0, 0)$ is the totally-unpolarized cross section. When one considers a pure S -wave deuteron, the tensor asymmetry (A_d^T) vanishes. Thus, measurements of A_d^T can provide insight into the tensor component of the internucleon potential. In addition, the beam-vector asymmetry (A_{ed}^V) when the proton is detected exhibits sensitivity to various reaction mechanisms.

2. The BLAST Spectrometer and Experimental Setup

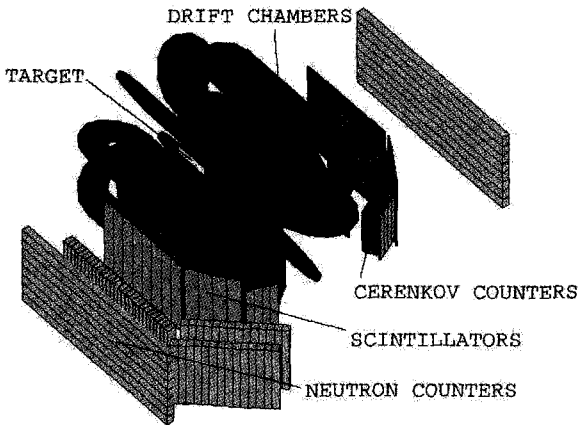


Fig. 1. The BLAST spectrometer

This measurement is being performed at the MIT-Bates Linear Accelerator Center using the BLAST (Bates Large-Acceptance Spectrometer Toroid) detector. A longitudinally polarized 0.850 GeV electron beam is incident on an internal atomic beam source (ABS) polarized deuterium target. The deuterium target sequentially switches between three polarization states, $(P_z, P_{zz}) = (p_z, p_{zz})$, $(-p_z, p_{zz})$, and $(0, -2p_{zz})$.

The beam polarization is measured via a Compton polarimeter; the target's vector and tensor polarizations are determined via fits of the data to Monte Carlo results. By flipping the beam's helicity as well as the target's polarization states, it is possible to measure all five of the asymmetries listed in Eq. 1.

Scattered particles are detected in the BLAST detector (see Fig. 1). The detector is based around an eight sector toroidal magnet with two opposing sectors instrumented with left/right symmetric detectors. Each detector sector is equipped with three drift chambers (for momentum reconstruction) as well as a layer of Cerenkov counters (for electron/pion discrimination), a layer of scintillators (for time-of-flight measurements), and a layer of neutron counters. In addition, the right sector is instrumented with an additional three layers of neutron counters. The drift chambers have a large acceptance, allowing measurements to be made over a Q^2 range of 0.1 to 0.5 GeV².

The target's polarization vector is aligned in-plane within the left sector so as to form a 32° angle with the beam line. By doing so, it is possible to isolate various parallel/perpendicular asymmetry components. For example, an electron passing through the left (right) sector has a corresponding three-momentum transfer vector, q , that lies within the right (left) sector, and thus q is approximately perpendicular (parallel) to the target polarization vector, s_d . Thus, electrons detected in the left (right) sector will emphasize asymmetry components that go as the cosine (sine) of the angle between q and s_d .

3. Preliminary Results

Figures 2 and 3 show our asymmetry results as compared to a theoretical model from H. Arenhovel et. al. [4] Systematic errors, though expected to be small, have not yet been incorporated into the analysis; all error bars in the figures are purely statistical.

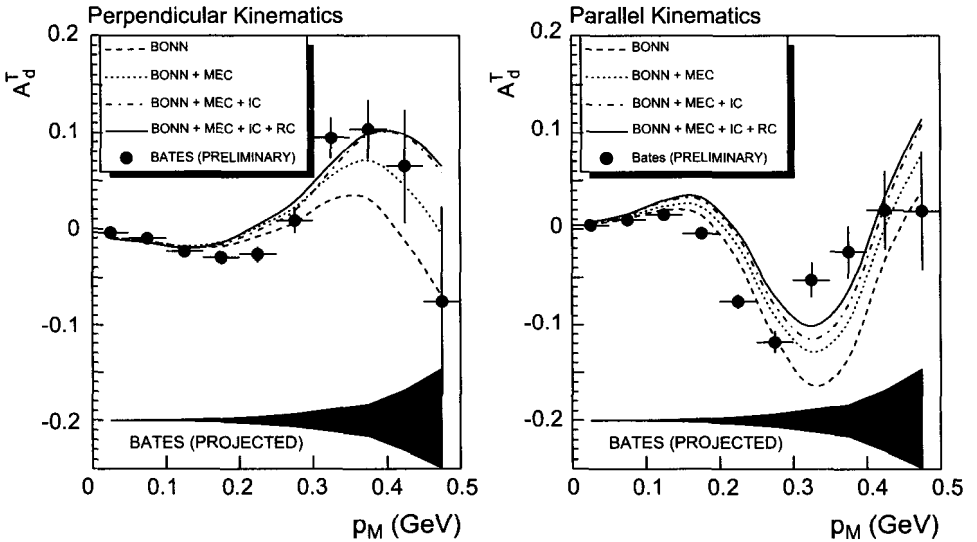


Fig. 2. ${}^2\text{H}(e, e'p)n$ Tensor Asymmetry, A_d^T , versus missing-momentum, p_M

The reconstructed tensor asymmetries show the same high missing-momentum “hump” as the theoretical ones, supporting the existence of a tensor component of the inter-nucleon potential. The reconstructed beam-vector asymmetries show the expected rise at high missing-momentum and supply evidence for the necessity for the inclusion of reaction mechanism effects. The results presented here are for roughly half of the total ${}^2\text{H}(e, e'p)n$ data expected to be collected. The projected errors for the full amount of data show that our results should go far to help discriminate between various reaction mechanism contributions.

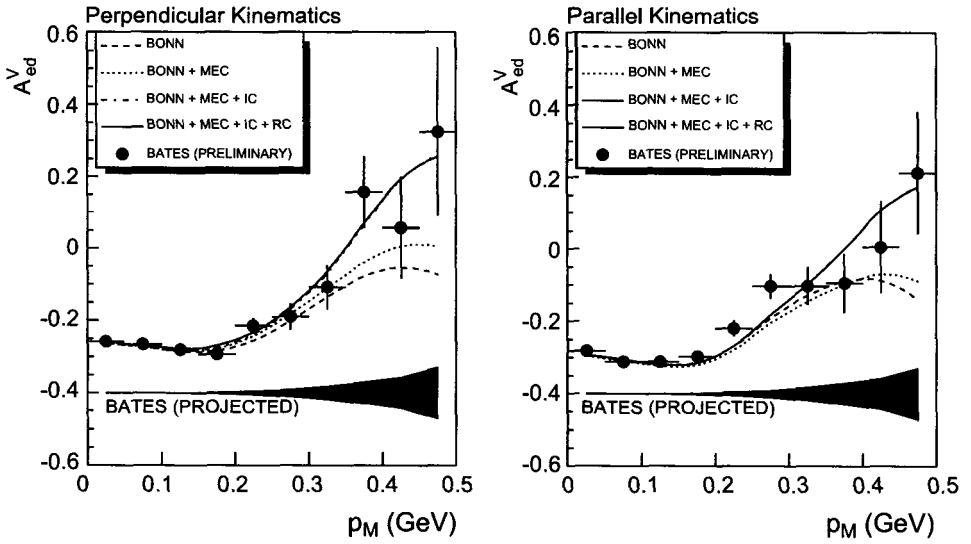


Fig. 3. ${}^2H(e, e'p)n$ Beam-Vector Asymmetry, A_{ed}^V , versus missing-momentum, p_M

References

1. B. R. Plaster, Ph.D. thesis, Massachusetts Institute of Technology, 2004 (unpublished)
2. R. Mady, et. al., *Phys. Rev. Lett.*, **91**, 122002 (2003)
3. BLAST proposed-approved experiment 00-03, "A Study of the Deuteron Structure Using Tensor Polarized Deuterium and the BLAST Detector", spokesperson: Z. Zhou, 2000, p.3
4. H. Arenhovel, W. Leidemann, and E. L. Tomusiak, *Phys. Rev. C*, **46**, 455 (1992)

Λ POLARIZATION IN EXCLUSIVE ELECTRO- AND PHOTOPRODUCTION

M. D. MESTAYER

Thomas Jefferson National Accelerator Facility, Newport News, USA

(representing the CLAS Collaboration)

I present recent results from the CLAS collaboration on Λ and Σ^0 polarization for both electroproduction and photoproduction of $K^+\Lambda$ and $K^+\Sigma^0$ exclusive states. I interpret these data using a simple quark model, leading to the surprising conclusion that the s and \bar{s} quarks are produced with spins anti-aligned, in apparent contradiction to the popular 3P_0 model of quark pair creation.

One of the important goals of hadronic physics is to understand the strong interaction which binds quarks into hadrons. The hypothesis that gluonic fields coalesce into a “flux-tube” can be tested by studying “tube-breaking” through quark-pair creation [1, 2]. A series of papers [3–6] attempted to explain meson-decay data by applying various models for the operator representing quark-pair creation. A consensus developed that the 3P_0 state dominates $q\bar{q}$ creation but it is only partially tested. Measuring Λ polarization in exclusive production is also sensitive to the spin state of the $s\bar{s}$ pair and can further test the “ 3P_0 hypothesis”.

1. Experiment Description and Analysis

I describe two experiments published by the CLAS collaboration. The first [7] is a measurement of induced Λ and Σ^0 polarization in photoproduction of $K^+\Lambda$ and $K^+\Sigma^0$ with unpolarized beam and target. The second [8] is a measurement of spin transfer from a polarized electron beam to the polarized Λ in $K^+\Lambda$ production from an unpolarized proton target.

These experiments were performed in Hall B at Jefferson Lab. Kaons were identified using the tracking and time-of-flight capabilities of the CLAS detector [9]. The recoil Λ (or Σ^0) was identified by missing mass. The data were binned in $\cos\theta_K^*$ and W where $\cos\theta_K^*$ is the cosine of the K^+ angle and W the total energy in the hadronic center-of-mass system. We also detected the decay proton (from $\Lambda \rightarrow p\pi^-$) and fitted the distribution of events to a form $1 + \alpha \cdot P \cdot \cos\theta_p$, where α is the Λ decay analyzing power value of 0.642, P is the polarization of the Λ sample, and $\cos\theta_p$ is the cosine of the proton’s angle relative to a chosen axis in the Λ rest frame.

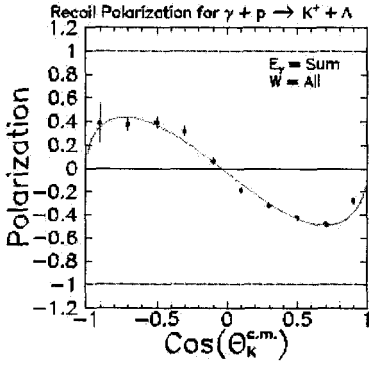


Fig. 1. Recoil polarization in $\gamma p \rightarrow K^+ \Lambda$ events averaged over all E_γ .

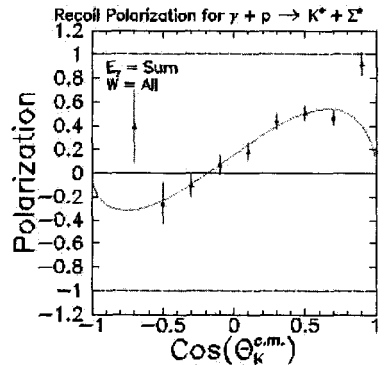


Fig. 2. Recoil polarization in $\gamma p \rightarrow K^+ \Sigma^0$ events averaged over all E_γ .

Because parity is conserved in $K^+ \Lambda$ production and the photon beam was unpolarized, the polarization in the photoproduction experiment can only be non-zero along the normal (\hat{n}) axis where $\hat{n} = \hat{q} \times \hat{p}_K$. For each bin in W and $\cos \theta_K^*$ the Λ polarization was obtained by a fit of the proton's decay angle distribution, as explained above. The Σ^0 polarization was determined by a fit to $1 + \alpha_\Sigma \cdot \alpha \cdot P \cdot \cos \theta_p$, where $\alpha_\Sigma = -1/3$ accounts for the polarization transfer from the Σ^0 to Λ decay. See Figs. 1 and 2 for the fitted Λ and Σ^0 polarization plotted versus $\cos \theta_K^*$, averaged over all incident photon energies. The curve is a phenomenological fit which is constrained to equal 0 at the endpoints. The Λ 's are negatively polarized (opposite the normal to the hadronic plane) for kaons produced in the forward hemisphere and positive for backward-going kaons. Interestingly, the Σ^0 polarization values are approximately equal in magnitude but opposite in sign from the Λ values.

For the second experiment we used a polarized electron beam. The existence of this pseudo-vector (the electron's spinor) means that polarization is allowed along any of the three axes in the Λ 's rest frame. Averaging the data over ϕ (the angle between the electron and hadronic planes) integrates the normal component to zero. In Figure 3 we plot the Λ polarization transfer along z (top) and x (bottom) as a function of $\cos \theta_K^*$ for three values of W , where z is along the virtual photon direction and x is perpendicular to z but in the electron scattering plane.

The x -polarization transfer is consistent with zero whereas the z -polarization transfer is large (about 75%) and is flat or shows a slow rise with $\cos \theta_K^*$. The polarization is approximately independent of center-of-mass energy, W . The curves are from hydrodynamic models [10]; see our recent paper [8] for details.

2. Observations and Conclusions

The observed polarizations are large and show a simple phenomenology. These results can constrain the parameters of hydrodynamic models, but the simple phenomenology begs a

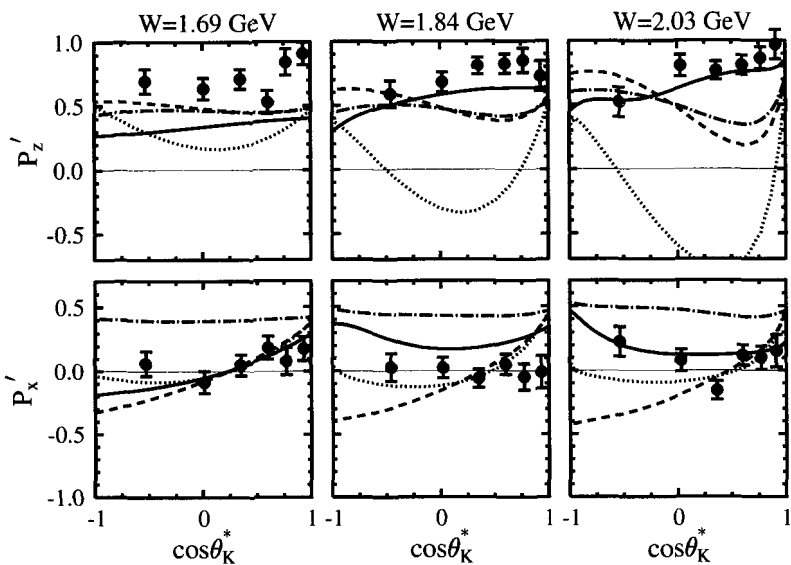


Fig. 3. Transferred Λ polarization components P'_x and P'_z plotted versus $\cos\theta_K^*$, summed over all Q^2 and Φ for three w bins centered at 1.69, 1.84 and 2.03 GeV.

quark model explanation. The equal but opposite induced polarizations for Λ and Σ^0 are natural if there is an underlying mechanism which polarizes the s -quark because, in $SU(3)$, the polarization of the Λ is parallel to the spin of the s -quark, whereas the polarization of the Σ^0 is anti-parallel.

Following arguments in a recent publication [11], I speculate that there is a spin-orbit force which polarizes the u -quark anti-parallel to \hat{n} . For the K^+ to have spin-zero, the \bar{s} quark's spin is selected to be parallel to \hat{n} . Since we observe the Λ 's polarization to be anti-parallel to \hat{n} , we infer that the s and \bar{s} were produced with spins anti-aligned. A similar argument explains our electroproduction results, although here the virtual photon polarizes the u -quark directly.

What is the angular momentum state of $q\bar{q}$ pairs which “break” the flux-tube? Our data seem to show that the s and \bar{s} quarks are produced with spins anti-aligned, presumably in an $S = 0$ state, inconsistent with the 3P_0 model. We eagerly await a more rigorous theoretical treatment of our data to unravel this paradox.

Acknowledgments

This paper represents the work of the entire CLAS collaboration, although some of the speculations are my own. I wish to recognize the important help and encouragement provided by Nathan Isgur.

References

1. L. Micu, *Nucl. Phys.* **B10**, 521 (1969); R. Carlitz and M. Kislinger, *Phys. Rev.* **D2**, 336 (1970), LeYaouanc, Oliver, Pene and Raynal *Phys. Rev.* **D8**, 2223 (1973).
2. A. Casher, H. Neuberger, and S. Nussinov *Phys. Rev.* **D20** 179 (1979).
3. Richard Kokoski and Nathan Isgur, *Phys. Rev.* **D35**, 907 (1987).
4. S. Kumano and V.R. Pandharipande, *Phys. Rev.* **D38**, 146 (1988).
5. Paul Geiger and Eric Swanson, *Phys. Rev.* **D50**, 6855 (1994).
6. E.S. Ackleh, T. Barnes and E.S. Swanson, *Phys. Rev.* **D54**, 6811 (1996).
7. J.W.C. McNabb *et al.*, *Phys. Rev.* **C69**, 042201 (2004), J.W.C. McNabb thesis, Carnegie Mellon University, (2002), unpublished.
8. D.S. Carman *et al.*, *Phys. Rev. Lett.* **90**, 131804 (2003).
9. B. Mecking *et al.*, *Nucl. Instr. and Methods* **A503**, 515 (2003).
10. R.A. Williams *et al.*, *Phys. Rev.* **C46**, 1617 ,(1992), T. Mart and C. Bennhold, *Phys. Rev.* **C61**, 012201, (2000), S. Janssen *et al.*, *Phys. Rev.* **C65**, 015201, (2002).
11. Liang Zuo-tang and C. Boros *Phys. Rev.* **D61**, 117503 (2000).

SPIN ASYMMETRIES A_{et} AND A_t IN EXCLUSIVE η ELECTROPRODUCTION FROM THE PROTON

P. E. BOSTED

Jefferson Lab, Newport News, USA

(for the CLAS Collaboration)

For the first time, measurements were made of the double-spin asymmetry A_{et} and the target single-spin asymmetry A_t in the exclusive reaction $p(e, e' p)\eta$ in kinematics dominated by the excitation of the $S_{11}(1535)$ resonance. Both A_{et} and A_t are found to be in agreement with the Eta-MAID model, which predicts strong dominance of $S_{11}(1535)$ excitation in the region studied, $0.3 < Q^2 < 1 \text{ GeV}^2$ and $1.49 < W < 1.59 \text{ GeV}$.

1. Introduction

It has long been known that exclusive electroproduction of the light pseudoscalar mesons is dominated by a single prominent resonance near threshold. In the case of the pion, this is the $P_{33}(1233)$, while in the case of the η it is the $S_{11}(1535)$. At a higher final state mass W , additional wide and overlapping resonances are excited. A continuous non-resonant background also plays a role. The η final state is of particular interest, as only N^* ($I = 1/2$) resonances can be excited due to the isoscalar nature of the η . In global fits to electroproduction data, the η final state is in principal very useful, as only approximately one half of the nucleon resonances play a role. In practice, measurements are difficult because most N^* resonances have small branching ratios to decay to $p\eta$ (of order 10% or less). The exception is the low-mass $S_{11}(1535)$ resonance, which has a large branching ratio (of order 50% [1]). This is reflected in the total spin-average exclusive η photoproduction cross section, which drops rapidly from about $15 \mu b$ near $W = 1.535 \text{ GeV}$ to a fairly constant value of a few μb above $W = 1.6 \text{ GeV}$ [2].

To disentangle the relative contributions of the background and resonant terms, spin asymmetries are particularly useful. For a pure $S_{11}(1535)$ excitation, only the helicity non-flip term $\sigma_{1/2}$ can contribute, while $\sigma_{3/2} = 0$, which leads to large double spin asymmetries A_{et} in scattering of longitudinally polarized electrons from polarized protons. In addition, the single spin target asymmetry A_t and beam asymmetry A_b are zero if there are no interference terms. While the latter has been studied in photoproduction [3], it has not been studied in electroproduction, and neither A_{et} nor A_t have been studied using real or virtual photons at all.

2. Experiment

The goal of the present study is to investigate A_{et} and A_t in exclusive η electroproduction to test and constrain models of N^* and non-resonant production, such as the unitary isobar models Eta-MAID [4]. Data were analyzed from the EG1b experiment in Hall B at Jefferson Lab, which ran in 2000-2001, with a longitudinally polarized electron beam with energies of 1.6 to 5.7 GeV and polarization P_b averaging 70%, incident on a longitudinally polarized NH_3 target with average polarization P_t of 70%. The analysis closely follows the approach taken in analyzing the exclusive π^0 electroproduction reaction from the first phase of the experiment (EG1a) [5]. Due to small signal to noise at higher W , only the $S_{11}(1535)$ region ($1.49 < W < 1.59$ GeV) was studied for η electroproduction.

Electrons were identified from a large background of negative pions by requiring a substantial signal in the gas Cherenkov counter and a large energy deposition in the electromagnetic calorimeter. Protons were primarily selected from a background of pions and kaons using time-of-flight (TOF) information. Photons, if any, were identified using TOF and the absence of a track pointing to an energetic cluster in the calorimeter.

The exclusive $p\eta$ final state was identified from the ep missing mass spectrum. A large background from nitrogen, helium and aluminium in the target was corrected for using spectra measured with the carbon target, normalized to fit the NH_3 spectra on either side of the η peak. Thus the background subtraction included both Fermi-smearred η production as well as two-pion production from the free proton.

The double-spin asymmetry A_{et} was calculated from the asymmetry in the raw rates (after subtraction of background from He, N, and Al, based on the C target spectrum), divided by $P_b P_t$, the product of beam and target polarization, as determined from the analysis of ep elastic events. The sign was chosen to agree with the MAID convention, and corresponds to A_{et} being negative for ep elastic scattering (or $\sigma_{3/2} - \sigma_{1/2}$). Note, on the figures we plot $-A_{et}$, which is +1 for ep elastic scattering and the $N \rightarrow S_{11}$ transition. The actual asymmetry is smaller than unity due to the de-polarization of the virtual photon, approximately given by

$$D = (1 - \varepsilon E'/E),$$

where E is the incident electron energy, E' is the scattered electron energy, and $\varepsilon = 1/[1 + 2(1 + v^2/Q^2)\tan^2(\theta/2)]$, where $v = E - E'$, θ is the electron scattering angle, and $Q^2 = 4EE'\sin^2(\theta/2)$. Numerically, $D \approx 0.75$ for the $E = 1.6$ GeV data, and $D \approx 0.25$ for the $E = 5.7$ GeV data.

The results for $-A_{et}$ at $E = 1.6$ GeV are plotted in Fig. 1 as a function of $\cos(\theta^*)$ (averaged over ϕ^*), for four bins in W near the S_{11} peak. The average Q^2 is about 0.4 GeV^2 (1.0 GeV^2) for $E = 1.6$ ($E = 5.7$ GeV). The results are in good agreement with strong dominance of the $N \rightarrow S_{11}$ transition in this W range, as evidenced by values that are close to the average value of D , independent of $\cos(\theta^*)$. The results are also in good agreement with the predictions of Eta-MAID [4], which was fitted to photoproduction data, and also assumes $N \rightarrow S_{11}$ dominance below $W = 1.59$ GeV.

Since both the data and the model show little dependence on W , we have averaged the

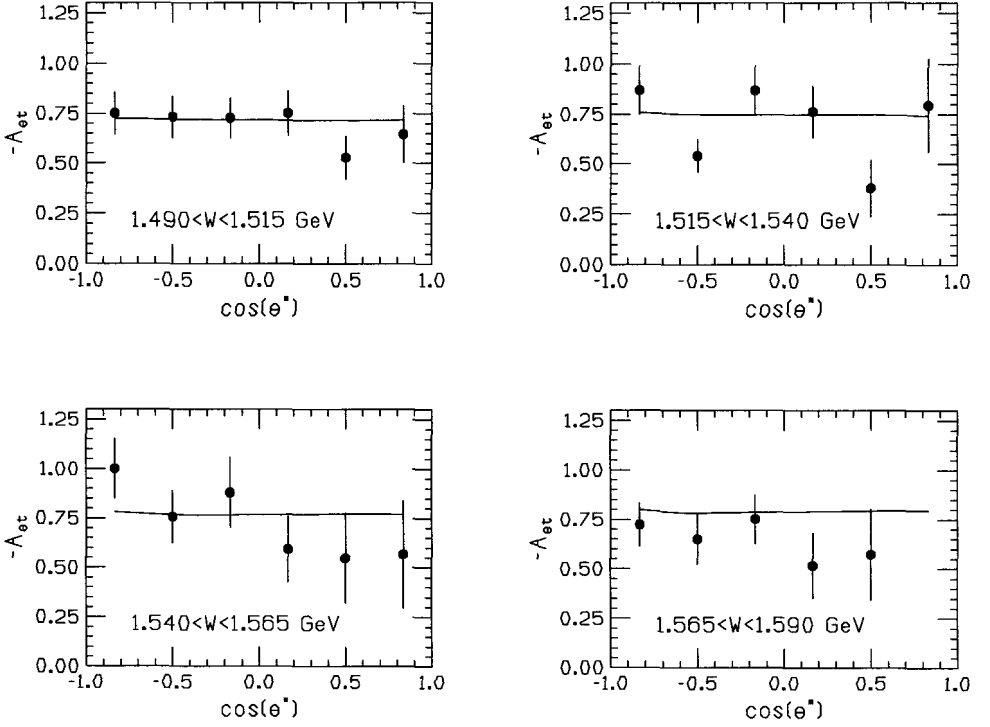


Fig. 1. Double-spin asymmetry $-A_{et}$ for exclusive eta electroproduction from the proton for $E = 1.6$ GeV, averaged over ϕ^* , as a function of $\cos(\theta^*)$ for the four indicated bins in W . The curve is the prediction of Eta-MAID.

data over $1.49 < W < 1.59$ GeV, and extracted the quantity $-A_{et}$ as a function of ϕ^* for six bins in $\cos(\theta^*)$. Due to the poor acceptance for low momentum protons, the statistical errors are large for backward η angles and become smaller at forward angles. As expected for $N \rightarrow S_{11}$ dominance, there is little dependence on ϕ^* in both the data and the model.

Finally, we examined the W dependence at and beyond the S_{11} peak, averaged over angles. The results are shown in Fig. 2. Due to the small cross section above an increasing multi-pion background, the errors increase rapidly above $W = 1.6$ GeV. Nonetheless, the data are consistent with the Eta-Maid model within errors. We also evaluated the target single spin asymmetry A_t , formed as the difference over the sum of rates with longitudinal target polarization pointing up-beam versus down-beam. The data are in agreement with the predictions, which are very close to zero in this region due to the strong dominance of the $S_{11}(1535)$ resonance relative to background.

References

1. Particle Data Group, Phys. Rev. D 66 (2002) 012002.
2. The CB-ELSA Collaboration, V. Crede *et al.*, hep-ex/0311045 and references therein.
3. The GRAAL Collaboration, D. Rebreyend *et al.*, Nucl. Phys. A663 (2000) 436-439.

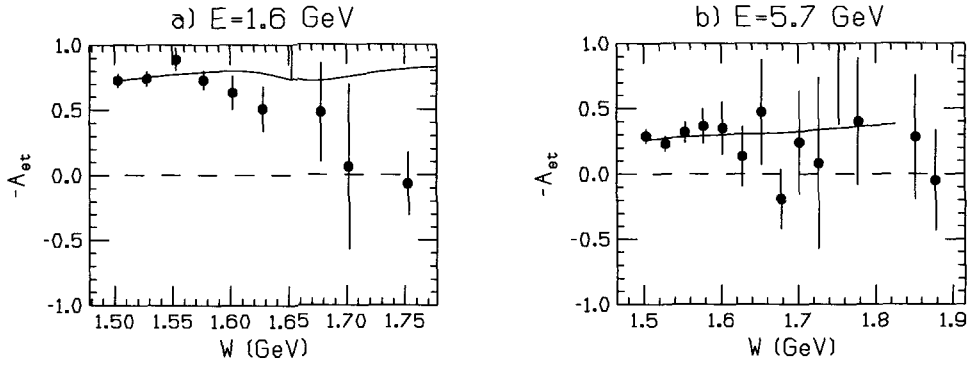


Fig. 2. Preliminary double-spin asymmetry $-A_{et}$ for exclusive η electroproduction from the proton, averaged over ϕ^* and $\cos \theta^*$, as a function of W for: a) $E = 1.6$ GeV; b) $E = 5.7$ GeV. The curves are the prediction of Eta-MAID.

4. W.-T. Chiang, S.-N. Yang, L. Tiator, D. Drechsel, Nucl. Phys. A **700**, 429 (2002) and www.kph.uni-mainz.de/MAID/eta/etamaid.html.
5. The CLAS Collaboration, A. Biselli *et al.*, Phys. Rev.C68, 035202 (2003).

MEASUREMENT OF THE Q^2 -EVOLUTION OF THE BJORKEN INTEGRAL AT LOW Q^2

A. DEUR

Thomas Jefferson National Accelerator Facility, Newport News, USA

We report on the extraction of the Q^2 -dependence of the Bjorken sum for $0.16 < Q^2 < 1.1 \text{ GeV}^2$. A twist analysis performed on these data shows that the higher twist corrections are small due to a cancellation between the twist-4 and 6 terms. The extraction of an effective strong coupling constant is discussed.

1. Bjorken Sum Rule

The Bjorken sum rule [1] played a central role in verifying in the spin sector that QCD is the correct gauge theory of the strong interaction. It reads:

$$\int_0^1 (g_1^p - g_1^n) dx = \frac{g_a}{6} \left[1 - \frac{\alpha_s}{\pi} - 3.58 \left(\frac{\alpha_s}{\pi} \right)^2 - 20.21 \left(\frac{\alpha_s}{\pi} \right)^3 + \dots \right] + \sum_{i=1}^{\infty} \frac{\mu_{2i+2}^{p-n}}{Q^{2i}} \quad (1)$$

where the coefficients μ_{2i+2}^{p-n} are sums of elements of twist no higher than $2i$ and which Q^2 -dependence is given by DGLAP equations. The sum rule has been verified experimentally at $Q^2=5 \text{ GeV}^2$ to better than 10%.

Taking the $Q^2 \rightarrow 0$ limit relates the Bjorken sum rule to the Gerasimov-Drell-Hearn (GDH) sum rule [2] that stands at $Q^2 = 0$. This connection triggered the generalization of the GDH sum [3] at finite Q^2 . Because the generalized GDH sum is in principle calculable at any Q^2 , it can help to study the transition from the hadronic to partonic degrees of freedom of strong interaction. However, the validity domains of the chiral perturbation theory (χ PT) at low Q^2 and pQCD calculations at higher Q^2 do not overlap. Lattice QCD should bridge the two domains but no calculation is available yet. The relation between the Bjorken and generalized GDH sum is:

$$\int_0^{1^-} g_1^p - g_1^n dx = \frac{Q^2}{16\pi^2\alpha} (\text{GDH}^p(Q^2) - \text{GDH}^n(Q^2)) \quad (2)$$

Hence the Bjorken sum is essentially the $p - n$ flavor non-singlet part of the GDH sum, which yields simplifications: more reliable estimations of the unmeasured low- x part of the integral, simpler pQCD evolution equations, and less complicated χ PT calculations. This

might help in linking the validity domains of pQCD and χ PT [6]. Hence the Bjorken sum appears as an important quantity to measure to understand the hadron-parton transition.

Precise data on the proton [7], deuteron [8], and ^3He [9] are available from the Thomas Jefferson National Accelerator Facility (JLab). We used them to extract the Bjorken sum from $Q^2 = 0.16$ to 1.1 GeV^2 . To combine proton and neutron data, the ^3He data were re-analyzed at the same Q^2 as the proton data. For consistency, the unmeasured low- x part of the integral was re-evaluated for the three data sets using a consistent prescription. The results are shown on Fig. 1, left panel, together with SLAC E143 results in the resonance region [10]. The elastic contribution is not included. The systematic uncertainties are given by the horizontal bands. At low Q^2 χ PT calculations can be compared to the data. Calculation done in the heavy Baryon approximation [12] may be more reliable since they agree with data, up to about $Q^2 = 0.25 \text{ GeV}^2$ (to be compared to $Q^2 = 0.1 \text{ GeV}^2$ typically for singlet quantities). However, the results from Bernard *et al.* [11] which do not use this approximation, do not support this conclusion. The improved model of Soffer and Teryaev [14] and the calculation from Burkert and Ioffe [15] agree well with the data. The pQCD result at third order in α_s and leading twist is shown by the grey band. The width comes from the uncertainty on α_s . Somewhat surprisingly, the data agree with the leading twist calculation down to quite low Q^2 , which indicates that higher twist terms are small or cancel each other. We quantitatively addressed the question by performing a higher twist analysis [13] that shows that the coefficient μ_4^{p-n} of the $1/Q^2$ correction has opposite sign and similar magnitude to the coefficient μ_6^{p-n} of the $1/Q^4$ correction at $Q^2 = 1. \text{ GeV}^2$: $\mu_6^{p-n}/Q^4 = 0.09 \pm 0.02$ and $\mu_4^{p-n}/Q^2 \simeq -0.06 \pm 0.02$. Higher Twist analyses were also done separately on the proton [16] and neutron [17].

2. The Effective Strong Coupling Constant

The simple α_s -dependence of the Bjorken sum makes it an ideal tool to extract α_s . However, higher twists have to be known or negligible. This is not the case for us. This difficulty is avoided when using the concept of effective coupling constants [18]. Here, higher twists and QCD radiations at orders higher than α_s^2 are folded into α_s^{eff} . We obtain a quantity that is well defined at any Q^2 , well behaved when crossing Λ_{QCD} or a quark mass threshold, and that is renormalization scheme independent. However, α_s^{eff} becomes process dependent. This is not a problem since process-dependent coupling constants can be related using equations called “commensurate scale relations” that connect observables without scheme or scale ambiguity [19, 20]. The extracted α_s^{eff} is shown in Figure 1, right panel. Also plotted is the pQCD calculation of α_s^{eff} (light grey band), α_s calculated to order β_0 (pink band), α_s^{eff} calculated using the model of Burkert and Ioffe, and α_s^{eff} as extracted from SLAC E155 (open squares). Satisfactorily, α_s^{eff} merges with α_s at large Q^2 , as expected since their difference is due to pQCD radiative corrections and higher twists. At low Q^2 , the behaviour of α_s^{eff} is constrained by the GDH sum rule. This, together with the steep rise α_s^{eff} at larger Q^2 , strongly hint that α_s^{eff} has no significant scale dependence at low Q^2 . This possible “freezing” of α_s^{eff} at low Q^2 is a debated issue. Lower Q^2 data [21, 22] will have the definite word on this feature of α_s^{eff} .

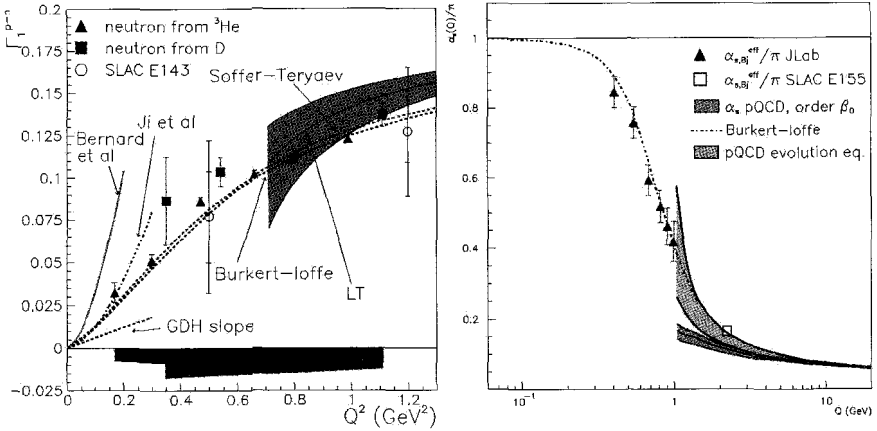


Fig. 1. Left: Q^2 -evolution of the Bjorken sum. The Bjorken sum formed using neutron data extracted from ^3He (D) data is shown by the triangles (squares). Right: Effective strong coupling constant.

3. Summary and Outlook

We have extracted the Bjorken sum in the Q^2 range of 0.16-1.1 GeV^2 . The parton to hadron gap, if smaller, is not bridged yet. The magnitudes of the higher twists were extracted. The higher twist effects appear to be small, due to a cancellation of the $1/Q^2$ and $1/Q^4$ terms. We extracted a physical coupling for the strong interaction. Data hint that α_s^{eff} loses its scale dependence at low Q^2 .

Acknowledgments

This work was supported by the U.S. Department of Energy (DOE) and the U.S. National Science Foundation. The Southeastern Universities Research Association operates the Thomas Jefferson National Accelerator Facility for the DOE under contract DE-AC05-84ER40150.

References

1. J. D. Bjorken, Phys. Rev. **148** 1467 (1966).
2. S. Gerasimov, Sov. J. Nucl. Phys. **2**, 1966. S. D. Drell and A. C. Hearn, Phys. Rev. Lett. **16**, 908 (1966).
3. M. Anselmino, B.L. Ioffe and E. Leader, Sov. J. Nucl. **49**, 136, (1989), X. Ji and J. Osborne, J.Phys. G27 127 (2001).
4. V. Bernard, T. R. Hemmert and Ulf-G. Meißner, Phys. Rev. D **67**, 076008 (2003), X. Ji, C. W. Kao and J. Osborne, Phys. Lett. **B472**, 1 (2000).
5. J. Ellis and R.L. Jaffe, Phys. Rev. **D9** 1444 (1974).
6. V. D. Burkert, Phys. Rev. D **63**, 097904 (2001).
7. CLAS collaboration: R. Fatemi *et al.*, Phys. Rev. Lett. **91**, 222002 (2003).
8. CLAS collaboration: J. Yun *et al.*, Phys. Rev. C **67**, 055204 (2003).
9. E94-010 collaboration: M. Amarian *et al.*, Phys. Rev. Lett. **89**, 242301 (2002); Phys. Rev. Lett. **92**, 022301 (2004).

10. K. Abe *et al.*, Phys. Rev. Lett. **78**, 815 (1997).
11. V. Bernard, T. R. Hemmert and Ulf-G. Meißner, Phys. Rev. D **67**, 076008 (2003).
12. X. Ji, C. W. Kao and J. Osborne, Phys. Lett. **B472**, 1 (2000).
13. A. Deur *et al.* hep-ex/0407007.
14. J. Soffer and O. V. Teryaev, hep-ph/041022
15. V. D. Burkert and B. L. Ioffe, Phys. Lett. **B296**, 223 (1992); J. Exp. Theor. Phys. **78**, 619 (1994).
16. M. Osipenko *et al.*, hep-ph/0404195.
17. E94-010 collaboration: Z. E. Meziani *et al.*, hep-ph/0404066.
18. G. Grunberg, Phys. Lett. **B95** 70 (1980); Phys. Rev. **D29** 2315 (1984)
19. S. J. Brodsky, H. J. Lu, Phys. Rev. **D51** 3652 (1995))
20. S.J. Brodsky, et al, Phys. Lett. **B372** 133 (1996)
21. J.P. Chen, A. Deur and F. Garibaldi, JLab experiment E97-110
22. M. Battaglieri, A. Deur, R. De Vita and M. Ripani, JLab experiment E03-006



SESSION 6

Spin Physics in Nuclear Interactions

This page intentionally left blank

${}^4\text{He}(p,2p)$ REACTIONS FOR STUDYING IN-MEDIUM NN INTERACTIONS

S. ASAJI, T. NORO, K. FUJITA*, Y. H. K. HATANAKA*, T. I. M. ITO*, S. KISHI†, Y. N. M. NAKAMURA‡, K. S. H. SAKAGUCHI†, Y. SAKEMI*, Y. SHIMIZU*, H. TAKEDA‡, Y. TAMESHIGE*, S. TERASHIMA†, M. UCHIDA†, T. W. Y. YASUDA†, H. P. YOSHIDA*, M. YOSOI†, T. YONEMURA

Department of Physics, Kyushu University, Fukuoka, Japan

*Research Center for Nuclear Physics, Osaka University, Osaka, Japan

†Department of Physics, Kyoto University, Kyoto, Japan

‡Institute for Chemical and Physical Research, Wako, Japan

A_y has been measured for the ${}^4\text{He}(p,2p)$ reaction at 392 MeV. The measured value of A_y at 0 MeV/c is 30% lower than the value of A_y from calculation, but the effect of central high density of the ${}^4\text{He}$ nucleus is not observed clearly as the reaction might take place at the outside of the nucleus. The cross section has also been measured under three kinematic conditions, the results agreeing to within 10% FWHM.

1. Introduction

The modification of hadron properties in the nuclear field is one of the most interesting topics in nuclear physics. If the properties are modified, the interaction is also expected to be modified because the meson exchange model describes the interaction reasonably well. Our interest is to study the NN interaction in the nuclear field. A direct way to do this is to examine the difference between NN interactions in free space and in nuclear medium. We therefore study $(p,2p)$ scattering as an example of NN scattering taking place in nuclear medium.

There is a long-standing problem in A_y , as deduced from calculations by using the NN interaction in free space [1, 2]. Experiments have been done with several target nuclei at RCNP, with the result that A_y reduces monotonically with effective mean density as defined in [3], which is estimated with a DWIA. On the other hand, the two-body process is off-energy-shell in the $(p,2p)$ reaction. Energy is needed to knock out a proton from a target nucleus, and the two-body kinetic energy in the final state is smaller than in the initial state. This off-energy-shell may also cause deviations of A_y . A_y is also reduced monotonically depending on separation energy. The central density of ${}^4\text{He}$ nucleus is twice that of other nuclei. We can determine the key parameter of A_y reduction by measuring it in the ${}^4\text{He}$ nucleus.

The $p,2p$ reaction is also interesting because it allows the experimental deduction of the momentum distribution of a bound nucleon. At RIKEN, the construction of a radioactive

isotope beam facility is under way, and the study of unstable nuclei by using this reaction, with inverse kinematics, is planned. The unstable nuclei to be studied include light ones such as He and Li isotopes. There are difficulties specific to studies of light nuclei with this reaction, such as the recoil effect. Thus it is valuable to study the ${}^4\text{He}(p,2p)$ reaction precisely because the structure of ${}^4\text{He}$, one of the lightest nuclei, is now well known. The second purpose of our study is to examine how accurately we can deduce the momentum distribution of the protons in this light nucleus.

2. Experimental Setup

We have measured the cross-section and A_y for the $(p,2p)$ reaction, using the ring cyclotron complex at RCNP, Osaka University. A polarised proton beam was accelerated to 392 MeV and transported to a cooled ${}^4\text{He}$ gas target at the centre of the scattering chamber. The momenta of the two protons emitted from the target were analyzed by using a high-resolution magnetics spectrometer “Grand Raiden (GR)” and a “Large Acceptance Spectrometer (LAS)”.

Measurements were performed under three kinematic conditions. In the first, the kinetic energies of the two outgoing protons and one of the detection angles θ_{gr} were kept fixed, and the angle θ_{las} was changed. In the second, the kinetic energies of the two outgoing protons were fixed as before and their angles were changed, keeping the momentum of the residual nucleus parallel to the momentum of incident proton. In the third condition, both the detection angles were fixed and the energies of the two detected protons were changed. All three conditions included a kinematical restriction whereby $\theta_{gr}=38.5^\circ$, $\theta_{las}=48.5^\circ$, and $E_{gr}=242$ MeV, where E_{gr} is the energy of protons corresponding to the central orbit of GR. This corresponds to the situation where the momentum of the recoil nucleus, and therefore the Fermi momentum of the knocked-out proton in the plane wave limit, is zero.

3. Results and Discussion

Experimental data for A_y are shown in Figure 1. The A_y values were compared with PWIA and DWIA calculations. The measured value of A_y at 0 MeV/c was 0.19. This is 30% lower than the value calculated by the PWIA, which corresponds to proton-proton elastic scattering in free space. On the other hand, it was shown in a previous study that A_y for $1s_{1/2}$ -proton knockout from a ${}^{12}\text{C}$ target is 50% lower than the calculated value. We therefore conclude that the effect of the high central density of the ${}^4\text{He}$ nucleus is not being observed clearly.

In addition, we measured A_y for this reaction on various light nuclei from ${}^2\text{H}$ to ${}^{16}\text{O}$, and extracted from the results a key parameter of the variation in A_y . The left panel of Figure 2 shows a plot of the data as a function of the effective mean density. Instead of A_y values themselves, ratios of observed values and PWIA calculations are plotted in order to eliminate a trivial kinematical effect caused by finite separation energies. The same ratios are plotted as a function of separation energy in the right panel. This means that the separation energy, i.e. the difference between initial and final energies, is likely to be the key parameter.

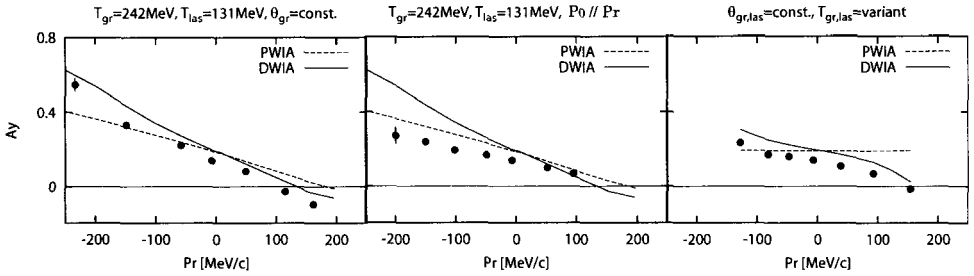


Fig. 1. Experimental data of A_y with PWIA and DWIA calculations.

Quasi-free scattering is the dominant process at incident energies of several hundred MeV, and the present kinematic condition, a zero-recoil condition for $s_{1/2}$ knockout, corresponds to the cross-section peak. From this and other experimental evidence, it is almost certain that any contribution of multi-step processes is small. The present result requires a new theoretical picture which explains this phenomenon in this dominant process.

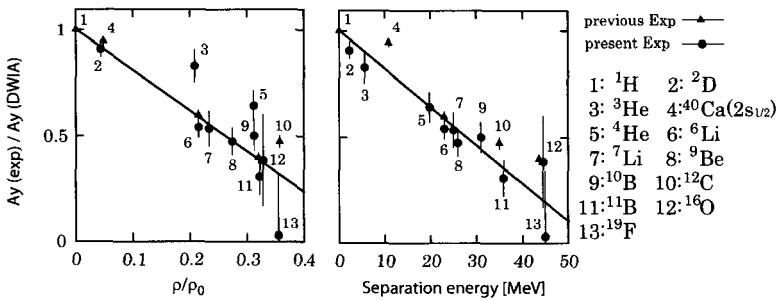


Fig. 2. Experimental result (solid circle). The vertical axis shows the ratio of observed A_y values to PWIA calculations. The horizontal axis shows the effective mean density in the left panel, and the separation energies in the right panel. The ratios are better aligned in the right panel, which suggests that the separation energy is a key parameter of A_y reduction. Results of the previous experiment are also plotted (solid squares). All the data except ^{40}Ca are those corresponding to proton knock-out from $1s_{1/2}$ orbits. The ^{40}Ca data corresponds to $2s_{1/2}$ knock-out.

Data for the differential cross-sections are shown in Figure 3, along with DWIA calculations. As can be seen, the experimental data for all kinematical conditions are consistent to within 10% in FWHM. In other words, the momentum width of bound wave function can be deduced to 10% accuracy by comparison with simple DWIA calculations. Theoretical progress is required for further study.

References

1. J. A. McGill *et al.*, Phys. Lett. **134B**, 157 (1984).
2. C. A. Miller *et al.*, Phys. Rev. **C57**, 1756 (1998).
3. K. Hatanaka *et al.*, Phys. Rev. Lett. **78**, 1014 (1997).

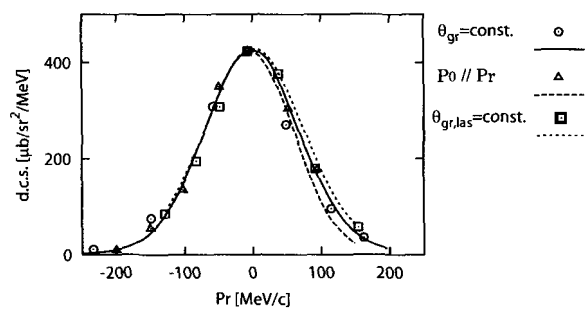


Fig. 3. Experimental data for differential cross sections and DWIA calculations. The solid line and circles show the calculation and the data, respectively, under the condition that the two outgoing protons and one of their angles were fixed. The dashed line and triangles correspond to a condition where two outgoing protons and the direction of the recoil momentum are fixed. The dotted line and squares correspond to a condition where two outgoing angles are fixed and the energies were changed.

SPIN CORRELATION PARAMETER C_{yy} OF $p + {}^3\text{He}$ ELASTIC BACKWARD SCATTERING AT INTERMEDIATE ENERGY

Y. SHIMIZU, K. HATANAKA, T. ADACHI^a, K. F. K. ITOH^b, T. KAWABATA^c, T. KUDOH^d,
H. M. H. OHIRA^d, H. OKAMURA^c, K. SAGARA^d, Y. S. Y. SASAMOTO^c, Y. S. H. P. YOSHIDA^d, K. SUDA^c,
Y. T. A. T. M. TOMIYAMA^d, M. U. T. UESAKA^c, T. WAKASA^d, T. WAKUI^c

Research Center for Nuclear Physics (RCNP) Osaka University, Ibaraki, Japan

^aDepartment of Physics, Osaka University, Toyonaka, Japan

^bDepartment of Physics, Saitama University, Urawa, Japan

^cCenter for Nuclear Study (CNS), University of Tokyo, Wako, Japan

^dDepartment of Physics, Kyushu University, Hakozaki, Japan

^eCyclotron and Radioisotope Center (CYRIC), Tohoku University, Sendai, Japan

It is possible to use nucleon-nucleus scattering as a probe of the spin structure of nuclei, since target related observables are extremely sensitive to small spin-dependent parts of the target wave function. In addition, one can gain information about the nucleon-nucleus reaction mechanism, the spin dependence of the nucleon-nucleon interaction in the nuclear medium, and off-shell behavior of the nucleon-nucleon amplitudes. For ${}^3\text{He}(p, {}^3\text{He})p$ elastic backward scattering (EBS), only a small amount of data exists for the differential cross-section and none exists for spin-dependent observables. We have developed a spin-exchange polarised ${}^3\text{He}$ target and measured the spin correlation parameter C_{yy} at 200, 300, and 400 MeV.

1. Introduction

For several decades considerable efforts have been made to investigate the structure of the lightest nuclei (d , ${}^3\text{He}$, ${}^4\text{He}$) at short distances between constituent nucleons. Significant progress has been achieved in both theory and experiment, first of all because high quality data on spin-dependent observables were obtained with both hadronic and electromagnetic probes. A large part of these investigations consisted of studies of elastic backward (in the center of mass system) proton-nucleus scattering (EBS). This process involves large momentum transfer and therefore a belief exists that EBS can provide access to high-momentum components of the wave function of the lightest nuclei.

The $p{}^3\text{He}$ EBS is studied in much less detail than the pd EBS. Today, however, high-intensity beams of polarised protons in combination with polarised ${}^3\text{He}$ targets offer an opportunity to perform detailed studies of $p{}^3\text{He}$ EBS, including spin-dependent observables. This in turn demands careful theoretical studies of the reaction mechanism. There are several cross-section data on $p{}^3\text{He}$ EBS, mainly at energies higher than 400 MeV. Analyzing powers were measured for $p{}^3\text{He}$ elastic scattering at TRIUMF at 200 ~ 500 MeV,

but measurements were limited to relatively forward angles [1]. We have measured the differential cross-section and the spin-correlation parameter C_{yy} of the $p^3\text{He}$ EBS at 200, 300, and 400 MeV.

2. Experiment

The measurements were performed at the Research Center for Nuclear Physics (RCNP), Osaka University. We used vertically polarised protons at incident energies of 200, 300, and 400 MeV. The beam intensity was 10 to 40 nA, which was limited by counting rates. The proton polarisation was about 70%. Elastically scattered ^3He particles were measured by the Grand Raiden spectrometer [2], set at 0° . In order to stop the beam and integrate the current a Faraday cup was installed inside and near the exit of the first dipole magnet of the spectrometer.

A spin-exchange polarised ^3He target has been developed at RCNP. The cell, made of borosilicate glass (Corning7056), consists of two parts, a target cell and a pumping cell, connected by a transfer tube. To reduce background, the cell windows are as thin as 150 μm . During operation the pumping cell is heated to about 460 K to achieve a sufficient Rb vapour density for optical pumping and spin-exchange collisions. Polarised ^3He atoms are transferred to the target cell by diffusion. By using two cells we can avoid problems of large backgrounds from the Rb atoms and of depolarising effects. A high-power diode laser, which is a Fiber Array Packaged Laser (COHERENT FAP79-30C-800LB), and optical elements were introduced to polarise the Rb atoms in the pumping cell. The ^3He polarisation is measured by the Adiabatic Fast Passage (AFP) NMR method. However, this method gives only the relative value of the polarisation. The target polarisation is calibrated independently by using the $^3\text{He}(p, \pi^+)^4\text{He}$ reaction, where polarisation is inferred from beam related asymmetries [3]. The spin signature of the reaction is $\frac{1}{2} + \frac{1}{2} \rightarrow 0^+ + 0^-$, and the spin correlation parameter C_{yy} takes the constant value of 1. Finally, the AFP NMR amplitude was calibrated by the following:

$$P_{^3\text{He}} [\%] = (6.62 \pm 0.16) \times 10^2 \cdot V_{\text{NMR}} [\text{mV}]. \quad (1)$$

3. Result and Discussion

Figure 1 shows the differential cross-section and the spin correlation parameter C_{yy} of the $p^3\text{He}$ EBS at $E_p = 200, 300, \text{ and } 400$ MeV. In this figure, the open circles show results of this work, and other symbols are values [4]~ [7] extrapolated to $\theta_{cm} = 180^\circ$ by us. For the differential cross-section, the present results are consistent with previous data. For the spin-correlation parameter C_{yy} , these are measured for the first time.

Several calculations exist for the differential cross-section and the spin-correlation parameter C_{yy} of the $p^3\text{He}$ EBS [8]~ [10]. For the differential cross-section, calculations are in good agreement with experimental data up to $E_p \sim 150$ MeV. However there are discrepancies at higher energies. Around 200 ~ 500 MeV, the reaction is dominated by rescattering of the intermediate pion off the deuteron (PI mechanism) [10]. The contribution of the singlet $NN(^1S_0)$ pairs is important. In contrast to the deuteron term, the singlet $NN(^1S_0)$

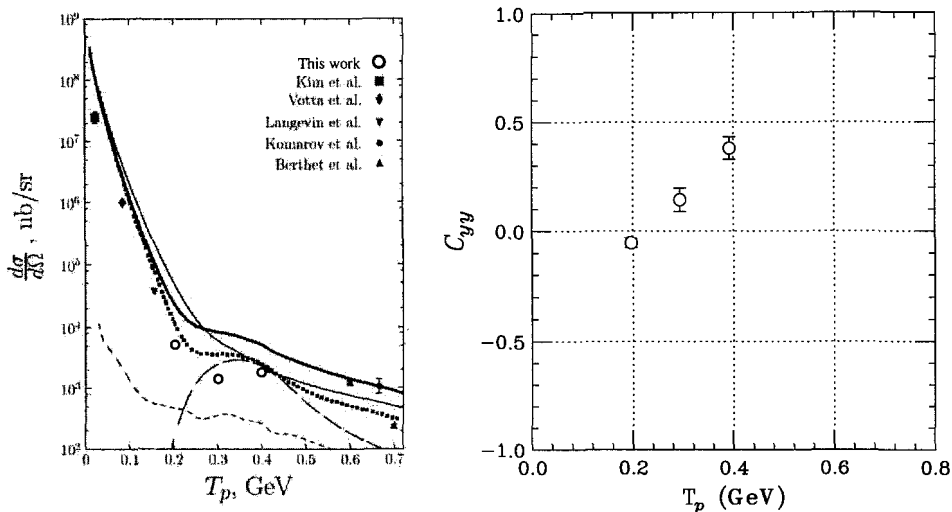


Fig. 1. The left panel shows the differential cross-section of the $p^3\text{He}$ EBS. Open circles show results of this work, and other data [4]~ [7] are extrapolated to $\theta_{cm} = 180^\circ$ by us. The solid curves include $(np)_1 + (np)_3$ exchange together with PI mechanism (the bold and thin curves are for Paris and CD-Bonn potential, respectively.) The one-deuteron exchange together with direct and PI mechanisms is shown by dotted line. The contribution of direct and PI mechanism are shown by long- and short-dashed lines, respectively. The right panel shows the spin-correlation parameter C_{yy} of the $p^3\text{He}$ EBS.

terms contribute only to the spin-independent part of the amplitude, and consequently have a strong influence on the spin-correlation parameter C_{yy} . We hope that our results on the spin-correlation parameter C_{yy} will provide an impetus for more sophisticated theoretical models to be considered.

Acknowledgments

We thank the RCNP staff for their support during the experiment. We also wish to thank Professor H. Toki for his encouragement throughout the work. This experiment was performed under Program No. E180 at the RCNP. This work was supported in part by the Grant-in-Aid for Scientific Research, Grant No. 14340074, of the Ministry of Education, Culture, Sports, Science and Technology of Japan.

References

1. D.K. Hasell *et al.*, Phys. Rev. Lett. **74**, 502 (1986); E.J. Brash *et al.*, Phys. Rev. C **52**, 807 (1995); R. Tacik *et al.*, Phys. Rev. Lett. **63**, 1784 (1989);
2. M. Fujiwara *et al.*, Nucl. Instrum. Methods Phys. Res. A **422**, 484 (1999).
3. G.G. Ohlsen, Rep. Prog. Phys. **35**, 760 (1972).
4. P. Berthet *et al.*, Phys. Lett. **106B**, 465 (1981); R. Frascaria *et al.*, Phys. Lett. **66B**, 329 (1977).
5. C.C. Kim *et al.*, Nucl. Phys. **58**, 32 (1964).
6. L.G. Votta *et al.*, Phys. Rev. C **10**, 520 (1974).
7. H. Langevin-Joliot *et al.*, Nucl. Phys. **A158**, 309 (1978).

8. Yu.N. Uzikov and J. Haidenbauer, *Phys. Rev. C* **68**, 014001 (2003); Yu.N. Uzikov, in *Proceedings of the Nuclear Many-Body and Medium Effects in Nuclear Interactions and Reactions, Fukuoka, Japan, 2002*, edited by K. Hatanaka, T. Noro, K. Sagara, H. Sakaguchi, and H. Sakai (World Scientific, Singapore, 2003), p. 137; Yu.N. Uzikov, *Nucl. Phys.* **A644**, 321 (1998).
9. L.D. Blokhintsev *et al.*, *Nucl. Phys.* **A597**, 487 (1996).
10. A.P. Kobushkin *et al.*, nucl-th/0112078 (2003). Submitted to *Phys. Lett. B*.
11. G. Fäldt *et al.*, *Nucl. Phys.* **A587**, 769 (1995); L.A. Kondratuyk *et al.*, *JETP Lett.* **63**, 1 (1996).

EXPERIMENTAL INVESTIGATION OF THE QUASIELASTIC SCATTERING OF POLARISED PROTONS ON NUCLEI AT THE JINR VB LHE SYNCHROPHASOTRON

A. A. YERSHOV, V. A. BODIAGIN, N. A. KRUGLOV, A. A. POPEKO, L. I. SARYCHEVA*

Skobel'syn Institute of Nuclear Physics, Moscow State University, Moscow, Russia

A. G. LITVINENKO, V. P. LADYGIN, S. V. AFANASIEV, L. S. AZHGIREY, A. Y. ISUPOV, V. I. IVANOV, A. N. KHRENOV, A. I. MALAKHOV, P. A. RUKOJATKIN, G. D. STOLETOV, V. N. ZHMYROV, L. S. ZOLIN

Joint Institute for Nuclear Research, Dubna, Moscow, Russia

Experimental investigation of quasi-elastic scattering of polarised protons on nuclei has been carried out at the JINR VB LHE Synchrophasotron (Dubna, Russia). The analyzing power of proton-nucleus scattering was measured using a beam of stripped polarised protons at 2.5, 3.0 and 3.6 GeV. The goal of the experiment was to test the effect of the analyzing power reduction on proton scattering on intranuclear protons and neutrons, in comparison with scattering on free nucleons.

1. Introduction

The investigation of single-spin asymmetry in the scattering of polarised protons by intranuclear nucleons looks important for an understanding of the role of spin in strong interactions, and for the development of nuclear polarimetry. The spin observable discussed is the analyzing power (A.P.) $A(\theta)$, defined as

$$\sigma(\varphi, \theta) = \sigma_0(\theta)(1 + A(\theta)(P \cdot n)). \quad (1)$$

By comparing A for scattering on free and intranuclear nucleons, the parameter R in the reduction of A.P. can be calculated as

$$R_{pN} = \frac{(p+n) \cdot A_{qe}}{p \cdot A_{pp} + n \cdot A_{pn}} \quad (2)$$

for scattering on an arbitrary intranuclear nucleon N (p and n are numbers of protons and neutrons), or

$$R_{pp} = \frac{A_{qe}^p}{A_{pp}} \quad (3)$$

*Work partially supported by the RF Federal Program "Fundamental Nuclear Physics".

for scattering on an intranuclear proton p . We further consider A.P. reduction in the region of the first A.P. maximum. There are two types of experimental performance: the measurement of A.P. in the reaction $X(p, pN)$ with detection of the leading proton only [1–3]; and the measurement of A.P. in $X(p, 2p)$ with detection of both the leading and recoil protons [4–6].

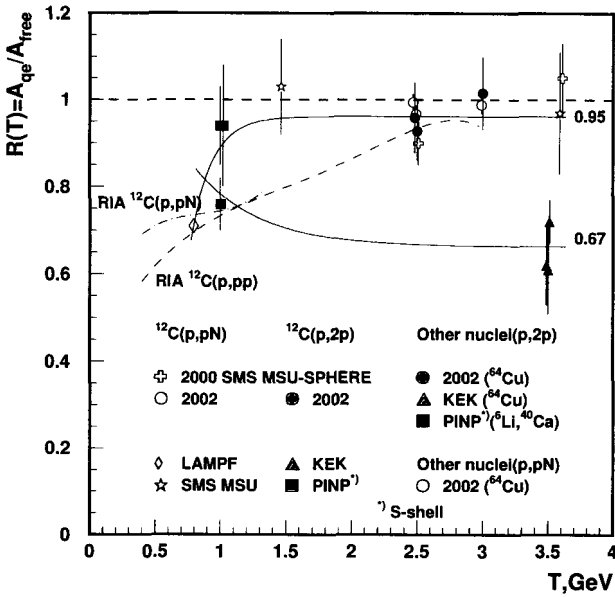


Fig. 1. Compilation of experimental data for $R_{pN} = A_{qe} / A_{pN}$ (open symbols) and $R_{pp} = A_{qe}^p / A_{pp}$ (closed symbols). Tendencies of $R(T)$ behaviour are shown by solid lines; RIA calculations are shown by dashed and dash-dotted lines.

Based on the [1, 2, 4, 5] data compilation, the $R(T)$ dependence on the initial proton kinetic energy is presented in Figure 1. Model-dependent analysis of the data [3, 6] is also taken into account to define the tendency of the $R_{pN}(T) \rightarrow 0.95$ and $R_{pp}(T) \rightarrow 0.67$ behaviour. This difference looks inexplicable, but the event kinematical conditions were significantly different. This was the reason for proposing an experiment to measure both values simultaneously.

2. Experiment description

The initial beam of polarised protons was produced by stripping the polarised deuteron beam and selecting the half-momentum proton. The polarisation of the beam was continuously measured using a double-arm intermediate energy polarimeter [7]. The values of the polarisation were $P(+/-, Run2000) = 0.575/0.397$ and $P(+/-, Run2002) =$

0.483/0.454, and were stable during the runs. The quasi-elastic channel was selected by spectrometric analysis of the leading proton momentum, together with detection of the recoil proton, and "time-of-flight" measurements. The A.P. was measured as the difference of the $\sigma(\theta)$ with different beam polarisation directions.

3. Results and conclusions

The results of the measurement are presented in Table 1 and Figure 2.

Table 1. Quasi-elastic scattering A.P. data from Run 2000 and Run 2002.

Reaction	T, GeV	$\Theta, \text{deg(l.f.)}$	A_{qe}	A_{pN}
$C(d, pN)$	2.51	9.0	0.169 ± 0.020	0.197
$C(p, pN)$	2.51	9.0	0.178 ± 0.010	0.197
$C(d, pN)$	3.60	6.7	0.087 ± 0.019	0.130
$C(p, pN)$	3.60	6.7	0.137 ± 0.010	0.130
$C(p, pN)$	2.51	9.1	0.191 ± 0.004	0.197
$C(p, 2p)$	2.51	9.1	0.243 ± 0.018	0.262
$Cu(p, pN)$	2.51	9.1	0.190 ± 0.004	0.191
$Cu(p, 2p)$	2.51	9.1	0.251 ± 0.021	0.262
$C(p, pN)$	3.00	7.9	0.160 ± 0.003	0.162
$C(p, 2p)$	3.00	7.9	0.231 ± 0.019	0.227

One can see that in our experiment the quasi-elastic scattering A.P. follows the corresponded free scattering A.P. Calculated $R_{pN}(T)$ and $R_{pp}(T)$ are shown in Figure 1 by open and closed circles.

There is no indication of a difference in measured values between the two types of measurements, or between scattering on carbon and copper. Further, anomalous A.P. reduction was not observed. The data obtained are in agreement with $R(T)$ estimation from RIA calculations [8–10], but it looks critical to carry out the measurement at $T = 1 - 2 \text{GeV}$. This experiment is planned in 2005 at the VB LHE Nuclotron.

References

1. J.A. McGill et al., *Phys. Lett.* **B134**, 157 (1984).
2. E.V. Anoshina et al., *Phys. of Atom. Nucl.* **60**, 224 (1997)
3. V.G. Vovchenko et al., *Preprint LINP 484*, (1979).
4. C. Ohmori et al., *Phys. Lett.* **B234**, 29 (1990).
5. J. Bystricky et al., *Lett. Nuovo Cim.* **40**, 15 (1984).
6. V.A. Andreev et al., *Phys. Rev.* **C69**, 024604 (2004).
7. L.S. Azhgirej et al., *Nucl. Inst. and Meth.* **A497**, 340 (2003).
8. A.A. Yerшов, *Czech. J. Phys.* **52**, C325 (2002).
9. C.J. Horowitz and M.J. Iqbal, *Phys. Rev.* **C33**, 2059 (1986).

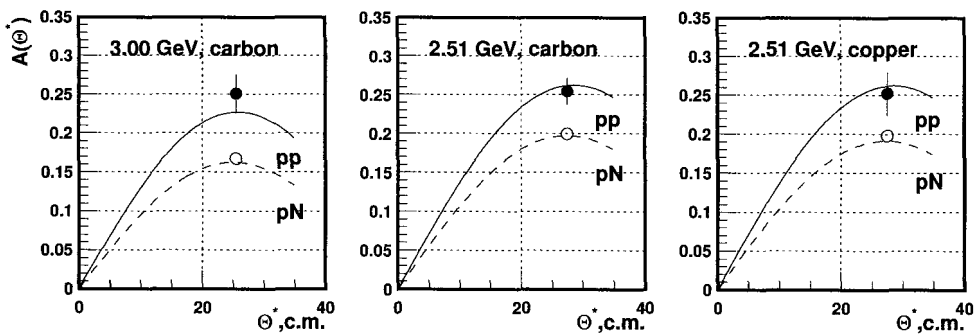


Fig. 2. Comparison of the measured values of quasi-elastic scattering analyzing power with the approximation of world data for the scattering on free nucleons. Solid lines and closed symbols correspond to pp scattering; dashed lines and open symbols correspond to pN scattering on an arbitrary nucleon.

10. R.A. Arndt, I.I. Strakovsky and R.L. Workman., *Phys.Rev.* **C62**, 034005 (2000).

MEASUREMENTS OF $n + d$ ELASTIC SCATTERING AT 250 MeV AND THE THREE-NUCLEON FORCES

Y. MAEDA, H. SAKAI, T. KAWABATA, K. SUDA, K. YAKO, M. HATANO, T. SAITO, H. KUBOKI, M. SASANO, K. HATANAKA^a, Y. SAKEMI^a, A. TAMII^a, J. KAMIYA^A, Y. SHIMIZU^a, K. FUJITA^a, H. OKAMURA^b, T. WAKASA^c, T. KUDOH^c, Y. HAGIWARA^c, Y. NAGASUE^c, K. SEKIGUCHI^d, K. ITOH^e, M. B. GREENFIELD^f, H. KAMADA^g.

University of Tokyo, Tokyo, Japan

^aResearch Center for Nuclear Physics, Osaka University, Osaka, Japan, ^bCYRIC, Tohoku University, Japan

^cKyushu University, Japan, ^dRIKEN, Japan, ^eSaitama University, Japan

^fInternational Christian University, Japan, ^gKyushu Institute of Technology, Japan

To study three-nucleon force (3NF) effects in a Coulomb-free system, the differential cross sections and the vector analyzing powers for $n + d$ elastic scattering at $E_n = 250$ MeV have been measured at $\theta_{cm} = 10^\circ - 180^\circ$. To cover the wide angular region, the experiments were performed by using two different methods at the (n, p) facility and at the NTOF facility at the Research Center for Nuclear Physics (RCNP). The results were compared with theoretical predictions based on Faddeev calculations with modern nucleon-nucleon (NN) forces combined with three-nucleon forces (3NF). The inclusion of 3NFs leads to a good description of the cross-section except for the backward angles. The results were also compared with theoretical predictions based on Faddeev calculations with relativistic corrections. The direct data-to-data comparison of the cross sections of the $n + d$ and $p + d$ is reported.

1. Introduction

One of the interesting problems in the few-nucleon system is the study of three-nucleon force (3NF) properties in the three-nucleon continuum.

Recently, highly precise measurements of the $d + p$ elastic scattering for deuteron energies of $E_d^{lab} = 140, 200$ and 270 MeV have been performed [1]. The calculations including NN forces only fail to reproduce cross-section and vector analyzing power data, but these discrepancies are removed by adding 2π exchange 3NFs. These results support the prediction that $N + d$ elastic scattering at intermediate energies is a good probe to study 3NF effects. However, it should be noted that all discussions are made by the comparing the precise $p + d$ data with rigorous $n + d$ Faddeev calculations, because performing three-body calculations in the presence of long-range Coulomb repulsion is extremely difficult.

To study 3NF effects in a Coulomb-free system, we have observed $n + d$ elastic scattering at 250 MeV at the Research Center for Nuclear Physics (RCNP). We measured differential cross sections and vector analyzing powers for $\theta_{cm} = 10^\circ - 180^\circ$. To cover such a wide angular region, we applied two techniques to perform the forward and backward

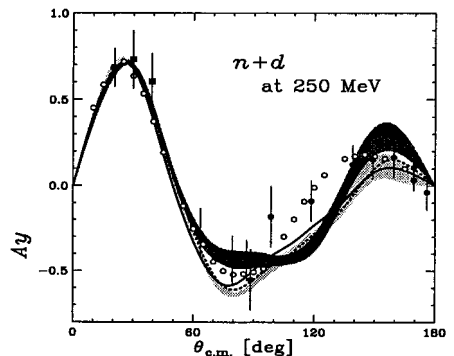
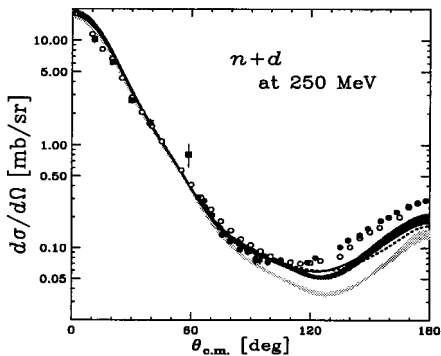


Fig. 1. Differential cross sections and vector analyzing powers for $n+d$ elastic scattering at $E_n = 250$ MeV. The solid circles and squares (open circles) are the results of $n+d$ ($p+d$) measurements. Statistical errors are shown. The Faddeev calculations, including various NN potentials with (dark shaded band) and without (light shaded band) TM-3NF, AV18+UrbanaIX (solid line) and CD-BONN+TM'-3NF (dotted line) are also shown.

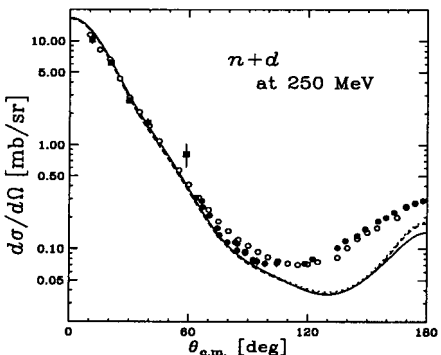


Fig. 2. Differential cross sections for nd elastic scattering at 250 MeV (solid circles and squares). The solid line is the prediction with CDBonn only; the two kinds of relativistic predictions with different approximations (dashed and dotted lines) are also shown.

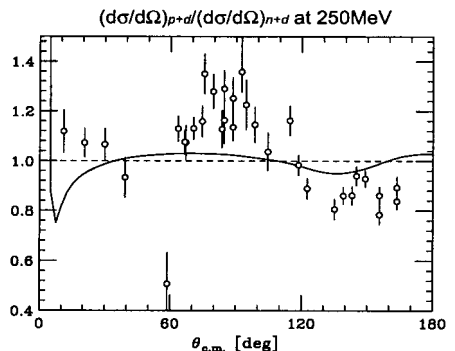


Fig. 3. The ratio of $p+d$ to $n+d$ cross-sections. The circles show the results deduced from the data from this work and $p+d$ data. The solid line shows theoretical predictions deduced including the Coulomb interaction approximately.

measurements.

2. Experiment

Measurements in the backward angular region ($\theta_{cm} \geq 60^\circ$) were carried out at the (n, p) facility [2] at RCNP. The nearly mono-energetic polarised neutron beam was produced by the ${}^7\text{Li}(p, n){}^7\text{Be}(\text{g.s.}+0.4 \text{ MeV})$ reaction at 250 MeV. We used the self-supporting deuterated polyethylene (CD_2) sheets [3], 100 – 220 mg/cm^2 thick, as the deuteron targets. The targets were mounted in the multi-wire drift chamber (MWDC). In this work, we also measured the $n+p$ scattering for normalization, using polyethylene (CH_2) sheets, 90 – 190 mg/cm^2 thick, as proton targets. The recoil deuterons or protons were momentum analyzed by the Large Acceptance Spectrometer (LAS).

Measurements in the forward angular region ($\theta_{cm} \leq 60^\circ$) were carried out at the neutron time-of flight (NTOF) facility [4] at RCNP. The polarised neutron beam was also produced by the ${}^7\text{Li}(p, n)$ reaction. The produced neutrons bombarded the deuteron target, which was located 2 m downstream from a ${}^7\text{Li}$ target. The deuterated liquid scintillator BC537 was used as the deuteron target, and coincidence measurements were performed. To remove background events originating from gamma rays, we used an $n\gamma$ discrimination method. The scattered neutrons travelled 70 m and were detected by NPOL II. The energy of the detected neutron was determined by TOF.

3. Results and Discussion

The results of the differential cross sections and vector analyzing powers are shown in Figure 1 by solid circles and squares with statistical errors only. Concerning the differential cross sections, it can be seen that the calculations including 3NF reproduce the data better, but are still too low in the backward region. These discrepancies may be an indication of relativistic effects [5] which are not taken into account in the present calculations. The data of the vector analyzing powers contain large statistical errors, but are consistent with the $p + d$ data within the systematic error of the $n + d$ data. We can see that the calculations fail to reproduce the angular distribution of the data at $\theta_{cm} = 110^\circ \sim 140^\circ$. Very recently, relativistic Faddeev calculations have been performed for $n + d$ elastic scattering at 250 MeV [6, 7]. In Fig. 2, we show the non-relativistic (solid line) and relativistic (dashed and dotted lines) predictions. It should be noted that no relativistic calculations include 3NF. We can see that the fully relativistic calculations improve the fit to the data at $\theta_{cm} \geq 160^\circ$, but the improvements are not enough.

We have also carried out $p + d$ measurements at 250 MeV [8]; these results are shown by open circles. This allows us to compare the $n + d$ and $p + d$ data directly. In Figure 3, the ratio of the cross-sections is plotted with open circles. The solid line represents the theoretical prediction at 250 MeV [9] which is based on CDBonn. In the calculation of the $p + d$ elastic scattering, the Coulomb force is included in an approximate way [10]. Although the discrepancies from unity are much larger for the data than for the prediction, the angles where the data cross the value of unity around $\theta_{cm} = 110^\circ$ are well reproduced by the theoretical prediction.

References

1. K. Sekiguchi *et al.*, *Phys. Rev C* **65**, 034003 (2002).
2. K. Yako *et al.*, *Nucl. Phys.* **A684**, 563c (2001).
3. Y. Maeda *et al.*, *Nucl. Instrum. Meth. A* **490**, 518 (2002).
4. H. Sakai *et al.*, *Nucl. Instrum. Meth. A* **369**, 120 (1996).
5. H. Witała *et al.*, *Phys. Rev. C* **57**, 2111 (1998)
6. H. Witała, private communication.
7. H. Kamada *et al.*, *Phys. Rev. C* **66**, 044010 (2002).
8. K. Hatanaka *et al.*, *Phys. Rev. C* **66**, 044002 (2002).
9. H. Kamada, private communication.
10. P. Doleschall *et al.*, *Nucl. Phys.* **A380**, 72 (1982).

A THREE-BODY EFFECT IN THE DOUBLE POLARISED ${}^3\text{He}(d, p){}^4\text{He}$ REACTION NEAR THRESHOLD

S. ORYU, S. GOJUKI*

Tokyo University of Science, Noda, Japan

A three-body Faddeev calculation for the n-p- ${}^3\text{He}$ system is carried out using the AV14 NN potential and including a Pauli corrected N- ${}^3\text{He}$ potential. Two sharp resonances ($5/2^+$, $3/2^+$) and one broad resonance ($1/2^+$) were found above the d- ${}^3\text{He}$ threshold in the region from 300 keV to 400 keV. Polarised and unpolarised cross sections are compared. Converged cross sections include full two-body partial waves and three-body spin-parity states at less than $J^\pi = 9/2^\pm$. The polarised angular dependence is very sensitive to the reaction rate; the 90° case is larger. The polarised cross section is enhanced by more than a factor of two compared with the unpolarised cross section, except near the $1/2^+$ resonance. A Coulomb correction was included in both the initial and final states.

1. Introduction

The study of low-lying resonances above the ${}^3\text{H}$ -d and ${}^3\text{He}$ -d thresholds is very interesting, not only for application problems but also for primordial nucleosynthesis. Improvements in polarisation techniques could provide additional experimental data. Three-body Faddeev calculations [1] for the n-p- ${}^3\text{He}$ system is one practical use for realistic nucleon-cluster interactions. For the NN potential, the ${}^1\text{S}_0$, ${}^3\text{S}_1$ - ${}^3\text{D}_1$, ${}^1\text{P}_1$, ${}^3\text{P}_0$, ${}^3\text{P}_1$, ${}^3\text{P}_2$ - ${}^3\text{F}_2$, ${}^1\text{D}_2$, and ${}^3\text{D}_2$ partial waves from the AV14 model are available [2]. For the nucleon-cluster interactions, we obtained sophisticated p- ${}^3\text{He}$ and n- ${}^3\text{He}$ potentials by combining a Pauli-corrected Resonating Group Method (RGM) with the Orthogonal Condition Model (OCM). This gives partial waves ${}^1\text{S}_0$, ${}^3\text{S}_1$, ${}^1\text{P}_1$, ${}^3\text{P}_0$, ${}^3\text{P}_1$, ${}^3\text{P}_2$, ${}^3\text{D}_1$, ${}^1\text{D}_2$, ${}^3\text{D}_2$, and ${}^3\text{D}_3$ (Ref. [3]) in which the potential difference between p- ${}^3\text{He}$ and n- ${}^3\text{He}$ depends on the p-p Coulomb interaction.

2. Three-body Faddeev calculation

Recently we investigated an n-p- ${}^3\text{He}$ model for the ${}^3\vec{\text{He}}(\vec{d}, p){}^4\text{He}$ fusion reaction by using the three-body Faddeev method [5], including selected two-body channels: ${}^1\text{S}_0$, ${}^3\text{S}_1$ - ${}^3\text{D}_1$ for n-p in a rank-1 separable potential approximation to the so-called AV14 potential [2], and ${}^1\text{S}_0$ (rank 1) for n- ${}^3\text{He}$ and p- ${}^3\text{He}$ from the RGM modified OCM (or RGM-OCM) interactions [3] with three-body total spins and parities of $J^\pi = 1/2^\pm, \dots, 9/2^\pm$. Our preliminary

*Present address: SGI Japan Ltd., Yokohama city, Japan

results indicated that the polarisation effect was very important for the ratio of polarised and unpolarised total cross sections. However our previous calculation with selected two-

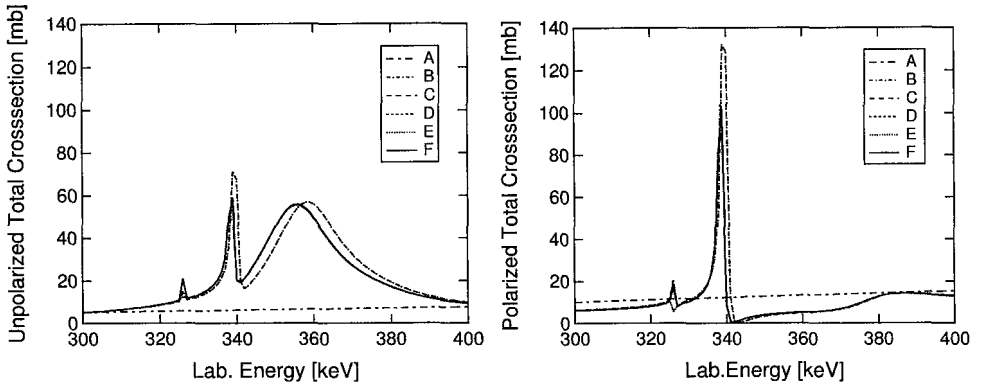


Fig. 1. a) Convergence with respect to N - ${}^3\text{He}$ partial waves for total cross-sections of the ${}^3\text{He}(d,p){}^4\text{He}$ reaction is shown (left figure). Three resonances, $5/2^+$, $3/2^+$, and $1/2^+$, appear from left to right. Lines A, B, C, D, E, F show the upper limit of the adopted partial waves in the N - ${}^3\text{He}$ interactions: 1S_0 (for A), ${}^3S_1, {}^1P_1, {}^3P_0, {}^3P_1, {}^3P_2$ (for B), 1D_2 (for C), 3D_1 (for D), 3D_2 (for E), 3D_3 (for F), respectively. b) Polarised total cross sections of the ${}^3\text{He}(d,p){}^4\text{He}$ reaction are shown (right figure). Partial waves are as in (a). The $1/2^+$ resonance is completely suppressed when both polarised angles are 90° with respect to the incident beam direction.

body states was not adequate to obtain good convergence when the number of two-body states increased. In this paper we would like to present a complete calculation using the full set of states from AV14 and the corresponding states for the N - ${}^3\text{He}$ potential. In particular, convergence with respect to the N - ${}^3\text{He}$ partial waves for the total cross section of the ${}^3\text{He}(d,p){}^4\text{He}$ reaction is investigated.

The N - ${}^3\text{He}$ two-body states ${}^1S_0, {}^3S_1, {}^1P_1, {}^3P_0, {}^3P_1, {}^3P_2, {}^3D_1, {}^1D_2, {}^3D_2,$ and 3D_3 are selectively used to explore the convergence. All partial waves for the AV14 NN interaction are included. Two narrow resonances, $5/2^+$ (lowest) and $3/2^+$ (middle), and a broad resonance, $1/2^+$ (highest), were found in the energy region from 300 keV to 500 keV. Finally the calculation shows that the polarised cross section is twice as large as the unpolarised one at a polarisation angle of 90° .

3. Conclusion and discussion

It was found that the double-polarised cross-section of ${}^3\text{He}(\vec{d}, p){}^4\text{He}$ is enhanced by a factor of 2 over the unpolarised one. It

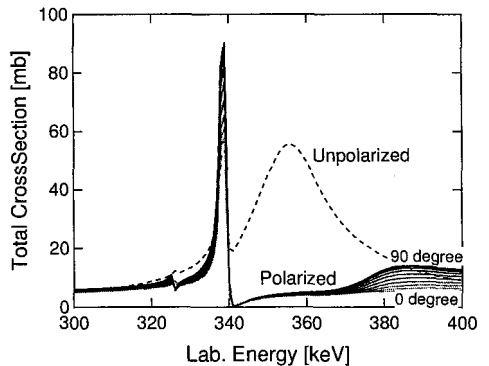


Fig. 2. The cross section enhancement of the double-polarised ${}^3\text{He}(d,p){}^4\text{He}$ reaction, with respect to the polarisation angles between 0° (lowest) and 90° (highest), compared with the unpolarised cross section.

seems that a three-body effect could be brought into play by the degrees of freedom of the constituent nucleons in the deuteron and in strongly dissociated ${}^3\text{He}$. Furthermore, three resonances in the region from 300 keV to 400 keV were found. The difference between the calculated resonance energy and the experimental one around $E_{lab} = 450$ keV could be attributed to Coulomb repulsion effects and to the off-shell behavior of the potentials used, which are all rank 1. Although a Coulomb correction is taken into account in our initial and final states, the method is not adequate to calculate a precise resonance spectra.

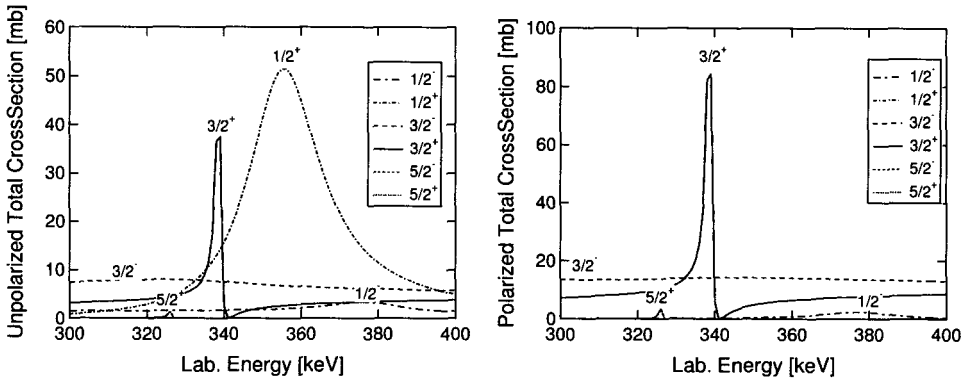


Fig. 3. a) Contribution of three-body states with respect to total spin and parity J^π , for unpolarised ${}^3\text{He}(d, p){}^4\text{He}$ cross sections (upper figure). b) For polarised cross sections (lower figure).

Needless to say, in order to test our results a very low energy accelerator facility should be set up; however such experiments could also be done by using a high energy polarised deuteron beam in collision with a high energy polarised ${}^3\text{He}$ beam at small angles. If a synchronization technique with a small collision angle could be developed, then one could obtain any energy in the region of $|E(d) - E({}^3\text{He})| \leq E \leq E(d) + E({}^3\text{He})$. As a result, one could tune a proper resonance energy by varying the collision angle between zero and 180° .

Acknowledgments

Numerical calculations were carried out using computer facilities in *FRCCS* in Tokyo University of Science, and the computer center of *JAERI*.

References

1. L. D. Faddeev, Zh. Eksp. Theor. Fiz. **39**, 1459 (1960) [Sov. Phys. JETP **12**, 1365 (1961)].
2. R. B. Wiringa, R. A. Smith, T. A. Ainsworth, Phys. Rev. **C29** 1207 (1984).
3. S. Gojuki, S. Oryu, and S. A. Sofianos, available from the Los Alamos e-print archive as **nucl-th/0112020**.
4. S. Oryu and S. Gojuki, Prog. Theor. Phys. Suppl. **154**, 285 (2004)
5. S. Gojuki and S. Oryu, Few-Body Systems Suppl. **14** 135 (2003).

THE ROLE OF SPIN OBSERVABLES IN QUASI-FREE η MESON PHOTOPRODUCTION FROM NUCLEI

B. I. S. van der VENTEL, G. C. HILLHOUSE

Department of Physics, Stellenbosch University, Stellenbosch, South Africa

L. J. ABU-RADDAD

Department of Infectious Diseases Epidemiology, Imperial College Faculty of Medicine, St Mary's Campus, London, United Kingdom

Quasi-free eta meson photoproduction is studied within a relativistic plane wave impulse approximation. The sensitivity of the unpolarized differential cross-section, the recoil nucleon polarization, and the photon asymmetry are investigated. The results indicate that the spin observables are sensitive to subtle effects that are not accessible by only looking at the unpolarized differential cross-section.

1. Introduction

The η electro- and photo-production processes continue to enjoy significant investigations using a variety of approaches. In this work, we assume the impulse approximation but provide a fully relativistic study in both the reactive content and the nuclear structure. The goal here is to shed light on the elementary process $\gamma N \rightarrow \eta N$ by furnishing a different physical setting from the on-shell point for studying the elementary amplitude. We also examine the possibility of using this process to extract medium modification effects to the propagation of the S_{11} and D_{13} resonances. We provide special attention in our work to the polarization observables, the recoil polarization of the ejected nucleon, and the photon asymmetry, as they are very sensitive to the fine details in the reactive content and are effective discriminators of subtle physical effects compared to the unpolarized differential cross-section. Moreover, the quasi-free polarization observables, while very sensitive to the fundamental processes, are insensitive to distortion effects.

2. Formalism

The transition matrix element for eta meson photo-production is given by

$$\mathcal{M} = \int d^4x_1 \cdots d^4x_N \bar{\psi} \phi J^\mu(x_1 \cdots x_N) A_\mu U_{\alpha,m} \quad (1)$$

where ψ is the nucleon wave function, ϕ is the eta meson wave function, A^μ is the incident photon wave function, and $U_{\alpha,m}$ is the wave function for the bound proton. By neglecting distortion effects on the eta and outgoing nucleon, we obtain from Eq. (1):

$$|\mathcal{M}|^2 = \delta(p_0 + k_0 - p_0 - k'_0) \sum_m \sum_s |\bar{U}(p', s) T(s, t) U_{\alpha,m}(p)|^2. \quad (2)$$

In Eq. (2) $U(p', s)$ is the usual free-particle Dirac spinor, and $T(s, t)$ is the interaction as a function of the Mandelstam variables s and t . The bound-state wave function $U_{\alpha,m}(p)$ is calculated within a relativistic mean-field approximation to the Walecka model [1], and is given by

$$\mathcal{U}_\alpha(\mathbf{p}) \equiv \mathcal{U}_{E\kappa m}(\mathbf{p}) = \frac{4\pi}{p} (-i)^l \begin{pmatrix} g_{E\kappa}(p) \\ f_{E\kappa}(p)(\boldsymbol{\sigma} \cdot \hat{\mathbf{p}}) \end{pmatrix} \mathcal{Y}_{\kappa m}(\hat{\mathbf{p}}). \quad (3)$$

If the impulse approximation is assumed then $T(s, t)$ in the medium is taken to be identical to that in free space, and therefore the following model-independent parametrization may be written down [2]:

$$T(\gamma p \rightarrow K^+ \Lambda) = F_T^{\alpha\beta} \sigma_{\alpha\beta} + iF_P \gamma_5 + F_A^\alpha \gamma_\alpha \gamma_5, \quad (4)$$

where the tensor, pseudoscalar, and axial-vector amplitudes are defined through

$$F_T^{\alpha\beta} = \frac{1}{2} \varepsilon^{\mu\nu\alpha\beta} \varepsilon_\mu k_\nu A_1(s, t), \quad (5)$$

$$F_P = -2i \left[(\boldsymbol{\varepsilon} \cdot \mathbf{p})(\mathbf{k} \cdot \mathbf{p}') - (\boldsymbol{\varepsilon} \cdot \mathbf{p}')(\mathbf{k} \cdot \mathbf{p}) \right] A_2(s, t), \quad (6)$$

$$F_A^\alpha = \left[(\boldsymbol{\varepsilon} \cdot \mathbf{p})k^\alpha - (\mathbf{k} \cdot \mathbf{p})\boldsymbol{\varepsilon}^\alpha \right] A_3(s, t) + \left[(\boldsymbol{\varepsilon} \cdot \mathbf{p}')k^\alpha - (\mathbf{k} \cdot \mathbf{p}')\boldsymbol{\varepsilon}^\alpha \right] A_4(s, t). \quad (7)$$

The elementary interaction $T(s, t)$ is the key input in the calculation, and it is parametrized by four independent functions A_1 , A_2 , A_3 , and A_4 . Our calculations uses as input the four functions as determined from the effective Lagrangian approach of Benmerrouche, Zhang, and Mukhopadhyay. [3]

3. Results

Results based on the formalism briefly outlined in the previous section are now presented. There are a number of key issues that may be investigated, such as (i) the role of the Born and vector terms, the S_{11} and the D_{13} resonances, (ii) uncertainties associated with the ηNN vertex, (iii) medium modifications of the resonance properties, as well as (iv) nuclear target effects. Here we will focus on issue (ii), but a full compendium of our results may be found in [2]. By way of illustration we show in Fig. 1 the recoil nucleon polarization and the photon asymmetry as a function of the eta meson scattering angle. The calculation was done not far from threshold for an incident photon energy of 750 MeV and fixed missing momentum of $|p_m| = 100$ MeV. The calculation employed both the S_{11} and D_{13} resonances, together with the Born and vector meson terms. This figure beautifully illustrates how the different spin observables are sensitive to different aspects of the ambiguity at the ηNN vertex.

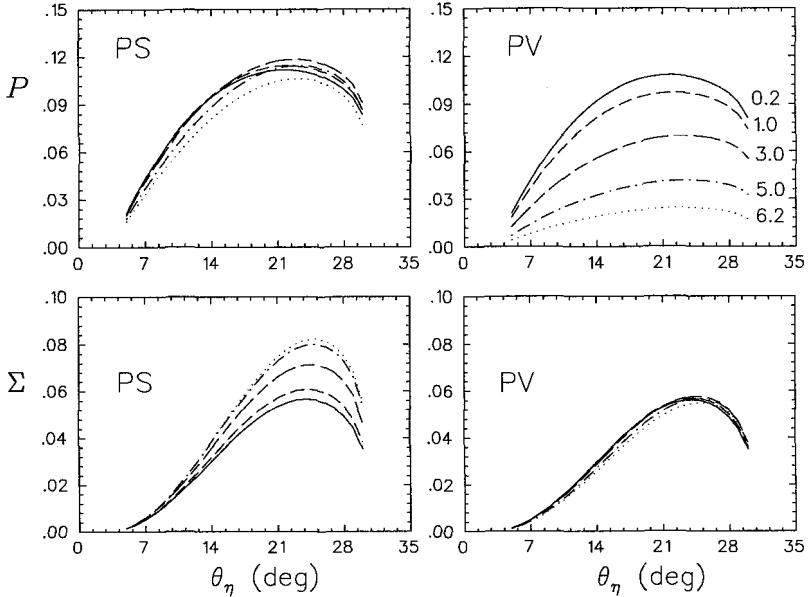


Fig. 1. Variation of the recoil nucleon polarization (\mathcal{P}) and the photon asymmetry (Σ) with respect to a change in the value of the η meson coupling constant (g_η) where $0.2 \leq g_\eta \leq 6.2$. The graphs on the left-hand-side (right-hand-side) are for PS (PV) coupling at the ηNN vertex. The values of the coupling constant chosen in the range specified above are shown on the graph of the polarization for pseudovector coupling. The calculations shown are for proton knockout from the $1p^{3/2}$ orbital of ^{12}C for an incident photon energy of 750 MeV and fixed missing momentum, $|p_m| = 100$ MeV. The calculation employed both the S_{11} and D_{13} resonances together with the Born and vector meson terms.

4. Summary and Conclusions

In this paper we have studied quasi-free η photoproduction via the calculation of the differential cross-section, the recoil nucleon polarization and the photon asymmetry using a relativistic plane wave impulse approximation formalism. The emphasis was on the polarization observables, since they are very sensitive to the underlying dynamics but largely insensitive to distortion and nuclear target effects.

Our results indicate that the nucleon polarization is practically target independent, whereas the asymmetry exhibits some small sensitivity. The polarization observables are very sensitive to the elementary amplitude. We find that, in contrast to coherent η photoproduction, the S_{11} resonance completely dominates the unpolarized cross-section. However, the two spin observables are dominated by the background processes in the elementary amplitude and specially sensitive to the D_{13} resonance contribution. As a consequence, the polarization and asymmetry are considerably sensitive to variations in the mass of the D_{13} resonance. Indeed, a variation in the mass of this resonance leads to significant effects in the polarization and asymmetry. The polarization (asymmetry) is insensitive to the magnitude of the coupling constant for pseudoscalar (pseudovector) coupling. However, the polarization (asymmetry) does indeed exhibit a sensitivity to the magnitude of the coupling constant for pseudovector (pseudoscalar) coupling.

The quasi-free differential cross-section provides an excellent tool to study medium modifications to the S_{11} resonance in order to distinguish between various models that attempt to understand the S_{11} resonance. The basic message of our results is now clear: to probe medium modifications to the S_{11} resonance, measure the differential cross-section, to study the background processes and their medium modifications, measure the polarization observables.

References

1. G. A. Lalazissis, J. König, and P. Ring, *Phys. Rev. C* **55**, 540-543 (1997).
2. B. I. S. van der Ventel, L. J. Abu-Raddad, and G. C. Hillhouse, *Phys. Rev. C* **68**, 024601 (2003).
3. M. Benmerrouche, N. C. Mukhopadhyay, and J. F. Zhang, *Phys. Rev. D* **51**, 3237 (1995).

UNIFIED UNDERSTANDING OF SPIN ISOSPIN RESPONSE FUNCTIONS OF NUCLEI

M. ICHIMURA

Faculty of Computer and Information Sciences, Hosei University, Koganei, Japan

T. WAKASA

Department of Physics, Kyushu University, Higashi, Japan

H. SAKAI

Department of Physics, The University of Tokyo, Bunkyo, Japan

Recent (p, n) and (n, p) experiments at intermediate energies provided reliable data on nuclear spin-isospin responses. We investigated them with emphasis on the contrasting phenomena of the quenching of the total strength of the Gamow-Teller transition, and the enhancement of the pionic response in the quasielastic region, in a unified theoretical framework, that is the continuum RPA with the $\pi + \rho + g'$ model, incorporated with DWIA and two-step calculations. We extracted a common set of the Landau-Migdal parameters, $g'_{NN}=0.6-0.7$ and $g'_{N\Delta}=0.2-0.4$ for both low and high momentum transfers.

Information on spin-isospin responses is being accumulated and becoming more reliable through experimental progress in (p, n) and (n, p) reactions at intermediate energies. Here we report a unified theoretical study of the Gamow-Teller (GT) giant resonance (GTGR) spectrum and the quenching of the total strength of the GT transition with respect to the GT sum rule value, which were obtained by the multipole decomposition analysis (MDA) of the (p, n) and (n, p) data at 295 MeV [1, 2], and the spin-longitudinal cross sections ID_q of (p, n) at 346 MeV [3, 4] and at 494 MeV [5], which well represent the pionic response function R_L .

Our main interest is to understand two contrasting phenomena simultaneously: the quenching of the total GT transition strength, and the enhancement of the pionic response in the quasielastic scattering (QES) region, which is a good signature of the precursor of pion condensation [6].

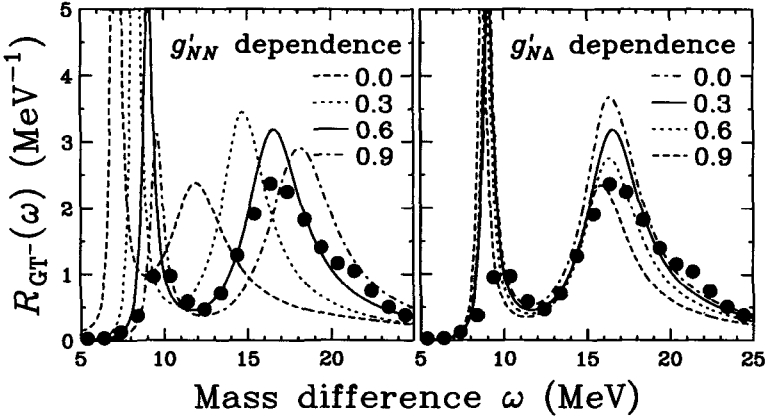


Fig. 1. The GT strength distribution from ^{90}Zr to ^{90}Nb . The curves denote the continuum RPA results with different g'_{NN} (left) and with different $g'_{N\Delta}$ (right).

To all these phenomena we applied [7] a common method, that is continuum RPA with the $\pi + \rho + g'$ model, incorporating DWIA [8] and two-step calculations. Here the effective interaction is the sum of the one- π and one- ρ exchange interactions, and the Landau-Migdal (LM) interaction V_{LM} specified by the LM parameters g'_{NN} , $g'_{N\Delta}$, $g'_{\Delta\Delta}$ as

$$\begin{aligned}
 V_{\text{LM}} = & \left[\frac{f_{\pi NN}^2}{m_\pi^2} g'_{NN} (\tau_1 \cdot \tau_2) (\sigma_1 \cdot \sigma_2) \right. \\
 & + \frac{f_{\pi NN} f_{\pi N\Delta}}{m_\pi^2} g'_{N\Delta} \{ ((\tau_1 \cdot T_2) (\sigma_1 \cdot S_2) + \text{h.c.}) + (1 \leftrightarrow 2) \} \\
 & \left. + \frac{f_{\pi N\Delta}^2}{m_\pi^2} g'_{\Delta\Delta} \{ (T_1 \cdot T_2^\dagger) (S_1 \cdot S_2^\dagger) + (1 \leftrightarrow 2) \} \right] \delta(r_1 - r_2). \quad (1)
 \end{aligned}$$

We used a local effective mass $m^*(r) = m_N - (m_N - m^*(0)) f_{\text{WS}}(r) / f_{\text{WS}}(0)$ with the Woods-Saxon radial form $f_{\text{WS}}(r)$. In this framework we looked for the g' 's best suited to reproduce the experimental data.

The left panel of Fig. 1 shows the g'_{NN} dependence of the GTGR peak position with fixed $g'_{N\Delta} = 0.3$ and $m^*(0)/m_N = 0.7$. The right panel shows the $g'_{N\Delta}$ dependence with fixed $g'_{NN} = 0.6$ and $m^*(0)/m_N = 0.7$. We also studied the $m^*(0)$ dependence. Dependences on $g'_{N\Delta}$ and $m^*(0)$ are not so sensitive as g'_{NN} . This analysis implies $g'_{NN} = 0.6 \pm 0.1$ with care for some $g'_{N\Delta}$ and m^* dependences. The high theoretical value around the peaks seen on the left could be redistributed by mixing of $2p2h$ states beyond GTGR. The right panel shows that the peak height depends strongly on $g'_{N\Delta}$, because it governs the coupling between ph and Δh states.

Figure 2 shows the $g'_{N\Delta}$ dependence of the quenching factor Q of the total GT strength on the sum rule value $3(N - Z)$, which is defined as

$$Q = (S_{\text{GT}^-}^{\text{exp}} - S_{\text{GT}^+}^{\text{exp}}) / \{3(N - Z)\}, \quad (2)$$

where $S_{\text{GT}^\pm}^{\text{exp}}$ is the measured total β^\pm type transition strength. The latest experimental value

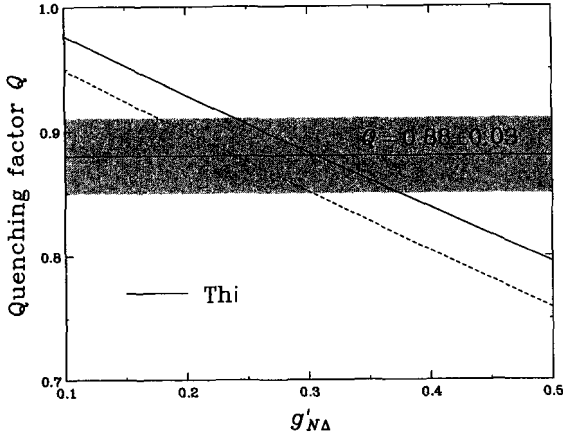


Fig. 2. Quenching factor Q vs. $g'_{N\Delta}$ with fixed $g'_{NN} = 0.6$ and $m^*(0)/m_N = 0.7$.

is $Q = 0.88 \pm 0.03$ obtained by MDA from the $^{90}\text{Zr}(p, n)$ and $^{90}\text{Zr}(n, p)$ data by Yako *et al.* [2].

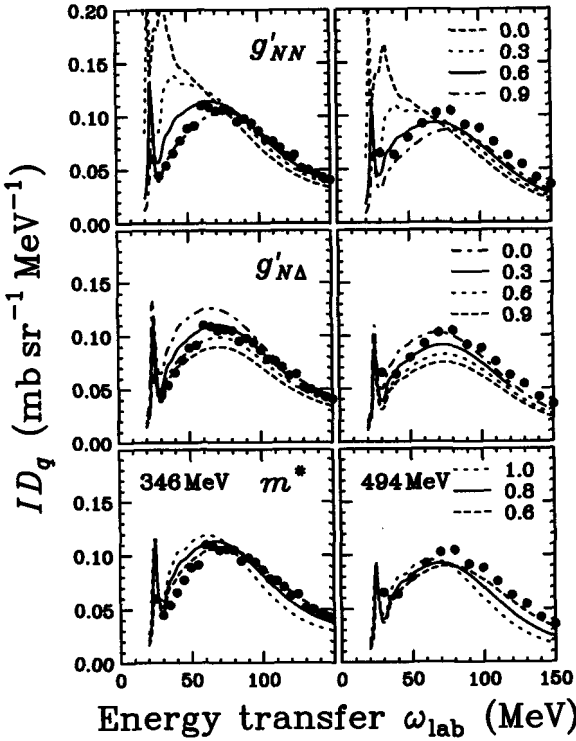


Fig. 3. ID_q for $^{12}\text{C}(p, n)$ at $T_p=346$ MeV (left) and 494 MeV (right).

The solid line shows our continuum RPA results, while the dashed line is given the Suzuki-Sakai formulas [9], derived with pure V_{LM} and a Fermi gas model. The comparison gives $g'_{N\Delta} = 0.31 \pm 0.07$. The difference between the present and the Suzuki-Sakai results is due to the π and ρ exchange interactions, with help of nuclear finite size [10].

Figure 3 shows g'_{NN} , $g'_{N\Delta}$, and $m^*(0)/m_N$ dependences of spin-longitudinal cross sections ID_q for $^{12}\text{C}(p, n)$. We performed DWIA and two-step calculations with the continuum RPA response functions. The top panels suggest $g'_{NN} = 0.7 \pm 0.1$. The middle panels suggest that suitable values of $g'_{N\Delta}$ are about 0.4 and 0.2 for the 346 MeV and 494 MeV data, respectively. Thus we could estimate $g'_{N\Delta} = 0.3 \pm 0.1$, which is consistent with that obtained from

Q. The bottom panels imply $m^*(0)/m_N \approx 0.7-0.6$, consistent with the standard theoretical estimations.

In summary, our unified approach leads to a common set of the LM parameters, $g'_{NN}=0.6-0.7$ and $g'_{N\Delta}=0.2-0.4$ for the above contrasting phenomena.

References

1. T. Wakasa *et al.*, *Phys. Rev.* **C55**, 2909 (1997).
2. K. Yako *et al.*, *nucl-ex/0411011*.
3. T. Wakasa *et al.*, *Phys. Rev.* **C59**, 3177 (1999).
4. T. Wakasa *et al.*, *Phys. Rev.* **C69**, 054609 (2004).
5. T. N. Taddeucci *et al.*, *Phys. Rev. Lett.* **73**, 3516 (1994).
6. W. M. Alberico, M. Ericson and A. Molinari, *Phys. Lett.* **B92**, 153 (1980).
7. T. Wakasa, M. Ichimura and H. Sakai, *nucl-ex/0411055*.
8. K. Kawahigashi *et al.*, *Phys. Rev.* **C63**, 044609 (2001).
9. T. Suzuki and H. Sakai, *Phys. Lett.* **B455**, 25 (1999).
10. A. Arima *et al.*, *Phys. Lett.* **B499**, 104 (2001).

ISOVECTOR AND ISOSCALAR SPIN-FLIP M1 STRENGTHS IN ^{11}B

T. KAWABATA

Center for Nuclear Study, Graduate School of Science, University of Tokyo, Wako, Japan

The $M1$ transition strengths provide important information on nuclear structure because they could offer a good way to test theoretical nuclear models. Recently, the $M1$ transition strengths have attracted interest from the viewpoints not only of the nuclear physics but also neutrino astrophysics, because the spin part of the $M1$ operator is identical to the relevant operator's mediation of neutrino-induced reactions.

Raghavan *et al.* pointed out that the ^{11}B nucleus can be used as a possible neutrino detector to investigate stellar processes [1]. High-energy neutrinos from stellar processes like the proton-proton fusion chain in the sun and supernova explosions excite low-lying states in ^{11}B and ^{11}C by $M1$ and Gamow-Teller (GT) transitions via neutral-current (NC) and charged-current (CC) processes, respectively. Such neutrinos can be detected by measuring electrons emitted by the CC reaction, and γ rays from the de-excitations of the low-lying states. Since the isospin of the ground state of ^{11}B is $T = 1/2$, low-lying states in ^{11}B are excited by both isovector and isoscalar transitions. Both isoscalar and isovector spin-flip $M1$ strengths are therefore needed for estimating the CC and NC cross-sections.

The cross-sections of hadronic reactions provide a good measure for the weak interaction response, since the relevant operators in the hadronic reactions are identical to those in β -decay and neutrino capture processes. Thus, we recently measured cross-sections for the $^{11}\text{B}(^3\text{He}, t)$ and $^{11}\text{B}(d, d')$ reactions to determine the isovector and isoscalar spin-flip $M1$ strengths in ^{11}B .

The experiment was performed at the Research Center for Nuclear Physics, Osaka University, using 450-MeV ^3He and 200-MeV deuteron beams. The measured cross-sections were shown in Figs. 1 and 2. Since the ground state of ^{11}B has non-zero spin, the cross-sections for the $^{11}\text{B}(^3\text{He}, t)$ and $^{11}\text{B}(d, d')$ reactions are described by an incoherent sum over the cross-section of the different multipole contributions,

$$\frac{d\sigma}{d\Omega} = \sum_{\Delta J} \frac{d\sigma}{d\Omega}(\Delta J).$$

In order to determine the spin-flip $M1$ strengths, the cross-section for each ΔJ transition is needed to extract the $\Delta J = 1$ contribution.

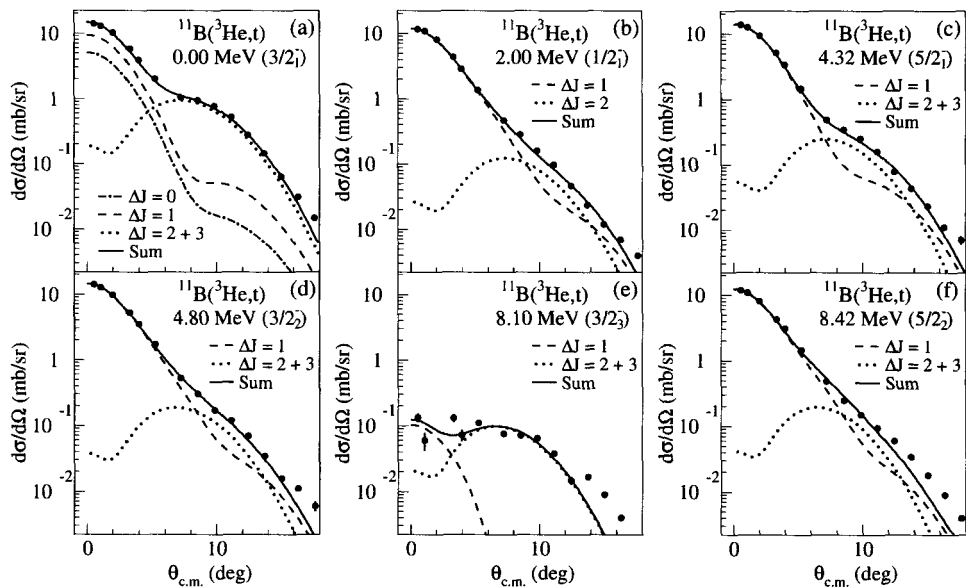


Fig. 1. Cross-sections for the $^{11}\text{B}(^3\text{He},t)$ reactions compared with the DWIA calculation. The dash-dotted, dashed, and dotted curves show $\Delta J = 0$, $\Delta J = 1$, and $\Delta J \geq 2$ contributions, respectively. The solid curves are sums of all the multipole contributions.

For the $^{11}\text{B}(^3\text{He},t)$ analysis, the cross-section for the each ΔJ transition was calculated by the distorted wave impulse approximation (DWIA) as seen in Fig. 1. Since the GT strength $B(\text{GT})$ for the ground-state transition is known to be 0.345 ± 0.008 from the β -decay strength, the cross-sections for the $\Delta J = 1$ transitions to the excited states in ^{11}C can be related to the $B(\text{GT})$ values by assuming a linear proportional relation. The $B(\text{GT})$ values obtained are compared with the previous (p,n) result [2] in Table 1. The present results are consistent with the (p,n) result, although several states are not separately resolved due to the poor energy resolution in the (p,n) measurement. Assuming isospin symmetry is conserved, the GT strengths are easily related to the isovector spin-flip $M1$ strength $B(\sigma\tau_z)$,

$$\frac{B(\text{GT})}{B(\sigma\tau_z)} = \frac{8\pi}{3} \frac{\langle T_i, T_{iz}, 1, \pm 1 | T_f, T_{fz} \rangle^2}{\langle T_i, T_{iz}, 1, 0 | T_f, T_{fz} \rangle^2}.$$

Although the isospin-symmetry breaking changes this ratio, the effect is usually small. Therefore, the GT strengths obtained from the charge exchange reaction are still useful in the study of isovector spin-flip $M1$ strengths.

For the $^{11}\text{B}(d,d')$ analysis, the cross-section for each ΔJ transition was determined from the $^{12}\text{C}(d,d')$ reaction. Since the ground state of ^{12}C has zero spin, transitions to the discrete states in ^{12}C are expected to be good references for the angular dependence

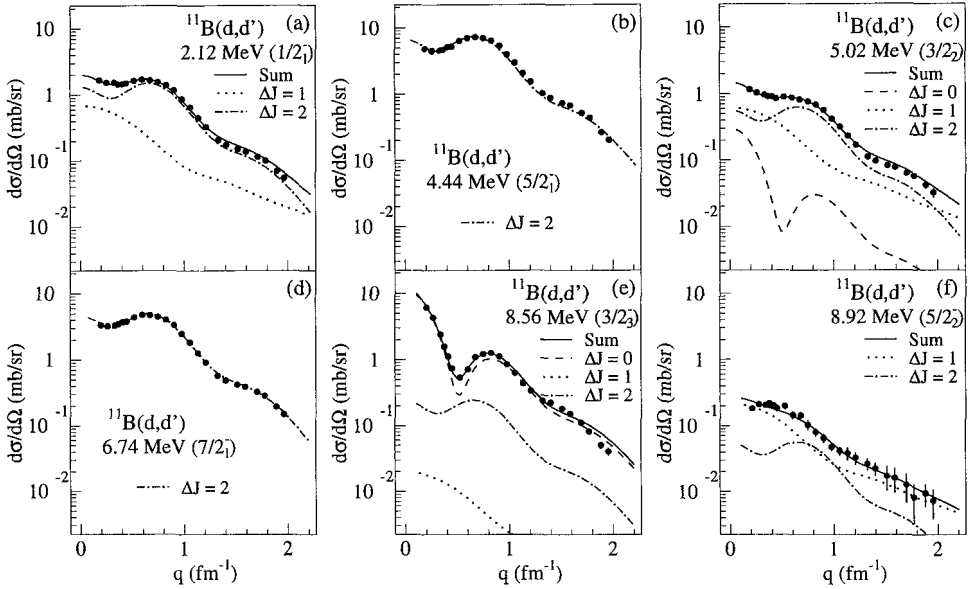


Fig. 2. Cross-sections for the $^{11}\text{B}(d,d')$ reactions. The dashed, dotted, and dash-dotted curves show $\Delta J = 0, 1,$ and 2 contributions, respectively. The solid curves are sums of all the multipole contributions.

Table 1. Measured $B(\text{GT})$ values compared with the (p,n) result.

E_x (MeV)	J^π	$B(\text{GT})$	
		Present	(p,n)
0.00	$3/2^-$	0.345 ± 0.008	
2.00	$1/2^-$	0.402 ± 0.031	0.399 ± 0.032
4.32	$5/2^-$	0.454 ± 0.026	} 0.961 ± 0.060
4.80	$3/2^-$	0.480 ± 0.031	
8.10	$3/2^-$	≤ 0.003	} 0.444 ± 0.010
8.42	$5/2^-$	0.406 ± 0.038	

of the cross-sections for certain ΔJ transitions. As shown in Fig. 2, the cross-section for the $^{11}\text{B}(d,d')$ reaction was successfully decomposed into the ΔJ contributions. Although the 4.44-MeV ($5/2^-$) state can be excited by both the $\Delta J = 1$ and 2 transitions, the main part of the transition is due to $\Delta J = 2$. This result is explained by the fact that the strong coupling between the ground and 4.44-MeV states is expected since the 4.44-MeV state is considered to be a member of the ground-state rotational band. Since the observed $\Delta J = 2$ transition strength is much larger than the expected $\Delta J = 1$ strength, the $\Delta J = 1$ component of the transition strength can not be reliably extracted for the 4.44-MeV state. The transition strength for the 6.74-MeV ($7/2^-$) state is also dominated by the $\Delta J = 2$ component, and the $\Delta J = 1$ transition to this state is not allowed. The isoscalar spin-flip $M1$ strength $B(\sigma)$ for the transition to the 2.12-MeV ($1/2^-$) state is known to be 0.037 ± 0.008 from the γ -decay widths of the mirror states and the $B(\text{GT})$ value [3]. Using this value, the cross-section for the $\Delta J = 1$ transitions to the other excited states can be related to the $B(\sigma)$ values. Since the

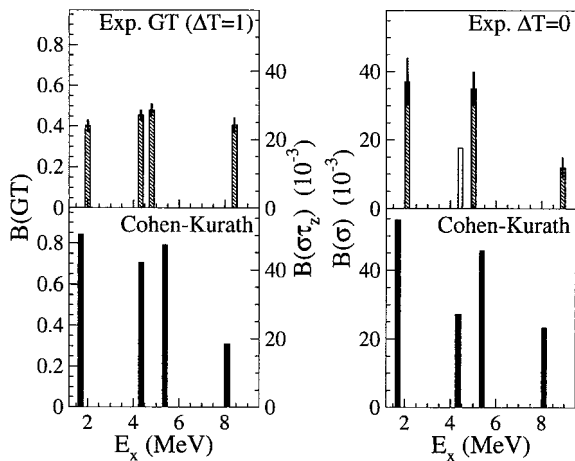


Fig. 3. Measured $B(\text{GT})$ [$B(\sigma\tau_z)$] and $B(\sigma)$ values are compared with the shell-model predictions using the Cohen-Kurath wave functions [?]. The open bar in the right-upper panel shows the $B(\sigma)$ value for the 4.44-MeV state estimated from $B(\text{GT})$ (see text).

$\Delta J = 1$ cross-section for the 4.44-MeV state was not reliably obtained in the (d, d') analysis, the isoscalar spin-flip $M1$ strength was determined from the measured $B(\text{GT})$ value and the relative strength of the isoscalar transition to the isovector transition calculated by using the Cohen-Kurath wave functions (CKWF) [4].

The measured $B(\text{GT})$ [$B(\sigma\tau_z)$] and $B(\sigma)$ values are compared with the shell model predictions using the CKWFs in Fig. 3. The CKWFs reasonably explain the experimental result, except for the quenching, by a factor of 0.5-0.7. The present result will be useful in the measurement of stellar neutrinos using the NC and CC reactions on ^{11}B .

References

1. R. S. Raghavan *et al.*, Phys. Rev. Lett. **57**, 1801 (1986).
2. T.N. Taddeucci *et al.*, Phys. Rev. C **42**, 935 (1990).
3. J. Bernabéu *et al.*, Nucl. Phys. **B378**, 131 (1992).
4. S. Cohen and D. Kurath, Nucl. Phys. **73**, 1 (1965).

TENSOR ANALYZING POWER OF THE $^{16}\text{O}(d, ^2\text{He})$ REACTION AT 0 DEGREES AND STRUCTURE OF THE SPIN-DIPOLE RESONANCES

K. SUDA^a, H. OKAMURA^b, T. UESAKA^a, R. SUZUKI^c, H. KUMASAKA^c, T. IKEDA^c, K. ITOH^c,
H. SAKAI^{a,d}, A. TAMII^e, K. SEKIGUCHI^f, K. YAKO^d, Y. MAEDA^a, M. HATANOD^d, T. SAITOD^d,
H. KUBOKI^d, N. SAKAMOTO^f, Y. SATOU^g

^aCenter for Nuclear Study, University of Tokyo, Bunkyo, Japan

^bCyclotron and Radioisotope Center, Tohoku University, Sendai, Japan

^cDepartment of Physics, Saitama University, Saitama, Japan

^dDepartment of Physics, University of Tokyo, Bunkyo, Japan

^eResearch Center for Nuclear Physics, Osaka University, Ibaraki, Japan

^fRIKEN (The Institute of Physical and Chemical Research), Wako, Japan

^gDepartment of Physics, Tokyo Institute of Technology, Meguro, Japan

The tensor analyzing power A_{zz} of the $^{16}\text{O}(d, ^2\text{He})^{16}\text{N}$ reaction at $E_d = 270$ MeV has been measured at 0° . A model-independent spin-parity determination method is applied to the observed states in the residual nucleus ^{16}N . Data are compared with the adiabatic coupled-channels Born approximation calculation.

1. Introduction

In recent years, the spin-dipole resonance (SDR) in ^{16}O has received attention in association with the detection of supernova neutrinos [1]. Recent study of the ^{16}O nucleus shows that the spin-parity states appear in the order 2^- , 1^- , and 0^- in the excitation energy spectra, and that they overlap each other. In such a study, the determination of spin-parity states relies largely on the shell-model calculations. For further study of SDRs, a model-independent determination is desired.

The $(d, ^2\text{He})$ reaction is one of the most effective tools for the study of SDR states [2]. Recently, a model-independent spin-parity determination method using the tensor analyzing power A_{zz} at 0° has been proposed [3]. The tensor analyzing power A_{zz} of the $(d, ^2\text{He})$ reaction on even-even targets shows extreme values at $\theta = 0^\circ$ and 180° for some J^π residual states, solely due to parity-conservation [3, 4]:

$$A_{zz}(0^\circ, 180^\circ) = \begin{cases} -2, & \text{if } J^\pi = 0^-, \\ +1, & \text{if } \pi = (-)^J. \end{cases} \quad (1)$$

By using Eq. (1), we can determine two of the three SDR states unambiguously. This method was successfully applied to a ^{12}C target, where a 0^- state in the residual nucleus

^{12}B was identified at $E_x = 9.3$ MeV [3]. We apply this method to ^{16}O targets, and study the structure of the SDR states in ^{16}N , the isobaric analog of ^{16}O .

2. Experiment

The experiment was performed at the RIKEN Accelerator Research Facility, using a tensor-polarised deuteron beam at $E_d = 270$ MeV. The solid oxygen target [5, 6], with a thickness of 5 – 40 mg/cm², was bombarded by the deuteron beam. Scattered protons were momentum analyzed by the magnetic spectrograph SMART [7], and detected at the first focal plane [8].

3. Results and Discussion

Figure 1 shows the energy spectra and the tensor analyzing power A_{zz} for the $^{16}\text{O}(d, ^2\text{He})^{16}\text{N}$ reaction at $\theta_{\text{c.m.}} = 0^\circ - 1^\circ$. In the upper panel, the energy spectra for two

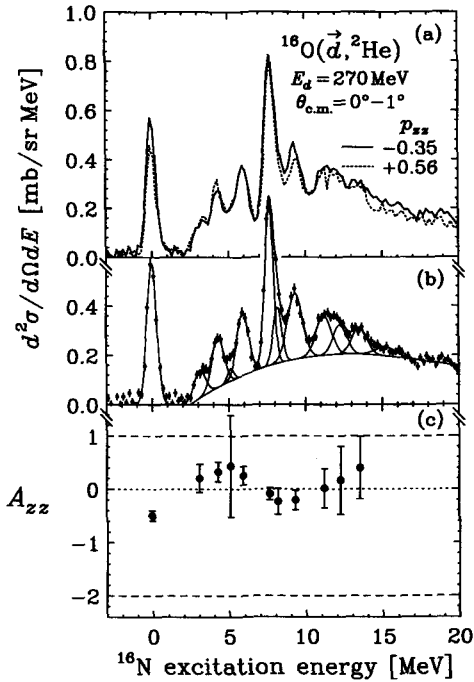


Fig. 1. (a) Energy spectra of the $^{16}\text{O}(d, ^2\text{He})^{16}\text{N}$ reaction at $\theta_{\text{c.m.}} = 0^\circ - 1^\circ$ for two tensor polarised beams. (b) the peak-fitting result of the spectrum and (c) A_{zz} values for each peak.

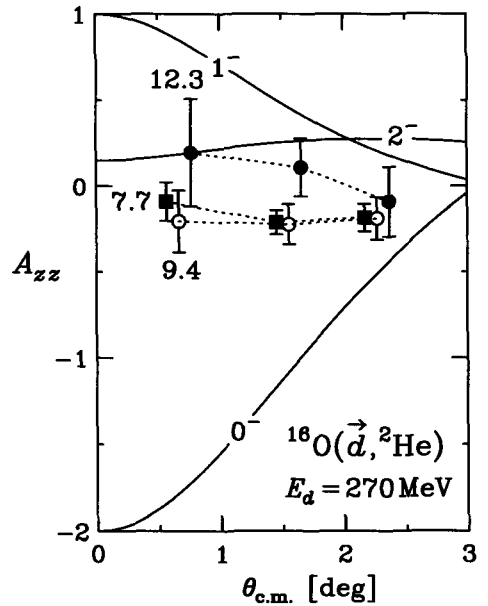


Fig. 2. Angular distribution of tensor analyzing power A_{zz} for the peaks at $E_x = 7.7, 9.4,$ and 12.3 MeV. Theoretical calculations for the spin-dipole states are shown by solid curves.

polarisation modes of the deuteron beam ($P_{zz} = -0.35$ and $+0.57$) are shown. The energy resolution was estimated to be 0.7 MeV at FWHM. A prominent peak was observed at

$E_x = 7.7$ MeV. In order to extract the tensor analyzing power A_{zz} , a Gaussian peak fit is performed. The non-resonant continuum background caused by the quasi-free scattering is subtracted using a semi-phenomenological function [9]. In the middle panel, the result of the energy spectrum fit for one of the polarisation modes ($P_{zz} = -0.35$) is shown. In the lower panel, the deduced A_{zz} corresponding to each peak is shown. At $E_x = 7.7$ MeV, the A_{zz} value is nearly equal to zero, and is significantly different from -2 and $+1$, which correspond to $J^\pi = 0^-$ and 1^- , respectively [see Eq. (1)]. Thus, the A_{zz} result suggests that 2^- state is dominant at $E_x = 7.7$ MeV. In order to confirm this 2^- dominance, we performed an adiabatic coupled-channel Born approximation calculation [10], and compared the angular distribution of A_{zz} . The one-body transition densities were obtained from the wave functions of Millener and Kurath [11], using the shell model code OXBASH [12]. The shell model calculation was performed within $1 \hbar\omega$ configuration space. Figure 2 compares the A_{zz} data with calculation for three SDR states. The monotonic distribution of A_{zz} for the peaks at $E_x = 7.7, 9.4,$ and 12.3 MeV is well reproduced by the calculation for 2^- state, indicating that 2^- states are dominant for these states.

Figure 3 compares the energy spectrum with the calculated strength for SDR states at $\theta_{\text{c.m.}} = 3.5^\circ$. The calculated ones are smeared by a Gaussian function with the width of the experimental resolution. The overall strength is well reproduced normalized by a factor

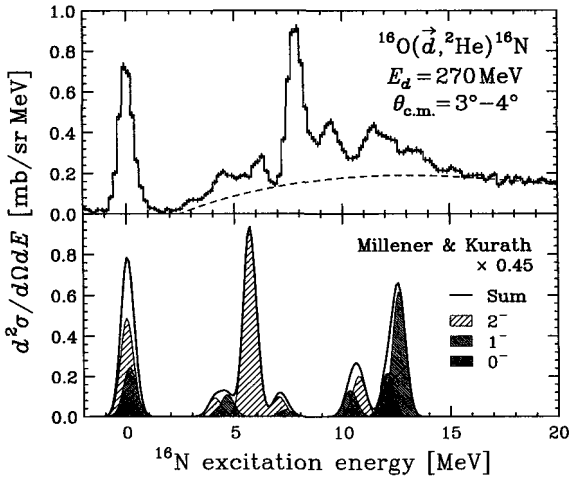


Fig. 3. Comparison of the energy spectrum and the calculated strength for the spin-dipole states at $\theta_{\text{c.m.}} = 3.5^\circ$. The upper panel shows the experimental result. The lower panel shows the calculated spectra for 2^- , 1^- , and 0^- states as well as their sum. The calculated strengths are smeared by a Gaussian function with the width of the experimental resolution. The overall strength is normalized by a factor of 0.45.

of 0.45. The observed peak at $E_x = 7.7$ MeV corresponds to the calculated 2^- state at $E_x = 5.7$ MeV. In contrast, at $E_x \sim 12.6$ MeV no concentration of the strength of the 1^- state are observed. This missing strength of the 1^- state may be attributed to higher-order effects such as $3p$ - $3h$ configuration mixing or tensor correlation [13].

Acknowledgments

The authors gratefully acknowledge Dr. T. Kawabata for valuable discussion. They also express their gratitude to all the staff of RIKEN Accelerator Research Facility. One of the authors (K. Suda) would like to acknowledge the financial support of the Junior Research Associate program of RIKEN.

References

1. K. Langanke et al., *Phys. Rev. Lett.* **76**, 2629 (1996).
2. H. Okamura et al., *Phys. Lett. B* **345**, 1 (1995).
3. H. Okamura et al., *Phys. Rev. C* **66**, 054602 (2002).
4. J. A. Kuehner et al., *Phys. Rev. Lett.* **35**, 423 (1975).
5. R. Suzuki et al., *RIKEN Accel. Prog. Rep.* **36**, 188 (2003).
6. T. Uesaka et al., *CNS-REP-59*, 56 (2003).
7. T. Ichihara et al., *Nucl. Phys.* **A569**, 287c (1994).
8. H. Okamura et al., *Nucl. Instrum. Methods Phys. Res. A* **406**, 78 (1998).
9. K. J. Raywood et al., *Phys. Rev. C* **41**, 2836 (1990).
10. H. Okamura, *Phys. Rev. C* **60**, 064602 (1999).
11. D. J. Millener et al., *Nucl. Phys.* **A255**, 315 (1975).
12. B. A. Brown et al., *The Oxford-Buenos-Aires-MSU Shell-Model Code*, Michigan State University Cyclotron Laboratory Report 524 (1986).
13. T. Suzuki et al., *Nucl. Phys.* **A637**, 547 (1998).

SPIN EFFECTS AND NEUTRINO OPACITY TO COLD NEUTRON MATTER

O. BENHAR^a, A. FABROCINI^b, S. FANTONI^c, G. I. LYKASOV^d

^a INFN, Sezione Roma 1, Roma, Italy

^b Dipartimento di Fisica "E.Fermi", Università di Pisa,
and INFN, Sezione di Pisa, Pisa, Italy

^c International School for Advanced Studies (SISSA) and INFN, Sezione di Trieste, Trieste, Italy

^d JINR, Dubna, Russia

The weak dynamic form factors of cold neutron matter have been calculated within correlated basis function (CBF) theory using a realistic Hamiltonian. The results show that the effects of nucleon-nucleon correlations on the density and spin-density responses are different. The role of long-range correlations has been investigated, comparing the CBF responses to those resulting from Landau theory of Fermi liquids. The neutrino mean free path has been obtained by combining the two approaches.

Neutrino processes in a nuclear medium play an important role in astrophysics. For instance, neutrino propagation in dense neutron or proto-neutron matter yields relevant information about stellar evolution and structure [1, 2] and [3, 4]. The key ingredient in neutrino transport calculation is the neutrino opacity. Its theoretical evaluation, however, involves several approximations in the calculation of the neutrino cross sections; see for example [5].

In this paper we focus on the analysis of the density-density and spin-density dynamic form factors (FF) constructed within the different approaches, and apply them to the calculation of the elastic and quasi-elastic neutrino cross-section and its mean free path. An approach which takes some care of the nucleon–nucleon interaction and of the consequent nucleon property modifications based on the CBF is suggested. This effect turns out to be sizable, based on calculations performed within the Fermi gas approximation. Comparing the calculated FF with the corresponding results obtained within the Landau Fermi liquid theory (LT), we find some differences. We therefore match the LT and CBF approaches to calculate the elastic neutrino mean free path due to the neutral weak current.

The description of nuclear responses in the quasi-elastic region is based upon the approach developed in [6]. The basic Ansatz consists in assuming that the nuclear excited states can be described as a product of a Slater determinant and a many-body correlation function, which is the same correlation function that describes the ground state [7]. The weak vector FF $\mathcal{S}_V(\mathbf{q}, \omega)$ and the axial-vector FF $\mathcal{S}_A(\mathbf{q}, \omega)$ are related to the correspond-

ing response functions $\chi_{V,A}(\mathbf{q}, \omega)$ [8]

$$\mathcal{S}_{V,A}(\mathbf{q}, \omega) = \frac{1}{2\pi n} \frac{1}{1 - \exp(-\beta\omega)} \text{Im}(\chi_{V,A}(\mathbf{q}, \omega)) \quad (1)$$

where $\beta = 1/k_B T$, k_B is Boltzman's constant, T is the temperature, and n is the density of neutron matter. They can be calculated, for example within the Landau Fermi liquid theory [1, 9].

Let us apply the response function to the analysis of neutrino propagation in a cold pure neutron matter at low energies. Actually the weak responses in symmetric nuclear matter have been calculated recently in [10] within the CBF theory using the Tamm-Dankoff approximation. We will compare our calculations with the results presented there, and find some differences. The weak response of nuclei has also been studied in [11], and a difference between the electromagnetic and weak FFs has been shown.

Using these forms for the leptonic and hadronic currents, one can derive an equation for the rate of neutrino-neutron elastic scattering in pure neutron matter at low energies; see for example [1, 5] and [4].

$$W_{fi} = \frac{G^2 n}{4V} [C_V^2 (1 + \cos(\theta)) \mathcal{S}_V(\mathbf{q}, \omega) + C_A^2 (3 - \cos(\theta)) \mathcal{S}_A(\mathbf{q}, \omega)] \quad (2)$$

However, the hadronic vector $\bar{\psi}_n \psi_n \delta_0^\mu$ current and the axial $\bar{\psi}_n \sigma_i \psi_n \delta_i^\mu$ current can be modified in a medium. The vector and axial constants C_V, C_A are renormalized; however they can be changed in a medium by about 10-15%. We therefore neglect this effect here.

Let us apply the form obtained for the density and spin-density FF to the computation of the mean free path l at zero temperature ($T = 0.$) for the nondegenerate neutrino case. Then, according to [1]

$$1/l = V \int \frac{d^3 q}{(2\pi)^3} W_{fi} \quad (3)$$

The Gamow-Teller part $1/l_{GT}$ of $1/l$ is related to W_{fi}^{GT} with help of Eq.(3), where

$$W_{fi}^{GT} = \frac{G^2 n}{4V} C_A^2 (3 - \cos(\theta)) \mathcal{S}_A(\mathbf{q}, \omega) \quad (4)$$

We have matched two different calculations, valid at low values of q and moderate momentum transfers, respectively, and calculated the elastic neutrino mean free path l . In Fig.1 the Gamow-Teller part l_{GT} of l calculated within the suggested hybrid approach as a function of the neutrino energy E_ν is presented and compared with a calculation performed within the Fermi gas approximation (FG) at the saturation nuclear density $n = 0.16(fm)^{-3}$. Here Q_0 is the momentum transfer at which we match the LT and the CBF approaches. In Fig.2 the total neutrino mean free path l for neutron matter at $n = 0.16(fm)^{-3}$, including both dynamic FFs calculated within the suggested approach and the FG approximation, are presented. Let us note that the neutrino mean free path in neutron stars and symmetric nuclear matter have been analyzed recently in [12, 13] within the Brueckner-Hartree-Fock approximation at finite temperatures, and [10] for cold symmetric nuclear matter. Actually, there is no contradiction between these results and ours at moderate neutrino energies, $E_\nu >$

20.(MeV.). Let us also stress that at low neutrino energies, for example $E_\nu < 20.(MeV.)$, the LT makes the main contribution to the elastic neutrino mean free path.

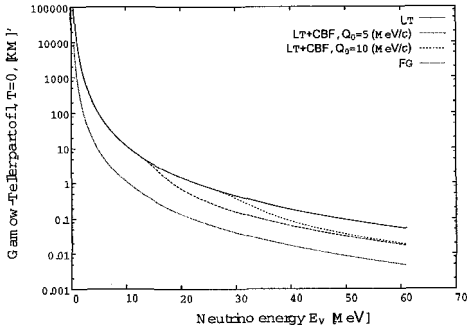


Fig. 1. The Gamow-Teller part of the elastic neutrino mean free path at $T = 0$ for the equilibrium density of neutron matter $n = 0.16(fm)^{-3}$ as a function of the initial neutrino energy E_ν at the different matching points Q_0 .

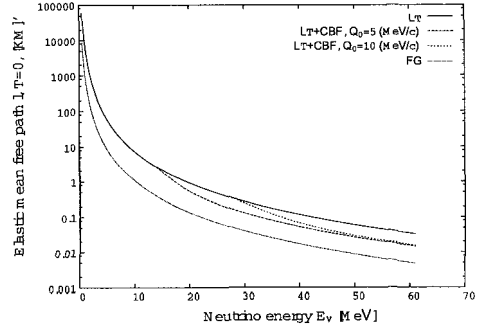


Fig. 2. Same as in Fig.1 for the elastic neutrino mean free path.

The analysis presented of the neutrino propagation in neutron matter at normal density and zero temperature has shown the following. The difference between the mean free paths calculated in the CBF and FG approximation is about 3 times that in [10]. On the other hand, the application of LT leads to a larger difference, about 5-6 times at $E_\nu < 4. - 5.(MeV)$. The Gamow-Teller part l_{GT} of the neutrino mean free path is due to the axial-vector FF or the spin-density response function χ_A . Its calculation within the suggested approach results in values much larger (about 10 times) than in the FG model at $E_\nu < 4. - 5.(MeV)$. One can therefore conclude that the contribution of the spin effects for a neutrino opacity at low E_ν is sizable.

Acknowledgements

The authors are very grateful to Prof. C.J.Pethick and Prof. I.Bombaci for useful discussions and comments.

References

1. Naoki Iwamoto and C.J.Pethick, Phys Rev. **D25** 313 (1982)
2. M.Prakash, I. Bombaci, M.Prakash, P.J.Ellis, J.M.Lattiner, R.Knorren, Phys.Rep.280 (1997) 1,
3. M.Prakash, Phys.Rep. 242 (1994) 297.
4. S.Reddy, M.Prakash J.M.Lattiner and J.A.Pons, Phys.Rev. **D59** 28888 (1999).
5. G.Raffelt, D.Seckel, Phys.Rev. **D52** 1780 (1995).
6. S.Fantoni, V.R.Pandharipande, Nucl.Phys. **A473** 234 (1987)
7. J.E.Amaro, F.Arias de Saaveda, A.M.Lallena, G.Co, A.Fabocini and S.Rashad, nucl-th/9910024
8. Philippe Nozie' res, David Pines, "The Theory of Quantum Liquids", Perseus Books, Cambridge, Massachusetts.

9. L.D.Landau, Zh.Eksp.Teor.Fiz.,v.32,N59(1957) [Sov.Phys.JETP, v.5,101(1957)].
10. S.Cowel and V.R.Pandharipande, Phys.Rev. **C70** 035801 (2004)
11. A.Botrugno and G.Co, nucl-th/0409041
12. Caiwan Shen, U.Lombardo, N.Van Giai and W.Zue, Phys.Rev. **C68**, 055802 (2003).
13. J.Marguren, I.Vidaia and I.Bombaci, Phys.Rev. **C68** 055806 (2003).

ASYMMETRY MEASUREMENT OF CHARGED HADRON PRODUCTION IN p↑A COLLISIONS AT 40 GeV

V. ABRAMOV, P. GONCHAROV, A. KALININ, A. KHMELNIKOV, A. KORABLEV, Y. KORNEEV,
A. KOSTRITSKI, A. KRINITSYN, V. KRYSHKIN, A. MARKOV, V. TALOV, L. TURCHANOVICH,
A. VOLKOV

Institute for High Energy Physics, Protvino, Russia

The single-spin asymmetry of charged hadron production by a 40 GeV proton beam with 39% transverse polarisation incident on nuclei (C, Cu) has been measured using the Focusing Double Arm Spectrometer (FODS). The measurements were carried out for hadrons with high x_T (82° in C.M.S.) and with high x_F (one arm at 51° and the other arm at 99° in C.M.S.). The results are presented for charged pions, kaons, protons and anti-protons with high x_T .

We have measured the single-spin asymmetry A_N of the inclusive charged pion, kaon, proton and anti-proton production cross sections at high x_T and high x_F for a 40 GeV/c proton beam incident on nuclei (C, Cu), where A_N is defined as

$$A_N = \frac{1}{P_B \cdot \cos\phi} \cdot \frac{N\uparrow - N\downarrow}{N\uparrow + N\downarrow}, \quad (1)$$

where P_B is the beam polarisation, ϕ is the azimuthal angle of the production plane, and $N\uparrow$ and $N\downarrow$ are event rates for the beam spin up and down respectively. The measurements were carried out at IHEP, Protvino. The polarised protons are produced by the parity - nonconserving Λ decays [1]. The up or down beam transverse polarisation is achieved by the selection of decay protons with angles near 90° in the Λ rest frame by a movable collimator. At the end of the beam line, two magnets correct the vertical beam position on the spectrometer target for the two beam polarisations. The intensity of the 40 GeV/c momentum polarised beam on the spectrometer target is 3×10^7 ppp, $\Delta p/p = \pm 4.5\%$, the transverse polarisation is $39_{-3}^{+1}\%$, and the polarisation direction is changed each 18 min, taking 30 s. The beam intensity and position are measured by ionization chambers and scintillation hodoscopes. Two Cherenkov counters identify the beam particle composition to check background contamination. At the spectrometer magnet entrance are two scintillation hodoscopes to measure the vertical coordinates of particles emitted from the target.

The measurements have been carried out with the FODS [1] spectrometer. It consists of an analyzing magnet, drift chambers, the Cherenkov radiation spectrometer (SCOCH)

for particle identification (π^\pm , K^\pm , p and \bar{p}), scintillation counters, and hadron calorimeters to trigger on high energy hadrons. To further suppress background there are two threshold Cherenkov counters using air at atmospheric pressure within the magnet. Inside the magnet there is also a beam dump made of tungsten and copper. There are two arms which can be rotated around the target centre situated in front of the magnet to change the secondary particle angle. The Cherenkov radiation spectrometer consists of a spherical mirror with diameter 110 cm, and 24 cylindrical lenses to focus the Cherenkov light onto the hodoscope photomultipliers. By measuring the particle velocity using SCOCH and its momentum in the magnetic field, one can determine the particle mass squared M^2 . The SCOCHs are filled with Freon 13 at 8 atm.

In 1994 a study of the single-spin asymmetry (A_N) in inclusive charge hadron production was started using FODS:

$$p \uparrow + p(A) \rightarrow h^\pm + X, \quad (2)$$

$$p \uparrow + p(A) \rightarrow h^\pm + h^\pm + X, \quad (3)$$

where h^\pm is a charged hadron (pion, kaon, proton or anti-proton). The experimental program consists of measuring the charge hadron single-spin asymmetry at high x_T and x_F in pp and pA collisions, to study the asymmetry dependence on the quark flavours u, d, s, and kinematical variables.

The pilot measurements of A_N for the charged hadrons carried out in 1994 on a hydrogen target for small x_F [1] are presented below for comparison with data obtained with nuclei.

The measurements of A_N in the range $-0.15 \leq x_F \leq 0.2$ and $0.5 \leq p_T \leq 4$ GeV/c are carried out with symmetrical arm positions at angles of ± 160 mrad. The results from the two arms are averaged, partially cancelling systematic uncertainties connected with the variation of the vertical beam position, the intensity monitor, and apparatus drift.

Figure 1a depicts the π^+ meson production asymmetry. Within the errors there is no difference in A_N with C and Cu targets. A_N for these targets in the range $1 \leq p_T \leq 2$ GeV/c is approximately 4% higher than for the hydrogen target. For the central region such a difference can be connected with the smaller proportion of u quarks in the nuclear target, which contains neutrons. Fragmentation of u quarks ($u \rightarrow \pi^+$) in the polarised beam protons, as well as u quarks in the target, contribute to the asymmetry. Because the target protons are not polarised, their contribution in the central region reduces the measured polarisation. For nuclear targets containing less u quarks in comparison with d quarks, the decrease of the asymmetry is not so substantial. Quark scattering in nuclei must also lead to a decrease of the asymmetry.

The asymmetry for π^- meson production is presented in Figure 1b. In the range $0.9 \leq p_T \leq 1.6$ GeV/c it is about 4% higher for the nuclear targets than for the hydrogen target. In the central region such differences can be connected with the larger proportion of d quarks in the nuclear targets. The major fragmentation contribution is d quarks ($d \rightarrow \pi^-$) from polarised beam protons and the target. For π^- mesons in pp collisions, the asymmetry is therefore negative. Due to the large contribution of the unpolarised target in the central

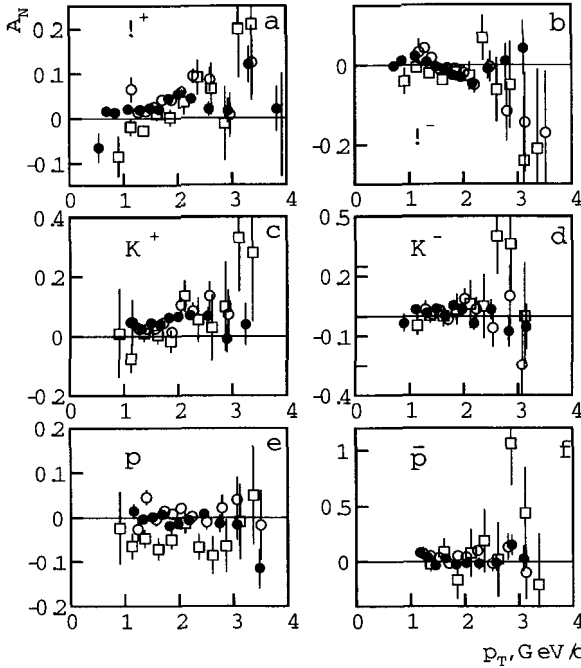


Fig. 1. A_N dependence on p_T for $p\uparrow+p(A)\rightarrow h^\pm+X$, where $h = \pi^+$ (a), π^- (b), K^+ (c), K^- (d), p (e), \bar{p} (f). Closed circles correspond to C target, open circles - Cu, square - proton.

regions, the asymmetry for nuclear targets is shifted into the positive region.

Figure 1c shows the asymmetry for K^+ production. There is no significant difference in A_N for the two nuclear targets (C and Cu) and A_N is about 3% higher than for the hydrogen target. The reason for this may be the same as for π^+ mesons.

Figure 1d presents A_N for K^- mesons. Within the errors there is no appreciable difference in A_N for all targets (p, C and Cu), and A_N is close to zero. This is expected because K^- does not contain valence quarks from the beam proton.

Figure 1e depicts the asymmetry for proton production, which is close to zero in nuclear targets. For the hydrogen target it is slightly negative.

The asymmetry for anti-proton production presented in Figure 1f shows no difference for all targets (p, C and Cu), and is close to zero. This result is expected because the produced anti-proton does not contain valence quarks from the beam proton. Sea quarks in most models are expected to be unpolarised. The upper limit for the asymmetry for anti-protons and K^- mesons is given by the sensitivity of the experiment (4%).

Two features of the results can be stressed:

- (1) There is no significant difference for the two nuclear targets (C, Cu);
- (2) For the positive charge mesons the asymmetry has a maximum at $p_T = 2.2$ GeV/c and decreases to zero at $p_T = 2.9$ GeV/c.

The analysis for high x_F is still under way.

References

1. V.V. Abramov, A.S. Dyshkant, V.N. Evdokomov et al., *Nucl. Phys.* **B492**, 3 (1997).

TENSOR ANALYZING POWER $A_{\gamma\gamma}$ IN DEUTERON INCLUSIVE BREAKUP AT LARGE P_T AND SPIN STRUCTURE OF THE DEUTERON AT SHORT INTERNUCLEONIC DISTANCES*

V. P. LADYGIN, L. S. AZHGIREY, S. V. AFANASIEV, V. V. ARKHIPOV, V. K. BONDAREV, Y. T. BORZOUNOV, L. B. GOLOVANOV, A. Y. ISUPOV, A. A. KARTAMYSHEV, V. A. KASHIRIN, A. N. KHRENOV, V. I. KOLESNIKOV, V. A. KUZNEZOV, A. G. LITVINENKO, S. G. REZNIKOV, P. A. RUKOYATKIN, A. Y. SEMENOV, I. A. SEMENOVA, G. D. STOLETOV, A. P. TZVINEV, V. N. ZHMYROV, L. S. ZOLIN

Joint Institute for Nuclear Researches, Dubna, Russia

G. FILIPOV

Institute of Nuclear Research and Nuclear Energy, Sofia, Bulgaria

N. P. YUDIN

Moscow State University, Moscow, Russia

$A_{\gamma\gamma}$ data for deuteron inclusive breakup of hydrogen and carbon at a deuteron momentum of 9.0 GeV/c and large p_T of emitted protons are presented. The large values of $A_{\gamma\gamma}$ independent of the target mass reflect the sensitivity of the data to the deuteron spin structure. The data obtained at fixed x and plotted versus P_t clearly demonstrate the dependence of the deuteron spin structure at short internucleonic distances on two variables. The data are compared with the calculations using Paris, CD-Bonn and Karmanov's deuteron wave functions.

1. Introduction

The interest in the (d, p) reaction at relativistic energies is mostly due to its sensitivity to non-nucleonic degrees of freedom and relativistic effects in the simplest bound system.

Large amounts of polarisation data in deuteron breakup obtained at zero degrees in the last few years can be interpreted from the point of view NN^* configurations in the deuteron, where relativistic effects are taken into account by the minimal relativization

*This work is supported by the RFFR under grant No. 03-02-16224.

scheme with the dependence of the deuteron structure on a single variable k . In addition, multiple scattering must be considered to obtain agreement with the data [1].

On the other hand, it has been shown that T_{20} data for the pion-free deuteron breakup process $dp \rightarrow ppn$ in the kinematical region close to that of backward elastic dp scattering depended on the incident deuteron momentum in addition to k [2]. Recent measurements of the tensor analyzing power A_{yy} of deuteron inclusive breakup on nuclear targets [3]– [5] have demonstrated a significant dependence on the transverse secondary proton momentum p_T at a fixed value of the longitudinal proton momentum. This suggests that the description of this quantity requires an additional independent variable besides k .

In this report the angular dependence of A_{yy} in deuteron inclusive breakup on hydrogen and carbon at 9 GeV/c is presented. The results are compared with relativistic calculations using Paris, CD-Bonn and Karmanov's deuteron wave functions (DWFs).

2. Experiment

The experiment has been performed using a tensor polarised deuteron beam from the Dubna Synchrophasotron and the SPHERE setup described elsewhere [3, 4]. The tensor polarisation of the beam has been measured from the asymmetry of protons from deuteron breakup on nuclear targets, $d + A \rightarrow p + X$, at zero angle and momentum $p_p \sim 2/3p_d$ [6]. The vector polarisation of the beam has been measured from the asymmetry of quasi-elastic pp scattering on a CH_2 target [7]. The tensor and vector polarisations, p_{zz} and p_z , were $p_{zz}^+ = 0.798 \pm 0.002(stat) \pm 0.040(sys)$, $p_{zz}^- = -0.803 \pm 0.002(stat) \pm 0.040(sys)$, $p_z^+ = 0.275 \pm 0.016(stat) \pm 0.014(sys)$ and $p_z^- = 0.287 \pm 0.016(stat) \pm 0.014(sys)$, respectively.

A slowly extracted deuteron beam with a typical intensity of $\sim 5 \cdot 10^8 \div 10^9$ d/spill was directed onto a liquid hydrogen target of 30 cm length or onto carbon targets with different lengths. The data at 9 GeV/c of the deuteron initial momentum were obtained at secondary proton emission angles of 85, 130 and 160 mr, and proton momenta between 4.5 and 7.0 GeV/c, on hydrogen and carbon. The separation of the protons and inelastically scattered deuterons was done by measuring their time-of-flight (TOF) over a base line of ~ 34 m. The residual background was completely eliminated by the requirement that particles are detected in at least two prompt TOF windows.

3. Results and discussion

The results on A_{yy} versus the momentum of the secondary protons are represented in Fig. 1 by the solid and open symbols for carbon and hydrogen targets, respectively. The circles are the data of this experiment, while the triangles represent the data obtained earlier [3]. The dashed, dash-dotted and solid lines are the relativistic calculations using Paris [8], CD-Bonn [9] and Karmanov [10] DWFs.

The data obtained on hydrogen and carbon are in good agreement. Hence multiple scattering processes play a minor role, and the information obtained reflects the internal deuteron structure.

The calculations performed in the framework of light-front dynamics [11] with the use of Paris and CD-Bonn DWFs fail to reproduce the A_{yy} data, while a prediction using Karmanov DWF depending on two internal variables, k and p_T , is in reasonable agreement with the data obtained at 85 mr.

A_{yy} data obtained at fixed proton momenta of 6.0, 6.5 and 7.0 GeV/c are plotted versus transverse proton momenta p_T . The symbols and curves are the same as in Fig.1. Again the use of DWF depending on two variables [10] gives better agreement with the data. To summarize, the observed features of the A_{yy} data suggest that the deuteron structure

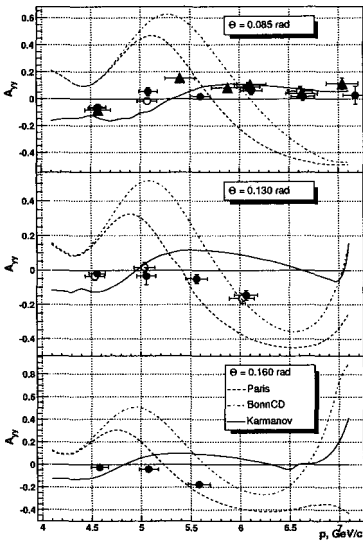


Fig. 1. The A_{yy} data plotted versus secondary proton momentum. The curves are the relativistic calculations with different DWFs.

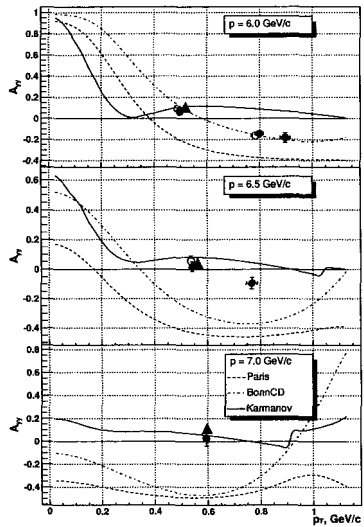


Fig. 2. The A_{yy} data obtained at fixed proton momenta in the lab., and plotted versus transverse proton momentum p_T .

function at short distances, where relativistic effects are significant, depends on more than one variable.

References

1. A.P.Kobushkin et al., *Phys.Lett.* **B421**, 53 (1998).
2. L.S. Azhgirey et al., *Phys. Lett.* **B391**, 22 (1997); *Yad. Fiz.* **61**, 494 (1998).
3. S.V. Afanasiev et al., *Phys. Lett.* **B434**, 21 (1998).
4. V.P. Ladygin et al., *Few-Body Systems* **32**, 127 (2002); L.S. Azhgirey et al., *Yad. Fiz.* **66**, 719 (2003).
5. L.S. Azhgirey et al., *Phys.Lett.* **B595**, 151 (2004).
6. L.S. Zolin et al., *JINR Rapid Comm.* **2[88]-98**, 27 (1998).
7. L.S. Azhgirey et al., *Nucl.Inst.and Meth. in Phys.Res.* **A497**, 340 (2003).

8. M. Lacombe et al., *Phys.Lett.* **B101**, 139 (1981).
9. R. Machleidt, *Phys. Rev.* **C63**, 024001 (2001).
10. V.A. Karmanov and A.V. Smirnov, *Nucl. Phys.* **A575**, 520 (1994); J. Carbonell et al., *Phys. Rep.* **300**, 215 (1998).
11. L.S. Azhgirey and N.P. Yudin, *nucl-th/0311052*; *Yad. Fiz.*, in press.

STUDY OF CORRESPONDING HOMOLOGOUS STATES IN ^{41}K AND ^{42}Ca VIA (p, α) REACTIONS

P. GUAZZONI, L. ZETTA

Dipartimento di Fisica dell'Università and I.N.F.N., via Celoria 16, I-20133 Milano, Italy

F. DELLA VEDOVA, S. M. LENZI, A. VITTURI

Dipartimento di Fisica dell'Università and I.N.F.N., via Marzolo 8, I-35131 Padova, Italy

G. GRAW, R. HERTENBERGER, H. WIRTH

Sektion Physik der Universität München, am Coulombwall 2, D-85748 Garching, Germany

M. JASKÓLA

Soltan Institute for Nuclear Studies, Hoza Street 69, Warsaw, Poland

To investigate the spectator role of the $1f_{7/2}$ unpaired proton outside the $Z=20$ closed shell, the reactions $^{44}\text{Ca}(p, \alpha)^{41}\text{K}$ and $^{45}\text{Sc}(p, \alpha)^{42}\text{Ca}$ have been measured in high resolution experiments at 24.6 MeV incident proton energy.

1. Introduction

During the last few years, with the advent of very powerful experimental devices and techniques together with new developments on the theoretical side, a renewed interest has been aroused in the study of the spectroscopy of medium-light nuclei. In particular, special attention has been devoted to $1f_{7/2}$ -shell nuclei where a wide variety of interesting phenomena has been emerged, such as rotational behaviour, proton-neutron pairing, and band termination [1–3].

It has been shown that the structure of these nuclei depends strongly on the competition of the different fp orbitals for the natural parity states, and on the contribution of other major shells to the unnatural parity states.

Experimentally these studies have been done mainly in fusion-evaporation reactions induced by heavy ions, but the information has to be complemented by the results of transfer reactions, which are essential to better specify the nature of the different states. Of particular interest is the occurrence of corresponding homologous states in neighbouring systems, which imply the persistence of preferred structures that survive after the addition of one particle, that, in these cases, behaves as a spectator, as we have already tested in the $Z=40$, $Z=50$, and $Z=82$ regions [4–6].

In order to investigate the spectator role of the $1f_{7/2}$ unpaired proton outside the $Z=20$ closed shell in the ^{45}Sc nucleus, and to test the validity of the homologous concept also in this region, the $^{44}\text{Ca}(p, \alpha)^{41}\text{K}$ and $^{45}\text{Sc}(p, \alpha)^{42}\text{Ca}$ reactions have been studied.

2. The experiment and the results

The angular distributions of cross sections $\sigma(\theta)$ and analyzing powers $A_y(\theta)$ of the triton-pickup reactions $^{44}\text{Ca}(p, \alpha)^{41}\text{K}$ and $^{45}\text{Sc}(p, \alpha)^{42}\text{Ca}$ have been measured from 10° to 60° , in high resolution experiments, with the 24.6 MeV proton beam of the Munich MP Tandem Accelerator, using the Stern-Gerlach source for intense, bright beams of negatively polarized hydrogen ions [7]. The reaction products were analyzed with the Q3D magnetic spectrograph and detected in the new light ion focal plane detector [8]. The beam current was up to $1.5 \mu\text{A}$ and the beam polarization 60%.

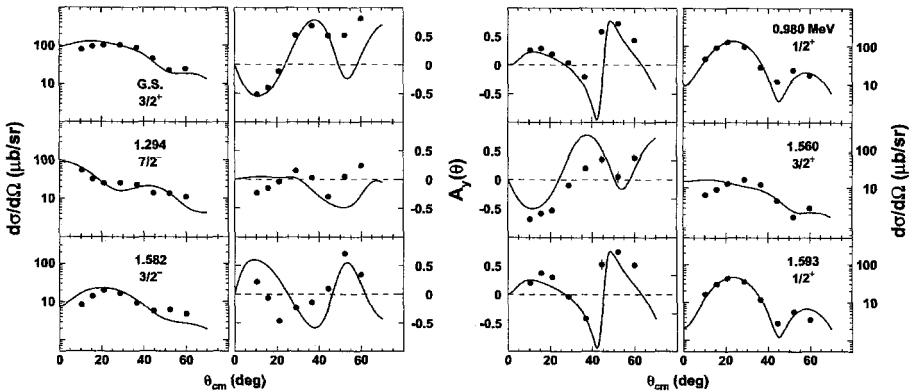


Fig. 1. Comparison between experimental and theoretical $\sigma(\theta)$ and $A_y(\theta)$ for some low-lying ^{41}K levels.

A DWBA analysis of $\sigma(\theta)$ and $A_y(\theta)$ was performed assuming a semimicroscopic triton cluster pickup mechanism. The calculations have been done in finite-range approximation with the code TWOFNR [9] using a Gaussian proton-triton interaction potential. Fig. 1 shows the comparison between experimental and calculated $\sigma(\theta)$ and $A_y(\theta)$ for some ^{41}K levels.

The spin and parity assignment to the homologous levels populated in the daughter reaction $^{45}\text{Sc}(p, \alpha)^{42}\text{Ca}$ is carried out following our methodology based on the homology

concept [4]. In this way the multiplet of states of ^{42}Ca homologous to the $\frac{3}{2}^+$ ground state of ^{41}K has been identified. The weak coupling model predicts in ^{42}Ca a quartet of states homologous to the parent state $^{41}\text{K}\frac{3}{2}^+$ G.S., with $J^\pi = 2^-, 3^-, 4^-, 5^-$. We have identified the following levels: 3.954 MeV, $J^\pi = 4^-$, 4.100 MeV, $J^\pi = 5^-$, and 4.117 MeV, $J^\pi = 3^-$, while the 2^- level is missing.

In Fig.2 the comparison between the measured $\sigma(\theta)$ and $A_y(\theta)$ for the transitions to the multiplet of ^{42}Ca states (dots) homologous to the G.S. $\frac{3}{2}^+$ of ^{41}K is presented. The last measured cross section is scaled for each level by the proper factor $\frac{(2J_i+1)}{\sum_i(2J_i+1)}$ (solid line).

Exploratory shell model calculations, involving one-hole excitation from the $d_{3/2}$ shell to the full fp shell, have been performed and reproduce some features of our experimental results. Calculations have been carried out with the code ANTOINE [10] and the interaction *spdf.sm* [11] for both ^{41}K and ^{42}Ca . In the case of ^{41}K the dominant configuration of the $\frac{3}{2}^+$ G.S. is $\pi(d_{3/2}^{-1})\nu(f_{7/2}^2)$. For ^{42}Ca we have calculated the low-spin negative parity states $J^\pi = 2^-, 3^-, 4^-, 5^-$.

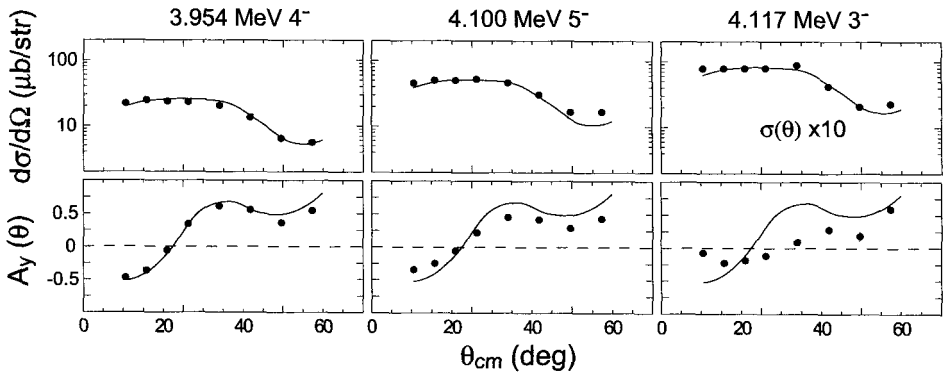


Fig. 2. Comparison between the measured $\sigma(\theta)$ and $A_y(\theta)$ for the transitions to the ^{42}Ca states (dots) homologous to the G.S. $\frac{3}{2}^+$ of ^{41}K (solid line) (see text).

The relative excitation energies of the $3^-, 4^-, 5^-$ states are in good agreement with the experimental data. The dominant configuration of these states is $\pi(f_{7/2}^1, d_{3/2}^{-1})\nu(f_{7/2}^2)$, as would be expected in the hypothesis of homologous states. The 2^- state, however, has a very different structure, as shown in Table 1. This is in agreement with the fact that this state is not populated in the $^{45}\text{Sc}(p, \alpha)^{42}\text{Ca}$ reaction.

References

1. E. Caurier et al., *Phys. Rev. Lett.* **75** 2466 (1995).
2. S. M. Lenzi et al., *Phys. Rev.* **C56** 1313 (1997).
3. F. Brandolini et al., *Phys. Rev.* **C66** 024304 (2002).
4. P. Guazzoni et al., *Z. Phys.* **A356** 381 (1997).
5. P. Guazzoni et al., *AIP Conference Proc.* **675** 664 (2003).
6. J. N. Gu et al., *Phys. Rev.* **C55** 2395 (1997)

Table 1. Main components of the wave functions of the different states

		neutron					proton					total %		
p1	f5	p3	f7	d3	s1	d5	p1	f5	p3	f7	d3		s1	d5
⁴¹K G.S. 3/2⁺ Parent State														
0	0	0	2	4	2	6	0	0	0	0	3	2	6	87.8
0	0	1	1	4	2	6	0	0	0	0	3	2	6	1.4
0	0	2	0	4	2	6	0	0	0	0	3	2	6	3.2
0	2	0	0	4	2	6	0	0	0	0	3	2	6	2.9
⁴²Ca 3⁻ Total Homologous 77.6 %														
0	0	0	2	4	2	6	0	0	0	1	3	2	6	64.7
0	0	1	1	4	2	6	0	0	0	1	3	2	6	8.5
0	0	2	0	4	2	6	0	0	0	1	3	2	6	2.5
0	2	0	0	4	2	6	0	0	0	1	3	2	6	1.9
⁴²Ca 4₁⁻ Total Homologous 82.4 %														
0	0	0	2	4	2	6	0	0	0	1	3	2	6	74.1
0	0	1	1	4	2	6	0	0	0	1	3	2	6	3.8
0	0	2	0	4	2	6	0	0	0	1	3	2	6	2.3
0	2	0	0	4	2	6	0	0	0	1	3	2	6	2.2
⁴²Ca 5₁⁻ Total Homologous 78.4 %														
0	0	0	2	4	2	6	0	0	0	1	3	2	6	68.9
0	0	1	1	4	2	6	0	0	0	1	3	2	6	4.6
0	0	2	0	4	2	6	0	0	0	1	3	2	6	2.6
0	2	0	0	4	2	6	0	0	0	1	3	2	6	2.3
⁴²Ca 2₁⁻ Not Homologous														
0	0	0	2	4	2	6	0	0	0	1	3	2	6	29.4
0	0	1	1	4	2	6	0	0	0	1	3	2	6	18.6
0	0	2	0	4	2	6	0	0	0	1	3	2	6	1.9
0	2	0	0	4	2	6	0	0	0	1	3	2	6	—

7. R. Hertenberger et al., *AIP Conference Proc.* **570** 825 (2001).
8. H.-F. Wirth *Ph. D. Thesis*, Technische Universität, München, 2001).
9. M. Igarashi *Computer code TWOFNR* unpublished, (1977).
10. E. Caurier *Computer code ANTOINE*, Strasbourg (1989-2002).
11. S. Nummela et al., *Phys.Rev.* **C63** 044316 (2001).

HIGH-ACCURACY MEASUREMENT OF THE SPIN-DEPENDENT NEUTRON SCATTERING LENGTH OF THE DEUTERON

B. van den BRANDT, P. HAUTLE, J. KOHLBRECHER, J. A. KONTER, A. MICHELS

Paul Scherrer Institute, Villigen, Switzerland

H. GLÄTTLI

Commissariat à l'Energie Atomique CE Saclay/SPEC, Gif-sur-Yvette Cedex, France

H. W. GRIESSHAMMER, F. M. PIEGSA, O. ZIMMER

Physics Department, Technische Universität München, Garching, Germany

The experiment aims at a significant improvement of accuracy of the doublet nd scattering length a_2 , which at present is only poorly known. The expected result will provide a key input to theoretical descriptions of few-nucleon systems, both in potential models and new effective field theory approaches. The value of a_2 is obtained from a linear combination of the spin-dependent nd scattering length, $a_{i,d}$, and the spin-independent one, $a_{c,d}$. Whereas the latter is rather well known, the former is limiting the total accuracy. We plan to measure $a_{i,d}$ with 10^{-3} accuracy at PSI using the technique of nuclear pseudomagnetic precession of polarised neutrons in a polarised target. The set up and test of the Ramsey apparatus, which will be employed to detect the pseudomagnetic precession, is described here.

1. Introduction

A better knowledge of nuclear three-body (3N) forces is essential for the theoretical description of few-nucleon systems at low energy. In many cases phenomenological nucleon-nucleon (NN) potentials fail to reproduce experimental values even with "ad hoc" admixtures of 3N-forces. [1] Recently the application of effective field theories to nuclear physics has made great progress. [2] Taking only nucleons, or nucleons and pions as explicit degrees of freedom, they provide a systematic approach, permitting an estimate of theoretical uncertainties. Accurate predictions of cross sections and their energy dependence become possible with the knowledge of only a few so-called low-energy constants that can be fixed experimentally. Provided these values are known with sufficient accuracy, observables in processes involving three nucleons at very low energy can be computed on the 1 % level of

accuracy. [3] Particularly suited to fix three-body forces is the doublet nd scattering length a_2 , which is currently known with only 6 % accuracy. It can be obtained from a linear combination of the spin-independent, coherent scattering-length, $a_{c,d}$, and the spin-dependent, incoherent one, $a_{i,d}$, which is only poorly known. Potential models use a_2 as additional input, or check their predictions against data to ensure that 3N-forces are accurately accounted for.

2. Layout of the Experiment

The incoherent neutron scattering length $a_{i,d}$ can be determined directly using the phenomenon of pseudomagnetic precession: [4, 5] owing to the spin-dependent refractive index, the spin of neutrons passing through a polarised target precesses around the axis of nuclear polarisation, the precession angle being proportional to the incoherent scattering length a_i of the nuclear species present in the sample. [6] The angle can be measured very accurately using Ramsey's well-known atomic beam technique, [7] adapted to neutrons. [8] Figure 1 shows the scheme of the Ramsey apparatus. From the white polarised

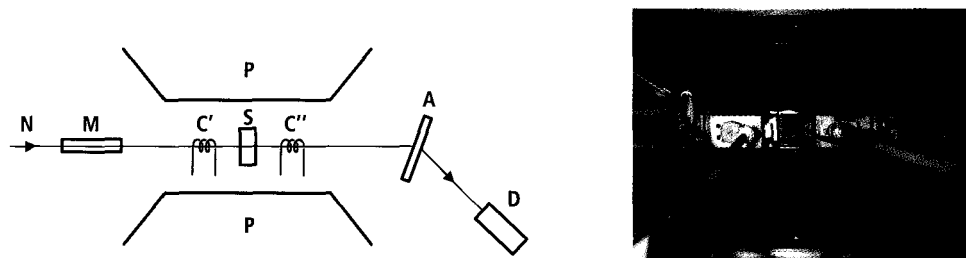


Fig. 1. Left: Scheme of the Ramsey apparatus: N, white polarised neutron beam; M, monochromating supermirror; C', C'', $\pi/2$ -flipper rf coils; S, sample; A, supermirror polarisation analyser; D, ^3He neutron counter; P, magnet pole pieces. Right: View from top between the magnets pole pieces, the coil simulating the sample can be seen positioned between the two $\pi/2$ -flippers.

cold neutron beam (N) FUNSPIN at PSI, a monochromating supermirror (M) selects neutrons with a wavelength of $\lambda = 4.6 \text{ \AA}$ with a bandwidth of $\Delta\lambda/\lambda \approx 16\%$ (FWHM). Two high-frequency coils (C' and C'') located between the pole pieces of an electromagnet, are operated at about 72.4 MHz, corresponding to the neutron resonance frequency at 2.5 T. These coils flip the spin of the neutrons by $\pi/2$. Subsequently, a polarisation analysis is performed with a supermirror polariser (A). The so-called Ramsey resonance pattern is then obtained by measuring the neutron count rate in the detector (D) as a function of the frequency of the phase stabilised flippers C' and C''. In a later stage of the experiment, a polarised deuteron target will be positioned between the two $\pi/2$ -flippers. In order to simulate its pseudomagnetic effect by a real magnetic field, an auxiliary coil was mounted at the sample position (S) with a field direction parallel to the main field. Figure 2 shows two Ramsey patterns measured with different currents through the auxiliary coil. From similar signal shifts the pseudomagnetic precession angle will be extracted in measurements with the polarised target. More details are given elsewhere. [6, 9, 10]

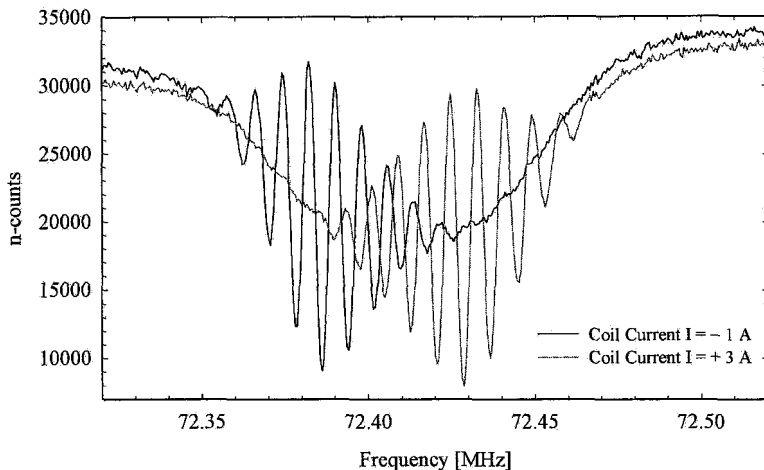


Fig. 2. The Ramsey pattern shifts when the current through the auxiliary coil is changed. A similar shift is expected from the pseudomagnetic effect of the polarised target.

3. Performance of the Ramsey Apparatus

To attain the proposed accuracy of 10^{-3} in the measurement of the incoherent scattering length $a_{i,d}$, a determination of the neutron precession angle to better than 1 degree is indispensable. This imposes stringent requirements on the stability of different parts of the apparatus. The 2.5 T electromagnet is stabilised with the help of NMR probes to ± 6 mG, corresponding to $\Delta B/B = \pm 2 \times 10^{-7}$. The RF amplitude and phase of the $\pi/2$ -flippers are controlled via a PC. From each flipper an amplitude and a phase signal are extracted. The phase signals are fed to a phase detector which provides a DC signal proportional to the phase difference. By means of a general purpose DAQ-card, a LabView program reads the DC signals and sets the corresponding control voltages for the attenuators and an analog phase shifter. A phase stability of $\pm 0.05^\circ$ and an amplitude stability of $\pm 0.25\%$ is reached with this control loop.

Considering the more than 6000 Larmor precessions a neutron performs on its 8 cm long flight path between the spin flippers, the need to control long-term drifts of the whole apparatus becomes obvious. We therefore implemented a two-beam method: the incoming neutron beam has been split into two partial beams which are analysed separately. In this way, phase drifts occurring simultaneously in both beams can be controlled very effectively. Even with phase changes of more than 10° , as observed for each of the individual beams during a day/night cycle, it was found that the phase jitter between the two beams is limited to $\pm 0.5^\circ$. In the final set up one partial beam will serve as reference beam and is foreseen to pass below the polarised sample.

4. Concluding Remarks

We have set up and commissioned a Ramsey resonance apparatus for cold neutrons for the measurement of the spin-dependent nd scattering length. With a newly developed spin

flipper stabilisation and the implementation of a two beam method, we achieve the required precision in the determination of the neutron precession angle. In the next phase of the experiment we will integrate a dedicated polarised target, the construction of which is almost completed, and perform the actual measurement.

References

1. H. Witala, A. Nogga, H. Kamada, W. Glöckle, J. Golak, R. Skibinski, *Phys. Rev.* **C68**, 034002 (2003).
2. P.F. Bedaque, U. van Kolck, *Ann. Rev. Nucl. Part. Science* **52**, 339 (2002).
3. H.W. Griebhammer, *Nucl. Phys.* **A744**, 192 (2004).
4. V. Baryshevsky, M. Podgoretsky, *Sov. Phys. JETP* **20**, 704 (1965).
5. A. Abragam, G.L. Bacchella, H. Glättli, P. Meriel, M. Pinot, J. Piesvaux, *Phys. Rev. Lett.* **31**, 776 (1973).
6. B. van den Brandt, H. Glättli, H.W. Griebhammer, P. Hautle, J. Kohlbrecher, J.A. Konter, O. Zimmer, *Nucl. Instr. Meth.* **A526**, 91 (2004).
7. N. Ramsey, *Molecular Beams* (Oxford Univ. Press, Oxford, 1956).
8. A. Abragam, M. Goldman, *Nuclear magnetism: order and disorder* (Clarendon Press, Oxford, 1982).
9. P. Hautle, *Nucl. Instr. Meth.* **A526**, 76 (2004).
10. F.M. Piegsa, Diploma Thesis, Technische Universität München (2004) (in German).

SESSION 7

Acceleration, Storage and Polarimetry of Polarized Beams

This page intentionally left blank

RHIC POLARIZED PROTON NEW WORKING POINT COMMISSIONING*

M. BAI, R. TOMÁS, L. AHRENS, K. BROWN, A. DREES, C. J. GARDNER, J. W. GLENN, W. FISCHER,
U. I. ARIZ, H. HUANG, Y. LUO, F. PILAT, W. W. MACKAY, G. MARR, C. MONTAG, V. PITISYN,
T. ROSER, T. SATOGATA, S. TEPIKIAN, N. TSOUPAS, J. Van ZEIJTS

Brookhaven National Laboratory, Upton, U.S.A.

The RHIC 2003 polarized proton run showed a limitation on the luminosity due to the beam-beam effect at a betatron tune working point of (0.225, 0.235). The integer parts of the horizontal and vertical betatron tunes are 28 and 29, respectively. The polarization transmission efficiency was also compromised because of the tight tune space due to the snake resonances. It was decided to explore the RHIC pp luminosity capability as well as the polarization capability with new working points during the RHIC pp 2004 Run. The working point (0.690, 0.685) at a RHIC stored energy of 100GeV/c was found to ameliorate the beam-beam effect, and also improve the polarization transmission efficiency as well as polarization lifetime during store. This paper reports the commissioning efforts and results of the new working point commissioning during the latest RHIC polarized proton run.

1. Introduction

The Brookhaven Relativistic Heavy Ion Collider (RHIC) is designed to provide collisions of polarized proton beams with longitudinal polarization for two high-luminosity detectors: PHENIX and STAR. It can also provide collisions with transversely polarized proton beam for the other two detectors: BRAHMS and PHOBOS. The nominal beta functions at the collision points of the STAR and PHENIX experiments are 1 m, and 3 m at the other two experiments. During its first polarized proton run for physics data taking at an energy of $\sqrt{s} = 200\text{GeV}$ in 2003, a strong beam-beam effect was observed. The large difference in beam lifetime for bunches colliding at 2, 3 and 4 experiments, respectively, demonstrated that the beam-beam effect was the main contribution to the deterioration of beam lifetime during a store [1].

In a collider, the beam-beam effect comes from the Coulomb interaction between the two colliding beams [2, 3]. For the same charge species, the beam-beam force behaves as a defocusing force near the center of the beam, and then becomes highly non-linear at about one rms beam size. It causes not only the shift of the betatron tune of the beam as a whole but also increases the tune spread. For a proton-proton collider, the coherent betatron tune shifts downward while the tunes for the high amplitude particles are not affected much. The

*This work is supported by us department of energy.

effect of beam-beam on the beam lifetime as well as luminosity lifetime is very sensitive to the working point.

A set of working point candidates were simulated and a subset of them were also studied carefully during the RHIC Au 2004 run at injection prior to the proton run [4]. Table. 1 lists the results of the working point studies. Here, $\nu_{x,y}$ are the tunes of the horizontal and vertical

Table 1. RHIC working point candidates

working point	ν_x	ν_y	available tune space with beam-beam	distance to a major snake resonance
RHIC design	0.19	0.18	0.008	0.01
RHIC operation	0.225	0.235	0.005	0.015
SPS operation	0.69	0.685	N/A	0.01
RHIC pp FY04	0.738	0.735	0.007	0.015

betatron oscillations. During the RHIC 2004 run, the working points in the two rings were located on either side of the $\nu_x = \nu_y$ resonance to avoid beam-beam driven resonances. The working point at the SPS operation tune could not be studied with the Au beam at injection due to the strong 3rd order resonance driven by the sextupole field component from persistent currents in the RHIC bending dipoles.

Another requirement on the RHIC working point is that it has to be in a region free of spin depolarizing resonances. The spin dynamics in a planar machine like RHIC is governed by the Thomas-BMT equation [5]. In a perfect accelerator, the spin vector precesses around the vertical direction $G\gamma$ times during one orbital revolution. Here, G is the anomalous gyromagnetic ratio. In a real machine, because of the errors and misalignments of magnets as well as the intrinsic betatron oscillations, the acceleration of polarized beam often encounters two types of spin depolarizing resonances [5]: imperfection at $G\gamma = nP$, and intrinsic spin resonances at $G\gamma = nP \pm Q_y$. Here, n is an integer and P is the accelerator super-periodicity. In RHIC, two Siberian helical snakes were installed in each ring to preserve the beam polarization [6]. However, it was discovered by simulation [5] and recently confirmed in RHIC [7] that a new type of spin depolarizing resonance can also cause beam polarization loss when the following condition is met.

$$\nu_s = m\nu_y + k. \quad (1)$$

Here ν_s is the spin precession tune, and m and k are integers.

2. Commissioning results

During the RHIC 2004 run, the RHIC working point at injection was set to (0.72,0.73) in the window of snake resonances at 0.7 and 0.75. The ramp was developed to accelerate the polarized proton beam with this working point. Two working points (0.738, 0.735) and (0.69, 0.685) were carefully studied at store. A tune swing from (0.73,0.72) to (0.69,0.685)

was successfully implemented at stored energy before the final beta squeeze [4]. Both working points yielded similar tolerance to the beam-beam effect. The luminosity lifetime with working point (0.745, 0.735) was also evaluated under the beam-beam limit with bunch intensity of 1.7×10^{11} protons. However, it was discovered that the beam polarization lifetime at this working point was significantly shorter than the polarization lifetime with (0.69,0.685) working point during a 5 hour store. The possible reason could be that the tunes of particles at high amplitudes are higher than the tune of the beam as a whole and hence closer to the snake resonance at 0.75. Careful studies will be required to confirm this. Fig. 1 shows the results of the beam lifetime as a function of beam betatron tune. The lower plot shows the proton loss rate as a function of the tunes.

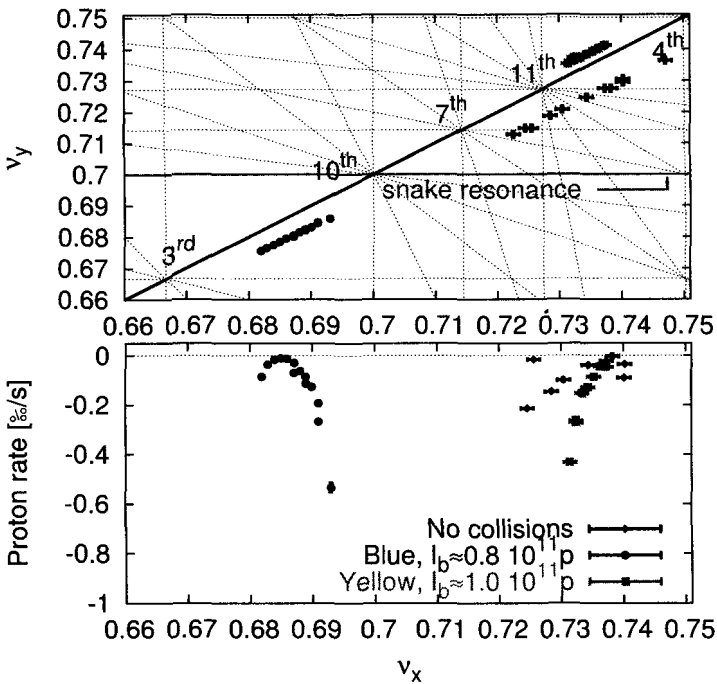


Fig. 1. Scan of beam lifetime as a function of working point at store with beam in collision.

3. Conclusion

Two new working points were investigated during the RHIC 2004 polarized proton run. Both showed an improved luminosity lifetime. However, due to the strong snake resonance at 0.75, the working point at (0.69,0.685) yields better polarization transmission efficiency and polarization lifetime at store.

Acknowledgement

The authors would like to thank the Operation Group of the C-A Department. The authors would also like to thank P. Cameron, K. Vetter, R. Michnoff and many others for their support during the polarized proton run.

References

1. W. Fischer, et al; *Summery of Beam-beam Observation during Stores in RHIC Proceedings of Halo'03 and Beam-beam'03 Workshop AIP Conference Proceedings*, 693 (2003).
2. H. Wiedemann; *Particle Accelerator Springer* (2003)
3. Eberhard Keil; *Beam-Beam Dynamics CERN SL/94-78* (1994)
4. R. Tomas, et al; *Quest of New Working Point Proceedings of EPAC04* (2004)
5. S. Y. Lee; *Spin Dynamics and Snakes in Synchrotrons World Scientific* (1997).
6. *RHIC Spin Design Manual* (1998).
7. V. Ptitsyn, et al; *Snake Resonances Observed in RHIC these proceedings*.

SNAKE RESONANCE OBSERVED IN RHIC*

V. PTITSYN, M. BAI, H. HUANG, W. W. MACKAY, T. ROSER, S. TEPIKIAN

Brookhaven National Laboratory, Upton, U.S.A

A pair of Siberian snakes is employed in each RHIC ring to avoid depolarization by imperfection and intrinsic spin resonances during the proton beam acceleration. Still, depolarization can happen in the vicinity of some betatron tune values due to high-order spin resonances called "snake" resonances. In this paper experimental evidence is presented from the latest RHIC run for the $\{Q_y\} = 3/4$ snake resonance. The depolarization produced by the resonance was observed in two circumstances: during a vertical betatron tune scan, and during a snake current scan.

1. Introduction

Polarized proton beams with $\sim 45\%$ polarization at 100 GeV energy have been achieved in RHIC [1]. To preserve the beam polarization during acceleration from the injection energy of 24 GeV to 100 GeV, a pair of Siberian snakes is used in each RHIC ring. The snakes hold the spin tune $\nu_s = 1/2$ independently of beam energy, effectively eliminating first-order intrinsic and imperfection spin resonances: $\nu_s = Q_\beta + k$ and $\nu_s = k$ respectively, where Q_β represents betatron tune and k is an integer. Nevertheless beam depolarization has been observed in previous RHIC runs at higher-order spin resonances: $\nu_s = mQ_\beta + k$ where k and m are integers. Taking into an account that with errors in RHIC $\nu_s = 1/2 + \delta\nu_s$, where $\delta\nu_s$ is a spin-tune error due to orbit or snake imperfections, the resonance condition can be rewritten as:

$$Q_\beta = \frac{2k+1}{2m} + \frac{\delta\nu_s}{m} \quad (1)$$

These resonances were investigated first by S.Y. Lee and S. Tepikian [2] and were named snake resonances, reflecting the fact that they can produce beam depolarization even in an accelerator with snakes. It was also demonstrated that in an accelerator with two snakes, the snake resonances corresponding to even m originate from the interference of intrinsic and imperfection resonances, hence depending on vertical closed orbit and snake imperfections. Also, imperfections cause a spin tune shift $\delta\nu_s$ which, according to equation (1), leads to resonance splitting and shifts the resonance location.

*Work performed under the auspices of the United States Department of Energy and RIKEN of Japan.

Previous RHIC runs used betatron tunes with fractional parts in the $[0.2, 0.25]$ interval. The snake resonances were observed [3] at fractional tune values $\{Q_{x,y}\} = 3/14$ and $\{Q_y\} = 3/4$ and required good betatron coupling correction as well as careful betatron tune and orbit control during acceleration to reduce beam depolarization.

2. Betatron tune scan

RHIC Run 2004 used a new working point [4] with fractional betatron tune parts in $[0.68, 0.75]$. In this interval snake resonances which may cause problems are expected at $\{Q_\beta\} = 3/4$ and $7/10$.

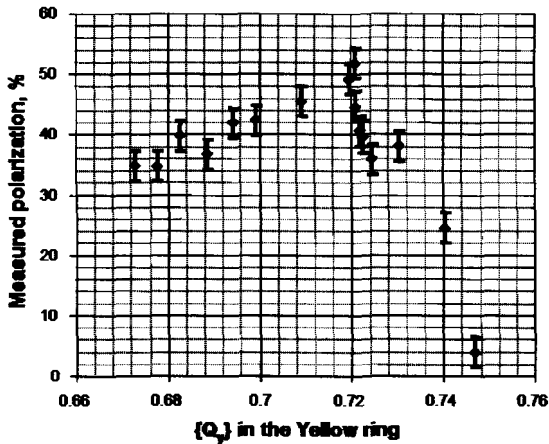


Fig. 1. Yellow ring polarization measurements during Q_y scan at the injection. The inner magnet snake current was at 326A.

No clear evidence of depolarization coming from $7/10$ resonance was observed at injection or at store energies. On the other other hand, the second-order snake resonance $\{Q_\beta\} = 3/4$ was clearly seen, and was probably a main depolarizing factor. Figure 1 shows a clear example of this resonance during a vertical tune scan in the Yellow ring at injection energy. The snake magnets were not tuned optimally at the time of the scan, so the resonance location was at 0.747 instead of 0.75.

The polarization preservation on the ramp was noticeably improved when the betatron tunes were put further away (between 0.68 and 0.695) from the $3/4$ snake resonance before the β^* -squeeze. The β^* -squeeze leads to considerably larger β functions in interaction region triplets. It increases betatron tune spread due to nonlinear fields and higher-order chromaticities, causing a larger probability for a portion of the beam to get into a resonance area.

3. Snake current scan

The condition $\{Q_y\} = 3/4$ presents not only the spin resonance but also a resonance in beam transverse motion generated by octupole nonlinear fields in the machine. When the betatron tune is moved close to $3/4$ the beam lifetime is considerably spoiled. In order to avoid beam losses during spin resonance studies, another technique was applied. In that case the fractional part of the vertical betatron tune was held at 0.74, while the spin tune was detuned from $1/2$. The spin resonance location was then shifted towards the resonance condition in accordance with the Equation (1). The spin tune shift was created by varying the current in inner magnets of both Siberian snakes. The inner magnet current changes lead to a change $\delta\phi$ of the relative angle between snake rotation axes of the snakes, which shifts the spin tune according to $\delta\nu_s \approx -\delta\phi/\pi$.

With the spin tune shifted away from $1/2$ by $\delta\nu_s$, the position of the snake resonance is shifted by $\delta\nu_s/2$. Figure 2 shows the polarization measurements done during the inner-snake magnet scans. The shift of spin resonance position also is plotted. The beam was completely depolarized in the vicinity of $\delta\nu_s/2 = \pm 0.01$. The total resonance width exceeds 0.01 although a considerable part of it comes from the betatron tune spread in the beam. The snake current scan helped to identify the optimal snake current settings which gives $\nu_s = 1/2$ and minimizes the depolarization.

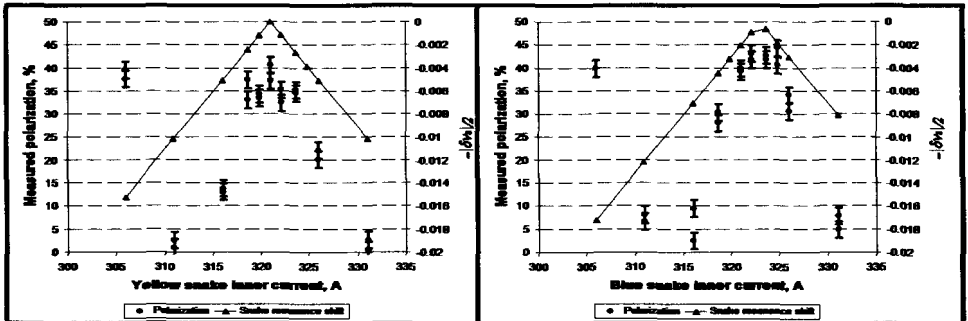


Fig. 2. The polarization versus snake inner magnet current scan in Yellow (top) and Blue (bottom) rings (circles). The shift of the snake resonance from $3/4$ is also shown (triangles).

Since the $\{Q_y\} = 3/4$ resonance is an even-order snake resonance the optimal snake settings also reduce the width of the resonance itself. An important factor in decreasing the $\{Q_y\} = 3/4$ resonance width is a better vertical orbit, which assumes both compensation of vertical misalignments and improved quality of the orbit correction.

4. Conclusions

The snake resonance $\{Q_y\} = 3/4$ was observed by means of betatron tune and snake current scans during the last RHIC run. Minimizing imperfections of snake and vertical orbit reduces the resonance width. Another remedy would be to put betatron tunes further away from the resonance.

References

1. W.W. MacKay et al., *these proceedings*.
2. S. Y. Lee and S. Tepikian, *Phys. Rev. Let.* **56**, 1637 (1986).
3. V. Ranjbar et al., *Phys. Rev. Let.* **91**, 034801 (2003).
4. M. Bai et al., *these proceedings*.

ACCELERATION OF POLARIZED PROTONS IN THE AGS WITH A HELICAL PARTIAL SNAKE*

H. HUANG, L. AHRENS, M. BAI, K. BROWN, C. GARDNER, W. GLENN, A. U. LUCCIO, W. W. MACKAY, C. MONTAG, V. PTITSYN, T. ROSER, S. TEPIKIAN, N. TSOUPAS, A. ZELENSKI, K. ZENO

Brookhaven National Laboratory, Upton, U.S.A.

M. OKAMURA, J. TAKANO

Radiation Laboratory, Saitama, Japan

The RHIC spin program requires 2×10^{11} proton/bunch with 70% polarization. As the injector to RHIC, AGS is the bottleneck for preserving polarization: there is no space for a full snake to overcome numerous depolarizing resonances. An AC dipole and a partial snake are used to preserve beam polarization. A helical dipole partial snake was commissioned successfully during recent operation. With less coupling from the new partial snake, 50% polarization has been achieved at AGS extraction. The results pave the way for using multiple partial snakes in the AGS to preserve polarization up to 24 GeV.

1. Introduction

Acceleration of polarized proton beams in a synchrotron is complicated by the numerous depolarizing spin resonances. It is particularly difficult in the medium energy range since there are limited straight sections in existing synchrotrons, and the typical large orbit excursions make it very hard to construct a full Siberian snake [1] to correct all depolarizing spin resonances.

There are mainly two kinds of resonances: imperfection resonances due to magnet field errors and misalignments, and intrinsic resonances due to betatron motion in quadrupoles. The imperfection resonance happens when $G\gamma = \text{integer}$, where $G = (g - 2)/2 = 1.7928$ is the anomalous factor of the magnetic moment and γ is the Lorentz factor. The intrinsic resonance happens when $G\gamma = mP \pm \nu$, where m is an integer, P is the super-periodicity of the synchrotron and ν is the betatron tune. In the AGS, $P = 12$, and the nominal betatron tune is around 8.7. In general, the intrinsic resonance is only associated with the vertical betatron tune ν_y . However, when coupling between the two transverse planes is present, the

*This work was supported by the US DOE and RIKEN of Japan.

resonance could also occur at the location of the horizontal betatron tune: $G\gamma = mP \pm \nu_x$. The so-called coupling resonance strength is proportional to the coupling and to the strength of the original resonance [2].

The Brookhaven AGS has been accelerating polarized protons since the 1980s. In the early days, the polarization was preserved by non-adiabatic techniques. A betatron tune-jump was used for intrinsic resonances, and harmonic orbit corrections were used for imperfection resonances [3]. Effectively, these two methods make the resonance strength small or crossing speed fast, to minimize the effect of the resonances. However, there are disadvantages associated with these two methods. A fast tune jump requires a large tune space, and more importantly, it causes emittance growth. The harmonic orbit correction method is tedious and very time consuming.

Over the years, adiabatic techniques have prevailed. In the AGS, a 5% partial solenoidal Siberian Snake has been used successfully to overcome imperfection resonances [4]. A coherent spin resonance excited by an AC dipole was used to overcome the four strong intrinsic spin resonances in the AGS [5]: $G\gamma = 0 + \nu_y, 12 + \nu_y, 36 \pm \nu_y$. The three weak ones at $G\gamma = 24 \pm \nu_y, 48 - \nu_y$ were left uncorrected. The AC dipole generated a full spin flip without significant emittance growth. Effectively, a partial snake and an AC dipole increase the strength of the resonances to a level such that full spin flip can be achieved. In general, the imperfection resonance strength is proportional to beam energy. At low energies, the snake strength can be less than 5% and still preserve polarization through imperfection resonances in the AGS. Actually, the solenoidal snake was run with a mixed percentage function in the past: 3% at injection and ramped up to 5% before $G\gamma = 12 + \nu_y$. This was a compromise between higher percentage required at higher energies and larger coupling associated with stronger snake.

2. Helical Partial Snake Commissioning

A partial Siberian snake can be constructed by a solenoid or dipoles. A solenoid magnet causes significant coupling between the two transverse planes, while the dipole snake causes a significant orbit excursion, especially at low energies. It is not practical to use a dipole partial snake in the AGS energy range. A helical snake design [6] can reduce the orbit excursion, but orbit matching around the helical snake is still a problem. It is the double pitch design that solved the problem and made it possible to use a helical dipole snake with much less coupling in the AGS. A helical partial snake with this novel design was recently designed and built by RIKEN of Japan. It was installed and used in AGS and resulted in higher polarization at AGS extraction.

The accelerator complex of RHIC is shown in Fig.1 of Ref. [7]. The polarized H^- beam from the optically pumped polarized ion source was accelerated through a radio frequency quadrupole and the 200 MeV linac. The beam polarization measured by the 200 MeV polarimeter was 80%. The beam was then strip-injected and accelerated in the AGS Booster up to 1.5 GeV kinetic energy or $G\gamma = 4.5$. Only one bunch of the twelve rf buckets in the AGS was filled, and the beam intensity varied between $0.7 - 1.2 \times 10^{11}$ protons per fill. In the AGS, the polarized proton beam was accelerated up to $G\gamma = 46.5$ or 24.3 GeV, passing

through 42 imperfection resonances and seven intrinsic resonances.

The helical snake magnet was run in the ring at 2700A with constant field. The snake strength has a weak energy dependence at low energies. It is an 8% and 6% partial snake at injection and extraction, respectively. Due to the smaller coupling, there are fewer parameters to worry about (one can ignore the horizontal emittance and horizontal tune). The lattice distortion from the snake insertion was manageable. Consequently, the AGS setup was easier with the new helical snake, as soon as the correct orbit bumps near the snake were applied.

Polarization was measured at flattop $G\gamma = 46.5$ and also along the ramp for diagnostic ramps. However, the analyzing power is only known at certain beam energies; this limited our ability to pinpoint all polarization losses along the ramp. Fig. 1 shows the asymmetries measured during the energy ramp. The lower asymmetry along the energy ramp was a combination of lower analyzing power, beam polarization profile, and possible polarization loss. Preliminary analysis shows that the polarization at AGS extraction was 50% with intensity of 10^{11} per bunch this year—a factor of 1.3 gain from last year. The gain factor consists of gains of 1.08 from source polarization; 1.1 from $0 + \nu$ and 1.1 from $36 + \nu$. The last two were due to the reduced effect of coupling. The remaining polarization loss has several sources: the limited aperture at $0 + \nu$ prevents the AC dipole exercising its full power; the limited power of the AC dipole at $36 + \nu$; the three uncorrected weak intrinsic resonances located at $24 \pm \nu$, and $48 - \nu$, since they are too weak to be overcome by an AC dipole.

3. Conclusion

50% polarization at AGS extraction has been achieved with the AC dipole and a helical partial snake. The new helical partial snake greatly reduced the coupling between the horizontal and vertical planes. As a result, the polarization at AGS increased from 40% (with a solenoid partial snake) to 50% this year. The uncertainty of A_N limits our ability to pinpoint the polarization loss. A polarized jet [8] run in RHIC with lower energies (10GeV) will be very valuable to get A_N as a function of beam energy. The success of the new helical snake commissioning also paves the way for the future plan to use two snakes [9] to overcome all

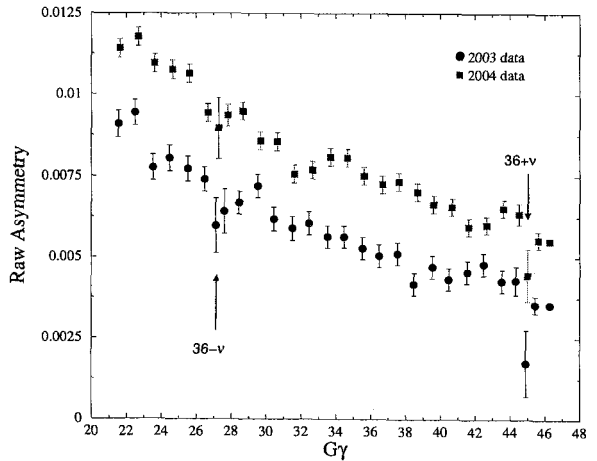


Fig. 1. Absolute values of raw asymmetries measured during AGS energy ramp. The dips of asymmetry with large error bars near $36 \pm \nu$ were measurements during spin flip induced by AC dipole pulses.

imperfection and intrinsic resonances.

References

1. Ya.S. Derbenev and A.M. Kondratenko, *Part. Accel.* **8**, 115 (1978).
2. H. Huang, T. Roser, A. Luccio, *Proc. of 1997 IEEE PAC, Vancouver, May, 1997*, p.2538.
3. F.Z. Khiari, et al., *Phys. Rev. D***39**, 45 (1989).
4. H. Huang, *et al.*, *Phys. Rev. Lett.* **73**, 2982 (1994).
5. M. Bai, *et al.*, *Phys. Rev. Lett.* **80**, 4673 (1998).
6. V.I. Piitsyn and Yu.M. Shatunov, *NIM A***398**, (1997)126.
7. W.W. MacKay, et al., these proceedings.
8. T. Wise, et al., these proceedings.
9. T. Roser, et al., these proceedings.

ACCELERATION OF POLARIZED BEAMS USING MULTIPLE STRONG PARTIAL SIBERIAN SNAKES *

T. ROSER, L. A. AHRENS, M. BAI, E. D. COURANT, J. W. GLENN, R. C. GUPTA, H. HUANG,
A. U. LUCCIO, W. W. MACKAY, N. TSOUPAS, E. WILLEN

Brookhaven National Laboratory, Upton, U.S.A.

M. OKAMURA, J. TAKANO

Radiation Laboratory, RIKEN, Saitama, Japan

Acceleration of polarized protons in the energy range of 5 to 25 GeV is particularly difficult since depolarizing spin resonances are strong enough to cause significant depolarization, but full Siberian snakes cause intolerably large orbit excursions. Using a 20 - 30 % partial Siberian snake, both imperfection and intrinsic resonances can be overcome. Such a strong partial Siberian snake was designed for the Brookhaven AGS using a dual pitch helical super-conducting dipole. Multiple strong partial snakes are also discussed for spin matching at beam injection and extraction.

1. Introduction

Accelerating polarized beams requires the control of both orbital motion and spin motion. The evolution of the spin direction of a beam of polarized protons in external magnetic fields, such as those existing in a circular accelerator, is governed by the Thomas-BMT equation [1],

$$\frac{d\vec{P}}{dt} = - \left(\frac{e}{\gamma m} \right) \left[G\gamma \vec{B}_\perp + (1 + G)\vec{B}_\parallel \right] \times \vec{P}$$

where the polarization vector \vec{P} is expressed in the frame that rotates with the particle's velocity. Comparison with the Lorentz force equation shows that, in a purely vertical field, the spin rotates $G\gamma$ times faster than the orbital motion. Here $G=1.7928$ is the anomalous magnetic moment of the proton and $\gamma = E/m$. $G\gamma$ gives the number of full spin precessions for every revolution and is also called the spin tune ν_{sp} .

During acceleration, a depolarizing spin resonance is crossed whenever the spin precession frequency equals the frequency with which spin-perturbing magnetic fields are

*This work was performed under the auspices of the US DOE and RIKEN of Japan.

encountered. The resonance conditions for imperfection depolarizing resonances, driven by magnet errors and misalignments, arise when $\nu_{sp} = G\gamma = n$, where n is an integer. Imperfection resonances are separated by only 523 MeV energy steps. The conditions for intrinsic resonances, driven by the focusing fields, are $\nu_{sp} = kP \pm \nu_y$, where k is an integer, ν_y is the vertical betatron tune, and P is the super-periodicity of the machine lattice.

All imperfection resonances can be overcome by introducing a local spin rotator ("partial Siberian snake") [2] that effectively increases the strength of all imperfection resonances to the point that they all introduce complete spin flip. The resonance strength ϵ_{ps} caused by a spin rotator that rotates the polarization by δ around a horizontal direction is $\delta/2\pi$. Note that with a partial Siberian snake the closest approach of the spin tune to an integer value is ϵ_{ps} . This is a special case of the formula for the spin tune of a ring with a partial Siberian snake:

$$\nu_{sp} = \frac{1}{\pi} \cos^{-1} \left[\cos \left(\frac{\delta}{2} \right) \cos(\pi G\gamma) \right]$$

2. Strong partial siberian snake

With a strong enough partial snake, it is possible to increase the gap between the spin tune and an integer enough that it becomes possible to place the fractional part of the betatron tune, and therefore the intrinsic resonance, inside this gap, as has been demonstrated at the Brookhaven AGS [3]. Tracking calculations revealed that for strong intrinsic resonances this betatron tune window is reduced by higher order depolarizing resonances that are similar to snake resonances. The strongest higher order resonance is located in the middle of the gap, but sufficient room is still available for placing the betatron tune.

If it is possible to build such a strong partial Siberian snake a single device would eliminate depolarization from all spin resonances and allow for polarized proton acceleration in medium energy accelerators. For the AGS the challenge amounts to building a 36° spin rotator with a maximum length of 2.6 m and internal orbit excursion of less than about 4 cm. The most compact solution consists of a 3 Tesla helical dipole, whose helical pitch at the ends is twice that at the centre. This field profile allows for compact matching of the outside orbit to the helical orbit inside the magnet.

3. Multiple partial siberian snakes

With a partial Siberian snake, the stable spin direction reverses direction at all imperfection resonances, but is very close to the vertical direction at half-integer values of $G\gamma$ as long as the partial snake is relatively weak. It is therefore possible to inject and extract vertically polarized beam at these energies without much loss of polarization. The AGS injection and extraction are set to occur at $G\gamma = 4.5$ and 46.5, respectively.

For a strong partial snake however, polarization losses at injection and extraction are no longer negligible. A 20% snake will lead to a 10% polarization loss due to this spin direction mismatch. This could be solved with appropriate spin rotators in the injection and extraction beam lines. However, a single additional partial snake located in the AGS

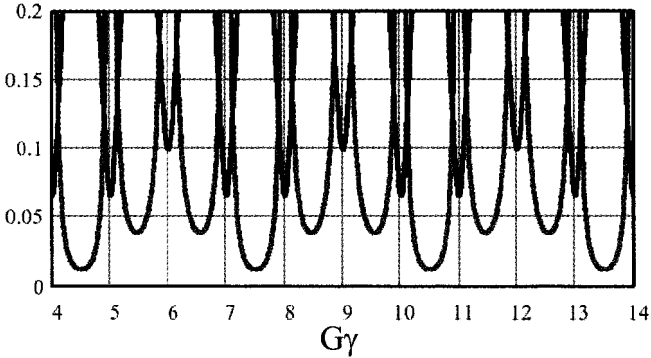


Fig. 1. Deviation from an integer for the spin tune (blue, dark) and vertical component of the stable spin direction (red, light) for 5% and 15% partial Siberian snakes separated by 120° orbital deflection angle as a function of $G\gamma$.

can provide the spin direction matching at injection and extraction, and also increase the effective partial snake strength if its position is chosen properly.

The location and the precession axis direction of multiple partial Siberian snakes has to be chosen very carefully to maintain control of the spin tune in a similar way as is necessary for multiple full Siberian snakes. For practical partial Siberian snakes, the precession axis direction is always very close to longitudinal, which leaves only the location and strength of the partial snakes as free parameters.

The spin tune for two partial Siberian snakes with rotation angle δ_1 and δ_2 and separated by $1/m$ of the ring is given by:

$$v_{sp} = \frac{1}{\pi} \cos^{-1} \left[\cos \left(\frac{\delta_1}{2} \right) \cos \left(\frac{\delta_2}{2} \right) \cos(\pi G\gamma) - \sin \left(\frac{\delta_1}{2} \right) \sin \left(\frac{\delta_2}{2} \right) \cos \left(\frac{\pi(m-2)}{m} G\gamma \right) \right]$$

The maximum effective strength of $\delta_1 + \delta_2$ occurs at mn where n is an integer. The minimum effective strength of $|\delta_1 - \delta_2|$ and also the maximum vertical component of the stable spin direction occurs at $G\gamma = mn + m/2$. For the maximum strength to occur at the strong intrinsic resonances, m has to be a common factor of both the vertical betatron tune and the machine super-periodicity. In addition, in order to avoid having the minimum strength at an imperfection resonance, m needs to be an odd integer.

At the AGS the vertical betatron tune is about 9 and the the super-periodicity is 12. All the above conditions can therefore be fulfilled for $m = 3$. With both snakes at equal strength δ , $v_{sp} = \delta/\pi$, effectively doubling the strength of the partial snakes. At the injection and extraction energies, for which $G\gamma = 3n + 1.5$, the two snakes cancel. The polarization direction is therefore exactly vertical and no polarization is lost due to spin direction mismatch.

Even using the currently installed normal-conducting helical partial Siberian snake [4], with a rotation angle of 9°, a very substantial reduction of the injection and extraction spin mismatch can be achieved. At the same time the effective strength of the partial snakes

at the intrinsic resonances is significantly increased. Figure 1 shows the spin tune and the vertical component of the spin direction in the AGS, with two partial snakes with rotation angles of 9° (5% partial snake) and 27° (15% partial snake), respectively. Both the injection and extraction regions have to be located between the two partial Siberian snakes. In this case the polarization loss due to injection and extraction mismatch is only 2.4%.

References

1. L.H. Thomas, *Phil. Mag.* **3**, 1 (1927); V. Bargmann, L. Michel, V.L. Telegdi, *Phys. Rev. Lett.* **2**, 435 (1959)
2. H. Huang et al., *Phys. Rev. Lett.* **73**, 2982 (1994)
3. H. Huang et al., *Phys. Rev. ST Accel. Beams* **7**, 071001 (2004)
4. J. Takano et al., "Field Measurements in the AGS Warm Snake", proceedings of the 2004 European Particle Accelerator Conference

SPIN MANIPULATING 2 GeV/c POLARIZED PROTONS AND DEUTERONS STORED IN COSY*

A. D. KRISCH¹, M. A. LEONOVA¹, V. S. MOROZOV¹, R. S. RAYMOND¹, D. W. SIVERS¹, V. K. WONG¹,
K. YONEHARA², R. GEBEL³, A. LEHRACH³, B. LORENTZ³, R. MAIER³, A. SCHNASE³,
H. STOCKHORST³, D. EVERSHEIM⁴, F. HINTERBERGER⁴, H. ROHDJESS⁴, K. ULBRICH⁴,
W. SCOBEL⁵

¹Spin Physics Center, Univ. of Michigan, Ann Arbor, USA

²Dept. of Physics, Illinois Inst. of Technology, Chicago, USA

³Forschungszentrum Jülich, Inst. für Kernphysik, Jülich, Germany

⁴Helmholtz-Inst. für Kernphysik, Univ. Bonn, Bonn, Germany

⁵Inst. für Experimentalphysik, Univ. Hamburg, Hamburg, Germany

We recently studied the spin manipulation of a vector and tensor polarized deuteron beam stored at 1.85 GeV/c in COSY. We manipulated the deuteron's polarization by sweeping the frequency of a ferrite RF dipole through an RF-induced spin resonance. We first experimentally determined the resonance's frequency and then varied the RF dipole's Δf and Δt to maximize the spin-flip efficiency. We obtained a measured vector spin-flip efficiency of about $97 \pm 1\%$. We also studied the detailed behavior of the tensor polarization during spin manipulation.

We later studied higher-order spin resonances using 2.1 GeV/c stored vertically polarized protons. By changing the vertical betatron tune within the range 3.51 to 3.71, with the horizontal tune fixed at 3.575, we found full spin flip when the 1st-order spin resonance was crossed; we also found partial depolarization near several 3rd-order resonances and possibly near one 2nd-order resonance.

We also spin-flipped 2.1 GeV/c vertically polarized protons stored in COSY, by sweeping the frequency of a strong ferrite RF dipole through an RF-induced spin resonance. After finding the resonance's frequency, we varied the RF dipole's strength, frequency ramp time Δt and frequency range Δf to maximize the spin-flip efficiency. We then used the multiple spin flip technique to measure a spin-flip efficiency of $99.92 \pm 0.04\%$.

1. Spin Flipping 1.85 GeV/c Polarized Deuterons

Recently, polarized deuteron experiments have become an accessible and interesting area of subatomic physics. Studying the polarization dynamics of polarized deuteron beams is an important step towards polarized deuteron, and thus polarized neutron, scattering experiments. The deuteron beam's vector and tensor polarizations can be manipulated by sweeping an RF magnet's frequency through an RF-induced spin resonance [1]. We recently used an RF dipole to study the spin manipulation of a vector and tensor polarized deuteron beam stored at 1.85 GeV/c in the COSY Cooler Synchrotron.

*Supported by research grants from the German BMBF Science Ministry.

Describing the polarization of spin-1 particles requires three vector polarization components and five independent second-rank tensor components [2]. A vertically polarized beam's vector and tensor polarizations are [2]:

$$P_v \equiv (N_+ - N_-)/N; \quad P_T \equiv 1 - 3(N_0/N) \quad (1)$$

where N_+ , N_0 , and N_- are the number of particles in $m = +1$, 0, and -1 states and $N = N_+ + N_0 + N_-$ is the total number of particles.

In any flat circular accelerator or storage ring, with no horizontal magnetic fields, each deuteron's spin precesses around the vertical fields of the ring's bending magnets. The spin tune ν_s (the number of spin precessions during one turn around the ring) is proportional to the deuteron's energy $\nu_s = G\gamma$, where $G \equiv (g - 2)/2 = -0.142987$ is the deuteron's gyromagnetic anomaly and γ is its Lorentz energy factor.

The deuteron's polarization can be perturbed by the horizontal RF magnetic field from either an RF solenoid or an RF dipole. At a resonant frequency the perturbations can add coherently to induce an RF spin resonance. The RF-induced spin resonance's frequency is

$$f_r = f_c(k \pm \nu_s), \quad (2)$$

where f_c is the deuteron's circulation frequency and k is an integer.

The beam's vector P_v and tensor P_T polarizations, after ramping an RF dipole's frequency through a spin resonance, can be related to the beam's initial vector P_v^i and tensor P_T^i polarizations and the ramp's frequency range Δf and ramp time Δt as [1]

$$\frac{P_v}{P_v^i} \equiv -\eta_v = (1 + \eta_v^i) \exp \left[\frac{-(\pi \epsilon_v f_c)^2}{\Delta f / \Delta t} \right] - \eta_v^i, \quad (3)$$

$$\frac{P_T}{P_T^i} = \frac{3}{2} \left\{ (1 + \eta_T^i) \exp \left[\frac{-(\pi \epsilon_T f_c)^2}{\Delta f / \Delta t} \right] - \eta_T^i \right\}^2 - \frac{1}{2}, \quad (4)$$

where η_v is the vector spin-flip efficiency, $\Delta f / \Delta t$ is the resonance crossing speed, η_v^i and η_T^i are the maximum achievable vector and tensor spin-flip efficiencies while ϵ_v and ϵ_T are the vector and tensor resonance strengths.

The apparatus used for this experiment, including the COSY storage ring, the EDDA detector, the low energy polarimeter, the injector cyclotron, the polarized ion source, and the RF dipole, were discussed in a few earlier publications [3–5]. To reduce our systematic errors, we cycled the polarized source through the five vertical polarization states:

$$|P_v P_T\rangle = |00\rangle, |-\frac{2}{3}0\rangle, |-\frac{1}{3}-1\rangle, |-11\rangle, \text{ and } |11\rangle.$$

We obtained the polarization in COSY with the EDDA detector as follows. First, the vector and tensor analyzing powers were measured for p-d elastic scattering at 1850 MeV/c. Then we measured the scalar asymmetries for all scattering into the four quadrants of the EDDA detector. We related these measured asymmetries to the deuteron vector and tensor polarizations using the detector's measured efficiencies and effective analyzing powers.

We first calculated the spin resonance frequency f_r using Eq. (2) and then experimentally determined it by running the RF dipole at different fixed frequencies near this f_r . The frequency range $\Delta f = 200$ Hz seemed sufficient to cover the resonance. We next flipped the deuteron beam by linearly ramping the RF dipole's frequency from $f_r - 0.1$ to $f_r + 0.1$ kHz,

with various ramp times Δt , and measured the polarizations after each frequency ramp as shown in Fig. 1.

After optimizing Δt and Δf for the maximum spin-flip efficiency at our maximum $\int B_{rms} dl$, we more precisely determined the spin-flip efficiencies by simultaneously measuring, after n frequency sweeps, the vector and tensor polarizations P_V^n and P_T^n . We fit these data using [1]

$$P_V^n/P_V^i = (-\eta_v)^n; \quad P_T^n/P_T^i = \left[\frac{3}{2}(-\eta_r)^2 - \frac{1}{2} \right]^n, \quad (5)$$

to obtain vector and tensor spin-flip efficiencies of $\eta_v = 96.4 \pm 0.9\%$ and $\eta_r = 98.3 \pm 0.9\%$, respectively. Combining them gives a measured spin-flip efficiency of about $97 \pm 1\%$.

2. Higher-Order Spin Depolarizing Resonances

Accelerating and storing polarized proton beams in a ring is difficult because of many first-order and higher-order spin resonances. An intrinsic spin resonance occurs whenever the spin precession frequency is correlated with the betatron oscillation frequencies. We studied higher-order spin

resonances using 2.1 GeV/c vertically polarized protons stored in COSY. Each proton's spin precesses around the vertical fields of the ring's dipole magnets. The number of precessions during one turn around the ring is called the spin tune ν_s . A spin resonance can

Fig. 1. (LEFT) The measured vector and tensor deuteron polarizations at 1850 MeV/c are plotted against the RF dipole ramp time Δt . The RF dipole's frequency half-range $\Delta f/2$ was 100 Hz, and its $\int B_{rms} dl$ was 0.54 T·m. The curves in the top part are fits using Eq. (3). The curves in the bottom part are fits using Eq. (4).

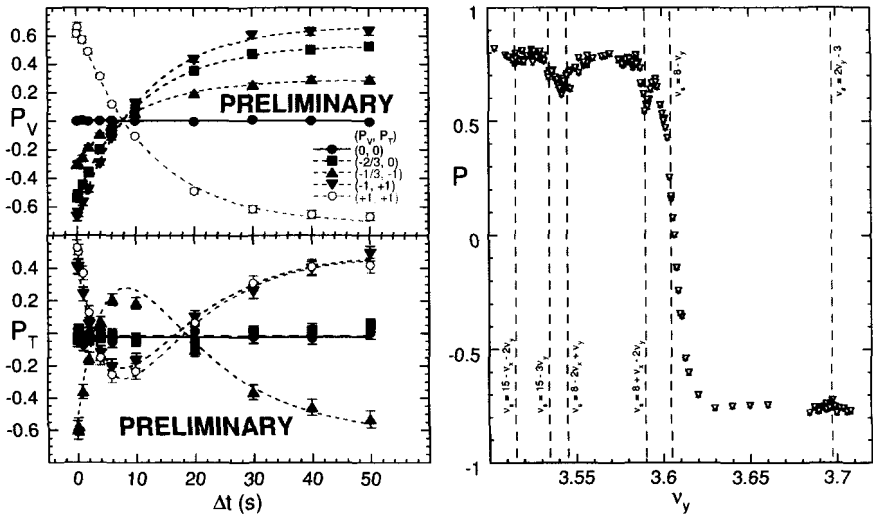


Fig. 2. (RIGHT) The measured vertical polarization of 2.1 GeV/c protons is plotted against the vertical betatron tune's final value after the quadrupole current ramps. The initial ν_y value was 3.525. ν_x was fixed at 3.575.

occur when

$$v_s = kv_x + lv_y + m, \quad (6)$$

where k , l and m are integers; v_x and v_y are the horizontal and vertical betatron tunes, respectively. The imperfection depolarizing resonances occur when $k = l = 0$. The intrinsic depolarizing resonances occur when either $k \neq 0$ or $l \neq 0$, or both; the sum $|k| + |l|$ defines each resonance's order.

During injection and acceleration from 294 to 2100 MeV/c v_x and v_y were kept fixed at 3.575 and 3.525, respectively. After acceleration, we rapidly changed v_y from 3.525 to some value between 3.51 – 3.71, with v_x fixed at 3.575. Next we slowly varied v_y through a very small tune range of 0.002 and then measured the polarization; this slow tune sweep enhanced the effect of any spin resonance in each small v_y range. The measured polarizations are plotted against the final v_y value in Fig. 2. We found full spin-flip when the 1st-order spin resonance was crossed; we also found partial depolarization near several 3rd-order resonances and possibly near a 2nd-order resonance. The 3rd-order $v_s = 8 + v_x - 2v_y$ resonance seems much stronger than the 2nd-order $v_s = 2v_y - 3$ resonance. These results suggest that many significant 3rd and possibly higher-order spin resonances must be overcome to accelerate and store polarized protons above 100 GeV.

3. Spin Flipping 2.1 GeV/c Polarized Protons

Many polarized scattering experiments require frequent spin-direction reversals (spin-flips), while the polarized beam is stored, to reduce their systematic errors. Spin resonances induced by either an RF solenoid or RF dipole can produce these spin-flips in a well-controlled way. At very high energy, the spin-flip efficiency with an RF-dipole should become almost independent of energy, mostly due to the Lorentz invariance of a magnet's transverse $\int Bdl$ [5]; this invariance is quite important for very high energy polarized proton rings. To confirm this we recently used an RF dipole to study the spin flipping of 2.1 GeV/c polarized protons stored in the COSY ring.

The proton polarization behaves in the same way as a deuteron's vector polarization. Thus, all discussion in Section 1 of using an RF-induced spin resonance to spin-flip a deuteron's vector polarization also applies to spin-flipping protons including Eq. (2), Eq. (3), and the vector part of Eq. (5). We also used the same equipment with the protons and deuterons [3–5].

We started by experimentally finding the spin resonance's frequency whose approximate value was calculated using Eq. (2). Then, with $\Delta f/2$ set at 6 kHz, we measured the polarization after 11 spin-flips P_{11} , while varying the RF-dipole's frequency ramp time Δt . We obtained the single-spin-flip efficiency η from the equation [5] $\eta = \sqrt[11]{-P_{11}/P_i}$, where P_i is the initial polarization. We then plotted this measured η against Δt in Fig. 3. Using Fig. 3, we set Δt at 0.1 s, where the spin-flip efficiency was high, while Δt was small enough to allow many spin flips fairly quickly.

After setting Δt and Δf to maximize the spin-flip efficiency η , we then determined it much more precisely by measuring the vertical polarization while varying the number of

spin-flips, up to 51, with Δt , Δf , and $\int B dl$ all fixed at their optimum values. These polarization data points are plotted against the number of spin-flips in Fig. 4. We fit these data to the vector part of Eq. (5) to obtain a measured spin-flip efficiency of $\eta = 99.92 \pm 0.04\%$ [5]. This result confirms that, due to the Lorentz invariance of an RF-dipole's magnetic field integral, an only slightly stronger RF-dipole should allow efficient spin flipping in very high-energy proton rings, such as the 100-250 GeV RHIC at Brookhaven or perhaps even someday at the 7 TeV LHC at CERN.

Acknowledgments

We thank the entire COSY staff for the successful operation of COSY, and A.W. Chao, E.D. Courant, Ya.S. Derbenev, G. Fidecaro, W. Haeblerli, H. Huang, T. Roser, H. Sato, and others for their help and advice. This research was supported by grants from the German BMBF Science Ministry.

References

1. V.S. Morozov *et al.*, Phys. Rev. Lett. **91**, 214801 (2003).
2. *Madison Convention, Proc. 3rd International Symposium on Polarization Phenomena in Nuclear Physics, Madison, 1970*, ed. H.H. Barschall and W. Haeblerli (Univ. of Wisconsin Press, Madison, WS, 1971), p. xxv.
3. K. Yonehara *et al.*, AIP Conf. Proc. No. 698 (AIP, Melville, NY, 2003), p. 763.
4. V.S. Morozov *et al.*, Phys. Rev. ST Accel. Beams **7**, 024002 (2004).
5. M.A. Leonova *et al.*, Phys. Rev. Lett. **93**, 224801 (2004).

Fig. 3. (LEFT) The proton spin-flip efficiency η at 2.1 GeV/c, measured after 11 spin-flips, is plotted against the RF-dipole's ramp time Δt . The RF-dipole's $\Delta f/2$ was 6 kHz; its $\int B_{rms} dl$ was 0.46 T-mm. The arrow indicates the Δt used in Fig. 4.

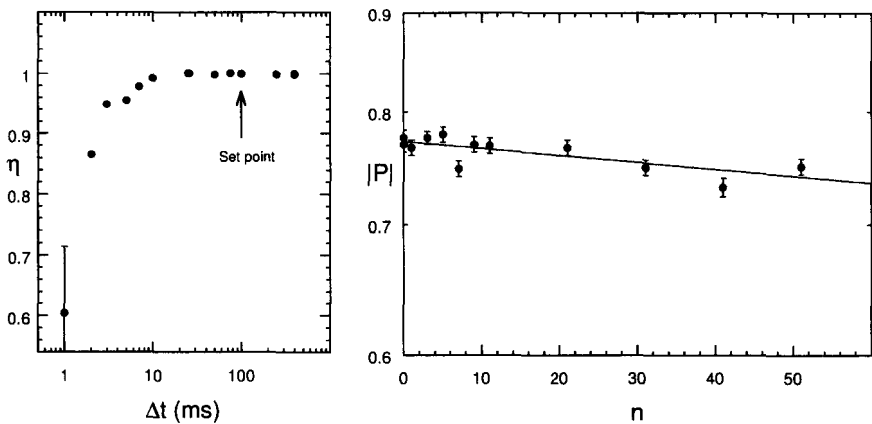


Fig. 4. (RIGHT) The magnitude of the measured proton polarization at 2.1 GeV/c is plotted against the number of spin-flips. The RF-dipole's frequency ramp time Δt was 0.1 s; its frequency half-range $\Delta f/2$ was 6 kHz, and its $\int B_{rms} dl$ was 0.46 T-mm. The line is a fit using the vector part of Eq. (5).

POLARISED DEUTERONS AT THE JINR ACCELERATOR NUCLOTRON *

Y. K. PILIPENKO, S. V. AFANASIEV, L. S. AZHGIREY, A. Y. ISUPOV, V. P. ERSHOV, V. V. FIMUSHKIN,
L. V. KUTUZOVA, V. F. PERESEDOV, V. P. VADEEV, V. N. ZHMYROV, L. S. ZOLIN

Joint Institute for Nuclear Research, Dubna, Russia

For the first time since the old Synchrophasotron machine was shut down, polarised deuterons have been accelerated at the new SC Nuclotron accelerator. The polarisation of the beam was measured by several polarimeters: after the 10 MeV linac, inside the accelerator ring, and after beam extraction. The high value of the vector polarisation P_z of the deuteron beam during acceleration was confirmed by all polarimeters to be $+0.62$ and -0.56 . The intensity of the polarised deuteron beam in a short one-turn injection mode ($8 \mu s$) was observed to be $1.3 \cdot 10^8 \uparrow d/pulse$. To increase the intensity of the accelerated polarised beam, multiturn charge exchange injection should be used. A polarised $\uparrow D^-$ ion source is required. The existing $\uparrow D^+$ source POLARIS was rebuilt as a $\uparrow D^-$ source. A new plasma $\uparrow D^-$ charge exchange ionizer was developed and tested. First results of the beam polarisation measurements are presented.

1. $\uparrow D^+$ source POLARIS

An intensive study of polarisation phenomena was carried out at the Dubna 10 GeV synchrophasotron during the last 20 years. In the fall of 2002 the last polarised beam run took place. During that time the cryogenic source POLARIS, designed at the end of the 1970s, was used to produce polarised deuteron beams [1]. The source atomic beam forming process is required to pump a large mass of injected gas. Instead of conventional pumping, cryocondensation of deuterium molecules on cooled surfaces was used. POLARIS is an atomic beam source with internal 4.2 K surfaces for effective gas cryopumping, cold nozzle, and superconducting magnets. It consists of two LHe cryostats: a pulsed atomic beam stage with SC sextupole magnets, and a Penning ionizer with a high-field SC solenoid. The energy of the deuteron beam is about 3 keV, and the current 0.3-0.4 mA. The vector and tensor polarisations are $P_z = \pm 0.56$ and $P_{zz} = \pm 0.76$.

The commissioning of the new SC accelerator Nuclotron assumes the continuation of the spin physics program. A first test polarised run at the new machine took place. Simulations show that depolarising resonances are absent for polarised deuteron acceleration over almost the full energy range of the Nuclotron.

*This work is supported by Russian Fund of Fundament. Res., the Grant 04-02-17410.

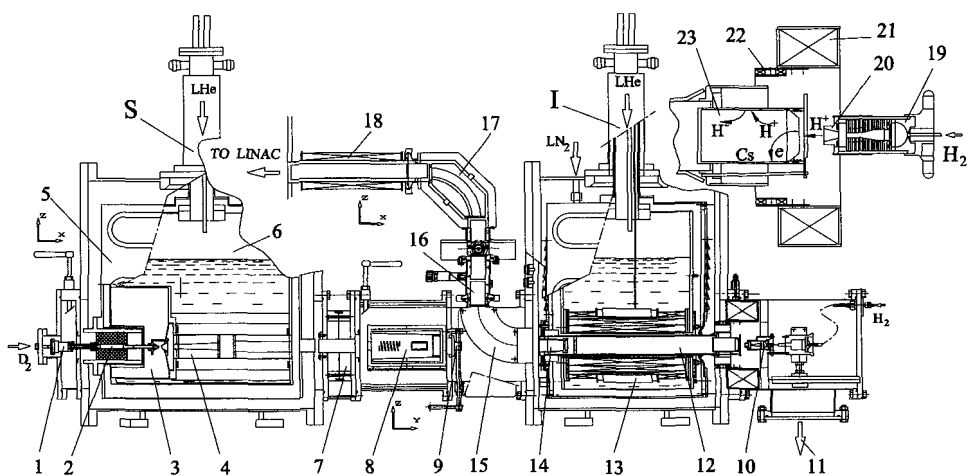


Fig. 1. Schematic view of the polarised deuteron source POLARIS. S: polarised atomic source, I: charge exchange ionizer, 1: pulsed D_2 valve, 2: dissociator, 3: nozzle chamber, 4: SC sextupole magnets, 5: nitrogen shield, 6: helium cryostat, 7: permanent sextupole, 8: RF cell, 9: vacuum gate, 10: H^- plasma generator, 11: 500 l/s turbopumps, 12: HV charge exchange space, 13: SC solenoid, 14: extraction electrodes, 15: 90° bending magnet, 16: ion optics, 17: electrostatic mirror, 18: spin-precessor solenoid, 19: Cu cathode, 20: anode, 21: magnetic coil, 22: transverse magnetic filter, 23: molybdenum converter.

2. Charge Exchange Ionizer

The new Nuclotron has short one-turn injection ($8 \mu s$) of positive ions (a factor 50 less than the synchrotron). To obtain a high-beam current a new plasma charge-exchange ionizer has been developed [2] (Fig. 1). It has a similar Penning ionizer to the LHe cryostat. A short pulse ($300 \mu s$) H^+ arc plasma generator is installed at the SC solenoid entrance. $0.05\text{--}0.1 \text{ cm}^3$ H_2 gas is injected into a hollow cathode space in the plasma generator to produce a high-current arc discharge pulse of H^+ plasma. A nuclear polarised deuterium atomic beam is moved into the solenoid space towards the plasma beam. The charge exchange reaction $\uparrow D^0 + H^+ = \uparrow D^+ + H^0$ takes place inside a HV space. The acceleration potential of the plasma generator and the HV pipe is +15 kV. The three plasma components $\uparrow D^+$, H^+ , and H_2^+ are extracted by grids.

Using the POLARIS atomic beam stage, about 1 mA polarised D^+ (mass 2) current, accompanied by 9 mA H_2^+ (mass 2) background from the plasma generator, have been measured behind the 90° bending magnet. To get proper vertical orientation of the spin, the polarised beam is passed through the electrostatic mirror and spin rotator. The efficiency of the new ionizer is 3-5% as compared to 1-2% for the our old Penning ionizer.

To reach accelerated polarised beam intensities of up to $0.7\text{--}1 \cdot 10^{10} \uparrow d/\text{pulse}$, multiturn charge exchange injection (20-30 turns) should be used. This is done by injecting $\uparrow D^-$ ions into the Nuclotron, and stripping them inside the ring. A $\uparrow D^-$ beam from the source is required.

The existing D^+ plasma charge exchange ionizer has been modified to accept $\uparrow D^-$ by

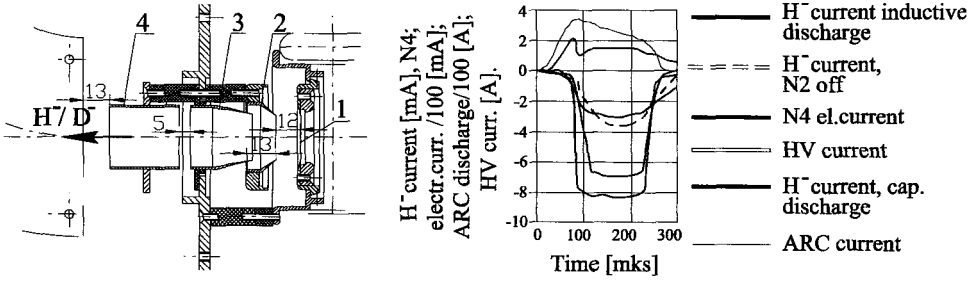


Fig. 2. Extraction electrodes and the H^- current pulse.

the use of an external converter-emitter [2,3]. At the output of the H^+ plasma generator, a molybdenum surface converter produces H^- ions. Caesiated molybdenum surfaces of the converter are exposed to an intense flux of superheated hydrogen atoms and positive ions, and generate H^- ions. H^- ions, space charge compensated by residual H^+ ions, enter the axial region and fill up a HV charge exchange space (-20 kV), where the $\uparrow D^0 + H^- = \uparrow D^- + H^0$ reaction takes place. The 90° bending magnet separates accelerated H^- plasma and polarised $\uparrow D^-$ ions.

Reconstruction of the ionizer and its cryogenic tests have been done. Some configurations of the H^+ generator and H^- molybdenum converter have been tested (Fig.2). The conditioning of the converter surfaces and the Cs layer is very important. The H^- current is raised slowly with time. It depends on the quantity of injected gas, arc voltage, pulse frequency, converter temperature, and the Cs layer. The 10 mA H^- current was observed under existing vacuum conditions. We estimate that 0.3-0.5 mA $\uparrow D^-$ beam should be obtainable, using the POLARIS atomic stage. The plasma charge exchange ionizer can be used as an intense source of unpolarised proton or deuteron. Development of the ionizer will be continued.

3. Test run at the Nuclotron

A test run has been carried out at the Nuclotron using the $\uparrow D^+$ source POLARIS. The beam polarisation is measured by a low energy polarimeter with He^4 target after the 10 MeV linac, by an internal target polarimeter, and by a two-arm relative polarimeter with polyethylene target.

The results of measurements are:

Beam polarisation	Pz (1-4)	Pz (3-6)
- behind the linac	- 0.56+/-0.07	0.62+/-0.07
- inside the ring at 3.5 GeV/c	-0.58+/-0.04	0.59+/-0.04
- at 5.0 GeV/c	-0.56+/-0.03	0.60+/-0.03
- extracted beam at 3.5 GeV/c	-0.54+/-0.02	0.56+/-0.02
- at 5.0 GeV/c	-0.66+/-0.02	0.60+/-0.02

The vector polarisation of the deuteron beam is retained during acceleration, as confirmed by all polarimeters. As expected, the intensity of the polarised deuteron beam in

one turn injection mode is observed to be $1.3 \cdot 10^8$ \uparrow d/pulse. Multiturn charge exchange injection is required.

Acknowledgments

This work is supported by Russian Fund Fundamental Research, the Grant 04-02-17410.

References

1. N.G. Anischenko *et al.*, 5th Int. Symp. on High Energy Spin Physics, Brookhaven 1982, AIP Conf. Proc. N.Y. **N95**, 445 (1983).
2. V.P. Ershov *et al.* Int. Workshop on Polarized Sources and Targets, Erlangen 1999, (Druckerei Lengenfelder, Erlangen) 456 (1999).
3. V.P. Ershov *et al.*, Int. Workshop on Polarized Sources and Targets, Nashville 2001, (World Scientific, Singapore) 225 (2002).

SPIN DEPENDENCE IN ELASTIC SCATTERING IN THE CNI REGION

A. BRAVAR¹, I. ALEKSEEV², G. BUNCE^{1,3}, S. DHAWAN⁴, R. GILL¹, H. HUANG¹, W. HAEBERLI⁵,
O. JINNOUCHI³, A. KHODINOV⁷, A. KPONOU¹, K. KURITA⁸, Y. MAKDISI¹, W. MENG¹, A. NASS¹,
H. OKADA⁹, N. SAITO^{3,9}, H. SPINKA¹⁰, E. STEPHENSON¹¹, D. SVIRIDA², D. UNDERWOOD¹⁰,
C. WHITTEN⁶, T. WISE⁵, J. WOOD⁶, A. ZELENSKI¹

¹Brookhaven National Laboratory, Upton, USA

²ITEP, Moscow, Russia

³RIKEN BNL Research Center, Upton, USA

⁴Yale University, New Haven, USA

⁵University of Wisconsin, Madison, USA

⁶UCLA, Los Angeles, USA

⁷SUNY at Stony Brook, Stony Brook, USA

⁸Rikkyo University, Toshima-ku, Japan

⁹Kyoto University, Sakyo-ku, Japan

¹⁰Argonne National Laboratory, Argonne, USA

¹¹Indiana University, Bloomington, USA

The interference of the electromagnetic spin-flip amplitude with a hadronic spin-nonflip amplitude in the elastic scattering of hadrons leads to significant spin dependencies at very low 4-momentum transfer t ($0.001 < |t| < 0.01$ (GeV/c)²). This kinematical region is known as the Coulomb Nuclear Interference (CNI) region. First results on spin effects in polarized proton-proton elastic scattering in the CNI region at 100 GeV from the 2004 polarized proton run at RHIC are presented. Preliminary results on A_N in the elastic scattering of polarized protons off a carbon target over a wide energy range from 4 GeV to 100 GeV from AGS and RHIC are presented as well. These results allow us to further investigate the spin dependence in elastic scattering and the mechanisms at work.

In some sense, elastic scattering of hadrons is the simplest and the most basic type of nuclear interaction (see Figure 1), yet elastic scattering phenomena have eluded a detailed and satisfactory explanation from general principles for a long time. The formalism for polarized elastic scattering is well developed in terms of five independent helicity amplitudes $\phi_i(t)$ with, however, little understanding of the mechanisms at work. The region of low 4-momentum transfer t is associated with long distance phenomena, and therefore is in the domain of non-perturbative QCD, where no precise predictions can be made. Several meson exchange models based on Regge phenomenology have been developed to describe the observed data. Naively one would expect that simple concepts like angular momentum

conservation and helicity conservation in the s -channel would lead to simple and predictable spin effects in elastic scattering. Most of these models, that otherwise seemed to work, failed to predict the observed spin dependencies.

In this talk I will discuss recent A_N results in pp and pC elastic scattering in the very low t region of $|t| < \text{few} \times 10^{-2}(\text{GeV}/c)^2$, from the 2004 polarized proton run at RHIC using internal targets. The analyzing power A_N is a measure of the left-right asymmetry of the cross section in the scattering plane normal to the beam or target polarization. A_N arises from the interference between a spin-flip and spin-nonflip amplitude, and thus provides basic information on the spin dependence of the interaction.

In high energy pp and pA elastic scattering at very low 4-momentum transfer t , A_N originates from the interference between the real electromagnetic (Coulomb) spin-flip amplitude, which is generated by the proton's anomalous magnetic moment, and the imaginary hadronic (Nuclear) spin-nonflip amplitude (CNI = Coulomb Nuclear Interference). A_N reaches a predicted maximum value of about 4–5 % around a t value of $3 \times 10^{-3} (\text{GeV}/c)^2$, and decreases with increasing $|t|$.

The existence of a potential hadronic spin-flip amplitude interfering with the electromagnetic spin-nonflip amplitude introduces a deviation in shape and magnitude for A_N calculated

with no hadronic spin-flip. [1]. While the former contribution is fully calculable, the latter can be tackled only in Regge-inspired phenomenological approaches [2]. Note that the conservation of angular momentum imposes restrictions on the helicity-flip amplitudes in the forward direction (i.e. for $|t| \rightarrow 0$) and $\phi_5(t) \propto \sqrt{|t|}$. The hadronic spin-flip amplitude carries important information on the static properties and on the constituent quark structure of the nucleon, since the $|t|$ dependence of this hadronic spin-flip amplitude at small $|t|$ is tightly connected with the structure of hadrons. Within Regge phenomenology, one can probe the long-standing issue of the magnitude of the Pomeron spin-flip through the study of A_N in the CNI region. In a quark-diquark picture of the proton the magnitude of the Pomeron spin-flip amplitude can be associated with the diquark separation, the smaller this separation the bigger the effect, suggesting that the spin part of the Pomeron probes the smallest distances in the proton.

$p p^\uparrow \rightarrow p p$

Using internal targets (atomic hydrogen jet target and carbon ribbons) the RHIC accelerator can be operated in a fixed target mode, with typical energies of $\sqrt{s} = 7 - 22$ GeV. The main motivation for studying polarized elastic scattering in the CNI region comes from a need for very precise beam polarization measurements at RHIC. For details of the RHIC polarimeters see D. Svirida's talk at this Symposium [3].

Figure 2 shows the schematic layout of the pp elastic scattering experiment. In the CNI region, recoil protons from pp elastic scattering emerge at close to 90° with respect to the beam direction. In this t region, the elastic process is fully constrained by the recoil particle only; thus the detection of the scattered beam proton is not mandatory. The recoil protons were detected using an array of silicon detectors located at ~ 80 cm from the jet target

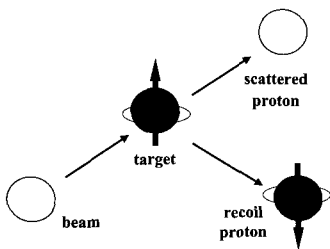


Fig. 1. The elastic scattering process: sometimes the recoil proton flips its spin yielding the left-right scattering asymmetry, A_N .

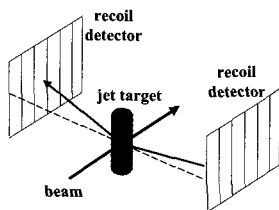


Fig. 2. Layout of the pp elastic scattering setup. The atomic beam crosses the RHIC beam from above.

axis on both sides of the beam, and covering an azimuthal angle of $\sim 15^\circ$ on each side. These detectors provided energy ($\Delta T_R \leq 60$ keV), polar angle ($\Delta \vartheta_R \sim 1.6$ mrad, horizontal segmentation of the recoil detectors ~ 4 mm), and time of flight ($\Delta \text{ToF} \sim 3$ ns, from intrinsic resolution and bunch length) measurements of the recoil particles. In the t range of $0.001 < |t| < 0.01$ (GeV/c^2), the recoil protons were fully absorbed in the recoil detectors. Recoil protons were identified on the basis of the $\text{ToF} - T_R$ non-relativistic relation $T_R = \frac{1}{2} M_p (\text{dist}/\text{ToF})^2$, and selected on the basis of the $\vartheta_R - T_R$ relation $T_R \simeq 2 M_p \vartheta_R^2$. The estimated background below the elastic peak was less than 5%. For additional information on the experiment, event selections and results see H. Okada's talk at this Symposium [4]. The atomic hydrogen beam crossed the RHIC beams from above with its polarization directed vertically.

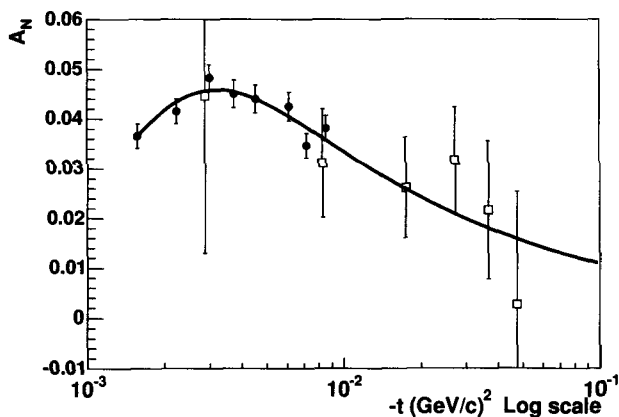


Fig. 3. $A_N(t)$ in pp elastic scattering; filled circles: this experiment, open squares: E704 at Fermilab [6]. The errors shown are statistical only. For details on the systematic errors see text. The solid line is the CNI - QED prediction with no hadronic spin-flip.

The state-of-the-art atomic polarized source delivered protons with a polarization of 0.924 ± 0.018 (the dilution from molecular hydrogen is included in this figure), a density in excess of 10^{12} p/cm^2 in its center, and a FWHM profile of less than 6 mm. The target polarization was reversed each 5 to 10 minutes, thus cancelling most of systematic effects associated with the asymmetric extraction. The jet target, its properties, performance and operation have been discussed in detail at this Symposium by A. Nass, T. Wise and

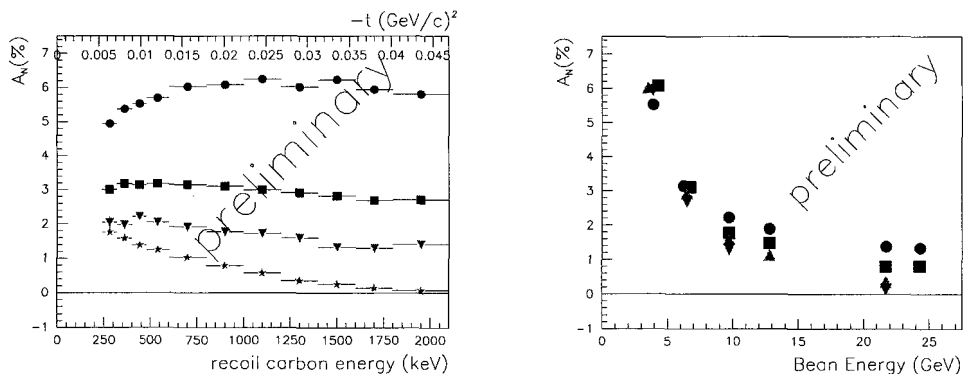


Fig. 4. **left:** A_N in % for $pC \rightarrow pC$ as function of T_R at 4 different beam energies: starting from top $E_B = 3.9$ GeV, 6.5 GeV, 9.7 GeV, and 21.7 GeV. The displayed errors are statistical only. **right:** A_N as a function of E_B for different intervals of t : full circles $|t| \sim 0.01 \text{ GeV}^2/c^2$, squares $|t| \sim 0.02 \text{ GeV}^2/c^2$, up triangles $|t| \sim 0.03 \text{ GeV}^2/c^2$, down triangles $|t| \sim 0.04 \text{ GeV}^2/c^2$. At larger values of E_B there appears to be a weak or no energy dependence; this behavior is suggestive of the onset of an asymptotic regime.

A. Zelenski [5].

Figure 3 shows the analyzing power $A_N(t)$ for pp elastic scattering in the t range of $0.001 < |t| < 0.01 \text{ (GeV}/c)^2$ at $\sqrt{s} \simeq 14 \text{ GeV}$. The displayed errors are statistical only. The two major sources of systematic errors come from the backgrounds and the error on the target polarization: the former is estimated to be around $\delta A_N^{sys} = 0.0015$ for each measured data point; the latter represents a normalization uncertainty of 2.0%. These data are also compared to a previous, much less precise, measurement from the Fermilab E704 experiment at $\sqrt{s} \simeq 20 \text{ GeV}$ [6].

These data are well described by the CNI prediction with no hadronic spin-flip terms ϕ_5^{had} [1]. In Figure 3 the A_N data are fitted with the CNI prediction with a free normalization factor N : $\chi^2/\text{d.o.f.} \simeq 5/7$ with $N = 0.98 \pm 0.03$. The interpretation, therefore, does not require additional hadronic spin-flip terms; the sensitivity on ϕ_5^{had} in this t region, however, is limited. A_N data in the larger t range of $0.01 < |t| < 0.03 \text{ (GeV}/c)^2$ will soon become available. Data on the double spin asymmetry A_{NN} in the same t range will be soon available, as well. That will allow us to perform more extensive studies of the spin dependence in pp elastic scattering and of the mechanisms at work, and draw firmer conclusions on ϕ_5^{had} .

$p^\dagger C \rightarrow pC$

A setup conceptually similar to the one shown in Figure 2 is used for the pC elastic scattering measurements. A carbon ribbon target, as thin as $3.5 \mu\text{g}/\text{cm}^2$, is inserted from time to time into the AGS and RHIC polarized proton beams. On the basis of ToF – T_R correlation for recoiling carbon ions, pC elastic scattering events are identified. For more details on the setup and analysis see O. Jinnouchi's talk at this Symposium [7].

Figure 4 shows the A_N results for pC elastic scattering as a function of the recoil carbon

energy T_R ($T_R = |t|/2M_C$), at several incident beam energies from 4 to 22 GeV using the AGS polarized proton beam. At beam energies below 10 GeV, a very weak $|t|$ dependence and much larger asymmetries are observed compared to the CNI-type behavior at larger energies. The normalization uncertainty is $\sim 10\%$ for the lowest energy data points, and increases to $\sim 20\%$ for the highest ones. The systematic error, which comes mainly from backgrounds below the elastic pC peak, pileup and electronic noise, is estimated to be $< 15\%$ relative.

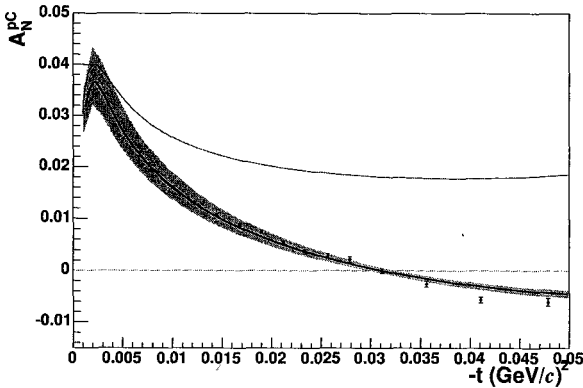


Fig. 5. $A_N(t)$ for pC elastic scattering at 100 GeV. The shaded band represents the systematic uncertainties of the measurement. The solid line in the band is a fit to the data including a significant hadronic spin-flip contribution (see text). The result is significantly different from the no-hadronic spin-flip prediction (top curve).

Figure 5 shows the A_N data as a function of t for pC elastic scattering at 100 GeV, using the RHIC polarized proton beam over a wide t interval. For this measurement $P_B = 0.386 \pm 0.033$, as measured with the jet target. The systematic errors, displayed as a band in Figure 5, come mainly from the normalization uncertainty $\Delta P_B/P_B \sim 8.5\%$, and the energy scale in determining the recoil carbon energy T_R . The systematic errors on the raw asymmetry measurement alone, however, are very small.

In Figure 5 these data are fitted with a phenomenological model developed in Ref. 2, which introduces a hadronic spin-flip contribution to A_N via the ω , f_2 , and Pomeron trajectories. Contrary to the pp elastic scattering case, these data require a significant hadronic spin-flip contribution. For the fit results of r_5 and discussion see Ref. 7. Comprehensive studies and modeling of A_N over the whole energy range should allow us to better understand and disentangle the various contributions to A_N , the role of the hadronic spin-flip amplitudes, and the possible onset of asymptotic regimes.

We would like to thank the Instrumentation Division at BNL for their work on the silicon detectors and electronics, and W. Lozowski at IUCF for providing the carbon ribbon targets. This work is performed under the auspices of U.S. DOE contract Nos. DE-AC02-98CH10886 and W-31-109-ENG-38, DOE grant No. DE-FG02-88ER40438, NSF grant PHY-0100348, and with support from RIKEN, Japan.

References

1. N.H. Buttimore *et al.*, Phys. Rev. D **59**, 114010 (1999).
2. B.Z. Kopeliovich and T.L. Trueman, Phys. Rev. D **64**, 034044 (2001).
3. Contribution of D. Svirida at this Symposium;
A. Bravar *et al.*, Proceedings of the Spin 2003 Workshop, Dubna 2003.
4. Contribution of H. Okada at this Symposium.
5. Contributions of A. Nass, T. Wise and A. Zelenski at this Symposium.
6. N. Akchurin *et al.*, Phys Rev. D **48**, 3026 (1993).
7. Contribution of O. Jinnouchi at this Symposium.

DEUTERON POLARIZATION DETERMINATION AT HIGH ENERGIES

N. H. BUTTIMORE

University of Dublin, Trinity College, Dublin, Ireland

T. L. TRUEMAN

Physics Department, Brookhaven National Laboratory, Upton, U.S.A.

In the event that polarized deuterons will be accelerated to high energy, to enable a spin study of neutron collisions for example, there will be a need to evaluate the level of polarization. Measurement of the analyzing power for polarized deuteron carbon collisions provides a method for the relative calibration of polarization when scattering angles are close to those of the electromagnetic hadronic interference region of momentum transfer. The use of carbon recoils has been effective in the case of the relative polarimetry for high-energy spin-half protons. A theoretical analysis of the corresponding process involving spin one deuterons scattering on a spin-zero carbon target is presented. The nuclear effects associated with small-angle polarized deuteron carbon collisions are incorporated.

1. Introduction

Considerable progress has been made in using polarized protons to elicit the partonic spin structure of the nucleon. To provide a more complete picture of the isotopic spin sector [1], it may be beneficial to use a probe more rich in the down quark such as the deuteron or a helium-three ion. The possibility of using deuteron carbon elastic scattering in the small angle interference region as a deuteron polarimeter is explored. Expectations for the analyzing power are presented and discussed.

2. Helicity amplitudes

The parity-conserving and time-reversal invariant helicity amplitudes for a spin-one deuteron of mass m scattering elastically off a spinless carbon nucleus are [2]

$$\begin{aligned} H_1 &= H_{++} = H_{--}, & H_2 &= H_{+0} = H_{0-} = -H_{0+} = -H_{-0} \\ H_3 &= H_{+-} = H_{-+}, & H_4 &= H_{00} \end{aligned} \quad (1)$$

where the subscripts refer to the helicity states of the scattered and incoming deuteron respectively. With centre-of-mass three-momentum k the spin averaged and spin aligned total cross sections are normalized according to

$$\begin{aligned} 4\pi \text{Im}[2H_1(s,0) + H_4(s,0)]/3 &= k\sqrt{s}\sigma_{\text{tot}}(s), \\ 8\pi \text{Im}[H_1(s,0) - H_4(s,0)]/3 &= k\sqrt{s}\sigma_{\text{tot}}^{\text{al}}(s). \end{aligned} \quad (2)$$

As in the case of proton-proton elastic collisions, there is a spin-dependent amplitude $H_1 - H_4$ which does not vanish in the forward direction. [3]

3. Coulomb amplitudes

Interference phenomena result from the inclusion of electromagnetic effects due to one-photon exchange. Omitting contributions from the quadrupole-moment form factor $F_2^{\text{d}}(t)$ as they involve a factor t , the helicity amplitudes for a deuteron of mass m colliding with a spin-zero nucleus of charge Ze and electromagnetic form factor $F_0(t)$ are (including the low $-t$ approximation)

$$\begin{aligned} \frac{H_1^{\text{em}}}{Z\alpha F_0} &= \left(F_1^{\text{d}} \frac{s-u}{2t} - G_1^{\text{d}} \right) \left(1 + \frac{t}{4k^2} \right) \approx F_1^{\text{d}} \frac{s}{t} \\ \frac{H_2^{\text{em}}}{Z\alpha F_0} &= \left[\left(F_1^{\text{d}} \frac{s-u}{4} - \frac{t}{4} G_1^{\text{d}} \right) \sqrt{\frac{1}{m^2} + \frac{1}{k^2}} - \frac{k\sqrt{s}}{2m} G_1^{\text{d}} \right] \sqrt{\frac{2}{-t} - \frac{1}{2k^2}} \approx F_1^{\text{d}} \frac{s}{\sqrt{-2t}} \left(\frac{1}{m} - \frac{\mu_d}{2m_p} \right) \\ \frac{H_3^{\text{em}}}{Z\alpha F_0} &= - \left(F_1^{\text{d}} \frac{s-u}{4} + \frac{t}{4} G_1^{\text{d}} \right) \frac{1}{k^2} \approx 0 \\ \frac{H_4^{\text{em}}}{Z\alpha F_0} &= F_1^{\text{d}} \frac{s-u}{4} \left(\frac{2}{t} + \frac{1}{m^2} + \frac{1}{k^2} \right) - G_1^{\text{d}} \left[1 + \frac{s-u}{4m^2} + \frac{t}{4k^2} + \left(\frac{1}{m^2} + \frac{1}{k^2} \right) \frac{t^2}{16k^2} \right] \approx F_1^{\text{d}} \frac{s}{t}. \end{aligned} \quad (3)$$

Two of the electromagnetic form factors of the deuteron have normalisations $F_1^{\text{d}}(0) = 1$ and $G_1^{\text{d}}(0)/m = \mu_d/m_p$ in units involving the proton mass m_p . [4]

4. Spin observables

Observables for scattering initially polarized deuterons on carbon are [2]

$$\begin{aligned} I_0 &\equiv t_{00}^{00} = 2|H_1|^2 + |H_4|^2 + 4|H_2|^2 + 2|H_3|^2 \\ (i/\sqrt{6})t_{11}^{00} I_0 &= -\text{Im}H_2^*(H_1 + H_4 - H_3) \\ (1/\sqrt{2})t_{20}^{00} I_0 &= |H_1|^2 - |H_4|^2 - |H_2|^2 + |H_3|^2 \\ (1/\sqrt{6})t_{21}^{00} I_0 &= \text{Re}H_2^*(H_1 - H_4 - H_3) \\ (1/\sqrt{3})t_{22}^{00} I_0 &= 2\text{Re}H_1^*H_3 - |H_2|^2. \end{aligned} \quad (4)$$

In the case where the amplitudes $H_1 - H_4$ and H_3 are negligible at high energies and low momentum transfers, the asymmetry parameter is

$$i\sqrt{3}t_{11}^{00} = -\frac{2\text{Im}\sqrt{2}H_2^*H_1}{|H_1|^2 + \frac{2}{3}|\sqrt{2}H_2|^2} \quad (5)$$

and the correspondence with the proton carbon case is evident. [5] It is useful to introduce the following hadronic amplitudes with a kinematically scaled ratio $\tau(s, t)$ between helicity flip and helicity non flip hadronic amplitudes

$$F = \frac{1}{2k\sqrt{s}} \frac{2H_1 + H_4}{3}, \quad \tau F = \frac{m_p}{2k\sqrt{s}} \sqrt{\frac{2}{-t}} H_2 \quad (6)$$

so that the analyzing power may be written using equation (3) as

$$\frac{A_N}{4\pi} \frac{d\sigma}{dt} = \frac{\sqrt{-t}}{m} 2\text{Im}(F + F^{\text{em}})^* \left[\tau F + \left(\frac{\mu_d}{2} - \frac{m_p}{m} \right) F^{\text{em}} \right] \quad (7)$$

where the deuteron carbon amplitudes comprise a hadronic part $F(s, t)$ and an electromagnetic part with $Z = 6$, form factor F_C , and Coulomb phase δ

$$F^{\text{em}} = 6\alpha F_1^d F_C e^{i\delta} / t. \quad (8)$$

If the proton-carbon elastic scattering amplitude $f(q)$ is assumed equal to the neutron carbon amplitude, the deuteron-carbon amplitude may be calculated at a particular value of s using an approximate Glauber method [5]

$$F(t) = 2f(q)f_d(q/2) + i \int \frac{d^2q'}{\pi} f(q/2 + q')f(q/2 - q')f_d(q'). \quad (9)$$

The figure shows the analyzing power for d-C scattering when there is no hadronic helicity flip amplitude. By comparison with the interference peak in proton-carbon elastic scattering, [6], the smaller interference trough near $-t = 0.002 \text{ GeV}/c^2$ results from the low negative value of the deuteron anomalous magnetic moment, in addition to the inhibiting effect of total cross section ratios. The depth of the trough is very sensitive to the value of the hadronic helicity flip amplitude, and can even change sign with moderate values. The figure of merit of the peak at higher $-t$ should also be studied in the context of polarimetry for deuterons. It seems likely that measuring the polarization of high-energy deuterons presents an interesting challenge.

Acknowledgments

This manuscript has been authored under contract number DE-AC02-98CH10886 with the U.S. Department of Energy. Accordingly, the U.S. Government retains a non-exclusive, royalty-free license to publish or reproduce the published form of this contributions, or allow others to do so, for U.S. Government purposes. TLT was partially supported by the Visiting Professorships and Fellowships Benefaction Fund of Trinity College of the University of Dublin.

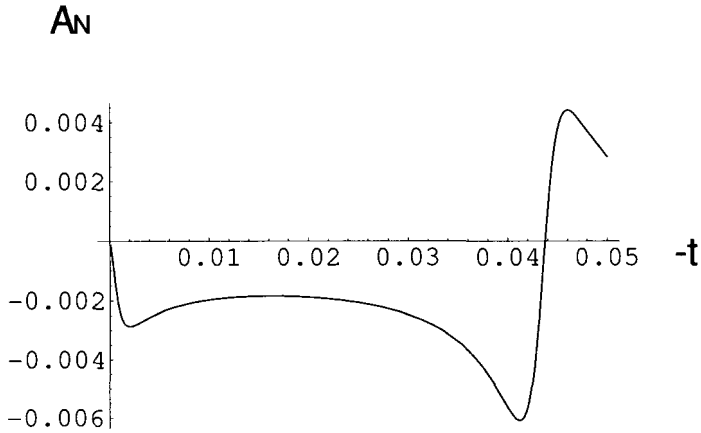


Fig. 1. The analyzing power for d-C scattering with zero hadronic helicity flip.

References

1. G. Bunce, N. Saito, J. Soffer and W. Vogelsang, *Ann. Rev. Nucl. Part. Sci.* **50**, 525 (2000).
2. R. A. Arndt, I. I. Strakovsky, R. L. Workman, *Phys. Rev. C* **50**, 1796 (1994).
3. N. H. Buttimore, B. Z. Kopeliovich, E. Leader, J. Soffer and T. L. Trueman, *Phys. Rev. D* **59**, 114010 (1999).
4. S. Waldenstrøm and H. Olsen, *Nuovo Cimento A*, 491 (1971) and references.
5. B. Z. Kopeliovich and T. L. Trueman, *Phys. Rev. D* **64**, 04004 (2001).
6. J. Tojo, I. Alekseev, M. Bai *et al.*, *Phys. Rev. Lett.* **89**, 05202 (2002).

DESIGN AND TEST OF A PROTOTYPE CAVITY FOR A STERN-GERLACH POLARIMETER *

P. R. CAMERON¹, M. CONTE², N. D'IMPERIO¹, W. FRANKLIN³, D. A. GOLDBERG⁴, A. U. LUCCIO¹,
W. W. MACKAY¹, M. PALAZZI⁵, M. PUSTERLA⁶, K. VETTER¹, T. ZWART³

1-BNL, Upton, USA;

2-Sezione INFN di Genova, Genova, Italy;

3-MIT-Bates Laboratory, Boston, USA;

4-Lawrence Berkeley National Laboratory, Berkeley, USA;

5-AMS Naval Systems, Genova, Italy;

6-Università e Sezione INFN di Padova, Padova, Italy

We present the design, simulations and measurements of a prototype passive RF cavity polarimeter, with a transversely polarized electron beam interacting with the longitudinal gradient of the transverse component of magnetic field in the TE₀₁₁ mode of the cavity. Signal levels at the MIT-Bates storage ring may approach a microwatt, permitting fast and accurate polarization measurement.

1. Polarimeter at MIT-Bates

The magnetic moment signal power [1,2] expected from the cavity polarimeter TE₀₁₁ mode at MIT-Bates [3] is

$$\frac{dU}{dt} = \frac{4Qf(\mu\tau n\gamma^2 P)^2}{\pi\epsilon_0 c^2 V} \quad (1)$$

where $Q = 5000$, $f = 2.856$ GHz is the bunching frequency, ϵ_0 is the permittivity of free space, $V \sim 500$ cm³ is the cavity volume, μ is the magnetic dipole moment of the electron, $\tau \sim 0.7$ is the transit time factor, $n = 10^8$ is the number of electrons per bunch for all buckets filled and 50 ma beam current, $\gamma = 2000$ is the Lorentz factor at 1 GeV, $P \sim 0.5$ is the beam polarization, and c is the speed of light. Due to unavoidable misalignments, the electric charge interaction with the same mode is

$$\frac{dU}{dt} = \frac{2Qf(q\tau nd \tan \phi)^2}{\pi\epsilon_0 V} \quad (2)$$

where $d = 6$ cm is the cavity length, and ϕ is the angular misalignment of the beam axis relative to the cavity axis. Figure 1 shows moment and charge power as a function of cavity alignment. Alignment of better than 1 μ rad is achievable with reasonable ease. These calculations indicate that, in the case of MIT-Bates, the moment signal can be discriminated

*Work performed under the auspices of the U. S. DOE (Contract # DE-AC02-98CH10886).

from the charge signal without kicking the spin away from the stable spin direction. The -45 dBm level of signal power is worthy of note. In comparison, Schottky signals are typically -150 dBm or less, and thermal background is -174 dBm/Hz. From the figure we see

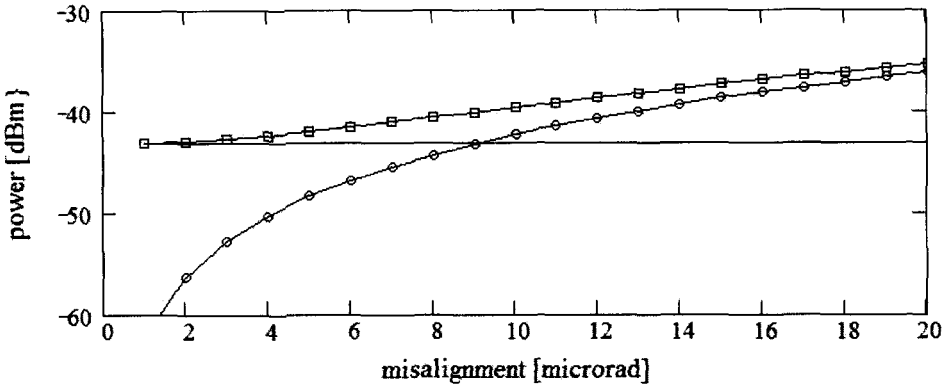


Fig. 1. Moment (straight line at ~ -44 dBm) and charge (open circles) powers and their sum (open squares) as a function of beam/cavity alignment.

that the interaction of the magnetic moment with the pickup has been enhanced sufficiently to permit easy observation, and that with a properly aligned TE_{011} mode this enhanced signal is not overwhelmed by the electric charge interaction. The remaining point which must be considered is the interaction of the beam charge with other cavity modes, and the overlap of those modes with the signal mode. Figure 2 shows frequencies and relative

freq[GHz]	mode	Ex at probe	effect of probe position	Ez at beam	effect of beam position
2.382	TM110	0.0E+00	position of probe in z only	7.1E+02	weak
2.724	TE011	6.4E+02	weak	0.0E+00	weak
3.203	TM111	7.5E+02	weak	9.6E+02	weak
3.766	TM120	0.0E+00	position of probe in y and z	0.0E+00	position of beam in y
3.766	TM210	0.0E+00	position of probe in z only	0.0E+00	position of beam in x
4.332	TM121	0.0E+00	position of probe in y only	0.0E+00	position of beam in y
4.332	TM211	1.0E+03	weak	0.0E+00	position of beam in x
4.764	TM220	0.0E+00	position of probe in y and z	0.0E+00	position of beam in x and y
4.900	TM112	0.0E+00	position of probe in z only	1.5E+03	weak
5.223	TM221	0.0E+00	position of probe in y only	0.0E+00	position of beam in x and y
5.326	TM130	0.0E+00	position of probe in z only	4.8E+03	weak
5.703	TM122	0.0E+00	position of probe in y and z	0.0E+00	position of beam in y
5.703	TM212	0.0E+00	position of probe in z only	0.0E+00	position of beam in x
6.740	TM131	4.1E+03	weak	5.2E+03	weak
6.073	TM230	0.0E+00	position of probe in z only	0.0E+00	position of beam in x
6.406	TM222	0.0E+00	position of probe in y and z	0.0E+00	position of beam in x and y
6.439	TM231	4.5E+03	weak	0.0E+00	position of beam in x
6.834	TM132	0.0E+00	position of probe in z only	6.1E+03	weak
7.431	TM232	0.0E+00	position of probe in z only	0.0E+00	position of beam in x

Fig. 2. Mode Frequencies and Strengths

strengths of the TE_{011} mode and the various TM modes. Of the eighteen TM modes listed there, the coupling of twelve to the beam is minimized by beam centering in the cavity. The remaining six (shown in bold) will contribute strongly to the longitudinal impedance seen

by the beam. This requires further attention from the perspective of machine stability, and may require that the machine be run with low beam current. Of the six modes that couple strongly to the beam, all except two (italicized) couple weakly to the pickup probe. To first order, we can divide Eq. 1 by Eq. 2 to find a scaling factor for relative power between the charge and moment interactions.

$$\text{ratio} = 2 \left(\frac{\mu \gamma^2 P}{qdc \tan \phi} \right)^2 = \frac{8 \times 10^{-11}}{\tan^2 \phi} \quad (3)$$

The charge interaction is about 100 dB greater than the moment interaction. Assuming that the nearest and most dangerous TM_{111} mode has a Lorentzian line shape, power at the ~ 2.8 GHz frequency of the TE_{011} signal mode due to the undamped TM_{111} mode is down by ~ 120 dB, or 20dB below the moment signal.

2. The prototype cavity

A prototype cavity made from square aluminum tubing has been built, with initial dimensions $8.9 \text{ cm} \times 8.9 \text{ cm} \times 7 \text{ cm}$. Commercially available feedthroughs, mounted on mini-CF flanges, are implemented as TE_{011} mode probes. S21 measurements have been done on this cavity; both with the ends blanked off and with the beampipes installed. Results are shown in Fig. 3. The frequencies for the closed box were evaluated both analytically and with finite element software, and are in good agreement with the measured frequencies. From the table in Fig. 2, we expect to see transmission only in those modes with non-zero transverse electric field at the probe location. This happens for the TE_{011} and $\text{TM}_{111,211,131}$ modes, as shown in the third column of the table. Figure 3 shows these modes, together with the TE_{031} mode. Adding the beampipes, the TM mode frequencies are slightly perturbed, whereas the TE_{011} mode is significantly shifted and the TE_{031} mode is strongly damped. Two unexpected new modes appear and are under investigation. Measured Q 's with beampipes are ~ 2500 , much less than the expected ~ 5000 . This difference is under investigation. The cavity length has been shortened to bring the TE_{011} mode closer to the 2.856 GHz frequency, and further measurements are under way. Based on the measurement results shown in Fig. 3 a cavity length has been calculated to bring the TE_{011} mode closer to the 2.856 GHz RF frequency. The cavity has been trimmed to this length, and further measurements are underway.

3. Conclusion

The present collaboration has at least three clearly defined goals. The first is to verify that there exists γ^2 dependence in the interaction of the beam magnetic moment with the selected cavity mode. The second is to utilize this interaction in the realization of fast and accurate polarimetry, first at MIT-Bates, and then at RHIC. The third, given the γ^2 scaling, is to promote the possibility of implementing the reciprocal device, the spin-splitter, for the purpose of providing polarized proton and anti-proton beams. The second iteration of prototype cavity measurements is underway, and we expect to begin fabrication of the final vacuum-compatible cavity shortly. Our intent is to install this cavity at MIT-Bates early in calendar year 2005.

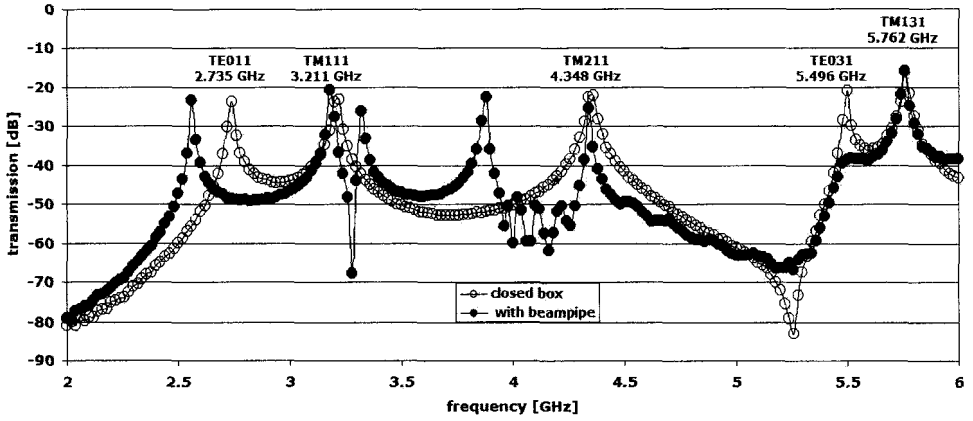


Fig. 3. S21 measurements of the prototype.

References

1. M. Conte *et al.*, "The Stern-Gerlach interaction between a traveling particle and a time varying magnetic field", INFN/TC-00/03, <http://xxx.lanl.gov/list/physics/0003>, preprint 0003069
2. P. R. Cameron *et al.*, "Proposal for a Cavity Polarimeter at MIT-Bates", PAC 2001, Chicago.
3. T. Zwart *et al.*, "Polarized Electrons in the MIT-Bates South Hall Ring", PAC 2001, Chicago.

THE MIT-BATES COMPTON POLARIMETER FOR THE SOUTH HALL RING *

W. A. FRANKLIN

MIT-Bates Linear Accelerator Center, Middleton, USA

(for the BLAST Collaboration)

Storage ring experiments with polarized electrons require a non-destructive mechanism for measuring the beam polarization. During a series of experiments with 850 MeV polarized electrons at intensities up to 175 mA, the MIT-Bates Compton Polarimeter has provided precise beam polarization data on a continuous basis. An overview of its design is presented in this paper, emphasizing features developed for intense low-energy beams. The polarimeter has been combined with a dynamic spin flipper and other consistency checks to minimize systematic errors. Preliminary polarization results are shown and discussed.

MIT-Bates has an ongoing research program to study comprehensively nucleons and light nuclei at low momentum transfer ($Q^2 < 1$ GeV) [1]. In these experiments, intense beams of electrons at 850 MeV, circulating in the South Hall Ring (SHR), are incident on a thin internal target of polarized hydrogen or deuterium produced by an atomic beam source [2]. The Bates Large Acceptance Spectrometer Toroid (BLAST) is used to measure double polarization asymmetries for several reactions. BLAST contains a symmetric set of detectors, subtending scattering angles from $20^\circ < \theta_{lab} < 90^\circ$ in the horizontal plane. The symmetry and large acceptance of the spectrometer permits the extraction of nucleon form factor ratios without independent measurements of the absolute beam or target polarization. Nevertheless, in order to maximize the electron beam polarization, a fast, reliable polarimeter is essential

Compton polarimetry is a technique which utilizes the well-understood spin dependence of the electromagnetic interaction. In the lab frame, low energy photons from a laser beam interacting with a highly energetic electron beam predominantly scatter in the direction defined by the electron momentum, *i.e.* backwards. Typically, the scattered photons receive a substantial energy boost allowing detection by a compact gamma ray detector. Varying the circular polarization of photons yields an asymmetry as a function of energy

*This work is supported by the U. S. Department of Energy under Cooperative Agreement BEFC294ER40818.

in the detected photon spectra which is dependent on the longitudinal polarization of the electron beam.

Compton scattering was initially established as a viable method of polarimetry at multi-GeV energy machines [3]. Although the analyzing power for Compton scattering (A_{pol}) can be very large in this regime, it falls to a few percent for electron energies below 1 GeV. Additionally, in low-energy experiments, the maximum kinematically allowable energy for scattered photons (the Compton edge) is low compared to the maximum bremsstrahlung energy, making separation of the signal from background difficult. The typical SHR beam lifetime is approximately 30 minutes, necessitating optimization of the signal to achieve a statistically precise measurement for each ring fill.

The design of the MIT-Bates Compton Polarimeter was influenced heavily by the NIKHEF Compton polarimeter [4], the first device to operate in an electron storage ring at energies below 1 GeV. The Bates polarimeter is located upstream of the BLAST target to minimize bremsstrahlung background with a small correction made to account for spin precession between the polarimeter and the target. The apparatus includes a solid-state 5-watt laser with an optical transport system designed to preserve the polarization of 532 nm light. A set of remotely controllable mirrors permits the laser to intercept the electron beam at a crossing angle of less than 2 mrad. Scattered photons are detected with a pure CsI calorimeter chosen for its combination of energy and time resolution.

A number of provisions have been made in the experimental apparatus and data acquisition (DAQ) system to facilitate high-intensity operation. A movable lead collimator defines an azimuthally symmetric acceptance for the backscattered photons to minimize background from beam halo. The calorimeter is equipped with a photomultiplier tube and base engineered for linear operation at very high rates, although saturation does occur at the highest SHR intensities. To circumvent this problem, a set of variable thickness stainless steel absorbers was installed to attenuate the photon flux in a manner nearly independent of energy and insensitive to photon polarization. Typical photon rates in the calorimeter are of the order of 100 kHz, necessitating a DAQ processor with high readout and sorting speeds. The DAQ system was locally developed and features an externally triggered 12-bit flash ADC with pulse sampling capability at 100 MHz for pulse-shape discrimination and pile-up rejection. The DAQ system is synchronized with the BLAST event stream and integrated with the BLAST analysis.

Data analysis involves conversion of raw ADC spectra to helicity-based asymmetries. The energy calibration of the calorimeter is monitored continuously by tracking the position of the ADC pedestal and the Compton edge. The analyzing power for the polarimeter has been calculated using a detailed GEANT simulation of the apparatus. The polarimeter provides results for each SHR storage cycle with a typical precision of $\Delta P \approx .04$ for a fifteen minute fill.

Figure 1 shows the extracted polarization as a function of time for a representative set of data over a period of a few hours. The direction of the beam polarization at injection is reversed each time the SHR is filled. The beam polarization can also be adiabatically reversed while the beam is stored by ramping the driving frequency of a spin-flipping RF dipole [5]

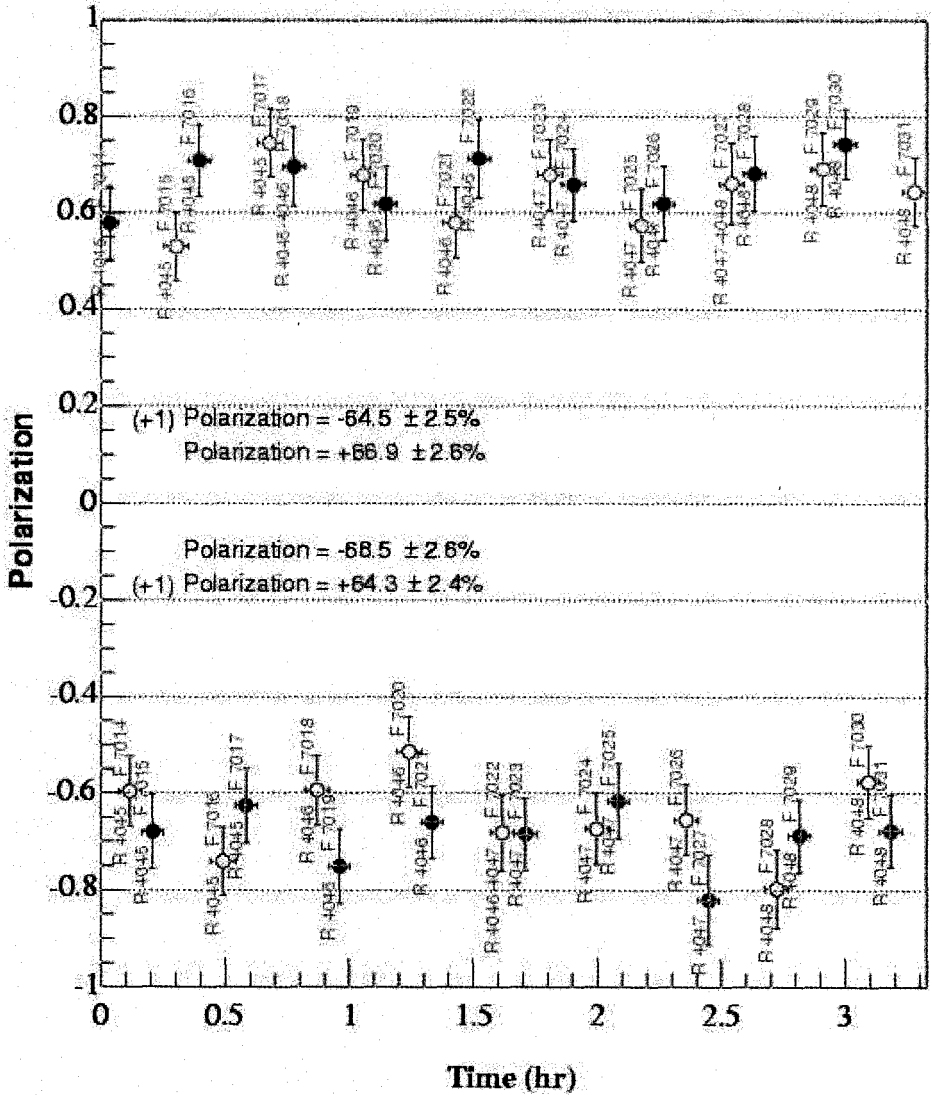


Fig. 1. Preliminary polarization measurements in the SHR.

through a depolarizing resonance of the SHR. This highly efficient device is helpful in constraining instrumental asymmetries resulting from effects such as helicity-correlated steering and polarization induced transport asymmetries (PITA) in the laser optical system. In Fig. 1, dark circles represent measurements of the initial polarization in the SHR, while open circles denote measurements following operation of the spin flipper. The average SHR beam polarization in 2004 is 0.66 with the results displaying a gaussian profile.

Long term uncertainties in the beam polarization are dominated by systematic uncer-

Table 1. Estimated systematic uncertainties for the MIT-Bates Compton Polarimeter.

Systematic Uncertainty Contribution	ΔP
A_{pol}	0.03
Pile-up	0.01
Beam alignment and PITA	0.02
Laser circular polarization	0.01
Spin precession uncertainty	0.01
Total	0.04

tainties in the polarimeter. Results have been compiled into a database for the BLAST experiment, allowing a detailed look at systematic behavior of the device. Consistency checks, including comparisons to low-energy polarization measurements in the polarized source and variation of the polarization angle upon injection into the SHR, are also used to assess the overall accuracy of the instrument. Table 1 provides a preliminary estimate of the error contributions from various sources to the overall level of systematic uncertainty. Much of the uncertainty results from uncertainties in modeling the analyzing power of the device, a quantity which is still being improved. Overall systematic error control and calibration uncertainty meet the levels required for completion of the BLAST program.

References

1. C. Crawford, A. Maschinot, and V. Ziskin, in these proceedings.
2. E. Tsentalovich, in these proceedings.
3. D. Barber et. al., *Nucl. Instr. and Meth.* **A329**, 79 (1993).
4. I. Passchier et. al., *Nucl. Instr. and Meth.* **A414**, 446 (1998).
5. V. Morozov et. al., *Phys. Rev. ST Accel. Beams* **4** 104002 (2001).

LOCAL POLARIMETRY FOR PROTON BEAMS WITH THE STAR BEAM BEAM COUNTERS

J. KIRYLUK

Massachusetts Institute of Technology, Cambridge, USA

(for the STAR Collaboration)

STAR collected data in proton-proton collisions at $\sqrt{s} = 200$ GeV with transverse and longitudinal beam polarizations during the 2003 running period at RHIC. We present preliminary results on single transverse spin asymmetries A_N in the production of forward charged hadrons detected with the Beam-Beam Counters (BBC). The asymmetries A_N measured at pseudorapidities $3.9 < |\eta| < 5.0$ are found to be of the order of 10^{-2} , while asymmetries measured at smaller pseudorapidities $3.4 < |\eta| < 3.9$ are found to be consistent with zero. The BBC and its associated scaler system for fast data recording provides the first local polarimeter at STAR. The set-up has been successfully used to tune the spin rotator magnets and to verify longitudinal polarization at STAR.

STAR is one of two large experimental facilities at the Relativistic Heavy Ion Collider (RHIC) at Brookhaven National Laboratory. One of the goals of the STAR physics program is to study the internal spin structure of the proton using collisions of longitudinally polarized protons at $\sqrt{s} = 200 - 500$ GeV. The stable beam polarization direction in RHIC is transverse, and thus needs to be rotated at the STAR Interaction Region (IR) to become longitudinal [1]. The magnitude of the beam polarization is measured at a different IR by the RHIC Coulomb-Nuclear Interference (CNI) pC polarimeter [1]. During the first (transversely) polarized proton running period in 2002, STAR measured single transverse spin cross-section asymmetries $A_N = (\sigma_{\downarrow} - \sigma_{\uparrow}) / (\sigma_{\downarrow} + \sigma_{\uparrow})$ at $\sqrt{s} = 200$ GeV in neutral pion [2] and charged hadron [3] production in the forward region. Additional sets of magnets were installed before and after the STAR IR before the second proton running period at RHIC in 2003 to obtain longitudinal polarization. Local polarimetry had been developed to measure the radial and vertical polarization components. We discuss the instrumentation and results below.

The Beam-Beam Counters (BBC) are scintillator annuli mounted around the beam pipe beyond the east and west poletips of the STAR magnet, 374 cm from the nominal IR. The small tiles of the BBC shown in Fig.1(a) provide full azimuthal coverage $\Delta\phi = 2\pi$ in the pseudorapidity range of $3.4 < |\eta| < 5.0$. A coincident signal from any of the 18 tiles on the east side and any of the 18 tiles on the west side of the IR constitutes a BBC coincidence.

The number of BBC coincidences is a measure of the luminosity \mathcal{L} . The BBC acceptance amounts to 53% of the total proton-proton cross section of $\sigma_{\text{tot}}^{pp} = 51$ mb. The BBC are used in STAR during proton runs to provide triggers, to monitor the overall luminosity, and to measure the relative luminosity for different proton spin orientations [3]. An example of the luminosity versus the bunch crossing number is shown in Fig. 1(b). Each bunch crossing can be uniquely related to the relative spin orientations of the protons in the colliding beams. The statistical accuracy of the relative luminosity measurement is typically $10^{-4} - 10^{-3}$. The high accuracy requires a fast BBC data acquisition system, consisting of a scaler board system^a. The scaler board is a 24 bit and 10 MHz VME memory module [4] with 2^{24} cells. Each cell is 40-bits deep to keep a continuous and deadtimeless record for up to 24 hours of operation at 10 MHz, which is the bunch crossing frequency at RHIC. Seven of the 24 bits are used to keep the bunch crossing number. The remaining 17 bits contain data from the fast detectors, such as the BBC. The BBC data input to the scalers consist of discriminator outputs from 16 individual PMTs and logic levels produced by the STAR level 0 trigger electronics (a BBC coincidence signal). In the spin asymmetry analysis described below, we used the data from two scaler boards for the BBC, one each on the east and west sides of the STAR IR. In an experiment with a transversely polarized beam and a left-right symmetric

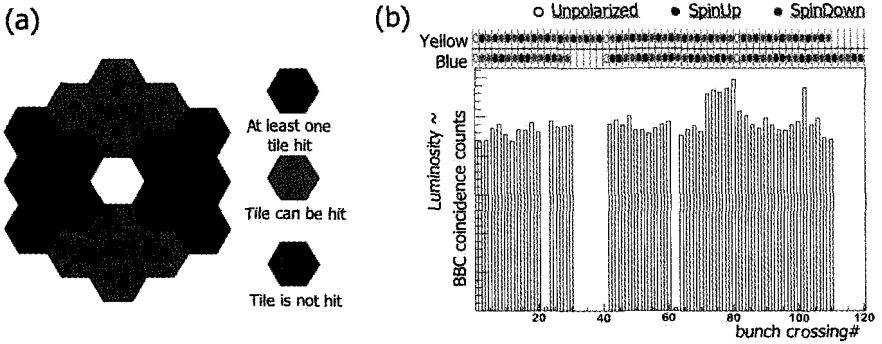


Fig. 1. (a) Schematic view of the BBC small tiles and event topology for charged particle Right scattering at $3.9 < \eta < 5.0$. (b) The number of coincidences between the BBC on either side of the IR versus bunch crossing for one data run.

detector, such as the BBC, the single spin asymmetry can be determined by measuring the beam polarization and the asymmetry of yields,

$$\epsilon_{\text{BBC}} = \frac{r_{ij} - 1}{r_{ij} + 1} \simeq \begin{cases} A_N^{\text{BBC}} \times P_v \times \langle \cos \phi \rangle & i, j = \text{Left, Right} \\ A_N^{\text{BBC}} \times P_r \times \langle \sin \phi \rangle & i, j = \text{Up, Down} \end{cases} \quad (1)$$

in which $r_{ij} = \sqrt{(N_i^\uparrow N_j^\downarrow) / (N_i^\downarrow N_j^\uparrow)}$ and $N_{i(j)}^{\uparrow(\downarrow)}$ are the spin dependent yields from the detector on the $i, j = \text{Left(Right)}$ or Up(Down) side of the beam, and $P_{v(r)}$ is the vertical (radial) beam polarization component. At RHIC both beams are polarized. Therefore, one needs to sum the yields for both spin orientations of one beam to measure a single spin asymmetry. False asymmetries due to differences in luminosities and acceptances cancel in Eq. 1. The BBC

^aAt average luminosities $\mathcal{L}_{\text{ave}} = 3.0 \times 10^{30} \text{ cm}^{-2} \text{ s}^{-1}$ the BBC coincidence rates are about 80 kHz, orders of magnitude higher than the STAR DAQ can handle.

segmentation allows the classification of the counted events by pseudorapidity (2 bins: Inner $3.9 < \eta < 5.0$ and Outer $3.4 < \eta < 3.9$ BBC rings) and azimuth. The group of four small tiles labeled by PMT numbers 1, 7 and 8 in Fig. 1(a) is referred to as Up, whereas the group of tiles 4, 12, and 13 is called Down. The remaining small tiles are labeled Left (Right) for the groups of tiles on the left (right). An example of the hit topology for the Inner-Right BBC event is shown in Fig. 1(a). Figure 2(a) shows the time variation of the

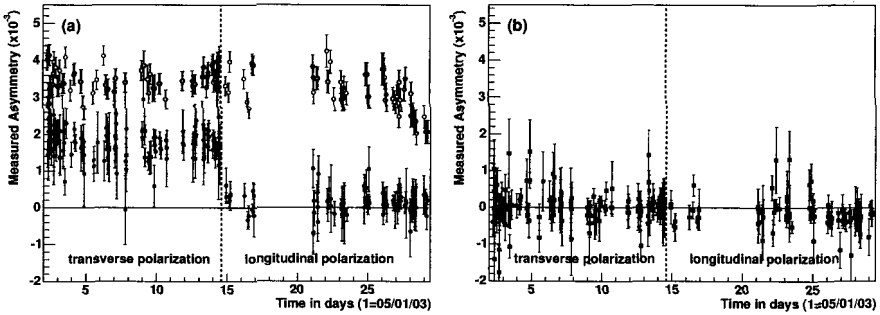


Fig. 2. Measured (a) 'Left-Right' (b) 'Up-Down' asymmetries (in parts per thousand) as a function of time (in days) since May 1 2003: BBC asymmetries (filled points) and CNI asymmetries (open points).

charged particle asymmetries determined with the BBC for $3.9 < \eta < 5.0$ (filled points) and the asymmetry measured with the RHIC CNI polarimeter [5] (open points). Each data point corresponds to one STAR run, which typically lasts for 30–60 min. The indicated uncertainties on the CNI and BBC asymmetries are statistical only. The dashed line indicates when the spin rotators at STAR were turned on and the transverse polarization direction in RHIC was made longitudinal at the STAR IR. From the data with transverse beam polarization at STAR we find that $A_N^{\text{BBC}} = 0.67(8) \times A_N^{\text{CNI}} \sim 1\%$ for $3.9 < \eta < 5.0$, while for smaller pseudorapidities, $3.4 < \eta < 3.9$, the BBC asymmetries are found to be $A_N^{\text{BBC}} = 0.02(9) \times A_N^{\text{CNI}}$ consistent with zero. The systematic uncertainty on the measured BBC asymmetry was estimated to be smaller than the statistical uncertainty, $\delta\epsilon_{\text{sys}} = 5 \times 10^{-5}$. The Left-Right asymmetries in the BBC are sensitive to the transverse polarization component, cf. Eq. 1. Their numerical values when the rotator magnets were on, that is when the beam polarization was longitudinal at the STAR IR, were significantly smaller. The currents in the rotator magnets were adjusted to make these asymmetries consistent with zero, while at the same time the CNI polarimeter - located at a different RHIC IR - continued to measure non-zero beam polarization. The asymmetries have also been evaluated with the Up and Down groups of tiles in the BBC, and are found to be close to zero for both transverse and longitudinal beam polarizations, cf. Fig. 2(b), as expected. In summary, the BBC and its associated scaler system provided the first local polarimeter at STAR. The measurement is based on the single transverse spin asymmetry A_N in the detection of charged hadrons produced at forward rapidities, and is fast and non-destructive. The set-up has been successfully used to tune the spin rotator magnets at STAR and to monitor residual vertical and radial

beam polarization components when the beam polarization was longitudinal.

References

1. Special Issue: RHIC and Its Detectors, Nucl. Instrum. Meth.A **499** (2003).
2. STAR, J. Adams et al., Phys. Rev. Lett. **92** (2004) 171801.
3. J. Kiryluk, AIP Conf. Proc. **675** (2003) 424.
4. H. Crawford, F. S. Bieser and T. Stezelberger, *The STAR Scaler Board, A 10 MHz 24-bit VME Memory Module*, to be published in Nucl. Instrum. Meth.
5. O. Jinnouchi et al., RHIC/CAD Accelerator Physics Note 171 (2004).

***p*-CARBON CNI POLARIMETERS AT BNL: THE FASTEST PHYSICS SETUP IN THE WORLD**

I. ALEKSEEV¹, A. BRAVAR², G. BUNCE^{2,3}, S. DHAWAN⁴, R. GILL², H. HUANG², G. IGO⁵,
O. JINNOUCHI³, V. KANAVETS¹, K. KURITA⁶, Z. LI², H. OKADA⁷, S. RESCIA², N. SAITO⁷,
H. SPINKA⁸, D. SVIRIDA¹, D. UNDERWOOD⁸, C. WITTEN⁵, J. WOOD⁵

¹ITEP, ²BNL, ³RBRC, ⁴Yale Univ.,
⁵UCLA, ⁶Rikkyo Univ., ⁷Kyoto Univ., ⁸ANL

Recent years of polarized proton running at BNL have proved the effectiveness of using the analyzing power of pC elastic scattering in the CNI region for proton beam polarimetry. Excellent performance of the polarimeters at both RHIC and AGS allowed fast and detailed beam polarization studies, including polarization loss, during the accelerator ramp, profile measurements, and spin rotation. Based on the latest achievements of digital electronics, the DAQ system uses signal waveform processing in FPGA crystals, and allows on-the-flight selection of up to 500 million elastic pC events per second with no dead time. Principles of operation of the polarimeters and of the DAQ system are presented, together with selected performance examples.

The research program with polarized protons at the BNL collider-accelerator complex demands a fast and cost effective tool for beam polarization measurements in a wide energy range with a few percent accuracy. In 1999 the experiment E950 [1] at AGS proved the general concept of using pC elastic scattering in the CNI region for proton polarization measurements, and evaluated the analyzing power of the process. This appeared very promising because of the small energy dependence of A_N predicted by theory [2], and the nearly fixed 90° recoil kinematics in the whole energy range. Yet the small value of the analyzing power of several percent requires huge statistics of about $2 \cdot 10^7$ for a single polarization measurement. Fortunately the large cross section of the process allows the collection of such statistics in seconds, at event rates of millions per second. In addition to the rate issue, recoil carbon identification is necessary for background suppression along with measurement of transferred momentum, because of the strong $-t$ dependence of A_N . Moreover, a system dead time, if correlated with polarization sign change, can produce unrecognizable false asymmetries. Thus the most critical part of the setup is a very fast (dead-timeless) DAQ system meeting the above requirements.

Such a system was built based on fast waveform digitizer [3] (WFD) modules recently developed at Yale University. Signals from Si strip detectors are preamplified, transferred

and shaped to obtain short (40 ns FW) pulses with amplitude proportional to the charge deposited in the detector. The pulse shapes are then digitized at the equivalent frequency of 420 MHz and analyzed inside the modules, providing the recoil carbon deposited energy and time of flight. The events are then filtered through lookup tables (LUT), checking the kinematic correspondence between the obtained values for carbon identification. The selected events are used to increment scalers and histograms in the modules, and can be stored in the on-board memory. The main advantage of such an approach is that there is no data transfer to the host computer during a data taking run, which makes the system really dead-timeless. The analyzing part is capable of processing of one event per RHIC bunch crossing period (110 ns), resulting in a maximum of $\approx 10^7 \text{ s}^{-1}$ events per channel.

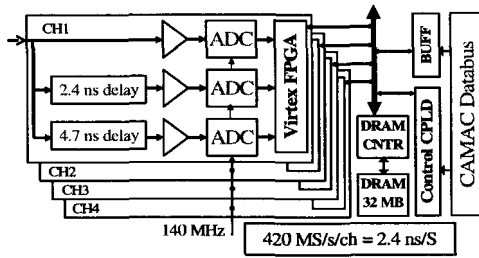


Fig. 1. Block diagram of the WFD module.

The WFD is a CAMAC module hosting four independent channels (Figure. 1) with common storage SDRAM (64 Mbyte) and CAMAC control circuitry. In each channel the input signal is split into three, two of which are delayed by 1/3 and 2/3 of the ADC digitization period. Three 8-bit ADCs synchronously start conversions at 140 MHz, resulting in triple equivalent digitization frequency. All the waveform analysis is done inside the Virtex-E Xilinx FPGA [4] chip at 70 MHz clock frequency. The analysis algorithm is rather specific since it has to process six waveform points in parallel (the FPGA clock is only 1/6 of the digitization frequency). The block diagram of the analyzing circuits in the FPGA is shown in Figure. 2. The input signal passes through a digital filter for noise reduction and partial compensation for different amplifications of delayed sub-channels. A level trigger is used to determine the presence of a significant signal in a particular bunch crossing period, and if the signal is not detected, the ADC values are used for baseline calculations. The baseline is determined individually for all three sub-channels to compensate for different amplifier offsets, and is averaged over the 16 latest bunch crossing periods with no significant signal. The baseline is then subtracted and the signal is stored in a FIFO, from which it can be directly read out as a waveform or taken for further analysis. The analysis is of the conveyor type and takes up to 5 stages, each stage corresponding to a sequential bunch crossing. On the first stage the whole waveform is used to define the signal amplitude (maximum), integral, and time at maximum. The second stage implements 1/4 constant fraction discriminator (CFD) based on the amplitude value defined in the first stage. The CFD time and amplitude are then used to filter the event through a LUT, which is preprogrammed

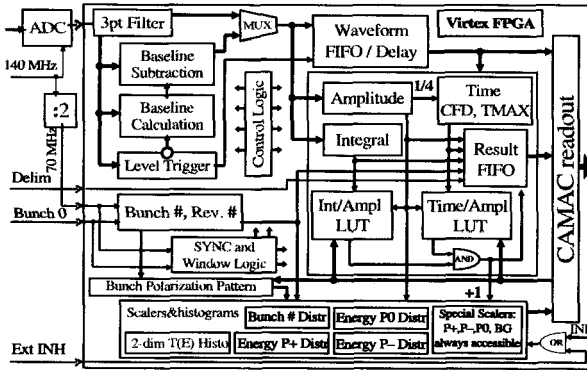


Fig. 2. Simplified block diagram of one WFD channel.

to respond to the energy-TOF correlation specific for carbon nuclei. Another LUT is used to compare the amplitude and integral values, which deviate from proportionality if two particles arrive within one bunch crossing. If both LUTs report a positive result, all signal parameters are stored in the result FIFO and used to fill the on-board histograms. The FPGA keeps track of the bunch and revolution numbers, as well as of the bunch polarization pattern, which allows a variety of histograms, including distributions of the energy (polarization sorted), bunch number and 2D time-amplitude histograms. Their contents can be read out after the data taking and is sufficient for beam polarization determination. Yet for better understanding and debugging purposes the signal parameters from the result FIFO can be transferred to the on-board storage memory, limiting the maximum event rate to $3 \cdot 10^6 \text{ s}^{-1}$ per channel.

With the carbon event rate up to 10^6 s^{-1} and 20–60 s target-in-the-beam time for a typical $2 \cdot 10^7$ event polarization measurement, about a thousand regular measurements were done at RHIC in proton run-2004. The extremely flexible and powerful design due to the use of FPGA allows a variety of specific beam studies in RHIC and the AGS, including polarization loss on the ramp (Figure 3a), polarization profile, and bunch by bunch polarization measurements (Figure 3b). Good spin physics is also done with the polarimeters, including measurements of the $-t$ dependence of the pC analyzing power at different energies (see [5]). The shape of the dependence reveals the non-vanishing contribution of the hadronic spin flip amplitude to the process. Thus the pC CNI polarimeters at the BNL collider complex with the dead-timeless DAQ system based on the WFD has proved to be a real success during the last few years.

References

1. J. Tojo et al., *Phys. Rev. Lett.* **89**, 052302 (2002).
2. N.H. Buttimore et al., *Phys. Rev.* **D59**, 114010 (1999).
3. S. Dhawan, private communication.
4. <http://direct.xilinx.com/bvdocs/publications/ds022.pdf>.
5. O. Jinnouchi et al., A. Bravar et al., *these proceedings*.

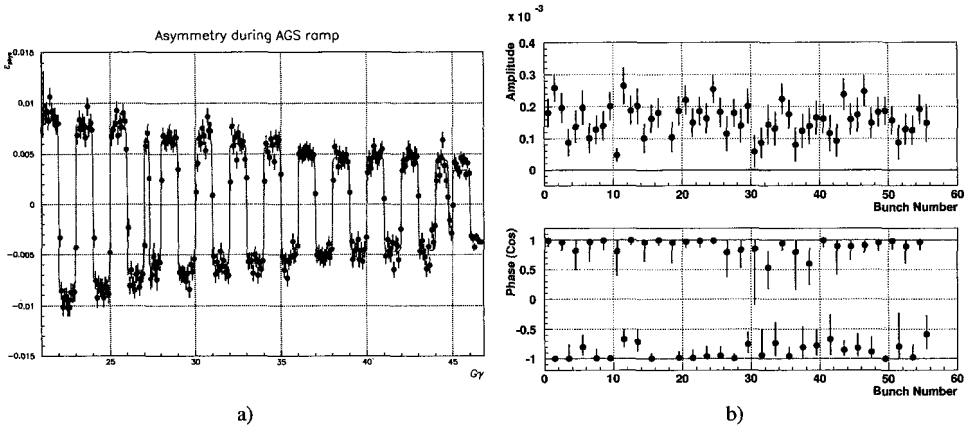


Fig. 3. Polarimeter performance examples: a) raw asymmetry during the AGS acceleration ramp, spin flips every $G\gamma = 1$ and at depolarizing resonances, beam energy is $E_{\text{beam}} = 0.524 \cdot G\gamma$; b) bunch by bunch raw asymmetry (upper) and spin orientation (lower) from a single typical measurement, RHIC, 55 bunch mode.

SPIN OSCILLATIONS IN STORAGE RINGS

A. J. SILENKO

Institute of Nuclear Problems, Belarusian State University, Minsk, Belarus

The dependence of the particle rotation frequency on the particle orbit perturbations is found. The exact equation of spin motion in the cylindrical coordinate system is derived. The calculated formula for the frequency of $g-2$ precession is in excellent agreement with previous results. Nevertheless, this formula contains an additional oscillatory term that can be used for fitting. The influence of spin oscillations on the spin dynamics in the EDM experiment is negligible.

The goal of this investigation is to obtain general formulae for spin oscillations in storage rings. The problem is very important because such oscillations change spin motion parameters. The spin oscillations are caused by coherent betatron oscillations (CBOs) and field distortions. In the particle rest frame, coherent betatron oscillations lead to oscillations of magnetic field acting on the particle and its spin. As a result, the spin oscillates. These oscillations result in a change of the spin rotation frequency in the $g-2$ experiment. If the particle possesses an electric dipole moment (EDM), they change the vertical spin motion measured in the EDM experiment. Perhaps spin oscillations can also affect other experiments.

It is quite natural to describe spin motion in a cylindrical coordinate system. However, the axes of this system are defined by the position of the particle, which rotates and oscillates. The transformation of the Bargmann-Michel-Telegdi (BMT) [1] equation to cylindrical coordinates should be performed with an allowance for oscillatory terms in the particle motion equation.

It is convenient to use the unit vector, $n = p/p$, which defines the direction of particle motion. The particle motion equation takes the form

$$\frac{dn}{dt} = \omega \times n, \quad \omega = -\frac{e}{\gamma m} \left(B - \frac{n \times E}{\beta} \right),$$

where ω is the angular velocity of the particle rotation.

Vertical and radial CBOs change the planes of particle and spin motion. The (pseudo)vectors of the angular velocities are tilted. The angle Φ between two positions of any rotating vector n does not equal the angle ϕ between two corresponding horizontal

projections. Therefore, any additional field changes the instantaneous frequencies of particle and spin motion. The average frequencies of particle or spin motion in the tilted and horizontal planes are the same.

The instantaneous angular velocity of particle or spin rotation in the horizontal plane is

$$\dot{\phi} = \frac{(n_{\parallel} \times \dot{n}_{\parallel}) \cdot e_z}{|n_{\parallel}|^2} = \omega_3 - \frac{(\omega_1 n_1 + \omega_2 n_2) n_3}{1 - n_3^2}, \quad (1)$$

where $1 \Rightarrow e_x$ or e_{ρ} , $2 \Rightarrow e_y$ or e_{ϕ} , $3 \Rightarrow e_z$. This equation is exact.

Usually we take into account only perturbations of particle orbits caused by vertical and radial CBOs. In this case,

$$n_1 = n_{\rho} = p_{\rho}/p = \rho_0 \sin(\omega_y t + \alpha), \quad n_3 = n_z = p_z/p = \psi_0 \sin(\omega_p t + \beta).$$

The second term in Eq. (1) is of the third order in the angular amplitudes of oscillations, ρ_0 and ψ_0 . Moreover, it oscillates, and therefore averages to zero. If we take into account only second-order terms in the angular amplitudes, the last term in Eq. (1) is negligible. Approximately, $\dot{\phi} = \omega_3$. The horizontal axes (e_{ρ} and e_{ϕ}) rotate with the instantaneous angular velocity $\omega' = \dot{\phi} e_z$.

Formulae for the electric dipole moment (EDM) can be obtained from the corresponding formulae for the anomalous magnetic moment by the substitution $B \rightarrow E$, $E \rightarrow -B$, $g-2 \rightarrow \eta$. The inclusion of the particle EDM leads to the following modification of the BMT equation:

$$\begin{aligned} \frac{ds}{dt} &= \Omega \times s, \quad \Omega = \Omega_{BMT} + \Omega_{EDM}, \\ \Omega_{BMT} &= -\frac{e}{m} \left[\left(a + \frac{1}{\gamma} \right) B - \frac{a\gamma}{\gamma+1} \beta(\beta \cdot B) - \left(a + \frac{1}{\gamma+1} \right) (\beta \times E) \right], \\ \Omega_{EDM} &= -\frac{e\eta}{2m} \left(E - \frac{\gamma}{\gamma+1} \beta(\beta \cdot E) + \beta \times B \right), \quad a = \frac{g-2}{2}, \end{aligned} \quad (2)$$

where Ω means the angular velocity of spin rotation in Cartesian coordinates, and Ω_{BMT} is defined by the BMT equation. The EDM does not affect the particle motion. As a rule, we can neglect the term $\frac{\gamma}{\gamma+1} \beta(\beta \cdot E)$.

The spin motion equation in the cylindrical coordinate system takes the form

$$\begin{aligned} \frac{ds_{\rho}}{dt} &= \frac{ds}{dt} \cdot e_{\rho} + s \cdot \frac{de_{\rho}}{dt} = s \cdot (e_{\rho} \times \Omega) + \dot{\phi} s_{\phi}, \\ \frac{ds_{\phi}}{dt} &= \frac{ds}{dt} \cdot e_{\phi} + s \cdot \frac{de_{\phi}}{dt} = s \cdot (e_{\phi} \times \Omega) - \dot{\phi} s_{\rho}, \\ \frac{ds_z}{dt} &= s \cdot (e_z \times \Omega). \end{aligned} \quad (3)$$

We can introduce a coordinate system with axes e_1, e_2, e_3 , corresponding to the axes e_{ρ}, e_{ϕ}, e_z , respectively. For such a system, Eq. (3) can be rewritten in the form:

$$\frac{ds}{dt} = \omega_a \times s, \quad \omega_a = \Omega - \dot{\phi} e_3 \quad (4)$$

or

$$\begin{aligned} \omega_a &= -\frac{e}{m} \left\{ aB - \frac{a\gamma}{\gamma+1} \beta(\beta \cdot B) + \left(\frac{1}{\gamma^2-1} - a \right) (\beta \times E) + \frac{1}{\gamma} [B_{\parallel} \right. \\ &\left. - \frac{1}{\beta^2} (\beta \times E)_{\parallel}] + \frac{\eta}{2} \left(E - \frac{\gamma}{\gamma+1} \beta(\beta \cdot E) + \beta \times B \right) \right\} + \frac{(\omega_1 n_1 + \omega_2 n_2) n_3}{1 - n_3^2} e_3, \end{aligned} \quad (5)$$

where the sign \parallel means the components parallel to the x_1x_2 -plane. Eqs. (4) and (5) are exact, and ω_a is the angular frequency of g-2 precession. These equations describe the spin motion in an arbitrary storage ring, with an allowance for the particle and spin oscillations and the EDM. As a rule, the last term in Eq. (5) is negligible.

In the g-2 experiment, the influence of the vertical CBO (pitch) on the spin rotation frequency has been calculated by Farley [2, 3]. The result has been confirmed by Field and Fiorentini [4] and computer simulations.

The horizontal CBO (yaw) does not give any significant corrections.

With the above formulae, the theory of spin oscillations in the g-2 experiment can be developed in a very general form. The spin motion perturbed by the vertical CBO is described by the equation

$$\frac{ds}{dt} = \{a_0 + a_3 \cos[2(\omega_p t + \phi_p)]\} (e_3 \times s) + a_2 \cos(\omega_p t + \phi_p) (e_2 \times s) + a_1 \sin(\omega_p t + \phi_p) (e_1 \times s), \quad (6)$$

where a_1 and a_2 are first-order quantities and a_3 is a second-order quantity in the angular pitch amplitude. The quantity ω_p is the angular pitch frequency.

This equation has an exact solution. The averaged g-2 frequency is

$$\omega_a = \omega_0(1 - C), \quad C = \frac{1}{4} \psi_0^2 \left[1 - \frac{\omega_0^2}{\gamma^2(\omega_0^2 - \omega_p^2)} - \frac{\omega_p^2(f-1)(f-1+2/\gamma)}{\omega_0^2 - \omega_p^2} - \frac{(\gamma-1)^2\omega_0^2 - f^2\gamma^2\omega_p^2}{\gamma^2(\omega_0^2 - \omega_p^2)} \langle \cos[2(\omega_0 t + \phi_0)] \rangle \cdot \frac{1 + s_3^{(0)2}}{1 - s_3^{(0)2}} \right], \quad (7)$$

where

$$f = 1 + a\gamma - \frac{1+a}{\gamma} = 1 + a\beta^2\gamma - \frac{1}{\gamma} \quad \text{and} \quad f = 1 + a\gamma$$

for electric and magnetic focusing, respectively.

The average value of the last term oscillating with frequency $2\omega_0$ is zero. Therefore, formula (7) is in agreement with previous results [2–4] found for the particular case $s_3^{(0)} = 0$. However, it is possible to include the oscillatory term in a fitting process instead of eliminating it. In the current g-2 experiment, $f = 1$, $s_3^{(0)} = 0$, $\gamma \gg 1$, ϕ_0 equals 0 or π , and formula (7) takes the form

$$\omega_a = \omega_0(1 - C), \quad C = \frac{1}{4} \psi_0^2 [1 - \langle \cos(2\omega_0 t) \rangle].$$

This formula shows that the inclusion of the oscillatory term in a fitting process is possible.

In the EDM experiment, the spin motion in the horizontal plane is strongly restricted by the radial electric field. In this case, spin rotation about the radial axis becomes very important because this rotation imitates the EDM effect.

The vertical CBO leads to spin motion described by the equation

$$\frac{ds}{dt} = \{a_0 + a_3 \cos(\omega_p t + \phi_p)\} (e_3 \times s) + a_1 \sin(\omega_p t + \phi_p) (e_1 \times s),$$

where $1 \Rightarrow e_\phi$, $2 \Rightarrow e_z$, $3 \Rightarrow e_\rho$, and a_1 and a_3 are first-order quantities in the pitch amplitude. This equation also has an exact solution. The averaged angular frequency is given by

$$\omega_a = a_0 + \frac{a_0 a_1^2}{4(a_0^2 - \omega_p^2)} \left[1 + \langle \cos[2(a_0 t + \phi_0)] \rangle \cdot \frac{1 + s_3^{(0)^2}}{1 - s_3^{(0)^2}} \right] + \frac{a_1 a_3}{2\omega_p} \cdot \frac{s_3^{(0)}}{s_{\parallel}^{(0)}} \langle \sin(a_0 t + \phi_0) \rangle .$$

In the EDM experiment

$$\omega_a = \omega_0 \left(1 - \frac{\alpha^2 \omega_c^2}{2\omega_p^2} \psi_0^2 \right),$$

where ω_c is the cyclotron frequency.

The yaw correction for the EDM experiment is nonzero:

$$\omega_a = \omega_0 \left[1 + a(\gamma - 1)\gamma \left(\frac{\omega_p^2}{2\omega_c^2} - \frac{1}{g} \right) \rho_0^2 \right].$$

However, vertical and radial CBOs give only small corrections to the systematic errors caused by the vertical electric field. Since these systematic errors must be eliminated, the corrections for the vertical and radial CBOs are negligible.

References

1. V. Bargmann, L. Michel, and V. L. Telegdi, *Phys. Rev. Lett.* **2**, 435 (1959).
2. F. J. M. Farley, *Phys. Lett. B* **42**, 66 (1972).
3. F.J.M. Farley and E. Picasso, in *Quantum Electrodynamics*, ed. by T. Kinoshita (World Scientific, Singapore, 1990).
4. J.H. Field and G. Fiorentini, *Nuovo Cim.* **A21**, 297 (1974).

SUPPRESSION OF COHERENT BETATRON OSCILLATIONS IN THE MUON (g-2) EXPERIMENT

I. A. KOOP, A. V. OTBOEV, E. A. PEREVEDENTSEV, P. Y. SHATUNOV, Y. M. SHATUNOV

Budker Institute for Nuclear Physics, Novosibirsk, Russia

1. Introduction

The concept of the muon g-2 experiment is to detect electrons from muon decays $\mu^\pm \rightarrow e^\pm + \nu$ [1]. The counting rate $\dot{n}(t)$ of such events in any local electron counter depends on muon spin direction, which changes from turn to turn due to anomalous spin precession ω_a in a homogeneous magnetic field. In the ideal case, the electron counting rate changes with time as:

$$\dot{n}(t) \sim N_0 \cdot e^{-\frac{t}{\tau_\mu}} \cdot [1 + A \cos(\omega_a t + \phi)], \quad (1)$$

where N_0 is the initial number of muons; τ_μ is the muon life time at the experimental energy 3.095 GeV.

However, it appears that residual coherent betatron oscillations of the beam centroid due to imperfect injection lead to additional parasitic amplitude and phase modulations of $\dot{n}(t)$. The result is to complicate the spin precession frequency determination, and introduces a serious systematic error.

The modulation effect decreases in time due to the “natural” chromaticity of the betatron oscillations, which slightly mix the phases of the particle oscillations. Unfortunately the decoherence time is about 20 times longer than the muon life time $\tau_\mu = 6.43 \cdot 10^{-5} \text{ sec}$ at the energy of the experiment. This paper proposes to introduce fast phase mixing by inserting in the machine lattice a nonlinear focusing element. The nonlinearity creates a dependence of betatron tunes ($\delta Q/\delta a^2$) on oscillation amplitudes [2], and mixes particles in transverse phase space.

These considerations show that CBO modulation could be minimized during several tens of turns. Much longer times (up to $0.8 \cdot \tau_\mu \approx 300$ turns) have been used in experiments on beam scraping by pulsed closed-orbit distortion. The proposed method will scrape the beam while at the same time making the CBO vanish.

2. Nonlinear tracking

The rectangular symmetry of the vacuum chamber allows only an octupole coil to be installed inside it. We have chosen a two-metre long coil, located in a section free of electrostatic focusing and kickers. A number of tracking simulations with 10000 muons have been done for the real g-2 ring with various starting angles and for different octupole strengths. Assuming homogeneous vertical and radial phase-space distributions at injection, up to 100 turns were tracked within the aperture limitations ($\approx \pm 4.5\text{cm}$). The result of one tracking run with octupole “on” is presented in Fig. 1, where (“a” and “b”) are initial and (“c” and “d”) are final distributions. One can see the disappearance of the horizontal asymmetry, as with beam scraping. Particle losses do not exceed 50 percent and are not sensitive to reasonable variations of the residual angle.

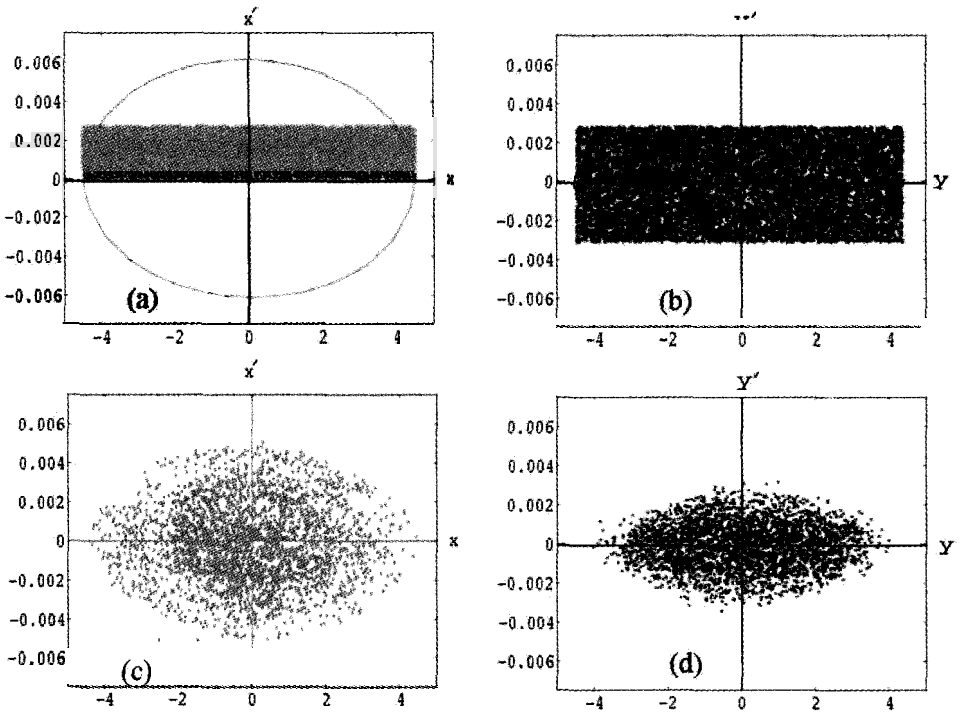


Fig. 1. Initial and final phase space distributions

Numerically the amplitude of the CBO can be evaluated after each turn by the expression:

$$A = \sqrt{\gamma_x \langle x \rangle^2 + 2\alpha_x \langle x \rangle \langle \dot{x} \rangle + \beta_x \langle \dot{x} \rangle^2 + \gamma_y \langle y \rangle^2 + 2\alpha_y \langle y \rangle \langle \dot{y} \rangle + \beta_y \langle \dot{y} \rangle^2}, \quad (2)$$

where $\langle x \rangle \langle \dot{x} \rangle$, $\langle x \rangle^2$, $\langle y \rangle \langle \dot{y} \rangle$, $\langle y \rangle^2$ are averaged over the ensemble coordinates and angles, and their squares. α , β and γ — are the corresponding Twiss parameters.

The Fig. 2 shows the behaviour of the CBO amplitude versus turn number for different octupole strengths. The CBO vanishes at around the 30th turn with octupole gradient 0.8 Gauss/cm². The tracking also shows this dip, and the later beating of the amplitude does not depend on the residual angle. It must be underlined that simultaneously with the CBO, a beam size modulation at twice the betatron frequency, caused by a mismatch between the machine and transfer channel, also disappears.

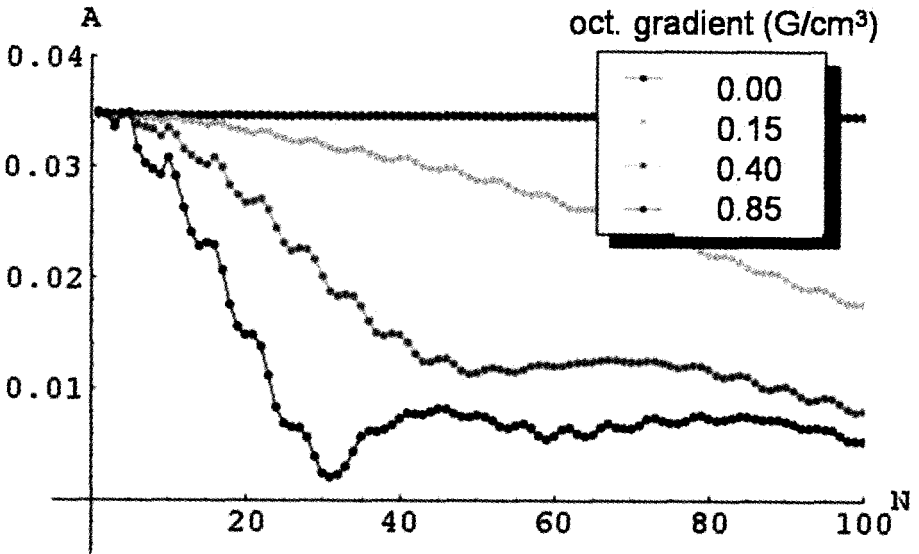


Fig. 2. Behaviour of the CBO amplitude

3. Octupole parameters

To leave the machine aperture free, the coil has to be wound around an area of 6 cm radius. The optimal octupole of gradient 0.8 Gauss/cm² in such a design can be obtained with a coil current of 2.5 kA.

It is clear that the octupole field has to be zeroed after CBO suppression. Modern electronics can easily form an arbitrary current pulse shape. But, since the simulations for a cosine pulse show no big difference from a rectangular one, we suggest using half a period ($T \approx 20 \mu\text{sec}$) of a simple generator: a capacitor "C" discharges through the octupole coil synchronously with the injection, and charges back through a bypass to a required voltage V_0 . It is then easy to estimate that $C \approx 1 \mu\text{F}$, and V_0 has to be $\approx 6.0 \text{ kV}$. The octupole coil can be made from water-cooled copper pipe of 1 cm diameter. The energy dissipated in such a coil is about 20 J per pulse.

It is also clear that the pulsed octupole field is confined practically within the vacuum chamber due to its wall thickness, which is about 15 skin depths at 50 kHz)

Alternatively, an electrostatic octupole is able to do the same, but its realization looks much less practical.

4. Conclusion

Tracking simulations have shown that the proposed pulsed octupole is able to reduce CBO oscillations to the stochastic level, the same size as beam modulations during 30 turns before the tracking. Additional beam scraping is not required.

To estimate real beam losses induced by the octupole, more careful tracking is needed with calculated beam phase space distributions at injection.

The construction and installation of this octupole coil and its power supply are not demanding.

The fall out octupole magnetic field will be not essential for the fixed NMR probe measurements.

Acknowledgments

We would like to thank members of the g-2 community for interest in this work and useful discussions.

References

1. G.W.Benett et al, "Measurement of the positive muon anomalous magnetic moment to 0.7 ppm", *Phys.Rev.Lett.* 89(2002)101.
2. L.D.Landau, E.M.Lifshitz, "Mechanics", Moscow "Nauka" (1988)

THE MIT-BATES SOUTH HALL RING: A UNIQUE INSTRUMENT FOR STUDYING POLARIZATION *

W. A. FRANKLIN

MIT-Bates Linear Accelerator Center, Middleton, USA

(for the BLAST Collaboration)

The MIT-Bates South Hall Ring (SHR) is a unique facility for carrying out experiments with polarized electron beams and polarized internal targets at energies up to 1 GeV. In its storage mode, the SHR delivers one of the most intense polarized electron beams in the world. This paper describes the characteristics of the SHR electron beam during experiments with the BLAST Spectrometer. Preliminary measurements of the beam polarization are shown and discussed.

The MIT-Bates Linear Accelerator Center is a facility which delivers intense polarized electron beams for a diverse set of experiments. The accelerator can operate in several distinct modes. In the standard mode, polarized electrons are accelerated from a polarized source through a 500 MeV linac at repetition rates as high as 600 Hz. The beam may be recirculated to reach energies of up to 1 GeV. This mode has been used for fixed target experiments such as SAMPLE [1].

Electron pulses from the accelerator may also be injected into the South Hall Ring (SHR) to achieve beams of high duty cycle. The South Hall Ring has a racetrack design with two long straight sections and a 190 m circumference. It contains 16 dipoles and a single RF cavity operating at 2.856 GHz. The SHR can operate in a pulse stretcher mode in which beams circulate for a limited number of turns while being slowly extracted for external target experiments. More often, the SHR is operated in its storage mode, in which electron pulses are gradually stacked in the ring to yield a long-lived continuous-wave beam. The beam usually circulates for several minutes, and passes through a thin internal target on each turn.

Since 2002, the SHR has been used almost exclusively to deliver stored beam to experiments with the Bates Large Acceptance Spectrometer Toroid (BLAST). Properties of the beam in storage mode are therefore tailored to meet the needs of the BLAST experimental

*This work has been supported by the U. S. Department of Energy under Cooperative Agreement BEFC294ER40818.

program, which requires a beam with high average intensity and high duty cycle. BLAST experiments utilize a spectrometer with an open configuration, a sensitive set of detectors, and a narrow internal target storage cell with a very delicate coating. This combination imposes strict limits on the tolerable levels of beam halo and experimental background. Finally, the experiments demand a high degree of longitudinal polarization at the target. Typical operating conditions for BLAST experiments at 850 MeV feature peak currents of 175 mA and 65% polarization, making the SHR polarized electron beam among the most intense in the world.

Stored beam in the SHR is achieved through a highly automated filling cycle based on the EPICS Control System. Pulses, of typical duration 2.3 μ s and peak intensity 2 mA, are injected into the SHR at a rate of 10 Hz to allow for the ring's damping time. The filling cycle is linked with the BLAST high voltage control software, allowing detectors to be gated off during injection. The entire filling cycle typically requires about 90 seconds, whereas stored beams usually circulate for a period of at least 15 minutes. Beam lifetime is governed by the internal target thickness, but can exceed 40 minutes in the absence of a target.

To achieve the very high beam quality required for BLAST experiments, the SHR is outfitted with a comprehensive set of diagnostics, including 32 sets of beam position monitors and a synchrotron light monitor which yields information on the beam profile. A tune sweeper permits measurements of dynamic properties of the beam at the outset and conclusion of a filling cycle. These elements are essential for steering the beam through the target cell, which forms an aperture 15 mm in diameter and 60 cm in length, and the 10-mm diameter tungsten collimator which shields it. To achieve best performance, slightly different orbits are used for injection and storage, with the SHR steering correctors ramped to make a smooth transition between the two. A set of plastic scintillators located close to the beamline provides rapid feedback on the level of beam halo and on the position of a set of halo slits used to minimize background.

Several devices work in conjunction to produce high longitudinal polarization at the BLAST internal target. Longitudinal polarization at injection into the SHR can be dialed in using a Wien filter in the Bates polarized source. Because the beam polarization precesses as it traverses the ring, a full Siberian Snake is required to restore longitudinal polarization at the BLAST target. The beam polarization is measured continuously by a Compton polarimeter [2] located upstream of the BLAST target. An RF dipole [3] is located downstream of the target, which can be used to adiabatically reverse the polarization direction of the stored beam with high efficiency. The frequency at which the RF dipole induces a spin flip provides a very sensitive measurement of the SHR spin tune, and was used to establish a calibration of the fractional snake strength with accuracy better than 0.1%.

The polarization in the South Hall Ring has averaged 0.66 ± 0.04 (systematic) in 2004 and is generally stable as a function of time to within a few percent. This figure is consistent with measurements at low energy in the polarized source. Preliminary measurements of the SHR longitudinal polarization during a portion of the 2004 run are shown in Figure 1. During the early stages of beam development, substantial losses of polarization were observed

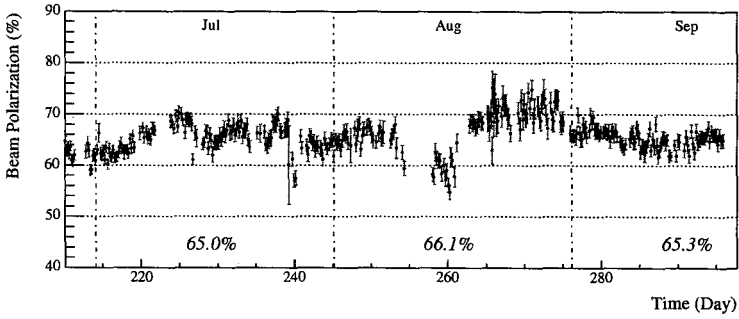


Fig. 1. Preliminary polarization measurements during SHR operation in 2004.

for certain ring parameters. Such effects were most pronounced for high intensity beams, and were correlated with tune spreading in the electron beam. Although this study was too limited in scope to produce a detailed resonance map, it led to restricting the betatron tunes used for ring operation during BLAST experiments ($\nu_x = .38 \pm .02, \nu_y = .17 \pm .01$). Similar issues will need to be addressed by future high intensity devices based on storage rings, such as a proposed electron-ion collider [4].

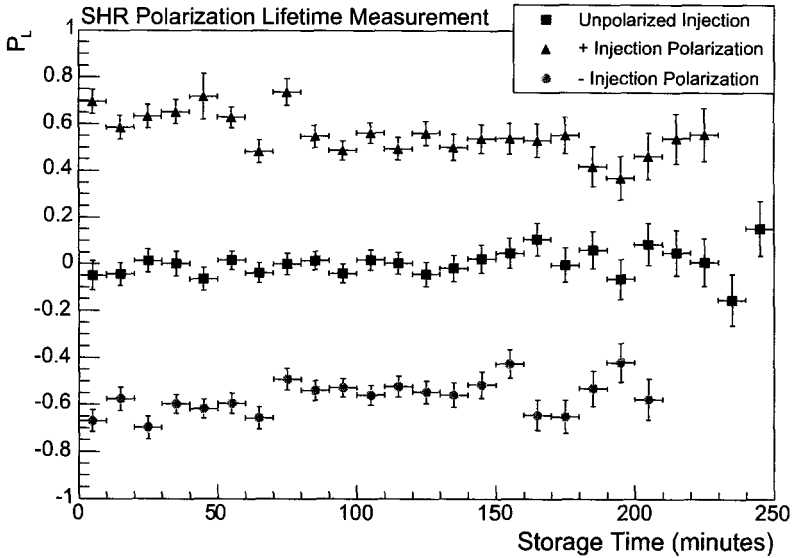


Fig. 2. Preliminary polarization measurements vs. storage time in the SHR.

The SHR polarization lifetime is very long compared to the beam lifetime. Measurements were carried out in which beams were injected into the Ring at 190 mA and allowed to circulate for several hours. Preliminary polarization data taken for these conditions are in Fig. 2. For very long storage times, the beam current decays to the point that it is no longer

possible to obtain a statistically accurate measurement. Measurements were performed with two different initial electron polarization directions and with initially unpolarized beams. From these data a mean polarization lifetime of 810 ± 190 minutes was extracted, a number which is slightly shorter than predictions of 1100 minutes. No conclusive evidence of radiative polarization of the beam was observed.

In summary, operation of an intense polarized electron beam in the SHR is now routine for polarized internal target experiments. Integrated charge is accounted for on a daily basis with more than 10 kiloCoulombs of charge typically delivered to the SHR internal target. This beam has enabled the success of a frontier experimental program using BLAST [5].

References

1. R. Hasty et. al., *Science* **290**, 2117 (2000).
2. W.A. Franklin, *AIP Conf. Proc.* **675**, 1058 (2003).
3. V.S. Morozov et. al., *Phys Rev. ST Accel. Beams* **4** 104002 (2001).
4. L. Ahrens et. al., eRHIC Zeroth-Order Design Report (2004).
5. C. Crawford, V. Ziskin, A. Maschinot in these proceedings.

POLARISATION IN THE eRHIC ELECTRON (POSITRON) RING

D. P. BARBER

Deutsches Elektronen-Synchrotron (DESY), Hamburg, Germany

(for the eRHIC Team [1])

We report on the status of, and plans for, calculations of the spin polarisation in the electron (positron) ring of the eRHIC complex.

Introduction

This article gives an update on calculations of electron and positron (e^\pm) polarisation for the 5–10 GeV ring in the ring–ring version of eRHIC. This is the proposed high luminosity e^\pm –proton(ion) facility in which longitudinally polarised e^\pm would collide with high energy longitudinally polarised protons or with ions in the Relativistic Heavy Ion Collider (RHIC) at Brookhaven National Laboratory (BNL). The basic concepts of the project are described in the Zeroth–Order Design Report [1]. See Fig. 1.

Polarisation in the e^\pm ring and calculations

e^\pm circulating in the (vertical) guide field of a storage ring emit synchrotron radiation (SR) and can become polarised by the Sokolov–Ternov (S–T) effect. In the case of an ideal simple flat ring the polarisation reaches a value of $\frac{8}{5\sqrt{3}} = 92.4\%$ and points along the guide field in the arcs [2]. The polarisation rate is proportional to the fifth power of the energy. For example, for the e^\pm ring of eRHIC the S–T polarisation time is about 11 hours at 5 GeV and 20 minutes at 10 GeV.

However, real rings delivering beam to experiments often have strong solenoids and so-called spin rotators, and the particles experience beam–beam forces. Moreover, a ring is inevitably slightly misaligned. Then the SR can also lead to depolarisation due to the stochasticity of photon emission. If this has a time scale comparable to, or shorter than the S–T time scale, the attainable polarisation can be much lower than 92.4%. The depolarising rate can be especially high compared to the S–T rate at the so-called spin orbit resonances [2, 3], and tends to increase strongly with energy. However, depolarisation can often be substantially overcome by arranging for “spin transparency” (see below) and by careful adjustment of the closed orbit. Detailed accounts of the theory and phenomenology of these effects can be found in [1–3].

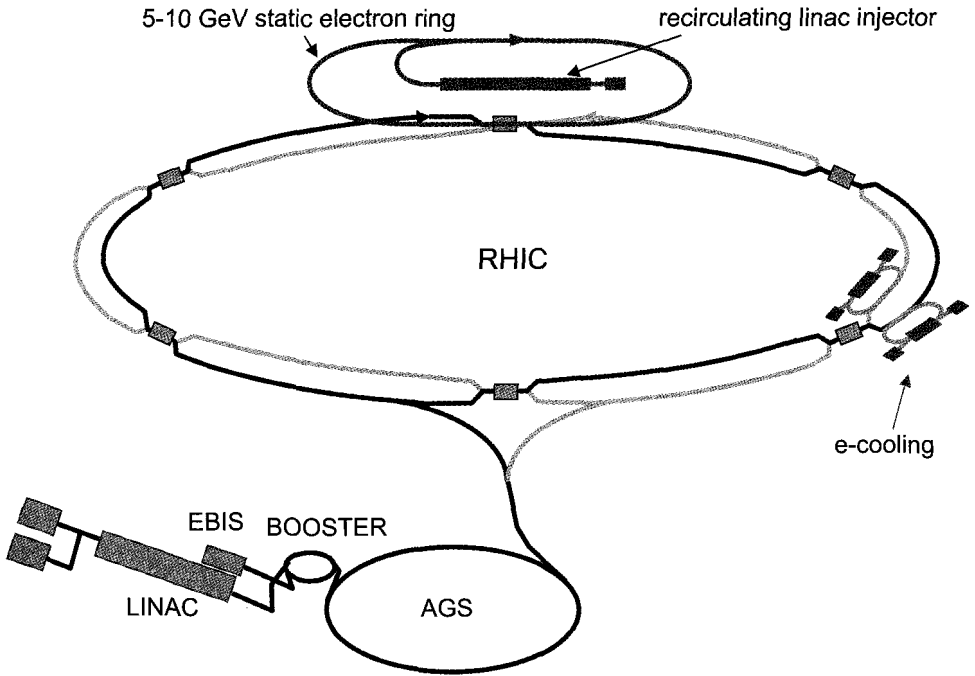


Fig. 1. The layout of eRHIC in the ring-ring version [1].

Although the e^\pm could in principle become polarised by the S-T effect, this would take too long in the energy range 5–8.5 GeV. Thus for electrons a prepolarised beam would be injected at full energy, even up to 10 GeV. For details of the source and the linear accelerator see [1]. Since no simple sources of polarised positrons exist, measurements with positrons will be restricted to 9–10 GeV where the S-T time scale is short enough.

The polarisation vector must be close to the vertical in the arcs in order for the S-T process to function and to prevent depolarisation. On the other hand the high energy physics programme needs longitudinal polarisation at the interaction point. This is obtained with the aid of the spin rotators [4] sketched in Fig. 2 whereby vertical polarisation in the arcs is brought into the horizontal plane by a pair of solenoids, rotated to longitudinal for the interaction point by dipoles, and then returned to the vertical by dipoles and solenoids of reversed polarity. However, such a system can also lead to strong depolarisation. Fortunately, it can be made “spin transparent” [2] by a special choice of the strengths of the quadrupoles between the solenoids in each pair [1, 4]. Then, in the absence of misalignments, almost all depolarising effects should be eliminated.

This is confirmed by analytical calculations with the code SLICK [1]. However, with misalignments, strong depolarisation can still occur. This is unlikely to be too important at 5 GeV, but it would certainly need attention at the high end of the energy range, where a small

The solenoid spin rotators

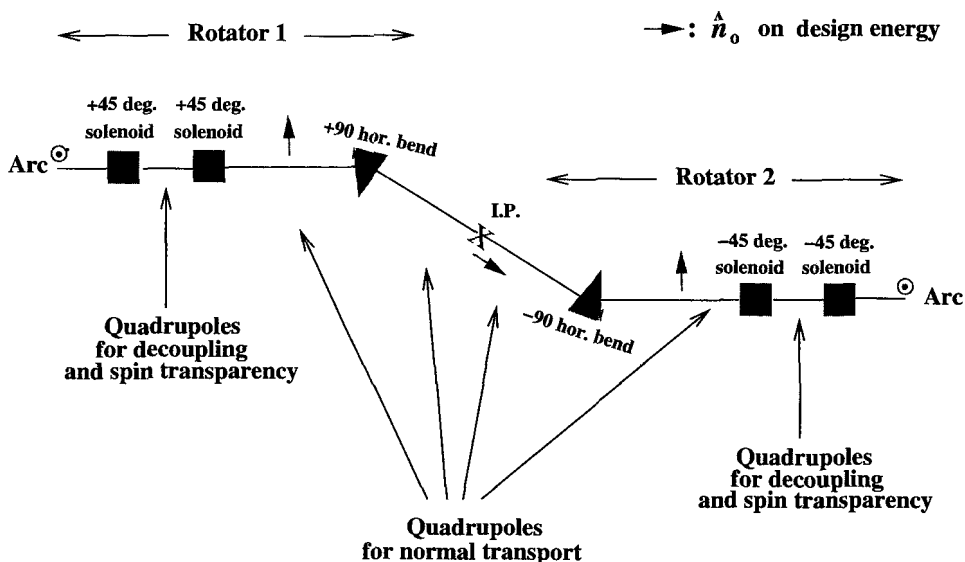


Fig. 2. Schematic of the spin rotators [4] in the e^\pm ring.

depolarisation time would lead to an unacceptably low equilibrium polarisation. Note that even with an injected electron polarisation of 80%, the polarisation would settle down (or up) to the equilibrium polarisation determined by the state of the ring and on a time scale shorter than the smaller of the polarisation and the depolarisation time scales. A positron beam would be injected with 0% polarisation. Thus a careful study of the attainable equilibrium polarisation is needed, at least above 8 GeV. SLICK uses a linearisation of the spin motion. The calculations can then only exhibit first order spin-orbit resonances. Typical results from SLICK for the equilibrium polarisation in the range 9.25–10.58 GeV with realistic misalignments and subsequent optimisation of the closed orbit are shown in [1], where one sees that polarisations of up to 80% are reached. The corresponding S-T and depolarising times for 9.25–9.69 GeV are shown in Fig. 3. The first order spin-orbit resonances are clearly visible. The best way to estimate the effects of higher order resonances, including the effects of nonlinear orbit motion and beam-beam forces, is to simulate the effects of stochastic photon emission in a Monte-Carlo (M-C) spin-orbit tracking code which operates on a large ensemble of particles and includes the full 3-D spin motion. Analytical methods [2] lack the required power and generality. The M-C is being implemented in the code SLICKTRACK, an extended version of SLICK. A sample result, for calibration of the concept, of running the Monte-Carlo with linearised spin motion under the same conditions as in the basic (i.e. analytical) SLICK, is shown in Fig. 3. It is clear that the M-C model is good even at energies where the depolarisation time is large with the consequence that its “measurement” can be imprecise. The M-C approach was pioneered

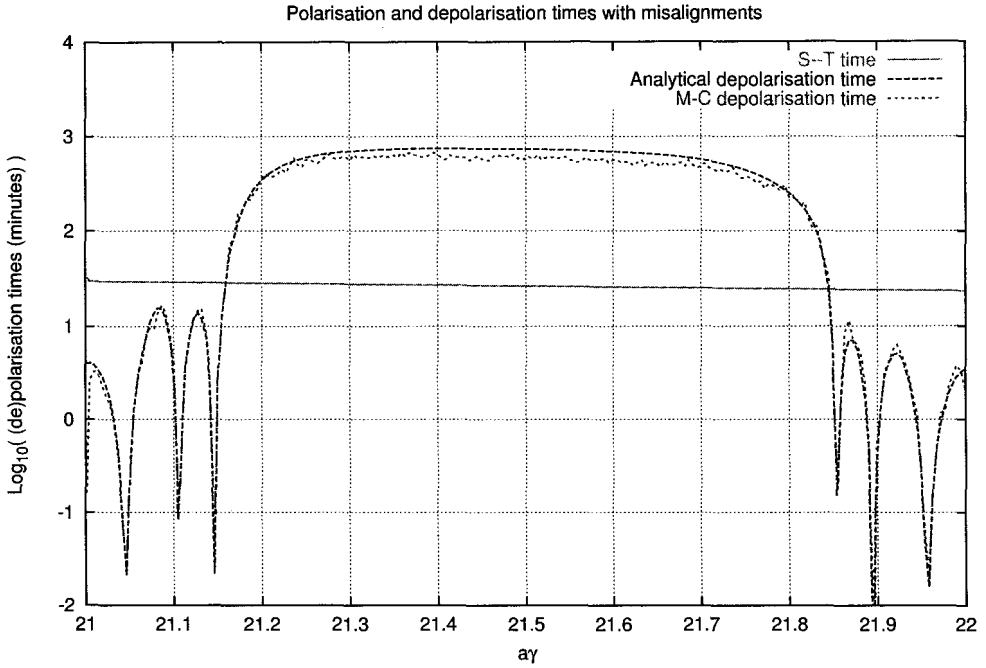


Fig. 3. The S-T time and first order estimates of the depolarising time vs. design orbit spin tune.

in the early 1980's in the code SITROS [2] but with SLICKTRACK, advantage has been taken of the subsequent huge increase in available computer power and of experience, to create a new, much simpler, software architecture. This in turn facilitates detailed investigation of the depolarisation process and of the effect of lack of spin transparency of sections of the ring under the heading "diagnostics", so that the potential for unreliable results is minimised. It is intended that SLICKTRACK should provide a powerful general tool for studying polarisation in all the e^\pm accelerators and rings of the eRHIC complex.

References

1. eRHIC Zeroth-Order Design Report BNL Report C-A/AP/142 (2004).
2. D.P. Barber, G. Ripken in *Handbook of Accelerator Physics and Engineering*, Eds. A.W. Chao and M. Tigner, World Scientific, 2nd edition (2002).
3. D.P. Barber et al., in *Proceedings of ICFA workshop "Quantum Aspects of Beam Physics"*, Monterey, U.S.A., 1998, World Scientific (1999).
4. A.A. Zholents, V.N. Litvinenko, BINP (Novosibirsk) Preprint 81-80 (1981). English translation: DESY Report L-Trans 289 (1984).

POLARIZED BEAMS IN THE HIGH-ENERGY STORAGE RING OF THE FUTURE GSI PROJECT

A. LEHRACH, R. MAIER, D. PRASUHN

Forschungszentrum Jülich, Jülich, Germany

I. KOOP, A. OTBOYEV, Y. M. SHATUNOV

Budker Institute of Nuclear Physics, Novosibirsk, Russia

A. U. LUCCIO

Brookhaven National Laboratory, Upton, USA

Acceleration and storage of polarized proton and antiproton beams in medium and high energy circular accelerator are complicated by numerous depolarizing spin resonances. In this paper possible scenarios for accelerating and storing polarized beams in the High Energy Storage Ring (HESR) of the future GSI Facility for Antiprotons and Ions Research (FAIR) [1] are discussed.

1. Introduction

The HESR is proposed as a storage ring for antiproton physics with high quality beams over a broad momentum range from 1.5 to 15 GeV/ c . An important feature of this new facility is the combination of phase space cooled beams with internal targets (e.g. PANDA [1]), which opens new capabilities for high-resolution and precision experiments with high luminosity. In 1992 an experiment at the Test Storage Ring (TSR) at MPI Heidelberg proved the feasibility of polarizing a 23 MeV proton beam by spin-dependent interaction of the stored beam with an electron-polarized hydrogen target [2]. A Letter-of-Intent has been submitted by the PAX collaboration [3], proposing to utilize this technique to provide a polarized antiproton beam for the FAIR project (invited contribution by F. Rathmann). A dedicated Antiproton-Polarizer Ring (AP) with a large acceptance angle is needed in order to polarize antiprotons to the high degree of 30 to 40% [4]. To perform spin-physics experiments in antiproton-proton interactions, the polarized beam would have to be accelerated and stored in the HESR.

2. Polarized Beams in the HESR

The spin motion in an external electro-magnetic field is governed by the so-called Thomas-BMT equation [5], leading to a spin tune of $\nu_{sp} = \gamma G$. G is the anomalous magnetic moment of the particle and $\gamma = E/m$ the Lorentz factor. The G -factor is quoted as 1.792847337(29) for protons, 1.800(8) for antiprotons (see Particle Data Booklet). In a strong-focusing ring like the HESR, imperfection and intrinsic spin resonances can depolarize the beam. In total 25 imperfection resonances ranging from $\gamma G = 4$ to 28, and 50 intrinsic resonances from $\gamma = 12 - Q_y$ to $20 + Q_y$, where Q_y is the vertical betatron tune, have to be crossed during acceleration. The strength of the resonances depends on the orbit excursions for imperfection resonances, and focusing structure of the lattice and beam emittance for intrinsic resonances, and ranges from 10^{-2} to 10^{-6} for the expected beam parameters. Due to coupling introduced by the 15 Tm solenoid of the electron cooler, strong coupling spin resonances are also excited. The large number of resonances to be overcome in the HESR makes it very hard to apply techniques of individual manipulation of single spin resonances [6]. Siberian snakes seem to be the only option to guarantee a set-up with low polarization losses during acceleration.

2.1. Siberian Snake with Combined Fields

In the HESR momentum range it is difficult to use a RHIC-type [7] helical dipole snake, due to the large orbit excursions shown in the upper left plot of Fig. 1. A solenoidal field would require a rather high integrated field strength of roughly 60 Tm . A magnet system with a combination of both field types was therefore investigated, consisting of four RHIC-type helical dipole magnets with a maximum field of 2.5 T and a 15 Tm solenoid (see upper right plot in the same Figure). To provide a full spin flip in the whole momentum range, the snake magnets have to be ramped according to the values given in the lower left plot, where s is the solenoid and $d1, d2$ are the two helical dipole field values. The resulting spin motion at 15 GeV/c is shown in the lower right plot. This magnet system provides a full spin flip in the whole momentum range by keeping the maximum closed orbit excursion below 5 cm. Spin rotation induced by the DC cooler solenoid at any possible field level can be compensated by the rampable 15 Tm snake solenoid, if snake and cooler are installed in the same straight section.

2.2. Siberian Snake with Solenoidal Fields

The second proposed scheme contains four solenoids grouped on either side of the cooler (see upper sketch of Fig. 2) with the same total integrated field strength of 15 Tm as the cooler solenoid. From injection up to about 7.5 gev the five solenoids will provide a full snake. At higher momenta they will be less effective, reducing to about 50% partial snake at top momentum. To compensate for coupling, two groups of four quadrupole magnets are needed with rotation angles up to 8.6, 6.3, 4.3 and 4.3 degree. The rotation angles of the quadrupoles have to be adjusted for different solenoid fields and beam momenta. The whole magnet insertion provides a betatron phase advance of π and 2π in the two

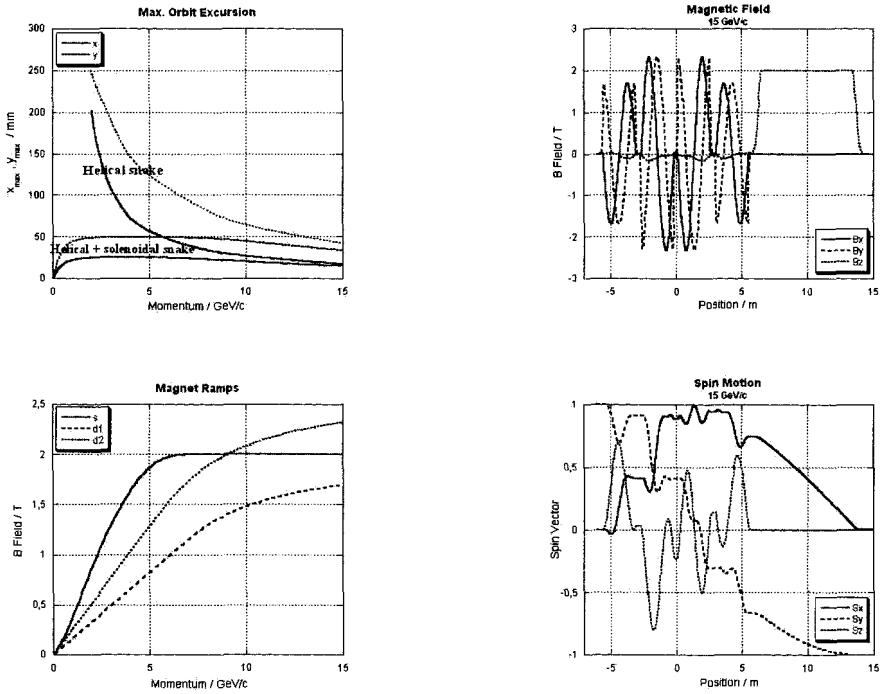


Fig. 1. Layout of a full Siberian snake with combined magnetic fields.

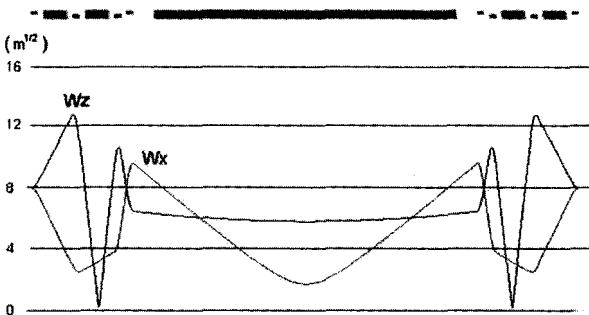


Fig. 2. Layout of a Siberian snake with solenoidal fields (top) and optical functions (bottom).

transverse planes, and has a total length of $56m$. To preserve polarization at first order spin resonances, the fractional part of the betatron tune has to be kept close to integer in the range $.75 < Q_{frac} < .25$. This scheme does excites no orbit excursions, and compensates for transverse phase space coupling. With higher integrated solenoidal field strength, it could also serve as a full Siberian snake.

3. Conclusion

The most serious drawback of a combined field scheme is the large orbit excursion in the snake, which could be a major restriction for the beam quality in the HESR. Furthermore, rampability of the super-conducting snake magnets remains to be solved. Good field quality of super-conducting ring magnets, in order to keep the strength of higher-order spin resonances small, combined with high flexibility of the lattice allowing for betatron tunes close to integers, are essential in a partial Siberian snake. A decision for one of the proposed schemes should be taken after intense particle and spin tracking, including field errors and technical layout of the snake magnets.

References

1. GSI Future Project, Conceptual Design Report, November 2001, <http://www.gsi.de/GSI-Future/cdr/>.
2. F. Rathmann et al., *Phys. Rev. Lett.* **71**, 1379 (1993).
3. PAX collaboration, Letter-of-Intent, January 2004, <http://www.gsi.de/documents/DOC-2004-Jan-125-1.ps>.
4. F. Rathman et al., hep-ex/0410029, accepted for publication by PRL.
5. L.H. Thomas, *Phil. Mag.* **3**, 1 (1927);
V. Bargman, L. Michel, V.L. Telegdi, *Phys. Rev. Letters* **2**, 43 (1959).
6. F.Z. Khiari et al., *Phys. Rev.* **39**, 45 (1989); H. Huang et al., *Phys. Rev. Lett.* **73**, 2982 (1994); M. Bai et al., *Phys. Rev. Lett.* **80**, 4673 (1998).
7. see <http://www.agrhome.bnl.gov/RHIC/Spin>.

POLARIZED PROTON ACCELERATION AT THE J-PARC ACCELERATOR COMPLEX

H. SATO, C. OHMORI, T. TOYAMA, Y. MORI

KEK-PS & J-PARC, Tsukuba, Japan

K. HATANAKA

RCNP, Ibaraki, Japan

M. OKAMURA

RIKEN, Wako, Japan

Japan Proton Accelerator Research Complex (J-PARC), which is JAERI and KEK Joint Project, is now under construction at the Tokai campus of JAERI. The purpose of the project is to provide a high intensity proton beam for nuclear/particle physics and material sciences. A need for polarized proton beam for various experiments is also expected. In this report, the J-PARC accelerator complex will be described and the polarized proton acceleration scheme will be discussed

1. Introduction

The High Intensity Proton Accelerator Facility aims to pursue frontier science in particle physics, nuclear physics, materials science, life sciences, and nuclear technology, using a new proton accelerator complex with the highest beam power in the world. The plan is managed jointly by the High Energy Accelerator Research Organization (KEK) and the Japan Atomic Energy Research Institute (JAERI) [1]. Previously these institutions proposed the Japan Hadron Facility (JHF) at KEK and the Neutron Science Project(NSP) at JAERI, respectively. These accelerators will be constructed at the Tokai campus of JAERI, about 130km north-east of Tokyo.

Because the time of operation of J-PARC is approaching (beam commissioning will start in 2007 JFY), it is a good time to create a mechanism to reflect voices from the user community much more efficiently than before, and a workshop was organized [2]. There are several Letters of Intent concerning polarization phenomena at 50 GeV, so it will be

worthwhile to discuss the feasibility of polarized proton beam acceleration at the J-PARC accelerator complex.

2. General Description of J-PARC Accelerator Complex

The accelerator complex consists of the following accelerators: 400-MeV normal-conducting Linac, superconducting Linac to increase the energy from 400 to 600 MeV, 3 GeV rapid cycling synchrotron (3-GeV RCS), and 50 GeV synchrotron ring (50-GeV MR). At the 50-GeV MR, which provides 0.75MW proton beams, nuclear/particle physics experiments using kaon beams, antiproton beams, hyperon beams, and primary proton beams are planned, as are experiments on neutrino oscillation using Super-Kamiokande as a detector. The 3-GeV RCS, which provides proton beams at 1MW, will be used as a booster synchrotron for the 50-GeV MR. In addition, it is designed to provide 1 MW of beam power for the extensive physics programs which cover nuclear/particle physics, condensed matter physics, materials sciences, and structural biology. The major highlights are materials sciences and structural biology, using neutrons produced in proton+nucleus spallation reactions. Muon beams are also important, in which muon SR (muon spin rotation/relaxation), muon catalyzed fusion, and other materials science, can be conducted. Radioactive beams produced from the 3-GeV RCS are also useful in nuclear/astro physics research. Finally, the high current 600-MeV Linac will be used for R&D for accelerator-driven nuclear transmutation.

Significant Beam Parameters are as follows [3],

- (1) Linac; Ions: Negative Hydrogen, Energy for RCS injection: 400 MeV(200MeV in the first stage), Energy for ADS: 600 MeV, Peak Current: 50 mA, Repetition Rate: 50 Hz.
- (2) 3-GeV RCS; Extraction Beam Energy: 3 GeV, Repetition: 25 Hz, Extraction Scheme: Fast, Beam Intensity: 8.3×10^{13} ppp, Circumference: 348.333 m, Typical Tune: (6.68, 6.27), Total Number of Cells: 27, Super Periodicity: 3, Number of Bending Magnets: 24, Number of Quadrupoles: 60, Number of Families: 7, Harmonic Number: 2, Painting Emittance at Injection: 216 mm.mrad, Physical Aperture: 486 mm.mrad, Beam Emittance at Extraction: 81 mm.mrad.
- (3) 50-GeV MR; Extraction Beam Energy: 50 GeV, Repetition: 0.3 Hz, Extraction Scheme: Fast and Slow, Beam Intensity: 3.3×10^{14} ppp, Circumference: 1567.5 m, Typical Tune: (22.3, 17.3-22.3), Number of Bending Magnets: 96, Total Number of Quadrupoles: 216, Number of Family: 11, Harmonic Number: 9, Beam Emittance at Injection: 54 mm mrad, Beam Emittance at Extraction (30 GeV): 10 mm mrad, Beam Emittance at Extraction (50 GeV): 6.1 mm mrad.

Construction of Phase I of the project was approved starting in April, 2001, and will be completed by March, 2007. In Phase I the linac will be constructed only for RCS injection (200 MeV). The 50-GeV synchrotron will be operated at an energy of 30 GeV for slow extraction. The neutrino production target area will not be constructed in Phase I either. However, the full power system will be constructed for the pulsed spallation neutron source. Approval of Phase II will be applied for immediately in order to start the long-

base line neutrino experiment and ADS. The polarized beam acceleration project should be considered in the same period of Phase II construction.

3. Polarized Beam Acceleration at the J-PARC Accelerator Complex

There are spin depolarizing resonances in the circular accelerator, such as intrinsic, imperfection and higher order resonances. If some of these resonances cause spin depolarization, correction of the depolarizing resonances will be necessary. Typical calculated depolarizing resonances are shown in Tables 1, 2, 3. In the 3-GeV RCS, no depolarization is expected for

Table 1. Imperfection resonances in the 3-GeV RCS.

n	γ	E_p (GeV)	ϵ	P_f	ϵ	P_f
			COD = 38 mm rms		COD = 38 mm rms	
3	1.673	0.632	0.00201	0.707	0.000139	0.998
4	2.231	1.155	0.00128	0.875	0.000106	0.999
5	2.789	1.678	0.00280	0.471	0.000123	0.999
6	3.347	2.202	0.00249	0.567	0.000360	0.990
7	3.904	2.725	0.00604	-0.523	0.000947	0.931

Table 2. Intrinsic resonances in the 3-GeV RCS
(200 π mm rad at injection).

	γ	E_p (GeV)	ϵ	P_f
$-3 + \nu$	2.155	1.084	0.01173	-0.991
$12 - \nu$	2.865	1.750	0.01474	-1.000
$0 + \nu$	3.828	2.654	0.01662	-1.000

Table 3. Strong intrinsic resonances in the 50-GeV PS.

	γ	E_p (GeV)	ϵ	P_f	ϵ	P_f
			300p mm-mrad		150p mm-mrad	
$-9 + \nu$	4.675	3.448	0.00536	-0.352	0.00379	0.139
$3 + \nu$	11.368	9.728	0.00495	-0.236	0.00350	0.236
$9 + \nu$	14.715	12.868	0.00537	-0.354	0.00379	0.136
$27 + \nu$	24.755	22.289	0.00365	0.185	0.00258	0.539

the imperfection resonances if COD is small, and spin-flip will be expected for the intrinsic resonances if the emittance is large. However, there is a serious disadvantage in the beam line from the 3-GeV RCS to the 50-GeV MR. Because of the 4.1 m difference between the levels of RCS and MR, a 2.61-degree sloping section is required. There will be some rotation of the vertical spin, and a method of compensating this will be needed. Alternatively, we could consider another injector, such as an FFAG, or direct injection from the LINAC, if it can be upgraded to higher energy. This would also be useful to avoid time-sharing the 3-GeV RCS.

In the 50-GeV MR, all of the imperfection resonance will be overcome by the partial Siberian Snake. There are four strong intrinsic resonances, and a fast betatron tune jump and/or coherent betatron oscillation excitation will be necessary. The full Siberian Snake is effective even for a symmetric machine, but 50-GeV MR has three-fold symmetry. Alternatively, two strong partial Siberian Snakes, as suggested by T. Roser [4], is an attractive method to overcome intrinsic resonances. We have to investigate in detail the feasibility of polarized proton acceleration at the J-PARC accelerator complex, including locating a suitable installation point.

4. Summary

The J-PARC accelerator complex is now under construction and the lattice structure will be changed slightly. As soon as the machine parameters are fixed, we have to investigate polarized beam acceleration in detail, studying not only conventional techniques but also Siberian Snakes. Further, another injector machine instead of 3-GeV RCS should be considered. A start on this work has been made.

References

1. "The Joint Project for High-Intensity Proton Accelerators", KEK Report 99-4, JHF-99-3 and JAERI-Tech 99-056 (1999).
2. NP04: The 3rd International Workshop on Nuclear and Particle Physics at J-PARC, August 2-4, 2004 at Tokai, Ibaraki, Japan
3. Accelerator Technical Design Report for J-PARC Accelerator Group JAERI/KEK Joint Project Team
4. Tomas Roser, Presented in this symposium.

This page intentionally left blank



SESSION 8

Polarized Sources, Targets and Polarimetry

This page intentionally left blank

BEAM INDUCED DEPOLARIZATION IN THE HERMES TRANSVERSELY POLARIZED HYDROGEN TARGET

D. REGGIANI

Physikalisches Institut der Universität Erlangen-Nürnberg, Erlangen, Germany

(on behalf of the HERMES Collaboration)

The HERMES polarized hydrogen target is situated in the HERA electron storage ring in Hamburg. For the transverse spin program at HERMES, the magnetic holding field of the target is perpendicular to the HERA positron beam. An unwanted consequence is that the beam-induced resonance between hydrogen hyperfine states with $\Delta m_F = 0$, which was previously forbidden, can occur. The shape and spacing of these resonances will be shown. In order to prevent these resonances from reducing the nuclear polarization in the target cell, a pair of correction coils has been added to improve the field homogeneity. The success of these measures will be demonstrated.

1. Introduction

The HERMES transversely polarized hydrogen gas target [1, 2] has been operational since 2001 in the HERA electron storage ring at DESY. The polarized gas, produced by an atomic beam source (ABS) [3], is injected into a storage cell [4] through which the 27.6 GeV HERA electron beam passes. A sample of gas diffuses from the middle of the cell into a Breit-Rabi Polarimeter (BRP) [5], which measures the atomic polarization, or into a Target Gas Analyzer (TGA) [6], measuring its atomic and molecular content. A magnet surrounding the storage cell provides a holding field defining the polarization axis, and prevents spin relaxation by effectively decoupling the spin of electrons and nucleons.

A potential source of target depolarization is related to the interaction of the transient magnetic fields generated by the bunched electron beam with the polarized nucleons of the target. This effect has already been studied at HERMES with the longitudinally polarized target [7]. In the transverse case, the occurrence of new densely spaced resonances makes this problem soluble only with the use of a very uniform target magnetic field.

2. Target depolarization by beam interaction

Bunch field induced resonant depolarization in the HERMES target may originate when the frequency of an RF-harmonic, induced by the HERA e-beam, matches the frequency difference between two different hyperfine states present in the storage cell. The probability

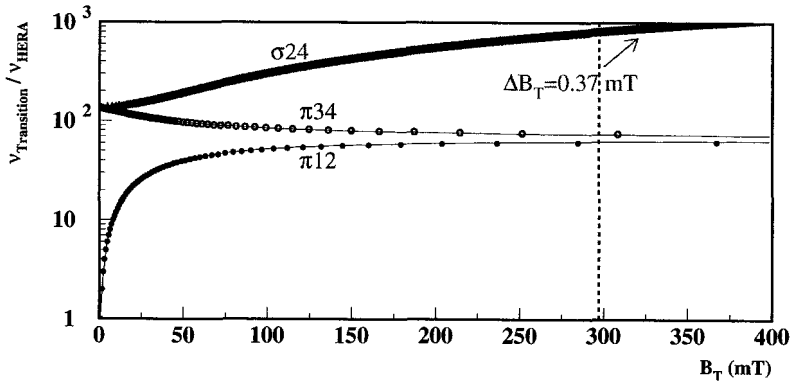


Fig. 1. Nuclear depolarizing resonances in the hydrogen case. The frequency difference between pairs of hydrogen hyperfine states whose transitions would lead to a nuclear depolarization are plotted as a function of the holding field. The frequency values are normalized for $v_{HERA} = 10.41$ MHz. The marks representing the resonance condition are clearly distinguishable for the π transitions, while they overlap with each other in the σ case. The dashed line denotes the target working field.

of such an event is proportional to the square of the beam current. In order to determine the values of the target holding field for which this mechanism is effective, one has to study the harmonic structure of the time dependent magnetic field induced by the 220 bunches of the electron beam. As the distance between two adjacent bunches is $\tau=96$ ns, the frequency spacing between two harmonics is given by $\nu=\frac{1}{\tau}=10.41$ MHz. Since the gaussian shaped bunch is very narrow ($\sigma_t=37.7$ ps), a huge number of harmonics with non-negligible amplitude can contribute to inducing RF-fields.

Depending on the pair of hyperfine states involved, transitions are distinguished between π , occurring when the RF-field component is perpendicular to the static one, and σ , taking place when the two fields are parallel. Around the working point of the target magnet (297 mT), the π resonances are easily avoidable with a field uniformity at the percent level. This is not the case for the σ resonances, whose spacing is only 0.37 mT (Fig. 1). Due to the relative orientations of the beam induced magnetic field and the static holding field, the σ transitions are present in the transverse case only.

3. The transverse magnet design

In order to avoid beam induced depolarization inside the target cell, during the design of the transverse target dipole magnet a field uniformity around 0.15 mT was requested. Due to geometrical constraints, this requirement could be fulfilled only along the longitudinal and vertical target cell directions ($\Delta B_z=0.05$ mT and $\Delta B_y=0.15$ mT respectively) but not throughout the transverse horizontal one ($\Delta B_x=0.70$ mT). A solution to this problem, making use of two correction coils embodied inside the storage cell support structure, was designed after the installation of the magnet in the HERMES hydrogen target (July 2001), and eventually implemented in July 2003. Fed with 60 A current, these coils provide a uniform correction along the length of the cell, improving the x non-uniformity from 0.7 to

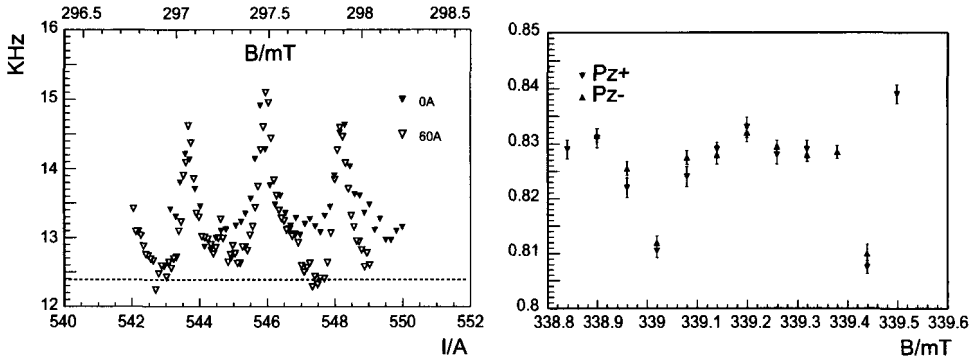


Fig. 2. Beam induced depolarization measurements. Left panel: BRP count rate versus holding field during a flip-in measure. Right: $\sigma|2\rangle \leftrightarrow |4\rangle$ resonances highlighted during a polarization measurement while increasing the holding field strength. More details in the text.

0.2 mT.

4. Measurements

At HERMES, a very effective method that can be applied in order to measure beam-induced hyperfine transition is the so-called *flip-in* measurement. This technique consists of injecting a defined hyperfine state into the target cell, while slowly increasing the target holding field, in order to match one or more resonance conditions and let the BRP measure the changing hyperfine population. The left panel in Fig. 2 shows the result of such a measurement, where state $|4\rangle$ was injected from the ABS and states $|1\rangle$ and $|2\rangle$ detected by the BRP, so that two possible transitions, namely $\pi|1\rangle \leftrightarrow |4\rangle$ (electron only) and $\sigma|2\rangle \leftrightarrow |4\rangle$, could be revealed. Both transitions present the same spacing in terms of magnetic field (0.37 mT), nevertheless the peaks can be attributed to $\pi|1\rangle \leftrightarrow |4\rangle$, whose intrinsic probability is larger [8]. The scan was performed twice, with correction coils turned off and on. Although the peaks are clearly resolved in both cases, with coils off at no point did the BRP rate sink to the level of no HERA beam (dashed line), pointing to the fact that the magnet uniformity is insufficient, and making it impossible to completely avoid the resonance. The situation clearly improves with the coils on, suggesting that the field uniformity improves substantially.

A clear way to identify the $\sigma|2\rangle \leftrightarrow |4\rangle$ resonances is to perform a polarization measurement while injecting, for instance, states $|1\rangle$ and $|4\rangle$, as shown in the right panel of Fig. 2. This scan, obtained at a beam current of around 33 mA, indicates how the atomic polarization drops in the presence of a resonance, allowing at the same time the working field to be set to where the depolarization effect is minimum.

5. Conclusion

Densely spaced beam induced depolarizing σ resonances have recently been observed in the HERMES hydrogen transverse gas target. In order to limit this unwanted effect, a hold-

ing field with a homogeneity better than 10^{-4} has been conceived thanks to the implementation of a pair correction coil at the edge of technical feasibility. The polarization drop has been limited to 1.5 % even at high HERA beam current.

References

1. A. Airapetian et al., The HERMES Polarized Hydrogen and Deuterium Gas Target in the HERA Electron Storage Ring *Nucl. Instrum. and Meth. A* (in press).
2. P. Lenisa, The HERMES Polarized Hydrogen and Deuterium Internal Gas Target, contribution to these Proceedings.
3. A. Nass et al., *Nucl. Instrum. and Meth. A*, **496** (2003), 277.
4. C. Baumgarten et al., *Nucl. Instrum. and Meth. A*, **496** (2003), 263.
5. C. Baumgarten et al., *Nucl. Instrum. and Meth. A*, **482** (2002), 606.
6. C. Baumgarten et al., *Nucl. Instrum. and Meth. A*, **508** (2003), 268.
7. K. Ackerstaff et al., *Phys. Rev. Lett.*, **82** (1999), 1164.
8. D. Reggiani, Ph.D. Thesis, University of Ferrara, January 2003.

POLARIZED HYDROGEN JET TARGET FOR MEASUREMENT OF RHIC PROTON BEAM POLARIZATION

T. WISE, M. CHAPMAN, W. HAEBERLI

University of Wisconsin, Madison, USA*

D. GRAHAM, A. KPONOU, G. MAHLER, Y. MAKDISI, W. MENG, A. NASS, J. RITTER, A. ZELENSKI

Brookhaven National Laboratory, Upton, USA

S. KOKHANOVSKI, V. ZUBETS

INR, Moscow, Russia

The performance and unique features of the RHIC polarized jet target, and our solutions to the important design constraints imposed on the jet by the RHIC environment are described. The target polarization and thickness were measured to be $0.924 \pm 2\%$ and $1.3 \pm 0.2 \times 10^{12}$ atoms/cm² respectively.

Introduction

The jet target was installed in the RHIC beam line for the polarized proton run in spring 2004. During this time the source produced a highly polarized gas target with record thickness for a polarized jet. We required vertical target polarization with a strong (0.12 T) and uniform ($\Delta B/B < 5 \times 10^{-3}$) vertical guide-field. The field uniformity is necessary to avoid depolarizing bunch field induced resonances from the circulating RHIC beam. The source, see Fig. 1, is mounted vertically to allow freedom in the midplane for recoil particle detection near 90°. Nass et al., this conference, describe the conventional design of the source and the measurement of the jet density and polarization. Here we point out some of the unique features we believe are responsible for the record intensity of 12.4×10^{16} atoms/s, significantly higher than the prediction of modeling codes [1, 2]. We employed improved RF coupling in the dissociator and pre-cooling of the dissociated gas before final thermal

*Work supported by United States Department of Energy grant number DE-FG02-88ER40438

accommodation in the usual 2 mm diameter expansion nozzle cooled to 75 K. More details are given in A. Zelenski et al., this conference. Large bore permanent 6-pole focusing magnets allow the beam to expand to 32 mm diameter over an unusually long 650 mm drift length before refocusing to a 5.8 mm FWHM target spot of $1.3 \pm 0.2 \times 10^{12}$ atoms/cm² thickness. The larger bore of the six-pole magnets implies both an increased gas conductance inside the magnets and a reduced beam density over much of the beam trajectory compared to other designs. These two factors may be responsible for a portion of the increased beam intensity.

Magnetic field configuration

The magnetic fields experienced by the atomic H beam are crucial for preservation of its nuclear polarization. To avoid non-adiabatic field changes we required that, in the atomic beam rest frame, the applied magnetic field direction may rotate no faster than $10^{-3} \omega_L$, the Larmor precession rate ($\gamma_p B$). Unfortunately, the target guide field configuration we employed to minimize the deflection of low energy (< 10 MeV) recoil protons resulted in two distinct locations where the field seen by the atomic beam reverses direction and strongly violates the adiabatic condition. Use of massive iron shielding allowed us to move the violation regions. In one case it was moved into the middle of a six-pole magnet, and in the other into the field of a 2-4 RF transition. The transverse fields in these regions restored the adiabatic condition. Nass et al., this conference, show that the residual depolarization is below 0.4%.

Vacuum

The source is divided into 9 pumping stages, 6 for the beam formation and target region and 3 for the BRP (Breit-Rabi Polarimeter). We utilized two Varian 1000 liter/s turbo pumps (2×10^6 compression ratio for hydrogen) in each stage except for the first stage which has 3 pumps. Application of a fourth pump would achieve an intensity increase of 3.5%. We achieved an operating pressure in the target region of 1.4×10^{-8} Torr and a base (jet OFF) of 4×10^{-9} Torr.

Breit-Rabi polarimeter

The layout of the BRP is shown in Fig. 1. In the usual BRP polarization measurement, all possible combinations of RF transitions are used to solve for the fractional hyperfine occupation numbers. In our case it is sufficient to determine the efficiency of the two RF transitions located upstream of the interaction region.

Furthermore it is possible to operate the two upstream transitions simultaneously. If those transitions have 100% efficiency, no chopped beam should reach the BRP detector. The ideal situation is nearly realized for our setup. We observed a rate of 52 Hz in the detector with both upstream transitions on, and a rate of about 20,900 Hz with the transitions off, leading to a lower limit to the average of the RF transition efficiencies of 99.7%.

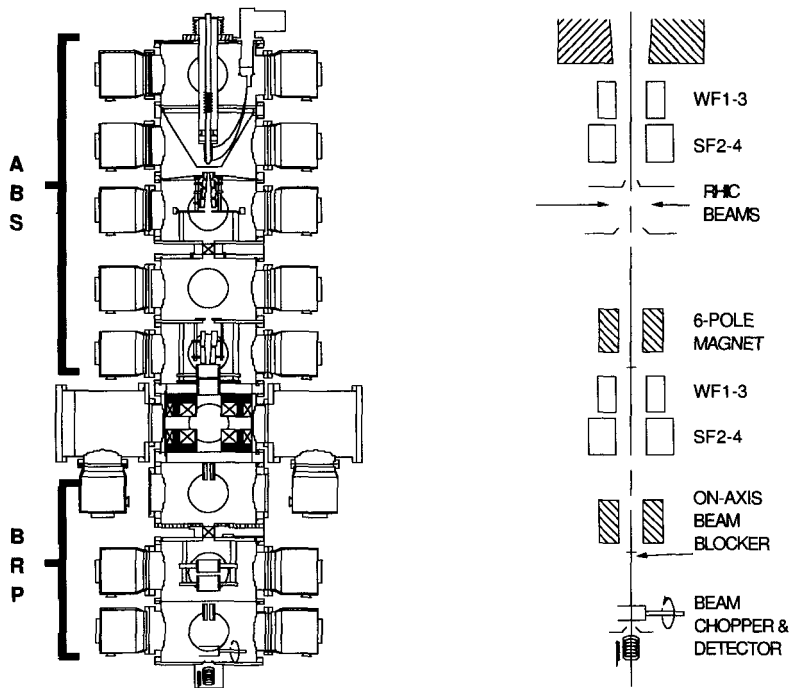


Fig. 1. Left, the overall layout of the jet to scale. The third turbopump on the first stage and the massive iron shielding are not shown. The large centrally located chambers house silicon recoil detectors for calibration of the RHIC beam polarization. Right, the configuration of the lower portion of the jet assembly showing the arrangement of RF transitions, beam blockers, six-pole magnets and beam chopper. The BRP detector is a commercial ion gauge biased with low ripple power supplies.

Jet polarization

Even with perfect RF transition efficiency the jet polarization will deviate from 100% because of several factors. At 0.12 T guide field, state 2 and 4 atoms have polarization $|P| = 0.921$, whereas state 1 and 3 atoms have $|P| = 1$, giving a two-state (1+4 or 2+3) theoretical $|P_{\max}| = 0.961$. In addition, the jet beam includes a dilution of approximately 3% nucleons of unpolarized H_2 gas measured with a QMA located at the RHIC beam interaction point. Although there was a possible depolarization from bunch field interaction with the circulating RHIC beam, none was observed. Combining the above factors yields a jet polarization of $P_+ = 0.923 \pm 2\%$ and $P_- = -0.925 \pm 2\%$. The difference between P_+ and P_- is due to a small but consistent difference in the efficiency of the 1-3 and 2-4 RF transitions. The quoted errors are entirely dominated by the uncertainty in the molecular dilution. Construction and calibration of hardware for a more precise measurement of the molecular content of the jet is in progress.

References

1. T. Wise et al., Design of a polarized atomic H source for a Jet Target at RHIC. *AIP Conference Proceedings 675, 15th International Spin physics Symposium, Upton, NY, (2002)*, Y. Makdisi, A. U. Luccio and W. W. MacKay, eds.
2. A. Zelenski et al., Absolute Polarized H-Jet Polarimeter Development for RHIC, *Proc. PST 2003, NIM A 26367* (2004).

ATOMIC BEAM STUDIES IN THE RHIC H-JET POLARIMETER

A. ZELENSKI, D. GRAHAM, S. KOKHANOVSKI, G. MAHLER, Y. MAKDISI, A. NASS, J. RITTER,
V. ZUNETS

Brookhaven National Laboratory, Upton, USA

W. HAEBERLI, T. WISE

Department of Physics, University of Wisconsin-Madison, Madison, USA

The results of atomic beam production studies are presented. Improved cooling of the atoms before jet formation in the dissociator cold nozzle apparently reduces the atomic beam velocity spread and improves beam focusing conditions. A carefully designed sextupole separating (and focusing) magnet system takes advantage of the high brightness source. As a result, a record beam intensity of a $12.4 \cdot 10^{16}$ atoms/s was obtained within 10 mm acceptance at the collision point. A 3% polarization dilution factor (by the hydrogen molecules at the collision point) was measured with a modified Quadrupole Mass Analyzer.

A polarized H-jet polarimeter is based on elastic proton-proton scattering in the Coulomb-Nuclear Interference (CNI) region. Due to particle identity, the polarization of the accelerated proton beam can be directly expressed in terms of proton target polarization, which can be precisely measured by a Breit-Rabi polarimeter. A detailed H-jet polarimeter description and results of the beam intensity and density measurements were presented at the PST 2003 in Novosibirsk [1]. Atomic polarization measurements and the H-jet project overview are presented at this conference (A. Nass et al. and T. Wise et al.). The focus of this paper is atomic beam production, dissociator long-term performance, and our first measurements of polarization dilution factor by molecular hydrogen.

Dissociator. In a conventional dissociator design, hydrogen atoms are produced in an RF-discharge with velocities equivalent to a few thousand degrees gas temperature. The atoms are cooled down in collisions with the pyrex or quartz walls of the dissociator discharge tube. The tube is usually cooled by a water jacket, and only the aluminium nozzle at the end of the tube is cooled to 30-100 K temperatures. As was described in [1], a new dissociator design has an extended 12 cm cold tube section upstream of the nozzle that is cooled by

cryocooler to 70-140 K. This allows a reduction in wall surface recombination, improves hydrogen thermal equilibrium conditions, and possibly reduces the beam velocity spread.

A number of different dissociator “neck” and nozzle cooling system modification were tested over the last year. These cooling improvements resulted in beam intensity increases for the same nozzle temperature. They also allowed the dissociator operation at higher RF-power. The operational power was increased to 250 W. At a higher power of 280-300 W, the beam intensity is about 10% higher, but the nozzle cooling is insufficient. At this power the RF-discharge penetrates further into the cold “neck” where wall recombination is reduced at 80-140 K temperatures. Also an ice layer formation on the tube and nozzle surfaces reduced recombination. There is a significant heat transfer to the heat sink copper clamp (attached to the cryocooler) from plasma cooling and recombination. This heat transfer varies in time for the same input RF-power, and depends on the tube wall conditions and the quality of the thermal contact between the copper clamp and the quartz tube. Better contact actually reduces the heat load due to a decrease in the tube wall temperature, which reduces recombination. The copper clamp-quartz tube thermal conductance is limited in all of our tested designs. At present a thin (~ 0.2 mm) layer of “Apiezon” cryogenic vacuum grease (instead of finger springs [1]) is used to provide the heat conductance between copper and quartz. It worked quite reliably during the RHIC run, but the reproducibility of the grease application is still a problem and needs to be improved.

The production of silicon oxide in the discharge plasma reaction with the quartz tube sometimes causes nozzle plugging by a “snow-ball” of SiO_2 . The oxide is accumulated in the region of the plasma boundary. The plasma penetrates about halfway into the cold dissociator “neck”, where the wall temperature is about 130 K. During continuous operation the oxide is bounded, perhaps by ice, and stable dissociator operation for up to three weeks was recorded. But sometimes the “snow-ball” plugged the nozzle completely after only five days. The procedure of vacuum cleaning of the dissociator with a plastic tube attached to a vacuum pump was developed and was effectively used during the H-jet run in the RHIC. Less than 0.5-hour ring access was required for this procedure.

In the H-jet dissociator, the cold surface area of the “neck” and nozzle is much larger than in the conventional dissociator, where only the nozzle is cold. The water vapour, which is produced mostly in the discharge, condenses and freezes upstream of the nozzle, and there is no need to warm the dissociator up to clean ice from the nozzle. During three weeks of continuous operation there was a steady increase (about 10%) in the beam intensity. This effect can be explained by a reduction in recombination due to better wall coating by the ice.

Atomic Beam Intensity Measurements. The total beam intensity in the collision chamber was measured with a compression tube 10 mm in diameter and 100 mm in length. The compression tube was calibrated by the conventional technique [1]. The maximum atomic beam intensity of $(12.4 \pm 0.2) \cdot 10^{16}$ atoms/sec was measured at ~ 75 sccm flow, the dissociator RF-power was 280 W, and the nozzle temperature 75 K (see Fig. 1a). The maximum intensity is significantly higher than in other ABS. Remarkably the HERMES ABS intensity of a $6.4 \cdot 10^{16}$ atoms/s was obtained at just 30 sccm H_2 flow i.e. three times less gas supply

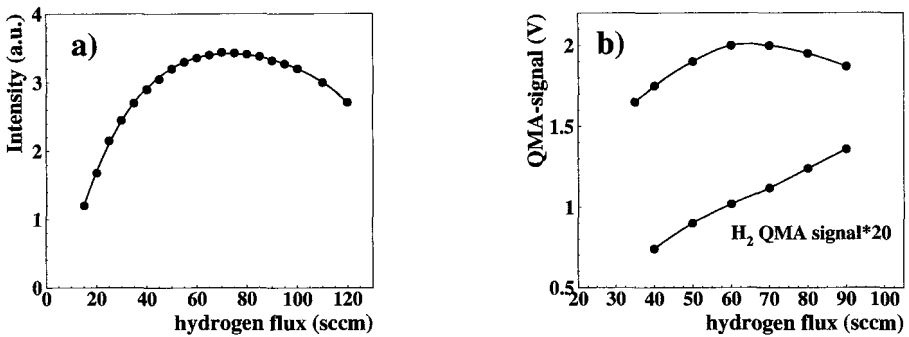


Fig. 1. Atomic beam intensity vs. H₂ flow in dissociator (a). Atomic and molecular hydrogen density vs. H₂ flow as measured by the QMA (b).

in the dissociator than HERMES ABS [2] utilized to obtain that intensity. This intensity dependence was measured after the dissociator cooling upgrade. The intensity decrease rate is not as fast as before [1], and the maximum is shifted to the higher flow. Apparently precooling the atoms before the nozzle improves beam formation out of the nozzle, and insufficient cooling limits the intensity increase. At higher H₂ flow the heat load to the dissociator “neck” is increased, and the plasma penetrates further into the “neck”. This may change the equilibrium velocity distribution and affect the beam quality. The dissociation ratio might also decrease. The operational temperature of the cooling bracket in the top part of the “neck” is about 140 K, which is close to minimum for recombination reduction at the quartz. But the inside wall temperature can be significantly higher. Further cooling system improvements are still required.

The target polarization dilution by molecular hydrogen. Atomic beam polarization close to 96% was measured in the Breit-Rabi polarimeter (A. Nass et al. at this conference). The target polarization dilution by the molecular hydrogen (at the collision point) was measured by a modified quadrupole mass analyzer. The original RIBEN QMA sensitive area was expanded from 5mm to 10 mm to accommodate the full 9mm beam width and significantly reduce atomic beam recombination at the QMA electrodes, which was observed in the first measurements. The QMA signal amplitude dependence on hydrogen flow in the dissociator is presented in Fig. 1b. The maximum of the QMA atomic beam signal is shifted to a lower flow from the compression tube maximum. The difference from a compression tube is because the QMA measures the beam density, not intensity. The density is the figure of merit for the H-jet target. Therefore the maximum of the QMA signal (at 60 sccm flow) is the best operational point. The absolute atomic beam density of about $1.0 \cdot 10^{12}$ atoms/cm³ at the collision point can be calculated from the atomic beam intensity, the beam profile, and the velocity. The QMA sensitivity factor to the molecular hydrogen was calibrated at different hydrogen pressures (hydrogen gas was supplied to the collision chamber through a needle valve) measured by a hot filament ion gauge closely positioned to the QMA sensor. The molecular hydrogen density of about 1.5% of the atomic beam den-

sity was determined from these measurements, which provide a preliminary measurement of the polarization dilution factor of about 3% at 60 sccm H₂ flow in dissociator. This gives an effective H-jet target polarization of a $93^{+1}_{-2}\%$. To meet the project goal of a 1% absolute accuracy for H-jet target polarization, new diagnostics devices are under development. A device for off-line measurements is based on electron beam ionizer and magnetic analysis of the ion components. For on-line polarization dilution monitoring, an optical technique development is in progress. It is based on detection of a luminescence light from atoms and molecules excited by the RHIC proton beam.

References

1. A. Zelenski et al., Proc. PST 2003, NIM A 26367 (2004).
2. A. Nass et al., Nucl. Inst. and Meth. A505 (2003), 633.

POLARIZED ELECTRON PHOTOINJECTOR FOR FUTURE LINEAR COLLIDERS USING THE PLANE WAVE TRANSFORMER (PWT) DESIGN*

D. YU, A. BAXTER, P. CHEN, M. LUNDQUIST, Y. LUO, A. SMIRNOV, J. YU

DULY Research Incorporated, Rancho Palos Verdes, CA USA

PWT photoinjectors being developed by DULY Research Inc. are rf guns capable of operation in ultra high vacuum and moderate field gradient. The expected performance of a modified L-band polarized electron PWT injector for the International Linear Collider is presented. The projected normalized transverse rms emittance is an order of magnitude lower than that produced with a DC polarized electron gun and subharmonic bunchers.

1. Introduction

A multi-cell, standing-wave, S-band, -mode, plane-wave-transformer (PWT) photoinjector, with an integrated photocathode in a novel linac structure [1], has been under development at DULY Research Inc. This design is extended here to L-band (Figure 1), which may be directly applicable as a polarized electron source for the International Linear Collider (ILC). A highly polarized ($> 80\%$) electron beam is produced from a strained lattice GaAs photocathode illuminated by a circularly-polarized laser ($\lambda \approx 800$ nm). The projected normalized transverse rms emittance is of the order of a few mm mrad or less. Thus, the PWT photoinjector may drastically reduce the cost of the complicated damping ring in the ILC. Unlike conventional SLAC-type disk loaded structures, the PWT cavities are formed by disks suspended by cooling rods inside a large cylinder. The "open" cavities are strongly coupled electro-magnetically, transforming a TEM-like mode in the open annular space between the tank and the disks into a TM₀₁-like mode on beam axis.

2. Load Lock, Pumping Box, Vacuum-RF Sieve

The 10+2/2 cell, S-band PWT polarized electron photoinjector has a load lock [2] that is attached to the PWT photoinjector via a gate valve. This enables activation and reprocessing of the GaAs cathode while maintaining ultra high vacuum. A full-scale model of the load lock has been built to test the puck transfer and handling of this system (Figure 2.c).

*Work supported by U.S. Department of Energy SBIR grants.

Several new features have been added to the existing S-band design to improve the vacuum and thermal hydraulic design of the polarized electron source. These include a pumping box that straddles the PWT tank, which is connected to the pumping box through a vacuum-RF sieve (Figure 2a,b). A large number of holes through the sieve allow efficient pumping; the holes are sufficiently small, however, to keep the RF power inside the PWT.

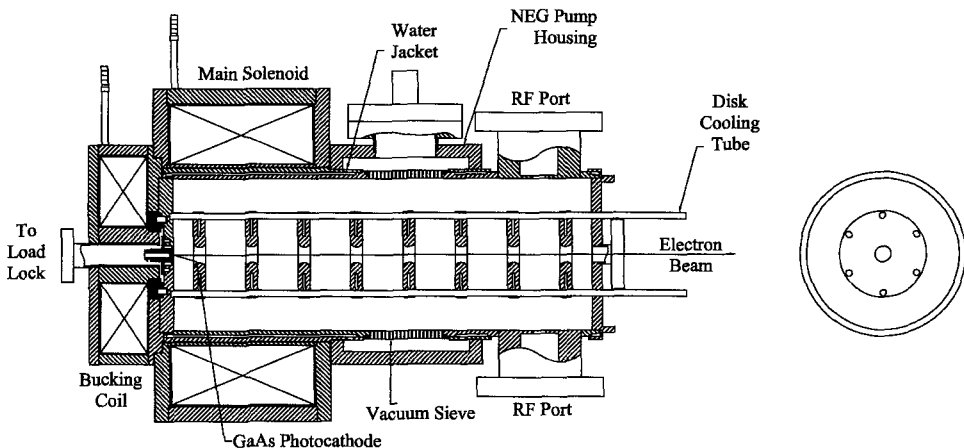


Fig. 1. Side and end view schematics of an L-band PWT polarized photoelectron linac.

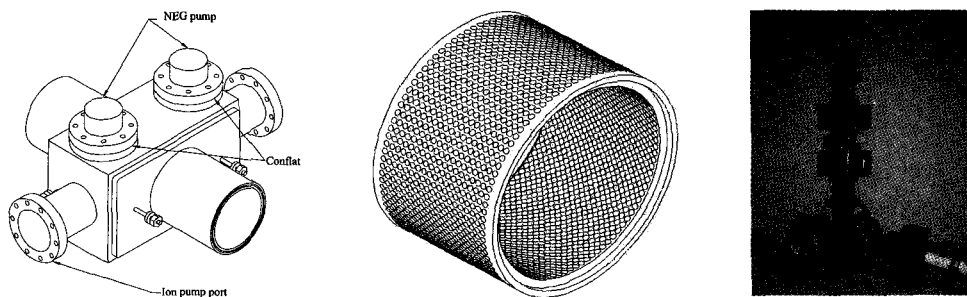


Fig. 2. Drawing of (a) pumping box, (b) vacuum-RF sieve, and (c) picture of load lock model.

3. L-Band PWT Polarized Electron Photoinjector Design

Compared with the 2.856 GHz S-band design, a 1.3 GHz L-band PWT polarized electron photoinjector will have better vacuum and cooling because of its larger vacuum conductance and larger pipes. In addition, fabrication and alignment tolerances will be relaxed. Preliminary results of simulations and analysis are compared with the current TESLA design in Table 1.

RF design - The 3-cm aperture is chosen for the PWT design because the injector can produce a beam with excellent transverse beam dynamics (see Table 1). A smaller aperture has the benefit of slightly increasing the shunt impedance. From Parmela simulations, we find that in order to capture the electron beam into the PWT, the peak field should be greater than 14 MV/m. A higher peak field results in a lower transverse emittance. In order to minimize dark current [3], however, we choose an operating peak field of 20 MV/m. A baseline design consists of a 7+2/2 cell structure with 6 disk-cooling pipes and a large stainless steel tank. Using two 10-MW klystrons to provide RF power results in a 10 MeV beam, with a normalized transverse rms emittance of 3.2 mm-mrad. This is more than an order of magnitude reduction from the best simulation result (42 mm-mrad) of the DC gun plus subharmonic bunchers [4]. Substantial improvements are also found for the rms bunch size, bunch length and energy spread (Table 1). We are currently considering several methods to improve the shunt impedance, such as adding peripheral rods (Figure 3.e) and enlarging the nose of the irises to form re-entrant cavities (Figure 3.b), thereby possibly reducing the number of klystrons required from 2 to 1.

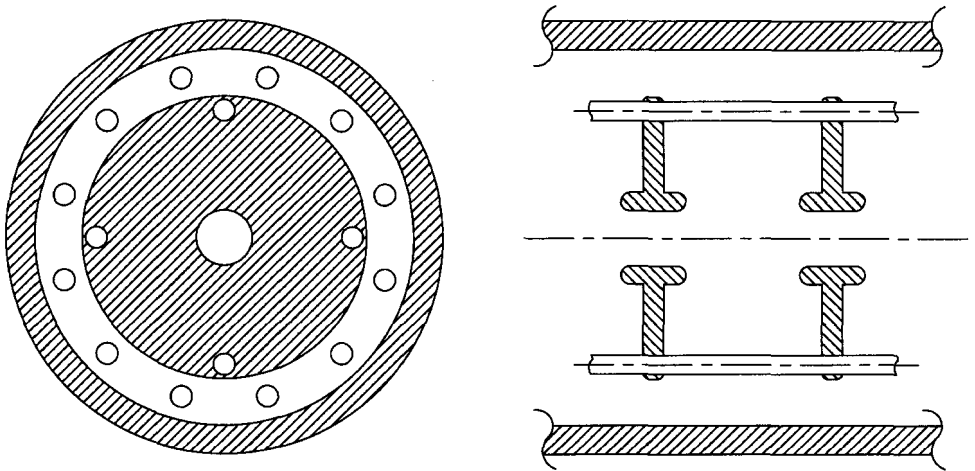


Fig. 3. (a) Photonic band gap design consisting of 12 peripheral rods; here only 4 cooling rods between disks are shown. (b) Side view of a re-entrant cavity, with an enlarged iris nose on each end.

Vacuum design - Scaling the dimensions of an L-band PWT from S-band increases the vacuum conductance, due in part to the larger holes of the vacuum-RF sieve. The large pumping box can accommodate several high capacity NEG pumps to offset the higher outgassing rate of the large stainless steel tank and copper surfaces, resulting in a pressure at the cathode of less than 10-11 Torr. In addition, the load lock for an L-band PWT can be scaled from the S-band design.

Thermal hydraulic design - The L-band linear collider uses substantial average RF power. The preliminary L-band PWT design uses two phase synchronized klystrons, each with a long RF pulse of 1370 microseconds, 10 MW peak power and 5 Hz rep rate. The

Table 1. Preliminary design of an L-band polarized electron injector.

	PWT L-band	TESLA design 2001 Tech Report	
		N cells	7+2/2
Length, m	0.922	1.15	1.96
Aperture radius a, cm	1.5	2.6	
Shunt impedance, M/m	17.1	31.9	35.4
E _{peak} , MV/m	19.2	16.6	13.4
Q-factor	20330	~21500	
Heat, kW (5Hz, 1.37ms, 10MW per klystron)	137 (2 klystrons)	68.5	
Beam parameters for q=3.7nC per bunch			
Energy	10	11.3	
Laser pulse length, ns	0.015	2	
Bunch length (rms), mm	2.0	3.4	
Energy spread (rms), keV	4.0	45	
Norm. emittance (rms), mm mrad	3.2	42.5	
Beam size (rms), mm	0.8	2.6	

heat transferred to the tank can be readily removed with cooling channels inside the large tank wall. Heat transferred to the suspended disks must be removed by cooling pipes and channels inside the disks. To prevent differential thermal expansion among disks (which may detune the RF cavities), equal coolant flow should be maintained in all the disks. This will be accomplished using an increasingly larger inlet pipe orifice for each downstream disk channel. Separating the six 1.09-cm ID cooling pipes into three independent cooling circuits allows each circuit to feed water in parallel into sets of 2 or 3 disks. Each of the eight PWT disks and the 6-rod segments supporting it would absorb 8 kW heating power. To remove the heat, the required flow in each disk channel is 22.5 liters/min, for a convection film temperature difference of 30°C. The required external pressure for the L-band PWT is 22.6 psig for a total flow of 67 liters/min. The cooling capacity of the PWT is therefore adequate.

Photocathode and laser issues - Scaling data from the SLAC DC gun with a 20 mm GaAs photocathode operating at 1.8 MV/m (giving a peak space charge limit current of 15 A) [5], the L-band PWT operating at 20 MV/m could have over 500 A of peak current and still be within the space charge limit. This is within the required current for ILC. To generate a polarized electron beam with the required time structure within each macropulse, a Ti-Sapphire mode-locked laser producing pulsed, circularly polarized light, such as the scheme suggested by Hovater and Poelker [6], may be used. Thus there is a laser solution and, based on scaling the SLAC DC gun, the space charge limit is not in principle exceeded.

4. Conclusion

An RF photoinjector with the plane-wave-transformer design is suitable as a low-emittance, polarized electron source for future linear colliders. The electromagnetic, vacuum, thermal hydraulic, and mechanical design of an S-band PWT polarized electron injector has been completed. An L-band PWT version is proposed as a polarized electron source for the International Linear Collider.

References

1. D. Yu, J. Clendenin, R. Kirby, U.S. Patent No. 6,744,226.
2. D. Yu *et al.*, Proc. of Particle Accelerator Conference, May 2003, p. 2129.
3. Y. Luo *et al.*, Proc. of Particle Accelerator Conference, May 2003, p. 2126.
4. TESLA Design Report, DESY, 2001.
5. R. Alley *et al.*, Nucl. Inst. and Meth. A365, 1 (1995).
6. C. Hovater and M. Poelker, Nucl. Inst. and Meth. A418, 280 (1998).

POLARIZATION MEASUREMENTS OF THE POLARIZED ^3He TARGET WITH WATER AND DPPH

W. KIM, S. S. STEPANYAN, S. WOO

Department of Physics, Kyungpook National University,
Daegu, Republic of Korea

We have designed and constructed an NMR setup for the polarization measurement of a polarized ^3He target. The experimental setup, including the Helmholtz coils, NMR electronics and laser system, has been constructed and tested. The system has been calibrated using water and a free radical, 2,2-diphenyl-1-picrylhydrazil. The setting is optimized for the Adiabatic Fast Passage NMR technique.

The stable free radical 2,2-diphenyl-1-picrylhydrazil (DPPH) is frequently used as a free-radical scavenger and as a standard in electron spin resonance spectroscopy [1, 2]. The experimental g -factor for DPPH is 2.039 ± 0.023 . This investigation was carried out to determine the polarization of a ^3He target by comparing NMR signal height of ^3He with that of DPPH. In a ^3He target, polarization is produced by spin-exchange. We also present a detailed study of thermal equilibrium signals from distilled water.

Polarized ^3He produced by spin exchange with optically pumped Rb metal [3] has recently been used for precision measurements of the neutron spin structure functions, tests of fundamental symmetries [4], neutron polarizers, and for MRI of the human body [5, 6]. In many of these cases it is important to know accurately the absolute ^3He polarization. At present, the most common polarimetry method is NMR (Nuclear Magnetic Resonance), usually on the basic technique of Adiabatic Fast Passage (AFP) [7]. While the Signal-to-Noise-Ratio (SNR) provided by this technique is excellent, absolute measurements require a complicated calibration which usually has limited precision [8, 9].

The ^3He target cell is placed in an homogenous magnetic field produced by a Helmholtz coil pair. At the same time an RF field is produced by a pair of RF coils orthogonal to the Helmholtz coil. The AFP sweep is produced by holding the RF frequency fixed and sweeping the main magnetic field through the RF resonance. At resonance, the spins flip, and this is detected by a pair of pickup coils wrapped around the cell. For DPPH, 10 turns of coil were wrapped around an ampoule containing 5g of material. The quality factor of the pickup coils was about 100 [9]. The quality factor is defined as proportional to L/R , where L is inductance and R is resistance.

The induced AC voltage in the pickup coils is detected with a lock-in amplifier referenced to the RF frequency. Usually absolute polarization can be determined by calibrating the NMR apparatus with a water sample. The polarization of the water sample is known in advance, as it follows from Boltzman distribution for thermal equilibrium situation. From Faraday's law one could calculate the voltage at the terminals of the coil. The susceptibility of the protons is 3×10^{-10} in water at room temperature. This calculation depends on the filling factor, which describes how the sample was filled inside the entire coil.

The voltage of the pickup coils is proportional to the impedance of a parallel AC LRC circuit. The voltage is related to the filling factor, quality factor and magnetic susceptibility. The NMR signal appears as a very small modulation. The AFP is the only method that gives tolerable signal-to-noise ratios(SNR).

The most troublesome factor in performing a water calibration is the poor SNR. This is usually overcome by averaging many sweeps together. The NMR signals accumulate coherently, while the random noise averages to zero. This can be a quite tedious procedure, as dozens of sweeps are usually needed before the NMR peak grows from the background. There are two ways to improve the SNR.

- (1) Boost the signal. Increase the number of proton spins within the coils simply by adding some extra water.
- (2) Decrease the background. This could be done by decreasing the RF amplitude. The pickup coil signal also decreases as the RF signal decreases. To prevent this, we should increase the pickup coil gain from the preamplifier. When the observed water signal is boosted, water must be removed. Then the RF amplitude could be increased [9]. The lock-in amplifier should be located as far as possible from the other electronic devices. Efforts should be made to isolate the pickup coils from any currents or vibrations, as these lead to microphonic noise in the pickup coils.

There are many noise sources which in real life can disturb water signal measurements. Thus we get DPPH as an alternative material for calibration measurements. One can show that Thermal Equilibrium Polarization can be described as the following ;

$$P_{DPPH} = \tanh \frac{\mu_B B}{kT} \quad (1)$$

where μ_B is Bohr magneton for electron, k is a Boltzman's constant and T is temperature of the sample. The Bohr magneton for electron is about 2000 times larger than for the proton. SNR could be good enough depending on the quantity of the material. 3cm^3 of DPPH could satisfy SNR conditions. For polarization measurements of the ^3He cell we should use the ratio of measured signals from ^3He and DPPH. We can calculate ^3He polarization based on the following relation:

$$\frac{\text{Gain}_{^3\text{He}} \times \mu_{^3\text{He}} \times \rho_{^3\text{He}} \times \text{signal}_{^3\text{He}}}{\text{Gain}_{DPPH} \times \mu_{DPPH} \times \rho_{DPPH} \times \text{signal}_{DPPH}} \quad (2)$$

The magnitude of the RF field and frequency sweep rate were adjusted to satisfy the AFP conditions. Figures 1 and 2 show signals from 5g DPPH in X and Y channels, respec-

tively. The plot for water NMR signal is shown in Figure 3. We can improve the SNR just by increasing the amount of material inside the cell.

We have presented a concept for ^3He polarimetry based on measuring the DPPH signal as a standard for calibration. This, with existing methods of water calibration and frequency shift of the Rb Zeeman resonance, could be used for precision polarimetry of ^3He polarized targets. This would allow easy polarization measurements.

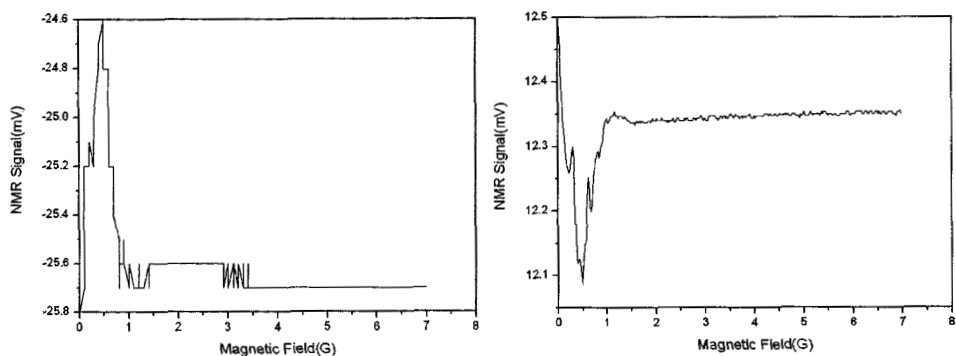


Fig 1. Plot for X absorption part of DPPH NMR signal Fig 2. Plot for Y dispersion part of DPPH NMR signal

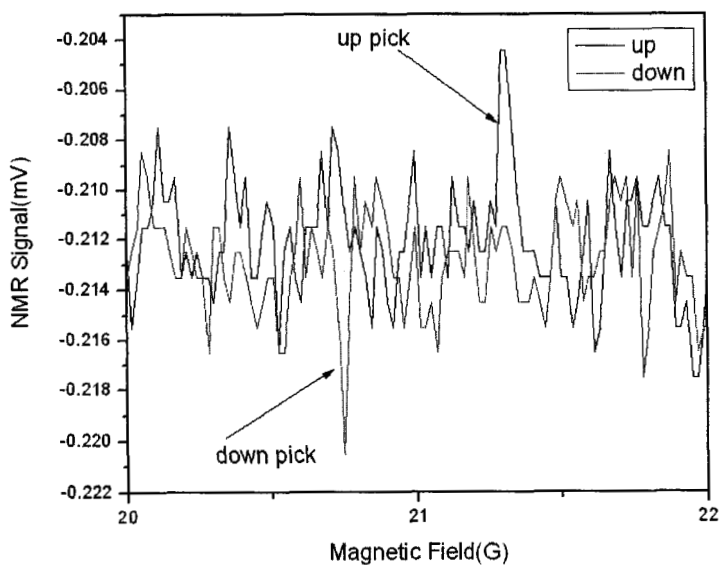


Fig 3. Plot for water NMR signal

References

1. J.H. Lee and D.B. Min, Nuclear magnetic resonance (NMR) study on the electron donating ability of beta-carotene by using 2,2-diphenyl picrylhydrazyl (DPPH), 2002 Annual Meeting and Food Expo - Anaheim, California
2. Q. Zhuang, F. Scholz, F. Pragst, The voltammetric behaviour of solid 2,2-diphenyl-1-picrylhydrazyl (DPPH) microparticles, Elsevier (1999).
3. T.E. Chupp, R.J. Hoare, R.L. Walsworth, and Bo Wu, Phys. Rev. Lett. B **72**, 2363 (1994).
4. G.L. Greene, A.K. Thompson, and M.S. Dewey, Nucl. Instrum. Methods Phys. Res. A **356**, 177 (1995).
5. H. Middleton, Magn. Reson. Med. **33**, 271 (1995).
6. M.V. Romalis et al., Nucl. Instrum. Method. Phys. Res. A **402**, 260 (1998).
7. A. Abragam, Principles of Nuclear Magnetism, Oxford University Press, New York, 1961.
8. M.V. Romalis and G.D. Cates, Phys. Rev. A **58**, 4 (1998).
9. K.Slifer, Improving SNR for water calibration of the polarized ^3He NMR system, Polarized ^3He Lab. Technical Note, Temple University, 2001.

IUCF POLARIZED ION SOURCE CIPIOS FOR JINR ACCELERATOR NUCLOTRON

N. N. AGAPOV, V. V. FIMUSHKIN, V. P. VADEEV

Joint Institute for Nuclear Research, Dubna, Russia

V. P. DERENCHUK

Indiana University Cyclotron Facility, Bloomington, USA

A. S. BELOV

Institute for Nuclear Research of the Russian Academy of Sciences, Moscow, Russia

There is a proposal to make a polarized deuteron beam in the JINR superconducting accelerator Nuclotron. The installation of the IUCF polarized ion source CIPIOS at the accelerator complex of JINR, Dubna will allow us to continue within a very short time research on the fundamental problems of the structure of nuclear matter and special features of strong interactions. The goal is to accelerate 10 mA D⁺ polarized deuteron beam up to 5 GeV/nucleon.

The Laboratory of High Energies (LHE) of the Joint Institute for Nuclear Research (JINR) has been carrying out basic research on the structure of light nuclei, including deuterons, and special features of strong interactions, with beams of polarized deuterons using the accelerator with a weak focusing system - the 10 GeV Synchrophasotron - since the middle of the 80s. The research is being carried out with the participation of scientists from many countries. In this research many phenomena not predicted by existing theoretical models have been discovered. The study of polarization characteristics has resulted in the discovery of some effects which necessitate reexamination of the standard idea of the nucleus as a set of nucleons, in the region where the distances between the nucleons are less than their size. Since 2003 this research has continued on a new superconducting accelerator with a strong focusing magnet system and different injection parameters - the Nuclotron. The source of polarized particles used up to now (0.4 mA D⁺ cryogenic source POLARIS [1, 2]), unfortunately, cannot provide some of the key parameters of the beams necessary for continued

research in the framework of international collaboration. JINR was greatly impressed by the performance of the atomic beam polarized ion source CIPIOS-IUCF, and would like to implement this source at the Nuclotron accelerator complex. The modifications of CIPIOS will provide high quality polarized deuteron beams at the Nuclotron. The Cooler Injector Polarized IOn Source (CIPIOS) [3] was developed at the Indiana University Cyclotron Facility (IUCF) in collaboration with the Institute for Nuclear Research of Russian Academy of Sciences (INR) in 1999. CIPIOS is intended for polarized and unpolarized $H^- D^-$ beam generation. The source consists of an atomic beam section that uses permanent magnet sextupoles for focusing, and radio frequency transition units to polarize the atoms before they are focused into the ionizer. The resonant charge-exchange ionizer produces pulses of negative ion plasma inside a solenoid. The atomic beam pulse is focused through the extraction system into the solenoid where the atoms are ionized by a highly efficient charge exchange reaction [4, 5]. Tens of milliamperes of unpolarized negative ions may be extracted directly from the ionizer without using the Atomic Beam Source (ABS). The ion beam is formed with a 25 kV extraction potential in a 100 μs to 400 μs wide pulse at a rate of 0.8 Hz to 4 Hz. As a first step it is planned to modify CIPIOS for use as a source of vector or tensor D^+ polarized deuterons. The installation of the polarized source CIPIOS-IUCF at the accelerator complex of LHE JINR will allow us to continue within a very short time research on the fundamental problems of the structure of nuclear matter and special features of strong interactions in the region where quark-gluon degrees of freedom are manifested. The goal is to accelerate 10 mA D^+ polarized deuteron beams up to 5 GeV/nucleon and increase the intensity of the accelerated polarized beam up to $(0.7 - 1) \times 10^{10}$ d/pulse. Agreement has been reached between IUCF & JINR about the transfer of CIPIOS from Bloomington, Indiana, USA to Dubna, Russia. The next tasks are the transport of CIPIOS from IUCF, assembly and setup improvements, and D^+ bench test and source commissioning at JINR (Laboratory of High Energies).

References

1. N.G. Anischenko et al., - In: The 6th Int. Symp. on High Energy Spin Physics, Marseille 1984, Journ. De Phys., Colloque C2, Supplement an n^o 2, 46, C2-703, (1985).
2. V.P. Ershov et al., - In: Int. Workshop on Polarized Beams and Polarized Gas Target, Cologne 1995, (World Scientific, Singapore), 193, (1996).
3. V.P. Derenchuk et al., - In: 2001 Particle Acc. Conf., eds. P. Lucas, S. Webber, IEEE 01CH37268, 2093, (2001).
4. A.S. Belov et al., - In: Proc. of Polarized Sources and Targets 2001, eds. V.P. Derenchuk and B.v. Przewoski, World Scientific, 205 (2002).
5. A.S. Belov et al., *Nucl. Inst. & Meth.* **A333**, 256, (1993).

ATOMIC BEAM POLARIZATION MEASUREMENT OF THE RHIC POLARIZED H-JET TARGET

A. NASS, D. GRAHAM, A. KPONOU, G. MAHLER, Y. MAKDISI, W. MENG, J. RITTER, A. ZELENSKI

Brookhaven National Laboratory, Upton, USA

M. CHAPMAN, W. HAEBERLI, T. WISE

Department of Physics, University of Wisconsin-Madison Madison, USA

S. KOKHANOVSKI, V. ZUBETS

INR, Moscow, Russia

The RHIC polarized H-Jet measures the polarization of the RHIC proton beam via elastic scattering off a nuclear polarized atomic hydrogen beam. The atomic beam is produced by a dissociator, a beam forming system and sextupole magnets. Nuclear polarization is achieved by exchanging occupation numbers of hyperfine states using high frequency transitions. The polarization was measured using a modified form of a Breit-Rabi polarimeter, including focusing magnets and another set of high frequency transitions. The sampling of a large part of the beam and low noise electronics made it possible to measure the polarization to a high degree of accuracy in a very short time (1 min). Using this system, we measured no depolarization of the atomic beam due to the RF fields of the bunched proton beam. Time-of-Flight measurements were done using a fast chopper and a QMA at the position of the RHIC interaction point, to determine the areal density of the atomic beam seen by the RHIC beam.

1. The H-Jet Setup

The H-Jet experiment consists of nine vacuum chambers in a vertical arrangement (see T. Wise et al. these proceedings). The hydrogen gas is dissociated in a RF-dissociator and expands through a cold nozzle into the vacuum of the first chamber. A high brilliance beam is formed using a skimmer and a collimator. Based on the Stern-Gerlach principle, sextupole magnets are used to separate atoms with electron spin state $+1/2$ (hyperfine states $|1\rangle$ and $|2\rangle$) and $-1/2$ ($|3\rangle$ and $|4\rangle$). These magnets also focus the atomic beam into the target region. Nuclear polarization is achieved using high frequency transitions (HFT) by exchanging the occupation numbers of the hyperfine states. After passing the RHIC beam the sextupoles of the so-called Breit-Rabi polarimeter (BRP) focus a large part (1/3) of the

atomic beam into the BRP-detector. The efficiencies of the HFTs and thus the polarization of the atomic beam are determined by comparing the detector signals while running several combinations of these transitions.

The HFTs consist of a resonator cavity in case of the strong field transition (SFT) of a high frequency coil in case of the weak field transition (WFT). All transitions are immersed in a static magnetic field whose strength and gradient along the atomic beam path can be individually adjusted. For the upper transitions a magnetic shield had to be build to reduce the large z-field of the main target holding field magnet and avoid non adiabatic regions (see below). This shield reduces the pumping in this region, and possibly a plasma was created inside the SFT cavity which slowed down the turn on of this transition but didn't affect the polarization of the atoms. To solve this problem the dissociator was pulsed for a short time (10ms) to reduce the gas density inside the cavity.

2. The Accuracy of the BRP Measurement

The sampling of approximately 1/3 of the atomic beam [1] and a high signal to noise ratio (noise reduction, amplification, proper grounding, background subtraction with chopper) lead to a very precise measurement (relative error < 0.1%). Operating different HFTs the efficiencies of these transitions (WFT: $(1 - \epsilon_{1-3})$, SFT: $(1 - \epsilon_{2-4})$, BRP-WFT: $(1 - \epsilon'_{1-3})$, BRP-SFT: $(1 - \epsilon'_{2-4})$) are determined in a short time (< 1 min). Since the remaining atoms in states $|3\rangle$ and $|4\rangle$ are rejected due to the beam blockers, the polarization of the atoms can be calculated:

$$P^+ = \frac{1 + (\cos \theta) \frac{N_2}{N_1} - 2(\cos \theta) \epsilon_{2-4} \frac{N_2}{N_1}}{1 + \frac{N_2}{N_1}} \quad (1)$$

$$P^- = \frac{-1 - (\cos \theta) \frac{N_2}{N_1} + 2\epsilon_{1-3} \frac{N_2}{N_1}}{1 + \frac{N_2}{N_1}} \quad (2)$$

where N_2/N_1 is the transmission ratio of state $|2\rangle$ and $|1\rangle$ through the sextupole system and $\theta = \arctan B_c/B$ ($B_c=50.7$ mT, B -target holding field). The very stable polarization values of the atoms for the 2004 run were $P^+ = 0.957 \pm 0.001$ and $P^- = -0.959 \pm 0.001$ (Fig. 1).

3. Depolarization Effects

If the change of direction of magnetic field in the rest frame of the atoms along the atomic beam path is too rapid, **Majorana depolarization** can occur. To avoid this the field changes have to be adiabatic, i.e. slow compared to the Larmor time $t_L \sim 1/B$. Therefore directional changes in a low field have to be more gradual than in a higher field. Fig. 2 shows this behaviour in the HFT region as a function of the target magnetic field which is penetrating into this region. The measurement was done with the SFT and WFT above the RHIC interaction point, operating at maximum efficiency. While changing the target magnetic field, the changing signal in the detector, which is directly related to the depolarization, was monitored.

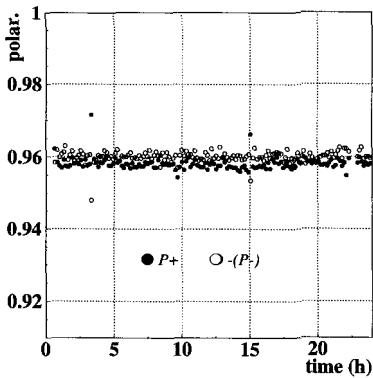


Fig 1. The polarization measurement over one day.

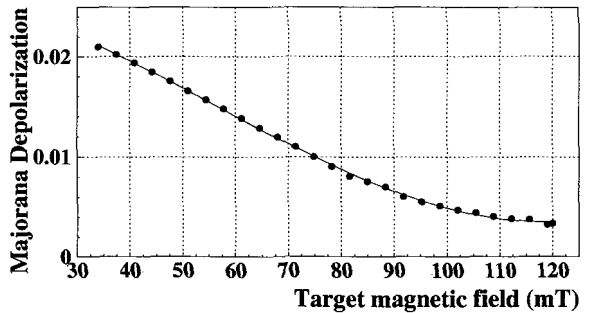


Fig 2. Majorana depolarization in the HFT region (H-Jet working point 120 mT).

Beam induced depolarization can occur due to the transient magnetic fields transverse to the beam direction of the bunched RHIC proton beam. These result in closely spaced depolarizing resonances in the usable range of the surrounding target holding field. Therefore a high uniformity of that field is required over the range of the transient fields (required and achieved for the H-Jet: $\Delta B/B = 5 \cdot 10^{-3}$). No depolarization at the 0.1% level was detected with 60 proton bunches and 10^{11} protons per bunch in RHIC. The measurement was done using SFT and WFT and monitoring the zero signal at the detector.

4. Time-of-Flight (TOF) Measurements and H-Jet Density

These measurements were done using a fast chopper (up to 300 Hz) in chamber #4 and a QMA at the position of the RHIC beam interaction point. The TOF signal is affected by the opening function of the chopper window. Since this influence decreases at higher motor speeds, the flight time was measured at different chopper speeds, and an extrapolation to infinite speed was made to determine the non-affected distribution. The mean velocity was (1562 ± 50) m/s for the working point of the dissociator (nozzle temperature $T = 75$ K, hydrogen flux $Q = 60$ sccm). The variation of the dissociator parameters (T , Q) showed only small (± 50 m/s) variation in the velocity spectrum since it is almost fixed by the transmission of the sextupole magnets. Taking the measured intensity [2] ($12.4 \cdot 10^{16}$ atoms/s) and beam profile [2] (FWHM = 5.8 mm), the areal density of the H-Jet can be calculated to be $(1.3 \pm 0.2) \cdot 10^{12}$ atoms/cm².

References

1. T. Wise et al., Design of a polarized Atomic H source for a Jet Target at RHIC, and A. Zelenski et al., Polarized H-Jet Polarimeter For Absolute Proton Polarization Measurement in RHIC, *AIP Conference Proceedings 675, 15th International Spin Physics Symposium, Upton, NY, (2002)*, Yousef Makdisi, Alfredo U. Luccio, and William W. MacKay eds.
2. A. Zelenski et al., Absolute Polarized H-Jet Polarimeter Development for RHIC, *PST 2003 Workshop on Polarized Sources and Targets, Novosibirsk, Russia*.

ESTIMATES OF INTRA-BEAM SCATTERING IN ATOMIC BEAM SOURCES

M. STANCARI, G. CIULLO, S. ATUTOV, L. BARION, M. CAPILUPPI, M. CONTALBRIGO, P. F. DALPIAZ,
F. GIORDANO, P. LENISA, M. STATERA, M. WANG

INFN and Università di Ferrara, Ferrara, ITALY

The intensity of atomic beam sources has reached a limit in recent years of around 10^{17} atoms/s, limiting in turn the luminosity of HEP experiments utilizing polarized gas targets inside storage rings. It has been suggested that this intensity limit is a result of intra-beam scattering, although this has not been decisively proven. A method to estimate these losses, based upon the calculated beam density, has been developed. The first results are compared with data from both the molecular beam of the Ferrara SpinLab test bench and the atomic beam of the HERMES source.

1. Intra Beam Scattering

Today's atomic beam sources (ABS) all reach a maximum intensity of about 10^{17} atoms/s, despite a large range of design and operating parameters such as input flux, nozzle temperature and magnet strength and geometry. This unexpected limit is a clear signal that the attenuation mechanisms are not yet understood. In this paper, we present a numerical method that estimates the attenuation due to intra-beam scattering (IBS).

The number of collisions dv in a volume dV and a time dt for a beam with density n is given by $dv = \sigma n^2 v_{rel} dV dt$ where σ is the elastic scattering cross section and v_{rel} is the average relative velocity of two random beam particles [1]. This equation can be easily solved numerically for particle loss along the beam axis, using a model for the initial density and divergence of the expanding beam called a *starting generator*^a and assuming that the transverse beam density is uniform. Subdividing the beam into small segments dz_i along the beam axis, the density loss in each segment is

$$dn_i = -2\sigma \frac{\Delta v}{v_{mean}} n_i^2 dz_i \quad (1)$$

where $n_i = \frac{n'_{i-1}}{n^0_{i-1}} n_i^0$, and n_i^0 is the beam density in the absence of scattering, Δv and v_{mean} are the FWHM and average values of the beam's velocity distribution. The resulting density of the beam is $n'_i = n_i(1 - dn_i)$.

^aIn this application, the beam particles are uniformly distributed in the transverse plane while the particle direction is distributed as $\cos^{n_p} \theta$, where θ is the angle between the direction and the beam axis and n_p , the *peaking exponent*, is generally set equal to 1.

2. Molecular Beam Measurements

The Ferrara SpinLab test bench, shown schematically in Figure 1, consists of two chambers for beam formation and two for diagnostics, separated by a compression tube and volume that can be sealed with a valve at the downstream end for beam intensity measurements. With the valve open, the beam passes freely to the diagnostic chambers where the time of flight (TOF) spectrum is recorded.

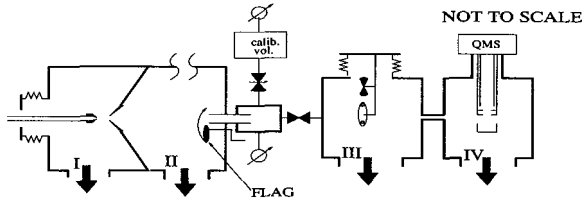


Fig 1. The layout of the Ferrara SpinLab test bench.

The beam intensity was measured as the increase in pressure in the compression volume with the beam blocker (labelled FLAG in Figure 1) removed. A value for $\Delta v/v_{mean}$ was obtained from the measured TOF spectra. The intensity measurements and predictions are shown in Figure 2, for a scattering cross section $\sigma(H_2 \cdot H_2) = 2 \times 10^{14} \text{ cm}^2$ [2].

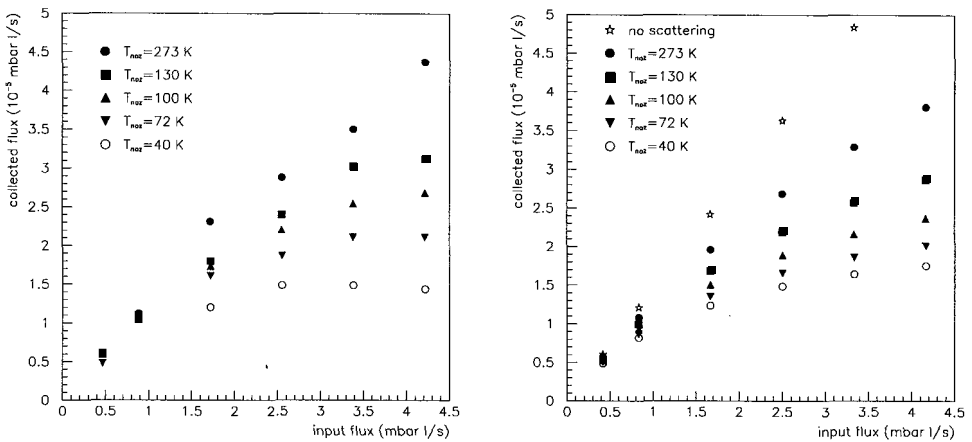


Fig 2. The molecular beam measurements and the corresponding predictions.

3. Atomic Beam Measurements

Two measurements made with the HERMES ABS can be compared with the calculations. The first is the collected beam intensity, $(6.5 \pm 0.6) \times 10^{16}$ atoms/s [4]. The second is a direct measurement of IBS, accomplished using the RF transitions between the two magnet

chambers to reduce the beam density by a factor of 2. The ratio of the measured intensities for normal and reduced density is a direct measure of the loss to IBS in the second half of the ABS, and the measured value is $\delta = (8.4 \pm 1.6)\%$ [3].

The algorithm in section 2 can be applied to the focused beam of the HERMES source by carefully defining a weighted average density

$$\bar{n}(z) = \frac{\int n_{env}(z,r)n_{tot}(z,r)dA}{\int n_{env}(z,r)dA}. \quad (2)$$

The subscript *env* indicates the subset of atoms which are collected by the compression tube, and *tot* the density of all the atoms present, including the defocused ones that have not yet collided with a surface. Figure 3A shows \bar{n} calculated for the HERMES ABS. The uppermost curve is the density without scattering, and the subsequent curves show the loss in density for scattering cross sections $(0.5 - 5.0) \times 10^{-14} \text{ cm}^2$. The predicted intensity of the HERMES ABS is obtained from the density at $z = 1.16 \text{ m}$, and these predictions are shown as the points in Figure 3C, where the measured value and its uncertainty are indicated by the horizontal band. In Figure 3B, the survival fraction, $\bar{n}'(z)/\bar{n}^0(z)$ is plotted.

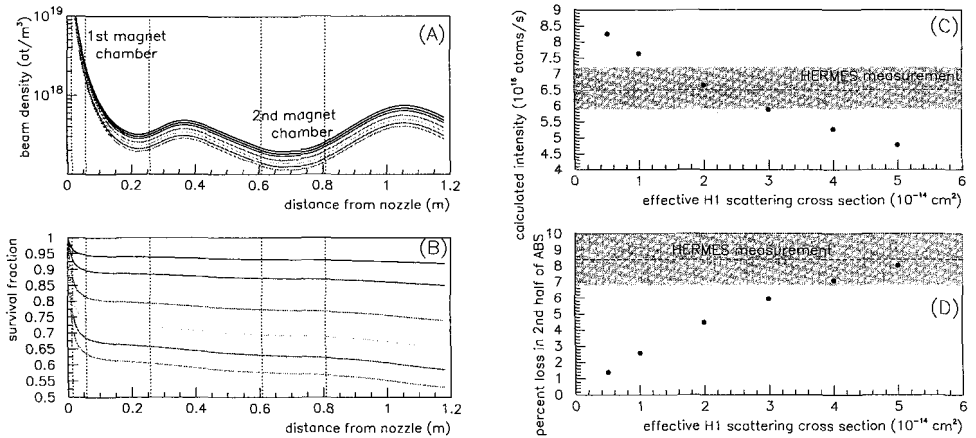


Fig 3. See description in text.

From these numbers, the calculated loss in the second half of the ABS ($0.6 < z < 1.16 \text{ m}$) is extracted and shown as the points in Figure 3D.

4. Conclusions

An new approach has been made to absolute numerical estimation of IBS losses in an ABS hydrogen beam, available for the first time. The calculation requires 1-2 minutes and thus is suitable for a parameter search that optimizes the intensity of an ABS design. Although still in a preliminary state, the first results are promising. When compared with molecular beam measurements, there is good absolute agreement at low fluxes. At high fluxes, the

attenuation is underestimated, probably due to losses from rest gas attenuation that are not yet included in the calculation.

The discrepancy in the HERMES calculations and measurements can be explained in two ways. The first is to use a peaking exponent in the starting generator of 2-3 instead of 1, with the consequence that the total IBS losses are 40-50%. The second explanation is that two corrections to $v_{rel} = \Delta v$ have been neglected. One increases (decreases) v_{rel} for a converging (diverging) beam. The other accounts for changes in the velocity distribution along the beam axis, with the consequence that v_{rel} is larger for the second half of the HERMES ABS. Either correction would increase the calculated attenuation only for the second half of the ABS, and the total losses to 20-30%. A further refinement of the method for estimating IBS losses is foreseen that includes these corrections and additional measurements.

References

1. L. D. Landau and E. M. Lifshitz, *The Classical Theory of Fields* (Pergamon Press, New York, 1975; p. 34 English edition).
2. P. S. Krstic and D. R. Schultz, *Phys. Rev.* **A60**, 2118 (1999).
3. Z. Ye, these proceedings.
4. A. Nass et. al., *Nucl. Inst. and Meth.* **A505**, 633 (2003).

DIRECT MEASUREMENT OF INTRA-BEAM SCATTERING IN ATOMIC BEAM SOURCES

Z. YE

DESY, Hamburg, Germany

(for the HERMES Target Group)

A method to directly measure the beam intensity loss due to Intra-Beam Scattering in Atomic Beam Sources by using a set of high frequency transitions between the two sextupole magnet subsystems of the atomic beam sources is introduced. Measurements done by means of this method on the HERMES-ABS are presented.

1. Introduction

The working principle of ABS, namely spin separation by sextupole magnets and transition between hyperfine states by high frequency transitions (HFT), has been reviewed by Steffens and Haerberli [1]. The quest for higher beam intensity constitutes one of the key issues in ABS development. The limitation of the ABS beam intensity has been traced back to residual gas attenuation (RGA) and intra-beam scattering (IBS) [2] effects. In particular the IBS effect is far from being understood. In this paper a method to directly measure the IBS effect in the ABSs by using the HFTs between two sextupole magnet subsystems is introduced. Measurements performed on the HERMES-ABS by means of this method are presented.

2. ABS Intensity

The effect of an HFT, exchanging atoms in state $|a\rangle$ and $|b\rangle$, on the hyperfine populations of the hydrogen atoms can be described by a 4×4 matrix \mathbf{T}_{ab} :

$$n_i^{new} = \sum_j (\mathbf{T}_{ab})_{ij} \cdot n_j^{old} \quad (1)$$

where $n_i^{new(old)}$ is the hyperfine population number of hydrogen atoms in state $|i\rangle$, describes the status after (before) the transition, and \mathbf{T}_{ab} is the matrix of the transition efficiencies in which the element $(\mathbf{T}_{ab})_{ij}$ describes the probability that an atom in state $|j\rangle$ is exchanged to state $|i\rangle$ by the HFT.

The sextupole magnets serve to focus atoms with electron spin $m_s = +\frac{1}{2}$ (hyperfine state^a $|1\rangle$ and $|2\rangle$) and deflect atoms with $m_s = -\frac{1}{2}$ (hyperfine state $|3\rangle$ and $|4\rangle$). With a set of HFTs in between the sextupole magnet system of an ABS, the probability for a hydrogen atom to be transmitted by the sextupole system can be represented as a 4×4 matrix. The element of the matrix σ_{ij} describes the probability of an atom transmitted through the ABS which is in state $|i\rangle$ before and in state $|j\rangle$ after the HFTs between the two sextupole subsystems.

With the knowledge of the transition efficiencies of the HFTs and of the transmission probabilities of the sextupole system, the ABS delivered beam intensity can be determined. If ρ_{IBS} and ρ_{RGA} denote the intensity loss in the ABS due to the IBS and RGA effects respectively, the ABS beam intensity can be expressed as:

$$I = I_0 \cdot (1 - \rho_{RGA}) \cdot (1 - \rho_{IBS}) \cdot \sum_{i,j} (\mathbb{T})_{ij} \cdot \sigma_{ji} \quad (2)$$

where I_0 is the beam intensity at the beginning of the ABS, \mathbb{T} denotes the product of the transition matrices of the HFTs between the two sextupole subsystems.

3. Intra-Beam Scattering Measurement

Intra-Beam Scattering is caused by collisions between particles with different velocities (or angles) in the beam. In a simple model considering a beam of parallel particles with velocity spread Δv over the mean velocity \bar{v} , the beam intensity $\Phi(z)$ can be described by the following equation [2]:

$$\frac{d\Phi}{\Phi} = -\frac{\sigma_{IBS} \cdot \Delta v \cdot \Phi}{\bar{v}^2} \cdot dz \quad (3)$$

with σ_{IBS} being the IBS loss cross section. Hence the relative beam intensity loss, $d\Phi/\Phi$, is proportional to the beam intensity Φ . Therefore, by varying the beam intensity and keeping the velocities, trajectories and distribution of the particles within the beam unchanged, the loss due to the IBS effect can be varied and measured. These conditions can be accomplished by using the HFTs between the two sextupole subsystems of the HERMES-ABS.

The HERMES-ABS is described in Ref [3]. A Weak Field Transition (WFT) 1-3^b and a Strong Field Transition (SFT) 2-4 are installed between the two sextupole subsystems. Different ABS injection modes can be selected via these HFTs. Four different ABS injection modes have been employed in the measurement, as listed in Tab. 1.

^aThe notation is based on the Breit-Rabi basis [1] $|a\rangle = |m_s, m_l\rangle$:

$$\begin{aligned} |1\rangle &= |1/2, 1/2\rangle \\ |2\rangle &= \cos\theta |1/2, -1/2\rangle + \sin\theta |-1/2, 1/2\rangle \\ |3\rangle &= |-1/2, -1/2\rangle \\ |4\rangle &= -\sin\theta |1/2, -1/2\rangle + \cos\theta |-1/2, 1/2\rangle \end{aligned}$$

where m_l is the nuclei spin, $\theta = \frac{1}{2} \arctan \frac{B_c}{B}$ is the mixing angle and B_c the critical magnetic field (50.7mT for hydrogen).

^bIt can be retuned as a Medium Field Transition (MFT).

Table 1. ABS injection modes used in the measurements. The table shows the corresponding measurement No., the HFTs between the two sextupole subsystems of the ABS employed, the hyperfine states ideally injected into the target cell by the ABS, and the relative beam intensity measured by a Breit-Rabi polarimeter.

Meas. No.	HFTs employed	injected states	BRP count rates
1	-	$ 1\rangle+ 2\rangle$	66.5 ± 0.3 kHz
2	SFT2-4	$ 1\rangle$	41.8 ± 0.2 kHz
3	WFT1-3	$ 2\rangle$	38.2 ± 0.3 kHz
4	SFT2-4, WFT1-3	no state	10.9 ± 0.1 kHz

Since the HFTs have no influence on the trajectories of the atoms, the ABS beam intensities of the injection modes listed in Tab. 1 are identical until the beginning of the second sextupole subsystem. Therefore the intensity loss due to the RGA and IBS effects in the first part of the ABS is the same for all these modes. Hence this measurement only deals with the second part of the ABS.

Because the nucleon magnetic moment is negligible compared to the electron one, the influence of the sextupole magnets on the motion of atoms in states $|1\rangle$ and $|2\rangle$ can be regarded as the same. We can then assume that the injection mode with state $|1\rangle$ is identical to the injection mode with state $|2\rangle$, as the atoms in these modes have the same trajectory and velocity distribution within the beam, and that the injection mode with injection state $|1\rangle + |2\rangle$ has the same density distribution but twice the intensity in the second part of the ABS compared to the injection modes with only state $|1\rangle$ or $|2\rangle$. The beam intensity losses in the second part of the ABS due to the IBS effect can therefore be related:

$$\rho_{IBS,|1\rangle+|2\rangle}^{(2)} = x \approx 2\rho_{IBS,|1\rangle}^{(2)} \approx 2\rho_{IBS,|2\rangle}^{(2)} \quad (4)$$

Here we have introduced $x = \rho_{IBS,|1\rangle+|2\rangle}^{(2)}$. For the fourth injection mode with ideally no atoms injected, we assume $\rho_{IBS, \text{no state}}^{(2)} \approx 0$. From Ref [4,5], we know that the RGA effect in the second part of this ABS can be considered as negligible. Taking all these into account, from Eq. (2) and (Eq. 4) we have:

$$\frac{x}{2(1-x)} - \frac{x}{2} \cdot \frac{I^{no}}{I^{1|1+2}} = \frac{(I^{1|1} + I^{2|2}) - (I^{1|1+2}) + I^{no}}{I^{1|1+2}} + \delta_{\text{WFT}} \cdot \frac{1 - \frac{x}{2}}{1 - x} \quad (5)$$

where

$$\delta_{\text{WFT}} = \frac{\sum_{ij} (\mathbf{I}_{4 \times 4} + \mathbf{W}_{13} \cdot \mathbf{S}_{24} - \mathbf{W}_{13} - \mathbf{S}_{24})_{ij} \cdot \sigma_{ji}}{\sum_i \sigma_{ii}} \quad (6)$$

describe the correlation terms between \mathbf{S}_{24} and \mathbf{W}_{13} . Since SFT 2-4 and WFT 1-3 exchange different hyperfine states, $\delta_{\text{WFT}} = 0$.

Because recombination of hydrogen atoms into molecules in the HERMES target cell [6] is independent of the target density and spin states [7], the total intensity of the sampled atomic beam measured by a Breit-Rabi Polarimeter [8] is a good measure of the ABS beam intensity. Deriving x from Eq. (5) with the ABS beam intensities measured with the Breit-Rabi polarimeter (as listed in Tab. 1), we find the beam intensity loss due to IBS in the

second part of the ABS to be $x = 8.4 \pm 1.6\%$. Measurements were also performed with the SFT 2-4 and a MFT 1-3 inbetween the sextupoles, the result was in agreement with the result reported here.

4. Conclusion

By using HFTs between the sextupole magnets and the defocusing action of the downstream sextupole magnets, it has been possible to vary the atomic beam intensity in a controlled way, and to directly measure the loss of the beam intensity due to the IBS effect in the second part of the HERMES-ABS. For the injection mode with two states, the beam intensity loss in the second part of the HERMES-ABS due to the IBS effect was measured to be $8.4 \pm 1.6\%$.

References

1. E. Steffens and W. Haeberli, Rep. Prog. Phys. , 66 (2003) 1887.
2. E. Steffens, Proceedings of 7th International Workshop on Polarized Gas Targets and Polarized Beams, (Urbana-Champaign IL, 1997).
3. A. Nass et al, Nucl. Instrum. Methods A, 505 (2003) 633.
4. T. Wise et al, Nucl. Instrum. Methods A, 336 (1993) 410-422.
5. F. Stock et al, Nucl. Instrum. Methods A, 343 (1994) 334.
6. C. Baumgarten et al, Nucl. Instrum. Meth. A, 496 (2003) 277.
7. C. Baumgarten et al, Nucl. Instrum. Meth. A, 496 (2003) 263.
8. C. Baumgarten et al, Nucl. Instrum. Meth. A, 482 (2002) 606.

POLARIZED ELECTRONS FOR LINEAR COLLIDERS*

J. E. CLENDENIN, A. BRACHMANN, E. L. GARWIN, R. E. KIRBY, D. -A. LUH, T. MARUYAMA,
C. Y. PRESCOTT, J. C. SHEPPARD, J. TURNER

Stanford Linear Accelerator Center, Menlo Park, USA

R. PREPOST

Department of Physics, University of Wisconsin, Madison, USA

Future electron-positron linear colliders require a highly polarized electron beam with a pulse structure that depends primarily on whether the acceleration utilizes warm or superconducting RF structures. The International Linear Collider (ILC) will use cold structures for the main linac. It is shown that a DC-biased polarized photoelectron source such as successfully used for the SLC can meet the charge requirements for the ILC micropulse with a polarization approaching 90%.

1. Charge

The SLAC Linear Collider (SLC) established that reliable electron beams with a polarization at high energy approaching 80% can be provided over periods of years. However, the beam pulse structures planned for future colliders present new demands. The ILC beam at the interaction point (IP) is expected to consist of a train of micropulses spaced ~ 300 ns apart. If one assumes that at the source it is prudent to be able to generate at least twice the charge required at the IP, then the charge, pulse length, and average current for each micropulse are indicated in Table 1 and compared with both the Next Linear Collider (NLC) and SLC designs. The ILC linac will use superconducting (SC) L-band (LB) RF for the main linac, but normal conducting (NC) RF is a possibility for the initial acceleration including the injector.

Highly polarized electrons for linac beams are generated by illuminating a p-doped GaAs (or its analogues) crystal with circularly polarized monochromatic light tuned to the band-gap edge. The absorbed photons promote electrons from filled valance band states to the conduction band (CB). If an atomically-clean crystal surface is treated with a Cs-oxide layer, then combined with band-bending, the work function can be lowered to below

*This work is supported by Department of Energy contract DE-AC02-76SF00515.

the vacuum level, resulting in a negative electron affinity (NEA) surface from which CB electrons reaching the surface are readily extracted by applying a negative bias.

The activated cathode is extremely sensitive to any contamination. To reduce field emission to near-zero, the SLC gun was operated with a bias of only -120 kV, which resulted in fields of ~ 1.8 and 7 MV/m on the cathode crystal and electrode respectively [1]. Under these conditions, space charge will limit the peak current that can be extracted to 11 A, assuming a fully illuminated round crystal of diameter 2 cm. A practical micropulse with temporal and spatial shapes approximating a Gaussian will be limited to average currents that are significantly lower than the space charge limit (SCL); e.g., ~ 7 A in the SLC case [2].

If the beam generated by the source can be accelerated with the same micropulse spacing as at the IP, then Table 1 shows there is no SCL problem regardless of whether the initial accelerating RF is SC or NC. However, if the initial accelerating RF is NC-SB to accommodate some possible damping ring designs, then the SCL could become a problem as illustrated in the 3rd column of values.

Table 1. Collider charge requirements at the source and the space charge limit.

		NLC	ILC	ILC	SLC
		NC-SB	SC-LB	inj: NC-SB linac: SC-LB	Design (2-cm)
n_e	nC	2.4	6.4	6.4	20
Δt	ns	0.5	2	0.5	3
$I_{\mu pulse.avg}$	A	4.8	3.2	12.8	6.7
$I_{\mu pulse.pk}$	A				(SCL) 11

2. Polarization

The highest electron-beam polarization is achieved using crystals in which the natural degeneracy of the heavy- and light-hole energy bands at the valence-band maximum is removed. This is accomplished by introducing a lattice mismatch with the substrate, or by using a short-period superlattice structure for the epilayer. By using a combination of both techniques, a separation of 50-80 meV is readily achieved. This is sufficient to tune a laser to promote electrons to the CB from the heavy-hole band only, promising 100% polarization. In practice polarizations $\geq 90\%$ have been reported [3], and the recent parity-violating asymmetry experiment at SLAC using the 50-GeV polarized electron beam, E-158, measured $P_e = 85\%$ in the early phase with a strained-layer crystal, and in the final phase an online value of $P_e = 90\%$ using a strained superlattice crystal. In Table 2, a comparison of polarization results for three photocathodes representing these two structures is presented. The crystal operating temperature was either warm ($\sim 20^\circ$) or cold ($\sim 0^\circ$).

The polarization of accelerator beams is made at low energy with Mott polarimeters and at high energy with typically Møller or Compton polarimeters. The two offline Mott polarimeters developed for the SLC are still in use. These polarimeters gave results that were consistent with the SLC Compton polarimeter (accuracy of $< 0.5\%$) within 2% after corrections for known depolarization in the transmission to the IP.

Table 2. Comparison of three photocathodes representing two structures.

Cathode Structure	Growth Method	$P_{e,max}$	λ_0 (nm)	$QE_{max}(\lambda_0)$	Polarimeter	Ref
1a GaAsP/GaAs strained SL	MOCVD	≥ 0.90	775	0.004	Mott	[3]
			warm		Nagoya	
1b GaAsP/GaAs strained SL	MBE	0.86	783	0.012	CTS Mott	[4]
			warm		SLAC	
		0.90	780	0.008	Møller E158-III	
			cold		SLAC	
2 GaAsP/GaAs strained-layer	MOCVD	0.82	805	0.001	CTS Mott	[5]
			warm		SLAC	
		0.85	800	0.004	Møller E158-I	[6]
cold	SLAC					

Since the electron polarization can vary significantly from one crystal to another for the same crystal structure, and can even vary by a few percent for a single crystal depending on surface conditions, it has been very difficult to compare the polarization results between different facilities. Some insight into the accuracy of the polarimeters themselves was recently gained in an experiment at JLAB, in which the polarized electron beam was switched on a pulse-to-pulse basis between three different Møller polarimeters and a Compton polarimeter, all at high energy, and compared with an inline Mott polarimeter at low energy [7]. Undetected systematic effects and errors in the simulated values of the effective analyzing powers were revealed at the level of several percent.

As shown in Table 2, the higher polarization using cathode 1b relative to cathode 2 is the same when measured by two independent polarimeters. If the E158 Møller polarization data—corrected for the 1% depolarization between source and polarimeter—for a GaAsP/GaAs strained superlattice crystal is combined with the SLAC Mott measurements made with a cathode crystal cut from the same wafer, the result is a polarization at the source of $(88 \pm 4)\%$.

References

1. R. Alley, H. Aoyagi, J. Clendenin *et al.*, *Nucl. Instrum. and Meth. A* **365**, 1 (1995).
2. K. R. Eppley, T. L. Lavine, R. A. Early *et al.*, in *Conf. Record of the 1991 IEEE Part. Acc. Conf.*, 1964 (1991).
3. O. Watanabe, T. Nishitani, K. Togawa *et al.*, in *SPIN 2000*, AIP Conf. Proc. **570**, 1024 (2001).
4. T. Maruyama, D. A. Luh, A. Brachmann *et al.*, *Appl. Phys. Lett.* **85**, 2640 (2004).

5. T. Maruyama, A. Brachmann, J. E. Clendenin *et al.*, *Nucl. Instrum. and Meth. A* **492**, 199 (2002).
6. P. L. Anthony, R. G. Arnold, C. Arroyo *et al.*, *Phys. Ref. Lett.* **92**, 181602 (2004).
7. J. M. Grames, C. K. Sinclair, J. Mitchell *et al.*, *Phys. Rev. ST-AB* **7**, 042802 (2003).

THE COMPASS POLARIZED TARGET

F. GAUTHERON, G. BAUM, Y. KISSELEV

Physics Department, University of Bielefeld, Bielefeld, Germany

N. DOSHITA, S. GOERTZ, J. KOIVUNIEMI, K. KONDO, W. MEYER, G. REICHERZ

Physics department, University of Bochum, Bochum, Germany

J. BALL, A. MAGNON, C. MARCHAND

CEA, DAPNIA/SPhn Saclay, Gif-sur-Yvette, France

The COMPASS experiment runs the largest polarized target system ever built to study the spin structure of the nucleon by the deep inelastic muon scattering process. This target, largely reusing the Spin Muon Collaboration target apparatus, consists of two cells oppositely polarized in a 2.5T field, and filled up with granulated ${}^6\text{LiD}$ as a deuteron target. The excellent stability and polarization performance of the target system allowed two ${}^6\text{LiD}$ world polarization records to be set under these conditions between 2001 and 2004.

1. The goal and the challenge

The main goal of the COMPASS muon program is to determine the gluon contribution to the nucleon spin by measuring the double spin asymmetry accessible through open charm leptoproduction and high- p_T hadron pair events from the scattering of a 160 GeV polarized muon beam on a longitudinally and oppositely polarized deuteron double cell target.

The double spin asymmetry is experimentally given by

$$A^{exp} = \frac{N^{\uparrow\uparrow} - N^{\uparrow\downarrow}}{N^{\uparrow\uparrow} + N^{\uparrow\downarrow}} = P_B P_T f A^{\mu N \rightarrow q\bar{q}X}, \quad (1)$$

$A^{\mu N \rightarrow q\bar{q}X}$ is the cross section asymmetry that would be directly measured for a pure target material, target and beam 100% polarized. N is the counting rate for parallel and antiparallel spin orientations between the beam and the target. P_B is the beam polarization, P_T the target polarization, and the dilution factor f is the ratio of the polarizable nucleons to the total nucleons. For a given beam polarization P_B the quantity $P_T \cdot f$, which depends on the target material, must be maximized. The challenge for such a target is:

- (1) to run the largest solid polarized target to get a high luminosity to obtain higher statistics,
- (2) to achieve the highest possible polarization requested in Eq. (1),
- (3) to measure the polarization without disturbing the experiment,
- (4) to reduce multiple scattering for an efficient reconstruction of events by minimizing the non-target material,
- (5) to allow frequent changes of the sign of the polarization to combat false asymmetries arising from acceptance changes.

2. The target system overview

The COMPASS muon program has restarted the SMC target system [1, 2]. This is mainly composed of two in-line target cells, each of 3cm in diameter and 60cm long, separated by a 10cm gap and cooled by a $^3\text{He}/^4\text{He}$ dilution refrigerator. The cells filled with ^6LiD are located in an homogeneous longitudinal 2.5 T magnetic field and irradiated by microwaves to build up the polarization by the dynamic nuclear polarization (DNP) process. A nuclear magnetic resonance (NMR) system measures the polarization.

2.1. The dilution refrigerator

A powerful dilution refrigerator is used to cool the 350g of ^6LiD grains loaded into the two target cells [1]. Its high cooling power can absorb the microwave power during the DNP process, where more than 350mW is necessary at the beginning. From 200-350mK when polarizing, this dilution refrigerator can lower and maintain the target at about 50mK in the frozen spin mode to slow down the spin-lattice relaxation when the microwave are switched off.

2.2. The superconducting magnet system

This consists of a main solenoid producing a 2.5T longitudinal field with respect to the beam axis, and a dipole generating a perpendicular 0.5T field. A longitudinal field homogeneity $\Delta B/B$ as good as $3.5 \cdot 10^{-5}$ over the target volume is guaranteed by 16 additional correction coils along the solenoid. The dipole is used to perform the magnetic field rotation procedure or to allow transverse target polarization to investigate transverse cross section asymmetry. The procedure of magnetic field rotation is used to reverse the target spin orientation which is needed to combat false asymmetries coming from the difference between the spectrometer acceptance of the two target cells. This procedure also helps to reduce systematic errors coming from time dependant variation of the spectrometer efficiency or beam intensity.

Polarization reversal by magnetic field is very useful because it takes only 33 minutes and can be carried out every eight hours automatically. This avoids having to repolarize by DNP because the polarization build-up time is considerably longer in the case of ^6LiD (see Sec. 2.4). The procedure also guarantees that the field is never below 0.5T, to preserve the degree of polarization.

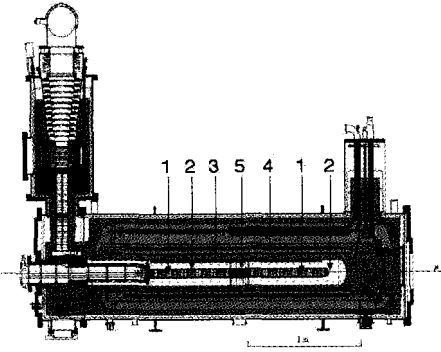


Fig 1. Side view layout of the target system. The muon beam enters the cryostat from the left. (1) target cells, (2) microwave cavity, (3) solenoid, (4) dipole, (5) microwave stopper

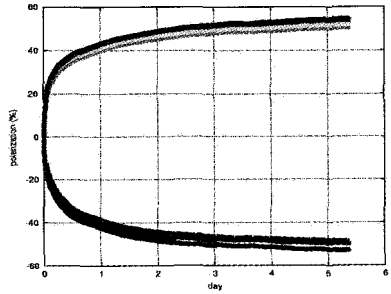


Fig 2. Typical ⁶LiD polarization build-up curve at 2.5 T. The four curves for positive/negative polarization are the response from the four NMR coils used for each cell.

2.3. The target material

The most important criteria in selecting a suitable target material are the degree of polarization and the dilution factor. Because the quantity $N^{\uparrow} + N^{\downarrow}$ in Eq. (1) is proportional to the measuring time, the beam time t to reach a certain statistical accuracy ΔA shows the dependency

$$t^{-1} \propto \rho (fP)^2 \tag{2}$$

where ρ stands for the density of the material. From Eq. (2) it is clear that the higher the product $f \cdot P$, the shorter is the required beam time for a given statistical accuracy. To characterize the material we define a figure of Merit (FoM) given by

$$FoM = \rho k (fP)^2 \tag{3}$$

including the packing factor k corresponding to the ratio of the volume occupied by the material to the volume of the target cell.

The Table 1 shows the values needed to determine the FoM of ⁶LiD used in COMPASS and also of the materials from the previous SMC experiment. ⁶LiD and D-Butanol have an equivalent degree of deuteron polarization, which is much lower than for the proton target NH₃, but the FoM is better for ⁶LiD due to a much higher dilution factor. Here we do not discuss the residual space between the pieces of material occupied by the ³He/⁴He mixture, which slightly reduces the dilution factor [3, 4].

2.4. The microwave system

Two independent EIO^a tubes are used to polarize the two target cells in opposite spin directions. Both cells are located in the microwave cavity but isolated one from the other

^aExtended Interaction Oscillator

Table 1. Comparison of the quantities of Eq. 3 and figure of merit for different target materials.

	SMC	SMC	COMPASS
Material	NH ₃	D-butanol	⁶ LiD
Density	0.85	1.10	0.84
Polarization	<i>H</i> :~0.90	<i>D</i> :~0.50	<i>D</i> :~0.50
Packing factor <i>k</i>	0.60	0.60	0.55
Dilution factor <i>f</i>	0.176	0.238	~0.50
FoM	10.3	6.7	16.0

by a microwave stopper (see Fig. 1). For ⁶LiD at 2.5T, the frequencies used for positive (negative) polarization are [70.180 - 70.238]GHz ([70.285 - 70.245]GHz). The frequencies and powers are continuously adjusted depending on the degree of polarization reached. In addition, frequency modulation of about 5MHz at a rate of 500Hz is used during the process to optimize the speed and the degree of the polarization [5]. From Fig. 2 it can be seen that $|P|=40\%$ after one day of DNP. This can be compared to the 5-6 hours needed to get the same degree of polarization with D-butanol. After more than five days of DNP the average polarizations are about $+55\%/-51\%$ but with a strong asymptotic behaviour, making it meaningless to continue polarization build-up thereafter.

2.5. The NMR system

The polarization is determined from eight NMR coils distributed along the target cells and tuned to the deuteron Larmor frequency at 2.5 T. They are driven simultaneously by a radiofrequency synthesizer with a frequency sweep of $\pm 50\text{kHz}$ around the deuteron Larmor frequency (16.38MHz) [6]. The spectra obtained from this scan are the direct result from the change of the coil impedance through inductance change induced by the change of magnetic susceptibility $\chi(\omega)$ of the material, which is proportional to the polarization [7]. A Q-meter determines the resulting voltage variation. The background signal is acquired by driving the magnetic field out of resonance. Subtracting it from the raw signal give access to the “real” line shape, which is integrated over a suitable frequency range to extract the polarization value.

3. Results and perspectives

The large COMPASS polarized target has run since 2001 in a very reliable way. A first world record of ⁶LiD polarization with $+56.8\%$ and -52.7% was reached in 2002. In 2004 a second world record was set with $+57.1\%$ and -53.0% , still at 2.5T. In order to increase the acceptance for hadrons from 70 mrad to 180 mrad a new solenoid with a larger diameter is under construction and will be combined with a dedicated microwave cavity. A promising trytil-doped D-butanol material with a substantial improvement of the maximum polarization is under investigation at Bochum university [8, 9]. A deuteron polarization higher than

80% seems to be accessible with this material, which would increase the FoM to 21 - 22. These features would improve the statistical accuracy of the double spin asymmetry by 30% for a given beam time.

References

1. D. Adams et al. *Nucl Instr and Meth A* **437**, 23-67 (1999).
2. N. Doshita et al. *Nucl Instr and Meth A* **526**, 138-143 (2004).
3. N. Doshita et al. Proc. Spin-Praha-2004 conference, to be published.
4. J. Koivuniemi et al. COMPASS note 2003-5.
5. Yu Kisselev, *Nucl Instr and Meth A* **356**, 99-101 (1995).
6. K. Kondo et al. *Nucl Instr and Meth A* **526**, 70-75 (2004).
7. M. Goldman, *J. Magn. Res.* **17**, 393-298 (1975)
8. St. Goertz et al. *Nucl Instr and Meth A* **526**, 43-52 (2004).
9. *CERN Courier*. September 2003, "Bochum breaks deuteron polarization records".

POLARIZATION BUILD UP IN COMPASS ${}^6\text{LiD}$ TARGET

J. KOIVUNIEMI, N. DOSHITA, S. GOERTZ, K. KONDO, I. L. GARCIA, W. MEYER, G. REICHERZ

Physics Department, University of Bochum, Bochum, Germany

F. GAUTHERON

Physics Department, University of Bielefeld, Bielefeld, Germany

The CERN COMPASS experiment uses a large double 424 cm³ cell polarized ${}^6\text{LiD}$ target for the muon program. High nuclear spin polarization $|P| > 50\%$ is obtained, typically in five days. The high cooling power of the COMPASS dilution refrigerator helps to build up the polarization fast at temperatures around 300 mK. At lower microwave power with lower spin and lattice temperatures, the polarization build up is slower. We discuss these features of the dynamic nuclear polarization of our ${}^6\text{LiD}$ target.

The COMPASS polarized target and the nuclear magnetic resonance technique to determine the nuclear polarization have been described in recent papers [1–4]. In the ${}^6\text{LiD}$ target material [5], the ${}^6\text{Li}$ is diluted with 4.2 % of ${}^7\text{Li}$. About $10^{-4} - 10^{-3}$ paramagnetic centers per nucleus have been created by irradiation in an electron beam [6]. The theory of dynamic nuclear polarization has been discussed in the literature [7, 8] and in recent review papers [9, 10]. High deuteron polarization $|P| > 40\%$ in a 2.5 T field is reached in 24 hours with a ${}^3\text{He}$ flow in the dilution cryostat of 80 - 120 mmol/s. The maximum polarization $|P| > 50\%$ is reached in five days. For each cell the power of the 70 GHz microwave pumping of the electron spins is reduced from 200 mW in the beginning to 25 mW during the polarization process. At the same time the optimum microwave frequency shifts 40 MHz up (down) for positive (negative) polarization [2]. The dynamic nuclear polarization can also be seen as a nuclear cooling process [11, 12], in which heat is removed from the spin system to the lattice.

The deuteron and ${}^6\text{Li}$ in the target material have nuclear spin quantum number 1. In a homogeneous magnetic field, three energy levels E_+ , E_0 and E_- are possible for them if the interaction between the spins is neglected. Each energy level has a population p_+ , p_0 and p_- with $p_+ + p_0 + p_- = 100\%$. In the absence of quadrupole splitting, only one narrow

nuclear magnetic resonance line, 3 kHz wide, is seen [13], and $E_+ - E_0 = E_0 - E_- = hf_0$. Here f_0 is the nuclear magnetic resonance frequency of the spin system. The intensity of the absorption signal integrated over the frequency is proportional to the population difference [8]

$$I = \frac{1}{f_0} \int_{f_0-\Delta}^{f_0+\Delta} \chi''(f) df = -a \cdot (p_- - p_+) = -a \cdot P, \quad (1)$$

where P is the vector polarization, $\chi''(f)$ the dynamic susceptibility, and $\Delta = 50$ kHz is much larger than the NMR-line width. The constant a is positive and is determined during a thermal equilibrium calibration [3], when the spin temperature is the same as the measured lattice temperature T_L . For positive polarization the signal intensity I is negative since $p_- > p_+$. The nuclear polarization is given by the Brillouin function [11, 12]

$$P_J(x) = \frac{2J+1}{2J} \coth\left(\frac{2J+1}{2J}x\right) - \frac{1}{2J} \coth\left(\frac{1}{2J}x\right), \quad (2)$$

where the spin number $J = 1$ for deuteron and ⁶Li, and $J = 3/2$ for ⁷Li. Here $x = hf_0/k_B T_S$ with k_B the Boltzmann constant and T_S the spin temperature. The thermal equilibrium calibration of the polarization [3] is done around 1 K temperature at the nominal NMR field of 2.506 T, corresponding to the resonance frequency f_0 of 16.379 MHz. The spin-lattice relaxation time is typically 3 hours and a good thermal equilibrium between the spin system and the lattice is reached in about 15 hours. The deuteron polarization from Eq. 2 at $T_S = T_L \sim 1$ K is about +0.05 %.

Typical polarization build up is shown in Fig. 1. The target material is heated up to 0.1 K - 0.3 K by the microwaves [2]. Even if the spin system could be cooled to 0.1 K, the resulting nuclear polarization would still be very low. The electron spin system cools down due to microwave pumping, and heat from the bulk nuclear spin system is transferred to the paramagnetic centers by a nuclear spin diffusion process [9, 14]. After the dynamic nuclear polarization the thermal energy of the nuclear spin system has been reduced to $T_S \sim \pm 0.9$ mK. We have carefully checked that during the polarization all the nuclei share the same spin temperature [1]. Thus the calculation of the polarizations of ⁶Li and ⁷Li can be done from Eq. 2, using the measured deuteron polarization and the resonance frequencies for ⁶Li and ⁷Li in the 2.506 T field. The nuclear heat capacity in a constant field for independent spins is [11, 12]

$$C_S/R = (x/2)^2 \sinh^{-2}(x/2) - ((2J+1)x/2)^2 \sinh^{-2}((2J+1)x/2) \quad (3)$$

with R the universal gas constant. The heat capacity depends on the polarization through Eq. 2. At the maximum polarization values obtained it is 3.1 J/mol·K for D and ⁶Li and 4.3 J/mol·K for ⁷Li. The nuclear cooling power can be estimated from the rate of polarization build up $\dot{Q}_S = n \cdot C_S(T_S) \cdot dT_S/dt$. In the beginning it is 100 μ W for one target cell and drops fast below 1 μ W when polarization $|P| > 20\%$ is reached. This is small compared to the 25 - 200 mW from the microwaves, since the energy needed for electron spin flip is about $5 \cdot 10^3$ higher than for nuclear spin flip. The electron spin normally has a very short relaxation time to the lattice phonon system [8]. The lattice heat conductivity is [15]

$$\kappa = 1/3 \cdot C_V \cdot v_s \cdot l = 4/5 \cdot \pi^4 \cdot R \cdot n_V \cdot v_s \cdot l \cdot (T_L/\theta_D)^3, \quad (4)$$

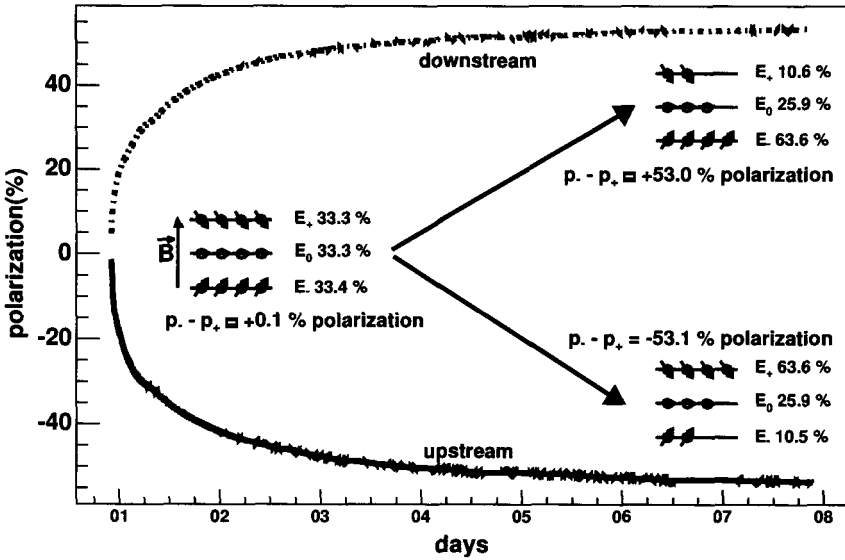


Fig 1. Typical deuteron polarization build up from 2004. Both upstream and downstream target cells are polarized simultaneously. About $\pm 40\%$ polarization is reached in 24 hours after starting the microwave pumping of electron spins. The build up then slows and the final polarization is reached in about five days from the start. The initial and final level populations for spin 1 deuteron are shown in the figure. The vector polarization $P = p_- - p_+$ is given by the population difference between the lowest and the highest energy levels. Since the gyromagnetic ratio of the deuteron is positive, the minimum energy E_- is achieved when the spin is aligned along the magnetic field. The tensor polarization can be estimated to be $T = 1/2(1 - 3p_0) = 11\%$ at the maximum. The highest polarizations correspond to a spin temperature T_S of 0.87 mK or -0.87 mK for negative polarization. From Eq. 2 the polarization of ${}^6\text{Li}$ can be estimated to be $\pm 51.3\%$ and the polarization of ${}^7\text{Li}$ $\pm 92.4\%$.

where C_V is the heat capacity per volume, $\theta_D \sim 1000$ K the Debye temperature [16], v_s sound velocity, n_V the molar density, and l the phonon mean free path. Since the dominant phonon wave length [11] $\theta_D/T_L \cdot 2 \text{ \AA} \sim 2 \mu\text{m}$ is much larger than the size of crystal defects, the phonon scattering takes place only at boundaries. Thus l is the crystal size $\sim 2 - 4$ mm. The probability for a phonon to cross the boundary between ${}^6\text{LiD}$ and helium [11] gives the relaxation time $\sim 70 \cdot l/v_s \sim 10 - 100 \mu\text{s}$. The phonon thermalization at boundaries is fast compared to the single electron spin flip rate $\sim (hf_0 N_e)/\dot{Q}_S \sim 30 - 300$ s, with $\dot{Q}_S \sim 0.1$ nW/crystal. At the same time the electron spin flips give heat $\dot{Q}_e \sim 400$ nW/crystal. The lattice heat capacity is negligible compared to that of the helium. Thus the high helium temperature limits the achievable maximum polarization [7, 9], and a high ${}^3\text{He}$ flow rate helps to build up polarization faster due to more efficient removal of heat from the paramagnetic centers.

References

1. J. Ball *et al.*, *Nucl. Instr. and Meth. A* **498**, 101 (2003).

2. N. Doshita *et al.*, *Nucl. Instr. and Meth. A* **526**, 138 (2004).
3. K. Kondo *et al.*, *Nucl. Instr. and Meth. A* **526**, 70 (2004).
4. N. Doshita *et al.*, submitted to Czech. J. Phys. for 2005.
5. S. Neliba *et al.*, *Nucl. Instr. and Meth. A* **526**, 144 (2004).
6. A. Meier, Ph.D. Thesis, University of Bochum, Germany (2001).
7. M. Goldman, *Spin Temperature and Nuclear Magnetic Resonance in Solids*, Oxford University Press, Oxford (1970).
8. A. Abragam, *The Principles of Nuclear Magnetism*, Oxford University Press, Hong Kong (1989).
9. S. T. Goertz, *Nucl. Instr. and Meth. A* **526**, 28 (2004).
10. St. Goertz, W. Meyer, G. Reicherz, *Prog. Part. Nucl. Phys.* **49**, 403 (2002).
11. O.V. Lounasmaa, *Experimental Principles and Methods Below 1 K*, Academic Press, London (1974).
12. F. Pobell, *Matter and Methods at Low Temperatures*, Springer-Verlag, Berlin (1996).
13. J. Koivuniemi *et al.*, *Nucl. Instr. and Meth. A* **526**, 100 (2004).
14. B. van den Brandt *et al.*, *Nucl. Instr. and Meth. A* **526**, 81 (2004).
15. N. W. Ashcroft, N. D. Mermin, *Solid State Physics*, Saunders College, Hong Kong (1987).
16. B. W. James, H. Kheyrandish, *J. Phys. C: Solid State Phys.* **15**, 6321 (1982).

THE POLARIZED INTERNAL GAS TARGET OF ANKE AT COSY *

K. GRIGORIEV¹, R. ENGELS², A. GUSSEN³, P. JANSEN³, H. KLEINES⁴, F. KLEHR³, P. KRAVTSOV¹,
B. LORENTZ², M. MIKIRTYTCHIANTS¹, M. NEKIPELOV¹, V. NELYUBIN¹, H. P. g. SCHIECK⁵,
F. RATHMANN², J. SARKADI⁴, H. SEYFARTH², E. STEFFENS⁶, H. STROHER², V. TROFIMOV¹,
A. VASILYEV¹, K. ZWOLL⁴

(1) Petersburg Nuclear Physics Institute, Gatchina, Russia

(2) Institute für Kernphysik, Forschungszentrum Jülich, Germany

(3) Zentralabteilung Technologie, Forschungszentrum Jülich, Germany

(4) Zentrallabor für Elektronik, Forschungszentrum Jülich, Germany

(5) Institut für Kernphysik, Universität zu Köln, Germany

(6) Physikalisches Institut II, Universität Erlangen-Nürnberg, Germany
for the ANKE Collaboration.

For future few-nucleon interaction studies with polarized beams and targets at COSY-Jülich, a polarized internal storage cell gas target is currently being developed and will be implemented at ANKE shortly after unpolarized internal storage cell gas target tests in 2005. At present, tests with Atomic Beam Source and cell prototypes at the laboratory of the Institute for Nuclear Physics (IKP, Forschungszentrum Jülich) have been prepared. The results of these tests with the Lamb-Shift polarimeter indicate that the signal from the polarized atoms can be distinguished from the background. At the same time, cell tests at ANKE for determination of the dimensions of the stored COSY beam have been performed.

1. Introduction

At present a polarized internal gas target (PIT) of ANKE^a at COSY^b is being developed. It is now being prepared for installation in the internal storage ring at COSY. The main parts of the PIT are : *Atomic Beam Source, Lamb-Shift polarimeter, and a Storage Cell*. The description of these components given here is only brief.

The ABS was used to feed a gas-storage cell with polarized hydrogen or deuterium atoms. Due to the space limit at the magnetic spectrometer ANKE [1] it will be installed vertically as shown in Fig. 1. Using a storage cell will increase the luminosity by about two orders of magnitude compared to an atomic gas jet crossing the stored, circulating, COSY beam [2]. A Lamb-Shift polarimeter

measures the polarization of atoms effusing from the storage cell into the polarimeter.

*This work is supported by BMBF, COSY-FFE, FZJ.

^aApparatus for Studies of Nucleon and Kaon Ejectiles, Forschungszentrum Jülich

^bCooler SYncrotron COSY, Forschungszentrum Jülich, Germany

The major parameter of storage cell design is its inner diameter, which should not be too small and cut beam at injection when the beam diameter is much bigger than after acceleration.

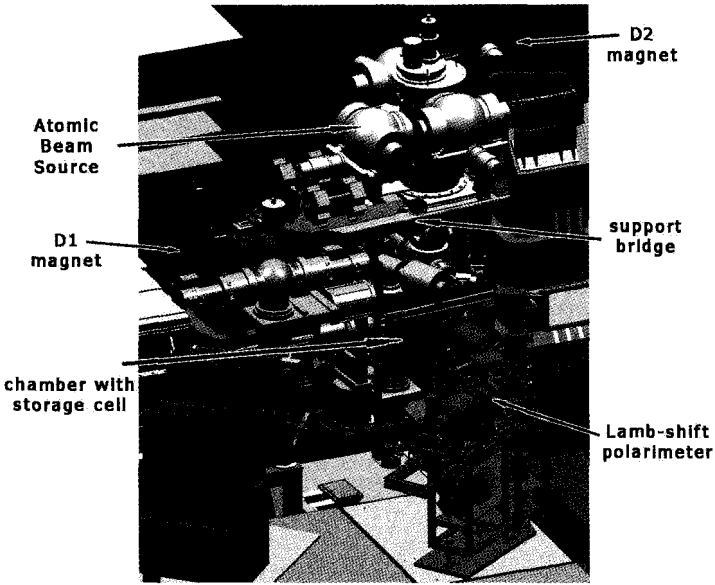


Fig 1. Polarized internal gas target set-up at ANKE.

At the laboratory of the Institute for Nuclear Physics of Forschungszentrum Jülich, this set-up gives a good signal which can be easily separated from background. In spring 2004, the storage cell prototype for PIT at ANKE was investigated and first tests were performed to determine the dimensions of the stored COSY beam. The results of these tests give an estimated storage cell dimensions.

2. PIT set-up at ANKE

The complete set-up, including ABS, LSP, and target chamber with storage cell, has to move together while the scattering angle of the ANKE spectrometer is changed. For this purpose a bridge (see Fig. 1) between magnets D1 and D2 was built. The position of PIT is fixed by the bridge at about 50 cm away from D2. Numerical calculations of the stray field have been done with the MAFIA computer program. The results obtained from the field map calculations in the most significant points of the set-up allow all devices to be used without additional shielding.

Because the COSY-ring tunnel is narrow, some changes in the current LSP construction are needed. This is one reason why the polarimeter operates at 60 degrees.

3. Apertures tests at COSY

For the COSY beam dimension tests at ANKE, a frame with a number of apertures was installed in the new target chamber, as shown in Fig. 2.

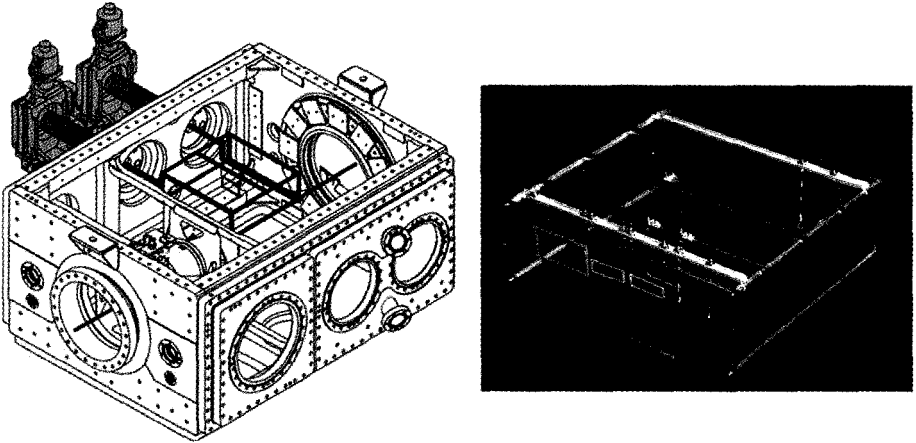


Fig 2. New target chamber with frame and apertures.

These tests were done with a large aperture whose inner size originally was larger than the beam diameter at injection, and of course after acceleration. At the beginning of the measurement, the centre of the aperture was always on the assumed beam axis, so that the beam shape was always the same at first. Using an XY-table (see Fig. 2), the aperture was moved away from the beam. At the same time, the beam intensity was measured with the BCT monitor^c. As soon as the aperture edge touched the beam, the intensity immediately dropped. This measurement gave real beam dimensions at energies about 2 GeV^d. Estimated beam shapes are shown in Fig. 3)

4. Conclusions

The MAFIA calculations gave the result that magnetic field shielding is not necessary. The best storage cell dimensions after the next tests at ANKE with the storage cell prototype can be estimated.

References

1. G. Pang and H. Zhao, *J. Phys. A: Math. Gen.* **25**, L527 (1992).
2. W. Haerberli, Proc. 2nd Int. Symp. On Polarization Phenomena, eds. P. Huber and H. Schopper, *Experientia Suppl.* **12** (Birkhauser, Basel, 1966), p. 64.

^cBeam Current Transmitter monitor.

^dCell tests at ANKE, February 11-12, 2004.

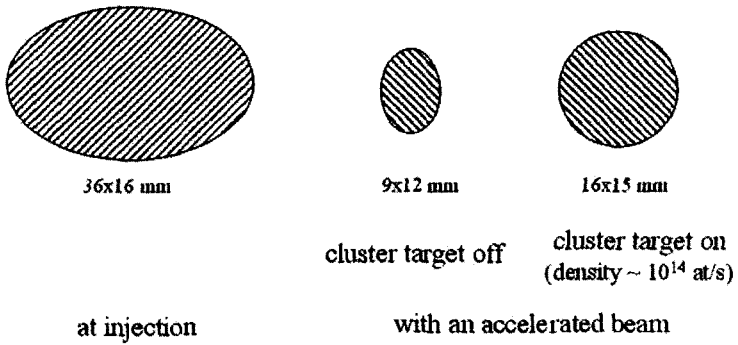


Fig 3. Estimated beam shapes during the run.

3. M. Nekipelov *et al.*, Compression Tube Measurements of the ANKE ABS Beam Intensity. // Proc. 8th Int. Workshop on Polarized Sources and Targets (PST99), eds. A. Gute, S. Lorenz, E. Steffens, (Universitat Erlangen-Nurnberg, 1999) pp. 486-489.
4. R. Engels *et al.*, Nuclear polarization measurement of H/D atoms extracted from a storage cell with a Lamb-shift polarimeter, accepted by NIMA, 2004

MICHIGAN ULTRA-COLD SPIN-POLARIZED HYDROGEN JET TARGET*

R. S. RAYMOND, A. D. KRISCH, M. A. LEONOVA, V. G. LUPPOV, V. S. MOROZOV, C. C. PETERS

Spin Physics Center, University of Michigan, Ann Arbor, USA

We are developing an ultra-cold high-density jet target of proton-spin-polarized hydrogen atoms (the Ultra-cold Michigan Jet) for use in polarized scattering experiments in storage rings. Most of the Jet has been fabricated and assembled; it now operates regularly. Data from recent runs of the Ultra-cold Jet is presented.

A layout of the Michigan Jet is shown in Fig. 1. Atomic hydrogen is produced with a room-temperature RF dissociator and guided to the ultra-cold (170 mK) separation cell, which is coated with superfluid ^4He to suppress the surface recombination of hydrogen atoms. The double walls of the cell form the mixing chamber of a $^3\text{He}/^4\text{He}$ dilution refrigerator. The cell's entrance and exit apertures are respectively located at about 95% and 50% of the superconducting solenoid's 12 T magnetic field. After the hydrogen atoms are thermalized by collisions

with the cell surface, the magnetic field gradient physically separates the atoms according to their electron-spin states. The "high-field-seeker" atoms in the two lowest hyperfine states ($|3\rangle$ and $|4\rangle$) are attracted up toward the high field region and most escape from the cell; they quickly recombine on bare surfaces and are cryopumped away. The "low-field-seeker" atoms in the two higher hyperfine states ($|1\rangle$ and $|2\rangle$) accelerate toward the low field region and effuse from the exit aperture, forming a monochromatic electron-spin-polarized beam.

To increase the Jet's density, we use a gold-plated copper focusing mirror with a polished surface covered with a ^4He superfluid film [1]. After an RF transition unit [2, 3], which will change state $|2\rangle$ atoms into state $|4\rangle$ atoms, the beam passes through the superconducting sextupole magnet. The sextupole focuses state $|1\rangle$ atoms into the interaction region and defocuses state $|4\rangle$ atoms, which are then cryopumped away. The proton-spin-polarized beam will then pass through the interaction region where it can collide with a proton beam in a high energy storage ring.

*Previously supported by a research grant from the U.S. Department of Energy.

Most of the Michigan Jet parts have been fabricated, successfully tested, and used. This hardware includes a 12 T superconducting solenoid with a very sharp gradient at its downstream end, a dilution refrigerator with a cooling power of about 22 mW at 170 mK, a 20 cm long superconducting sextupole magnet with a 0.31 T field at its iron poles' 10.5 cm diameter bore, the catcher [4] to keep the storage ring's vacuum uncontaminated with a measured cryocondensation pumping speed of 1.2×10^7 liters·s⁻¹, and a hydrogen maser polarimeter capable of monitoring the polarization with a precision of about $\pm 2\%$ in a few minutes.

We studied a beam of polarized hydrogen atoms, which were focused by the superconducting sextupole into a compression tube detector that measured the polarized atoms' intensity. To avoid the superfluid ⁴He film creeping out of the ultra-cold region, we installed three film burners above the mixing chamber, as shown in Fig. 2. Each film burner consists of a double-walled cell and a heater which is wound outside the cell. The superfluid ⁴He film which creeps into the film burner cell is evaporated by the heater; the ⁴He gas then recondenses inside the double-walled cell. We recently added two multiple knife edges, also shown in Fig. 2, to further restrict the superfluid ⁴He film flow from the inside surfaces of the separation cell and mirror. The resulting increase in the film thickness on

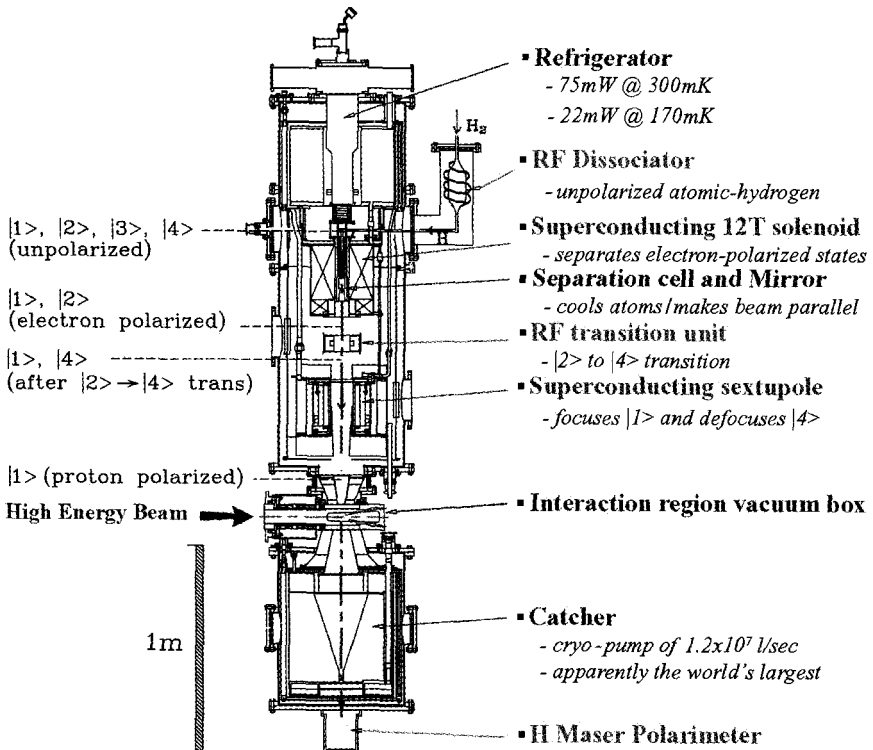


Fig 1. Layout of the Michigan Ultra-Cold Jet.

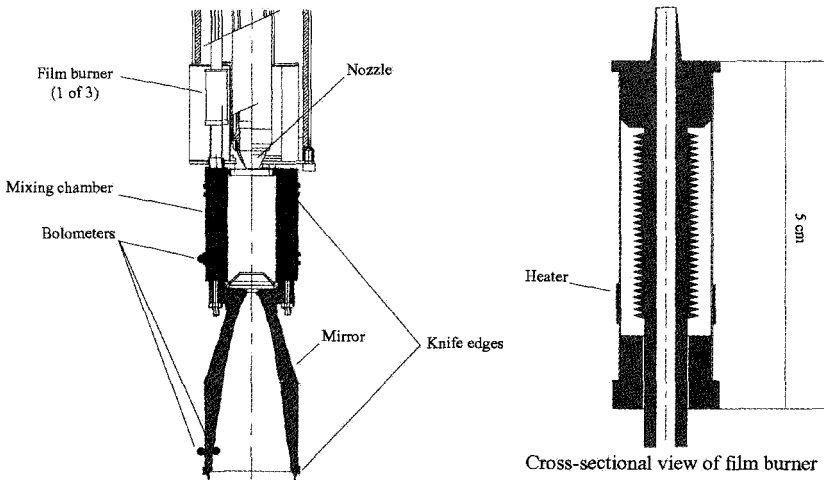


Fig 2. Details of the Jet's film burners.

these inside surfaces should further reduce the recombination of hydrogen atoms and allow a higher-intensity polarized beam. We measured and automatically controlled the film thickness inside the mirror using a resistor of about $2 \times 2 \times 0.3$ mm called a bolometer. We supplied power to it and measured the time needed to evaporate its film, which determines its film thickness. The ^4He flow was then automatically adjusted to maintain the preset thickness.

By maintaining this thick ^4He superfluid film, we were able to produce a high intensity spin-polarized hydrogen beam, which operated with good stability during an 18-hour run, until our liquid ^4He supply was depleted; the data is shown in Fig. 3. The average measured hydrogen intensity, into the 11 mm by 1.4 mm compression tube slot, was about 1.1×10^{15} $\text{H}\cdot\text{s}^{-1}$, which corresponds to a hydrogen Jet thickness of 0.8×10^{12} $\text{H}\cdot\text{cm}^{-2}$; the maximum fluctuation was about $\pm 20\%$. We can heat the separation cell to about 40 K to remove the frozen H_2 molecules; this usually takes about 2 hours, but was not needed during this 18-hour run. The compression tube can measure the beam's intensity at different radii; as shown in Fig. 4, this gave a measured beam size of about 8 mm.

References

1. V.G.Luppov *et al.*, *Phys. Rev. Lett.* **71**, 2405 (1993).
2. B.B.Blinov *et al.*, *AIP Conf. Proc.* No. 570 (AIP, New York, 2001), p. 856.
3. R.S.Raymond *et al.*, *Proc. Int'l Workshop Polarized Sources & Targets*, ed. A. Gute *et al.* (Univ. Erlangen-Nurnberg, Erlangen, 1999), p. 494.
4. V.G.Luppov *et al.*, *Proc. 12th Int'l Symp. High-Energy Spin Physics, Amsterdam, 1996*, ed. C.W. de Jager *et al.* (WorldScientific, Singapore, 1996), p. 434.
5. V.G.Luppov *et al.*, *Proc. 9th Int'l Workshop Polarized Sources & Targets*, ed. V.P. Derenchuk and B.v.Przewoski (WorldScientific, Singapore, 2002), p. 32.

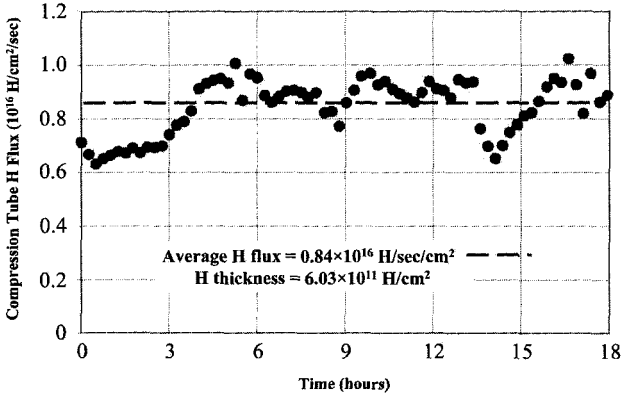


Fig 3. The observed hydrogen Jet intensity entering the compression tube during an 18-hour run.

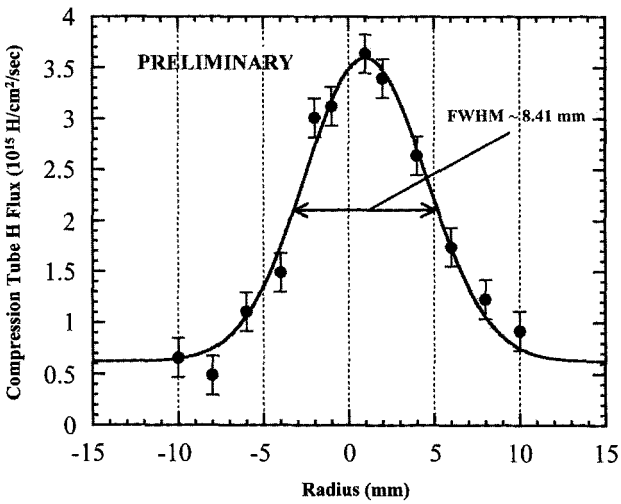


Fig 4. The observed radial hydrogen intensity entering the compression tube through 1.4 mm diameter holes.

PERFORMANCE OF THE HERMES POLARIZED HYDROGEN AND DEUTERIUM GAS TARGETS

P. LENISA

Università di Ferrara and INFN - sez. Ferrara, Ferrara, Italy

(on behalf of the HERMES Target Group)

The HERMES hydrogen and deuterium nuclear polarized targets have been in use since 1996. A description of the apparatus and a summary of the target performance is presented.

1. Introduction

The HERMES experiment at HERA (DESY, Hamburg) aims at the study of the quark-gluon spin structure of the nucleon by deep-inelastic scattering (DIS) of longitudinal polarized electrons/positrons from an internal polarized gas target.

During the first year of operation, 1995, the target was run with polarized ^3He gas produced by a different source based on optical pumping. Since 1996, the present target apparatus for polarized hydrogen and deuterium has been in operation. During the 1996-97 runs, longitudinally polarized hydrogen ($H_{||}$) was used. In the years 1998-2000 the target was switched to longitudinally polarized deuterium ($D_{||}$), and in 2001 the currently running transversely polarized hydrogen target (H_{\perp}) was installed.

2. Target set-up

A beam of H/D atoms is generated in a RF or MW dissociator which forms part of the atomic beam source (ABS) [1]. These atoms are electron polarized by means of Stern-Gerlach separation in a sextupole magnet system. The electron polarization is transferred to the nucleons by means of two sets of adiabatic high frequency transitions.

The beam of nuclear polarized atoms is injected into the centre of the thin-walled storage cell [2] via a side tube, and the atoms then diffuse to the open ends of the cell where they are removed by a high speed pumping system. The cell consists of a 40 cm long Al tube of elliptical cross section (21 mm \times 8.9 mm), coated with Drifilm in order to minimize wall interaction effects. The cell is immersed in a magnetic holding field. In the 1997-2000 runs, a longitudinal magnetic field of approximately 330 mT was maintained over the cell volume by a superconducting magnet coil. Since 2001 a transverse field produced by a conventional dipole magnet has been used.

A second side tube is provided to sample the gas within the target cell. The beam emerging from this tube is analysed with a Target Gas Analyser (TGA) [3] to determine its atomic fraction, and a Breit-Rabi polarimeter (BRP) [4] to measure its hyperfine occupation in order to calculate the atomic polarization.

The layout of the target is shown in figure 2.

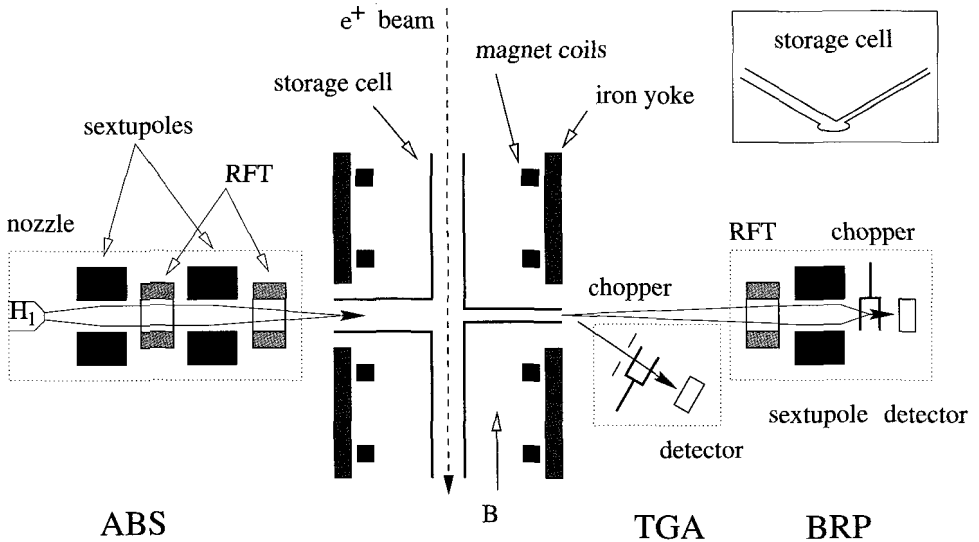


Fig 1. A schematic view of the HERMES polarized target.

3. Performance

The average target polarization can be written as [5]:

$$P^T = \alpha_0[\alpha_r + (1 - \alpha_r)\beta]P_a \quad (1)$$

where α_0 is the injected atomic fraction inside the cell, α_r represents the atomic fraction which survived recombination on the cell wall, P_a is the atomic polarization and β ^a is the ratio between molecular and atomic polarization.

Tab. 1 summarizes averaged values for the target properties during the various running periods.

A comparison between the longitudinally polarized hydrogen and deuterium target leads to the following conclusions. At the same guide field, in the case of deuterium the spin exchange and wall relaxation processes are suppressed by a factor $(B_C^H/B_C^D)^2 \simeq 20$

^aThe molecular polarization has been recently measured by exploiting the 1997 longitudinally polarized hydrogen data [6] and found to be $\beta = 0.64 \pm 0.19$.

Table 1. Summary of the HERMES target performance in the years 1997, 2000 and 2002. The tabulated values are averaged over the respective running periods. The ΔP_i s represent the polarization losses arising from the listed process (see text).

	$H_{ }$ (1997)	H_{\perp} (2002)	$D_{ }$ (2000)
α_0	0.960 ± 0.010	0.918 ± 0.032	0.919 ± 0.026
α_r	0.945 ± 0.035	0.979 ± 0.023	0.997 ± 0.017
P_{z+}	$+0.908 \pm 0.016$	$+0.859 \pm 0.032$	$+0.927 \pm 0.017$
P_{z-}	-0.908 ± 0.016	-0.859 ± 0.032	-0.915 ± 0.010
$-\Delta P_{SE}$	0.035	0.055	≤ 0.001
$-\Delta P_{WD}$	0.02	0.055	≤ 0.01
$-\Delta P_{BI}$	absent	0.015	absent
P_+	$+0.851 \pm 0.031$	$+0.783 \pm 0.041$	$+0.851 \pm 0.029$
P_-	-0.851 ± 0.031	-0.783 ± 0.041	-0.840 ± 0.026
t (10^{14} nucleons/cm ²)	0.7	1.1	2.1
FOM ($P^2 t$) (10^{14} /cm ²)	0.5	0.67	1.5

compared to hydrogen. The positive and negative P_z values for hydrogen coincide very well, while for deuterium there is a clear difference. This is due to the larger number of efficiencies and transmissions involved.

From the table it is possible to deduce departures from the optimal performance, such as the amount of recombination ($\Delta\alpha_r = 1 - \alpha_r$), and the depolarization due to the various depolarizing mechanisms: spin-exchange collisions (ΔP_{SE}), wall-depolarization (ΔP_{WD}), and beam-induced fields (ΔP_{BI}). The target density integrated over the cell length, or areal density t , is also shown, together with a relative factor of merit (FOM) that takes into account both the polarization and the density. It is worthwhile to mention that in 1997 the target cell had a larger cross-section (29 mm \times 9.8 mm), implying a higher conductance and a correspondingly lower density (about 40%). The table also illustrates the optimal performance of the $D_{||}$ target in 2000. For this target no recombination ($\Delta\alpha_r = 0$), and no depolarization phenomena ($\Delta P_{WD} = \Delta P_{SE} = \Delta P_{BI} = 0$), have been observed. This excellent behaviour has to be attributed to the lower critical field of deuterium (11.7 mT) compared to hydrogen (50.7 mT), and to an improvement in the knowledge and preparation of the cell surface coating. The improved surface coating is also responsible for the better performance of the 2002 H_{\perp} target compared to the 1997 $H_{||}$ target, as far as the amount of recombination is concerned.

On the other hand, in 2002, due to the higher density obtained and the higher number of wall collisions, spin-relaxation effects became more important, causing a loss in polarization of about 11%, and limiting the gain in the factor of merit with respect to the 1997 running due to the increase in density. This indicates how an enhancement in the figure of merit of the target might be obtained by increasing the holding field proportionally to the density, in order to limit the spin relaxation effects.

4. Conclusion

The HERMES polarized hydrogen/deuterium target has been reliably operating since 1996. It provides high polarization and total systematic uncertainties of only 3–4%. The system-

atics of both the recombination and depolarization processes in the storage cell are fully under control.

References

1. A. Nass et al., *Nucl. Instrum. and Meth. A*, **505/3** (2003), 633.
2. C. Baumgarten et al., *Nucl. Instrum. and Meth. A*, **496** (2002), 263.
3. C. Baumgarten et al., *Nucl. Instrum. and Meth. A*, **508** (2003), 265.
4. C. Baumgarten et al., *Nucl. Instrum. and Meth. A*, **482** (2002), 606.
5. A. Airapetian et al. *The HERMES polarized hydrogen and deuterium gas target in the HERA electron storage ring* to appear on NIM A.
6. A. Airapetian et al. *Eur. Phys. J. D* **29** (2004) 21.

FROZEN-SPIN POLARIZED HD TARGET FOR SPIN ASYMMETRY EXPERIMENTS *

T. KAGEYA^{1,6}, C. M. BADE^{1,4}, C. GIBSON^{1,5},
H. GLÜCKLER², F. LINCOLN¹, M. M. LOWRY¹, J. MAHON⁴,
M. PAP², A. M. SANDORFI¹, H. SEYFARTH²,
H. STRÖHER², X. WEI¹, C. S. WHISNANT³

- (1) Brookhaven National Laboratory, Upton, USA
- (2) Forschungszentrum, Jülich, Germany
- (3) James Madison University, Harrisonburg, USA
- (4) Ohio University, Athens, USA
- (5) University of South Carolina, Columbia, USA
- (6) Virginia Polytechnic Institute and State University, Blacksburg, USA

Pion photo-production experiments have been performed with a longitudinally polarized HD target and circularly as well as linearly polarized photon beams at the Laser-Electron-Gamma-Source (LEGS) facility at BNL. A Hydrogen-Deuteron target, polarized and aged for 86 days at 15 Tesla in a dilution refrigerator which reached a base temperature of 8 mK, reached a frozen-spin state with polarizations of $15.1 \pm 0.7\%$ and $59.9 \pm 1.5\%$ for deuterons (D) and protons (H), respectively. The target was transferred to an In-beam Cryostat which held the it at 0.9 Tesla and a temperature of 250 mK. Relaxation times in IBC for D and H have been measured to be about 5 months for both. Preliminary double-polarization data are presented.

1. Frozen-spin HD target

An H₂ molecule which consists of two identical protons has two spin states, with spins either antiparallel (para) or parallel (ortho). The ortho-H₂ is readily polarized at a high magnetic field and a low temperature while the para-H₂ is not. At a low temperature, the ortho-H₂ decays into the para-H₂ with a half life of about six days.

Due to a spin-spin coupling between an H in H₂ and an H in HD, a polarized ortho-H₂ can transfer its polarization to HD. A small concentration of polarized ortho-H₂ (of the order of 10^{-4}) is used to polarize HD, and in a couple of months most of the ortho-H₂ decays into the para state. There are no phonons to couple an S-wave HD to its crystal lattice; thus once polarized, HD has an extremely long relaxation time.

HD gas was solidified in a Production Dewar (PD) which is a ⁴He cryostat. Thermal Equilibrium (TE) calibrations were done at 4.2 K in this dewar in August, 2004, when the

*Supported by a research grant from the u.s. department of energy under contract no. de-ac02-98ch10886 and the u.s. national science foundations.

relaxation time was still relatively short. The HD target was then transferred to a Dilution Refrigerator (DR), polarized at low temperature and high field (base temperature of 8 mK and 15 Tesla) and simply held in this state for 86 days (aging) to reach a frozen spin-state.

In October 2004, the target was transferred back to the PD and polarizations were measured to be $15.1 \pm 0.7 \%$ and $59.9 \pm 1.5 \%$ for D and H, respectively. For NMR, a cross coil method has been used to detect interference signals between two coils by sweeping the magnetic fields [1].

The target was transferred to an In-Beam-Cryostat (IBC) cooled with a horizontal dilution refrigerator to a temperature of 250 mK with a holding field of 0.9 Tesla (maximum field is 1 Tesla). Polarizations were monitored with NMR in the IBC every four hours for D and about 2 days for H. Very long relaxation times were observed over the course of a 17 day run, approximately 5 months for both D and H.

Pion production data were taken for spin orientations of both D and H parallel to the holding field for 9 days, and H directions antiparallel to the field for 8 days. H spins were flipped with an allowed RF transition by scanning the magnetic field at fixed frequency. The same scan also caused a forbidden $H \leftrightarrow D$ transition. As a result, D polarizations were observed to increase from 15 % to 17 % while H polarizations were changed from + 57 % to about - 40 %.

Table 1. Cryostat comparison, temperatures and holding fields.

	Temperature (K)	Holding field (Tesla)
PD	1.8	2
DR	0.012	15
IBC(present)	0.25	1.0
IBC(previous)	1.3	0.65
TC(present)	1.8	0.12
TC(previous)	1.8	0.016

For the target transfers from one cryostat to another, a transfer cryostat (TC) has been used, constructed in collaboration with Forschungszentrum Jülich, Germany. The TC has 0.12 Tesla holding field supplied by a permanent Halbach dipole and a temperature of 1.8 K; the field has been improved by a factor of seven compared with a previous TC. The transfers take from 30 to 60 minutes in most cases. The relaxation times of D and H in the TC are shortest at a higher temperature and lower field. The temperature and field conditions in our various cryostats are summarized in Table 1). Polarization losses are most likely when a target is in the TC, and they depend on the aging time. The average losses per transfer from PD to IBC for D and H are approximately 0.1 % and 2.7 %, respectively. (The in-beam polarizations in IBC are calculated based on the above measurements of losses, and they are preliminary.)

A new IBC has been constructed by Quantum Technology Corp., and has been used for

the present experiments. The relaxation times observed in this experiment are very much longer than those of a test run in 2001. We attribute this mainly to the lower operating temperature of the new IBC.

After the experimental runs, saturated forbidden transitions of H polarization to D were carried out successfully in the PD. For the next experiments scheduled for Spring 2005, this transition will be applied to obtain higher D polarization.

2. Preliminary spin asymmetry

Figure 1 shows missing energy distributions of π^0 where the distributions have been subtracted by those of background scattering with the target cell (Ke1-F) and thin aluminum wires to cool down the HD solid [2]. (This background amounts to about 20 %.) Figure 1(a) shows the distribution when the spin direction of the circularly polarized photons is antiparallel to that of HD target, while Figure 1(b) corresponds to parallel alignment. Figure 1(c) is obtained by subtracting (b) from (a). The data were taken using 340 MeV photon beams and the polar angle region detected in the CM was from 70 to 100 degrees. A clear spin asymmetry has been observed. The distributions are preliminary.

References

1. A. Caracappa and C. Thorn, *Proceedings of 15th International Spin Symposium, Upton, New York*. 867 (2002).
2. T. Kageya *etal*, *Proceedings of 15th International Spin Symposium, Upton, New York*. 857 (2002).

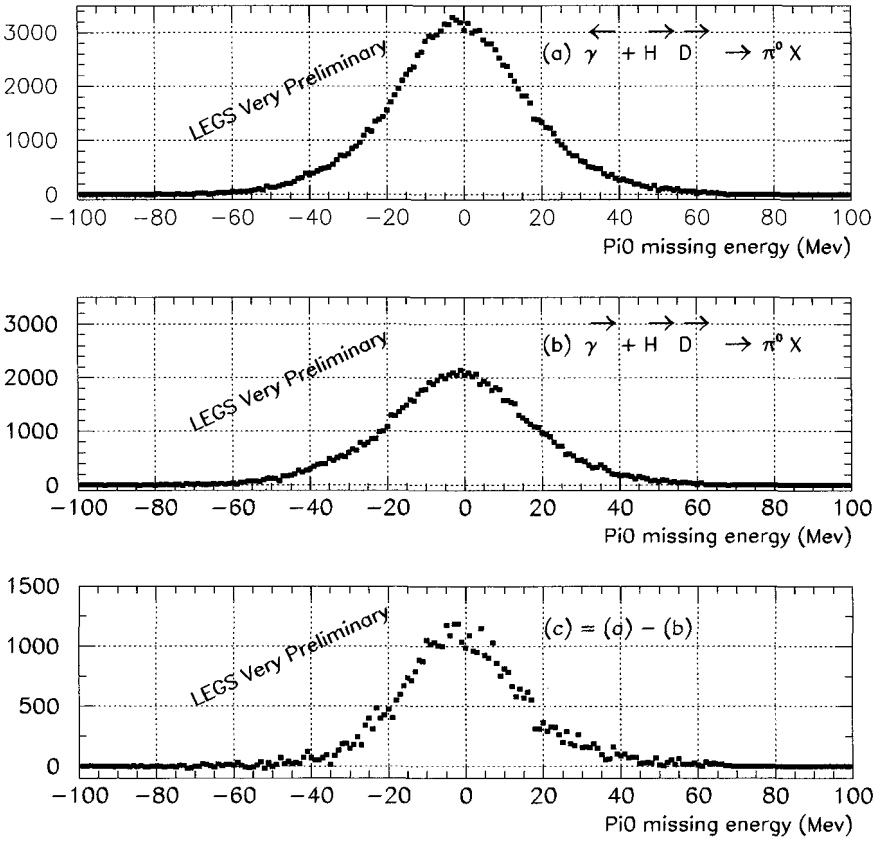


Fig 1. π^0 missing energy distributions for $E_\gamma \approx 340$ MeV and $\Theta = 70 - 100$ degrees. (a) spin direction of γ is antiparallel to those of HD; (b) parallel. (c) difference between (a) and (b).

FEATURES OF DYNAMIC NUCLEAR POLARIZATION IN IRRADIATED LiD TARGET MATERIAL

Y. KISSELEV, N. DOSHITA, S. GOERTZ, K. KONDO, W. MEYER, G. REICHERZ

Physics Department, University of Bochum, Bochum, Germany.

G. BAUM, F. GAUTHERON

Physics Department, University of Bielefeld, Bielefeld, Germany.

J. BALL, A. MAGNON

CEA Saclay, DAPNIA, Gif-sur-Yvette, France

Relaxation times with measured dependency on the nuclear polarization and spectral resolved spin radiation were observed for LiD in the large COMPASS twin target at CERN. The record deuteron polarizations (-53% and +57%) reached in the target may be restricted not only by the material properties but also by the target environment.

Nuclear polarization of irradiated LiD is obtained by the Dynamic Nuclear Polarization (DNP) method. As follows from theory [1], the maximum nuclear polarization depends mainly on the EPR-line structure of F-centers and the different relaxation mechanisms connecting the electron and nuclear spin species with the relatively “warm” lattice.

The actual target is located in a complex environment. Polarized spins have inductive couplings with the NMR coils, microwave (MW) cavity walls, cables, and sense wires. These couplings enable radiation or damping losses; usually there are MW dielectric losses and heat transport difficulties during the DNP process. As a consequence, the maximum polarization can also depend on the design of the target environment.

The COMPASS twin-target operates at 2.5 T field in the $0.065 \div 0.25$ K temperature region. Its material incorporates an atomic fraction of 0.953 for ${}^6\text{LiD}$, 0.044 for ${}^7\text{LiD}$ and 0.003 for ${}^6\text{LiH}$ in a total weight of 175 grammes per cell. Due to the high polariza-

tions reached and the large molar spin numbers $n_D \approx n(^6\text{Li}) \approx 21, n(^7\text{Li}) \approx 0.95, n(\text{H}) \approx 0.065, n(e) \approx 0.007$, the nuclear subsystems possess a large heat capacity given by:

$$C(\mu_{I,S}) = n_{I,S} \cdot R \cdot x^2 \frac{dB_{I,S}(x)}{dx}, \quad (1)$$

where R is the gas constant, B_I is the Brillouin function, $x = \mu_{I,S}B/(kT_s)$, $\mu_{I,S}$ is the magnetic moment of I, S -spins, $B=2.5$ T field, k is the Boltzmann constant, and T_s is the spin temperature. At 50% deuteron polarization ($T_s \approx 0.9$ mK), Eq. 1 yields of the order of 60 J/K for D($I=1$), 60 for ^6Li ($I=1$), 5 for ^7Li ($I=3/2$), 1 for ^1H ($I=1/2$) and only about 0.02 for S-spins.

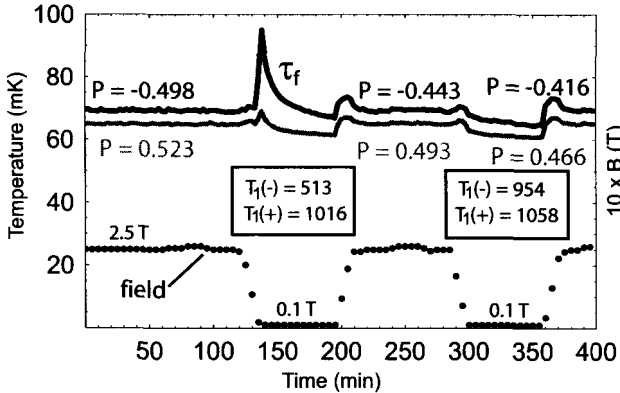


Fig 1. Bolometer detection of the fast energy release of spin energy with $\tau_f \approx 18$ min during the first exposure with clear indication of very different relaxation times of $T_1(-) \ll T_1(+)$ for the opposite deuteron polarizations; a fast energy release is absent in the second exposure, and here $T_1(-) \approx T_1(+)$.

in the second exposure. This shows an additional mechanism of the energy release, needed to explain the dependency of the measured relaxation times on the sign of polarization.

To determine the mechanism of the fast process we estimate the average energy released from D and ^6Li during the τ_f -period.

$$\Delta W \approx 2n_D N_A \mu_D B \cdot \Delta P_D, \quad (2)$$

where the factor 2 takes D and ^6Li into account, and N_A is Avogadro's constant. Setting $\mu_D \approx \mu_{Li} \approx 4.3 \cdot 10^{-27} \text{ J} \cdot \text{T}^{-1}$, the difference of polarization of $\Delta P_D = 0.055$, measured by NMR at $B=2.5$ T before and after the first exposure, we obtain the energy of $\Delta W \approx 0.15$ J. This gives the average power of $\Delta W/\tau_f \approx 14 \mu\text{W}$, which is negligible in its influence on the temperature of $^3\text{He} / ^4\text{He}$ mixture. On the other hand, the bolometer sensitivity of the order of 10^{-9} W allows the detection of radiation on such a level. Thus we conclude that we see radiation losses from the polarized LiD.

Figure 2 shows the first observation of the spectro-resolved radiation in LiD, received by the bolometer, without additional fields applied to the material.

We could observe an energy release using Speer 220 bolometers and NMR polarization measurements. Fig. 1 shows the measured dynamics of the temperatures, the deuteron polarizations, and the measured relaxation times (T_1) for the two sequential one-hour exposures of the target at 0.1 T and at about 65 mK. One can see that the bolometer of the negatively polarized cell detects a fast energy release with $\tau_f \approx 18$ min only during the first exposure; it is absent

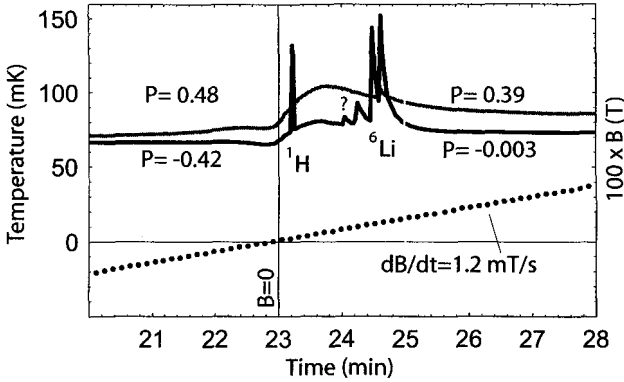


Fig. 2. The spectro-resolved spin radiation (from left to right): ^1H (28.9 mT), non-identified (90.1 mT), ^7Li (101 mT), D (121 mT), ^6Li (127 mT).

frequencies of I - nuclear species, ξ is a fitting parameter, μ_S is the electron magnetic moment, r_{SS} is the effective radius per electron spin, $r_{SS}^3 = 3/(4\pi N_S)$, and $N_S = 9.8 \cdot 10^{-21} \text{ cm}^{-3}$ is the S -spin concentration in LiD, we finally obtain $\xi = (0.5 \div 1.0)$, which explains the position of resonances in Fig. 2. It follows that the spin species radiate in sequence, all at approximately the same frequency of about 1.0 MHz. The first spike in Fig. 2 belongs to the proton spins having the highest gyromagnetic ratio, then comes ^7Li , D and ^6Li .

The point is that MHz-radiation is not possible without the inductive coupling of polarized spins with a resonance system [2]. This coupling produces an additional channel for the fast spin energy dissipation through conductive losses in the circuit. In our tests the effect is seen as the fast losses in Fig. 1, and as the background and the resonances in Fig. 2.

Two mechanisms explain the detected radiation [3]: thermal induced superradiation (SR) and maser-like generation (MG). SR acts during the radiation time τ_R of the order of T_2 , where $T_2 \approx 3 \cdot 10^{-4} \text{ s}$ is the transverse relaxation time of D and ^6Li estimated from NMR line shapes. In our case, however, $\tau_R \approx 6 \gg T_2 \approx 3 \cdot 10^{-4} \text{ s}$, so that SR is absent, or our slow control system with a resolution of 2 s is unable to see it.

MG explains the radiations shown in Fig. 1 and 2. MG lasts longer than crossing over the bandwidth of the resonant circuit, which is easily estimated as the product of the field rate and τ_R or $1.2 \text{ mT/s} \cdot 6 \text{ s} = 7.2 \text{ mT}$ or 47 kHz for the deuteron spike. This yields a circuit quality factor of $Q_{\text{circ}} = 10^6/4.7 \cdot 10^4 \approx 20$. The main difference between the radiations shown in Fig. 1 and 2 comes from the initial temperatures of the electron dipolar subsystems of about $-4 \cdot 10^{-5}$ and -10^{-7} K respectively, which determine the intensity of alternating local fields.

We estimate the minimum threshold product $(\eta \cdot Q)_{\text{min}}$, where η is the filling factor, at which this process starts to act against the deuteron polarization build up, and we have [2]

$$(\eta Q)_{\text{min}} = ((2\pi)^2 M_0 \gamma_D T_2)^{-1} \approx 2.1, \quad (3)$$

where M_0 is the average magnetic moment per unit volume, in our case $M_0 \approx 6.1 \mu\text{T}$ at 50 % polarization, and $\gamma_D \approx 6.54 \text{ Hz}/\mu\text{T}$ is the gyromagnetic ratio. Setting $\eta_{\text{coil}} \approx 0.25$ for

Its pulse components have the approximate duration of $\tau_R \approx 0.1 \text{ min}$, hence $\tau_R \approx 0.1 \ll \tau_f \approx 18 \ll T_1 \approx 1000 \text{ min}$. This means that the spin-lattice relaxation is switched off, and only the alternating local fields of LiD lead to these resonances. Assuming that the Zeeman nuclear energy equals the energy of dipole-dipole interactions of electron spins, $h\nu_I = \xi \cdot \mu_S^2 / r_{SS}^3$, where h is Plank's constant, ν_I are Larmor frequencies

the NMR coils and $\eta_{cav} \approx 0.016$ for the MW cavity yield $Q_{min} \approx 9$ and ≈ 130 for NMR coils and the MW cavity respectively. Eq. 3 does not depend on the magnetic field. Also the observed value of $Q_{cav} \approx 20 > Q_{min}$ is satisfied for NMR coils, but not for the MW cavity. From this it can be argued that a high enough Q_{coil} might be a reason for the lower negative polarization of (-53 %) in comparison with positive (+57%) polarization reached in our 2001-2004 measurements.

References

1. A. Abragam, M. Goldman, *Nuclear Magnetism: Order and Disorder*, Clarendon Press, Oxford, (1982).
2. N. Blombergen and R.V. Pound, *Phys.Rev.* **95**, 8 (1954).
3. Yu.F. Kisselev, *Phys. of Part. and Nucl.* **31**, 354 (2000).

OPTICAL SPECTROMETER FOR MEASURING THE RATIO OF ATOMIC HYDROGEN AND MOLECULAR HYDROGEN IN AN ABS

S. N. ATUTOV, L. BARION, G. CIULLO, M. CONTALBRIGO, P. F. DALPIAZ, F. GIORDANO, P. LENISA, M. STANCARI, M. STATERA, L. TOMASSETTI, M. WANG

INFN and Università di Ferrara, Ferrara, Italy

At the test bench in Ferrara, we constructed an optical spectrometer that measures the relative population of the atomic and molecular hydrogen in the discharge tube of our atomic beam source (ABS). The spectrometer consists of a rotating grating, achromatic lenses, slits, and a sensitive photo-detector connected to a computer. Due to the rotation of the grating, the optical spectrum is scanned over the detector, and the intensities of hydrogen spectral lines are recorded. The intensity ratio of recorded hydrogen atomic lines to hydrogen molecular lines gives qualitative information about the degree of dissociation. With the device's high sensitivity and spectral resolution, it will be possible to monitor vacuum conditions and gas impurities in the ABS discharge tube.

1. Introduction

We have constructed a simple optical spectrometer for studying hydrogen gas discharges in an atomic beam source (ABS). The main goal of this study is to measure the ratio of the atomic hydrogen and molecular hydrogen fraction (the dissociation) in an ABS discharge tube. The ratio can be written in the following form:

$$A = \frac{I_a}{I_a + I_m} \quad (1)$$

where I_a is the sum of intensity of all atomic hydrogen Balmer lines, and I_m the intensity of molecular hydrogen lines.

2. Description

The spectrometer consists of a grating, an objective, two slits, and a low noise sensitive photo-detector connected to a computer. The grating has both a large number of lines per mm (2500) and a large size (50×50 mm), and allows us to obtain a high enough spectral resolution despite the relatively small focal length of the objective. The small focal length provides a great optical solid angle, essential for detecting very weak hydrogen molecular lines (and lines of any gaseous impurities in the discharge) in the presence of strong atomic hydrogen spectral lines. Because the focal length of optical lenses depends on the frequency

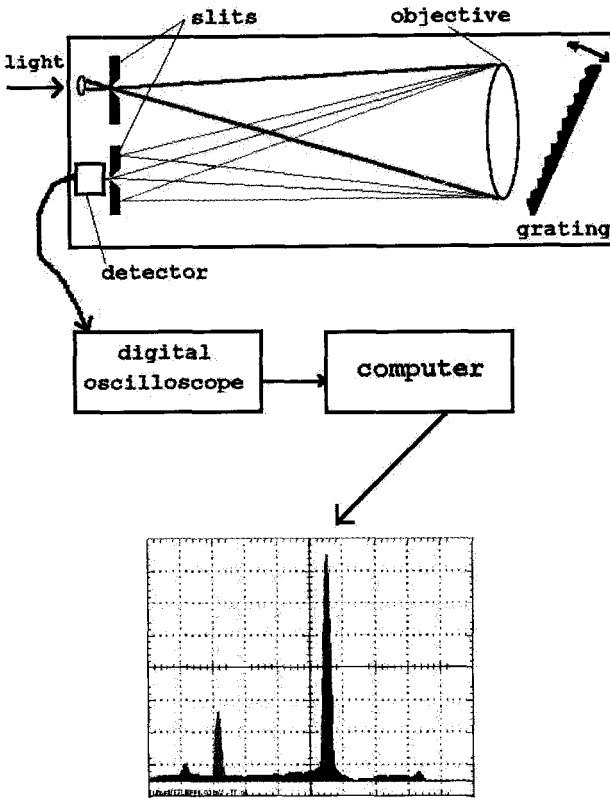


Fig 1. Scheme of the optical spectrometer.

optical spectrum is scanned on the output slit and the intensity of atomic hydrogen, molecular hydrogen, and other gas impurities spectral lines are recorded by a sensitive photodiode with integrated amplifier. This technical solution allows us to avoid the use of any expensive detectors like CCD cameras, and to obtain averaged spectra of very high quality. For these test experiments a glass cylindrical cell connected to a valve and a turbo pump was used. The cell has a length of 800 mm and a diameter of 15 mm. In preparation for the experiment, the cell was extensively cleaned to remove contamination (e.g. traces of oil, nitrogen) which can deform hydrogen spectra. The cell was working in a closed regime without gas through-put at a hydrogen pressure in the range of a few mbars. The source of RF power consists of an RF generator tuned to a resonance frequency of 124 MHz, and an RF amplifier with power up to 100 W connected to two cylindrical electrodes placed on the tube. The length of the discharge in the tube can be varied from 3 cm to 15 cm, and the discharge can be fixed anywhere along the tube by simply shifting the electrodes. Light was taken from one end of tube through an output window. The shifting of discharge zone was used to verify the absence of any deformation of recorded spectra by light absorption by

of the light, the quality of the objective is important. The objective must produce images of spectral lines on the output slit in a wide (from blue to infra-red) spectral range. In order to avoid any remarkable difference in size of these images in this wide spectral range (which would decrease the spectral resolution), a good achromatic objective was chosen. For the simplicity of the spectrometer, which might be important for working in polluted and noisy conditions of the test bench environment, the spectrometer was constructed as a compact, auto-collimated device with just one objective which produces at the same time collimation of the discharge light on the grating, and focuses the light on the output slit. Due to the rotation of the grating, the ABS

the gas column between the discharge and the cell output window. An example of the discharge spectra is shown in Fig. 2. These spectra are taken at hydrogen pressure ~ 1 mbar, RF frequency 124 MHz and power ~ 25 W. Besides the Balmer H_α , H_β and H_γ lines (the most

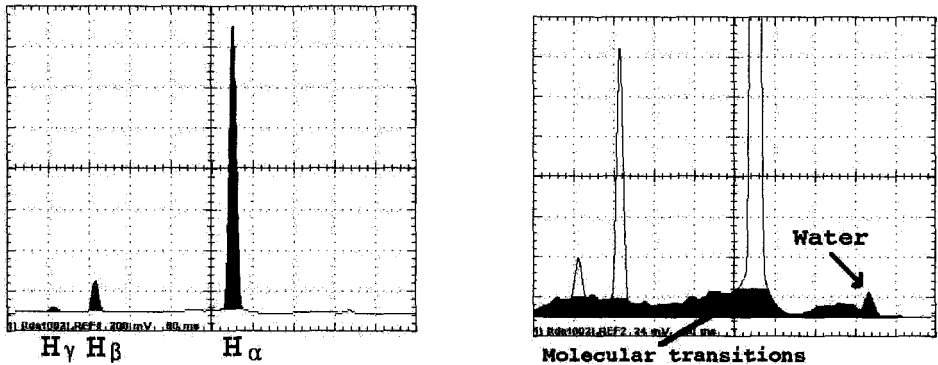


Fig 2. The observed spectrum on two different vertical scales.

intense is red H_α line at 656.3 nm) the green - red molecular continuous emission spectrum is clearly seen. This continuum is due mostly to optical transitions in hydrogen molecules (see [1]). It is important to note that a relatively small but well resolved peak of molecular water transition exists near 700 nm. This was verified by adding a small amount of water to the cell, leading to an increase in the intensity of the peak. When the vacuum conditions in the cell were worse than usual a continuous spectrum of nitrogen was recorded.

3. Results

Figure 3 presents the measured ratio A of the atomic and molecular hydrogen (in arbitrary units) in the cell discharge versus RF power. In complete accordance with expectations, the

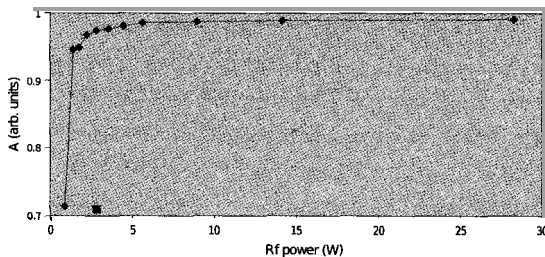


Fig 3. The degree of dissociation as a function of RF power.

graph shows a small fraction of hydrogen atoms at low RF power. Then with increasing

power, the atomic fraction sharply increases till it saturates at maximum power. The rectangular point at ~ 2.5 W shows the ratio A after 9 hours of continuous discharge running in a closed cell at constant hydrogen pressure and power. We believe that the relatively small atomic hydrogen fraction in this case is due to the destruction of water on the inner glass walls by plasma electron bombardment. This leads to a great increase of hydrogen atom recombination on the cell wall and, as a result, to decreasing dissociation.

References

1. A. M. Goyette *et.al.*, J. Phys. D:Appl. Phys. **29** 1197 (1996).

HYDROGEN/DEUTERIUM POLARIZED TARGET AT MIT-BATES

E. IHLOFF, H. KOLSTER, N. MEITANIS, R. MILNER, A. SHINOZAKI, E. TSENTALOVICH, V. ZISKIN,
Y. XIAO, C. ZHANG

MIT-Bates Linear Accelerator Center, Middleton, USA

MIT-Bates Linear Accelerator Center conducts experiments with a polarized internal target in the electron storage ring. The target includes an Atomic Beam Source (ABS), a storage cell and a polarimeter. Bates ABS is the first installation of the kind operated inside a magnetic spectrometer in the presence of a magnetic field exceeding 2 kG. The paper describes the specific features of the ABS operation in a magnetic field. High ABS intensity ($2.5 \cdot 10^{16}$ at/sec) and high polarization ($\approx 70\%$) inside the storage cell have been achieved.

1. Introduction

Recently, experiments with internal target in the storage ring started at MIT-Bates. The facility includes a polarized electron source, a linear accelerator with a recirculator, and the South Hall storage ring (SHR). The experiments are conducted at an electron energy of 850 MeV. The injected current into the ring is 150-170 mA, and the average current is 110-120 mA. A Siberian Snake built in the Budker Institute for Nuclear Physics (Novosibirsk) was installed in the ring. It allows the longitudinal beam polarization in the internal target area to be kept at an average value of 67%. The BLAST (Bates Large Acceptance Spectrometer Toroid) magnetic spectrometer [1] is used to detect scattered electrons and secondary particles in coincidence. BLAST is an open geometry detector with a toroidal magnetic field. The experiments are conducted on polarized hydrogen and deuterium targets. The ABS produces a jet of polarized atoms and injects it into the T-shaped storage cell (60 cm length, 15 mm diameter) cooled to about 100°K. The surface of the cell is coated with dri-film to minimize wall depolarization. A small outlet allows some fraction of the jet to go through the cell for polarization analysis in Breit-Rabi Polarimeter (BRP).

2. The Atomic Beam Source

The ABS is of a convenient design. Atoms leave the RF dissociator through a 2.1 mm nozzle, followed by a skimmer and a diaphragm. The focusing system consists of 2 sets of permanent sextupole magnets. The MFT transition unit is located between the sextupoles, SFT and WFT units follow the second sextupole. For the deuterium target, we switch between 3 target states:

- (1) Vector + : $P_z=1, P_{zz}=1$
- (2) Vector - : $P_z=-1, P_{zz}=1$
- (3) Tensor - : $P_z=0, P_{zz}=-2$

The ABS was originally designed and built in Amsterdam [2]. It was shipped to Bates after AmPs was closed. However most of the ABS components had to be redesigned due to the unique environment. The ABS is located inside the BLAST magnetic spectrometer, which is spatially very cramped and has a strong magnetic field.

These conditions narrowed our choice of vacuum pumps. Large turbopumps do not fit into the available space, and they do not work in a magnetic field. Still they are the best pumps for the first stages of ABS, where the gas load is high. We installed four turbopumps with a total pumping speed of 5240 l/sec outside the magnetic field, and shielded them to reduce the residual field. Those turbos pump the first two stages of ABS via long (1.5 m) pipes of very large diameter (30 cm).

In the past the sextupole magnet chamber was pumped with 2 NEG pumps with pumping speed 1300 l/sec each. However, the use of NEG pumps might be dangerous, since they can overheat permanent magnets during the activation. Also, we found that they do not operate with specified pumping speed in our environment. The pumping speed degrades fast after activation, and the pumps saturate much faster than they should. We attribute these effects to poisoning of the NEG surfaces by non-hydrogen species originated from degassing of coils in RF transition units. Lately, we have replaced the NEGs with cryopumps of compact design and high pumping speed (3000 l/sec each). It should be noted that these cryopumps break beyond repair in a strong magnetic field (due to demagnetization of the valve mechanism) and need to be shielded to reduce the effective field below .5 kG.

We observed an interesting effect of the BLAST magnetic field affecting the focusing in sextupoles. Although the BLAST field is rather uniform, and it does not change the amplitude or direction of the gradients in a sextupole magnet, it changes the direction of magnetic momentum of the atoms relative to the direction of the gradient. Generally, the force acting on the magnetic dipole is $F = \nabla \cdot (\mu \cdot B)$, and since dipoles follow the direction of the magnetic field $\mu = \mu \cdot B/B, F = \mu \cdot \nabla B$.

In ideal sextupole ($B_x = G(x^2 - y^2); B_y = -G \cdot 2xy$) with no external field, the force has only a radial component: $F = 2G\mu r; \frac{F}{F} \cdot \frac{r}{r} = 1$. An external magnetic field B_0 applied in the x-direction (so that $B_x = G(x^2 - y^2) + B_0$) does not affect the amplitude of the force, but it does change its direction:

$$\frac{F}{F} \cdot \frac{r}{r} = \frac{1 + b \cdot \cos(2\theta)}{\sqrt{1 + b^2 + 2b \cdot \cos(2\theta)'}}$$

where b is the ratio of external field and sextupole field at the given point $b = B_0/B_6$, and θ is the polar angle. One can see that in the regions where the external field exceeds the sextupole field, the

y-component of the force changes sign and becomes defocusing! Since the BLAST field is over 2 kG, and the sextupole field is zero at the magnet centre and about 10 kG at the pole tip, the effect is very significant and reduces the ABS intensity by factor of 2. We

encased our sextupoles in magnetic shields and reduced the effect to less than 10%.

3. The Breit-Rabi Polarimeter

The convenient BRP with a permanent sextupole magnet, a chopping wheel, and quadrupole mass analyzer (QMA) could not be used in our environment. QMA does not work in strong magnetic fields, unless it is placed at the very bottom of BLAST pit, some 2 m away from the target. At such a distance, the signal was too weak for reliable measurements. The only natural way to enhance the signal - compression tube - has too slow a response time to be combined with a chopping wheel.

Instead, we used BRP with a dipole magnet. The magnet has very strong (about 2.5 kG/cm) and uniform gradient and was placed after a small (2 mm) diaphragm below the outlet of the storage cell. Three compression tubes (CT) have been installed 1.5 m below the magnet. With the magnet off, the central CT collects both atoms and molecules. With the magnet on, atoms are deflected into the left or right CT depending on their polarization. Our BRP allows measuring both degrees of dissociation in the discharge tube (ABS sextupole magnets have been moved out for these measurements) and polarization in the jet. Moreover, we could monitor the polarization of the atomic beam during the production run by observing the signals from the left and right CTs. The drawback of the system is that only the central trajectories of the atomic beam are sampled in BRP, and therefore absolute measurements of polarization contain significant systematic errors.

4. The Ion Polarimeter

The Ion Polarimeter was designed and build in Amsterdam, and it was only partially implemented at Bates. The electron beam ionizes atoms and molecules in the storage cell. A set of electrostatic lenses extracts ions from the cell and accelerates them to 2.5 kV. A spherical deflector guides ions into the Wien filter, where they are mass analyzed. The full version includes deuteron ions scattering on a tritium target to measure the polarization, but this apparatus was not installed at Bates. Even the limited version allowing the analysis of the mass spectrum of the ions, and therefore the measurement of the atomic fraction in the target, proved to be very useful. In the early commissioning phase we detected a very low atomic fraction (less than 50%) for both hydrogen and deuterium, which explained the low asymmetries we measured at that stage. We identified the problem as damage to the cell surface caused by either Synchrotron Radiation (SR) or charged particles during the injection flash.

Later we removed the Ion Polarimeter and installed a tungsten collimator just upstream of the storage cell. It has an internal diameter just smaller than that of the cell, and its shape was designed to protect the cell from the SR and charged particles, and also minimize the background rate in the detectors. With the collimator in place, we ran for several months and did not detect any degradation of the cell.

5. The Target Performance

Target intensity and polarization are monitored on a daily basis by measuring the rate and asymmetry of the elastic and inelastic scattering. The ABS flow into the cell for both hydrogen (one state) and deuterium (two states) was about $2.5 * 10^{16} \text{at/sec}$, which produced a target thickness of $7 * 10^{13} \text{at/cm}^2$. The measured polarization of the deuterium target was $P_z \approx 72\%$, $P_{zz} \approx 68\%$. The polarization of the hydrogen target was $P_z \approx 78\%$.

References

1. Proceedings of the 2nd Workshop on Electro-Nuclear Physics With Internal Targets and the BLAST Detector, May 1998, Cambridge MA, *World Scientific Publishing*; ISBN: 981024004X
2. Van Buuren L.D. etc., *NIM A* **474**, 209 (2001).

This page intentionally left blank



PARTICIPANTS

This page intentionally left blank

PARTICIPANTS

Alekseev Igor

ITEP
B. Chermushkinskaya 25
117259 Moscow – Russian Federation
Igor.Alekseev@itep.ru

Alexakhin Vadim

Particle Physics Laboratory, JINR
Joliot-Curie 6
141980 Dubna – Russian Federation
Vadim.Alexakhine@cern.ch

Andreev Viktor

Dep. of Phys., Gomel State University
Sovetskaya str. 102,
246019 Gomel – Belarus
andreev@gsu.unibel.by

Anselmino Mauro

University of Turin
Via Giuria 1
10125 Torino – Italy
mauro.anselmino@to.infn.it

Arends Hans-Jürgen

University of Mainz
Institut für Kernphysik J.-J. Becher-Weg 45
D-55099 Mainz – Germany
arends@kph.uni-mainz.de

Armeni Massimo

Pirelli International Award manager
Pirelli & C. S.p.A. Ufficio di Roma
Foro Romano, 3
00186 Roma – Italy

Asaji Shun

Kyushu University
Hakozaki 6-10-1,
812-8581 Higashi – Japan
shun@kutl.kyushu-u.ac.jp

Aschenauer Elke-Caroline

DESY - Hermes Building 1e/407
Notkestrasse 85
22603 Hamburg – Germany
Elke.Aschenauer@desy.de

Aslanyan Petros

Joint Institute for Nuclear Research
Joliot-Curie 6
141980 Dubna – Russian Federation
paslan@jinr.ru, aslanyan@sunhe.jinr.ru

Atutov Sergei

INFN
Via Paradiso 12
44100 Ferrara – Italy
atutov@fe.infn.it

Aulenbacher Kurt

Institut für Kernphysik, Uni. Mainz
J.J. Becherweg-45
55099 Mainz – Germany
aulenbac@kph.uni-mainz.de

Babich Alexander

Gomel Technical University
October Avenue 48,
246746 Gomel – Belarus
babich@gomel.gstu.by

Bacchetta Alessandro

Regensburg University
Theoretische Physik Universitaetstr. 31
93040 Regensburg – Germany
alessandro.bacchetta@physik.uni-regensburg.de

Badelek Barbara

Inst. of Exp. Physics
Warsaw University
Hoza 69
00-681 Warsaw – Poland
badelek@fuw.edu.pl

Bai Mei

Brookhaven National Lab.
C-A Department, Bldg 911B
11720 Upton – United States
mbai@bnl.gov

Balestra Ferruccio

Dipartimento di Fisica Generale A. Avogadro
University of Turin
Via P. Giuria 1
10125 Torino – Italy
balestra@to.infn.it

Barber Desmond

DESY
Notkestrasse 85
22607 Hamburg – Germany
mpybar@mail.desy.de

Barion Luca

INFN - Ferrara
via Paradiso, 12
44100 Ferrara – Italy
barion@fe.infn.it

Barish Kenneth

Department of Physics
University of California
Riverside, CA 92521 – United States
Kenneth.Barish@ucr.edu

Barone Vincenzo

Dipartimento di Scienze
Università del Piemonte Orientale 'A. Avogadro'
Piazza Ambrosoli 5
15100 Alessandria – Italy
barone@to.infn.it

Bazilevsky Alexander

Brookhaven National Laboratory
Pennsylvania Ave
11973 Upton – United States
shura@bnl.gov

Belostotski Stanislav

Petersburg Nucl. Phys. Institute
Gatchina, St.Petersburg region
188300 St.Petersburg – Russian Federation
belostot@desy.de

Bertini Raimondo

Dipartimento di Fisica Generale A. Avogadro,
University of Torino
Via P. Giuria 1
10125 Torino – Italy
bertini@to.infn.it

Bianchi Nicola

INFN - LNF
via E. Fermi 40
00044 Frascati – Italy
bianchi@lnf.infn.it

Birsa Renato

INFN, Sezione di Trieste
Area di Ricerca Padriciano 99
34012 Trieste – Italy
renato.birsa@ts.infn.it

Bisplinghoff Jens

HISKP
University of Bonn
Nüßallee 14-16
D 53115 Bonn – Germany
jens@iskp.uni-bonn.de

Bland Leslie

Physics Department Bldg. 510a
Brookhaven National Laboratory
11973 Upton, New York – United States
bland@bnl.gov

Boglione Mariaelena

University of Turin
Via P. Giuria 1
10125 Torino – Italy
boglione@to.infn.it

Bosted Peter

Jefferson Lab
MS 12H 12000 Jefferson Avenue
Newport News, VA 23606 – United States
bosted@jlab.org

Brachmann Axel

SLAC
M/S 18 2575 Sand Hill Road
Menlo Park, CA 94025 – United States
brachman@slac.stanford.edu

Bradamante Franco

Dipartimento di Fisica
University of Trieste
Via A. Valerio 2
34100 Trieste – Italy
franco.bradamante@ts.infn.it

Bravar Alessandro

Brookhaven National Laboratory
P.O. Box 5000
NY-11793 Upton – United States
bravar@bnl.gov

Bressan Andrea
 Dipartimento di Fisica
 University of Trieste
 via Valerio 2
 34129 Trieste – Italy
 Andrea.Bressan@cern.ch

Brona Grzegorz
 Institute of Experimental Physics
 Warsaw University
 Hoza 69
 00-681 Warszawa – Poland
 Grzegorz.Brona@fuw.edu.pl

Bunce Gerry
 Physics Department, BNL
 Upton, NY 11973 – United States
 bunce@bnl.gov

Bunyatova Elionora
 Joint Institute for Nuclear Research
 Joliot Curie 6
 141980 Dubna – Russian Federation
 bunyatel@nusun.jinr.ru

Burinskii Alexander
 NSI Russian Academy Sciences
 B. Tulsakaya 52
 115191 Moscow – Russian Federation
 bur@ibrae.ac.ru

Bussa Maria Pia
 Dipartimento di Fisica Generale A. Avogadro
 University of Turin
 Via P. Giuria 1
 10125 Torino – Italy
 bussa@to.infn.it

Buttimore Nigel
 School of Mathematic
 University of Dublin
 Hamilton Building – Trinity College
 2 Dublin – Ireland
 nhb@maths.tcd.ie

Calucci Giorgio
 Abdus Salam ICTP
 Strada Costiera 2
 34100 Trieste – Italy
 Giorgio.Calucci@ts.infn.it

Cameron Peter
 Bldg 817
 Brookhaven National Laboratory
 Upton, NY 11973 – United States
 cameron@bnl.gov

Carlini Roger
 Jefferson Laboratory
 12000 Jefferson Avenue
 Newport News, VA 23606 – United States
 carlini@jlab.org

Chernitskii Alexander
 St. Petersburg Electrotechnical Univer.
 Prof. Popov str. 5
 197376 Saint Petersburg – Russian Federation
 aa@cher.etu.spb.ru

Christova Ekaterina
 Inst. of Nucl. Research and Nucl. Energy
 Tzarigradsko Chausee 72
 1784 Sofia – Bulgaria
 echristo@inrne.bas.bg

Ciullo Giuseppe
 INFN - Ferrara
 via del Paradiso 12
 44100 Ferrara – Italy
 ciullo@fe.infn.it

Cledenin James
 SLAC
 2575 Sand Hill Rd.
 Menlo Park, CA 94025 – United States
 clen@slac.stanford.edu

Colantoni Marialaura
 Dipartimento di Fisica Generale A. Avogadro
 University of Turin
 Via P. Giuria 1
 10125 Torino – Italy
 colanton@to.infn.it

Contalbrigo Marco
 Dipartimento di Fisica
 University of Ferrara
 Via Paradiso 12
 44100 Ferrara – Italy
 contalbrigo@fe.infn.it

Conte Mario
 Dipartimento di Fisica Sezione
 University of Genova
 Via Dodecaneso 33
 16146 Genova – Italy
 Mario.Conte@ge.infn.it

Crabb Donald
 Physics Department
 University of Virginia
 382 McCormick Rd.
 Charlottesville, VA 22903 – United States
 dgc3q@virginia.edu

Crawford Christopher

MIT-LNS
25 Evergreen Ln
Arlington, MA 02476 – United States
chris2@ins.mit.edu

Crawford John

RST Radar Systemtechnik
Hengelweg 37
CH-5303 Würenlingen – Switzerland
john.crawford@psi.ch

D'Alesio Umberto

Dipartimento di Fisica
University of Cagliari
Cittadella universitaria S.P. Monserrato-Sestu
09042 Cagliari – Italy
umberto.dalesio@ca.infn.it

Dalla Torre Silvia

INFN-Sezione di Trieste
Area di Ricerca, Padriciano 99
34012 Trieste – Italy
silvia.dallatorre@ts.infn.it

Darwish Eed M.

Physics Department
South Valley University
82524 Sohag – Egypt
eeddarwish@yahoo.com

De Jager Kees

Jefferson Lab
12000 Jefferson Avenue
Newport News, VA 23606 – United States
kees@jlab.org

De Sanctis Enzo

INFN-Laboratori nazionali di Frascati
Via E. Fermi, 40
00044 Frascati – Italy
desanctis@lnf.infn.it

De Vita Raffaella

Istituto Nazionale di Fisica Nucleare
via Dodecaneso 33
16146 Genova – Italy
devita@ge.infn.it

Del Fabbro Giulietta

Central Europe Initiative
Via Genova 9
34100 Trieste – Italy
delfabbro@cei-es.org

Denisov Oleg

INFN-Torino
via Pietro Giuria 1
10125 Torino – Italy
denisov@to.infn.it

Deshpande Abhay

Department of Physics & Astronomy
C-101, SUNY-Stony Brook
Stony Brook, NY 11974 – United States
abhay@skipper.physics.sunysb.edu

Deur Alexandre

Jefferson Lab
Mailstop 12/B127 – 12000 Jefferson Avenue
Newport News, VA 23606 – United States
deurpam@jlab.org

Di Nezza Pasquale

INFN, LNF
via E. Fermi 40
00044 Frascati (Roma) – Italy
Pasquale.DiNezza@lnf.infn.it

Di Salvo Elvio

Dipartimento di Fisica
University of Genova
Via Dodecaneso 33
16146 Genova – Italy
disalvo@ge.infn.it

Dick Louis

CERN
1211 Geneve 23 – Switzerland
Louis.Dick@cern.ch

Dorokhov Alexander

Joint Institute for Nuclear research
Joliot Curie str., 6
141980 Dubna – Russian Federation
dorokhov@thsun1.jinr.ru

Dosselli Umberto

INFN Sezione di Padova
Via Marzolo 8
I-35131 Padova – Italy
dosselli@padova.infn.it

Duic Venicio

Dipartimento di Fisica
University of Trieste
via Valerio 2
34129 Trieste – Italy
duic@mail.cern.ch

Dutz Hartmut

Physikalisches Institut Universität Bonn
Nussallee 12
53115 Bonn – Germany
dutz@physik.uni-bonn.de

Dyug Maxim

Budker Institute of Nuclear Physics
Lavrentieva av. 11
630090 Novosibirsk – Russian Federation
M.V.Dyug@inp.nsk.su

Efremov Anatoly

Lab. Theor. Phys., JINR
Joliot Curies st. 6
141980 Dubna – Russian Federation
efremov@thsun1.jinr.ru

Ermolaev Boris

Ioffe Physico-Technical Institute
Polytechnicheskaya, 26
194021 St.Petersburg – Russian Federation
boris.ermolaev@cern.ch

F. Dalpiaz Paola

Ferrara University
Via Paradiso 12
44100 Ferrara – Italy
pfd@fe.infn.it

Fabbri Riccardo

HERMES - DESY
Notkestraße 85
22607 Hamburg – Germany
rfabbri@mail.desy.de

Fantoni Alessandra

INFN - LNF
Via E. Fermi, 40
00044 Frascati (RM) – Italy
fantoni@lnf.infn.it

Fantoni Stefano

SISSA / ISAS
Via Beirut 4
I-34014 Trieste – Italy
fantoni@sissa.it

Felix Julian

Instituto de Física, UGTO
Lomas del Bosque 103, Lomas del Campestre
37150 Leon – Mexico
felix@fisica.ugto.mx

Ferrero Andrea

University of Turin
Via Pietro Giuria, 1
10125 Torino – Italy
aferrero@to.infn.it

Ferrero Livio

Dipartimento di Fisica Generale A. Avogadro
University of Turin
Via P. Giuria 1
I-10124 Torino – Italy
ferrero@to.infn.it

Fidecaro Giuseppe

CERN
CH-1211 Geneva 23 – Switzerland
fideg@mail.cern.ch

Fields Douglas

UNM/RBRC
Department of Physics and Astronomy
800 Yale Boulevard NE
Albuquerque, Nm 87131 – United States
fields@unm.edu

Fimushkin Victor

Cryogenic Department - JINR
Joliot Curie 6
141980 Dubna – Russian Federation
fimush@sunhe.jinr.ru

Finger Michael

CTU Prague
Sluknovska 312
CZ-190 00 Praha 9 – Czech Republic
michael.finger@cern.ch

Finger Miroslav

Charles University
V Holesovickach 2
CZ-180 00 Praha 8 – Czech Republic
miroslav.finger@cern.ch

Fischer Horst

University Freiburg
Hermann-Herder-Str. 3
Freiburg D-79104 – Germany
Horst.Fischer@cern.ch

Forte Stefano

Dipartimento di Fisica
University of Milan
via Celoria 16
I-20133 Milano – Italy
forte@mi.infn.it

Franklin Wilbur

Bates Linear Accelerator Center
P.O. Box 846
Middleton, MA 01949 – United States
wafrankl@mit.edu

Friedrich Jan

Physik Department E18
Technical University Munich
James-Franck-Str. 1
85748 Garching Bei München – Germany
Jan.Friedrich@ph.tum.de

Fukao Yoshinori

Department of Physics, Bld. 510A
Brookhaven National Laboratory
Upton, NY 11973-5000 – United States
fukao@bnl.gov

Furlan Giuseppe

Dipartimento di Fisica Teorica
University of Trieste
Strada Costiera 11
I-34014 Trieste – Italy
gfurlan@ictp.trieste.it

Gamberg Leonard

Science Division, Penn State University
Berks – Lehigh Valley College
Tulpehocken Road PO Box 7009
Reading, PA 19610-6009 – United States
lpg10@psu.edu

Garfagnini Raffaello

Dipartimento di Fisica Generale A. Avogadro
University of Turin
Via P. Giuria 1
I-10125 Torino – Italy
garfagnini@to.infn.it

Garçon Michel

SPhN - Saclay
bat. 703 CEA-Saclay
91191 Gif-sur-Yvette – France
mgarcon@cea.fr

Gasimova Rasmiiya

Nakhchivan State University
Nizami 61/31
AZ7012 Nakhchivan – Azerbaijan
gasimovar@yahoo.co.uk

Gautheron Fabrice

CERN
1211 Geneva 23 – Switzerland
fabrice.gautheron@cern.ch

Ghirardi Giancarlo

Consorzio per la Fisica – Trieste
Strada Costiera 11
I-34014 Trieste – Italy
ghirardi@ictp.it

Giordano Francesca

Università di Ferrara
Via Paradiso 12
44100 Ferrara – Italy
giordano@fe.infn.it

Giorgi Marcello

Dipartimento di Fisica
University of Trieste
Via A. Valerio 2
I-34127 Trieste – Italy
marcello.giorgi@ts.infn.it

Gobbo Benigno

INFN - Sezione di Trieste
Area di Ricerca – Padriciano 99
I-34012 Trieste – Italy
benigno.gobbo@ts.infn.it

Goloskokov Sergey

BLTP, JINR
Joliot-Curie 6
141980 Dubna – Russian Federation
goloskkv@thsun1.jinr.ru

Goradia Shantilal

AEP
3003 Royal Huntsman Court
South Bend, IN 48837 – United States
ShantilalG1@juno.com

Goshtasbpour Mehrdad

Department of Physics
Shahid Behashti University
Evin
19834 Tehran – Iran
goshtasb@sbu.ir

Goto Yuji

RIKEN BNL Research Center, Bldg.510A
Brookhaven National Laboratory,
Upton, NY 11973 – United States
goto@bnl.gov

Grajek Oleg

HEP Division, SINS
Hoza 69
PL-00-681 Warsaw – Poland
oleg@fuw.edu.pl

Grigoriev Kirill

Institute for Nuclear Physics (IKP)
LeoBrandt Strasse,
52425 Juelich – Germany
k.grigoriev@fz-juelich.de

Grosse Perdekamp Matthias

UIUC and RBRC
Loomis Laboratory
1110 W. Green Street
Urbana, IL 61856 – United States
mcp@uiuc.edu

Guazzoni Paolo

Milan University
via Celoria 16
20133 Milano – Italy
paolo.guazzoni@mi.infn.it

Haerberli Willy

University of Wisconsin-Madison
1150 University Avenue
Madison, WI 53706 – United States
haerberli@wisc.edu

Hasch Delia

INFN-LNF
via E. Fermi, 40
00044 Frascati – Italy
delia.hasch@inf.infn.it

Hatanaka Kichiji

RCNP, Osaka University
10-1 Mihogaoka
Ibaraki, Osaka 567-0047 – Japan
hatanaka@rcnp.osaka-u.ac.jp

Hautle Patrick

Paul Scherrer Institut
WLGA/U129
5232 Villigen PSI – Switzerland
patrick.hautle@psi.ch

Heinsius Fritz-Herbert

Universitat Freiburg
Hermann-Herder-Str. 3
79104 Freiburg – Germany
heinsius@axfr01.physik.uni-freiburg.de

Hinterberger Frank

H-ISKP, Univ. Bonn
Nußallee 14-16
D-53115 Bonn – Germany
fh@iskp.uni-bonn.de

Hobbs Robert

University of New Mexico
1813 Ridgecrest Dr. SE
Albuquerque NM 87108 – United States
rhobbs@unm.edu

Huang Haixin

BC-A Department
Brookhaven National Lab
Upton, NY 11973-5000 – United States
huanghai@bnl.gov

Hughes Emlyn

California Institute of Technology
1200 East California Boulevard
Pasadena, CA 91125 – United States
emlyn@caltech.edu

Hughes Miryam

Physics Department
Yale University
P.O.Box 208121
New Haven, CT 06520 – United States

Huseynov Vali

Nakhchivan State University
Azadlig prospekti 44/11
AZ7012 Nakhchivan – Azerbaijan
vgusseinov@yahoo.com

Ichimura Munetake

Faculty of Computer and Information Science
Hosei University
3-7-2, Kajinocho, Koganeishi
184-8584 Tokyo – Japan
ichimura@k.hosei.ac.jp

Illarionov Alexei

Laboratory of High Energy
Joint Institute for Nuclear Research
141980 Dubna – Russian Federation
Alexei.Illarionov@jinr.ru

Imai Kenichi

Department of Physics
Kyoto University
606 Kyoto – Japan
imai@nh.scphys.kyoto-u.ac.jp

Jiang Xiaodong

Rutgers University
MS 12 H 12000 Jefferson Ave.
Newport News, VA 23606 – United States
jiang@jlab.org

Jinnouchi Osamu

RIKEN BNL Research Center
BLDG. 510A, BNL
UPTON, NY 11973-5000 – United States
josamu@bnl.gov

Johansson Tord

Department of Radiation Sciences
Uppsala University
Box 535
S-75121 Uppsala – Sweden
tord.johansson@tsl.uu.se

Joosten Rainer

University Bonn
Nussallee 14-16
53115 Bonn – Germany
rainer.joosten@cern.ch

Jungmann Klaus

KVI
Rijksuniversiteit Groningen Zernikelaan 25
9747AA Groningen – Netherlands
jungmann@kvi.nl

Kacharava Andro

IKP FZJ
Forschungszentrum Juelich
Leo-Brandt-Str. 1
D52428 Juelich – Germany
a.kacharava@fz-juelich.de

Kageya Tsuneo

LEGS group, Bld. 510A
Brookhaven National Lab.
Upton, NY 11973-5000 – United States
kageya@bnl.gov

Kawabata Takahiro

CNS, University of Tokyo
c/o RIKEN, Hirosawa 2-1
351-0198 Wako, Saitama – Japan
kawabata@cns.s.u-tokyo.ac.jp

Kawall Dave

RIKEN-BNL Research Center, Bldg 510A
Brookhaven National Lab
Upton, NY 11973-5000 – United States
kawall@bnl.gov

Khorramian Alinaghi

IPM-Institute for Studies in Theoretical Physics & Mathematics
19395-5531 Tehran – Iran
khorramiana@theory.ipm.ac.ir

Kim Wooyoung

Department of Physics
Kyungpook National University
1370 Sankyukdong, Pookgu
702-701 Daegu – Korea (KR)
wooyoung@knu.ac.kr

Kinney Edward

Department of Physics
University of Colorado
Boulder, CO 80309-0390 – United States
Edward.Kinney@colorado.edu

Kiryuk Joanna

Massachusetts Institute of Technology
P.O. Box 114
Upton, NY 11973 – United States
joanna@ins.mit.edu

Kisselev Yuri

CERN
1211 Geneva 23 – Switzerland
Yuri.kisselev@cern.ch

Koivuniemi Jaakko

CERN
1211 Geneve 23 – Switzerland
Jaakko.Koivuniemi@cern.ch

Konter Ton

Paul Scherrer Institut
WLG/U125
5232 Villigen PSI – Switzerland
ton.konter@psi.ch

Kosmachev Oleg

LHE JINR
Joliot-Curie, 6
141980 Dubna – Russian Federation
kos@thsun1.jinr.ru

Kotzinian Aram

Dipartimento di Fisica
University of Turin
via Pietro Giuria 1
10125 Torino – Italy
aram.kotzinian@cern.ch

Krisch A. D.

Spin Physics Center
University of Michigan
Ann Arbor, MI 48109-1120 – United States
krisch@umich.edu

Kryshkin Victor

Institut for High Energy Physics
Pobeda st. 1
142281 Protvino – Russian Federation
Victor.Kryshkin@ihep.ru

Kubart Jiri

Technical University
Halkova 6
46117 Liberec – Czech Republic
jiri.kubart@cern.ch

Kubo Ken-ichi

Tokyo Metropolitan University
1-1 Minami-Osawa, Hachioji-shi
192-0397 Tokyo – Japan
kubo@comp.metro-u.ac.jp

Kurek Krzysztof

Soltan Institute for Nuclear Studies
Hoza 69
00 681 Warsaw – Poland
kurek@fuw.edu.pl

Ladygin Vladimir

LHE-JINR
Joliot Curie 6
141980 Dubna – Russian Federation
ladygin@sunhe.jinr.ru

Lamanna Massimo

CERN
1211 Geneve 23 – Switzerland
Massimo.Lamanna@cern.ch

Leader Elliot

High Energy Physics, Blackett Laboratory
Imperial College
Prince Consort Road
SW7 2BW London – United Kingdom
e.leader@imperial.ac.uk

Lehrach Andreas

Institut für Kernphysik Geb. 9.7
Forschungszentrum Jülich
52425 Jülich – Germany
a.lehrach@fz-juelich.de

Lenisa Paolo

Università di Ferrara
via Paradiso, 12
44100 FERRARA – Italy
lenisa@hermes.desy.de

Lhuillier David

CEA Saclay
DAPNIA/SPhN Bat.703
91191 Gif-sur-Yvette – France
dlhuillier@cea.fr

Liang Zuo-tang

Department of Physics
Shandong University
250100 Jinan – China
liang@sdu.edu.cn

Litvinenko Anatoly

Laboratory of High Energy
Joint Institute for Nuclear Research
Joliot Curie 6
RU-141980 Dubna – Russian Federation
litvin@moonhe.jinr.ru

Lowenstein Derek

C-A Department, Bldg. 911B
Brookhaven National Laboratory
35 Lawrence Drive P.O. Box 5000
Upton, NY 11973-5000 – United States
lowenstein@bnl.gov

Luccio Alfredo U.

C-AD Department, Bldg. 911B
Brookhaven National Laboratory
Upton, NY 11973-5000 – United States
luccio@bnl.gov

Lykasov Gennady

Joint Institute for Nuclear Research
Joliot Curie 6
141980 Dubna – Russian Federation
lykasov@nusun.jinr.ru

Lyuboshitz Valery

Joint Institute for Nuclear Research
Joliot-Curie str., 6
141980 Dubna – Russian Federation
Valery.Lyuboshitz@jinr.ru

MacKay William

Brookhaven National Lab
Upton, NY 11973-5000 – United States
waldo@bnl.gov

Maeda Yukie

RIKEN
Hirosawa 2-1, Wako city
351-0198 Saitama – Japan
yukie@nucl.phys.s.u-tokyo.ac.jp

Maggiora Angelo

INFN
Via P. Giuria 1
101025 Torino – Italy
maggiora@to.infn.it

Maggiora Marco

Dipartimento di Fisica Generale A. Avogadro
Università di Torino
Via P. Giuria 1
I-10125 Torino – Italy
marco.maggiora@to.infn.it

Makdisi Yousef

Collider Accelerator Department
Brookhaven National Laboratory
Upton, NY 11973 – United States
makdisi@bnl.gov

Mallot Gerhard

PH Department CERN
1211 Geneva 23 – Switzerland
Gerhard.Mallot@cern.ch

Mankoc Borstnik Norma Susana

University of Ljubljana
Jadranska 19,
1000 Ljubljana – Slovenia
norma.s.mankoc@ijs.si

Martin Anna

Dipartimento di Fisica
University of Trieste
via A. Valerio 2
34127 Trieste – Italy
anna.martin@ts.infn.it

Marukyan Hrachya

Yerevan Physics Institute
Alikhanian Brothers st. 2
375036 Yerevan – Armenia
marukyan@mail.desy.de

Maruyama Takashi

Stanford Linear Accelerator Center
2575 Sand Hill Road
Menlo Park, CA 94025 – United States
tvm@slac.stanford.edu

Maschinot Aaron

Massachusetts Institute of Technology
149 Derby ST APT A
SALEM, MA 01970 – United States
AJMASCH@MIT.EDU

Mestayer Mac

Jefferson Lab
12000 Jefferson Ave.
23606 Newport News, Va. – United States
mestayer@jlab.org

Metz Andreas

Institute for Theoretical Physics II
Ruhr-University Bochum
44780 Bochum – Germany
metza@tp2.ruhr-uni-bochum.de

Meyer Werner

Institut für Experimentalphysik Gebäude NB2/135
Ruhr-Universität Bochum
D-44780 Bochum – Germany
meyer@ep1.rub.de

Michels Andreas

Paul Scherrer Institut
WLG/UA129
5232 Villigen PSI – Switzerland
andreas.michels@psi.ch

Mielech Adam

INFN - Sezione di Trieste
Padriciano 99
34-012 Trieste – Italy
mielech@ts.infn.it

Mikes Petr

Technical University
Halkova 6
46117 Liberec – Czech Republic
petr.mikes@centrum.cz

Milner Richard

MIT-Bates
77 Massachusetts avenue
Cambridge, MA 02139 – United States
milner@mitlms.mit.edu

Mirjalili Abolfazl

Physics Department
Yazd University
89195-741 Yazd – Iran
a.mirjalili@yazduni.ac.ir

Mochalov Vasily

Department of Experimental Physics
IHEP
1 Pobeda str
142281 Protvino – Russian Federation
mochalov@jlab.org

Mukherjee Asmita

Lorentz Institute
University of Leiden
2300 RA Leiden – The Netherlands
E-mail: asmita@lorentz.leidenuniv.nl

Murgia Francesco

INFN - Sezione di Cagliari
Cittadella Universitaria di Monserrato, C.P. 170
09042 Monserrato (CA) – Italy
francesco.murgia@ca.infn.it

Musulmanbekov Genis

JINR
Joliot Curie 6
RU-141980 Dubna – Russian Federation
genis@jinr.ru

Nagaytsev Alexander

JINR
Joliot-Curie 6
141980 Dubna – Russian Federation
nagajcev@mail.desy.de

Nass Alexander

BNL, bld. 930
Upton, NY 11973 – United States
nass@bnl.gov

Nassalski Jan

Soltan Institute for Nuclear Studies
Hoza 69
05-816 Warsaw – Poland
jan.nassalski@fuw.edu.pl

Neyret Damien

CEA Saclay
DAPNIA/SPhN bat 703
route de Saclay
91191 Gif Sur Yvette – France
dneyret@cea.fr

Nurushev Sandibek

Institute for high energy physics
5 Moskovskaya Str, app. 35,
142281 Protvino – Russian Federation
nurushev@mx.ihep.u

Ogawa Akio

Brookhaven National Laboratory,
Upton, NY 11973-5000, USA
akio@bnl.gov

Okada Hiromi

RIKEN BNL Center, Bldg. 510A
Brookhaven National Laboratory
Upton, NY 11973 – United States
okadah@bnl.gov

Okada Kensuke

RBRC
BNL bldg.510a
UPTON, NY 11973 – United States
okada@bnl.gov

Oryu Shinsho

Tokyo University of Science
2641-Yamazaki
278-8510 Noda – Japan
oryu@ph.noda.tus.ac.jp

Pagano Paolo

INFN - Sezione di Trieste
via Valerio, 2
I-34127 Trieste – Italy
Paolo.Pagano@ts.infn.it

Pagnini Maria Paola

Comune di Trieste
Piazza Unità d'Italia 4
I-34100 Trieste – Italy
PagniniMP@sp.univ.trieste.it

Pankov Alexander

Technical University of Gomel
October Av. 48
246746 Gomel – Belarus
pankov@ictp.ts.it

Panzieri Daniele

Dipartimento di Fisica Generale A. Avogadro
University of Turin
via P. Giuria 1
I-10125 Torino – Italy
panzieri@to.infn.it

Paul Stephan

Physik Department E18
Technische Univ. Muenchen
James Franck Str
85747 Garching – Germany
stephan.paul@ph.tum.de

Paver Nello

Dip. di Fisica Teorica
University of Trieste
str. Costiera, 11
I - 34014 Trieste – Italy
nello@ts.infn.it

Penzo Aldo

INFN - Sezione di Trieste
Area di Ricerca Padriciano 99
I-34012 Trieste – Italy
penzo@ts.infn.it

Peshekhonov Dmitry

JINR
Joliot-Curie 6
141980 Dubna – Russian Federation
Dimitri.Pechekhonov@cern.ch

Pijlman Fetze

Vrije Universiteit Amsterdam
De Boelelaan 1081 (room U2.21)
NL-1081 HV Amsterdam – Netherlands
fetze@nat.vu.nl

Pilipenko Yuri Konstantinovich

Laboratory High Energy
Joint Institute for Nuclear research
Joliot Curie str., 6
141980 Dubna – Russian Federation
pilipen@sunhe.jinr.ru

Piragino Guido

Dipartimento di Fisica Generale A. Avogadro
University of Turin
Via P. Giuria 1
I-10125 Torino – Italy
piragino@to.infn.it

Piskunov Nikolay

Joint Institute for Nuclear Research
6 Joliot-Curie str.
141980 Dubna – Russian Federation
piskunov@sunhe.jinr.ru

Polak Jaroslav

Faculty of Mechatronics
Technical University
Halkova 6
46117 Liberec – Czech Republic
jaroslav.polak@cern.ch

Prepost Richard

University of Wisconsin
1150 University Av. Madison, WI 53706 – United States
prepost@hep.wisc.edu

Prescott Charles

Stanford Linear Accelerator Center
2575 Sand Hill Road
Menlo Park, CA 94025 – United States
prescott@slac.stanford.edu

Prokofiev Alexander

Petersburg Nuclear Physics Institute
Gatchina
188300 St.Petersburg – Russian Federation
prokan@mail.pnpi.spb.ru

Prokudin Alexei

University of Turin
Via Pietro Giuria, 1
10125 Torino – Italy
prokudin@to.infn.it

Ptitsyn Vadim

C-AD, Bldg.911B
Brookhaven National Laboratory
Upton, NY 11973 – United States
vadimp@bnl.gov

Pusterla Modesto

Dipartimento di Fisica
University of Padua
Via Marzolo 8
I-35131 Padova – Italy
pusterla@pd.infn.it

Raccanelli Andrea

Physikalisches Institut
Universitaet Bonn
Nussallee 12
53115 Bonn – Germany
araccan@physik.uni-bonn.de

Ramsey Gordon

Loyola University Chicago
6460 N. Kenmore
Chicago, IL 60626 – United States
gpr@hep.anl.gov

Ratcliffe Philip G.

Università dell'Insubria
via Valleggio 11
22100 Como – Italy
philip.ratcliffe@uninsubria.it

Rathmann Frank

Institut für Kernphysik
Leo-Brandt-Str. 1
52425 Juelich – Germany
f.rathmann@fz-juelich.de

Raymond Richard

Randall Lab of Physics
University of Michigan
Ann Arbor, MI 48109 – United States
rraymond@umich.edu

Reggiani Davide

Physikalisches Institut
 Universität Erlangen-Nuernberg
 Erwin-Rommel-Str. 1
 91058 Erlangen – Germany
 reggiani@mail.desy.de

Riazuddin

National Center for Physics
 Quaid-e-Azam University
 45320 Islamabad – Pakistan
 riazuddins@yahoo.com

Richard Jean-Marc

University Joseph Fourier
 LPSC, 53 avenue des Martyrs
 38023 Grenoble – France
 jean-marc.richard@ipsc.in2p3.fr

Riedl Caroline

Hermes building 1e/403
 DESY
 Notkestr. 85
 22607 Hamburg – Germany
 criedl@mail.desy.de

Rivas Martin

Theoretical Physics Department
 University of the Basque Country,
 Apdo 644
 48940 Bilbao – Spain
 wtpripem@lg.ehu.es

Roberts B. Lee

Department of Physics
 Boston University
 590 Commonwealth Ave
 Boston, MA 02215 – United States
 roberts@bu.edu

Roche Julie

Jefferson Lab
 12H/C113 12000 Jefferson Avenue
 Newport News, VA-23608 – United States
 jroche@jlab.org

Romeo Domenico

University of Trieste
 Rettorato Piazzale Europa 1
 I-34127 Trieste – Italy
 rettore@units.it

Rondio Ewa

Soltan Institute for Nuclear Studies
 Hoza 69
 PL-00-681 Warszawa – Poland
 ewar@fuw.edu.pl

Roser Thomas

Bldg. 911B Collider-Accelerator Dept.
 Brookhaven National Laboratory
 Upton, NY 11973-5000 – United States
 roser@bnl.gov

Rostomyan Armine

Yerevan Physics Institute
 Notkestrasse 85
 22607 Hamburg – Germany
 armine.rostomyan@desy.de

Rubin Joshua

Physics Department
 University of Illinois Urbana-Champaign
 1110 W. Green St.
 Urbana, IL 61801 – United States
 jrubin@uiuc.edu

Rykov Vladimir

Main Research Building Rm. 254
 RIKEN
 2-1 Hirosawa
 351-0198 Wako, Saitama – Japan
 rykov@riken.jp

Ryltsov Vladislav

ITEP
 B. Chermushkinskaya 25,
 117218 Moscow – Russian Federation
 Vladislav.Ryltsov@itep.ru

Saito Naohito

Physics Department
 Kyoto University
 Kitashirakawa-Oiwake-Cho Sakyo-ku
 606-8502 Kyoto – Japan
 saito@nh.scphys.kyoto-u.ac.jp

Sandacz Andrzej

Soltan Institute for Nuclear Studies
 Hoza 69
 PL 00-681 Warsaw – Poland
 sandacz@fuw.edu.pl

Sapozhnikov Mikhail

Laboratory of Particle Physics
 JINR
 Joliot Curie 6
 141980 Dubna – Russian Federation
 sapozh@sunse.jinr.ru

Sato Hikaru

KEK
 I-I Oho
 Tsukuba, Ibaraki 305-0801 – Japan
 hikaru.sato@kek.jp

Schiavon Paolo

Dipartimento di Fisica
University of Trieste
via A. Valerio, 2
34127 Trieste – Italy
Paolo.Schiavon@ts.infn.it

Schill Christian

Physikalisches Institut
Universität Freiburg
Hermann-Herder Str. 3
D-79104 Freiburg – Germany
christian.schill@cern.ch

Schnell Gunar

Department of Physics
Tokyo Institute of Technology
2-12-1 O-okayama, Meguro
152-8551 Tokyo – Japan
gunar.schnell@desy.de

Seidl Ralf

Loomis Laboratory of Physics
University of Illinois at Urbana-Champaign
1110 Green Street
Urbana, IL 61801-3080 – United States
ralf.seidl@web.de

Selyugin Oleg

Institute de Physique
Université de Liège
141980 Liège – Belgium
selugin@thsun1.jinr.ru

Seto Richard

Physics Department
University of California
Riverside, CA 92521 – United States
richard.seto@ucr.edu

Shaikhatdenov Binuradden

JINR
Joliot-Curie str., 6
141980 Dubna – Russian Federation
sbg@thsun1.jinr.ru

Shatunov Petr

BINP Novosibirsk
Zolotodolinskaya str 31/1-67
630090 Novosibirsk – Russian Federation
P.Shatunov@gsi.de

Shatunov Yuri

Budker Institute of Nuclear physics
11 Lavrentiev av.
630090 Novosibirsk – Russian Federation
shatunov@inp.nsk.su

Shekhovtsova Olga

NSC KIPT Institute of Theoretical Physics
Akademicheskaya str., 1
61108 Kharkov – Ukraine
shekhovtsova@kipt.kharkov.ua

Shevchenko Oleg

Joint Institute for Nuclear Research
Joliot-Curie 6
141980 Dubna – Russian Federation
Oleg.Chevchenko@cern.ch

Shimizu Youhei

RCNP
Osaka University
10-1 Mihogaoka, Ibaraki
567-0047 Osaka – Japan
yshimizu@rcnp.osaka-u.ac.jp

Si Lakhhal Bahia

Physics Department
University Saad Dahlab of Blida
P.O Box 270 Sourmaa
09000 Blida – Algeria
silakhhal@wissal.dz

Sikach Sergey

Institute of Physics BAS
Fr. Skoryna ave. 68
220072 Minsk – Belarus
sikach@dragon.bas-net.by

Silenko Alexander

Belarusian State University
11 Bobruiskaya street
220080 Minsk – Belarus
silenko@inp.minsk.by

Soergel Volker

Max Planck Institute for Physics
Föhringer Ring 6
80805 Munich – Germany
soergel@mppmu.mpg.de

Solovieva Tatiana

IHEP
Pobeza st.1
RU-142284 Protvino – Russian Federation

Sowinski James

Indiana University
IUCF 2401 Milo B. Sampson Ln
Bloomington, IN 47408 – United States
sowinski@iucf.indiana.edu

Sozzi Federica

Dipartimento di Fisica
University of Trieste
via Valerio 2
34129 Trieste – Italy
federica.sozzi@ts.infn.it

Stamenov Dimitar

Institute for Nuclear Research
blvd. Tzarigradsko chausee 72
1784 Sofia – Bulgaria
stamenov@inrne.bas.bg

Stancari Michelle

University of Ferrara
Via Paradiso,12
44100 Ferrara – Italy
michelle@fe.infn.it

Statera Marco

INFN - Sezione di Ferrara
V. Paradiso 12
44100 Ferrara – Italy
statera@fe.infn.it

Steffens Erhard

Physikalisches Institut
University of Erlangen-Nürnberg
Erwin-Rommel-Str. 1
91058 Erlangen – Germany
steffens@physik.uni-erlangen.de

Stewart Jim

DESY
Notkestrasse 85
22607 Hamburg – Germany
Stewart@hermes.desy.de

Stibunov Victor

Nuclear Physics Institute Tomsk
Lenin Avenue, 2A
634050 Tomsk – Russian Federation
stib@npi.tpu.ru

Stolarski Marcin

Warsaw University
Hoza 69
00-861 Warszawa – Poland
Marcin.Stolarski@cern.ch

Suda Kenji

Center for Nuclear Study
University of Tokyo
2-1 Hirosawa, Wako
351-0198 Saitama – Japan
suda@cns.s.u-tokyo.ac.jp

Sumachev Viktorin

Petersburg Nuclear Physics Institute
str. Koli Podryadchikova, 11, fl. 183
188308 Gatchina – Russian Federation
sumachev@pnpi.spb.ru

Svirida Dmitry

ITEP
25 B. Chermushkinskaya
117218 Moscow – Russian Federation
Dmitry.Svirida@itep.ru

Tannenbaum Michael

Physics Department
Brookhaven National Lab, 510c
Upton, NY 11973-5000 – United States
mjt@bnl.gov

Teryaev Oleg

BLTP JINR
Joliot Curie str., 6
Dubna – Russian Federation
teryaeв@thsun1.jinr.ru

Tessaro Susanna

Dipartimento di Fisica
University of Trieste
Via A. Valerio 2
I-34127 Trieste – Italy
tessaro@ts.infn.it

Tessarotto Fulvio

INFN - Sezione di Trieste
Area di Ricerca –Padriciano 99
34012 Trieste – Italy
fulvio.tessarotto@ts.infn.it

Tikhonin Feodor

Institute for High Energy Physics
Pobeda str, 1
142284 Protvino – Russian Federation
tikhonin@mx.ihep.su

Togawa Manabu

Kyoto University
Oiwakekyo, Kitashirakawa, Sakyo-ku
606-8502 Kyoto – Japan
togawa@nh.scphys.kyoto-u.ac.jp

Toorsunov Ergash

Institute of Nuclear Physics
Beruni st 4-2, Ulugbek
702132 Tashkent – Uzbekistan
tursune@inp.uz

Toporkov Dmitry

Budker institute of nuclear physics
prospect Lavrentieva 11
630090 Novosibirsk – Russian Federation
D.K.Toporkov@inp.nsk.su

Troshin Sergey

IHEP
Pobeda 1,
142280 Protvino – Russian Federation
Sergey.Troshin@ihep.ru

Trueman T Laurence

Brookhaven National Laboratory
P.O. Box 5000
Upton, NY 11786 – United States
trueman@bnl.gov

Tsentalovich Evgeni

MIT - Bates
PO Box 846
21 Manning Rd
Middleton, MA 01949-2846 – United States
evgeni@mit.edu

Tsytrynau Andrei

Laboratory for Physical Study
Pavel Sukhoi State Technical University
October Avenue, 48
246746 Gomel – Belarus
tsytrin@gstu.gomel.by

Tuniz Claudio

Abdus Salam ICTP
Strada Costiera 11
I-34014 Trieste – Italy
ctuniz@ictp.it

Tyurin Nikolay

Institute for High Energy Physics
1 Pobedy str.,
142281 Protvino – Russian Federation
tyurin@mx.ihep.su

Underwood David

HEP - Bldg 362
Argonne National Lab
9700 S. Cass Ave
Argonne, IL 60439 – United States
dgu@hep.anl.gov

Uzikov Yuri

Joint Institute for Nuclear Researches
Joliot Curie, 6
141980 Dubna – Russian Federation
uzikov@nusun.jinr.ru

Vacchi Andrea

INFN - Sezione di Trieste
Area di Ricerca
Padriciano 99
I-34012 Trieste – Italy
andrea.vacchi@ts.infn.it

Van Den Brandt Ben

Paul Scherrer Institute
WLGA-127
CH-5232 Villigen – Switzerland
Ben.vandenBrandt@psi.ch

Van Der Nat Paul

NIKHEF
Kruislaan 409
1098 SJ Amsterdam – Netherlands
natp@nikhef.nl

Van Der Ventel Brandon

Department of Physics
University of Stellenbosch
Private Bag X1, Matieland,
7602 Stellenbosch – South Africa
bventel@sun.ac.za

Van Oers Willem T.H.

TRIUMF
4004 Wesbrook Mall
Vancouver, BC V6T 2A3 – Canada
vanoers@triumf.ca

Vogelsang Werner

BNL Nuclear Theory, Bldg. 510a
Brookhaven National Laboratory
Upton, NY 11973 – United States
wvogelsang@bnl.gov

Von Przewoski Barbara

Indiana University Cyclotron Facility
Milo B. Sampson Lane
Bloomington, IN 2401 – United States
przewoski@iucf.indiana.edu

Wagner Marcus

RBRC - Bldg. 510A
Brookhaven National Lab
Upton, NY 11973-5000 – United States
mwagner@rcf.rhic.bnl.gov

Wakamatsu Masashi

Department of Physics
Osaka University
Machikaneyama-cho 1-1 Toyonaka
560-0043 Osaka – Japan
wakamatu@phys.sci.osaka-u.ac.jp

Wang Meng

INFN - Sezione di Ferrara
via Paradiso 11
44100 Ferrara – Italy
wang@fe.infn.it

Windmolders Roland

University of Bonn
Nussallee 14-16
D-53115 Bonn – Germany
roland.windmolders@cern.ch

Wise Thomas

Department of Physics
University of Wisconsin
1150 University Avenue
Madison, WI 53706 – United States
wise@uwnc0.physics.wisc.edu

Wislicki Wojciech

Soltan Institute
Hoza 69
Pl-00-681 Warszawa – Poland
wislicki@fuw.edu.pl

Wong Victor

University of Michigan
1071 Beal Ave
48109 Ann Arbor, Michigan – United States
vkw@umich.edu

Xu Qinghua

Physics Department
Shandong University
250100 Ji'nan – China
xuqh@sdu.edu.cn

Yashchenko Sergey

Universität Erlangen-Nuernberg
Wiesenstrasse 6g
D-52428 Juelich – Germany
s.yaschenko@fz-juelich.de

Ye Zhenyu

Deutsches Elektronen-Synchrotron
Notkestrasse 85
22607 Hamburg – Germany
yezhenyu@mail.desy.de

Yershov Alexander

Scobeltsyn Institute of Nuclear Physics
Moscow State University
Leninskie gory, 1(2),
119992 Moscow – Russian Federation
e@lav01.sinp.msu.ru

Yoshimi Akithiro

RIKEN
2-1 Hirosawa, Wako, Saitama
351-0198 Wako – Japan
yoshimi@rarfap.riken.jp

Yu David

DULY Research Inc.
1912 MacArthur Street
Rancho Palos Verdes, CA 90275 – United States
davidyu@pacbell.net

Zajc W.A.

Physics Department
Columbia University
New York, NY – United States
zajc@nevis.columbia.edu

Zamiralov Valeri

Scobeltsyn Institute of Nuclear Physics
Moscow State University
Leninskie gory, 1(2),
119992 Moscow – Russian Federation
zamir@depni.npi.msu.ru

Zanetti Anna Maria

INFN - Sezione di Trieste
Padriciano 99
34012 Trieste – Italy
zanetti@ts.infn.it

Zavada Petr

Institute of Physics
Na Slovance 2
CZ-182 21 Prague – Czech Republic
zavada@fzu.cz

Zelenski Anatoli

Brookhaven National Lab.
Bldg.930, BNL
Upton, NY 11973 – United States
zelenski@bnl.gov

Zetta Luisa

University of Milan
via Celoria 16
20133 Milano – Italy
luisa.zetta@mi.infn.it

Ziskin Vitaliy

MIT
21 Manning Rd
Middleton, MA 01949 – United States
vziskin@mit.edu

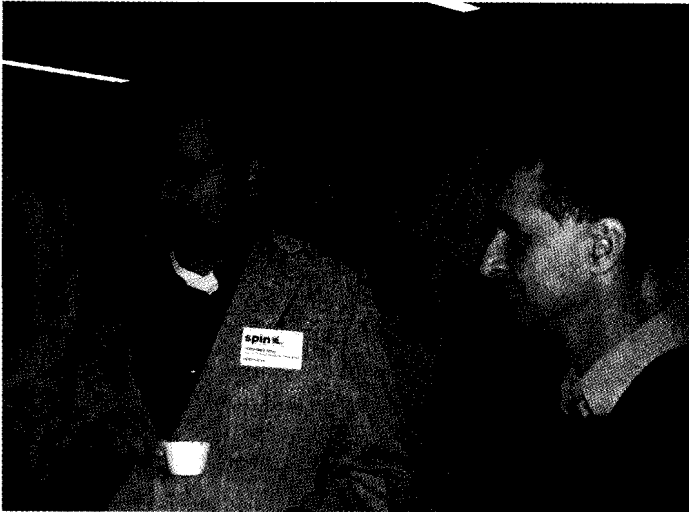
Zolin Leonid

JINR
Joliot Curie str, 6
141980 Dubna – Russian Federation
zolin@sunhe.jinr.ru

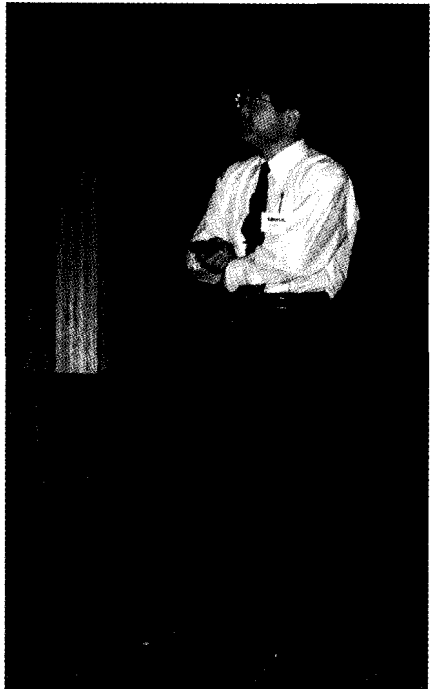
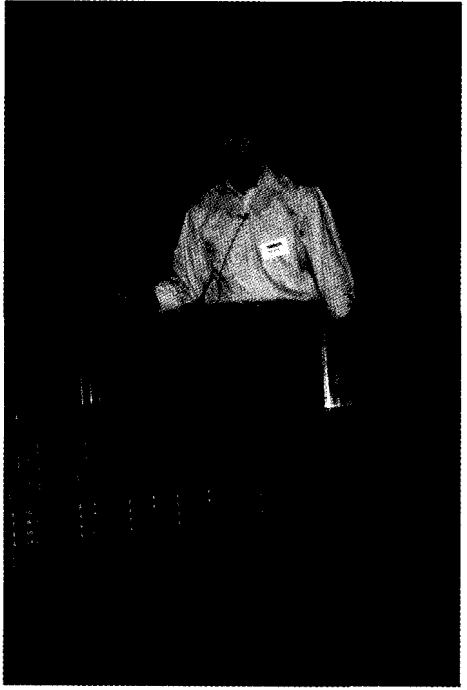
This page intentionally left blank



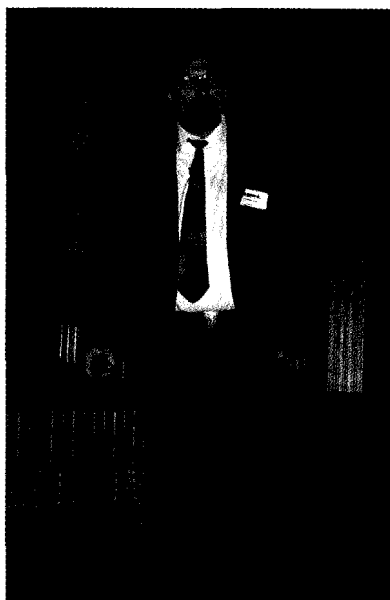
PHOTOS

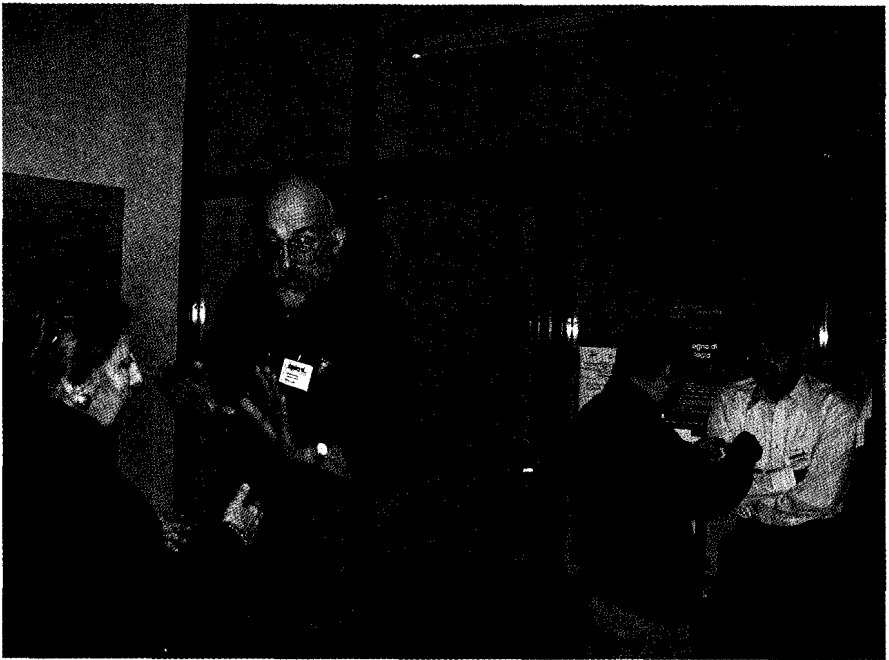
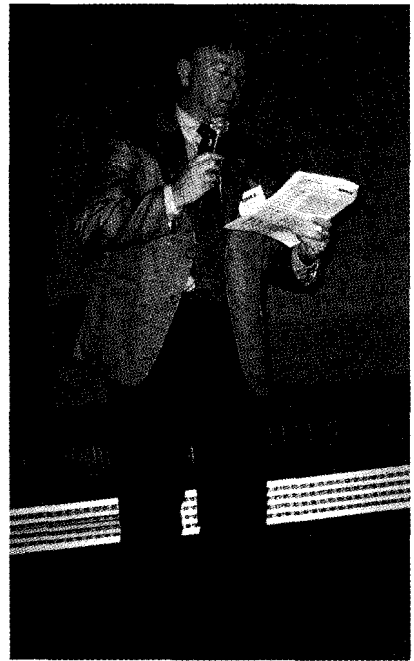
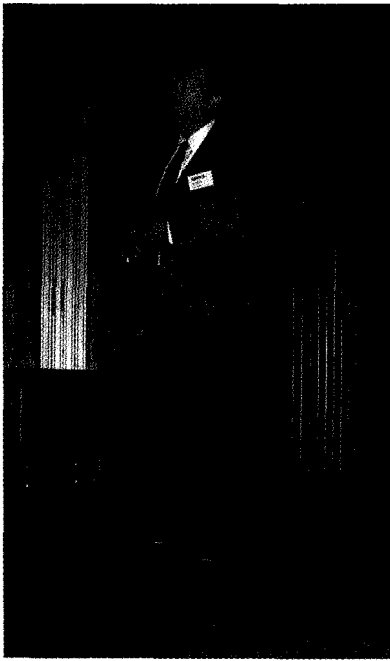


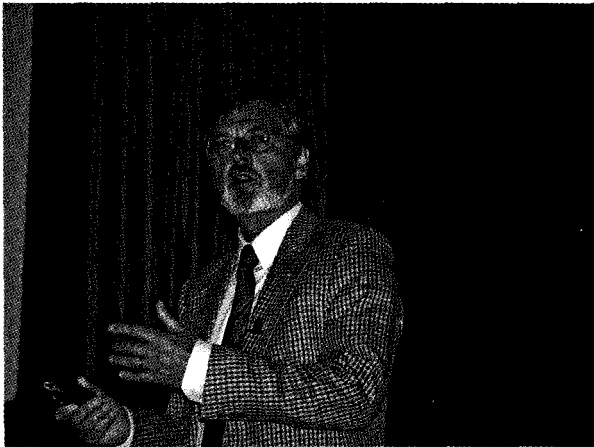
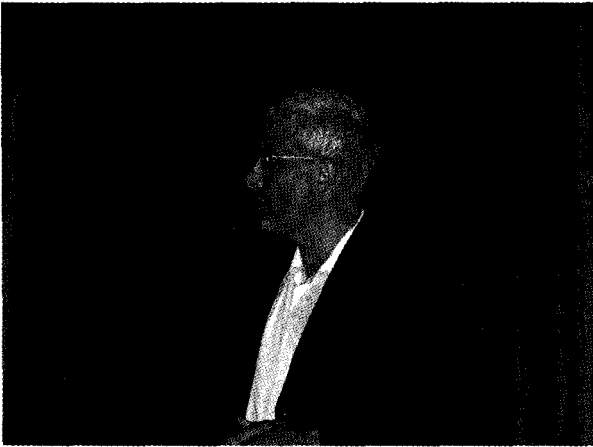


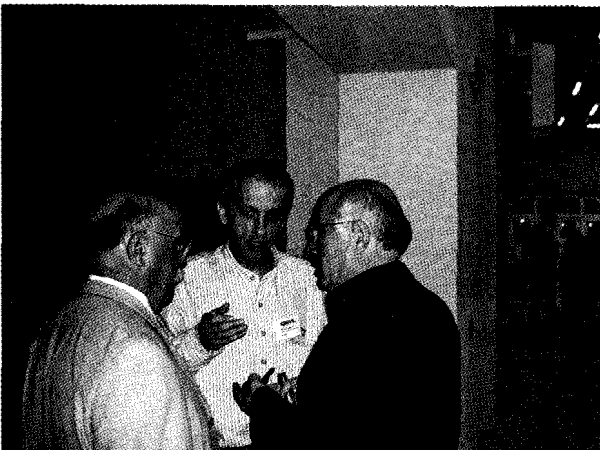
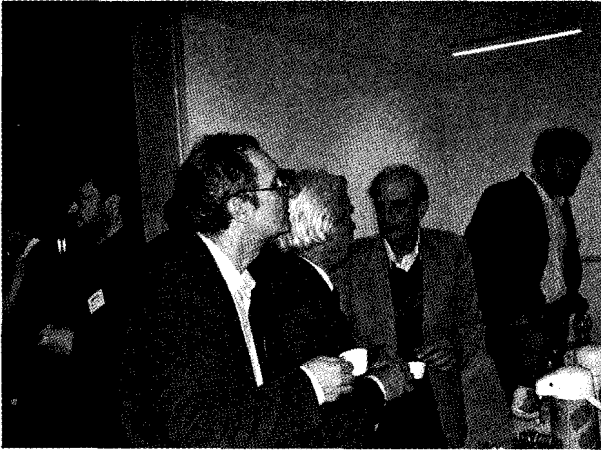


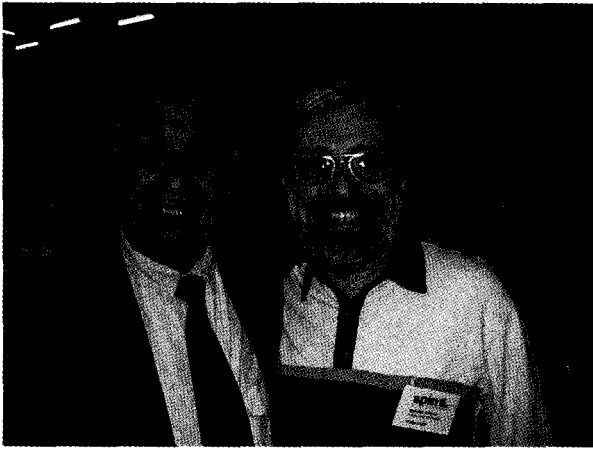


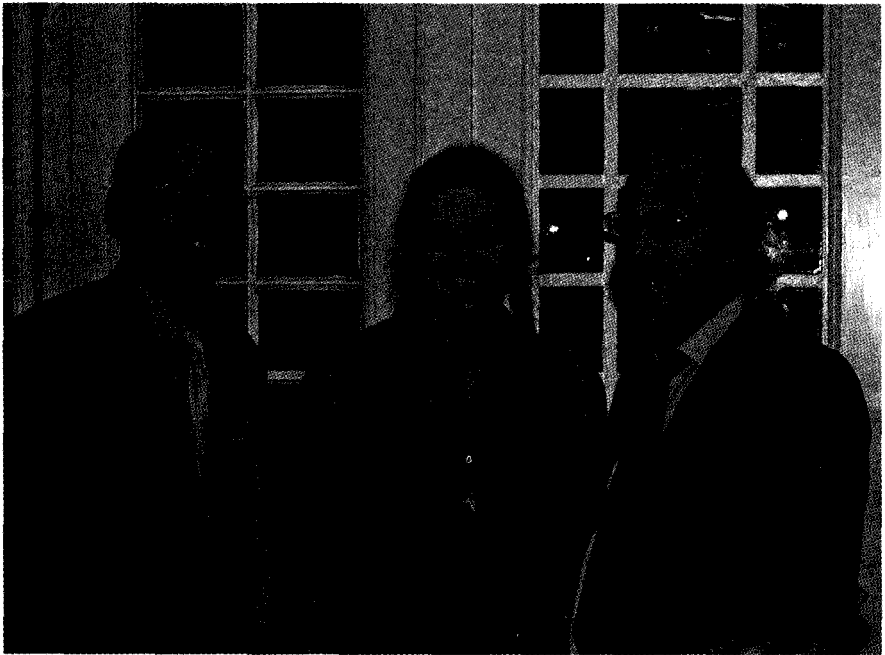
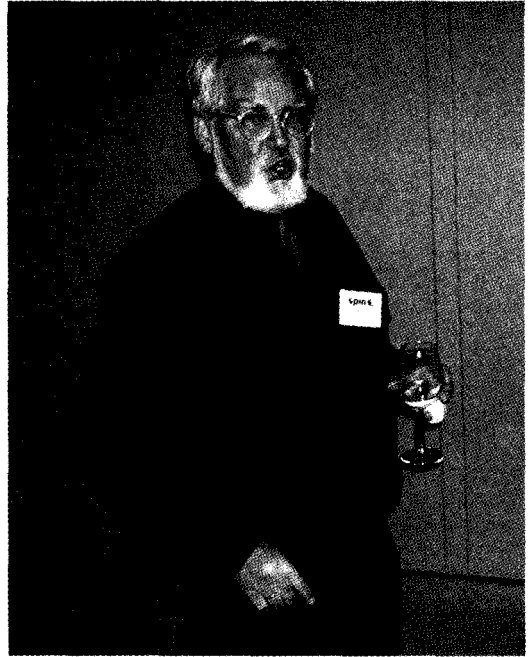
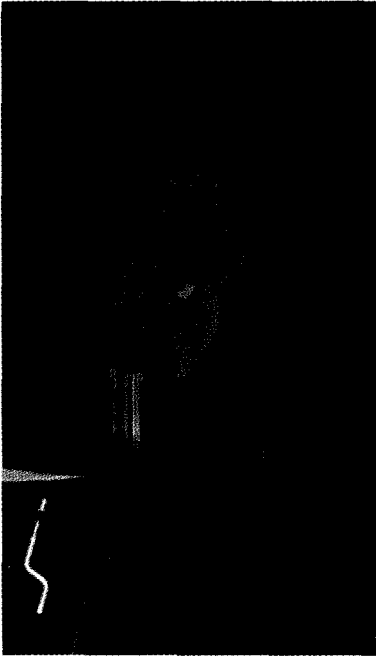


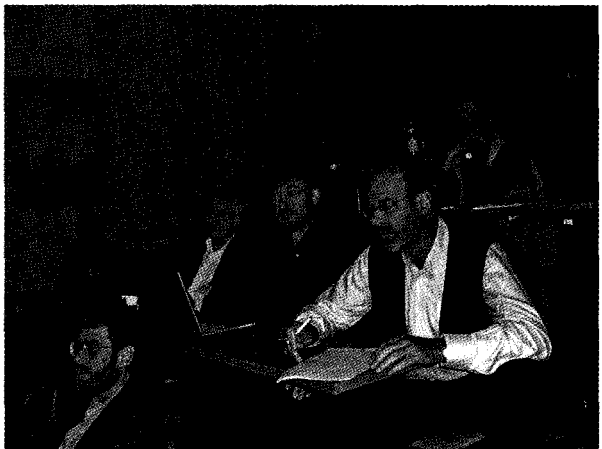
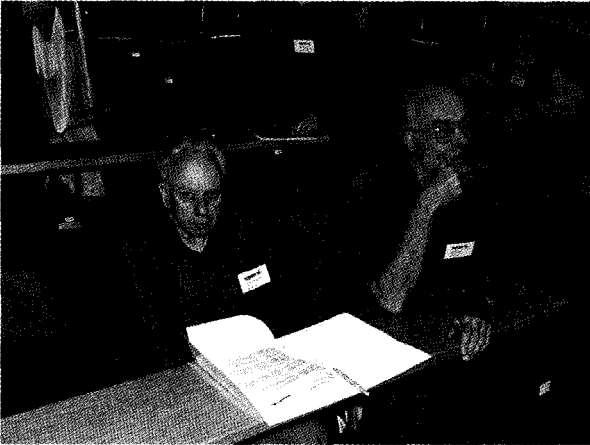


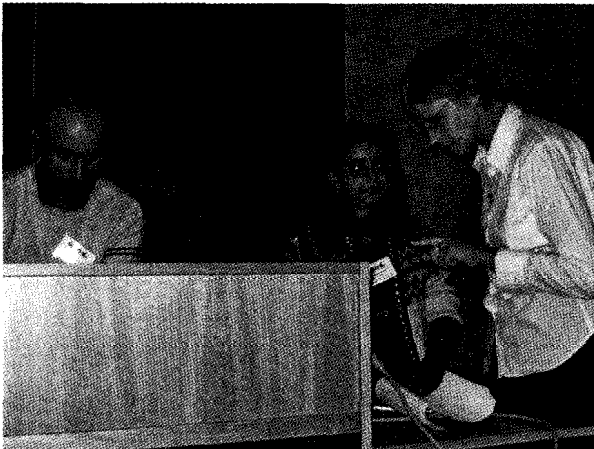
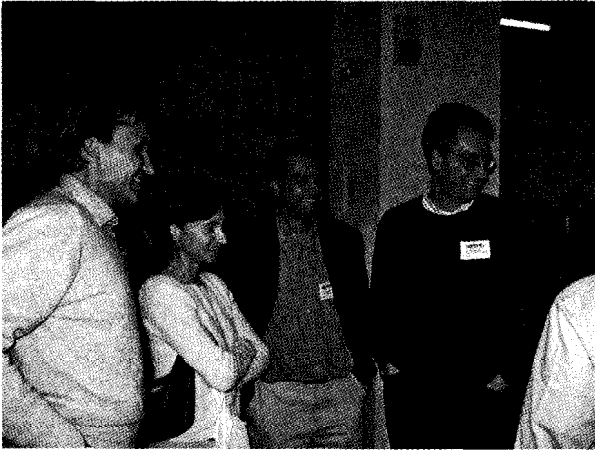


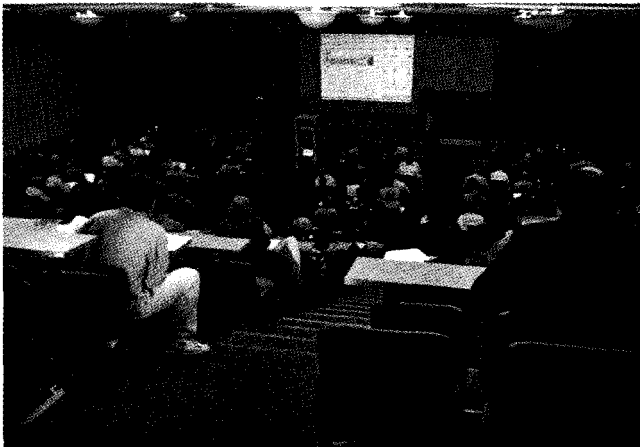
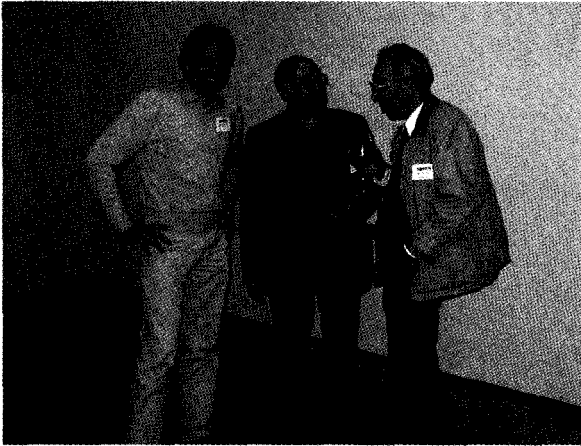


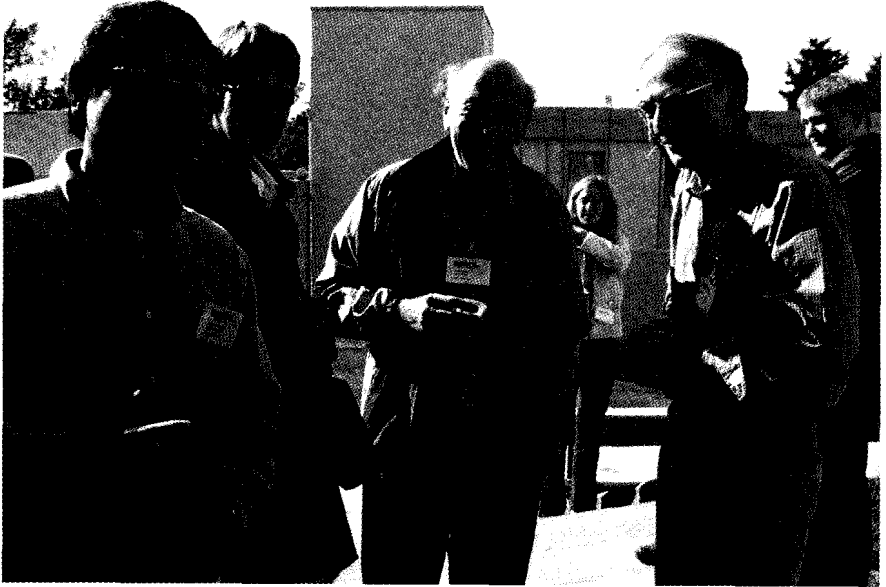
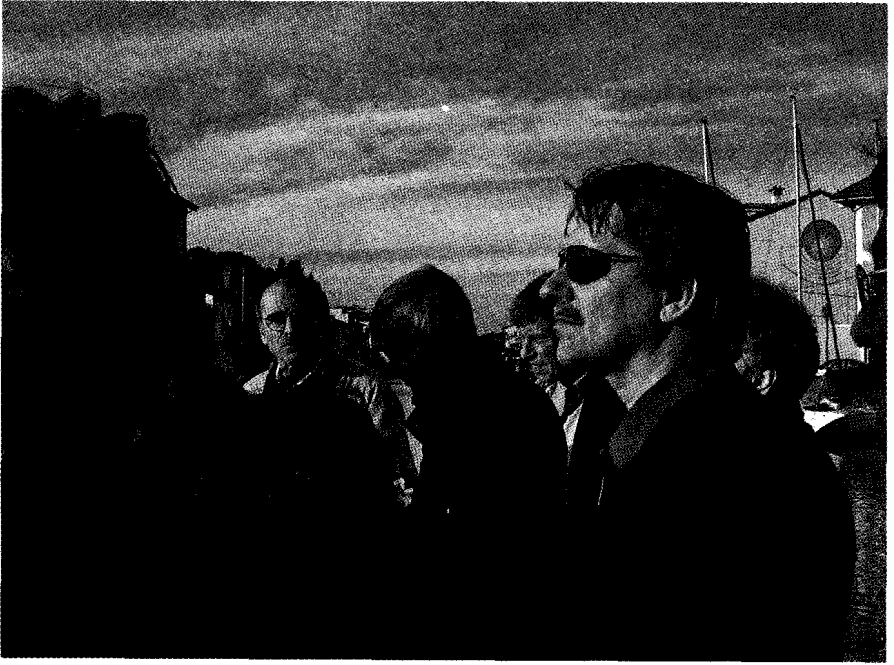




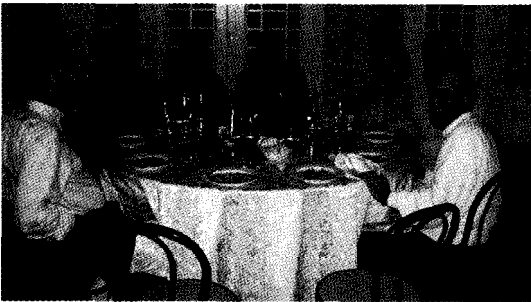
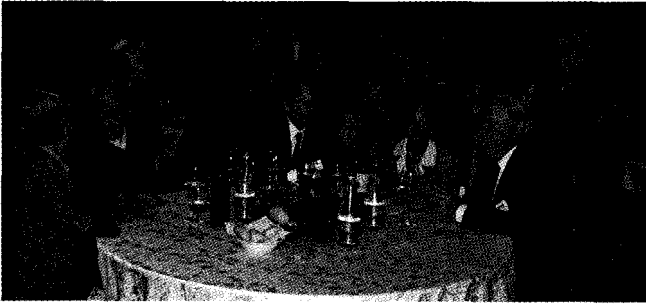










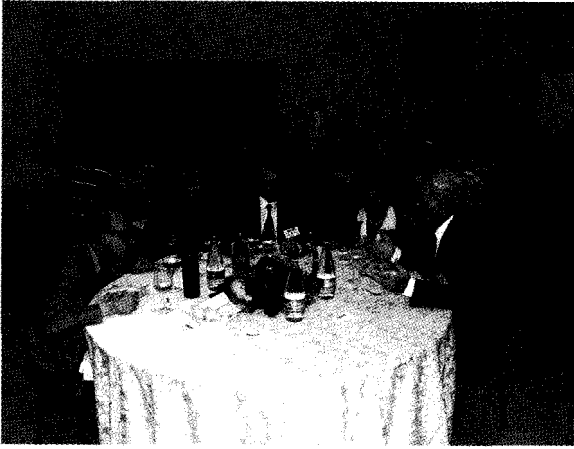










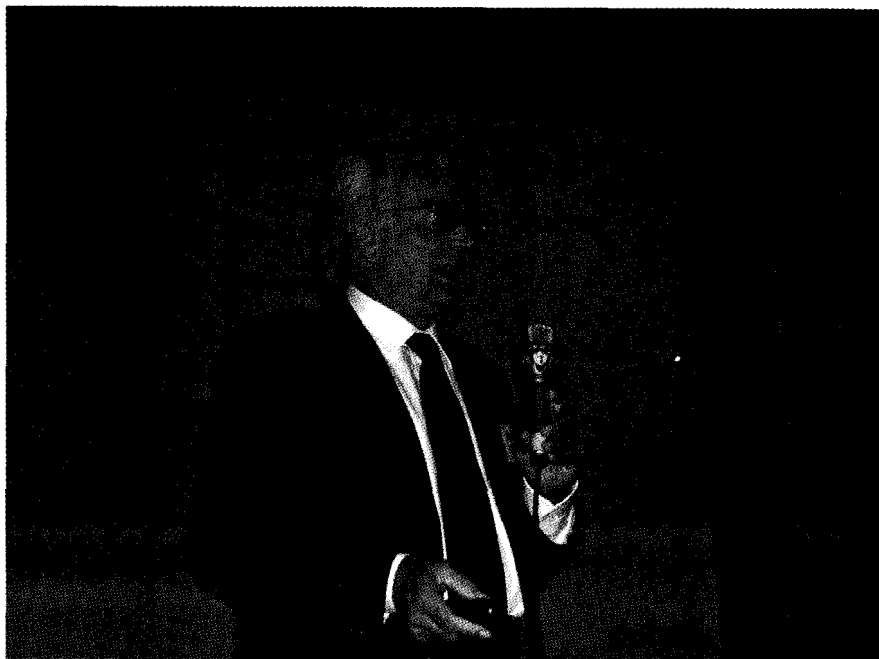












THE ABOVE SALAM BEEH

Ph.D. Andre Salim
Special thanks to my
organizers and sponsors
for making this possible

CPH gives opportunities to
fellow scientists from Africa and
other countries to experience
the full and the excitement of
world class research. Some
times the ONLY opportunity to
be a scientist at that level. Here
the tools and people to discuss
things!

A special personal thanks to the
SPINOSA Organizers for making
me to give this talk!



Novosibirsk Deuteron Collaboration

D.K. Toporkov, L.M. Barkov, V.F. Dmitriev, M.V. Dyug, A.V. Grigoriev, B.A. Lazarenko, S.I. Mishnev, I.A. Rachek, R.Sh. Sadykov, Yu.V. Shestakov, S.A. Zevakov

BINP, 630090 Novosibirsk, Russia

A.Yu. Loginov, A.V. Osipov, A.A. Sidorov, V.N. Stibunov

INP TPU, 634050 Tomsk, Russia

H. Arenhövel

IKP, JGU, D-55099 Mainz, Germany

S.L. Belostotsky, V.V. Nelyubin, V.V. Vikhrov

PINP, Gatchina 188350 St.Petersburg, Russia

R. Gilman

Rudgers University, Piscataway, NJ 08855, USA

R.J. Holt, D.H. Potterveld

Argonne National Laboratory, Argonne, IL 60439, USA

C.W. de Jager

TJNAF, Newport News, VA 23606, USA

E.R. Kinney

Colorado University, Boulder, CO 80309, USA

H. de Vries

NIKHEF, P.O.Box 41882, 1009 DB Amsterdam, The Netherlands

workshop on
polarized electron
sources and polarimeters

mainz, germany
october 7_9 2004

editor_
kurt aulenbacher
[mainz university]

This page intentionally left blank

PREFACE

The workshop 'Polarized Electron Sources and Polarimeters' (PESP) has been serving as a 'satellite' to the spin physics symposia for many years. PESP is usually located in an institution that is performing experiments with polarized electrons and which is reasonably close to the site of the main conference. This was the case for the preceding workshops at MIT-Bates, Nagoya and St. Petersburg which were corresponding to the SPIN symposia at Brookhaven, Osaka and Protvino. It is good practice that the workshop takes place just before the SPIN symposium.

Following this tradition the PESP-2004 workshop took place at the institute for nuclear physics at the Johannes-Gutenberg university in Mainz, Germany from 7-9 of October 2004. We hosted 34 participants from 16 institutions, 25 talks were presented in 8 sessions. A round table discussion was devoted to target main issues for polarized source construction at the next linear electron/positron collider. Several additional aspects were presented in a poster session.

The production and diagnostics of polarized electron beams requires research and development in a wide variety of fields. Consequently it is not surprising that talks addressed very different issues ranging, e.g., from the growth and characterization of semiconductor heterostructures to the operation of polarized electron sources at parity violation experiments with their extreme requirements towards beam stability and diagnostics.

We had lively and often exciting discussions throughout the workshop period. The organizers wish to take this opportunity to thank all our guests for their participation and contributions which have made PESP-2004 a productive workshop.

The workshop was supported by the Deutsche Forschungsgemeinschaft (DFG) and by the Johannes-Gutenberg Universität in Mainz. The support and encouragement we have received by the international committee for spin physics symposia is especially acknowledged.

The organizing committee

Gerhard Arz
Kurt Aulenbacher
Roman Barday
Roman Bolenz
Doris Jacob
Valeri Tioukine
Monika Weis

This page intentionally left blank

PESP 2004 Scientific Programm

Thursday October,7, 2004

8:30 - 9:00	Registration		
9:00 - 9:15	Opening address		
Session 1	Operation of polarized sources for accelerators: Chair: Y. Mamaev		
9:15 - 9:50	M. Poelker	JLAB	The Status of Gallium Arsenide Photoemission Guns at Jefferson Lab Operation of the MIT-Bates Polarized Source for A High Average Current Storage Ring Present status of 200keV Polarized Electron Gun at Nagoya University
9:50 - 10:25	M. Farkhondeh	MIT-Bates	
10:25 - 11:00	M. Yamamoto	Nagoya	
Session 2	Strained layer superlattices-1: Chair: G. Lampel		
11:15 - 11:50	L.G.Gerchikov	St. Petersburg	Maximal Spin Orientation in Electron Photoemission from Strained Semiconductor Superlattices High Performance Polarized Electron Photocathodes based on InGaAlAs/AlGaAs Superlattices Polarized electron emission from strained GaAs/GaAsP superlattice photocathodes
11:50 - 12:25	Y. Mamaev	St. Petersburg	
12:25 - 13:00	T. Maruyama	SLAC	
13:00 - 14:30	Lunch		
Session 3	Strained layer Superlattices-2/Innovative Polarimeters: Chair: M. Poelker		
14:30 - 14:55	K. Aulenbacher	Mainz	Time resolved depolarization measurements on superlattices with strained wells The Compton Backscattering Polarimeter of the A4-Experiment Ferromagnetic Thin Layers for Spin Polarimetry Highly-Polarized Electron Emission from Strain-compensated AlInGaAs-GaAsP Superlattices
14:55 - 15:20	Y. Imai	Mainz	
15:20 - 15:55	D. Lamine	Polytechnique	
15:55 - 16:30	L.G. Gerchikov	St. Petersburg	
16:50 - 18:00	Poster Session: Posters may be visited at: http://www.kph.uni-mainz.de/de/events/conferences/pep2004/		

Friday October, 8 2004

Session 4	Electron and laser beam parameters: Chair: Kurt Aulenbacher		
9:00 - 10:00	Round table discussion: Polarized lepton sources for future colliders		
10:00- 10:25	A. Brachmann	SLAC	Laser Development for Future Photocathode Research at SLAC Performance of the cold photocathode gun at the electron target of the Heidelberg TSR
10:25- 11:00	D. Orlov	MPI-Heidelberg	
Session 5	Material research for high lifetime photocathode: Chair: T. Maruyama		
11:20 - 11:45	J. Grames	JLAB	Lifetime Measurements using the Jefferson Lab Load-Lock Electron Gun Recent PES Photocathode R&D at Nagoya University Material Properties and Application Issues of Chalcopyrite Thin Films (*)
11:45 - 12:20	M. Kuwahara	Nagoya	
12:20 - 13:00	Th. Schedel-Niedrig	HMI-Berlin	
13:00 - 14:30	Lunch		
Session 6	Photocathode and beam quality characterization: Chair: A. Terekhov		
14:30 - 15:05	A. Terekhov	Novosibirsk	Quality characterization of NEA-photocathode for PES by means of photoemission from defect states Properties of field emission dark current from Molybdenum and Titanium electrodes The Mainz A4 Parity Violation Experiment: Single Spin Asymmetries in Elastic Scattering
15:05 - 15:40	M. Yamamoto	Nagoya	
15:40 - 16:15	F. Maas	Mainz	
16:30 - 18:00 18:00	Guided tour: MAMI-B/C-Accelerator and its experimental areas Conference dinner		

Saturday October, 9 2004

Session 7	Photocathode surface research: Chair: D. Orlov		
9:00 - 9:35	K. Aulenbacher	Mainz	Photocathode life time research at MAMI Cesium adsorption on GaAs(001) surface: adsorbates geometry and Sb influence Atomic Hydrogen Cleaning of Polarized GaAs Photocathodes
9:35 - 10:10	S.E.Kulkova	Tomsk	
10:10 - 10:45	T. Maruyama	SLAC	
Session 8	New challenges at new accelerators: The future of polarized e^+ / e^- -sources: Chair: K. Aulenbacher		
11:00 - 11:35	M. Farkhondeh	MIT-Bates	Polarized Electron Sources for Future Electron Ion Colliders Helical Undulator Based Production of Polarized Positrons and Status of the E166 Experiment Polarized Positron Generation Experiment at KEK (*)
11:35 - 12:10	K. Laihem	DESY-Zeuthen	
12:10 - 12:45	T. Omori	KEK	
12:45	End of Workshop		

(*) Contribution is not included in the proceedings.



This page intentionally left blank

PESP 2004 WORKSHOP AGENDA

Thursday October, 7 2004

8:30-9:00 *Registration*

9:00-9:15 Welcome address by the director of the nuclear physics institute,
Professor Thomas Walcher

SESSION 1 - Operation of polarized sources for accelerators

Chair: Y. Mamaev

- 9:15-9:50 M. Poelker The Status of Gallium Arsenide Photoemission
Guns at Jefferson Lab
- 9:50-10:25 M. Farkhondeh Operation of the MIT-Bates Polarized Source for
A High Average Current Storage Ring
- 10:25-11:00 M. Yamamoto Present status of 200keV Polarized Electron Gun
at Nagoya University

SESSION 2 - Strained layer superlattices-1

Chair: G. Lampel

- 11:15-11:50 L.G. Gerchikov Maximal Spin Orientation in Electron Photoemis-
sion from Strained Semiconductor Superlattices
- 11:50-12:25 Y. Mamaev High Performance Polarized Electron Photocath-
odes based on InGaAlAs/AlGaAs Superlattices
- 12:25-13:00 T. Maruyama Polarized electron
emission from strained GaAs/GaAsP superlattice
photocathodes

13:00-14:30 *Lunch*

SESSION 3 - Strained layer Superlattices-2/Innovative Polarimeters

Chair: M. Poelker

- 14:30-14:55 K. Aulenbacher Time resolved depolarization measurements on
superlattices with strained wells
- 14:55-15:20 Y. Imai The Compton Backscattering Polarimeter of the
A4-Experiment

15:20-15:55	D. Lamine	Ferromagnetic Thin Layers for Spin Polarimetry
15:55-16:30	L.G. Gerchikov	Highly-Polarized Electron Emission from Strain-compensated AlInGaAs-GaAsP Superlattices
16:50-18:00	Poster Session	

Friday October, 8 2004

9:00-10:00 Round table discussion: Polarized lepton sources for the next electron positron collider.

SESSION 4 - Electron and laser beam parameters

Chair: Kurt Aulenbacher

10:00-10:25	A. Brachmann	Laser Development for Future Photocathode Research at SLAC
10:25-11:00	D. Orlov	Performance of the cold photocathode gun at the electron target of the Heidelberg TSR

SESSION 5 - Material research for high lifetime photocathode

Chair: T. Maruyama

11:20-11:45	J. Grames	Lifetime Measurements using the Jefferson Lab Load-Lock Electron Gun
11:45-12:20	M. Kuwahara	Recent PES Photocathode R&D at Nagoya University
12:20-13:00	Th. Schedel-Niedrig	Material Properties and Application Issues of Chalcopyrite Thin Films

13:00-14:30 *Lunch*

SESSION 6 - Photocathode and beam quality characterization

Chair: M. Farkondeh

14:30-15:05	A. Terekhov	Quality characterization of NEA-photocathode for PES by means of photoemission from defect states
15:05-15:40	M. Yamamoto	Properties of field emission dark current from Molybdenum and Titanium electrodes
15:40-16:15	F. Maas	The Mainz A4 Parity Violation Experiment: Single Spin Asymmetries in Elastic Scattering
16:30-18:00	<i>Guided tour: MAMI-B/C-Accelerator and its experimental areas</i>	

Conference dinner

Saturday October, 9 2004

SESSION 7 - Photocathode surface research

Chair: D. Orlov

9:00-9:35	K. Aulenbacher	Photocathode life time research at MAMI
9:35-10:10	S.E.Kulkova	Cesium adsorption on GaAs(001) surface: adsorbates geometry and Sb influence
10:10-10:45	T. Maruyama	Atomic Hydrogen Cleaning of Polarized GaAs Photocathodes

SESSION 8 - New challenges at new accelerators: The future of polarized e^+e^- -sources

Chair: K. Aulenbacher

11:00-11:35	M. Farkhondeh	Polarized Electron Sources for Future Electron Ion Colliders
11:35-12:10	K. Laihem	Helical Undulator Based Production of Polarized Positrons and Status of the E166 Experiment
12:10-12:45	T. Omori	Polarized Positron Generation Experiment at KEK

End of Workshop

This page intentionally left blank

THE STATUS OF GALLIUM ARSENIDE PHOTOEMISSION GUNS AT JEFFERSON LAB

M. POELKER, P. ADDERLEY, M. BAYLAC, J. BRITTIAN, D. CHARLES, J. CLARK, J. GRAMES, J. HANSKNECHT, R. KAZIMI, M. STUTZMAN, K. SURLES-LAW

Thomas Jefferson National Accelerator Facility, Newport News, USA

Highlights of the polarized beam program at CEBAF at Jefferson Lab will be presented. These include successful completion of portions of parity violation experiments G0 Forward Angle and HAPPEX-II. Experience with commercial modelocked Ti-Sapphire lasers and high polarization strained-superlattice GaAs photocathodes will be discussed. Finally, gun charge lifetime measurements made over the course of many years following charge extraction of nearly 3000 C will be presented.

1. Parity Violation Experiments

The past year has seen the successful completion of scheduled portions of the parity violation experiments HAPPEX-II and G0 Forward Angle. These experiments were demanding from a polarized source perspective, requiring new lasers, new laser-table optical devices, new pockels cell alignment procedures, new injector beamline settings and new software tools to map and set the beam envelope through the machine [1]. Rigorous monitoring of beam properties was required throughout each experiment to maintain consistent and reliable results. For both experiments, the helicity-correlated beam asymmetries were maintained within acceptably small limits (see Table 1).

Table 1. Preliminary run-averaged helicity-correlated beam asymmetries for parity violation experiments recently conducted at CEBAF. Numbers may change slightly as data reduction continues. Error bars are forthcoming.

Experiment	Intensity	Position X	Position Y	Energy
G0 Forward Angle	0.14 ppm	3 +/- 4 nm	4 +/- 4 nm	10 ppb
HAPPEX-II He	0.4 ppm	3 nm	2 nm	2.6 ppb
HAPPEX-II H	0.2 ppm	2.2 nm	2.3 nm	2 ppb

The two experiments faced different challenges. The G0 Forward Angle experiment was lengthy, consisting of two preliminary stages of beam delivery (engineering and commissioning runs) followed by production running. Although production running was only

~8 weeks, the total calendar time for all stages of this experiment was over 12 months. The G0 Forward Angle experiment relied on time-of-flight detection which necessitated low duty factor beam at the bunch repetition rate of ~31 MHz, which is the sixteenth sub-harmonic of standard 499 MHz CW beam delivered to each experiment hall. Two styles of modelocked Ti-Sapphire lasers were constructed at Jefferson Lab to meet this beam specification however, both lasers proved inadequate. Each laser was ~5 m long, with numerous folding mirrors to provide a relatively small footprint. The first version used an intra-cavity acousto-optic modulator (AOM) to initiate modelocked operation. Unfortunately, optical pulses were too long (~300 ps) to provide adequate electron beam transmission through the CEBAF injector chopper with 111 ps acceptance. This was likely a result of difficulty obtaining a large depth of modulation (i.e., high absorbed rf power) within the AOM. The second version was seeded with light from a gain-switched diode laser with a pulse repetition rate of 31 MHz [2]. This laser produced 150 ps pulses but the output was contaminated with low-level light at multiples of 31 MHz. In addition, both homemade lasers were "free running", i.e., without active cavity length stabilization. As a result, the phase of the electron beam produced by these lasers would vary by small amounts over time, effecting transmission and beam orbit through the machine in subtle ways. These minor cavity length changes would probably have gone unnoticed by many experiments but they were problematic for a parity violation experiment, where it is extremely important that conditions remain constant. The third and final version of the G0 laser was purchased from commercial vendor Time-Bandwidth Products. This laser also had a ~5 m cavity length but modelocked operation was obtained using a saturable absorber mirror [3]. The laser proved to be very reliable with output power 300 mW and active cavity length stabilization to produce an optical pulse train with very low timing jitter. Options were purchased that allowed operation at two wavelength ranges centered at 780 nm and 845 nm and with four different optical pulsewidths between 10 and 70 ps.

The G0 Forward Angle experiment required only 40 μA , a modest value by CEBAF standards, however it proved to be a difficult matter to deliver this beam to the G0 target because bunch charge was much higher than usual. Transporting 40 μA at 31 MHz repetition rate was equivalent to delivering 640 μA at the normal pulse repetition rate of 499 MHz, in terms of equivalent bunch charge. Space charge induced emittance growth caused the G0 electron bunches to rapidly expand in space and time and it was impossible to deliver the requested beam current using injector settings that had been adequate for normal CEBAF operations. This is obvious in Figure 1, where 100 kV electron bunch length grows from ~100 ps at 0.5 μA to ~350 ps at 40 μA . The transverse beam profile also grew as a function of beam current and significant aberrations could be seen at high current. Eventually, injector settings were empirically determined that provided 40 μA beam to the endstation with ~80% transmission. The biggest adjustments were made to the laser spot size at the photocathode, solenoid focusing magnet settings and prebuncher amplitude.

High bunch charge and associated less-than-unity injector transmission created problems for parity-quality beam delivery during G0 Forward Angle. Helicity-correlated beam parameters - position, charge and energy - are coupled. For example, helicity-correlated po-

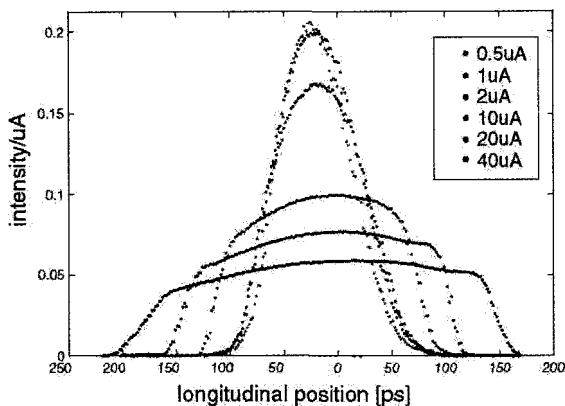


Fig 1. G0 electron bunchlength measured at 100 kV beam energy using the injector chopper. Individual pulse heights were scaled to provide equal area under each curve.

sition asymmetry at the photocathode creates helicity-correlated charge asymmetry downstream of apertures. And helicity-correlated charge asymmetry produces rf-beam loading at accelerating cavities which in turn produces helicity-correlated position and energy asymmetry at the target. Consequently, it was important to eliminate helicity-correlated asymmetries as early in the machine as possible, i.e., at the photocathode. The G0 collaboration used a rotating halfwave plate downstream of the pockels cell to obtain a “coarse minimum” of helicity-correlated position and charge asymmetry. Helicity-correlated charge asymmetry was further reduced by modulating laser power at the photocathode using a device referred to as the IA cell, which consists of a waveplate, a pockels cell driven at low voltage and a fixed linear polarizer. A pzt-driven mirror was used to actively minimize position asymmetry. Typical results are shown in Figure 2, where the plots indicate helicity-correlated beam parameters approach zero as the feedback algorithms take effect.

The HAPPEX-II collaboration hoped to conduct their experiment without using position feedback. To this end, they spent considerable time in advance of the experiment studying pockels cell behavior to develop a test regiment to identify cells with small birefringence gradient and an alignment procedure that placed the laser beam at the precise geometric center of the cell, a location that provides the smallest helicity-correlated laser beam steering [4]. The small helicity-correlated beam asymmetries identified in Table 1 suggests this work was worth the effort. The run-averaged position asymmetries were small and within specifications, without using active position feedback.

There were however, complications associated with HAPPEX-II, which consisted of measurements using two target materials, helium and hydrogen. The intended beam current for this experiment was $80 \mu\text{A}$ but radiation heating of the superconducting spectrometer magnets limited beam current to $\sim 40 \mu\text{A}$. This made it difficult to obtain reasonable statistical accuracy during the allotted time period for the experiment. To help overcome this shortcoming, strained-superlattice GaAs photocathode material from commercial vendor SVT Associates [5, 6] was installed in one of the CEBAF photoguns. This material pro-

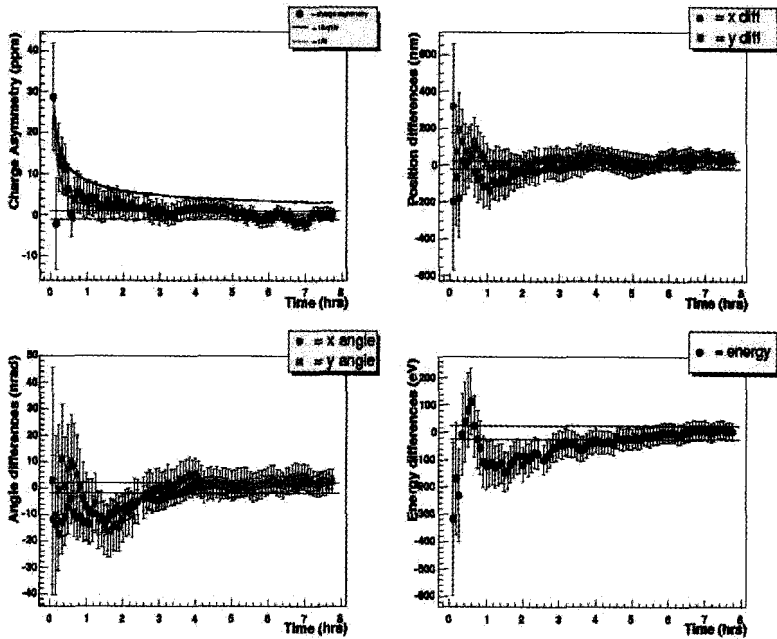


Fig. 2. Clockwise from top left; helicity correlated charge, position, energy and angle asymmetries as feedback algorithms take effect.

vided $\sim 86\%$ beam polarization, considerably higher than what is typically obtained from strained-layer GaAs (between 75 and 78%) and the highest value yet measured at CEBAF. Stable beam properties were observed while helium was studied and other halls were not requesting much beam. However, when the collaboration switched to hydrogen and a neighboring hall began to receive high current beam, it was discovered that photocathode lifetime was very poor. To maintain requested beam currents at all halls, the laser spot was moved to “fresh” photocathode locations daily. The rapidly decaying QE and slightly different beam orbits through the injector from each photocathode location created subtle variations in the injector transmission that made it difficult to obtain stable beam conditions on a parity-scale. As a result, the collaboration requested that measurements with the hydrogen target be completed using beam from the other gun, with lower polarization but longer operating lifetime. Figure 3 shows position asymmetry plotted versus run number for beam obtained from each of the CEBAF guns, first using strained-superlattice GaAs and then strained GaAs. Position asymmetries were stable and close to zero while operating from “gun2”, the gun with longer operating lifetime.

Both collaborations will return in 2005 and 2006 to complete additional portions of their experiments; HAPPEX will continue their experiment to obtain more accuracy and G0 will conduct backward scattering-angle measurements. The lessons learned during 2004 should make future efforts go smoothly. Other collaborations have taken note of recent success. As a result, it is likely more demanding parity violation experiments will receive approval

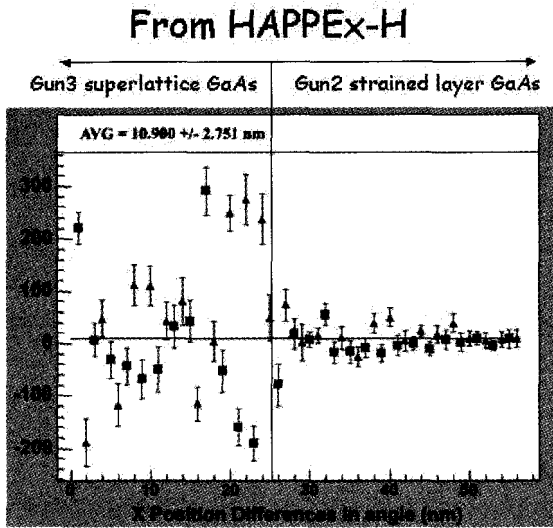


Fig 3. Helicity-correlated position asymmetry plotted versus run number for insertable halfwave plate IN and OUT (red boxes, blue triangles). Left side of plot for beam from strained superlattice GaAs and gun with poor lifetime, right side of plot for beam from strained GaAs and gun with long lifetime.

for beam time at CEBAF, for example Qweak and Lead Parity.

2. Gun Charge Lifetime

On a note unrelated to parity violation experiments, a dedicated effort has been made to accurately monitor the charge lifetime of each gun at the CEBAF injector over the past four years, with nearly 3000 C extracted from the guns. Photocathode QE is measured at least daily and plotted as a function of extracted charge. An exponential fit is applied to the data and charge lifetime is defined as the amount of charge that can be extracted from the photocathode before QE falls to $1/e$ of the initial value. The results for measurements obtained with both guns using the Hall C laser are shown in Figure 4. There is considerable scatter to the data, likely due to the fact that conditions were not constant during this long period of time. For example, gun, photocathode material, laser wavelength and laser spot size at the photocathode were often changed to best suit the needs of the experiment program. Despite this lack of control of important experimental variables, there are sections of the plot that reveal interesting trends. During 2003, “gun2” charge lifetime was observed to steadily decrease from ~ 250 C to < 100 C. To address this problem the non-evaporable getter pumps were replaced and the gun re-baked. The charge lifetime steadily increased throughout 2004, achieving a value exceeding 500 C, suggesting new NEG pumps and subsequent vacuum recovery following the bakeout had significantly improved the vacuum within the gun. This observation suggests NEG pumps have a limited lifetime, at least under CEBAF operating conditions, i.e., relatively high average current with guns vented and re-baked frequently compared to load-locked guns.

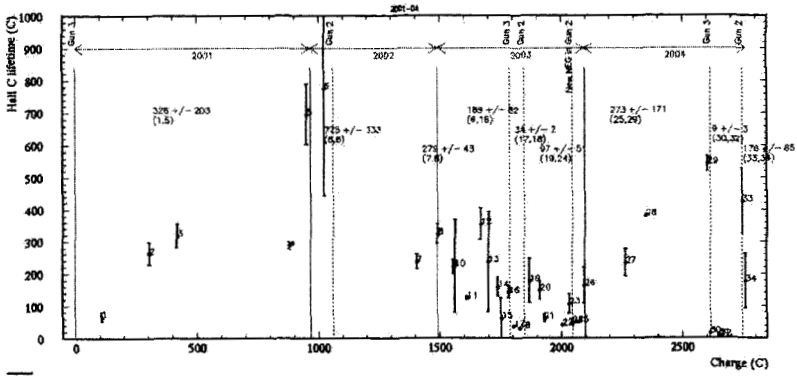


Fig 4. Gun charge lifetime measured over four years with nearly 3000 C extracted charge. The period of time between 2003 and 2004 is of interest and is described in the text.

Acknowledgments

This work was supported by the U.S. DOE Contract No. DE-AC05-84-ER40150.

References

1. Separate contributions by R. Kazimi *et al.* and Y. Chao *et al.*, *Proceedings of the 2004 European Particle Accelerator Conference*, July 5-9, 2004, Lucerne, Switzerland.
2. C. Hovater and M. Poelker, *Nucl. Instrum. and Meth.* **A418**, 280-4 (1998).
3. View many articles referenced at the vendor's web page; <http://www.tbwp.com>.
4. K. Paschke *et al.*, *Proceedings of SPIN 2004*, Trieste, Italy, Oct 10-16, 2004.
5. T. Maruyama *et al.*, SLAC-PUB-10331 (Feb 2004), submitted to *Appl. Phys. Lett.*, J.E. Clendenin, proceedings to the *10th Workshop on Polarized Sources and Targets*, Novosibirsk, Russia, 22-26 Sep 2003.
6. SVT Associates, Inc., <http://www.svta.com>.

OPERATION OF THE MIT-BATES POLARIZED SOURCE FOR A HIGH AVERAGE CURRENT STORAGE RING*

M. FARKHONDEH, W. FRANKLIN, E. TSENTALOVICH, T. ZWART, E. IHLOFF

MIT-Bates Linear Accelerator Center, Middleton, USA

For the past few years, the MIT polarized injector has been delivering highly polarized beams to the South Hall Ring for nuclear physics experiments with the BLAST spectrometer and an internal target fed by a polarized atomic beam source. Photoemission is produced from a high gradient-doped GaAsP photocathode with peak polarization of about 70% at 810 nm, which matches the radiation wavelength of a fiber-coupled diode array laser system. Pulses with $2\mu\text{s}$ width and 4 mA peak intensity are fed to the linac at 10–20 Hz and stored in the ring to reach beam currents up to 200 mA. Source operation lifetimes of many months between activations are achieved with occasional cesiation. A Siberian Snake system maintains a longitudinal polarization in the internal target area, and a high degree of beam polarization is carefully maintained with continuous monitoring of the betatron tune and a Compton backscattering polarimeter. Operational features of the source and the ring storage mode for the BLAST experiment will be presented.

1. Introduction

The MIT-Bates accelerator complex has been utilized for the past few years to inject high polarization beams into the South Hall Ring (SHR) for nuclear physics experiments. The experiments utilize the Bates Large Acceptance Spectrometer (BLAST), a polarized internal target based on an atomic beam source of hydrogen or deuterium, and stored polarized electron beams of up to 200 mA. DC pulses of $2\mu\text{s}$ width and 4 mA peak from the polarized source are injected at 10–20 Hz into the accelerator, chopped and bunched to the 2856 MHz frequency of the accelerating structure, accelerated to 850 MeV in the linac-recirculator complex, and injected into the storage ring.

The storage mode of operation of the accelerator and SHR complex and the ring stacking capability reduce both the peak and average current requirements from the polarized source. This mode of operation for the polarized source system is considerably less demanding than the long pulse, high average current mode of operation used in fixed target experiments. It is also far less demanding than the extraction mode of operation of the SHR that requires both high peak current and high repetition rate injections. Injected pulses of 2 mA peak at 10–20 Hz are stacked in the ring for 20–30 seconds to provide circulating

*This work is supported by the department of energy under a cooperative agreement # bef0294er40818.

average currents of 200 mA. The stored beam circulates in the ring for 10–15 minutes and passes through the storage cell every turn. When the stored current falls below an optimum value, the beam is dumped and a new fill begins. The accelerator and the polarized source are idle while the beam is stored in the ring, with a macroscopic duty cycle of order 10^{-5} and a negligible average current from the photocathode. This low average current in the source results in a long lifetime for the photocathode. In this paper, we describe the MIT polarized source including the laser system and the high polarization photocathode. We briefly present operation of the source for the BLAST experiment and SHR, and present and discuss the measured beam polarization in the ring using a laser backscattering Compton polarimeter. Finally, the future plans for the MIT-Bates accelerator center and the polarized source are briefly presented.

2. Polarized Source for Storage Mode

The MIT polarized source uses a high-gradient-doped $GaAs_{0.95}P_{0.05}$ photocathode [1] with peak polarization at 810 nm. With 5% phosphate concentration, the peak of polarization is shifted to 810 nm matching the wavelength of our high power diode laser system [2]. The top 10 nm layer of this sample is GaAs and is heavily zinc doped (5×10^{19}) to minimize the surface charge limit effect often present in strained samples at high laser power densities. However, diffusion of zinc during heat cleaning at 600° C will cause a depletion of the dopant concentration in the top layer causing a surface charge limit effect. The heat cleaning for these photocathodes is therefore limited to below 575° C for 10 minutes intervals.

The BLAST experiments require average circulating currents of 80 mA with an operational time between each fill of order 15 minutes. Because the damping time is about 100 milliseconds for SHR at 850 MeV, pulse trains with peak currents of 2 mA from the accelerator complex are injected into the ring at 10–20 Hz for 20–30 seconds. A typical accelerator-to-ring capture efficiency of order 10–20 % is achieved during each fill. The capture efficiency of the accelerator for the source was increased in 2003 from a nominal 33% to about 50–60% by adding a “pre-prebuncher” cavity a few meters upstream of the pre-buncher, but downstream of the polarized injector immediately following the 300 kV acceleration column. This is a 2856 MHz pillbox cavity designed using the SUPERFISH and PARMELA groups of codes for rf and beam dynamics simulations. As a result, the peak current requirement from the source was reduced by about a factor of two, thus increasing the operational lifetime of the photocathode.

The MIT-Bates polarized source has three identical gun assembly systems which can be certified for performance before installation on the main injector. At any time, there will be at least one fully certified photocathode stored as a backup for the main injector. A 60 keV test beam setup with a Mott polarimeter decoupled from the accelerator complex is used for the photocathode certification. A manual gate valve isolates the UHV gun chamber and the photocathode from the atmosphere. A baked gun with an activated photocathode is first installed on the test beam setup, then a small transition section of the beam line downstream of the valve is evacuated and baked to 200° C. Using the valve, the gun is opened to the beamline, the beam polarization and the photocathode quantum efficiency are measured,

and the high voltage performance is characterized. With the valve closed, the assembly is removed and stored for later use.

A multimode fiber-coupled diode array laser system [2] capable of producing peak power up to 150 W (unpolarized) at $\lambda = 810 \pm 3$ nm is used on the main injector. A similar system is also used on the test beam setup. The large 200 mm-mrad emittance of this laser precluded use of the 20-m long transport line utilized in the past for the Ti:Sapphire laser system. A wide-aperture 4-m long laser transport system matching the emittance of the diode laser system was designed and installed in 2002. The output end of the fiber bundle and the associated optics transport system was installed on an optical board aligned at a 53° inclined angle to aim the radiation onto a viewport on the gun chamber with a direct line of sight to the photocathode. The transport line also includes 3-inch aperture focusing lenses, a polarizer, a quarterwave plate and a remotely removable halfwave plate for helicity control of the light. The intensity of the unpolarized laser is reduced by a factor of two after passing through the polarizer. The intensity of the circularly polarized light at the photocathode is about 60 W maximum. With the 37° incident angle, the refracted angle at the surface of the GaAs based material is about 8° to the vertical due to a large index of refraction of GaAs ($n \approx 4.5$), resulting in an almost negligible drop of polarization.

In the storage mode, the photoemission from the source occurs every 15 minutes for a 20–30 second duration to fill the ring. With 60 W of polarized laser at 810 nm and the high-gradient-doped GaAsP photocathode, the source produces 4 mA peak for months before a heat cleaning and activation is needed. However, more frequent cesiation is needed every few weeks to few days depending on the elapsed time from the activation cycle. The present gun was installed in January of 2004 and is still in use with a total of three activations so far. The latest heat cleaning for this photocathode consisted of a rapid temperature increase to 570° C, 10–15 minutes at 570° C and a fast cooldown.

The surface charge limit effect was negligible on the present photocathode when the gun was first installed. After a few months, the effect became more prominent, although it is partially removed with each heat cleaning. The existing polarized source and the photocathode lifetime is more than sufficient for the requirements of the storage mode operation. However, the surface charge limit effects and the necessary periodic but infrequent cesiation indicate that a) the zinc dopant on the surface may be depleting with each heat cleaning, b) the photocathode surface pollutant is not completely removed with each heat cleaning, and c) the UHV condition in the gun chamber may need further improvement.

3. Operation of Polarized Beam for BLAST

The beam operation for the BLAST experiments requires a synchronization of a series of beam and detector actions. Each fill cycle is as follows: The BLAST detector high voltages are lowered to a standby value, a set of beam scraping slits in the ring are moved out, several viewing targets are placed in the path of the beam and the stored beam is dumped on these targets. The source is turned on and the state of the half-wave plate in the source laser path is reversed from its previous state. The refilling of the ring begins with photoemission from the source, injection into the ring stacking to 200 mA, the slits are moved into a

predetermined position to optimize background and the detector high voltages are ramped up to the operation values. Finally, the data acquisition is resumed again. This automated process takes about 1.5 minutes for each 15 minute data-taking period and is optimized for maximum beam delivery to the experiment. The source and the accelerator remain idle during the data-taking interval. The EPICS control system is utilized for these repetitive tasks. The daily integrated charge delivered to the BLAST experiments is averaging 10 kilocoulombs.

4. Beam Polarization in the Ring

The helicity of the stored beam is determined by the state of the half-wave plate in the polarized injector laser optics. This state remains the same during each fill and alternate from fill to fill. The Wien filter in the polarized source is set to inject a longitudinally polarized beam in the internal target region of the ring. A Siberian Snake system consisting of a pair of superconducting solenoids is used to preserve this longitudinal polarization in the internal target region. There are many spin depolarization resonances in the ring that must be carefully avoided. A map of the betatron tune shift in x-y plane was created, a region free of resonances was selected and the optics of the ring was set for that region and constantly monitored. The beam polarization is constantly monitored with a laser backscattering Compton polarimeter [3]. A 6% relative statistical accuracy in beam polarization is achieved during each standard 15 minutes running period. It was determined that the betatron tune shift in the vertical direction must remain within a tight window to keep the entire beam away from nearby depolarization resonances, thus keeping the beam polarization maximized. The betatron tune shift is measured for each fill before the beam is dumped. Figure 1 shows the measured beam polarization in the ring for a period of 3 months in 2004. The polarization for this photocathode was measured during the certification process by a Mott polarimeter on the 60 keV test setup and the result was $P=68 \pm 2$ (stat) $\pm 2\%$ (sys). The systematic error originates from the uncertainty in the Sherman function.

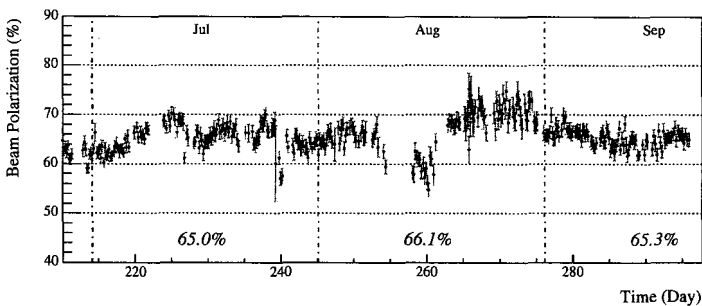


Fig 1. Preliminary beam polarization measured in the ring with a Compton polarimeter for a three month period in 2004.

5. Future Polarized Source Activities at Bates

The nuclear physics user program funded by US Department of Energy (DOE) at the Bates Linear Accelerator Center will come to an end in 2005 and the center will transition to new directions. There are two major initiatives envisioned for the MIT-Bates center beyond 2005. These include

- (1) *Research and Engineering Laboratory (R&E laboratory)*
- (2) *Center for Accelerator Science and Technology (CAST)*

The R&E Laboratory will consist of a total of fifteen personnel including physicists, engineers and technicians to support the nuclear physics research activities of the MIT faculty in the Laboratory for Nuclear Science. The polarized source R&D will remain part of this laboratory. CAST is an initiative under consideration at MIT to establish an inter-departmental center for education and R&D in accelerator science and technology. It is proposed to use the Bates accelerator-ring complex and the polarized source for R&D and student training for CAST. The R&E laboratory activities will begin in 2005. The CAST proposal has strong support at MIT and is being submitted to DOE for funding beginning in 2006. Polarized source R&D will continue at Bates under R&E, and CAST if the initiative is funded. It is envisioned that the initial polarized source R&D at Bates will have two major components. The first component is a collaboration with the Jefferson Laboratory Polarized Injector Group to enable the CEBAF main injector to use a load lock system that can accept photocathodes that are fully tested and certified on the test setup without exposure to atmosphere. The second activity will be in the area of polarized source development for eRHIC [4], a future Electron Ion Collider based on the RHIC ion beam at BNL. The polarized source group at MIT-Bates played a major role in developing the design of the electron beam for eRHIC initiative.

References

1. Bandwidth Semiconductor Inc., Bedford, NH.
2. Spectra-Physics, Opto Power diode laser model OPC-DO60-mmm-FC.
3. W. Franklin, *et al.*, "The MIT-Bates Compton Polarimeter for the South Hall Ring", these proceedings.
4. Zero Design Report (ZDR), http://www.agrhichome.bnl.gov/eRHIC/eRHIC_ZDR/ZDR_start.pdf

PRESENT STATUS OF 200 KEV POLARIZED ELECTRON GUN AT NAGOYA UNIVERSITY

M. YAMAMOTO, N. YAMAMOTO, T. NAKANISHI, S. OKUMI, F. FURUTA, M. MIYAMOTO,
M. KUWAHARA, K. NANIWA, K. YASUI

Nagoya University, Dept. of Physics, Nagoya, Japan

M. KURIKI, H. MATSUMOTO, M. YOSHIOKA

KEK High Energy Accelerator Research Organization, Tsukuba, Japan

A proto-type of 200 keV electron gun for a future linear collider has been constructed at Nagoya University. The degradation of a negative electron affinity (NEA) surface of a GaAs photocathode is known as a major problem for such a high field gradient gun, since the gun is required to produce the high intensity and low emittance beam. In order to improve the NEA lifetime (~ 40 h) for the initial gun operation, the vacuum pumping speed was reinforced by using non-evaporable getter (NEG) modules. As a preliminary result, the total pressure was improved to 5.7×10^{-10} Pa and the lifetime was extended to ~ 150 hours. A relation between the NEA lifetime and the partial pressures of CO_2 and H_2O was evaluated by assuming a simple model for a mechanism of NEA degradation. An emittance measurement system based on a pepper pot method was also build and a preliminary measurement has been started.

1. Introduction

A 200keV polarized electron source (PES) has been constructed at Nagoya University for applications for a future linear collider [1]. As well known, the design of ILC injector of the polarized electron gun requires the beam with high intensity (≥ 4.5 nC/bunch), multi-bunch structure (~ 2 ns bunch width, 337 ns separation) and low emittance ($\leq 8\pi mm \cdot mrad$) at gun exit [2]. In such applications, the negative electron affinity (NEA) surface makes an indispensable role to extract polarized electrons in conduction band minimum into vacuum. The high polarization ($P \sim 90\%$) and high quantum efficiency ($QE \sim 0.5\%$) were achieved by using the GaAs-GaAsP superlattice photocathode developed at Nagoya University [3].

The NEA surface is realized by a mono-layer of electric dipole moment of Ga(-)-Cs(+) formed by the Cs deposition to the GaAs surface. These electric dipoles easily destroyed by various disturbance [4, 5], and thus NEA surface has a serious lifetime problem. Three major mechanism are considered to degrade the NEA surface,

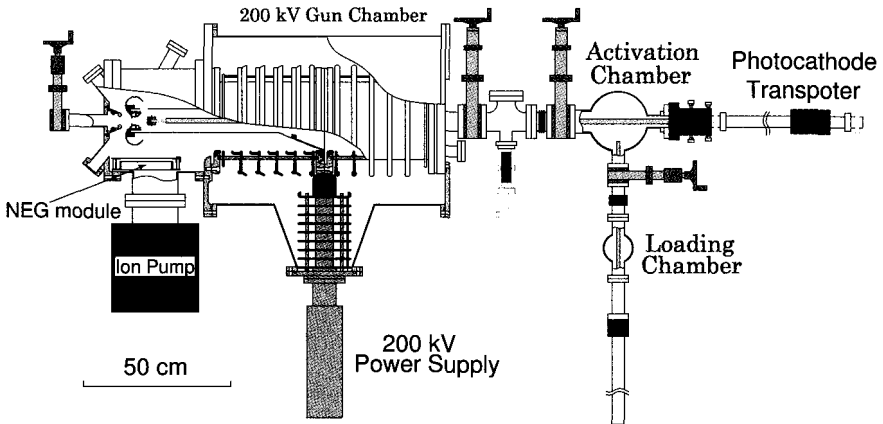


Fig 1. Schematic view of the 200 keV polarized electron source

- (1) Adsorption of residual gas molecules. Especially, CO_2 and H_2O give bad influences on the NEA surface.
- (2) Desorption of additional gas molecules from high voltage electrode due to the dark currents.
- (3) Positive ion back-bombardment to the NEA surface. They are produced by collisions of the beam itself with residual molecules.

In order to reduce these effects of (2) and (3), the dark current must be suppressed below 10 nA level. On the other hand, the higher field gradient on the NEA surface is required to prevent the divergence of a beam due to space charge effect. Therefore, the choice of materials and fabrication procedure for making the high voltage electrode become more important.

Concerning of the vacuum system, it is indispensable to create a ultra high vacuum (UHV) condition. In particular, the fraction of harmful residual molecules must be reduced to relax the influences of (1) and (3) effect.

2. Mechanical Structure of 200 keV Gun

The structure of the 200 keV gun is shown in Fig. 1. The gun consists of three chambers which are isolated by gate valves. The photocathode is transferred between these chambers by two magnetic manipulators. The loading chamber introduces the photocathode into the UHV chamber, and makes the surface cleaning by atomic hydrogen. Then the photocathode is transferred to activation chamber and further cleaned by the RF heating method. Finally, the NEA activation is made by deposition of Cs and O_2 or NF_3 and the photocathode is transferred to the gun chamber.

High voltage of -200 kV is applied to a center of double ceramic insulators, to which the cathode supporting tube is also fixed. In order to suppress the leakage currents along

the ceramic surface and the corona discharge to ground, dry nitrogen is fulfilled into an insulation gas tank with a pressure above 3.6 atm.

The high quality UHV is indispensable for the long lifetime of NEA surface. The original pumping system of the gun chamber was designed to have a 360 l/s ion pump and an 850 l/s non-evaporable getter (NEG) pump. The total pressure and partial pressures of residual gas were monitored by an extractor gage (IE514; Leybolt) and a residual gas analyzer (TH200; Leybold), respectively. After baking of the gun chamber at 200 °C for a week, the base pressure fell down to 3.2×10^{-9} Pa and partial pressures of H_2O and CO_2 were 1.1×10^{-10} Pa and 2.3×10^{-10} Pa, respectively.

Under this UHV condition, the lifetime was rather short of ~ 40 hours, in either case of the CW beam operation (200keV, ~ 100 nA), or the intermittent beam supply (5keV, ~ 100 nA) for QE measurement which is so called as dark lifetime measurement. These data suggested that the QE lifetime was limited by degradation of the NEA surface due to adsorption of harmful residual gases. Thus the following improvements were employed to achieve the extra-high-vacuum ($\leq 10^{-10}$ Pa).

- (1) Gate valves used in the gun chamber were replaced from viton-seal to metal-seal for high temperature baking (≥ 200 °C).
- (2) Additional NEG pumping modules were installed to reinforce the pumping speed as shown in Table 1. and Fig. 2.

3. NEA Lifetime Improvement

3.1. Vacuum System

The total pumping speed was reinforced up to 4650 l/s using eight NEG pump modules (WP950 \times 8; Saes Getters) that were installed surrounding the photocathode. They are fixed to a frame as shown in Fig. 2. The design value of activation temperature was ~ 450 °C with 35 A supplied current for each module. The mesh of stainless steel is used to cover inner side of the frame for masking the NEG modules from the high voltage electrode. The NEG module system was electrically insulated from ground so that the amount of dark current emitted from the cathode electrode to the mesh could be monitored.

3.2. Preliminary Results of UHV and Dark Lifetime Measurements

The results of preliminary UHV test are as follows. The baking of the gun chamber including various parts was done at 200 °C for 100 hours. The heating temperature of NEG modules was as same as the baking temperature of 200 °C, due to a trivial accident of current supply circuit. In spite of this incomplete activation of the NEG modules, the base pressure was improved from 3.2×10^{-9} Pa to 5.7×10^{-10} Pa. The partial pressures of harmful gasses were also reduced to 2.6×10^{-11} Pa for H_2O and 5.1×10^{-11} Pa for CO_2 , respectively. They are summarized in Table 2.

A preliminary dark lifetime measurement was done using a He-Ne laser ($\lambda = 633$ nm) at a bias voltage of -5 kV under the same UHV condition. The QE decrease as a function of time is shown in Fig.3. The dark lifetime was improved from 40 hours to 150 hours, and

	NEG pump	Ion pump	total
Before	850 l/s	360 l/s	1210 l/s
After	4290 l/s	360 l/s	4650 l/s

Table 1. Increase of the pumping speed of the gun chamber.

	Before	After
B. P.	3.2×10^{-9} Pa	5.7×10^{-10} Pa
H_2O	1.1×10^{-10} Pa	2.6×10^{-11} Pa
CO_2	2.3×10^{-10} Pa	5.1×10^{-11} Pa

Table 2. Comparison of base pressures and partial pressures of residual gases in the gun chamber, before and after increasing the pumping speed.

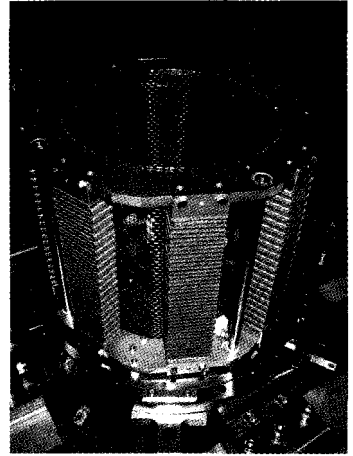
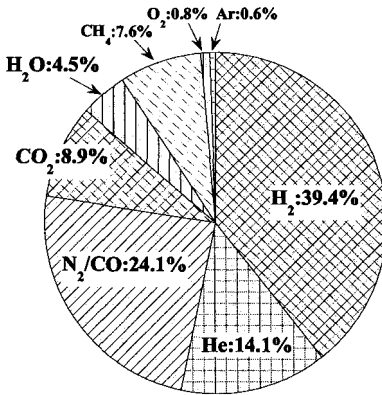


Fig 2. The NEG modules fixed to the rigid frame



Base Pressure : 5.7×10^{-10} Pa

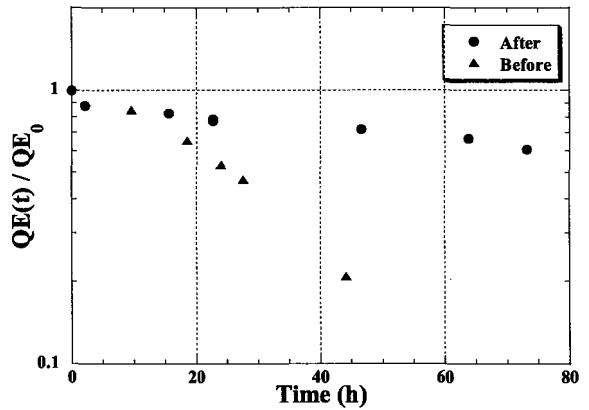


Fig 3. The preliminary results of residual gas analysis and preliminary dark lifetime measurement.

it is reconfirmed that the reduction of harmful residual gasses (in particular, H_2O, CO_2) is so important to preserve the good NEA condition. The result of dark lifetime measurement is simply interpreted if we assume the NEA degradation is dominated only by adsorption of H_2O and CO_2 on to the NEA surface. In this case, the ratio of the number of destructed electric dipoles by one harmful molecule adsorption is estimated to be ~ 2.5 .

4. Emittance Measurement System

An emittance measuring system employing a pepper pot technique was introduced to our gun system. It was originally developed at KEK for the emittance measurement of

a thermionic cathode gun [6] and now modified for our NEA-GaAs cathode gun. As shown in Fig.4, The pepper pot mask is fixed on a linear manipulator at a distance of $\sim 1m$ from the photocathode. Then the electron beamlet passing through hole of the pepper pot mask drifts in free space (56 mm) and hits a scintillator film screen.

This scintillation light ($\lambda = 375nm$) passes through an IR-cut-filter to eliminate the background of laser lights ($\lambda = 780nm$ for Ti:Sapphire, $\lambda = 633nm$ for a He-Ne laser). Then small luminous spots on the screen are magnified by a telescope, amplified by an image intensifier and finally converted into the electrical images by a CCD camera.

As a preliminary result of the emittance measurement, $\epsilon_{rms} \sim 1.1\pi mm \cdot mrad$ was obtained for a 80 keV CW beam with 100 nA.

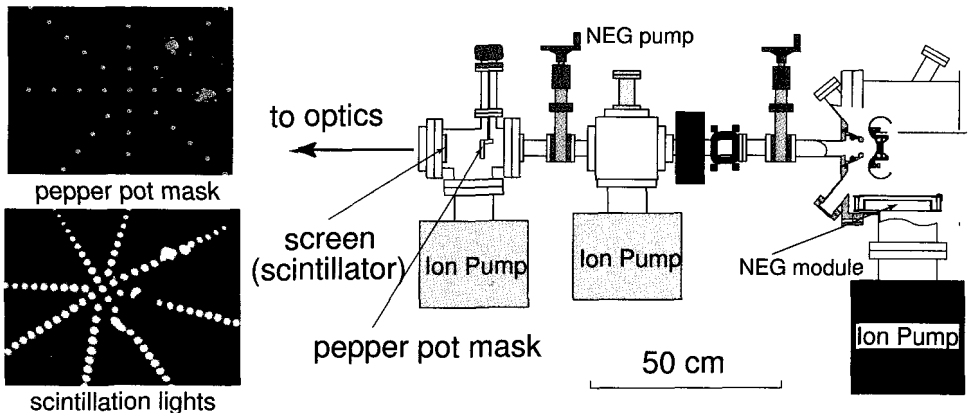


Fig 4. A pepper pot type emittance measurement system

5. Summary

We have tried to improve the lifetime of NEA-GaAs photocathode in the 200 keV gun by reinforcing the pumping speed and also making the high temperature baking for the gun chamber. The dark lifetime was extended to 150 hours, and the longer lifetime will be obtained by increasing the NEG activation temperature from 200°C to 450°C. The precise measurement of source emittance becomes also possible. Further studies to improve the dark lifetime and increase the field gradient by a new electrode having a Mo-cathode and a Ti-anode are in progress [7–9].

References

1. T. Nakanishi, et al., KEK Report **97-01**, 36-48 (1997)
2. R. Brinkmann, et al., "The Accelerator" TESLA TDR Part2 (2001)
3. M. Kuwahara, et al., This proceedings.
4. T. Nakanishi, et al., Proceedings of LINAC2004, MOP76

5. R. Alley, et al., *Nucl. Instr. and Meth. A* **356**, (1995) 1.
6. Y. Yamazaki, et al., *Nucl. Instr. and Meth. A* **322**, (1992) 139.
7. F. Furuta, et al., This proceedings.
8. F. Furuta, et al., to be published in *Nucl. Instr. and Meth.*
9. T. Nakanishi, et al., Proceedings of LINAC2004, THP23

MAXIMAL SPIN ORIENTATION IN ELECTRON PHOTOEMISSION FROM STRAINED SEMICONDUCTOR SUPERLATTICES

L. G. GERCHIKOV, A. V. SUBASHIEV

St. Petersburg State Polytechnic University, St. Petersburg, Russia

Various channels of the electron spin polarization losses in strained semiconductor superlattices including smearing of the photoabsorption band edge, indirect optical transitions and the contribution of low-polarized absorption in the surface GaAs layer are analyzed to evaluate the maximal electron polarization in spin polarized electron photoemission. The optimal design of the strain superlattice photocathode for highly polarized emission is discussed.

The strained superlattice (SL) based heterostructures for the photocathode applications has been actively studied as the most effective sources of highly spin-polarized electron beams [1–3]. High electron polarization is obtained by a spin optical orientation in excitation from the valence band splitted both by the strain and the hole confinement in the layers forming quantum wells (QW) for the holes. Though the theoretically predicted initial electronic polarization in the conduction band the near the absorption edge is expected to be close to $|P| = 100\%$, the experimentally observed values of the emitted electron polarization are typically in the interval from 80 to 86 % (e.g., see Refs. [4, 5] this volume), the origin of this spread being poorly understood. These results call for a reexamination of possible contributions to the electron polarization losses, including smearing of the photoabsorption edge due to the hole scattering processes and the fluctuations of the layer composition, polarization losses during electron extraction to the surface layer and emission into vacuum, and generation of low polarized photoelectrons in the surface layer.

We calculate the generation rate of photoelectrons in the working layer under the circularly polarized light excitation and their initial polarization using the multiband Kane model [6]. The absorption coefficients $\alpha_{\uparrow,\downarrow}$ including contributions of the direct and indirect optical transitions at the polarization maximum near the absorption edge are formed by the transitions between the first heavy hole, hh1, the first light hole, lh1, and the electron, e1, minibands. The main contribution comes from direct hh1-e1 transition populating one ($|\uparrow\rangle$) conduction-band spin state.

The electron generation in the second spin state ($|\downarrow\rangle$) of the conduction band is mainly due to indirect optical transitions which contribute to α_{\downarrow} via the virtual transition from

hh1 to the lh1 miniband at the absorption edge near the center of the Brilluin zone, $\hbar\omega = \varepsilon_{e1}(\mathbf{0},0) - \varepsilon_{hh1}(\mathbf{0},0)$. The corresponding contribution to the absorption coefficient can be written as

$$\alpha_{\downarrow}(\omega) = \frac{2\pi e^2 \omega}{c} \int |M_{lh1el}(\mathbf{k},q)|^2 \frac{\gamma(\varepsilon_{hh})}{(\varepsilon_{hh} - \varepsilon_{lh})^2 + (\gamma(\varepsilon_{hh})/2)^2} \frac{d\mathbf{k}dq}{(2\pi)^3}, \quad (1)$$

Here $M_{lh1el}(\mathbf{k},q)$ is the dipole matrix element of the optical transition between lh1 and e1 states and $\varepsilon_{lh} = \varepsilon_{lh1}(\mathbf{k},q)$ is the energy of the intermediate light hole state, ε_{hh} is the energy of the initial heavy hole state determined by the energy conservation

$$\varepsilon_{hh1} = \varepsilon_{e1}(\mathbf{k},q) - \hbar\omega \mp \hbar\Omega. \quad (2)$$

The last term in Eq.(2) indicates the energy conservation in the processes of absorption and emission of a phonon with the energy $\hbar\Omega$; it is absent in the case of impurity scattering. The width of the Lorentian in Eq. (1) is determined by the rate of hh1-lh1 transitions and therefore is energy dependent

$$\gamma(\varepsilon) = 2\pi \int |\langle \Psi_{lh1,q,k} | \hat{H}_i | \Psi_{hh1,k',q'} \rangle|^2 \delta(\varepsilon_{hh1}(\mathbf{k},q) - \varepsilon) \frac{d\mathbf{k}'dq'}{(2\pi)^3}. \quad (3)$$

Here \hat{H}_i stands for the Hamiltonian responsible for the hh1-lh1 interaction. It follows from Eq. (2) that both direct and indirect optical transitions near the band edge occur at rather small momenta, so that the momentum q, \mathbf{k} of the light-hole state in Eq. (3) can be taken equal to zero, γ being dependent only upon the heavy-hole energy. Therefore, one can neglect the optical phonon dispersion as well as the contribution of the hole scattering by the acoustical phonons. We have calculated the corresponding transition rate, $\gamma(\varepsilon)$,

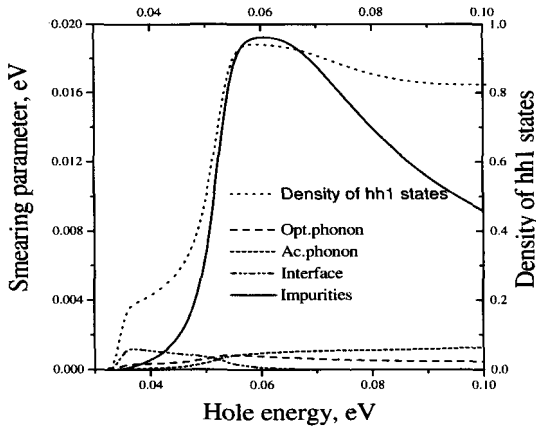


Fig 1. Transition rate γ calculated using Eq. (3) for the light to heavy-hole miniband transition rate for different scattering mechanisms and the density of the final states for $\text{In}_{0.18}\text{Al}_{0.14}\text{Ga}_{0.68}\text{As}-\text{GaAs}_{0.83}\text{P}_{0.17}$ 4×4 superlattice.

for different mechanisms of hh-lh scattering. Contributions to γ of the main competing

scattering mechanisms are depicted in Fig. 1. For the impurity scattering we use a short-range model for the impurity potential contributing to transitions with alterations of the hole angular momentum. Shown are results of the calculations for $p = 10^{18} \text{cm}^{-3}$ and the impurity scattering length $f = 5 \text{nm}$. These parameters correspond to the in-plane mobility of the heavy holes $\mu = 2 \cdot 10^2 \text{cm}^2/\text{V}$, typically observed for these type of structures at room temperature. Fig. 1 demonstrates that for taken parameters the scattering on the impurities provides the width by the order of magnitude larger than the other mechanisms.

The energy dependence of $\gamma(\varepsilon)$ reflects variation of the density of the final states in the hh1 miniband and decreases to zero at $\varepsilon = \varepsilon_{hh1}$. Therefore the relevant value of the broadening parameter γ and the shape of the calculated polarization maximum is sensitive to the processes resulting in smearing of the hole density of states and exhibiting themselves as the tails in the interband absorption. Having in mind to allow the influence of smearing of the absorption edge on the indirect transitions, we include the fluctuation effects by calculating an average value of the smearing parameter $\gamma(\varepsilon)$ as

$$\langle \gamma(\varepsilon) \rangle = \int_{-\infty}^{\infty} \gamma(\varepsilon)(\varepsilon + V)f(V)dV, \quad (4)$$

$$f(V) = \frac{s}{\Gamma(1/s)\delta} \exp\left(-\frac{|V|^s}{\delta^s}\right), \quad (5)$$

here δ is the smearing parameter taken to be equal for the light-hole and heavy-hole minibands, s is the parameter depending on the dominant band tailing mechanism; $s = 1$ for a regular case of exponential decrease of the interband absorption on the low-energy tail (Urbach's rule). An estimate for the smearing parameter δ can be obtained from the comparison of the calculations of the absorption spectrum with the spectral dependence of the quantum yield on the excitation energy below the absorption edge. However, the tailing parameter is not identical to the energy width of the absorption tail since it relies on the contribution of the lh-e transitions to the absorption at the hh-e absorption edge. Therefore, this parameter should also depend on the hh1-lh1 splitting, being smaller in the structures with larger separation of the hh1- and lh1- valence band states.

To identify the relative polarization losses at different stages of photoemission we calculate polarization, $P(h\nu)$, and quantum yield, $Y(h\nu)$, spectra for various values of width γ at the valence band edge and smearing parameter δ . In energy region above the first polarization maximum initial polarization: (i) is not sensitive to the smearing parameters in a reasonably taken variation range; (ii) follows closely the experimental spectra for different strained SLs; (iii) exceeds the observed polarization of emitted electron by a constant value which does not depend on the photon energy. Therefore this depolarization factor can be attributed to the steps associated with electron transport to the surface and escape in vacuum through the activation layer. For the best photocathodes it does not exceed 5%, in line with time-resolved photoemission data [7]. Shown in Fig. 2 are the calculated $P(h\nu)$ and $Y(h\nu)$ spectra for the $\text{In}_{0.18}\text{Al}_{0.14}\text{Ga}_{0.68}\text{As}-\text{GaAs}_{0.83}\text{P}_{0.17}$ SL containing 20 periods with 5 nm- thick wells and 4-nm barriers in the excitation energy region near the first polarization maximum (with included 5% depolarization factor). Fig. 2a demonstrates variations of the amplitude of the first polarization maximum with δ and γ . It is seen that for realistic values

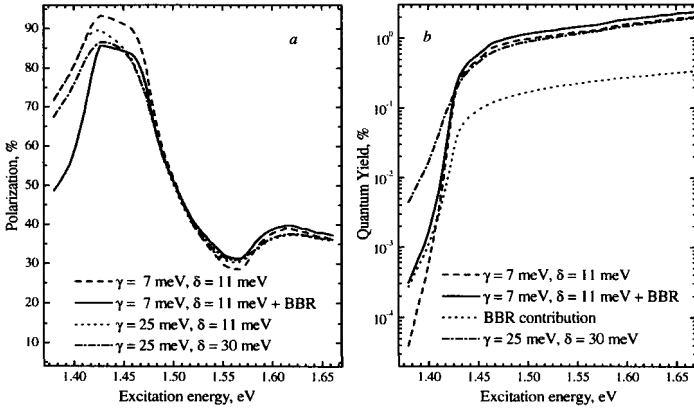


Fig 2. Calculated $P(h\nu)$ (a) and $Y(h\nu)$ spectra (b) of the emitted photoelectrons for $\text{In}_{0.18}\text{Al}_{0.14}\text{Ga}_{0.68}\text{As-GaAs}_{0.83}\text{P}_{0.17}$ SL for varying parameters of valence band smearing δ and hh-lh scattering width γ . Dotted line in the right panel (b) shows the separate contribution of photoabsorption in BBR layer to the $Y(h\nu)$ spectrum.

$\gamma = 7$ meV and $\delta = 11$ meV only 3% polarization losses occurs at the photoabsorption stage. This rather small value is due to a large enough valence band splitting in this SL, $\Delta\varepsilon_{hh-lh} = \varepsilon_{hh1}(0,0) - \varepsilon_{lh1}(0,0) = 50$ meV, resulting in a decrease of all effects of hh-lh mixing. Fig. 2 shows that typical experimental values of maximal polarization $P_{max} < 90\%$ can result only from unrealistically large values of δ , $\gamma \geq 25$ meV, inconsistent with our calculations of the rate of hh1-lh1 indirect transitions. Besides, the enlarged smearing parameters would result in much slower decline of $Y(h\nu)$ below the absorption edge than the experimentally observed.

An additional origin of polarization losses is contribution of the optical absorption in the surface GaAs layer forming the Band Bending Region (BBR) to the photoemission response. The position of the main polarization maximum is close to SL absorption where photoabsorption coefficient is rather small. Thus the contribution of the relatively thin BBR with smaller band gap in this frequency region can be sizable (see Fig. 2b). Since the spin orientation of photoelectrons generated in BBR is less than 50% the BBR photoabsorption can reduce the value of polarization in its maximum. The results of calculations of the $P(h\nu)$ and $Y(h\nu)$ spectra of electron emission accounting for BBR absorption in a BBR layer with a thickness of 0.055 of the thickness of the working layer is shown in Fig. 2 by a solid line. The calculated polarization spectrum shows that photoabsorption in BBR layer lowers resulting electron polarization value in the maximum by 6% demonstrating the importance of this contribution to the total polarization losses near polarization maximum.

For the present the maximal experimental value $P_{max} = 91\%$ was apparently observed for the $\text{GaAs/In}_{0.2}\text{Al}_{0.21}\text{Ga}_{0.59}\text{As}$ strained barrier SL structure [4]. Our analysis shows that, in addition to the enlarged valence band splitting $\Delta\varepsilon_{hh-lh} = 70$ meV, which reduces all processes of hh-lh mixture (2% of polarization losses at the photoabsorption stage), this photocathode has polarization losses in transport and emission in vacuum of about 5% (typical for the best photoemitters) and extremely small BBR contribution ($\approx 2\%$) presumably due

to more precise modulation doping.

The present study gives a guidance on the optimization of photoemitter structure to obtain maximum electronic polarization. First, to reduce the effects of the polarization losses in excitation, the enlarged value of the valence band splitting is essential. However, the strain-induced splitting and the splitting caused by the quantum confinement do not combine additively, so the choice of the working layer structure must be based on the optimization of miniband spectrum. The maximum splitting is found in the strained well superlattices, while the splitting in strain-compensated structures is smaller and also in the barrier strained structures due to lower barriers for the light holes.

However strain-compensated SL's have an advantage of no restriction to the working layer thickness and therefore decreased contribution of BBR, while strained-barrier structures have minimal polarization losses in transport. To lessen depolarization losses in the BBR one can exploit modulation doping to reduce the BBR width and also carefully chosen BBR composition to minimize weakly polarized absorption in the vicinity of the polarization maximum. Imperfections in the low quality SL structure lead to the smearing of the valence band edge and cause a strong heavy - light hole mixture that can depreciate the effect of large valence band splitting. Analysis of the P variation due to these factors shows that optimization of the SL-based photoemitter structures can increase the maximum polarization of the emitted electrons up to 95%.

This work was supported by Russian Fond of Basic Research under grant 04-02-16038, CRDF under grant RP1-2345-ST-02, by NATO under grant PST.CLG 979966, by Russian Ministry of industry, science and technology under contracts # 40.012.1.1.1152 and # 40.072.1.1.1175.

References

1. T. Otori, Y. Kurihara, Y. Takeuchi, M. Yoshioka, T. Nakanishi, S. Okumi, M. Tsubata, M. Tavada, K. Togava, Y. Tanimoto, C. Takahashi, T. Baba and M. Mixuta, *Jpn. J. Appl. Phys.*, **33**, 5676 (1994).
2. T. Saka, T. Kato, T. Nakanishi, S. Okumi, K. Togava, H. Horinaka, T. Matsuyama, and T. Baba, *Surf. Sci.* **454-456** 1042 (2000).
3. T. Maruyama, D.-A. Luh, A. Brachmann, J. E. Clendenin, E. L. Garvin, S. Harvey, J. Jiang, R. E. Kirby, C. Y. Prescott, R. Prepost, and A. M. Moy, SLAC-Pub-10331, Feb. (2004)
4. Yu. A. Mamaev, et al., Proceedings of PESP 2004 (this volume), p....
5. A. V. Subashiev, et al., Proceedings PESP 2004 (this volume), p....
6. A.V. Subashiev, L. G. Gerchikov, A. N. Ipatov *Journ. Appl Physics* **96**,1511 (2004).
7. K. Aulenbacher, J. Schuler, D. v. Harrach, E. Reichert, J. Roethgen, A. Subashev, V. Tioukine, Y. Yashin, *J. Appl. Phys.*, **92**, 7536 (2002).

HIGH PERFORMANCE POLARIZED ELECTRON PHOTOCATHODES BASED ON InGaAlAs/AlGaAs SUPERLATTICES

Y. A. MAMAEV, A. V. SUBASHIEV, Y. P. YASHIN, L. G. GERCHIKOV

St. Petersburg State Polytechnic University, St. Petersburg, Russia

D. LUH, T. MARUYAMA, J. E. CLENDENIN

Stanford Linear Accelerator Center, Menlo Park, USA

V. M. USTINOV, A. E. ZHUKOV

Ioffe Physico-Technical Institute, RAS, St. Petersburg, Russia

Highly efficient emitters of polarized electrons based on the InAlGaAs/AlGaAs superlattice give an optimistic prognosis to explorations of such structures as the sources for accelerators. A new set of these SL structures with minimized conduction band offset was designed and recently tested. A new technology of surface protection in MBE growth leads to a significantly reduced heat-cleaning temperature. At these lowered cleaning temperatures, the thermal degradation of the working structure parameters is avoided. As a result a polarization P of up to 91% at corresponding quantum efficiency (QE) of 0.3% was achieved at room temperature. A 50% increase in the photocathode lifetime has been achieved with Sb coverage.

1. Introduction

The spin-polarized electron sources (PES) based on photoemission from GaAs or its relatives under excitation by circularly polarized light has proved to be the best for high energy electron accelerators applications [1]. New progress in development of polarized electron sources can be based on new structures with good structural quality, large valence band splitting and spin relaxation times resulting in larger polarization and quantum efficiency. The most obvious prospects for optimization of the PES structure are to increase both the quantum efficiency and electron spin polarization using superlattice (SL) structures with specially designed layer thickness and compositions. They consist of several thin strained films separated by layers of unstrained larger-bandgap material, specially designed to cause barriers for the hole transport but keep electron mobility high. From the point of view of

growth of a perfect crystal, every separate strained film of the SL can be grown thinner than the critical thickness (CTh), but with a total thickness which can exceed CTh and be sufficient to obtain high quantum efficiency (QE). To suppress the depolarization during the transport to the band bending region (BBR), the working part of a structure has to be low p-doped (about $5 \times 10^{17} \text{ cm}^{-3}$), which should help to suppress Bir - Aronov - Pikus spin relaxation mechanism [2]. At the same time the request for high QE at maximum polarization requires the top of a structure to be heavily p-doped to achieve high quality Negative Electron Affinity (NEA) surface. These two requirements can be simultaneously fulfilled with the modulation doping profile. Very high (not less than $5 \times 10^{19} \text{ cm}^{-3}$) doping of the top layer helps as well to overcome surface charge limit (SCL), which appears at high pumping light power [3, 4]. Below our recent results with InAlGaAs/AlGaAs superlattices are discussed. All SL samples were grown by solid-source molecular beam epitaxy on GaAs(100)-oriented substrates.

2. Highly strained InAlGaAs/AlGaAs SL structures

The main advantage of SL-based photoemitters is the possibility to vary the properties of the active layer over a wide range by the appropriate choice of layer composition, thickness, and doping profile. The initial polarization P_0 can be increased by choosing structures with a higher valence band splitting. The SL structures with strained quantum well (QW) layers in which heavy and light hole bands, in addition to the strain splitting, are moved aside due to different light and heavy-hole confinement energy in the QW layers, are the best for this purpose. The other benefit of the SLs is the possibility of a precise modulation doping providing small polarization losses during electron escape from the active layer and the band bending region into vacuum.

New InAlGaAs/AlGaAs SL structures with thin (close to 2 nm) quantum well layers and the highest possible (up to 35 %) concentrations of In within the QW layers were developed and tested. The studies of polarization spectra obtained at lowered activation temperatures revealed a rather wide plateau in the vicinity of the maximum polarization (about 85 %) and a sharp edge of the quantum yield spectrum, which indicates the good structural qualities of these samples. Record high values of strain splitting are reproducibly obtained, though further optimization of the overall photocathode structures is still needed. InAlGaAs/AlGaAs SL structures are favorable candidates for photocathodes since they can be grown by a standard MBE technology and the structures are well controlled and reproduced during the growth. This gives an optimistic prognosis to explore such structures in the sources attached to accelerators.

3. InAlGaAs/GaAs SL structures with minimized conduction band offset

A new strained-barrier short-period $\text{Al}_x\text{In}_y\text{Ga}_{1-x-y}\text{As}/\text{GaAs}$ superlattice with a minimal conduction-band offset was proposed in [1]. The main advantage of such SL results from the band line-up between the semiconductor layers of the SL. The Al content determines the formation of a barrier in the conduction band, while adding In leads to conduction band

lowering, so the conduction band offset can be completely compensated by appropriate choice of x and y , while barriers for the holes remain uncompensated. As a result high vertical electron mobility and simultaneously a small spin relaxation rate is achieved while also a large enough valence-band splitting remains.

For the thermalised electrons at room temperature the influence of the resulting periodical potential should be negligible. Besides, as a result of the conduction-band line up, the residual 4-nm barriers for the electrons in the SL are transparent. Thus the changes of electron mobility and spin relaxation rate from the values typical for the bulk GaAs should be small. Using the structures based on quaternary $\text{Al}_x\text{In}_y\text{Ga}_{1-x-y}\text{As}$ alloy one can change

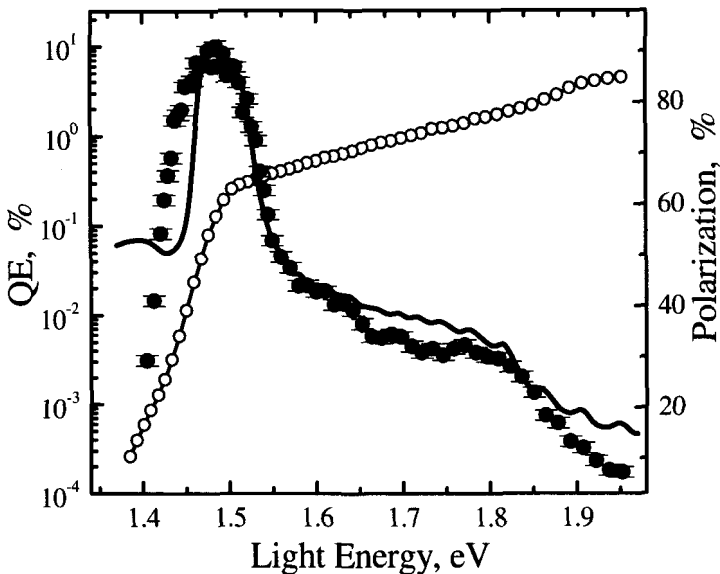


Fig 1. Polarization (solid circles) and quantum efficiency (open circles) spectra of $\text{Al}_{0.21}\text{In}_{0.2}\text{Ga}_{0.69}\text{As}$ (4nm)/GaAs(1.5nm) 18.5 periods Superlattice sample at room temperature. Heat cleaning temperature is 450°C . Solid line: calculated energy dependence of $P(h\nu)$.

the band gap by varying the Al content in the layers keeping In concentration unchanged to maintain high deformation and strain-induced valence band splitting. The choice of the layer thickness is dictated by the need to split the hole minibands. The splitting grows when barriers are broad enough and wells are narrow and deep.

A new set of the InAlGaAs/GaAs SL structures with minimized conduction band offset was designed and tested. The optimization of the design of these structures has recently become possible only with the development of more accurate calculation programs. In addition, a new technology of surface protection in MBE growth enabled us to significantly reduce the heat-cleaning temperature (for optimal activation it should not exceed 450°C). At these lowered cleaning temperatures, the thermal degradation of the modulation doping profile is avoided. As a result a polarization P of up to 91% at corresponding quantum

efficiency QE of 0.3% was achieved at room temperature (see Fig. 1). These results are significantly better than our previous ones and are equal to or superior to the best results achieved anywhere. The lowered activation temperatures open the possibility for further improvements in photocathode parameters via optimization of the doping profile.

4. Photocathode lifetime improvement

The possibility to protect the activation layer by an additional co deposition of Sb on the Cs-O activated surface was investigated. Several types of co-adsorption processes with antimony addition to oxygen during Yo-Yo- cycles as well as Sb co-deposition at the final stage of the activation cycles were tested. The quantum efficiency attenuation and the lifetime of the cathodes was measured for the varying activation conditions. For the studied activation process with antimony deposition at the final activation stage it was found that highly strained InGaAs/AlGaAs SL photocathodes have about 2 times smaller quantum efficiency, but result in a 50% increase in the photocathode lifetime.

5. Summary

New structures based upon highly QW-strained InAlGaAs/AlGaAs SLs and barrier-strained InAlGaAs/GaAs SLs with minimized conduction band offset have been developed and tested. InAlGaAs/AlGaAs SL structures are favorable candidates for photocathodes since they can be grown by a standard MBE technology and the structures are well controlled and reproduced during the growth. A new technology of surface protection in MBE growth leads to considerable reduction of the heat-cleaning temperature (not more than 450°C). At these lowered cleaning temperatures, the thermal degradation of the working structure parameters is avoided. As a result a polarization P of up to 91% at corresponding quantum efficiency (QE) of 0.3% was achieved at room temperature. A 50% increase in the photocathode lifetime has been achieved with Sb coverage.

Acknowledgments

This work was supported by RFBR under grant 04-02-16038, Russian Ministry of industry, science and technology, CRDF under grant RP1-2345-ST-02, NATO under grant PST.CLG 979966 and the US Department of Energy under grant DE-FG02-01ER8332.

References

1. A. V. Subashiev, Yu. A. Mamaev, Yu. P. Yashin, and J. E. Clendenin, *Phys. Low-Dim. Struct.* **1/2**, 1 (1999).
2. F. Meier and B. P. Zakharchenya eds., *Optical orientation*, (North-Holland, 1984).
3. G. A. Mulhollan, A. V. Subashiev, J. E. Clendenin, E. L. Garwin, R. E. Kirby, T. Maruyama, and R. Prepost, *Phys. Lett. A* **282**, 309 (2001).
4. T. Maruyama, A. Brachmann, J. E. Clendenin, T. Desikan, E. L. Garwin, R. E. Kirby, D.-A. Luh, J. Turner, and R. Prepost, *Nucl. Instr. and Meth. A* **492**, 199 (2002).

POLARIZED ELECTRON EMISSION FROM STRAINED GaAs/GaAsP SUPERLATTICE PHOTOCATHODES*

T. MARUYAMA[†], D. LUH[†], A. BRACHMANN[†], J. E. CLENDENIN[†], E. L. GARWIN[†], S. HARVEY[†],
J. JIANG[†], R. E. KIRBY[†], C. Y. PRESCOTT[†], R. PREPOST[‡], A. M. MOY*

[†]Stanford Linear Accelerator Center, Menlo Park, USA

[‡]Department of Physics, University of Wisconsin, Madison, USA

*SVT Associates, Inc., Eden Prairie, USA

Spin-polarized electron photoemission has been studied for GaAs/GaAs_{1-x}P_x strained superlattice cathodes grown by gas-source molecular beam epitaxy. The superlattice structural parameters are systematically varied to optimize the photoemission characteristics. The heavy-hole and light-hole transitions are reproducibly observed in quantum efficiency spectra, enabling direct measurement of the band energies and the energy splitting. Electron-spin polarization as high as 86% with over 1% quantum efficiency has been observed.

1. Introduction

Single strained GaAs photocathodes were introduced for the SLAC polarized electron source in 1993. After 10 years of experience with many cathode samples, the maximum polarization using the GaAs/GaAsP single strained-layer cathode remains limited to 80%, while the quantum efficiency (QE) for a 100-nm epilayer is only 0.3% or less. Two known factors limit the polarization of these cathodes: 1) a limited band splitting; and 2) a relaxation of the strain in the surface epilayer since the 10-nm critical thickness for the 1% lattice-mismatch is exceeded. Strained superlattice structures, consisting of very thin quantum well layers alternating with lattice-mismatched barrier layers are excellent candidates for achieving higher polarization since they address these two issues. Due to the difference in the effective mass of the heavy- and light-holes, a superlattice exhibits a natural splitting of the valence band, which adds to the strain-induced splitting. In addition, each of the superlattice layers is thinner than the critical thickness. This paper presents an investigation of strained GaAs/GaAsP superlattice samples in which the principal structural parameters are systematically varied to define the optimum structural details [1].

*This work was supported in part by the U. S. Department of Energy under contract numbers DE-AC02-76SF00515 (SLAC), and DE-AC02-76ER00881 (UW).

2. Experiment

Four parameters specify the superlattice structure: the GaAs well width, the GaAs_{1-x}P_x barrier width, the phosphorus fraction, and the number of periods. Table 1 summarizes the eleven superlattice samples studied here.

Table 1. Strained GaAs/GaAs_{1-x}P_x superlattice samples.

Sample	Well (nm)	Barrier (nm)	x	No. Period
1	4	4	0.25	12
2	4	4	0.30	12
3	4	4	0.36	12
4	4	4	0.40	12
5	4	4	0.36	9
6	4	4	0.36	15
7	4	4	0.36	20
8	4	4	0.36	30
9	3	3	0.36	16
10	4	3	0.36	14
11	5	3	0.36	12

Figure 1 shows the polarization and QE as a function of the excitation photon energy for Sample 3. The peak polarization is 86% with 1.2% QE. The QE spectrum shows two distinct steps as expected from the density of states for the two dimensional structure. The first step corresponds to the heavy-hole (HH) band to the conduction band excitation, while the second step corresponds to the light-hole (LH) band to the conduction band excitation. The energy splitting between the HH- and LH-bands is 82 meV.

When the phosphorus fraction is varied, the lattice-mismatch between the well and the barrier changes, thus the superlattice strain can be varied. While a larger phosphorus fraction generates a larger strain and therefore a larger energy splitting between the HH and LH bands, the strain within a layer may relax. For Samples 1, 2, 3, and 4, the phosphorus fraction was increased from 0.25 to 0.40 keeping the total superlattice thickness constant. Figure 2 shows the peak polarization and QE anisotropy [2] as a function of the phosphorus fraction for constant total thickness. The measured HH-LH energy splitting is also shown in the figure. Although the HH-LH energy splitting increased from 60 meV to 89 meV, the peak polarization and the QE anisotropy did not change significantly at about 85% and 1.7%, respectively, indicating that this degree of energy splitting is sufficient to maximize the spin polarization.

Using samples with the same well (4 nm)/barrier (4 nm) thickness and phosphorus fraction ($x=0.36$), the total superlattice thickness was varied. Figure 3 shows the peak polarization and QE anisotropy as a function of the number of superlattice periods using Samples 3, 5, 6, 7, and 8. Also shown in Figure 3 is the strain relaxation in the superlattice

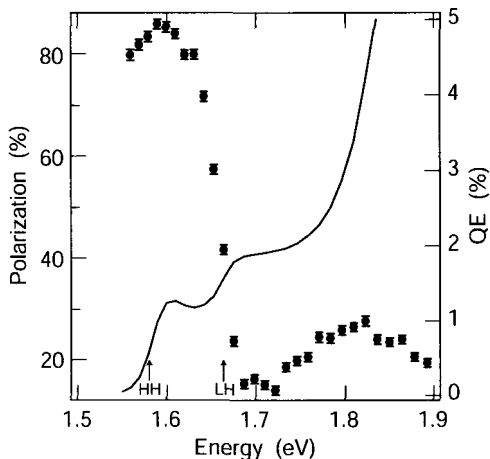


Fig 1. Polarization and QE as a function of excitation light energy

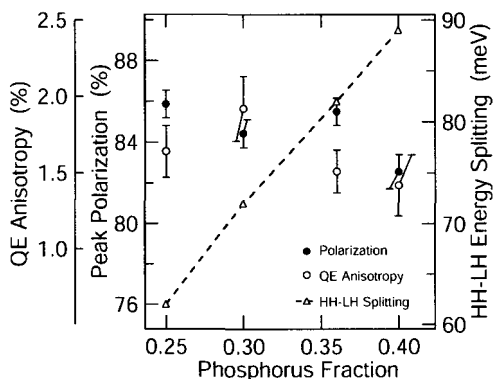


Fig 2. Peak polarization (solid circles), QE anisotropy (open circles), and measured HH-LH energy splitting (triangles) as a function of the phosphorus fraction.

GaAs well layers measured using x-ray diffraction. Although the well width is smaller than the critical thickness, increased superlattice periods will result in strain relaxation. As the strain relaxation steadily increases with the superlattice thickness, the peak polarization and QE anisotropy appear constant at 85.5%, and 1.5%, respectively, for less than 15 periods. At more than 20 periods, however, the peak polarization decreases and the QE anisotropy increases rapidly.

The QE and polarization spectra can be understood in terms of the superlattice band structure. In particular, the band structure is very sensitive to the well width. Using samples with the same barrier thickness (3 nm) and phosphorus fraction ($x=0.36$), the well thickness was varied while the number of periods was adjusted to keep the same total superlattice thickness. Figure 4 shows the spin polarization as a function of the excitation photon energy for Samples 9, 10, and 11. As the well thickness was increased, the polarization

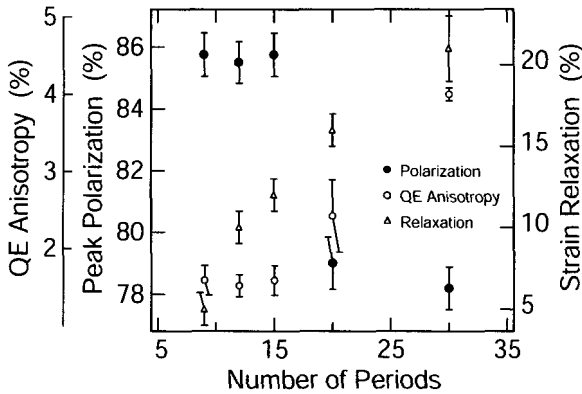


Fig 3. Peak polarization (solid circles), QE anisotropy (open circles), and strain relaxation (triangles) as a function of the superlattice period.

spectra shifted towards lower energy. The peak polarization was, however, independent of the well thickness. While the changes in the band structure differentially affected the polarization spectra for energies above the polarization peak, the maximum polarization remained constant at about 86%, indicating that the valence-band splitting for this range of well thicknesses was sufficient.

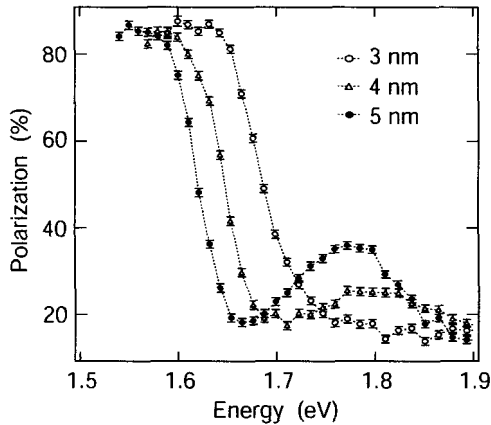


Fig 4. Polarization as a function of the excitation light energy for the three samples with a different well width; 3 nm (open circles), 4 nm (triangles), and 5 nm (solid circles).

3. Conclusions

We have investigated polarized photoemission from strained GaAs/GaAsP superlattice structures by systematically varying the superlattice parameters. The heavy- and light-hole excitations have been observed for the first time in the QE spectra, enabling direct measurements of the heavy- and light-hole energy bands. Spin polarization as high as 86% is

reproducibly observed with the QE exceeding 1%. The superlattice structures have superior polarization and QE compared to the single strained-layer structures of GaAs/GaAsP photocathodes.

References

1. T. Maruyama, D.-A. Luh, A. Brachmann, J.E. Clendenin, E.L. Garwin, S. Harvey, J. Jian, R.E. Kirby, C.Y. Prescott, R. Prepost and A.M. Moy *Appl. Phys. Lett.* **85**, 2640 (2004).
2. R.A. Mair, R. Prepost, H. Tang, E.L. Garwin, T. Maruyama and G. Mulhollan, *Phys. Lett.* **A212**, 231 (1996).

TIME RESOLVED DEPOLARIZATION MEASUREMENTS ON SUPERLATTICES WITH STRAINED WELLS *

K. AULENBACHER, R. BOLENZ, V. TIOUKINE, M. WEIS

Institut für Kernphysik der Universität Mainz, Mainz, Germany

A. V. SUBASHEV, Y. YASHIN

Sankt Petersburg State Polytechnical University, St. Petersburg, Russia

Strained well superlattices of the InAlGaAs/AlGaAs type were investigated. Conventional measurements of c.w.-Polarization and quantum efficiency show good polarization ($\approx 80\%$) and high q.e. ($> 1\%$). Surprisingly the pulse response is rather slow. We demonstrate that polarizations at the beginning of the pulse response can approach or even exceed the value of 90%, whereas the average polarization of the response is reduced by almost 10%.

1. Introduction

In the photoemission process after photoexcitation electrons undergo depolarization processes during their transport from the semiconductor conduction band (CB) to the surface. Investigation of the time response of a photocathode after excitation with a subpicosecond light pulse may serve as a useful tool to explore these effects. We have been able to demonstrate that emission processes from thin strained layer- and superlattice-photocathodes are very fast ($< 2 ps$) [1]. If we assume reasonable depolarization times in the CB it follows that the transport process leads to loss of $< 3\%$ in polarization [2]. However it is by no means evident that all types of newly developed cathodes show this behavior. Different structure design may lead, e.g., to a smaller diffusion constant and hence to slower transport.

We have investigated the time response of strained-well superlattice structures (SL) with a basic period of 3.5 nm $In_{.16}Al_{.20}GaAs$ and 4 nm $Al_{.28}GaAs$ layers. This period is repeated 15 times leading to an active layer thickness of 112.5 nm. The layer content is chosen to give a sufficient ($> 50 meV$) valence band splitting between the light and heavy-hole minibands. However it is obtained at the expense of rather high barriers for the electrons in the CB. The working layer is capped with a 6 nm thick GaAs quantum well structure. The

*Work supported by the Deutsche Forschungsgemeinschaft within Sonderforschungsbereich 443.

application of this highly doped surface layer leads to a minimized band bending region thickness and allows to achieve large values of NEA leading to high escape probabilities. The capping layer itself produces electrons of low polarization, however they contribute only a fraction of less than 1% to the total emission. Consequently high values of quantum efficiency ($QE > 1\%$) and polarization $\approx 0.80\%$ were obtained.

2. Pulse responses

Figure 1 shows the pulse response of the SL at excitation wavelengths of 830 and 780 nm. At the long wavelength the active layer structure is transparent, so that only the GaAs capping layer contributes to the emission. This response is limited by the experimental resolution of about 2.5 ps FWHM. The response at 780 nm is far more extended in time. The energy width of the emitted beam could be large because of the high NEA-value, thus leading to an increased time spread during the acceleration in the source. However the observed pulse profile cannot be explained with realistic NEA values within the parameters of our apparatus. Therefore the long response implies lower electron mobility. Note that it can not be attributed only to an increase of electron effective mass but predominantly to a more intense electron scattering on the defects of the interfaces as consequence of high barriers in the CB. The sufficient length of the response - compared to our time resolution of 3 ps for this type of experiment - allows to perform a time resolved polarization measurement (also displayed in fig. 1).

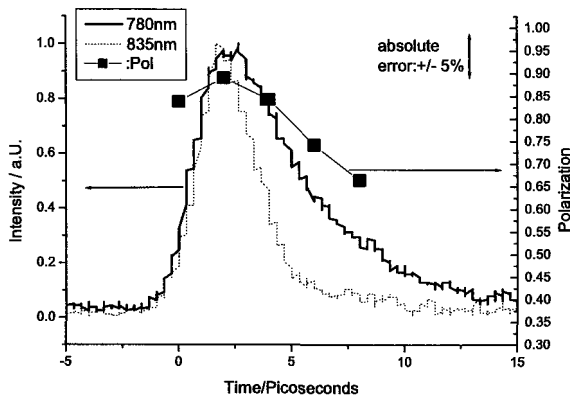


Fig 1. Pulse response of superlattice at two different excitation wavelengths. Polarization data are for the 780nm response.

A considerable depolarization takes place. From the experimental data we can estimate the depolarization time constant τ_s to be of the order 30 ps, which is significantly lower than the values for the individual SL-components in the bulk and also implies high scattering at the interfaces. The average polarization of the emitted bunch is therefore reduced by

about 10% if compared with the polarization at the onset of the response. This leads to the conclusion that polarizations in excess of 90% can be observed directly at the beginning of the emitted pulse. However, a large fraction of the emitted charge is located within the time interval that corresponds to the experimental resolution, so that the real polarization of the first electrons cannot be measured directly. We made use of pulse enlargement by space charge to increase the 'effective' resolution for our experiment.

3. Space charge expansion

The mutual repulsion of the electrons leads to pulse lengthening during the electron flight to the detection region. For our conditions we find a pulse enlargement in time of a factor ten at bunch charges of about 4 fC [2]. Then, a smaller fraction of the pulse intensity is located within the 3 ps resolution time. Provided that the order of electrons is conserved during expansion we have therefore effectively increased our resolution.

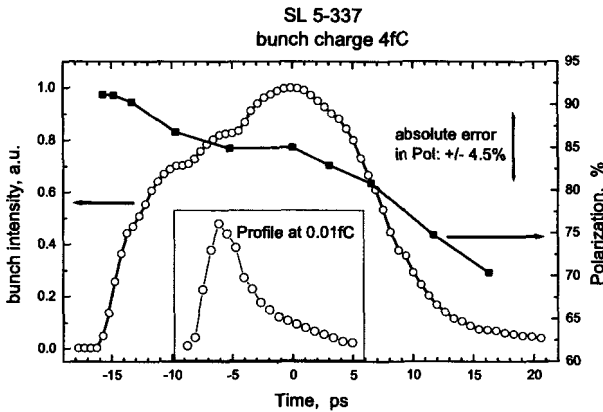


Fig 2. Time resolved polarization measurement for expanded pulse from SL-cathode.

Figure 2 shows the pulse length of a superlattice at 4 fC bunch charge and in addition for negligible charge. Because of complexity of factors contributing to the pulse shape during the space charge induced bunch expansion we do not try to give an interpretation of the expanded pulse profile. Still, the measurement shows the expected behavior. At the onset of the pulse we observe an electron polarization of $91.4 \pm 4.5\%$. This observation is in agreement with theoretical statements that the maximum available polarization after excitation is well above 90% [3]. It is obvious that a better absolute calibration of our Mott polarimeter is desirable. It can be improved to $\approx 2\%$ using known - but tedious - systematic investigations [4].

4. Summary

Even though the q.e. and maximum polarization of the SL's investigated here are quite satisfactory we have found that the pulse response is longer than expected for structures with working layer thicknesses in the 100 nm range apparently due to high barriers in the conduction band. This reduces the observed average beam polarization to $\approx 80\%$. It may be possible to improve the transport properties of the structure in a way that a time response can be achieved so that is comparable to a strained layer structure of similar thickness. In this case the average polarization of the beam may approach or even exceed 90%.

References

1. J. Schuler, K. Aulenbacher, T. Baba, D. v. Harrach, H. Horinaka, T. Nakanishi, S. Okumi, E. Reichert, J. Röthgen, and K. Togawa in Proceedings SPIN2000, AIP 570 p.926 (2000)
2. K. Aulenbacher, J. Schuler, D. v. Harrach, E. Reichert, J. Röthgen, A. Subashev, V. Tioukine, Y. Yashin *Journ. Appl. Phys* **92,12**, 7536 (2002).
3. L. G. Gerchikov et al. This conference.
4. T.J. Gay, M.A. Khakoo, J.A. Brand, J.E. Furst, W. V. Meyer and W. Wijayaratna *Rev. Sci. Instr.* 63(1) 114 (1992)

THE COMPTON BACKSCATTERING POLARIMETER OF THE A4 EXPERIMENT *

Y. IMAI[†]

Institut für Kernphysik, Universität Mainz, Mainz, GERMANY

(for the A4 Collaboration)

We have set up a new type of Compton backscattering polarimeter at the Mainz Microtron (MAMI) which uses the internal cavity design. To increase the limited luminosity achievable with commercial laser systems, the electron beam is guided directly through the resonator of the used laser. Intra-cavity intensities of up to 90W have been measured with polarization optics installed. In August 2003, first backscattered photons have been detected. In July 2004, we have measured first Compton asymmetries.

1. Introduction

The A4 experiment at the MAMI facility is designed to investigate the nucleon structure by measuring single-spin asymmetries in the elastic electron-nucleon-scattering with polarized beams. The measured asymmetry A_{exp} is related to the physics asymmetry via:

$$A_{exp} = P_e A_{phys} \quad (1)$$

P_e is the beam polarization, which therefore has to be monitored closely. For an absolute measurement, a Compton backscattering polarimeter using a new design approach has been installed in the A4 beamline.

2. Compton Polarimetry

Compton polarimetry is a long-proven method to determine the polarization of lepton beams [1]. The cross-section for polarized light on polarized electrons can be separated into four parts of different polarization dependence [2]:

$$\frac{d\sigma}{d\Omega} = \frac{d\sigma_0}{d\Omega} + Q \frac{d\sigma_l}{d\Omega} - V P_e^{long} \frac{d\sigma_{long}}{d\Omega} - V P_e^{tr} \cos\varphi \frac{d\sigma_{tr}}{d\Omega} \quad (2)$$

P_e^{long} and P_e^{tr} denote longitudinal and transverse electron polarization, Q and V the Stokes parameters describing the light polarization and φ the azimuthal photon scattering angle.

*This work is supported by the Deutsche Forschungsgemeinschaft and the U.S. DOE.

[†] comprises part of PhD thesis

When using circular light, switching the light or electron helicity leads to an asymmetry in the energetic and spatial photon distributions from which P_e^{long} and P_e^{tr} can be extracted. The luminosity depends on the focusing, intensities, and the crossing angle of both beams. The A4 experiment is run at $20\mu A$, so the maximum luminosity achievable with present-day commercial lasers is about $4kHz/barn$ (green light, $10W$ of power). Even under ideal conditions without background, this results in a statistical accuracy of only 5% in $15min$. In order to improve it, the light intensity has to be increased.

3. Polarimeter Layout

One method is to feed the laser beam into an external Fabry-Pérot (F-P) cavity. Such a system has been set up successfully [3], but needs a complex laser frequency stabilization due to the small bandwidth of high-gain cavities. We implement for the first time the 'internal cavity' approach [4]: the resonator of a laser is already a F-P cavity, and the output light only a fraction of the internally circulating light. We extend the cavity in length, use high-reflective mirrors at both ends and guide the electron beam through the resonator where it interacts with the higher intra-cavity intensity. A frequency stabilization is not necessary, because the laser medium adapts to cavity length fluctuations. However, the maximum power is lower than with an external cavity.

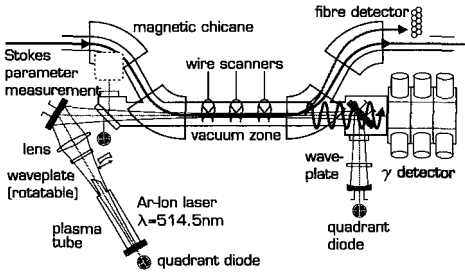


Fig 1. Schematic view of the polarimeter

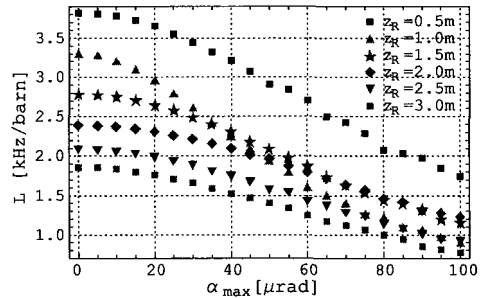


Fig 2. Average luminosity for different laser focusings as a function of mirror vibration amplitude

The polarimeter is shown schematically in Fig.1. The electron beam is deflected in a magnetic chicane so that a collinear beam geometry is possible. We use an Ar-Ion laser designed for $10W$ at $514.5nm$. A lens focuses the light in the interaction region while keeping the original profile in the laser medium. To establish overlap, the positions of both beams are measured simultaneously using three wire scanners. The backscattered photons have a maximum energy of $26.2MeV$ and are detected in a NaI calorimeter. The electrons involved in the scattering lose energy and are therefore displaced behind the chicane. A scintillating fibre array is used to detect them and improve the data quality using the coincidence technique. The circular polarization is created by two quarter waveplates. One is rotatable to select the light helicity. We use one vacuum window as a beamsplitter to extract 0.6% of the light and measure its polarization state.

In order to maximize the luminosity, a long overlap region is necessary. The resonator is therefore very long and vulnerable to vibrations of the optical elements. It now has a total length of 7.8m. All resonator parameters have been optimized in Monte-Carlo simulations to find the best compromise between required space, peak luminosity, and stability against beam axis fluctuations due to vibration (Fig.2). The chosen values allow for a luminosity of 2.1kHz/barn per 10W of laser power. In addition, a stabilization system for the laser beam position has been designed to reduce fluctuations and long-term drifts of the beam axis. The position is measured with quadrant diodes and stabilized using piezo tilt-platforms for selected mirrors, thereby keeping the overlap once established.

4. Status and Results

The beamline of the polarimeter has been set up in December 2002. The A4 experiment has been operated with chicane and the beam quality is not deteriorated. We have set up and commissioned the laser system. After installation of the polarization optics, intra-cavity powers of up to 90W have been measured. The system is stable and works reproducibly. We have developed procedures to establish beam overlap and were able to measure first backscattered photons in August 2003. The NaI calorimeter is calibrated using radioactive sources and muons from cosmic radiation, where the deposited energy is defined by confining the muon tracks with trigger scintillators.

In beginning of 2004 we have installed the electron detector, and were able to improve the signal-to-noise ratio from 1:7.1 to 1:2.1 by imposing a coincidence condition between electrons and photons. The laser beam stabilization system has been set up, and tests have shown significant reductions of beam axis fluctuations. On the beam splitter vacuum window, the long-term drift was reduced from 25 $\mu\text{m}/\text{h}$ to 0.7 $\mu\text{m}/\text{h}$, and the short-term fluctuations from 10 $\mu\text{m}/\text{h}$ to less than 1.1 $\mu\text{m}/\text{h}$. The measurement device for the laser Stokes parameters has also been installed and tested. In July 2004, we have performed first tests with circularly polarized light and were able to measure Compton asymmetries by switching the electron helicity. When inserting a half waveplate at the polarized electron source which interchanges the electron helicities, these asymmetries also clearly change sign (Fig.3).

With the results achieved so far, we are already able to reach a statistical accuracy for the asymmetry of 12% in 5min without laser beam stabilization. This value will improve when operating the polarimeter with stabilization. Systematic uncertainties for the extraction of the polarization can arise from the photon detector response and the measurement of the

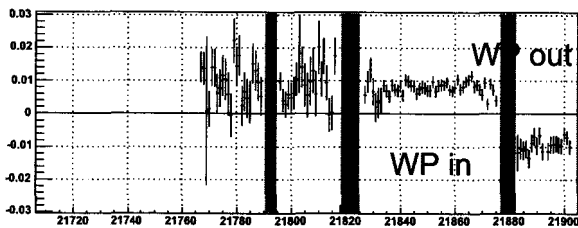


Fig 3. Average asymmetry over Compton energy range vs. run-number. The grey shaded areas are background runs.

laser polarization. Work is going on to control these sources.

We are also performing analyses of stress birefringence in the vacuum windows which alters the polarization state and keeps the circular polarization below the possible maximum. The statistical uncertainty will further im-

prove after solving this problem, because the analyzing power is proportional to the laser polarization. For the future, it is planned to install a position-sensitive photon detector to measure also the transverse electron polarization.

The internal cavity concept is a new and elegant approach to Compton polarimetry. Without background, a statistical accuracy of 2.5% in 15min seems achievable. Even with background, this value will be around 5%.

References

1. V. Baier and V. Khoze, *Sov. J. Nucl. Phys* **9**, 238 (1969)
2. F. Lipps and H. Tolhoek, *Physica* **XX**, 395 (1954)
3. N. Falletto et. al., *N.I.M.* **A459**, 412 (2001)
4. M. Düren, HERMES internal report **00-005** (2000)

FERROMAGNETIC THIN LAYERS FOR SPIN POLARIMETRY

D. LAMINE, G. LAMPEL, Y. LASSAILLY, J. PERETTI

Laboratoire de Physique de la Matière Condensée, CNRS - Ecole Polytechnique, Palaiseau, France

N. ROUGEMAILLE

Lawrence Berkeley National Laboratory, Berkeley, USA

We present a study of spin filtering effect in a ferromagnetic metal/semiconductor (Pd/Fe/oxide/GaAs) junction and discuss the application to electron spin polarimetry. Spin-polarized electrons are injected from vacuum in the metallic layer and the current I_C transmitted through the junction is collected in the semiconductor substrate. When reversing the magnetization of the Fe layer, a spin-dependent component of the transmitted current ΔI_C is measured. The transmission spin asymmetry $\Delta I_C/2I_C$ is proportional to the polarization P_0 of the incident electrons. Both I_C and ΔI_C increase over several orders of magnitude with the energy E_P of the incoming electrons. We show that adjusting E_P allows to optimize the measurement of P_0 .

1. Introduction

Spin analysis brings key information on scattering processes in high energy physics as well as in solid state physics. However, the measurement of free electron spin polarization still relies on heavy-handling techniques, based on Mott scattering or spin-polarized low energy electron diffraction [1–4], which require severe operating conditions (high voltage, surface preparation, . . .). The development of more convenient electron spin detectors would be of great interest especially in view of applications to spin-resolved electron spectroscopy and microscopy. The discovery of spin filtering effects in ultra-thin magnetic films [5–7] has offered a new possible approach of free electron spin polarization measurement; but, up to now, no spin-filtering polarimeter, as efficient as Mott detectors, is actually available.

Following a previous work [8], we present here an extended study of spin-dependent electron transmission in ferromagnetic metal/oxide/semiconductor junctions (FM/Ox/SC) as a function of the incident electron energy. We will show that adjusting the operating energy allows to increase by orders of magnitude the sensitivity, of such a device to the incident electron polarization, with an optimum operating energy of the order of 1 keV. We compare the characteristics of spin filters with Mott polarimeter and discuss further improvements.

2. Experiment

The principle of the experiment, schematized in Figure 1 (left), consists in measuring the spin-dependent transmission of electrons through a FM/Ox/SC junction.

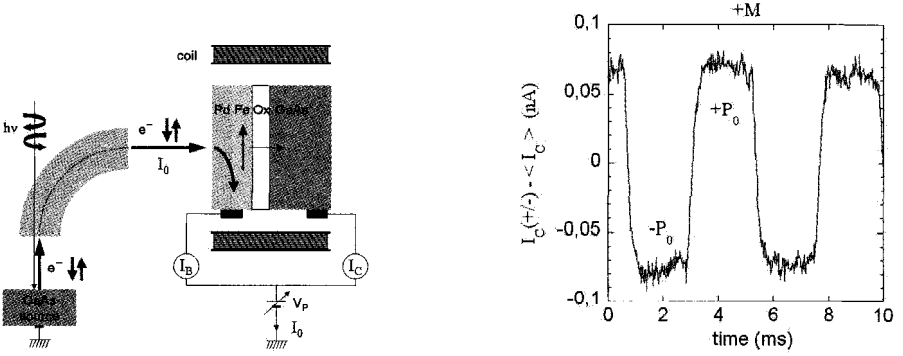


Fig 1. (Left) Schematic view of the experimental set-up. (Right) Variation of I_C , as a function of time, when reversing periodically the polarization P_0 of the incident electrons. $\langle I_C \rangle$ refers to the spin-independent part of the collected current I_C .

Under circularly-polarized light excitation, the GaAs source produces an electron beam of longitudinal spin polarization $P_0 = \pm 25\%$. After a 90° electrostatic deflection, the beam polarization is turned into a transverse one and the electrons are injected into the junction with an incident energy defined by the sample potential V_P and with a typical incident current I_0 of 40 nA. The sample is in-plane magnetized and the magnetization is oriented by pulse-operation of two magnetic coils. The currents I_B and I_C are measured independently, and verify in the whole energy range $I_0 = I_B + I_C$.

3. The Spin Filter as a Polarimeter : Analysis.

The spin filter effect is evidenced by measuring the change in the collected current I_C when modulating either the incident polarization (between $\pm P_0$) or reversing the Fe layer magnetization (from $+M$ to $-M$). This effect is shown in Figure 1 (right). I_C varies between two values : $I_C^\pm = (T \pm \Delta T)I_0 = TI_0(1 \pm SP_0)$. In this expression, T is the average transmission $T = \frac{I_C^+ + I_C^-}{2I_0}$, ΔT the spin dependent part of the transmission $\Delta T = \frac{I_C^+ - I_C^-}{2I_0}$ and S the Sherman function of the spin filter, i.e. the spin discriminating power which relates the transmission asymmetry to the incident polarization $P_0 = \frac{1}{S} \frac{\Delta T}{T}$. The quantities T and S characterize the quality of the polarimeter.

The uncertainty δP_0 on the determination of P_0 is related to the noise δI_C^\pm in the measurement of I_C^\pm and, in a bandwidth $\Delta\nu$, is given by : $(\delta I_C^\pm)^2 = 2e\Delta\nu I_C^\pm (1 + I_C^\pm/I_0) + 4k_B\tau\Delta\nu/R + (\delta i)^2$, where τ is the temperature. The first term in the above expression is the shot noise on I_C^\pm . In the present experiment, the amplifier noise $(\delta i)^2$ can be neglected with respect to the Johnson noise $4k_B\tau\Delta\nu/R$. Introducing the saturation current of the junc-

tion $I_S = k_B \tau / eR$ ($\approx 0.6 \mu A$ in the present experiment) and neglecting $(SP_0)^2$ with respect to unity, one gets straightforwardly :

$$(\delta P_0)^2 \approx \frac{2e\Delta v [T(1+T)I_0 + 2I_S]}{2(STI_0)^2} \tag{1}$$

Two cases can be distinguished depending on the relative value of the quantities $2I_S$ and $T(1+T)I_0$. When $2I_S \gg T(1+T)I_0$, the measurement is limited by the Johnson noise of the junction, and one gets $(\delta P_0)^2 \approx \frac{2e\Delta v I_S}{(STI_0)^2}$. When $2I_S \ll T(1+T)I_0$, the measurement is limited by the shot noise, and then $(\delta P_0)^2 \approx \frac{\Delta v e}{I_0} \frac{1+T}{S^2 T}$. As S and T strongly depend on the incident electron energy E_P , the uncertainty on the measurement of P_0 can be consequently minimized by adjusting E_P .

4. Results

Figure 2 shows a logarithmic plot of the transmission T , its spin dependency ΔT , and the Sherman function S as a function of E_P . Between $E_P = 250 \text{ eV}$ and $E_P = 500 \text{ eV}$, ΔT in-

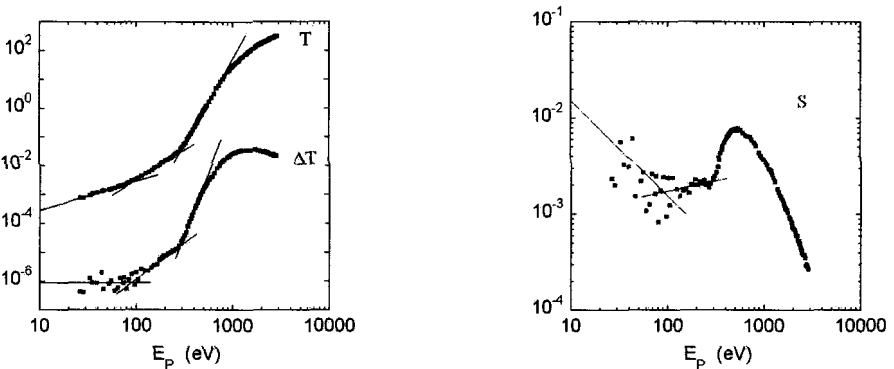


Fig 2. (Left) Variation of the transmission T and its spin dependency ΔT , and (right) of the Sherman function S , deduced from the expression : $SP_0 = \Delta T/T$, where $P_0 = 25\%$, as a function of the incident electron energy E_P .

creases dramatically, even faster than T , by about three orders of magnitude, yielding a net increase of S by about a factor 4 in this energy range. The different features in the variation of T , ΔT and S are related to different regimes of hot-electron transport through the metal layer. This transport is dominated by electron-electron collisions [9] yielding efficient secondary electron excitation which has two main consequences : current multiplication and correlated polarization dilution. A detailed analysis based on a transport model taking into account the Schottky and the oxide barriers will be presented elsewhere [10]. Here, we will focus on the behavior, versus operating energy, of the spin-polarimeter characteristics of the junction. According to (1), the increase in T , when increasing the incident energy E_P , may allow to reach a shot-noise-limited detection regime. In such a regime, the noise δI_C should increase proportionally to $[I_C(1+I_C)]^{1/2}$, i.e. first to $I_C^{1/2}$ and then to I_C . The

experimental values of δI_C measured (with a bandwidth of 1Hz) when increasing E_P up to 3 keV are plotted, as a function of I_C , in Figure 3 (left-hand curve). For low values of I_C , i.e. for low injection energy, δI_C remains constant because the Johnson noise dominates. At higher I_C , δI_C increases and becomes proportional to I_C , indicating that the measurement is limited at high E_P by the shot noise term proportional to I_C . Let us now consider the quantity F defined as :

$$F = \frac{e\Delta\nu}{I_0} \frac{1}{(\delta P_0)^2} \simeq \frac{S^2 T^2}{T(1+T) + 2I_S/I_0}$$

For the Mott detector, F represents the figure of merit and takes a typical value of about 10^{-4} . In our FM/Ox/SC junction, the variation of F as a function of E_P , deduced from the experimental values of S and T , is plotted in Figure 3 (right-hand graph). The curve, obtained for $I_0 = 40$ nA, yields $2I_S/I_0 = 30$ and shows an optimum value of F of $2 \cdot 10^{-5}$, for $E_P = 700$ eV. When decreasing the incident current I_0 , the optimum shifts towards higher energy and F decreases. Indeed, in order to reach the detection regime limited by the shot noise, one has to increase T . This is obtained by increasing E_P , but up to a range where S starts to decrease.

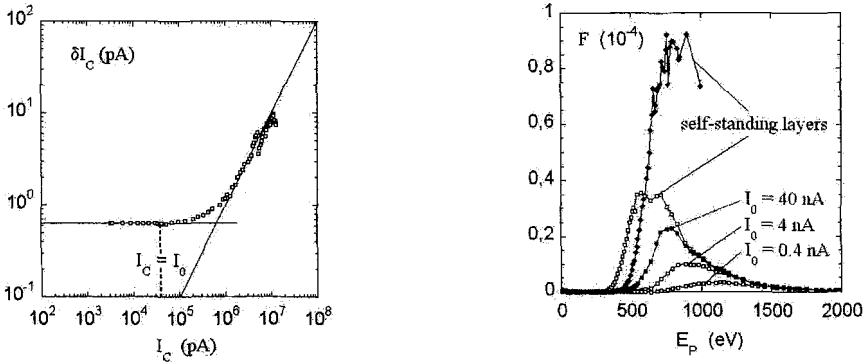


Fig 3. (Left) Experimental variation of δI_C versus I_C for $\Delta\nu = 1\text{Hz}$. (Right) Variation of F with E_P for $I_0 = 40$ nA, 4 nA, 0.4 nA, i.e. for $2I_S/I_0 = 30, 300, 3000$. The variation of F , that one would obtain if $2I_S/I_0 = 0$, is plotted for two different structures : Pd(2nm)/Fe(2.5nm) (opened symbols) and Pd(5nm)/Fe(3.5nm) (plain symbols).

In order to improve F for low incident currents, one can decrease the Johnson noise by improving the quality of the junction, reducing the area of the junction or cooling down its temperature. In any case one would then be limited by the constant noise in the measurement of an analog current. The decisive improvement would be to eliminate the junction. This could be obtained by measuring the spin dependent transmission through self-standing magnetic layers [6]. In such a configuration, the electrons would be re-emitted into vacuum over the work-function barrier 5 eV (comparable with the oxide layer barrier height) of the back metallic layer surface. Then counting techniques can be used and the detection

would be only limited by the shot noise. The figure of merit would be therefore independent on I_0 : $F = \frac{S^2 T}{1+T}$. The variation of F that one could expect with a self-standing layer of same characteristics (2nm-Pd/2.5nm-Fe) is plotted in Figure 3 (right) (open symbols). An optimum value of about $3.5 \cdot 10^{-5}$ is obtained at E_P of the order of 600 eV. The value of F could even be further improved by optimizing the thicknesses of the metallic layers. Indeed, we have performed experiments on a junction of different characteristics : Pd(5nm)/Fe(3.5nm)/Ox/GaAs. We have measured S and T as a function of E_P . From these measurements, we have deduced the variation of F that one would obtain for a self-standing layer made of 5 nm of Pd and 3.5 nm of Fe (plain symbols in Figure 3 (right)). The optimum value of F is reached in an incident energy range between 700 eV and 900 eV. In this operating energy range, F is comparable to the typical figure of merit of a Mott detector.

5. Conclusion

We have presented a study of spin-polarized electron transport in ferromagnetic metal/oxide/semiconductor junctions, when varying the incident energy of the incident electrons from 20 eV to 3 keV, and we have discussed the potentiality of magnetic spin-filters in terms of applications to spin polarimetry. We have shown that, increasing the operating energy allows to reach an electron transport regime in the metallic layer which favors the improvement of the spin sensitivity of the device. Values of the figure of merit comparable with a Mott detector could be predicted for realistic self-standing magnetic layers under operation at energy of the order of 1 keV. Such a polarimeter may have many advantages, when compared to available instruments, because of its compactness, low operation voltage, insensitivity to surface chemical contamination.

References

1. N. F. Mott, *Proc. R. Soc. London* **124**, 425 (1929).
2. V. N. Petrov, V. V. Grebenshikov, B. D. Grachev, and A. S. Kamochkin *Rev. Sci. Instrum.* **74**, 1278 (2003).
3. J. Kessler, *Polarized electrons*, Springer-Verlag, Berlin (1985).
4. J. Kirschner, *Polarized electrons in surface physics*, ed. by R. Feder, World Scientific Publishing, Singapour (1985).
5. G. Schönense and H. C. Siegmann, *Ann. Physik* **2**, 465 (1993).
6. Y. Lassailly, H.-J. Drouhin, A. Van der Sluijs, G. Lampel, and C. Marliere, *Phys. Rev.* **50**, 13054 (1994).
7. H.-J. Drouhin, A. Van der Sluijs, Y. Lassailly, and G. Lampel, *J. Appl. Phys.* **79**, 4734 (1996).
8. N. Rougemaille, G. Lampel, J. Peretti, H.-J. Drouhin, Y. Lassailly, A. Filipe, T. Wirth and A. Schuhl, *Proceedings of the 15th International Spin Physics Symposium and Workshop on Polarized Electron Sources and Polarimeter*, ed. by Y. I. Makdisi, A. V. Luccio and W. W. MacKay; *AIP Conference Proceedings*, 675 (2002).
9. A. J. Dekker, *Secondary Electron Emission, in Solid State Physics*, ed. by F. Seitz and D. Turnbull, *Academic Press*, **6**, 251-311 (1958).
10. N. Rougemaille, G. Lampel, Y. Lassailly, and J. Peretti, *to be published*.

HIGHLY-POLARIZED ELECTRON EMISSION FROM STRAIN COMPENSATED InAlGaAs -GaAsP SUPERLATTICES

A. V. SUBASHIEV, L. G. GERCHIKOV, Y. A. MAMAEV, Y. P. YASHIN

St. Petersburg State Polytechnic University, St. Petersburg, Russia

J. S. ROBERTS, P. A. HOUSTON

Department of Electronic Engineering University, Sheffield, UK

D. LUH, T. MARUYAMA, J. E. CLENDENIN

Stanford Linear Accelerator Center, Menlo Park, USA

New results from experimental and theoretical studies of spin-polarized electron emission from InAlGaAs-GaAsP superlattice photocathodes with opposite strain in the quantum well and barrier layers are presented. The measured values of maximum polarization and quantum yield for the structure with a 0.18 μm -thick working layer are close to the best results reported for strained superlattice photocathode structures, demonstrating the high potential of strain compensation for future photocathode applications. An analysis of the photoemission spectra is used to estimate the parameters responsible for the polarization losses.

Highly spin-polarized electron photoemission from strained short-period superlattice (SL) structures have been the subject of a number of studies; e.g., see [1–3]. In these structures, the heavy-hole (hh) and light-hole (lh) minibands are split due to the difference in the hh and lh confinement energies in the SL quantum wells, which adds to the separation due to strain alone. The enlarged valence band splitting results in a high initial electron polarization in the conduction band under excitation by circularly polarized light. However, the thickness of the stressed photocathode working layer necessary for achieving a high value of quantum yield exceeds the critical thicknesses for strain relaxation, which results in structural defects, smaller residual strain and thus lower polarization. To overcome these problems the use of strain-compensated structures with the composition of the SL barrier layers chosen to have opposite (tensile) strain from that of the quantum well layers was

proposed [4]. Thus considerably larger strain values in the SL wells can be achieved with no limitations on the overall thickness of the SL structure [5], which should ensure high electronic polarization. Here we present the results of the studies of these SLs.

The SL structures were grown by metal-organic vapor phase epitaxy (MOVPE), which provides high structural quality and low defect densities at the interfaces [6]. The working layer consisted of 8 to 30 pairs of compressively strained $\text{In}_x\text{Al}_y\text{Ga}_{1-x-y}\text{As}$ quantum well layers alternated by tensile strained $\text{GaAs}_z\text{P}_{1-z}$ barrier layers. On top of the SL working layer a 6-nm thick GaAs surface layer was deposited with Zn - doping concentration enlarged to $1 \times 10^{19} \text{ cm}^{-3}$.

The range of available compositions of the $\text{In}_x\text{Al}_y\text{Ga}_{1-x-y}\text{As}$ quantum well layer is restricted to x values which give maximum valence band splitting while retaining a high structural quality (i.e. $x \approx 16\text{-}18\%$) and the y values that result in the SL band gap larger than that in GaAs ($y \geq 12\%$). The phosphorus content in the $\text{GaAs}_z\text{P}_{1-z}$ barrier layers should provide sufficient deformation to compensate strain in the wells. However at large z values the SL becomes of a type II for the light holes so that the energy splitting of the hh1-lh1 minibands is lowered. To test this variation three sets of samples with $z = 8, 17$ and 18% various working-layer thicknesses were studied.

The experimental quantum yield, $Y(h\nu)$, and polarization, $P(h\nu)$, spectra (for pre-activation heating temperature T_h close to optimal) for the photocathode based on $\text{In}_{0.18}\text{Al}_{0.14}\text{Ga}_{0.68}\text{As}\text{-GaAs}_{0.83}\text{P}_{0.17}$ SL containing 20 periods with 5 nm-thick wells and 4-nm barriers is presented in Fig. 1. The parameters of the photocathode, i.e. the maximum polarization value, $P_{max} = 84\%$, and yield at the maximum, $Y(h\nu) = 0.4\%$, are close to the best results reported for any strained superlattice photocathode structures, evidencing the high potential of strain compensation. The spectral dependence of $P(h\nu)$ shown in Fig. 1 is typical for all considered samples. It includes a high-polarization peak at the band-edge absorption and a second peak at higher energies with a well pronounced dip between them. These features follow the sequence of the miniband transitions hh1 \rightarrow e1, hh2 \rightarrow e2 and lh1 \rightarrow e1 respectively, the edges of these transition being close to the energies corresponding to maximal slope in $P(h\nu)$ are shown in Fig. 1 by the vertical lines.

To estimate the photocathode parameters, we have calculated optical absorption and the initial polarization of photoelectrons in the working layer as a function of excitation energy using the multiband Kane model [7]. The electron depolarization during the transport to the surface and emission into vacuum was assumed to be 5% [8]. The calculated maximum polarization value at the top of the first polarization maximum is sensitive to the broadening of the absorption edge associated with two mainfactors. The first is the inter band absorption smearing due to the band edge fluctuations, which can be evaluated by fitting the $Y(h\nu)$ dependence. The second factor originates from the processes of hole scattering between the hh and lh states, which leads to a non-zero contribution of the lh1 miniband to the absorption near the edge and that populates the second spin state. The calculated spectra for scattering rate $\gamma = 7 \text{ meV}$ and smearing energy $\delta = 11 \text{ meV}$ are depicted in Fig. 1 by the dashed line giving the maximum value of electron polarization $P_{max} \approx 92\%$.

Note that a sizeable decrease of the polarization maximum comes from the surface

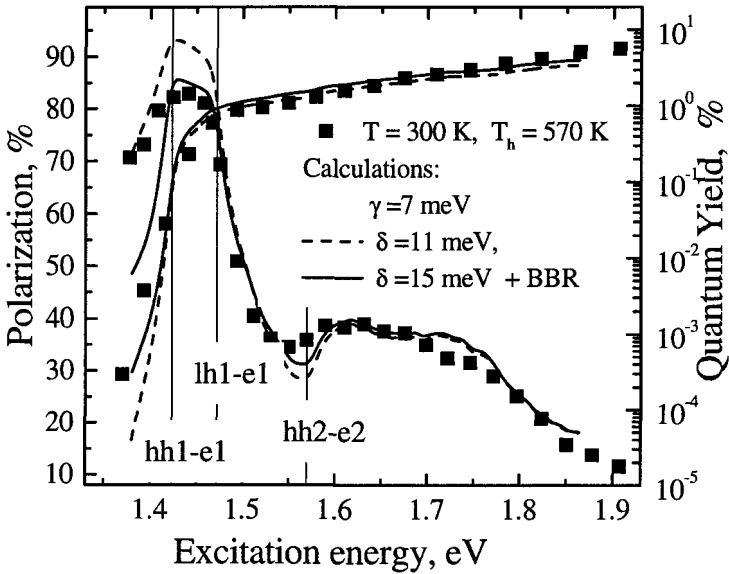


Fig 1. Polarization and quantum yield spectra of the emitted photoelectrons for $\text{In}_{0.18}\text{Al}_{0.14}\text{Ga}_{0.68}\text{As-GaAs}_{0.83}\text{P}_{0.17}$ superlattice and the calculated energy dependence of $P(h\nu)$ and $Y(h\nu)$ spectra with the valence band smearing and hole scattering (dashed), and with the contribution of the BBR added (solid lines).

CaAs layer (BBR) since it has smaller band gap and the polarization of electrons excited in this layer does not exceed 50%. The results of the calculation of the $P(h\nu)$ and $Y(h\nu)$ spectra allowing absorption in a BBR layer with a thickness of 10 nm are shown in Fig. 1 by the solid line. The good agreement with experimental data shows the importance of this contribution to the total polarization losses.

To summarize, newly designed photocathode superlattice structures with strain compensation have been grown and studied as candidates for highly polarized electron emission. These photocathodes are based on InAlGaAs-GaAsP structures grown by MOVPE. The structures are found to be advantageous due to the prevention of strain relaxation and the smaller relative contribution of the BBR region in comparison with strained-well structures.

This work was supported by CRDF under grant RP1-2345-ST-02, by NATO under grant PST.CLG 979966, by Russian Ministry of industry, science and technology under contracts # 40.012.1.1.1152 and #40.072.1.1.1175, by UK EPSRC under grant GR/R65534/01, and also supported in part by the U.S. Department of Energy under contract DE-AC02-76SF00515.

References

1. T. Omori, Y. Kurihara, Y. Takeuchi, M. Yoshioka, T. Nakanishi, S. Okumi, M. Tsubata, M. Tavada, K. Togava, Y. Tanimoto, C. Takahashi, T. Baba and M. Mixuta, *Jpn. J. Appl. Phys.*, **33**, 5676 (1994).

2. T. Saka, T. Kato, T. Nakanishi, S. Okumi, K. Togava, H. Horinaka, T. Matsuyama, and T. Baba, *Surf. Sci.* **454-456** 1042 (2000).
3. T. Maruyama, D.-A. Luh, A. Brachmann, J. E. Clendenin, E. L. Garvin, S. Harvey, J. Jiang, R. E. Kirby, C. Y. Prescott, R. Prepost, and A. M. Moy, SLAC-Pub-10331, Feb. (2004)
4. Yu. P. Yashin, J. S. Roberts, L. G. Gerchikov, P. A. Houston, A. N. Ipatov, Yu. A. Mamaev, A. V. Rochansky and A. V. Subashiev, *11th Int. Symp. "Nanostructures: Physics and Technology" (NANO 2003)* (St. Petersburg, 2003) p. 61.
5. J.C. Dries, M.R. Gokhale, K.J. Thomson, S.R. Forrest, *Appl. Phys. Lett.* **73**, 2263 (1998).
6. R.P. Green, A. Krysa, J.S. Roberts, D.G. Revin, L.R. Wilson, E.A. Zibik, W. H. Ng, and J. W. Cockburn, *Apl. Phys. Lett.* v. 83, 1921(2003).
7. A.V. Subashiev, L. G. Gerchikov, A. N. Ipatov *Journ. Appl Physics* **96**, 1511 (2004).
8. K. Aulenbacher, J. Schuler, D. v. Harrach, E. Reichert, J. Roethgen, A. Subashev, V. Tioukine, Y. Yashin, *J. Appl. Phys.*, **92**, 7536 (2002).

LASER DEVELOPMENT FOR FUTURE PHOTOCATHODE RESEARCH AT SLAC*

A. BRACHMANN, K. CONE, J. E. CLENDENIN, E. L. GARWIN, R. E. KIRBY, D. LUH, T. MARUYAMA,
R. PREPOST, C. Y. PRESCOTT

Stanford Linear Accelerator Center, Menlo Park, USA

This report summarizes results of recent upgrades to SLAC's polarized source drive laser system. A Q-switching system has been incorporated into the flashlamp-pumped Ti:Sapphire laser system. The Q-switched laser provides energies up to 5 mJ for a 200 ns long pulse. Slow Q-switching provides control over length and shape of the laser pulse. A peak current of > 5.5 A has been demonstrated using a GaAs photocathode illuminated by this laser system.

1. Introduction

Since 1993 a flashlamp-pumped Ti:Sapphire laser is used at SLAC polarized electron source. Details about this system and its modifications can be found in the literature [1]. This paper describes modifications of the laser cavity and summarized results of Q-switched operation. The motivation for this work was to increase the laser pulse energy available for photocathode research. An important aspect was to develop a system that provides flexibility for future photocathode research projects.

2. Laser Cavity Modifications

Two Pockel's cells have been introduced into the Ti:Sapphire cavity and allow controlled electro-optical switching of the stimulated emission. Figure 1 shows a scheme of the cavity layout.

One Pockel's cell is operated such that the HV pulse acts as an inhibitor of stimulated emission and thereby increasing the population of the upper lasing level. The amount of stored energy can be controlled by HV pulse height and length and relative timing of flashlamp and Pockel's cell trigger. A second Pockel's cell is operated as a slow Q-switch by applying a ramped HV pulse. A programmable function generator determines the overall length and slope of the ramp. This allows controlled release of the stored energy. The result is a flexible system with adjustable energy, length and shape of the laser pulse. Also,

*This work is supported by Department of Energy contract DE-AC02-76 SF00515.

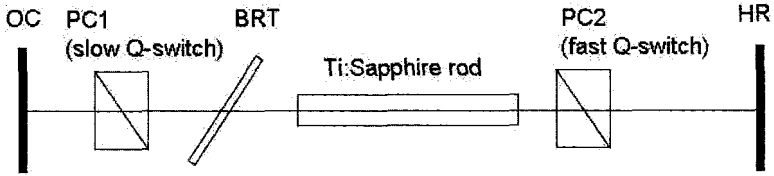


Fig 1. Scheme of Ti:Sapphire laser cavity; OC: output coupler, PC: Pockel's cell, BRT: birefringent tuner, HR: high reflector

concerns regarding optical damage can be addressed by controlled switching of the laser cavity. We performed a large number of experiments to determine the optimum operating conditions for the use of this laser system at our polarized source.

3. Results

Q-switched operation using only one Pockel's cell with a square switching pulse of 600 ns produced a 5 mJ pulse with a Gaussian temporal shape of ~ 200 ns FWHM. This is an increase of laser energy by one order of magnitude compared to un-Q-switched operation. Further energy increase is possible by extending the length of the 'hold-off' pulse. To reduce the risk of optical damage of cavity components we decided not to explore laser energies above 5 mJ. A comparison of both operational modes is given in Figure 2.

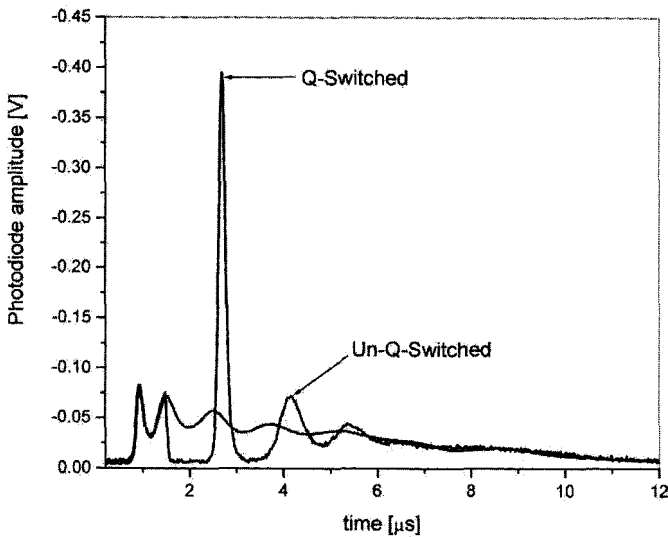


Fig 2. Temporal pulse shape comparison of Q-switched and un-Q-switched cavity.

The second Pockel's cell is used for slow release of the stored energy. A pulse length of ~ 1000 ns was achieved. Appropriate relative timing of the square 'hold-off' and shaped

'release' also allows temporal shaping of the pulse. Figure 3 illustrates the evolution of the pulse's profile when the timing of 'hold-off' and 'release' is varied with respect to each other. Initial experiments at our test facility result in an peak electron beam current in excess of 5.5 A. Figure 4 compares the performance of a strained GaAs cathode when used with standard and Q-switched laser system.

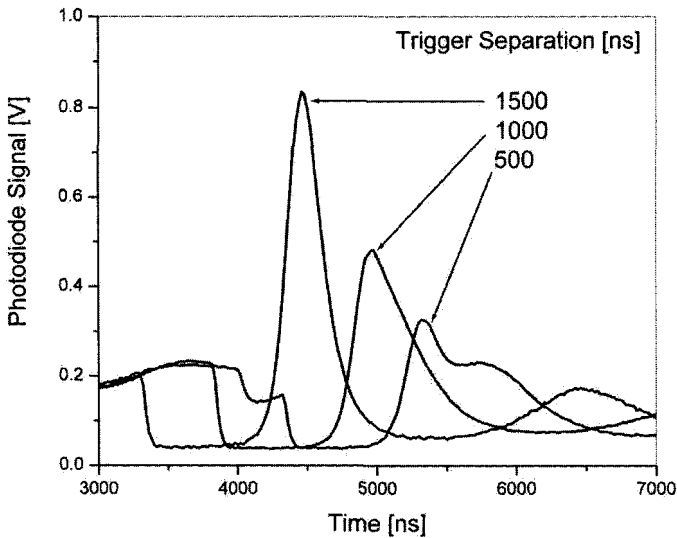


Fig 3. Illustration of temporal pulse shaping effect by separation of Pockel's cell trigger (PC1 and PC2).

4. Summary

SLAC's flashlamp-pumped Ti:Sapphire polarized source laser has been successfully modified for Q-switched operation and provides pulse energies in excess of 5 mJ. A peak current of > 5.5 A has been extracted from a strained GaAs cathode. Appropriate timing of cavity Pockel's cells allows flexibility in pulse energy and shape.

References

1. T. B. Humensky et al., *Nucl. Instrum. Meth.* **A521**, 261 (2004).

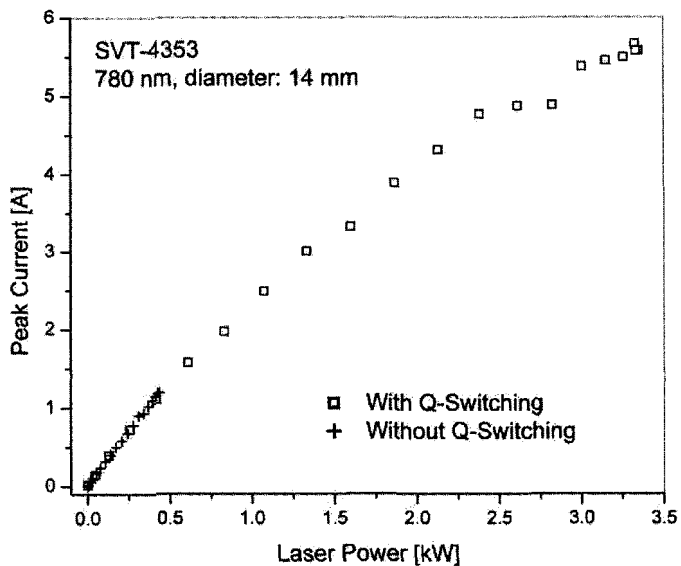


Fig 4. Cathode peak photo-current vs. laser power.

PERFORMANCE OF THE COLD PHOTOCATHODE GUN AT THE ELECTRON TARGET OF THE HEIDELBERG TSR

D. A. ORLOV, U. WEIGEL, M. LESTINSKY, F. SPRENGER

Max–Planck–Institut für Kernphysik, Heidelberg, Germany

A. S. TEREKHOV

Institute of Semiconductor Physics, Novosibirsk, Russia

D. SCHWALM, A. WOLF

Max–Planck–Institut für Kernphysik, Heidelberg, Germany

A source of ultra cold (≤ 10 meV) magnetically guided *dc* electron beams with a transmission mode GaAs-photocathode recently started to be operated at the electron target of the Heidelberg Test Storage Ring. Photocathodes, cooled by liquid nitrogen, show lifetimes of about 10–15 hours at 0.2 mA currents. Atomic hydrogen cleaning was found extremely useful to keep the photocathodes in a closed cycle of operation without removing them from the vacuum setup and allows accordingly almost non-stop measurements with a cold electron target.

1. Introduction

A cold intense electron source with a GaAs photocathode has been developed for the Heidelberg TSR to study inelastic electron-ion interactions [1–3]. Photoemitted electrons are extracted in the space charge mode and then undergo adiabatic magnetic expansion as well as adiabatic acceleration to obtain an ultra cold electron beam which is overlapped with the stored ion beam in a straight section of the ring. The first merged beam experiments with a cold electron target demonstrated unprecedented resolution with a transverse temperature of the electron beam below 1 meV [4, 5].

In this paper the performance of the cathode under experimental conditions will be described and attention will be paid to atomic hydrogen cleaning which allows us to use the photocathodes in a close cycle of operation without removing them from the vacuum setup.

2. Setup and photocathode handling

We use transmission mode GaAs photocathodes consisting of a two layer GaAs/AlGaAs heterostructure bonded to a sapphire substrate. The vacuum setup consists of a loading, a preparation and a gun chamber, separated by all-metal gate valves, with base pressures of 10^{-10} , 10^{-12} and 3×10^{-11} mbar, respectively. Inside the vacuum the samples are transferred by magnetically coupled feedthroughs. In the preparation chamber samples are fixed on a carousel capable to keep four cathodes. The carousel can be rotated into different positions for thermal cleaning and activation of the photocathodes with cesium and oxygen. The quantum yield of a fully activated cathode is about 20-25%, while the effective quantum yield of cold electrons is about 1-2% [6]. In the electron gun the sapphire substrate of the cathode is pressed to the copper cold head by a spring force of 100 N in order to obtain a good thermocontact [3]. The photocathode is illuminated in transmission mode with a 800 nm diode laser capable to apply a power of 1.7 W. The photocathode is run in the space charge mode. The gun perveance is about $1 \mu\text{Perv}$.

3. Atomic hydrogen cleaning

Cleaning of a GaAs surface based on atomic hydrogen exposure is found to remove effectively contaminations as well as As- and Ga-oxides even at moderate temperatures (300–450°C). Common sources of atomic hydrogen are based on plasma discharge, on hot tungsten filaments, or on capillary cracking. To avoid the risks of higher energetic particles hitting the cathode surface, of pollution by evaporated tungsten and of uncontrolled heating of the sample we have built a capillary source, originally proposed by Bischler and Bertel [7]. It basically consists of a tungsten capillary traversed by molecular hydrogen and heated at the outlet by electron bombardment. The capillary temperature of only about 1500–1700°C is enough to achieve nearly total H_2 dissociation. The atomic hydrogen leaves the capillary with a narrow angular distribution.

The atomic hydrogen source (Fig.1) is attached to the loading chamber, equipped with a turbo pump (Pfeiffer, TPH 180). The base pressure of about 10^{-10} mbar is reached after one day of a chamber baking at 150–180°C. Before hydrogen treatment of the cathode the capillary and filaments are outgassed carefully for about one hour. The parameters of the source were optimized to reach the best quantum yield for samples which degraded due to multiple heating and (Cs,O) re-activation.

Molecular hydrogen is supplied to the vacuum system by diffusion through a Pd-filter heated to about 200°C. The flux of the hydrogen is regulated by a leak valve. Hydrogen pressure at the entrance of the capillary was monitored by a Pirani gauge. The recovering effect of the photocathode was found to be independent on the H_2 doses in the test range between $10 \text{ min} \times 0.2 \text{ mbar}$ to $60 \text{ min} \times 2 \text{ mbar}$. Molecular hydrogen reaches the tungsten capillary through a supply tube connected via an insulated ceramic. The capillary is about 50 mm long and has an internal diameter of 0.6 mm. Close to the front end of the capillary a thoriated tungsten filament of 0.2 mm diameter is located. A filament emission current of about 45 mA and acceleration voltage of 500 V heats the front end (about 5 mm) of the capillary to about 1600°C. Water cooled copper shielding with an opening of 2 mm

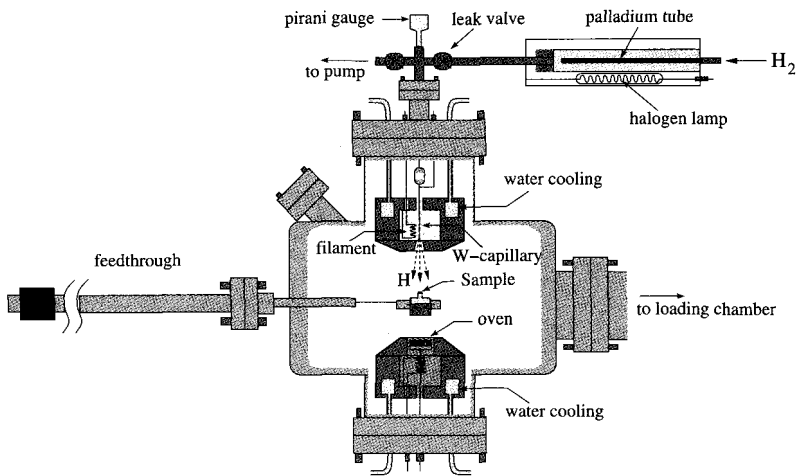


Fig 1. Outline of the atomic hydrogen chamber attached to the loading chamber

diameter prevents the sample from radiation heating by the tungsten filament and by the capillary.

To perform the atomic hydrogen cleaning the sample is kept by a holder at the manipulator head and positioned 30 mm underneath the capillary outlet. An oven heats the cathode radiatively from below up to about 420–470°C. It takes about 15 min to reach the final temperature and then atomic hydrogen is applied for about 10 min. The working molecular hydrogen pressure was about 1–2 mbar, while the hydrogen pressure in the main part of the chamber was below 10^{-5} mbar. After this procedure we close the leak valve and when the pressure falls below 10^{-9} mbar (in 10–15 min) the cathode is transferred to the preparation chamber. Then additional heating (30–40 min up to 450°C and 5 min at 500°C) and subsequent (Cs,O)-activation are applied.

4. Photocathode performance

Presently the photocathodes, cooled with liquid nitrogen, are typically run at emission currents of about 0.2 mA during 10–15 hours with a current stability of about 5%. Then the electron current rapidly falls down due to the rise of the work function so that the vacuum level reaches the position of the conduction band in the bulk. The increase of the current from 0.2 mA to about 1 mA decreases the lifetime of the cathode to about 1 hour. Measurements of electron current profiles show “black” zones, while the rest of the cathode still demonstrates high current performance. The picture of degradation is known to be due to a back-stream of ions, ionized by electrons in the acceleration section, where the vacuum conditions are not optimal. Another problem encountered is the fast degradation of cathodes if the temperature approaches LN₂ temperature. It was never observed previously in the test setup, where the vacuum conditions were better. The reason of this degradation might be cryosorption of the rest gas (such as CH₄, CO). At present, the temperature of the cathodes is kept slightly above LN₂ temperature to avoid fast degradation due to gas

condensation.

The problems with relatively bad vacuum conditions in the gun region are connected with the following reasons. The acceleration section of 1.5 m length is pumped only from the sides, where pressures of $3\text{--}5 \times 10^{-11}$ mbar are measured. There is a limitation of 180°C for the baking temperature of the acceleration tube, much lower than the temperature for bakeout of the photocathode chamber (250–300°C). Hence, wall-outgassing of the acceleration tube can be relatively high and due to the limited conductance of the long tube (which has a diameter of 0.1 m) the pressure inside the tube can be much higher than that at the sides. In addition the electron current, reflected from the collector, partly returns to the electron gun following the magnetic field, and hits the electrodes close to the cathode. This is an additional source of outgassing at high electron currents. Clearing electrodes at the toroid sections help to decrease this effect but it still has to be optimized. The installation of a cryofinger close to the cathode is planned to improve the vacuum.

As soon as the cathode starts to show a current decrease it is changed against another one stored in the preparation chamber. It takes about 5 min to change the sample and then about 20 min to cool the cathode down close to LN₂ temperature. The samples were usually re-used 3–5 times by radiative heating and re-activation in the preparation chamber before they lose their performance. Sometimes, after re-activation the samples showed strong photovoltage effects at low temperatures despite high quantum yields and long lifetimes at room temperature. The heating of these samples at higher temperatures did not solve the problem with the photovoltage.

An atomic hydrogen cleaning technique was used to recover the properties of the cathode by removing contaminations, as well as As- and Ga-oxides and old (Cs,O) layers. With hydrogen cleaning, the cathodes were recovered with respect to photovoltage and no degradation of quantum yield and energy spreads were found even after multiple cycles (15 times) of atomic hydrogen treatment of the cathodes. In total, we had 4 samples which were used for all measurements starting from June 2004 without removing them from the vacuum chamber.

5. Conclusion

A new source of cold electrons with a GaAs photocathode was developed for electron-ion merged experiments at the Heidelberg TSR. It provides electrons with energy spreads below 10 meV at currents of 0.2 mA and lifetimes of about 10–15 hours. With atomic hydrogen cleaning the performance of the photocathodes was recovered inside the UHV setup. This strongly simplified the operation of the target and allowed us to run the target in almost non-stop mode.

References

1. D.A. Orlov, M. Hoppe, U. Weigel, D. Schwalm, A.S. Terekhov and A. Wolf, *Appl. Phys. Lett.* **78**, 2721 (2001).
2. D.A. Orlov, U. Weigel, D. Schwalm, A.S. Terekhov and A. Wolf, *NIM A* **532**, 418 (2004).
3. U. Weigel, D.A. Orlov, S.N. Kosolobov, D. Schwalm, A.S. Terekhov and A. Wolf, *NIM A*, in press (2004).

4. D.A. Orlov, F. Sprenger, M. Lestinsky, U. Weigel, D. Schwalm D and A. Wolf, *Journal of Physics: Conference Series*, to be published (2005).
5. H. Buhr *et al*, to be published (2005).
6. D.A. Orlov, U. Weigel, M. Hoppe, D. Schwalm, A.S. Terekhov and A. Wolf, *Proceedings of the 9-th International Workshop on Polarized Sources and Targets*, ed. by V.P. Derenchuk and B. v. Przewoski, 151 (2001).
7. U. Bischler and E. Bertel, *J. Vac. Sci. Technol. A* **11**, 458 (1993).

LIFETIME MEASUREMENTS USING THE JEFFERSON LAB LOAD-LOCK ELECTRON GUN

J. GRAMES, P. ADDERLEY, M. BAYLAC, J. BRITTIAN, D. CHARLES, J. CLARK, J. HANSKNECHT,
M. POELKER, M. STUTZMAN, K. SURLES-LAW

Thomas Jefferson National Accelerator Facility, Newport News, USA

Lifetime measurements of bulk GaAs using a 100 kV load-lock electron gun and beam line were made. Initial tests used anodized samples to study lifetime under various conditions (gun vacuum, laser spot location, activated area). Subsequent tests used a mechanical mask to limit the active area and included improved monitoring of the gun chamber and beam line vacuum pressure. Results of these measurements support claims made at past workshops, namely photocathode lifetime improves when gun vacuum is enhanced and when electron emission from the edge of the photocathode is eliminated. The dependence upon laser spot location is less certain. Tests studying lifetime at higher beam intensity ($I \sim 8$ mA) have begun.

1. Introduction

Present and future accelerators require photocathodes having high and sustainable quantum efficiency (QE). For example, the CEBAF photoinjector at Jefferson Laboratory must provide up to 200 μ A of polarized electrons for long periods of time (about 20 C/day) without interruption. Long photocathode lifetime benefits the nuclear physics program because experiments are not interrupted to replace or repair photocathodes. Future accelerators expect to operate at even higher currents. Of course, if QE is initially exceptionally large or laser power is unlimited, then then degradation of QE might be tolerable, but these conditions are not practical. Additionally, non-uniformities in QE across the illuminated photocathode surface may be intolerable for some parity violation experiments because of position dependent charge asymmetry.

2. Experiment Configurations

Photocathode lifetime is defined as the amount of charge extracted as the QE falls to 1/e of the initial value. A series of measurements were made at Jefferson Lab during 2003-2004 aimed at characterizing charge lifetime of bulk GaAs within a 100 kV DC photoemission gun [1] under various operating conditions. The dominant mechanism that limits charge lifetime is ion backbombardment, where the electron beam ionizes residual gas within the chamber. These positive ions are accelerated toward the photocathode causing QE damage

that can be repaired by heating and reactivating the photocathode. Other mechanisms might effect charge lifetime, for example, chemical poisoning of the photocathode surface by residual gas, or field emission from the cathode electrode surface, but these mechanisms were considered secondary and were assumed to be much smaller than effects from ion backbombardment. The results are summarized below.

2.1. Period 1 - Summer/Fall 2003

Initial measurements used a 780 nm diode laser (DC beam) focussed to 500 μm at the photocathode. For the tests described in this section the laser power was adjusted (de-

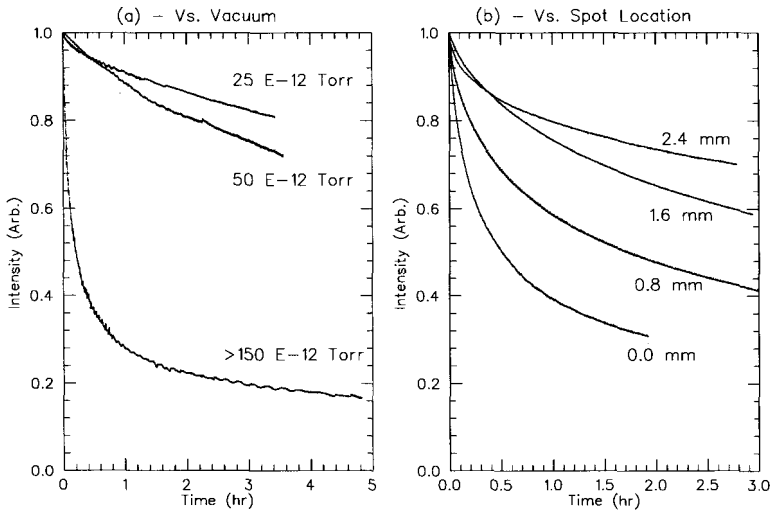


Fig 1. (a) For a fixed laser spot location (center), the cathode lifetime improves as the gun vacuum level decreases. (b) For a nearly constant vacuum level ($<10 \text{ E-12 Torr}$), the cathode lifetime improves as the laser spot location moves further from the cathode center.

pending upon the starting QE) to achieve 150 μA and then fixed for the remainder of the measurement. Initially, as a consequence of beam line vacuum leaks suffered during commissioning, lifetime was measured at a variety of vacuum levels. Once the best vacuum was achieved, the dependence on laser spot location was measured. Results are shown in Figure 1, indicating that lifetime improves as the vacuum improves and as the laser spot is moved further from the electrostatic center. Lifetime was also measured as a function of photocathode active area. To accomplish this task, an oxide layer was grown on the edge of the photocathode surface, to intentionally eliminate QE from regions of the photocathode that produce extreme beam trajectories. The oxide layer was obtained via the process of anodization [2], where the photocathode sample is placed in an electrolytic solution under applied electrical bias. In this manner, four photocathode samples were studied, with different active areas; 11 mm (the exposed portion of a 12.8 mm square sided cathode behind the cathode electrode), 9 mm, 7 mm and 5 mm. The results for the most different samples

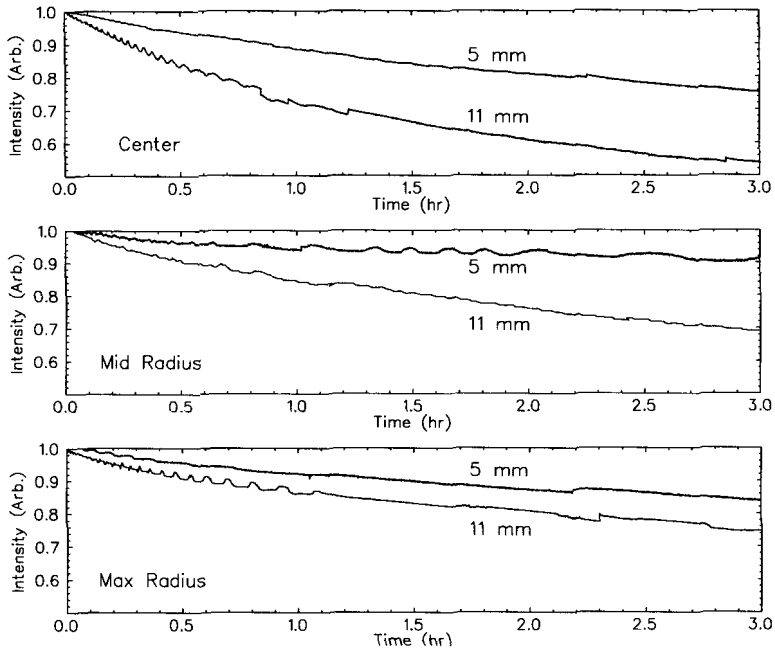


Fig 2. For three laser spot locations (center, mid-radius, max-radius), the cathode lifetime improves as the outer annulus of exposed photocathode is anodized, prohibiting photoemission there.

studied (11 mm and 5 mm), shown in Figure 2, indicate lifetime improves with smaller active area.

2.2. Period 2 - Spring/Summer 2004

At a later time, a mechanical mask, like that produced at MAMI [3], was used to define the photocathode area, mitigating the need for chemical anodization. This routinely produced a well defined region of uniform QE. In addition, ion pump power supplies with nanoamp resolution vastly improved vacuum monitoring of the gun and beam line during tests. Charge lifetime measurements using 7 mm and 9 mm masks over a range of 150-600 μ A were made for three spot locations. Although the lifetimes were not exceptional, in each case, the cathode with reduced active area performed better, as shown in Figure 3. Next, measurements of lifetime versus laser spot location were repeated, however, these disagreed with prior results. In this case, the lifetime degraded as the laser spot was located further from the cathode center. While unexpected, the dependence on the beam optics or unknown parameters is uncertain and requires further study.

A brief series of tests were made prior to the workshop, to investigate lifetime trends at higher intensities (8 mA achieved). A 532 nm Nd:YVO4 laser (DC beam), focussed to 1 mm at the photocathode, was used to take advantage of the higher QE at this wavelength. Although a QE of \sim 17% was achieved at 300 V, this value dropped to 1.5% at 100 kV, steady over a broad range of laser power. Two features of the lifetime measurements are

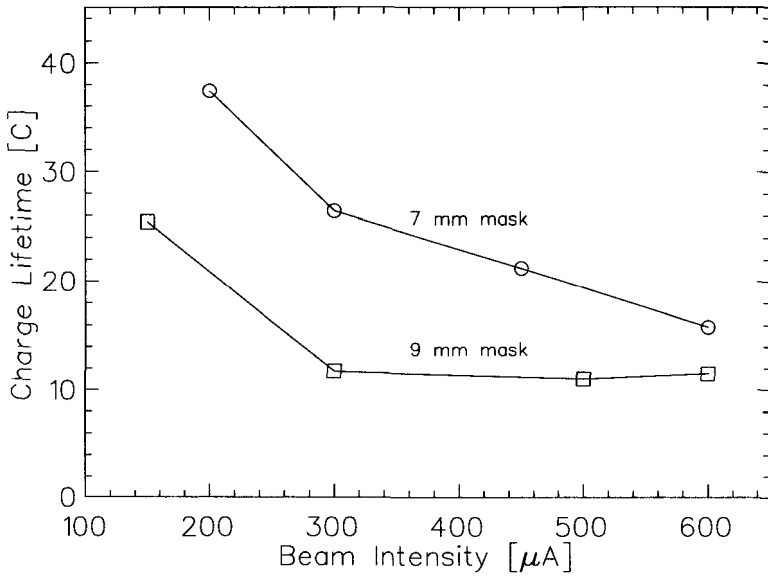


Fig 3. In contrast to chemical anodization, the mask method for limiting the large radius cathode photoemission also improves lifetime. These tests were made up to significantly higher beam intensity (600 μA versus 150 μA , described earlier).

notable. First, above 1 mA a very short lifetime (<0.1 C) occurred, followed by a typical lifetime (10-50 C). Second, while the gun vacuum pressure was stable, the photocurrent would instantaneously change shape, between two distinct charge lifetimes. This is not yet understood.

3. Conclusion

We are using a 100 keV load-lock photoemission electron gun and beam line to study photocathode lifetime versus gun operating parameters. Measurements consistently indicate that improved vacuum levels in the gun chamber and limited activated area enhance photocathode lifetime. Measurements also indicate that photocathode lifetime as a function of laser spot location may depend upon a greater set of parameters than expected, for example, the beam line optics settings and laser spot size. In forthcoming measurements emphasis will be placed to develop a quantitative lifetime model, better able to describe collected data and design future measurements.

Acknowledgments

This work was supported by the U.S. DOE Contract No. DE-AC05-84-ER40150.

References

1. M. Stutzman *et al.*, *SPIN 2002: 15th International Spin Physics Symposium and Workshop on Polarized Electron Sources and Polarimeters*, Upton, New York (USA) 9-14 September 2002, p. 1078-82.
2. P. Rutt and A. Day, *Active Area Definition of GaAs Photocathodes via Anodization*, Jefferson Laboratory Technical Note JLAB-TN-01-030, (2001).
3. K. Aulenbacher *et al.*, *SPIN 2002: 15th International Spin Physics Symposium and Workshop on Polarized Electron Sources and Polarimeters*, Upton, New York (USA) 9-14 September 2002, p. 1088-92.

RECENT PES PHOTOCATHODE R&D AT NAGOYA UNIVERSITY

M. KUWAHARA, T. NAKANISHI, S. OKUMI, M. YAMAMOTO, F. FURUTA, M. MIYAMOTO,
N. YAMAMOTO, K. NANIWA, K. YASUI

Graduate School of Science, Nagoya University, Nagoya, Japan

T. NISHITANI

Kansai Research Establishment, Japan Atomic Energy Research Institute, Tokai, Japan

O. WATANABE, Y. TAKEDA, H. KOBAYAKAWA, Y. TAKASHIMA

Graduate School of Engineering, Nagoya University, Nagoya, Japan

K. TOGAWA

RIKEN/SPring-8, Harima Institute, Hyogo, Japan

The strained-layer superlattice structures have been exhibiting the most promising performance as a photocathode for the polarized electron source (PES). In our experiments, the GaAs-GaAsP photocathode achieved maximum polarization of $92\pm 6\%$ with quantum efficiency of 0.5%, while the InGaAs-AlGaAs photocathode provided higher quantum efficiency (0.7%) with lower polarization ($77\pm 5\%$). Criteria for achieving high spin polarization and high quantum efficiency using superlattice photocathodes were clarified by employing the spin-resolved quantum efficiency spectra.

However, it seems that major problems still remained for the PES R&D are to improve (1) beam emittance and (2) NEA lifetime under gun operations for high peak current and high average current, respectively. In order to overcome these problems simultaneously, we started a development of a new type photocathode using field emission mechanism. First, we tried to use a pyramidal shape GaAs (tip-GaAs). Using the tip-GaAs, electrons can be emitted from a small area at the top of pyramid, and thus the beam emittance is expected to be small. This emission mechanism also enables to extract electrons from the poor NEA or small PEA surface into vacuum, and it helps to relax the NEA lifetime problem. Preliminary results were already obtained.

1. Introduction

A strained-layer superlattice (SL) photocathode shows high performance as PES. Especially, the GaAs-GaAsP strained-layer SL has achieved the highest spin polarization of $92\pm 6\%$ with high QE(0.5%) [1]. Furthermore, polarized electron beam with sub-nanosecond multi-bunch structure (peak current density $1A/cm^2$) has been produced from strained-layer SL with heavy surface doping [2, 3], and it means the surface charge limit (SCL) problem was overcome. The criteria for achieving high polarization and high QE using SL were clarified by analyzing the spin resolved QE spectra as described in a section 2.2. A new type of GaAs photocathode has been also studied recently. It employs two fundamental physical mechanisms, 1)optical orientation method to create polarized electrons in bulk GaAs and 2) field emission mechanism to extract the electrons into vacuum. We are interested in such a cathode, because it will be possible to produce a smaller emittance beam than an ordinary plane cathode, and also the NEA lifetime problem may be relaxed by help of field emission mechanism. First, we tried to test a pyramidal shaped GaAs (tip-GaAs), and preliminary results are reported in section 3.

2. Strained Layer Superlattice Photocathode

2.1. Experiment and Results

The InGaAs-AlGaAs SL samples were fabricated by molecular beam epitaxy (MBE) at NEC, and the GaAs-GaAsP SL samples were made by metal-oxide chemical vapor deposition (MOCVD) at Nagoya University. A number of different SL samples with various materials and crystal parameters were fabricated and tested, but in this paper, the SLSPA#02 and SLSP#16 samples are selected from InGaAs-AlGaAs and GaAs-GaAsP SL families. The crystal structure and dopant density of SLSP#16 are shown in Fig. 1. The crystal structure of SLSPA#02 was already given in Ref. 3 as a SL-3 sample. The thicknesses of the well and barrier layers were chosen so as to obtain the large hh-lh energy splitting, and the total thickness of active layer was about $100nm$, set to minimize spin depolarization.

ESP and QE were measured using a compact cathode test system with a $4keV$ DC gun and a $100keV$ Mott polarimeter [4]. The ESP and QE spectra of the SLSP and SLSPA cathodes are shown in Fig. 2, as a function of laser wavelength. Most of the SLSP cathodes achieved maximum ESPs about 90%, especially SLSP#16 reached 92% with QE of 0.5%

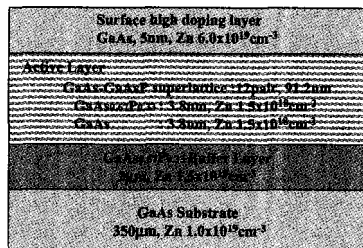


Fig 1. Crystal microstructure and dopant density of SLSP#16

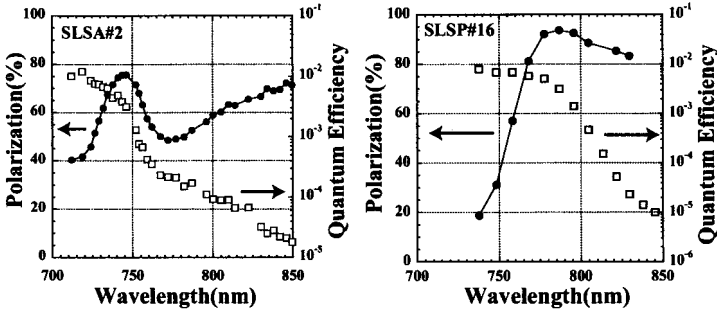


Fig 2. Observed polarization and QE as a function of wavelength

at 778nm. The SLSA cathodes showed lower ESPs of about 80%, but the highest QE of 0.7% was reached by SLSA#02 at 741nm with the ESP of 77%. Concerning the SCL effect, we demonstrated that a multi-bunch beam can be also produced using the GaAs-GaAsP SL photocathode in combination with a 70keV DC gun and a 0.7ns double-bunch laser.

2.2. Data Analysis and Discussion

The maximum ESP depends on the initial polarization (P_i) of excited electrons in the conduction band, and P_i is also related to the coefficients of photo-absorption from the hh (A_{hh}) and lh (A_{lh}) mini-bands. The explicit relations are given by $A_{hh} = A_i(1 + P_i)/2$ and $A_{lh} = A_i(1 - P_i)/2$, where A_i is the total absorption coefficient. These photo-absorption coefficients A_{hh} and A_{lh} are proportional to the joint density of states (JDOS) between conduction and hh or lh bands. The typical behaviors of these JDOSs in the threshold region are shown in Fig. 3. For comparison the experimental data with the above JDOS-based A_{hh}

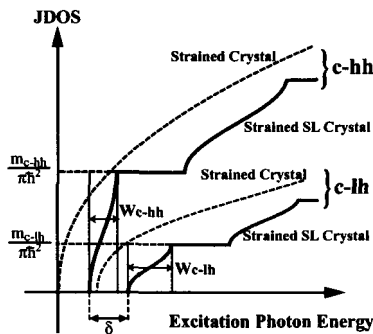


Fig 3. Schematic of JDOS's behavior as a function of excitation photon energy. the dotted line shows strained layer's, and solid line shows strained SL layer's. Both widths of absorption edge are indicated for the hh and lh absorption.

and A_{lh} spectra, it is convenient to use the spectra of spin-resolved quantum efficiencies for left-handed (Q_L) and right-handed (Q_R) electrons in an emitted beam plotted as functions

of excitation photon energy. The experimental Q_L and Q_R spectra are plotted in Fig. 4. A step-like jump in QE is clearly observed in the Q_L spectra for SLSP#16. The parameters of the JDOS-based A_{hh} and A_{lh} spectra were determined for the SLSP and SLSA cathodes using threshold energies for hh and lh excitations calculated by the Kronig-Penny model, where the strain relaxation effect was taken into account by using the Matthews formula.

The mechanism that determines the maximum ESP was clarified through these phenomenological data analyses of spin-resolved QE spectra. It was found that the most important factors for achieving high ESP and QE simultaneously are 1) large hh-lh energy (δ) separation, 2) narrow joint widths (W_{c-hh}) between the conduction and hh-band, and 3) minimal depolarization inside the SL layers. Combining 1) and 2), $\delta \geq W_{c-hh}$ was derived as the most important condition. The above criteria can explain why the GaAs-GaAsP strained SL photocathode can achieve such high ESP (92%) and QE (0.5%) simultaneously.

3. Tip-GaAs

The pyramidal shaped GaAs was fabricated on the Zn-doped GaAs (100) substrate ($p=2 \times 10^{19} \text{ cm}^{-3}$) by anisotropic wet etching using H_3PO_4 solutions [5]. As shown in Fig. 5, the sample had a tip radius of about 25 nm , and a distance between tip to tip of $200 \mu\text{m}$.

In the experiment, we used a 70 keV DC gun system [3] and a 20 keV DC gun for which the gap separation of electrodes was variable. The 20 keV gun could apply a high-gradient dc field of 3.8 MV/m to the photocathode surface under UHV (10^{-11} Torr) condition. Figure 6(a) shows Fowler-Nordheim (F-N) plots of the emission current obtained by laser light irradiation ($\lambda = 780 \text{ nm}$). The data was roughly fitted by a straight line, that is inversely proportional to $1/E$. This behavior suggests that the excited electron was extracted into vacuum by tunneling effect. Figure 6(b) shows the QE as a function of excitation photon energy under a high gradient field of 3.4 MV/m . The solid line is a fitting curve using a calculation of tunneling yield based on WKB approximation. The QE is rising quickly at 1.6 eV . Such a behavior is not observed for the bulk-GaAs with NEA surface. Figure 7 shows ESP and QE of tip-GaAs under application of high gradient field and irradiation of circular laser light together with the ESP of NEA-GaAs. The ESP of tip-GaAs has some dip and bump structures between 20% and 40%, but it has higher values than bulk-GaAs in wavelength region below 760 nm . This wavelength corresponds to the rising edge of QE at 1.6 eV . These experimental results indicate that the spin polarized electrons can be ex-

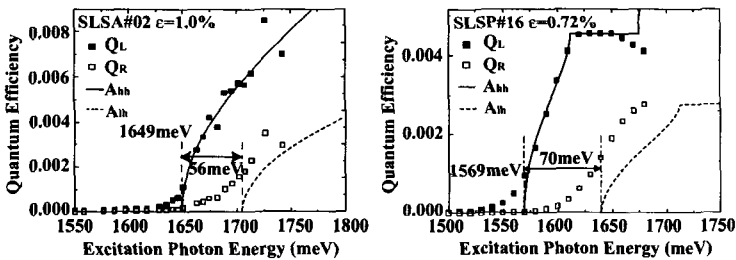


Fig. 4. The Q_L and Q_R spectra, and the JDOS-based A_{hh} and A_{lh} spectra for SLSA#02 and SLSP#16



Fig 5. SEM images of tip-GaAs fabricated by anisotropic wet etching

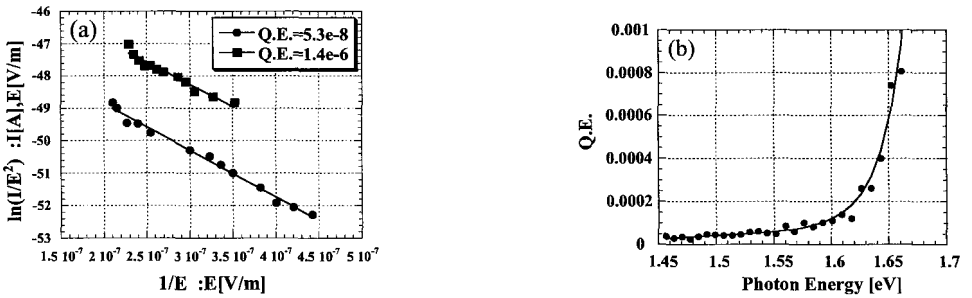


Fig 6. (a) F-N plot of photo-electron extracted from tip-GaAs, (b) QE of tip-GaAs under impressing high gradient field as a function of excitation photon energy.

tracted from the conduction band into vacuum through the tip of GaAs without serious depolarization. Further experimental study will be continued to establish the feasibility of such field emission type PES photocathodes.

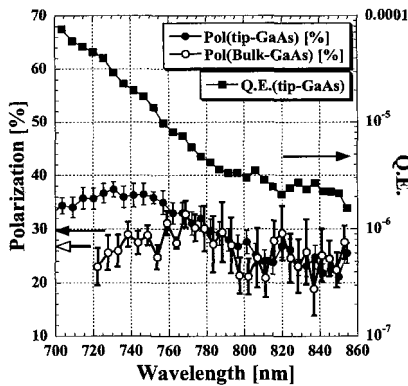


Fig 7. ESP and QE of tip-GaAs as a function of wavelength. ESP of NEA-GaAs was also plotted for comparison.

Acknowledgments

We thank T. Saka, K.Kato and T. Baba for providing us photocathode samples, and K. Yamaguchi of the University of Electro-Communications for collaboration the tip-GaAs fabrication.

References

1. T. Nakanishi et al., *Linac2004 Proceedings* (<http://www.linac2004.de>) THP24
2. K. Togawa, et al., *Nucl.Instr. Meth.* **A455**, 109 (2000).
3. K. Togawa, et al., *Nucl.Instr. Meth.* **A414**, 431 (1998).
4. T. Nakanishi, et al., *Jpn. J. Appl. Phys.* **25**, 766 (1986).
5. K. Yamaguchi, et al., *J. Electrochem. Soc.* **Vol.143, No.8**, 2616 (1996).

QUALITY CHARACTERIZATION OF NEA-PHOTOCATHODE FOR PES BY MEANS OF PHOTOEMISSION FROM DEFECT STATES

A. A. PAKHNEVICH⁽²⁾, A. V. YAZKOV⁽²⁾, V. V. BAKIN⁽¹⁾, O. E. TERESHCHENKO^(1,2),
H. E. SCHEIBLER⁽¹⁾, A. S. JAROSHEVICH⁽¹⁾, S. N. KOSOLOBOV⁽¹⁾, A. S. TEREKHOV^(1,2)

⁽¹⁾Institute of semiconductor physics, Novosibirsk, Russia

⁽²⁾Novosibirsk State University, Novosibirsk, Russia

The photoemission from surface and bulk defect states of NEA photocathodes was measured. It is shown, that the relative contribution of defect-related photoemission to the total photocurrent at photon energy near the band gap (ϵ_g) may be as high as $\sim 10\%$ or more. The photoemission from defect states is assumed to be unpolarized and therefore can be responsible for the loss of electron polarization.

1. Introduction

Semiconductor photocathodes with the state of effective negative electron affinity (NEA) play the key role in the development of polarized electron sources for experiments in solid state, atomic and high energy physics. The theoretical limit for polarization of electrons emitted from semiconductor heterostructures with splitted valence band is equal to 100%. The experimentally demonstrated polarization is of about 10% below the theoretical limit. We have assumed that unpolarized photoemission from electron states, related to the activation layer and to crystal defects within band bending region (BBR) could be responsible for the lowering electron polarization below the theoretical limit. The study of near band gap photoemission from unstrained GaAs - photocathodes and highly strained and relaxed GaN - photocathodes gave us experimental arguments to support our assumption.

2. Experiment

To study the photoemission from defects states, two photocathode materials were used. The photoemission from surface states related to surface defects and to the activation layer was measured with unstrained, thick p-GaAs(Cs,O) - photocathodes. In order to evaluate the contribution from bulk defects, p-GaN - epitaxial layers, grown on sapphire substrate were used. To remove oxides the surfaces of both photocathode materials were first cleaned with HCl-isopropanol in the pure N₂ - atmosphere and then heat cleaned in the UHV-chamber. The details of these procedures are given in [[1], [2]]. After the heat cleaning, photocathodes were activated by (Cs,O) coadsorption at room temperature. Activated photocathodes

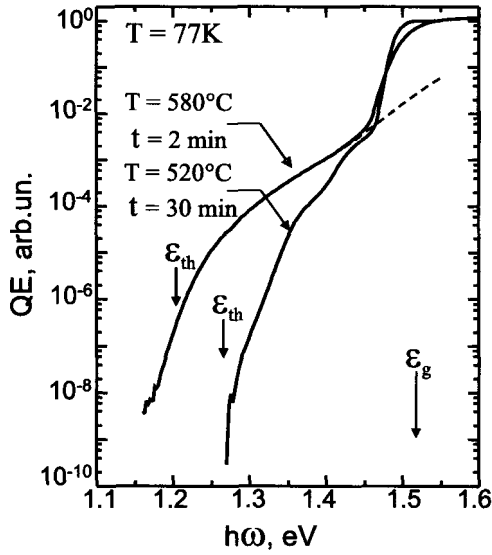


Fig 1. Quantum efficiency spectra of two p-GaAs(Cs,O)-photocathodes with different surface preparation procedures.

were sealed within the vacuum-tight metal-ceramic envelopes with an optical window and anode. The anode was made of a flat Cu-mesh and enabled one to measure the electron distribution curves (EDCs) by the retarding potential method [[3]]. Grating monochromator with halogen and deuterium lamps was used as a light source. More details concerning the quantum efficiency (QE) and EDC measurements procedures are given in [[3]].

3. Results and discussion

The QE spectra measured with p-GaAs(Cs,O)-photocathodes are shown in Figure 1. Two photocathodes with different surface preparation procedures were used in these experiments. The first one was heat cleaned at 580°C for 2 minutes and activated to the maximum of QE. The second one was heat cleaned at lower temperature, but for longer time and activated with a thin activation layer to about 0.7–0.8 of the expected maximum value of QE. One can see from Figure 1 that photoemission consists of two contributions. For photon energies $\hbar\omega \gtrsim \epsilon_g$ the QE spectrum is dominated by the photoelectron emission from the valence band (ϵ_v). For $\hbar\omega \lesssim 1.45$ eV photoemission from surface states is responsible for the formation of a broad shoulder in QE spectrum which covers the photon energy interval between the photoelectron threshold energy (ϵ_{th}) and the ϵ_g . To demonstrate the different nature of photoemission from valence band and from surface states, the electron distribution curves (EDCs) were measured. The results are presented in Figure 2. One can see that for $\hbar\omega = 1.50$ eV the EDC line shape is approximately rectangular and covers the energy interval from the conduction band in the bulk (ϵ_c) up to the vacuum level (ϵ_{vac}), which is equal to NEA value. For the photoemission from surface states (at $\hbar\omega = 1.40$ eV) the

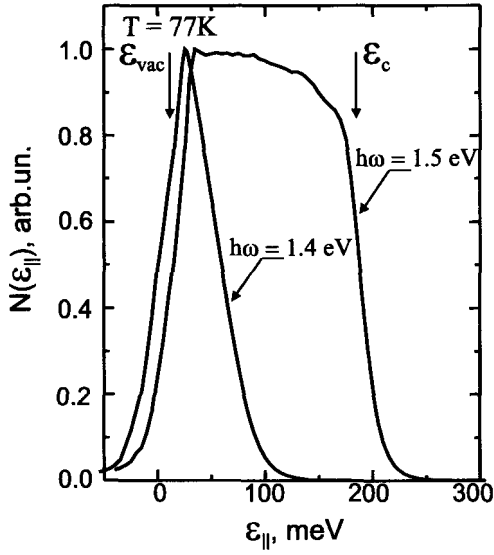


Fig 2. Photoelectron energy distributions of p-GaAs(Cs,O)-photocathodes measured for photon energies in the vicinity and below the energy gap of GaAs.

EDC is narrow with a maximum near the vacuum level. The high energy tail of this EDC depends on the surface states energy distribution below the Fermi level.

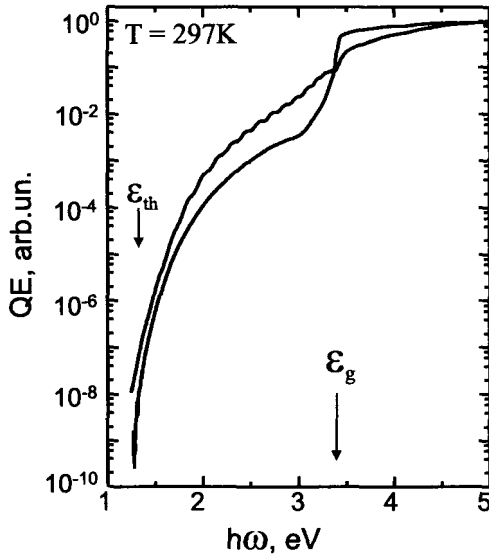


Fig 3. Quantum efficiency spectra of two p-GaN(Cs,O)-photocathodes with different different density of bulk defects.

To evaluate the contribution of unpolarized photoemission from surface states to the total photoemission at $\hbar\omega = \varepsilon_g$, we have extrapolated the QE spectrum, related to photoemission from surface states to the photon energies, where this photoemission overlaps with photoemission from the bulk states. This extrapolation is shown in Figure 1 with a dotted line. One can see, that at $\hbar\omega = 1.50$ eV the extrapolated QE spectrum from the surface states is of about 1% of the valence band photoemission. In our photocathode the thickness of GaAs layer is equal to $1.5 \mu\text{m}$, which is enough to absorb $\simeq 90\%$ of photons with $\hbar\omega \simeq 1.50$ eV. The thicknesses of the active layer of strained photocathodes are of about $0.1 \mu\text{m}$. Therefore, the relative contribution of photoemission from the surface states to the total photocurrent at $\hbar\omega = 1.50$ eV for thin strained photocathodes should be as high as 10 – 15%. This means that the electron polarization from highly strained GaAs photocathode should not exceed 85 – 90% at 77 K due to the contribution of unpolarized photoemission from the surface states. At room temperature the GaAs band gap decreases down to ~ 1.40 eV, while the ε_{th} does not depend on temperature. Consequently, the relative contribution of surface states to the total photocurrent measured for $\hbar\omega \simeq \varepsilon_g$ at 297 K will be lower in comparison with the measurement at 77 K. We should mention, that the spectra shown in Figure 1 demonstrated the lower limit of surface state density for GaAs - photocathodes. If one use high temperature (~ 600 °C) heat cleaning for about one hour or other cleaning procedures which generate near-surface defects and the GaAs activation with a thick (Cs,O)-activation layer [4], the surface state density increases. Photoemission from these states lowers the photoelectron polarization. The non-radiative recombination of photoelectrons via surface states decreases QE. In addition to surface defects, bulk defects within BBR may also contribute to the unpolarized photoemission. For unstrained semiconductors this contribution is negligible, but for strained and partly relaxed heterostructures it can be relatively high. To demonstrate this we used p-GaN(Cs,O) - photocathodes grown on sapphire substrates. Due to 12% lattice mismatch [5] between GaN and sapphire, the dislocation density within GaN layer may be as high as 10^9 cm^{-2} [5]. The QE-spectra of (Cs,O)-activated p-GaN - heterostructures from two different vendors are shown in Figure 3. One can see, that both photocathodes demonstrate pronounced photoemission for photon energies below $\varepsilon_g \simeq 3.4$ eV and that for one photocathode defect-related photoemission is nearly equal to the photoemission from the valence band states.

4. Summary

Contributions to the total photoemission from the valence band, from defect states in BBR and from the surface states in (Cs,O)-activation layer are summarized in Figure 4. The relative contributions of bulk- and surface-related defects states depend on the bulk defect (dislocations) density and on the quality of the surface cleaning and activation procedures. To optimize these procedures it is helpful to measure both photoemission QE spectra at $\hbar\omega \leq \varepsilon_g$, which enable one to evaluate the contribution of unpolarized photoemission from surface and bulk defect states to the total photocurrent.

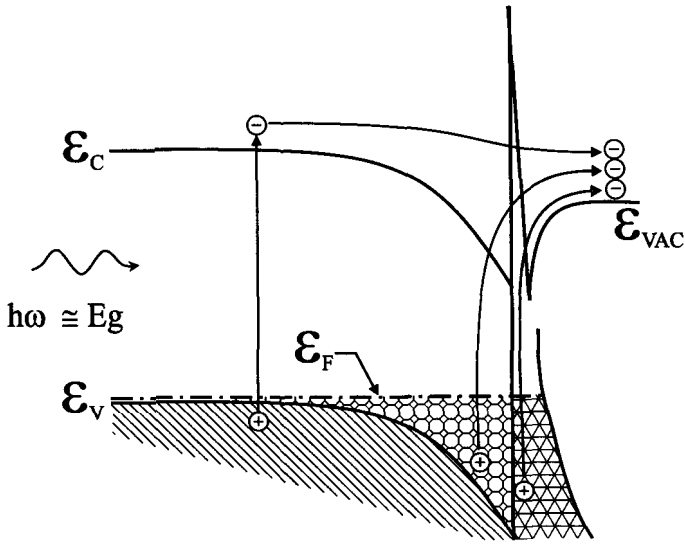


Fig 4. Photoemission from valence band and from near-surface defect states.

Acknowledgments

This work was partly supported by the Russian Foundation for Basic Research (grant 04-02-16639) and by the Russian Academy of Sciences (program "Spintronics").

References

1. O. E. Tereshchenko, S. I. Chikichev, A. S. Terekhov, *J. Vac. Sci. Technol.* **A17**, 2655 (1999).
2. O. E. Tereshchenko, H. E. Sheibler et al., *Phys. of Sol. St.* **46**, 1949 (2004).
3. A. A. Pakhnevich, V. V. Bakin et al., *Pis'ma Zh. Eksp. Teor. Fiz.* **79**, 592 (2004) [*JETP Lett.* **79**, 479 (2004)].
4. S. More, S. Tanaka et al., *Sur. Sci.* **454-456**, 161 (2000).
5. O. Ambacher, B. Foutz et al., *J. Appl. Phys.* **87**, 334 (2000).

PROPERTIES OF FIELD EMISSION DARK CURRENT FROM MOLYBDENUM AND TITANIUM ELECTRODES

F. FURUTA, M. YAMAMOTO, T. NAKANISHI, S. OKUMI, T. GOTOH, M. MIYAMOTO, M. KUWAHARA,
N. YAMAMOTO, K. NANIWA, K. YASUI

Nagoya University, Dept. of Physics, Nagoya, Japan

H. MATSUMOTO, M. YOSHIOKA

KEK High Energy Accelerator Research Organization, Tsukuba, Japan

K. TOGAWA

SPring-8, RIKEN, Mikazuki-cho, Sayo-gun, Japan

The dark current generally contains two components produced by the primary field emission from cathode and the secondary enhanced emission due to electron and ion bombardments of anode and cathode. However, using the dark current dependence on the electrode gap separation we can separate these components. By analyzing the observed dark currents from molybdenum (Mo) and titanium (Ti), it is shown that Mo exhibits very low primary field emission current as a cathode, while Ti exhibits a lower enhancement effect as an anode. An electrode configuration of Mo cathode and Ti anode is thus examined, and it is confirmed that a field gradient as high as 130MV/m is possible for 1nA total dark current for a gap of 0.5mm and an effective cathode area of $7mm^2$.

1. Introduction

It is well known that a field emission dark current induces degradation of a negative electron affinity (NEA) surface. Therefore, reduction of a dark current is a key technology for development of a high field gradient polarized electron gun [1].

We have studied the dark current properties of metal electrodes by using a test stand constructed at KEK (Fig. 1, left). The SUS and Cu electrode properties were already studied and it was clarified that the magnitude of dark current depends not only on the electrode fabrication procedure, but also on the purity of materials [2]. As a next step, Mo and Ti were examined as more promising materials than SUS and Cu.

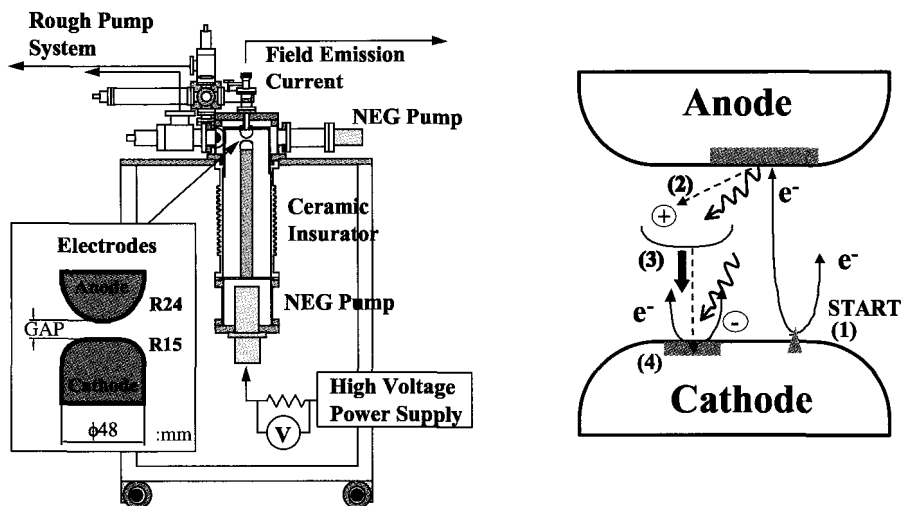


Fig 1. Schematic view of test stand (left) and enhancement effect of dark current by electron and ion bombardment on electrodes (right)

1.1. Model of Dark Current Growth

The F-N theory provides a fundamental viewpoint for the field emission phenomena [3], but the real dark current phenomenon can not be explained sufficiently by this theory. For example, it can not predict the gap separation dependence of dark current under the same magnitude of field gradient.

Usually it is assumed the dark current consists of a primary field emission and a secondary enhanced emission. The primary field emission is considered to be induced at tips or non-metallic contamination on the metal surface. These primary electrons are accelerated toward the anode with the same kinetic energies proportional to bias voltage and hit the anode electrode. As a result, the various molecules including positive ions and X-rays are ejected from the anode. The positive ions are also created by collisions of electrons with residual gas molecules and accelerated again toward the cathode. These ions and X-rays may generate secondary electrons by hitting the cathode surface. This feedback loop stimulates the growth of total dark current as shown in Fig.1 (right).

Therefore, it is necessary to suppress not only the primary emissions but also the secondary enhanced emissions to reduce the total dark current.

1.2. Preparation of Mo and Ti Electrodes

The test stand of Fig 1. (left) was used for studies of field emission dark currents from various metal electrodes under the high DC field gradient ($\sim 200\text{MV}/\text{m}$) with ultra high vacuum ($< 10^{-9}$ Pa).

The applied field gradient could be changed by controlling bias voltage (0-100kV) and gap separation of the electrode (0-20mm). In this experiment, 7mm^2 area at the center of the

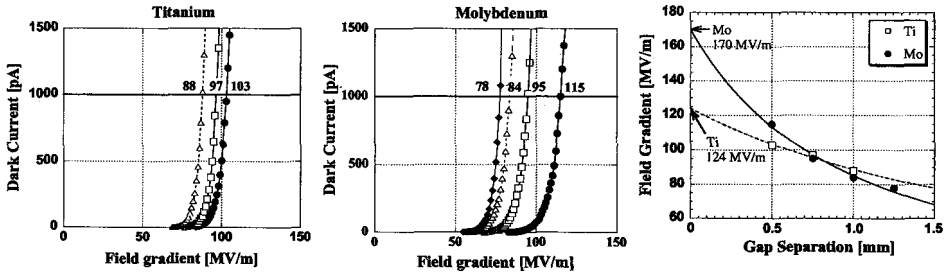


Fig 2. Dark current from titanium and molybdenum electrodes as a function of applied maximum field gradient at the cathode surface. Gap separations are 0.5 mm (●), 0.75 mm (□), 1.0 mm (△), 1.25 mm (◇). The right-side figure shows gap separation dependence of a field gradient corresponding to a dark current of 1nA.

cathode surface was exposed to the maximum field gradient. The anode electrode was fixed on a linear manipulator which is electronically insulated from ground. Total dark current was measured by a pico-ammeter connected between the manipulator and ground.

The electrode materials of JIS grade-2 pure Ti and polycrystalline Mo with purity of 5N were prepared in this experiment. Mirror-like surface polishing were done by buff polishing for Ti and diamond paste buff polishing for Mo electrodes, respectively. The high pressure rinsing with ultra pure water ($80kg/cm^2, 80M\Omega cm, 5min$) was done before installation of the electrode to the vacuum chamber. The vacuum pressure fell down to 8×10^{-10} Pa after 250 °C baking for 1 week.

2. Results of Dark Current Measurement

The measured dark currents from Ti and Mo electrodes are shown in Fig.2. These results are plotted for several gap separations as a function of applied field gradient on the cathode surface.

The gap separation dependence is observed for both electrodes, and it is more significant for Mo rather than Ti. As shown in Fig. 2 (center and left), the best performance is achieved by Mo electrode at narrow gap condition, while Ti exhibits an advantage for wide gap condition ($\geq 1.0mm$).

3. Analysis of Primary Field Emission

The gap separation dependence of field gradient corresponding to dark current of 1 nA is shown in Fig. 2 (right). Based on the model picture of dark current growth (Fig 1, right), the primary field emission current is considered to be equivalent to the total emission current at zero gap separation. Thus, the field gradient at zero gap separation can be obtained by extrapolating several experiments data of the field gradient of $E(I, d)$ (MV/m) which is the field gradient giving total dark current of I (A) at gap separation of d (mm). The explicit relation is given by the following formula,

$$E(I, d) = \frac{E(I, 0)}{1 + \alpha d} \tag{1}$$

where α is a constant representing the enhancement effect (mm^{-1}), and $E(I, 0)$ is the field gradient at zero gap separation corresponding to the magnitude of the field gradient giving the field emission current of I .

In general, the primary field emission current for any electrodes can be estimated by the following procedure, as shown in Fig. 3 (left).

- (1) Measure the dark current as a function of applied field gradient at the cathode surface for several gap separations.
- (2) Estimate a field gradient of zero gap separation $E(I, 0)$ by using Eq.(1) and the experiment data of field gradients $E(I, d)$ as a function of gap separation d for the fixed dark current I .
- (3) Plot the estimated $E(I, 0)$ values for various I values as a function of field gradient.

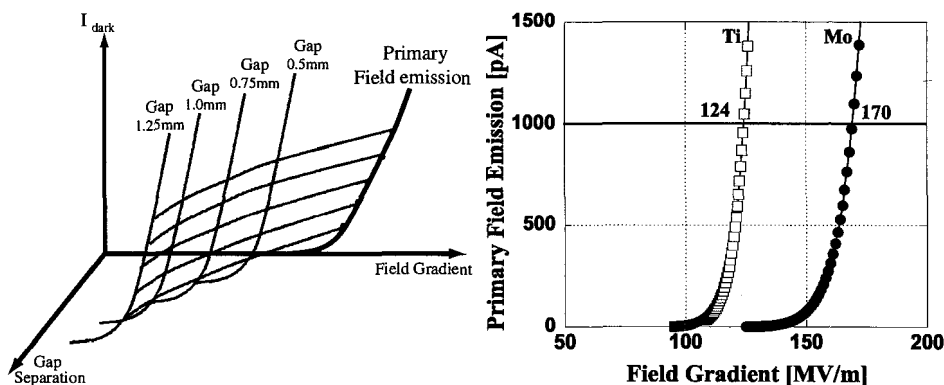


Fig. 3. An illustration of how to separate a primary field emission from the gap separation dependence measurements (left), and the result of estimated primary field emissions from titanium and molybdenum electrode as a function of a field gradient (right).

The primary field emissions estimated for Mo and Ti electrodes are plotted in Fig. 3 (right). The field gradients for 1nA primary field emission are given as 170 MV/m for Mo, and 124 MV/m for Ti, respectively. The values of α corresponding to magnitude of enhancement effect were obtained as $0.4 \pm 0.02(mm^{-1})$ for Ti and $1.0 \pm 0.04(mm^{-1})$ for Mo.

From these analyses, it is clarified that Mo is fine material for suppression of the primary field emissions, and Ti is effective to reduce the secondary enhanced emissions.

4. Reduction of Dark Current

As a conclusion of our analysis, a configuration of Mo cathode and Ti anode (Mo-Ti) is considered to be most suitable for a reduction of dark current. For such a Mo-Ti electrode, the dark current was measured also at several gap separations. The results of experiment and data analysis are shown in Fig. 4.

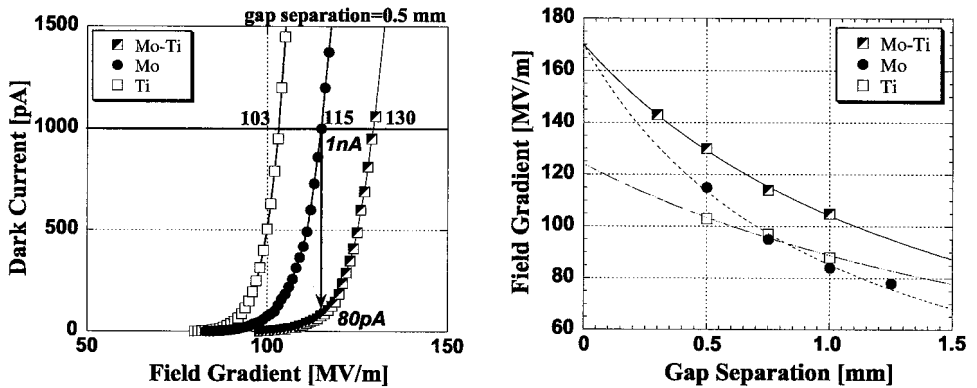


Fig 4. Dark current measurement for Mo-Ti configuration as a function of field gradient with 0.5 mm gap separation, and the result of gap dependence of field gradient corresponding to dark current of 1 nA.

The applicable field gradient was improved from 115 MV/m (Mo-Mo) to 130 MV/m (Mo-Ti) for dark current level of 1 nA, and the parameter α also reduced to be $0.6 \pm 0.01 (\text{mm}^{-1})$. Therefore, the Mo-Ti configuration exhibited the best performance in comparison with both of Ti-Ti and Mo-Mo configurations.

In addition, the field gradient at zero gap separation for Mo-Ti electrode has the same value of Mo-Mo configuration. It means that the Mo performance for the primary field emission can be well reproduced for different measurements and the estimation procedure for the primary field emission is reliable.

5. Conclusion

Dark current measurements using Mo and Ti electrode were performed. The applicable field gradients of 115 MV/m for Mo and 103 MV/m for Ti were observed at 0.5 mm gap separation for 1 nA dark current. A new method to separate the primary field emission from total dark current was proposed based on the analysis of gap separation dependence of dark current. By this method, it is suggested that a high field gradient of 170 MV/m with the primary field emission of 1 nA can be applicable for the Mo-cathode.

The reduction of dark current by using a new electrode with Mo cathode and Ti anode was also successful and the applicable field gradient for 1 nA dark current was improved to 130 MV/m at 0.5 mm gap separation. The fundamental research of dark current phenomena for other materials such as tungsten (W) and tantalum (Ta) have been planned by using an improved test apparatus with a load lock system for the electrode exchange.

References

1. R. Alley, et al., *Nucl. Instr. and Meth. A* **365**, (1995) 1.
2. C. Suzuki, et al., *Nucl. Instr. and Meth. A* **462**, (2001) 337.
3. R. H. Fowler, L. Nordheim, *Proc. Roy Soc. A* **119**, (1927) 173.
4. F. Furuta, et al., to be published in *Nucl. Instr. and Meth.*.

5. T. Nakanishi, F Furuta, et al., Proceedings of LINAC 2004, Luebeck, Germany, August 2004. p716. (THP23)

THE MAINZ A4 PARITY VIOLATION EXPERIMENT* SINGLE SPIN ASYMMETRIES IN ELASTIC SCATTERING

F. E. MAAS

Johannes-Gutenberg Universität Mainz, Institut für Kernphysik, Mainz, Germany

(for the A4 Collaboration)

We report here on recent measurements of the parity violating (PV) Asymmetry in the scattering of polarized electrons on unpolarized protons performed with the setup of the A4-collaboration at the MAMI accelerator facility in Mainz. This experiment is the first to use counting techniques in a parity violation experiment. The kinematics of the experiment is complementary to the earlier measurements of the SAMPLE collaboration at the MIT Bates accelerator and the HAPPEX collaboration at Jefferson Lab. After discussing the experimental context of the experiments, the setup at MAMI and preliminary results are presented.

1. Strangeness in the Nucleon

The understanding of quantum chromodynamics (QCD) in the nonperturbative regime of low energy scales is crucial for understanding the structure of hadronic matter like protons and neutrons (nucleons). In this context the contribution of strange quarks plays a special role since the nucleon has no net strangeness, and any contribution of strange quarks to the nucleon structure observables is a pure sea-quark effect. Parity violating (PV) electron scattering off nucleons provides experimental access to the strange quark vector current in the nucleon $\langle N | \bar{s} \gamma_\mu s | N \rangle$ which is parameterized in the electromagnetic form factors of proton and neutron, G_E^s and G_M^s [1]. A determination of the weak vector form factors of the proton (\tilde{G}_E^p and \tilde{G}_M^p) by measuring the PV asymmetry in the scattering of longitudinally polarized electrons off unpolarized protons allows the determination of the strangeness contribution to the electromagnetic form factors G_E^s and G_M^s . The interference between weak (Z) and electromagnetic (γ) amplitudes leads to a PV asymmetry $A_{LR}(ep) = (\sigma_R - \sigma_L)/(\sigma_R + \sigma_L)$ in the elastic scattering cross section of right- and left-handed electrons (σ_R and σ_L respectively), which is given in the framework of the Standard Model [2]. $A_{LR}(ep)$ is of order parts per million (ppm). The asymmetry can be expressed as a sum of three terms, $A_{LR}(ep) = A_V + A_s + A_A$. A_V represents the vector coupling at the proton vertex where the possible strangeness contribution has been taken out and has been put into

*This work had been supported by DFG in the framework of SFB 201 and SPP 1034

A_s , a term arising only from a contribution of strangeness to the electromagnetic vector form factors. The term A_A represents the contribution from the axial coupling at the proton vertex due to the neutral current weak axial form factor \tilde{G}_A^p . We average $A_0 = A_V + A_A$ over the acceptance of the detector and the target length in order to calculate the expected asymmetry. The largest contribution to the uncertainty of A_0 comes from the uncertainty in the axial form factor G_A , the electric form factor of the proton G_E^p , and the magnetic form factor of the neutron G_M^n .

2. The A4 Experimental Setup and Analysis

The A4 experiment [3–7, 9] at MAMI is complementary to other experiments since for the first time counting techniques have been used in a scattering experiment measuring a PV asymmetry. Therefore possible systematic contributions to the experimental asymmetries and the associated uncertainties are of a different nature as compared to previous experiments, which use analogue integrating techniques. From the source to the target, the

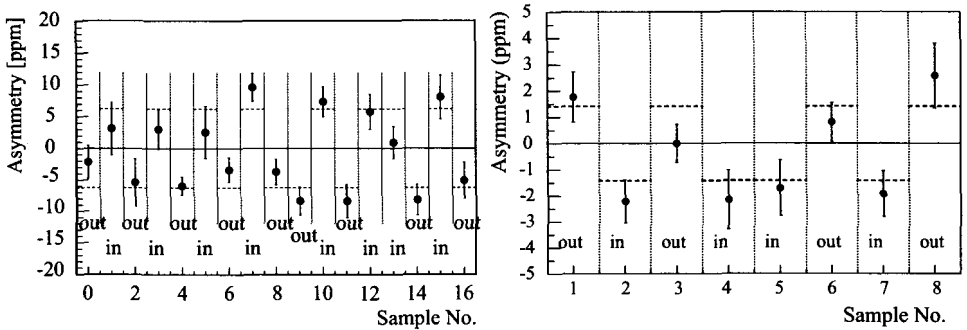


Fig 1. The left plot shows the data samples of 854.3 MeV data with the $\lambda/2$ -plate in and out. The right plots represents the data sample for the 570.4 MeV data with the $\lambda/2$ -plate in and out as described in the text.

electron beam develops fluctuations in beam parameters such as position, energy and intensity which are partly correlated to the reversal of the helicity from +P to -P. We have used a system of microwave resonators in order to monitor beam current, energy, and position in two sets of monitors separated by a drift space of about 7.21 m in front of the hydrogen target. In addition, we have used a system of 10 feed-back loops in order to stabilize current, energy [8], position, and angle of the beam. The 10 cm high power, high flow liquid hydrogen target was optimized to guarantee a high degree of turbulence with a Reynolds-number of $R > 2 \times 10^5$ in the target cell in order to increase the effective heat transfer. For the first time, a fast modulation of the beam position of the intense cw 20 μ A beam could be avoided. The luminosity L was monitored for each helicity state (R, L) during the experiment using eight water-Cerenkov detectors (LuMo) that detect scattered particles symmetrically around the electron beam for small scattering angles in the range of $\theta_e = 4^\circ - 10^\circ$, where the PV asymmetry is negligible. From the beam current helicity

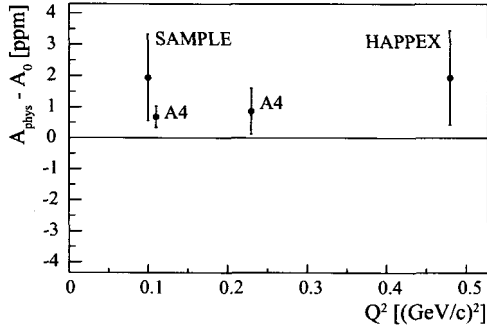


Fig 2. Difference between the measured parity violating asymmetry in electron proton scattering $A_{LR}(ep)$ and the asymmetry A_0 without vector strangeness contribution from the Standard Model for the SAMPLE experiment at backward angles, and the HAPPEX and the two A4 results at forward angles. The new experimental result at $Q^2=0.109$ (GeV/c)² presented here is the most accurate measurement.

pair data $I^{R,L}$ and luminosity monitor helicity pair $L^{R,L}$ data we calculated the target density $\rho^{R,L} = L^{R,L}/I^{R,L}$ for the two helicity states independently.

To detect the scattered electrons we developed a new type of a very fast, homogeneous, total absorption calorimeter consisting of individual lead fluoride (PbF₂) crystals [4, 9]. The material is a pure Cerenkov radiator and has been chosen for its fast timing characteristics and its radiation hardness. This is the first time this material has been used in a large scale calorimeter for a physics experiment. The crystals are dimensioned so that an electron deposits 96% of its total energy in an electromagnetic shower extending over a matrix of 3×3 crystals. Together with the readout electronics this allows us a measurement of the particle energy with a resolution of $3.9\%/\sqrt{E}$ and a total dead time of 20 ns. For the data taken at 854.3 MeV only 511 out of 1022 channels of the detector and the readout electronics were operational, for the 570.4 MeV data all the 1022 channels were installed. The number of elastic scattered electrons is determined for each detector channel by integrating the number of events in an interval from $1.6 \sigma_E$ above pion production threshold to $2.0 \sigma_E$ above the elastic peak in each helicity histogram, where σ_E is the energy resolution for nine crystals. These cuts ensure a clean separation between elastic scattering and pion production or Δ -excitation which has an unknown PV cross section asymmetry. We calculate the raw normalized detector asymmetry as $A_{\text{raw}} = (N_e^R/\rho^R - N_e^L/\rho^L)/(N_e^R/\rho^R + N_e^L/\rho^L)$. The possible dilution of the measured asymmetry by background originating from the production of π^0 's that subsequently decays into two photons where one of the photons carries almost the full energy of an elastic scattered electron was estimated using Monte Carlo simulations to be much less than 1% and is neglected here. The largest background comes from quasi-elastic scattering at the thin aluminum entrance and exit windows of the target cell. Corrections due to false asymmetries arising from helicity correlated changes of beam parameters were applied on a run by run basis. The analysis was based on the five minute runs for which the counted elastic events in the PbF₂ detector were combined with the correlated beam parameter and luminosity measurements. In the analysis we applied

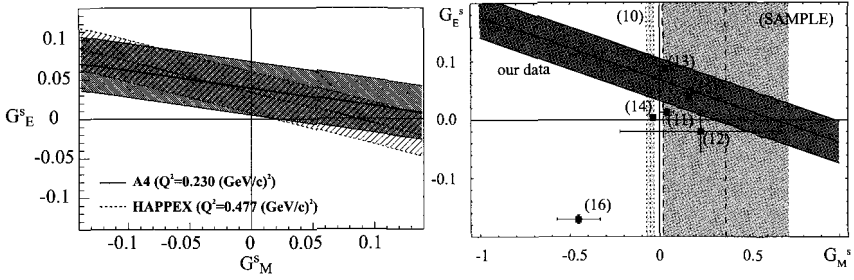


Fig 3. Left: The solid line represents all possible combinations of $G_E^s + 0.225G_M^s$ as extracted from the work presented here at a Q^2 of 0.230 (GeV/c)². The densely hatched region represents the 1- σ uncertainty. The recalculated result from the HAPPEX published asymmetry at Q^2 of 0.477 (GeV/c)² is indicated by the dashed line, the less densely hatched area represents the associated error of the HAPPEX result. Right: The solid lines represent the result on $G_E^s + 0.107G_M^s$ as extracted from our new data presented here. The hatched region represents in all cases the one- σ -uncertainty with statistical and systematic and theory error added in quadrature. The dashed lines represent the result on G_M^s from the SAMPLE experiment. The dotted lines represent the result of a recent lattice gauge theory calculation for μ_s . The boxes represent different model calculations and the numbers denote the references.

reasonable cuts in order to exclude runs where the accelerator or parts of the PbF₂ detector system were malfunctioning. The analysis is based on a total of 7.3×10^6 histograms corresponding to 4.8×10^{12} elastic scattering events for the 854.3 MeV data and $4.8 \cdot 10^6$ histograms corresponding to $2 \cdot 10^{13}$ elastic events for the 570.4 MeV data.

For the correction of helicity correlated beam parameter fluctuations we used multi-dimensional linear regression analysis using the data. The regression parameters have been calculated in addition from the geometry of the precisely surveyed detector geometry. The two different methods agree very well within statistics. We have taken half of our data with a second $\lambda/2$ -plate inserted between the laser system and the GaAs crystal. This reverses the polarization of the electron beam and allows a stringent test of the understanding of systematic effects. The effect of the plate can be seen in Fig. 1: the observed asymmetry extracted from the different data samples changes sign, which is a clear sign of parity violation if, as in our case, the target is unpolarized. Our measured result for the PV physics asymmetry in the scattering cross section of polarized electrons on unpolarized protons at an average Q^2 value of 0.230 (GeV/c)² is $A_{LR}(ep) = (-5.44 \pm 0.54_{stat} \pm 0.26_{syst})$ ppm for the 854.3 MeV data [5] and $A_{LR}(ep) = (-1.36 \pm 0.29_{stat} \pm 0.13_{syst})$ ppm for the 570.4 MeV data [6]. The first error represents the statistical accuracy, and the second represents the systematical uncertainties including beam polarization. The absolute accuracy of the experiment represents the most accurate measurement of a PV asymmetry in the elastic scattering of longitudinally polarized electrons on unpolarized protons. Fig. 2 shows the present situation of all the published asymmetry measurements in elastic electron proton scattering. From the difference between the measured $A_{LR}(ep)$ and the theoretical prediction in the framework of the Standard Model, A_0 , we extract a linear combination of the strange electric and magnetic form factors of $G_E^s(Q^2=0.230(\text{GeV/c})^2) + 0.225G_M^s(Q^2 = 0.230 \text{ (GeV/c)}^2) = 0.039 \pm 0.034$ for the 854.3 MeV data and $G_E^s(Q^2=0.109(\text{GeV/c})^2) \pm$

$0.105 G_M^s(Q^2 = 0.109(\text{GeV}/c)^2) = 0.071 \pm 0.036$ for the 570.4 MeV data, where statistical and systematic error of the measured asymmetry and the error in the theoretical prediction of A_0 are added in quadrature. In Fig. 3 the results for both data sets are displayed. A recent very accurate determination of the strangeness contribution to the magnetic moment of the proton $\mu_s = G_M^s(Q^2 = 0 (\text{GeV}/c)^2)$ from lattice gauge theory [10] would yield a larger value of $G_E^s = 0.076 \pm 0.036$ if the Q^2 dependence from 0 to $0.109 (\text{GeV}/c)^2$ is neglected. The theoretical expectations for another quenched lattice gauge theory calculation [11], for SU(3) chiral perturbation theory [12], from a chiral soliton model [13], from a quark model [14], from a Skyrme-type soliton model [15] and from an updated vector meson dominance model fit to the form factors [16] are included into Fig. 3.

We are preparing a series of measurements of the parity violating asymmetry in the scattering of longitudinally polarized electrons off unpolarized protons and deuterons under backward scattering angles of $140^\circ < \theta_e < 150^\circ$ with the A4 apparatus in order to separate the electric (G_E^s) and magnetic (G_M^s) strangeness contribution to the electromagnetic form factors of the nucleon. Following our first results on the measurement [7] of a transverse single spin beam asymmetry A_\perp , we are preparing a further set of measurements for A_\perp too.

Acknowledgments

This work has been supported by the DFG in the framework of the SFB 201 and SPP 1034. We are indebted to K.H. Kaiser and the whole MAMI crew for their tireless effort to provide us with good electron beam. We are also indebted to the A1-Collaboration for the use of the Moeller polarimeter.

References

1. David B. Kaplan et al., Nucl. Phys. B **310**, 527 (1988).
2. M.J. Musolf et al., Phys. Rep. **239**, 1, (1994).
3. F. E. Maas et al., Eur. Phys. J. A **17**, 339 (2003).
4. P. Achenbach et al., Nucl. Ins. Meth. A **465**, 318 (2001).
5. F. E. Maas et al., Phys. Rev. Lett., **93**, 022002 (2004).
6. F. E. Maas et al., nucl-ex/0412030, (2004).
7. F. E. Maas et al., nucl-ex/0410013 accepted for publication by Phys. Rev. Lett., (2004).
8. M. Seidl et al., Proc. of the EPAC 2000, 1930 (2000).
9. F. E. Maas et al., Proc. of the ICATPP-7, page 758, World Scientific, 2002.
10. D. B. Leinweber et al., hep-lat/0406002, (2004).
11. R. Lewis et al., Phys. Rev., **D 67**, 013003 (2003).
12. T. R. Hemmert et al., Phys. Rev., **C 60**, 045501 (1999).
13. A. Silva et al., Eur. Phys. J., **A 22**, 481 (2004).
14. V. Lyubovitskij et al., Phys. Rev., **C 66**, 055204 (2002).
15. H. Weigel et al., Phys. Lett. B, **353**, 20 (1995).
16. H.-W. Hammer et al., Phys. Rev., **C60**, 045204 (1999).

PHOTOCATHODE LIFE TIME RESEARCH AT MAMI *

K. AULENBACHER, G. ARZ, R. BARDAY, V. TIOUKINE

Institut für Kernphysik der Universität Mainz, Mainz , Germany

The degradation of Photocathode quantum efficiency was studied under different experimental conditions at MAMI. We find that current induced effects become dominant at currents higher than $65 \mu\text{A}$. At smaller currents the lifetime of the photocathode is limited to a few weeks by the vacuum conditions in operation. We intend to improve the situation by using extensive NEG coating. Further studies of source lifetime under high average currents are presented.

1. Present status of photocathode lifetime at MAMI

Beam time scheduling at MAMI is characterized by production periods of typically two weeks followed by a one or two day maintenance period. Photocathode lifetime is sufficient to supply the experiments. With the aid of the load-lock system the photocathode reactivation can be handled conveniently during the maintenance interval. Consequently beam time losses due to photocathode problems were negligible during the last years. However, lifetime improvement is still desirable since the photocathode reactivation process can only be repeated for about 6 to 10 times. Therefore photocathodes have to be replaced periodically. Even if a new cathode will yield adequate simultaneous values for quantum efficiency (q.e.) and polarization, an adaptation of the working point of the semiconductor laser system will in general be necessary due to the different band gap.

We have therefore decided to start a lifetime research program at MAMI. Our investigations are also dedicated to explore the limits of continuous charge production of GaAs-NEA photosources. The necessary investment for new accelerator projects could be considerably reduced if the present limitation of charge production (several hundreds of Coulombs) can be increased by a factor of more than 10. In the following text the term 'lifetime' indicates the reduction of initial q.e. by a factor of $1/e$.

2. Identification of different lifetime limiting effects

We investigate a simple model in order to sort out different processes that contribute to photocathode degradation: If we assume that all processes act in parallel and independently

*Work supported by the Deutsche Forschungsgemeinschaft within Sonderforschungsbereich 443

we find^a the following formula for the observed lifetime:

$$\tau_{obs}^{-1} = \sum_i \tau_i^{-1} \quad (1)$$

The values of the individual τ_i are determined by the experimental conditions which will be discussed in the following subsections.

2.1. 'Vacuum-lifetime' during shutdown

The lifetime during shutdown is limited by the residual gas/NEA-surface interaction. We were able to measure it after a four week interruption of polarized source operation during which beam was delivered by a thermionic source. From the reduction of q.e. during this time we find $\tau_{obs} = \tau_{vac} \approx 1200$ hours.

2.2. 'Vacuum-lifetime' in operation

In operation backstreaming gas from the accelerator may reduce the lifetime. In addition, application of the d.c.-accelerating field in the source may cause a small field emission current of the order of Nanoamperes which will also shorten the lifetime (Lifetime is of the order of hours only if field emission currents in the μA -range are emitted.) In our case we found $\tau_{obs} = 850$ hours. This time constant was measured during an experiment which required negligible current. If we make use of the independent measurement of τ_{vac} above, we find from equation 1 that the time constant caused by field emission and backstreaming is $\tau_{FE} = 3000$ hours. The effect is therefore not dominant but it contributes.

2.3. Influence of emission current

Harmful gas components that are generated by beam losses in the collimation system as well as ion backbombardment created by the ionization of molecules in the acceleration stage of the source will tend to decrease τ_{obs} . Since the contribution of these mechanisms should be proportional to the emission current it seems reasonable to assume that an additional lifetime summand in equation 1 is given by

$$\tau_l = \frac{k}{I}. \quad (2)$$

In order to test this assumption τ_{obs} was determined under different currents (figure 1). Except for $200\mu A$ the measurements were done parasitically during operation for experiments at MAMI. The largest current could not be accelerated in MAMI since the installed r.f.-power is too small. Here the current was dumped at 100 keV in a water cooled faraday cup.

By increasing the current we pass from a 'vacuum-lifetime' regime to a situation where current induced effects are dominant. This is clearly indicated by the exponential fits to the

^aSuch a simple model will of course not be able to explain the wide variety of phenomena associated with the degradation of the NEA-surface, e.g. the q.e. may remain relatively constant for some time before an exponential decay appears.

data in figure 1: The curve for $10\mu A$ is very close to the vacuum lifetime under operation whereas for the $200\mu A$ curve lifetime is reduced by almost a factor 4.

Determining the different time constants and taking into account the operational vacuum lifetime and plugging them into equations (1) and (2) leads to $k = 200 \pm 60$ Coulomb. The value of k can be regarded as the amount of charge that will be produced under emission of a constant current during the lifetime of the photocathode if τ_I is much smaller than all other time constants, i.e. at very high current. The influence of τ_I^{-1} is in our case equal to the sum of the current independent effects at a current of $65\mu A$. For the present time it is therefore our first priority to improve basic vacuum since most experiments at MAMI require less current.

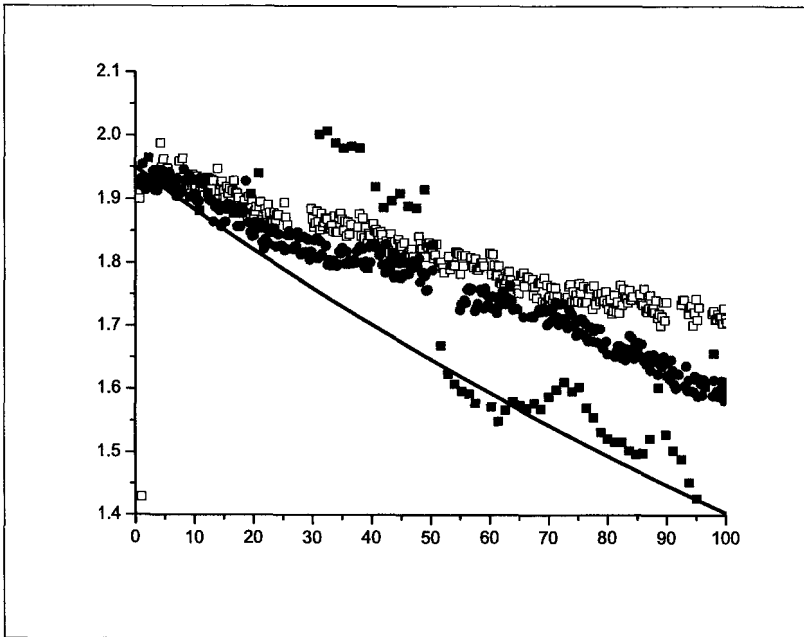


Fig 1. Decay of q. e. at MAMI in different operating conditions (at constant current). Open squares: $10\mu A$, filled circles: $30\mu A$, filled squares: $200\mu A$. Q.e.'s at $t = 0$ are normalized to the same value. The temporary increase (with ongoing decay of same τ) of q.e. for the $200\mu A$ data is probably due to a laser spot movement.

3. Vacuum improvement and high current test bench

The basic pressure of our vacuum system may be reduced by either increasing the pumping speed or by decreasing the outgassing rate of the apparatus. A combination of both possibilities may be achieved by non evaporable getter (NEG) coating, a technology developed at CERN [1]. Coating of the source inner surface - several thousand square centimeters - will therefore increase the total pumping speed, though not by orders of magnitude. However, the main advantage seems to be that any area coated with NEG will be transferred from

a source of gas into a gas sink. Furthermore it was found [1] that electron impact desorption of NEG coated surfaces is by orders of magnitude lower if compared to stainless steel surfaces. Therefore virtually all effects discussed in the preceding sections will be reduced.

3.1. NEG coating technology at MAMI

NEG coating is done with the so called magnetron sputtering technique: The vacuum vessel is placed into a homogenous magnetic field ($10^{-2}T$), and filled with Krypton gas at 0.06 mbar. Cathodes made from different elements (Titanium, Zirkonium, Vanadium) are placed inside the vessel. This configuration allows for a stable gas discharge. Depending on the geometry and the number of electrodes we have achieved growth rates of up to 2 micrometer/day. During deposition the temperature of the vacuum chamber was kept at 80°C. By analyzing test surfaces with scanning X-ray micrography we found that the homogeneity of the layer in thickness and elementary composition ($Zr_{.51}Ti_{.66}Va$) was satisfying. After applying an activation temperature of 220 °C we have observed a specific pumping speed of $0.2l/(s * cm^2)$ for Hydrogen. So far vacuum chambers with inner surfaces of up to 4000 cm^2 have been coated. We therefore believe that it will be possible to coat most of the vacuum surfaces of the source and the injection beamline.

3.2. High current test bench

A copy of the MAMI source is available for life time studies. It is intended to study the effects of NEG coated parts in this apparatus before using them at the MAMI source itself. As a first experiment - before starting the application of NEG parts - we decided to investigate the present performance under high average current.

We cannot accelerate the 100 keV beam in the test apparatus but have to dump it in a water-cooled Faraday cup which is located about 3 m downstream from the source. NEG coating of the cup was applied in order to minimize gas desorption from electron beam impact. Additional pumping with a cryopump was installed in order to further minimize additional backstreaming. Since polarization is not an issue in these experiments we operated bulk GaAs photocathodes with a d.c. laser excitation at 532 nm wavelength. Quantum efficiency was up to 13% ($58\mu A/mW$). Since we envisage operation at currents of 10 mA where space charge forces are non negligible we have increased the laser spot diameter on the cathode to 2 mm. Beam losses in the vicinity of the anode are minimized by using the mask activation technique [2]. We find a relative beam loss of $5 \cdot 10^{-6}$ at 1 mA current at an isolated beam tube directly behind the anode. Figure 2 shows q.e.-decays with initial currents of 1 mA. In this case the laser power -initially 28 mW (lower curve) - was constant allowing for a decrease of emitted current. After about 70 hours the current had decreased to roughly 1/e of the initial value, then the initial current was restored by increasing the laser power. The following decay (upper curve) allowed to extract at least the same amount of charge in one lifetime than before. Therefore it seems that the cathode tolerates 80 mW of laser power without a large reduction of lifetime. Altogether more than 330 Coulomb have been produced continuously in two lifetimes, yielding a similar value for k than the

one we have found at the MAMI source. In addition we have demonstrated that it is possible to transport beams with increased emittance ($\approx 3\pi\text{mmrad}$) without severe effect on lifetime.

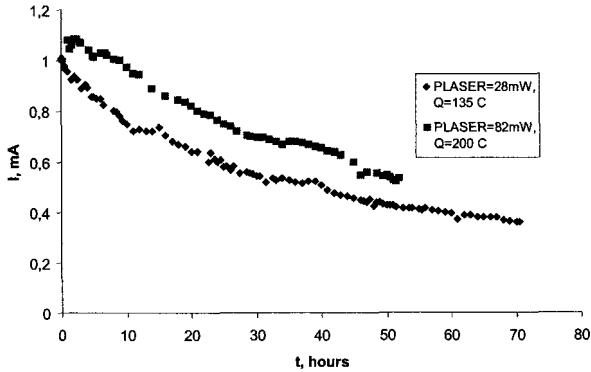


Fig 2. Quantum efficiency decay with constant laser power. Upper curve is the continuation of experiment after passing one lifetime.

4. Outlook

Extensive NEG coating of the electron source and the beamline will be studied with the prospect of increase of vacuum lifetime. Besides this we hope to demonstrate an improvement in the value of extractable charge at very high average current. To do so effectively - the measurement times are already quite long even at 1 mA - we will try to increase the average beam current to values of the order ≥ 10 mA. The potential problem of thermal heating by the laser power can be handled by methods similar to the ones described by Orlov et. al [3].

To handle the electron beam power we will use the 'suppressed collector' technique in order to decelerate the beam to kinetic energies below 1 kV.

References

1. C. Benvenuti, P. Chiaggiato, F. Cicoira and Y.L' Aminot *J. Vac. Sci Technol. A* **16** (1) 148 (1998)
2. K. Aulenbacher, V. Tioukine, M. Wiessner and K. Winkler, Proc. of 15th international Spin physics symposium (SPIN-2002), AIP Vol.675 1088 (2003)
3. D. Orlov et al. this conference.

CESIUM ADSORPTION ON GaAs(001) SURFACE: ADSORBATES GEOMETRY AND Sb INFLUENCE *

S. E. KULKOVA, S. V. EREMEEV

Institute of Strength Physics and Materials Science of SB RAS, Tomsk, Russia

A. V. SUBASHIEV

St. Petersburg State Polytechnic University,
Politekhnicheskaya 29, St. Petersburg, 195251, Russia

Ab-initio full-potential linearized augmented-plane-wave (FLAPW) method is applied for calculations of the electronic structure of ideal GaAs(001) surface and Sb-covered GaAs (001) surface. The change of local densities of states in the surface and subsurface layers upon Cs adsorption on Sb-covered GaAs (001) surface is analyzed for several adsorbates sites. The role of oxygen coadsorption on GaAs(001) surface during cesium adsorption is also investigated. Among considered adsorption sites the T3 site (Cs is on an atom belonging to third atomic layer) is found to have the largest adsorption energy. The formation of activation layer and its electronic structure is discussed.

1. Introduction

Based on successful applications of materials design to the development of new methods of the spin state control for semiconductor spintronics, it is expected that ab-initio calculations will be powerful tool with considerable potential. The calculations can quantitatively predict the electronic structure and physical properties of materials. Modern generation of highly polarized electron sources is based on photoemission from semiconductor nanostructures. To improve both emitted charge and electron polarization the optimization of cathode heterostructure parameters including parameters of the surface layer becomes necessary. The adsorption of alkali metals on both GaAs (001) and (110) surfaces leads to a drastic decrease of the work function (ϕ). This process of the surface activation to a state with a negative electron affinity plays the key role in operation of the photoemitters of highly spin-polarized electrons [1].

Several models of structure are used in order to explain the Ga-rich GaAs(001) surface [2–6]. The difficulty in determination of stable surface structure is connected with

*This work was supported by CRDF grant RP1-2345-ST-02

small difference in total energy for considered models which results in a rich variety of the observed surface reconstructions, depending of surface composition. In view of the complexity of surface (001) atomic structure and great computer time needed for calculations, (2×1) structure with Ga-dimer in top layer is often used in total energy calculations. This approach allows to obtain reasonable physical trends in the interaction of surface states with adsorbates at least in the nearest to Ga-dimer region.

The main goal of the present studies is to explore the mechanism of Cs adsorption on the Sb-covered GaAs(001) surface and influence of Sb sublayers on electronic properties of Cs-covered GaAs surface.

2. Calculation details

The full-potential linearized augmented plane wave method (FLAPW [7]) in the local density approximation for the exchange-correlation potential was applied for investigation of electronic structure of clean and Sb-covered GaAs(001) surface. The surface was simulated by repeated slabs separated in the one direction by a vacuum region ($\sim 10 \text{ \AA}$). The lateral lattice parameter was set equal to the experimental lattice constant for the bulk GaAs (5.6537 \AA). The calculated equilibrium lattice parameter (5.6264 \AA) was found to be 0.5% less than the experimental one. For the surface simulation we used the slabs with 9–17 atomic layers. The multipole expansion of the crystal potential and electronic density inside the muffin-tin spheres was cut at $l_{\max} = 10$. Non-spherical contributions to the charge density and potential within muffin-tin spheres were considered up to $l_{\max} = 4$. In the interstitial region the plane waves with reciprocal lattice vectors up to $|G| = 7 \text{ a.u.}^{-1}$ were included. The k -space integration was carried out using 6 and 15 k -points in the two-dimensional (2D) irreducible part of the Brillouin zone (IPBZ). We evaluated the work function as a difference between the vacuum level and the highest occupied energy level. The vacuum level was determined as the value of the self-consistent, in-plane averaged potential between the slabs.

3. Results and discussion

In our previous paper [8] we investigated the electronic structure of GaAs(110) and alkali metal (Na, K, Cs) adsorption at this surface as well as Cs adsorption on GaAs(001). The removal of both filled and empty surface states from the band gap due to the surface relaxation was found and the values of adsorption energies for Na on GaAs(110) were obtained, in agreement with results of Hebenstreit and Scheffler [9]. For a clean GaAs(001) surface the calculated Ga-Ga dimer bond length (2.4 \AA) and the first interlayer distance agree well with previous calculation [9].

Here we have calculated the electronic structure of the Ga-terminated GaAs(001) surface with adsorbed Sb and Sb-dimers on GaAs(001)- (2×1) surface structure. The sum of local DOS in surface and subsurface atoms for GaAs(001) and Sb/GaAs(001) are shown in Fig. 1. (top panels). As one can see the electronic structure (ES) changes substantial in comparison with clean surface. Nevertheless the influence of Sb decreases sharply in the bulk region. In the case of Sb-covered surface we also suggested the dimer formation with

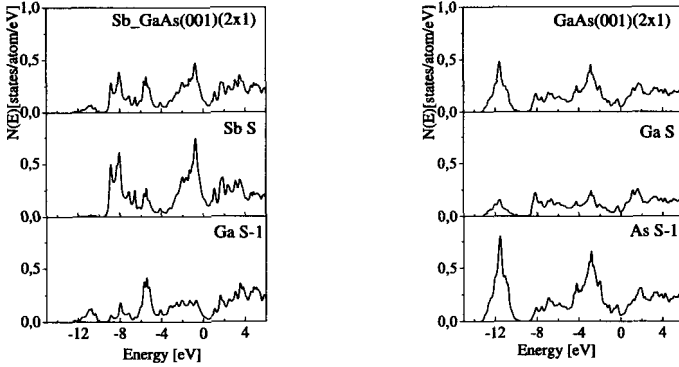


Fig. 1. Surface and local DOS of surface (S) and subsurface (S-1) atoms for Sb-covered GaAs(001) and clean GaAs(001).

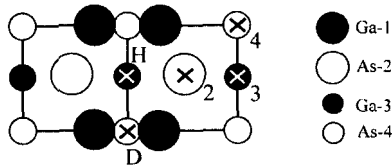


Fig. 2. Adsorbate sites for Cs (top view) near Ga-Ga dimers.

an increased bond length $\sim 3.04 \text{ \AA}$. To the best of our knowledge there is no experimental data about possible atomic structure and the positions of Sb onto surface. It is known that the formation of Ga-dimer leads only to a partial disappearance of the surface states within the band gap and to a decrease of the number of partially occupied dangling bonds, furthermore the rehybridization leads to the gain in the total energy. The similar behavior is observed in the case of 1 ML Sb-covered surface. In line with the work of Hogan et al. [5], in which the As-rich GaAs(001) surface was investigated, several possible adsorbate sites (Fig. 2.) have been considered. They are labeled as D for dimer site and as T_n for trench sites on an atom belonging to n -th atomic layer. Actually we have studied the positions which do not differ significantly from those for $\beta_2(4 \times 2)$ model near Ga-dimer region [6]. In addition, we have studied a so-called "hollow" position (H) between two Ga-dimers. We determine the symmetry character of the bonds and surface states. The detailed analysis of the clean GaAs(001) surface states and charge density distribution showed that the Ga-dangling states can be modified by the surface structure and the bonding with adsorbate depending on its position. The layer-resolved densities of states for Cs adsorption in the Ga-bridge (D) and hollow (H) positions are shown in Fig. 3. It is seen that Cs contributes mainly in the region below -10 eV , where the lower valence band (VB) of GaAs is located. It has primarily s -As character. We find no significant changes in ES for both cases. The decrease of the Cs local DOS and its shift to higher energy are observed when Cs is adsorbed in the H-position. The same behavior is found for T3 (Cs is located above Ga in the

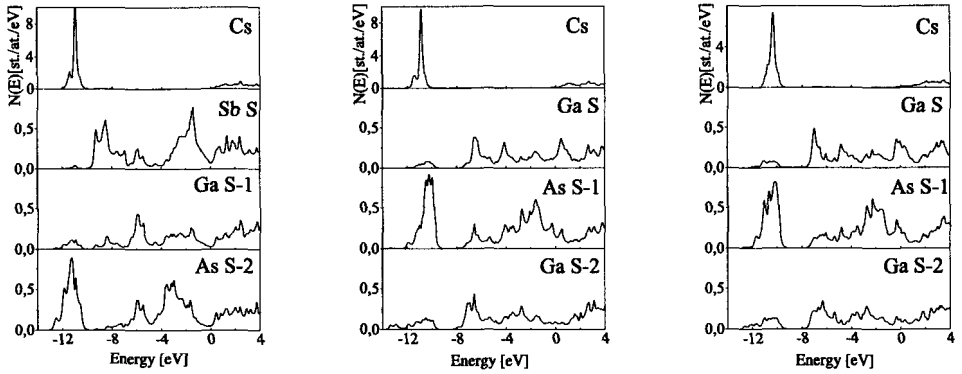


Fig 3. Layer-resolved DOS for 0.5 ML Cs in Sb-bridge on Sb-covered GaAs(001) surface (left) and in Ga-bridge (middle) and hollow (right) positions on GaAs(001).

third layer) and T4 (above As in the fourth layer) positions. The lower VB of As in sub-surface layer becomes somewhat wider due to the interaction with Cs. Among investigated adsorbate sites T3 has the highest adsorption energy of 2.45 eV. This results is in line with a conclusion of Hogan et al. [5] that the T3 position is the most preferable for adsorption onto the As-rich GaAs(001) $\beta_2(2 \times 4)$ surface. The value of E_{ad} in the H position is lower by 0.66 eV. For other positions the obtained adsorption energies are given in Table 1. In the case of a Sb-covered surface the density of states in the region where Cs gives contribution is significantly lowered though the higher valence band of Sb is shifted towards to Cs band. Moreover, the effects of Sb adsorption on the Ga states manifest in a decreased gap between the two valence subbands. It is possible to conclude that the interaction between Cs states and the substrate is stronger compared to that on a clean GaAs(001) surface. The

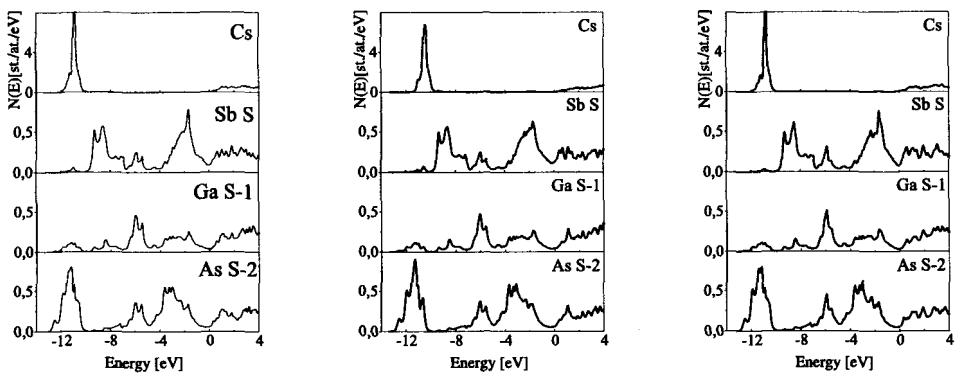


Fig 4. Layer-resolved DOS for Cs in T2 (left), T3 (middle) and T4 (right) sites on Sb-covered GaAs(001) surface.

layer resolved DOS for Cs in T2, T3 and T4 positions on Sb/GaAs(001) is given in Fig. 4.

The difference in the energy bands is primarily connected with Cs peak, the Cs contribution being substantially dependent on its adsorption geometry. To find the equilibrium positions for Cs the total energy was calculated as a function of the distance between adsorbate and surface layer. Similarly to the clean GaAs(001) surface, the highest adsorption energy of 2.48 eV is obtained in the T3 site. For Cs in the Sb-hollow site it is by ~ 0.3 eV lower with respect to T3 site (Table 1). Finally our calculations showed that ϕ changes with respect to adsorption sites on the clean and the Sb-covered GaAs(001) surfaces. The calculated values of ϕ are presented in Table 1.

Table 1. Adsorption energies and the work function (in eV) for Cs in different adsorbate sites on clean and Sb-covered GaAs(001) surface.

	D	H	T2	T3	T4	D	H	T3	T4
	0.5 ML Cs on Sb/GaAs(001)					0.5 ML Cs on GaAs(001)			
E_{ad}	1.68	2.16	1.79	2.48	1.87	1.18	1.79	2.45	1.67
ϕ	2.16	1.95	2.12	1.58	1.93	2.09	1.65	2.01	1.80

4. Conclusion

In summary, we have studied the electronic structure of GaAs(001) (2×1) surface and its adsorption properties using ab-initio approach. Among considered adsorption sites the T3 site is found to have the largest adsorption energy. This conclusion is valid for the case of Sb-covered GaAs(001) surface. The value of work function is found to be the smallest for this T3 adsorbate site (1.58 eV) whereas it is smaller in H (hollow) position on a clean surface. The calculated variations in the work function due to the composition of the surface and subsurface layers and the adsorbate positions are within the range of $\sim 0.1 - 0.5$ eV.

References

1. A. V. Subashiev, *Physics-Uspokhi* **44**, 1311 (2001).
2. N. Moll, A. Kley, E. Pehlke, M. Scheffler, *Phys. Rev.* **B54**, 8844 (1996).
3. W. G. Schmidt, S. Mirbt, *Phys. Rev.* **B62**, 8087 (2000).
4. W. G. Schmidt, *Appl. Phys.* **A75**, 89 (2002).
5. C. Hogan, D. Paget, Y. Garreau, M. Sauvage, G. Onida, L. Reining, P. Chiaradia, V. Corradini, *Phys. Rev.* **B68**, 205313 (2003).
6. Sung-Hoon Lee, W. Moritz, M. Scheffler, *Phys. Rev. Lett.* **18**, 3890 (2000).
7. P. Blaha, K. Schwarz, G. K. M. Madsen, D. Kvasnicka, J. Luitz, *Wien2k*, Vienna University of Technology, Austria, 2001, ISBN 3-9501031-1-2.
8. S. E. Kulkova, D. V. Khanin, A. V. Subashiev, *Nuclear Instruments and Methods in Physics Research A* (2004). (in press)
9. J. Hebenstreit, M. Scheffler, *Phys. Rev.* **B46**, 10134 (1992).

ATOMIC HYDROGEN CLEANING OF POLARIZED GaAs PHOTOCATHODES*

T. MARUYAMA[†], D. LUH[†], A. BRACHMANN[†], J. E. CLENDENIN[†], E. L. GARWIN[†], S. HARVEY[†],
R. E. KIRBY[†], C. Y. PRESCOTT[†], R. PREPOST[‡]

[†]Stanford Linear Accelerator Center, Menlo Park, USA

[‡]Department of Physics, University of Wisconsin, Madison, USA

Atomic hydrogen cleaning followed by heat cleaning at 450°C was used to prepare negative-electron-affinity GaAs photocathodes. When hydrogen ions were eliminated, quantum efficiencies of 15% were obtained for bulk GaAs cathodes, higher than the results obtained using conventional 600°C heat cleaning. The low-temperature cleaning technique was successfully applied to thin, strained GaAs cathodes used for producing highly polarized electrons. No depolarization was observed even when the optimum cleaning time of about 30 seconds was extended by a factor of 100.

1. Introduction

Recently the high-gradient-doping technique has been applied to photocathode structures to successfully overcome the surface charge limit effect while maintaining high spin polarization. The high-gradient-doping technique consists of a thin (10 nm), very-highly-doped ($5 \times 10^{19} \text{ cm}^{-3}$) surface layer with a lower density doping ($5 \times 10^{17} \text{ cm}^{-3}$) in the remaining active layer. High dopant density promotes recombination of the minority carriers trapped at the surface. Trapped carriers increase the surface barrier in proportion to the arrival rate of photoexcited conduction band (CB) electrons. Because CB electrons depolarize as they diffuse to the surface of heavily doped materials, the highly doped layer must be very thin, typically no more than a few nanometers. However, to achieve high quantum efficiencies, an negative-electron-affinity (NEA) surface is required, which in turn must be prepared on an atomically clean surface. The conventional way to achieve a surface free of all surface oxides and carbon-related contaminants is to heat the crystal to 600°C for about 1 hour. After only about 2 hours at this temperature, diffusion of the dopant in the thin, highly-doped layer results in the re-appearance of the surface charge limit effect. Therefore, high temperature heat cleaning should be avoided.

Atomic hydrogen cleaning (AHC) is a well known technique for removing oxides and carbon-related contaminants at relatively low temperatures. While As-oxides and Ga₂O-like oxides are liberated at temperatures less than 450°C, the removal of Ga₂O₃-like oxides

*This work was supported in part by the U. S. Department of Energy under contract numbers DE-AC02-76SF00515 (SLAC), and DE-AC02-76ER00881 (UW).

requires a higher temperature. Under atomic hydrogen irradiation, Ga₂O₃-like oxides are converted to more volatile Ga₂O-like oxides. On the other hand, it has been well demonstrated that atomic hydrogen can passivate both shallow donor and acceptor impurities. The passivation rate increases rapidly with the doping concentration. Since the band-bending in the photocathode is controlled by the *p*-type doping, the dopant passivation may have an adverse effect on QE.

In the present paper, a systematic study of AHC in a vacuum-loading system is reported. The AHC system and the associated analysis system remain under UHV, while the sample is introduced in the UHV system through a loading chamber, and transferred between the AHC and analysis systems under vacuum [1].

2. Experiment

Two types of GaAs samples were used. Samples (13 × 13 mm²) cut from Zn-doped ($1 \times 10^{19} \text{ cm}^{-3}$) bulk GaAs (001) wafers were used for optimizing the AHC conditions. Strained GaAs samples with the active 100-nm GaAs layer Zn-doped at $5 \times 10^{18} \text{ cm}^{-3}$ were used for studying the AHC effect on polarization. Prior to installation in the loading chamber, a sample was degreased in a boiling solution of trichloroethylene and chemically cleaned in NH₄OH to remove native oxides on the surface. Since NH₄OH etches only oxides without disturbing the stoichiometry of GaAs, it was used for the epitaxial photocathodes as well. Some samples were installed without the NH₄OH cleaning to intentionally leave native oxides on the surface.

The experiments were carried out in a three-chamber UHV system consisting of a loading chamber, an AHC system and an analysis system called Cathode Test System (CTS). The AHC system was equipped with an rf plasma discharge source, a heater tower, and a linear translator. The surface temperature during AHC was maintained at 300 - 350°C. The heater tower was electrically isolated from the AHC system so that a bias voltage could be applied to the GaAs sample during AHC. Atomic hydrogen was produced by dissociating molecular hydrogen in a 2.5 cm diameter Pyrex glassware surrounded by a helical rf resonator following the design used at Jefferson Lab. [2] To study the effect of hydrogen ions generated by the rf dissociator, the GaAs sample could be biased negatively to enhance ion collection. To reduce the ion current, a transverse magnetic field was applied at the exit of the dissociator using a permanent magnet. With the magnet in place, the ion current was negligible ($< 1 \text{ nA}$).

Activation to an NEA surface, and measurement of QE and polarization were made in the CTS. After AHC, the sample was transferred to the CTS under vacuum when the AHC system pressure dropped to a few 10^{-8} Torr, typically within 30 minutes after AHC. The cathode activation method used to obtain an NEA surface consisted of heat cleaning for 1 hour, cool-down for an hour, followed by application of cesium until the photo-yield peaked, and then cesium and nitrogen-trifluoride co-deposition until the photo-yield was again maximized.

AHC was performed on NH₄OH-cleaned bulk GaAs samples under three different conditions that control the ion current: 1) with no bias and no magnet, 2) with a negative 88-Volt

bias and no magnet to enhance the ion effect, and 3) with magnet and no bias to eliminate the ion effect. For each AHC, a fresh cathode sample was used and only the AHC time was varied while all other conditions were fixed. After AHC, the sample was transferred to the CTS under vacuum, heat-cleaned at 450°C, activated, and the QE measured. Figure 1 shows the QE at 670 nm as a function of the AHC time. QEs as high as 16% were obtained with only 15 - 30 seconds of AHC. The QE decreased with prolonged cleaning, yielding only 1.8% after 40 minutes of AHC. The QE was higher when the ion current was eliminated using the magnet, and lower when the ion current was enhanced using the negative bias. The data indicate that the excessive absorption of atomic hydrogen in GaAs is detrimental for the QE. Under atomic hydrogen irradiation, the native oxides on the surface are converted to more volatile oxides and get liberated. If the irradiation continues, atomic hydrogen is absorbed in the GaAs, passivating the *p*-type dopants in the band bending region. Since the doping concentration at the surface controls the band bending, dopant passivation raises the vacuum level, resulting in a lower QE. Acceptor passivation by hydrogen proceeds through ion pair formation of negatively charged acceptors and positively charged hydrogen ions. [3] Ions are more effective than atomic hydrogen at passivating the dopants.

AHC was also performed on bulk GaAs samples without the NH_4OH cleaning. QEs as high as 14% were obtained after 1 hour of AHC (open square in Figure 1). The sample with native oxides produced a high QE after prolonged AHC, indicating the oxide layer was protecting the GaAs surface from impinging atomic hydrogen. [4] This indicates the AHC time must be optimized depending on the oxide level on the GaAs surface. The NH_4OH etching establishes a reproducible level of native oxides.

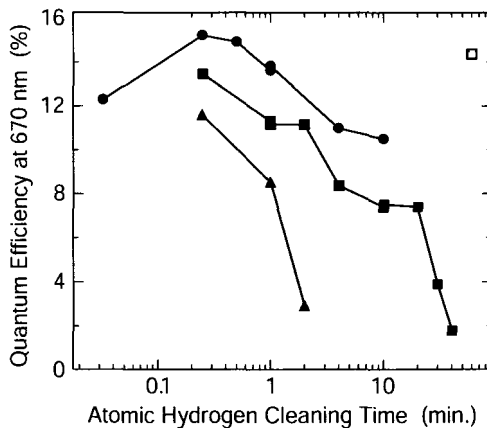


Fig 1. QE at 670 nm as a function of the AHC time. Three different conditions are used to control ions: solid circles are no bias and with magnet, squares are no bias and without magnet, and triangles are with -88 V negative bias without magnet. One sample (open square) was not cleaned in NH_4OH .

Studies at Jefferson Lab [5] indicate that a significant depolarization may occur as a result of long exposures to atomic deuterium. The electron polarization was measured in the

present experiment as a function of the AHC time using thin strained photocathodes. The sample was heat-cleaned at 570°C without AHC and the polarization was measured. Then, a sequence consisting of 15 minutes of AHC followed by polarization measurements was repeated four times for the same sample. The AHC was performed with the magnet and no bias voltage. Figure 2 shows the polarization spectrum for 1) no AHC, 2) 30 minutes AHC, and 3) 60 minutes AHC. All three data sets are consistent within the statistical errors. No depolarization was observed after 60 minutes, which is ~ 100 times longer exposure time than the optimum time, of AHC.

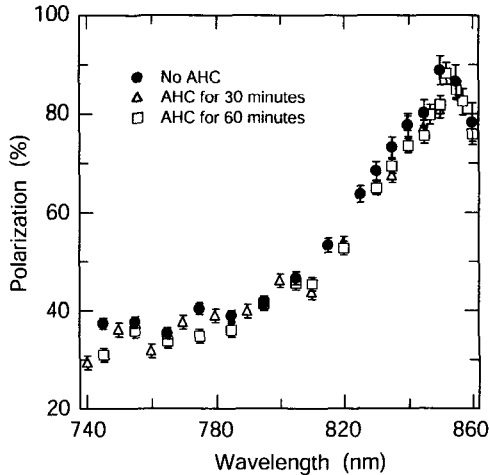


Fig. 2. Polarization as a function of wavelength. Solid circles are measurements without AHC, triangles are measurements after 30 minutes of AHC, and squares are measurements after 60 minutes of AHC.

3. Conclusions

Atomic hydrogen cleaning can be used to prepare high-QE GaAs photocathodes at the lower heat-cleaning temperature of 450°C. Photocathode quantum efficiencies as high as 15% were obtained when hydrogen ions were eliminated. Extended exposure to atomic hydrogen was found to have no effect on the electron polarization.

We thank Matt Poelker of Jefferson Lab for providing useful information about the AHC technique used at his laboratory.

References

1. T. Maruyama, D.-A. Luh, A. Brachmann, J.E. Clendenin, E.L. Garwin, S. Harvey, R.E. Kirby, C.Y. Prescott, and R. Prepost, *Appl. Phys. Lett.* **82**, 4184 (2003).
2. C. K. Sinclair, B. M. Poelker, and J. S. Price, *Proceedings of the 1997 IEEE Particle Accelerator Conference*, 12-16 May 1997, Vancouver, B.C., Canada, p. 2864.
3. S.J. Pearton, J.W. Corbett, and M. Stavola, *Hydrogens in Crystalline Semiconductors*, (Springer-Verlag, Heidelberg, 1992).

4. Y. Ide and M. Yamada, *J. Vac. Sci. Technol.* **A12**, 1858 (1994).
5. M. Baylac, *Proceedings of the 15th International Spin Physics Symposium*, 9-14, September 2002, Upton, New York, p. 1073.

POLARIZED ELECTRON SOURCES FOR FUTURE ELECTRON ION COLLIDERS *

M. FARKHONDEH, W. FRANKLIN, T. ZWART

MIT-Bates Linear Accelerator Center, Middleton, USA

For the past few years an initiative in the US to build an Electron-Ion collider (EIC) has gathered momentum. This machine would probe the structure of hadrons in terms of their quark and gluon constituents and provide insight into the evolution of quarks and gluons into hadrons. The most mature option, eRHIC, is based on a ring-ring architecture with a 5–10 GeV electron ring and the existing RHIC ion ring at design energies of 250 GeV and 100 GeV per nucleon for e-p and e-A collisions respectively. Design luminosities of order $10^{33} \text{ cm}^{-2}\text{s}^{-1}$ are expected for eRHIC. Electron bunches from the polarized injector must be precisely synchronized with proton bunches in the RHIC ring. The eRHIC polarized source requirements are demanding. Another more futuristic option for EIC is a design initiated by Jefferson Lab (ELIC) based on a superconducting linac, a circulating electron ring and a hadron storage ring. The polarized source requirements for this option are also very demanding. In this paper, we present an overview of EIC design parameters, the polarized source requirements, and the design concepts for the laser systems under consideration for eRHIC.

1. Introduction

Some of the basic questions about hadronic matter are the structure of hadrons in terms of their quark and gluon constituents, and the evolution of quarks and gluons into hadrons. Lepton probes with high luminosities are very suitable for answering these questions. An Electron-Ion Collider (EIC) can directly probe the quark gluon distribution in nucleons over a wide range of x , the fraction of proton momentum carried by the struck quark and gluon. Such a facility will need to have high center-of-mass energy, high luminosity for precision, polarized leptons and polarized nucleons, and a complete range of nuclear targets and optimum detectors. Substantial international interest in high luminosity ($10^{33} \text{ cm}^{-2}\text{s}^{-1}$) polarized lepton-ion colliders over the past decade resulted in several international workshops in the US and in Europe. An important aspect of EIC is the polarization of both lepton and ion beams.

There are two major initiatives in the US considered for EIC:

- (1) **eRHIC**: An electron-ion collider based on the existing RHIC accelerator at BNL.

*This work is supported by the U.S. Department of Energy under a Cooperative Agreement # BEFC294ER40818.

- (2) **ELIC:** An Electron Light-Ion Collider based on an energy recovery linac (ERL) utilizing the CEBAF accelerator at Jefferson Lab.

Both of these designs entail injecting polarized electron beams into a linac. In 2004, physicists from several institutions, including BNL and MIT-Bates, produced a comprehensive zeroth order design report (ZDR) [1] for eRHIC. Also in recent years at Jefferson-Lab, a concept for Electron Light-Ion Collider emerged [2] that is based on a 3–7 GeV ERL electron linac, a new electron circulator ring and a new light ion ring. In the next two sections, we present polarized source requirements for these EIC concepts. Also, a preliminary polarized source design developed at MIT will be presented for the eRHIC injector.

2. Polarized Source for eRHIC

2.1. Ring-Ring Design

The present main design for eRHIC calls for a 0.5 A electron storage ring with full-energy injection from a linac with a polarized electron source. Although the electron ring will be self-polarizing, the polarization build-up time for 5 GeV beams will be several hours, meaning that the ring must be injected with a highly polarized beam. Furthermore, use of a highly polarized source will allow operation of the storage ring in top-off mode, permitting the electron beam intensity to remain high at all times. For a CW storage ring, the achievement of 0.5 A of highly polarized electrons would represent a modest technical requirement based on present state-of-the-art polarized source technology. However, because eRHIC is a collider, synchronized bunches of electrons must precisely match the time structure of the proton bunches in the RHIC ring. This presents a great challenge to the injector configuration and the polarized source design. The polarized source must address two primary challenges: the time and bunch structure of the ring-ring collider, and the necessary laser power required to achieve the charge per bunch for the stated luminosity for the collider. A detailed evaluation of the eRHIC luminosity ($10^{33}\text{cm}^{-2}\text{s}^{-1}$) design value shows that peak currents of at least 20 mA from the source are required. The corresponding charge per bunch is 1.3 pC for bunches 70 picoseconds long produced at 28 MHz synchronous with the collider ring. This is a challenging technical requirement for a photoinjector. It should be noted that alternative designs for eRHIC, involving a linac-ring collider, present even greater challenges for the polarized source. The specifications of the eRHIC ring-ring option are summarized in Table 1. A schematic diagram of the time structure for the ring-ring eRHIC is shown in Figure 1.

Photoemission in the eRHIC polarized injector will be produced by illuminating high polarization GaAs-based photocathodes with circularly polarized laser light at 780–830 nm. For this range of wavelengths, a laser peak power of at least 50 W will be needed for the beam specifications given in Table 1, assuming a quantum efficiency of order 5×10^{-3} . Currently, designs based on two different types of laser systems are being considered [3]. These two options differ in the time structure of the photoemission drive laser systems and in the electron beam line for bunching and chopping functions. The first option is based on a mode-locked diode laser [4] capable of producing laser bunches synchronized with

Table 1. Beam specification for the eRHIC ring-ring polarized electron source design.

	Quantity	Value	Unit
Collider ring	Stored current	480	mA
	Frequency	≈ 28	MHz
	Ring circumference	4.3	μs
	Number of bunches	120	
	Charge per macro bunch	20	nC
	(stacking) pulse train rep. rate	25	Hz
	Duration	10	minutes
	Total pulse train	15,000	
Photoinjector	Bunch duration	70	ps
	Bunch charge	1.3	pC
	Peak current	20	mA
Linac	Microscopic duty cycle	0.002	
	Macropulse average current	40	μA

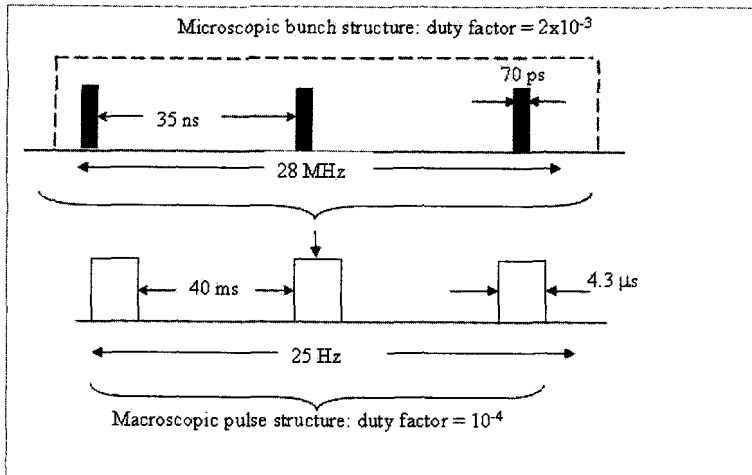


Fig 1. Schematic diagram of time structure of the ring-ring design for eRHIC.

pulses in the storage ring. A schematic diagram of the first option based on a mode-locked laser system is shown in Figure 2.

The second option relies on a high-powered DC fiber-coupled diode array laser system similar to one employed for the MIT-Bates polarized source [5]. In this case, bunching and chopping elements in the linac injector are used to produce bunches synchronized with the collider ring. This option employs a commercial high power diode laser system. A schematic view of this option is shown in Figure 3. The laser produces DC or pulsed radiation with no microscopic structure. The challenge of this option is to ascertain the degree to which the complex bunching and chopping of the electron beam at multiple frequencies is possible.

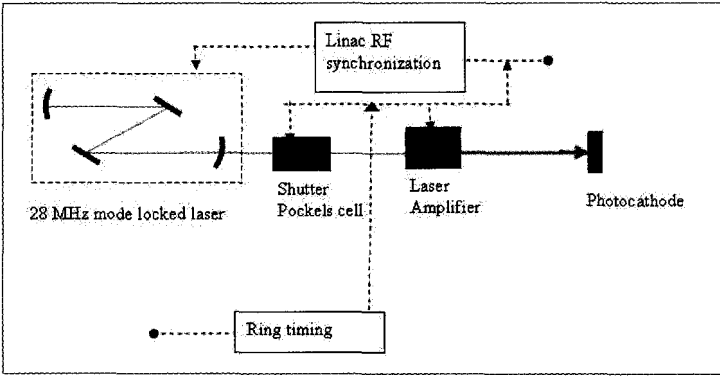


Fig 2. Schematic diagram of the mode-locked laser option for the eRHIC polarized injector.

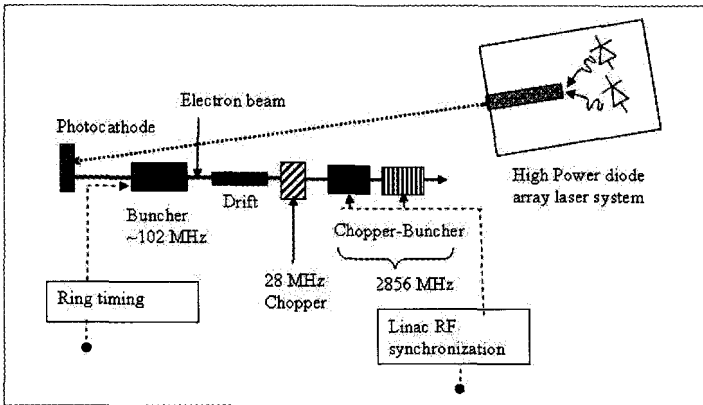


Fig 3. Schematic diagram of the laser and the electron beam layout for the DC fiber-coupled diode laser option for the eRHIC injector (Option Two).

2.2. Linac-Ring Concept

In addition to the baseline ring-ring design of eRHIC, a linac-ring design is also under consideration at BNL. In this design, a 5–10 GeV superconducting energy recovery linac (ERL) [1] is considered. For the eRHIC design luminosity of order $10^{33} \text{ cm}^{-2}\text{s}^{-1}$, an average current of 400 mA is required from the linac. Therefore, a polarized injector capable of producing these very high average currents with the correct time structure synchronous with the RHIC ion beam is required. This very demanding requirement is beyond the present state of the art by three orders of magnitude. One method envisioned so far is to direct high power lasers onto a relatively large photocathode 7–10 cm in diameter. Assuming that scaling principles hold in photoemission, laser power on the order of 1 kW is required for this injector. One concept for such a laser system, described in Appendix A of the ZDR [1] document, is the use of the output of a dedicated low energy ERL-FEL at 780–830 nm range as the drive laser for this collider. To produce 100% circularly polarized light, an FEL based

on a helical wiggler must be used. Photocathode surface charge limits are of great concern for these high power laser densities. A major R&D effort is required to assess the feasibility of this design of a polarized gun.

3. Polarized Source for ELIC

For the ELIC design, a high power ERL electron linac is used to inject bunches of electrons into a circulating figure-8 electron circulator synchronously with light ion bunches in the ion ring. The ELIC design has similarities to the ring-ring design and the linac-ring design for eRHIC. The circulating ring [2] will use the electron bunches for about 100 turns, thus reducing the bunch charge required from the polarized injector by a factor of about 100 compared to a linac-ring collider of same luminosity. The ELIC timing structure is shown schematically in Figure 4. Depending on the design luminosities of ELIC (10^{33} – $10^{35} \text{ cm}^{-2} \text{ s}^{-1}$), peak currents of 2.5 mA to 25 mA are required from the ELIC injector. For the time structure shown in Figure 4, microbunch charges of 1.6 nC are required at 150 MHz initially and at 1.5 GHz for the higher luminosity design. The collider nature of the bunches requires a complex design for the polarized source drive laser with higher powers than exist today. R&D on the laser system is essential for this photoinjector [6].

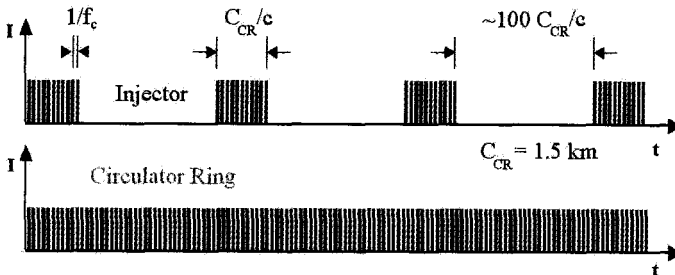


Fig 4. Schematic diagram of the ELIC timing structure. The top graph shows the bunches in the injector and the bottom illustrates the circulating bunches.

References

1. Zeroth order Design Report (ZDR), http://www.agrsrichome.bnl.gov/eRHIC/eRHIC.ZDR/ZDR_start.pdf
2. L. Merminga *et al.*, and Y. Derbenev, Proc. European Particle Accelerator Conference (2002).
3. M. Farkhondeh, 2nd EIC Accelerator Workshop, Jefferson Lab, March 15-17, 2004.
4. Time-Bandwidth mode-locked laser used for the G0 experiment at Jefferson Lab.
5. Spectra-Physics Opto Power diode laser model OPC-DO60-mmm-FC. See also E. Tsentalovich, AIP Conf. Proc 675 (2002) 1019.
6. M. Poelker, 2nd EIC Accelerator Workshop, Jefferson Lab, March 15-17, 2004.

HELICAL UNDULATOR BASED PRODUCTION OF POLARIZED POSITRONS AND STATUS OF THE E166 EXPERIMENT

K. LAIHEM

Deutsches Elektronen-Synchrotron DESY, Zeuthen, Germany

(for the E166 Collaboration)

This paper describes the status of the E166 experiment. The experiment is dedicated to test the helical-undulator-based polarized positron source for the international linear collider. The physics motivation for having both electrons and positrons polarized in collision is crucial and a demonstration experiment for the undulator-based production of polarized positrons is summarized. The E166 experiment uses a 1 meter long helical undulator in the 50 GeV Final Focus Test Beam at SLAC to provide MeV photons with circular polarization. These photons are then converted in a thin (0.5 radiation length X_0) target into positrons (and electrons) with about 50% degree of longitudinal polarization. In this experiment, the polarization of both photons and positrons is measured simultaneously using photon transmission polarimetry.

1. Introduction

The full exploitation of the physics potential of an International Linear Collider (ILC) will require the development of polarized positron beams [1, 3, 4]. Having both positron and electron beams polarized in the e^+e^- collision will be a decisive improvement for many physics studies, providing new insight into structures of couplings and thus access to the physics beyond the standard model. The concept of a polarized positron source is based mainly on the development of a circular polarized photons source. Those photons are then converted by pair-production in a relatively thin target to generate longitudinally polarized positrons and electrons. To date, two different approaches have been developed to generate the polarized photons. While in an experiment at KEK [6] Compton back scattering of polarized laser beam off an electron beam is used, the E166 experiment [7] uses a 1 meter long helical undulator in the FFTB 50 GeV beam line to produce MeV photons with circular polarization [1, 2].

1.1. The E166 Experiment

1.1.1. Photon Production (Helical-Undulator)

The undulator [1, 2] consists of a 0.6 mm diameter copper wire bifilar helix, wound on a stainless steel support tube with an inner diameter of 0.89 mm. The current in the two he-

lically wound wires flows in opposite directions. The longitudinal magnetic field cancels. Inside remains a transverse magnetic field that rotates as one moves along the axis. The 50 GeV FFTB electron beam [9] (see Fig. 1) passes through the center of the undulator and radiates circularly polarized photons with a cutoff energy of 9.6 MeV. The photons generated in the undulator can be understood as the result of the electron beam backscattering of virtual undulator photons. After passing through the undulator, the electron beam is bent down towards the beam dump. While the undulator photons go to positrons production target.

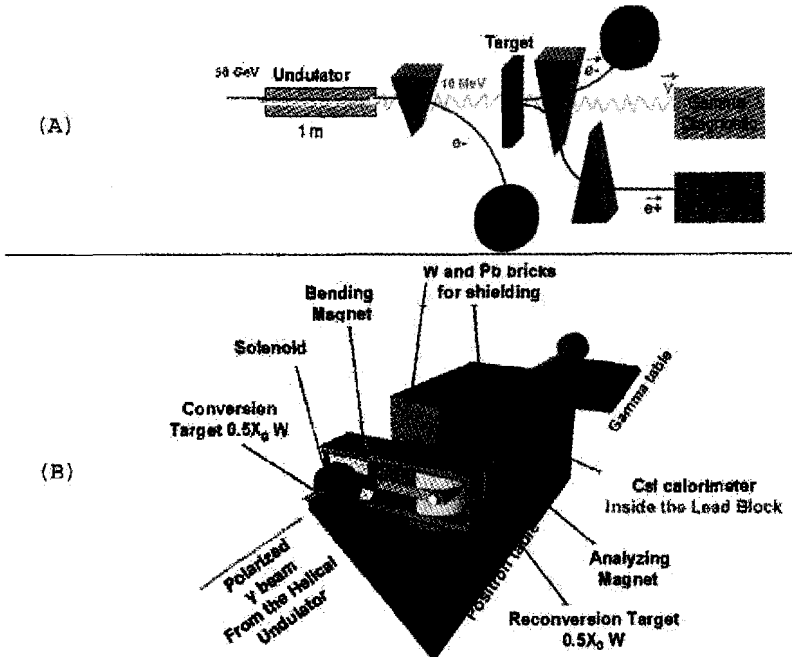


Fig 1. A) Conceptual scheme of the E166 experiment and B) Geometry based GEANT4 of the E166 experimental setup.

1.1.2. Positron Production

By pair-production, circularly polarized photons create an e^+e^- pair in a thin target of $0.5 X_0$ Ti or W [7]. The spin of the photon is transferred to the outgoing leptons [5, 8]. The achievable polarization scales with the energy transferred in the conversion process. Energy loss of positrons by bremsstrahlung in the target causes depolarization. Simulation studies based on modified GEANT3 code indicate that a target of about $0.5 X_0$ delivers positrons of the highest polarization. Figure 2 gives the longitudinal polarization (solid curve) and energy spectrum (histogram) of positrons emitted from a $0.5 X_0$ Titanium target. The polarization of the total sample is about 53%.

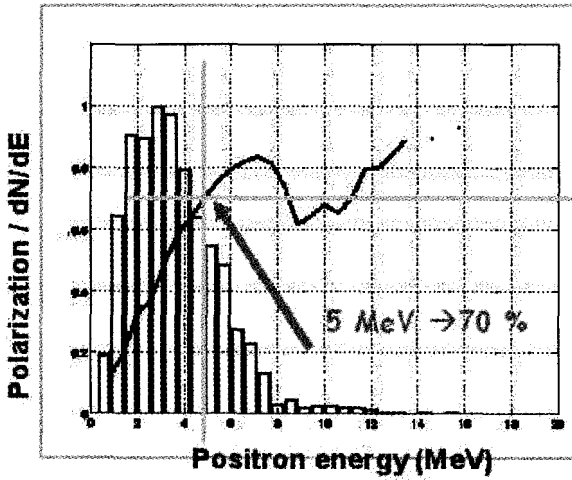


Fig 2. Energy Spectrum (histogram) and polarization (curve) of the generated positrons in the production target.

1.1.3. Polarimetry

In the E166 experiment, both the circular polarization of the undulator photons and the longitudinal polarization of positrons are measured. The transmission polarimetry of photons through a thick magnetized iron is used. This method is based on the spin dependence of Compton scattering of atomic target electrons. For the positron polarization measurement, the positrons are converted back into polarized photons by bremsstrahlung in a thin reconversion target.

A) Photon polarimeter

The photon polarimeter consist of two main components: the analyzer magnet with a reversible iron core and a SiW calorimeter for the energy and flux measurement. The iron is 14 cm thick and is magnetized to saturation (2/26% polarized electrons for saturated iron).

The transmission [7] is given by equation 3.

$$T = N e^{-nL(\sigma_{pair} + \sigma_{photo} + \sigma_{Compton})} e^{-nL\sigma_{Pol}P_{Ph}P_e} \tag{1}$$

Where L is the thickness of the iron core, n the density, σ_{pair} , σ_{photo} , $\sigma_{Compton}$ are cross sections of the pair production, photo effect and the Compton scattering respectively. The last term depends on the photon polarization P_{Ph} and the electron polarization P_e . σ_{Pol} stands for the polarization dependent part of the Compton scattering cross section.

When flipping the iron magnetization and for a thick absorber the asymmetry factor can be approximated to

$$\delta = \frac{T_+ - T_-}{T_+ + T_-} \approx nL\sigma_{Pol}P_{Ph}P_e = A_{Ph}P_{Ph}P_e \tag{2}$$

A_{Ph} is the analyzing power. The magnetization P_e is known and the photon polarization can be calculated

$$P_{Ph} = \frac{\delta}{A_{Ph}P_e} \quad (3)$$

The analyzing power (Determined from Monte Carlo) depends on the energy of the photons and must therefore be convoluted over the photon spectrum.

B) Positron polarimeter

The same concept is used for the positron polarization measurement. The positrons have to be reconverted into bremsstrahlung or annihilation photons to use the photon transmission polarimetry. The positron polarimeter consist of the reconversion target a magnetized iron ($\simeq 7\text{cm}$) and a CsI(Tl) calorimeter. This photon transmission polarimetry has the advantage that low energy background photons are suppressed in the energy measurement. About 1500 bremsstrahlung photons per bunch with a total energy of about 6 GeV from the reconversion target are expected to reach the CsI-calorimeter .

1.1.4. CsI(Tl) Calorimeter

The CsI calorimeter consists of a stack of 3x3 CsI(Tl) crystals with the dimensions 6cm x 6cm x 28cm. They are read-out with two 2 cm^2 PIN diodes each. The whole setup sits in a brass box which acts as an RF-shield. In the E166 setup, a strong Pb shielding is needed around the calorimeter to suppress background noise. Each crystal is calibrated with a 228Th source that emits 2.6 MeV photons. It is also calibrated in addition with cosmic muons that deposits about 40 MeV in the crystals. The pedestal has a width of about 250 keV and the signals are well separated. The light-yield is about 4600 PhE/MeV. The signal that is expected in the experiment is about 6 GeV, the PIN diodes and the preamplifiers have to cover a large dynamic range.

2. Simulation Tools

Substantial efforts has been put into Monte Carlo simulation of the E166 experiment. Initially a GEANT3 code modified for polarization has been used. This demonstrated the feasibility of such an experiment. Also, GEANT3 studies were used for background optimization. In the last 6 months, a new GEANT4 based Monte Carlo has been started. The whole experiment will be implemented. however, one has to mention that additional effort is needed to implement new classes for polarization which are still missing in GEANT4.

3. Conclusions and Outlook

Since its approval in June 2003, the E166 experiment has made a considerable progress. All the components are ready and work properly. The experiment was initially scheduled to run in October 2004 and January 2005 but for external reasons at SLAC the first run has been

canceled. We are confident to achieve a positron polarization of 50%. This will demonstrate the feasibility of undulator-based production of polarized positrons for an international linear collider.

Acknowledgements

I would like to thank all my colleagues on E-166 for an enjoyable and fruitful collaboration.

References

1. V.E.Balakin and A.A.Mikhailichenko, Budker Institute of Nuclear Physics, Preprint BINP 79-85 (1979)
2. A.A.Mikhailichenko, Cornell CBN 02-10, SLAC LCC106 (Sept.16,2002).
3. T.Hirose et al., JLC ,Nucl.Instr. and Meth.A455 ,15 (2000).
4. G.Moortgat-Pick and H.M.Steiner, EPJdirect C,vol.1,C6 ,1 (2001),hep-ph/0106155.
5. H.Olsen and L.C.Maximon, Phys.Rev.114 ,887 (1959).
6. M.Fukuda,T.Aoki,K.Dobashi,T.Hirose,T.Iimura,Y.Kurihara,T.Okugi,T.Omori, I.Sakai,J.Urakawa,and M.Washio, KEK Preprint 2003-05,submitted to Phys.Rev.Lett.
7. M.Woods et al., SLAC LCC-0107 (Nov.6,2002),
8. C.Fronsdahl and H.Uberall, Phys.Rev.111 ,580 (1958);Nuovo Cim.8 ,163 (1958).
9. Achim W. Weidemann et al. Polarized Positrons at a Future Linear Collider and the Final Focus TestBeam (SLAC-PUB-10581 July 2004).

This page intentionally left blank

PESP2004 – PARTICIPANTS

Kurt Aulenbacher

Johannes-Gutenberg-Universität
Institut für Kernphysik
Johann-Joachim-Becher-Weg 45
55099 Mainz - Germany
aulenbac@kph.uni-mainz.de

Roman Barday

Johannes-Gutenberg-Universität
für Kernphysik
Johann-Joachim-Becher-Weg 45
55099 Mainz – Germany
rbarday@kph.uni-mainz.de

Rustam Berezov

Johann Wolfgang Goethe Universität
Institut für angewandte Physik
Robert-Mayer Str. 2-4
60325 Frankfurt a.M. – Germany
Berezov@Physik.Uni-Frankfurt.de

Axel Brachmann

Stanford Linear Accelerator Center
M/S 18, 2575 Sand Hill Road
Menlo Park, CA 94025 – USA
brachman@slac.stanford.edu

James Clendenin

Stanford Linear Accelerator Center
2575 Sand Hill Rd.
Menlo Park, CA 94025 – USA
clen@SLAC.Stanford.EDU

Henri -Jean Drouhin

Ecole Polytechnique
Route de Saclay
91120 PALAISEAU - France
HJ.Drouhin@Polytechnique.fr

Joachim Enders

Technische Universität Darmstadt
Schlossgartenstraße 9
64289 Darmstadt – Germany
enders@ikp.tu-darmstadt.de

Manouchehr Farkhondeh

MIT-Bates Laboratory
P.O. Box 846
Middleton, MA 01949 - USA
manouch@mit.edu

Leonid Gerchikov

State Polytechnical University
Department of Experimental Physics
Politeknicheskaya 29
195251 St. Petersburg - Russia
leonid@priv.hop.stu.neva.ru

Joseph M. Grames

Thomas Jefferson National Accelerator Facility
12000 Jefferson Avenue MS 5A
Newport News, VA 23430 - USA
grames@jlab.org

Christoph Hessler

Technische Universität Darmstadt
Schlossgartenstraße 9
64289 Darmstadt - Germany
hessler@ikp.tu-darmstadt.de

Wolfgang Hillert

Universität Bonn
Nussallee 12
53115 Bonn - Germany
hillert@physik.uni-bonn.de

Gheorghe Iancu

Technische Universität Darmstadt
Schlossgartenstraße 9
64289 Darmstadt - Germany
iancu@ikp.tu-darmstadt.de

Yoshio Imai

Johannes-Gutenberg-Universität
Institut für Kernphysik
Johann-Joachim-Becher-Weg 45
55099 Mainz - Germany
imai@kph.uni-mainz.de

Svetlana Kulkova

Institute of Strength Physics and Materials Science of SB
RAS
Akademicheskyy 2/1
634021 Tomsk - Russia
kulkova@ms.tsc.ru

Makoto Kuwahara

Nagoya University
Department of Physics
Furo-cho, Chikusa-ku
464-8602 Nagoya, Aichi - Japan
kuwahara@spin.phys.nagoya-u.ac.jp

Driss Lamine

Ecole Polytechnique
Route de Saclay
91120 PALAISEAU - France
driss.lamine@polytechnique.fr

Georges Lampel

Ecole Polytechnique
91128 PALAISEAU
France
georges.lampel@Polytechnique.fr

Karim Laihem

DESY-Zeuthen
Platanenallee 06
15738 Zeuthen - Germany
karim.laihem@desy.de

Frank Maas

Johannes-Gutenberg-Universität
Institut für Kernphysik
Johann-Joachim-Becher-Weg 45
55099 Mainz - Germany
maas@kph.uni-mainz.de

Yuri Mamaev

State Polytechnical University
Department of Experimental Physics
Politekhnicheskaya 30
195251 St. Petersburg - Russia
mamaev@spes.stu.neva.ru

Takashi Maruyama

Stanford Linear Accelerator Center
2575 Sand Hill Road
Menlo Park, CA 94025 - USA
tvm@SLAC.Stanford.edu

Tsuneiko Omori

KEK
Institute of Particle and Nuclear Studies
Oho 1-1
305-0801 Tsukuba-shi, Ibaraki-ken - Japan
Tsuneiko.Omori@kek.jp

Dmitry Orlov

Max-Planck-Institut für Kernphysik
Saupfercheckweg, 1
69117 Heidelberg - Germany
Dmitry.Orlov@mpi-hd.mpg.de

Mathew Poelker

Thomas Jefferson National Accelerator Facility
12000 Jefferson Avenue MS 5A
Newport News, VA 23430 - USA
poelker@jlab.org

Yuliya Poltoratska

Technische Universität Darmstadt
Schlossgartenstrae 9
64289 Darmstadt - Germany
yuliya@ikp.tu-darmstadt.de

Charles Prescott

Stanford Linear Accelerator Center
P.O. Box 20450
Stanford, CA 94309 - USA
prescott@SLAC.Stanford.edu

Thomas Schedel-Niedrig

Hahn-Meitner-Institut Berlin GmbH
Glienicke Strasse 100
14195 Berlin - Germany
schedel-niedrig@hmi.de

Claus Dieter Schröter

Max-Planck-Institut für Kernphysik
Saupfercheckweg, 1
69117 Heidelberg - Germany
c.schroeter@mpi-hd.mpg.de

Alexander Terekhov

Institute of Semiconductor Physics
Zolotodolinskaya str. 33,5
630090 Novosibirsk - Russia
terek@thermo.isp.nsc.ru

Valeri Tioukine

Johannes-Gutenberg-Universität
Institut für Kernphysik
Johann-Joachim-Becher-Weg 45
55099 Mainz - Germany
tioukine@kph.uni-mainz.de

Wolther v. Drachenfels

Universität Bonn
Nussallee 12
53115 Bonn - Germany
drachen@physik.uni-bonn.de

Jürgen Wittschen
Universität Bonn
Nussallee 12
53115 Bonn - Germany
wittsche@cip.physik.uni-bonn.de

Masahiro Yamamoto
Nagoya University
Department of Physics
Furo-cho, Chikusa-ku
464-8602 Nagoya, Aichi - Japan
yamamoto@spin.phys.nagoya-u.ac.jp

This page intentionally left blank

AUTHOR INDEX

- A4 Collaboration, 926, 970
Abramov, V., 657
Abu-Raddad, L. J., 637
Adachi, T., 623
Adderley, P., 891, 948
Afanasiev, S., 565
Afanasiev, S. V., 627, 661, 696
Agapov, N. N., 774
Ahrens, L., 163, 675, 683
Ahrens, L. A., 687
Alarcon, R., 577
Alekseev, I., 700, 722
Alekseev, I. G., 163, 507, 511, 515, 540
Alexakhin, V. Y., 393
Andreev, V. V., 231
ANKE Collaboration, 531
Anselmino, M., 341, 345, 389
Arends, H., 136
Ariz, U. I., 675
Arkhipov, V. V., 661
Arz, G., 975
Asahi, K., 247
Asaji, S., 619
Aslanyan, P. Z., 569
Atutov, S., 779
Aulenbacher, K., 215, 922, 975
Azhgirey, L., 565
Azhgirey, L. S., 627, 661, 696
- Bacchetta, A., 373
Bai, M., 163, 675, 679, 683, 687
Bakin, V. V., 959
Bakker, B. L., 438
Ball, J., 791, 816
Barber, D. P., 738
Barday, R., 975
Barion, L., 779, 820
Barone, V., 12
Barsov, S., 537
Baum, G., 791, 816
Baxter, A., 765
- Baylac, M., 891, 948
Bazhanov, N. A., 540
Beloglazov, Y. A., 540
Belostotski, S. L., 400
Belov, A. S., 774
Benhar, O., 653
BLAST Collaboration, 577, 581, 601, 714, 734
Bodiagin, V. A., 627
Bogliione, M., 341, 345, 389
Bolenz, R., 922
Bondarev, V. K., 661
Borštnik, N. M., 489
Borisov, N. S., 548, 551
Borzounov, Y. T., 661
Bosted, P., 446
Bosted, P. E., 609
Bračić, A. B., 489
Brachmann, A., 787, 917, 939, 985
Brandt, B. van den, 669
Bravar, A., 163, 507, 515, 700, 722
Bressan, A., 48
Brittian, J., 891, 948
Brown, K., 163, 675, 683
Budkovsky, P. E., 540
Bunce, G., 103, 163, 507, 515, 700, 722
Bunyatova, E. I., 540
Burinskii, A., 255
Buttimore, N. H., 706
- Calaga, R., 163
Cameron, P. R., 710
Capiiluppi, M., 779
Carlini, R. D., 497
Chapman, M., 757, 776
Charles, D., 891, 948
Chen, P., 765
Christian, D. C., 555
Christova, E., 317
Church, M. D., 555
Ciullo, G., 779, 820

- Clark, J., 891, 948
 CLAS Collaboration, 605, 609
 Clendenin, J. E., 787, 913, 917, 935, 939, 985
 COMPASS Collaboration, 48, 265, 294, 369, 381, 393, 396, 425
 Cone, K., 939
 Contalbrigo, M., 779, 820
 Conte, M., 710
 Courant, E. D., 163, 687
 Crawford, C. B., 581
 Cudell, J., 527
- D'Alesio, U., 282, 341, 345, 389
 D'Imperio, N., 710
 Daito, I., 565
 Dalpiaz, P. F., 779, 820
 Davidenko, A. M., 548, 551
 Day, D., 446
 de Jager, K., 117
 De Vita, R., 70
 Della Vedova, F., 665
 Derenchuk, V. P., 774
 Derevschikov, A. A., 548, 551
 Deshpande, A., 192
 Deur, A., 613
 Dhawan, S., 507, 515, 700, 722
 Di Salvo, E., 409
 Dorokhov, A. E., 235
 Doshita, N., 791, 796, 816
 Doushita, N., 565
 Drees, A., 163, 675
 Dutz, H., 221
 Dymov, S., 537
- E166 Collaboration, 995
 Efremov, A. V., 205
 Efremov, A. V., 413
 Emelyanenko, V. N., 569
 Emori, S., 247
 Engels, R., 800
 Erenee, S. V., 980
 eRHIC Team, 738
 Ermolaev, B. I., 290
 Ershov, V. P., 696
 Eversheim, D., 691
- Félix, J., 555
 Fabbri, R., 429
 Fabrocini, A., 653
 Fantoni, S., 653
- Farkhondeh, M., 897, 990
 Fedorov, A. N., 548, 551
 Filimonov, E. A., 540
 Filipov, G., 661
 Fimushkin, V. V., 696, 774
 Finger, M., 210
 Fischer, W., 163, 675
 Forbush, M., 555
 Forte, S., 154
 Franklin, W., 710, 897, 990
 Franklin, W. A., 714, 734
 Friedrich, J. M., 396
 Fujita, K., 619, 631
 Fukao, Y., 325
 Fukui, S., 565
 Furuta, F., 902, 953, 964
- G0 Collaboration, 585
 Gabbert, D., 361
 Gamberg, L. P., 385
 Garçon, M., 30
 Garcia, I. L., 796
 Gardner, C., 163, 683
 Gardner, C. J., 675
 Garwin, E. L., 787, 917, 939, 985
 Gasimova, R. E., 239
 Gautheron, F., 791, 796, 816
 Gebel, R., 537, 691
 Geis, E., 577
 Gerchikov, L. G., 908, 913, 935
 Gill, R., 507, 700, 722
 Giordano, F., 779, 820
 Glättli, H., 669
 Glenn, J. W., 163, 675, 687
 Glenn, W., 683
 Goeke, K., 413
 Goertz, S., 791, 796, 816
 Gojuki, S., 634
 Goldberg, D. A., 710
 Goldstein, G. R., 385
 Goloskokov, S. V., 421
 Golovanov, L. B., 661
 Goncharov, P., 657
 Goshtasbpour, M., 466
 Gotoh, T., 964
 Gottschalk, E. E., 555
 Graham, D., 757, 761, 776
 Grames, J., 891, 948
 Graw, G., 665
 Greco, M., 290

- Greenfield, M. B., 631
 Griebhammer, H. W., 669
 Griffioen, K., 377
 Grigoriev, K., 800
 Grishin, V. N., 548, 551
 Grosse-Perdekamp, M., 361
 Guazzoni, P., 665
 Gupta, R., 163
 Gupta, R. C., 687
 Gussen, A., 800
 Gutierrez, G., 555
- Haeberli, W., 507, 700, 757, 761, 776
 Hagiwara, Y., 631
 Hall A Collaboration, 589
 Hansknecht, J., 891, 948
 Hartmann, M., 537
 Hartouni, E. P., 555
 Harvey, S., 917, 985
 Hasch, D., 38
 Hasuko, K., 361
 Hatanaka, K., 78, 623, 631, 746
 Hatanaka, Y. H. K., 619
 Hatano, M., 631, 649
 Hautle, P., 669
 HERMES Collaboration, 38, 286, 302, 365,
 377, 400, 429, 434, 454, 458, 753
 HERMES Target Group, 783, 808
 Hertenberger, R., 665
 Hillhouse, G. C., 637
 Hinterberger, F., 691
 Holmes, S. D., 555
 Horikawa, N., 565
 Houston, P. A., 935
 Huang, H., 163, 515, 675, 679, 683, 687, 700,
 722
 Hughes, E. W., 126
 Huseynov, V. A., 239
 Huson, F. R., 555
- Ichimura, M., 641
 Igo, G., 163, 515, 722
 Ihloff, E., 824, 897
 Ikeda, T., 649
 Imai, Y., 926
 Iriso, U., 163
 Isupov, A., 565
 Isupov, A. Y., 627, 661, 696
 Ito, T. I. M., 619
 Itoh, K., 631, 649
- Itoh, K. F. K., 623
 Ivanov, O. N., 313
 Ivanov, V. I., 627
 Iwata, T., 565
- Jansen, P., 800
 Jaroshevich, A. S., 959
 Jaskóla, M., 665
 Jensen, D. A., 555
 Jiang, J., 917
 Jiang, X., 446
 Jinnouchi, O., 163, 507, 515, 700, 722
 Jones, M., 446
 Joosten, R., 381
 Jungmann, K. P., 108
- Kacharava, A., 531
 Kacharava, a., 537
 Kageya, T., 812
 Kalinin, A., 657
 Kamada, H., 631
 Kamiya, J., 631
 Kanavets, V., 722
 Kanavets, V. P., 515, 540
 Kartamyshev, A. A., 661
 Kashirin, V. A., 661
 Kawabata, T., 623, 631, 645
 Kazimi, R., 891
 Khmelnikov, A., 657
 Khodinov, A., 507, 700
 Khodyrev, V. Y., 548, 551
 Khorramian, A. N., 481, 485
 Khoukaz, A., 537
 Khrenov, A., 565
 Khrenov, A. N., 627, 661
 Kim, W., 770
 Kirby, R. E., 787, 917, 939, 985
 Kiryluk, J., 718
 Kishi, S., 619
 Kisselev, Y., 791, 816
 Klehr, F., 800
 Kleines, H., 800
 Knapp, B. C., 555
 Kobayakawa, H., 953
 Kohl, M., 577
 Kohlbrecher, J., 669
 Koivuniemi, J., 791, 796
 Kokhanovski, S., 757, 761, 776
 Kolesnikov, V. I., 661
 Kolster, H., 824

- Komarov, V., 537
 Kondo, K., 565, 791, 796, 816
 Konter, J. A., 669
 Koop, I., 742
 Koop, I. A., 730
 Korablev, A., 657
 Korneev, Y., 657
 Koroleva, L. I., 540
 Kosolobov, S. N., 959
 Kostritski, A., 657
 Kotzinian, A., 389, 404
 Kovalev, A. I., 540
 Kponou, A., 507, 700, 757, 776
 Kravtsov, P., 800
 Kreisler, M. N., 555
 Krinitsyn, A., 657
 Krisch, A. D., 134, 691, 804
 Kroll, P., 421
 Kruglov, N. A., 627
 Kruglov, S. P., 540
 Kryshkin, V., 657
 Kubo, K., 558
 Kuboki, H., 631, 649
 Kudoh, T., 623, 631
 Kulessa, p., 537
 Kulikov, A., 537
 Kulkova, S. E., 980
 Kumasaka, H., 649
 Kurbatov, V., 537
 Kuriki, M., 902
 Kurita, K., 163, 515, 700, 722
 Kutuzova, L. V., 696
 Kuwahara, M., 902, 953, 964
 Kuznezov, V. A., 661

 Ladygin, V., 565
 Ladygin, V. P., 627, 661
 Laihem, K., 995
 Lamine, D., 930
 Lampel, G., 930
 Lang, N., 537
 Lassailly, Y., 930
 Leader, E., 306, 317, 341, 345, 438
 Lehmann, I., 537
 Lehrach, A., 186, 691, 742
 Lenisa, P., 779, 808, 820
 Lenzi, S. M., 665
 Leonova, M. A., 691, 804
 Lestinsky, M., 943
 Lhuillier, D., 589

 Li, Z., 722
 Liang, Z., 562
 Litvinenko, A., 565
 Litvinenko, A. G., 627, 661
 Lorentz, B., 537, 691, 800
 Luccio, A. U., 163, 683, 687, 710, 742
 Luh, D., 913, 917, 935, 939, 985
 Luh, D. -A., 787
 Lukhanin, A. A., 548, 551
 Lundquist, M., 765
 Luo, Y., 163, 675, 765
 Luppov, V. G., 804
 Lykasov, G. I., 653
 Lyuboshitz, V. L., 251
 Lyuboshitz, V. V., 251

 Maas, F. E., 970
 Macharashvili, g., 537
 Mackay, W. W., 163, 675, 679, 683, 687, 710
 Maeda, Y., 631, 649
 Magnon, A., 791, 816
 Mahler, G., 757, 761, 776
 Maier, R., 691, 742
 Makdisi, Y., 163, 269, 507, 700, 757, 761, 776
 Malakhov, A. I., 627
 Mallot, G. K., 176
 Mamaev, Y. A., 913, 935
 Marchand, C., 791
 Markov, A., 657
 Marr, G., 163, 675
 Marukyan, H., 454
 Maruyama, T., 787, 913, 917, 935, 939, 985
 Maschinot, A., 601
 Matafonov, V. N., 548, 551
 Matsumoto, H., 902, 964
 Matulenko, Y. A., 548, 551
 Meitanis, N., 824
 Melnick, Y. M., 548, 551
 Meng, W., 507, 700, 757, 776
 Mersmann, T., 537
 Merzliakov, S., 537
 Meschanin, A. P., 548, 551
 Mestayer, M. D., 605
 Metz, A., 3
 Meyer, W., 791, 796, 816
 Michels, A., 669
 Mikirtychiants, M., 800
 Mikirtychiants, S., 537
 Milner, R., 577, 824

- Mirjalili, A., 481, 485
 Miyamoto, M., 902, 953, 964
 Mochalov, V. V., 548, 551
 Montag, C., 163, 675, 683
 Mori, Y., 746
 Morozov, B. V., 540
 Morozov, V. S., 691, 804
 Moy, A. M., 917
 Mukherjee, A., 349
 Muon ($g - 2$) Collaboration, 22
 Murgia, F., 282, 341, 345, 389
 Mussgiller, A., 537
 Musulmanbekov, G., 243
- N. atutov, S., 820
 Nagasue, Y., 631
 Nagaytsev, A., 450
 Nakamura, Y. N. M., 619
 Nakanishi, T., 902, 953, 964
 Naniwa, K., 902, 953, 964
 Nass, A., 163, 507, 700, 757, 761, 776
 Neganov, A. B., 548, 551
 Nekipelov, M., 800
 Nelyubin, V., 800
 Nesterov, V. M., 540
 Neyret, D., 425
 Nioradze, M., 537
 Nishitani, T., 953
 Nogach, L. V., 548, 551
 Noro, T., 619
 Novinsky, D. V., 540
 Novosibirsk Deuteron Collaboration, 593,
 597
 Nurushev, S. B., 548, 551
- Ogawa, A., 337, 361
 Ohira, H. M. H., 623
 Ohm, H., 537
 Ohmori, C., 746
 Ohnishi, Y., 462
 Okada, H., 163, 507, 515, 700, 722
 Okada, K., 329
 Okamura, H., 623, 631, 649
 Okamura, M., 163, 683, 687, 746
 Okumi, S., 902, 953, 964
 Orlov, D. A., 943
 Oryu, S., 634
 Oshima, S., 247
 Otboev, A. V., 730
 Otboev, A., 742
- Özpıneci, A., 493
- Pagano, P., 369
 Pakhnevich, A. A., 959
 Palazzi, M., 710
 Pankov, A. A., 473, 477
 Penev, V., 565
 Peresedov, V., 565
 Peresedov, V. F., 696
 Peretti, J., 930
 Perevedentsev, E. A., 730
 Peshekhonov, D., 294
 Peters, C. C., 804
 PHENIX Collaboration, 269, 325, 329, 333
 Piegsa, F. M., 669
 Pijlman, F., 442
 Pilat, F., 163, 675
 Pilipenko, Y., 565
 Pilipenko, Y. K., 696
 Pitisyn, V., 675
 Plis, Y. A., 548, 551
 Poelker, M., 891, 948
 Popeko, A. A., 627
 pp2pp Collaboration, 511
 Prasuhn, D., 537, 742
 Predazzi, E., 527
 Prepost, R., 787, 917, 939, 985
 Prescott, C. Y., 787, 917, 939, 985
 Prokudin, A., 389
 Prudkoglyad, A. F., 548, 551
 Przewoski, B. von, 86
 Ptitsyn, V., 163, 679, 683
 Pusterla, M., 710
- Qassemi, F., 466
 Qweak Collaboration, 497
- Radici, M., 373
 Ramsey, G. P., 310
 Ratcliffe, P. G., 278
 Rathmann, F., 145, 537, 800
 Raymond, R. S., 691, 804
 Reggiani, D., 753
 Reicherz, G., 791, 796, 816
 Rescia, S., 722
 Reznikov, S. G., 661
 Richard, J. M., 95
 Riedl, C., 286
 Rikhkvitzkaya, G. G., 569
 Ritter, J., 757, 761, 776

- Rivas, M., 259
Roberts, B. L., 22
Roberts, J. S., 935
Roche, J., 585
Rohdjess, H., 691
Rondio, E., 298
Roser, T., 163, 201, 675, 679, 683, 687
Rostomyan, A., 434
Rougemaille, N., 930
Rubin, J. G., 302
Rukojatkin, P. A., 627
Rukoyatkin, P. A., 661
Rykov, V. L., 353
Ryltsov, V. V., 540
Ryskin, M. G., 548
- Sagara, K., 623
Saito, N., 58, 163, 507, 515, 700, 722
Saito, T., 631, 649
Sakaguchi, K. S. H., 619
Sakai, H., 631, 641, 649
Sakamoto, N., 649
Sakemi, Y., 619, 631
Sarkadi, J., 800
Sarycheva, L. I., 627
Sasamoto, Y. S. Y., 623
Sasano, M., 631
Sato, H., 746
Satogata, T., 163, 675
Satou, Y., 649
Scheibler, H. E., 959
Schieck, H. P. g., 800
Schill, C., 265
Schleichert, R., 537
Schnase, A., 691
Schnell, G., 365
Schwalm, D., 943
Schweitzer, P., 413
Scobel, W., 691
Seidl, R., 361
Sekiguchi, K., 631, 649
Selyugin, O. V., 527
Semenov, A. Y., 661
Semenov, P. A., 548, 551
Semenova, I. A., 661
Seyfarth, H., 537, 572, 800
Shatunov, P. Y., 730
Shatunov, Y. M., 730, 742
Shchedrov, V. A., 540
Sheppard, J. C., 787
Shestermanov, K. E., 548, 551
Shevchenko, O. Y., 313
Shimizu, Y., 631
Shimizu, Y., 619, 623
Shinozaki, A., 824
Sidorov, A. V., 306
Silenko, A. J., 726
Sissakian, A. N., 313
Sivers, D. W., 691
Smirnov, A., 765
Soloviev, L. F., 548, 551
Sowinski, J., 321
Spin Muon Collaboration (SMC), 298
Spinka, H., 163, 507, 515, 700, 722
Sprenger, F., 943
Stamenov, D. B., 306
Stancari, M., 779, 820
STAR Collaboration, 321, 337, 718
Statera, M., 779, 820
Steffens, E., 800
Stein, H. J., 537
Stepanyan, S. S., 770
Stephenson, E., 700
Stephenson, E. J., 163, 507
Stern, B. J., 555
Stewart, J., 458
Stibunov, V. N., 593
Stockhorst, H., 691
Stoletov, G. D., 627, 661
Ströher, H., 537
Stratmann, M., 349
Stroher, H., 800
Stutzman, M., 891, 948
Subashev, A. V., 922
Subashiev, A. V., 908, 913, 935, 980
Suda, K., 623, 631
Suda, K., 649
Sudoh, K., 353
Sulimov, A. D., 540
Sumachev, V. V., 540
Surles-Law, K., 891, 948
Suzuki, K., 558
Suzuki, R., 649
Svirida, D., 700, 722
Svirida, D. N., 163, 507, 515, 540
- Takano, J., 163, 683, 687
Takashima, Y., 953
Takeda, H., 619
Takeda, Y., 953

- Talov, V., 657
 Tameshige, Y., 619
 Tamii, A., 631, 649
 Tehrani, S. A., 481, 485
 Tepikian, S., 163, 675, 679, 683
 Terashima, S., 619
 Terekhov, A. S., 943, 959
 Tereshchenko, O. E., 959
 Teryaev, O. V., 171, 205, 357
 Tioukine, V., 922, 975
 Togawa, K., 953, 964
 Togawa, M., 333
 Tomás, R., 675
 Tomas, R., 163
 Tomassetti, L., 820
 Tomiyama, Y. T. A. T. M., 623
 Toporkov, D. K., 209, 597
 Toyama, T., 746
 Trautman, V. Y., 540
 Trofimov, V., 800
 Troshin, S. M., 523
 Troyan, S. I., 290
 Trueman, T. L., 438, 519, 706
 Tsentalovich, E., 824, 897
 Tsoupas, N., 163, 675, 683, 687
 Tsytrinov, A. V., 477
 Turchanovich, L., 657
 Turner, J., 787
 Tursunov, E. M., 544
 Tyurin, N. E., 523
 Tzvinev, A. P., 661

 Uchida, M., 247, 619
 Uesaka, M. U. T., 623
 Uesaka, T., 649
 Ulbrich, K., 691
 Underwood, D., 163, 700, 722
 Uribe, J., 555
 Usov, Y. A., 548, 551
 Ustinov, V. M., 913
 Uzikov, y., 537
 Uzikov, Y. N., 572

 Vadeev, V. P., 696, 774
 van der Nat, P. B., 377
 van der Ventel, B. I. S., 637
 Vasiliev, A. N., 548, 551
 Vasilyev, A., 800
 Vetter, K., 710
 Vitturi, A., 665

 Vogelsang, W., 273, 349
 Volkov, A., 657

 Wakamatsu, M., 462
 Wakasa, T., 623, 631, 641
 Wakui, T., 623
 Wang, M., 779, 820
 Wang, M. H. L. S., 555
 Watanabe, O., 953
 Wehmann, A., 555
 Weigel, U., 943
 Weis, M., 922
 Whisnant, C. S., 812
 White, J. T., 555
 Whitten, C., 163, 700
 Wiencke, L. R., 555
 Willen, E., 687
 Wirth, H., 665
 Wise, T., 184, 507, 700, 757, 761, 776
 Witten, C., 722
 Wolf, A., 943
 Wong, V. K., 691
 Woo, S., 770
 Wood, J., 163, 700
 Wood, J., 515, 722

 Xiao, Y., 824

 Yako, K., 631, 649
 Yakovlev, S. B., 493
 Yakutin, A. E., 548, 551
 Yamamoto, M., 902, 953, 964
 Yamamoto, N., 902, 953, 964
 Yaschenko, S., 537
 Yashin, Y., 922
 Yashin, Y. P., 913, 935
 Yasuda, T. W. Y., 619
 Yasui, K., 902, 953, 964
 Yazkov, A. V., 959
 Ye, Z., 783
 Yershov, A. A., 627
 Yonehara, K., 691
 Yonemura, T., 619
 Yoshida, H. P., 619
 Yoshida, Y. S. H. P., 623
 Yoshimi, A., 247
 Yoshioka, M., 902, 964
 Yosoi, M., 619
 Yu, D., 765
 Yu, J., 765

Yudin, N. P., 661

Závada, P., 417

Zalikhanov, B., 537

Zamiralov, V. S., 493

Zeijts, J. Van, 675

Zeijts, J. van, 163

Zelenski, A., 163, 507, 683, 700, 757, 761,
776

Zeno, K., 163, 683

Zetta, L., 665

Zhang, C., 824

Zhang, S. Y. , 163

Zhmyrov, V., 565

Zhmyrov, V. N., 627, 661, 696

Zhukov, A. E., 913

Zhuravlev, N. , 537

Zhurkin, V. V., 540

Zimmer, O., 669

Ziskin, V., 577, 824

Zolin, L., 565

Zolin, L. S., 627, 661, 696

Zubets, V., 757, 776

Zunets, V., 761

Zwart, T., 897, 990

Zwart, T. , 710

Zwoll, K., 800

This page intentionally left blank

spin 2004
16th international spin physics symposium
trieste, italy
october 10_16 2004



workshop on polarized electron
sources and polarimeters
mainz, germany
october 7_9 2004

World Scientific
www.worldscientific.com
5812 hc

